RRFM

EUROPEAN RESEARCH REACTOR CONFERENCE 2014



Transactions

Ljubljana, Slovenia
30 March-3 April 2014

EUROPEAN NUCLEAR SOCIETY

ENS CONFERENCE

organised in collaboration with:

IAEA
International Atomic Energy Agency

Nuclear Society of Slovenia

© 2014
European Nuclear Society
Avenue des Arts 56
1000 Brussels, Belgium
Phone + 32 2 505 30 54
Fax +32 2 502 39 02
E-mail ens@euronuclear.org
Internet www.euronuclear.org

ISBN 978-92-95064-20-1

These transactions contain all contributions submitted by 29 March 2014.

The content of contributions published in this book reflects solely the opinions of the authors concerned. The European Nuclear Society is not responsible for details published and the accuracy of data presented.



Programme Committee

Edgar Koonen, SCK•CEN, Belgium (*Chairman)*
Pablo Adelfang, IAEA, Austria
Xavier Domingo, Areva, France
Helmuth Böck, TU-Vienna, Austria
André Chabre, CEA, France
Stephen Curr, Rolls-Royce plc, United Kingdom
Gunter Damm, Jülich Research Center, Germany
Jacob de Vries, RID Delft, The Netherlands
Heiko Gerstenberg, Technische Universität München, Germany
Dominique Geslin, CERCA (AREVA Group), France
José Marques, Instituto Tecnologico de Nuclear, Portugal
István Vidovszky, AEKI, Hungary
Nikolay Arkhangelskiy, ROSATOM, Russia
Vlastimil Juricek, NRI REZ, Czech Republic

TABLE OF CONTENT

International Projects

RRFM2014-A0020	ARE RADIOISOTOPE SHORTAGES A THING OF THE PAST?: MOLYBDENUM-99/TECHNETIUM-99M SUPPLY AND DEMAND FORECAST, 2015-2020	Peykov, P. (1); Cameron, R. (1) 1 - OECD - Nuclear Energy Agency (NEA), France
RRFM2014-A0062	2014 PROGRESS REPORT ON HEU MINIMIZATION ACTIVITIES IN ARGENTINA	Cristini, P. (1); De Lio, L. (1); Falcon, M. (1); Lopez, M. (1); Gonzalez, A. G. (1); Picchetti, B. (1); Taboada, H. (1); Vaccaro, J. (1) 1 - COMISION NACIONAL DE ENERGIA ATOMICA, Argentina
RRFM2014-A0001	VIENNA RELOAD, USED TRIGA FUEL BURNS AGAIN (A PACKAGING AND TRANSPORT STORY)	Adam, J. (1) 1 - NAC International Inc., United States
RRFM2014-A0028	PRELIMINARY ANALYSIS OF THE IMPACT OF FUEL DENSITY ON THE RESEARCH REACTOR FUEL CYCLE	Ryu, H. J. (1); Seo, C. G. (2); Adelfang, P. (3) 1 - Korea Advanced Institute of Science and Technology, Korea, republic of 2 - Korea Atomic Energy Research Institute, Korea, republic of 3 - International Atomic Energy Agency, Austria
RRFM2014-A0121	IAEA ASSISTANCE IN THE DEVELOPMENT OF NEW RESEARCH REACTOR PROJECTS	Borio di Tigliole, A. (1); Bradley, E. (1); Zhukova, A. (1); Adelfang, P. (1); Shokr, A. (1); Ridikas, D. (1) 1 - International Atomic Energy Agency, Austria

Key areas of the nuclear fuel cycle

RRFM2014-A0034	ISOTHERMAL TRANSFORMATION KINETICS IN URANIUM MOLYBDENUM ALLOYS	Säubert, S. (1); Jungwirth, R. (1); Zweifel, T. (1); Chiang, H. .-Y. (1); Breitkreutz, H. (1); Petry, W. (1) 1 - Forschungs-Neutronenquelle Heinz Maier-Leibnitz (FRM II), Germany
RRFM2014-A0043	UMO POWDER ATOMIZED / HYDRIDED.COMPARISON BASED ON INTERACTION ANNEALING AND OUT-OF-PILE SWELLING TEST CONDUCTED ON DISPERSION TYPE MINIPLATES	Olivares, L. (1); Lisboa, J. (1); Marin, J. (1); Chavez, J. C. (1); Barrera, M. (1) 1 - Chilean Commission for Nuclear Energy, Chile

RRFM2014-A0069	MODELING OF U-MO FUEL SWELLING TO HIGH BURNUP	Ye, B. (1); Kim, Y. S. (1); Rest, J. (1); Hofman, G. (1) 1 - argonne national laboratory, United States
RRFM2014-A0070	SEM CHARACTERIZATION OF THE HIGH BURN-UPMICRO STRUCTURE OF U-7MO ALLOY	Keiser, D. (1); Jue, J.-F. (1); Gan, J. (1); Miller, B. (1); Robinson, A. (1); Medvedev, P. (1); Wachs, D. (1) 1 - Idaho National Laboratory United States
RRFM2014-A0093	STABILITY STUDY OF THE RERTR FUEL MICROSTRUCTURE	Gan, J. (1); Keiser, D. (1); Miller, B. (1); Wachs, D. (1) 1 - Idaho National Laboratory, United States

RRFM2014-A0030	IN-PILE IRRADIATED U-MO/AL(SI) DISPERSED NUCLEAR FUEL BEHAVIOUR UNDER THERMAL ANNEALING: FISSION GAS RELEASE AND MICROSTRUCTURE EVOLUTIONS	Zweifel, T. (1); Valot, C. (1); Pontillon, Y. (1); Lamontagne, J. (1); Blay, T. (1); Petry, W. (2); Palancher, H. (1) 1 - CEA, DEN, DEC, France 2 - Forschungs-Neutronenquelle Heinz Maier-Leibnitz (FRM II), Germany

RRFM2014-A0091	TEM CHARACTERIZATION OF HIGH BURN-UP MICROSTRUCTURE OF U-7MO ALLOY	Gan, J. (1); Miller, B. (1); Keiser, D. (1); Robinson, A. (1); Madden, J. (1); Medevedev, P. (1); Wachs, D. (1) 1 - Idaho National Laboratory, United States
RRFM2014-A0092	CHARACTERIZATION OF FUEL-CLADDING BOND STRENGTH USING LASER SHOCK	Smith, J. (1); Cottle, D. (1); Rabin, B. (1) 1 - Idaho National Laboratory, United States
RRFM2014-A0101	SHUTDOWN-INDUCED TENSILE STRESS IN MONOLITHIC MINIPLATES AS A POSSIBLE CAUSE OF PLATE PILLOWING AT VERY HIGH BURNUP.	Medvedev, P. (1); Ozaltun, H. (1); Rabin, B. (1); Robinson, A. (1) 1 - Idaho National Laboratory, United States
RRFM2014-A0104	POST-IRRADIATION ANALYSIS OF U-SILICIDE-COATED OR U-NITRIDE-COATED U-MO DISPERSION FUEL IN AL TESTED IN KOMO-5	Kim, Y. S. (1); Park, J. M. (2); Lee, K. H. (2); Yoo, B. O. (2); Ryu, H. J. (3) 1 - ANL, United states 2 - KAERI, Korea, Republic of 3 - KAIST, Korea, Republic of

RRFM2014-A0064	UMO MONOLITHIC FUEL DEVELOPMENT PROGRESS IN AREVA-CERCA	Stepnik, B. (1); Grasse, M. (1); Coullomb, C. (1); Jarousse, C. (1); Geslin, D. (1); Petry, W. (2); Jungwirth, R. (2); Breitkreutz, H. (2); Röhrmoser, A. (2); Huber, T. (2); Wachs, D. (3) 1 - AREVA-CERCA, France 2 - TUM-FRM2, Germany 3 - INL, United States
RRFM2014-A0067	ADVANCES IN GTRI FUEL FABRICATION CAPABILITY TECHNOLOGY	Burkes, D. (1); Paxton, D. (1); Maple, S. (1); Senor, D. (1); Longmire, H. (2); Dombrowski, D. (3); Cole, L. (4) 1 - Pacific Northwest National Laboratory, United states 2 - Y-12 National Security Complex, United States 3 - Los Alamos National Laboratory, United States 4 - Idaho National Laboratory, United States
RRFM2014-A0103	FRM II / CERCA UMO ATOMIZER PROJECT PROGRESS	Schenk, R. (1); Petry, W. (1); Stepnik, B. (2); Grasse, M. (2); Bourdat, G. (2); Moyroud, C. (2); Coullomb, C. (2); Jarousse, C. (2) 1 - FRM II, Technische Universität München (TUM), Germany 2 - AREVA CERCA, France
RRFM2014-A0109	Y-12 NATIONAL SECURITY COMPLEX COUPON FABRICATION	Gambrell, M. (1); Langham, C. (1); Moore, A. (1); Gooch, J. (1); Demint, A. (1) 1 - Y-12 NATIONAL SECURITY COMPLEX , United States
RRFM2014-A0124	INTERFACE FRACTURE CHARACTERIZATION OF PLASMA SPRAYED AND HIP BONDED METALLIC COATINGS USING BULGE TESTING	Hollis, K. (1); Liu, C. (1); Lovato, M. (1); Dombrowski, D. (1) 1 - Los Alamos National Laboratory, United States

RRFM2014-A0128	PROGRESS IN OPTIMIZATION OF U-10MO FUEL CASTING BY MODELING AND EXPERIMENT	Aikin, R. (1); Dombrowski, D. (1) 1 - Los Alamos National Laboratory, United States

RRFM2014-A0133	FUEL ELEMENT DESIGN AND ANALYSIS FOR ADVANCED TEST REACTOR CONVERSION TO LEU FUEL	Dehart, M. (1); Pope, M. (1); Nigg, D. (1); Jamison, K. (1); Morrell, S. (1) 1 - Idaho National Laboratory, United States

RRFM2014-A0023	INFLUENCE OF DEPLETED MOLYBDENUM-95 ON MONOLITHIC UMO FUEL PLATE DESIGNS FOR FRM II	Breitkreutz, H. (1); Röhrmoser, A. (1); Petry, W. (1) 1 - Forschungs-Neutronenquelle Heinz Maier-Leibnitz (FRM II), Technische Universität München, Germany
RRFM2014-A0098	TEST PLAN FOR MINI PLATES IRRADIATION AND PIE FOR U-7MO FUEL QUALIFICATION	Yim, J. S. (1); Tahk, Y. W. (1); kim, H. J. (1); Oh, J. Y. (1); Lee, B. H. (1); Park, J. M. (1); Jeong, Y. J. (2); Lee, K. H. (2) 1 - Nuclear Fuel Design for Research Reactor, KAERI, Korea, republic of 2 - Research Reactor Fuel Development, KAERI, Korea, Republic of
RRFM2014-A0108	RESULTS OF THE TRIAL OF LEAD TEST ASSEMBLIES IN THE WWR-K REACTOR	Arinkin, F. (1); Chakrov, P. (1); Chekushina, L. (1); Gizatulin, S. (1); Koltochnik, S. (1); Shaimerdenov, A. (1); Hanan, N. (2); Garner, P. (2); Roglans-Ribas, J. (2) 1 - The Institute of Nuclear Physics, Atomic energy committee, Ministry of Industry and New Technology, Kazakhstan 2 - The Argonne National Laboratory, United States
RRFM2014-A0113	LOW ENRICHMENT URANIUM FUEL ELEMENT DESIGNS WITH MONOLITHIC U-10MO FUEL AND UN-FINNED CLADDING FOR THE MIT RESEARCH REACTOR	Wilson, E. (1); Bergeron, A. (1); Yesilyurt, G. (1); Dunn, F. (1); Stevens, J. (1); Hu, L. W. (2); Newton, T. (2) 1 - Argonne National Laboratory, United States 2 - MIT, United States
RRFM2014-A0117	EVALUATION OF U10MO FOR THE CONVERSION OF KUCA DRY CORES	Morman, J. (1); Aliberti, G. (1) 1 - Argonne National Laboratory, United States
RRFM2014-A0041	THE NEWEST CASK DESIGN FOR INTERNATIONAL SHIPMENTS IN SUPPORT OF RESEARCH REACTOR AND LABORATORIES STAKEHOLDERS: TN-LC PACKAGE	Guibert, N. (1) 1 - AREVA TN, United States

RRFM2014-A0044	RADIOACTIVE WASTE ANALYSIS OF RESEARCH REACTOR SPENT FUEL	Khan, R. (1); Hussain, I. (1); Muhammad, A. (2); Khan, S. (1); Stummer, T. (3) 1 - Pakistan Institute of Engineering and Applied Sciences (PIEAS), Pakistan 2 - Pakistan Institute of Nuclear Science and Technology (PINSTECH), Pakistan 3 - Atominstitut/Vienna University of Technology, Austria
RRFM2014-A0080	GLOBAL THREAT REDUCTION INITIATIVE'S U.S.-ORIGIN NUCLEAR MATERIAL REMOVAL PROGRAM: 2014 UPDATE	Messick, C. (1); Galan, J. (1) 1 - U.S. Department of Energy - National Nuclear Security Administration, United States
RRFM2014-A0084	PREPARATIONS FOR THE DECOMMISSIONING OF THE FINNISH TRIGA FIR 1 – SPENT FUEL BACK-END MANAGEMENT AND DISTRIBUTION OF THE UNSPENT FUEL	Auterinen, I. (1); Viitanen, T. (1); Räty, A. (1); Häkkinen, S. (1); Kotiluoto, P. (1) 1 - VTT Technical Research Centre of Finland, Finland
RRFM2014-A0135	DEPLETION / DECAY CHARACTERISTICS OF PARR-1 LEU FUEL	Mahmood, T. (1); Muhammad, A. (1); Iqbal, M. (1) 1 - PINSTECH, Pakistan
RRFM2014-A0015	AIR SHIPMENT OF SPENT NUCLEAR FUEL FROM THE BUDAPEST RESEARCH REACTOR	Dewes, J. (1); Gajdos, F. (2); Vidovszky, I. (2) 1 - Savannah River National Laboratory, United states 2 - MTA Centre for Energy Research, Hungary
RRFM2014-A0052	AVAILABLE REPROCESSING AND RECYCLING SERVICES FOR RESEARCH REACTOR SPENT NUCLEAR FUEL (INTRODUCTION OF A NEW IAEA REPORT)	Tozser, S. (1); Adelfang, P. (1); bradley, E. (1); Budu, M. (2); Chiguer, M. (3) 1 - International Atomic Energy Agency, Austria 2 - Research and Development Company SOSNY, Russian Federation 3 - AREVA, France
RRFM2014-A0110	STATUS OF SILICIDE FUELS TREATMENT AT LA HAGUE PLANT	Eysseric, C. (1); Valery, J.-F. (2); Domingo, X. (2) 1 - CEA DEN/DRCP/DIR, France 2 - AREVA NC, France

Utilisation of Research Reactors

RRFM2014-A0017	PRODUCTION OF RADIOISOTOPES FOR MEDICAL USE ON THE JULES HOROWITZ REACTOR	Antony, M. (1); Coulon, J.-P. (1); Gay, S. (1); Martin, G. (1) 1 - CEA, France
RRFM2014-A0025	ADVANCED REACTOR PHYSISCS EXERCISES AT THE TRIGA MARK II REACTOR	Snoj, L. (1); Rupnik, S. (1); Jazbec, A. (1) 1 - Jozef Stefan Institute, Slovenia
RRFM2014-A0054	MEASUREMENTS OF THE IN-CORE NEUTRON FLUX DISTRIBUTION AND ENERGY SPECTRUM AT THE TRIGA MARK II REACTOR OF THE VIENNA UNIVERSITY OF TECHNOLOGY/ATOMINSTITUT	Cagnazzo, M. (1); Bock, H. (1); Raith, C. (1); Stummer, T. (1); Villa, M. (1) 1 - Vienna University of Technology / Atominstitut, Austria

RRFM2014-A0038	CAPABILITIES AND CAPACITIES OF RESEARCH REACTORS TOWARDS DEPLOYMENT OF INNOVATIVE NUCLEAR ENERGY SYSTEMS AND TECHNOLOGIES. IAEA CATALOGUE UNDER DEVELOPMENT.	Khoroshev, M. (1); Bradley, E. (1); Borio di tigliole, A. (1) 1 - IAEA, Austria

RRFM2014-A0072	THERMOHYDRAULIC DESIGN OF THE LORELEI EXPERIMENTAL SETUP IN JHR	Katz, M. (1); Gitelman, D. (2); Shenha, H. (2); Weiss, Y. (2); Sasson, A. (2); Tarabelli, D. (3); Ferry, L. (3); Gonnier, C. (3) 1 - NRCN, Israel 2 - ROTEM Ind., Israel 3 - French Atomic Energy Commission (CEA) − Cadarache Centre, France
RRFM2014-A0122	PRIMARILY POSITIVE PERCEPTIONS: A SURVEY OF RESEARCH REACTOR OPERATORS ON THE BENEFITS AND PITFALLS OF CONVERTING FROM HEU TO LEU	Dalnoki-veress, J. (. (1) 1 - James Martin Center for Nonproliferation Studies (CNS), Monterey Institute of International Studies, , United States
RRFM2014-A0140	EXPERIMENTAL PROGRAMS OUTLOOKS IN MTRS FOR SUPPORTING DEVELOPMENT OF SODIUM COOLED FAST REACTOR FUELS AND MATERIALS	Phélip, M. (1); Le Flem, M. (2); Parrat, D. (1); Pelletier, M. (1); Jaecki, P. (3) 1 - Commissariat à l'énergie atomique et aux énergies alternatives, Nuclear Energy Division, Fuel Study Department, France 2 - Commissariat à l'énergie atomique et aux énergies alternatives, Nuclear Energy Division, Nuclear Material Deparment, France 3 - Commissariat à l'énergie atomique et aux énergies alternatives, Nuclear Energy Division, Reactor Study Department, RJH, France

New Research Reactor Projects

RRFM2014-A0004	JULES HOROWITZ REACTOR: ORGANISATION FOR THE PREPARATION OF THE COMMISSIONING PHASE AND NORMAL OPERATION	Estrade, J. (1); Fabre, J.-L. (1); Marcille, O. (1); Bignan, G. (1); Blandin, C. (1) 1 - CEA , France
RRFM2014-A0040	RESEARCH REACTOR PROJECTS IN TUNISIA : CASE OF THE TUNISIAN SUB-CRITICAL ASSEMBLY PROJECT	Ben-ismail, A. (1); Dridi, W. (1); Ben-abdallah, M. (1); Nasri, M.-A. (1); Kahlaoui, N. (1); Reguigui, N. (1) 1 - National Center for Nuclear Sciences and Technology, Tunisia

RRFM2014-A0120	RMB: THE NEW BRAZILIAN MULTIPURPOSE RESEARCH REACTOR	Soares, A. (1); Perrotta, J. (1) 1 - Comissão Nacional de Energia Nuclear, Brazil

Innovative Methods in Research Reactor Analysis and Design

RRFM2014-A0019	ANALYSIS OF SMALL RESEARCH REACTOR WITH UMO FUEL USING MCNPX AND MULTI-GROUP NODAL DIFFUSION METHOD	Jaradat, M. (1); Alkhafaji, S. (1); Park, C. J. (2); Lee, B. (2) 1 - Jordan Atomic Energy Commission, Jordan 2 - Korea Atomic Energy Research Institute, Korea, Republic of
RRFM2014-A0031	Calculation of Kinetics parameters of the JSI TRIGA reactor with Tripoli 4 and MCNP	Henry, R. (1); Snoj, L. (2); Lengar, I. (2) 1 - Jozef Stefan Institute, Reactor Engineering Divison (R4), Slovenia 2 - Jozef Stefan Institute, Reactor Physics (F8), Slovenia
RRFM2014-A0033	NEUTRONIC AND THERMAL HYDRAULIC CHARACTERISTICS OF U-MO FUEL MINI PLATES IRRADIATED IN HANARO REACTOR	Jo, D. (1); Kim, H. (1); Chae, H. (1); Seo, C. G. (1) 1 - Korea Atomic Energy Research Institute, Korea, Republic of
RRFM2014-A0088	A 3D Thermo-Mechanical model to predict ballooning and burst behavior of Zircaloy-4 fuel cladding during LOCA transients in LWR, employing commercial numerical simulation software.	Landau, E. (1); Weiss, Y. (2); Szanto, M. (2) 1 - Department of Nuclear Engineering, Ben Gurion University, Israel 2 - Rotem Industries LTD , Israel
RRFM2014-A0097	Measurement and characterization of the integral and fast neutron flux distribution in the TRIGA Mark II reactor core.	Chiesa, D. (1); Clemenza, M. (1); Nastasi, M. (1); Pozzi, S. (1); Prata, M. (2); Previtali, E. (3); Salvini, A. (2); Scionti, G. (1); Sisti, M. (1) 1 - Università degli Studi di Milano-Bicocca, Dipartimento di Fisica, Italy 2 - Università di Pavia, Laboratorio di Energia Nucleare Applicata (LENA), Italy 3 - Istituto Nazionale di Fisica Nucleare sez. Milano-Bicocca, Italy
RRFM2014-A0106	Experimental Study of Thermosiphon Circulation of Water through a Triangle Rod Bundle	Aharon, Y. (1); Hochbaum, I. (1) 1 - NRCN, Israel
RRFM2014-A0107	Fuel burnup modelization with the Monte Carlo code MCNP5 and core reconfiguration prediction for the TRIGA Mark II reactor at the University of Pavia	Alloni, D. (1); Cammi, A. (2); Chiesa, D. (3); Clemenza, M. (3); Manera, S. (1); Pozzi, S. (3); Prata, M. (1); Previtali, E. (4); Salvini, A. (1); Sartori, A. (2); Sisti, M. (4); Zanetti, M. (2) 1 - Laboratorio Energia Nucleare Applicata (L.E.N.A.) of the University of Pavia, Italy 2 - Energy Department of Polytechnical University of Milan, Italy 3 - Physics Department "G. Occhialini" of the University of Milano-Bicocca, Italy 4 - INFN Section of Milano Bicocca, Italy
RRFM2014-A0112	REVERSAL OF OFI AND CHF IN RESEARCH REACTORS: APPLICATION TO THE BR2 HEU AND LEU CORES	Kalimullah, M. (1); Olson, A. P. (1); Feldman, E. E. (1); Dionne, B. (1); Kalcheva, S. (2); Van den branden, G. (2); Koonen, E. (2) 1 - Argonne National Laboratory, USA 2 - SCK•CEN, BR2 Reactor Department, Belgium
RRFM2014-A0011	MODELING THE CLADDING-OXIDE GROWTH AND ITS EFFECTS ON THE THERMO-MECHANICAL PERFORMANCE OF	Tentner, A. (1); Bergeron, A. (1); Kim, Y.-S. (1); Stevens, J. (1); Van den Berghe, S. (2); Kuzminov, V. (2)

RRFM2014-A0112	REVERSAL OF OFI AND CHF IN RESEARCH REACTORS: APPLICATION TO THE BR2 HEU AND LEU CORES	Kalimullah, M. (1); Olson, A. P. (1); Feldman, E. E. (1); Dionne, B. (1); Kalcheva, S. (2); Van den branden, G. (2); Koonen, E. (2) 1 - Argonne National Laboratory, United States 2 - SCK•CEN, BR2 Reactor Department, Belgium
RRFM2014-A0060	STATUS AND CALL FOR PROJECT PROPOSALS RELATED TO THE NEW IAEA CRP ON "BENCHMARKS AGAINST EXPERIMENTAL DATA ON FUEL BURNUP AND TARGET/MATERIAL ACTIVATION"	Ridikas, D. (1); Peld, N. (1); Borio, A. (1); Kennedy, W. (1) 1 - IAEA, Austria

RRFM2014-A0081	MULTI-CHANNEL THERMAL HYDRAULIC ANALYSIS OF PLATE TYPE RESEARCH REACTORS	Albati, M. (1); Jo, D. (2); Alkhafaji, S. (1); Al-yahia, O. (1) 1 - Jordan Atomic Energy Commission (JAEC), Jordan 2 - Korea Atomic Energy Research Institute (KAERI), Korea, Republic of

Research Reactor Operation and Maintenance

RRFM2014-A0018	CORROSION BEHAVIOR FOR CARBON STEEL IN RSG-GAS SECONDARY WATER COOLANT	Sunaryo, G. R. (1); Santoso, M. I. (2); Rahmat, A. (1) 1 - PTRKN - BATAN, Indonesia 2 - STTN - BATAN, Indonesia
RRFM2014-A0037	COMPARISON OF MEASURED AND CALCULATED INTEGRAL AND DIFFERENTIAL REACTIVITY WORTH OF CONTROL RODS IN A TRIGA REACTOR	Merljak, V. (1); Merljak, V. (2); Lengar, I. (2); Trkov, A. (2) 1 - Faculty of Mathematics and Physics, University of Ljubljana, Slovenia 2 - Reactor physics department, 'Jožef Stefan' Institute , Slovenia

RRFM2014-A0056	RESEARCH ACTIVITIES IN BATAN FOR THE BURNUP MEASUREMENT OF SILICIDE FUEL	Sembiring, T. M. (1) 1 - National Nuclear Energy Agency of Indonesia - BATAN, Indonesia
RRFM2014-A0126	IMPACT OF HEU TO LEU FUEL CONVERSION ON THE LIFETIME AND EFFICACY OF THE UNIVERSITY OF MISSOURI RESEARCH REACTOR BERYLLIUM REFLECTOR	Foyto, L. (1); Mckibben, J. C. (1); Peters, N. (1); Saddler, J. (1) 1 - University of Missouri-Columbia Research Reactor, United States
RRFM2014-A0057	DEVELOPMENT OF REACTOR INFORMATION SYSTEM AT JSI TRIGA MARK II REACTOR	Jazbec, A. (1); Snoj, L. (1); Smodis, B. (1) 1 - Jozef Stefan Institute, Slovenia
RRFM2014-A0059	REACTIVITY MEASUREMENTS AT THE TRIGA REACTOR USING SIGNAL FROM MULTIPLE FISSION CELLS	Lengar, I. (1); Merljak, V. (1) 1 - Jozef Stefan Institute, Slovenia
RRFM2014-A0102	FUEL MANAGEMENT AT ENEA TRIGA RC-1 REACTOR	Falconi, L. (1); Carta, M. (1); Palomba, M. (1); Sepielli, M. (1) 1 - ENEA, Italy
RRFM2014-A0123	THE RESULTS OF REPLACEMENT OF THE PUMPS IN PRIMARY FUEL CHANNEL COOLING CIRCUIT IN MARIA REACTOR.	Krzysztoszek, G. (1); Pytel, K. (1) 1 - National Centre for Nuclear Research, Poland

RRFM2014-A0021	TRANSIENT ANALYSIS OF THE IR-8 REACTOR MIXED LOADINGS DURING CONVERSION FROM HEU TO LEU	Nasonov, V. (1); Pesnya, Y. (1); Sidorenko, A. (1); Hanan, N. (2); Garner, P. (2) 1 - National Research Centre «Kurchatov Institute» (NRC KI), Russian federation 2 - Argonne National Laboratory (ANL), United States
RRFM2014-A0022	PROGRESS IN ASSESS SAFETY OF THE IR-8 REACTOR DURING CONVERSION TO LEU FUEL	Erak, D. (1); Nasonov, V. (1); Taliev, A. (1); Pesnya, Y. (1); Sidorenko, A. (1); Dubovskiy, Y. (1); Pavlenko, V. (1); Smirnov, L. (1); Danichev, V. (1) 1 - National Research Centre «Kurchatov Institute» (NRC KI) , Russian Federation
RRFM2014-A0027	SAFETY ANALYSIS FOR CONVERSION OF IRT MEPHI RESEARCH REACTOR TO LEU FUEL	Alferov, V. P. (1); Kryuchkov, E. F. (1); Shchurovskaya, M. V. (1); Hanan, N. A. (2); Garner, P. L. (2); Kontogeorgakos, D. (2) 1 - National Research Nuclear University MEPhI , Russian Federation 2 - Argonne National Laboratory, United States
		2 - SCK-CEN, Belgium
RRFM2014-A0014	TRANSIENT ANALYSIS BEHAVIOR FOR THE JRTR RESEARCH REACTOR UNDER LOSS OF ELECTRICAL POWER ACCIDENT	Al-yahia, O. (1); Jo, D. (2); Alkhafaji, S. (1); Albati, M. (1) 1 - Jordan Atomic Energy Commission , Jordan 2 - Korea Atomic Energy Research Institute, Korea, Republic of

Poster

RRFM2014-A0003	STUDY OF METHODS FOR PHASE CHARACTERIZATION IN INTERMETALLIC UALX	Durazzo, M. (1); Conturbia, G. D. L. C. (1); Garcia, R. H. L. (1); Saliba-silva, A. M. (1) 1 - Nuclear and Energy Research Institute - IPEN-CNEN/SP, Brazil
RRFM2014-A0006	BENCHMARK CRITICALITY EXPERIMENTS FOR URANIUM-WATER HETEROGENEOUS CONFIGURATIONS WITH LOW ENRICHMENT UZRCN FUEL	Sikorin, S. (1); Mandzik, S. (1); Polazau, S. (1); Hryharovich, T. (1); Soltan, I. (1); Gohar, Y. (2); Talamo, A. (2); Zhong, Z. (2); Bolshinsky, I. (3); Tukhvatulin, S. (4); Zhalilov, R. (4); Vishnevsky, V. (4); Daragan, I. (4) 1 - Joint Institute for Power and Nuclear Research − Sosny, Belarus 2 - Argonne National Laboratory, United States 3 - Idaho National Laboratory, United States 4 - Scientific Research Institute Scientific Industrial Association "LUCH", Russian Federation
RRFM2014-A0008	PASSIVE RESIDUAL HEAT REMOVAL SYSTEM OF AN OPEN-POOL TYPE RESEARCH REACTOR USING GRAVITY CORE COOLING TANK	Lee, K.-Y. (1); Chi, D.-Y. (1); Kim, S. H. (1); Seo, K. (1); Yoon, J. (1) 1 - Korea Atomic Energy Research Institute, Korea, Republic of
RRFM2014-A0009	SERPENT CODE SIMULATION OF IPR-R1 TRIGA REACTOR	Araújo silva, V. (1); Meireles, S. (1); Dos santos, A. A. (1); Campolina, D. (1); Mesquita, A. (1); Pereira, C. (2) 1 - Centro de Desenvolvimento da Tecnologia Nuclear (CDTN/CNEN), Brazil 2 - Departamento de Engenharia Nuclear da Universidade Federal de Minas Gerais (DEN/UFMG), Brazil
RRFM2014-A0012	ASSESMENT OF GLOBAL UNCERTAINTY WITH 5-MW POOL-TYPE RESEARCH REACTOR	Yum, S. (1); Park, S. (1); Chung, Y. (1) 1 - Korea Atomic Energy Research Institute (KAERI), Korea, Republic of
RRFM2014-A0024	BIOLOGICAL SHIELDING CALCULATIONS AND DESIGN FOR THE SCRW-FQT TEST LOOP AT THE LVR-15 REACTOR	Soltes, J. (1); Vojacek, A. (1); Ruzickova, M. (1); Frybort, O. (1) 1 - Research Centre Rez, Czech Republic
RRFM2014-A0029	UTILIZATION OF A UNIVERSITY REACTOR FOR PUBLIC ACCEPTANCE	Kim, M. H. (1) 1 - Kyung Hee University, Korea, Republic of

RRFM2014-A0039	INTERDIFFUSION STUDIES BETWEEN A U7WT%MO ALLOY AND ZIRCALOY-4	Araldi Cardoso, K. (1); Fontenele Urano Carvalho, E. (1); Durazzo, M. (1); Gracher Riella, H. (2) 1 - Nuclear and Energy Research Institute , Brazil 2 - Santa Catarina Federal University, Brazil
RRFM2014-A0046	IRRADIATION TEST CONDITIONS OF U-7MO DISPERSION FUEL FOR KJRR FUEL QUALIFICATION	Tahk, Y.-W. (1); Kim, H.-J. (1); Oh, J.-Y. (1); Lee, B.-H. (1); Park, J.-M. (1); Yim, J.-S. (1) 1 - Korea Atomic Energy Research Institute, Korea, Republic of
RRFM2014-A0051	INFLUENCE OF THERMAL ANNEALING ON THE SPECIFIC HEAT OF DIFFERENT DISPERSION U-(7-8)WT%MO FUEL	Reiter, C. (1); Huber, T. (1); Breitkreutz, H. (1); Petry, W. (1); Zweifel, T. (1) 1 - Forschungsneutronenquelle Heinz Maier-Leibnitz (FRM II), Technische Universität München, Germany
RRFM2014-A0055	INSPECTION SYSTEM OF U-MO PLATE FUELS USING X-RAY TESTING AND ULTRASONIC TESTING METHODS.	Lee, Y.-S. (1); Lee, K.-H. (1); Sim, C.-M. (1); Jeong, Y.-J. (1); Lee, H.-I. (1); Park, J.-M. (1) 1 - Korea Atomic Energy Research Institute, Korea, Republic of
RRFM2014-A0065	IMPROVED POWER MEASUREMENTS AT THE JSI TRIGA REACTOR IN LJUBLJANA USING MULTIPLE DETECTORS	Žerovnik, G. (1); Snoj, L. (1); Trkov, A. (1); Barbot, L. (2); Fourmentel, D. (2); Villard, J.-F. (2) 1 - Jožef Stefan Institute, Slovenia 2 - CEA Cadarache, France
RRFM2014-A0071	COATED U(MO) FUEL: AS-FABRICATED MICROSTRUCTURES	Perez, E. (1); Keiser, D. (1); Leenaers, A. (2); Van den berghe, S. (2) 1 - Idaho National Laboratory, United States 2 - SCK CEN, Belgium
RRFM2014-A0074	THERMAL DESIGN OF THE LORELEI TEST DEVICE USING A COMSOL INVERSE SOLVER	Shenha, H. (1); Gitelman, D. (1); Preker, I. (1); Arbel-Haddad, M. (2); Ferry, L. (3); Weiss, Y. (1); Katz, M. (2) 1 - ROTEM Ind., Israel 2 - NRCN, Israel 3 - French Atomic Energy Commission (CEA) − Cadarache Centre, France

RRFM2014-A0076	NUMERICAL SIMULATION OF A SINGLE-PHASE CLOSED-LOOP THERMOSYPHON IN THE LORELEI TEST DEVICE	Gitelman, D. (1); Tarabelli, D. (2); Shenha, H. (1); Weiss, Y. (1); Katz, M. (3); Gonnier, C. (2); Sasson, A. (1) 1 - ROTEM Ind., Israel 2 - French Atomic Energy Commission (CEA) − Cadarache Centre, France 3 - NRCN, Israel
RRFM2014-A0085	FISSION-INDUCED CREEP OF U-MO/AL DISPERSION FUEL	Kim, Y. S. (1); Jeong, G. Y. (2); Sohn, D.-S. (2) 1 - ANL, United States 2 - UNIST, Korea, Republic of
RRFM2014-A0089	CONCEPT OF THE LORELEI TEST DEVICE FOR LOCA EXPERIMENT IN THE JHR REACTOR	Szanto, M. (1); Moran, N. (1); Ferry, L. (2); Azulay, A. (1); Mileguir, O. (1); Weiss, Y. (1) 1 - Rotem Industries LTD, Israel 2 - French Atomic Energy Commission (CEA) - Cadarache Centre, France, France
RRFM2014-A0099	DEVELOPMENT OF U(MO) FUEL MINIPLATES DISPERSED IN AL(SI) MATRIX. MICROSTRUCTURAL CHARACTERIZATION.	Mirandou, M. (1); Aricó, S. (1); Balart, S. (1); Fabro, J. (1) 1 - Comisión Nacional de Energía Atómica (CNEA), Argentina
RRFM2014-A0100	NEUTRON IRRADIATION OF U3SI5 AND AL43MO4U6 COMPOUNDS. FIRST RESULTS.	Mirandou, M. (1); Gonzalez, R. (1); Aricó, S. (1); Fortis, A. (1) 1 - Comisión Nacional de Energía Atómica (CNEA), Argentina
RRFM2014-A0119	INSIGHTS ON THE KINETIC AND MECHANISM BEHAVIORS OF LAYER FORMATION IN UAL2-AL DIFFUSION COUPLE.	Moussa, C. (1); Tougait, O. (1); Pasturel, M. (1); Peron, I. (1); Geslin, D. (2); Jarousse, C. (2); Stepnik, B. (2) 1 - Institut des Sciences Chimiques de Rennes, UMR-CNRS 6226, Université de Rennes, France 2 - AREVA-CERCA, France
RRFM2014-A0125	PROGRESS IN DEVELOPMENT OF LARGE, FORMED HIP CANS FOR CLADDING OF U-MO FUEL	Clarke, K. (1); Crapps, J. (1); Tucker, L. (1); Dvornak, M. (1); Hudson, R. (1); Aikin, B. (1); Dombrowski, D. (1) 1 - Los Alamos National Laboratory, United States
RRFM2014-A0129	EFFECT OF COLD DEFORMATION AND ANNEALING TEMPERATURE ON U-10MO FUEL FOIL GEOMETRY	Alexander, D. (1); Clarke, K. (1); Scott, J. (1); Montalvo, J. (1); Dombrowski, D. (1) 1 - Los Alamos National Laboratory, United States

RRFM2014-A0136	METALLOGRAPHIC STUDY ON ALLOY ZYR-4 USED IN MANUFACTURE OF MONOLITHIC MINIPLATES	Gonzalez, A. G. (1); Munoz, C. A. (1); Arnaldo, G. J. (2) 1 - Nuclear Fuel Cycle Management, Constituyentes Atomic Center, National Commision of Atomic Energy, Argentina 2 - Materials Management, Department of Characterization and fracture mechanics, National Commision of Atomic Energy, Argentina
RRFM2014-A0138	DIGITAL SAFETY AND I&C SYSTEMS AND NEUTRON INSTRUMENTATION SUBSYSTEMS	Matousek, J. (1); Kochova, M. (1) 1 - I&C, dataPartner s.r.o, Czech Republic
RRFM2014-A0139	DETERMINATION OF UNCONTROLLED PARAMETERS OF WWR-KN EFAS	Techerepnin, Y. S. (1); Sokolov, S. A. (1); Bulkin, S. Y. (1); Lukichev, V. A. (1); Kravtsova, O. A. (1); Radaev, A. I. (1); Derikot, A. P. (1) 1 - JSC 'NIKIET', Russian Federation



International Programmes

ARE RADIOISOTOPE SHORTAGES A THING OF THE PAST?

PAVEL PEYKOV, DR. RON CAMERON
OECD Nuclear Energy Agency, 12 Boulevard des Iles, 92130 Issy-les-Moulineaux, France

ABSTRACT

Since June 2009, the NEA and its High-level Group on the Security of Supply of Medical Radioisotopes (HLG-MR) have examined the causes of ^{99}Mo/^{99m}Tc supply shortages and developed a policy approach, including principles and supporting recommendations to address those causes. The NEA has also reviewed the global ^{99}Mo/^{99m}Tc supply situation periodically, using the most up-to-date data from supply chain participants, to highlight periods of reduced supply and underscore the case for implementing the HLG-MR policy approach in a timely and globally-consistent manner.

In 2012, the NEA released a ^{99}Mo supply and demand update for the period up to 2030 (A Supply and Demand Update of the Molybdenum-99 Market, OECD/NEA, 2012), identifying periods of low supply relative to demand. This paper presents the preliminary results from an updated ^{99}Mo supply and demand forecast, focusing on the potentially critical 2015-2020 period, when two major ^{99}Mo producers (the NRU reactor in Canada and the OSIRIS reactor in France) are scheduled to cease ^{99}Mo irradiations.

On the demand side, the NEA had previously released a study with the results from a global survey of future demand for ^{99}Mo/^{99m}Tc (OECD-NEA, 2011), devising a scenario based on a data assessment by an expert advisory group. In the current analysis, the expected demand growth rate and total demand have been modified, based on the latest information from supply chain participants.

On the supply side, the NEA has updated the list of current and planned new ^{99}Mo/^{99m}Tc irradiation and processing projects. The modelling results incorporate revisions to production start/end dates, potential additional projects, and impacts of converting to the use of low-enriched uranium (LEU) targets on ^{99}Mo/^{99m}Tc capacity and production. The supply forecast horizon (2015-2020) has been chosen to reflect upcoming, important changes in global production capacity – the planned shutdowns in Canada and France, and the expected commissioning of new reactor- and non-reactor-based projects in Europe, the United States, South America, and Australia.

1. Introduction

At the request of its member countries, the Organisation for Economic Co-operation and Development (OECD) – Nuclear Energy Agency (NEA) became involved in global efforts to ensure a secure supply of ^{99}Mo/^{99m}Tc. Since June 2009, the NEA and its High-level Group on the Security of Supply of Medical Radioisotopes (HLG-MR) have examined the causes of supply shortages and developed a policy approach, including principles and supporting recommendations to address those causes. The NEA has also reviewed the global ^{99}Mo supply situation periodically, using the most up-to-date data from supply chain participants, to highlight periods of reduced supply and underscore the case for implementing the HLG-MR policy approach in a timely and globally-consistent manner.

In 2012, the NEA released a ^{99}Mo supply and demand forecast up to 2030, identifying periods of low supply relative to demand. This report updates the 2012 forecast[1], focusing on the shorter and potentially critical 2015-2020 period. In that period, one of the largest irradiators for medical isotopes, the National Research Universal (NRU) reactor in Canada, will cease ^{99}Mo production and the OSIRIS reactor in France will permanently shut down operations. In the same period, new reactor- and non-reactor-based ^{99}Mo/^{99m}Tc projects are expected to be commissioned in various countries. It is important to analyse the overall impact of these supply events to understand how global supply might be affected.

2. Demand Update

In 2011, the NEA released a study with the results of a global survey of future demand for ^{99}Mo/^{99m}Tc (OECD/NEA, 2011), developing a scenario based on a data assessment by an expert advisory group. The study showed ^{99}Mo/^{99m}Tc demand growth up to 2030 in both mature and emerging markets, with stronger growth forecast in emerging markets.

In a subsequent report, *A Supply and Demand Update of the Molybdenum-99 Market (OECD/NEA, 2012)*, the NEA estimated global ^{99}Mo demand at 10,000 6-day curies per week[2]. This was a decrease from the previously estimated 12 000 6-day curies per week, resulting from a number of changes that had occurred in the market as a consequence of the 2009-2010 supply shortage. These changes included: better use of available ^{99}Mo/^{99m}Tc, more efficient elution of ^{99m}Tc generators and patient scheduling, and an increased use of substitute diagnostic tests/isotopes.

As a starting point, the demand scenarios in this report use the NEA 2012 estimate of 10 000 6-day ^{99}Mo curies from processors. However, the NEA has modified the expected demand growth rate from the 2011 study, based on more recent information from supply chain participants.

The NEA continues to treat outage reserve capacity (ORC)[3] as an increase in demand for irradiation and processor capacity, as this capacity is required to be 'set-aside' in order to ensure reliability of supply. As a result, similar to the 2012 ^{99}Mo supply and demand update, a range for demand is presented, including two situations: no ORC demanded and 33% ORC demanded[4].

3. Supply scenarios and assumptions

The NEA has updated the list of current and planned new ^{99}Mo/^{99m}Tc irradiation and processing projects, based on the most recent information available. The updates include: revisions to production start/end dates, additional potential projects and

[1] The future scenarios presented by the NEA in this report should not be construed as a prediction, forecast or expectation of which projects will proceed and when. The scenarios are only meant to be illustrative of possible future situations, whether planned new projects materialize or not.

[2] A 6-day curie is the measurement of the remaining radioactivity of ^{99}Mo six days after it leaves the processing facility (i.e. at the end of processing – EOP).

[3] Outage reserve capacity is required to ensure a reliable supply chain by providing back-up irradiation and/or processing capacity that can be called upon in the event of an unexpected or extended shutdown.

[4] The requirement for 33% ORC is based on a derived model showing that a system with somewhat effective, but not perfectly ideal, co-ordination with a large reactor in the fleet could maintain necessary ORC levels if each reactor kept, on average, 33% of their capacity as ORC when they operate.

impacts of converting to using low-enriched uranium (LEU) targets on ^{99}Mo capacity and production. It should be noted that not all planned, new production facilities may be operational by the stated times or at all, particularly projects that rely on commercial funding, given the prevailing below-full-cost-recovery prices in the market and the resulting challenges to develop solid business cases.

The supply forecast horizon is five years (2015-2020) to reflect important changes in global production capacity – the planned cessation of ^{99}Mo production at the NRU reactor in Canada and the OSIRIS reactor in France, and the expected commissioning of new reactor- and non-reactor-based projects in Europe, North and South America, and Australia.

This paper presents a summary of the results from three scenarios for the 2015-2020 period, presented in 6-month intervals (January-June and July-December):

- Reference scenario – a baseline case that includes only current irradiation capacity and processing production;
- 'New infrastructure' scenario that starts from the reference scenario and adds some (but not all) of the planned, new ^{99}Mo production capacity; and,
- 'Challenges' scenario that starts from the reference scenario and adds the same new projects as in the 'new infrastructure' scenario, but delays their start dates by one year; also delays LEU conversion by one year and assumes reduced available capacity for one major ^{99}Mo producer.

Irradiation capacity in all three scenarios, for each 6-month forecast interval, is forecast based on historical reactor operating schedules. This approach improves the irradiation capacity forecast, compared to an even 50/50 split between the two 6-month periods in a year, although the NEA recognises that actual future capacity in a given 6-month period may still vary over time.

It should be noted that the reference scenario (and by extension, the two alternative scenarios) does not include all announced, new projects[5]. Some projects have been excluded due to the uncertainty of their commissioning within the announced timelines. This is not to suggest that these projects will not become operational, but that they are not likely to be in the chosen forecast horizon (2015-2020).

In this paper, the NEA assumes that the impact from LEU conversion on ^{99}Mo production capacity is high given the significant economic and technical challenges to conversion that processors are experiencing, which have led to an extension of their timelines for full conversion.

4. Supply Forecast: Reference Scenario

4.1 Global Irradiation Capacity

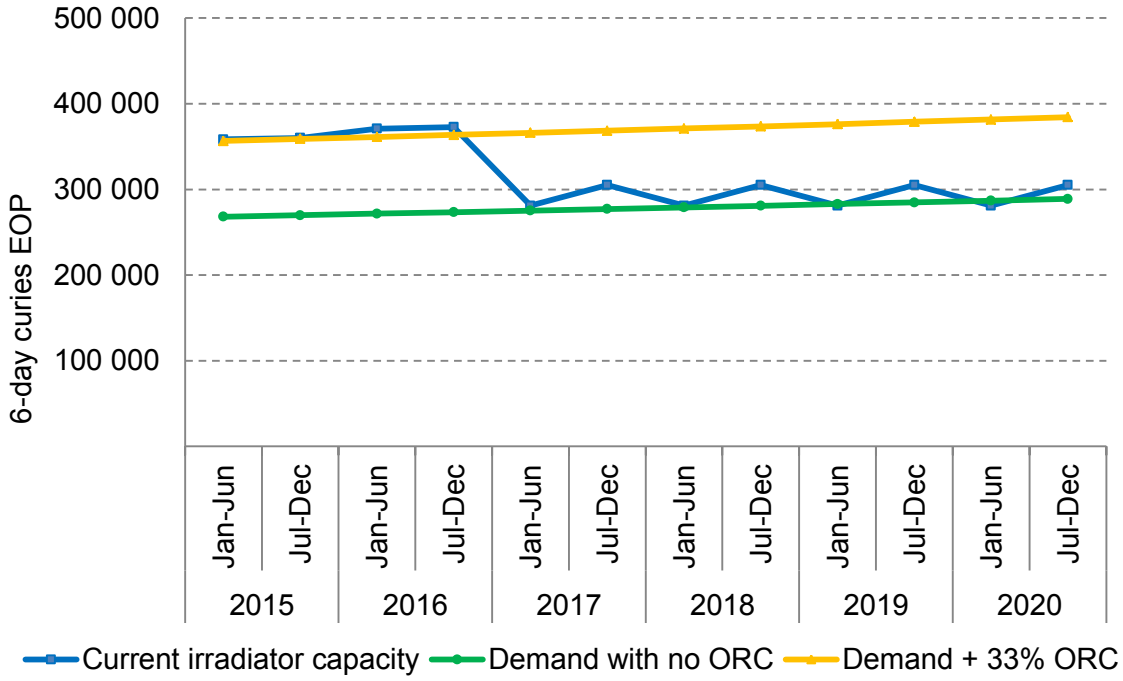
As discussed in previous NEA studies, the current fleet of irradiators is ageing and some are expected to stop irradiating targets for ^{99}Mo production within the next few years, while others may experience extended or more frequent periods of maintenance/refurbishment. The planned exit from the global supply chain of the NRU and OSIRIS reactors will significantly decrease the available irradiation capacity, while

[5] The NEA supply forecast includes only major projects that have a minimum production capacity of 1,000 six-day curies per week EOP. The only exception is the RA-3 reactor in Argentina, which has available capacity of 400 6-day curies per week.

sufficient new capacity may not be commissioned in time to compensate for this loss. Figure 4.1 shows the projected 2015-2020 global ^{99}Mo supply and demand based on the capacity of the current fleet of irradiators.

Figure 4.1 starts with a reduced available irradiation capacity in January-June 2015, as the BR-2 reactor in Belgium enters a planned major refurbishment, expected to last sixteen months (until well into 2016). The drop in capacity in January-June 2017 reflects NRU's exit. OSIRIS' exit is not as clearly evident, as its lost capacity will be offset by the return to service of the BR-2. In addition to the permanent loss of capacity from the exit of the NRU and OSIRIS, the full conversion to LEU targets in 2016 at most of the existing irradiators will further reduce available capacity from the current fleet, although this is also not directly identifiable in Figure 4.1, as again, the return of the BR-2 will provide an offset.

Figure 4.1 Current irradiation capacity and projected future demand, 2015-2020



The ^{99}Mo demand curve with no outage reserve capacity (ORC) in Figure 4.1 lies below the ^{99}Mo supply curve. However, should ORC be demanded, for example by the unplanned shutdown of one reactor, irradiation capacity becomes insufficient in the 2017-2020 period. The kinks in the supply curve in that period represent fluctuations in the available irradiation capacity between the two six-month intervals modelled, January-June and July-December in each year. This is a result of reactor capacity for ^{99}Mo irradiations tending to be higher in the July-December time interval, based on historical reactor operating schedules.

Despite Figure 4.1 showing no projected supply shortages in the 2015-2020 period (unless ORC is demanded), the gap between supply and demand without ORC is too small to assert that supply will be secure. In fact, at its lowest point relative to demand (January-June 2020), supply is only 98% of demand, while at its highest point (January-June 2016), supply is 137% of demand in the market. Historically, this has been shown to be insufficient. Overall, irradiation capacity is gradually decreasing in

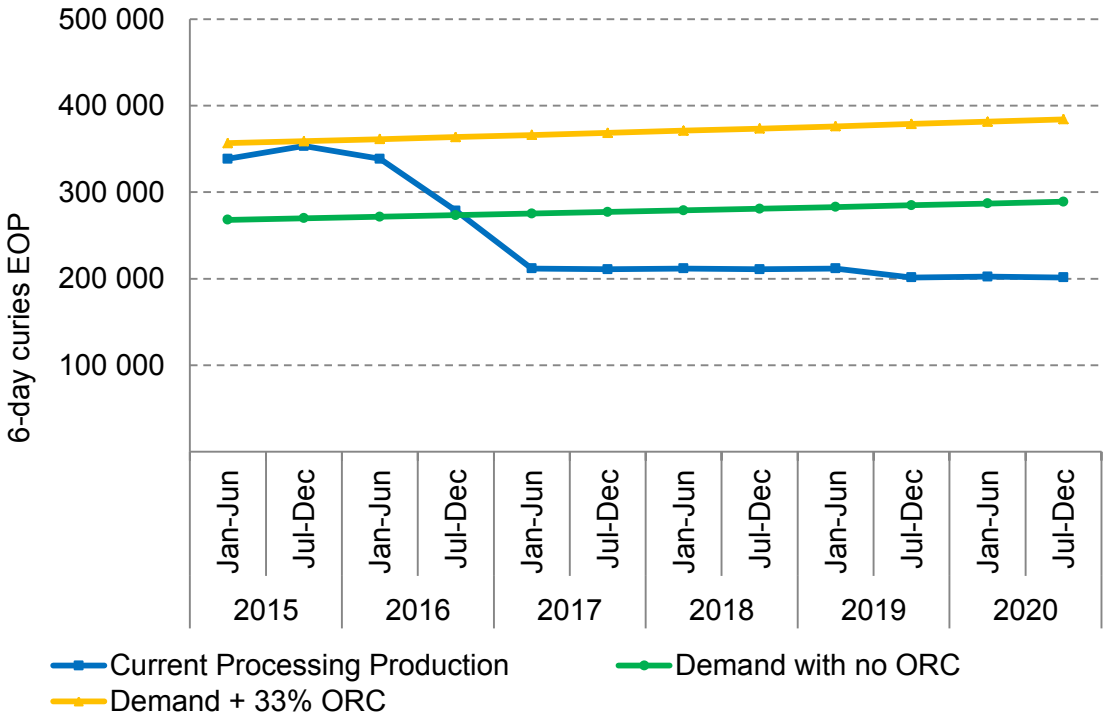
the 5-year forecast period, with a sharp drop in January-June 2017, whereas demand is slowly increasing. Consequently, the supply-demand gap is decreasing over the period, increasing concerns about the security of supply.

4.2 Global Processing Production

Although useful in understanding the global supply situation, irradiation capacity presents only a partial picture and does not account for geographical limitations relating to the production of bulk ^{99}Mo. Not all ^{99}Mo-irradiating reactors have associated processing facilities, which results in regional constraints on processing production and loss of product through higher decay during transportation. This is especially the case in Europe, where irradiation capacity exceeds processing capacity and production. Therefore, for a more complete analysis of ^{99}Mo supply, it is important to consider processing production. Figure 4.2 below shows current processing production, versus projected demand for ^{99}Mo.

In 2015 and 2016, processing production is projected to be greater than demand without an ORC requirement. However, should ORC be demanded, processing production would be insufficient to meet demand. In the rest of the forecast period (2017-2020), the supply curve drops below the demand curve, indicating a potential supply shortage. The main reason for the sharp drop observed in 2016 is the anticipated end of ^{99}Mo irradiations at the NRU reactor, which will directly affect the associated processing production in Canada. In addition, conversion to low-enriched uranium (LEU) targets by processors would further reduce ^{99}Mo production from 2016 onward.

Figure 4.2 Current processing production and projected future demand, 2015-2020



The regional limitations on ^{99}Mo production mentioned earlier can be seen when one compares the supply curves in Figures 4.1 and 4.2. If plotted on the same graph, the supply curve representing processing production would lie below the supply curve

representing irradiation capacity, which shows a smaller amount of bulk ^{99}Mo supplied to the global market than the larger irradiation capacity would imply. The next section attempts to overcome regional limitations to processing by presenting a regional breakdown of processing production. There is a clear conclusion from the analysis above that processing production is the major determinant of supply and that will be insufficient without additional processing capacity.

5. 'New infrastructure' Scenario

The 'new infrastructure' scenario is an extension of the reference scenario, presented in the previous section, and includes selected new reactor- and non-reactor-based projects around the world, in addition to the existing irradiation capacity and processing production. It should be mentioned that not all of the announced new projects have been included in this scenario, given the uncertainty over whether some of them will be operational within the 2015-2020 forecast horizon. More specifically, the NEA has decided to consider only new projects that are most likely to be commissioned at least one year before the end of the forecast horizon[6] and exclude projects that have yet to receive full financing or have unspecified construction start and commissioning dates. By making such a determination, the NEA is not suggesting that excluded projects will never materialise, but rather that they may not be commissioned within the forecast period. In the longer term, after 2020, the ^{99}Mo supply-demand schedule may look different with these projects online, with potentially greater supply available in the market.

There is one notable exception to the assertion above – the proposed Molybdenum 2010 processing facility in Poland. Should this project materialise in the announced timeframe (by 2017), it would increase processing production in Europe enough to push supply above demand with an ORC requirement, significantly improving the regional security of supply. However, financing has not yet been provided for this project, hence its future production is excluded from the 'new infrastructure' scenario.

Another exception is the planned new reactor and processing facility in the Republic of Korea, which would be important for ^{99}Mo security of supply in Asia. Again, this capacity may not be fully operational in the 2015-2020 forecast horizon.

5.1 Global Irradiation Capacity

Under this scenario, global capacity looks to be sufficient to meet projected demand, even with an ORC requirement, throughout the 5-year forecast period, assuming demand increases only slightly. Notwithstanding the expected cease of production at the NRU and OSIRIS reactors, new capacity in North America and Europe should more than compensate for this capacity loss. However, there could still be a period from the end of 2016 to sometime in 2017 when capacity may be insufficient, depending on the exact dates of operation of new production facilities. Later in the forecast period, the supply-demand gap increases due to the commissioning of new reactor capacity and associated processing production in South America and Asia.

[6] In order to include their full capacity in the forecasting model, based on the assumption that new projects need ramp-up time before they reach full production capacity. The ramp-up time is assumed to be one year, so a project needs to be commissioned no later than July-December 2019 to be included in the forecast.

5.2 Global Processing Production

If all new projects under this scenario are commissioned within the announced timelines, global processing production should be sufficient (without an ORC requirement) throughout the forecast period to meet projected global demand. However, with an ORC requirement, ^{99}Mo supply fluctuates above and below the demand curve up to mid-2017, resulting in the potential for difficulties in ensuring sufficient supply. Although ^{99}Mo supply appears to be sufficient to meet global demand in the latter part of the 2015-2020 forecast period under this scenario, ^{99}Mo supply in the first half of the period remains somewhat fragile and vulnerable to unexpected producer outages.

From 2018 onwards, the projected processing production far exceeds demand and, hence, there must be concerns over the continued viability of those projects that require sustainable prices.

6. 'Challenges' Scenario

The 'challenges' scenario has been developed from the reference scenario, but represents a more conservative version than the 'new infrastructure' scenario. The planned, new ^{99}Mo production capacity included in this scenario is the same as in the 'new infrastructure' scenario, in addition to the existing capacity, however, the following assumptions are also made:

- The selected new projects will be delayed by one year from their announced dates for commissioning.
- Full LEU conversion will be delayed by one year from the current commitment of 2016.
- Available capacity is reduced at a major irradiator, given recent extended outages, based on its actual ^{99}Mo irradiation time over the last five years (2009-2013).

This scenario provides an alternative (but still realistic) picture of ^{99}Mo supply to the one presented in the 'new infrastructure' scenario. Given the technical complexity of new reactor-based projects and the ground-breaking efforts in reaching large-scale, commercial production by non-reactor-based technologies, it is not unreasonable to experience delays in full project implementation. Furthermore, the majority of the new projects included in this scenario intend to apply full-cost recovery for their future ^{99}Mo production and need to develop distribution networks for their product, which provides an additional challenge to implementation.

Compared to the 'new infrastructure' scenario, ^{99}Mo supply in the 'challenges' scenario is projected to fluctuate more in the 2015-2017 period due to the combined effects and timing of the capacity loss from the NRU and OSIRIS reactors, the delayed new capacity and LEU conversion. On the one hand, delayed new capacity and the assumed lower available irradiation capacity at a major producer will have a negative effect on total irradiation capacity, but on the other, delayed LEU conversion will have the opposite effect. Over the 2015-2020 forecast period, except for July-December 2016, the 'delayed new capacity' effect will dominate, resulting in lower total irradiation capacity.

Global processing production under the 'challenges' scenario is projected to fall below the demand curve in 2016 and 2017 (regardless of ORC), creating a potential risk of

shortages. Post-2017 supply appears to be sufficient to meet demand with or without an ORC requirement.

7. Preliminary Conclusions

During the entire forecast horizon (2015-2020) existing global irradiation and processing capacity appear insufficient for security of supply, even with all current producers operating under normal conditions, i.e. without any unplanned or extended outages, which suggests a need for additional capacity. When new capacity is added (in the two alternative scenarios in this report), the global ^{99}Mo/^{99m}Tc outlook improves, albeit with remaining periodic challenges to ensure sufficient supply.

This ^{99}Mo/^{99m}Tc supply and demand update confirms previous forecasts of tight and potentially insufficient supply in the short term. The planned exit of the NRU and OSIRIS reactors from the global supply chain poses challenges to ensure that there is enough supply to meet rising demand in 2016-2017, particularly with an ORC requirement. On the other hand, the scheduled commissioning of new capacity as early as 2015 raises hopes that these short-term challenges can be overcome. However, any potential delays in production from that capacity could cause supply difficulties.

Despite the (overly) optimistic outlook for ^{99}Mo/^{99m}Tc supply post-2017 under all three scenarios in this report, it should be noted that much of the expected new production capacity to come online towards the end of the current decade may not be commercially-based. This, in addition to the projected over-capacity in the market in that period, would present future challenges for suppliers who have or will have implemented full-cost recovery by then, and other new projects that are being planned to operate on full-cost recovery. In the limit, such suppliers could be forced to exit the market, which emphasises the need for all countries to implement the six HLG-MR policy principles in a timely and globally consistent manner.

The results in the updated 2015-2020 supply forecast reinforce the need to an economically sustainable ^{99}Mo/^{99m}Tc supply chain as quickly as possible to enable investment in new/replacement, non-HEU-based production capacity and its timely entry in operation, and provide sufficient amounts of ORC to the market. The ageing fleet of research reactors – the backbone of global ^{99}Mo production at present – and recent extended outages at major suppliers, underscore the importance of universally adopting full-cost recovery and ORC. Furthermore, the supply chain should continue its communication and co-ordination efforts to identify potential challenging periods for supply and minimise the impact on end-users. This is critical for the long-term sustainability of the ^{99}Mo/^{99m}Tc market and the security of supply.

References

Available at www.oecd-nea.org/med-radio:

1. OECD-NEA (2012), *Market Impacts of Converting to Low-enriched Uranium Targets for Medical Isotope Production*, OECD, Paris.

2. OECD-NEA (2012), *A Supply and Demand Update of the Molybdenum-99 Market*, OECD, Paris.

3. OECD-NEA (2011), The Supply of Medical Radioisotopes: An Assessment of Long-term Global Demand for Technetium-99m, OECD, Paris.

2014 PROGRESS REPORT ON HEU MINIMIZATION ACTIVITIES IN ARGENTINA

Pablo Cristini, Liliana de Lio, Alfredo G. Gonzalez, Marisol López,
Bianca Picchetti, Horacio Taboada; Jorge Vaccaro

COMISIÓN NACIONAL DE ENERGÍA ATÓMICA
Av. Del Libertador 8250 (1429) Buenos Aires, Argentina

In Marrch 2010 a contract extension between CNEA and the NNSA DoE to enhance the final national HEU inventories minimization, to the original RA-6 reactor core conversion one, was signed. To that end, CNEA reserved a small inventory of HEU for R&D uses in fission chambers, neutronic probes and standards. The minimization comprises all fresh and irradiated HEU remnant inventories coming from fuels and Mo99 irradiation targets fabrication and irradiated HEU-oxides retained in production filters and solutions. The contract goal is to recover, down-blend into LEU and purify those inventories or to waste part of them if the recovery is not advisable or feasible.

CNEA has focused its R&D program on very high density fuel fabrication technology on monolithic U-Mo alloy (Zry-4 cladding) miniplates to support the qualification activities of the RERTR program. Some monolithic 58% enrichment U and depleted U 8%Mo and 10%Mo miniplates were delivered to INL-DoE to be irradiated in the ATR reactor core. Full scale plates will take part of the ALT FUTURE irradiation at the BR II Belgium reactor.

CNEA, a worldwide leader on LEU technology for fission radioisotope production is providing Brazil with 1/3 of the national requirements on Mo99 by weekly deliveries. ANSTO is firmly producing several fission radioisotopes batches by week. Egypt´s MPR reactor is also producing fission radioisotopes, both based on CNEA's LEU technology provided by INVAP SE.

CNEA is also working in the design, construction and operation since 2017 of a new fission radioisotope research multipurpose research nuclear reactor, named RA-10, which main functions will be radioisotope production, material testing and a stationary neutron source of high intensity.

Future plans include:

- To recover and purify the LEU based inventories in Mo99 production filters, once the HEU minimization campaign is over.
- Development, fabrication and delivery of LEU very high density monolithic U-Mo fuel plates with Zr cladding for the FUTURE-MONO experiment in the frame of the RERTR program.

1. Introduction:

In March 2010, a supplementary agreement between CNEA and NNSA-DoE to the original one - involving the RA-6 reactor core conversion and the exportation to the US of 42 SNF in terms of the SNF FRR Program- was signed by both parties. This was done in the frame of the efforts for HEU minimization for civilian uses. From remaining HEU inventories, used in the past for fuel and target fabrication, a small amount of it for R&D purposes was reserved by CNEA (for further uses in fission chambers, neutronic probes and standards fabrication).

This minimization means the recovery, blending down and purification of fresh and irradiated HEU inventories contained in scraps from fuel and target fabrication and in fission Mo99 production filters, or the disposition as waste of those few inventories whenever its recovery is not advisable due to a cost-benefit consideration. These tasks are taking place and the corrected deadline is December 2015.

2. New tasks on HEU minimization

Previously it was informed about the inventories classification into 6 groups (see Table 1)

Description	Group Number	Form	U Mass (kg)	Enrichment	235 U Mass (kg)
Irradiated Mo-99 Targets And Solutions	**1**	**Solid and Liquid**	**1.928**	**89.73%**	**1.73**
UF6 Cylinder	**2**	**Gas / Solid (UO2F2)**	**0.65**	**90.14%**	**0.59**
Miscellaneous Solids (alloys, metal)	**3**	**Solid**	**0.397**	**87.15%**	**0.346**
Miscellaneous Solutions	**4**	**Liquid**	**0.228**	**89.91%**	**0.205**
Materials declared waste to dispose	**5**	**Solid**	**0.505**	**89.97%**	**0.453**
Ingot for MEU-Mo/Zr Miniplates Fabrication	**6**	**Solid**	**0.344**	**88.66%**	**0.305**
TOTAL			**4.05**		**3.63**

Tab. 1 HEU inventories

Regarding the progress of the tasks involved the present status can be seen in Table 2. Most of them are already finished.
Main importance has the Group 1, which comprises the refurbishment of a radiochemical laboratory (LFR lab), licensing of two transport casks, for irradiated solutions and solids contained in cartridge filters, among of the proper recovery, down blending and purification of the HEU inventory in the hot cells of the LFR lab. This task is ongoing and the actualized deadline is December 2015.
Group 2 to 6 are already treated, finished and previously informed, unless the marginal final waste of processes to be disposal
At present the balance can be seen in table II where it is informed.

GROUP	DESCRIPTION	HEU MASS (Kg)	RECOVERED AND DOWNBLENDED (Kg)	DECLARED WASTE OR TO BE WASTED (Kg)
1	IRRADIATED MATERIAL	1,928	-	-
2	5A CYLINDER CONTAINING HEU-F6	0,649	0,628	0,021
3	SOLIDS	0,378	0,374	0,004
4	LIQUIDS	0,228	0,140	0,086
5	MATERIAL TO DECLARE WASTE	0,505	0	0,505
6	HEU FOR MEU-Mo MINIPLATES & LEU-Mo PLATE FABRICATION	0,344	0,310*	0,154
TOTAL		4,032	1.452	0.770

Tab. 2 Recovery and downblending into LEU

3. R&D on VHD fuels

The development of CNEA miniplates using monolithic UMo alloy cores involves the use of the well known Zr alloy named Zircalloy-4 (Zry-4). Zry-4 is commonly used as nuclear fuels cladding for nuclear power plants. In this case Zry-4 is employed as cladding in top, cover and frame. The fuel material in the core is an alloy between Uranium (U) and Molybdenum (Mo) with different contents of Mo (between 7-10% wt/wt). These Mo percentages are enough to retain the gamma phase at low temperature but also not to penalize the reactor neutronics due to the capture cross section of Mo95 isotope. The fabrication process includes hot and cold co-rolling. In previous reports[I] was already informed. A special report on new findings in development will be presented in this meeting

LEU target and radiochemical technology for Mo99 and other fission radioisotopes production:

It is by far the largest contribution of CNEA to HEU minimization for civilian uses. It was already informed how CNEA found an adequate LEU replacement without changing its radiochemical technology.

CNEA has developed and is using high-density LEU-aluminum dispersion targets. The target meat has a density of 2.9 gU/cm3 obtained by increasing the ratio of uranium aluminide to aluminum in the target meat. The mass of U-235 in the target meat is about twice that of conventional uranium-aluminum alloy targets.

CNEA was able to convert to LEU-based production in the same set of hot cells that were being used for HEU-based production, without interrupting Mo-99 production.

CNEA's development showed that there are no technical barriers for the conversion of fission Mo-99 production from HEU targets to LEU targets. Production using LEU targets is technically

feasible and is being carried out by CNEA in Argentina, by the Australian National Nuclear Science and Technology Organisation and the Egytpian MPR reactor. Both institutes are using CNEA's radiochemical technology and LEU targets provided by INVAP to produce Mo-99 y other fission radioisotopes..

This new LEU technology satisfies the most stringent requirements of quality for its use in nuclear medicine applications. Mo-99 purity has been consistently higher than that produced using HEU targets[II]. Also in September 2005, CNEA began the regular production of high quality fission I-131, a by-product of Mo-99 production, meeting also international quality standards.

HEU-LEU production process comparison costs reveal that this new technology has no significant overall cost of 10% [III]. Due to the fact that CNEA was able to duplicate the LEU-based radioisotope weekly production rate, since 2010 provides Mo99 to Brazil covering 1/3 of the Brazilian market.

To support these activities CNEA is refurbishing a set of radiochemical cells where the spent LEU based material retained in the filters of the Mo99 production facility along these last 10 years will be separed from waste, recovered and purified to be reutilized in this or in other nuclear applications.

The National Atomic Energy Commission of Argentina is working since 2010 in the design, the construction and operation since 2017 of a new multipurpose research nuclear reactor, named RA-10. This project foresees the replacement of the RA-3 reactor, deploying the national capability in the design and construction of such kind of nuclear reactors. The aim is to achieve a qualitative increase in health, nuclear technology and material science development in our country and region.

Main goals are

- to account with an increased capability of fission radioisotope research and production able to hold the national and regional supply
- to consolidate the national nuclear fuel fabrication capability
- to bring to the national and regional science systems a stationary neutron source of high intensity,

The new plant will have a thermal power capacity of 30 MW. The reactor is a open pool type, running on low-enriched uranium fuel assemblies.

At present the project is being deployed having achieved planning, structure and site steps. Conceptual engineering is completed while the basic engineering is advanced under the frame of a CNEA-INVAP agreement to that end. Site studies had finished and the licensing plan is ongoing. It will be located in the Ezeiza Atomic Centre.

In the design of this new reactor are working professional and technician of different areas of CNEA. It will provide fission radioisotopes for health and industry applications in the local, regional and worldwide market, increasing the national production capability.

During the basic engineering development phase, common interests with a similar project being carried out by Brazil, where identified. Those similarities gave raise to joint activities in the frame of the nuclear cooperation on peaceful uses of the nuclear energy between both countries.

The new RA-10 reactor will be a key instrument in the field of materials science, engineering and other sciences requiring neutron beams as a knowledge tool, comparable to the most modern and advanced research reactors in the world, as the ANSTO's OPAL (Australia) and the Germany's FRM II. The utilization of the neutron sources through state-of-the-art design and construction of research devices will bring unique opportunities for a qualitative improvement in the national science and technology development.

.

4. Conclusions:

FINAL HEU MINIMIZATION: CNEA is minimizing the remnants HEU inventories, both fresh and irradiated from fuel and target fabrication scraps and fission RI production solutions and filters. All these tasks are scheduled to finish during 2014.
R&D ON LEU VHD FUELS: CNEA is actively supporting both R&D activities to achieve solutions for core conversions.
LEU TECHNOLOGY FOR FISSION RI PRODUCTION: No technical, quality or financial reasons make disadvantageous changing from HEU to LEU for fission Mo99 and other RI production. CNEA leads LEU based isotope production technology, and with INVAP built all LEU-based production systems in Australia and Egypt. This is by far the largest contribution of CNEA to the HEU minimization for civilian uses.
RA-10 reactor: the new reactor will have a thermal power capacity of 30 MW. The reactor is a open pool type, running on low-enriched uranium fuel assemblies. Main goals are: to account with an increased capability of fission radioisotope research and production able to hold the national and regional supply, to consolidate the national nuclear fuel fabrication capability and to bring to the national and regional science systems a stationary neutron source of high intensity,

---

I P. Cristini, L. De Lio, D. Gil, A. G. Gonzalez, M. López, O. Novara, H. Taboada "2012 Progress Report on LEU activities in Argentina" XII RRFM International Meeting, Prague,Cezch Republic, March 21-24, 2012
II Durán,A. 2005. Radionuclide Purity of Fission Mo-99 Produced from LEU And HEU. A Comparative Study. 2005 International RERTR Meeting, Boston, Massachusetts, USA, November 6-10, 2005. Available at http://www.rertr.anl.gov/RERTR27/PDF/S8-3_Duran.pdf.

III Cestau D., A. Novello, P. Cristini, M. Bronca, R. Centurión, R. Bavaro, J. Cestau, E. Carranza. HEU and LEU cost comparison in the production of molybdenum-99. 2008 International RERTR Meeting, Washington, DC, USA, 5-9 October 2008, and Cestau D., A. Novello, P. Cristini, M. Bronca, R. Centurión, R. Bavaro, J. Cestau, E.Carranza. 2007. HEU and LEU comparison in the production of molybdenum-99. 2007 International RERTR Meeting, Prague, Czech Republic, Sep. 23-27, 2007. Available at http://www.rertr.anl.gov/RERTR29/PDF/6-4_Cestau.pdf

VIENNA RELOAD, USED TRIGA FUEL BURNS AGAIN (A PACKAGING AND TRANSPORT STORY)

JAMES D. ADAM
Sr. Vice President, Site and Transportation Services
NAC International Inc.
3930 East Jones Bridge Road, Suite 200, Norcross, GA, USA
Street, Postal Code City – Country (10 pt, italics)

ABSTRACT

Used TRIGA fuel elements were mined out of dry storage at Idaho National Laboratory, INTEC facility and transported to the Atominstitut Vienna.
This reload LEU core permitted the discharge, packaging and return to USA transport of the used core, which included some HEU fuel elements.
The reload core enables the long term continued operation of the highly utilized research and test reactor in Vienna, Austria.
After the delivery of the replacement core, the used fuel, including the HEU and some damaged fuel, was packaged and shipped to Idaho National Laboratory.
This story is interesting due to the mining of what was presumed to be waste material for reuse, the round trip transport of the loaded cask, INF vessel, and the logistics of twice transiting a third country with no inherent interest in the project.
We even picked up a hitchhiker from Italy along the way back.

Topics

Vienna Institute of Technology, Atomistitut (ATI) - Burned core
HEU inventory & Damaged fuel
FRR Program return deadline
Shut down 5/2016 & Return by 5/2019
TRIGA fuel supply
TRIGA International & Alternatives
Mining used fuel from INL storage
Retrieval & Inspection
Packaging & Transporting new core in
Package, Loading, Road, Export, Marine, Transit, Unloading
Packaging & Transporting of old core out
Damaged fuel, Press, Hitchhiker

1. Introduction

The TRIGA Mark-II reactor of the Atominstitut Vienna began operations 7 March 1962 and has been a valuable, highly-utilized, research and test reactor supporting the Vienna Institute of Technology and the IAEA.

The reactor core consists of 80 fuel elements with a nominal power of 250kW and has been in operation now for 52 years.

In the Autumn of 2012, a replacement fuel core was brought to ATI and the used fuel elements were shipped back to the USA for disposition.
The ninety-one used fuel elements at ATI consisted of the following:

- 9 HEU
- 82 LEU

Of those 91 fuel elements, 11 had been deemed to be damaged in one way or another that required them to be canned prior to packaging.

2. FRR Program

The Foreign Research Reactor (FRR) return program is a temporary fuel take back initiative by the U.S. Department of Energy (DOE) to repatriate U.S. Origin fuel from research and test reactors located outside of the USA.

Under the terms of the FRR Return Program the reactor wishing to participate must stop irradiating the qualified U.S. origin fuel by May 2016 and ship the fuel back to the USA by May 2019.

ATI was successful in negotiating with the DOE a special agreement to allow the return of the replacement fuel core significantly after that deadline for continued operations of the reactor's usefulness to support IAEA personnel safeguards training. This agreement was critical to the reactors continued operating life, as no other viable back-end solution is available to ATI.

3. Replacement TRIGA fuel supply

With that agreement in place with the DOE, the search for replacement fuel began.
ATI needed a replacement core of 77 fuel elements. The first choice of course would be new fuel elements fabricated by TRIGA International.
Unfortunately at this time the TRIGA fuel fabrication line was having a planned disruption for regulatory required upgrades.
Also, an anticipated fuel element price increase due to fabrication costs and market conditions was being discussed as highly probable.

The some alternatives to new fuel element fabrication were also explored.

Shut down reactors
Idaho National Lab used TRIGA storage facility (INTEC)

4. Mining used fuel from INL

The idea of mining for fuel at INL was novel and the practice was unprecedented. However it was an elegant solution for this situation.

The retrieval & inspection of potential fuel elements took about two weeks with ATI personnel making the final decision on which fuel element they would take for use. As each

fuel element was selected it was immediately placed into the fuel basket designed and licensed for the selected transport package.

INL has several used inventories of TRIGA from which to pick. Ultimately ATI chose fuel from Musashi Institute of Technology, a TRIGA Mark II Reactor, in Japan. The fuel had a burn-up of only 1%.

5. Transport Package

The transport package selected was NAC International's workhorse transportation cask, the NAC-LWT.

Dimensions	inch	mm
Overall length	199.80	5075
Overall diameter	44.20	1120
Cavity length	180.90	4600
Cavity diameter	13.37	340
Weighs	**Tons**	**Metric Tons**
Loaded inside ISO	33.0	30.0
Empty cask	24	22.4
Package ID#s		
USA/9225/B(U)F-96	US NRC	Rev 58
USA/9225/B(U)F-96	US DOT	Rev 49
USA/9225/B(U)F-96 (DOE)	US DOE	Rev 6

NAC-LWT Cask basics 1

6. INL- INTEC

Fuel Inspection and selection performed September 2012
As each fuel element selection was agreed upon between DOE and ATI, it was placed into a NAC TRIGA fuel basket for packaging to await cask loading. The fuel element inspection and selection process took approximately two weeks to perform.
The NAC-LWT cask loading was performed in early October 2012 for transport to Austria.
Upon the cask return to INL with the ATI discharge fuel the unloading was performed in December 2012

7. Road Transport

The USA road transport was fairly routine. However it was necessary to apply for and obtain two new approved road routes within the U.S.A. from the U.S. NRC.
They are:

#242 - Eastbound, INL – SRS
#243 - Northbound, SRS – Charleston

8. Marine Transport

The marine transport of course was planned as a round trip between Charleston, South Carolina and Koper, Slovenia.
There was 10 days of ship demurrage between eastbound and westbound ship sailings.
One port (Koper) needed for 1st leg and two ports (Koper and Trieste) needed for the 2nd leg.
Ship fuel bunkering during the demurrage raised questions with the Slovenian authorities.

9. Port & Transit

The unique aspect of this shipment was that it was always planned as a round trip between INL and ATI. Needing to bring the LEU in and taking the HEU out.
Austria is land locked, with no access to marine ports without the help of neighboring coutries.
Obviously the project needed a port for the ship to dock and permission to transit through whichever country allowed use of the port.
Others denied port access & ground transit for our Class 7 cargo of irradiated nuclear fuel.
However, the Port of Koper in Slovenia has been used several times in the past to provide the needed port use and road transit access and they stepped up and permitted this access again this time, with a few conditions that the project was happy to concede to.

Thank You SLOVENIA !

10. Unloading/Loading at Vienna

Since the ship was waiting in the north Adriatic for the return cargo, the need to unload and reload the cask as quickly as possible was obvious. This was nominally scheduled as a one week long activity.
Set up equipment took place over the weekend preceding the arrival of the loaded cask.
The unloading of 77 elements happened without incident.
Then the reverse action of loading 91 the discharged fuel elements took place.
Included in the cask loading, it was necessary to package 11 damaged fuel elements into 5 sealed cans.

During the loading of the 2nd to last fuel element it was bumped upon the fuel basket and then it was noticed that a stream of tiny bubbles started to exit from the fuel element. Only one possible cause could be the origin of these bubbles and that was we had an emergent damaged fuel element, with a pin-hole leak in the cladding allowing the gas to escape from the confinement of the fuel cladding.
The issues that this caused our project was three-fold:

- We needed an additional sealed can to package for transport the leaking fuel element

And

- We needed INL to permit a cask receipt configuration change before we could transport which was to be done in two days.

And

- It was Saturday

A volunteer was quickly found in Idaho Falls to hand carry the can to Vienna. It was brought over by one of our good friends from the Idaho National Laboratory, Mr. Eric Woolstenhulme. He arrived with the can by the next morning and we had it loaded within a few hours after its arrival on site.

INL-INTEC support to change their internal procedures to permit the inclusion of an additional can of damaged fuel was immediate, swift, and positive. This reactor was critical to the success of the project in removing 100% of the used fuel from ATI.

Thanks INL!

Thank you Eric Woolstenhulme

The remaining work on site for preparing the now loaded cask for transport was routine.

Packing up all the tooling and equipment and preparing all of the transport, export documentation was done and trucks gathered to connect to trailers with ISO containers all in a line ready for the planned transport window, that night.

11. Team ATI

NAC International	TU Wien – Atominstitut
Edlow International Co.	Austrian Government
Secured Transportation Services	DOE-NNSA
Columbiana High-Tech	DOE-EM
Tri-State Motor Transit	DOE-Idaho
Atlantic Container Lines	INTEC
Nuclear Cargo + Service	DOE-Savannah River Site
Dusan Jovic	U.S. NRC
Port of Koper	Slovenia Government
Prangle	Joint Base Charleston
J. Poulsen Shipping	

12. Hitchhiker

When the Sogin Avogadro facility, in Italy heard about the Austria fuel shipment to the U.S.A. they requested the opportunity to join the ship on the westbound transit of the Atlantic and another NAC-LWT cask to repatriate 10 U.S. origin HEU MTR fuel loose plates
They did have a few facility infrastructure and administrative restrictions that necessitated the design and fabrication of a new piece of equipment that could perform a horizontal loading of the NAC-LWT cask with a single can containing the 10 loose fuel plates.

NAC took on the engineering duty and on an expedited basis completed the design, engineering and fabrication of the new designed tooling.
Time was so short however, that it needed to be air freight shipped to Italy to support the cask loading schedule. This is only mentioned as an issued due to the excessive weight of the lead shielded transfer device.

In addition to the equipment being provision being just in time and few other issues became critical path to the success of the project.

We needed several approvals by local authorities for the loading operations process, and tooling, and for the transit of the material across Italy to meet the ship at Trieste all of which seemed to only be accomplished at the last possible minute to allow the transport to be performed.

Just prior to the transport taking place there were press reports that detailed what our transport plans were and put the security of the transport into question. The DOE requested another security assessment take place and the word was given to proceed with the transport, which took place uneventfully.

The two casks arrived in the US at Joint Base Charleston in South Carolina and then were both trucked down to Savanah River Site (SRS). The Sogin fuel was taken to the L-Basin at SRS and the ATI fuel was trucked across the USA to the Idaho National Laboratory site in Idaho, where it was duly unloaded and placed into long term storage at the INTEC facility.

Thank you!

PRELIMINARY ANALYSIS OF THE IMPACT OF FUEL DENSITY ON THE RESEARCH REACTOR FUEL CYCLE

HO JIN RYU
Department of Nuclear and Quantum Engineering, Korea Advanced Institute of Science and Technology, 291 Daehakro, Yuseong, Daejeon 305-701, – Republic of Korea

CHUL GYO SEO
Reactor Core Design Division, Korea Atomic Energy Research Institute, 989-111 Daedeokdaero, Yuseong, Daejeon 305-353, – Republic of Korea

P. ADELFANG
Division of Fuel Cycle and Waste Management, International Atomic Energy Agency

ABSTRACT

Several major considerations related to the impact of uranium density of LEU fuel on the cost of research reactor fuel cycle are analyzed in order to identify significant factors affected by adopting higher uranium density fuel in research reactors, as a result of a cooperative activity of the International Atomic Energy Agency. Because of the complex character of multiple overarching factors of the fuel cycle, it is difficult for potential users of high density fuel to clearly understand what benefits are expected, for example, when U-Mo fuel with a uranium density higher than 4.8 g-U/cm^3 is used instead of U_3Si_2 fuel. While several studies on the impact of high density fuels are available for generic reactors and existing reactors, it is necessary to provide a comprehensive overview by considering potential benefits and limitations of using high density fuel. In this study, the impact of the use of increased density fuel on the annual consumption of fuel assemblies, the costs for the manufacturing and spent fuel management, the reactor performance parameters and irradiation capabilities are discussed.

1. INTRODUCTION

High density research reactor fuels may offer economic benefits, despite being more expensive initially, because they offer the prospect of higher burnup, thus reducing the number of assemblies that need to be procured, when compared to the currently qualified and commercially-available LEU fuels [1,2]. These high density fuels are still under development and are expected to be available in the near future after completing qualification tests. Because of the complex character of the various factors of the fuel cycle, it is difficult for potential users of the high density fuel to understand clearly what kind of benefits they can expect, for example, when 8.0 g-U/cm^3 U-Mo fuel is used instead of 4.8 g-U/cm^3 U_3Si_2 fuel.

In view of the above-mentioned potential advantages of using higher density fuels in research reactors, the IAEA hosted a consultancy meeting to discuss the impact of the use of a higher density research reactor fuel in March 2013 in Vienna. Consultancy participants initiated a comprehensive study on the impact of fuel density on the cost of the research reactor fuel cycle and several major considerations and case studies related to the impact were presented and discussed in detail during the second consultancy meeting in Dec. 2013 in Vienna. The objectives of the study were to collect the various studies prepared by the consultants and to

review the draft of an IAEA Nuclear Energy series report on the impact.

In this paper, the preliminary analyses developed by the consultancy group members, whose names are listed in the Acknowledgments, are highlighted. This study focuses more on the technical aspects regarding the possible use of high density dispersion fuel in research reactors, without preferentially promoting the use of any particular high density fuel. The cases regarding monolithic fuel and HEU-LEU conversion will not be included in this study in order to clarify the pure impact of fuel density changes.

2. THE STRUCTURE OF THE ANALYSES

Studies on the impact of uranium density of LEU fuel on the economy and performance of the research reactor fuel cycle were collected according to the preliminary Table of Contents for the planned technical report, as listed in Table 1. Analyses on the major impacts of increasing fuel density on fuel consumption, reactor performance, safety parameters, manufacturing, spent fuel management, and transportation are summarized in this paper. A simple parametric estimation on the cost saving as a result of using high density fuel is given based on the analyses of the consultancy group.

Case studies for existing reactors and generic reactors were collected and discussed for the drafting of the planned technical report, as listed in Table 2. The analyses of existing reactors include case studies of JMTR, Japan, KJRR, Korea, OPAL, Australia, and RP-10, Peru.

Chapter 1. Introduction
- 1-1 Purpose of the study a
- 1-2 Scope and limitation of the study

Chapter 2. Status of High Density Fuel

Chapter 3. Major Impacts of Increasing Fuel Density
- 3-1 General aspects related to changing high density fuels
- 3-2 Fuel consumption
- 3-3 Reactor performance
- 3-4 Safety and kinetic parameters
- 3-5 Manufacturing
- 3-6 Spent fuel management
- 3-7 Transportation
- 3-8 Qualification/licensing

Chapter 4. Cost impact estimation

Chapter 5. Conclusions

Annex. Case studies

Table 1. Table of contents of the planned technical report on the impact of fuel density.

Annex I. Case studies for existing reactors

- N. Takemoto, T. Imaizumi, H. Ide, M. Naka, T. Kusunoki and M. Ishihara, "Preliminary Analytical investigation on High density U-Mo Fuel Introduction to the JMTR", JAEA
- C.G. Seo, "Comparative Study on Fuel Material for the KIJANG Research Reactor", KAERI
- G. Broudakis, E.Villarino, "Study of change OPAL reactor fuel from U_3Si_2 to high density U-Mo", ANSTO and INVAP
- E. Villarino and D. Ferraro "RP-10 Research Reactor Higher density fuels utilization Analysis", INVAP

Annex II. Case Studies for generic reactors

- E. Villarino, D. Ferraro, C. Mazufri and P. Bouza, "Generic Reactor Fuel replacement from U_3Si_2 to U-Mo" INVAP and Instituto Balseiro
- C.G. Seo "Comparative Study on fuel density for the AHR", KAERI

Table 2. A list of case studies for the planned technical report on the impact of fuel density.

Because the impact of the use of high density fuel is dependent on the probable design changes of fuel assemblies and reactor cores, the cases are classified into three categories: direct replacement of the fuel zone, fuel assembly re-design and replacement of the fuel zone with core changes. In case of the direct replacement of the fuel zone, no re-design of fuel assemblies and no core upgrade are expected. By directly replacing fuel meat with high density uranium dispersion fuel, a higher discharge burnup is expected while the fuel assembly design might not be optimum for the high density. To optimize the fuel performance of the high density fuel, the re-design of fuel assemblies might be proposed, maintaining fixed core size, in the case of the fuel assembly re-design. The total number of fuel assemblies in the core might be decreased for the higher density fuel in case of the replacement of the fuel zone with core changes.

3. THE SUMMARY OF THE ANALYSES

The change to higher density fuel can lead to an extended cycle length and/or discharge burnup. As shown in Table 3, case studies on the impact of the replacement of U_3Si_2 fuel with U-Mo fuel, particularly for OPAL, KJRR and advanced HANARO [3-5], show that the replacement increases the cycle length by one-third and reduces the annual fuel assembly consumption by a factor of two, and the annual LEU consumption by approximately 17%.

	OPAL		KJRR		AHR	
Type of fuel	U_3Si_2	U-Mo	U_3Si_2	U-Mo	U_3Si_2	U-Mo
Density	4.8g/cc	8.0g/cc	4.8g/cc	8.0g/cc	4.0g/cc	6.0g/cc
Cycle length	30.0	40.5	37.5	50	31	50
Annual FA consumption	34.2	17.2	24	12		

Table 3. Comparison of the cycle length and annual consumption of fuel assemblies.

All parameters related to safety and design criteria must be analyzed because potential problems might arise related to shutdown margins, power peaking factor, reactivity coefficients and kinetic parameters, maximum discharge burnup and/or average irradiation time, and oxide layer growth.

The shutdown margin can be deteriorated by the use of high density fuel due to an increase in excess reactivity. Having higher initial uranium loads may reduce the capacity of the control rods to shutdown the reactor with the proper margins. Increasing cycle length and inclusion of burnable poisons can diminish the excess reactivity.

An increase in the power peaking factor for higher density fuel is expected when the capabilities of cooling systems are limited. For the cases where the use of higher density fuel leads to an unacceptable increase in the power peaking factor, the re-design of fuel assembly may be necessary. An appropriate fuel management strategy and/or inclusion of burnable poisons can reduce the power peaking factor

Changing fuel to high density can modify neutronic behavior that can impact in the main parameters regarding temporal response to transients, such as kinetic parameters and reactivity coefficients. When the use of higher density fuels is intended to increase the discharge burnup of the fuel, other related problems may arise such as large oxide layer growth. When the maximum discharge burnup has already been optimized for an original core operating with existing LEU fuel, the change to higher density fuel might present no advantage in fuel consumption because higher excess reactivity available cannot be used to improve the discharge burnup.

In order to address potential constraints regarding safety and performance of the changed core with high density fuel, several options including the modifications of fuel management strategies, the introduction of burnable poisons, modifications of fuel assembly design, and modifications of control rod positions should be considered, in addition to the core design modification,

4. IMPACT ON FUEL CYCLE COST

The fuel cycle cost includes the purchase of LEU, expenses for the manufacturing of the fuel elements, and the cost of spent fuel management. To give only a preliminary evaluation of the impact of an increased density on the cost of the fuel cycle, a rough breakdown of 20 to 33% for the purchase of LEU, and 33 to 40% for both fuel manufacturing and spent fuel management each were assumed in this study [6]. The transportation component, which represents only a few percent of the fuel cycle cost, is neglected. When 4.8 g-U/cm^3 U_3Si_2 is replaced with 8 g-U/cm^3 U-Mo, the annual consumption of fuel assemblies is reduced by a factor of two, as shown in the case studies [3-5]. It is expected that the change to high density fuel will increase the fuel fabrication cost because of the increased amount of fissile materials per fuel assembly, atomized powder production, matrix modification, increased scrap, and enhanced quality control. Fabrication cost for high density fuel may be significantly impacted if additional steps, such as coating, have to be added to an existing fabrication process. A cost evaluation with an acceptable uncertainty for spent fuel management of U_3Si_2 fuel and U-Mo fuel is not available at the moment.

If the cost for fuel manufacturing and spent fuel management are assumed to be increased up to 20%, the cost saving by replacement with high density fuel ranges from 32 to 43% as shown in Tables 4 and 5. It should be noted that this evaluation does not take into account the cost of R&D related to qualification, licensing, and conversion.

	SM=0%	SM=10%	SM=20%
FM=0%	43%	41%	39%
FM=10%	41%	39%	37%
FM=20%	39%	37%	35%

Table 4. Cost saving estimation of using high density fuel when the cost breakdown is 20% for LEU supply, and 40% for each of manufacturing and spent fuel management (FM: fuel manufacturing cost increase, SM: spent fuel management cost increase)

	SM=0%	SM=10%	SM=20%
FM=0%	39%	37%	36%
FM=10%	37%	36%	34%
FM=20%	36%	34%	32%

Table 5. Cost saving estimation of using high density fuel when cost breakdown is 33% each for the LEU supply, manufacturing, and spent fuel management

CONCLUSIONS

- Reduction of annual consumption of fuel assemblies by using higher density fuel owing to increased cycle length, burnup, and life time is expected.
- Reduction of fuel-related operation cost is attainable if costs for the manufacturing and spent fuel management for higher density fuel do not increase significantly.
- Comparison of fuel cycle costs between different fuel systems is affected by large uncertainties on different components including the back-end of the fuel cycle, manufacturing and qualification/licensing, among others.
- Increasing fuel density may affect a number of reactor performance parameters including thermal flux, control rod worth, shutdown margin, and power peaking factors. Adjustment of, *inter alia*, the designs of fuel assembly, core configuration, and irradiation facility and/or by introducing burnable poisons may be necessary to maintain reactor operation consistent with mission and safety requirements.
- Improved reactor performance is an additional potential benefit of using high density fuel. The latter includes increased experimental capability, increased neutron flux, the possibility of operating a more compact core, smaller reactivity swing, and reduced reactivity worth of experiment and irradiation targets.
- While several studies on the impact of high density fuels are available for generic reactors and existing reactors, it is necessary to provide a comprehensive overview by considering potential benefits and limitations of using high density fuel and a methodology to evaluate the impact on cost.

ACKNOWLEDGMENTS

The authors gratefully acknowledge the contributions of the following international experts who are participating in the drafting and review of the IAEA technical report: E. A. Villarino (INVAP, Argentina), D. Ferraro (INVAP, Argentina), G. Braoudakis (ANSTO, Australia), E. Koonen, (SCK/CEN, Belgium), M.-C. Anselmet (CEA, France), P. Lemoine (CEA, France), T. Kusunoki (JAEA, Japan), F. C. Klaassen (NRG, Netherlands), J. Roglans-Ribas (ANL, USA), and B. Dionne (ANL, USA).

REFERENCES

[1] M. M. Bretscher and J. E. Matos, “Neutronic Performance of High Density LEU Fuels in Water-Moderated and Water-Reflected Research Reactors”, ANL/TD/RP-91011, Argonne National Laboratory, July 1996.

[2] M. M. Bretscher, J. E. Matos, and J. L. Snelgrove, “Relative Neutronic Performance of Proposed High-Density Dispersion Fuels in Water-Moderated and D_2O-Reflected Research Reactors”, RERTR-2006, Seoul, Korea, October 7-10, 1996,

[3] E. A. Villarino, “Neutronic Performance of the U-Mo Fuel Type in the Replacement Research Reactor”, RERTR-2002. Bariloche, Argentina, November 3-8, 2002.

[4] E. A. Villarino, “Core Performance Improvements using High Density Fuel in research Reactors”, RRFM-2013, St Petersburg, Russia, APRIL 21-25, 2013.

[5] C.G. Seo et al., “Conceptual Neutronic Design of an Advanced HANARO Reactor using the U_3Si_2 and U-Mo Fuel”, RERTR-2006, Cape Town, South Africa, 2006.

[6] P. Lemoine, presentation in the IAEA consultancy meeting, Vienna, Dec. 2013.

IAEA ASSISTANCE IN THE DEVELOPMENT OF NEW RESEARCH REACTOR PROJECTS

A. BORIO DI TIGLIOLE[(1)]*, E. BRADLEY[(1)], A. ZHUKOVA[(1)], P. ADELFANG[(1)], A. SHOKR[(2)], D. RIDIKAS[(3)],

(1) Research Reactor Section, NEFW-NE
(2) Research Reactor Safety Section, NSNI-NS
(3) Physics Section, NAPC-NA
International Atomic Energy Agency
Vienna International Centre, PO Box 100, Vienna, AUSTRIA

*Corresponding author: A.Borio@iaea.org

ABSTRACT

A research reactor (RR) project is a major undertaking that requires careful preparation, planning, implementation and investment in time, money, and human resources. In recent years, the interest of IAEA Member States in developing RR programmes has grown significantly, and currently, several Member States are in different stages of new RR projects. The majority of these countries are building their first RR as a key national facility for the development of their nuclear science and technology programmes, including nuclear power.

In order to support Member States in such efforts, the IAEA in 2012 published the Nuclear Energy Series Report No. NP-T-5.1 on *Specific Considerations and Milestones for a New Research Reactor Project* (also known as *RR Milestones publication*), which provides guidance on the timely preparation of a RR project through specific development phases. The publication includes a detailed description of the range of infrastructure issues that need to be addressed and the expected level of achievement (or milestones) at the end of each phase of the project.

To provide further support, the IAEA also developed a document (presently in print) to assist Member States in the preparation of the technical requirements for the bidding process of a new RR (Nuclear Energy Series Report No. NP-T-5.6 *Technical Requirements in the Bidding Process for a Research Reactor*). This document supports the application of the RR Milestones publication and addresses the preparation phase of the bidding process as well as discusses criteria that may be used in the technical and safety evaluation of the bids.

In the framework of the RR Milestones publication and with the objective to continue facilitating the successful development of new RR projects, the IAEA is currently preparing a new publication to provide guidance in the assessment of the national infrastructure to support a new RR project.

The IAEA, in order to assist Member States in evaluating their national nuclear infrastructure status and to identify gaps and future development needs, is also developing integrated RR infrastructure assessment (IRRIA) missions. Such a service will be coordinated and led by the IAEA in the frame of the cross-cutting activities on RRs and participated by international experts appointed by the IAEA. Mission will be conducted on the basis of the above mentioned document under development, the IAEA RR Milestone publication, IAEA Safety Standards for RRs and other IAEA technical documentation, including RR utilization and applications.

The IAEA will also continue to provide assistance for human resources development of the Member States establishing their first RR, and to facilitate sharing experience and knowledge among Member States through its programmatic activities including expert mission services, technical meetings, training courses and workshops addressing relevant technical and safety topics.

This paper will present the IAEA assistance and services provided to the Member States establishing new RRs, with particular emphasis on those establishing their first RR, including elaboration on the services mentioned above.

1. INTRODUCTION

Many IAEA Member States have shown, in the recent years, interest in constructing a research reactor (RR), as their first major nuclear investment and opportunity to benefit from the peaceful uses of nuclear technology. These future RRs may have various roles, such as: a) promoting science and technology in industrial, agricultural and medical applications; b) serving as a major facility for nuclear education and training of young generations of scientists and technicians, and c) contributing to build expertise and national infrastructure to support a nuclear power programme. In responding to this trend, the IAEA published in 2012 the Nuclear Energy Series Report No. NP-T-5.1 on "Specific Considerations and Milestones for a Research Reactor Project" (also known as RR Milestones publication), which provides guidance on the timely preparation of a RR project through specific development phases [1]. The publication includes a detailed description of the range of infrastructure issues that need to be addressed and the expected level of achievement (or milestones) at the end of each phase of the project.

The feedback from the IAEA activities, in particular from Member State establishing their first RR, indicated the need for further guidance on the development of the technical specifications for the bidding process of a RR. In responding to this need, the IAEA has recently finalized the development of a Nuclear Energy Series Report on "Technical Requirements in the Bidding Process for a New Research Reactor" (presently in print) [2]. The scope of this publication covers the bidding process, from the definition of the technical requirements of the bid invitation specifications (BIS) until the selection of the RR design and the signature of the contract, including criteria for bids evaluation.

In the framework of the RR Milestones publication, to continue facilitating the successful development of new RR projects, the IAEA is currently developing a publication to provide guidance in the assessment of the national infrastructure that should be implemented to support a new RR programme. The publication is meant to be used as basis for Member States self-assessment of the status of the national infrastructure and as guidance for the implementation of a new IAEA service, the integrated research reactor infrastructure assessment (IRRIA) missions. Such a service aims at assisting Member States in evaluating their national nuclear infrastructure status and to identify gaps and future development needs. The envisaged IRRIA missions will be coordinated and led by the IAEA (in the frame of the IAEA cross-cutting activities for RRs) and with the participation of international experts. The mission will be conducted on the basis of the above mentioned document under development, the IAEA RR Milestones publication, IAEA Safety Standards for RRs and other IAEA technical documentation, including RR utilization and applications.

The IAEA will also continue to provide assistance for human resources development of the Member States establishing their first RR, and to facilitate sharing experience and knowledge among Member States through its programmatic activities including expert mission services, technical meetings, training courses and workshops addressing relevant technical and safety topics.

2. SPECIFIC CONSIDERATIONS AND MILESTONES FOR A RESEARCH REACTOR PROJECT

The IAEA RR Milestones publication [1] provides guidance on the timely preparation of a RR project through a sequential development process (phases), and includes a detailed description of the range of infrastructure issues that need to be addressed and the expected level of achievement (milestones), at the end of each phase of the project. Furthermore, the publication provides a discussion of the mechanisms for building stakeholder support, in particular user community development as well as utilization and strategic planning to justify a new RR, and addresses the evolution of infrastructure needs from the time a Member State first considers a RR and its

associated facilities, through the stages of planning, bid preparation, construction and preparation for commissioning. It includes technical, legal, regulatory and safety infrastructure, and emphasizes the development of qualified human resources needed for a RR.

The publication is divided in seven chapters. Session 1 provides the background, the objectives and defines the use of the publication. Session 2 presents the infrastructure development phases, namely the Pre-Project (phase 1), Project Formulation (phase 2) and Project Implementation (phase 3), considering the issues to be addressed during these phases. Session 3 is referring to the important phase of RR's justification; moreover, the chapter elaborates the process of identifying the stakeholders needs with emphasize on securing the long term government commitments associated with operation of a RR and considering regional and international cooperation while preparing the strategic plan. The next three Sessions, 4 to 6, describes in details the three milestones that indicate the completion of each phase, to be followed during a RR project: a) milestone 1: ready to make a knowledgeable commitment; b) milestone 2: ready to invite bids; c) milestone 3: ready to commission and operate the RR and its auxiliary facilities. Finally, in Chapter 7, a summary of the chapters of the publication together with recommendations for the implementation of the milestones approach are provided.

The milestones to be achieved at the end of each phase of the project are briefly described in the following paragraphs.

2.1 Milestone 1: ready to make a knowledgeable commitment

During phase 1, the country should have determined that there are scientific, industrial or medical needs that justify the construction of a RR. This achievement should be reflected in the completion of two documents, the Pre-Project Assessment Report (PPAR) and the Preliminary Strategic Plan (PSP), which aim to pride a sound basis for the reactor future utilization, including identifying potential stakeholders' support. However, before embarking in the RR project, the country should also develop a comprehensive understanding of the obligations and commitments involved, and ensure that there is a long term national strategy and resources available to discharge them. This work will culminate in the attainment of milestone 1 and the production of the Feasibility Study.

The Feasibility Study should demonstrate that the Member State is in a position to make an informed decision whether to proceed with the RR project. The Feasibility Study should incorporate and update the Pre-Project Assessment Report and the Preliminary Strategic Plan and integrate these with the analysis of the obligations, commitments, gaps and resources required based on the "19 Infrastructure Development Issues" listed in the RR Milestones publication.

2.2 Milestone 2: ready to invite bids for the RR

Following the policy decision to proceed with the development of a RR project, substantive work for achieving the necessary level of technical and institutional competence should be undertaken. Thus, phase 2 requires a significant and continuing commitment from the government and from the operating organization (OO). A dedicated team, the RR Project Implementation Commission (RRPIC), should be established to ensure that the necessary infrastructure and policies are in place prior to the construction of the reactor. RRPIC should also include representatives from the Regulatory Authority at this stage of the project.

During the second phase of the project, the State should carry out the work required to prepare for the construction of a RR. The nuclear legislation would need to be enacted before proceeding with a request for bid for the first RR. The regulatory body would need to be developed to a level at which it can fulfill all of its oversight duties.

Before the commencement of the bidding process, the licensing stages and activities to be licensed should be defined, including safety and security requirements for the bidding process itself. The

necessary infrastructure should be developed to the point of complete readiness to request a bid or enter into a commercial contract.

An effective management system and staff capabilities should be developed to ensure proper accomplishment of the OO obligations (the OO has a key role at this time in ensuring that it has developed the competences to manage a nuclear project, to achieve the level of organization, operational culture, and safety culture necessary to meet the regulatory requirements, and the ability to demonstrate that it is an adequately informed and effective customer).

Work performed during phase 2 would culminate having the Bid Specification prepared and being the OO ready to start the bidding process.

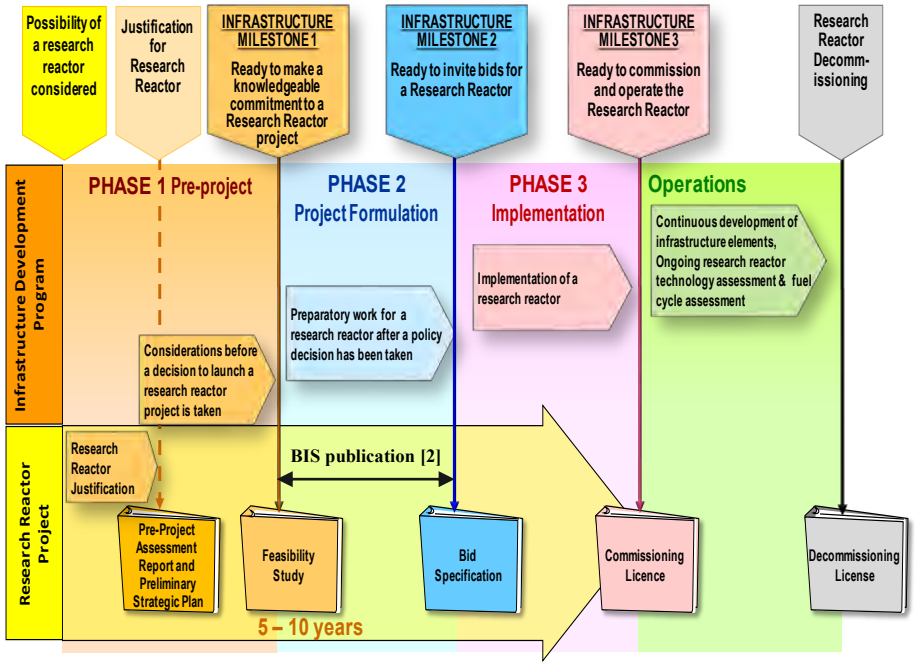
2.3 Milestone 3: ready to commission and operate the RR

Phase 3 of the project development includes all the activities necessary to implement the RR and complete most of the national nuclear infrastructure. During this phase, the greatest capital expenditures will occur. Attention by all organizations is crucial to the successful outcome and all have important roles to play.

At the end of this phase, the OO will have developed from an organization capable of ordering a RR to an organization that can accept responsibility for commissioning and operating one. Procedures and arrangements to ensure safe control of RR under all conditions should have been developed as well as significant development and training for all levels of staff. Work performed during Phase 3 will culminate with the obtainment of the RR Commissioning and Operating License.

While achieving the third milestone is a major accomplishment, it should be remembered that it is only the beginning of a long lasting commitment to the safe, secure and effective utilization of the RR.

FIG 1: Research Reactor project and infrastructure development programme [1]. The arrows indicate the place of the new IAEA publication [2] within the project.



3. TECHNICAL REQUIREMENTS IN THE BIDDING PROCESS FOR A NEW RESEARCH REACTOR

The scope of the recent IAEA publication Technical Requirements in the Bidding Process for a New Research Reactor [2] is to cover the bidding process for a new RR, from the preparation of the technical requirements for the bid invitation specifications (BIS) until the selection of the RR design and the signature of the contract, including criteria for bid evaluation. The publication is to be used in conjunction with the other IAEA publications on RR safety and utilization and the supporting IAEA Safety Standards. As such, the new document is to be used to bridge the gap between the Feasibility Study (milestone 1) and the Bid Specification (milestone 2), as depicted Fig. 1.

The guidance applies to all RR types and technologies, and therefore is not recommending a specific reactor type or technology or a specific design. However, it is assumed that the document will be used by a Member State that has already decided that general features as safe, sustainable, robust-design and easy-maintained RR is appropriate to be considered the country's needs, as it establishes its first nuclear installation. Moreover, the guidance provided in the publication is primarily oriented to countries developing its first RR. However, such guidance could be also used for the bidding process of a subsequent reactor in a country. Furthermore, the publication is mainly directed to the turnkey contractual approach. On the other hand, it also could be useful in other kinds of contractual approaches.

The publication discusses the general considerations of the bidding process, including description of the bidding process and its preconditions, the entities involved in the bidding process and their responsibilities, as well as other important aspects such as schedule of the bidding process and pre-qualifications of the bidders (Section 2). It provides description of the general considerations for developing the BIS, including, among others, the site selection and specification process, the general design requirements, the main issues regarding the fuel supply and the bid evaluation criteria (Section 3). These items are presented along with discussions on the relevant information that should be included in the technical specifications of the BIS. The publication addresses reactor utilization related design features (Section 4). A list of the various applications of RR [3] is presented along with the technical requirements that can shape the owner/operator's (Member State's) request from the vendor during the bidding process. Description of the fundamental design requirements for the research reactor that should be included in the technical specifications of the bid is provided in Section 5. Special emphasis is given to the IAEA Safety Requirements and to the requirements for safety demonstration to be included in the BIS. Guidance on the reactor organizational structure during operation phases together with the training requirements as well as the items to be requested from the vendor in this regard is provided in Section 6. The publication provides additional guidance on the technical documents to be requested from the reactor vendor as well as the technical documents that should be prepared by the OO based on inputs gathered from the vendor in the frame of the bidding process (Section 7). A list of infrastructure related facilities (including software) that have to be specified by the operator and supplied by the vendor to build, operate and safely utilize the new research reactors facility is provided in Section 8. The bid evaluation process and guidance on performing such an evaluation from technical and economical point of view is discussed in Session 9 together with suggested technical evaluation criteria for the bids.

4. ASSESSMENT OF THE NATIONAL NUCLEAR INFRASTRUCTURE TO SUPPORT A NEW RESEARCH REACTOR PROJECT

Member States requested IAEA additional guidance on determining how to assess the progress of their national infrastructure development for RRs programmes. In response to their request, the

IAEA has initiated to develop a publication with the tentative title of "Assessment of the National Nuclear Infrastructure to support a new Research Reactor Project; Reference Document for IAEA service Integrated Research Reactor Infrastructure Assessment (IRRIA) Mission".

The main objective of this publication is to provide a holistic approach for the evaluation of the progress in the development of the RR related nuclear infrastructure, based on the guidance contained in the RR Milestones publication. The evaluation approach will provide a comprehensive means to determine the status of the infrastructure conditions covering all the 19 issues [1]. It could be used either by a Member State wishing to evaluate its own progress (self-assessment) or as a basis for an external evaluation (international peer review) with the participation of the IAEA and independent international experts, where the Member State wishes to invite them to carry out an evaluation of its progress.

Based on both this new approach and on well-established services for RRs, the IAEA will, upon request, assist Member States in assessing and developing their national nuclear infrastructure for the implementation of a safe, secure and effective new RR project.

5. CONCLUSIONS

A RR that is appropriately conceived, managed, and supported is an extraordinary tool that contributes to country's scientific and technological development, improving health care, industrial and agricultural productivity and national nuclear capacity. However, its construction and operation requires recognition of important international responsibilities, and a well-defined and implemented national nuclear science and technology policy, regulatory, safety and technical infrastructure. These also include a legal framework, appropriate finances, human resources, and waste management resources.

The regulation, operations, spent fuel and waste management aspects of the RR represent costs that will be incurred for several decades. Addressing these issues requires a systematic approach that starts with a careful justification for the RR based on a sound utilization plan that includes user community and other stakeholder inputs. This approach helps ensure the long term sustainability (and thereby the long term funding) of the new facility.

If the RR can be justified, and sufficient users and sponsors found to support its construction and operation, then the focus should move to reviewing and implementing the necessary national infrastructure in addition to work on the RR project itself.

According to the IAEA RR Milestones publication, three phases of work can be identified each culminating in the achievement of milestones that demonstrate that the RR project is ready to move forward into its next phase. By following this systematic approach to decision making, stakeholder engagement, project and infrastructure development, the RR project will be safe, secure and cost effective, and therefore able to achieve its full expected potential.

To provide assistance to Member States in such efforts, the IAEA has published and is still developing specific guidelines to support the planning, formulation and implementation of new RR projects together with the assessment of the Member States' infrastructure needed to support such projects.

These publications should be used in conjunction with the IAEA publications on RR safety (such as e.g. [5], [6], [7], [8] and [9]) and utilization (such as e.g. [3] and [4]), in particular the Code of Conduct on the Safety of Research Reactors [10] and the IAEA Safety Standards.

The IAEA will also continue to provide assistance for human resources development of the Member States establishing their first RR, and to facilitate sharing experience and good practices among

Member States through its programmatic activities including expert mission services, technical meetings, training courses and workshops addressing relevant technical and safety topics. A new service that will be soon offered to Member States embarking in a new RR project is the integrated RR infrastructure assessment (IRRIA) mission that is designed to provide assistance in assessing national nuclear infrastructure status and to identify gaps and means to fill them.

6. REFERENCES

[1] INTERNATIONAL ATOMIC ENERGY AGENCY, Specific Consideration and Milestones for a RR Project, Nuclear Energy Series No. NP-T-5.1, IAEA, Vienna (2012).

[2] INTERNATIONAL ATOMIC ENERGY AGENCY, Technical Requirements in the Bidding Process for a New RR, Nuclear Energy Series No. NP-T-5.6 (in print in 2014).

[3] INTERNATIONAL ATOMIC ENERGY AGENCY, Applications of Research Reactors, Nuclear Energy Series No. NP-T-5.3 (in print in 2014).

[4] INTERNATIONAL ATOMIC ENERGY AGENCY, Strategic Planning for Research Reactors, TECDOC-1212, IAEA, Vienna (2001).

[5] INTERNATIONAL ATOMIC ENERGY AGENCY, Safety Assessment of RRs and Preparation of the Safety Analysis Report, Safety Standards Series No. SSG-20, IAEA, Vienna (2012).

[6] INTERNATIONAL ATOMIC ENERGY AGENCY, Safety Analysis for RRs Safety Reports Series No. 55, IAEA, Vienna (2008).

[7] INTERNATIONAL ATOMIC ENERGY AGENCY, Safety of RRs, Safety Standards Series No. NS-R-4, IAEA, Vienna (2005).

[8] INTERNATIONAL ATOMIC ENERGY AGENCY, Maintenance, Periodic Testing and Inspection for RRs, Safety Standards Series No NS-G-4.2, IAEA, Vienna (2007).

[9] INTERNATIONAL ATOMIC ENERGY AGENCY, Defence in Depth in Nuclear Safety, INSAG-10, IAEA, Vienna (1996).

[10] INTERNATIONAL ATOMIC ENERGY AGENCY, Code of Conduct on the Safety of Research Reactors, IAEA, Vienna (2006).



Key areas of nuclear fuel cycle

ISOTHERMAL TRANSFORMATION KINETICS IN URANIUM MOLYBDENUM ALLOYS

S. SÄUBERT[1)], T. ZWEIFEL[1,2)], R. JUNGWIRTH[1)], M. HÖLZEL[1)], M. HOFMANN[1)], W. PETRY[1)]

1) Forschungs-Neutronenquelle Heinz Maier-Leibnitz (FRM II), Technische Universität München, Lichtenbergstr. 1, 85747 Garching bei München - Germany

2) CEA, DEN, DEC, Cadarache, F13108 Saint Paul Lez Durance - France

ABSTRACT

Exposing uranium-molybdenum alloys (UMo) retained in the γ-phase to elevated temperatures, transformation reactions set in during which the γ -UMo phase decomposes into the thermal equilibrium phases, i.e. U_2Mo and α-U.

The present work deals with the isothermal transformation kinetics in an U8wt.-%Mo alloy for temperatures between 400 °C and 525 °C and annealing durations of up to 48 h. Thereby, annealed samples were examined at room temperature using either high-energy X-Ray diffraction (HE-XRD) or neutron diffraction. The obtained diffraction patterns were analysed with Rietveld refinement and, hence, the phase composition after thermal treatment was determined.

Moreover, in-situ annealing studies using neutron diffraction were performed. These measurements delivered the onset of phase decomposition by observing the peak intensities as a function of annealing time, i.e. peak growth curvatures.

While for temperatures of 400 °C and 425 °C the start of decomposition is delayed, for higher temperatures the first signs of transformation are already observable before 3 h of annealing. Not only the onset of phase decomposition at lower temperatures is delayed, but also the transformation itself takes place at a much slower rate compared to higher temperatures. The typical C-shaped curves in a TTT-diagram for the start and end of phase decomposition, respectively, could be determined in the observed temperature regime. Therefore, a revised TTT-diagram for U8wt.-%Mo between 400 °C and 525 °C and of up to 48 h is proposed.

1. Introduction

In order to reduce the amount of highly enriched uranium (HEU) fuel in the civilian nuclear fuel cycle, efforts are made to develop a fuel with higher uranium density which would allow the conversion of research and test reactors from HEU to lower enrichment while maintaining an equivalent neutron flux and quality.

Since Uranium compounds like U_3Si_2 and UAl_x do not provide the Uranium density, which is needed to convert high-performance research reactors, a new fuel has to be developed. Pure metallic Uranium, which would offer the highest Uranium density possible, is known to show unfavourable behaviour during irradiation to high burn-up [1-4]. Only the γ-phase of uranium has adequate properties to be used as a nuclear fuel [1]. Both, UMo and UZrNb alloys retain the U γ

phase in a metastable state at room temperature and have a sufficient uranium density. However, UZrNb showed a poor performance during both, annealing and in-pile irradiation experiments under research reactor conditions [5].
In contrast, UMo alloy showed good irradiation behaviour in the past and allows sufficiently high uranium densities.
Hence, the UMo alloy, well-known since the 50s of the last century, is currently the subject of the renewed interest of the international research-reactor-fuel developing community. The addition of 7 wt.-% to 10wt.-% of Mo to the U is the best compromise between a high uranium density and a good γ-stability of the UMo. Nevertheless, the high temperatures to which the fuel element is exposed during the manufacturing process may lead to a decomposition of the UMo γ-phase into α-U and U_2Mo. Although it has been shown that the decomposition is reversed during in-pile irradiation [6-8], it is preferable to avoid it during the fuel plate production. Therefore, the precise dynamics of the γ-UMo phase decomposition needs to be understood. Since the available TTT diagrams are based on data from the 50ies and 60ies of the last century, a new study applying more modern techniques seemed to be advised.
Further, during the manufacturing process of the fuel elements, temperatures above the room temperatures can be present. Elevated temperatures lead to transformation reactions and hence a decomposition of the γ-phase into the thermal equilibrium micro- structures, i.e. α-U and U_2Mo. Therefore, neutron diffraction as well as high-energy X-ray diffraction studies at room temperature was performed on annealed samples in order to obtain detailed crystallographic information on the state of decomposition as a function of time and temperature. Additionally, in-situ annealing studies with neutron diffraction have been used for the investigation of peak growth behaviour and hence the transformation kinetics of single phases.

2. Experimental Techniques

2.1 Sample Preparation

All samples analysed in this work originate from the same U8wt.-%Mo ingot provided by *AREVA-CERCA*. The samples were cut down from the ingot and melted with an electric arc furnace and cast into a cylindrical shape. After that, all samples were homogenized at 900°C for 48 h and water quenched to room temperature. In doing so, it was ensured that only the γ-phase is retained in the entire specimen before heat treatment. The presence of a single phase γ-UMo has been verified by neutron diffraction analysis on one sample which has been prepared as described.

2.2 Heat Treatment

Depending on annealing duration and temperature, the decomposition of the γ-phase is in a different stage of transformation. Therefore, after the homogenization, the samples have been annealed for different temperatures between 400 °C and 500 °C and annealing times of either 3 h, 6 h, 16 h, 24 h or 48 h in order to get a grid of measurement points with various stages of γ-UMo phase decomposition. Fig. 1 shows the measurement points investigated during this work.

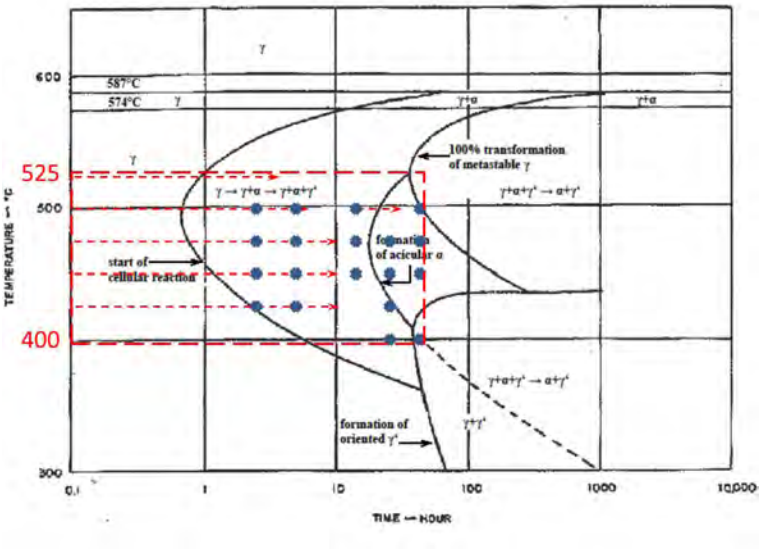


Fig. 1 TTT diagram of an U8wt.-%Mo alloy [9] where all measured samples are listed; highlighted in red is the temperature-time zone covered by the present work; i) blue dots: annealing time and temperature for the individual samples characterised at RT; ii) red arrow: neutron diffraction studies during in-situ annealing

2.3 Neutron Diffraction Experiments

Neutron diffraction experiments have been performed at the Forschungs-Neutronenquelle Heinz Maier-Leibnitz (FRM II) (Garching, Germany).

2.3.1 Crystallographic Phase Analysis

The study of the phase composition in pre-annealed samples has been performed at the High-Resolution Structure Powder Diffractometer SPODI at the FRM II. For the experiment, a germanium monochromator Ge(551) was chosen together with a take-off angle of 155 ° and a 5 m distance to the sample. The measurement of the NIST Si-640c standard along with a Rietveld refinement of the diffraction pattern determined the wavelength to λ = 1.548 Å. In total 12 samples have been analysed which were heat treated according to Fig. 1.

A diffraction pattern of each sample has been collected during a 15 min scan in order to get a first impression of the phase composition. With this information, the resolution has been chosen between 0.05 ° and 0.1 ° along with scan times between 6 h and 8 h. Data was collected in the angular range of [1.0 °; 151.8 °] 2θ, *i.e.* [0.006 $Å^{-1}$; 0.626 $Å^{-1}$] sin(θ)/λ.

2.3.2 In-Situ Annealing Studies

Diffraction studies on γ-UMo samples during in-situ annealing have been performed at the Materials Science Diffractometer STRESS-SPEC at the FRM II. For the experiment, a germanium monochromator Ge(311) and a 1.065 m distance to the sample was chosen. The measurement of the NIST Si-640c standard showed a wavelength of λ = 1.914 Å. Data was collected in the angular range of [37.8 °; 56.7 °] 2θ, *i.e.* [0.17 $Å^{-1}$; 0.25 $Å^{-1}$] sin(θ)/λ. Diffraction patterns were collected every 5 min. In total 6 specimens were investigated as shown in Fig. 1.

2.4 High-Energy X-Ray Diffraction Experiments

High-energy X-ray diffraction measurements have been carried out at the *Deutsches Elektronen-Synchrotron* (DESY) (Hamburg, Germany).

2.4.1 Crystallographic Phase analysis

The study of the phase composition in pre-annealed samples have been performed at the *High Energy Materials Science Beamline* (HEMS) at the *Positron-Electron Tandem Ring Accelerator III* (PETRA III) at the DESY. With an energy of E = 100 keV the wavelength is calculated to λ = 0.124 Å, which has been confirmed by the measurement with the NIST LaB_6-660a standard. In total 7 samples have been analysed which were heat treated according to Fig. 1.

Data was collected in the angular range of [0.0025 °; 7.6400 °] 2θ, i.e. [0.0004 $Å^{-1}$; 0.537 $Å^{-1}$] sin(θ)/λ.

3. Crystallographic Phase Analysis

3.1 Data Analysis

Diffraction data collected either by neutron or X-ray diffraction have been analysed using the *Rietveld Refinement Method* [10] and the *FullProf Suite* software package [11, 12]. Five phases have been included in the refinement process. Thereby, four of them describe the UMo-particles: γ-UMo-a, γ-UMo-b, α-U and U_2Mo. The γ-UMo-a represents the initial γ-phase and γ-UMo-b a molybdenum enriched γ-phase, which precipitates during the phase decomposition reactions. Hence, the latter phase has smaller lattice parameters. α-U and U_2Mo are the products of decomposition, whereas the α-phase can also be the distorted states α'-U or α''-U, dependent on the reaction temperature. Due to the inclusion of oxide and nitrite, one other phase has been added. Since UC and UN have the same space-group, *i.e.* Im-3m, and very similar lattice parameters, only one phase representing both of them has been included and named UC.

For the refinement, Pseudo-Voigt functions have been chosen to simulate the shapes of Bragg peaks. Selected background points and a linear interpolation between these points, rather than by mathematical functions, described the background. The steps include the refinement of scale factors, lattice parameters and peak shape parameters. Moreover, to improve the quality of the fit, the background points have been refined as well.

3.2 Crystallographic Composition

Since the Rietveld refinement method delivers quantitative information on the crystallographic composition in a sample, results from neutron diffraction and HE-XRD measurements can be directly compared.

Exemplary Rietveld refined diffraction patterns for both, HE-XRD and neutron diffraction, are shown in Fig. 2 and Fig. 3. Due to different wavelengths at the different instruments, the intensity is plotted over sin(θ)/λ rather than over 2θ in order to compare the diffraction patterns more easily. Neutron data extend to large values in reciprocal space. Both diffraction patterns were taken after annealing at 475 °C for either 16 h or 48 h. At this temperature the decomposition is already in an advanced stage after 16 h of annealing. In the time between 16 h and 48 h most of the remaining γ-UMo is decomposed into the equilibrium microstructures, i.e. α-U and U_2Mo.

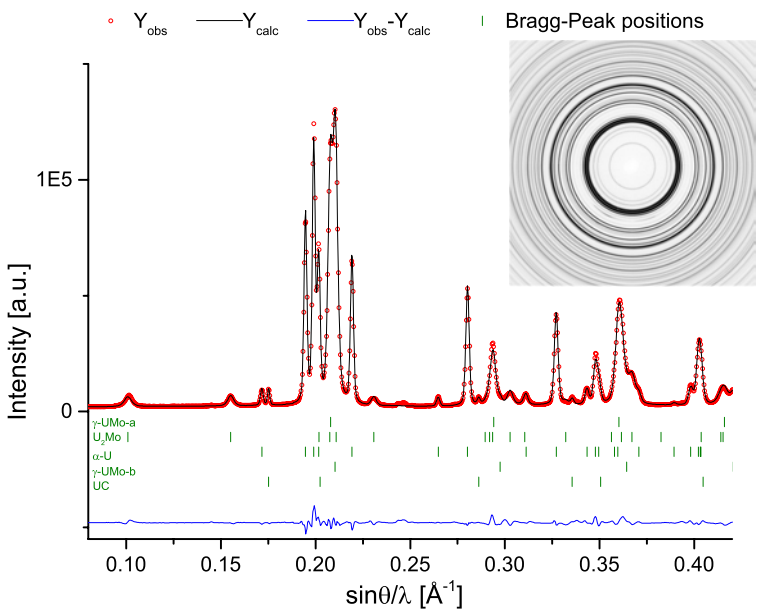


Fig. 2 Sample A-475C16h: γ-UMo decomposition after annealing at 475 °C for 16 h; sample investigated with HE-XRD; data analysed via Rietveld refinement

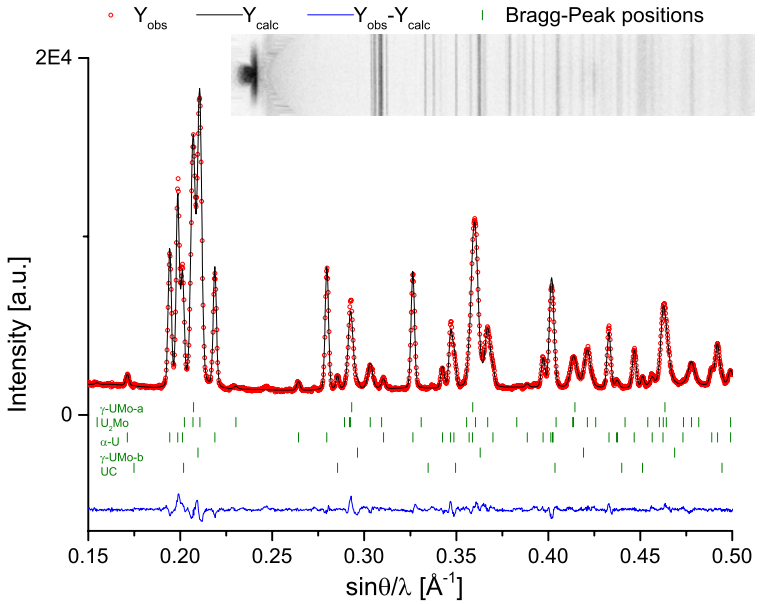


Fig. 3 Sample A-475C48h: γ-UMo decomposition after annealing at 475 °C for 48 h; sample investigated with neutron diffraction; data analysed via Rietveld refinement

Analysing severely decomposed materials gave insight on how advanced the γ-UMo decomposition is. The obtained data suggest that in the high temperature regime

(475 °C - 500 °C) the first products of decomposition are an enriched γ-UMo phase and α-U. Moreover, first signs of the formation of U_2Mo is observable. The decomposition starts early after reaching the designated temperature, which is indicated by the quite strong decomposition already after 3 h of annealing.
The decomposition takes place differently in the intermediate temperature regime (400 °C - 450 °C). While at 450 °C already a noticeable decomposition took place after 3 h of annealing, at the lower temperatures the beginning of phase decomposition is delayed. Not only the onset of phase decomposition is delayed, but also the transformation itself takes place at a much slower rate compared to higher temperatures.

4. In-Situ Annealing Studies

4.1 Data Analysis

The consecutive collected diffraction patterns, an example is shown in Fig. 4, have been analysed with *StressTextureCalculator* [13]. This software sequentially processes all diffraction patterns. It corrects the detector image via a dark measurement, allows subtracting the background and offers several possibilities for fitting the peaks.
The peak growth of a single peak was determined by observing the sum of intensities over an angular range as a function of time. Thereby, the angular range is the same for all diffraction patterns of one sequential measurement. This method was preferred over fitting each individual peak since the fit was not good for very small peaks, i.e. the beginning peak growth.

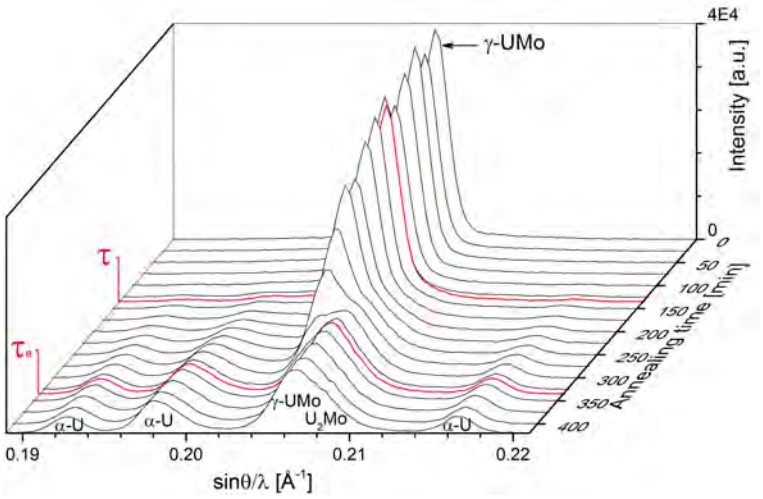


Fig. 4 Waterfall chart of the γ-UMo phase decomposition as a function of the annealing time at 500 °C; diffraction pattern for τ = 10 % and τ_e = 90 % are highlighted in red

The obtained peak growth curvatures were then analysed with a modified Avrami equation:

$$I(t) = \begin{cases} A(1 - \exp(-k(t - t_0)n)) + B & ; t > t_0 \\ B & ; t \leq t_0 \end{cases}$$

Where the parameters *n* and *k* describe the nucleation and growth process (for a detailed description of the nucleation and growth kinetics see [14, 15]), *A* is a scale factor for the intensity, *B* describes the background intensity and t_0, with a lower limit of $t_0 = 0$, was introduced in order to describe peak growth curvatures which not start at t = 0.
The peak intensity as a function of annealing time could only be described quantitatively for the α-U phase since, due to overlapping peaks, the quantitative extraction of the intensities of the other phases, i.e. the growth of U_2Mo and the decrease of γ-UMo, was not feasible.

4.2 α-U Phase Growth Kinetics

Peak growth curvatures were obtained for α-U at different temperatures indicated in Fig. 1. Based on the information obtained in these measurements, Avrami curves were calculated in order to determine the beginning and end of α-U phase growth as a function of annealing temperature. An exemplary peak growth is shown in Fig. 5.

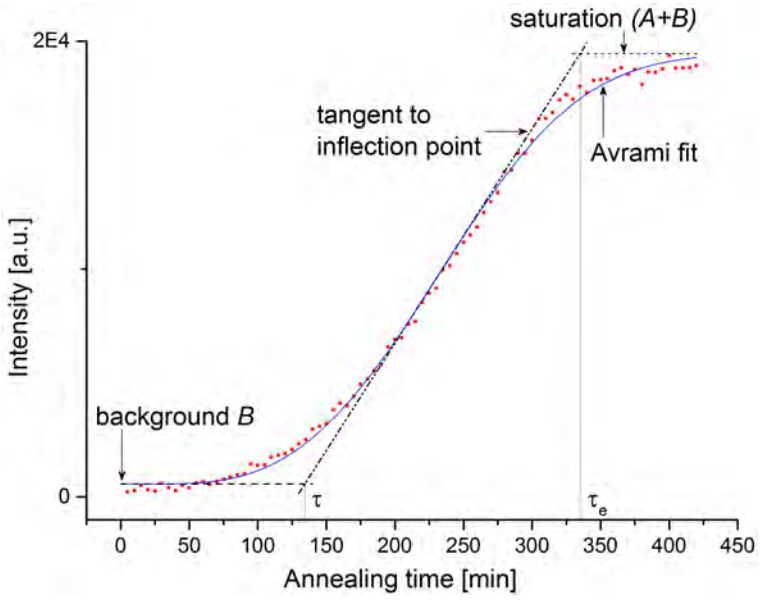


Fig. 5 Peak growth and Avrami curve for the $\alpha_{1\,1\,0}$-U phase during annealing at T = 500 °C

With the obtained fit parameters a definition for the times τ and τ_e was found by taking the intersection of the tangent to inflection point with the background and saturation, respectively. Moreover, with the Avrami equation any fraction of transformed phase can be calculated. Similar calculations were made for the individual measurements. The most important durations for transformed α-U as a function of annealing temperature are shown in Tab. 1.
The data shows the strong temperature dependence of the onset of phase decomposition. As expected the transformation starts earlier for higher temperatures, while it is delayed and much slower for lower temperatures.
After 10 h of annealing at 425 °C only the first signs of decompositions are visible. The collected data was not sufficient for the Avrami fit and, therefore, the beginning and end of peak growth could not be determined. Hence, data given for 425 °C only delivers an estimation for the beginning of phase decomposition.

Tab. 1 Overview over α-U growth depending on annealing temperature and time. t and τ indicate the weight fraction of α-U after the according annealing time. Data for 425 °C is estimated since the measurement time was insufficient to collect satisfying data.

Annealing Temp. [°]	**Fraction of transformed α-U; time in [min]**				
	t_0 = 1 %	**τ = 10 %**	**$t_{50\%}$ = 50 %**	**τ_e = 90 %**	**t_e = 99 %**
525	49	99	186	274	346
500	77	135	236	336	420
450	152	232	371	511	627
425	~360-420	~540-660	-	-	-

5. Discussion

The two experimental methods, crystallographic phase analysis and in-situ annealing studies, deliver information which can be combined in order to achieve quantitative information on the isothermal transformation kinetics in U8wt.-%Mo. While the performed in-situ annealing measurements determined the onset of phase decomposition as well as detailed information on the α-U phase growth, diffraction patterns at different points in time and temperature were used to derive the crystallographic phase composition at these points. Hence, in-situ measurements gave information on the time a phase starts to decompose, but not on the exact crystallographic composition as a function of time due to limited coverage in reciprocal space. Crystallographic phase analysis, on the other hand, delivered detailed information on the phase composition in the samples at a certain time and temperature, but none about how this state was reached. Therefore, a complementary consideration of both methods is required.

Comparing the growth curvatures with the data for crystallographic composition of annealed samples shows that, after the growth of the α-U peak has stopped as described by the S-shaped Avrami curve, the peaks intensity keeps growing with a linear like behaviour and much slower compared to the S-shaped growth. The linear-like growth approaches slowly the saturation of this phase.

Fig. 6 shows the α-U phase growth according to Tab. 1 and described by the Avrami equation. Since α-U is the first product of transformation, Fig. 6 describes the beginning of phase decomposition along with detailed information on α-U growth. Due to the limitations in analysing all other peaks within the angular range as detailed as α-U, the S-shaped growth of U2Mo was not observed.

Fig. 7 comprises the crystallographic phase composition at different measurement points. The data suggests that the S-shaped growth of U_2Mo and α-U starts together but rises differently. The growth of U_2Mo takes much longer. Comparing the data obtained for measurements on samples annealed for 24 h and 48 h, respectively, for the temperatures between 450 °C and 475 °C, suggest that U_2Mo keeps growing with a linear-like rise after the S-shaped growth. This is the same behaviour as observed for α-U. Therefore, the blue area drawn into Fig. 7 indicates

the beginning of the linear-like rise of U_2Mo and the approach to the end of phase decomposition since α-U already rises with a linear like behaviour.

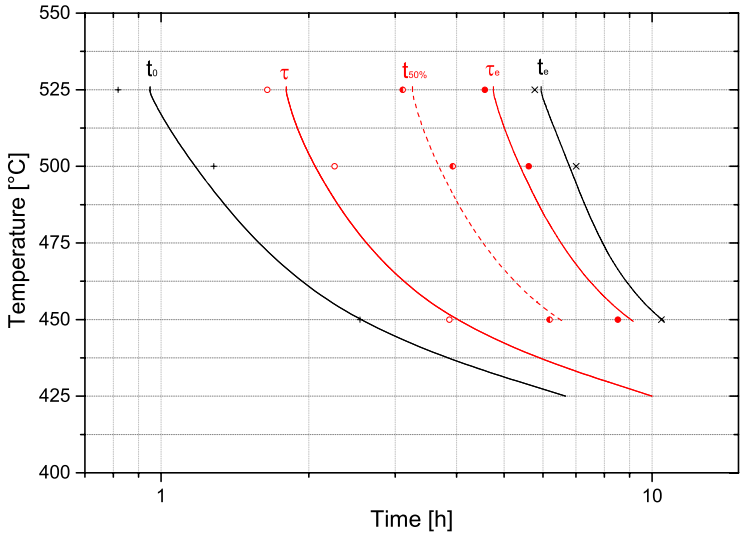


Fig. 6 Isothermal transformation curves for the α-U phase growth as determined by the Avrami equation

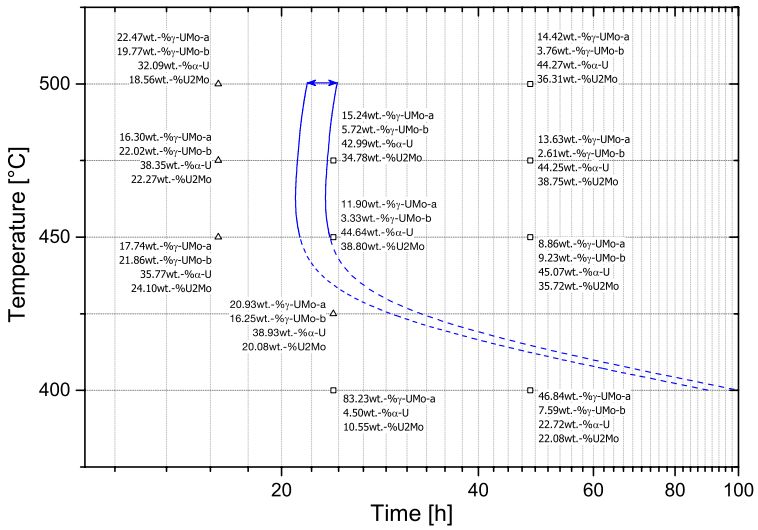


Fig. 7 Measuring points and their determined crystallographic composition along with the isothermal transformation curve describing the beginning of the linear-like rise of U_2Mo

This work complements previous similar experiments considering neutron diffraction of U-Mo/Al systems exposed to elevated temperatures between 400 °C and 475 °C and annealing times between 2 h and 52 h [16]. In the frame of this work, a wider range of annealing temperature and a more precise stepping in annealing time was considered in order to provide a more detailed investigation of growth kinetics.

Acknowledgements

The authors thank U.Bönberg from DESY's PETRA-III beamline for valuable help during the HE-XRD measurements.

Further, we gladly thank Herve Palancher from CEA Cadarache for valuable discussions and support during beamtimes and data treatment.

This study was supported by a combined grant (FRM0911) of the Bundesministerium für Bildung und Forschung (BMBF) and the Bayerisches Staatsministerium für Bildung und Kultus, Wissenschaft und Kunst (KM).

References

[1] B. Frost, *Material Science and Technology Volume 10A, Nuclear Materials.* 1994.

[2] G. L. Hofman et al., *Metallic fast reactor fuels.* In Brian Frost, editor, Material Science and Technology Volume 10A, Nuclear Materials, 1994.

[3] S. H. Paine et al., *Irradiation effects in uranium and its alloys.* Proceedings of the International conference on the peaceful uses of atomic energy, 1956.

[4] J. Rest et al., *Experimental and calculated swelling behaviour of U-10Mo under low irradiation temperatures.* Transactions of the RERTR, 1998.

[5] J. Snelgrove et al., *Development of very-high-density fuels by the RERTR program.* Transactions of the RERTR 1996.

[6] M. Bleiberg et al., *Phase changes in pile-irradiated uranium-base alloys.* Journal of Applied Physics, 27:1270-1283, 1956.

[7] S. Konobeevskii et al., *Effects of reactor radiation on the phase composition of low-alloyed uranium alloys.* Atomic Energy, 22:565-573, 1967.

[8] R. Jungwirth, *Irradiation behaviour of modified high-performance nuclear fuels.* PhD Thesis, Technische Universität München, 2011.

[9] P. E. Repas et al., *Transformation Characteristics of U-Mo and U-Mo-Ti Alloys.* Transactions of the American Society for Metals, 57:150-163, 1964.

[10] H. M. Rietveld, *A profile refinement method for nuclear and magnetic structures.* Journal of Applied Crystallography, 2:65-71, 1969.

[11] *FullProf Suite, Version 5.30, http://www.ill.eu/sites/fullprof/*, 2006.

[12] J. Rodríguez-Carvajal, *An introduction to the program FullProf.* Laboratoire Léon Brillouin (CEA-CNRS), 2001.

[13] C. Randau et al*., StressTextureCalculator: A Software Tool to extract Texture, Strain and Microstructure Information from Area-Detector Measurements.* Journal of Applied Crystallography, 44:641–646, 2011.

[14] J. W. Christian*, The theory of transformations in metals and alloys – Part I and Part II – Third Edition.* PERGAMON – An imprint of Elsevier Science, 2002.

[15] M. Avrami*, Kinetics of phase change I-III.* Journal of Chemical Physics, 1939-1941.

[16] H. Palancher et al*., UMo/Al nuclear fuel plate behavior under thermal treatment (425-550°C).* Powder Diffraction, 28:371–393, 2013.

UMo POWDER ATOMISED / HYDRIDED. COMPARISON BASED ON INTERACTION ANNEALING AND OUT-OF-PILE SWELLING TEST CONDUCTED ON DISPERSION TYPE MINIPLATES

LUIS OLIVARES, JAIME LISBOA, JORGE MARIN, MARIO BARRERA

Nuclear Materials Department
Chilean Commission for Nuclear Energy - CCHEN
95 Amunategui St., Postal Code 6500687
Santiago – Chile

JUAN CARLOS CHAVEZ
Office of Technical Cooperation and International Relations - CCHEN

ABSTRACT

UMo powder was produced by means of the Rotating Electrode Process - REP and using a laboratory system assembled at CCHEN. The powder particles, made of U + 7 wt% Mo alloy, exhibit morphologies near to spheres and multimodal size distribution, with 100 wt% below 150 µm and 19.9 wt% below 45 µm. Dispersion type miniplates with uranium densities between 6 and 8gU/cm^3 were manufactured using Al - 4wt% Si blend as matrix. For the highest density miniplates, typical defects as fishtail and stray particles were observed towards the ends, and thickening of the meat in the edges (dog bone).

This paper presents the results of an out-of-pile swelling test applied to a miniplate fabricated with highest density, and the results of the fuel/matrix interaction layer, IL, produced by an annealing at 500°C. The inspection of cross sections of particles by means of SEM reveals the formation of a thin IL after the fabrication processes. This IL and its evolution after 4 and 6,5 hours of annealing are shown and discussed. SEM+EDS microanalyses evidenced a strong fuel/matrix interaction characterized by the progressive growth of the IL. The swelling test reveals a total volume increasing close to 1,7% after 50 hours of annealing.

1. Introduction

Since 2003, CCHEN is working in a fuel development programme based on UMo alloys. The main milestones have been powder manufacturing by means of several techniques, and fabrication of dispersion type miniplates, and the main purpose of this programme has been the development of the manufacturing processes and inspection & evaluation methodologies [1].

To understand in advance the fuel behaviour into the reactor core, under irradiation fuel qualification and PIE examination are consider the proper tests to evaluate the interaction between UMo fuel and aluminium matrix [2]. Nevertheless, out-of-pile swelling test and interaction test, as alternative and previous tests [3], are methodologies generally accepted to characterise the behaviour of dispersion fuel plates subjected to controlled thermal treating aimed to activate atomic interdiffusion mechanisms involved in formation of the interaction layer, IL, and decomposition of UMo-γ (cubic gamma phase) [4], [5].

The results of SEM-EDS confirm the formation of an IL, for ground, hydrided and atomised powder. In any kind of UMo particles dispersed in Al – Si matrix, the interaction and IL formation with differences in morphology and composition, will occur. Besides powder size distribution and particle shape [6], there are others factors such as open and close porosity of particles, surface oxide layer, residual stress, among others, that will produce differences

in the performance of miniplates subjected to thermal treatments, before a qualification under irradiation [7]. This paper gives some of these differences based on experimental results.

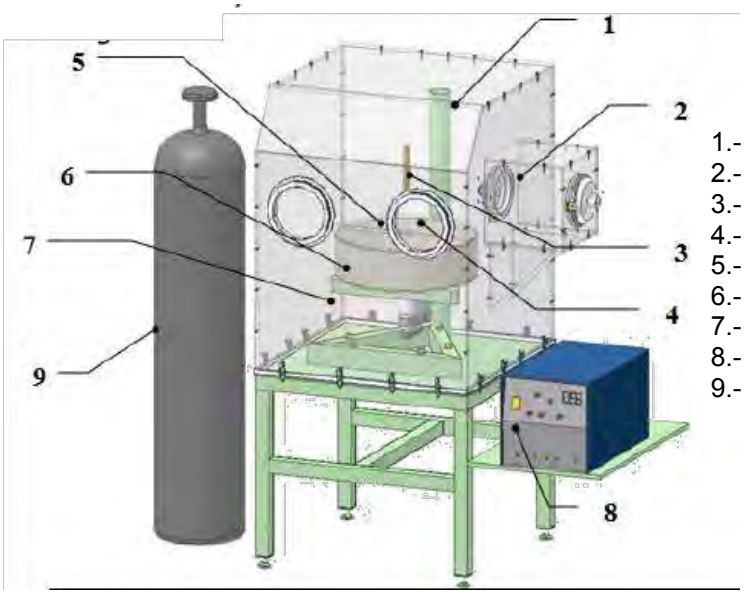
2. Experimental Methodology

2.1 Powder Preparation

UMo atomised particles were produced by the centrifugal atomisation of cylindrical bars or pins made of U-7wt% Mo cast alloy, previously obtained by means of induction melting of pure metals (Mo and U) and then poured into graphite mould, coated with alumina paint. Before atomisation, UMo pins were cleaned using a nitric acid solution, and were machined at one end to improve the alignment and to fit properly in a ¼" collet (Fig 1). The atomisation proceeded in a sealed glove box chamber with an argon atmosphere, shown in figure 2. The atomisation tests were carried out with rotational speed of 36000 RPM, with pin diameters of 6, 8 and 10 mm and an electrode currents of 40, 60 and 80 Amps, supplied by a TIG- AC/DC welding power supply. The characterisation of the atomised powder included granulometry analyses by sieving in Tyler series mesh, XRD for phase identification, and morphology and constitutional analysis by means of SEM with Energy Dispersive Spectroscopy (EDS) analyses.



Fig. 1.- At left, UMo pin in as cast condition ,and at right, the pin is placed in the collet at the centre of the collector chamber, ready for the atomisation by the Rotating Electrode Process



1.- Glove box
2.- Transfer port
3.- 5/32" Tungsten cathode
4.- Cover of the collection chamber
5.- Rotating pin electrode
6.- Collection chamber
7.- High speed motor
8.- Power supply
9.- Argon tank

Fig. 2. - Schematic of the centrifugal atomiser system

2.2 Miniplates Fabrication

The miniplates were manufactured by blending the UMo and Al-Si powders, followed by compacting, assembling (compact, covers and frame), welding, hot rolling, blister test, cold rolling and QC inspections. The miniplates were fabricated with uranium densities from 6.0 to 8.0 gU/cm^3. The powder mixture was compacted in a rectangular die of 18 x 22 mm. For all miniplates, the compacting pressure was 21 Tons applied to a 4 cm^2 area (564 MPa).

2.3 Miniplates characterisation

After completing the hot rolling process, the miniplates were subjected to a blister test annealing (480°C/30 min) and then, visually inspected. Meat metrology, inspection of manufacturing defects (stray particles, white points) and homogeneity in fuel distribution were done using radiographies. The meat/cladding bonding quality was verified by means of bending test and the cladding thickness was measured by an Eddy current technique. Metallographic cross sections taken from UMo-88 miniplate were used for direct measurements of the cladding – meat thickness through optical microscopy.

2.4 Out-of-Pile Swelling Test

The swelling was thermally induced by air annealing (350°C) of the UMo-89 entire miniplate. The original miniplate volume was measured by the Archimedes method at the beginning (as fabricated) and after 1 to 50 hours of annealing. The values of the volume increase in relation to the annealing time were included as data in a swelling graphic previously prepared with other UMo miniplates

2.5 Interaction Test

For the fuel/matrix interaction test, small samples were extracted from the meat zone of the UMo-88 miniplate. These samples were annealed to 500°C by 4 and 6,5 hours. After metallographic preparation, transverse cross sections of specimens in the as-fabricated condition and after the interaction annealing were inspected through SEM. The elemental composition of the interaction layers were revealed using energy dispersive X-ray spectroscopy (EDS) analysis

3. Experimental Results

3.1 Results of centrifugal atomisation

Details of the U-7% Mo pins preparation, atomisation and characterisation of powder has been presented in a previous paper [1].

The Centrifugal atomisation tests were carried out on five UMo pins with different diameters. Starting from a total amount of 185.9 g of UMo alloy, the weight of UMo powder produced was 140,3 g. After sieving and classification of the particles, the fuel powder used as source material for miniplates fabrication has the granulometry detailed in Table 1.

Table 1.- Granulometry of UMo atomised powder proper for fuel miniplates fabrication

Mesh (µm)	Material below	
	(g)	(%)
150	12.03	100.00
90	12.73	78.41
63	19.85	55.56
45	11.10	19.92
Total	55.71	

3.2 Results of the fabrication and inspection of miniplates

Table 2 summarizes the fabrication parameters for the complete batch of 6 miniplates. According to this information, the reduction rate was about 1:4, i.e, less than reduction values usually applied to U_3Si_2 plates (1:6 -1:7). Thereby, the total reduction applied to the UMo miniplates was in the order of 75%, lower than the applied to U_3Si_2 dispersion fuel plates, in which the total reduction is approximately 85%. When compared with miniplates made of hydrided UMo powder, the reduction rate and total reduction are slightly higher than those used for miniplates fabricated with hydrided UMo powder [8].

Table 2. Manufacturing parameters for miniplates based on atomised UMo powder

Miniplate Identification		UMo-84	UMo-85	UMo-86	UMo-87	UMo-88	UMo-89
						Interact test	Swelling test
Uranium density gU/cm^3		6,0	6,0	7,0	7,0	8,0	8,0
Fuel UMo Weight [g]		5,93	5,93	6,18	6,18	6,40	6,4
Matrix material weight (Al+4 wt% Si) [g]		1,52	1,52	1,27	1,27	1,05	1,05
Compacting Load [Tons.]		22	22	22	22	22	22
Volume of meat [cm^3]		1,12	1,13	1,05	1,05	0,99	1,00
Fuel volume fraction UMo		0,42	0,42	0,47	0,47	0,52	0,51
Matrix volume fraction Al-Si		0,50	0,50	0,45	0,45	0,39	0,39
Meat porosity (calculated) [%]		8,0	8,0	8,0	8,0	9,1	10,0
Miniplates measurements (preliminary cutting)	Length (mm)	129,49	130,22	130,92	131,04	130,33	129,64
	Wide (mm)	50,29	50,00	50,03	50,39	50,13	50,42
	Thickness (mm)	1,45	1,44	1,41	1,43	1,39	1,41
Thickness of assembly (before roll) [mm]		5,8	5,84	5,67	5,64	5,48	5,52
Total Reduction (%)		75,0	75,3	75,1	74,6	74,6	74,5
Reduction rate		1 : 4,00	1 : 4,06	1 : 4,02	1 : 3,94	1 : 3,94	1 : 3,91

3.3 Results of Out-of-pile Swelling Test

After 50 hours of annealing at 350°C, the miniplate manufactured with atomised UMo powder showed a volume increase of 1,7%, that is greater than the 0,68% volume increase measured for the miniplate prepared with UMo hydrided powder.

The blue line in the Figure 3 corresponds to the swelling detected in an UMo/Al miniplate based on UMo ground powder, without the addition of silicon in the matrix. Besides the positive effect of the silicon addition to the matrix on the swelling behaviour, this graphic shows that the miniplate made of atomised particles (red line) exhibits swelling values slightly higher than those measured for the miniplate based on hydrided UMo powder (purple line).

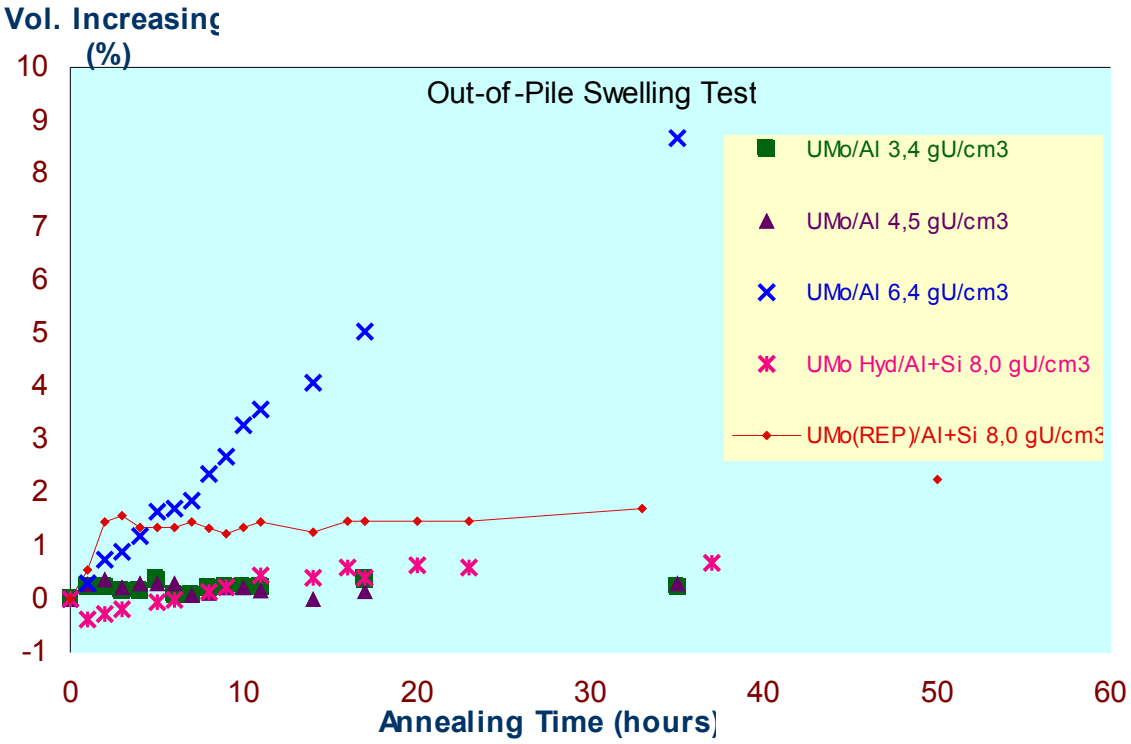


Figure 3. Out of pile thermal swelling applied to UMo miniplates

3.4 Results of Interaction Test

Based on SEM images shown in Figure 4, it is possible to compare the morphology of particles for hydrided and atomised UMo. These source materials exhibit irregular and spherical morphology respectively. In the atomised particles image is possible to observe the surface layer, composed mainly by uranium oxide, brittle and weakly adhered to particle.

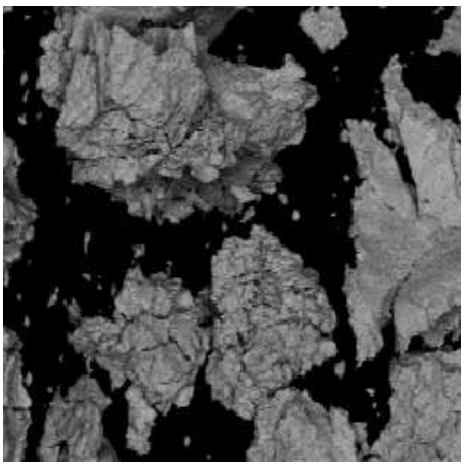
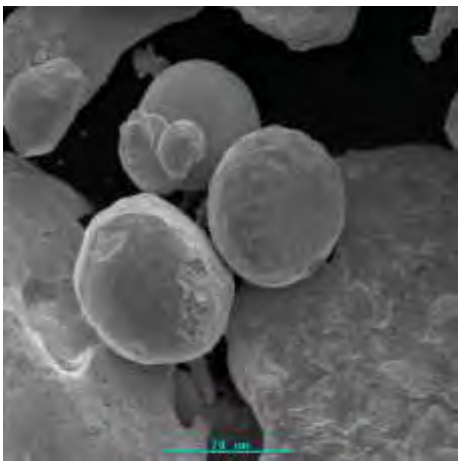
Source Material (UMo Powder)	
Hydriding – Dehydriding	Atomised (Rotating Electrode Process)
 500X	 500X

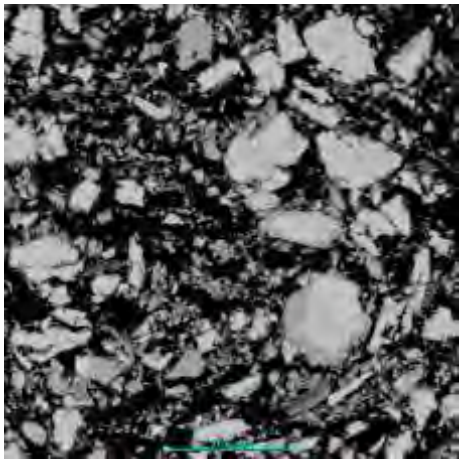
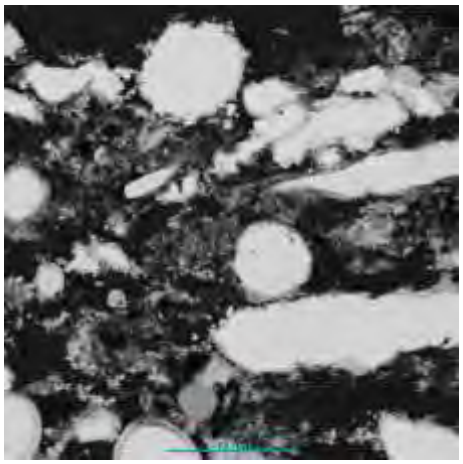
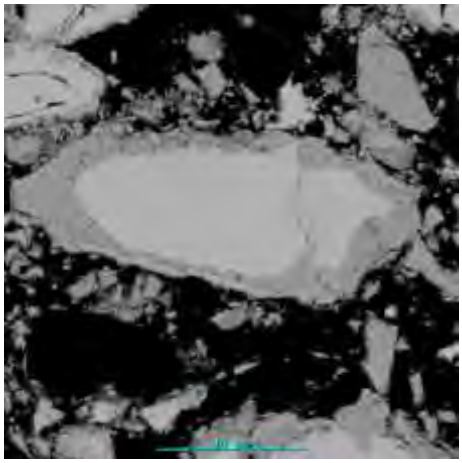
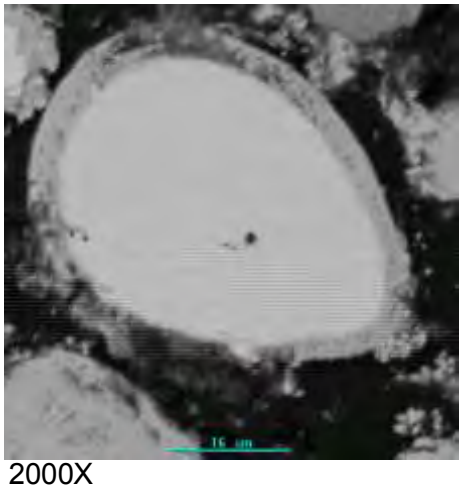
Figure 4. UMo particles fabricated at CCHEN. Left, by hydriding-dehydriding and at right, atomised by REP process

Figure 5 shows evidences of the early formation of the IL during the fabrication process of the miniplates, probably after annealing for hot rolling process and/or blister test. SEM micrographs of cross section specimens subjected to thermal treatments revealed some differences in performance of miniplates manufactured with each type of UMo particles. EDS analyses allowed to evaluate the effect of thermal treatment in the formation and evolution of the interaction layer. At the centre, the UMo particles exhibits practically the nominal composition, nevertheless in the IL, the contents of U, Al and Mo differs strongly between atomised and hydride condition.

In the as-fabricated condition, the atomised particles exhibited an IL with a homogeneous thickness around the particle surface, different to the irregular thickness of the IL formed in hydrided UMo particles. In both cases, the thickness of the IL is around 8 – 10 microns.

According to the information obtained from EDS analyses included in figures 5, 6 and 7, the aluminium content detected in the IL region for hydrided particles is higher than the same element detected in the IL for atomised UMo particles. Meanwhile, the uranium content present in the IL is lower for the hydrided particles than for the atomised particles.

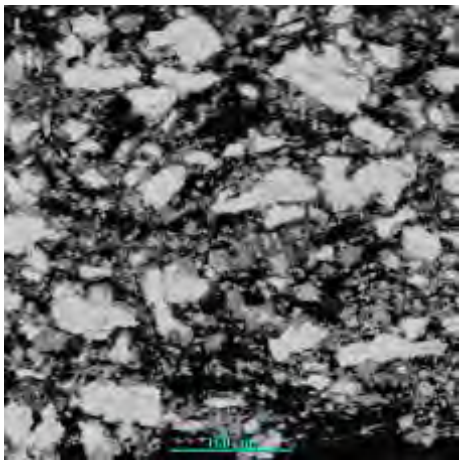
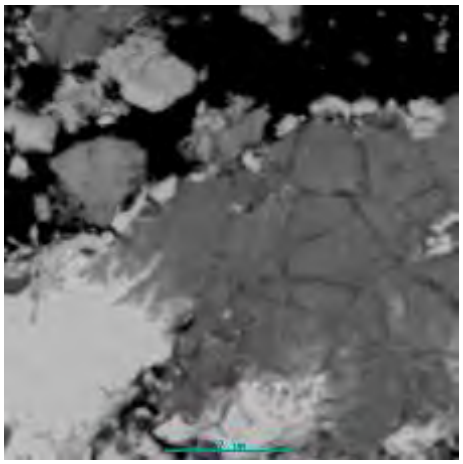
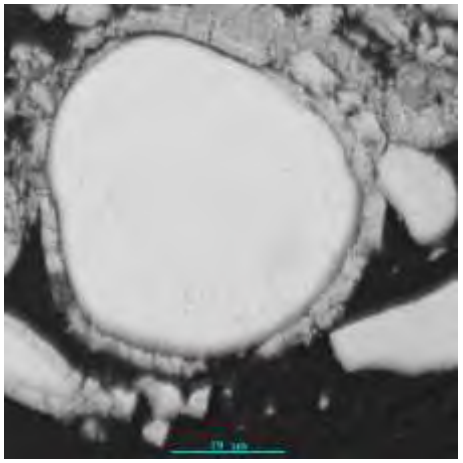
After the interaction annealing, the samples of atomised UMo particles exhibited an IL with important presence of open porosity, coalescence of pores, cracks and evidences of progressive detriment of particle integrity. These defects are less notorious in the IL of the hydrided particles, where the IL have a modified composition in relation to the particle core, but appears dense and without disintegration of particles.

As-fabricated (Sample of miniplate)					
Hydriding – Dehydriding (Miniplate UMo-54)			Atomised (Miniplate UMo-88)		
 200X			 500X		
 1000X			 2000X		
Composition at IL			Composition at IL		
Element	Atom %	Wt %	Element	Atom %	Wt %
Al	80.59	40.19	Al	5.47	0.69
Si	5.15	2.68	Si	4.88	0.36
Mo	2.13	3.77	Mo	0.32	0.14
U	12.13	53.36	U	89.33	98.81

Composition at centre of particle		
Element	Atom %	Wt %
Al	2.00	0.27
Si	6.22	0.50
Mo	13.44	6.42
U	78.34	92.82

Figure 5. SEM micrographs of UMo specimens of miniplates in as-fabricated condition

Annealed 4 hrs/500 °C

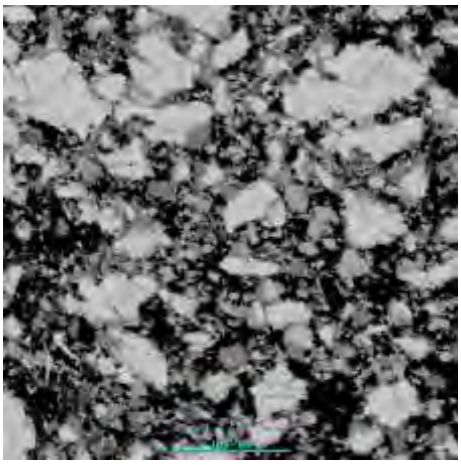
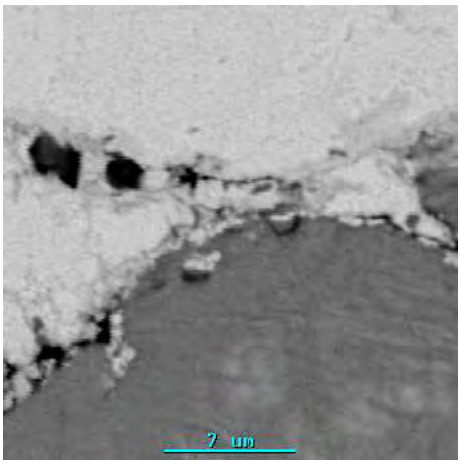
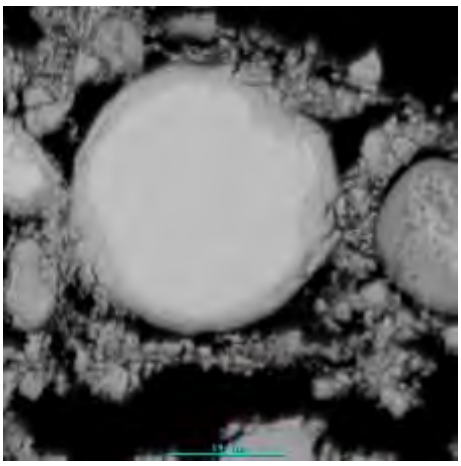
Hydriding – Dehydriding (Miniplate UMo-54)	Atomised (Miniplate UMo-88)
 200X  5000X	 1500X

Composition at IL (gray)			Composition at IL		
Element	Atom %	Wt %	Element	Atom %	Wt %
Al	66.65	25.55	Al	2.02	0.24
Si	10.33	4.12	Si	1.08	0.13
Mo	3.72	5.06	Mo	2.79	1.18
U	19.30	65.27	U	94.11	98.45

Composition in UMo particle (light)			Composition at centre of particle		
Element	Atom %	Wt %	Element	Atom %	Wt %
Al	2.85	25.55	Al	1.88	0.24
Mo	14.03	6.35	Si	1.21	0.16
U	83.12	93.29	Mo	11.68	5.22
			U	85.23	94.39

Figure 6. SEM micrographs of UMo specimens of miniplates after 4hrs/500 °C annealing

Annealed 6,5 hrs/500 °C

Hydriding – Dehydriding (Miniplate UMo-54)	Atomised (Miniplate UMo-88)
 200X  5000X	 1500X

Composition at IL (gray)			Composition at IL		
Element	Atom %	Wt %	Element	Atom %	Wt %
Al	64.39	26.06	Al	4.91	0.64
Si	15.93	7.71	Si	0.72	0.10
Mo	1.42	2.05	Mo	13.69	6.36
U	18.26	65.19	U	80.36	92.91

Composition in UMo particle			Composition at centre of particle		
Element	Atom %	Wt %	Element	Atom %	Wt %
Mo	13.05	5.70	Al	1.75	0.22
U	86.95	94.30	Si	0.88	0.11
			Mo	12.00	5.34
			U	85.36	94.32

Figure 7. SEM micrographs of UMo specimens of miniplates after 6,5 hrs/500°C annealing

4. Discussions and Conclusions

Although it was not possible to complete the IL characterisation with the analytical tools applied to this study, it is evident that the fuel/matrix interaction depends strongly of the surface condition of UMo particles. Some characteristics on the surface of the atomised UMo particles cause a high reactivity with Al/Si matrix.

The out-of-pile swelling test results indicates that this phenomena is present in an acceptable level for the atomised UMo particles; nevertheless the SEM/EDS results reveal an excessive interaction and interdiffusion in detriment of the UMo particle integrity.

The differences in composition of IL indicated by the EDS analyses for atomised and hydrided UMo particles could be an evidence of distinct types of compounds formed in these zones.

The results of this study confirm that is necessary to develop methodologies for the coating of the UMo particles, particularly for atomised powder.

5. References

[1] L. Olivares, J. Marin, M. Barrera, C. Gutierrez and J. Lisboa. ¨Dispersion fuel miniplates based on UMo powder produced by centrifugal atomization¨ Proceedings of RERTR 2012, Warsaw, Poland. October 2012.

[2] B. Miller, D. Keiser, JR., J. Gan, J. Jue, A. Robinson, P. Medvedev, M. Meyer and D. Wachs. ¨U7Mo alloy microstructure evolution during irradiation¨. Proceedings of RRFM 2013, Saint Petersburg, Russian Federation, April 2013.

[3] T. Zweifel, H. Palancher, A. Bonnin, F. Charollais, A. Leenars, S. Van Den Berghe, R. Jungwirth, W. Petryu and P. Lemoine ¨Study of Si and ZrN coated atomized particles using high energy XRD¨. Proceedings of RRFM 2012, Prague, Czech Republic, March 2012.

[4] H. Palancher, E. Welcomme, C. Sabathier, P. Partin, F. Mazaudier, C. Valot, S. Dubois, R. Tucoulou and P. Lemoine. ¨Characterisation of the interaction layer between decomposed UMo 7 and aluminium using micro-focused XRD on a single particle. Proceedings of RERTR 2008'', Washington, USA, October 2008.

[5] J. Allenou, X. Iltis, F. Charollais, M. C. Anselmet, O Tougait, M. Pasturel and P. Lemoine. ¨Effect of the addition of a third element in γ (U-Mo) fuel on the interdiffusion processes in U-Mo/Al-Si systems¨. Proceedings of RRFM 2010, Marrakech, Morocco, March 2010.

[6] R. Schenk, W. Petry, B. Stepnik, C. Jarousse, G. Bourdat, C. Moyroud, and M. Grasse. ¨FRM II/CERCA UMo atomised project status¨. Proceedings of RRFM 2013, Saint Petersburg, Russian Federation, April 2013.

[7] HERACLES Working Group ¨The development of disperse UMo as a high performance research reactor fuel in Europe¨. Proceedings of RRFM 2013, Saint Petersburg, Russian Federation, April 2013.

[8] L. Olivares, J. Marin, M. Barrera and J. Lisboa. ¨Microstructural characterization of dispersion fuel miniplates made of hydrided U + 7wt% Mo powder¨ Proceedings of RERTR 2010, Lisbon, Portugal, October 2010.

MODELING OF U-Mo FUEL SWELLING TO HIGH BURNUP

BEI YE, YEON SOO KIM, GERARD HOFMAN, JEFF REST

Nuclear Engineering Division, Argonne National Laboratory
9700 South Cass Ave, Argonne, IL 60439 USA

ABSTRACT

Acceleration of fuel swelling at high burnup (> $4x10^{21}$ fissions/cm^3) region in full-sized U-Mo/Al dispersion fuel plates has been observed in recent E-FUTURE and SELENIUM irradiation tests. This phenomenon is of great interest because the behavior of the fuel in the high burnup region of high performance reactors dictates the reliability of the fuel system under operating conditions. In order to interpret the fuel behavior at high burnup, the DART-THERMAL fuel performance code, developed at Argonne National Laboratory, has been utilized to simulate U-Mo fuel swelling up to very high burnup ($7.5x10^{21}$ fissions/cm^3). In previous studies, DART-THERMAL has demonstrated the capability to simulate U-Mo/Al dispersion fuel behavior of RERTR test fuel plates in the low burnup regime. As a fuel plate approaches high burnup, a fuel restructuring process occurs in which fuel grains become subdivided due to accumulated radiation damage (irradiation-induced recrystallization). In recrystallized fuel, fission gas bubble swelling is effectively enhanced due to the increased grain boundary area per unit volume. In order to capture this effect, a recrystallization model in the form of an Avrami equation has been implemented into DART-THERMAL. Fuel swelling was analyzed as a function of burnup. The results show good agreement with experimental data.

1. Introduction

Recent SELENIUM post-irradiation examination (PIE) results reveal that U-Mo dispersion fuel plates experience an increase in swelling rate at a burnup of > $4.5x10^{21}$ fissions/cm^3 (shown in Figure 1). This acceleration of fuel swelling can be explained by enhanced fission gas bubble growth resulting from a recrystallization process [1]. During this restructuring process, fuel grains are subdivided, which effectively enhances fission gas bubble swelling due to increased grain boundary area per unit volume [2]. Measured swelling by gas bubbles is shown in Figure 2. It is exhibited from the comparison of Figure 1 and 2 that both fuel swelling and fission gas swelling show acceleration at a burnup of ~ $4.5x10^{21}$ fissions/cm^3. Such similarity indicates that increased fission gas swelling causes rise of fuel swelling at high burnup.

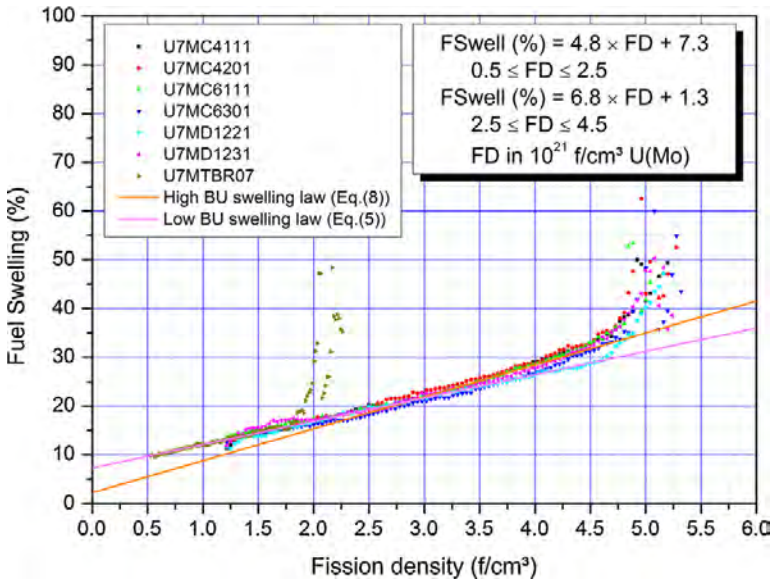


Figure 1. Fuel swelling versus fission density for SELENIUM and E-FUTURE plates [1].

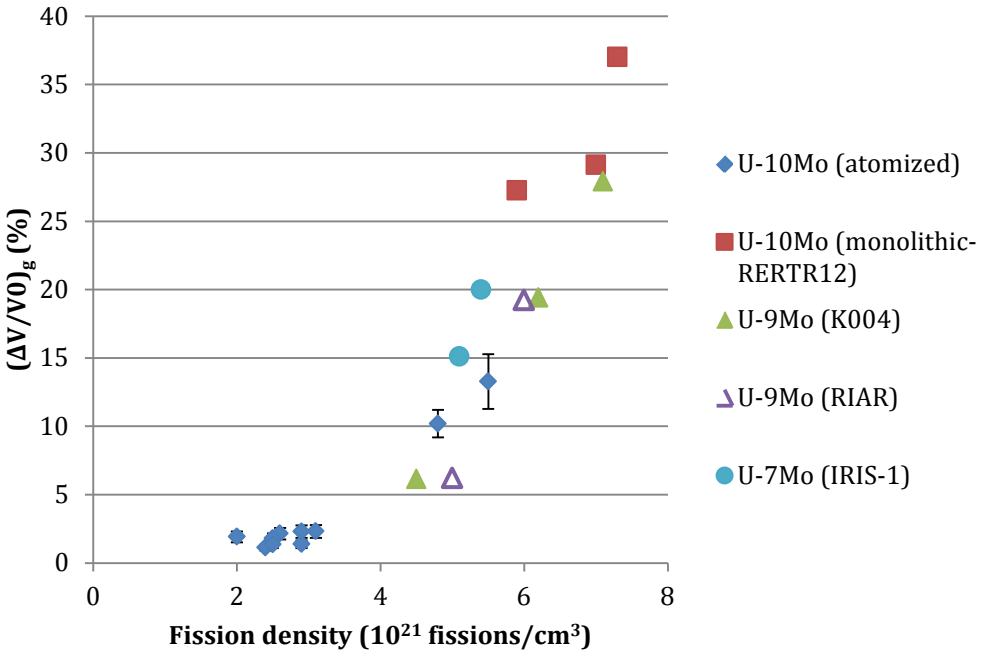


Figure 2. Fission gas bubble swelling versus fission density

The fuel recrystallization process has been observed not only in U-Mo fuels, but also in oxide fuels at high burnup. The driving force for recrystallization is the accumulation of interstitial loops due to irradiation. The grain subdivision process has been observed to start along the preexisting grain boundaries, progress toward the grain center and eventually consume the entire grain [3].

In order to simulate fuel swelling behavior in U-Mo fuel at high burnup, DART-THERMAL, the dispersion fuel performance code developed at ANL [4, 5], has been updated with a recrystallization correlation in [2]. Analysis of U-Mo fuel swelling at high burnup was carried out using the updated computation code. This paper describes the recrystallization model

implemented in DART-THERMAL, and the comparison between modeling results and measurement data.

2. Recrystallization model

A modified Avrami equation was used to describe the recrystallization process in the recrystallization model in [2]. The Avrami equation is commonly used to express the evolution of a new phase as a function of time [6], and the recrystallization process is similar to typical phase transformation reactions. Therefore, it is reasonable to describe the recrystallization process with an Avrami equation. The modified Avrami equation is given as follows [2]:

$$V_{rx} = 1 - \exp[-K(F - F_0)^n] \qquad (1)$$

where V_{rx} is the fuel volume fraction with subdivided grains, K is the recrystallization reaction constant, F is the fission density in 10^{21} fissions/cm^3, and F_0 is the incubation fission density in 10^{21} fissions/cm^3 below which recrystallization does not occur, and n is the Avrami exponent that is dependent upon the recrystallization nucleation and growth mechanism.

Constants K, F_0, and n were determined by fitting with experimental data in Figure 3, and their values are as follow:

$n = 2.6$;

$F_0 = 1.67$ for atomized powder fuel, and $F_0 = 1.38$ for ground power fuel;

$K = 0.1 \times [0.75(10 - x_{Mo}) + 1]$ where x_{Mo} is the Mo content in wt.%.

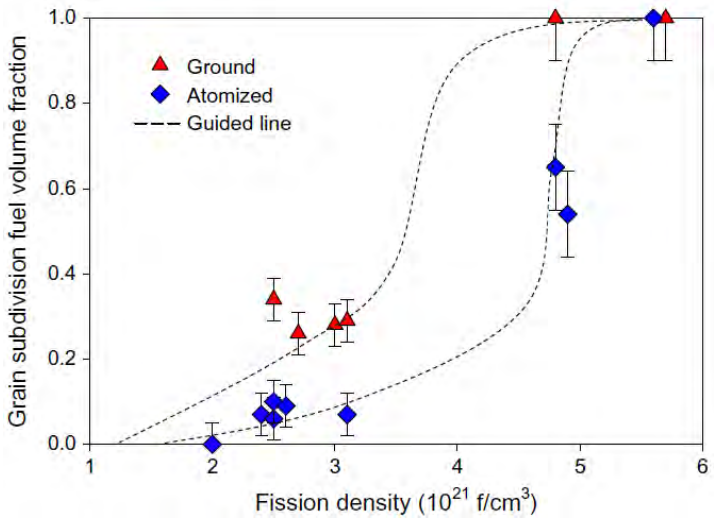


Figure 3. Measured recrystallized fuel volume fractions of U-10Mo [2].

When the correlation was implemented in DART-THERMAL, the incubation fission density F_0 was adjusted in order to reflect the different recrystallization behavior in U-7Mo and U-10Mo fuels. The adjustment details are described in Section 4.

3. Implementation approach

In DART-THERMAL, each fuel particle is divided into *n* shells with either equal volume or equal thickness, and recrystallization progresses shell by shell in a fuel particle. At each time step, the code checks each shell to determine if it becomes recrystallized. The detailed procedure is depicted in Figure 4.

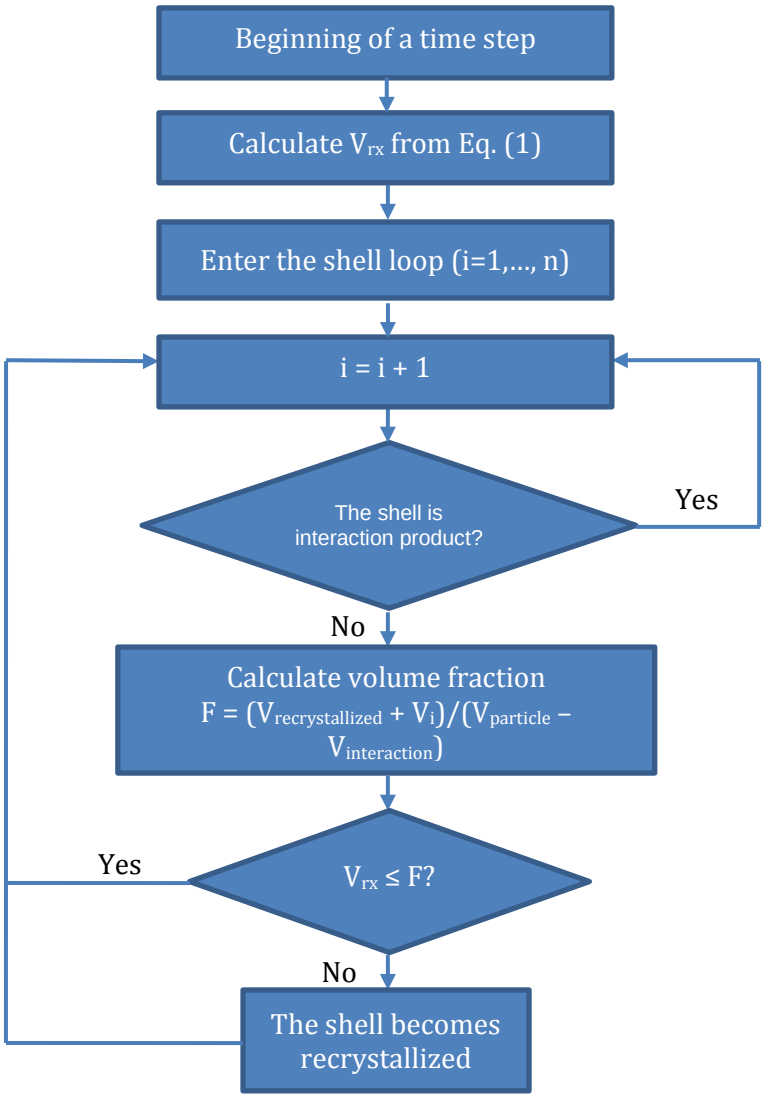


Figure 4. Flow chart of recrystallization progress in DART-THERMAL.

4. Fuel swelling calculation

The fuel phase swelling $(\frac{\Delta V}{V_0})_f$ calculation in DART-THERMAL is composed of two parts: fission-gas-bubble swelling $(\frac{\Delta V}{V_0})_g$ and solid fission product swelling $(\frac{\Delta V}{V_0})_{sp}$. Fission-gas-bubble swelling is calculated with a rate-theory fission gas behavior model [4, 5]. In this model, gas bubbles are grouped into many size classes, and the bubble size distribution inside grains and on grain boundaries is calculated. The swelling by fission-gas-bubble is the total volume of gas bubbles distributed at different locations (lattice, grain boundaries and triple points) and in all size classes. Before recrystallization starts, the majority of $(\frac{\Delta V}{V_0})_g$ comes from bubbles within grains. Subdivision of fuel grains results in an increased number of gas bubbles at grain boundaries and triple points. At the same time, substantial growth of intergranular gas bubbles occurs due to shortened gas atom diffusion distance from the center of a fuel grain to its boundary. These changes eventually lead to a significant increase of $(\frac{\Delta V}{V_0})_g$.

In the current calculations, solid fission product swelling is estimated to be:

$$(\frac{\Delta V}{V_0})_{sp} = 2.5F_d \qquad (2)$$

where $(\frac{\Delta V}{V_0})_{sp}$ is in %, and F_d is fission density in 10^{21} fissions/cm^3. There is no direct measurement data for swelling by solid fission products. Their existence status in fuel materials is not clear either. Some fission products can combine with lattice atoms to form compounds, and others might precipitate out to become an additional phase. Estimates can be made based on the atomic volume differences between solid fission products and uranium atoms. Hofman and Walters [8] estimated non-soluble fission products contribute 1.18% per burnup to fuel swelling in U-Pu-Zr fuel. Kim and Hofman [7] estimated $(\frac{\Delta V}{V_0})_{sp} = 4.0F_d$ for U-10Mo monolithic fuel, which includes swelling by very small gas bubbles (< 0.1 μm in diameter). Thus, $(\frac{\Delta V}{V_0})_{sp}$ can vary in a small range of 2.0 – 4.0% per 10^{21} fissions/cm^3. In DART-THERMAL calculations, swelling by small gas bubbles (< 0.1 μm in diameter) has been taken into account in $(\frac{\Delta V}{V_0})_g$, so $(\frac{\Delta V}{V_0})_{sp}$ is adjusted to be $2.5F_d$ to fit the experimental data.

In Eq. (1), the same onset fission density of recrystallization F_0 is applied for U-7Mo and U-10Mo fuels. However, grain subdivision in U-7Mo fuel may start earlier according to experimental observation (as shown in Figure 5). Therefore, it is valid to use a smaller F_0 value

for U-7Mo fuel than U-10Mo fuel. In current calculations, onset fission densities of $1.7x10^{21}$ fissions/cm^3 and $2.7x10^{21}$ fissions/cm^3 are used for U-7Mo and U-10Mo fuel respectively.

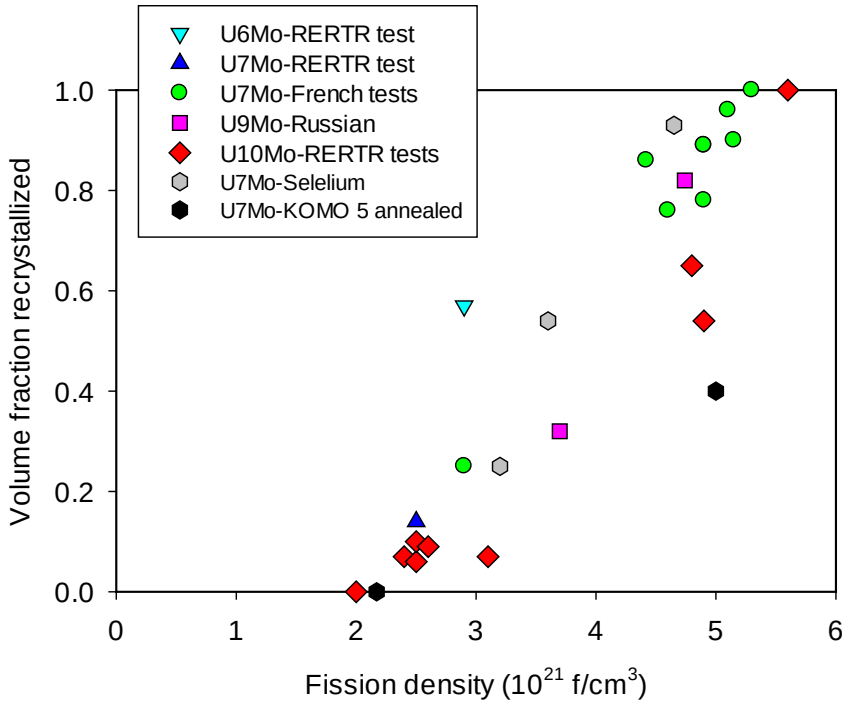


Figure 5. Measured volume fraction of recrystallized fuel versus fission density

5. Results

Calculated fuel swelling as functions of burnup for U-7Mo and U-10Mo fuels are shown in Figure 6, and they are compared with experimental data. The experimental data in Figure 6 were measured either from monolithic fuel or from dispersion fuel containing coated particles. In these fuel plates, interaction layer formation has a very minor effect on fuel swelling. Therefore, the interaction layer growth model was turned off in these calculations in order to obtain comparable irradiation conditions with experimental conditions. Reasonable agreement between experimental data and calculation results are seen in Figure 6, which show that DART-THERMAL is able to simulate fuel swelling behavior by using the empirical recrystallization model described in Section 2 with minor modifications. The results in Figure 6 confirm that U-10Mo fuel has a better swelling performance than U-7Mo fuel.

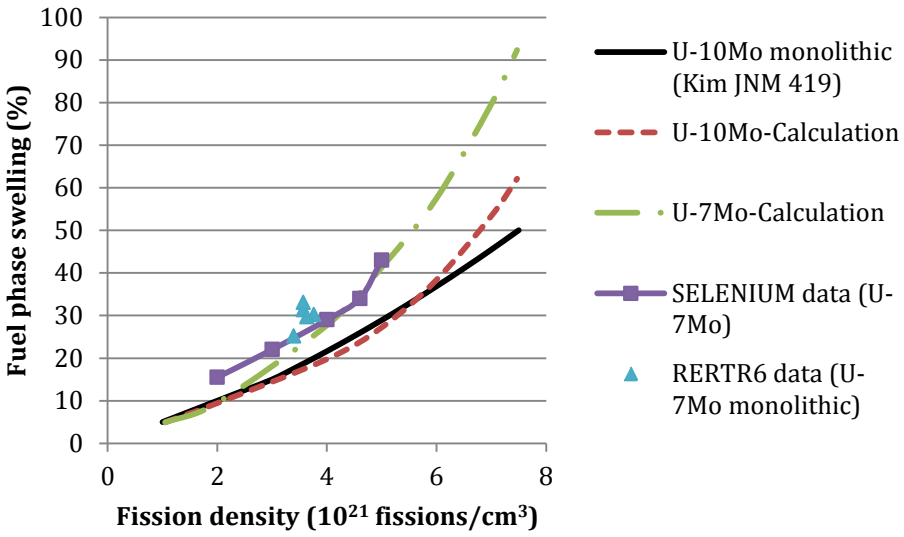


Figure 6. Comparison of calculated and experimental data for U-Mo fuels with various Mo contents.

In order to show the potential impact on fuel swelling behavior by using annealed fuel particles, a preliminary analysis was carried out. During annealing treatment, the average grain size in fuel particles increases and the grain boundary area per unit volume decreases, so that the number of recrystallization nucleation sites decreases. As such, it is reasonable to expect a lower rate of recrystallization with larger grain size. The annealing process also removes pre-existing defects within fuel grains, which leads to the ease of internal stresses caused by lattice displacement. Accordingly, the initiation of recrystallization delays at the same irradiation conditions.

Based on these analyses, two parameters in Eq. (1) need to be adjusted in order to simulate the annealing effect: a smaller exponential factor n to reflect a lower progression rate, and a larger incubation fission density F_0 to represent the delay of recrystallization. However, there are no sufficient experimental data to fit n and F_0 for annealed fuel particles. Therefore, a parameter sensitivity study was carried out, and the results are depicted in Figure 7. These results show that fuel phase swelling can be reduced by either decreasing n or increasing F_0. This preliminary analysis demonstrates that using annealed fuel particles can help improve fuel swelling. In order to simulate the annealing effect more accurately, it is necessary to obtain more measurement data for the model development. Additionally, a theoretical model of U-Mo recrystallization [3] which includes grain size effect will be implemented in the future development of DART-THERMAL.

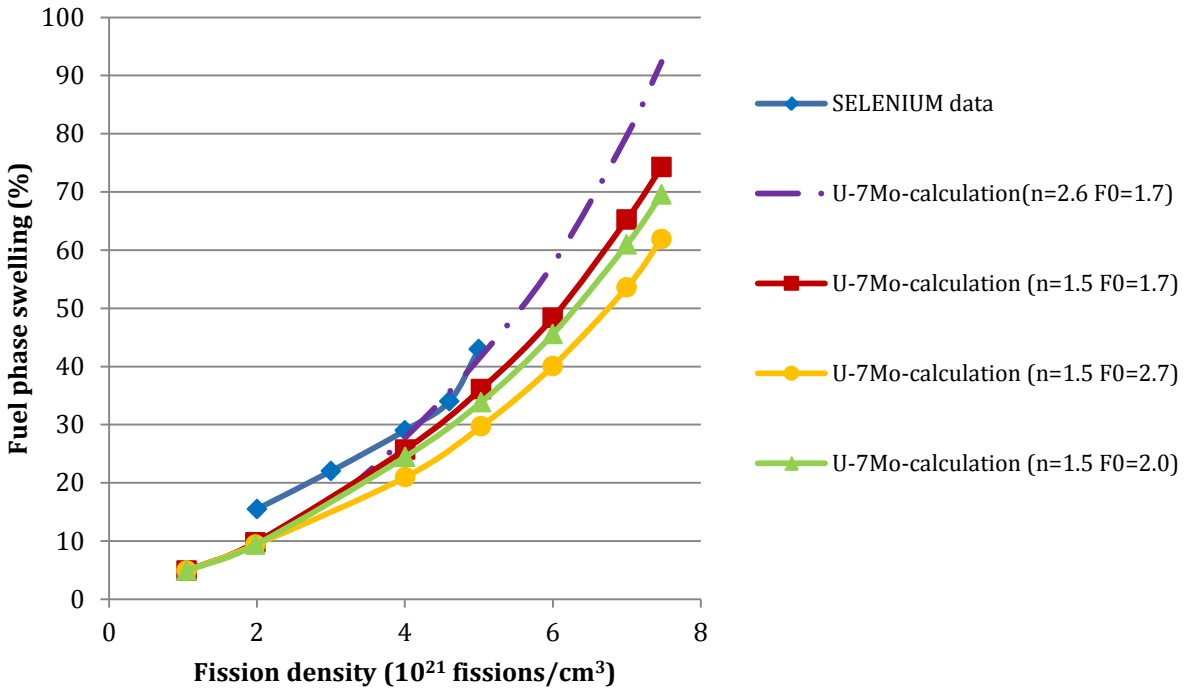


Figure 7. Calculation results for U-7Mo fuel with various *n* and F_0.

6. Conclusion

A recrystallization model describing the recrystallized fuel volume fraction as a function of burnup has been implemented into DART-THERMAL. The model is expressed in the form of an Avrami equation, and the constants in the model were fitted based on experimental measurements. With the implementation of the recrystallization model, DART-THERMAL is able to simulate U-Mo fuel swelling behavior at high burnup (> 4.5×10^{21} fissions/cm^3). Swelling of U-Mo fuels with various Mo contents (7-10 wt.%) were calculated up to 8×10^{21} fissions/cm^3. The calculation results are in reasonable agreement with the PIE data obtained from SELENIUM test U-7Mo fuel and RERTR tests U-10Mo monolithic fuel. The calculations also suggest that fuel swelling can be improved by the use of annealed U-Mo powder.

Acknowledgements

This work was supported by the U.S. Department of Energy, Office of Global Threat Reduction (NA-21), National Nuclear Security Administration, under Contract No. DE-AC-02-06CH11357 between UChicago Argonne, LLC and the Department of Energy.

This work is supported by the U.S. Department of Energy, Basic Energy Sciences, Office of Science, under contract # DE-AC02-06CH11357. The submitted manuscript has been created by UChicago Argonne, LLC, Operator of Argonne National Laboratory ("Argonne"). Argonne, a U.S. Department of Energy Office of Science laboratory, is operated under Contract No. DE-AC02-06CH11357. The U.S. Government retains for itself, and others acting on its behalf, a paid-up nonexclusive, irrevocable worldwide license in said article to reproduce, prepare derivative works, distribute copies to the public, and perform publicly and display publicly, by or on behalf of the Government.

Reference

[1] S. Van den Berghe, Y. Parthoens, G. Cornelis, A. Leenaers, E. Koonen, V. Kuzminov, C. Detavernier, J. Nucl. Mater. 442 (2013) 60-68.
[2] Y.S. Kim, G.L. Hofman, J.S. Cheon, J. Nucl. Mater. 436 (2013) 14-22.
[3] J. Rest, J. Nucl. Mater. 346 (2005) 226-232.
[4] J. Rest, ANL-95/36 (1995).
[5] B. Ye, J. Rest, Y.S. Kim, ANL/GTRI/TM-13/3 (2013).
[6] M. Avrami, J. Chem. Phys. 7 (1939) 1103.
[7] Y.S. Kim, G.L. Hofman, J. Nucl. Mater. 419 (2011) 291-301.
[8] G.L. Hofman, L.C. Walters, in: R.W. Cahn, P. Haasen, E.J. Kramer (Eds.), Materials Science and Technology A Comprehensive Treatment, in: Brian R.T. Frost (Ed.), Nucl. Mater., Vol. 10A, Weinheim, Newyork, 1994, P. 25.

SEM CHARACTERIZATION OF THE HIGH BURN-UP MICROSTRUCTURE OF U-7MO ALLOY

D. KEISER, JR., B. MILLER, J. JUE, J. GAN, A. ROBINSON, P. MEDVEDEV, J. MADDEN, M. TEAGUE, AND D. WACHS

Nuclear Fuels and Materials Division, Idaho National Laboratory
P. O. Box 1625, Idaho Falls, ID 83415-6188 U.S.A.

Corresponding Author Contact Information:
Dennis D. Keiser, Jr.
Idaho National Laboratory
P.O. Box 1625
Idaho Falls, ID, 83415-6146 U.S.A.
Phone: 1 (208) 533-7298
Fax: 1 (208) 533-7863
E-mail: Dennis.Keiser@inl.gov

For Publication in the Proceedings of the *Research Reactor Fuel Managment Conference*

(March 30-April 3, 2014 in Ljubljana, Slovenia)

This manuscript has not been published elsewhere
and has not been submitted simultaneously for publication elsewhere.

SEM CHARACTERIZATION OF THE HIGH BURN-UP MICROSTRUCTURE OF U-7MO ALLOY

D. KEISER, JR., B. MILLER, J. JUE, J. GAN, A. ROBINSON, P. MEDVEDEV, J. MADDEN, M. TEAGUE, AND D. WACHS

Nuclear Fuels and Materials Division, Idaho National Laboratory
P. O. Box 1625, Idaho Falls, Idaho 83403 USA

ABSTRACT

During irradiation, the microstructure of U-7Mo evolves until at a fission density near $5x10^{21}$ f/cm^3 a high-burnup microstructure exists that is very different than what was observed at lower fission densities. This microstructure is dominated by randomly distributed, relatively large, homogeneous fission gas bubbles. The bubble superlattice has collapsed in many microstructural regions, and the fuel grain sizes, in many areas, become sub-micron in diameter with both amorphous fuel and crystalline fuel present. Solid fission product precipitates can be found inside the fission gas bubbles. To generate more information about the characteristics of the high-fission density microstructure, three samples irradiated in the RERTR-7 experiment have been characterized using a scanning electron microscope equipped with a focused ion beam. The FIB was used to generate samples for SEM imaging and to perform 3D reconstruction of the microstructure, which can be used to look for evidence of possible fission gas bubble interlinkage.

1. Introduction

The Global Threat Reduction Initiative Fuel Development program is developing low-enriched uranium (LEU) fuel to reduce the demand of highly-enriched uranium (HEU) fuels currently used in research and test rectors throughout the world [1,2]. One fuel type is a U-Mo dispersion fuel. In order to support qualification of the fuel, it is critical to understand changes in the fuel microstructure due to irradiation [3]. One area of particular interest is the characteristics of the high-burnup microstructure. Recently, it has been observed that the EFUTURE and SELENIUM experiments exhibited a relatively large change in swelling behavior above 4.6 $x10^{21}$ f/cm^3 [4-6], and one potential cause of this behavior is a significant change in the swelling behavior of the U-7Mo fuel particles themselves at fission densities above this value. To improve understanding of characteristics of the U-7Mo microstructure at this high level of fission density, three fuel plates were characterized at their highest fission density regions using a scanning electron microscopy (SEM) and a focused ion beam (FIB) insitu lift out (INLO) technique for sample preparation. SEM analysis of FIBINLO samples was performed to investigate the size, morphology, and distribution of fission gas bubbles and solid fission product phases. The FIB was also employed to generate sample cubes that could be employed to perform a 3D reconstruction of the microstructure. A companion paper reports the results of TEM characterization of high fission density samples [7].

2. Experimental

The dispersion fuel plates that were characterized were irradiated in the Advanced Test Reactor as part of the RERTR-7A experiment. During irradiation, the plates were oriented edge on facing the core. This led to a significant fission rate variation across the plates. This provided a variation in fission densities across individual plates. Samples were produced from the high fission density side of three fuel plates (see Table 1) at the Hot Fuels Examination Facility (HFEF) at the Idaho National Laboratory in the form of 1-mm-diameter

by 1.4-mm-long fuel punchings. The samples were mounted and polished at the Electron Microscopy Laboratory for sample preparation and analysis in the scanning electron microscope (SEM). Both secondary electron (SE) and backscattered electron (BSE) images were produced from the polished samples. Additional characterization samples were produced from the mounted samples using a FEI Quanta3D Dualbeam FIB. The first step when generating a FIB sample is to deposit a Pt protective layer on the sample surface to reduce curtaining and minimize damage to the specimen surface during milling operations. This is followed by the generation of "lift-outs", which are ultimately obtained at specific locations by coarse trenching a 20 µm x10 µm x 1 µm sample. Figure 1 shows a polished surface for the R2R040 sample where six FIBINLO samples were produced for characterization. SE imaging was employed to evaluate the the size, morphology, and distribution of fission gas bubbles and solid fission product phases present in these samples. To produce information for 3D reconstruction, cubes ~(20 µm x 20 µm x 25 µm) were produced from the U-7Mo for each of three samples. Tens of nanometers of material was milled at a time from the cube, and an SEM image was produced after each milling step. The hundreds of images that were generated were used in combination with a software program to produce 3D reconstruction information.

Table 1: Calculated irradiation parameters for R3R050, R0R010, and R2R040 SEM samples

Sample	Heat flux, W/cm^2		Temperature, ^{o}C		Fission Density, fissions/cm^3	Average fission rate density, fissions/cm^3-s	Matrix
	BOL*	EOL**	BOL	EOL			
R3R050 (High flux)	267	227	124	136	5.2 x 10^{21}	6.6 x10^{14}	AA4043***
R0R010 (High flux)	282	245	119	125	5.6 x 10^{21}	7.2 x 10^{14}	Al
R2R040 (High flux)	337	307	121	119	6.3 x 10^{21}	8.1 x 10^{14}	Al-2Si

*Beginning-of-Life; **End-of-Life; ***Nominal composition (wt.%): (4.53Si-0.14Fe-0.09Cu-0.04Ti-0.01Zn-0.008Mg-balAl)

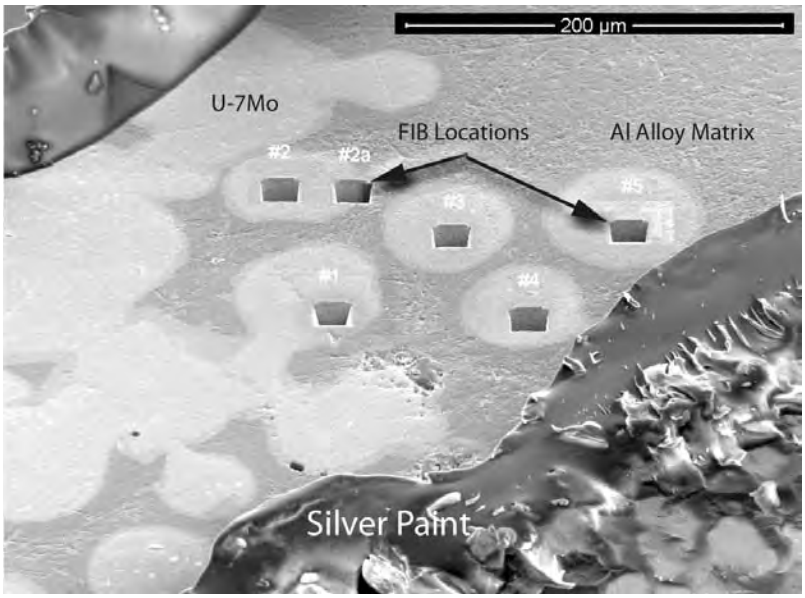
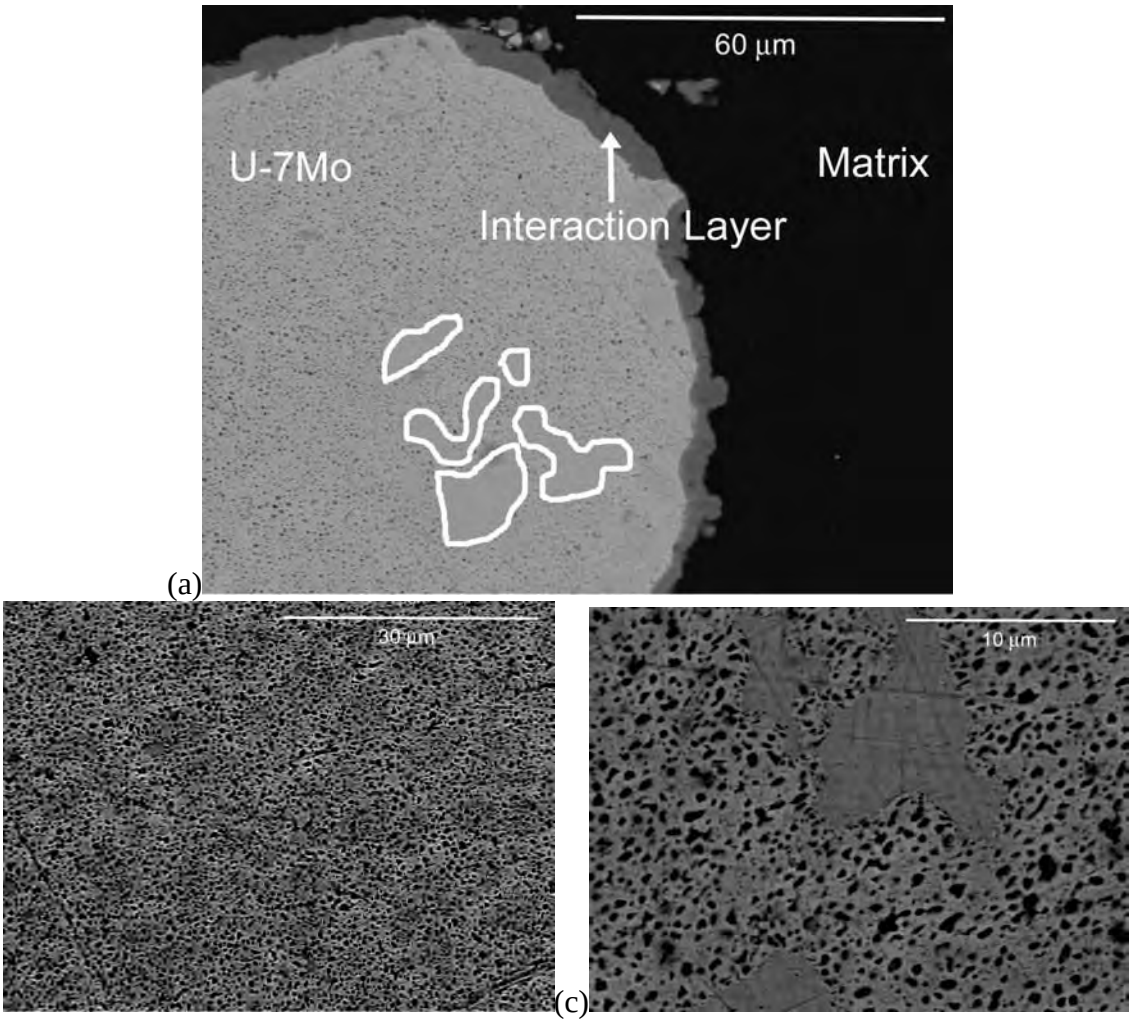


Figure 1. SE image of the locations where FIBINLO samples were produced from an irradiated fuel plate (R2R040). The darkest areas are where conductive silver paint was applied to the surface of the sample. Samples 1, 2, 3, 4, and 5 were produced to capture the U-7Mo microstructure.

3. Results

3.1 R3R050

Figure 2 shows the polished surface of a fuel particle for the R3R050 sample. A majority of the U-7Mo microstructure is comprised of relatively large fission gas bubbles. Some isolated areas could be found that contained no observable fission gas bubbles. A total of five FIBINLO samples were produced from the fuel particles in the R3R050 sample. Figure 3 shows representative SE images of the microstructure observed in these samples.



(a) (b) (c)

Figure 2. BSE images (a-c) of the polished surface of a U-7Mo fuel particle for sample R3R050. In (a), white lines identify regions where fission gas bubbles could not be observed. A higher magnification image of a region where only the relatively large fission gas bubbles could be observed is shown in (b) and of the localized regions without observable fission gas bubbles is shown in (c).

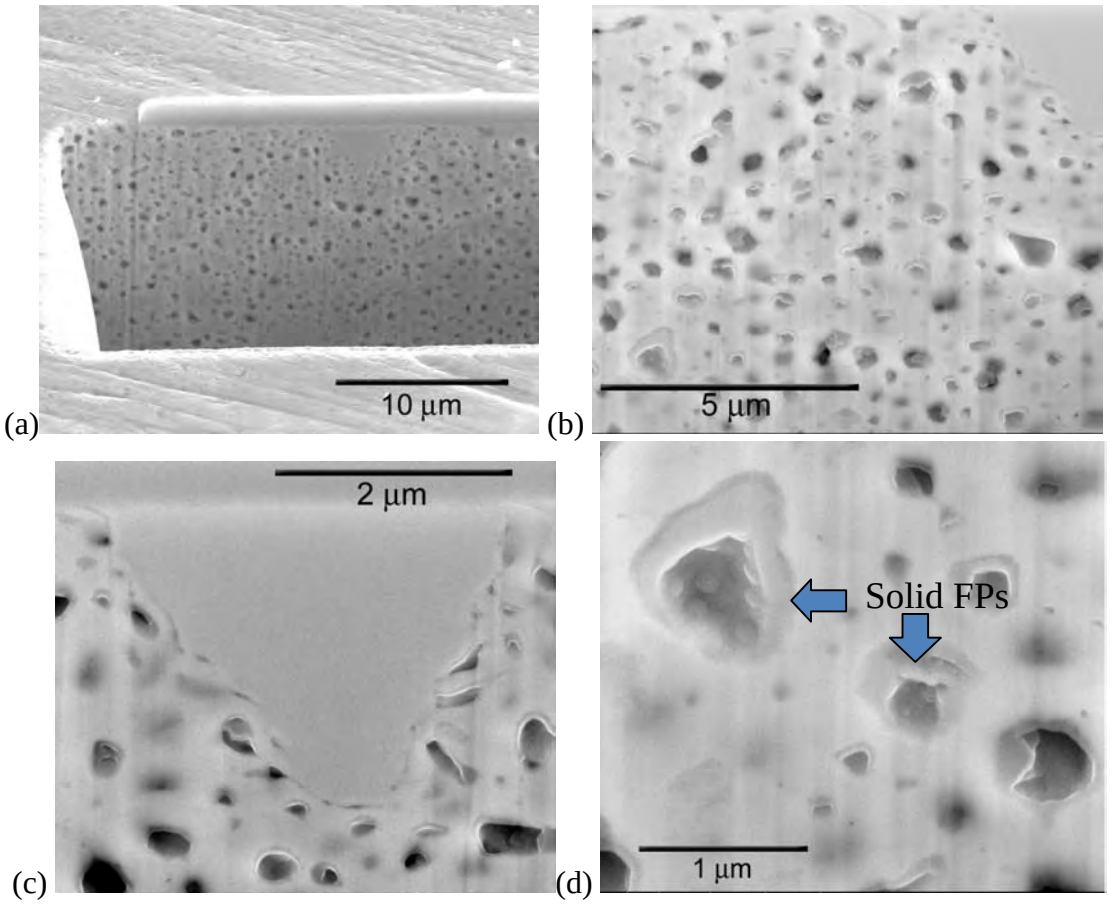


Figure 3. SE image (a) showing the microstructure that is revealed where a FIBINLO sample is generated from sample R3R050. The SE images in (b-d) show the uniform distribution of relatively large, faceted fission gas bubbles, and (b,c) shows a localized region without observable fission gas bubbles. (d) highlights solid fission product phases observed in some fission gas bubbles.

3.2 R0R010

Figure 4 shows SE images of FIBINLO samples produced from R0R010. Uniformly distributed, faceted fission gas bubbles can be observed that contain solid fission product phases. Figure 4(b) shows a crack that was observed in the microstructure that propagates from fission gas bubble to fission gas bubble. It is not clear if this crack was due to sample preparation or if it was already present in the sample. These types of features, if they are inherent to the U-7Mo at a specific stage of irradiation, are of interest in terms of how they may impact the release of fission gases.

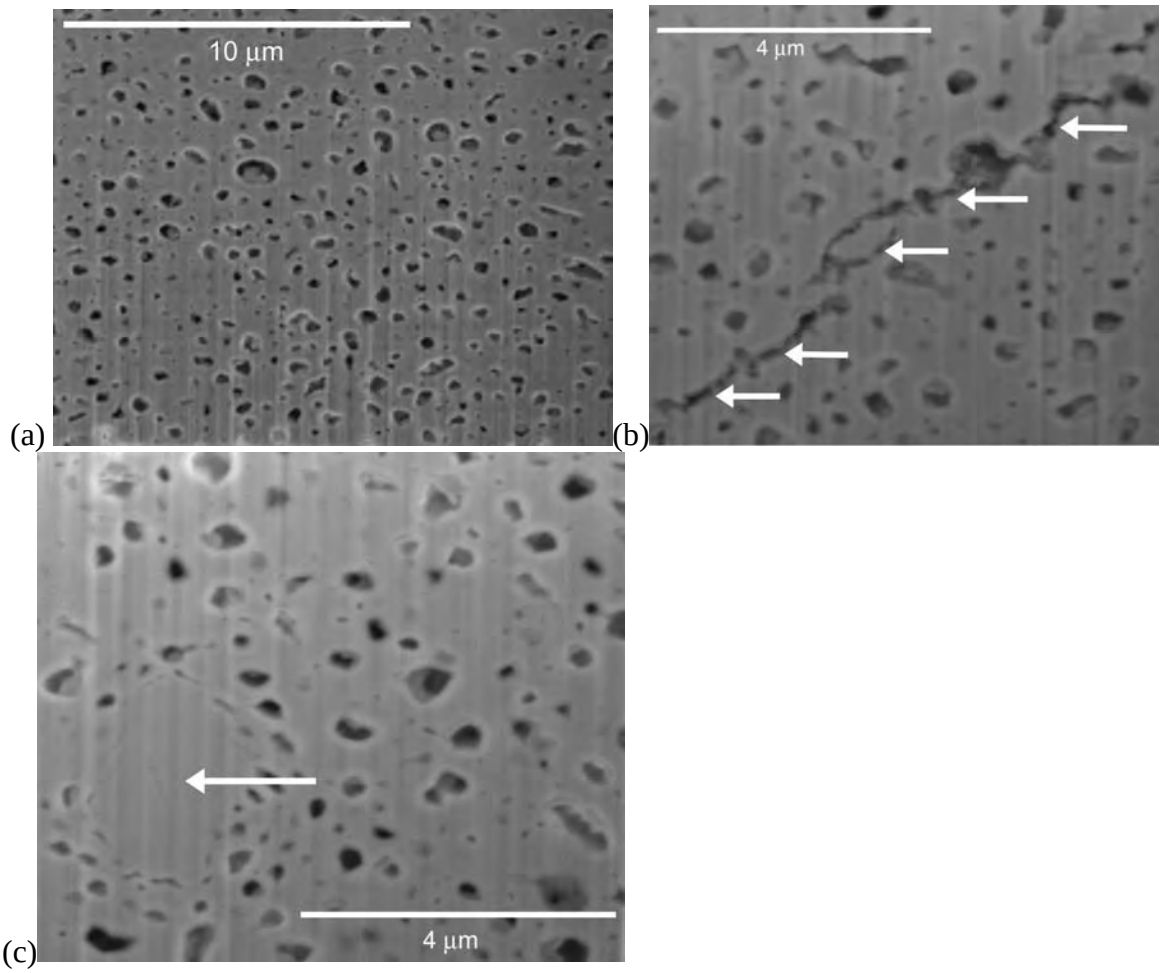


Figure 4. SE images (a-c) of the microstructure observed for U-7Mo FIBINLO samples generated from the R0R010 sample. (b) shows the propagation of a crack, as indicated by arrows, through the microstructure. (c) shows a small region (arrow) without the presence of relatively large fission gas bubbles.

3.3 R2R040

R2R040 was the highest fission density sample characterized (6.3 x 10^{21} fissions/cm^3). A total of five samples were FIBed from the U-7Mo for SEM analysis. Figure 1 shows an SE image that identifies where the FIB samples were taken from U-7Mo particles. Figure 5 shows SE images that are representative of the observed microstructure in the different samples. Like was the case for the the R3R050 and R0R010 samples, a fairly uniform distribution of fission gas bubbles is observed, and the size range for the bubbles is fairly wide. Solid fission product phases are present in the fission gas bubbles.

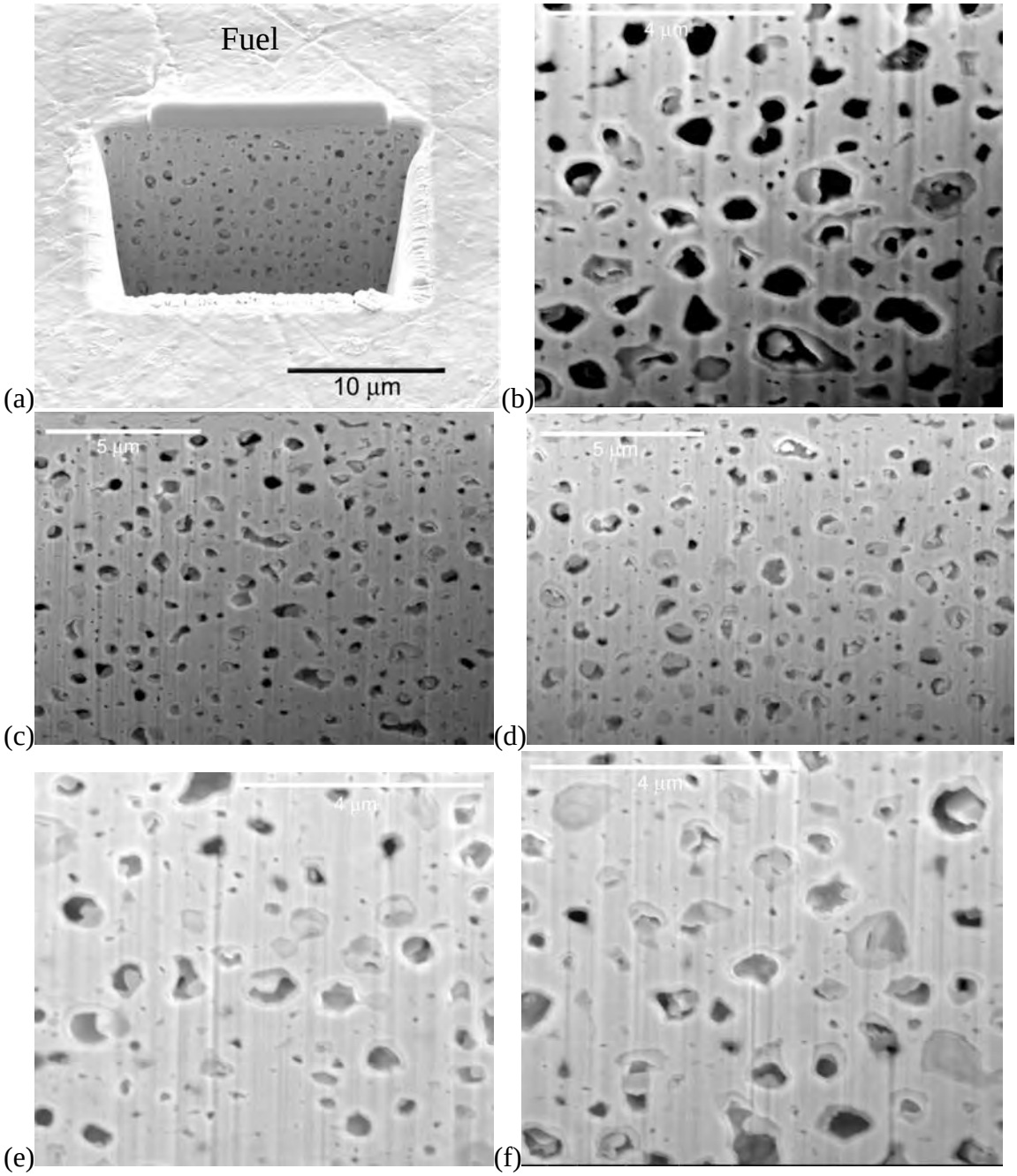


Figure 5. SE images (a-f) of the microstructure observed for the U-7Mo FIBINLO samples generated from the R2R040 sample. A fairly uniform distribution of fission gas bubbles is observed. There seems to be a fairly wide size range for the bubbles. Solid fission product phases are present within the fission gas bubbles.

3.4 3D Reconstruction

An SE image of a fuel particle in the R3R050 sample where a cube of the U-7Mo has been milled and is being lifted away from the sample is presented in Figure 6a. Generation of a small cube allows for serial sectioning and reconstruction of the 3D microstructure of the material without additional sample handling. [8] The cube at different stages of milling and imaging is shown in Figs 6(b-d). Also shown in Figure 6 is a computer-generated 3D reconstruction of the fission gas bubbles present in the microstructure, where colors are used to highlight localized regions where these bubbles may be interconnected.

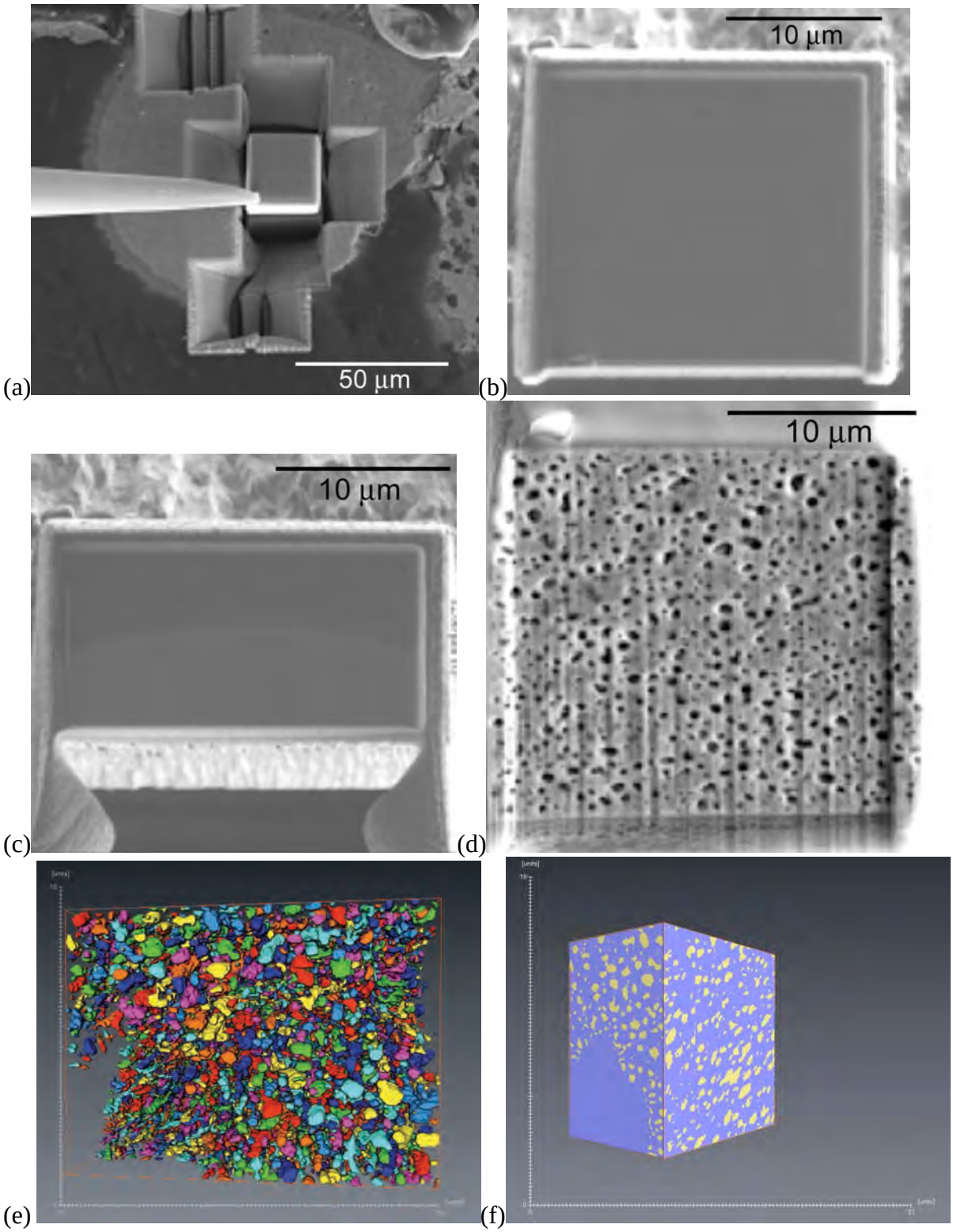


Figure 6. SE image (a) showing the top-view of a cube as it was being lifted out of sample R3R050 using the FIB. (b) shows a higher magnification SE image of the top view of the final sample before FIB milling and imaging was performed. (c) shows a top view of the sample after some FIB milling and imaging had occurred. (d) shows an SE image frontal view of the sample taken near the end of the process. (e) shows a 3D reconstruction that highlights with various colors the regions where different pores may have begun to interconnect. (f) shows a 3D reconstruction of the cube that highlights the pores (yellow) on the outer surfaces.

4. Discussion

As discussed in Reference [3], there is a marked difference between the microstructure of U-7Mo at low fission densities (e.g., 3.3 x 10^{21} f/cm^3) and those above 5 x 10^{21} f/cm^3. At the higher fission density, TEM analysis has shown that the U-7Mo has areas that are both crystalline and amorphous, and these regions are sub-micron in size, with sizes ranging down to 100 nm [3]. A few micron-sized grains are still present in the microstructure and within the areas with high density intergranular bubbles, the fuel grains are nano-sized. There is evidence that recrystallization has occurred in the microstructure of U-7Mo at higher fission densities. For the highest fission density sample (R2R040), the original ~10 µm grains have become much smaller (~200 nm) [7]. With respect to fission gas bubbles in U-7Mo at high fission density, the fission gas superlattice that is present in many grains of the microstructure at lower fission densities has collapsed in the bulk of the fuel grains. This has apparently "released" fission gas in the microstructure that has ended up in the larger fission gas bubbles. The larger bubbles appear to go threw a coarsening process, and the observed bubbles range in size from 0.1 µm to 1 µm. As far as behavior of the solid fission products, Zr, Sr, Y, Ce, Ba, Nd, Pd, and Te have been observed in the solid fission products that are present in many of the fission gas bubbles. [3, 7].

As mentioned earlier, the fuel plates in the EFUTURE and SELENIUM experiments that were irradiated in the BR-2 reactor, exhibited a change in swelling behavior at a fission density above 4.6 x 10^{21} f/cm^3. [4-6]. These experiment were performed at higher powers (470 W/cm^2 peak BOL power, local maximum burn-up of ~5.5 x10^{21} f/cm^3) than were the RERTR-7 plates discussed in this paper. In the EFUTURE and SELENIUM plates the high fission density microstructure of the U-7Mo should be very similar to what has been described in this paper, unless the exposure to higher power results in some significant microstructural differences. As discussed in [6], a change in the intrinsic nature of the U-7Mo fuel should be considered for explaining the changes in swelling behavior at higher fission densities. Based on the observations from anlysis of FIBINLO samples and 3D reconstruction of the irradiated U-7Mo microstructure, as discussed in the current paper, the U-7Mo microstructure is markedly different at high fission density, compared to the lower fission density microstructure. Instead of the low fission density microstructure where a fission gas superlattice is present internal to the grains and larger fission gas bubbles are observed on grain boundaries [9, 10], the microstructure at relatively high fission density (>4.6 x 10^{21} f/cm^3) consists of relatively large, uniformly distributed, fission gas bubbles (up to ~1 µm diameter) throughout the microstructure that are filled with solid fission products. The phenomena of solid fission product precipitate development (with potentially low molar volumes) and of fission gas bubble growth, with potential interconnection during irradiation, should be considered when trying to explain the observed changes in swelling behavior of the EFUTURE and SELENIUM experiments at higher fission densities.

5. Conclusions

When U-7Mo fuel particle are irradiated to a fission density of 5.2 x10^{21} f/cm^3, or higher, the microstructure will be comprised predominantly of large fission gas bubbles (up to 1 µm in diameter) that contain solid fission product precipitates. The effects of this microstructure, which is different than what is observed at lower fission densities, need to be considered when trying to explain changes in swelling behavior that can occur at fission densities above 4.6 x 10^{21} f/cm^3.

Acknowledgments

This work was supported by the U.S. Department of Energy, Office of Nuclear Materials Threat Reduction (NA-212), National Nuclear Security Administration, under DOE-NE Idaho Operations Office Contract DE-AC07-05ID14517. Personnel in the Hot Fuel Examination Facility are recognized for their contributions in destructively examining fuel plates.

References

[1]. J. Snelgrove et al., Nucl. Engr. Design 178 (1997) 119-126.
[2] D. Wachs et al., Proc. of *GLOBAL 2007*, Boise, ID, September 9-13, 2007.
[3]. B. Miller et al., *Proc. of the International Topical Meeting on Research Reactor Fuel Management (RRFM)*, Saint Petersburg, Russia, April 21–25, 2013.
[4]. S. Van den Berghe et al., *J. Nucl. Mater. 430 (2012) 246-258.*
[5]. A. Leenaers. et al., J. Nucl. Mater. 441 (2013) 439-448.
[6]. S. Van den Berghe et al., J. Nucl. Mater. 442 (2013) 60-68.
[7]. J. Gan et al., this conference.
[8] M. Teague et al., J. Nucl. Mater. 444 (2014) 475-480.
[9]. D. D. Keiser, Jr. et al., J. Nucl. Mater. 425 (2012) 156-172.
[10]. J. Gan et al., J. Nucl. Mater. 396 (2010) 234-239.

STABILITY STUDY OF THE RERTR FUEL MICROSTRUCTURE

J. GAN; D. D. KEISER, JR.; B. D. MILLER AND D. WACHS
Nuclear Fuels and Materials Division, Idaho National Laboratory
P. O. Box 1625, Idaho Falls, ID 83415, USA

M. KIRK
Materials Science Division, Argonne National Laboratory
9700 South Cass Ave.,, Argonne, IL 60439, USA

ABSTRACT

The irradiation stability of the interaction phases at the interface of fuel and Al alloy matrix as well as the stability of the fission gas bubble superlattice is believed to be very important to the U-Mo fuel performance. In this paper the recent result from TEM characterization of Kr ion irradiated U-10Mo-5Zr alloy will be discussed. The focus will be on the phase stability of Mo_2Zr, a dominant second phase developed at the interface of U-10Mo and the Zr barrier in a monolithic fuel plate from fuel fabrication. The Kr ion irradiations were conducted at a temperature of 200 °C to an ion fluence of 2.0E+16 ions/cm^2. To investigate the thermal stability of the fission gas bubble superlattice, a key microstructural feature in both irradiated dispersion U-7Mo fuel and monolithic U-10Mo fuel, a FIB-TEM sample of the irradiated U-10Mo fuel (3.53E+21 fission/cm^3) was used for a TEM in-situ heating experiment. The preliminary result showed extraordinary thermal stability of the fission gas bubble superlattice. The implication of the TEM observation from these two experiments on the fuel microstructural evolution under irradiation will be discussed.

1. Introduction

The most popular fuel design for the research and test reactors is the plate type of fuels either in dispersion or monolithic configuration sandwiched with aluminum alloy Al 6061 cladding on both sides. The advantage for a monolithic fuel plate is its higher uranium loading capacity compared to a dispersion fuel. To mitigate the undesired strong interaction between the U-Mo fuel and the Al 6061 cladding, a Zr thin foil of ~ 25 μm is added as a diffusion barrier between the U-Mo and Al 6061. It was found that the Zr foil also develops reaction product at both interfaces of U-Mo/Zr and Zr/Al 6061 from the fuel plate fabrication process [1]. A comprehensive microstructural characterization is required to investigate the radiation stabilities of the relevant interaction product phases at the fuel/cladding interface.

While neutron irradiation and the PIE is an essential part of a fuel development program, ion irradiation, with focus on certain aspect of a fuel material property, is very useful and complementary due to its cost effectiveness, quick turn-around cycle, well controlled irradiation conditions and negligible radioactivity of the sample. The previous ion irradiation study on the stability of interaction product phases at the U-Mo/Al-Si interface provided useful information [2,3]. The Mo_2Zr phase has been identified as a major interaction product developed at the U-Mo/Zr interface [4] or in the U-10Mo-χZr ternary alloy (χ = 1 to 6) [5]. In the open literature, the common crystalline structure for Mo_2Zr is $MgCu_2$ type (cF24, a_0 = 0.75875 nm) as listed in U-Mo-Zr ternary or Mo-Zr binary system phase diagrams [6]. There is also a less common structure for Mo_2Zr phase that is bcc type (cI2, with a_0 = 0.3185 nm) found in a two-phase Mo_2Zr compound where both bcc and $MgCu_2$ type structure co-exist [7,8]. The work by Osten shows that single phase Mo_2Zr in bcc structure cannot be obtained without an extremely fast

quenching of 10^5 K/sec following the arc melt [9]. The objective of this work is to investigate radiation stability of the Mo_2Zr phase as an interaction product. This work focuses on microstructure of the Mo_2Zr phase under Kr ion irradiation recorded in-situ along with more detailed post-irradiation TEM characterization.

Equally important to the radiation stability of interaction phase is the stability of fission gas bubble superlattice (GBS) in the U-Mo fuel. GBS is one of the most important microstructural features in the irradiated U-Mo fuel and its radiation and thermal stability may have a strong impact on the fuel performance. Although U-Mo fuel plate operation temperature is limited to below 250 °C due to corrosion of Al alloy cladding, the microstructural stability of U-Mo fuel itself is more or less controlled by the γ-phase stability. There is a great interest of investigating the thermal stability of the GBS in reference to its γ-phase stability. The thermal annealing study on the GBS in the irradiated fuel may be helpful to a better understanding of the U-Mo fuel performance as well as its potential to be used as an alternative fuel for other types of reactors.

2. Experiment

To investigate the radiation stability of the Mo_2Zr interaction phase, a U-10Mo-5Zr alloy was cast via arc melting followed by heat treatments relevant to the fuel fabrication process to produce Mo_2Zr phase for ion irradiation experiment. The cast material was first homogenized at 900 °C for 168 hours and water quenched. The following heat treatment was performed at 650 °C for 3 hours plus water quench which is relevant to the hot rolling process in fuel fabrication. The final step of heat treatment was carried out at 560 °C for 90 min followed by air cool which is representative to the process of hot isostatic press (HIP) as a last step of fuel fabrication. Scanning electron microscopy analysis and X-ray diffraction analysis were performed to confirm the presence of Mo_2Zr phase in the U-10Mo-5Zr alloy. Standard 3.0 mm samples for transmission electron microscopy (TEM) analysis were prepared through slicing, mechanical polishing, disc punching and fine polishing followed by electrical jet polishing to produce thin areas transparent to 200 keV electron beam.

The TEM samples were irradiated with 500 or 250 keV Kr ions at 200 °C to ion doses up to 2×10^{16} ions/cm^2 using the Intermediate Voltage Electron Microscope (IVEM) equipped with a tandem accelerator at Argonne National Laboratory. For 500 keV Kr ions, this corresponds to a peak displacement damage of ~ 145 displacements per atom (dpa) in Mo_2Zr (~ 100 nm thick) estimated from the SRIM calculation [10]. The specimen chamber vacuum is approximately 1.1×10^{-5} Pa (8.0×10^{-8} torr) during ion irradiation. The estimated local temperature uncertainty is approximately ±10 °C. With the selected ion energy of 500 keV or 250 keV, the retention of the injected Kr ions in the electron transparent area (~ 100 nm thickness) of the TEM foil were estimated to be 33% and 95%, respectively. The in-situ TEM analysis was performed using a Hitachi H-9000NAR transmission electron microscope operating at 300 keV during the Kr ion irradiation. Detailed post-irradiation examination (PIE) was performed using a 200 keV JEOL 2010 TEM/STEM system equipped with a LaB_6 filament, a Gatan UltraSacn-1000 digital camera for imaging and a Brukers Si drift detector for composition analysis with Energy Dispersive Spectroscopy (EDS). The TEM selected area diffraction (SAD) patterns from the major zones were used for structural analysis. A Java-version Electron Microscopy Simulation (JEMS) software developed by Stadelmann was used to assist in identifying the phase and indexing the diffraction patterns [11].

Thermal stability study of the GBS was conducted using a Gatan double-tilt TEM heating holder for an irradiated U-10Mo FIB-TEM sample (T_{irr} ~ 140°C, 3.5×10^{21} fissions/cm^3). The GBS

microstructure is monitored in-situ during the heating experiment. The temperature ramp rate was approximately 10°C/min where the temperature readout was based on the thermocouple spot-welded at the miniature furnace of the heating holder. The heating holder temperature was raised from room temperature to 700 °C in about 90 min, then kept at ~700 °C for about 30 min, continued to ~850 °C with a reduced rate of ~ 5 °C/min. GBS images at zone [110] were recorded at various points of the heating experiment for evaluation on its thermal stability.

3. Results and Discussion

3.1 Kr ion irradiation stability of Mo_2Zr phase

The alloy matrix remains the bcc structure of U-Mo in γ phase. A low magnification scanning-TEM (STEM) image of the U-10M-5Zr alloy general microstructure is shown in Figure 1 where all precipitates shown in the picture were identified to be Mo_2Zr phase. TEM diffraction analysis of the Mo_2Zr phase in the unirradiated sample confirmed the $MgCu_2$ type structure for Mo_2Zr phase in U-10Mo-5Zr alloy.

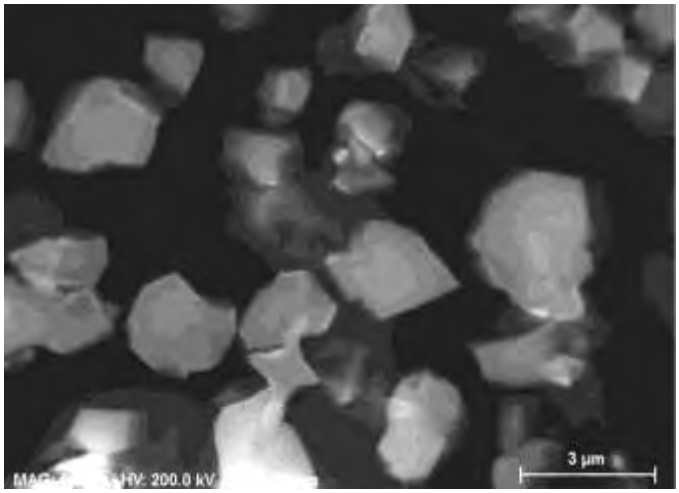


Figure 1. STEM overview image of U-10Mo-5Zr alloy showing Mo_2Zr phase (light contrast).

The microstructural evolution as a function of dose in Mo_2Zr phase under 500 keV Kr ion irradiation is shown in Figure 2. Low-magnification TEM overview images on the top reveal the microstructural change before and after Kr ion irradiation in the Mo_2Zr phase. Six high-magnification TEM images from the same area show the details of the microstructural development as a function of dose. The initial unirradiated microstructure contains a twin and its visibility dropped significantly at a low dose of 1×10^{14} ions/cm^2 and disappeared before the ion fluence of 5×10^{14} ions/cm^2. Significant dislocation development can be seen even at dose as low as 4×10^{13} ions/cm^2. At an ion does of 5×10^{14} ions/cm^2, the development of dislocation as a result of irradiation appears saturated with no significant change up to the final fluence of 2×10^{16} ions/cm^2. A high-resolution image in Figure 3 shows the details of the dislocation tangles and network at the final dose within the same Mo_2Zr precipitate shown in Figure 2. TEM imaging with under- and over-focus conditions at high magnification during both in-situ irradiation and PIE work could not reveal any bubbles in the 500 keV Kr ion irradiated Mo_2Zr phase. It appears Mo_2Zr is quite resistant to Kr ion radiation damage in terms of bubble formation.

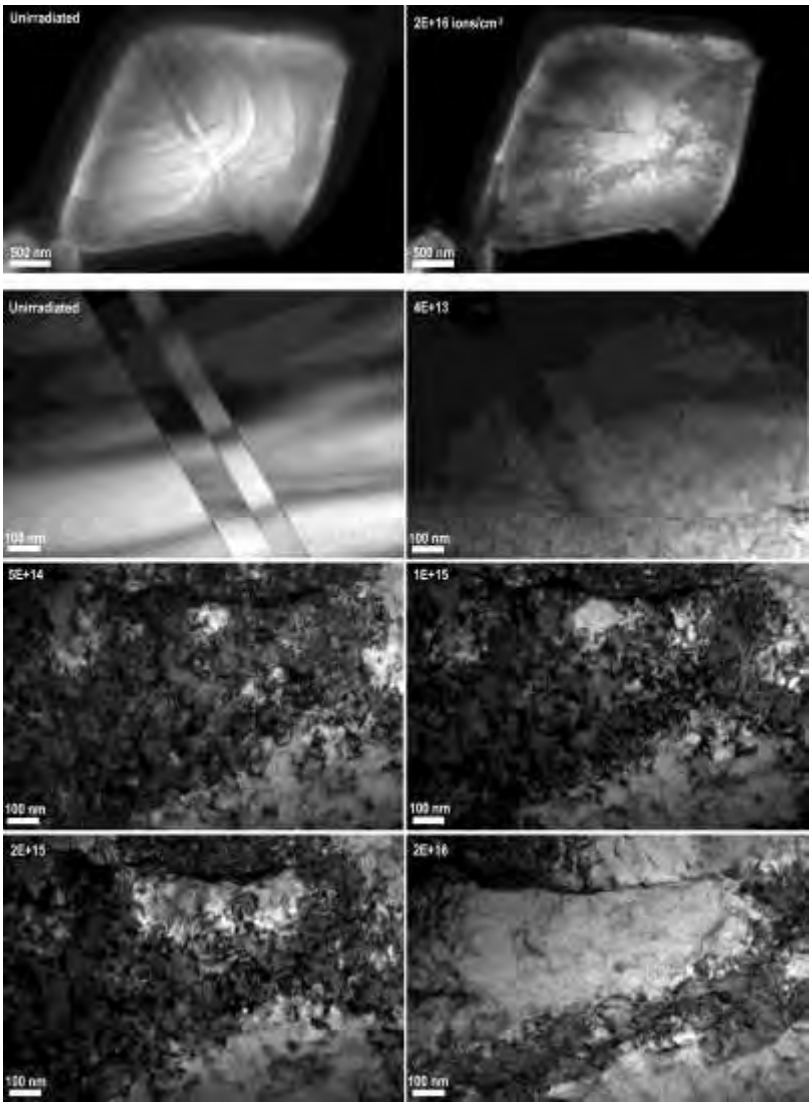


Figure 2. TEM images showing microstructure evolution from the same area in Mo_2Zr.

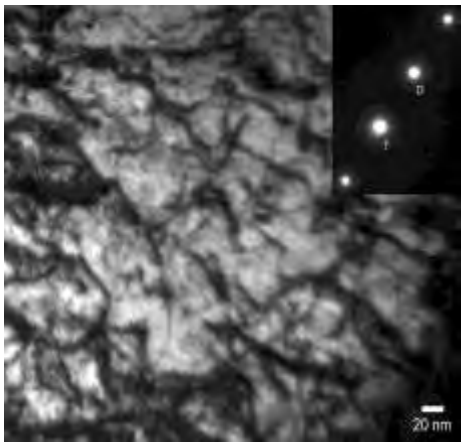


Figure 3. High resolution TEM image showing dislocation tangles and network imaged under g=0-11 from the same area in Figure 2 in bcc Mo_2Zr irradiated to 2×10^{16} ions/cm^2.

The most important finding from the PIE with detailed TEM microstructural characterization is the structural change of Mo_2Zr phase as a result of Kr ion irradiation. The TEM SAD patterns from three major zones ([001], [111] and [101]) for the Mo_2Zr phase in the unirradiated condition in comparison to that of the irradiated condition (2×10^{16} ions/cm^2) are shown in Figure 4. Although the SAD patterns of zone [001] and [111] between the two structures look similar, the corresponding indices are quite different between the two structures. For the irradiated Mo_2Zr, the missing of the original [101] zone pattern shown in the $MgCu_2$ type structure for the unirradiated Mo_2Zr plus the presence of zone patterns from a much smaller cubic structure such as zone [101] confirms the radiation induced structural change.

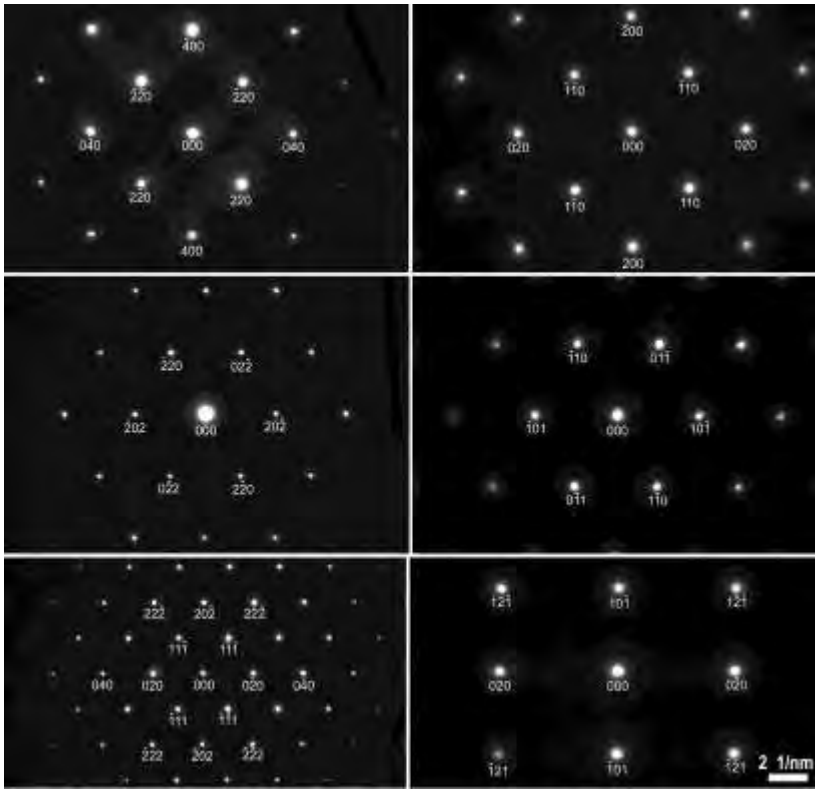


Figure 4. Comparison of SAD zone patterns in Mo_2Zr for unirradiated ($MgCu_2$ type, left) and irradiated to 2×10^{16} ions/cm^2 (bcc, right) at zone [001] (top), [111] (middle) and [101] (bottom).

The $MgCu_2$ type large cubic (a_0 = 0.7588 nm, containing 24 atoms) in the unirradiated Mo_2Zr has changed to the bcc type small cubic (a_0 = 0.3185 nm, containing 2 atoms) in the irradiated condition (2×10^{16} ions/cm^2). The associated volume contraction is estimated to be 11.3%. Unfortunately the exact irradiation doses where the structural transformation was occurring could not be identified in this work without additional Kr ion irradiation experiment using the IVEM due to limited availability for the facility. The transformed Mo_2Zr structure in bcc has a lattice constant similar to that for bcc molybdenum (a_0 = 0.315 nm). Recall that the single phase Mo_2Zr in bcc structure could not be obtained without an extremely fast quenching of 10^5 K/sec following the arc melt [9], the radiation-induced structural transformation for Mo_2Zr phase demonstrated that ion irradiation can lead to a microstructural change far from its thermodynamically stable state. Comparing to the previous work on Kr ion irradiation of U-Mo/Al-Si interaction products [2,3] and disregarding the structural change, the Mo_2Zr phase displayed exceptional radiation tolerance with clear SAD pattern and Kikuchi line pattern at even higher dose. Although the threshold ion dose for the structural transformation was not identified,

it is speculated that the threshold dose may be rather low therefore most part of the Kr irradiation was on Mo_2Zr phase with bcc structure which is known for its relative high resistance to swelling and bubble formation comparing to the initial more complex crystalline structure.

One of the objectives for this work is to investigate the bubble development and swelling behavior of the Mo_2Zr phase under Kr ion irradiation relevant to the U-10Mo/Zr/Al-6061 monolithic fuel plate. Since 500 keV Kr ion irradiation to 2×10^{16} ions/cm^2 was ineffective to introduce bubbles in Mo_2Zr phase, it demonstrated the high resistance to bubble formation. In order to develop bubbles under more aggressive condition, the ion energy was reduced to 250 keV to trap more Kr ions in the sample. The amount of Kr ions retained in Mo_2Zr was almost tripled with the reduced ion energy to the same ion fluence. Figure 5 shows the high concentration of small Kr ion bubbles in Mo_2Zr imaged with under- and over-focus conditions for the 250 keV Kr ion irradiation to 2×10^{16} ions/cm^2. The estimated bubble size is approximately ~ 2 nm.

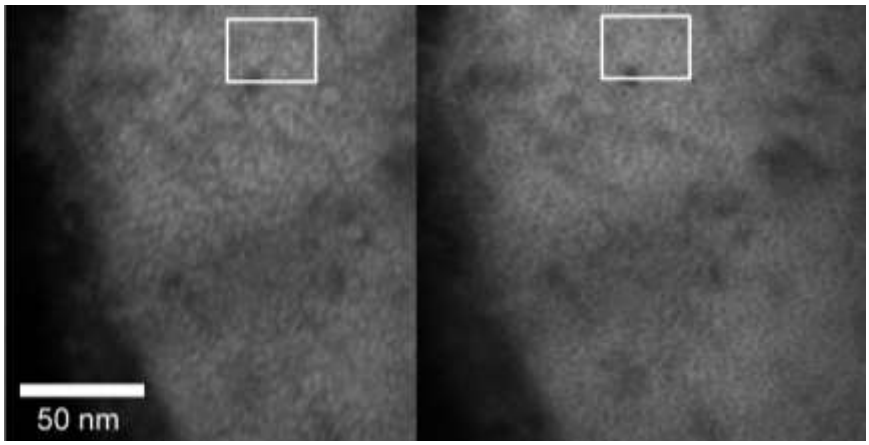


Figure 5. TEM images of under-focus (left) and over-focus (right) showing small Kr bubbles in Mo_2Zr phase irradiated with reduced energy of 250 keV Kr ions at 200 °C to 2×10^{16} ions/cm^2.

During post-irradiation TEM, it was found that there are small cracks present around the interface between the large Mo_2Zr precipitate (> 5 μm) and U-Mo-Zr alloy matrix. This is likely attributed to the volume contraction (11.3%) from radiation-induced structural change in Mo_2Zr phase that may create a tensile stress exceeding the bond strength at the interface. Interface cracks were not found for the small precipitates despite of the similar volume contraction, indicating less tensile stress built up at the precipitate and matrix interface. Perez et al found that the Mo_2Zr precipitates at the interface of U-Mo and Zr barrier layer in a fresh fuel tend to be quite small [1]. Therefore the cracks identified for the large Mo_2Zr as a result of radiation-induced structural change may not be a concern for the U-10Mo/Zr/Al-6061 monolithic fuel plate as long as the fuel fabrication process does not introduce large Mo_2Zr precipitates.

3.2 Thermal stability of gas bubble superlattice

The temperature vs. time curve for the TEM in-situ heating experiment for an irradiated U-10Mo FIB-TEM sample is shown in Figure 6. During the heating experiment, it requires frequent Z-height adjustment and correction for tilt and thermal drift to maintain the right imaging condition for GBS. Figure 7 shows the TEM bright field images of GBS at various temperatures from the

same sample area. It shows no significant degradation on the superlattice structure for GBS. The GBS images accquired at room temperature before and after the in-situ heating experiment are shown in Figure 8. They demonstrate the high thermal stability of the GBS. This is not a total surprise since GBS was developed in the U-Mo fuel under very aggressive fission fragment bombardement to very high atomic displacement damage while in the reactor. The temperature-transformation-time (TTT) diagram for U-10Mo indicates that for U-10Mo it may take more than 5 hours to decompose its γ-phase at 500°C [5]. Once passing 580°C, U-10Mo will be stable in its high temperature γ-phase (bcc). It is believed that GBS will collapse if γ-phase is decomposed.

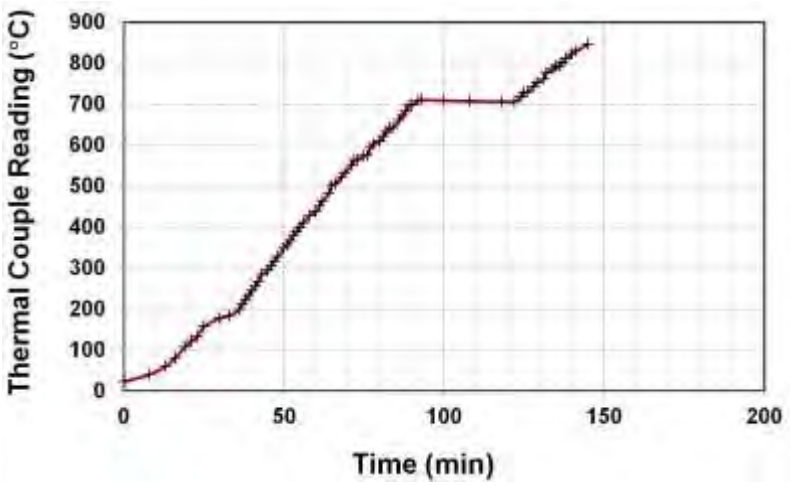


Figure 6. TC reading vs. time for TEM ins-itu heating test for an irradiated U-10Mo sample.

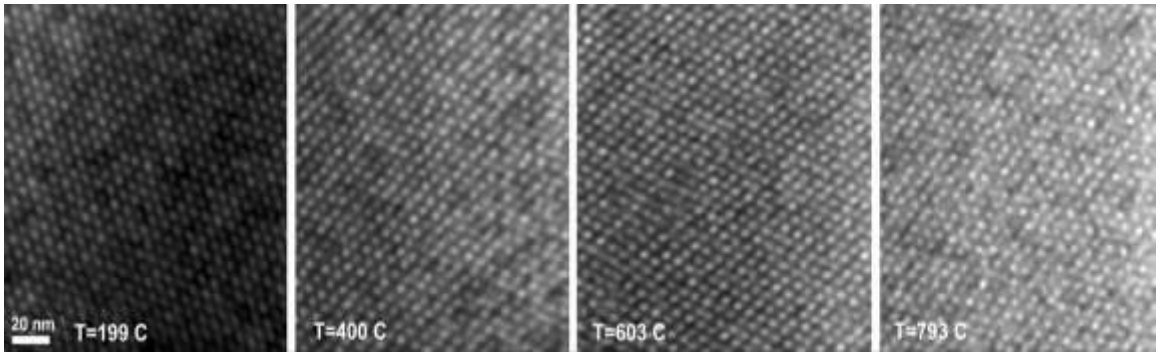


Figure 7. TEM bright field images of GBS at zone [110] at various temperatures.

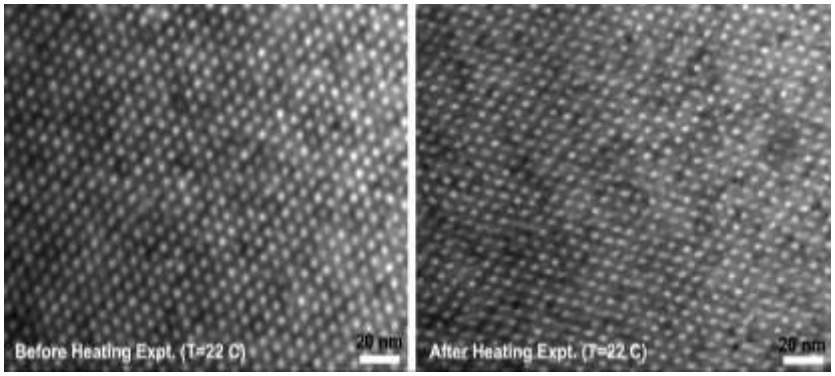


Figure 8. GBS images at room temperature before and after TEM in-situ heating experiment.

As a general concern for the in-situ TEM experiments, the small sample dimension plus the technical difficulty in calibrating the FIB-TEM spcimen temperature for the TEM heating holder, the observation from this work needs to be verified by the furnace annealing experiment of a bulk irradiated fuel sample followed by TEM characterization. This work has been planned and the results will be provided in the future publication or conference. To better understand the correlation between the γ-pahse stability on GBS stability in U-Mo fuel, it is desired to conduct heating experiment for the irradiated U-7Mo fuel instead of the U-10Mo fuel since the former may start the phase transformation in about 1 hour at 525°C which is much sooner than that of U-10Mo fuel.

4. Conclusions

The Mo_2Zr phase developed at U-10Mo/Zr interface from fuel fabrication has an $MgCu_2$ type large and complex cubic structure. Under Kr ion irradiation at 200 °C temperature to fluence of 2×10^{16} ions/cm^2, this phase changes its structure to a much smaller bcc cubic associated with a volume contraction of 11.3%. The irradiated defect structure mainly consists of dislocation tangles and network. Ignoring the radiation-induced structural change, the Mo_2Zr phase shows exceptional radiation tolerance on suppressing bubble formation and maintaining crystalline structure up to high dose of ~ 145 dpa. The preliminary result from TEM in-situ hjeating of an irradiated U-10Mo demosntrated the high thermal stability of gas bubble superlattice.

Acknowledgments

Acknowledgment is given to Glenn Moore for alloy fabrication and Francine Rice for help on TEM heating experiment at Idaho National Laboratory, and Pete M. Baldo for ion irradiation at Argonne National Laboratory. The in-situ ion irradiation and electron microscopy was accomplished at the Electron Microscopy Center for Materials Research at Argonne National Laboratory, a U.S. Department of Energy Office of Science Laboratory operated under Contract No. DE-AC02-06CH11357 by UChicago Argonne, LLC. This work was supported by the U.S. Department of Energy, Office of Nuclear Materials Threat Reduction (NA-212), National Nuclear Security Administration to the RERTR program, under DOE-NE Idaho Operations Office Contract DE-AC07-05ID14517. Accordingly, the U.S. Government retains a nonexclusive, royalty-free license to publish or reproduce the published form of this contribution, or allow others to do so, for U.S. Government purposes.

References

[1] E. Perez, B. Yao, D.D. Keiser Jr., Y.H. Sohn, J. Nucl. Mater. 402 (2010) 8-14.
[2] J. Gan, D.D. Keiser, B.D. Miller, M.A. Kirk, J. Rest, T.R. Allen, D.M. Wachs, J. Nucl. Mater 407 (2010) 48-54.
[3] J. Gan, D.D. Keiser Jr., B.D. Miller, D.M. Wachs, T.R. Allen, M. Kirk, J. Rest, J. Nucl. Mater. 411 (2011) 174-180.
[4] K. Huang, Y. Park, D.D. Keiser Jr., and Y.H. Sohn, “Interdiffusion Between Zr Diffusion Barrier and U-Mo Alloy”, Journal of Phase Equilibria and Diffusion, Vol. 33. No. 6 (2012) 443.
[5] C.A.W. Peterson, W.J. Steele, S.L. DiGiallonardo, “Isothermal Transformation Study of Some Uranium-Base Alloys”, Report: UCRL-7824, Metals, Ceramics, and Materials, UC-25, TID-4500 (34th Ed.), Lawrence Radiation Laboratory, Livermore, California, August, 1964.

[6] ASM Alloy Phase Diagrams Center, P. Villars, editor-in-chief; H. Okamoto and K. Cenzual, section editors; http://www1.asminternational.org/AsmEnterprise/APD, ASM International, Materials Park, OH, USA, 2006-2014.
[7] Ban, Z., Trojko, R., Blazina, Z., "High temperature equilibria in the Zr_{1-x} Hf_x M_2, Zr_{1-x} Ti_x M_2 and Hf_{1-x} Ti_x M_2 (M= Mo or W) systems", J. Less-Common Met. 83, 175 (1982).
[8] Blazina Z., Trojko R., Ban Z., "METAL-METALLOID EXCHANGE IN THE $Zr_{1-x}M_xMo_2$ (M = Ge, Si, Al) SYSTEM". J. Less-Common Met. 97, 91 (1984).
[9] Osten Rapp, J. Less-Common Met., 21 (1970) 27-44.
[10] J.F. Ziegler, J.P. Biersack, and U. Littmark, The Stopping and Range of Ions in Solid, Pergamon Press, New York, 1996.
[11] P. Stadelmann, http://cimewww.epfl.ch/people/stadelmann/jemsWebSite/jems.html.

IN-PILE IRRADIATED U-Mo/Al(Si) DISPERSED NUCLEAR FUEL BEHAVIOUR UNDER THERMAL ANNEALING: FISSION GAS RELEASE AND MICROSTRUCTURAL EVOLUTIONS

T. ZWEIFEL[1], H. PALANCHER, Ch. VALOT,
Y. PONTILLON, J. LAMONTAGNE, T. BLAY
CEA, DEN, DEC
F-13108 St. Paul-lez-Durance CEDEX - France

W. PETRY
Forschungs-Neutronenquelle Heinz Maier-Leibnitz (FRM II)
Lichtenbergstr. 1, D-85747 Garching - Germany

ABSTRACT

Thermal treatments have been performed on in-pile irradiated U-Mo/Al(Si) fuel plate samples (IRIS4 irradiation campaign) up to 1800°C with fisson gas release on-line monitoring. More than 70% of the FGs are released during two major FG release peaks around 500°C and 670°C. Additional characterizations of the samples by XRD, EPMA and SEM suggest that up to 500°C FGs are released from the IDL[2]/matrix interfaces. The second peak at 670°C representing the main release of FGs originates from the massive interaction between the U-Mo particles and the matrix in the vicinity of the cladding.

1. Introduction

During in-pile test irradiation, the growth of an interdiffusion layer (IDL) between the U-Mo fuel particles and the surrounding Al matrix strongly limits the performance of this fuel [1,2]. SEM and TEM indicated that the IDL is amorphous for irradiation temperatures below 200°C [3, 4, 5, 6, 7]. As the IDL exhibits a poor retention for fission gases (i.e. Xe), these gases eventually accumulate at the IDL/Al interfaces in large bubbles of more than 10 µm in diameter [4, 5]. Thus, one major goal of U-Mo/Al development is to understand this fission gas behaviour. The approach chosen for this work consists in combining in-situ monitoring of FG release during thermal treatments with destructive examinations of the annealed samples [8]. This methodology is aimed at defining the initial location of fission gas inside the fuel material and understanding their behaviour. Samples taken from the IRIS4 in-pile experiment, which is described in [9], have been selected for this study.

[1] Also at Forschungs-Neutronenquelle Heinz Maier-Leibnitz (FRM II)

[2] Interdiffusion Layer between U-Mo particles and the Al-based matrix, which has grown during in-pile irradiation.

2. Examinations before thermal treatments

2.1 IRIS 4 fuel plate manufacturing and fresh fuel plate characterization

The IRIS4 fuel plates consisted of atomized U-7wt%Mo particles (enrichment <20wt%) which were subsequently oxidized by a thermal treatment at 200-250°C during a few hours. Main crystallographic phase inside the obtained coating is UO_2 and its thickness is about 1.0 μm [10]. In total, four fuel plates were produced. The U-Mo particles were embedded in either a pure Al A5 matrix (2 plates labelled 8053 and 8054), or in an AlSi alloy matrix with 2.1wt% Si addition (2 plates labelled 8043 and 8044). The uranium density was 8 g/cc which equals to about 50 vol% U-Mo. The mixed powders have been compacted finally, further enclosed by an AG3NE frame and an AlFeNi cladding [11]. This composite has been hot-rolled [12], and a successive "blister test" has been performed at 425 ± 25°C for one hour. In this paper we focus on the study of the fuel plate containing Si in the matrix (no. 8043).
Prior to in-pile irradiation, the fresh fuel plates microstructures have been investigated by either high energy X-ray diffraction (HE-XRD) detailed in [13] or electron probe micro analysis (EPMA) shown in Fig. 1. No signs of elemental mixing between the U-Mo particles and the matrix after the fabrication step could be detected. HE-XRD indicated an UO_2 layer thickness increase by an average 0.5 μm. Additionally, EDX and HE-XRD indicated that a cracked UN_x layer has formed in the outer part of the oxide coating [13]. It is assumed that this nitrogen contamination has occurred during the oxidation treatment of U-Mo powder under air, as this UN layer is found around each U-Mo particle (not only around the closest from the frame).
At some U-Mo particle/oxide layer interfaces, a Si-rich diffusion layer (SiRDL) has formed. This has already been observed in prior similar fresh fuels [14, 15]. HE-XRD measurements have quantified this SiRDL's average thickness and the remaining Si concentration inside the matrix [13], [16]. In fuel plates with oxidised U-Mo particles the SiRDL thickness is smaller and the amount of Si remaining inside the matrix is higher. HE-XRD also confirmed a slight γ-U destabilisation into α"-U and U_2Mo during the plate manufacturing process. This destabilisation has probably enhanced Mo depletion at grain boundaries inside U-Mo atomised particles (as shown in Fig. 1) [13].

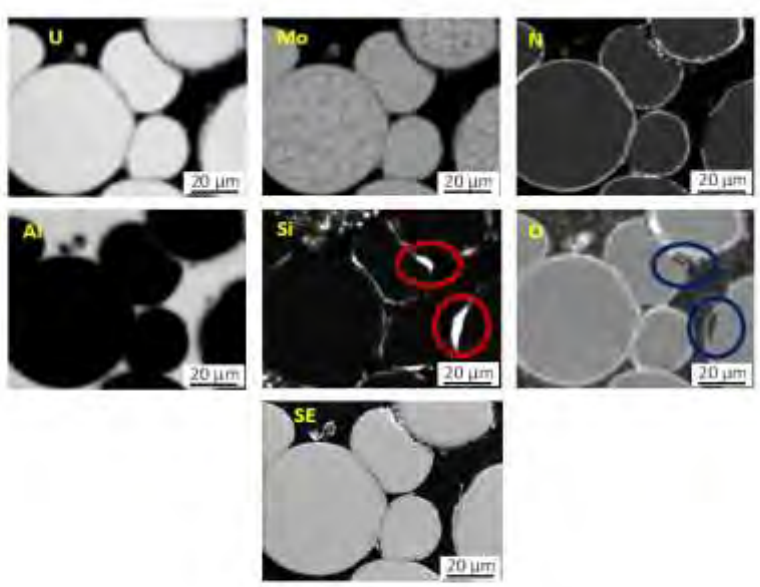


Fig. 1: EPMA local elemental analysis of the non-irradiated IRIS4 fuel meat. X-ray maps for U, Mo, Al, Si, O and N are given together with a secondary electron image (SE) of the same zone. Indicated in red (in the Si map) and in blue (in the O map) is the SiRDL location between the oxide layer and the U-Mo core.

2.2 Irradiation conditions

In 2009, the IRIS 4 irradiation campaign started in the OSIRIS material testing reactor [11]. The fuel plate no. 8043, from which the samples presented in this paper were retrieved, has been irradiated until a final 62% burn-up with an according fission density of 3.4×10^{21} f/cm^3 (mean value averaged over the whole fuel plate) [17]. The heat flux was 258 W/cm^2 at the maximum flux plane (MFP), while the outer cladding temperature was around 100°C [18].

2.3 Post irradiation experiments (PIE)

Destructive examinations including optical microscopy (OM), scanning electron microscopy (SEM), X-ray diffraction (XRD) and EPMA measurements were undertaken to characterise the fuel microstructure. Results are very close to those already published on the plate 8044, which had the same initial composition and which has been irradiated in very similar conditions [17]: From EPMA images taken in the main meat region of the fuel (see Fig. 2) the IDL formation around the U-Mo particles is visible. Considering that XRD indicated no $U_xMo_yAl_z$ intermetallic crystalline phases, it is assumed that the IDL is amorphous as expected from experiments performed under similar irradiation conditions [3, 4, 5].

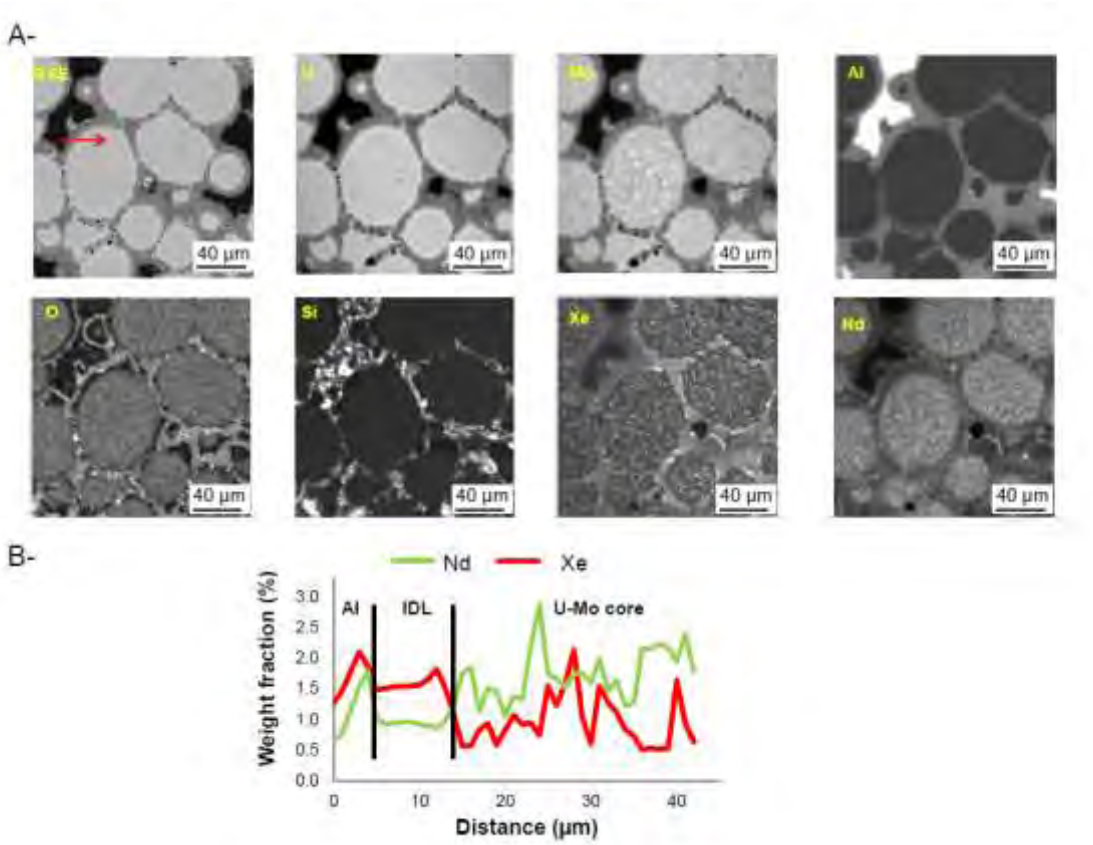


Fig. 2: EPMA local elemental analysis of the as-irradiated IRIS4 fuel meat. (A-) A back-scattered electron (BSE) image together with X-ray maps for U, Mo, Al, O, Si, Xe and Nd is shown. (B-) A quantitative EPMA linescan showing Nd and Xe elemental concentrations from U-Mo core towards matrix is shown (indicated by a red arrow on the BSE map).

Moreover, the IDL exhibits a so-called “duplex” structure [17], further referred to as an “internal” IDL near the U-Mo/IDL interface and an “external” IDL near the IDL/Al interface. The external IDL is oxygen-richer than the internal part of the IDL (see Fig. 2-A). Aluminium contents in both parts are very similar, with a slightly higher value in the external IDL (see tab. 1).

	(Al+Si)/(U+Mo) atomic ratio		Si concentration (at%)	
	Internal IDL	External IDL	Internal IDL	External IDL
After in-pile irradiation	4-5	5-6	---	---
After thermal treatment at 500°C	3-7	>7	2 - 4	--
After thermal treatment at 670°C	3.3 - 9.6 (no internal/external IDL; high values are close to the cladding; lower values in the meat center)		1-5 (relevant only for IDL around particles in the centre of the meat)	

Tab. 1: IDL elemental composition as determined by quantitative EPMA linescans on in-pile irradiated IRIS4 fuel. A comparison is made between as-irradiated and post-thermally annealed samples.

The internal IDL shows no detectable amount of Si. Only a small amount of Si has been consumed during irradiation. Si diffuses towards the particles to stabilise the U-Mo particles, i.e. reduce and slow down the IDL growth during irradiation. The fact that only a low Si diffusion towards the particles has been observed in the IRIS4 fuel could be attributed to the presence of the UO_2 layer around the particles. Concluding, the presence of an UO_2 layer around the particles in the IRIS4 experiment has not added to the beneficial effect of Si addition. The presence of the nitrogen layer mentioned previously does not result in any notable difference with respect to the general behaviour of the external oxide layer.
Considering the final density in the 8043 plate, recrystallization should have begun [19]. When comparing the Mo X-ray maps before (Fig. 1) and after irradiation (Fig. 2-A), the initial Mo grain structure remains at least in some particles, suggesting that recrystallization has not completed. Recrystallization would result in a collapse of the nanometre sized fission gas bubbles inside the U-Mo particles and lead to large bubbles up to 1 μm in size which would be more homogeneously distributed in the particles (not only located at grain boundaries)
Fission gas bubbles are also present at U-Mo/IDL interfaces (and even in the internal IDL part) and at IDL/IDL interfaces where no matrix remains in between. In these two last locations, they are larger than in the particle cores. If Xe is also found in the external part of the IDL, no significant precipitation can be detected (see Fig. 2-A). According to EPMA linescans across U-Mo particles, the IDL and the matrix (see Fig. 2-B), the Xe concentration is found to be almost constant in the IDL: this suggests that Xe has precipitated in very small bubbles within the IDL (0.1 μm or even lower). For FG diffusion, the Xe/Nd weight ratio is most often used, as Nd is non-volatile. Here, the weight ratio was determined to 1.1 inside the particles and about 1.6 in the external IDL (see Fig. 2-B). These values are in good agreement with those measured in the IDL inside U-Mo/Al(Si) fuel plates irradiated in close temperature conditions but with a higher surface power and up to a higher burn-up [20].

3 Experimental methods

3.1 Sample preparation

Three samples were cut from plate 8043 for further thermal treatments (TT). Their final size was 8 × 8 mm^2. The samples' locations are almost symmetrical with respect to the MFP and is very close to the sample analysed for describing the "as-irradiated" case. It is considered that their burn-up is identical in a first approximation.

3.2 Thermal Treatments (TT) and on-line FG release monitoring

The so-called "MERARG-2" device used for thermal treatments consists of a high frequency (50 kHz) induction furnace, located in a hot cell at the LECA-STAR facility at the CEA Cadarache centre, coupled with on-line gas release measurements [21]. On-line gamma spectrometry allows monitoring of inert gas release (i.e. ^{85}Kr or ^{133}Xe), while on-line gas chromatography allows observation of He, H_2 and other gases in specific dilution conditions (i.e. N_2, Kr, Xe). By taking into account fission gas dilution and flowing time between the furnace and the counting chamber, real fission gas release kinetics at the sample position can be reconstructed from the measured one at the γ detector position.
In this work, a slow temperature increase of 0.1 °C/s was chosen to obtain an accurate characterization of FG release kinetics. When the target temperature was reached, the furnace was switched off, which means the holding time at the maximal temperature was very short. After TT, transversal cross-section were cut from the samples and embedded in an eutectic Wood alloy for EPMA measurements. As very few material was available, all analyses (OM, EPMA, XRD) had to be performed on the same samples. This has an influence on the quality of measured data especially for XRD. EPMA itself is only sensitive to elements present in the first micrometre below the sample surface, therefore in case of precipitation, sample preparation may have induced a significant release of Xe by cutting bubbles. As a consequence, such measurements underestimate Xe concentration especially when they are located in large bubbles with diameters larger than 0.5 µm. For a more reliable quantification, secondary ion mass spectrometry (SIMS) would be needed.

4 Results

4.1 Gas release during annealing tests

The first heating test has been performed up to a very high temperature of 1800°C to determine the main temperature regions where fission gas output happens. At 1800°C, it can reasonably be assumed that only a negligible part of FG remains in the U-Mo samples since this temperature is higher than Al (matrix and cladding) and U-Mo melting temperatures. Fig. 3-A shows the release kinetics of ^{85}Kr in this first TT. Below 750°C, three temperatures are interesting: a broad peak below 400°C, a second more intense peak at about 500°C and a last very intense peak at 670°C. The most intense two peaks were chosen as maximal temperatures for the two successive TT. Associated ^{85}Kr release curves are given in Fig.3-B and Fig.3-C. Reproducibility between these TT is very well seen. Indeed, ^{85}Kr integral release was 1.5 and 1.5 $\times 10^{15}$ at/g for TT up to 500°C (TT1 and TT2 respectively) whereas it was 7.8 and 8.5 $\times 10^{15}$ at/g for TT up to 670°C (TT1 and TT3 respectively). Finally, the released ^{85}Kr fraction during sample cooling down to room temperature yields 26±3 % and 6±2 % of the total released ^{85}Kr quantity for TT up to 500 and 670°C respectively. Considering Xe and He, two main peaks of the same shape as for Kr are found at identical temperatures. This indicates that all gases are located at the same positions inside the fuel.

.

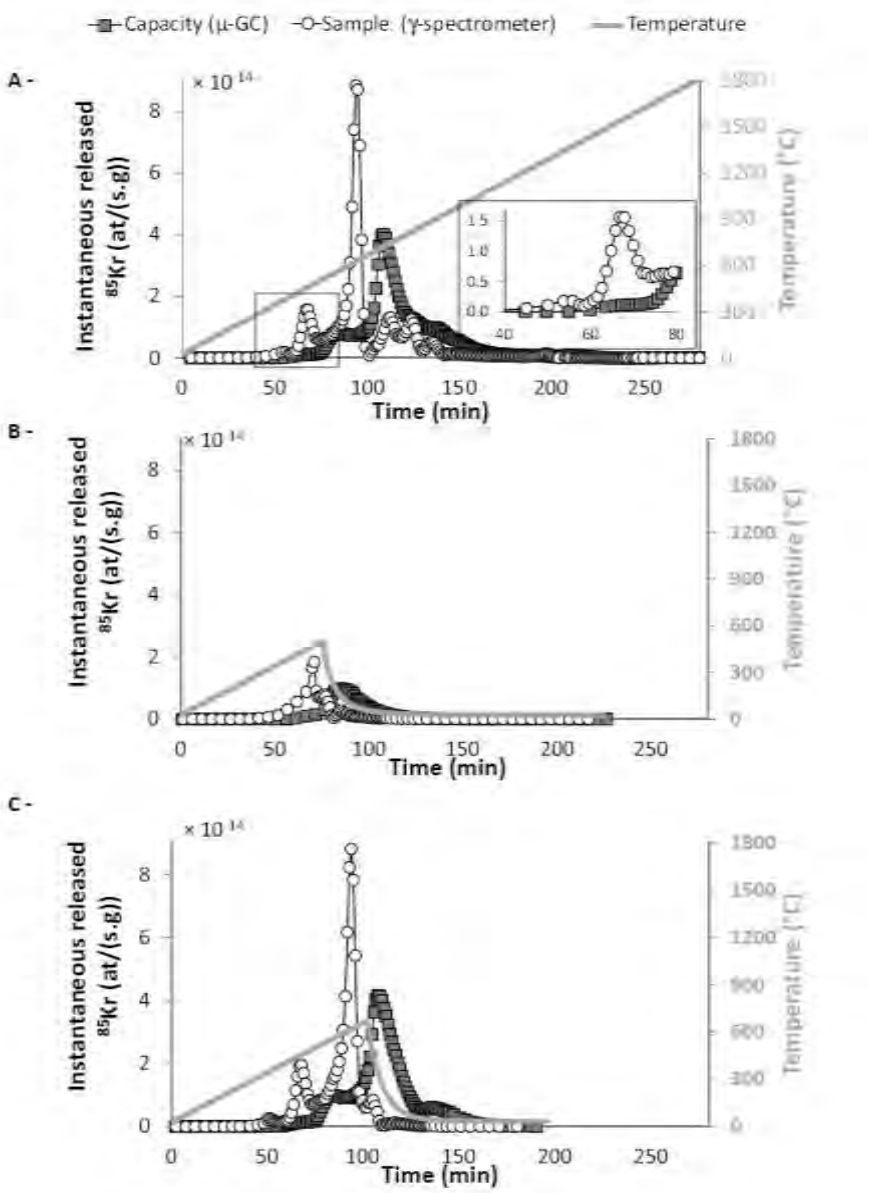


Fig. 3: Measured 85Kr output during the three different thermal treatments performed in the MERARG-2 loop using similar irradiated IRIS4 fuel samples. These TTs were performed up to 1800°C (A-), 500°C (B-) and 670°C (C-) respectively. The inset in (A-) shows a zoom in the capacity curve (in the [40;80] min time range) to indicate the presence of two FG output peaks. The associated temperatures are 400 and 500°C.

4.2 Post- Thermal Treatment results

A first global OM overview was carried out on both the 500°C and 670°C sample. At 500°C the sample microstructure (i.e. a clear distinction between the meat and the cladding) is still visible, while this is no longer the case for the 670°C sample. This is detailed in the following.

4.2.1 Thermal Treatment at 500°C

4.2.1.1 SEM characterisations

Inside U-Mo particles, big cracks of around 30 μm in length have been observed. In contrast, the Al matrix shows no signs of change. The cracks have the same size in both the centre and at the cladding interface. Considering the IDL thickness, no significant increase in its thickness can be observed at this step if compared to the pre-TT state. Moreover, large interconnected “holes” could be observed at the IDL/Al interfaces. These holes can also be observed after TT in similar conditions (475 °C 2h followed by an additional treatment at 550°C for 4 h) on non-irradiated U-Mo/Al fuel sample [22]. This clearly suggests that the origin of these holes is not due to fission gases.

4.2.1.2 EPMA

An overview of Si and Al X-ray mappings in both the meat centre region and the meat/cladding interface is shown in Fig. 4, while the location of Xe and Nd in the same areas is shown in Fig. 5.

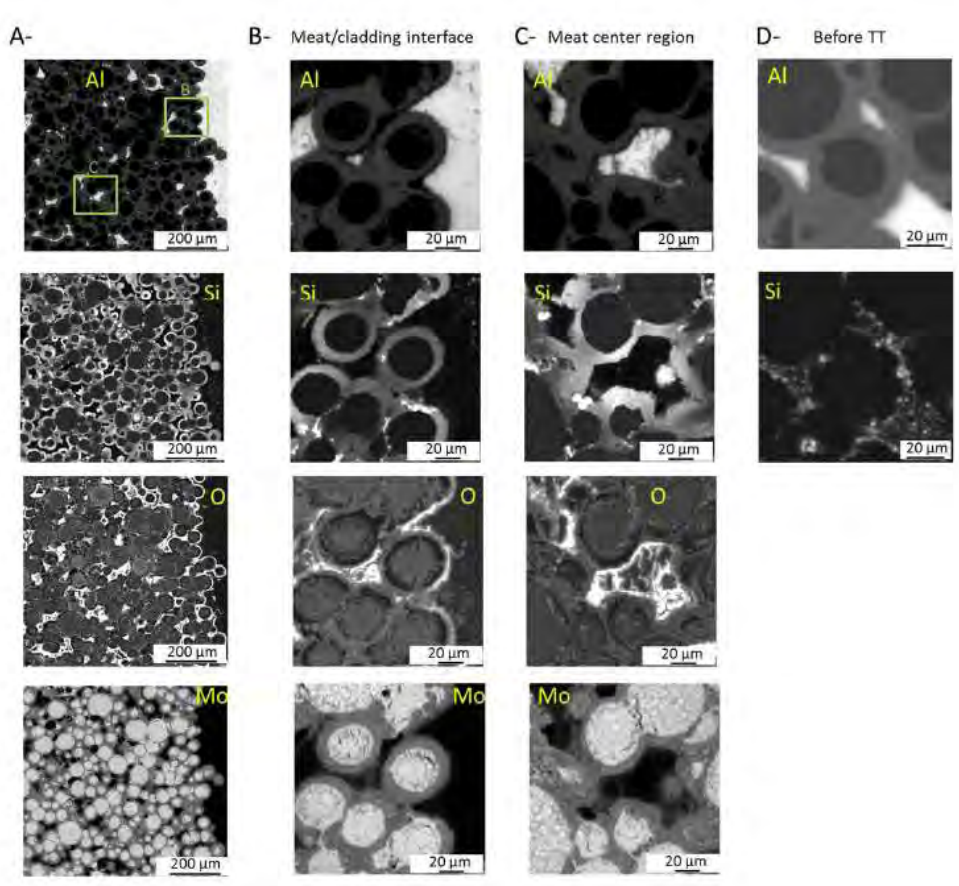


Fig. 4: Al, Si, O and Mo X-ray maps measured on IRIS4 thermally treated at 500°C (A- and B-) and on an as-irradiated sample before any TT (D-). Si accumulation inside the IDL is obvious after TT as shown in large maps (A-), as well as in more local characterisations close to the meat/cladding interface (B-) and the meat center (C-).

The biggest difference compared to the pre-TT state is the location of Si. Indeed, no Si remains in the Al matrix after TT at 500°C (see Fig.4-A): it has diffused towards U-Mo particles. It accumulates in the internal part of the IDL where its concentration may reach 4 at%. The IDL still exhibits a duplex structure with an oxygen-rich external part. However, the IDL seems to be Al richer (see Tab. 1).

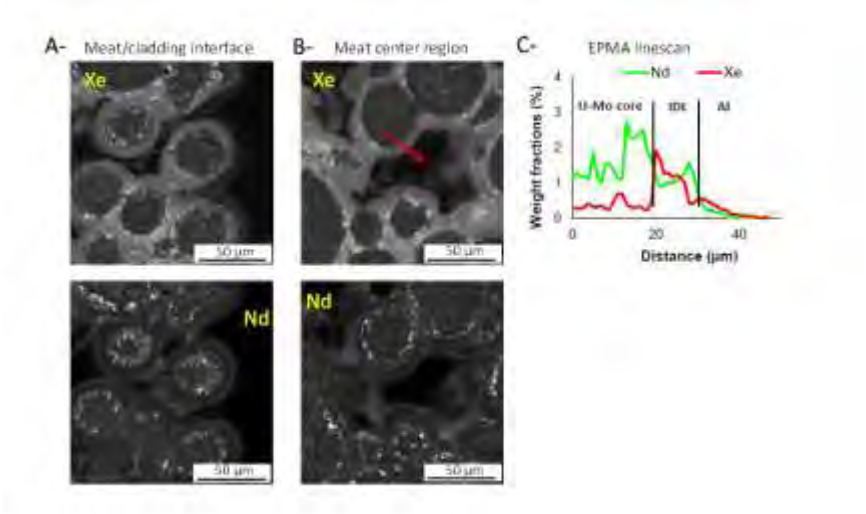


Fig. 5: Xe and Nd X-ray maps at both meat/cladding interface (A-) and meat centre region (B-). The same areas as in Fig. 4-B and –C have been selected. A quantitative EPMA linescan from U-Mo particle towards IDL and matrix shows the Nd and Xe weight fractions (C-). The linescan direction is indicated by a red arrow in (B-).

With respect to the as-irradiated case, distribution of Xe fission gas within U-Mo particles appears to be less homogeneous. Moreover EPMA linescans show a very low Xe average concentration within U-Mo cores (i.e. 0.17 wt%) (see Fig. 5-C), much lower than in the as-irradiated (before TT) case (0.33 wt%). However, based on these two observations, it should not be readily concluded that Xe has diffused out of U-Mo particles. Indeed these two measurements can also demonstrate a massive Xe precipitation in large bubbles which would have been cut during sample preparation prior to EPMA measurements. Inside the IDL, three different parts can be distinguished:

• Close to the U-Mo/IDL interface, in the internal part of the IDL, numerous Xe bubbles can be seen.
• A plateau in Xe concentration (1.3 wt%) is observed in the IDL which is probably associated with the presence of smaller Xe bubbles. In this location, the TT does not seem to have significantly modified the Xe concentration.
• Closer to the IDL/matrix interface, a decrease in the Xe concentration is found. If some Xe remains in the matrix close to the IDL (up to 0.5 wt%), no Xe accumulation can be measured in this area after TT at 500°C contrary to what has been measured in the as-irradiated case.

As a conclusion, Xe seems to have precipitated into larger bubbles in U-Mo cores as a consequence of the TT and has slightly diffused towards the internal IDL where it has also precipitated but into smaller bubbles. On both sides of the IDL/Al interface, Xe concentration is lower in the heat treated sample than before TT.

4.2.1.3 XRD

The main contributions to the XRD pattern in the 500°C sample are coming from α-U, γ-UMo, Al and UAl_3. The occurrence of α-U is attributed to the destabilisation of the γ-U-Mo metastable phase which is expected at 500°C [23]. The presence of the UAl_3 Bragg lines suggests that the IDL recrystallization has started.

4.2.2 Thermal Treatment at 670°C

4.2.2.1 SE/BSE characterisations

The U-Mo particle shape can only be detected in the very centre of the sample. For the rest of the sample, a complete interaction between Al and U-Mo particles happened, which could be a consequence of the expected melting point of both matrix and cladding which is below 700°C. In the meat centre, fissures can as well be detected, just as in the 500°C sample. Although the final temperature was higher, the fissures are not greater in size than in the 500°C U-Mo particles at comparable regions. Closer to the initial cladding location; particles can only be merely detected as huge porosities of up to several tens of micrometres in diameter have developed.

4.2.2.2 EPMA

Global X-ray maps for Mg and Fe show that these addition elements initially present in the frame and in the cladding have extensively diffused towards the meat centre. The behaviour of Al initially in the frame or in the cladding is more complex: it is assumed that it also diffused towards the meat centre, but on its way Al may have interacted with U-Mo particles.
Close to the meat/frame interface, a total interdiffusion between the U-Mo particles and the Al matrix has occurred: indeed, Al is now homogeneously distributed inside the particles (see Fig. 6-A). In the meat centre region, where a less drastic U-Mo/Al interaction occurred, the beginning Al diffusion inside the U-Mo particles can be observed (see white circles in Fig. 6-B).
When comparing Al, Si, U and Mo (Fig. 6-A) intensities and their location, it is visible that regions rich in U are lacking Al and Mo. Accordingly, Si can be found at the same spots as U. Therefore it is concluded that Al_xMo_y and U_xSi_y compounds have been created. Calculating the (Si+Al)/(U+Mo) atomic ratios from the meat centre towards the cladding, a value of 3.3 for the meat centre increasing to 9.6 at the sample outer limit was obtained (see Fig. 6-G).
Considering the elemental intensities of Xe (see Fig. 6-A and -B) this element is only very faintly detected at the cladding or frame interface while a higher amount can be found in the meat centre. Indeed, successive EPMA linescans close to the cladding or frame and in the meat centre show an average Xe weight fraction of 0.16 and 0.34 % respectively. Moreover EPMA linescan in the meat centre confirm that Xe diffuses more easily in the IDL than Nd: the Xe/Nd weight ratio evolves from 0.2 inside the particles up to 0.37 in the IDL.

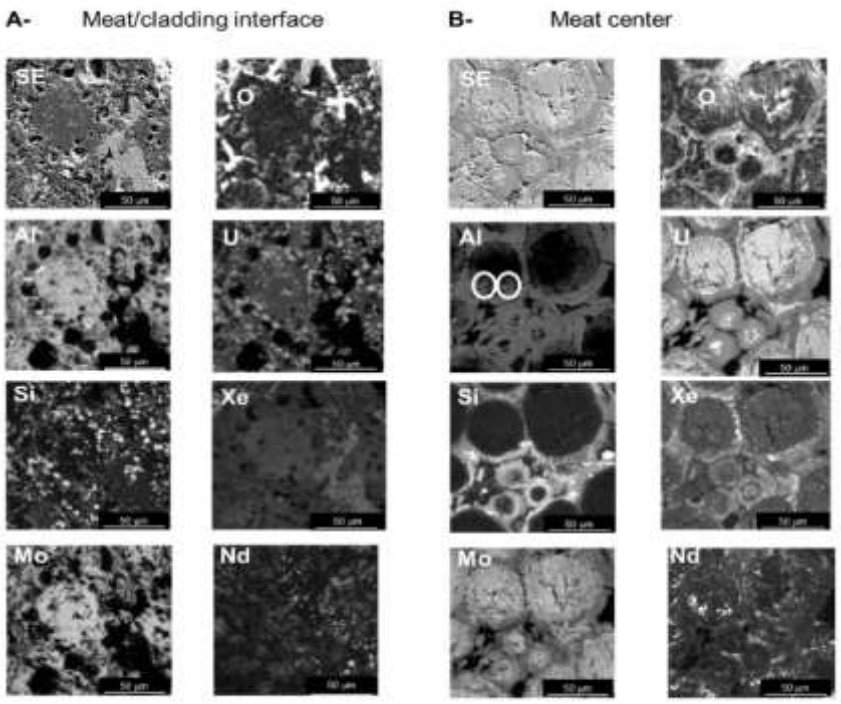


Fig. 6: SE images and X-ray maps (Al, Si, Mo, O, U, Xe, Nd) for two zones within the sample thermally treated at 670°C. The outer region at the meat/cladding or meat/frame interface is shown in (A-), while the meat centre region is shown in (B-). White circles represent areas where Si diffusion into the U-Mo particles has occurred.

5 Discussion

5.1.1 IDLs

At 500°C, the very limited increase in IDL thickness seems to have occurred all over the fuel plate meat and therefore will not be further discussed. This section is focused on the interpretation of the heterogeneous rate of U-Mo/Al interaction observed after TT at 670°C. As the heating rate of the samples was very low (0.1 °C/s), it is assumed that no thermal gradient has built up during the experiment. Instead the quantity of available Al throughout the meat thickness is the explanation for the heterogeneous rate of U-Mo/Al interaction. This interpretation is on the hand based on the behaviour of impurities (i.e. Mg) inside the cladding/frame that were found around interacted U-Mo particles, suggesting that Al from the cladding could also have been mobile during TT. On the other hand, an out-of-pile study confirms that the lower the U-Mo fractions in U-Mo/Al samples the higher the U-Mo/Al interaction rate [24]. Moreover in [24], it is reported that a very strong exothermic reaction occurs at 650°C. This temperature is in excellent agreement with the strong FG output detected at 670°C.

5.1.2 Si effects

Full diffusion of Si from the matrix into the internal part of IDL has been observed at 500°C. At higher temperatures (670°C), in fuel meat centre, this diffusion behaviour has not strongly evolved. Towards the outer sample part, in fully interacted zones, U_xSi_y compounds have

formed with a low Al and Mo content. At 670°C, both oxide and Si cannot prevent U-Mo/Al interaction.

5.1.3 U-Mo particles

Annealing at 500°C has induced the destabilisation of the metastable γ-U-Mo phase, which is a well-known effect [25]. This has been shown first by XRD. At 670°C, grains inside U-Mo particles are not observable anymore using X-ray maps (this was still possible at 500°C), and cracks inside U-Mo particles exhibit the same morphology and size.

5.2 Interpretation of Xe release kinetics

At temperatures below 400°C, 2.4% of the total fission gas release has been observed. In this case, the fission gas release may have happened out of volumes close to the sample surfaces.
Between 400°C and 500°C, 13.8% of the total FG release occurs. These fission gases are believed to be mainly located at matrix/IDL interface, in the IDL or even in the matrix. Indeed the IDL should have recrystallized, but the FG diffusion towards the IDL/matrix interface has not increased significantly. As a consequence, these 13.8% are mainly associated with FG located at the IDL/matrix interface in the as-irradiated fuel: this includes FG present in the external part of the IDL, in the matrix and those located in large porosities between matrix and IDL. The FG diffusion from the particle core to the IDL is neglected.
In the 500-670°C temperature range, an output of 57% of the total amount has been observed. This release is attributed to the remaining FG quantity inside U-Mo particles close to the cladding regions. This is due to total UMo/Al interaction in these zones.
For temperatures above 670°C, an increasing amount of U-Mo particles and IDLs are affected by the U-Mo/Al interaction process. Fission gas release (26.8% of the total amount) occurs until the whole sample (including the meat centre) is affected by interaction processes.

6 Conclusions

In this paper, a synthesis of the IRIS4 irradiation experiment has been performed with the goal to investigate FG behaviour in atomized U-Mo/Al(2.1wt%Si) nuclear fuels. The particles were protected with a 1 µm thick oxide layer. Previous experiments have demonstrated the better in-pile irradiation behaviour (with respect to the pure U-Mo/Al case) of fuel plates optimised with either Si added to the matrix, or U-Mo particles protected with an oxide layer. Microstructural analyses done here on in-pile irradiated oxidised U-Mo/Al(2.1wt%Si) fuels showed that positive effects of both solutions are not added. It is very likely that the presence of an oxide layer has reduced the Si diffusion kinetics towards U-Mo particles. This is visualized by the growth of a typical U-Mo/Al interdiffusion layer (IDL) around the particles which has not been enough delayed. It is well known that this Si diffusion can (besides irradiation) also be thermally activated. A striking illustration of this phenomenon has been obtained after thermal treatment up to 500°C of the in-pile irradiated fuel plate: Si has fully diffused towards the IDL.
Thermal treatments (TT) on in-pile irradiated fuel plate revealed two major FG release peaks around 500°C and 670°C. While the interpretation regarding the FG source giving rise to the peak at 500°C will require a confirmation, it is clear that the second peak (at 670°C) is due to a full interaction between U-Mo and matrix close to the cladding.
Further understanding of fission gas behaviour inside irradiated U-Mo/Al samples requires additional analytical methods. Therefore, secondary ion mass spectrometry (SIMS) in combination with EPMA could be used to clarify the location, the size of fission gas bubbles inside IDL after irradiation and U-Mo particles after TT at 500°C.

Acknowledgments:
Authors do acknowledge the MERARG team for their experimental work (CEA) and F. Charollais and B. Kapusta for their advices and comments.
This study was supported by a combined grant (FRM0911) of the Bundesministerium für Bildung und Forschung (BMBF) and the Bayerisches Staatsministerium für Wissenschaft, Forschung und Kunst (StMWFK).

7. REFERENCES

[1] P. Lemoine et al. in: Proceedings of the 8th International Topical Meeting on Research Reactor Fuel Management (RRFM), Munich, Germany, 2004.
[2] G.L. Hofman et al. in: Proceedings of the 26th International Topical Meeting on Reduced Enrichment for Research and Test Reactors (RERTR), Vienna, Austria, 2004.
[3] S. Van den Berghe et al., J. Nucl. Mater. 375 (2008), 340 – 346.
[4] J. Gan et al., J. Nucl. Mater. 396 (2010) 234 – 239.
[5] J. Gan et al., J. Nucl. Mater. 424 (2012), 43 – 50.
[6] A. Leenaers et al., J. Nucl. Mater. 412 (2011), 41 – 52.
[7] O.A. Golosov et al. in: 11th International Topical Meeting on Research Reactor Fuel Management (RRFM)/IFDWG, Lyon, France, 2007
[8] J. Lamontagne et al., J. Nucl. Mater. 440 (2013), 366 – 376.
[9] M. Ripert et al., Transactions of RRFM-2008, Hamburg, Germany, 2008.
[10] H. Palancher et al., J. Appl. Crystallogr. 45 (2012) 906-913.
[11] F. Charollais et al. in: Proceedings of the 13th International Topical Meeting on Research Reactor Fuel Management (RRFM) Vienna, Austria, 2009.
[12] Y.S. Kim, in: Comprehensive nuclear Materials (2012) 391-421.
[13] H. Palancher et al., J. Alloys Compounds 527 (2012) 53-65.
[14] M. Ripert et al. in: Proceedings of the 15th International Topical Meeting on Research Reactor Fuel Management (RRFM), Rome, Italy, 2011.
[15] D.D. Keiser et al., J. Nucl. Mater. 393 (2009) 311 – 320; D.D. Keiser et al., J. Nucl. Mater. 393 (2011) 226 – 234
[16] R. Jungwirth et al., J. Nucl. Mater, 438 (2013) 246–260.
[17] Ch. Valot et al. in: Proceedings of the 33th International Topical Meeting on Reduced Enrichment for Research and Test Reactors (RERTR), Santiago de Chile, 2011.
[18] M. Ripert et al. in: Proceedings of the 31st International Topical Meeting on Reduced Enrichment for Research and Test Reactors (RERTR), Beijing, China, 2009.
[19] Y.S. Kim et al., J. Nucl. Mater. 436 (2013) 14-22.
[20] A. Leenaers et al., J. Nucl. Mater. 441 (2013), 439 – 448.
[21] Y. Pontillon et al., J. Nucl. Mater. 385 (2009) 137–141.
[22] A. Bonnin et al., Zeit. Kristall. Proc. 1 (2011), 29 – 34.
[23] P.E. Repas et al., Trans. ASM, 1964, vol. 57, pp. 150–63.
[24] H.J. Ryu et al., J. Nucl. Mater. 321 (2003) 210 – 220.
[25] M.L. Bleiberg, J. Nucl. Mater. 1 (1959), 182–190.

TEM CHARACTERIZATION OF HIGH BURN-UP MICROSTRUCTURE OF U-7Mo ALLOY

J. GAN, B. D. MILLER, D. KEISER, JR. A. ROBINSON, J. MADDEN, P. MEDVEDEV AND D. WACHS

Nuclear Fuels and Materials Division, Idaho National Laboratory
P. O. Box 1625, Idaho Falls, ID 83415–6188, USA

ABSTRACT

As an essential part of global nuclear non-proliferation effort, the RERTR program is developing low enriched U-Mo fuels (< 20% U-235) for use in research and test reactors that currently employ highly enriched uranium fuels. One type of fuel being developed is a dispersion fuel plate comprised of U-7Mo particles dispersed in Al alloy matrix. Recent TEM characterizations of the ATR irradiated U-7Mo dispersion fuel plates include the samples with a local fission densities of 4.5, 5.2, 5.6 and 6.3 E+21 fissions/cm^3 and irradiation temperatures of 101−136°C. The microstructure of the irradiated U-7Mo fuel particles consists of fission gas bubble superlattice, large gas bubbles, solid fission product precipitates associated with the large gas bubbles, grain subdivision to tens or hundreds of nanometer size, collapse of bubble superlattice, and amorphization. This paper will describe the observed microstructures specifically focusing on the U-7Mo fuel particles. The impact of the observed microstructure on the fuel performance and the comparison of the relevant features with that of the high burn-up UO_2 fuels will be discussed.

1. Introduction

Transmission electron microscopy (TEM) characterization with high-resolution local microstructure and composition analysis in post-irradiation-examination (PIE) provides critical information in understanding the fuel performance in the reactors [1, 2]. With the recent advancement on TEM sample preparation using focused ion beam (FIB) technique for the irradiated fuels, site-specific TEM analysis from the areas of interest identified from scanning electron microscopy (SEM) become routinely available for the irradiated fuels [3]. TEM and SEM are two powerful complementary characterization tools to capture the microstructural information at different scales. A comprehensive SEM characterization of the high burn-up U-7Mo fuels for the research and test reactors can be found in a paper by Keiser et al in the forthcoming RRFM 2014 Transactions [4]. SEM can provide the general microstructure of the U-7Mo fuel particles, the interaction layer between the U-7Mo fuel particle and the Al-Si alloy matrix, as well as the overall bubble distribution within the fuel grains and at the fuel grain boundaries. TEM can reveal the microstructural details on both structure and composition for solid fission product distribution, fission gas bubble superlattice, defects development at the interaction layer and within the fuel particle with resolution down to ~ 1 nm.

The Reduced Enrichment Research and Test Reactor (RERTR) fuel development program is aiming to develop the reliable low-enriched fuel (U < 20%U-235) to support a safe and secured operation of the research and test reactors around the world. Fuel reactor irradiation test and the PIE are the critical part of the RERTR program. While publications or reports can be found in the open literature regarding the U-Mo fuel irradiation test and characterization, the detailed

TEM results of the irradiated fuels are still lacking [5,6,7]. Recent irradiation results from the SELENIUM test conducted in the BR-2 reactor in Belgium have shown increased fuel swelling rates for U(Mo)/Al(Si) dispersion fuel plates after a threshold fission density of ~ 4.5×10^{21} f/cm^3 [8]. In order to investigate the U-Mo fuel microstructural evolution at high fission density, it is necessary to carry out TEM characterization for the high burn-up microstructure.

Considering the threshold fission density that sets accelerated swelling rate with the break-away swelling, the microstructure detail around that turning point holds the key information about the mechanism driving the change in fuel swelling behavior and the potential mitigation that may be applied to the fuel to delay the onset of break-away swelling. It is believed that at high fission density the instability of fuel-matrix-interaction (FMI) and interlinking of large bubbles in the fuel grain are likely the causes leading to the break-away swelling. This paper focuses the recent TEM work on the high burn-up U-7Mo dispersion fuels tested in the Advance Test Reactor (ATR) at Idaho National Laboratory (INL). It is recommended to check the complement paper on the SEM high burn-up microstructure of U-7Mo for a better understanding of the TEM results.

2. Experiment

The irradiation conditions for the high burn-up U-7Mo dispersion fuels are listed in Table 1. Four sample conditions with their local fission densities at 4.5, 5.2, 5.6 and 6.3 $\times10^{21}$ fissions/cm^3 were characterized. A small 1 mm diameter fuel punch was produced from the irradiated dispersion fuel plate in a hot cell at the Hot Fuel Examination Facility (HFEF) at INL. The small punch sample was then transferred to the Electron Microscopy Laboratory. TEM samples were prepared either with conventional 3.0 mm disc sample preparation technique in a glove box or using FIB-TEM lift-out technique from an SEM sample. Schematic of 3 mm TEM disc sample preparation with a fuel punch (ϕ ~1 mm, h ~1.5 mm) and a Mo ring is shown in Figure 1. TEM characterization was performed using a 200 keV JEOL 2010 TEM/STEM system equipped with a LaB_6 filament, a Gatan UltraSacn-1000 digital camera for imaging and a Brukers Si drift detector for composition analysis with Energy Dispersive Spectroscopy (EDS). The TEM selected area diffraction (SAD) patterns from the major zones were used for structural analysis. The Java-version Electron Microscopy Simulation (JEMS) software developed by Stadelmann was used to assist in identifying the phase and indexing the diffraction patterns [9].

Table 1. Information of high burn-up dispersion fuel samples for TEM work.

Fuel plate ID	R2R010	R3R050	R0R010	R2R040
Fuel particle composition	U-7Mo	U-7Mo	U-7Mo	U-7Mo
Matrix composition	Al-2Si	Al-5Si	Pure Al	Al-2Si
U-235 enrichment (%)	19	58	58	58
Local fission density (10^{21} f/cm^3)	4.5	5.2	5.6	6.3
Fuel plate centerline temperature (°C)	105	130	122	120
TEM sample format	3 mm disc	FIB-TEM	FIB-TEM	3mm disc, FIB-TEM

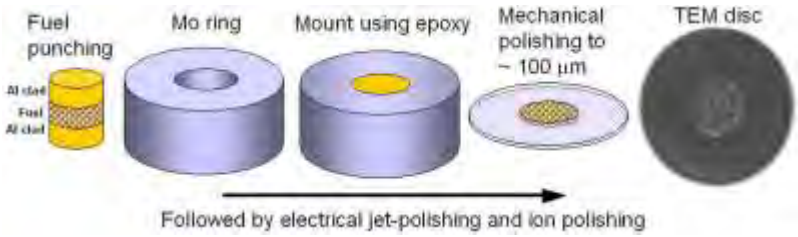


Figure 1. Schematic of TEM 3 mm disc sample preparation for irradiated dispersion fuel.

3. Results and Discussion

For fuel plate R2R010 sample with a local fission density of 4.5×10^{21} f/cm^3, the TEM work was performed on a 3 mm disc sample. Figure 2 reveals the key features of the irradiated microstructure. The overall microstructure is quite heterogeneous. From fuel particle interior to the Al alloy matrix, it typically consists of 4 different zones, namely crystalline U-Mo fuel (particle interior), a thin amorphous layer of U-Mo fuel with high Si content (3-13 at.%, fuel particle outer layer), amorphous FMI layer, and crystalline Al alloy matrix. The development of large bubbles in the U-Mo fuel particle interior and amorphous outer layer region is evident. The heterogeneous distribution of large bubbles in the FMI layer is more pronounced with area either containing just few scattered bubbles (see Figure (a)) or area filled with many bubbles (see Figure (c)). In the crystalline region of the fuel, most areas contain fission gas bubble superlattice (GBS) as shown in Figure 1 (b). It was found that the thin shell around the large bubble in the fuel is amorphous with a high content of solid fission products. No solid fission product precipitate (SFPP) was found in the areas with GBS.

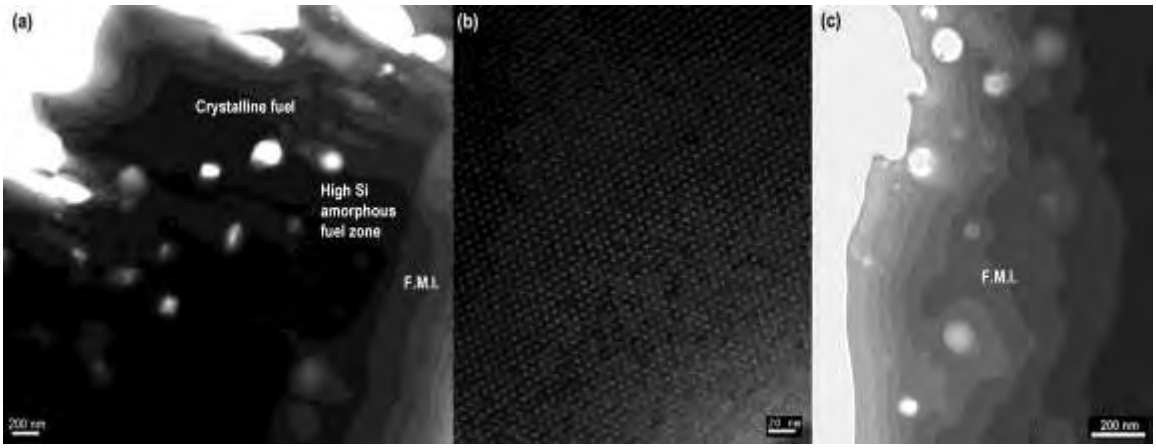


Figure 2. TEM bright field images of U-7Mo dispersion fuel (4.5×10^{21} fission/cm^3) show (a) general microstructural feature, (b) gas bubble superlattice in crystalline fuel grain and (c) another region of Fuel-Matrix-Interaction layer containing many large bubbles.

The detailed TEM analysis on GBS can be found in the previous work [2]. It is a 3D self-organized bubble superlattice with a face-center-cubic (FCC) structure coherent to the U-Mo body-center-cubic (BCC) structure. The measured average bubble size in the GBS is in the range of 3.1-3.6 nm with a superlattice constant in the range of 11-12 nm. It is believed that the crystalline U-Mo with GBS produces a high stress field in U-Mo that may significantly increase the diffusion barrier for solid fission products, therefore most solid fission products are believed to be kept in solution when the GBS is present and maintained. With the increase of solid fission product concentration in the U-Mo fuel, it could increase the solution energy, which may be one of the driving forces leading to the grain subdivision where the original large U-Mo grain (5-10 μm) breaks into much smaller submicron grains [10, 11, 12, 13]. It is intriguing that while Si addition in the Al alloy matrix seems to be effective in suppressing the growth of FMI, the diffusion of Si into the U-Mo fuel particle outer region creates an amorphous thin shell that is believed to be detrimental. The heterogeneous bubble development in the FMI layer may be related to the fluctuation of the actual local fission density as a result of imperfection of fuel particle distribution in the Al alloy matrix.

For the irradiated fuel plate R3R050 with a local fission density of 5.2×10^{21} f/cm^3, the TEM characterization was carried out on the FIB-TEM samples. The SEM data generated from the FIB-sectioned-surface provide more detailed information, compared to the conventional mechanically polished surface, which suffers from a smearing effect. Figure 3 reveals the general microstructure of the fuel particle interior with approximately 15% of the clean areas estimated from SEM. These clean areas retain crystalline structure and GBS fine bubbles as shown in the high magnification image in the middle. The measured Mo content in clean area is higher than that of the area with large bubbles (15 wt% vs. 13 wt%), indicating a more stable initial U-Mo structure. It is speculated that these clean areas may be associated with large initial grain size. The microstructural development at the fuel-matrix interface is shown in the image on the right where a white dashed line was added to mark the boundary between the amorphous and crystalline U-Mo. Compared to a sample irradiated to a fission density of 4.5×10^{21} f/cm^3, the width of the Si-rich amorphous zone increased and the bubbles with the largest size were found in this zone. It appears that the Si-rich zone grows inwards with the development of relatively large round-shaped bubbles due to surface energy constrain for the amorphous material. Another important feature is the preferential attachment of SFPP to the large bubbles as shown in Figure 4. In many cases, the SFPP formed inside the large bubbles and attached to the inner wall of the large bubbles. The EDS measurement in the STEM mode indicates these SFPP consist of Zr, Sr, Y, Ce, Ba, Nd, Pd, Te and Xe, which is different from the 5-metal: Pd, Rh, Ru, Tc and Mo found in the grain boundary bubbles in irradiated UO_2 [14]. This is likely due to the difference in diffusion kinetics of the SFP in U-Mo and UO_2 fuels.

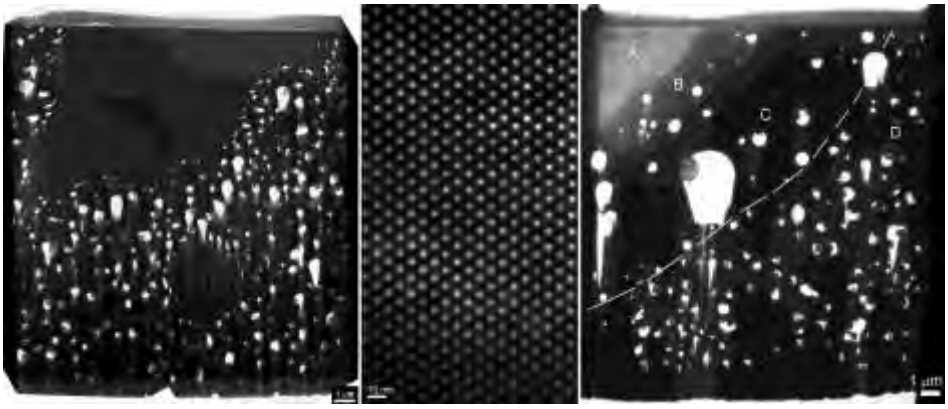


Figure 3. Bright field TEM images of irradiated U-7Mo fuel (5.2×10^{21} f/cm^3) reveal general microstructure (left), the GBS from the clean areas in the left (center), and multi-zone (right) microstructure of (A) Al alloy matrix, (B) FMI, (C) high Si amorphous zone in U-Mo and (D) crystalline fuel particle interior.

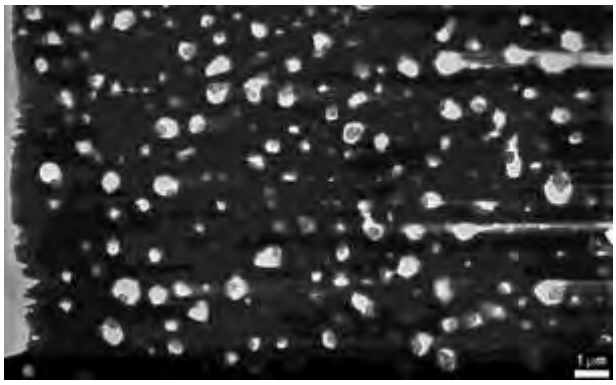


Figure 4. Low magnification TEM image of irradiated U-7Mo fuel (5.2×10^{21} f/cm^3) shows distribution of large bubbles and solid fission product precipitates preferentially attached to the large bubbles.

At this fission density, significant microstructural changes lead to the widely spread collapse of the GBS and the development of large bubbles throughout the fuel particle. The overall microstructure is still highly heterogeneous. Figure 5 reveals the development of large bubbles in the microstructural areas after GBS collapse. The EDS measurement for these areas provides the composition in wt% for U (81-86), Mo (13-16), Al (0.4-1.5) and Si (0.1-1.8). These areas are believed to remain crystalline with a GBS at the lower fission density. This is based on the composition data and the presence of a high concentration fine bubbles and the similar small bubble size in comparison to that of GBS bubbles. The formation of large bubbles after collapse of the GBS appears mainly through bubble coarsening. This is likely the mechanism that introduces large bubbles in the fuel grain interior at intermediate to high burn-up. Note that accelerated fuel plate swelling is observed in irradiated dispersion fuel plates once the average fission density reaches approximately 5×10^{21} fission/cm^3.

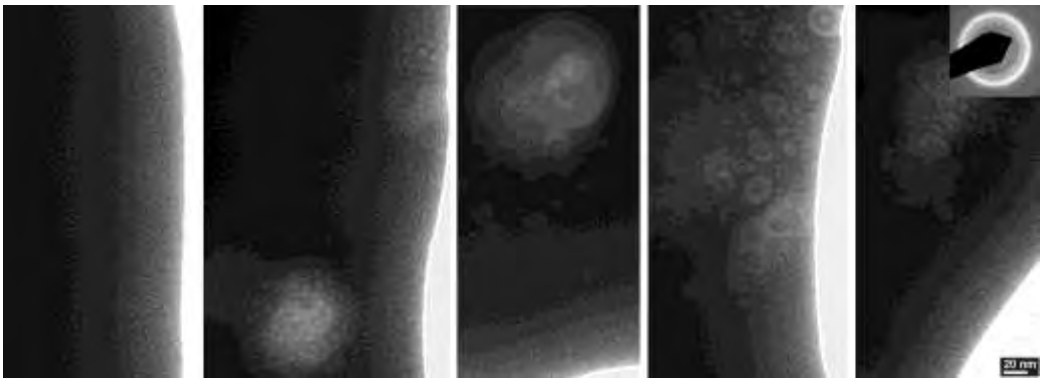


Figure 5. TEM images of neighboring amorphous areas in U-Mo fuel, revealing the development of large bubbles through bubble coarsening. Inset shows the SAD pattern from the region.

The sample made from irradiated fuel plate (R0R010) has a local fission density of 5.6×10^{21} f/cm^3. Figure 6 shows the STEM low magnification image of general microstructure on the left, and the high magnification TEM image of scattered residual GBS pocket on the right. At this fission density, although the general microstructure in the fuel particle interior looks quite similar to that of 5.2×10^{21} f/cm^3, the residual GBS was only found in small pocket in scattered areas of the crystalline region in the sample. Similar to the previous fuel plate (R3R050), the fuel interior is filled with large bubbles that exhibit a wide size range (0.1 – 1 μm). There is no evidence in TEM images of interlinking between the large bubbles. Since large bubbles tend to develop an amorphous shell filled with SFP, the increase in size and concentration of the large bubbles results in a noticeable decrease in the volume fraction of the crystalline regions of the U-Mo fuel. Note that the matrix is pure Al without Si, the Si rich amorphous outer layer did not form.

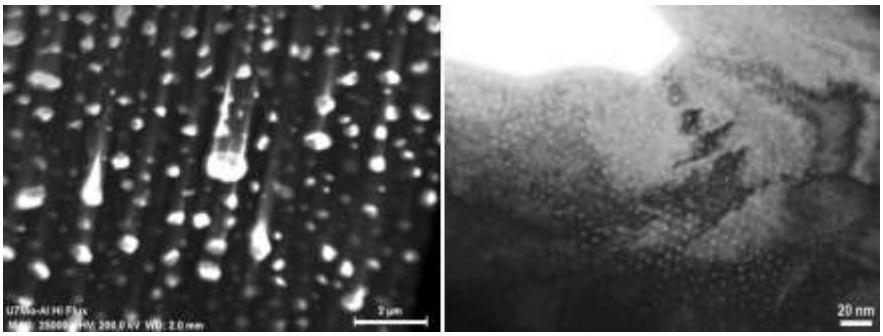


Figure 6. STEM image of the fuel particle interior for U-7Mo fuel at a fission density of 5.6×10^{21} f/cm^3 (left), and a TEM high magnification image of the residual GBS in the crystalline region (right).

The sample for fuel plate (R2R040) has the highest local fission density of 6.3×10^{21} f/cm^3. Both a conventional 3 mm disc sample and FIB-TEM samples were prepared for TEM characterization. Figure 7 shows the bright field images of an overview on the left and the detailed view of fuel interior at high magnification on the right. The SEM work identified potential interlinking of large bubbles in the fuel particle interior. The labels in the overview image on the left are for EDS composition measurement and the results are listed in Table 2. The Si-rich amorphous zone next to the FMI layer is not well defined in this case, likely the result of microstructural heterogeneities. Two important features are noticed in the high-resolution image. One is the residual GBS pocket still present in a certain part of the crystalline fuel region where the residual GBS shown in the picture was imaged at zone [100] direction. The other is the presence of fine grains known as grain subdivision, which is well known as a key microstructural feature of the rim structure in the high burn-up UO_2 pellet.

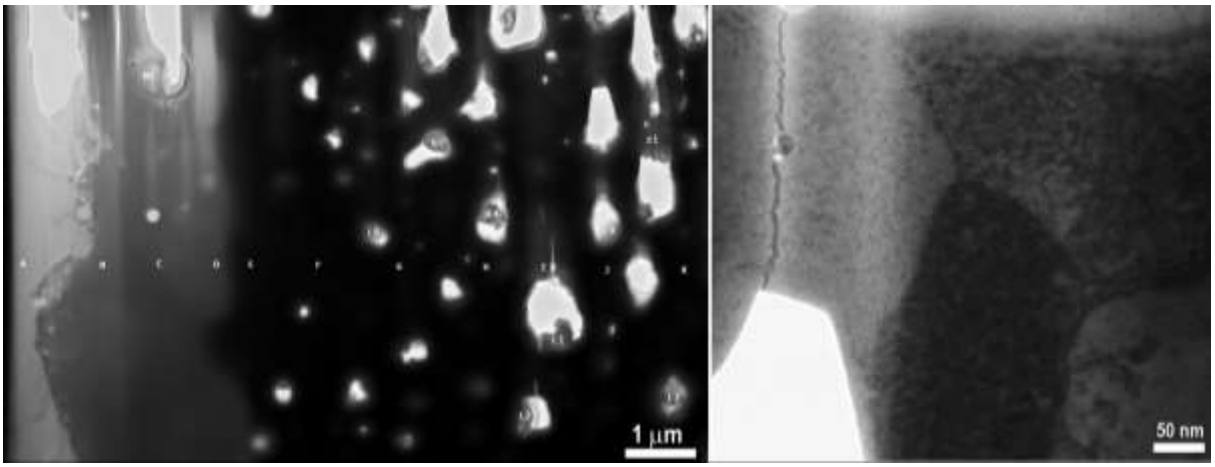


Figure 7. TEM images of irradiated U-7Mo fuel high burn-up (6.3×10^{21} f/cm^3) microstructure: overview (left) with marks for EDS composition measurement and the detailed view (right) showing grain subdivision and residual GBS.

Table 2. EDS measurement (wt%) of the spot marked in Figure 7.

ID	U	Mo	Al	Si	Other element
A	0.4	1.2	98.3	0.1	
B	52.4	6.0	34.8	6.8	
C	55.7	6.5	36.2	1.7	
D	60.2	7.5	31.8	0.5	
E	87.3	8.9	3.0	0.9	
F	88.4	9.2	0.8	1.6	
G	92.2	7.6	0	0.2	
H	91.0	8.7	0.1	0.1	
I	90.0	9.1	0.5	0.3	
J	91.7	8.1	0.1	0.2	
K	91.9	8.0	0.2	0	
L1	11.4	1.5	0.3	0	Sr_23, Ba_22, Y_19, Zr_7.6, Pd_5.6, Te_4.4, Pm_2.1
L2	5.5	0.8	0.2	0	Sr_30, Ba_37, Y_14, Zr_5.3, Pd_1.0, Te_3.0, Pm_2.1
L3	7.3	0.8	1.3	0	Sr_31, Ba_37, Y_12, Zr_6.4, Pd_0.8, Te_2.9
L4	26.2	4.7	0.3	0	Sr_23, Ba_22, Y_12, Zr_5.5, Pd_5.8, Te_1.0
L5	11.3	1.3	0.3	0	Sr_25, Ba_30, Y_15, Zr_8.7, Pd_8.0, Te_1.4
L8	16.4	4.5	0	0	Sr_29, Ba_18, Y_18, Zr_7.6, Pd_4.4
L9	10.3	0.3	0	0	Sr_32, Ba_45, Y_8.5, Zr_2.9, Pd_0.5
M1	44.2	3.4	22.6	0	Sr_2.3, Ba_0.4, Zr_27
Z1	90.0	7.9	0.2	0	Zr_1.5

For the irradiated U-7Mo fuel at high fission density, the original large fuel grains (~ 10 μm) break into much smaller grains (~ 200 nm). Unlike the original U-7Mo grain boundaries that are the preferential sites for the early development of large bubbles, the newly created boundaries from grain subdivision appear free of large bubbles other than the fine bubbles. One explanation is that these subdivided grain boundaries are mostly the small angle boundaries with low energy that is not an effective sink to attract defects, including Xe gas. This observation is consistent with that of UO_2 high burn-up rim structure [15]. EDS data in Table 2 indicates that most SFPPs associated with large bubbles consist of Sr, Ba, Y, Zr and Pd. The general microstructure of the fuel particle interior is a mixture of amorphous and crystalline regions as shown in Figure 8. Bubble coarsening continues in the amorphous region (image on the left), and small pockets of GBS can still be observed (image on the right).

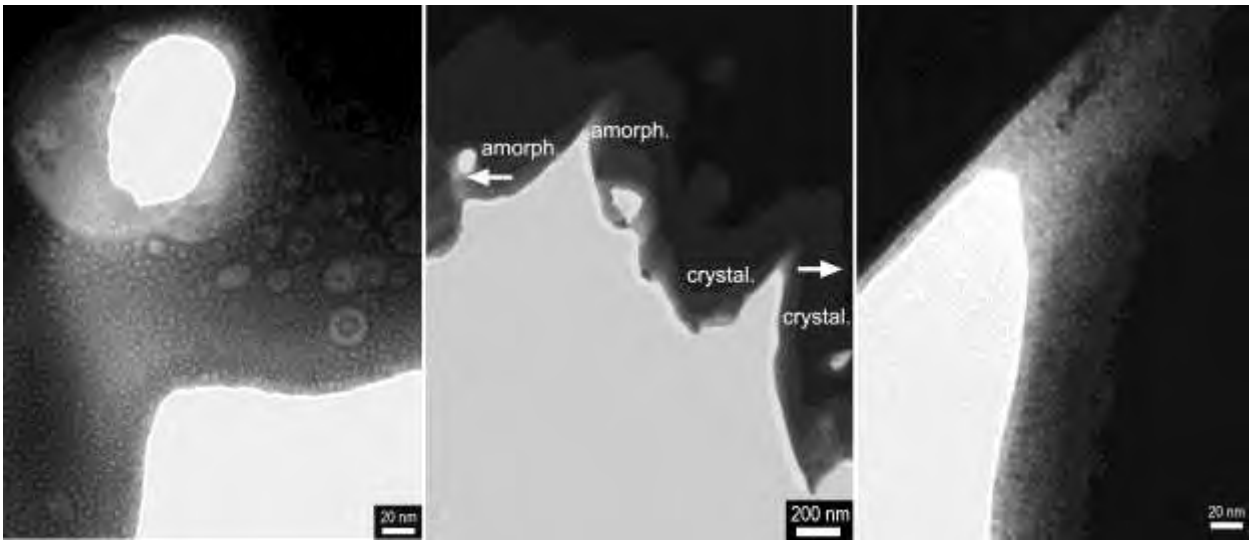


Figure 8. TEM image of high burn-up (6.3×10^{21} f/cm^3) U-7Mo fuel microstructure (middle) showing the mixture of amorphous region with bubbles (left) and the crystalline region with residual GBS (right). The light contrast around the large bubbles consists of high concentration solid fission products.

From the SEM work, it was found that at high burn-up, the development of large bubbles appears more pronounced around the grain boundaries. This appears to combine with the bubble coarsening occurring in the fuel, which seems to be the driving mechanism for the large bubble development. Linkage of large bubbles becomes evident at high burn-up. The interlinkage of large bubbles is attributed to the increase of large bubble concentration and the growth of large bubbles. It is speculated that when the microstructure is filled with a high concentration of large bubbles or linked bubbles, the vacancy partitioning to bubble growth becomes important, and the fuel swelling is then dominated by the vacancy production from irradiation rather than from fission gas and SFP production. One supporting evidence is that the break-away swelling occurs when fuel reaches high burn-up with reduced fission rate.

As most of the research and test reactors are the thermal neutron spectrum reactors, the additional fissions from Pu-239 as a result of U-238 transmutation has to be considered in fuel microstructure development. This effect may be associated with the fuel format, geometry and irradiation configuration in the reactor core. It is often called fission “peaking effect” which could lead to a local fission density much higher than eastimeted from U-235 from the Plate Code [16]. Besides the “peaking effect” from fuel plate geometry, which is anticipated to be similar for both dispersion fuel and monolithic fuel, the dispersion fuel is expected to have a stronger “peaking

effect" due to its larger surface to volume ratio for fuel particles in comparison to monolithic fuel foil for the comparable U-Mo fuel volume. This could be the partial explanation for the early break-away swelling observed in dispersion fuel, compared to what has been observed for monolithic fuel. Another major difference between dispersion and monolithic fuel is the fact that the U-7Mo particles in dispersion fuel compared to the U-10Mo foil in monolithic fuel are a thermodynamically less stable phase. The heterogeneous distribution of the dispersed U-7Mo fuel particles in as-fabricated dispersion fuel may also be partially responsible for the non-uniform irradiated microstructure from particle to particle, although the estimated local fission density is the same. This is because the Plate Code assumes a uniform particle distribution for a fission density calculation.

4. Conclusions

The high burn-up microstructure of irradiated U-7Mo dispersion fuels is dominated by large bubbles with size ranging from a few hundred nm to ~ 1 μm. Bubble coarsening is identified as an important mechnism in the devlopment of large bubbles. At a fission density of 5.2×10^{21} f/cm^3, there is roughly 15% of the particle area (clean fuel grain) that contains only the gas bubble superlattice of ~ 3.5 nm bubbles without large bubbles. The size of these areas varies from few μm up to more than ~ 10 μm. Small pockets of GBS bubbles are still present in the crystalline region at the highest fission density of 6.3×10^{21} f/cm^3, but with significantly reduced volume fraction, and the GBS pocket size is typically around a few hundred nm or below. The early development of large round bubbles is evident in the high Si amorphous layer next to the fuel-matrix-interaction layer. At high fission density, a significant portion of the original U-7Mo grains turn amorphous as a result of radiation-induced atomic displacement damage from high energy fission fragments as well as the local composition change due to fission product generation. The collapes of the GBS at high burn-up results in a rapid precipitation of the solid fission products at a thin amorphous shell around the large bubbles or inside the large bubbles. The observed microstructures from TEM analysis of high burn-up U-7Mo dispersion fuel plate samples has helped identify possible mechanisms for the eventual break-away swelling of U-7Mo fuel at high fission density.

Acknowledgments

This work was supported by the U.S. Department of Energy, Office of Nuclear Materials Threat Reduction (NA-212), National Nuclear Security Administration to the RERTR program, under DOE-NE Idaho Operations Office Contract DE-AC07-05ID14517. Accordingly, the U.S. Government retains a nonexclusive, royalty-free license to publish or reproduce the published form of this contribution, or allow others to do so, for U.S. Government purposes.

References

[1] S. Van den Berghe, W.Van Renterghhem, A. Leenaers, J. Nucl. Mater., 375 (2008) 340-346.
[2] J. Gan, D.D. Keiser Jr., D.M. Wachs, A.B. Robinson, B.D. Miller, T.R. Allen, J. Nucl. Mater., 396 (2010) 234-239.
[3] B.D. Miller, J. Gan, J. Madden, J.F. Jue, A. Robinson, D.D. Keiser, Jr., J. Nucl. Mater., 424 (2012) 38-42.
[4] D.D. Keiser, Jr., J.F. Jue, J. Gan, B.D. Miller, A.B. Robinson, P. Medvedev and D.M. Wachs, "High Burn-up Microstructure of U-7Mo Alloy", to be published in RRFM 2014 Transaction,

[5] A. Leenaers, S. Van den Berghe, J. Van Eyken, E. Koonen, F. Charollais, P. Lemoine, Y. Calzavara, H. Guyon, C. Jarousse, D. Geslin, D. Wachs, D. Keiser, A. Robinson, G. Hofman, Y.S. Kim, J. Nucl. Mater., 441 (2013) 439-448.
[6] S. Van den Berghe, Y. Parthoens, F. Charollais, Y.S. Kim, A. Leenaers, E. Koonen, V. Kuzminov, P. Lemoine, C. Jarousse, H. Guyon, D. Wachs, D. Keiser Jr, A. Robinson, J. Stevens, G. Hofman, J. Nucl. Mater., 430 (2012) 246-258.
[7] A. Leenaers, S. Van den Berghe, W. Van Renterghem, F. Charollais, P. Lemoine, C. Jarousse, A. Röhrmoser, W. Petry, J. Nucl. Mater., 412 (2011) 41-52.
[8] S. Van den Berghe, Y. Parthoens, G. Cornelis, A. Leenaers, E. Koonen, V. Kuzminov, C. Detavernier, J. Nucl. Mater., 442 (2013) 60-68.
[9] P. Stadelmann, http://cimewww.epfl.ch/people/stadelmann/jemsWebSite/jems.html.
[10] L. E. Thomas, C. E. Beyer, L. A. Charlot, J. Nucl. Mater., 188 (1992) 80-89.
[11] S. E. Donnelly, J. H. Evans, [ed.]. NATO Advanced Research Workshop on Fundamental Aspects of Inert Gases in Solids. New York : Plenum Press, 1191.
[12] L. M. Clarebrough, M. E. Hargreaves, M. H. Loretto. *Recovery and Recrystallization of Metals.* New York : Interscience, 1963.
[13] J-P. Crocombette, J. Nucl. Mater., 305 (2002) 29-36.
[14] Hj. Matzke and H. Blank, J. Nucl. Mater. 166 (1989) 120.
[15] I.L.F. Ray, Hj. Matzke, H.A. Thiele, M. Kinoshita, J. Nucl. Mater., 245 (1997) 115-123.
[16] Y. S. Kim, G.L. Hofman, P. G. Medvedev, G. V. Shevlyakov, A. B. Robinson, H. J. Ryu, 2006 International Meeting on Reduced Enrichment for Research and Test Reactors, “Post Irradiation Analysis and Performance Modeling of Dispersion and Monolithic U-Mo Fuels”.

CHARACTERIZATION OF FUEL-CLADDING BOND STRENGTH USING LASER SHOCK

J. A. SMITH, D. L. COTTLE AND B. H. RABIN
Nuclear Fuels and Materials, Idaho National Laboratory
2525 N. Fremont Avenue, Idaho Falls, Idaho, 83415 – USA

ABSTRACT

This paper describes new laser-based capabilities for characterization of fuel-cladding bond strength in nuclear fuels, and presents preliminary results obtained from studies on as-fabricated monolithic fuel consisting of uranium-10 wt.% molybdenum alloys clad in 6061 aluminum by hot isostatic pressing. Two complementary experimental methods are employed, laser-shock testing and laser-ultrasonic imaging. Measurements are spatially localized, non-contacting and require minimum specimen preparation, and are therefore ideally suited for applications involving radioactive materials, including irradiated materials. The theoretical principles and experimental approaches employed in characterization of nuclear fuel plates are described. The ability to measure layer thicknesses, elastic properties of the constituents, and the location and nature of laser-shock induced debonds is demonstrated, and preliminary bond strength measurement results are discussed.

1. Introduction

The U.S. National Nuclear Security Agency oversees the Global Threat Reduction Initiative (GTRI), which is tasked with minimizing the use of highly enriched uranium (HEU) worldwide. A key component of that effort is the conversion of research reactors from HEU to low-enriched uranium (LEU) fuels. The U.S. High Performance Research Reactors (USHPRR) program is developing and qualifying a new high-uranium density fuel to replace the HEU dispersion fuels currently used in certain high performance reactors [1]. The new LEU fuel is based on a fuel meat made from a monolithic uranium-10 wt.% molybdenum (U–10Mo) alloy foil (typically 0.2 to 0.4 mm thick) encapsulated in 6061 aluminum cladding using a hot isostatic pressing (HIP) process, with thin (typically 25 μm) Zr diffusion barrier interlayers between the U–10Mo and cladding, as shown schematically in Figure 1.

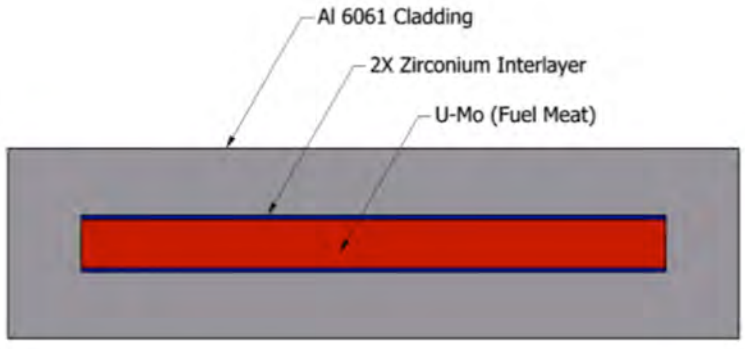


Figure 1. Schematic cross section of monolithic fuel plate.

One significant difference between monolithic fuel and historical dispersion fuels relates to the fuel-cladding interface. In monolithic fuel, a mismatch in properties exists across the fuel-cladding interface, resulting in localized stresses during fabrication and irradiation. Additionally, the interface involves complex microstructures that evolve over time. Characterizing the integrity of the fuel in both the as-fabricated (fresh) and irradiated

conditions has therefore been identified as being important for demonstrating safe reactor operations and assessing fuel performance. Requirements exist to ensure mechanical stability and cooling of the fuel are maintained, and to demonstrate that fuel-cladding bonding is sufficient to prevent delamination failures. Since the cladding serves as the primary barrier for fission product retention, there are additional requirements related to ensuring that cladding-cladding bonding is maintained during anticipated operating conditions. Measurement of bond strengths in fuel plates using conventional mechanical testing techniques is difficult. Therefore, a critical need exists to establish new evaluation methods and criteria for assessing interfacial bonding in fuel plate geometries and that can be applied to both fresh and irradiated fuels.

2. Background

In these methods, originally developed for application to measurements of the adhesion of thin films and coatings to substrates [2-7], a high-energy pulsed laser is used to generate a large-amplitude compression wave at the top surface of a specimen. The compressive shock wave travels through the material and after reaching the bottom of the specimen, the shock wave is reflected from the free surface as a tensile stress wave that travels back through the specimen. When of sufficient magnitude, the tensile stress generated will debond the film/coating from the substrate. By analyzing the specimen response, and with the aid of shock wave propagation models and/or dynamic simulations, the stress required to debond the film/coating from the substrate can be deduced. These techniques were later adapted for the purpose of characterizing the adhesion between layers in thicker structures such as epoxy bonded carbon-carbon composites [8], the approach that forms the basis for the methods described herein.

Advantages offered by LST include the ability to provide a spatially localized measurement without contacting the specimen, and with a minimum of specimen preparation. Since there is no propagation of the induced debond outside of the test area, the specimen remains intact. Compared to conventional testing techniques (e.g. pull testing, bend testing or double cantilever beam methods), these are significant advantages for applications involving radioactive materials. For example, nuclear fuel plates can be characterized remotely, improving operator safety, and fuel remains contained within the cladding, avoiding the potential for spreading radioactive contamination. It should be recognized that LST is a high strain-rate interrogation technique, relying upon the propagation of waves at the speed of sound in the material. The constitutive behavior of a material under shock loading conditions is significantly different compared to that observed using quasi-static (i.e. low strain-rate) testing methods. In particular, flow stresses in metals are significantly elevated and deformation mechanisms are different, therefore, the critical stress necessary to create a debond (i.e. the bond strength) as measured by LST may be several times greater than the values measured by quasi-static (i.e. low strain rate) methods such as pull testing [9].

3. Experimental

3.1. Methods

A high energy pulsed laser (shock laser) is fired at the top of a specimen, with incrementally increasing energy, in order to generate shockwaves with increasing magnitude within the sample. The goal is to determine the threshold necessary to create a debond at one of the internal interfaces. Because the shock wave energy imparted to the specimen is difficult to calculate or reproduce consistently, optical energy of the source laser is not an accurate predictor of internal stresses. For this reason, the system incorporates an optical interferometer whose purpose is to measure the bottom surface velocity of the specimen in real time during the shock experiments. The bottom surface velocity provides a more accurate representation of the energy actually imparted to, and transmitted through, the specimen, and is therefore used in calculations to estimate the internal stresses responsible for debonding. A pulse-echo laser-UT inspection is performed before and after each laser shot in order to determine when a debond has occurred, as well as to measure the through-

thickness location of the debond within the sample, information necessary to more accurately estimate the internal stress at the location where the debond actually occurred.

Previous publications [8,10] explain the strategy used to account for multiple reflections from internal interfaces, improving the accuracy and reproducibility of stress estimates. Plastic deformation may also occur in the materials under shock loading conditions, which changes the shape of the shock waves, dissipates energy, and further alters local stress distributions, making precise stress estimates more difficult. Preliminary bond strength calculations are simplified by assuming only elastic wave propagation.

A schematic diagram showing the configuration of the sample is provided in Figure 1. Experimentally, a Q-Switched neodymium doped: yttrium aluminum garnet (Nd:YAG) laser, which generates optical pulses of about 10 ns with a maximum energy of 3.5 J at 1064 nm wavelength, is used to induce shock waves for interrogating the top surface of fuel plates. During a shock experiment, the surface velocity of the bottom surface of the sample is recorded in real-time by an optical velocimeter based on a solid Fabry-Perot etalon. The velocimeter laser is a long pulse (>120 µs) Nd:YAG, operated at 1064 nm wavelength. Details of the etalon interferometer can be found in reference [11]. Laser-UT measurements are obtained using generation and detection laser beams applied on the bottom surface (i.e. pulse-echo mode), superimposed with diameter sizes of about 1 mm and 0.5 mm, respectively. During areal scanning, the step size of the scan is approximately 0.5 mm in the x and y directions on the sample surface. The generation laser is a Nd:YAG, operated at 532 nm wavelength with a full-width at half-maximum (FWHM) of 10 ns. The detection uses a long pulse (>120 µs) Nd:YAG laser, operated at 1064 nm wavelength and a photorefractive interferometer. The laser-ultrasonic inspection is similar to a conventional ultrasonic C-scan.

In order to avoid surface damage and to increase the efficiency of optical-to-mechanical transduction, the surface of the material is covered with an absorbing tape and then covered with a transparent plasma-constraining medium (such as water or transparent tape). The shock waves generated under the confinement layer produce large-amplitude molecular displacements of the sample surface, rather than surface ablation. Previous work [6,8,12,13] used a liquid-constraining medium (e.g. de-ionized water). The liquid-constraining medium works well, but the liquid overspray can contaminate equipment and optics, and may not be desirable in the hot cell environment, therefore recent work has focused on the use of transparent tape.

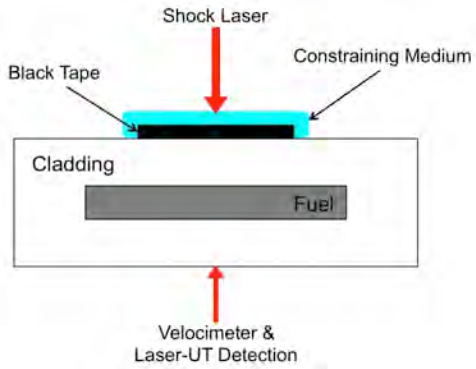


Figure 1. Schematic diagram showing the experimental configuration of a sample during analysis.

3.2. Stress Calculations

For clarity, the naming conventions for sample orientation and interfaces are shown schematically in Figure 2. The identifying aspects of the fuel plate (e.g. front surface, interface I_2, back cladding, etc.) are relative to the plate identification (ID), independent of the plate orientation. In the experimental reference frame, the laser shock is always carried out at the top of the specimen and velocimetry and laser-UT measurements are always

performed from the bottom. The Reference Orientation is the case where the plate ID is at the top and the Flipped Orientation is where the plate ID is at the bottom.

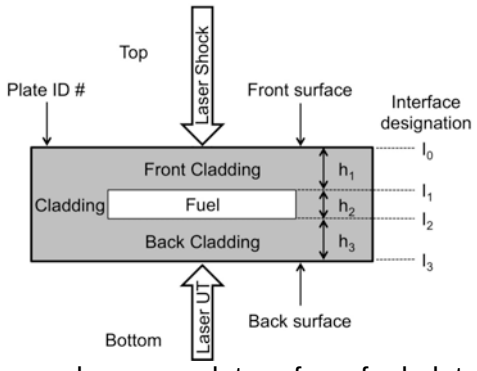


Figure 2. Geometry and sample nomenclature for a fuel plate tested the "Reference Orientation" (Plate ID at the top). Note that fuel plate characteristics are independent of the testing orientation.

The shock-wave source size (~laser spot size) is chosen to be at least two times the sample thickness (about 1.5 mm for the typical fuel plates under investigation) in order to better approximate one-dimensional (1-D) wave propagation. Under the 1-D approximation, shear stresses are neglected, and the initial shock wave is primarily compressive in nature. The generated compressive shock wave travels through the specimen and is then reflected by the bottom surface of the plate as a tensile wave, assumed to be solely responsible for creating debonds at internal interfaces within the sample.

Ignoring multiple and overlapping reflections, and assuming elastic, 1-D wave propagation and no attenuation, the measured bottom surface velocity, u_B, is related to stress at the bottom surface, σ_B, by Equation 1:

$$\sigma_B = \rho v u_B \tag{1}$$

where v is the speed of sound and ρ is the density. Laser-UT inspection can be used to accurately measure v by measuring the time, t, required for a compression pulse to travel through a sample having known thickness, h according to Equation 2:

$$v = \frac{h}{t} \tag{2}$$

The sample of known thickness can be a dedicated, calibrated reference standard or a location on the test specimen that has been dimensionally inspected by physical means. In this manner, speed of sound in 6061 Al, v_{Al}, has been determined to be 6,440 m/s. By knowing v_{Al} and by measuring the total plate thickness, h_{total}, at any location, the thickness of the individual layers, namely h_1, h_2 and h_3, and the speed of sound in the fuel meat, v_{fuel}, can be determined at any specific location.

The fundamental equation describing the speed of 1-D elastic wave propagation in a homogeneous, isotropic solid is given by Equation 3:

$$v = \sqrt{\frac{E}{\rho}} \tag{3}$$

where E is Young's modulus. Equation 3 allows changes in properties to be evaluated.

In practice, the stresses in the material are the result of several waves, not only the wave reflected from the bottom surface. To illustrate this, Figure 3 shows the time evolution of the stress amplitude in the specimen thickness caused by an elastic wave pulse generated normal to the top surface at time t=0. This diagram was generated by an elastic simulation assuming a 1-D propagation for thicknesses representative of fuel plates (h_1=600 µm,

h_2=280 µm, h_3=510 µm) for typical wave velocity, *v,* and density, ρ, values as follows: for Al, v = 6.4 mm/µs, ρ = 2.7 g/cm^3, for U-Mo, v = 3.2 mm/µs, ρ = 17.2 g/cm^3. The temporal profile of the pulse is assumed triangular and of duration T, with a sharp compression front and a slow release (rarefaction), in close agreement with previously measured loading [8]. Due to the reflections at the interfaces and surfaces, other tensile waves arise and cumulative effects result in large tensile stress concentrations at the interfaces. For this geometry, the propagation times in the three layers are almost equal. Bond strength is evaluated by increasing the laser pulse energy step-by-step to determine the stress at which debonding first occurs. To minimize cumulative effects of plastic deformation, it is preferable to apply a single shock at each location.

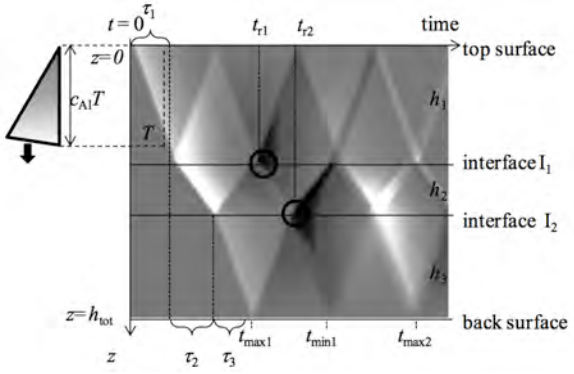


Figure 3. Time-space diagram of the propagation of a shock wave pulse. White and black areas represent the compression wave and the tensile wave, respectively.

The relation between the bottom surface velocity and the in-depth stress is calculated from the propagation of waves that reached the bottom surface, up to the desired depth, neglecting attenuation, consisting of two different sets of contributions: 1) back propagation and forward propagation (two terms), 2) including internal reflections (four terms). To illustrate, using the formulation proposed by Perton et al. [8, 10] consider the stress at interface I_1 at time t_{r1}, which is calculated from the particle velocities of the four waves present at that time and that position (Figure 3):

$$\sigma_1 = z_2 u_{01} - z_1 u_{0121} + z_2 u_{0101} - z_1 u_{012321} \tag{4}$$

where $z_i = \rho_i v_i$ is the acoustic impedance of the layer i, where u_{01}, u_{0121}, u_{0101} and u_{012321} refer to the waves that propagated from the top surface to the interface I_1, after successive reflections or transmissions denoted 0, 1, 2, 3, respectively for the top surface, the interfaces I_1, I_2 and the bottom surface. With the travel times (τ_1, τ_2, τ_3) in the different layers, the stress at the first interface becomes:

$$\sigma_1(t_{r1}) = \frac{z_3}{2T_{23}^P}\begin{pmatrix} u(t_{r1}+\tau_2+\tau_3) + R_{23}^p T_{21}^p u(t_{r1}-\tau_2+\tau_3) - R_{12}^p u(t_{r1}-2\tau_1+\tau_2+\tau_3) \\ - T_{23}^p T_{32}^p T_{21}^p u(t_{r1}-\tau_2-\tau_3) \end{pmatrix} \tag{5}$$

where $u(t)$ is the velocimeter signal at the bottom surface, and R_{ij} and T_{ij} are respectively the reflection and transmission coefficients in pressure amplitude between layers i and j. The stress value is positive for a compressive wave and negative for a tensile wave. If one considers only back propagation and forward propagation excluding internal reflections, one has Equation 5 with only the first and fourth terms. Note that the bottom surface velocity should only be used for time $t<t_{min1}$ in Figure 3. The stress at the interface I_2 at time t_{r2} is calculated in the same way. The full derivations of the stress expressions are given in [14].

Based on the above equations, a Labview™ software application was developed [15] that calculates the stress at both interfaces in the 3-layer medium using the maximum bottom surface velocity recorded by the velocimeter during a shock experiment. It's necessary to use this software in combination with the laser-UT inspection methods to confirm that the threshold for debonding has been established and to identify which interface has debonded, and therefore which calculated stress value corresponds to the measured bond strength.

3.3. Materials

Samples examined included experimental monolithic U-10Mo fuel mini-plates produced using fabrication processes described elsewhere [16-18], as listed in Table 1. The monolithic fuel plates typically contained DU-10Mo fuel with thin Zr diffusion barrier layers clad in 6061 by a HIP process, although some plates were also examined for comparison that either contained LEU instead of DU, or did not contain the Zr diffusion barrier layer. The "standard" HIP processing conditions involve 560 °C maximum temperature, 90 minutes hold time, 103 MPa maximum pressure, and a cooling ramp rate of 280 °C/hr. In contrast, the samples from HIP 88 involved the same conditions, except the hold time was reduced from 90 minutes to 60 minutes. Results are also shown for fuel plates fabricated during process development that employed stainless steel (SS) foil as a surrogate fuel material. These samples, HIP 45-2 and HIP 46-2, were fabricated using standard HIP conditions.

Table 1. Samples tested for which results are discussed in this paper.

PLATE ID	DESCRIPTION
HIP 45-2	Mini-plate, SS fuel meat, standard HIP processing conditions
HIP 46-2	Mini-plate, SS fuel meat (known weak bond due to intentional contamination with Neo-lube)
HIP 88-2	Mini-plate, DU-10Mo fuel meat, HIP hold time 60 minutes
HIP 88-3	Mini-plate, DU-10Mo fuel meat with Zr diffusion barrier layer, HIP hold time 60 minutes
HIP 88-5	Mini-plate, LEU-10Mo fuel meat with Zr diffusion barrier layer, HIP hold time 60 minutes
OSU-1-4	Approximately 2" x 1.75" sample section from larger plate, DU-10Mo fuel meat with Zr diffusion barrier layer, standard processing conditions

Additionally, a large-size fuel plate fabricated to support flow testing experiments was characterized. This fuel plate is representative of full-size monolithic fuel plates of interest. A sample sheared from this fuel plate is identified as OSU-1-4 in this paper.

4. Results and Discussion

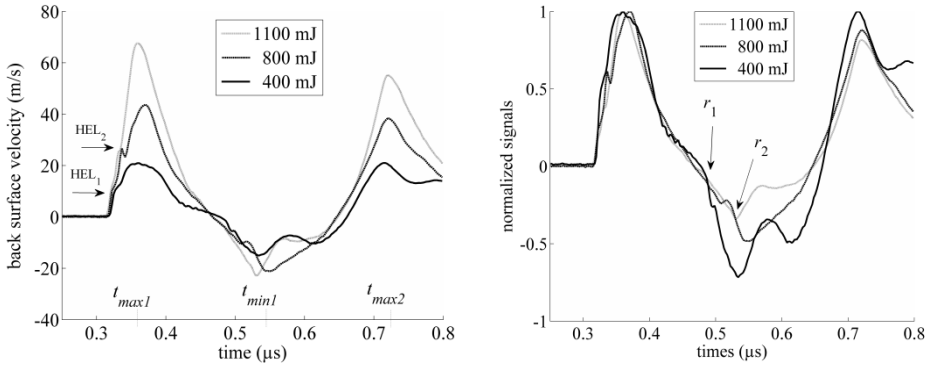
4.1. Data Acquisition

Figure 4 shows typical bottom surface velocity signals from measurements made on a fuel plate for three laser energies, starting from a value well below the debonding threshold, and increasing to values just above the debond threshold for interfaces I_1 and I_2. The first acoustic pulse, located between 300 and 450 µs corresponds to the generated wave that travels through the entire sample and arrived at time t_{max1} in Figure 3. A small step at about 10 m/s, denoted HEL_1, corresponds to the aluminum Hugoniot Elastic Limit (HEL, i.e. the threshold between elastic and plastic behaviour in aluminum at high strain rate). Another step at about 25 m/s, denoted HEL_2, is presumed to correspond to the HEL of the fuel. The wave propagation is clearly in the "elastic-plastic regime" [19-21].

For the signal at 400 mJ, the compression pulse (positive velocity) is followed by a tensile pulse (negative velocity between 450 and 650µs). When the signals are normalized, Figure 4b, distinct signatures (indicated by arrows) are observed for the two velocity signals obtained at higher laser energies. These are attributed to interfacial debonds that change the local reflection conditions.

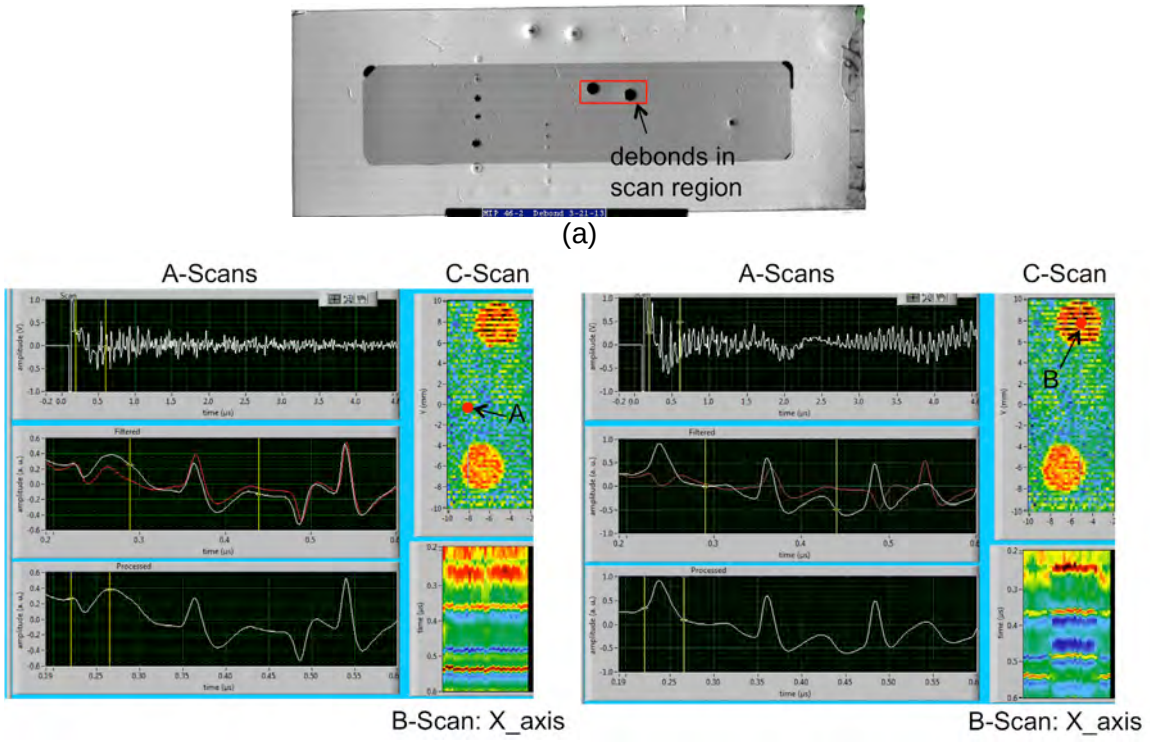
Figure 5 shows laser-UT performed on an area of fuel plate HIP 46-2 that contained debonds. Figure 5a is a convention ultrasonic C-scan image of the sample taken after the laser shock experiment, in which several debond indications are present. Figure 5b and 5c show the laser-UT signals obtained from the scan at well-bonded (position A) and debonded (position B) locations, respectively. By comparing the raw and filtered A-scan (amplitude vs. time) data from these cursor locations, the presence of the debond is clearly evident (note

the signal inversion in the A-scan at about 0.23 and 0.48 μs). The B-scan data, which represents the time history of amplitude along a line (x-axis here), clearly shows the presence of the original interfaces in Figure 5b and the multiple, new longitudinal and shear wave reflections created by the presence of the debond in Figure 5c. The depth of the debond is determined from the A-scan data by knowing the arrival time and the speed of sound in the material.



(a) (b)

Figure 4. (a) Example bottom surface velocity signals measured for laser shock pulse energies below any interface debond (400 mJ), at interface I_1 (800 mJ) and I_2 (1100 mJ) debond thresholds. (b) Same signals normalized.



(a)

(b) (c)

Figure 5. (a) Conventional ultrasonic C-scan image of laser shocked fuel plate HIP 46-2 showing debonds in example laser-UT scan area. Laser-UT scan with signals shown for cursor positioned at (b) well-bonded spot, and (c) debonded spot.

4.2. Laser-UT Debond Characterization

An example of a shocked fuel plate containing a debond at the front interface (interface I_1) scanned in the Reference Orientation is shown in Figure 6. Note the peak marked C in the red curve, taken from a well bonded region, that represents the wave that traveled from the bottom of the plate to the top surface where it was reflected and traveled back. In the white

curve, taken with the cursor positioned over the debond, this reflection is absent, and instead, peaks marked A and B appear. Peak A represents the wave that traveled from the bottom of the plate to the debond, where it was reflected and traveled back. Peak B represents the wave that is reflected once between interfaces I_1 and I_2 (i.e. reverberated within the fuel layer itself) and then travels back to the bottom surface.

The same fuel plate, when inspected in the Flipped Orientation, is shown in Figure 7. The signal in red, taken from a well bonded region, shows peaks marked B and C corresponding to reflections from interface I_1 and the top surface, respectively. In the signal taken from the debonded region, the signal does not pass interface I_1 and only the multiple reflections between I_1 and the bottom surface are observed.

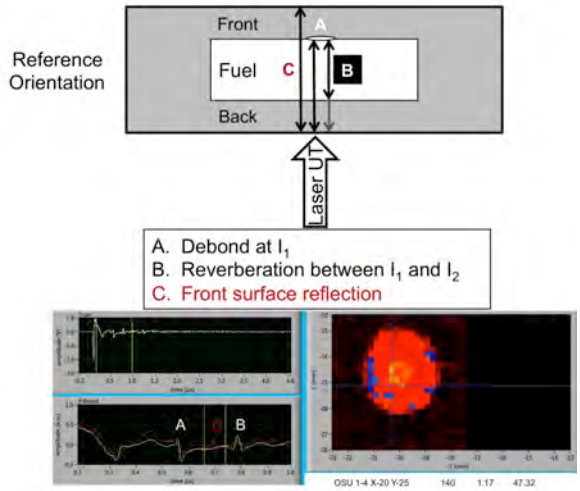


Figure 6. Example of shocked fuel plate containing a debond at interface I_1 inspected in Reference Orientation.

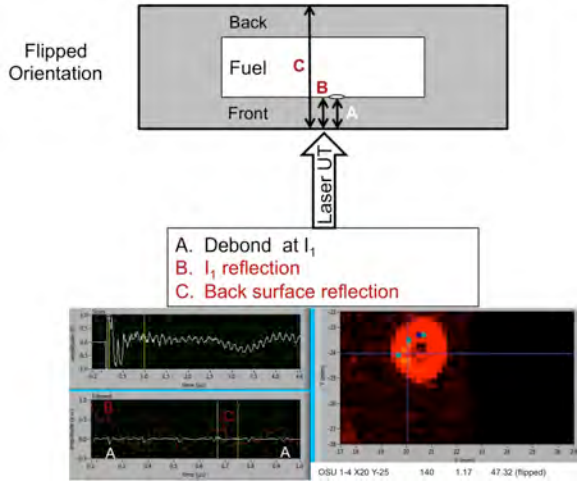


Figure 7. Example of shocked fuel plate containing a debond at interface I_1 inspected in Flipped Orientation.

4.3. Laser-UT Dimensional Characterization

Experiments performed on the OSU-1-4 fuel plate, listed in Table 2, demonstrate the geometrical and material properties that can be obtained. The thicknesses of the front and back cladding are calculated by noting the appropriate time of flight from each interface in the ultrasonic echo and knowing the (measured) speed of sound in the cladding. The fuel thickness is calculated by subtracting the sum of the front and back cladding thicknesses from the total (measured) plate thickness. The speed of sound in the fuel is measured by determining the time of flight (TOF) obtained from front and back surface reflections in the ultrasonic echo. The calculated fuel thickness and TOF are then used to calculate the

ultrasonic velocity in the fuel. Using this procedure, the mean and standard deviation (STD) thicknesses and fuel velocities were determined at several locations on the specimen. Note there is a significant difference between the front and back cladding thickness for this fuel plate, indicating the fuel is not centered within the plate. The impacts of asymmetry on fuel performance are not understood and are under investigation. Similar measurements were carried out on the HIP 88 mini-plates and these results are listed in Table 3.

Table 2. OSU-1-4 thickness and fuel velocity determined by laser-UT.

OSU 1-4 Location	Total thickness, mm	Front cladding thickness, mm	Back cladding thickness, mm	Fuel thickness, mm	Fuel velocity, mm/μs
X-10 Y-10	1.503	0.498	0.677	0.327	3.021
X-20 Y-25	1.508	0.473	0.694	0.341	3.112
X-10 Y-35	1.499	0.473	0.684	0.341	3.145
X-10 Y-05	1.503	0.460	0.684	0.359	3.203
X-15 Y-30	1.506	0.489	0.684	0.333	3.139
X-10 Y-25	1.505	0.477	0.723	0.306	2.985
Mean / STD	1.505 / 0.003	0.478 / 0.020	0.697 / 0.018	0.330 / 0.021	3.079 / 0.103

Table 3. HIP-88 thickness and fuel velocity determined by laser-UT.

HIP-88 Plate ID	Total thickness, mm (Mean/STD)	Front cladding thickness, mm (Mean/STD)	Back cladding thickness, mm (Mean/STD)	Fuel thickness, mm (Mean/STD)	Fuel velocity, mm/μs (Mean/STD)
88-2	1.66 / 0.001	0.74 / 0.007	0.62 / 0.004	0.30 / 0.003	3.36 / 0.019
88-3	1.68 / 0.018	0.74 / 0.011	0.62 / 0.003	0.32 / 0.014	3.61 / 0.130
88-5	1.71 / 0.012	0.76 / 0.009	0.64 / 0.006	0.31 / 0.002	3.26 / 0.033

The measurements on the HIP 88 plates demonstrate remarkable consistency for a laboratory scale fabrication process. The average sound velocity for 6061 Al in the HIP 88 plates is 6.44 mm/μs with a standard deviation of 0.024 mm/μs. Keep in mind that the "uncertainty" in the ultrasonic measurements is incorporated into the fuel thickness calculation, which is reflected in the correspondingly larger standard deviation values for fuel thickness in Tables 2 and 3. Table 3 indicates that LEU (HIP 88-3) fuel velocity is higher than DU. According to Equation 5, this suggests the Young's modulus of the LEU fuel is higher, although differences in fuel density cannot be ruled out since fuel density was not independently measured in this work.

4.4. Bond Strength Calculations

Bond strength calculations were performed by taking into account the multiple reflections involved in debonding, as described previously, based upon user input of the experimentally determined plate geometry, density and speed of sound for each layer. The software uses the measured maximum surface velocity to calculate the stress as a function of time at each interface location, assuming either two terms or four terms (see Section 3.2). The following example shows an experiment performed on the OSU-1-4 sample tested in the Reference Orientation at location X-10 Y-35, which exhibited a debond threshold at a maximum bottom surface velocity of 35.21 m/s. The velocimeter output, material and geometry inputs, and the results of the stress calculations are shown in Figure 8. It's possible to move the cursor position along the time axis and read the calculated stress value at each interface, allowing a comparison between peak interface stress and the velocimeter signal.

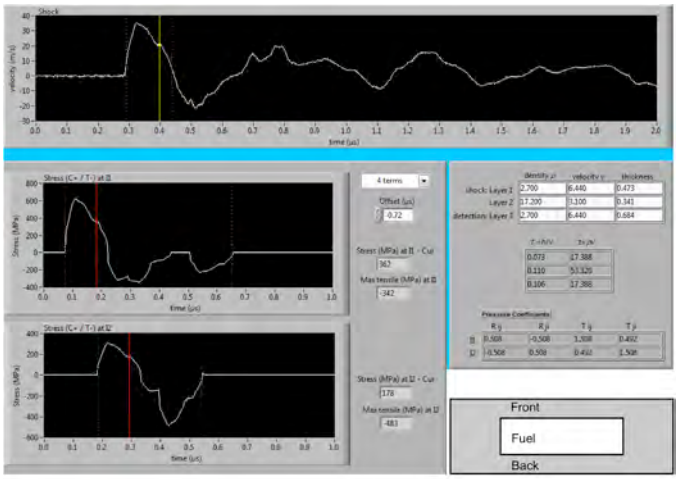


Figure 8. Example of bond strength calculation for the OSU-1-4 fuel plate sample after threshold testing in the Reference Orientation assuming four terms in the stress calculation.

Bond strength calculations for the HIP 88 fuel plates and the HIP 45-2 surrogate fuel plate tested in the Reference Orientation are shown in Table 4. The highlighted cells in Table 4 indicate which interface was observed to debond during the experiment. The calculations using two terms predict that the bottom interface always exhibits higher peak tensile stress, which is consistent with the observation that interface I_2 always debonded first. For the calculations using four terms, the interface stresses are nearly equal, which may explain why in some cases, both interfaces were observed to debond from a single laser shot that exceeded the debond threshold. These preliminary results suggest the bare fuel DU specimen (HIP 88-2) may exhibit slightly higher bond strength compared to the Zr barrier DU specimen (HIP 88-3), and that the DU/Zr specimen may exhibit slightly higher bond strength compared to the LEU/Zr specimen (HIP 88-5). Additional studies are needed to confirm these results. Note also that the stresses calculated for HIP 45-2 SS surrogate fuel plate are comparable to the uranium-bearing specimens. Interestingly, in the HIP 45-2 case, a significantly lower peak tensile stress is calculated for the top interface (I_1) in the four-term calculations. HIP 45-2 debonded at interface I_2, consistent with these predictions.

Table 4. Bond strength calculation results for the HIP 88 mini-plates.

Plate ID	Flash lamp delay (μs)	Maximum tensile stress, two terms (MPa)		Maximum tensile stress, four terms (MPa)	
		I_1	I_2	I_1	I_2
88-2	140*	341	734	712	701
	135	345	746	736	737
88-3[a]	150*	237	560	617	572
	140	296	675	700	691
	140*	280	642	674	639
88-5	150*	229	482	468	456
	145	237	499	502	535
	150*	264	562	556	552
45-2	160*	271	516	317	655
	155	241	470	300	562
	155	268	504	302	651

[a] Assumed the same density value as DU.
* Indicates multiple laser shocks at one location

Bond strength calculations for different OSU-1-4 fuel plate test locations are shown in Table 5. In general, the four term calculation predicts less difference in the peak stress values between the two interfaces compared to the two term calculation. In the Reference

Orientation, the peak stress for interface I_2 is little changed by the addition of the extra terms, whereas in the Flipped Orientation, there is a notable difference. For the OSU-1-4 specimen, regardless of orientation, the model predicts the bottom interface always exhibits a higher peak tensile stress, which is not in agreement with the observation for this sample tested in the Reference Orientation, where interface I_1, located near the top, always debonded first. When tested in the Flipped Orientation, interface I_1 is predicted to have the highest peak tensile stress, in agreement with the debond observations. The reason for this discrepancy is not clear at this time; possible explanations include the influence of residual stress, plasticity, or that interface I_1, for unknown reasons related to processing, may actually be weaker than interface I_2.

Table 5. Bond strength calculation results for the OSU-1-4 sample.

Plate ID	Flash lamp delay (μs)	Maximum tensile stress, two terms (MPa)		Maximum tensile stress, four terms (MPa)	
		I_1	I_2	I_1	I_2
Reference Orientation					
X-10 Y-35	155	225	463	349	481
X-30 Y-35	155	219	452	350	450
X-30 Y-05	155	217	453	324	424
X-20 Y-15*	155	196	398	275	396
X-20 Y-25	155	243	494	377	507
Flipped Orientation					
X25Y-20	150	559	275	559	543
X25Y-15*	155	552	272	552	549

* Indicates multiple laser shocks at one location

In summary, calculation results demonstrate the sensitivity of the peak tensile stress values at each interface to relative differences in input material properties and layer geometry. For the cases examined, the results predict that the bottom interface will consistently be exposed to the highest peak tensile stresses. Thus one would generally expect that the bottom interface (I_2 for the case of Reference Orientation) would debond first during testing. However, testing of the OSU-1-4 plate has shown that debonding occurred 100% of the time at interface I_1 which had the thinnest cladding, regardless of specimen orientation. Future work will continue to develop, validate and qualify the LST method, as well as to investigate the influences of cladding asymmetry, residual stresses, material properties, and local variability in interface strengths.

5. Acknowledgements

This work was supported by the U.S. Department of Energy, Office of Nuclear Materials Threat Reduction (NA-212), National Nuclear Security Administration, under DOE-NE Idaho Operations Office Contract DE-AC07-05ID14517. Accordingly, the U.S. Government retains a non-exclusive, royalty-free license to publish or reproduce the published form of this contribution, or allow others to do so, for U.S. Government purposes.

6. References

1. See http://nnsa.energy.gov/aboutus/ourprograms/dnn/gtri/convert
2. J. L. Vossen, ASTMM Spec. Tech. Publ., **640**, pp. 122-131 (1978).
3. Gupta V, Argon A S, Cornie J A and Parks D M, Measurement of interface strength by laser-pulse-induced spallation *Mater. Sci. Eng.* A **126,** 1990, 105–17.
4. Yuan J and Gupta V 1993 Measurement of interface strength by the modified laser spallation technique: I. Experiment and simulation of the spallation process *J. Appl. Phys.* **74** 2388–97

5. Gupta V and Yuan J 1993 Measurement of interface strength by the modified laser spallation technique: II. Applications to metal/ceramic interfaces *J. Appl. Phys.* **74** 2397–404
6. Yuan J, Gupta V and Pronin A 1993 Measurement of interface strength by the modified laser spallation technique: III. Experimental optimization of the stress pulse *J. Appl. Phys.* **74** 2405–10
7. C. Bolis, L. Berthe, M. Boustie, M. Arrigoni, S. Barradas, and M. Jeandin, Physical Approach to Adhesion Testing Using Laser- Driven Shock Waves, J. Phys. D: Appl. Phys., 2007, 40(10), p 3155-3163
8. M. Perton, A. Blouin and J.-P. Monchalin, “Adhesive bond testing of carbon–epoxy composites by laser shockwave”, J. Phys. D: Appl. Phys., 44(3), 2011, 034012.
9. M. Arrigoni, S. Barradas, M. Braccini, M. Dupeux, M. Jeandin, M. Boustie, C. Bolis, L. Berthe, Comparative study of three adhesion tests (EN 582 similar to ASTM C633 - LASAT (LASer Adhesion Test) - Bulge and blister test) performed on plasma sprayed copper deposited on aluminium 2017 substrates, Journal of Adhesion Science Technology, 20 (5) pp. 471–487 (2006)
10. M. Perton, et al., “Laser shockwave technique for characterization of nuclear fuel plate interfaces”, 39th Annual Review of Progress in QNDE, AIP Conf. Proc. 1511, 2013, 345-352.
11. M. Arrigoni, J.P. Monchalin, A. Blouin, S.E. Kruger, and M. Lord, Laser Doppler Interferometer Based on a Solid Fabry- Perot Etalon for Measurement of Surface Velocity in Shock Experiments, Meas. Sci. Technol., 2009, 20(1), p 015302.
12. J. A. Smith; D. L. Cottle and B. H. Rabin, “Laser Shockwave For Characterizing Diffusion Bonded Interfaces," to be published in AIP Conf. Proc. Vol. 151, D. O. Thompson, D. E. Chimenti, Editors, American Institute of Physics, Melville, NY, 2014.
13. J. A. Smith et al., “Laser Shockwave Technique For Characterization Of Nuclear Fuel Plate Interfaces”, RERTR 2012 — 34th International Meeting On Reduced Enrichment For Research And Test Reactors, Warsaw Marriott Hotel Warsaw, Poland, October 14-17, 2012.
14. J. A. Smith, D. L. Cottle and B. H. Rabin, “Characterization of Bond Strength of U-Mo Fuel Plates Using the Laser Shockwave Technique: Capabilities and Preliminary Results,” INL/EXT-13-30312, Idaho National Laboratory, September, 2013.
15. Software “INL@Analyze”, Version 3, developed for Idaho National Laboratory under contract by National Research Council of Canada, 2013.
16. Jue, J. F., Park, B. H., Clark, C. R., Moore, G. A., Keiser, D. D., “Fabrication of Monolithic RERTR Fuels by Hot Isostatic Pressing,” *Nuclear Technology,* 172.2 (2009), pp. 204-210.
17. G. A. Moore and M. C. Marshall, “Co-Rolled U10Mo/Zirconium-Barrier-Layer Monolithic Fuel Foil Fabrication Process”, INL/EXT-10-17774, Idaho National Laboratory, January 2010.
18. B. H. Park, C. R. Clark and J. F. Jue, “INL HIP Plate Fabrication”, INL/EXT-10-17792, Idaho National Laboratory, February 2010.
19. L. Davison, D. E. Grady, M. Shahinpoor, *High-Pressure Shock Compression of Solids II*, Springer-Verlag, New York, 1996.
20. J. R. Asay, M. Shahinpoor, *High-Pressure Shock Compression of Solids*, Springer-Verlag, New York, 1993.
21. R. A. Graham, Solids Under High-Pressure Shock Compression, Springer-Verlag, New York, 1993.

SHUTDOWN-INDUCED TENSILE STRESS IN MONOLITHIC MINIPLATES AS A POSSIBLE CAUSE OF PLATE PILLOWING AT VERY HIGH BURNUP

P. G. Medvedev, H. Ozaltun, A. B. Robinson, B. H. Rabin
Nuclear Fuels and Materials, Idaho National Laboratory
2525 N. Fremont Avenue, Idaho Falls, Idaho, 83415 – USA

ABSTRACT

Post-irradiation examination of Reduced Enrichment for Research and Test Reactors (RERTR)-12 miniplates showed that in-reactor pillowing occurred in at least 4 plates, rendering performance of these plates unacceptable. To address in-reactor failures, efforts are underway to define the mechanisms responsible for in-reactor pillowing, and to suggest improvements to the fuel plate design and operational conditions. To achieve these objectives, the mechanical response of monolithic fuel to fission and thermally-induced stresses was modeled using a commercial finite element analysis code. Calculations of stresses and deformations in monolithic miniplates during irradiation and after the shutdown revealed that the tensile stress generated in the fuel increased from 2 MPa to 100 MPa at shutdown. The increase in tensile stress at shutdown possibly explains in-reactor pillowing of several RERTR-12 miniplates irradiated to the peak local burnup of up to 1.11×10^{22} fissions/cm^3. This paper presents the modeling approach and calculation results, and compares results with post-irradiation examinations and mechanical testing of irradiated fuel. The implications for the safe use of the monolithic fuel in research reactors are discussed, including the influence of fuel burnup and power on the magnitude of the shutdown-induced tensile stress.

1 Introduction

The RERTR-12 miniplate irradiation experiment was conducted at the Idaho National Laboratory (INL) in the Advanced Test Reactor with an objective to investigate performance of the monolithic U-10Mo fuel to the burnup up to 1×10^{22} fissions/cm^3. The test included 56 monolithic U-10Mo miniplates whose operating conditions enveloped those expected in the U.S. high power research reactors [1,2]. Post-irradiation examination of the RERTR-12 experiment is in progress, and has revealed that most of the plates demonstrated acceptable performance, up to the average burnup of 7×10^{21} fissions/cm^3. However, the higher-burnup plates L1P754, L1P759, L1P785, and L1P7A0 exhibited pillows over a part of the fuel region, rendering performance of these plates unacceptable [3]. Despite the presence of pillows, no fission product release into the reactor coolant was detected. To illustrate the pillowing phenomenon, the appearance of a pillowed plate L1P785 is shown in Figure 1.

To address the in-reactor failures, efforts are underway to define the mechanisms responsible for the in-reactor pillowing, and to suggest improvements to the fuel plate design and operational conditions. To achieve these objectives, the mechanical response of monolithic fuel to fission and thermally-induced stresses was modeled using a commercial finite element analysis code.



Figure 1. Post-irradiation appearance of a pillowed plate L1P785.

This paper presents the modeling approach and calculation results, and compares results with post-irradiation examinations and mechanical testing of irradiated fuel. The implications for the safe use of the monolithic fuel in research reactors are discussed, including the influence of fuel burnup and power on the magnitude of the shutdown-induced tensile stress.

2 Modeling approach

To investigate the mechanical response of monolithic fuel to fission and thermally-induced stresses, a commercial finite element analysis code, ABAQUS, was utilized. A fully-coupled three-dimensional model of a monolithic miniplate with a capability to evolve mechanical and thermal properties of the constituent materials with irradiation time and burnup was developed. The model uses plate geometry, power history, and coolant conditions as input. The model output includes temperature, stress and deformation history in the fuel, cladding and zirconium diffusion barrier [4,5]. The behavior models include fission heat source, swelling due to solid and gaseous fission products [6], irradiation-induced creep [7], elasticity, thermal expansion, plasticity, and cladding hardening due to the fast neutron fluence. The fuel swelling model is coupled with the thermal conductivity model to account for the degradation of the thermal conductivity due to the formation of fission gas bubbles (pores) in the fuel during irradiation. As most of the physical and mechanical properties of irradiated U-10Mo are unknown, the modeling results are regarded as qualitative.

3 Plate power history and spatial power distribution

While the detailed description of the experiment conditions is given elsewhere [1,2], the power history and spatial power distribution in plates L1P785, L1P7A0, L1P756, analyzed in this study are shown in Figure 2. Spatial power distribution plots reveal power variations in the plate and highlight the high power regions. High power regions attain higher burnup and operate at higher temperatures.

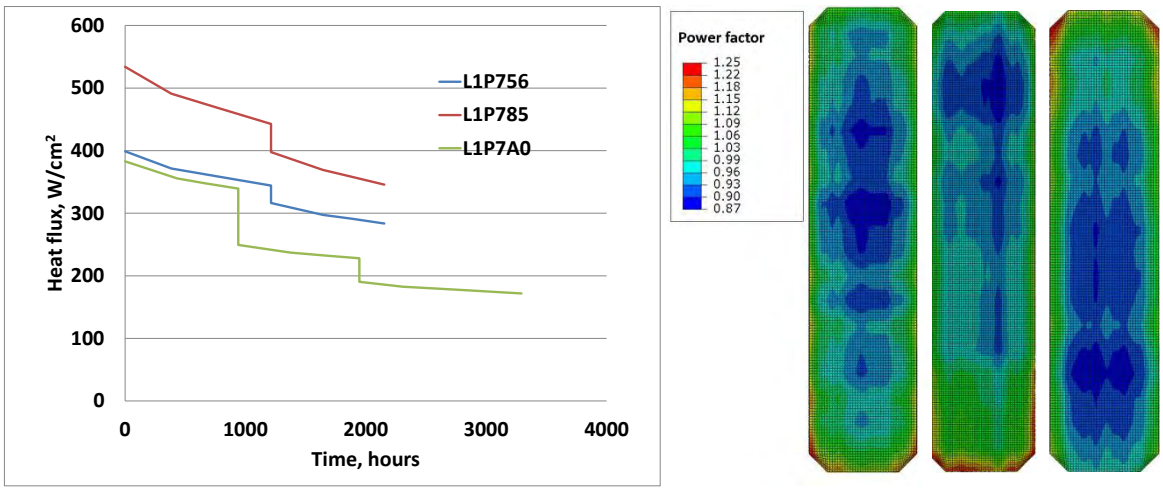


Figure 2. Power history and spatial power distribution in plates L1P785, L1P7A0, L1P756 (left to right).

4 Results

4.1 Shutdown-induced tensile stress in the fuel

The focus of the present paper is on the discovery of the tensile stress that develops in the fuel foil after the shutdown. In an event of a reactor shutdown, the plate power instantly reduced from its current value to zero and the temperature instantly reduced to the reactor coolant temperature. The existence of this stress is demonstrated by comparing stress patterns in the fuel before and after the shutdown. For the plate L1P785, this comparison is provided in Figure 3, where the calculated values of maximum principal stress during irradiation and after the shutdown are plotted along the length of the fuel. As evident from Figure 3, a shutdown results in a nearly 10-fold increase of the maximum principal stress in the bottom region of the plate. It should be noted, that the positive sign of the stress value is indicative of the tensile stress.

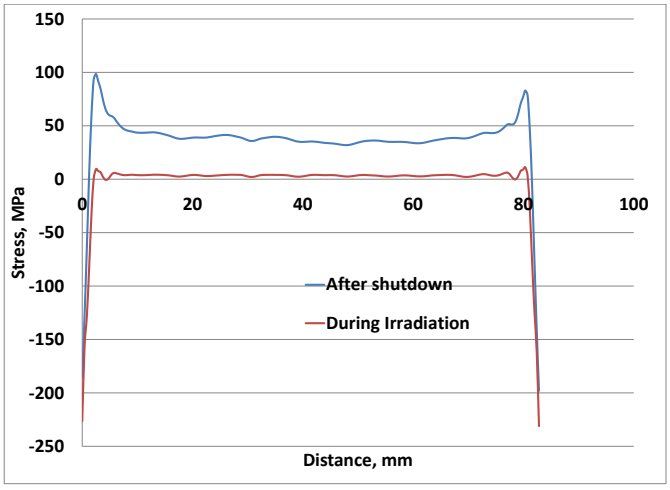


Figure 3. Comparison of the calculated values of maximum principal stress during irradiation and after the shutdown.

The neutron radiography image of the plate L1P785, the contour plot of the calculated maximum principal stress at the mid-plane of the fuel after the shutdown, and pre-shutdown fuel temperature are shown in Figure 4. Examination of Figure 4 and Figure 1 reveals that the pillow is found on the bottom of the plate where the maximum principal stress is the

highest. This observation establishes a possible correlation between the plate pillowing and high tensile stress in the fuel observed after the shutdown.

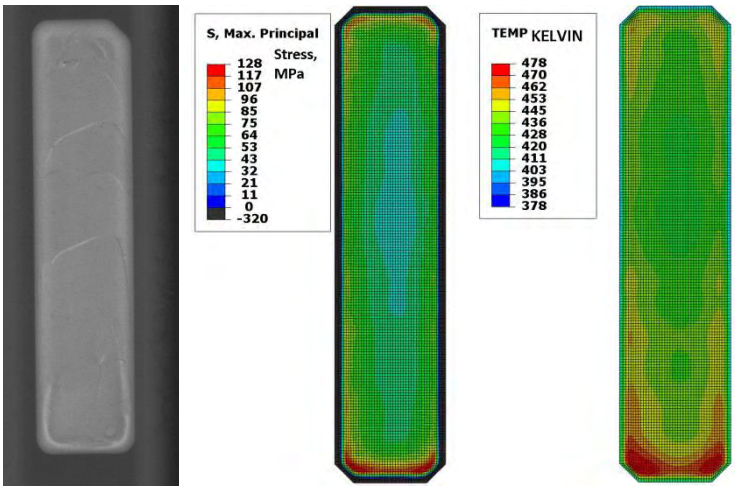


Figure 4. Left: neutron radiography image,
Center: contour plot of the maximum principal stress at the fuel mid-plane,
Right: the pre-shutdown fuel temperature.

Examination of the pre-shutdown fuel temperature contour shown in Figure 4, suggests that the peak stress is occurring at the peak temperature locations, which leads to a conclusion that the stress is due to thermal effects in the fuel. The temperature gradients are explained by the power gradients and by a more efficient cooling of the fuel edges. During the thermal transient occurring on the shutdown, the thermal strain, being a product of a thermal expansion coefficient and a temperature change, is greater in the locations of the fuel that operate at higher temperatures.

4.2 Comparison of the shutdown-induced tensile stress with the fuel strength

According to the maximum stress failure criterion, a material failure is expected if the maximum principal stress in the material exceeds its uniaxial tensile strength. Therefore, it is of interest to compare the values of maximum principal stress in the fuel with the fuel strength. Results of the bending strength measurements [8] performed at the INL on fuel foil samples taken from irradiated AFIP-3 plates are shown in Table 1.

Sample ID	Bending strength, MPa	Burnup, fissions/cm^3
3BZ-3	156.5	2.42
3BZ-4	114.9	2.03
3TT-3	25.2	5.24
3TT-4	84.1	5.39

Table 1. Bending strengths and fission densities of irradiated U-10Mo fuel.

The values of the fuel foil strength shown in Table 1 range from 25.2 MPa to 156.5 MPa, and a decrease of strength with burnup is evident. The peak value of maximum principal stress calculated in plate L1P785 is 128 MPa. Recognizing that plate L1P785 peak burnup is 1.1×10^{22} fissions/cm^3, which is nearly twice the burnup of the AFIP-3 plates subjected to fuel strength measurements, it is concluded that the stress plate L1P785 has most likely exceeded the fuel foil strength resulting in fuel failure manifested by cracking.

4.3 Porosity interconnection and fission gas release

It has been postulated that gaseous fission products generated in the U-10Mo fuel form fission gas bubbles (pores) that contribute to the fuel swelling [6]. It is also well known [9,10] that, when fission gas induced swelling in metal fuel reaches 33% (which corresponds to a porosity of 24%), the porosity begins to interconnect, and the fission gas is released. To demonstrate the likelihood of porosity interconnection and fission gas release in plate L1P785, the calculated values of fuel porosity are mapped in Figure 5. Also shown in Figure 5, are the locations where porosity interconnection and fission gas release is expected. As evident from Figure 5, porosity interconnection and fission gas release are expected in the corners and edges of the fuel foil, with the bottom region of the foil being affected the most. The location of the most pronounced porosity interconnection and fission gas release coincides with the location of the pillow shown in Figure 1. Therefore, the formation of the pillow at the bottom of the fuel foil may be explained by the porosity interconnection and fission gas release in that fuel region.

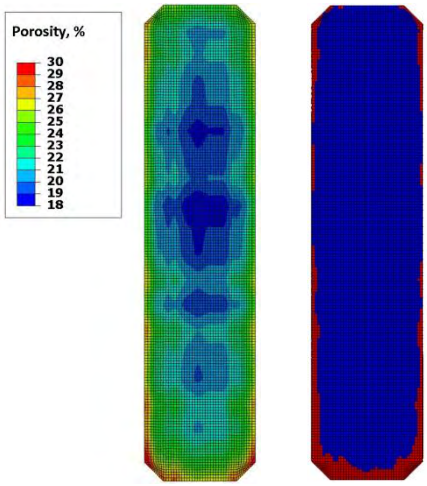


Figure 5. Left: map of fission gas porosity in the fuel;
Right: locations where porosity interconnection
and fission gas release are expected (shown in red).

4.4 Comparison with plates L1P7A0 and L1P756

To uncover possible fuel performance trends, the calculated values of temperature, stress, burnup, and porosity were compared among plates L1P785, L1P7A0, L1P756 listed in Table 2. Among the compared plates, plate L1P756 was the only plate that did not form a pillow. Examination of the data in Table 2 reveals that unlike the other two plates, plate L1P756 did not reach the 24% porosity threshold necessary for fission gas bubble interconnection and fission gas release. This observation may link plate pillowing to porosity interconnection and fission gas release. Recognizing that the fuel strength decreases with an increase of porosity, it is noted that the fuel strength would be the highest in plate L1P756, thus rendering it more resistant to the shutdown-induced stress. It appears that plate pillowing could be attributed either to the porosity interconnection, or to the shutdown-induced stress, or to both phenomena occurring simultaneously. Similar analysis for additional plates from the RERTR-12 experiment should be performed to better understand causes of pillowing. In addition, post-irradiation examinations seeking the evidence of porosity interconnection and fission gas release are needed.

Plate	Pre-shutdown temperature, C	Maximum principal stress after shutdown, MPa	Burnup, fissions/cm^3	Fission gas porosity, %	Plate pillowed?
L1P785	205	128	1.1×10^{22}	30	Yes
L1P7A0	135	73	1.0×10^{22}	27	Yes
L1P756	171	86	9.2×10^{21}	23	No

Table 2. Calculated peak values of temperature, stress, burnup, and porosity for plates L1P785, L1P7A0, L1P756.

4.5 Implications for the safe use of the monolithic fuel in research reactors

Based on the findings documented in this paper, the conditions for a destructive shutdown-induced stress are: (1) high pre-shutdown fuel temperature and (2) highly porous fuel featuring low strength. Because the maximum burnup expected in the low-enriched uranium (LEU) research reactor fuel is approximately 8×10^{21} fissions/cm^3, the maximum attainable fission gas porosity is 18.5%, as estimated using the methodology developed by Kim [6]. Maximum attainable fission gas porosity in LEU fuel is less than the porosity interconnection and fission gas release threshold (24%) and is less than the values calculated for plates L1P785, L1P7A0, L1P756 (23-30%). Therefore, the LEU fuel is not expected to reach porosity levels calculated in the pillowed RERTR-12 plates. Furthermore, LEU fuel operating at high burnup is unable to sustain high fission power necessary to achieve high fuel temperature. As shown in Figure 6, LEU fuel operating in a constant neutron flux exhibits a rapid power decrease due to the depletion of the fissile material. This is in contrast to the 70% enriched fuel used in RERTR-12 test capable of sustaining a heat flux of 300 W/cm^2 while having attained a burnup of 1×10^{22} fissions/cm^3. Indeed, due to lack of power generation, the temperature of the LEU fuel that has reached burnup of 8×10^{21} fissions/cm^3 is expected to be nearly equal to the coolant temperature, and development of significant shutdown-induced stresses in high-burnup LEU fuel does not seem possible. As the RERTR-12 experiment utilized highly-enriched uranium (HEU) fuel to achieve high fission rates in the available neutron flux, the power history of the RERTR-12 fuel was not prototypic of the LEU fuel; therefore, the fuel behavior observed in this experiment is also not prototypic of the LEU fuel. Nevertheless, the experiment has elucidated a new fuel failure mode and a definition of fuel operational limits.

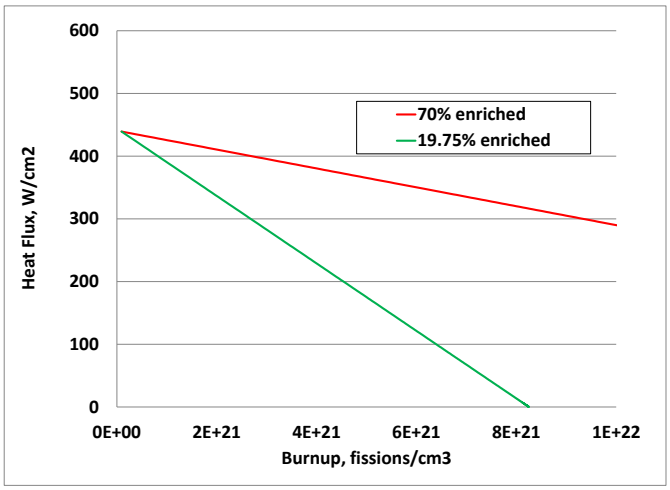


Figure 6. Heat flux in HEU and LEU fuels exposed to a constant neutron flux.

5 Conclusions

Based on the results of the thermo-mechanical analysis, pillowing in several RERTR-12 plates irradiated to a very high burnup has been attributed to a shutdown-induced stress in the fuel and/or to the fission gas release caused by interconnection of the fission gas porosity. These phenomena occurred because the fuel continued to operate at a considerable power while having attained burnup in excess of $1x10^{22}$ fissions/cm^3. Such a combination of burnup and power ensued because of high (70%) fuel enrichment used in the RERTR-12 experimental fuel plates.

The failure mode discussed in the present paper is not likely to occur in the LEU fuel, because the LEU fuel is not only unable to reach the burnup attained in RERTR-12 plates, but also unable to sustain the power necessary for development of shutdown-induced stress at the end of irradiation. Nevertheless, the experiment and modeling results yielded to a definition of operational limits of U-10Mo monolithic fuel.

Similar analysis for additional plates from RERTR-12 experiment should be performed to confirm the findings of this study. In addition, post-irradiation examinations seeking the evidence of porosity interconnection and fission gas release are needed. Finally, the calculations should be updated as better mechanical and thermal property data for the U-10Mo fuel become available.

6 References

[1] Perez, D. M., M. A. Lillo, G. S. Chang, and N. E. Woolstenhulme, *RERTR-12 Insertion 1 Irradiation Summary Report*, INL/EXT-11-24101.

[2] Perez, D. M., G. S. Chang, D. M. Wachs, G. A. Roth, and N. E. Woolstenhulme, *RERTR-12 Insertion 2 Irradiation Summary Report*, INL/EXT-12-27085.

[3] Robinson, Adam B., Francine J. Rice, Walter Williams, and Muhamid Abir, *RERTR-12 Non-Destructive PIE Report*, INL/LTD-13-30298.

[4] Miller, Samuel J., and Hakan Ozaltun, 2012, "Evaluation of U10Mo Fuel Plate Irradiation Behavior via Numerical and Experimental Benchmarking," *ASME 2012 International Mechanical Engineering Congress and Exposition, Volume 6: Energy, Parts A and B, Houston, Texas, USA*, November 9–15, 2012.

[5] Ozaltun, Hakan, Robert M Allen, and You Sung Han, 2013, "Effects of the Zirconium Liner Thickness on the Sress-Strain Characteristics of U10Mo Alloy Based Monolithic Mini-Plates," *Proceedings of the ASME 2013 International Mechanical Engineering Congress & Exposition, San Diego, California, USA*, November 13-21, 2013.

[6] Kim, Yeon Soo, and G.L. Hofman, "Fission product induced swelling of U–Mo alloy fuel," *Journal of Nuclear Materials, Volume 419*, Issues 1–3, December 2011, Pages 291-301.

[7] Kim, Yeon Soo, G.L. Hofman, J.S. Cheon, A.B. Robinson, and D.M. Wachs, "Fission induced swelling and creep of U–Mo alloy fuel," *Journal of Nuclear Materials, Volume 437*, Issues 1–3, June 2013, Pages 37-46.

[8] ECAR-1850, 2013, "Irradiated AFIP-3 fuel plate bend tests," B. Rabin and R. Lloyd, Idaho National Laboratory.

[9] Barnes, R. S., "A Theory of Swelling and Gas Release for Reactor Materials," *Journal of Nuclear Materials*, 11, 1964, 135 148.

[10] Hofman, G.L., L.C. Walters, and T.H. Bauer, “Metallic Fast Reactor Fuels,” *Progress in Nuclear Energy, Volume 31*, Issues 1–2, 1997, Pages 83–110.

Post-irradiation Analysis of U-silicide or U-nitride Coated U-7Mo/Al Dispersion Fuel

Yeon Soo KIM
Argonne National Laboratory
9700 S. Cass Ave, Argonne, IL 60439 – USA

J.M.PARK, K.H.LEE, B.O.YOO
Research Reactor Fuel Development Division, Korea Atomic Energy Research Institute
989-111 Daedeokdaero, Yuseong-gu, Daejeon 305-353 – Republic of Korea

H.J. RYU
Dept. of Nuclear and Quantum Engineering
Korea Advanced Institute of Science and Technology, 291 Daehak-ro, Yuseong, Daejeon 305-701 – Republic of Korea

ABSTRACT

Although effective in general, the addition of Si in the Al matrix to reduce interaction layer (IL) growth is limited by the decrease in homogeneity of fuel particle distribution and the effective Si content in the high U-loading test samples. Increasing Si in Al to cope with high power application raises the matrix toughness that makes plate rolling fabrication more difficult. To overcome these disadvantages, KAERI has developed technologies of U-silicide-coated U-Mo powders and U-nitride coated U-Mo powders. One of the objectives of the KAERI's most recent test campaign KOMO-5 was to examine the effectiveness of the coating methods. The KOMO-5 was in-pile tested in the HANARO. The U-loading of the test rods was 5 gU/cm^3, the test temperature was controlled at ~180^{o}C, and the burnup reached ~68% U-235 after 228 EFPD. This paper reports the PIE data and analysis results focusing on the effectiveness of the coating concept on IL growth and general fuel performance.

1. INTRODUCTION

A Si addition in the Al matrix to suppress interaction layer (IL) growth between U-Mo and Al has been proved effective in many in-pile tests (see [1] and references therein). It was also found that the suppression increased as the Si content increased [2]. This method is convenient to apply so that it requires neither considerable cost additionally nor technological improvement in the hot-rolling fabrication method. Although beneficial in general, however, the effectiveness of Si addition in the Al matrix weakens when the Si particle distribution in the matrix is inhomogeneous and/or the fuel particle distribution in the fuel meat is inhomogeneous. To boost the effectiveness of Si addition to achieve high-power and high-burnup in a demanding application, increasing the Si content in the Al matrix appears logical. However, this also increases the matrix toughness, which makes plate fabrication harder and the homogeneity of fuel particle distribution more difficult to achieve. The maximum Si content that can be obtained with a reasonable yield appears to be about 6% for the current hot-rolling technology.

To overcome these disadvantages, providing a direct diffusion barrier on U-Mo particles before plate fabrication has been proposed [3]-[5]. KAERI's method is to coat the fuel particles with a reaction layer of U-Si formed in a high-temperature heating process. One of the objectives of

KAERI's most recent test campaign, KOMO-5, was to examine the effectiveness of the coating methods, also including U-N coating on U-Mo particles. This paper reports the PIE data and analysis results focusing on the effectiveness of the coating concept on IL growth and general fuel performance.

2. Experimental

2.1 Sample fabrication

A U-7Mo alloy powder, manufactured using KAERI's atomization method [6], were mixed with a pure Si powder having 99% purity and size of -325 mesh (= 44 μm). The mixure was then heated in a vacuum of 1 Pa at 1000 °C for an hour [7]. As a result of the heating, a U-Si coating layer was formed on the U-7Mo particles with a thickness of ~5 μm. SEM examination of as-fabricated coating found that the coating was composed of two sub-layers. The outer layer was thicker than the inner layer. The Si/U ratio of the outer layer was approximately 1.6 and while that of the inner layer was approximately 0.6. Using a rough estimate, the Si content in the coat is equivalent to 4wt%Si addition in the matrix based on 5 gU/cm^3 loading. The external surface of the coat was relatively uniform compared to the inner surface on U-7Mo.

KAERI also developed a U-Nitride coating technology. The U-Nitride coating was obtained by heating the atomized U-7Mo powder at ~1000 °C for 30 min in a controlled argon and nitrogen gas mixture. Characterization of the as-coated powder showed that a coating of U-nitride with a thickness of about 5 μm was formed. SEM EDS was also performed to measure the elemental concentrations of the coat and the inner region ajacent to the coat. A substantial nitrogen concentration was measured not only in the coat but also in the inner region. In addition, considerable amount of oxygen was also found in both regions. This results suggests that nitrogen atom diffusion in the fuel particle rapidly occurred. Another remarkable finding was that the Mo concentration was lower than the nominal value (~16 at%). This is probably due to the lower affinity of Mo than uranium for nitrogen and oxygen.

The test rods were 200-mm long, partial-length long rods, compared to the full length driver fuel rod, which is 700 mm long. The test rods contained cylindrical fuel meat of coated U-7Mo particles in an Al matrix. The fuel meat was 6.4 mm in diameter, directly bonded to Al-1060 cladding with thickness of 0.76 mm. The cladding had 8 fins with height of ~1 mm to improve heat tranfer, which is the same feature as the HANARO driver fuel rods. The fuel particle size was in the range 140 - 210 μm. The U-loading in the meat was 5 gU/cm^3-meat. The U-Si coated fuel rod (557-SI1) and U-N coated fuel rod (676-NI1) were included in the fuel rod bundle as shown in **Fig. 1**.

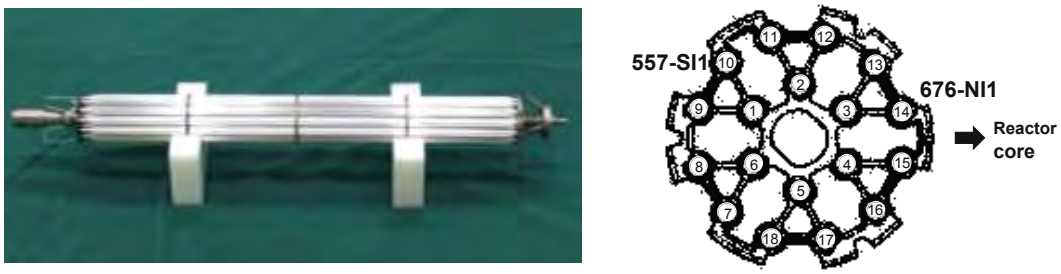


Fig. 1 Fuel rod test bundle and schematic of cross section of the test rod bundle. 557SI-1 is the U-Si coated fuel rod and 676NI-1 is the U-N coated fuel rod. Rod positions 1 – 6 were loaded with Al dummy rods and test rods were loaded in rod positions 7 – 18.

2.2 Irradiation test

Because the test rods were loaded in the upper region of the full size rod and the reactor axial power shape was a chopped-cosine shape, the lower part of the sample rod achieved higher power and burnup. This suggests that the temperature was higher at a lower part of the test rod. The axial cutting locations during PIE were 191 mm for 557-SI1 and 178 mm for 676-NI1 from the upper end plug.

The calculated test temperature and power histories of 557-SI1 and 676-NI1 were as shown in **Fig. 2**. The burnups at the axial cutting locations were 68% for 557-SI1 and 62% for 676-NI1 after the irradiation lasted for 228 EFPD. Although the 676-NI1 rod was closer than the 557-SI1 to the reactor core center (**Fig. 1**), the power, burnup and temperature were all lower than the 557-SI1 because the 577-SI1 was cut at a lower location than the 676-NI1.

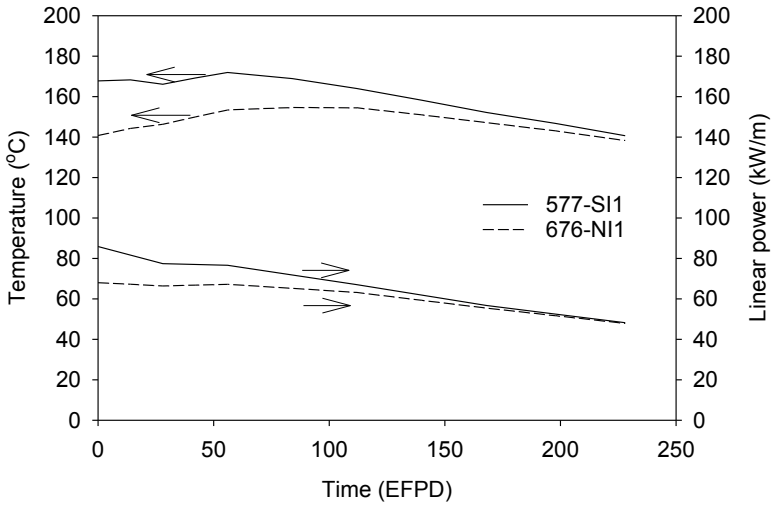


Fig. 2 Power and temperature histories of 557Si-1 and 676NI-1 rods at their respective PIE locations

3. Results

The U-Si coated U-7Mo fuel rod was post irradiation examined by performing metallography at the axial location with 68% BU. The effectiveness of the coating method was evaluated by measuring the interaction layer growth and meat swelling using optical microscopy (OM). The high-magnification OM images were taken across the diameter and used to compose a partial cross section image shown in **Fig. 3**. It appears that three kinds of interaction layers (ILs) were formed: ILs with apparently minimal thickness, less thick but irregular ILs, and thick and uniform ILs. These suggest that the coating quality was variable. The coat was perfect so that virtually suppressed IL growth completely, or it was imperfect so that yielded some IL growth, or it was removed or no coat was formed during the coating procedure so that IL growth without any restriction.

The U-N coated U-7Mo fuel rod metallography at location having 62% BU also received the same examinations as the U-Si coated rod. The image presented in **Fig. 4** is a composition of many higher magnification OM images to show a partial cross section of fuel meat across diameter. The ILs in this rod are more uniform than in the U-Si coated fuel rod, suggesting that the coat, either in good quality or bad, was uniform. The uniform coat thickness was possible because in the U-N coat process, the coating material was gas while the U-Si coat it was solid.

The thickest IL in 557-SI1 was ~45 μm while the average IL thickness in 676-NI1 was ~30 μm. The IL volume fractions were 20% and 22% for 577-SI1 and 676-NI1, respectively. The 557-SI1 was slightly better than 676-NI1 in terms of IL growth, suggesting the U-Si coating method was superior to the U-N coating.

Since there is negligible dimensional change in the length direction, fuel meat swelling was calculated by the change in the meat cross section area before and after the irradiation. The meat swelling obtained in this way was 10.3% for 557-SI1 and 9.2% for 676-NI1, respectively. Considering the similar IL growth for both samples, the slightly higher meat swelling for 577-SI1 is attributed to the fuel particle swelling due to higher burnup. For the meat swelling is the addition of fuel particle swelling by fission products and volume expansion by IL growth, subtracted by fuel and matrix consumption by IL growth.

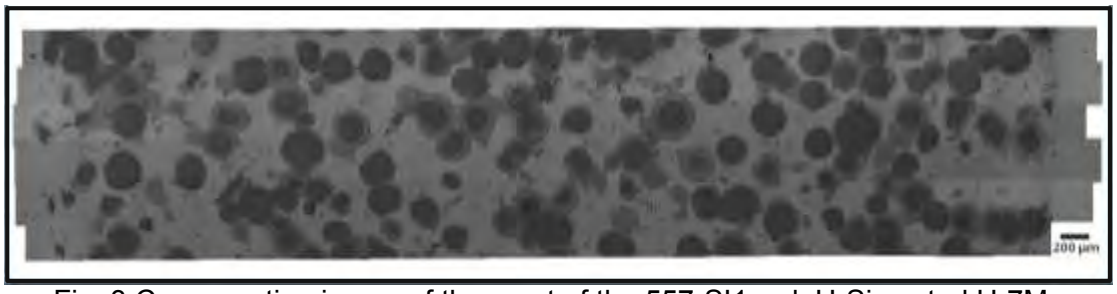


Fig. 3 Cross section image of the meat of the 557-SI1 rod. U-Si coated U-7Mo dispersion in Al irradiated to a burnup of 68% LEU equiv.

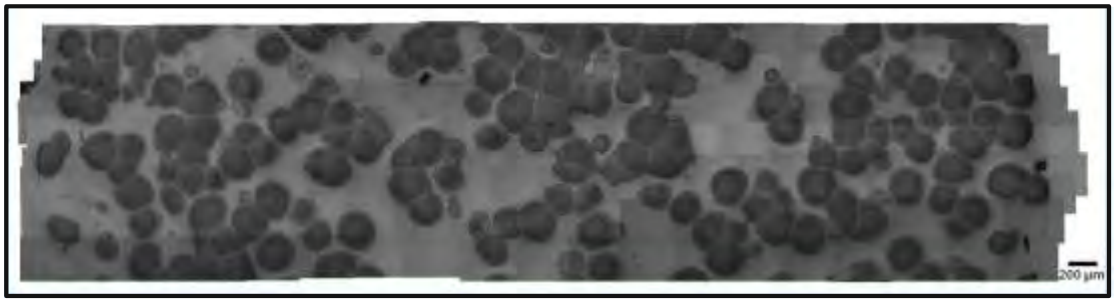


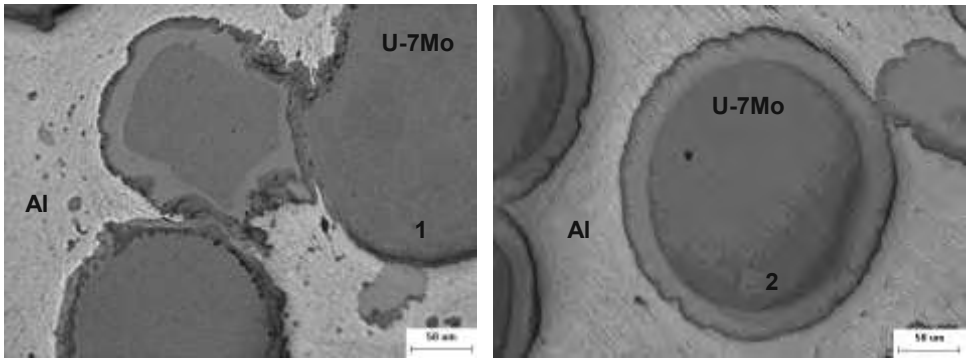
Fig. 4 Cross section image of the meat of the 676-NI1 rod. U-N coated U-7Mo dispersion in Al irradiated to a burnup of 62% LEU equiv.

EPMA measurements for concentration in the ILs were made. Two kinds of ILs were analyzed for the U-Si coated rod: one with thin IL, and the other thick IL. It was noticeable that the thin IL was formed on the U-Si coat while the thick IL was formed on a no-coat surface. Comparing with the as-coated concentrations, however, the Si concentration appeared to be diluted to a considerable extent. It was also remarkable that the IL was formed outside of the coat.

The U-N coated fuel rod showed that the nitrogen concentration was negligible in and around the IL, implying that the U-N coat was dissolved and disappeared during irradiation. The generally thick and uniform ILs formed in the U-N coating sample suggest that the U-N coat was inefficient as a diffusion barrier against Al in the IL.

Higher magnification images compared in **Fig. 5**, which clearly show the differences in the morphology of interaction layers between the U-Si coated and U-N coated fuel rods. Irregular thickness ILs in the U-Si coated particles and uniform ILs in the U-N coated particles are noticeable. A remarkable finding common for both images in **Fig. 5** was the large grain sizes in

the fuel particles such as ~25 μm for 557-SI1 and ~50 μm for 676-NI1. The grain boundaries are shown in lighter lines in the fuel particle marked by 1 in the U-Si coated fuel and in the fuel particle marked by 2 in the U-N coated fuel. Considering the typical grain size of ~10 μm observed for un-coated fuel particles [8], this large grains mean that considerable grain growth occurred by the heating during the coating process (~1000 ^{o}C for ~1 hour).



(a) (b)

Fig. 5 Optical post-irradiation images of (a) silicide-coated U-7Mo/Al (557-SI1), and (b) nitride-coated U-7Mo/Al (676-NI1).

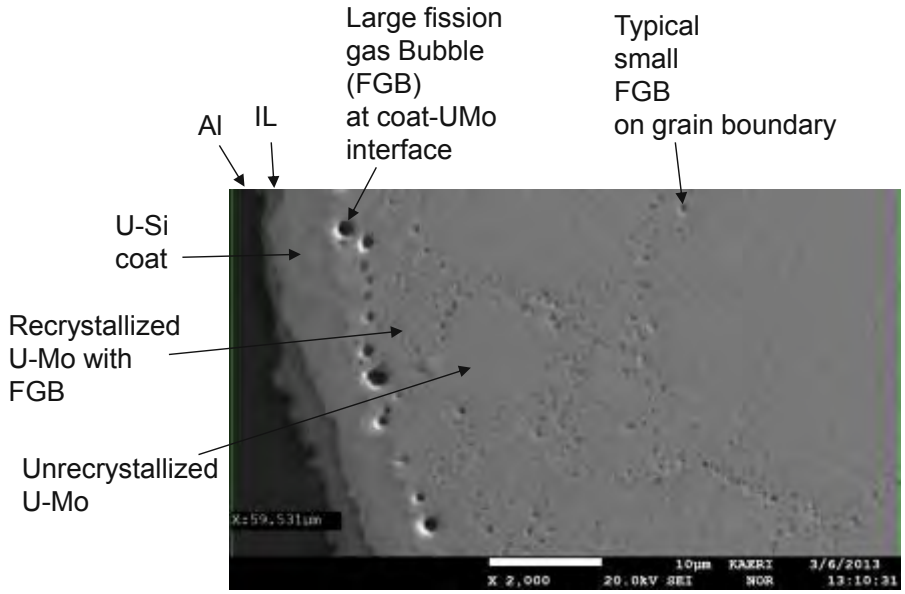


Fig. 6 SEM of U-Si coated fuel showing large fission gas bubbles at the interface between U-Si coat and U-Mo.

Because the U-Si coat is in fact a fuel, the coated fuel particle is a 'multiplex' fuel composed of the several layers of U-silicides at the periphery and inner U-Mo fuel. A true side-by-side comparison between U-silicide fuels and U-Mo fuel might be possible. A SEM in **Fig. 6** shows a number of large bubbles (larger than the typical inter-granular fission gas bubbles) are visible along the interface between the U-Si coat and U-Mo. This is possibly fission gas bubbles formed in U-rich U-silicide fuel with a Si/U ratio less than that of U_3Si, for which fission gas bubbles tend to be larger than U_3Si and U_3Si_2. No visible fission gas bubbles were found in the U-Si coat while small fission gas bubbles were visible in the recrystallized U-Mo. This suggests that U-silicide fuel with a high Si/U ratio is not only stable, but also excellent by suppressing fission gas bubble swelling.

4. Discussion

4.1 U-Si coated fuel

The U-Si coating of the fuel particles showed again effectiveness of a Si-rich layer as a diffusion barrier blocking Al diffusion in the IL between U-Mo and Al, consistent with the observation from the Si addition in the Al matrix (see Ref. [8]) that when a Si-containing IL is formed, the IL growth rate is reduced. Since the U-Si coating is a more effective method to provide Si on the fuel surface, the IL reducing effect would be more effective than Si addition to the matrix.

The observation of the irregular ILs indicates that the U-Si coating method provided non-uniform coat. Since the coating method practically transforms the fuel particle periphery to a U-Si fuel, it would provide a strong coat that will probably not be easily peeled off during rod fabrication. Hence the no-coat regions in the fuel surface is caused not by peeling off of a coat, but by the absence of a coat from the coating process.

To improve the effectiveness of the U-Si coating method, appying a uniform coat seems to be the key. One method of performing this is to using a continuously tumbling bed during coating.

4.2 U-N coated fuel

The effectiveness of the U-N coat during irradiation appeared to be small. EDS measurement of nitrogen in the IL was negligible, implying that the U-N had completely vanished. Where did the nitrogen go? This question was hard to answer because EDS failed to observe nitrogen accumulation anywhere. In an out-of-pile heating test, however, the U-N coat served as an efficient diffusion barrier for Al diffusion. The loss of U-N coat during irradiation is therefore thought to be due to an unknown mechanism. One possibility is the presence of fission product induced resolution of U-N coat and fission ehhanced diffusion of Al in the coat. When the U-N coat is dissolved and react with Al, the following reaction will be activated:

$$UN + 4Al \rightarrow UAl_4 + N \qquad (1)$$

The liberated nitrogen can then diffuse in the U-Mo and is diluted. By this process, nitrogen can vanish.

From the KOMO-5 result, the U-N coating method is concluded to be ineffective, contrasting to the positive results for ZrN coating [3][4].

4.3 Use of large fuel particles

The U-Mo particle size was in the range 140 – 210 μm, which is far larger than the typical size used in the US RERTR tests and European tests (~70 μm). The use of large fuel particles was possible in the present test because the test rods were fabricated by using the co-extrusion method other than in rolling methods for plates. The use of large fuel particles provided advantages such as less IL growth due to lower fuel specific surface area (lower S/V ratio) and higher meat thermal conductivity. In addition, fission product recoil release rate is also reduced because it is proportional to S/V ratio.

4.4 Heating effect during coating

The heating process during coating appeared to improve the U-Mo fuel particles by growing grains. The exceptionally large grains shown in the coated particles were attributed to the

heating. The large grains and perhaps the annealing during heating are advantageous because recrystallization of fuel is delayed. Recrystallization is known to be the key mechanism that determines the rate of fuel swelling and that occurs at the pre-existing grain boundaries [10]. The heating during coating was performed for both U-Si coating and U-N coating in the γ-phase. Hence, no deleterious α-phase transformation occurred -- only grain growth and annealing of defects. The effect of the γ-phase annealing was tested in the RERTR-3 test and the advantageous results were observed. The present results confirmed this effect. Therefore, to reduce fuel swelling, having a γ-phase annealing is recommended.

5. CONCLUSIONS

From the KOMO-5 test of U-Si coating and U-N coating methods, the following conclusions can be drawn.

1. The U-Si coating method used for the KOMO-5 test showed areas of improvement. The key area for improvement was believed to be to provide a uniform coating.
2. The U-N coating method showed negligible effective for reducing interaction layer growth.
3. The heating during coating (~1000 ^{o}C for ~0.5 hour) provided advantageous effect by grain growth that reduces fuel swelling.
4. The use of large fuel particles was beneficial by reducing IL growth and increasing meat thermal conductivity.

ACKNOWLEDGMENT

This study was supported by the National Nuclear R&D Program of Ministry of Education, Science and Technology (MEST) of Republic of Korea and the ANL contribution was supported by the UChicago Argonne, LCC as Operator of Argonne National Laboratory under Contract No.DE-AC-02-06CH11357 between UChicago Argonne, LLC and the US Department of Energy.

REFERENCES

[1] Yeon Soo Kim, G.L. Hofman, A.B. Robinson, D.M. Wachs, Nucl. Technol., 184 (2013) 42.
[2] Yeon Soo Kim, G.L. Hofman, H.J. Ryu, J.M. Park, A.B. Robinson, D.M. Wachs, Nucl. Eng. Technol., 45 2013) 827.
[3] A. Izhutov, V. Alexandrov, A. Novosyolov, V. Starkov, A. Sheldyakov, V. Shishin, V. Iakovlev, I. Dobrikova, A. Vatulin, G. Kulakov, V. Suprun, Proc. Int. Meeting on Reduced Enrichment for Research and Test Reactors (RERTR), Lisbon, Portugal, Oct. 10 - 14, 2010. http://www.rertr.anl.gov
[4] A. Leenaers, S. Van den Berghe, C. Detavernier, J. Nucl. Mater., 440 (2013) 220.
[5] H.J. Ryu, J.M. Park, K.H. Lee, B.O. Yoo, Y.H. Jung, Y.J. Jung, Y.S. Lee, Yeon Soo Kim, Trans. RRFM 2013, ENS, St. Petersburg, Russia, Apr. 21 -25, 2013.
[6] C.K. Kim, K.H. Kim, S.J Jang, H.D. Jo, I.H. Kuk, Proc. 1992 Internat. RERTR Meeting, ANL/RERTR/TM-19, CONF-9209266, Sept 27–Oct 1, 1992.
[7] H.J. Ryu, J.S. Park, J.M. Park, C.K. Kim, Nucl. Eng. Technol., 43 (2011) 159.
[8] Yeon Soo Kim, G.L. Hofman, J. Nucl. Mater., 419 (2011) 291.
[9] Yeon Soo Kim, J.M. Park, H.J. Ryu, J.H. Yang, G.L Hofman, J. Nucl. Mater., 430 (2012) 50.
[10] Yeon Soo Kim, G.L. Hofman, J.S. Cheon, J. Nucl. Mater., 436 (2013) 14.

RRFM 2014 INTERNATIONAL MEETING ON
EUROPEAN RESEARCH REACTOR CONFERENCE

March 30 – April 3, 2014
Ljubljana, in Slovenia

UMO MONOLITHIC FUEL DEVELOPMENT PROGRESS IN AREVA-CERCA

B. STEPNIK, M. GRASSE, C. COULLOMB, D. GESLIN, C. JAROUSSE
AREVA-CERCA
10, rue Juliette Récamier, F-69456 Lyon Cedex 06 – France

W. PETRY, R. JUNGWIRTH, H. BREITKREUTZ, A. RÖHRMOSER, T. K. HUBER, T. ZWEIFEL
Forschungs-Neutronenquelle Heinz Maier-Leibnitz (FRM II)
Technische Universität München (TUM), Lichtenbergstr. 1, 85747 Garching – Germany

D. M. WACHS
Idaho National Laboratory (INL)
P.O. Box 1625, Idaho Falls, ID 83415 – USA

ABSTRACT

The European high density fuel developments for the conversion of the European High Performance Research Reactors take place inside the HERACLES consortium.

Since 1999, AREVA has been involved in UMo fuel developments in close cooperation with international partners. First we focused on UMo dispersion fuel. Then, since 2005, we have been working on both UMo dispersion and UMo monolithic fuel.

In 2005-2008, full-size monolithic foil manufacturing was carried out by a TUM / CEA / AREVA-CERCA cooperation for the planned IRIS 5 irradiation. A more cautious strategy has been followed up since 2008. AREVA-CERCA, FRM II/TUM and INL are partners in the UMo monolithic fuel developments. The monolithic foils are produced by INL and the plates are manufactured by TUM and AREVA-CERCA.

This paper shows the status of the UMo monolithic fuel plate manufacturing developments. It addresses (1) the feasibility studies which have been performed until today by AREVA-CERCA and (2) the comprehension phase which will be studied in the framework of the HERACLES consortium.

1. Introduction

In a common international effort, for example under the Global Threat Reduction Initiative (GTRI), work is in progress to minimize the use of highly enriched Uranium (HEU) in the civilian nuclear fuel cycle. One part of these efforts is the conversion of the nuclear research reactor fuel from HEU to low enriched Uranium (LEU) which is pursued by a number of different programs, e.g. the Reduced Enrichment Research and Test Reactor (RERTR) program. In a first step, the medium performance research reactors were converted in the 1990's using U_3Si_2 fuel. After that, the TRIGA reactors were converted in the decade of 2000 using ZrH fuel. In both cases AREVA-CERCA participated in the fuel development and production [1, 2].

Currently, the international community is making considerable efforts to convert the high performance research reactors (HPRR) using uranium-molybdenum (UMo) fuel. The UMo fuel for research reactors was first proposed in 1996 [3, 4]. It is not a new fuel alloy but some historical experience exists: In the 1960's, for example, AREVA-CERCA produced the fuel of the French first-generation nuclear power plants (*Uranium Naturel Graphite Gaz*) using UMo alloys. Nevertheless and despite this existing experience, the conversion of the last HEU research reactors is a long and complex challenge due to the pronounced requirements of the HPRRs regarding the operation conditions of the HPRRs. Development work is in progress in several continents, but today no fuel is qualified for converting these HPRRs. The US conversion program "United States High Performance Research Reactors (USHPRR) Conversion Program" is dedicated to monolithic UMo fuel and is currently moving from R&D to industrial development [6, 7]. The European conversion program HERACLES, "High performance European Reactors Action for their Conversion into a Low Enriched Solution", is dedicated to both dispersion and monolithic UMo and is currently at the R&D stage [8].

This paper describes the status of the UMo monolithic fuel manufacturing developments performed in AREVA-CERCA. This work was accomplished in partnership with the European research reactor's institutes inside European programs since the last decade.

2. Past developments

The European preliminary UMo monolithic studies were performed by CEA, TUM and AREVA-CERCA between 2005 and 2008 in the framework of the planned IRIS 5 experiment [10, 11, 12, 13, and 14]. At that time, the UMo monolithic concept was proposed by the US program [15, 16] as an alternative to the dispersion fuel in order to achieve higher uranium densities and to reduce the interaction area between aluminium and fuel by eliminating the aluminium matrix, which was considered to be responsible for the anomalous swelling of this fuel.

The aim of the AREVA-CERCA development work was to establish techniques for foil and plate manufacturing. The work was split up into three sub-programs: ingot making, foil manufacturing and plate production [10, 11]:

- The UMo ingots were made using a high capacity induction furnace.

- UMo foils were manufactured by hot and cold rolling processes under air atmosphere. Full-size foils of about 250 µm thickness were achieved. However, the foil quality obtained was not sufficient and some cracks and oxidation appeared [12, 13].
- The plate fabrication consists of bonding an UMo foil into an aluminium cladding, therefore the interface between aluminium cladding and UMo foil was of major interest. Two manufacturing processes were implemented and tested: Friction Stir Welding [12, 13] and a new welding technique called C2TWP, "CEA CERCA TUM Welding Process" [14]. The tests were performed on surrogate material (stainless steel) and depleted uranium. The process achieved good adherence on surrogate material but poor adherence on UMo material.

Based on these European manufacturing results and the irradiation results from the US program that were obtained in the same time period [17, 18], it was recommended to deposit an intermediate layer of a suitable material on the UMo foil prior to plate assembly [19]. The selected material must allow formation of a mechanically-stable diffused junction during manufacturing phase and must preclude the formation of an amorphous interaction compound under irradiation, which is unable to retain fission products.

The European foil production development work was stopped in 2008 due to the new orientation of the US program and the high investments that would have been required for foil production [20]. It was decided that the European manufacturing approach would focus on plate fabrication rather than foil production.

3. Current developments

Since 2008, the European UMo monolithic studies were continued in the framework of the ALPS program, a mutual agreement between TUM and AREVA-CERCA [21]. The development work is dedicated to monolithic plate fabrication, the necessary UMo foils are provided in partnership with the US program by the Idaho National Lab (INL).

At the beginning, the ALPS technical program allowed for two options depending on the UMo/Zr oxidation: The continuation of the development work under air with the C2TWP process (option 1) or under vacuum with Hot Isostatic Pressing (HIP) (option 2). C2TWP is a hot rolling process between 300-600°C using a stretching rate between 0 and 50% with a surface preparation able to remove oxidations and pollutants. In mid 2010, the technical results obtained with surrogate material made it possible to choose the development under air as the main development branch.

Thereafter, the project program was composed of three manufacturing steps: full-size plate manufacturing using surrogate materials and mini-size and later full size plates using depleted UMo foils.

3.1. Manufacturing validation using monolithic Zr foils

In order to avoid the U and Al interaction, a diffusion barrier is interposed between the UMo foil and the cladding in the UMo monolithic fuel concept [20]. Zirconium (Zr) was chosen by the US monolithic project from in-pile and out of pile irradiation experiments [22] and confirmed by TUM heavy ion bombardment experiments [23, 24]. Therefore, Zr material was used as surrogate material.

Developments were started with mini-size plates using pure Zr foil dimensions of 45 x 30 x 0.125 mm and continued with full-size plates of 45 x 700 x 0.125 mm dimension, which are representative for the UMo mini-size and full-size plate dimensions usually used in irradiation experiments. The bonding process used was C2TWP which was selected during the preliminary studies (see §2).

The development work was fully successful using both mini-size and full-size pure Zr foils. The C2TWP process produced several monolithic plates that were in-line with the quality criteria using both AlFeNi cladding and AG3NE cladding. Therefore, a robust process was established and the important process parameters were determined.

3.2. Manufacturing validation using monolithic mini-size UMo foils

In mid-2010, AREVA-CERCA received 21 depleted U8Mo mini-size foils from INL. In these samples, the Zr coating was deposited by a co-rolling process. The mini-size foil dimensions were 84 x 33 x 0.31 mm and the coating was Zr with 25 µm thickness.

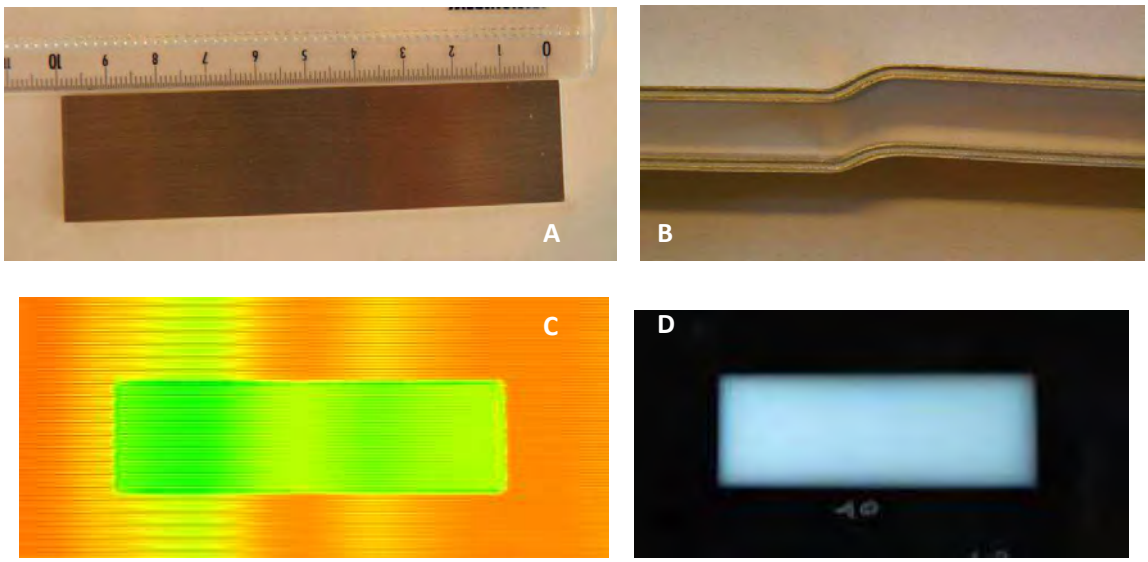


Figure 1: UMo monolithic mini-size plates: plate picture (A), bend test specimen picture (B), ultrasonic inspection picture (C), x-ray picture of the fuel loading picture (D).

The development work was also fully successful using mini-size UMo foils. The C2TWP process produced UMo monolithic mini-size plates with reproducible properties. All the last four plates were produced in compliance with standard inspection quality criteria [25]: dimensional inspections, visual inspection of bend test specimens, x-ray inspection of fuel loading and fuel out of zone, cladding thickness measurement, ultrasonic inspection for clad-clad bonding and visual inspection of surface flaws and cleanliness. As an example, figure 1 shows typical inspection pictures obtained for such plates.

Based on this success, LEU monolithic mini-size plates were produced with four foils provided by INL in the framework of the RERTR-11A experiment. Three LEU mini-size monolithic plates were produced in compliance with inspection quality criteria [25]; one was used for the destructive tests and two are ready to be irradiated.

An alternative coating technique to the INL co-rolling process which uses physical vapor deposition (PVD, "sputtering") is under development at TUM [26, 27, 28, and 29]. The process is able to cover UMo foils with 25 µm Zr [28] with the appropriate bond properties [29]. The production at AREVA-CERCA of monolithic mini-size plate with such foils is in progress.

3.3. Manufacturing validation using monolithic full-size UMo foils

In mid-2011, AREVA-CERCA received depleted U10Mo full-size foils from INL. In the samples, the Zr coating was deposited by the co-rolling process of INL. The full-size foil dimensions were 700 x 45 x 0.33 mm and the coating was Zr with 25 µm thickness. 8 foils were available for full-size plate production.

One of the major findings of this part of the program was the key role played by the UMo foil quality. During the ALPS program, the US monolithic program was still at the R&D stage [30, 31] where quality criteria were comprehensibly undefined as the focus was on feasibility. . Accordingly, the quality of these first foils was heterogeneous, leading to some uncertainties during the plate production development at AREVA-CERCA. To avoid these and in accordance with the matured US foil production program, detailed quality parameters and inspection programs will be defined between the parties in further development works.

Nevertheless, the development work was fruitful. No significant differences between AlFeNi and AG3NE cladding material were observed. Except the ultrasonic inspection, all other quality inspections were in compliance with standard inspection quality criteria [32], i.e. dimensional, bend, X-ray, cladding thickness, visual. During the ultrasonic inspection, small unbonded areas were found on all full-size plates produced. In the best case only two ultrasonic defects were observed (see figure 2). The largest one had an equivalent diameter of 2.5 mm which is only 1000^{th} of the plate surface. However, the quality criteria specify a maximum 1.5 mm [32] as cladding-meat contact faults can have dramatic thermal-hydraulic effects [33, 34].

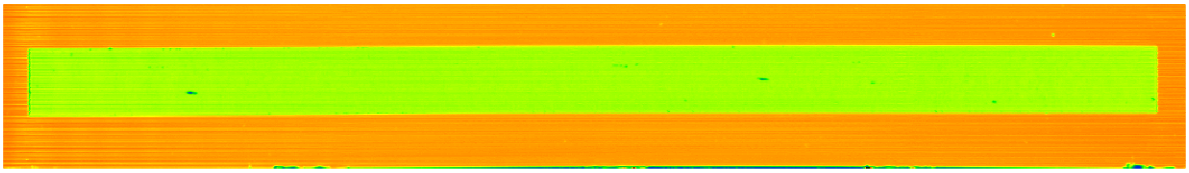


Figure 2: UMo monolithic full-size plate: ultrasonic inspection picture. The green zone is the fuel zone, the blue points are the unbond areas (ø2,5 mm size). The other colors are bonding areas.

The defects identified by ultrasonic inspection were randomly located on the fuel plate surface. Scanning Electron Microscope (SEM) pictures and Energy-dispersive X-ray spectroscopy (EDX) analysis were performed on 12 defect and non-defect samples. Figure 3.A and 3.B are the typical results for a non-defect interface. The Zr and Al welding are evidenced by the overlap of the corresponding curves in the EDX spectra. Three types of results were obtained for the defect samples:

1. No debonding evidence for the smallest defects. The Zr/Al interface defect has been missed or the defect is not located at the interface but could be a defect inside the foil itself.
2. A debonding evidence with a gap between the Zr and Al interface as presented in Figure 3.C. No trace of oxidation or polluting agent was found (Figure 3.D). As a trace of Al is observed on both sides of the gap, a contact has taken place between Zr and Al interface originally but the mechanical or thermal constraints were too strong to weld them.
3. In few places, debonding defects were correlated to Si polluting agent as seen in Figure 4. The Si most probably originates from the silicon spray, which covered the surface of the Zr co-rolled UMo foil after production to prevent oxidation. On some locations of the foil, the spray seemingly was not completely removed before the C2TWP and caused the debonding between cladding material and Zr layer.

Therefore, the causes for these defects can be attributed to the foil itself, a lack of foil cleaning and plate internal mechanical or thermal constraints. They provide important evidence on the ways to improve the C2TWP process. Nevertheless, these results demonstrate the technical feasibility of the C2TWP process to produce full-size monolithic UMo plates and underline that quality inspections and the cleaning of the foils is a crucial point for the produced plate quality.

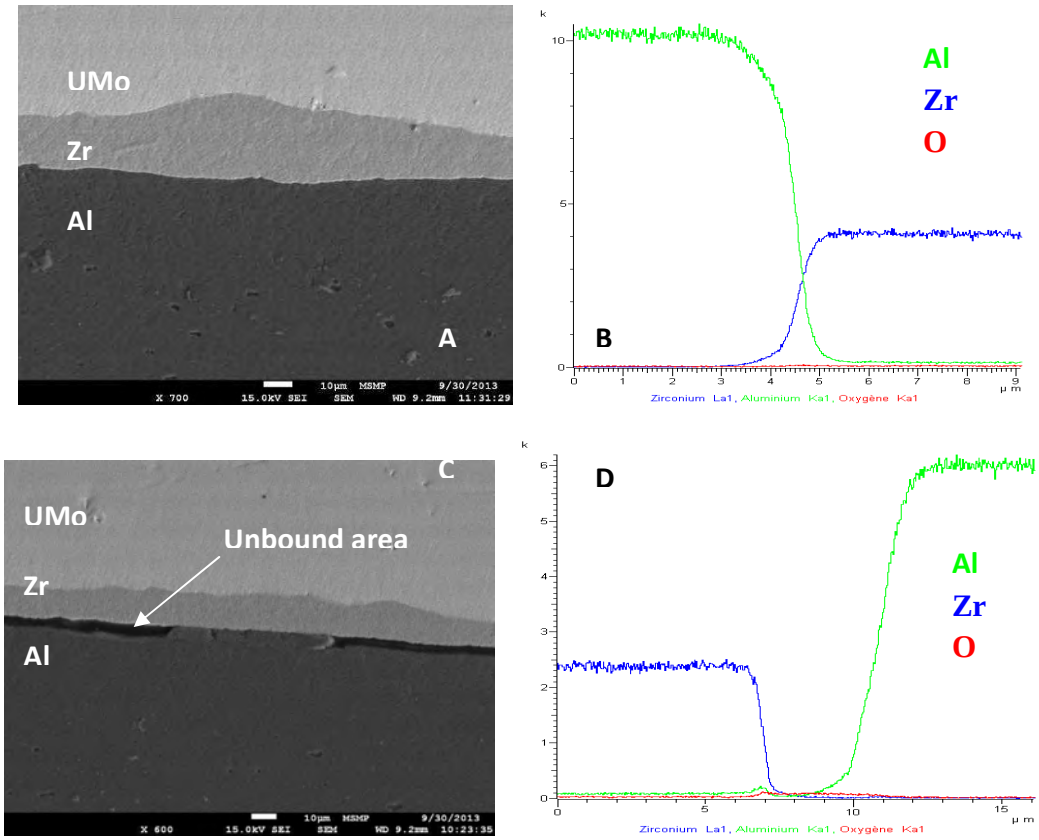


Figure 3: SEM pictures of interface area between Zr and Al resulting from the C2TWP process. (A) Bond interface; (B) Scan across interface evidencing the welding; (C) Unbond interface; (D) corresponding EDX scan across the gap: The measurements show no trace of oxidation, nor polluting agent.

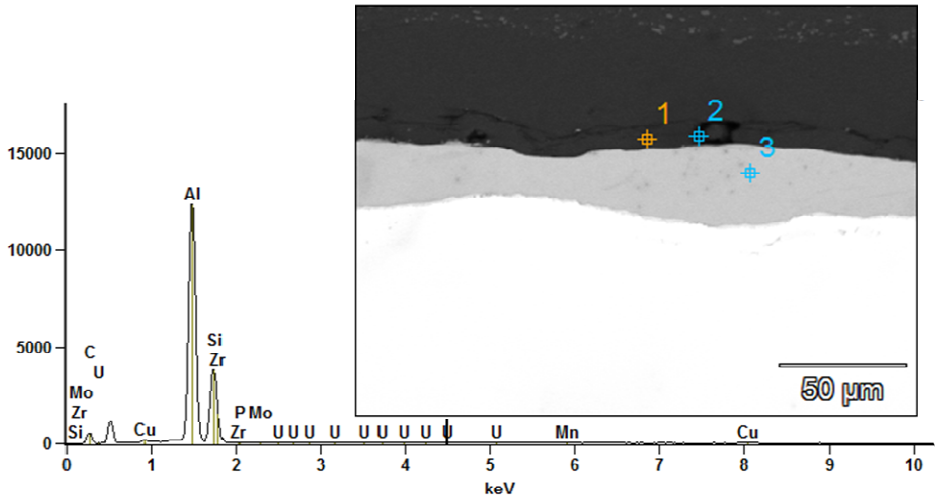


Figure 4: EDX analysis of ruptured structure on the surface between cladding material and Zr layer. The diagram shows the spectrum at location 2 in the SEM image with a Si peak at ~1.8keV.

4. Perspectives

In 2013, the European institutions, CEA, ILL, SCK-CEN, TUM and AREVA-CERCA teamed-up to form the HERACLES group [8, 9]. The group carries on from the existing European programs, ALPS [21] and LEONIDAS [35], which are merged together to increase efficiency and the chances for success. The goal of HERACLES is to develop and qualify a suitable high density fuel for the conversion of the European HPRRs. It is a common European group with a common strategy addressing both dispersion and monolithic fuels.

In the coming years, the HERACLES group will focus on a comprehension phase in order to secure and speed up the conversion process. From the monolithic fuel manufacturing point of view, the HERACLES program will cover a number of important items: Most important, the work in progress presented in section 3 will be continued, i.e. the measurements on ALPS ultrasonic defects will be finalized and monolithic plates with inter-diffusion barrier sputtered by TUM will be produced. Technical data will be exchanged with the US monolithic program, in particular about foil quality inspection. A mini-size plate irradiation experiment is planned to validate the results achieved so far. And, as a major step towards conversion, the industrial feasibility of the C2TWP process for the production of full-size monolithic plates will be studied.

5. Conclusion

Since 2005, AREVA-CERCA has been involved in UMo monolithic fuel manufacturing development work in partnership with the European research reactor's institutes inside European programs. The results achieved so far are fruitful and promising. A plate manufacturing process called C2TWP was set up, studied and its ability to produce UMo full-size monolithic plates was demonstrated. It is therefore an alternative process to the US process. Two LEU UMo mini-size monolithic plates were produced in compliance with standard inspection quality criteria and are ready to be irradiated.

From this year on, the European high density fuel development work (dispersion and monolithic) for the conversion of the European high performance research reactors is being conducted inside the HERACLES program. A roadmap has been built and work has started, i.e. AREVA-CERCA continues to develop UMo monolithic fuels, together with all the European institutions of HERACLES and in partnership with the US conversion program.

6. References

[1] J-P. Durand, B. Duban, Y. Lavastre, S. de Perthuis, “CERCA’s 25 years experience in U3Si2 fuel manufacturing”, Proceedings of RERTR 2003, Chicago, Illinois, USA, October 5-10, 2003.

[2] J-C. Macias, P. Colomb, T. Veca, “Progress and status of TRIGA reactor conversion carried out by TRIGA International”, Proceedings of RRFM 2011, Rome, Italy, March 20-24, 2011.

[3] J. L. Snelgrove, G.L. Hofman, C.L. Trybus, T.C. Wiencek, “Development of very-high density fuels by the RERTR program”, Proceedings of RERTR 1996, Seoul, Republic of Korea, October 7-10, 1996.

[4] J. L. Snelgrove, G.L. Hofman, M.K. Meyer, C.L. Trybus, T.C. Wiencek, ”Development of very-high-density low-enriched-uranium fuels”, Nucl. Eng. & Design, **178,** 119-126 (1997).

[6] D. E. Dombrowski, “Overview of LANL Progress in Process Development, Advanced Characterization Methods and Prototype Fabrication”, Proceedings of RERTR 2012, Warsaw, Poland, October 14-17, 2012.

[7] M.K. Meyer, D. M. Wachs, I. Glagolenko, D.D. Keiser, P. Medvedev, S. Miller, G. Moore, H. Ozatlun, F. Rice, B.H. Rabin, A. Robinson, N.E. Woolstenhulme, G.L. Hofman, Y.-S. Kim, “U.S. Progress in U-Mo Fuel Development”, Proceedings of RRFM 2013, Saint Petersburg, April 21-25, 2013.

[8] H. Breitkreutz, R. Jungwirth, A. Röhrmoser, W. Petry, S. Van den Berghe, A. Leenaers, E. Koonen, P. Lemoine, M. Ripert, H. Palancher, M-C. Anselmet, C. Jarousse, B. Stepnik, D. Geslin, J. Calzavara, H. Guyon, „The development of disperse UMo as high performance research reactor fuel in Europe – HERACLES working group“, Proceedings of RRFM 2013, Saint Petersburg, April 21-25, 2013.

[10] JM. Hamy, P. Lemoine, F. Huet, C. Jarousse, JL. Emin, “The French UMo group contribution to new LEU fuel development”, Proceedings of RRFM 2005, Budapest, Hungary, April 10-13, 2005.

[11] C. Jarousse, P. Lemoine, W. Petry, and A. Röhrmoser, “Monolithic U-Mo Full Size Prototype Plates Manufacturing Development”, Proceedings of RERTR 2005, Boston, USA, November 6-10, 2005.

[12] C. Jarousse, P. Lemoine, W. Petry, “Monolithic UMo full size prototype plates manufacturing development status as of April 2006”, Proceedings of RRFM 2006, Sophia, Bulgaria, April 30–May 3, 2006.

[13] C. Jarousse, P. Lemoine, P. Boulcourt, W. Petry, A. Röhrmoser, “Last manufacturing results of monolithic UMo full size prototype plates”, Proceedings of RERTR 2006, Cape Town, South Africa, October 26 - November 3, 2006.

[14] C. Jarousse, P. Lemoine, P. Boulcourt, W. Petry, A. Röhrmoser, “Monolithic UMo full size prototype plates for IRIS 5 Irradiation experiment”, Proceedings of RRFM 2007, Lyon, France, March 12-14, 2007.

[15] G.L. Hofmam, M.K. Meyer, "Progress in Irradiation performance of experimental Uranium molybdenum dispersion fuel", RERTR conference, San Carlos de Bariloche, Argentina, November 3-8, 2002.

[16] C.R. Clark, G.C. Knighton, M.K. Meyer, G.L. Hofman, "Monolithic fuel plate development at Argonne national laboratory", Proceedings of RERTR 2003, Chicago, Illinois USA, October 5-10, 2003.

[17] D.E. Burkes, N.P. Halliman, J. M. Wight, D. Chapple, « Update on friction bonding of monolithic U-Mo fuel plates », Proceedings of RERTR 2007, Prague, Czech Republic, September 23-27, 2007.

[18] J-F. Jue, B. Park, M. Chapple, G. Moore, D. Keiser, “Development of monolithic nuclear fuels for RERTR by hot isostatic pressing”, Proceedings of RERTR 2007, Prague, Czech Republic, September 23-27, 2007.

[19] G. Moore, C. Clark, J. Jue, W.D. Swank, D. Haggard, M. Chapple, D. Burkes, “Foil fabrication and barrier layer application for monolithic fuels”, Proceedings of RERTR 2007, Prague, Czech

Republic, September 23-27, 2007.
[20] D.M. Wachs, C.R. Clark, R.J. Dunavant, “Conceptual Process Description for the Manufacture of Low-Enriched Uranium-Molybdenum Fuel”, Idaho National Laboratory Report INL/EXT-08-13840, Feb. 2008.
[21] C. Jarousse, L. Halle, W. Petry, R. Jungwirth, A. Röhrmoser, W. Schmid, “FRM II and AREVA-CERCA common effort on monolithic UMo plate production”, Proceedings of RRFM 2009, Vienna, Austria, Mar. 22 – 25, 2009.
[22] G.A. Moore, F.J. Rice, N.E. Woolstenhulme, W.D. Swank, D.C. Haggard, J.F. Jue, B.H. Park, S.E. Steffer, N.P. Hallinan, M.D. Chapple, D.E. Burkes, « Monolithic fuel fabrication process at the INL », Proceedings of RERTR 2008, Washington, D.C., USA, October 5-9, 2008.
[23] R. Jungwirth, W. Petry, H. Breitkreutz, W. Schmid, H. Palancher, A. Bonin, M. Grasse, C. Jarousse, B. Stepnik, „Screening of different UMO/Al samples: protective oxide layers, TI addition to the matrix and ternary U-Mo-X alloys”, Proceedings of RRFM 2011, Rome, Italy, March 20-24, 2011.
[24] T. Zweifel, H-Y. Chiang, H. Palancher, A. Bonnin, L. Beck, P. Weiser, M. Döblinger, C. Sabathier, R. Jungwirth, F. Charollais, P. Lemoine, W. Petry, „Heavy ion irradiation on monolithic UMo/Al layer systems interdiffusion layer analysis using TEM and nano-XDR“, Proceedings of RRFM 2013, Saint Petersburg, April 2013, 21-25.
[25] G.A. Moore, N.E. Woolstenhulme, J.N. Campbell, J.F. Williams, S.G. Galbraith, G.N. Hoggard, “Specification for Experimental Plates for the RERTR-11A and RERTR-ALT Campaigns”, Idaho National Laboratory Report INL/SPC 1308, Nov. 2011.
[26] W. Schmid, R. Jungwirth, W. Petry, P. Böni, L. Beck, “Manufacturing of thick monolithic layers by DC magnetron sputtering”, Proceedings of RRFM 2008, Hamburg, Germany, March 2-5, 2008.
[27] W. Schmid, S. Dirndorfer, R. Grossmann, H. Juranowitsch, W. Petry, C. Jarousse, “Sputtering as a coating technique for monolithic UMo fuel foils”, Proceedings of RERTR 2010, Lisbon, Portugal, October 10-14, 2010.
[28] W. Schmid, S. Dirndorfer, R. Grossmann, H. Juranowitsch, W. Petry, C. Jarousse, “Sputtering as a Coating Technique for Monolithic U-Mo Fuel Plates”, Proceedings of RERTR 2011, Santiago, Chile, October 23-27, 2011.
[29] S. Dirndorfer, W. Schmid, H. Breitkreutz, R. Jungwirth, H. Juranowitsch, W. Petry, C. Jarousse, M. Hirsch, “Characterization of bond strength of monolithic two metal layer systems”, Proceedings of RRFM 2010, Marrakech, Morocco, March 21-25, 2010
[30] N. Woolstenhulme, D. Wachs, M. Meyer, “Design and Testing of Prototypic Elements Containing Monolithic Fuel”, Proceedings of RERTR 2011, Santiago, Chile, October 23-27, 2011.
[31] D. Wachs, D. Keiser, A. Robinson, G. Moore, N. Woolstenhulme, C. Clark, F. Rice, M. Lillo, D. Perez, G. Chang, J. Jue, D. Burkes, M. Meyer, “Fuel Performance Aspects of the Advanced Test Reactor U-Mo Monolithic Demonstration Assembly Safety Basis”, Proceedings of RERTR 2011, Santiago, Chile, October 23-27, 2011.
[32] “Specification for CERCA fuel plates for irradiation in FUTURE-MONO campaign”, Idaho National Laboratory Report INL/SPC 1311, October. 2011.
[33] H. Breitkreutz, W. Petry, “Thermal-hydraulic effects of cladding-meat contact faults”, Proceedings of RERTR 2011, Santiago, Chile, October 23-27, 2011.
[34] H. Breitkreutz, W. Petry, “Simulation of the time-evolution of oxide layers surrounding cladding-meat contact faults (non-bonds) and their thermal-hydraulic implication”, Proceedings of RRFM 2012, Prague, Czech Republic, March 18-22, 2012.
[35] B. Stepnik, M. Grasse, D. Geslin, C. Jarousse, F. Charollais, P. Lemoine, Y. Calzavara, H. Guyon, E. Koonen, S. Van Den Berghe, “LEONIDAS UMo dispersion fuel qualification program: Progress and perspectives - focus on the E FUTURE II fuel plate manufacturing”, Proceedings of RRFM 2012, Prague, Czech Republic, March 18-22, 2012.

ADVANCES IN GTRI FUEL FABRICATION CAPABILITY TECHNOLGY

D.E. BURKES, D.M. PAXTON, S.A. MAPLE, and D.J. SENOR
Pacific Northwest National Laboratory, P.O. Box 999, Richland, WA 99352 USA

H.A. LONGMIRE
Y-12 National Security Complex, P.O. Box 2009, Oak Ridge, TN 37831 USA

D. DOMBROWSKI
Los Alamos National Laboratory, P.O. Box 1663, Los Alamos, NM 87545 USA

L. COLE
Idaho National Laboratory, P.O. Box 1625, Idaho Falls, ID 83415 USA

ABSTRACT

The Fuel Fabrication Capability (FFC) is part of the U.S. Department of Energy's (DOE) National Nuclear Security Administration (NNSA) Global Threat Reduction Initiative (GTRI) Convert Program. The FFC is primarily responsible for the establishment of a fabrication process for the low-enriched monolithic uranium-molybdenum fuel currently under development for supply to the U.S. research and test reactor community. This presentation will focus on advancements that have been made in fabrication technology under consideration by the FFC over the past year, specifically in order to reduce scrap generation, increase material utilization, and increase process yield. This includes casting technology to produce alloy coupons, rolling processes to produce foils, alternative methods to apply a Zr diffusion barrier to foils, and plate fabrication processes. A particular focus has been placed on better understanding the relationship between fuel fabrication process parameters and fuel properties. The FFC criteria for selecting and advancing technologies and plans for the coming year will also be discussed.

1. Introduction

The mission of the GTRI is to reduce and protect vulnerable nuclear and radiological material located at civilian sites worldwide. This mission is accomplished through three main program areas. First, convert research reactors and isotope production facilities from the use of high-enriched uranium (HEU) to low enriched uranium. Second, remove and dispose of excess nuclear and radiological materials. Third, protect high priority nuclear and radiological materials from theft and sabotage. This paper will address the fabrication development of low-enriched uranium-molybdenum (LEU-Mo) monolithic fuel for use in U.S. research and test reactors.

Within the Convert Program, the FFC has been tasked with development and deployment of a cost-effective and efficient fuel production capability that supports the conversion and continued operation of High Performance Research Reactors (HPRR) within the U.S. In particular, the FFC is responsible for the development of commercial-scale fabrication processes for manufacturing the LEU-Mo monolithic fuel. The FFC process development efforts are conducted in a manner to ensure that a particular process or set of parameters does not adversely affect fuel performance or qualification. Further, there is a particular impetus to perform optimization of process steps to reduce eventual fuel manufacturing costs and improve material utilization. The FFC provides support to government and commercial fabricators by transferring knowledge developed at the lab and bench scale for use at a commercial scale, and is also responsible for fabricating experimental and demonstration fuel products requested by the Fuel Development and Reactor Conversion

pillars of the GTRI Convert Program. The FFC is a multi-laboratory effort, with activities conducted across the U.S. DOE Complex including Idaho National Laboratory (INL), Los Alamos National Laboratory (LANL), Oak Ridge National Laboratory (ORNL), Pacific Northwest National Laboratory (PNNL), and Y-12 National Security Complex (Y-12 NSC). The FFC interfaces with Babcock and Wilcox Nuclear Operations Group (B&W NOG) as the current fuel supplier to the U.S. HPRR, as well as with other commercial entities and universities. Currently, the FFC is focusing much of its efforts on technology maturation and scale-up of reference fabrication processes and alternative technologies that promise material utilization and cost improvements [1]. In general, development of a standard fabrication process to satisfy the requirements of each unique US HPRR fuel design is challenging since the fabrication processes used for a monolithic fuel are a significant departure from those processes currently in use for US HPRR HEU dispersion fuels. Figure 1 shows the general monolithic LEU-Mo fuel fabrication concept, comprised of five major processing steps.

The first step involves downblending HEU with a low enrichment diluent, typically natural or depleted uranium, and alloying with molybdenum using a vacuum induction melting process (VIM). The downblended, alloyed material is cast into an intermediate shape that is subsequently re-melted using VIM and cast into an LEU-Mo ingot. The ingot is sized and machined into a coupon, which is then coupled with the Zr diffusion barrier, canned, and subjected to a hot rolling process. Once at an intermediate thickness, the hot-rolled LEU-Mo sheet is removed from the can and cold-rolled to the final desired thickness. The cold-rolled sheet is sheared according to final required dimensions to produce foils and placed between two sheets of aluminum cladding. A series of cladding-foil-cladding assemblies are stacked into another can, evacuated and sealed, and subjected to a Hot Isostatic Press (HIP) process to hermetically seal the foil within the aluminum cladding. Fuel plates are machined from the HIPed assemblies and formed according to specification. The finished, formed fuel plates are then swaged or welded to side plates to produce a fuel element. Four major processes are currently being optimized and will be discussed in this paper.

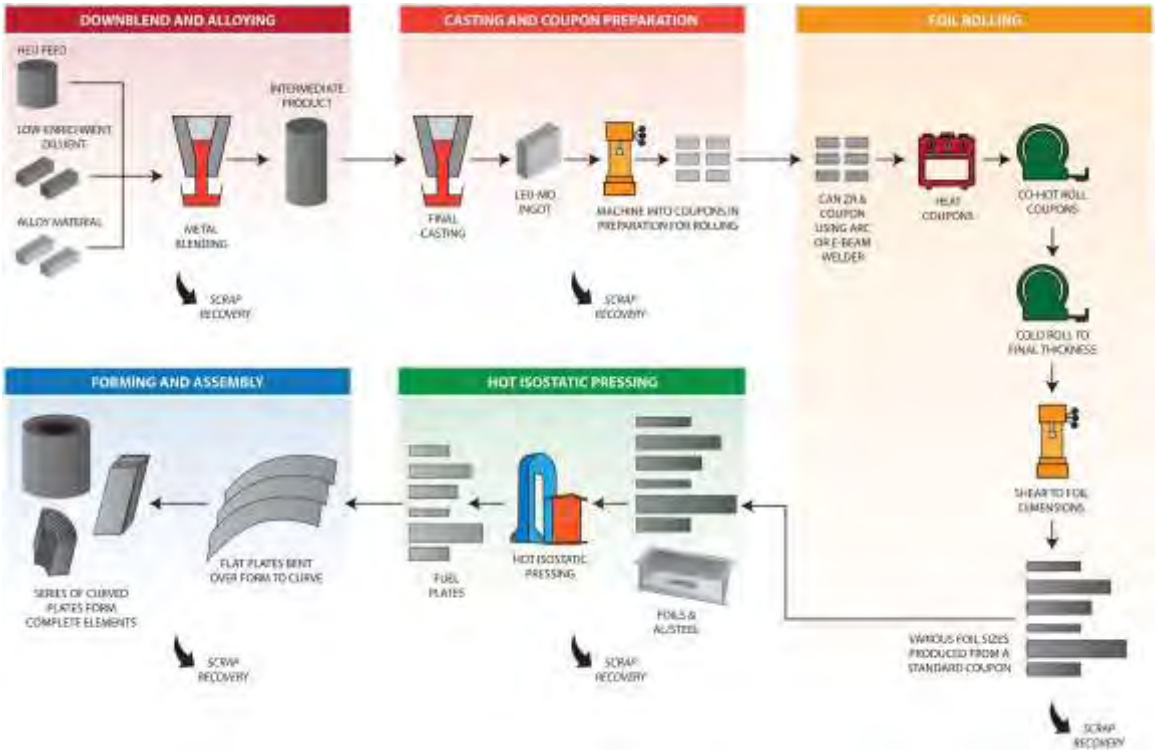


Fig. 1. Monolithic LEU-Mo Fuel Fabrication Reference Process

2. Casting and Coupon Preparation

Conducting downblending and alloying operations in a single step is non-optimal due to the significant difference in liquidus temperatures between uranium and molybdenum. This often leads to inhomogeneity in the cast product, e.g. undissolved molybdenum or coring, and requires the use of an intermediate casting step. Current efforts are investigating the production of a DU-Mo "master alloy" using a VIM/vacuum arc re-melt (VAR) process or an arc-melt button process. Because this operation involves depleted uranium (DU), it can be conducted outside high security facilities where enriched uranium is processed, ultimately lowering cost. Furthermore, the master alloy can be combined with HEU for downblending in a single VIM step, eliminating the need for an intermediate casting. Use of a master alloy also offers the promise of a product with improved homogeneity that pays dividends in downstream processing operations. An example of a composite electrode used for the VIM/VAR master alloy process at LANL is provided in Figure 2.

Coupons are currently prepared by machining the as-cast ingot to final thickness, resulting in a significant generation of LEU-Mo fines. Only about 35% of the cast product (mass basis) ends up as a coupon for rolling with the current process. Activities are underway to perform a rolling operation to reduce the thickness of the as-cast ingot to near final coupon thickness, minimizing the amount of machining required and in turn reducing the amount of machining scrap that is generated. Rolling the as-cast product also offers improvements in microstructure, where pores present from casting can effectively be closed and carbides present in the material can be distributed more evenly. Examples of rolled, as-cast material are provided in Figure 3.



Fig. 2. Example of composite electrode (Mo fins surrounded by cast DU) used for the VIM/VAR master alloy concept at LANL

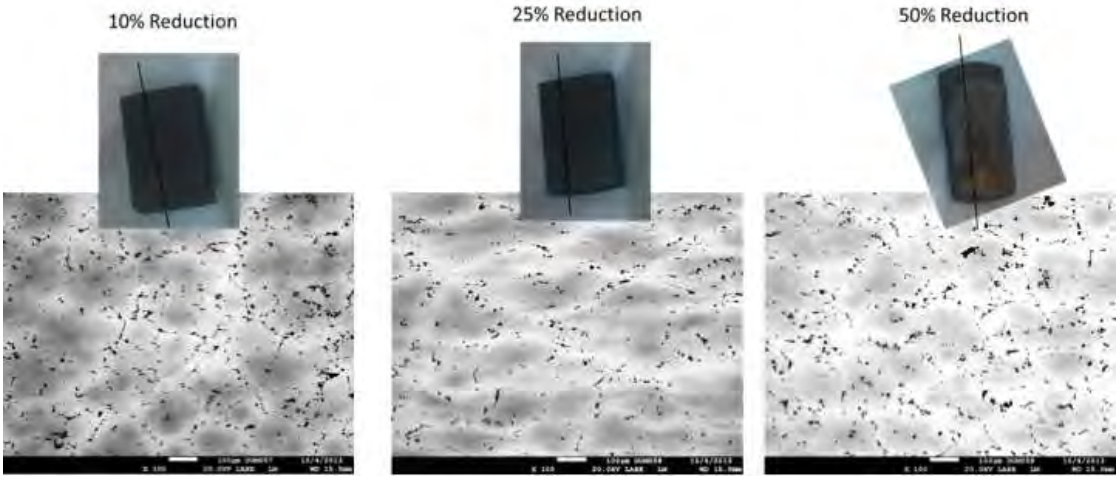


Fig. 3. Example micrographs of as-cast material subjected to three different rolling reductions to reduce thickness at PNNL. The coupons were initially 8.36 mm thick and were reduced at 800 ^{o}C. Images were obtained at the center of the rolled coupons.

3. Foil Trimming

Foils are currently trimmed from coupons rolled to final thickness using a mechanical shearing operation. If not properly optimized, this type of shearing could produce undesirable mechanical deformation resulting in a shear lip that causes poor fit in the cladding pocket prior to the HIP operation. Furthermore, it has been hypothesized that such a shear lip results in increased interaction between the uncoated fuel foil edge and the cladding that may result in undesirable performance characteristics. Shearing long, thin, relatively hard foils in this manner is challenging while trying to maintain physical and mass tolerances. One alternative to a mechanical shearing operation is a mechanical slitting operation, where both edges of the foil are trimmed simultaneously. While this may address physical and mass control issues, it may not completely alleviate concern with formation of a shear lip and foil bowing (camber) may occur when slitting foils that are not perfectly flat. Another alternative currently being investigated is a laser ablation method. This alternative uses a laser to locally vaporize the foil producing a cut edge. Technical challenges associated with this method that are currently being addressed include appropriate sizing of laser equipment to increase process throughput, addressing uranium vapor produced during the operation, and optimizing parameters (such as linear cutting speed) to produce clean edges without significant melting or spatter.

4. Barrier Coating Alternatives

The current co-rolling process to bond the Zr diffusion barrier to the LEU-Mo fuel foils is a time intensive process. There are several technical issues relating to the current process. First, the foil must be sheared from the Zr coated sheet, making determination of final U mass loading challenging without an accurate method to assess variability in the Zr layer thickness. Foil trimmings also contain Zr and cannot be returned directly to the U-Mo casting process. The Zr must first either be dissolved off and/or separated from the U using an expensive recovery operation. Alternate methods to apply the Zr layer are needed that allow for an accurate U mass loading as well as minimizing Zr contaminated U-Mo scrap.

Two methods to apply Zr to the foil after rolling the U-Mo to the specified thickness are currently being investigated. The first alternative is a plasma spray process being developed at LANL [2]. This method is capable of delivering relatively uniform, fine-grained Zr coatings of high density with adhesion comparable to that observed in roll-bonded foils [3]. Foils up to 61 cm long have been successfully coated using this process, but irradiation tests have yet to be performed. The second method involves electroplating Zr from a molten salt bath onto the foil. Initial tests with plating Zr onto surrogate foils have shown that this is a feasible method and warrants further investigation. In the surrogate tests, uniform, high-density Zr coatings have been applied to the substrate material. This technology offers the advantage of inherently coating foil edges with Zr, thereby fully encapsulating the LEU-Mo foil in Zr. Micrographs of Zr coatings applied using plasma spray and electroplating are provided in Figure 4.

One final alternative barrier coating method that is under investigation is co-extrusion [4]. The co-extruded billet, an example of which is shown in Figure 5, is passed through a series of rolls to produce a foil of the desired thickness. The rolls can be shaped, resulting in graded foils that are necessary for some reactor designs, e.g., the High Flux Isotope Reactor. While this method is similar to roll bonding, it offers the advantage of minimal post trimming operation, i.e., no trimming along the foil width is required. This also improves the ability to accurately estimate the U mass inside the foil, and also lends itself to using a standard billet size to produce multiple foil geometries, something that cannot be accomplished using a coupon in the rolling operation without generating significant quantities of scrap.

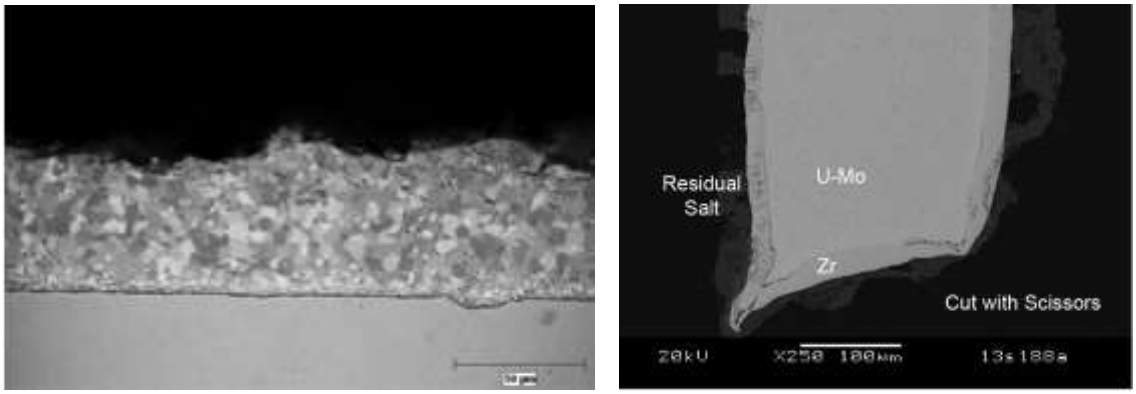


Fig. 4. Example micrographs of Zr coatings applied to foils using plasma spray at LANL (left) and electroplating at PNNL (right)


Fig. 5. Example of a U-Mo billet co-extruded with Zr to produce a rod that can then be passed through a series of rolls to produce a foil at PNNL.

5. HIP Process Optimization

Aluminum alloy 6061 (AA6061) is clad to the LEU-Mo monolithic fuel foils employing a hot isostatic pressing (HIP) process. The baseline process utilizes a stack-up of cladding and fuel foils separated by steel strongbacks housed inside a stainless steel can. The can is evacuated, inserted into the HIP chamber, and subjected to 103 MPa at 560 ^{o}C for roughly 90 minutes. The FFC is currently investigating methods to reduce the number of welds required to fabricate the stainless steel can. One option involves utilization of a HIP can made by sheet forming with a die. A formed can reduces the number of welds required from six down to one [5]. Further, this design can be sealed using electron beam (e-beam) welding, offering an additional advantage of evacuation and sealing in a single step, rather than two independent process steps. The formed and hydroformed cans are shown, along with an as-processed formed HIP can, in Figure 6.

Additional areas of HIP process optimization include the re-use of strongbacks in the HIP can for multiple HIP runs and the elimination of the stainless steel HIP can altogether. For the latter, e-beam welding is utilized to seal the foil inside the AA6061 cladding, again coupling evacuation with the welding step. The “canless” plates are placed in a fixture inside the HIP to provide constraint and the normal HIP process is carried out. Finally, alternatives to the HIP process, such as hot pressing, are also being investigated in order to reduce space and equipment infrastructure requirements since clad bonding via HIP essentially applies a uniaxial load. However, a significant amount of technology maturation is required to successfully demonstrate that these types of processes can be used for this application.

The characteristics of desirable foil-to-clad and clad-to-clad bonding must still be defined in order to compare the optimized and alternative processes to the baseline process that has been proven to survive irradiation. Further, process parameters such as time at temperature



Fig. 6. Example photographs of a HIP can formed from sheet with a die (upper left) and a hydroformed HIP can (lower left). A formed can sealed by electron beam welding is shown after being subjected to the HIP process (right) at LANL.

must continue to be optimized in order to avoid any deleterious impacts on fuel performance, such as increased intermetallic formation, especially at uncoated foil edges, and U-Mo decomposition. These characteristics continue to be investigated by both the Fuel Development and FFC Pillar teams as part of the GTRI Convert Program.

6. Conclusions

The FFC has been tasked with the development and deployment of a cost-effective and efficient fuel production capability that supports the conversion and continued operation of HPRRs within the U.S. The FFC process development efforts are conducted in a manner to ensure that a particular process or set of parameters does not adversely affect fuel performance or qualification. Further, there is a particular impetus to perform optimization of process steps to reduce eventual fuel manufacturing costs and improve material utilization. Currently, the FFC is focusing much of its efforts on technology maturation and scale-up of reference fabrication processes and alternative technologies that promise material utilization improvements. Examples of some of the most promising optimization and alternative process campaigns have been discussed. If determined suitable according to FFC fabrication criteria, most of the alternatives discussed here will be evaluated for irradiation performance in the Mini-Plate-1 experiment (MP-1).

7. Acknowledgements

The authors wish to acknowledge the numerous technical, administrative, and managerial support staff at INL, LANL, PNNL, the Y-12 NSC, and B&W NOG that enable the Fuel Fabrication Capability Pillar. The authors wish to acknowledge the sponsor, the Global Threat Reduction Initiative, for the opportunity to conduct and present this work.

8. References

1. D.J. Senor and D.E. Burkes, Fuel Fabrication Capability Research and Development Plan, Pacific Northwest National Laboratory Report PNNL-22528, June 2013.
2. K. Hollis, N. Mara, R. Field, T. Wynn, J. Crapps and P. Dickerson, “Characterization of Plasma Sprayed Zirconium on Uranium Alloy by Microcantilever Testing,” J. Thermal Spray Technology 22 (2013) 233-41.

3. K. Hollis, C. Liu, R. Leckie and M. Lovato, “Interface Fracture Characterization of Plasma Sprayed and HIP Bonded Zr Coatings on U-Mo Sheet Using Bulge Testing,” International Thermal Spray Conference, Barcelona, Spain, May 21-23, 2014.
4. C.A. Lavender *et al.*, Concept Feasibility Report for Using Co-Extrusion to Bond Metals to Complex Shapes of U-10Mo, Pacific Northwest National Laboratory Report PNNL-23045, December 2013.
5. K. Clarke, J. Crapps, J. Scott, B. Aikin, V. Vargas, M. Dvornak, A. Duffield, R. Weinberg, D. Alexander, J. Montalvo, R. Hudson, B. Mihaila, C. Liu, M. Lovato, D. Dombrowski, Hot Isostatic Press Can Optimization for Aluminum Cladding of U-10Mo Reactor Fuel Plates: FY12 Final Report and FY13 Update, Los Alamos National Laboratory Report LA-UR-13-26706, August 2013.

RRFM 2014 – EUROPEAN RESEARCH REACTOR CONFERENCE

March 30 – April 3, 2014
Ljubljana
Slovenia

FRM II / CERCA UMo ATOMIZER PROJECT PROGRESS

R. SCHENK, W. PETRY

Forschungs-Neutronenquelle Heinz Maier-Leibnitz (FRM II), Technische Universität München (TUM)
Lichtenbergstr. 1, 85747 Garching – Germany

B. STEPNIK, M. GRASSE, G. BOURDAT, C. MOYROUD, C. COULLOMB, C. JAROUSSE

AREVA CERCA
Les Bérauds ZI BP 1114, 26104 Romans sur Isère – France

ABSTRACT

FRM II and CERCA have launched a common project for the construction and operation of an UMo atomizer. The project aims at providing feedstock atomized UMo fuel powder for future irradiation tests and at gathering know-how for industrial scale fuel-powder production by means of atomization.

General operational readiness of the FRM II / CERCA UMo atomizer using surrogate material was confirmed in early 2013. After receipt of the nuclear operating licence and subsequent commissioning of both the production facility and dedicated uranium laboratory, initial powder production experiments on depleted uraniferous material were conducted.

This paper presents the project's progress and discusses first production results.

1. Introduction

High density reactor fuels are currently being developed so as to replace present highly-enriched fuels being used in European research reactors like FRM II. Amongst others, disperse uranium-molybdenum alloy (UMo) based fuels show promising mechanical and physical properties, though irradiation behaviour makes extensive irradiation tests inevitable.

In order to satisfy the subsequent demand of UMo fuel powder, FRM II and CERCA agreed in early 2010 on a cooperation to build up a dedicated powder production facility. Centrepiece of this facility will be the in-house developed and constructed FRM II / CERCA UMo atomizer, since atomization is a promising and widely used principle for metal powder

production. In addition to the atomizer, the facility includes an adapted and dedicated uranium laboratory, an induction furnace and two related custom glove boxes.

Commissioning of the uranium laboratory was accomplished in the middle of 2013, shortly after the nuclear operating licence for the laboratory was granted. Thereafter, both the glove box containing the induction furnace as well as the one containing the atomizer were sealed and approved for uraniferous commissioning. Subsequently, the induction furnace and atomizer were also put into 'hot' operation.

Eventually, first uraniferous production tests were performed involving depleted UMo melting, casting, atomization, and powder analysis.

2. Production process

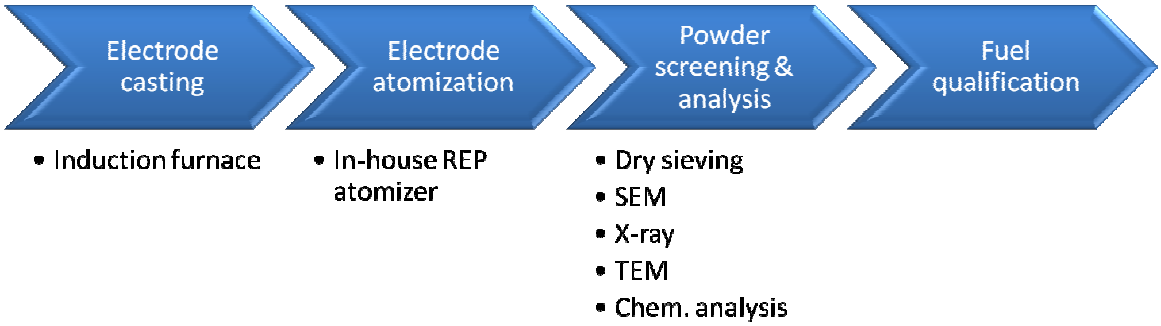


Figure 1 – Process chain for UMo powder production.

The UMo powder production at CERCA involves three basic process steps in order to obtain powder for the subsequent fuel qualification program: electrode casting, atomization and powder analysis (Figure 1). The pre-alloyed UMo is transferred from the feedstock to the new powder production facility for electrode casting and atomization, conducted in an induction furnace and REP[1] atomizer, respectively. Powder screening and analysis involves dry sieving, scanning electron microscopy (SEM), X-ray mapping, transmission electron microscopy (TEM), and chemical analysis.

[1] REP: rotating electrode process.

3. Electrode casting

3.1 Setup



Figure 2 – The induction furnace in its custom glove box before ‘hot’ commissioning.

The induction furnace is entirely housed in a custom glove box in order to avoid any dissemination of radioactive material (Figure 2).

The pre-alloyed U-8Mo is molten and cast in an induction furnace since induction is traditionally the most common melting technique for uranium and its alloys [1]. It is worth mentioning, that this particular furnace allows for melt-stirring by induction, thus enhancing alloy homogenisation before casting [2]. In addition, the furnace uses the gravity (drop) casting technique, thereby pouring the melt from below the pool. This is beneficial to cast metal purity since dross and slag tend to float to the pool top due to their lower density.

First experiments were carried out using uncoated graphite crucibles and moulds. The U-8Mo was molten under argon atmosphere and poured into cold, non-split moulds. This straightforward setup may serve as a starting point in order to evaluate the necessity of a more sophisticated procedure in terms of production quality, effort, and time; despite this, similar approaches were taken in [3]. However, feedstock material was mechanically polished before melting in the caster, for the oxide skin is suspected to complicate full melting of UMo coupons.

As a matter of course, mould dimensions were adapted to the solidification shrinkage in order to guarantee accurate electrode dimensions [4]. In particular, the electrode fitting is required to meet the intake dimensions of the atomiser collet chuck. Furthermore, a balanced geometry and mechanical integrity of the electrode are beneficial to both process stability and safety as REP atomization exposes the electrode to considerable centrifugal force.

3.2 Results



(a) (b)

(c) (d)

Figure 3 – Pictures showing polished depleted feedstock uranium (a) and U-8Mo (c) as well as the corresponding uranium (b) and U-8Mo electrode in their as-cast state.

Depleted Uranium and U-8Mo electrodes were successfully cast from feedstock material (Figure 3). Though, a substantial loss of around 20 % of the raw material occurred during the first melting and casting experiments. This relatively high value [3, 4] will be subject to optimisation in the further course of the project.

Due to their solidification shrinkage, U and U-8Mo electrodes were readily recovered from the non-split moulds. Subsequently, they were controlled for pouring defects such as misruns, cold shuts, and eccentric cavities as they might compromise the mechanical electrode-performance during atomization. In fact, visual and X-ray inspection did not reveal any of those defects. Though, as-cast U and U-8Mo electrodes showed visible surface pitting (Figure 3b, d) and shrinkage piping, causing a rough surface and a central cavity, respectively. These defects are likely due to the cold mould setup [3], but influenced neither atomization nor powder quality. The latter, though, might be compromised by carburisation of the melt, which is indicated by the dark and matt appearance of the electrode surfaces.

In summary, the as-cast U-8Mo electrodes were considered suitable for REP atomization.

4. Atomisation

4.1 Setup



Figure 4 – View of the glove box housing the REP atomizer and sieving machine before 'hot' commissioning.

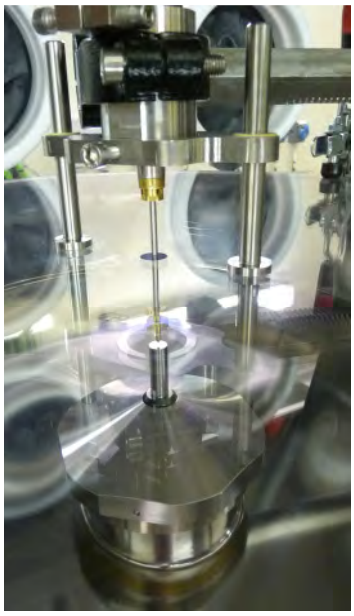


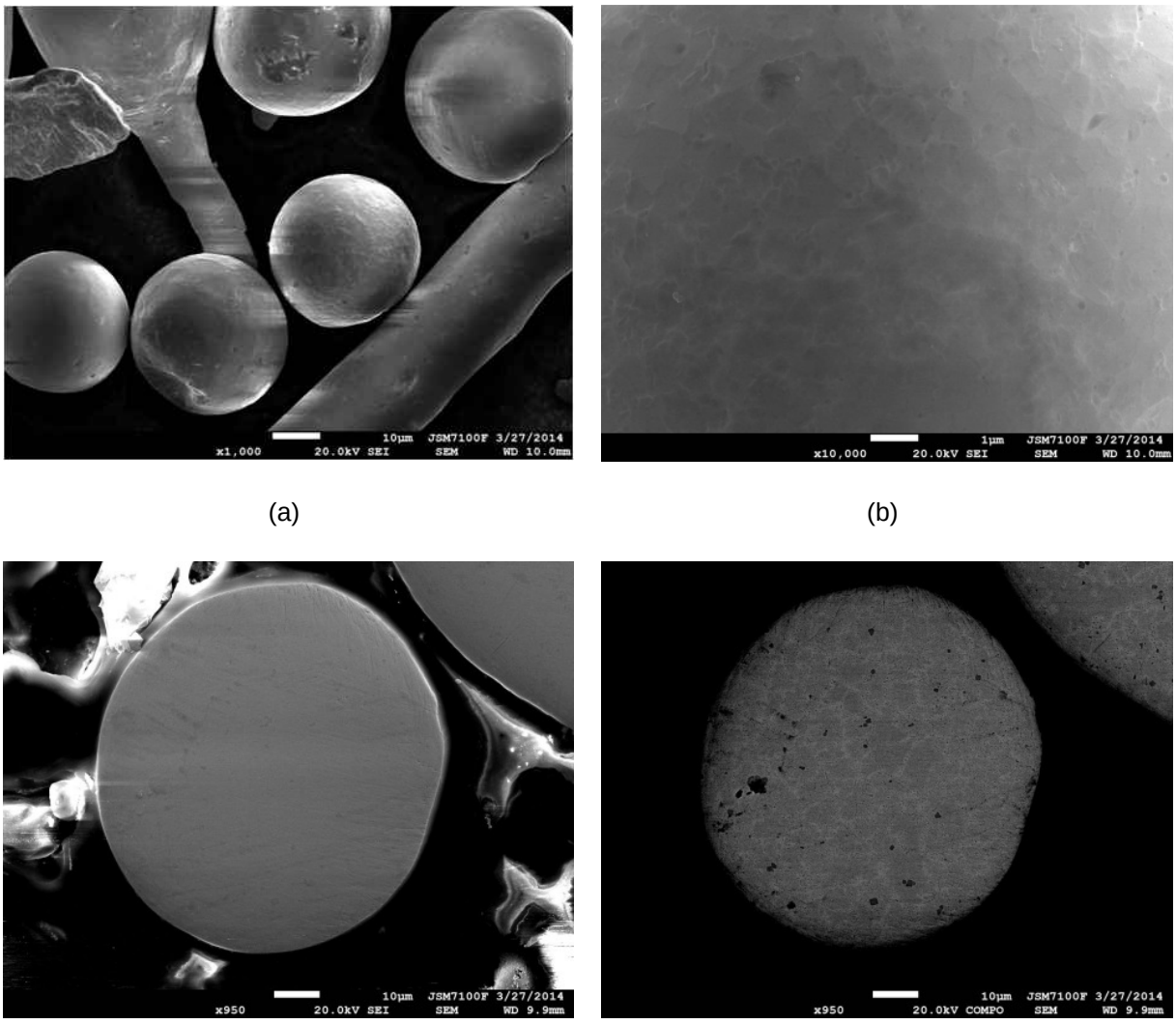
Figure 5 – Insight view of the REP atomizer recipient showing a mounted stainless steel electrode (bottom), the tungsten electrode (top), and the cover hood.

The atomizer is housed in a customized argon glove box (Figure 4). This installation accounts for radiation protection, safety, and powder quality as it inhibits dissemination of radioactive material, inflammation of reactive metal powders, and particle oxidation, respectively.

As presented at the RRFM 2013, this atomizer is based on the rotating electrode process (REP) [5], offering rotational speeds up to 50'000 rpm depending on the electrode's geometry and mass (Figure 5). For atomization, the consumable electrode is mounted on a collet chuck and rotated by a spindle shaft that is in turn powered by an in-house designed belt-drive system. In order to provide stable rotation, repeatability, and traceability of results, a speed sensor provides real-time data from the spindle to both the operator and motor loop-control. An electric arc fed by a TIG arc melter provides the heat that is needed to melt a UMo electrode. For convenience, the arc is ignited at full rotation speed by high frequency ignition.

The first U-8Mo electrode was atomised under argon atmosphere of less than 10 ppm and 5 ppm of oxygen and humidity, respectively. This parameter set was chosen as it efficiently worked for surrogate material, that is, atomized stainless steel particles had almost entirely a spherical shape and no visible oxidation [5].

4.2 Results



(a) (b)

(c) (d)

Figure 6 – Scanning electron microscopy (SEM) images using secondary electrons (SE) reveal a mixture of UMo spheres and fibres (a) showing generally regular surfaces without pores (b) and no porosity (internal voids) in sectioned particles (c). Though, backscattered electrons (BSE) reveal segregation of impurities (black) to the grains (dark grey) and grain boundaries (light grey) (d).

Scanning electron microscopy (SEM) of the first U-8Mo powder batch – atomised from an in-house cast electrode – revealed that the powder is composed of spheres and fibres (Figure 6a). It is suggested that the applied atomization parameter set caused droplet formation within the ligament formation regime – one of the three distinct droplet formation mechanisms of centrifugal atomization. In order to primarily obtain spherical shaped particles, a parameter set favouring direct droplet formation may be pursued [6, 7, 8]. Preceding experiments with surrogate material [5] back up this evaluation.

The atomized UMo particles have regular (smooth) surfaces showing neither pores nor oxidation (Figure 6b). In addition, no internal porosity or cavities were observed (Figure 6c).

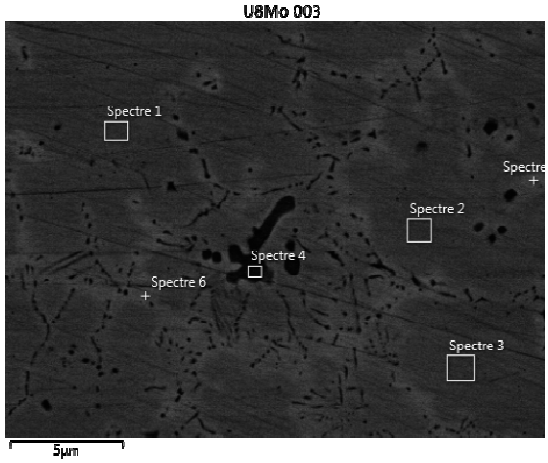


Table 1 – Elemental composition of EDS-scanned areas and points of a sectioned UMo particle.

Spectrum	Element	Mass-%
1, 2, 3	U	92
	Mo	8
4	U	77
	C	23
5, 6	U	96
	Mo	4

Figure 7 – Picture from a sectioned UMo particle showing different areas and points of spectral analysis by means of energy-dispersive X-ray spectroscopy (EDS). The corresponding element analysis is presented in Table 1.

Though, grains and grain boundaries show a different alloy composition of UMo. In particular, molybdenum content in the grain boundaries decreases to 50 % of its initial value, whereas the uranium content seems to compensate for this effect (Figure 7 and Table 1). However, UMo composition in the grains meets the initial and aimed ratio. This means that – after remelting of the alloy in both the induction furnace and atomiser and after subsequent atomisation of the melt – the initial element ratio of the alloy has generally remained the same throughout the entire production process. In addition, X-ray diffraction of the powder confirmed that the UMo crystallizes in the γ-phase during atomisation. This effect was already reported earlier by INL [9].

Segregation of impurities occurs in particular to the grain boundaries (Figure 6d, Figure 7). It is likely that these impurities primarily consist of carbon. In fact, chemical analysis of the U-8Mo powder revealed an overall carbon contamination of around 1400-1600 ppm[2] while other impurities do not exceed 200 ppm, though. The outstanding value is most probably due to the use of uncoated graphite crucibles and moulds [3, 4]. Electron-dispersive X-ray diffraction (EDS) confirms these measurements, notably in terms of segregation effects to the grain boundaries. However, the quantitative carbon content (Table 1) must be interpreted carefully as the sample was embedded into graphite resin. In fact, polishing could have transferred graphite from the resin matrix to internal particle voids. As a consequence, sample preparation will be subject to review. It should be mentioned, though, that the carbon content – although being elevated – does not exceed current fuel specification limitations.

About 60 % of the UMo-electrode was atomised. The particle size distribution of the first atomized U-8Mo batch was obtained by dry sieving (Figure 8). In order to provide comparable data, the obtained mass fraction in each size class was normalized[3] [7]. The normalized mass fraction allows for the determination of the distribution's shape and mode[4] which lies between 63 and 90 µm. The mass median diameter of about 122 µm was determined from the cumulative undersize distribution (Figure 8) by linear interpolation.

[2] Initial carbon content of feedstock U-8Mo was < 1000 ppm.

[3] Sieving mesh sizes are standardised and follow a geometric progression, rendering the interval between two successive mesh sizes greater as the mesh size increases. It is hence consistent to normalize the obtained result in each size class by the corresponding mesh size interval.

[4] Mode: value x or diameter at which the distribution reaches its maximum value.

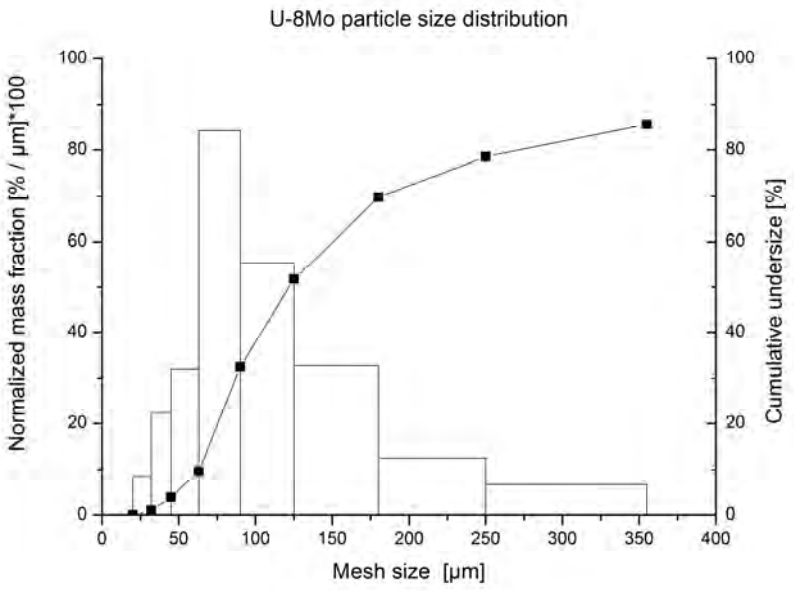


Figure 8 – Normalized mass fraction (bars) in each size class and cumulative undersize (sigmoidal curve) of the atomized U-8Mo powder in each size class. The latter results from sequently adding up the mass fractions of each size class and allows for the determination of the powder fraction below a certain diameter, or between any two diameters.

Sieve analysis assumes regular and spherical particles [7], though, which is not the case for the presented powder batch (Figure 6a). In fact, the measured characteristic diameters are roughly the smallest dimension of the particles, when assuming spherical or elongated particles of fairly constant and circular cross sections [7]. As a consequence, the presented particle size distribution does not show 'true' characteristic parameters.

5. Conclusion

The FRM II / CERCA atomizer project has succeeded in producing its first batch of atomized U-8Mo powder from an in-house cast electrode – using the internally designed and constructed REP atomizer and the recently implemented induction furnace, respectively. Furthermore, the project was conducted both in the defined schedule and within the budget while thoroughly considering safety aspects, process quality, and future industrialisation.

Associated with these project milestones were the successful 'hot' commissioning of a dedicated uranium laboratory, two custom glove boxes, an induction furnace, and the atomizer after all nuclear operating licences for the UMo production facility were granted.

Powder screening and analysis of the first atomized U-8Mo batch shows encouraging powder properties in terms of particle dimensions, surface morphology, oxidation, internal porosity, alloy composition, and microstructure. Particle shape is considered a matter of parameter set, that is, spherical particles may be produced by pursuing the direct droplet formation regime.

Consequently, atomizer parameterisation, process optimisation, and U-8Mo powder characterisation will be the next project steps, eventually leading to fuel irradiation tests. Beyond that, the gathered know-how will provide a substantial basis for the down selection process of a convenient atomization principle with regard to process industrialisation within the HERACLES program.

6. Acknowledgement

The authors would like to acknowledge the effort of AREVA, FRM II and TUM staff. INL provided know-how to the melting and casting process development presented in this work. SEM and X-ray image interpretation was assisted by CSM.
This project is supported by a combined grant (FRM0911) from the Bundesministerium für Bildung und Forschung (BMBF) and the Bayerisches Staatsministerium für Wissenschaft, Forschung und Kunst (StMWFK) as well as the cooperation agreement TUM-CERCA CJ/12.093.

7. References

[1] E. B. Ripley: *"Melting and Casting of Uranium"*, in J. S. Morrell et al. *"Uranium Processing and Properties"*, Springer, New York, (2013)

[2] E. J. Davies: *"Conduction and Induction Heating"*, IEE Power Engineering Series 11, Peter Peregrinus Ltd., London, (1990)

[3] J. J. Burke: *"Physical Metallurgy of Uranium Alloys"*, Proceedings of the 3rd Army Materials Technology Conference, First Edition, Brookhill Pub. Co., Chestnut Hill, (1976)

[4] W. D. Wilkinson: *"Uranium Metallurgy, Vol.1: Uranium Process Metallurgy"*, Interscience Publishers, New York, London, (1962)

[5] R. Schenk, W. Petry, B. Stepnik, C. Jarousse, G. Bourdat, C. Moyroud, M. Grasse: *"FRM II / CERCA UMo Atomizer Project Status"*, Proceedings of the RRFM 2013, St. Petersburg, (2013)

[6] A. Lawley: "*Atomization – The Production of Metal Powders",* Monographs in P/M Series No. 1, Metal Powder Industries Federation, Princeton, New Jersey, (1992)

[7] A. J. Yule, J. J. Dunkley: "*Atomization of Melts for Powder Production and Spray Deposition"*, Oxford Series on Advanced Manufacturing 11, Clarendon Press, Oxford, (1994)

[8] A. H. Lefebvre: "*Atomization and Sprays"*, Combustion: An International Series, Hemisphere Publishing Corp., (1989)

[9] C. R. Clark, B. R. Muntifering, J. F. Jue: *"Production and Characterization of Atomized U-Mo Powder by the Rotating Electrode Process"*, RERTR-2007 International Meeting on Reduced Enrichment for Research and Test Reactors, Prague, (2007)

RRFM 2014
EUROPEAN RESEARCH REACTOR CONFERENCE

30 March – 3 April 2014
Ljubljana, Slovenia

Y-12 NATIONAL SECURITY COMPLEX COUPON FABRICATION

Amy DeMint
Development Technologies
Y-12 National Security Complex
Oak Ridge, TN 37831 USA

Mike Gambrell
Uranium Metalworking Process Engineering
Y-12 National Security Complex
Oak Ridge, TN 37831 USA

Jack Gooch
Development Technologies
Y-12 National Security Complex
Oak Ridge, TN 37831 USA

Cary Langham
Uranium Metalworking Process Engineering
Y-12 National Security Complex
Oak Ridge, TN 37831 USA

Hollie A. Longmire
Nuclear Material Applications
Y-12 National Security Complex
Oak Ridge, TN 37831 USA

Alan Moore
Uranium Metalworking Process Engineering
Y-12 National Security Complex
Oak Ridge, TN 37831 USA

ABSTRACT

Y-12 National Security Complex (Y-12 NSC) participates in the Fuel Fabrication Capability (FFC) pillar of the U.S. Department of Energy's (DOE) National Nuclear Security Administration (NNSA) Global Threat Reduction Initiative (GTRI) Convert Pillar system. Y-12 NSC is primarily responsible for the establishment of a coupon fabrication process for the low-enriched uranium-molybdenum (LEU-Mo) fuel currently under development. This presentation will focus on LEU-Mo campaigns performed at Y-12 NSC. These campaigns utilized a depleted uranium-molybdenum (DU-Mo) master alloy and introduced a multi-plate mold in a production atmosphere.

DISCLAIMER

This work of authorship and those incorporated herein were prepared by Contractor as accounts of work sponsored by an agency of the United States Government. Neither the United States Government nor any agency thereof, nor Contractor, nor any of their employees, makes any warranty, express or implied, or assumes any legal liability or responsibility for the accuracy, completeness, use made, or usefulness of any information, apparatus, product, or process disclosed, or represents that its use would not infringe privately owned rights. Reference herein to any specific commercial product, process, or service by trade name, trademark, manufacturer, or otherwise, does not necessarily constitute or imply its endorsement, recommendation, or favoring by the United States Government or any agency or Contractor thereof. The views and opinions of authors expressed herein do not necessarily state or reflect those of the United States Government or any agency or Contractor thereof.

COPYRIGHT NOTICE

This document has been authored by a contractor/subcontractor of the U.S. Government under contract DE-AC05-00OR-22800. Accordingly, the U.S. Government retains a paid-up, nonexclusive, irrevocable, worldwide license to publish or reproduce the published form of this contribution, prepare derivative works, distribute copies to the public, and perform publicly and display publicly, or allow others to do so, for U. S. Government purposes.

1. Introduction

The Reduced Enrichment for Research and Test Reactors (RERTR) Program was initiated by the U.S. Department of Energy (DOE) to develop the technical means for the conversion of high powered research reactors (HPRRs) from HEU to LEU. The RERTR program cooperates with the research reactor community to achieve this goal of HEU to LEU conversion while maintaining reactor reliability and performance. The Y-12 National Security Complex (Y-12) is a participant in the NNSA NA-21 Convert Program, also known as RERTR, by performing development activities, supporting low enriched uranium (LEU)-molybdenum (Mo) research, and performing production activities in casting and machining.

The LEU-Mo reference baseline casting process is a two-step process, as depicted in *Figure 1:* First, highly enriched uranium (HEU) is blended with a diluent and molybdenum in an initial cylindrical casting. The cylindrical casting is sampled. Based on the results, the feed is adjusted and recast or the alloy is then broken and recast into a single plate form. The LEU-Mo coupons are fabricated from the plate casting. This process has a large molybdenum distribution range, typically from 8% to 12%, resulting in a higher than desired reject rate. One theory is that the initial casting step has too many process variables in a one unit operation to provide a repeatable and predictable casting. Y-12 is experimenting with LEU-Mo casting using a pre-alloyed diluent feedstock, labeled as UMoF, and a multi-plate casting form, as depicted in *Figure 2: Alternate Casting Process*.

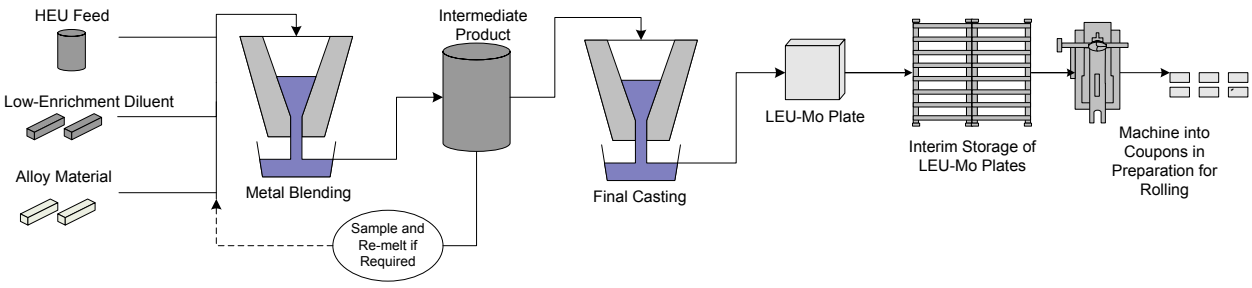


Figure 1: Baseline Coupon Fabrication Concept

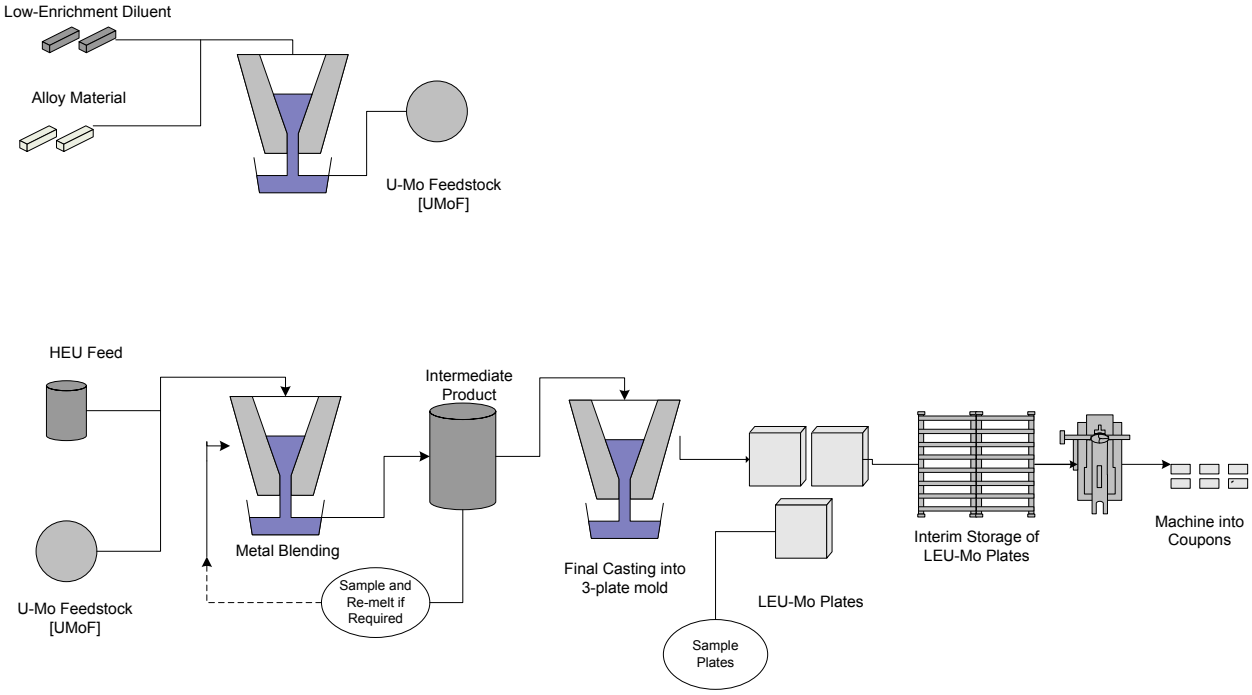
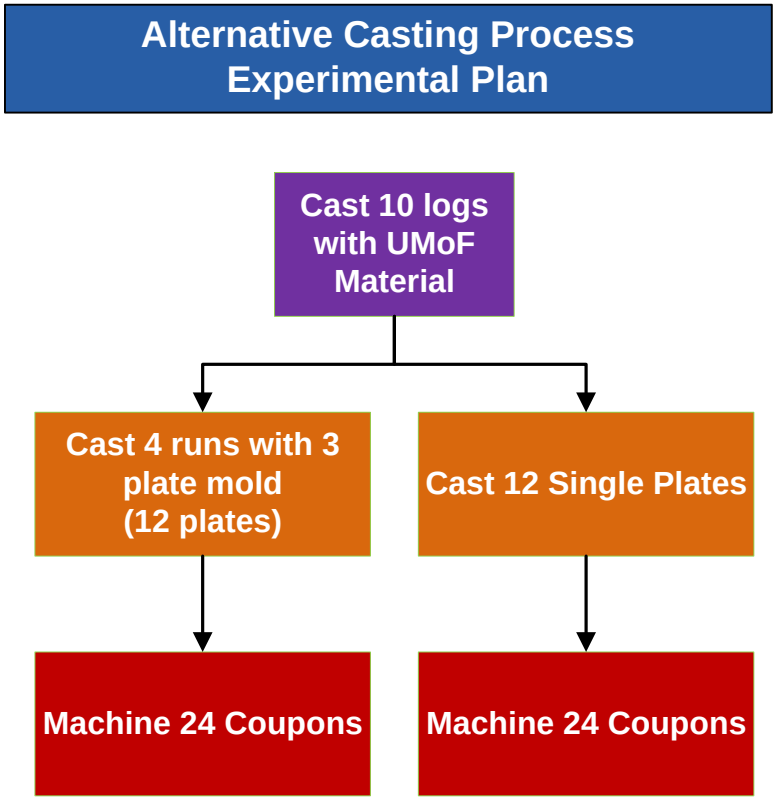


Figure 2: Alternate Casting Process

A small trial of the alternate casting process indicated there was a greater control of process parameters by pre-alloying the diluent. The alternate process also indicated that the molybdenum (Mo) and uranium-235 (U235) distribution throughout the casting were more uniform. In response to these findings, the Fuel Fabrication Capability developed an experimental plan to fabricate coupons with the alternate process, using both a single plate form and a multi-plate form. The intent is that the coupons will be fully characterized and then sent to the final fabricator for fuel fabrication. Then, data from the foil fabrication process could be used to provide feedback on the front end process.

2. Description of Experimental Plan

As part of the trial campaign, Y-12 fabricated LEU-Mo coupons and plans to ship the coupons to the foil fabricator as shown in *Figure 3: Alternative Casting Process Experimental Plan*. The plan was split into two batches, a single plate casting and a multi-plate casting. The plan assumed that each log would yield 2.5 plates; therefore, five logs were required for plate batch. From the five logs cast, twelve plates will be cast using the single plate mold and twelve plates will be cast using the three plate mold (i.e. 4 cast runs). This experimental plan assumed that there was no attrition for cast surface defects. The intent was to allow the final fabricator to process all of the coupons and provide feedback to determine the true defects of coupons that lead to foil failures during the fabrication process. Furthermore, the intent was to explore the use of the multi-plate form, with the understanding this will be the first introduction of the form and optimization may be needed.



Assumptions:

- 2 coupons per plate
- 2.5 plates per log
- Compare single plate to 3 plate mold
- Assumes less than 10% attrition, to account for a total failure
- No attrition for cast surface defects

Figure 3: Alternative Casting Process Experimental Plan

3. Progress of Experimental Plan

Y-12 completed the experiment described in *Figure 3: Alternative Casting Process Experimental Plan.*Y-12 utilized an arc melted UMoF feedstock as the pre-alloyed diluent. The UMoF had a rejected rate of approximately two percent.

For the single plate castings, there were no losses due to mis-pours. Therefore, twelve plants and twenty-four coupons were fabricated as planned. Samples were taken on the milled plate, which is representative of the coupon. Samples were taken at the top, middle and bottom of each plate. The chemical analyses were compared to targets. For molybdenum, the target was 10%±1%. For Uranium 235, the target was 19.75%±0.2%. The results are shown in *Figure 4: Molybdenum Distribution in Milled Single Plate Castings, Figure 5: Uranium 235 Distribution in Milled Single Plate Castings* and *Figure 6: Carbon Distribution in Milled Single Plate Castings*

.

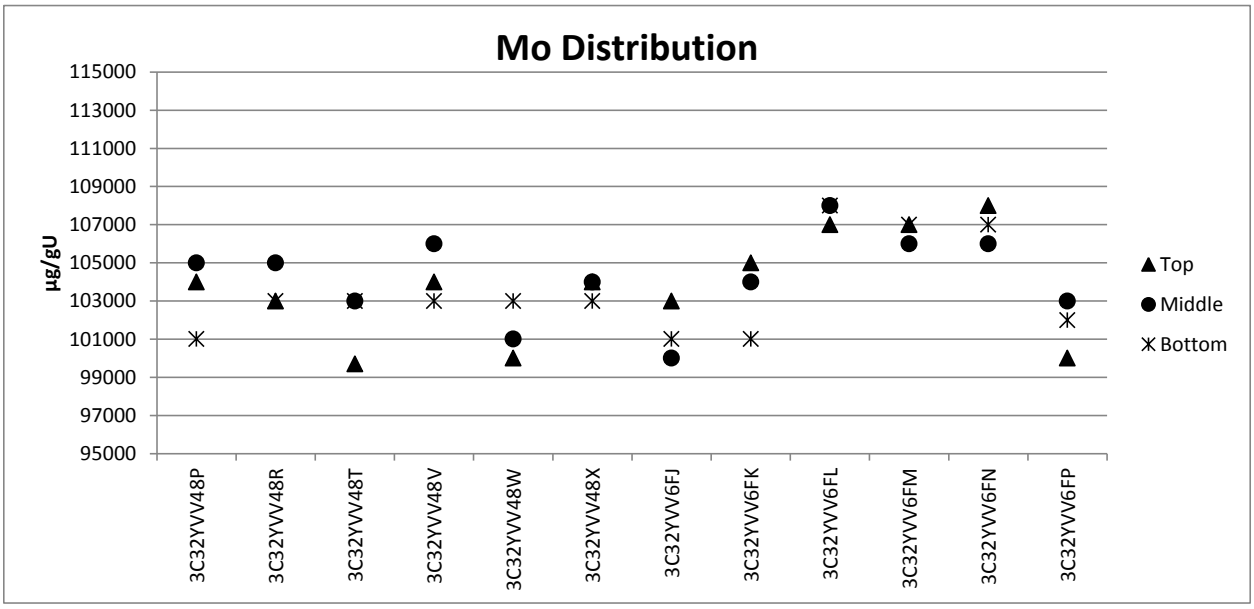


Figure 4: Molybdenum Distribution in Milled Single Plate Castings

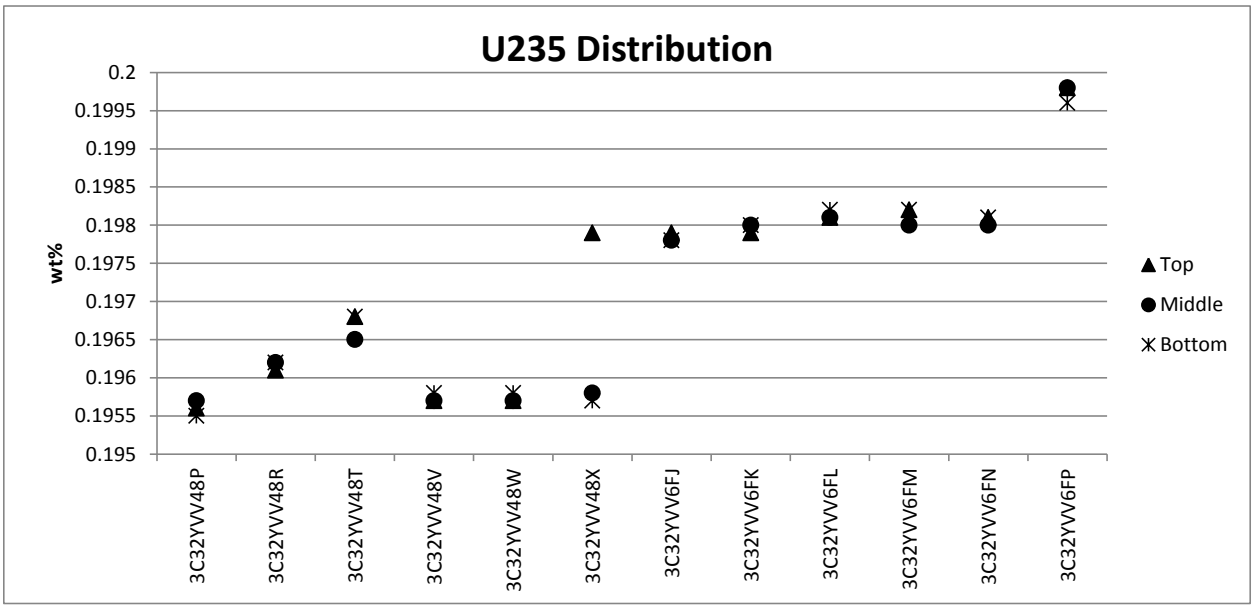


Figure 5: Uranium 235 Distribution in Milled Single Plate Castings

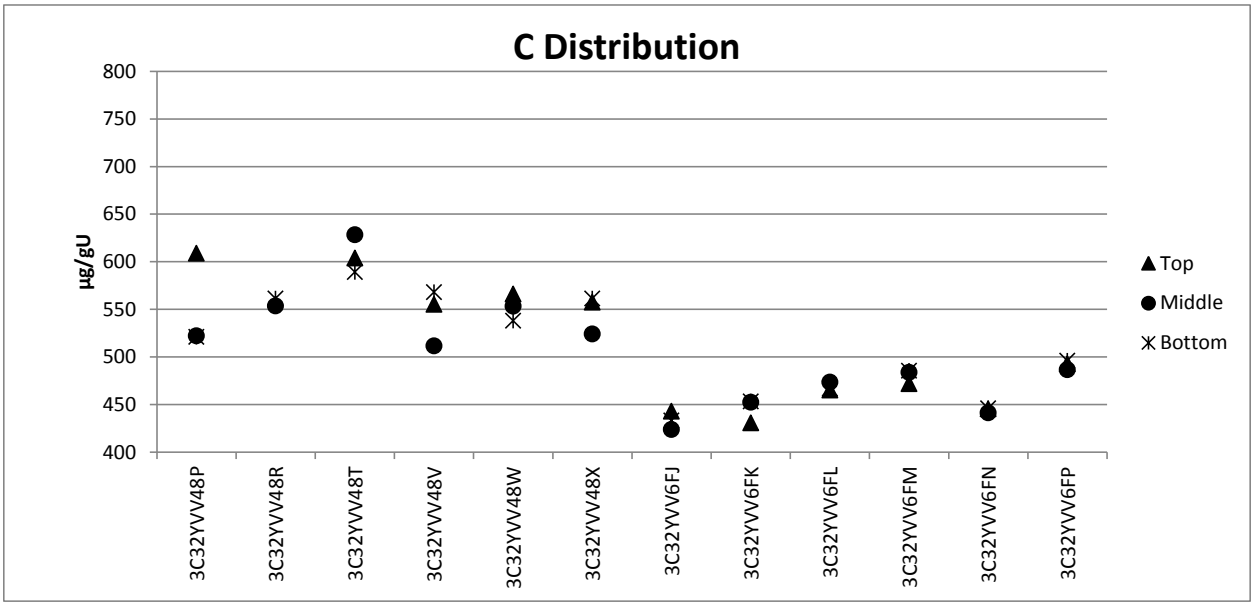


Figure 6: Carbon Distribution in Milled Single Plate Castings

Based on the data*, Figure 4* indicates that the Mo distribution range is smaller with the arc melted UMoF than with the previous process. Similarly, *Figure 5* indicates the U235 distribution is more precise than the previous process. There is one sample, 3D32YVV6FP, which indicates the U235 content is slightly above the desired target. Additional investigation is needed to determine the root cause of the results (i.e. log feed analysis). Another significant difference between the alternate casting process and the baseline reference process is the carbon levels. During the two step casting process previously used, carbon levels in the log casting would range from 500 to upwards of 800 ppm. *Figure 6: Carbon Distribution in Milled Single Plate Castings* indicates that carbon levels are lower than previously seen.

For the multi-plate castings, there were losses due to mis-pours. Therefore, seventeen of twenty-four coupons were fabricated. The new mold did not perform as intended fifty percent of the time, which resulted in short pours on the inner plates, which, in turn, resulted in fewer coupons. A design review of the mold indicated that tighter tolerances were required. For this batch, samples were taken on the milled plate, which is representative of the coupon. Samples were taken at the top, middle and bottom of each plate. The results are shown in *Figure 7: Molybdenum Distribution in Milled Multi-Plate Casting, Figure 8: Uranium 235 Distribution in Milled Multi-Plate Casting* and *Figure 9: Carbon Distribution in Milled Multi-Plate Casting*

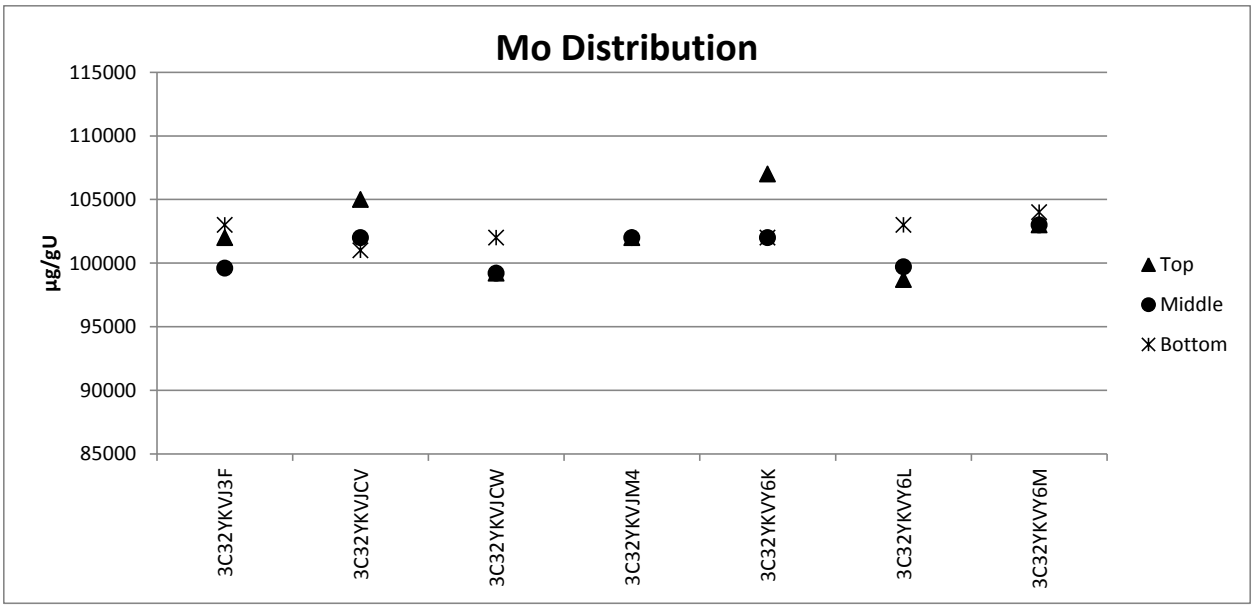


Figure 7: Molybdenum Distribution in Milled Multi-Plate Casting

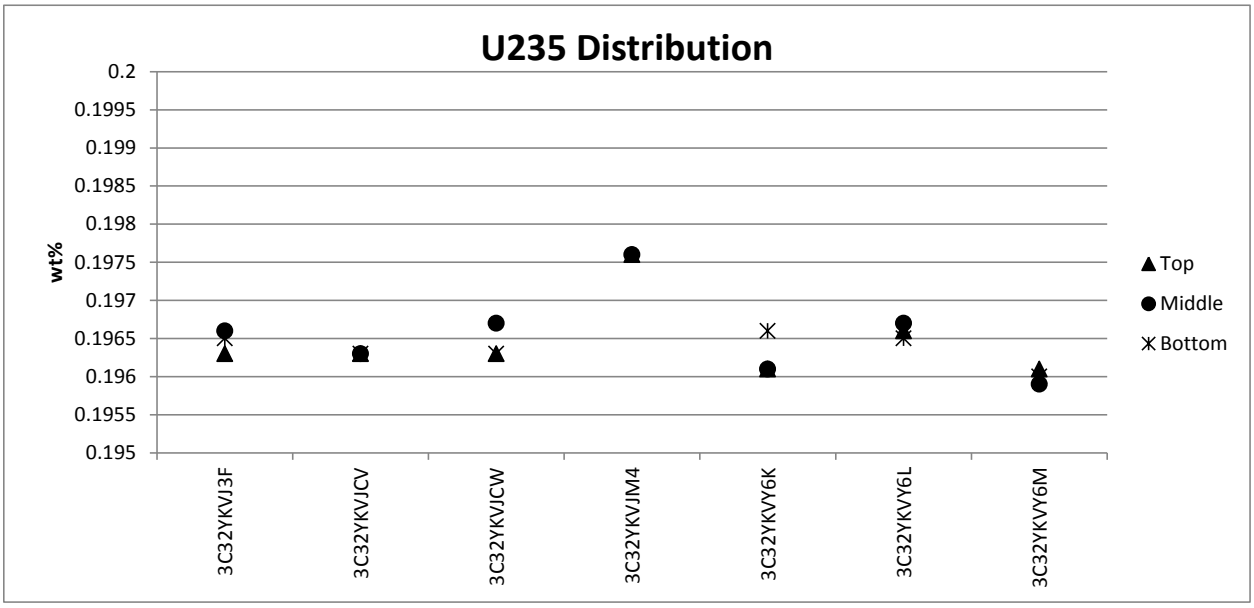


Figure 8: Uranium 235 Distribution in Milled Multi-Plate Casting

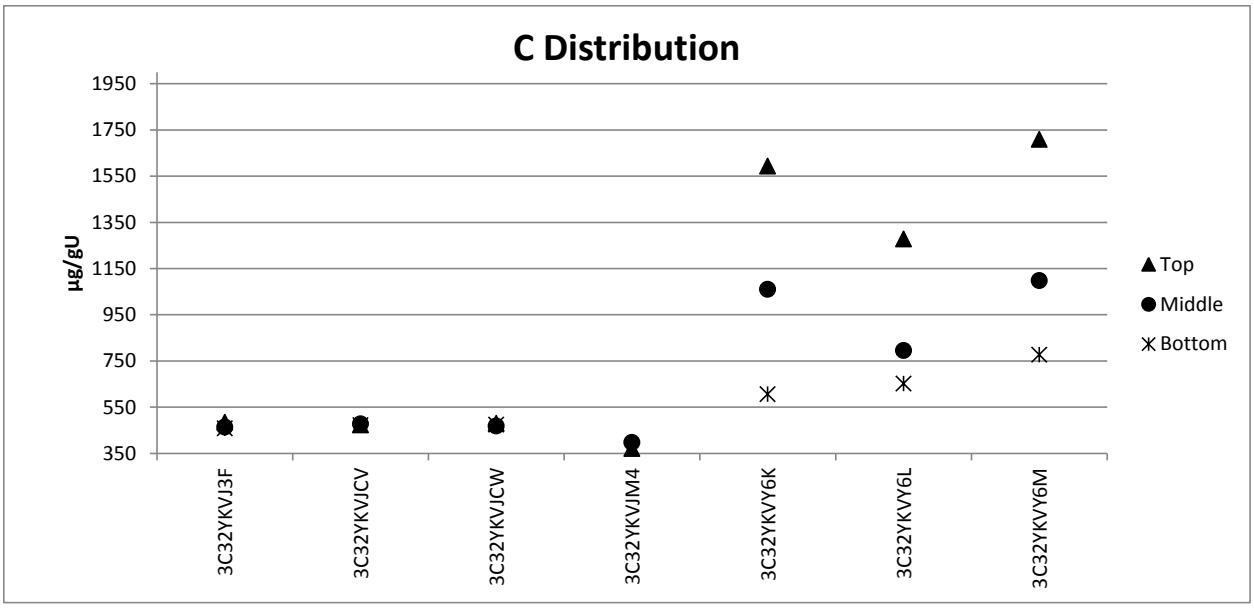


Figure 9: Carbon Distribution in Milled Multi-Plate Casting

As seen with the single plate casting data*, Figure 7* indicates that the Mo distribution range is smaller with the arc melted UMoF than with the previous process. Furthermore, *Figure 8* indicates the U235 distribution is more precise than the previous process, which was also noted with the single plate castings. Interestingly, *Figure 9* indicates the carbon distribution was initially less than 500 ppm and then there are three samples which indicate unusually large carbon distributions. Additional investigation is needed to determine the root cause of the results. Several factors can affect the carbon reading; material anomalies in casting, sampling, and quality of samples material. Samples are usually obtained through a drilling operation. If a drill bit starts to wear, carbon may be introduced into the samples. Furthermore, drilled samples are cleaned with an acetone prior to analyses. If the drilled sample contains small particles, the acetone may not completely evaporate prior to analysis, thus resulting in higher than normal carbon readings.

4. Summary

Y-12 fabricated LEU-Mo coupons using a pre-alloy diluent feedstock. The experimental plan also introduced a multi-plate mold. Based on the results, the pre-alloyed diluent allows for a tighter process control of material constituents. Furthermore, there are promising results on the reduction of carbon levels in the product. The multi-plate mold shows promising results to increase the throughput of material. Additional work is needed to become proficient on the mold use, but examining mold tolerances, material charges, etc.

INTERFACE FRACTURE CHARACTERIZATION USING BULGE TESTING OF MOCK LEU FUEL WITH A PLASMA SPRAYED DIFFUSION BARRIER LAYER

K. HOLLIS, C. LIU, R. LECKIE, M. LOVATO, D. Dombrowski
Materials Science and Technology Division, Los Alamos National Laboratory
P.O. Box 1663, Los Alamos, NM - USA

ABSTRACT

Bulge testing using a pressurized fluid to fracture the interface between bonded material layers along with three-dimensional digital image correlation to measure the sample distortion caused by pressurized fluid was applied to plasma sprayed coatings. The initiation fracture toughness associated with the bonded materials was measured during the testing. The bulge testing results of a uranium-molybdenum alloy plasma sprayed with zirconium and clad in aluminum are presented. The initiation fracture toughness was observed to increase with increasing cathodic arc cleaning current and the use of alternating polarity transferred arc current. This dependence was linked to the interface composition of oxide and mixed metal phases along with interface temperature during spray deposition.

1. Introduction

In support of the United States' nonproliferation and highly enriched uranium (HEU) minimization policies, the U.S. Department of Energy (DOE)/National Nuclear Security Administration's (NNSA) Global Threat Reduction Initiative (GTRI) is actively working to convert civilian research and test reactors from the use of HEU fuel to low enriched uranium (LEU) fuel. GTRI's Reactor Conversion program provides governments and facilities around the world with technical and economic assistance for conversion. If no suitable LEU fuels are available, the program contributes to the development of new LEU fuels. To date, GTRI has converted or verified the shutdown of 87 research reactors worldwide, including 20 domestic facilities. Of the remaining domestic research reactors, five U.S. high performance research reactors (USHPRRs) and one associated critical assembly will require a new high density LEU fuel and fabrication capability, which is currently under development, to convert. Existing qualified fuels do not meet the high fuel density requirements for the operation of these high-performance reactors, which include the Advanced Test Reactor (ATR) at Idaho National Laboratory, the High Flux Isotope Reactor (HFIR) at Oak Ridge National Laboratory, the University of Missouri Research Reactor (MURR), the Massachusetts Institute of Technology Reactor (MITR), and the Department of Commerce's National Bureau of Standards Reactor (NBSR). To maintain performance requirements, the Reactor Conversion program is developing a high-density monolithic plate fuel system which uses low enriched uranium 10wt% molybdenum (U10Mo) foils clad with aluminum [1].
A diffusion barrier between the 6061 Al layer and the U-Mo is needed to prevent reaction between these materials that could result in fuel swelling during reactor operation. Zirconium (Zr) is the currently preferred material for the barrier which is applied to both sides of the U-10Mo fuel [2,3]. Applying the Zr by plasma spraying is one possible manufacturing option. Characterization of the bonding between a plasma sprayed Zr coating and the U-Mo fuel on one side and between the Zr and the Al cladding layer on the other side are of significant interest for evaluating the plasma spraying technique for this application. The bonding at the U-Mo/Zr and the Zr/Al interfaces must be strong enough to allow the fuel to survive its irradiation cycle without delamination.
In order to investigate the bonding at the U-Mo/Zr and Zr/Al fuel interfaces, bulge testing is being evaluated at Los Alamos National Laboratory. Bulge testing uses the pressure of a

fluid to force separation between two bonded layers. The primary advantage of the bulge test for the present application is that it can simulate the scenario of fission gas accumulation in a reactor fuel and the propensity of the gas pressure to separate the layers of the fuel at either the U-Mo/Zr interface or the Zr/Al interface. Bulge testing also uses relatively simple equipment and does not require a load frame making implementation in a radioactive material handling area more feasible.
Although the first bulge-type testing reported was in 1961 [4], the use of bulge testing to characterize the bond between a thermal sprayed coating and substrate is a relatively new technique with only one known prior publication [5]. In this publication, substrate roughness, substrate temperature and spraying atmosphere (air or argon) were varied while plasma spraying a copper coating on an aluminum substrate. Bulge test results gave measured adhesion energy values of 30-75 J/m^2 [5].
The goal of this present study was to implement bulge testing for the reactor fuel plates described above. In particular, a determination of which interface (U-Mo/Zr or Zr/Al) was the stronger one and a measurement of the adhesion energy (also called initiation fracture toughness) of the weaker interface was the primary goal. In addition, understanding the variation in initiation fracture toughness with plasma spraying parameters was sought to guide future coating development work.

2. Experimental Procedure

2.1 Sample Preparation

The substrates used for this study were 19 mm x 95 mm x 0.35 mm depleted uranium alloy containing 10 weight percent molybdenum. The Zr powder was 99.2% minimum purity (ATI Wah Chang, Albany, OR, USA) with particle size range 50 μm to 5 μm. Prior to plasma spraying, the substrates were cleaned in a 50% nitric acid solution and a nitric/hydrofluoric acid solution was used for the desmut. The samples were hot air dried which resulted in the visible formation of an oxide layer before being loaded into the spray chamber.
Thin (40-70 μm) Zr coatings were deposited in a chamber filled with argon and maintained at 60 kPa. The oxygen level during deposition was approximately 100 ppm. An SG-100 plasma torch (Praxair/TAFA, Concord, NH, USA) operating at 850 A and 26 V with 40 standard liters per minute (slm) Ar, 18 slm He, 3 slm Ar powder carrier gas, powder flow rate of 5 g/min and a torch to substrate distance of 100 mm was used. Before, during and after deposition, a transferred arc (TA) between the torch face and the substrate was utilized for cathodic arc cleaning and substrate heating. The TA power supply produced direct current (DC) or alternating square-wave current (AC) at 100 Hz. TA cleaning and heating were performed for two torch passes without powder feed followed by eight torch passes with powder feed followed by two torch passes after the powder was turned off. Samples were produced for TA current of 0 A (sample No-TA), 30 A DC (sample 30ADC), 40 A DC (sample 40ADC) and 40 A AC (sample 40AAC).
Another method for applying Zr to the U-Mo is roll bonding where a thin foil of Zr is placed on each side of the U-Mo sheet then enclosed in a steel can to be rolled at elevated temperature [6]. One roll bonded sample (sample RB) was included in this investigation as a basis for comparison to the plasma sprayed coatings.
Following coating, the samples were layered between a top and bottom sheet of 6061 Al (sheet thickness 0.76 mm) and placed in a steel can. The can was evacuated and welded closed in the evacuated condition. The can and contents were hot isostatic press (HIP) bonded at 560°C and 103 MPa in Ar for a hold time of 4400 seconds at the peak temperature and pressure. The HIP operation compressed the can, bonded the Al sheets together around their edges and bonded the Al to the Zr coating on the top and bottom outside surfaces of the U-Mo samples.

2.2 Bulge Testing

The experimental setup for bulge testing is shown schematically in Fig. 1. The Al clad U-Mo/Zr sample was cut to a circular disk shape of 25 mm diameter by electro-discharge machining. A hole of 9.5 mm diameter was milled in the center of the disk through the Al to a depth near the interface between the Al and U-Mo. The Al layer on the side opposite the milled hole was ground down to be thinner than the U-Mo layer. The samples were then adhesively bonded to a stainless steel backing plate using Loctite E-214HP epoxy and cured at 120°C for 2 hours followed by a cure at 22°C for 4 hours. The adhesive has a typical tensile strength of 30.75 MPa according to the manufacturer. The sample and backing plate were inserted into the pressure cell where distilled water was injected into the cavity below the sample using a syringe pump. The sample surface was monitored by two CCD cameras arranged to allow stereoscopic imaging (Fig. 2) and 3D time evolved height mapping using a digital image correlation (DIC) calculation [7]. This 3D mapping allowed the measurement of the maximum bulge height (δ in Fig. 1). Simultaneous recording of the fluid pressure and bulge height occurred during the test. The pressure/bulge height curve is initially linear due to elastic deformation of the sample. As plastic deformation begins, the curve becomes non-linear and fluid pressure continues to increase until an abrupt change in bulge height occurs indicating a sudden separation between the layers in the sample.

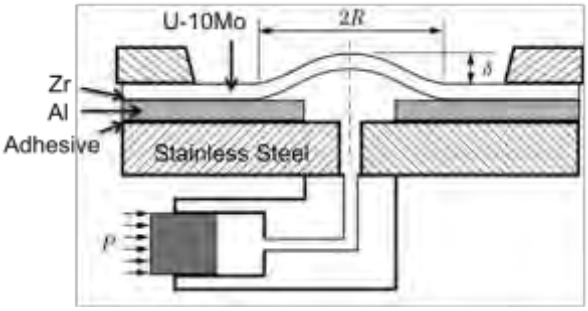


Fig 1. Cross-sectional schematic of bulge testing equipment configuration.

Classical Kirchhoff-Love plate theory [8] was used for interpreting the results of the bulge test even though plastic deformation of the samples occurred. At the test maximum pressure or critical pressure (P_{crit}), delamination along an interface occurred for every sample in an unstable and dynamic manner. The only energy available to cause delamination was the

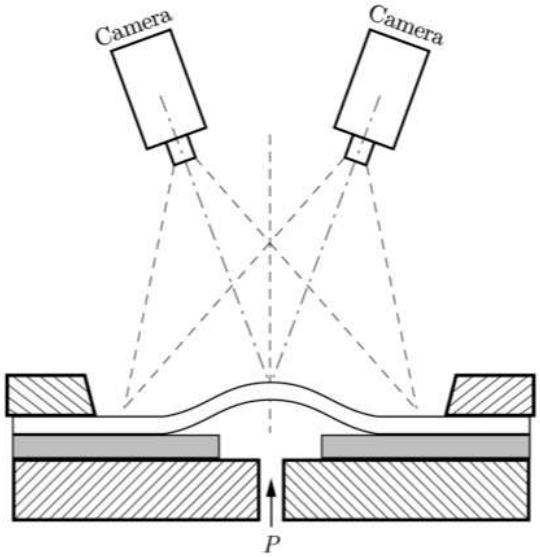


Fig 2. Bulge testing configuration showing the position of the CCD cameras with respect to the sample during testing.

stored elastic energy in the sample since the work done to generate plastic deformation was dissipated in the sample and was not recovered at fracture. The fluid pressure also did not contribute to the energy of fracture since the fluid pressure fell off rapidly in the fast

delamination event. The critical energy release at fracture, or the initiation fracture toughness (γ_{crit}), was related to the elastic stiffness of the deforming bulge (η) and the fluid pressure at the initiation of interface delamination (P_{crit}) according to Eq. 1 [9]:

$$\gamma_{crit} = P_{crit}^2 / 4\eta \qquad (1)$$

2.3 Sample Characterization

After bulge testing, the samples were cross sectioned, polished and examined using light optical microscopy (LOM) and a scanning electron microscope (SEM) (Inspect F, FEI Co., Hillsboro, OR, USA) equipped with an energy dispersive X-ray spectrometer (EDS) detector. Images were recorded in the back-scattered electron (BSE) mode and X-ray maps and spectra were recorded in order to identify the distribution of elements in the samples.

3. Results

An example of a bulge profile produced by the 3D-DIC calculation is shown in Fig. 3 for sample RB where δ is the bulge height and h is the bulging sample thickness. The bulge test plot of bulge height versus fluid pressure for all samples is shown in Fig. 4 with sample No-TA referenced to the scale on the right side of the figure and the other samples referenced to the scale on the left side of the figure. The maximum applied pressure (P_{crit}), the initial linear slope of the curve (η) and the fracture initiation toughness values (γ_{crit}) calculated using Eq. 1 are shown in Table 1. The P_{crit} and γ_{crit} values for sample No-TA are 1 and 2 orders of magnitude respectively lower than the other samples tested. A cross-section LOM image of sample 40ADC after testing is shown in Fig. 5. In this figure, the sample failed in the

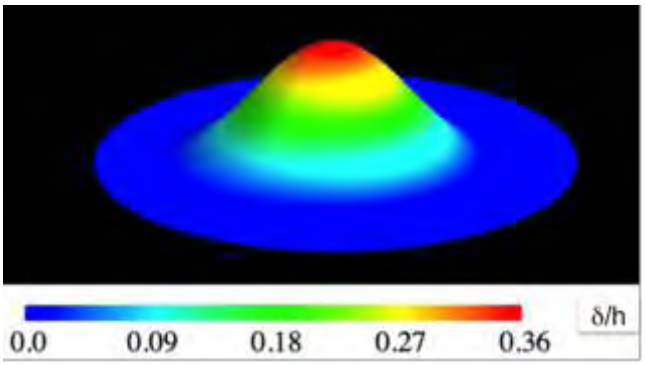


Fig 3. Bulge profile of sample RB during testing.

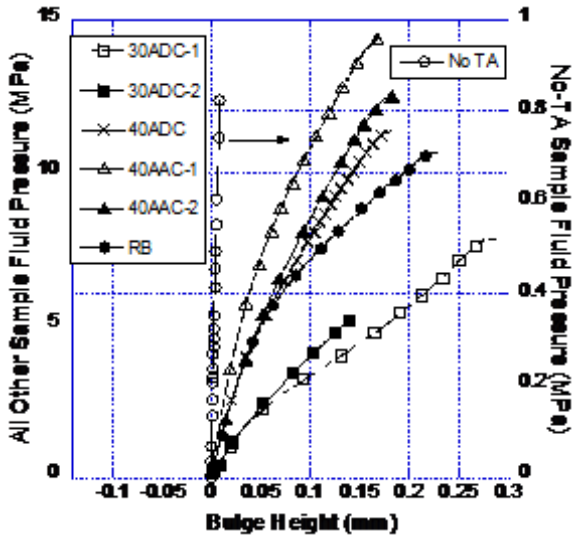


Fig 4. Bulge test experimental results for all samples.

Sample	η (MPa/mm)	P_{crit} (MPa)	γ_{crit} (J/m^2)
No-TA	104	0.8	1.6
30ADC-1	53	7.8	290
30ADC-2	49	5.2	134
40ADC	128	11.3	249
40AAC-1	176	14.4	296
40AAC-2	102	12.5	382
RB	118	10.6	240

Tab 1. Bulge testing results and calculated values.



Fig 5. LOM image of sample 40ADC after bulge testing showing delamination in the adhesive on the left side and between the U-Mo and Zr on the right side.

adhesive on the left side and between the Zr coating and the U-Mo substrate on the right side. Other tested samples failed either at the adhesive or between sample metallic layers appearing similar to either the left or right side of Fig. 5.

4. Discussion

4.1 Sample No-TA

The fracture surfaces of sample No-TA after bulge testing are shown in Fig. 6. The elemental distribution of the surfaces was investigated using SEM-EDS. There is a continuous uranium oxide layer of approximate thickness 2 μm attached to the U-Mo side of the fracture. The fracture is within the uranium oxide and between the uranium oxide and Zr coating with some uranium and uranium oxide attached to the Zr side of the fracture. No Zr was observed on the U-Mo side of the fracture. The low value for γ_{crit} is due to the weak and brittle nature of the oxide and the bond between the oxide and the Zr coating. The lack of TA cleaning has allowed the native oxide on the U-Mo alloy to remain in place during the Zr coating process. Regions of mixing between the Zr and the U-Mo are not observed in this sample.

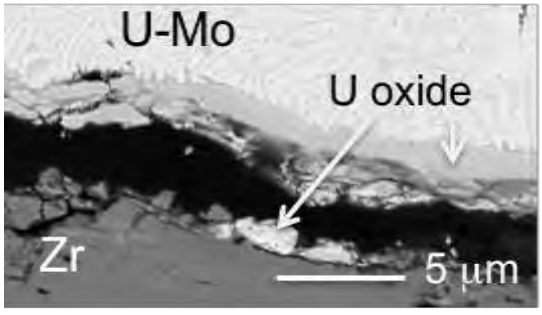


Fig 6. SEM-BSE image of the fracture surfaces of sample No-TA.

4.2 Samples 30ADC-1 and 30ADC-2

For samples 30ADC-1 and 30ADC-2, the U-Mo was thinned about 1/3 of its total thickness in the hole milling operation. This caused the stiffness of the bulge test samples (η) to drop

compared to the other samples with full thickness of the U-Mo. The P_{crit} value and γ_{crit} are much higher than for the No-TA sample. The fracture interfaces are shown in Fig. 7. There is not a continuous uranium oxide layer present as there was with sample No-TA. However, small, isolated uranium oxide regions are still present. Uranium is detected on the Zr side of the interface and Zr is detected on the U-Mo side of the interface. The fracture is within a region containing U-Mo and Zr intermixed with each other along with some uranium oxide. The reason for the difference in P_{crit} and γ_{crit} between 30ADC-1 and 30ADC-2 is not known and may represent the stochastic nature of the strength of the bond between the Zr and the U-Mo.

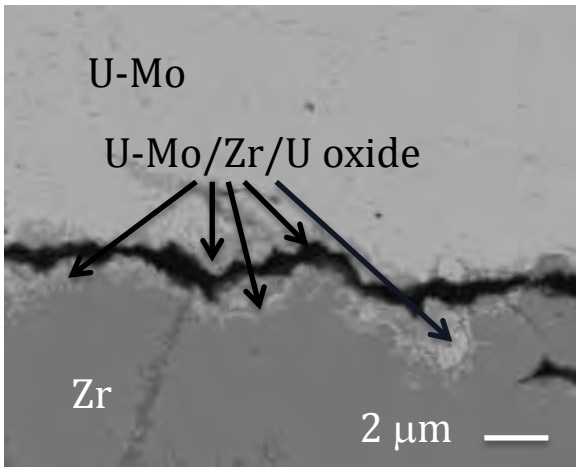


Fig 7. SEM-BSE image of the fracture surfaces of sample 30ADC-1.

4.3 Sample 40ADC

For sample 40ADC, the fracture was in the adhesive on one side of the sample and at the Zr/U-Mo interface on the other side of the sample as was shown in Fig. 5. A very small amount of uranium oxide is detected at the interface. The crack runs through a zone of mixed Zr and U-Mo with Zr and U detected on both sides of the crack. In some isolated areas, the fracture passes through the Zr coating up to 10 μm away from the interface. Fig. 8 shows the crack tip in the center of the image. At the left side, the crack has propagated through the Zr coating and at the center the crack has propagated through the Zr/U-Mo mixture region.

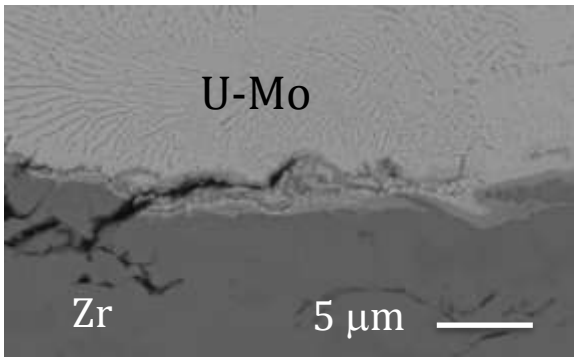


Fig 8. SEM-BSE image of the crack tip of sample 40ADC.

4.4 Samples 40AAC-1 and 40AAC-2

Sample 40AAC-1 is stiffer than sample 40AAC-2 as measured by the η values shown in Table 1. For 40AAC-1, the Al on top (opposite the pressurized fluid) is slightly thicker and the U-Mo sheet length is slightly shorter than for 40AAC-2 leading to the change in stiffness.

Sample 40AAC-1 failed at a higher pressure than sample 40AAC-2 but sample 40AAC-2 failed partly in the adhesive while sample 40AAC-1 failed along the Zr/U-Mo interface. This demonstrates variability in the adhesive failure strength. Fracture is in the adhesive or in the Zr/U-Mo mixture zone where a small amount of isolated uranium oxide is detected. Occasional fracture through the Zr coating is observed similar to sample 40ADC. The fracture surfaces of sample 40AAC-2 are shown in Fig. 9 and are qualitatively very similar to those of sample 40ADC with Zr and U detected on both sides of the fracture.

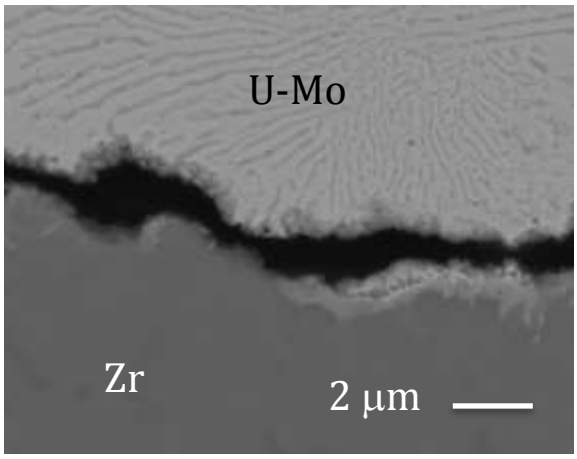


Fig 9. SEM-BSE image of the fracture surfaces of sample 40AAC-2.

4.5 Sample RB

The roll bonded sample (RB) failed in the adhesive on both sides of the fluid hole as is shown in Fig. 10. However, the pressure at failure was lower than for samples 40ADC, 40AAC-1 and 40AAC-2 again demonstrating the variability in adhesive strength. Since the failure was entirely within the adhesive, the γ_{crit} value of 240 J/m^2 represents a lower bound for roll bonding. In addition, it was not determined if the U-Mo/Zr or the Zr/Al bond was the weaker one for roll bonding. A stronger adhesive is needed to determine the initiation fracture toughness of the bonds in the roll bonded sample.



Fig 10. LOM image of sample RB after bulge testing showing delamination in the adhesive layer on both sides of the sample.

4.6 Sample Comparison

There is a clear decrease in adhesion for sample which was not TA cleaned (sample No-TA) compared to the other samples in this study. When the continuous oxide layer is removed as it is for the other plasma sprayed samples, the P_{crit} and γ_{crit} values increases significantly. This cleaning and adhesion behavior is consistent with other results [10-12] and is a significant advantage of plasma spraying using TA cleaning. The γ_{crit} values from Ref. 5 for plasma sprayed Cu on Al are between 30 and 75 J/m^2. The same samples in Ref. 5 were tested using EN 582 (similar to ASTM C633) with tensile adhesion strengths of 25-48 MPa. Compared to these Cu on Al samples, the No-TA sample bond is weaker while the other Zr/U-Mo samples are stronger. The mixed Zr/U-Mo region at the interface between coating and substrate for TA cleaned samples show that a diffusion bond has formed due to the removal of the continuous oxide layer and sufficient temperature at the interface for diffusion.

The much higher γ_{crit} value of this diffusion bond compared to the mechanical bond of the No-TA sample show the importance of oxide removal for strong bonding to U-Mo alloys.
It is unexpected that the No-TA sample showed a much lower γ_{crit} than the plasma sprayed samples from Ref. 5. The hole milling process for bulge test sample preparation could have damaged the brittle Zr/U-Mo bond in sample No-TA. Arrgoni et al. [5] milled the hole part way into the sample then chemically etched the remainder of the material rather than milling all the way to the interface. This is a more gentle process and is less likely to damage the bond at the interface resulting in a better estimation of the undisturbed bond strength. Therefore, the low P_{crit} and γ_{crit} values measured for the No-TA sample were lower bounds and may not accurately represent the undisturbed interface strength.
Among the TA cleaned samples, there was an increase in P_{crit} in the order 30ADC < 40ADC < 40AAC. The γ_{crit} averaged values for all samples produced under the sample conditions followed the same trend. However, some sample γ_{crit} values overlapped with samples produced under different conditions (non-monotonic trend). From this analysis, it appears that higher TA current levels and the use of AC current enhance bonding between the coating and substrate. The removal of oxide from the substrate has clearly been demonstrated for both DC and AC TA. During AC TA cleaning, there is cathodic arc cleaning of the substrate during the electrode positive (substrate negative) portion of the cycle along with efficient heating of the substrate during the electrode negative portion of the cycle. The added heating efficiency of the electrode negative portion of the cycle for AC TA likely caused the interface temperature to rise above that of the DC TA sample at the same current. Therefore, the effect of surface cleanliness and surface temperature during the initial coating pass are both responsible for the nature of the bond and the strength of the interface.
All samples failed at or near the Zr/U-Mo interface (except for adhesive failures). The Zr/Al interface showed no signs of cracks or delamination. Therefore, efforts to improve the adhesion strength of the plasma sprayed Zr fuel, if needed, should be focused on the Zr/U-Mo interface.

5. Conclusions

- All plasma sprayed samples failed at the U-Mo/Zr interface rather than the Zr/Al HIP bonded interface.

- Bulge test results show a significant increase in both failure pressure (P_{crit}) and initiation fracture toughness (γ_{crit}) values when using transferred arc (TA) cleaning prior to plasma spray deposition compared to not using TA cleaning.

-Increasing TA direct current (DC) from 30 A to 40 A resulted in higher P_{crit} and γ_{crit} values.

- Alternating current (AC) TA resulted in higher P_{crit} and γ_{crit} than DC for the same 40 A TA current level.

-The γ_{crit} values for Zr coatings on U-Mo are both much lower (sample No-TA) and much higher (all other samples) than those reported by Arrigoni et al. [5] for Cu plasma sprayed coatings on an Al substrate.

6. References

[1] http://nnsa.energy.gov/aboutus/ourprograms/ dnn/gtri/convert.
[2] Wachs, D., C. Clark, R. Dunavant: Conceptual Process Description for the Manufacture of Low-Enriched Uranium-Molybdenum Fuel. Idaho National Laboratory report INL/EXT-08-13840 (Feb. 2008).
[3] Hollis, K.: Zirconium Diffusion Barrier Coatings for Uranium Fuel used in Nuclear Reactors. Advanced Materials and Processes 168 (2010), Issue 11, pp. 57/9.

[4] Dannenberg, H.: Measurement of Adhesion by a Blister Method. Journal of Applied Polymer Science 5 (1961), pp. 125/34.
[5] Arrigoni, M., S. Barradas, M. Braccini, M. Dupeux, M. Jeandin, M. Boustie, C. Bolis, L. Berthe: A Comparative Study of Three Adhesion Tests (EN 582, Similar to ASTM C633, LASAT (Laser Adhesion Test), and Bulge and Blister Test) Performed on Plasma Sprayed Copper Deposited on Aluminum 2017 Substrates. Journal of Adhesion Science and Technology 20 (2006), Issue 5, pp. 471/87.
[6] Hollis, K., N. Mara, R. Field, T. Wynn, J. Crapps, P. Dickerson: Characterization of Plasma Sprayed Zirconium on Uranium Alloy by Microcantilever Testing. Journal of Thermal Spray Technology, 22 (March 2013), Issue 2-3, pp. 233/41.
[7] Liu, C., : The study of the Decohesion of Bimaterial Interfaces Using Miniature Bulge Test & 3D-DIC. Los Alamos National Laboratory Report, LA-UR-12-26131 (2012).
[8] Love, A.: A Treatise on the Mathematical Theory of Elasticity. Fourth edition (1927), Cambridge University Press.
[9] Liu, C., M. Lovato, K. Clarke, D. Alexander, W. Blumenthal: Miniature Bulge Test and Energy Release Rate in HIPed Aluminum/Aluminum Interfacial Fracture. Los Alamos National Laboratory Report LA-UR-14-20640 (2014).
[10] Castro, R., K. Hollis, C. Maggiore, A. Ayala, B. Bartram, R. Doerner: Negative Transferred Arc Cleaning: A method for roughening and Removing Surface Contamination from Beryllium and Other Metallic Surfaces. Fusion Technology 38 (2000), Issue 3, pp. 369/75.
[11] Davis, J., ed.: Handbook of Thermal Spray Technology. ASM International (2005), p. 70/2.
[12] Pawlowski, L.: The Science and Engineering of Thermal Spray Coatings. Wiley & Sons (1995), pp. 43/6.

7. Acknowledgements

The authors gratefully acknowledge Joel Montalvo for the metallographic preparation of the samples along with Beverly Aikin and Victor Vargas for the HIP cladding. The authors would like to acknowledge the financial support of the US Department of Energy Global Threat Reduction Initiative Reactor Convert program. Los Alamos National Laboratory, an affirmative action equal opportunity employer, is operated by Los Alamos National Security, LLC, for the National Nuclear Security Administration of the U.S. Department of Energy under contract DE-AC52-06NA25396.

PROGRESS IN OPTIMIZATION OF U-10Mo FUEL CASTING BY MODELING AND EXPERIMENT

R. M. AIKIN JR. AND D. DOMBROWSKI
Materials Science and Technology: Metallurgy, Los Alamos National Laboratory
P.O. Box 1663, Los Alamos, NM 87544

ABSTRACT

LEU U-10Mo fuel fabrication begins with a molten metal casting process which is feedstock for fuel foil fabrication by rolling. This work describes the experiments and modeling that have been performed on an initial plate shaped U-10%Mo casting design. The mold and casting cavity were instrumented with a number of thermocouples to determine the thermal history of the mold and casting. This information was then used to validate a process model of that casting. This validated model was then used to investigate process and mold geometry variations to develop a refined mold design and casting process parameters, with the goal of improving casting yield and minimizing casting defects such as porosity and Mo segregation. This refined design was then cast and the results are compared to the initial design.

1. Introduction

In support of the United States' nonproliferation and highly enriched uranium (HEU) minimization policies, the U.S. Department of Energy (DOE)/National Nuclear Security Administration's (NNSA) Global Threat Reduction Initiative (GTRI) is actively working to convert civilian research and test reactors from the use of HEU fuel to low enriched uranium (LEU) fuel. To maintain performance requirements, the Reactor Conversion program is developing a high density monolithic plate fuel system which uses low enriched uranium foils alloyed with 10wt% molybdenum and clad with aluminum.

The production of this low enriched U-10wt%Mo fuel begins with the vacuum induction melting (VIM) and casting of a rolling billet. For maximum efficiency it is important that the minimum amount of metal be used to produce the maximum sized casting. The cast metal billet should be free of porosity and have a uniform Mo concentration. This work discusses ongoing work to optimize the casting process of one potential cast billet geometry.

2. Initial Vertical Mold Design

2.1 Casting Procedure

The initial vertical mold design and process parameters were supplied by Y-12 [1]. This design is shown in Fig. 1. The mold stack is comprised of 4 parts: a bottom and top clamp, a left and right book mold body, and a crucible on top. The two halves of the book mold are together by the top and bottom mold clamps. The clamps also serve as a heat source on top and a chill on the bottom. The mold cavity is 18.4 cm tall by 13.0 cm wide by 2.5 cm thick. A standard 35 cm OD by 30 cm ID by 14 cm tall crucible is used. At Y-12 this crucible would be used with a knockout/rupture disk, but because of furnace differences, a stopper rod with 1.9 cm diameter pour hole was used at LANL.

The mold was machined from a log HLM grade graphite [2]. HLM is a medium-grain extruded graphite commonly used for molds and crucibles for the casting of uranium. To prevent chemical reaction between molten uranium and the graphite mold, those parts of the mold and crucible that come in contact with the molten uranium were coated with a yittrium-oxide mold coating [3]. This mold coating was applied with an automotive style paint sprayer and allowed to dry prior to mold assembly.

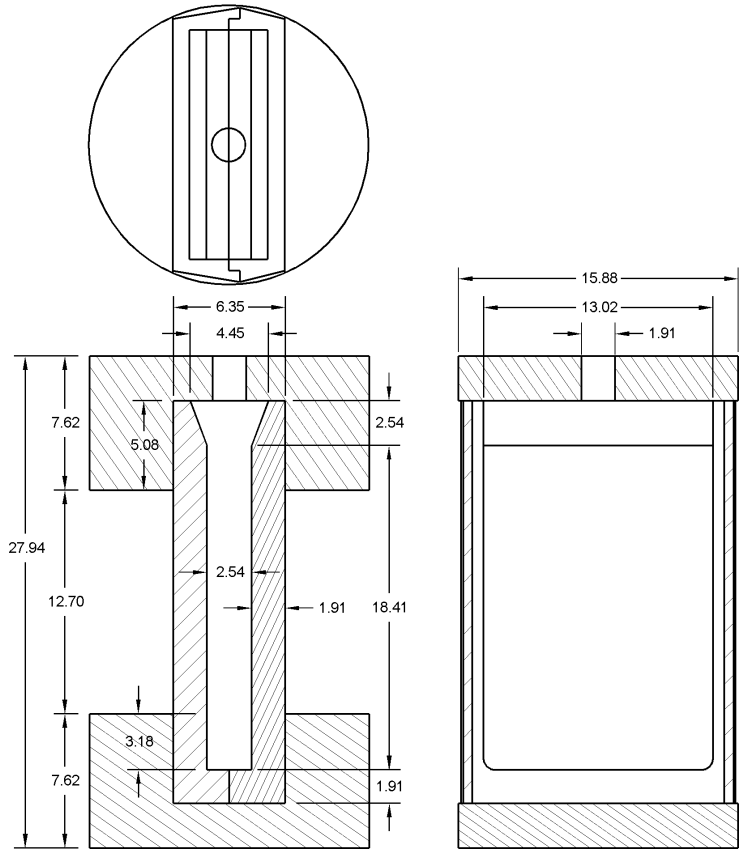


Fig. 1 Three views of the vertical mold design. Dimensions are in centimeters.

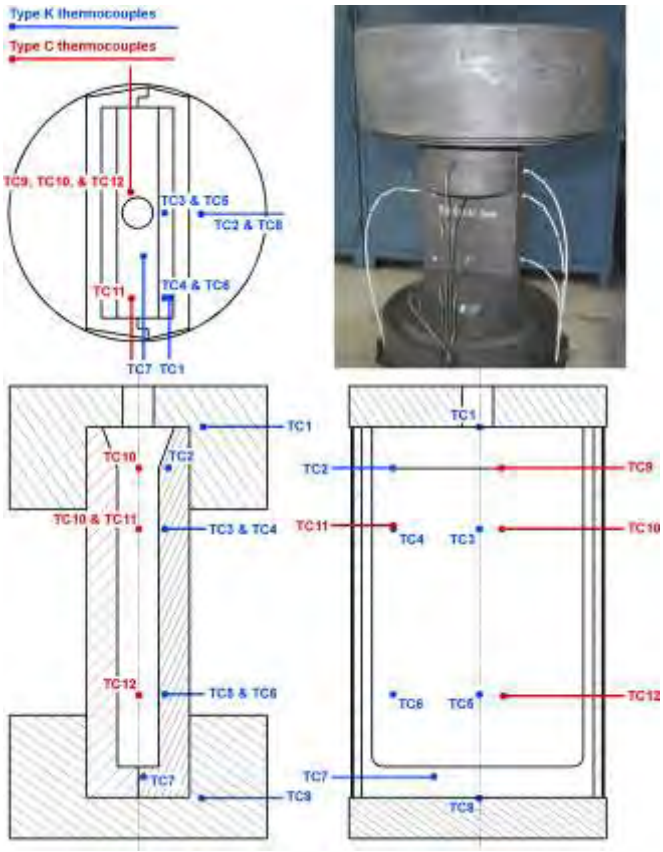


Fig. 2 Thermocouple positions in the vertical mold along with a photo of the mold stack prior to casting.

Stainless steel sheathed type-K thermocouples (chromel – alumel) were inserted into holes drilled in the graphite mold. Alumina sheathed type-C thermocouples (W-5%Re – W-26%Re) with a bare-bead tip were placed in the casting cavity and cemented in place. Locations of the thermocouples are shown in Fig. 2, along with a photo of this instrumented mold stack.

The crucible was charged 14.6 kg of U-10Mo buttons produced by non-consumable arc-melting. These buttons were approximately 2 kg each. The buttons were made from high purity depleted uranium plate with approximately 35 ppm carbon and 99.95% pure molybdenum. The metal was arc-melted in a copper tundish with a tungsten electrode. Each button was melted and flipped 3 times prior to charging into the VIM crucible.

The mold stack was placed in a vacuum induction furnace. The furnace has a single induction coil 46 cm in diameter by 91 cm long. Between the mold stack and induction coil is a 4 cm thick layer of refractory insulation. The mold stack was placed with the bottom of the stack at the same level as the bottom of the coil. The mold stack was supported by a 28 cm diameter graphite pedestal that was below the coil hot-zone; the mold and crucible were fully inside the hot-zone. The coil was powered by a 100kW / 3kHz solid-state power supply. Furnace vacuum was supplied by a blower backed by a rotary-vane vacuum pump.

2.2 Vertical Mold Design - 1400°C Pour Temperature

The initial casting strictly followed the Y-12 recommended processing procedure. Induction power of 60 kW was applied until the metal melted and the molten metal temperature reached 1400°C. The molten metal temperature was determined by a two-color pyrometer looking in though the furnace lid and aimed on the metal near the stopper rod. Once the metal reached 1400°C (43 minutes), power was reduced that the metal was held at 1400°C for an additional 10 minutes. The stopper rod was then removed and the molten metal allowed to flow into the mold cavity.

The liquidus of U-10Mo is 1230°C [4-5], thus the 1400°C pouring temperature represents 170°C of superheat above the liquidus. Figure 3 shows the temperature in the mold, as a function of position just prior to the removal of the stopper rod. It shows that with this heating procedure the top half of the mold was above the1230°C liquidus temperature at pour time. This combination hot mold and high superheat resulted in an extremely long solidification time, on order 10 minutes, in the top of the casting.

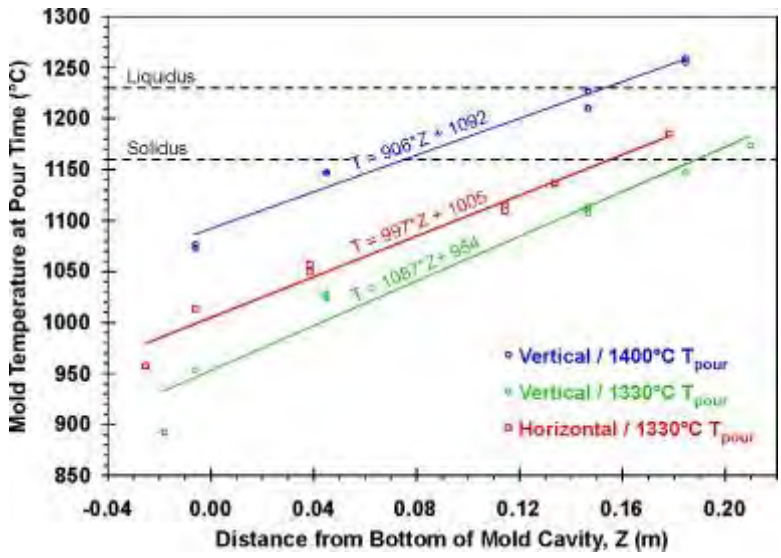


Fig. 3 Temperature as a function of position in the mold just prior to removal of the stopper rod showing initial thermal gradient in the mold for the 3 castings considered.

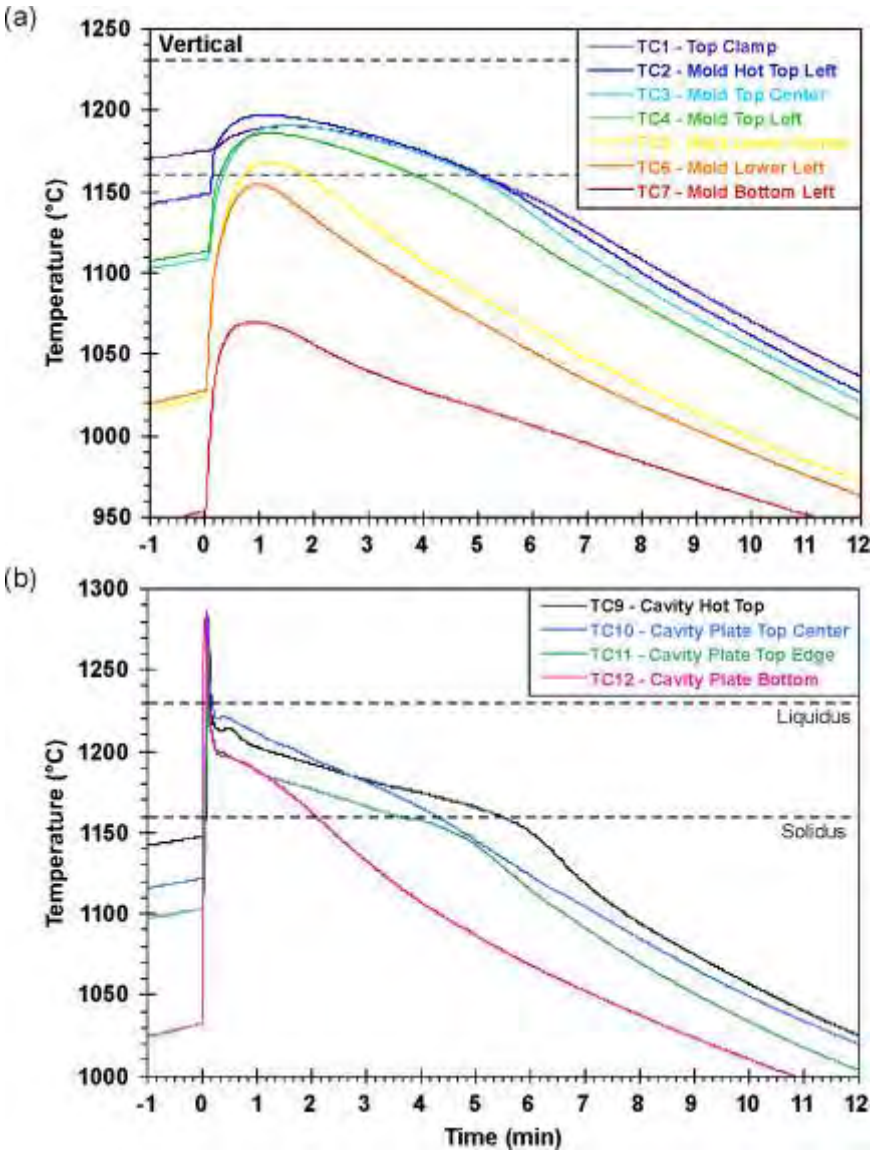


Fig. 4 Thermal history of vertical mold poured at 1330°C; (a) thermocouples in mold and (b) thermocouples in casting cavity.

2.3 Vertical Mold Design - 1330°C Pour Temperature

To reduce the solidification time, and reduce the likelihood of Mo segregation, the casting procedure was modified. The modified procedure used the same mold setup and initial furnace power setting, but the metal was heated to 1330°C (100°C superheat) and then held for 10 minutes prior to pouring.

The metal reached 1330°C in 31 minutes, was held at temperature for 10 minutes, and then the stopper rod was removed. Figure 3 shows the much lower mold temperature at pour time. Figure 4 shows the resulting cooling curves for the thermocouples in the mold and in the casting cavity. The resulting casting had a weight of 12.5 kg.

One major concern for the castings poured at both temperatures, is that (as shown in Fig. 4(b)) during the early part of solidification the hot top (TC9) was cooler than the top of the cast plate (TC10). As such, the hot top is unable to properly feed metal into the casting and this will result in castings porosity.

3. Process Modeling and Mold Redesign

To better understand the solidification behavior of the vertical mold, the process was simulated using the commercial computational fluid dynamics code Flow-3D [6]. FLOW-3D solves relevant time-dependent heat and fluid flow free-surface problems in three dimensions. The experimentally determined temperature of the mold at pour time was used as the initial conditions and the experimentally determined cooling curves were used to validate the code and parameters used. Only a portion of the results are presented here.

In Figure 5(a), the fraction solid as a function of time is shown for the vertical mold with 1330°C pour temperature. Simulation was done in quarter symmetry so that in this figure only a quarter of the billet is visible; we are looking at the two center-lines of the casting. The simulation shows a rapid removal of the super heat and a fraction solid of about 0.1 by 30 seconds. Solidification then advances from the sides and bottom, but leaves a deep region along the castings center-line (*e.g.* at 90 seconds). The chilling of the hot top is exacerbated by it's contact with the top clamp and subsequent heat removal.

Because of the 80°C difference between liquidus (approximately 1230°C) and solidus (1160°C) [4-5], U-10Mo will have inherent micro-porosity problems. To minimize porosity in an alloy casting the following principles should be applied to the mold and process parameter design [7]:

- maximize the thermal gradient to minimize the length of the dendrites and improve flow from the hot top to the dendrite roots.

In addition the hot top must be designed so that it:

- solidifies at the same time or later than the casting,
- contains sufficient liquid to compensate for the volume-contraction of the freezing metal,
- there must be a path from the hot top to allow feed metal to reach regions that need it.

From both the experimental and simulation results the vertical mold design clearly violates several of these principles and as such is expected to yield a cast billet with micro-porosity.

Macro-segregation refers to spatial variations in composition that occur in metal alloy castings and range in scale from several millimeters to centimeters or even meters. The cause of macro-segregation is relative movement or flow of segregated liquid and solid during solidification [8]. Since U-Mo is a peritectic with the uranium rich liquid being heavier than the Mo rich solid, buoyancy driven flow from should not be an issue. But, for minimum macro-segregation solidification time should me minimized.

Based on these design goals, and the results of the vertical mold castings, several mold design variations' were examined. The revised mold design had the following changes -

1) The casting was rotated from being 18 cm tall by 13 cm wide to 13 cm tall and 18 cm wide. This long dimension on the horizontal and short dimension on the vertical minimizes the molten metal feeding length. It also reduces the mold length, which for similar top and bottom clamp temperatures, increases the thermal gradient.
2) The size of the hot top was increased.
3) Head room was provided above the hot top to make sure that molten metal does not contact the top of the mold.

This revised horizontal mold design is shown in Fig. 6. In Fig. 5(b), the simulation results for the horizontal mold are shown. The simulation shows significantly less of a dip in the center of the casting. It also shows a higher thermal gradient that should help minimize micro-porosity.

2. Revised Horizontal Mold Design

Based on the simulation results, a graphite mold was machined from the horizontal mold design. As with the vertical mold, stainless steel sheathed type-K thermocouples and alumina sheathed type-C thermocouples with a bare-bead tip were placed in the casting

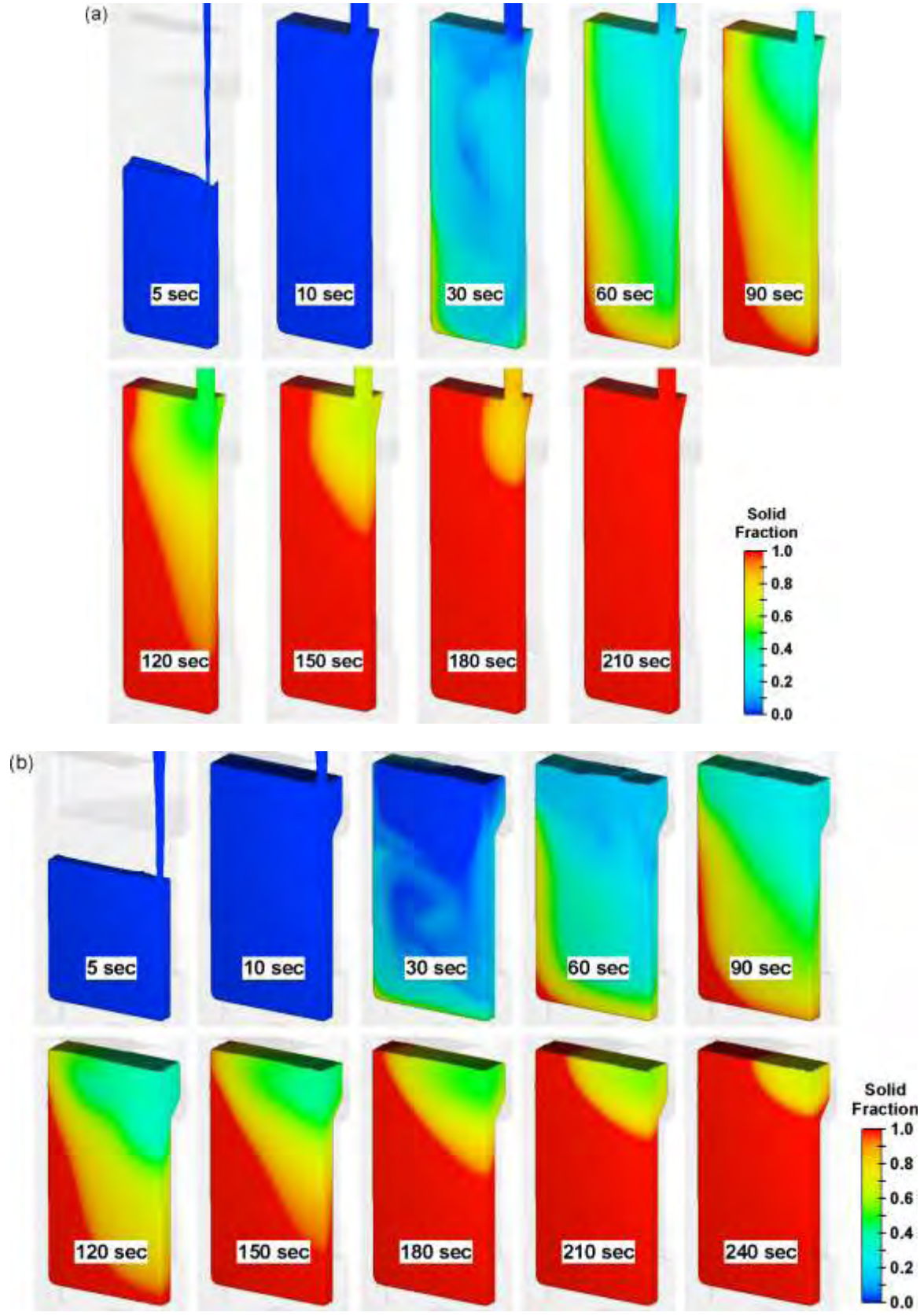


Fig. 5 Simulation results showing fraction solid as a function of time; (a) vertical mold and (b) horizontal mold.

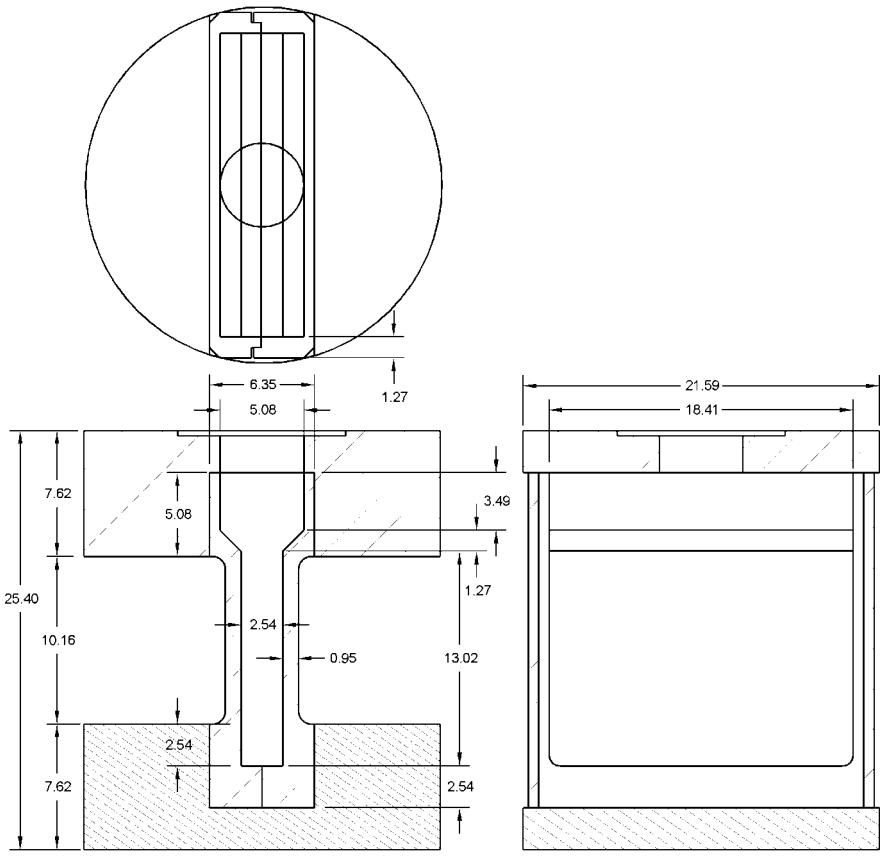


Fig. 6 Three views of the horizontal mold design. Dimensions are in centimeters.

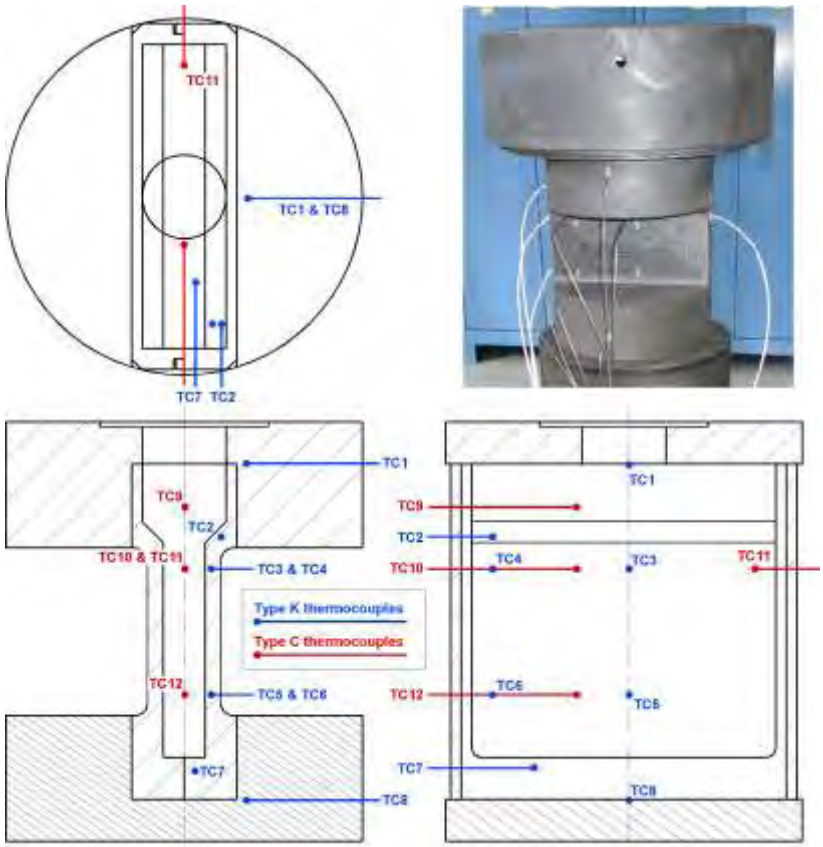


Fig. 7 Thermocouple positions in the horizontal mold along with a photo of the mold stack prior to casting.

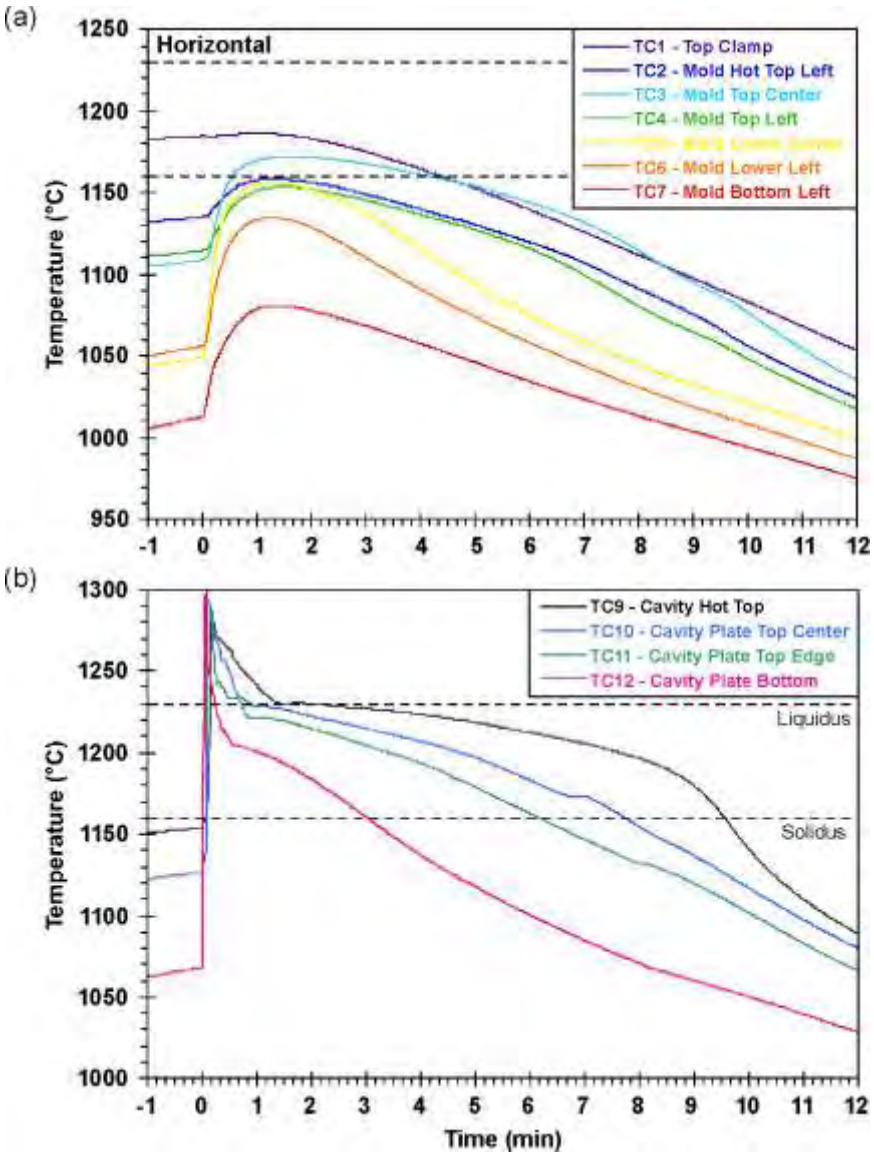


Fig. 8 Thermal history of horizontal mold poured at 1330°C; (a) thermocouples in mold and (b) thermocouples in casting cavity.

cavity and cemented in place. The location of the thermocouples and instrumented mold stack are shown in Fig. 7. Because of the larger hot top, the crucible was charged with 15.5 kg of U-10Mo arc-melted buttons. The casting was processed with the same 60 kW initial furnace power setting, and the metal was heated to 1330°C (100°C superheat) and held for 10 minutes prior to pouring.

The metal reached 1330°C in 33 minutes, was held at temperature for 10 minutes, and then the stopper rod was removed. Figure 3 shows the thermal gradient in the mold at pour time. An unintended consequence of the shorter overall mold stack, combined with use of the same heating procedure as used for in the vertical mold design, is that the overall mold temperature was hotter than in the vertical design. Figure 8 shows the resulting cooling curves for the thermocouples in the mold and in the casting cavity. The resulting casting had a weight of 14.0 kg.

5. Discussion

In considering the two mold designs, it is informative to examine the thermal gradient in the casting cavity as a function of time. Figure 9 shows a comparison of thermal gradients along the center set of thermocouples in the mold cavity as a function of time from pouring. For the

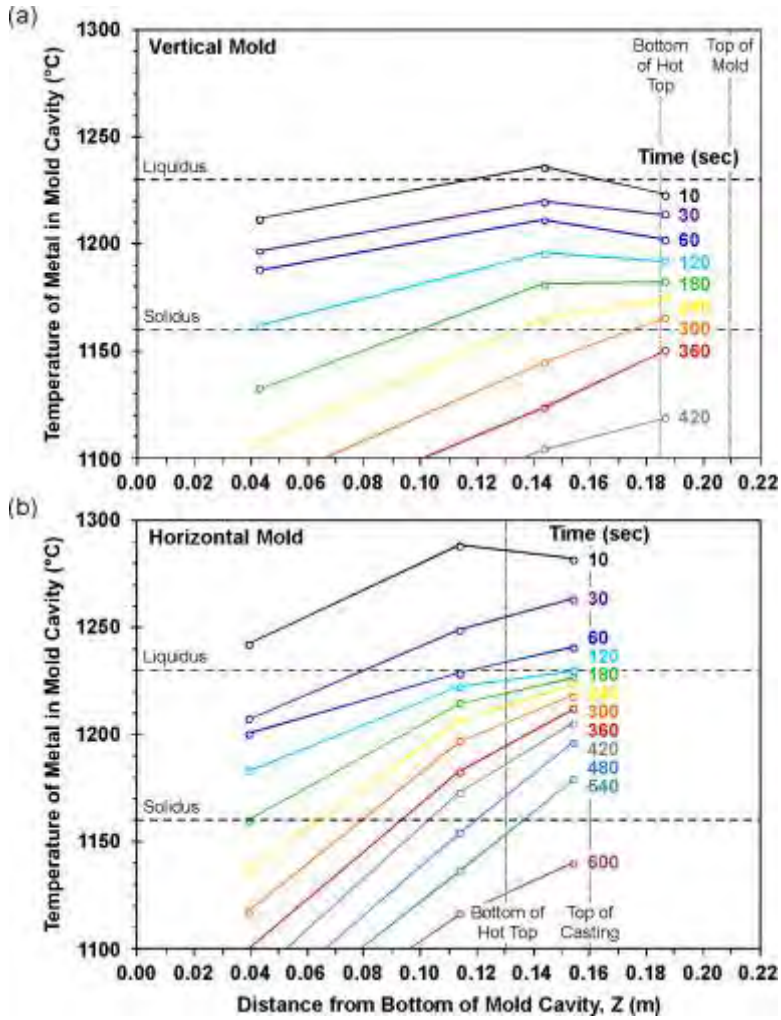


Fig. 9 Comparison of thermal gradients along the center set of thermocouples in the mold cavity as a function of time from pouring; (a) vertical mold and (b) horizontal mold. Both castings poured a melt temperature of 1330°C.

vertical mold design (Fig. 9(a)), it is clear that up to about 180 seconds there is a negative thermal gradient between the plate and hot top. Such a situation makes the hot top totally ineffective with porosity preferentially forming in the top of the casting rather than in the hot top. For the horizontal mold design (Fig. 9(b)), the thermal gradient remains positive between the plate top and hot top. Further the thermal gradient in the lower bulk of the casting is significantly higher and will promote feeding and minimize micro-porosity.

To aid x-ray radiographic examination of the two billets the "wings" of the hot tops were machined off. This gave a constant 2.5 cm thick plate that was more conducive to uniform contrast in x-ray radiography. Figure 10 shows the radiographic results of the two castings. The horizontal red line indicates the location of the hot top to cast plate transition. The dark horizontal lines are the alumina sheaths for the type-C thermocouples. The radiographs are unable to distinguish minor amounts of micro-porosity, but they do show rejoins of major micro-porosity in the hot top of both castings as dark clumps. Analysis of micro-porosity distribution awaits metallographic analysis of the two castings.

6. Conclusions

The instrumented castings of the initial vertical mold design showed an undesirable thermal gradient during solidification that likely results in micro-porosity and an undesirably low material yield. Based on the initial castings, good casting design practice, and process simulation, a revised horizontal design was developed. The redesigned horizontal mold had

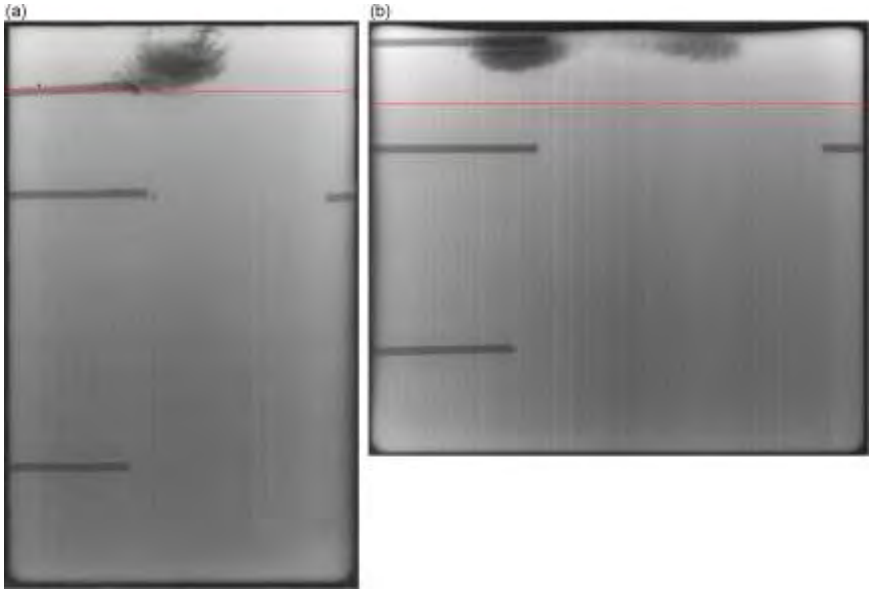


Fig. 10 Radiographic results of the two castings; (a) vertical and (b) horizontal mold geometry. The red line indicates the location of the hot top to cast plate transition. The dark horizontal lines are the alumina sheaths for the type-C thermocouples.

a larger hot top and exhibits a strong thermal gradient conducive to good feeding and a minimization of micro- and macro-porosity in the cast plate

Future work: Metallography to determine distribution and amount of micro-porosity still needs to be done for these two castings. In addition, measurement of composition as a function of position to determine any Mo macro-segregation must be performed.

Recommendations for future castings: (i) use the horizontal mold but with a lower charge (14.5 kg) this would give the two mold designs the same initial charge and as such same yield (be it with lower micro-porosity in the horizontal mold); (ii) lower metal pour temperature (100°C superheat is too much for this thick casting); (iii) lower the mold temperature by either holding for less than 10 minutes once temperature is reached or by heating faster.

Acknowledgement

The authors would like to acknowledge the financial support of the US Department of Energy Global Threat Reduction Initiative Reactor Convert program. Los Alamos National Laboratory, an affirmative action equal opportunity employer, is operated by Los Alamos National Security, LLC, for the National Nuclear Security Administration of the U.S. Department of Energy under contract DE-AC52-06NA25396.

7. References

[1] Vertical mold design and process parameters private communication J.G. Gooch, A.L. DeMint, and H.A. Longmire, Y-12 Nat. Secruity Complex, Oak Ridge, TN, USA.

[2] HML grade graphite by SGL Carbon, LLC., St. Marys, PA USA.

[3] Type YK nonaqueous-based yttrium oxide paint by ZYP Coatings, Oak Ridge, TN USA.

[4] P.C.L. Pfeil, J. Inst. Metals, v 77, pp. 553-570 (1950).

[5] S.P. Garg and R.J. Ackermann, J Nucl. Mater., v. 64, pp. 265-274 (1977).

[6] Flow-3D by Flow Science Inc., Santa Fe, NM USA.

[7] John Campbell, Complete Casting Handbook, Butterworth, Oxford UK (2011).

[8] C. Bekermann, “Macrosegregation”, ASM Handbook Vol. 15: Casting, pp. 348-352 ASM International (2008).

FUEL ELEMENT DESIGN AND ANALYSIS FOR ADVANCED TEST REACTOR CONVERSION TO LOW ENRICHED URANIUM FUEL

M.A. POPE, M.D. DEHART, D.W. NIGG, R.K. JAMISON, S.R. MORRELL
Idaho National Laboratory
2525 N. Fremont Avenue, Idaho Falls, Idaho, 83415, USA

ABSTRACT

Under the current long-term US Department of Energy (DOE) policy and planning scenario, both the Advanced Test Reactor (ATR) and its critical facility (ATRC) will be reconfigured at an appropriate time to operate with low-enriched uranium (LEU) fuel. This paper describes the progression of the LEU fuel design and the trade studies used to narrow the field of candidates based on Naval Reactor performance requirements and nuclear safety criteria. Ultimately, the fabricability and fuels performance questions associated with elements containing burnable absorbers led to the adoption of the Enhanced LEU Fuel (ELF) concept, a fuel element containing no poisons, which uses variation in fuel meat thickness to shape the radial (plate-to-plate) power peaking in the element. The ELF fuel is currently conceptualized in two forms, one with three unique fuel meat thicknesses (Mk 1A) and one with five (Mk 1B). Evaluation of the ELF Mk 1A and ELF Mk 1B designs against Naval Reactors (NR) and safety requirements is ongoing. Analyses are also ongoing regarding the impacts of uncertainty in fuel meat thickness. It was determined that there exist plate-to-plate interactions that can contribute to higher heat fluxes when neighboring plates have certain combinations of thicknesses. Therefore, a statistical approach is likely necessary in order to determine worst-case impacts of this uncertainty.

1. Introduction

The Advanced Test Reactor (ATR), located at Idaho National Laboratory (INL), is one of only a few high-power research reactors of its general type in the world. Its capabilities support a variety of missions involving accelerated testing of nuclear fuel and other materials in a very high neutron flux environment, medical and industrial isotope production, and several other specialized applications. Figure 1 shows a cross-sectional view of the ATR core. Along with its companion critical mockup, the ATR Critical Facility (ATRC), the ATR is one of the key nuclear engineering research and testing facilities within the US Department of Energy (DOE) National Laboratory Complex. The ATR and ATRC also serve as the centerpieces of the ATR National Scientific User Facility (NSUF), whose purpose is to facilitate the current trend toward broadening application of the ATR beyond its traditional base. Under the current long-term DOE policy and planning scenario, both the ATR and the ATRC will be reconfigured at an appropriate time to operate with low-enriched uranium (LEU) fuel. This will be accomplished under the auspices of the Reduced Enrichment for Research and Test Reactors (RERTR) Program of the Global Threat Reduction Initiative (GTRI), administered by the DOE National Nuclear Security Administration (NNSA).

2. Fuel Design Trade Studies

A number of activities related to LEU fuel design for the ATR are underway at INL. The primary focus has been on computational and experimental materials performance studies for uranium-molybdenum composites. Experimental work has been supplemented by a number of computational RERTR fuel studies to determine potential performance of different

fuel designs covering a broad range of fuel characteristics [1-6]. The following paragraphs summarize the design progression of the LEU conversion program and the trade studies used to narrow the field of candidates.

Prior to 2010, the design of a conceptual ATR LEU fuel element was performed by the Idaho National Laboratory (INL) GTRI Fuels Development (FD) group primarily because this group included analysts familiar with ATR design and operation. The scope of the GTRI FD work included design of a candidate test element to be inserted in an ATR fuel position. This design process was focused on development of a fuel concept that could be employed in a number of high performance research and test reactors that included but was not limited to ATR.

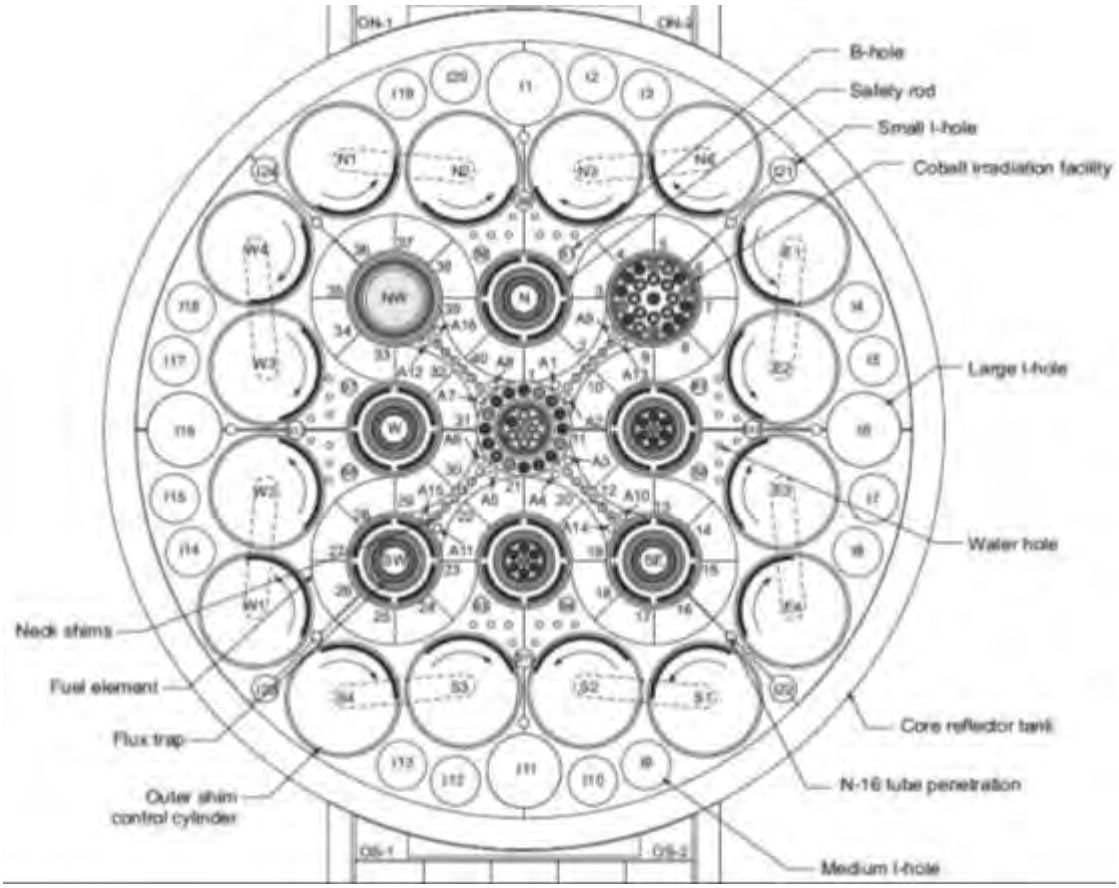


Fig 1. Cross-sectional view of the ATR core [7]. Note that irradiation positions are identified by compass locations, with the top of the figure representing north (N) on the compass.

As a result of this development process, a representative 'Full Element' (FE) design was proposed that would use 11 unpoisoned LEU fuel plates with reactivity and power peaking control provided by poisoned HEU fuel plates from the existing Mark 7F design. It was recognized, however, that for complete LEU deployment within the ATR some form of reactivity control would be needed. The FD team examined a broad number of options to accomplish this objective, in an informal and research-oriented approach. The set of candidate fuel designs selected by the FD team were identified as the Integral Cladding Burnable Absorber (ICBA). [3] Within this set of candidate fuel designs a number of different fuel meat and poison combinations were studied. Ultimately a design was recommended that closely approximated the ATR HEU element power profile and reactivity at beginning of life. This design was essentially a 7-layer sandwich that imbedded a thin layer of B_4C poison within the cladding of innermost and outermost fuel plates. While this design was theoretically very attractive, it did not meet performance requirements due to: (1) the

potential for formation of helium that could result in fuel blistering; and (2) the extreme difficulty and inherent cost associated with fabrication of such a complicated design.

In 2011, an ATR Conversion Project was formed at INL and a physics analysis team grew out of the ongoing Physics Methods upgrade project. The ICBA design was used as a basis for early evaluation of physics methods to determine appropriateness of the new methods for ATR LEU design and analysis. The challenges associated with this design process highlighted weaknesses in existing analysis approaches – specifically the challenge of doing scoping analyses for a variety of designs using HELIOS [8], limitations in three-dimensional multi-group Monte Carlo-based depletion calculations within the SCALE [9] system and lack of a robust depletion capability based on MCNP5. [10] Serpent was found to meet the near-term requirements for LEU design evaluations and was used for evaluation of subsequent LEU design concepts. [11]

Because of the possible performance limitations of the ICBA design, it was discarded. The GTRI program asked the ATR Conversion team to investigate alternatives to burnable absorbers integral to the fuel meat. In order to accommodate this request, a traditional engineering selection process was adopted to down-select an element design. First, local experts in fuel element design and analysis were assembled and a brainstorming session was held to collect all plausible designs. Nine concepts for an LEU fuel design were proposed with multiple variations of each. [12] By this point, it was already clear that variable fuel meat thicknesses (using U-10Mo meat) would be needed in fuel plates to mitigate radial (plate-to-plate) power peaking issues in the fuel, regardless of whether there would be burnable absorber anywhere in the element. Three of the nine identified concepts were found to meet the initial scoping performance requirements, which included Naval Reactor (NR) requirements (described in Section 2.4) and general fabricability, and were selected for further analysis against ATR safety and performance needs [13].

These three designs were designated as: (1) Integral Side-Plate Burnable Absorber – Cadmium (ISBA-Cd), (2) Integral Side-Plate Burnable Absorber – Boron (ISBA-B) and (3) Enhanced LEU Fuel (ELF). The following sections describe each of the three concepts and summarize the results of the trade studies; Table 1 provides the fuel meat thicknesses and ^{235}U masses for each of the three concepts evaluated. Figure 2 shows a modeled representation of two adjacent candidate LEU fuel elements for the ICBA-Cd design; it also illustrates the variation in fuel meat thicknesses that are similar for all three of the candidate fuel elements. All three designs are based on a U-10Mo fuel foil enriched to 19.75% ^{235}U, encased in a 0.00254 cm (1 mil) zirconium diffusion layer bonded to aluminum cladding. The zirconium barriers are present in the figure, but are too small to be clearly seen here.

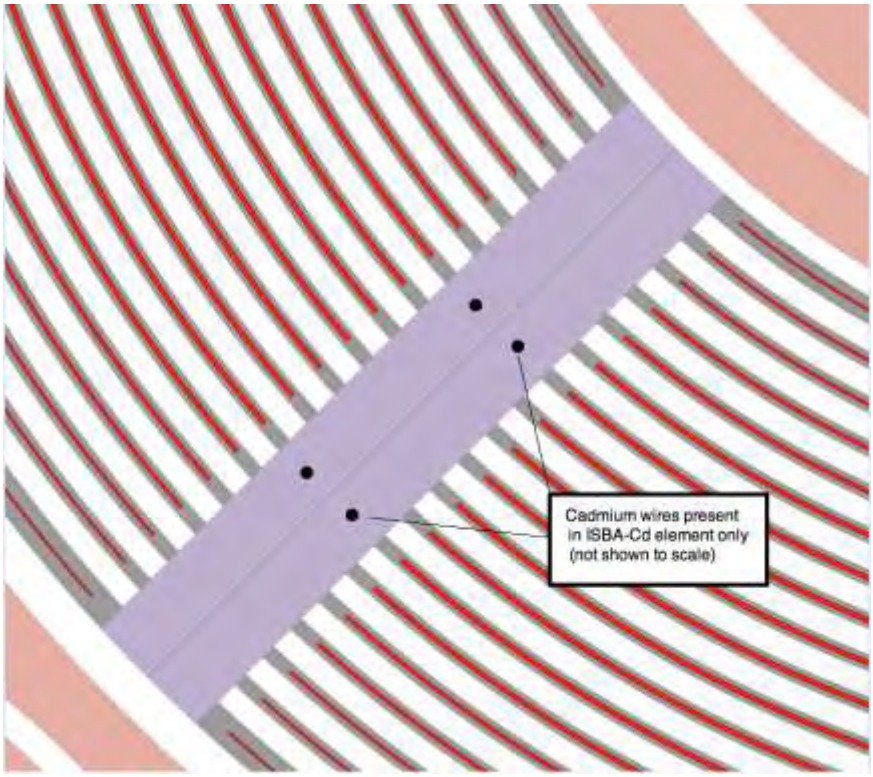


Fig 2. Interface between two ISBA-Cd fuel elements showing Cd wires in sideplates.

Tab 1. Fuel meat thicknesses and other parameters for three candidate element designs.

Parameter		ISBA-Cd		ISBA-B		ELF	
		(cm)	(mils)	(cm)	(mils)	(cm)	(mils)
Meat Thickness by Plate #	1	0.02286	9	0.02286	9	0.02032	8
	2	0.02286	9	0.02286	9	0.02286	9
	3	0.02540	10	0.02540	10	0.02540	10
	4	0.02794	11	0.02794	11	0.03048	12
	5	0.03302	13	0.03302	13	0.03302	13
	6	0.03683	14.5	0.03556	14	0.03556	14
	7	0.03683	14.5	0.03556	14	0.03810	15
	8	0.03683	14.5	0.03810	15	0.03810	15
	9	0.03683	14.5	0.03810	15	0.03810	15
	10	0.03683	14.5	0.03810	15	0.03810	15
	11	0.03683	14.5	0.03810	15	0.03810	15
	12	0.03683	14.5	0.03556	14	0.03810	15
	13	0.03683	14.5	0.03556	14	0.03810	15
	14	0.03302	13	0.03302	13	0.03556	14
	15	0.02794	11	0.02794	11	0.03048	12
	16	0.02540	10	0.02540	10	0.02794	11
	17	0.02032	8	0.02032	8	0.02286	9
	18	0.01778	7	0.01778	7	0.02032	8
	19	0.01524	6	0.01778	7	0.01778	7
Number of unique thicknesses		8		8		9	
^{235}U mass per element (g)		1397		1406		1465	

2.1 Integral Side-Plate Burnable Absorber – Cadmium (ISBA-Cd)

Figure 2 shows the top view of the ISBA-Cd LEU fuel element. The ISBA-Cd design uses variable fuel plate thicknesses (as do the other two candidates) to reduce radial power

peaking in the fuel element, but also uses cadmium wires within the aluminum side plates for control of excess reactivity at beginning of life. Two cadmium wires were added to each side plate having dimensions (1-mm-dia × 48-in.-length). Table 1 provides individual fuel meat thickness for each plate (i.e., U-10Mo thickness; it does not include Zr layer) along with ^{235}U mass. Figure 2 shows the top view of the ISBA-Cd LEU fuel element. (Note that the cladding and sideplates are constructed of two different aluminum alloy materials.) [14]

2.2 Integral Side-Plate Burnable Absorber – Boron (ISBA-B)

For the ISBA-B fuel design, reactivity control is achieved by using borated aluminum side plates containing 150 ppm ^{10}B. Table 1 provides individual meat thickness (i.e., U-10Mo thickness; it does not include Zr layer) and ^{235}U masses. Fig 2, viewed without the cadmium wires in the sideplates, can be used to provide an approximate visualization of the ISBA-B LEU fuel element. (Note once again that the cladding and sideplates are different aluminum alloy materials and that the Al cladding is not borated.) [15]

2.3 Enhanced LEU Fuel (ELF)

The ELF fuel closely resembles the other two candidate elements, but does not include the use of burnable poison. Radial power peaking is again accomplished through adjusted fuel meat thickness, which varies for each of the 19 plates where the fuel meat is centered in the aluminum cladding. Table 1 provides individual plate fuel thickness and ^{235}U masses for the ELF concept. The ELF design can again be visualized using Figure 2 with the cadmium wires omitted. [16]

2.4 Results of Trade Study

The LEU fuel element down selection process involved reactor physics and thermal-hydraulics analyses being performed on the three primary candidate designs assessing them against Naval Reactor performance requirements and nuclear safety criteria. From a technical performance perspective, the primary concern is the Naval Reactors (NR) requirements letter provided in 2007 to the GTRI program [17]. This document enumerates eight performance requirements that, if met, would allow the ATR LEU core to meet NR's needs. Five of these requirements directly relate to the physics performance of a core loaded with an LEU design, listed below:

- **NR-1:** Operational cycle length of 56 days at 120 MW
- **NR-2:** Fast-to-thermal neutron flux ratio within 5% of current values in a pressurized-water loop test
- **NR-3:** Greater than 4.8×10^{14} fissions per second per gram ^{235}U in a specimen with 1 gram ^{235}U per linear inch in a standard in-pile tube (SE or SW) operating at 60 MW
- **NR-4:** 3/1 lobe power split with south corner lobes operating at three times the lobe power of the northern lobes.
- **NR-5:** Gamma-to-neutron flux ratio within +10%/-10% of current values.

To evaluate the three design concepts, Serpent calculations were performed using a core configuration based on a fresh fuel benchmark developed from startup testing after the 1994 core internals change-out (94-CIC) [7]. The 94-CIC configuration was modeled faithfully with three exceptions: (1) outer shim control cylinders (OSCCs) were rotated to mid-position at 80°, (2) the northwest (NW) tube (see Fig. 1) was loaded with a prototypic experiment in place of the solid aluminum dummy described in the benchmark and (3) fresh HEU fuel was replaced with a representative core loading consisting of 18 fresh, 14 once-, and 8 twice-burned fuel elements, as illustrated in Fig 3. Rationale for these changes and details of the core loading are described in Ref. 15. Calculations were performed to address items NR-1 through NR-4 of the above list. The core model was modified slightly to evaluate item NR-3

by modeling a pseudo-experiment containing one gram of ^{235}U per linear inch in the southeast (SE) and southwest (SW) experiment tubes. Coupled neutron-gamma (n-γ) calculations needed to address requirement NR-5 above are currently beyond Serpent code capabilities and will ultimately be evaluated using a different approach such as MC21 [18] which has the capability to complete these calculations. It is anticipated that all three LEU fuel designs will demonstrate similar n-γ characteristics and therefore this is not expected to be a discriminating criterion between LEU candidate designs. However, the magnitude of changes in the n-γ source remains to be evaluated.

The Serpent calculations described above were verified by independent MCNP [10] calculations for a subset of fresh fuel evaluations and found to be in very close agreement. In addition, Serpent has been shown to match results of the ATR benchmark described in Ref. 7, along with element power distributions described for startup testing for various OSCC power splits [20]. Validation of Serpent depletion calculations has been performed informally by comparison to other depletion calculations and a formal qualification of Serpent is in progress. This is a requirement of the conversion project and is described in an internal project validation plan document.

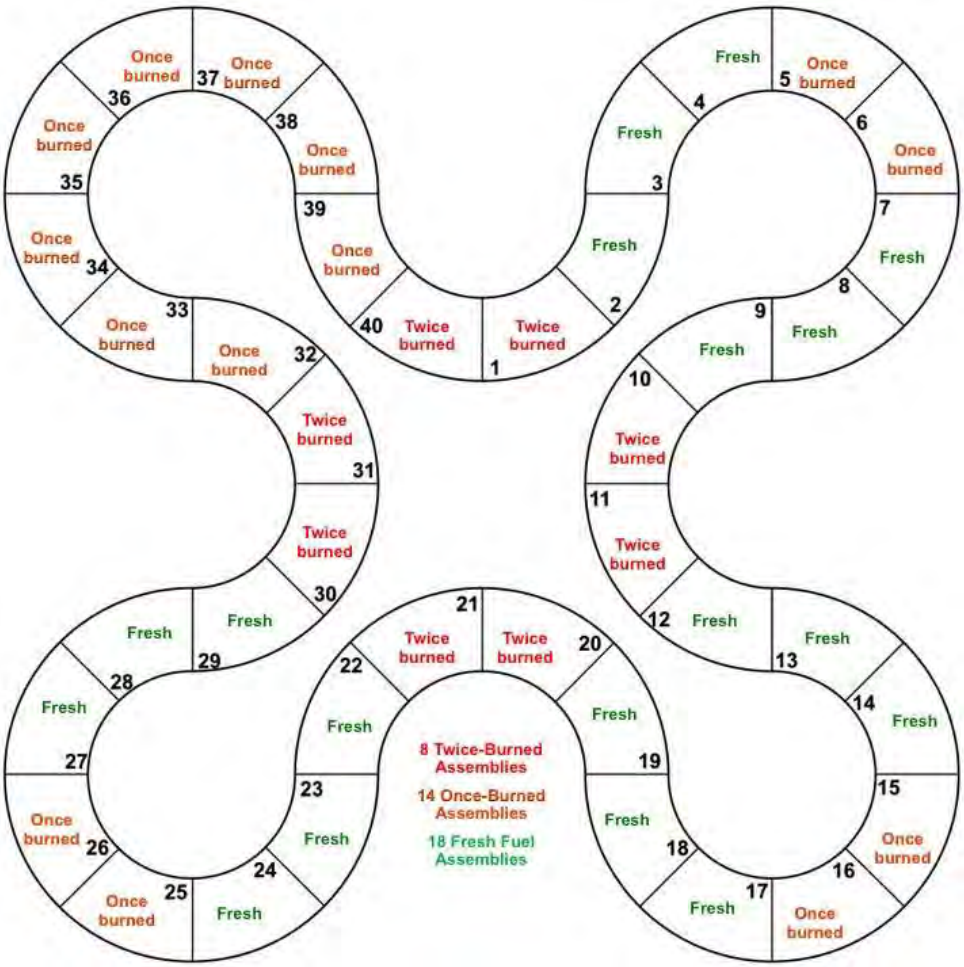


Fig 3. Loading pattern assumed for representative cycle calculations.

Figure 4 illustrates the core reactivity behavior as a function of burnup for the representative core loading operated without shim adjustment (OSCCs maintained at 80°, 22 neck shims fully inserted) for HEU and the three LEU designs. This plot shows the value of k_{eff} for the four fuel types (solid markers for the three LEU types, lower half of plot) and the reactivity of

the LEU fuels relative to the HEU fuel (open markers, upper half of plot). Among the three batches, the behavior of the reactor is most influenced by the reactivity of the fresh fuel elements (18 of 40 elements are fresh in this loading). The HEU fuel, with significantly more poison than the three LEU concepts, loses net reactivity more slowly; however, LEU fuels see a reactivity recovery later in the fuel cycle due to buildup of significant quantities of plutonium. The three LEU designs show a maximum reactivity deficit in the range of $2.50 to $3.50 (varying by design) compared to HEU. This deficit is addressed by addition of fuel (see Section 3) in subsequent work, and is not considered a differentiator between the LEU candidates. Therefore, all three of the LEU designs were judged capable of meeting the cycle length criterion (NR-1) once additional fuel is included by expanding fuel meat thicknesses.

Results of calculations of the fast-to-thermal ratio in pressurized loop locations are provided in Table 2 in terms of the change in the fast-to-thermal (F/T) ratio (assuming a 1.25 eV boundary) for each LEU design relative to the calculated ratio for the standard HEU fuel design. These results show that although the change in the F/T ratio is within NR requirements at beginning of cycle (BOC), the change exceeds the NR criterion of no more than a 5% increase at end of cycle (EOC). However, these results are misleading. Table 3 shows the percent change in F/T ratio at BOC and EOC for each fuel. The F/T ratio changes very little (~0.5-1% decrease) for the LEU designs over the length of the cycle, while there is a 2-3% decrease in the F/T ratio in the HEU core. Since a constant flux ratio is likely more important for an irradiation experiment (as seen with LEU designs), and LEU fuel meets the 5% change criterion at BOC, it is felt that these results are consistent with the intent of NR requirements.

Calculations performed to evaluate fission rates in the south (S) in-pile tube (IPT) positions show a slight reduction in sample fission rates for LEU relative to HEU at BOC, as shown in Table 4. The reduction is minor and still exceeds the minimum level of 4.8×10^{14} fissions per second specified by NR. However, note that this is highly dependent on the assumed water density in the pseudo-experiment. These results assume 1 g/cm^3 water density, and the effect of lower density is a lowering of fission rate. Subsequent calculations at experiment conditions indicate that neither HEU nor LEU designs can meet this criterion; subsequently further information on this specification has been requested from NR.

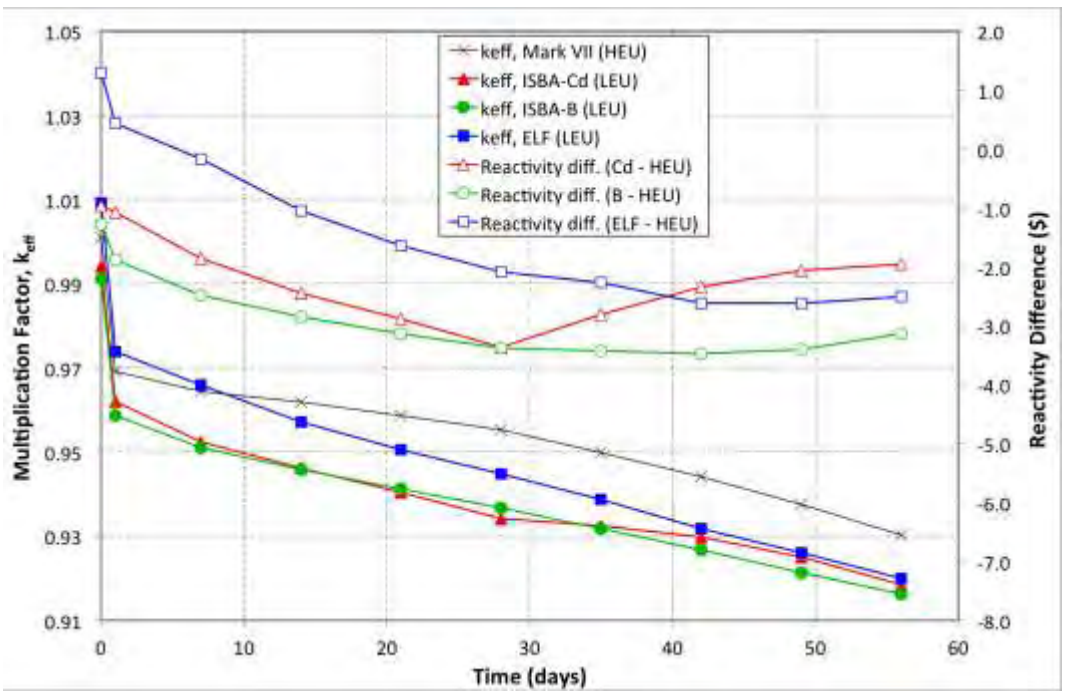


Fig 4. K_{eff} vs. depletion time in days for representative mixed 3-batch loading depletion on left axis. Reactivity Difference between each fuel and HEU on right axis.

Thermal-hydraulics (TH) analysis of these designs indicated that the ELF design maintained safety margins similar to or better than the current HEU fuel design. The ISBA-B design met safety margins for a mix of limiting criteria, but tended to have less margin than the ELF design. The ISBA-B design has design refinements, fuel meat thickness, and boron concentration that could be varied to regain additional safety margins for LOCA and RIA scenarios, if required, and offers a conversion option should the ELF design have an unexpected critical limit. ISBA-Cd met several safety margins, though a full thermal-hydraulic analysis was not performed because the results are expected to be very similar to the ISBA-B design. These results were not considered discriminating between the designs because the differences in TH performance are highly dependent on the distribution of fuel meat thicknesses, which would be further adjusted during the Conceptual Design Phase. The details of the TH analyses used in this trade study are therefore not presented here.

Table 2. Percent Change in Fast to Thermal Flux Ratio for LEU designs relative to HEU case for four locations.

Fuel	IPT	Burn Time (days)					
		0	1	14	28	42	56
ISBA-Cd	N	3.9	3.5	3.8	4.6	4.7	5.3
	W	3.5	3.4	4.0	4.3	4.9	5.1
	SW	3.7	3.8	4.1	4.6	5.0	5.5
	SE	3.8	3.7	4.3	4.4	5.0	5.4
ISBA-B	N	3.7	3.9	4.3	4.6	4.9	5.2
	W	3.7	3.8	4.2	4.5	5.2	5.3
	SW	4.0	3.9	4.3	4.6	5.1	5.4
	SE	4.0	4.1	4.6	4.9	4.8	5.1
ELF	N	3.9	4.0	4.5	4.7	5.3	5.8
	W	3.7	3.7	4.3	4.7	5.5	5.8
	SW	4.1	3.9	4.3	5.0	5.3	5.6
	SE	3.8	4.1	4.6	4.9	5.0	5.5

Table 3. Percent Change in Fast to Thermal Ratio from BOC to EOC.

Fuel	IPT	Change of F/T Flux Ratio (%)
Mark VII (HEU)	N	-2.3
	W	-2.5
	SW	-2.1
	SE	-1.9
ISBA-Cd (LEU)	N	-0.8
	W	-0.8
	SW	-0.3
	SE	-0.5
ISBA-B (LEU)	N	-1.1
	W	-1.2
	SW	-0.7
	SE	-0.9
ELF (LEU)	N	-1.1
	W	-1.2
	SW	-0.7
	SE	-0.9

Table 4. Fission Rate in HEU Plug in Two IPT Locations Normalized to a 60 MW Lobe Power.

Fuel	IPT	Fission Rate in HEU Plug (Fissions / s / in)
Mark VII (HEU)	SW	5.4×10^{14}
	SE	5.3×10^{14}
ISBA-Cd (LEU)	SW	5.2×10^{14}
	SE	5.2×10^{14}
ISBA-B (LEU)	SW	5.2×10^{14}
	SE	5.2×10^{14}
ELF (LEU)	SW	5.1×10^{14}
	SE	5.2×10^{14}

2.5 Selection of ELF for Further Analysis

For the three candidate LEU fuel elements analyzed in detail, neither neutronic nor TH performance provided discriminating information. Therefore, fabrication and fuels performance expectations were used to inform the down selection process. Fabrication challenges associated with placement of the Cd wire in the ISBA-Cd element sideplate resulted in this design being given a marginal rating under fabrication. In addition, where cadmium is considered a hazardous material (RCRA regulated metal), its introduction into the design may complicate fuel management. The introduction by the ISBA-B design of borated aluminum sideplates raises questions regarding swelling that could affect fuel handing, and would require additional qualification testing. From a fabrication perspective, all three of these fuel designs depend on variable fuel meat thickness for power peaking and reactivity control to some degree, though the ELF fuel design does not require the addition of a burnable absorber within the element itself, thereby simplifying overall fuel element assembly fabrication. The absence of burnable poison in the ELF design will introduce additional reactivity hold-down requirements at BOC. However, it is thought that this can be managed by a combination of operational changes to fuel loading, OSCC positioning, and, if needed, the possible addition of external burnable poisons in selected experiment positions (likely one of the numbered “B” holes shown in Fig. 1).

3 Modified ELF Fuel (“ELF Mk 1A” and “ELF Mk 1B”)

During reactor physics evaluation in support of the trade study described above, needs were identified for further refinement of the ELF fuel element before designating a conceptual design. As mentioned in Section 2.4, an increase in fuel mass was found to be needed to meet cycle length requirements in a representative mixed-loading core. Also, the desirability of specifying fewer unique fuel meat thicknesses was recognized to reduce the burden on manufacturing. A number of iterations were performed where fuel meat thicknesses were adjusted followed by evaluation of neutronic and TH performance. This process resulted in two candidates for conceptual design, designated Mk 1A and Mk 1B. Table 5 shows fuel meat thicknesses for these modified designs along with the total number of unique meat thicknesses. The ^{235}U mass per element is also given along with the percent increase in ^{235}U mass over the original ELF design. Note that the Mk 1A design results in the fewest number of fuel meat thicknesses, while Mk 1B provides a somewhat lower peak heat flux with the addition of two additional meat thicknesses. At this time, it is not know which parameter will be most important in the final design, so both options are being evaluated with a final down select anticipated in the future.

Tab 5. Fuel meat thicknesses and other parameters for ELF Mk 1A and ELF Mk 1B.

Parameter		ELF Mk 1A		ELF Mk 1B	
		(cm)	(mils)	(cm)	(mils)
Meat Thickness by Plate #	1	0.02032	8	0.02540	10
	2	0.03302	13	0.02540	10
	3	0.03302	13	0.03302	13
	4	0.04064	16	0.03302	13
	5	0.04064	16	0.03810	15
	6	0.04064	16	0.03810	15
	7	0.04064	16	0.04572	18
	8	0.04064	16	0.04572	18
	9	0.04064	16	0.04572	18
	10	0.04064	16	0.04572	18
	11	0.04064	16	0.04572	18
	12	0.04064	16	0.04572	18
	13	0.04064	16	0.03810	15
	14	0.04064	16	0.03302	13
	15	0.04064	16	0.03302	13
	16	0.03302	13	0.03302	13
	17	0.02032	8	0.02540	10
	18	0.02032	8	0.02032	8
	19	0.02032	8	0.02032	8
Number of unique thicknesses		3		5	
^{235}U mass per element (g)		1648		1657	
Mass increase from original ELF (%)		12.5		13.1	

Figure 5 illustrates the core reactivity behavior as a function of burnup for the representative core loading operated without shim adjustment (OSCCs maintained at 80°, 22 neck shims fully inserted) for HEU and the ELF Mk 1A and Mk 1B LEU designs. This shows that the modified designs now have sufficient fuel to meet the cycle length requirement (item NR-1 in Section 2.4). The two designs have approximately $3.0 and $3.3 of additional reactivity at BOC compared to HEU and $1.1 and $1.4 additional reactivity at EOC (Mk 1A and 1B, respectively). This suggests that a slightly different loading strategy, wherein some fresh or once-burned elements are displaced by once- or twice-burned elements, could be used with the LEU fuel designs. This strategy would give the same cycle length as HEU with fewer fresh elements. Based on the comparison in Fig 5, this would effectively lower the excess reactivity at EOC from $1.1 – $1.4 down to zero, and approximately the same would occur at BOC. Therefore, the additional hold down required for the ELF Mk 1A and 1B fuel is predicted to be approximately $2 for either design on a constant cycle length basis. Again, it is expected that this additional reactivity can be controlled by a combination of OSCC rotation and external burnable poisons in selected test positions of ATR, if necessary. Evaluation of the Mk 1A and Mk 1B designs against the other NR requirements is ongoing. However, it is expected that they will perform similarly to the original ELF design in this regard.

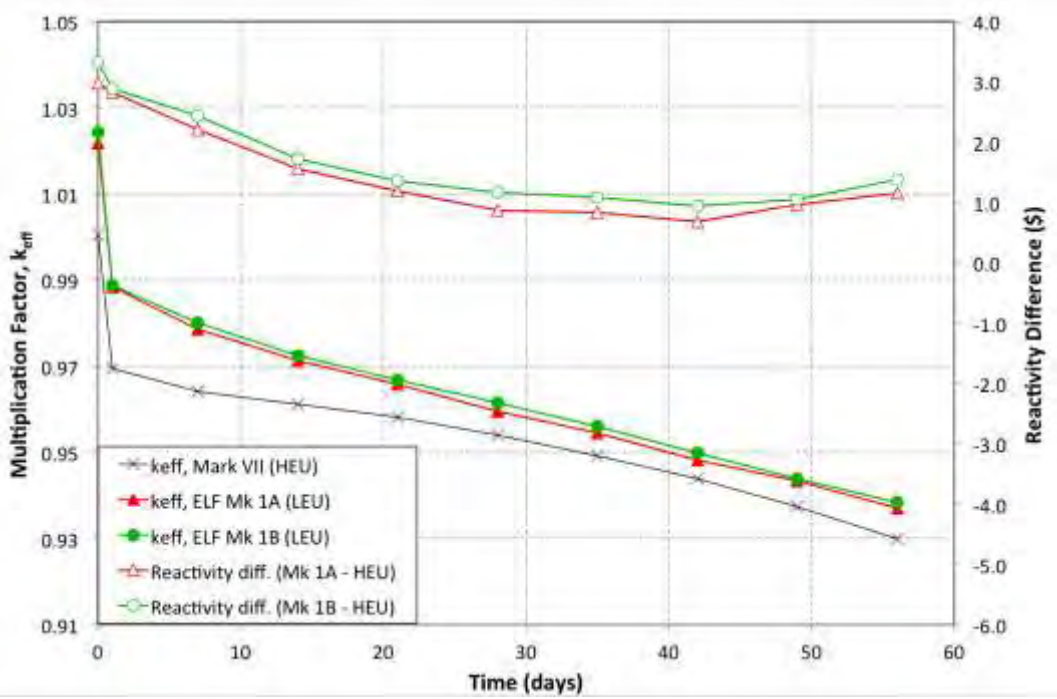


Fig 5. K_{eff} vs. depletion time in days for representative mixed 3-batch loading depletion on left axis. Reactivity difference between each fuel and HEU on right axis.

Once a set of fuel meat thicknesses was defined, Serpent calculations were performed in order to determine 1) peak heat flux in each plate, 2) peak fission rate density, and 3) element 18 power distributions in a 70 MW power split configuration.* Power distributions were used to evaluate the core's performance in a Small Break Loss of Coolant Accident (SBLOCA). From these evaluations, minimum margin to critical heat flux (CHF) and flow instability (FI) were compiled for ELF Mk 1A and Mk 1B. Results of SBLOCA analysis, typically the most limiting postulated accident scenario for ATR, suggest that both ELF Mk 1A and ELF Mk 1B are likely to meet all of the relevant safety requirements in the ATR Safety Analysis Report (SAR). [21] However, this work is ongoing and definitive statements to this effect are reserved until these analyses have been completed.

4. Impacts of Fuel Meat Thickness Uncertainty

As with any manufacturing process, the actual thicknesses of the fuel foils will vary about their nominal values by some uncertainty band. Variation of fuel meat thickness will alter the power (and thus heat flux) profile in a fuel element. This affects the margin to thermal-hydraulic limits set in the SAR such as critical heat flux (CHF) and flow instability (FI). The magnitude and exact nature of the uncertainty is not currently known. However, studies of the impact of some assumed uncertainties are of tremendous value in defining the requirements of the manufacturing process. The goal of this work was to begin evaluating what methods can be used to determine a worst-case heat flux profile from a given fuel meat thickness uncertainty definition. A manufacturing uncertainty of ±1 mil was assumed for this work. It was further assumed that the fuel meat uncertainties were independent from plate to plate and that a fuel foil has identically the same thickness axially and radially, wherever it falls within the tolerance. Several methods have been evaluated for determining a worst-case peak heat flux given this uncertainty assumption.

* The 70 MW power split is considered to be the enveloping case for safety analysis, and is based on OSCC drum rotations that would result in a 70 MW power in the SE lobe with core power at 230 MW. However, the ATR is limited to a maximum lobe power of 60 MW. Additionally, there is a 5% lobe power measurement uncertainty, meaning that if a lobe is reading 60 MW, the highest the power can be in a lobe is 63 MW. Therefore, the 70 MW power split case is used in Serpent to generate the power distribution in the hot assembly (assembly 18) and then these powers are scaled by a factor of 63/70 to arrive at a more realistic limiting power shape.

All 19 fuel plates of the hot element in this power condition (the 70 MW split described above) were divided into 10 axial and 20 azimuthal zones in which power was tallied during the Serpent calculations. These powers were converted to heat flux since this is the most useful indicator of the TH margins of present interest. Then, peak heat flux for each plate was determined and recorded for each calculation. Each Serpent calculation used 20,000 neutron histories per cycle and 10,000 active cycles. An additional 1,000 inactive cycles were used to develop the neutron source description. Each case was run in parallel on 32 processors (single compute node having four 8x2.4GHz AMD Opteron processor 6136) using shared memory, taking approximately 18 hours of wall time. Statistical uncertainty on peak heat flux was calculated to a standard deviation of ~1%.

In the first set of calculations, 0.00254 cm (1 mil) of meat thickness was added to each plate of the limiting (highest power) element, one at a time. This simple approach yields a peak heat flux for each of the 19 fuel plates in their perturbed (thickened) state. This method is a relatively fast and simple approach to finding an estimate of peak heat flux as a result of manufacturing uncertainty. However, for this to yield the true peak heat fluxes, it would have to be the case that power in each plate is independent from the fuel meat thickness of its neighbors. In other words, the peak heat flux of plate N only depends on the thickness of fuel meat in plate N. This assumption would be tested in subsequent analyses.

In the second analysis performed, it was proposed to increase the fuel meat thickness of all plates of the limiting element simultaneously in order to examine whether or not this would produce an absolute worst-case scenario with regard to peak heat flux. Allowing these to increase simultaneously was expected to increase the limiting element power, and likewise increase peak heat flux.

The third analysis performed involved a number of random variations of fuel meat thicknesses in the limiting element. A script was written that randomly generates an “actual” meat thickness for each plate, which varied within a band of ±1 mil about the nominal value. Here, the assumption was made that any deviation from nominal thickness would apply to an entire plate uniformly. Also, the fuel meat of each plate was assumed to be independent from all of the other plates. The probability density about the nominal thickness was assumed to be flat with any thickness in the ±1 mil band being equally likely. Once an actual fuel meat thickness distribution was generated, a new Serpent transport calculation was performed with the limiting element having the perturbed fuel meat thicknesses, and the power profile was tallied for this configuration. This was performed 300 times (distributed over 300 processors simultaneously) and statistics were generated for the peak heat flux values.

Results are given here only for ELF Mk 1B as an example of the phenomena that would be common between the two ELF designs. Figure 6 shows the results from the different approaches to handling the meat thickness uncertainty. The values presented have been scaled such that they represent a power of 63 MW in the SE lobe. Peak heat fluxes for each plate of the limiting element are given in the nominal thickness case along with the peak values from the various perturbed cases. The figure gives the peak heat flux in each plate resulting from the stepwise addition of 0.00254 cm (1 mil) of meat thickness to each plate individually. Using this method, the largest change in peak heat flux as a result of the additional fuel meat was approximately 12%, located in plate 18.[†]

Also presented in Fig 6 are the peak heat flux values resulting from the simultaneous +1 mil increase in all meat thicknesses. These data show that simultaneous increase of fuel meat thickness does not produce a limiting condition with regard to peak heat flux. The element

[†] Note that this 12% is not plotted in the figure. What is plotted is the result of random sampling, described below.

power increased from 8.58 MW to 8.78 MW, a ~2% increase from this uniform increase in meat thickness. The lobe power increased by a very small amount, well below the 5% measurement uncertainty on lobe power.

Serpent calculations were then performed for 300 randomly-generated sets of perturbed meat thicknesses for the limiting element. The black "×" markers in Fig 6 show the maximum peak heat flux from these random variations. On the right-hand axis is the percent change in peak heat flux from nominal to the random cases. From this, one sees that the random variation methodology yields a slightly higher peak heat flux (1-5%) than the aforementioned method of stepwise addition of 1 mil to each plate individually. The standard deviation on a given peak heat flux value from the Serpent Monte Carlo calculations is approximately 1%, so this amounts to a statistically meaningful difference. The fact that this is rather consistently positive across all plates suggests that there are plate-to-plate interactions that can contribute to higher heat fluxes when neighboring plates have certain combinations of thicknesses.

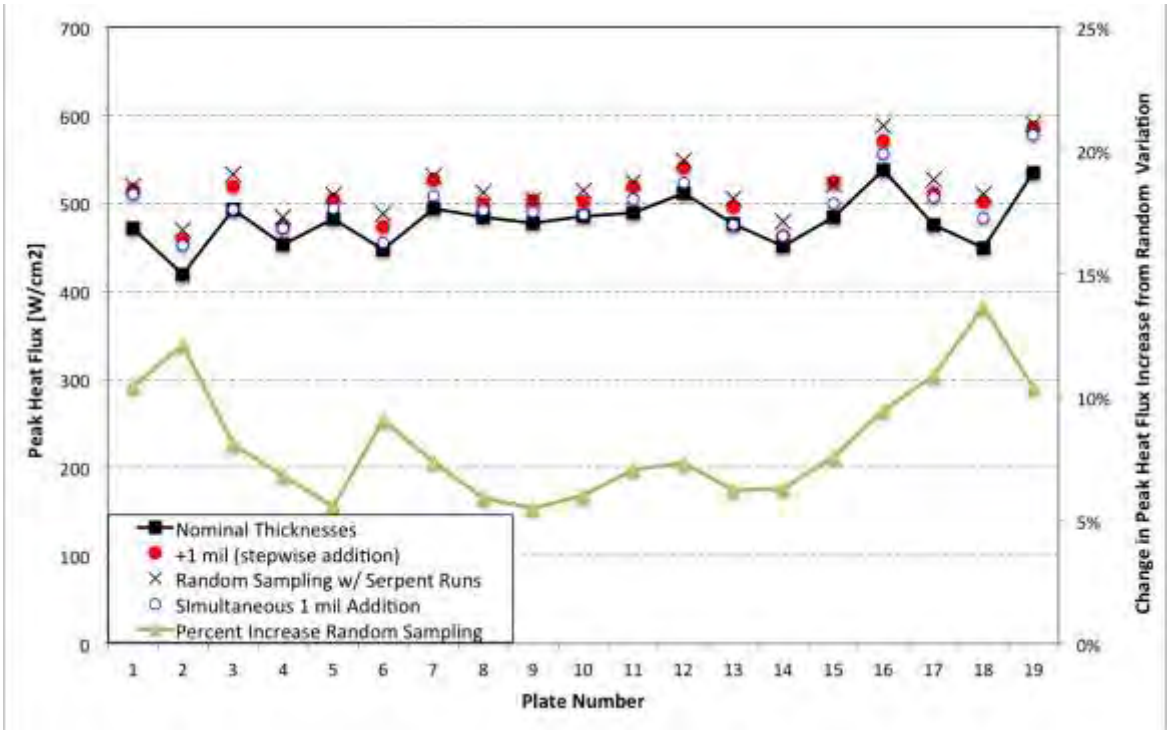


Fig 6. Peak heat flux in each plate of limiting element with different treatments of meat thickness uncertainty in ELF Mk 1B, 63 MW lobe.

4. Conclusions

The two ELF fuel element designs, ELF Mk 1A and ELF Mk 1B, have been identified as leading candidates for conceptual design for an LEU fuel element for ATR. This is the result of a traditional engineering selection process involving many design variations. The field was narrowed based on reactor physics evaluations and thermal-hydraulics (TH) analysis against Naval Reactor performance requirements and nuclear safety criteria. From the initial pool of candidates, three were selected for a detailed trade study, ISBA-Cd, ISBA-B, and ELF. All three of these use fuel meat thickness variation to achieve radial power flattening. From the neutronic and TH analyses performed in the trade study, no significant discriminators were found causing any of these three concepts to be discarded. Ultimately, the fabricability and fuels performance questions associated with elements containing burnable absorbers lead to the adoption of ELF, a fuel element containing no poisons. The ELF fuel is currently conceptualized in two forms, one with three unique fuel meat

thicknesses (Mk 1A) and one with five (Mk 1B). These have approximately 13% more fuel than the original ELF from the trade study, and they have far fewer unique fuel meat thicknesses. Evaluation of the ELF Mk 1A and ELF Mk 1B designs against NR and safety requirements is ongoing. Analyses are also ongoing regarding the impacts of uncertainty in fuel meat thickness. It was determined that there exist plate-to-plate interactions that can contribute to higher heat fluxes when neighboring plates have certain combinations of thicknesses. Therefore, some type of statistical approach is likely necessary in order to determine worst-case impacts of this uncertainty.

5. References

1. G.S. Chang, R.G. Ambrosek, M.A. Lillo, "Advanced Test Reactor LEU Fuel Conversion Feasibility Study (2006 Annual Report),' INL/EXT-06-11887, Idaho National Laboratory. Dec. 2006.
2. G.S. Chang, "ATR LEU Fuel and Burnable Absorber Neutronics Performance Optimization by Fuel Meat Thickness Variation," INL/CON-07-12949, *RERTR-2007 - International Meeting on Reduced Enrichment for Research and Test Reactors*, Prague, Czech Republic, Sept. 2007.5
3. G.S. Chang, "ATR LEU Monolithic Foil-Type Fuel with Integral Cladding Burnable Absorber Design – Neutronics Performance Evaluation," *RERTR 2011 – 33rd International Meeting on Reduced Enrichment for Research and Test Reactors*, Santiago, Chile, Oct. 2011.
4. M.D. DeHart, W.F. Skerjanc and B.K. Castle, "Evaluation of RERTR LEU Conversion Core Physics Analysis Methods," ECAR-1819, Idaho National Laboratory, Feb. 20, 2012.
5. M.D. DeHart, W.F. Skerjanc and S.R. Morrell, "Analysis of the Reactor Physics of Low-Enrichment Fuel for the INL Advanced Test Reactor in support of RERTR," *Proc. ANS Annual Meeting, American Nuclear Society*, Chicago, IL, June 2012.
6. M.D. DeHart, M.A. Pope, D.W. Nigg, R.K. Jamison and S.R. Morrell, "Fuel Element Design and Analysis for Advanced Test Reactor Conversion to LEU Fuel," *Proc. ANS Winter Meeting, American Nuclear Society*, Washington, D.C., November 10-14, 2013.
7. S.S. Kim, B.G. Schnitzler, "Advanced Test Reactor: Serpentine Arrangement of Highly Enriched Water-Moderated Uranium-Aluminide Fuel Plates Reflected by Beryllium," NEA/NSC/DOC/(95)03/II, Volume II, HEU-MET-THERM-022.
8. R. STAMMLER et al., "User's Manual for HELIOS," Studsvik/Scandpower (1994).
9. M. D. DeHART and S. M. BOWMAN, "High-Fidelity Lattice Physics and Depletion Analysis Capabilities of the SCALE 6.0 Code System Using TRITON," *Nuclear Technology*, **174**, 2, 196-213, May 2011.
10. X-5 MONTE CARLO TEAM, "MCNP – A General N- Particle Transport Code, Version 5," Tech. Rep. LA-UR-03- 1987, Los Alamos Scientific Laboratory (April 2003).
11. SERPENT, PSG2 / Serpent Monte Carlo Reactor Physics Burnup Calculation Code, 2011. http://montecarlo.vtt.fi/
12. Idaho National Laboratory, "ATR LEU Fuel Design Trade Study," TEV-1849, Rev. 1, Sept. 9, 2013.
13. M. D. DeHart, "Analysis of Candidate LEU Fuel Designs for ATR," ECAR-1997, Idaho National Laboratory, Aug. 29, 2012.
14. Pope, M. A., "Physics Analysis of the Integral Side-plate Burnable Absorber – Cadmium Wire Fuel (ISBA-Cd) Design," ECAR-2174, Idaho National Laboratory, March 30, 2013
15. M. D. DeHart, "Physics Analysis of the Integral Side-plate Burnable Absorber – Boron Fuel Design," ECAR-2140, Idaho National Laboratory, Mar. 1, 2013.
16. M. D. DeHart, "Physics Analysis of the Enhanced LEU Fuel (ELF) Design," ECAR-2202, Idaho National Laboratory, April 17, 2013.
17. A. P. Cochran Letter to A. J. Bieniawski, "Naval Reactors Functional Requirements for the Advanced Test Reactor," NR:RM:APCochran S#08-04461, Dec 11, 2008.
18. Sutton, T.M., et al., 2007, "The MC21 Monte Carlo Transport Code", Knolls Atomic Power Laboratory and Bettis Laboratory, LM-06K144.

19. X-5 MONTE CARLO TEAM, “MCNP – A General N- Particle Transport Code, Version 5,” Tech. Rep. LA-UR-03- 1987, Los Alamos Scientific Laboratory (April 2003).
20. S. S. Kim and J. A. McClure, “PDQ Reactor Physics Analysis for the ATR-FSAR Upgrade,” Internal Technical Report PG-T-92-003 Rev. 1, Sept. 1993.
21. SAR-153, “Upgraded Final Safety Analysis Report for the Advanced Test Reactor,” Rev. 35, January 2013.

INFLUENCE OF DEPLETED MOLYBDENUM ON MONOLITHIC UMO FUEL PLATE DESIGNS FOR FRM II

H. BREITKREUTZ, A. RÖHRMOSER, W. PETRY
Forschungs-Neutronenquelle Heinz Maier-Leibnitz, FRM II
Technische Universität München, Lichtenbergstr. 1, 85747 Garching, Germany

ABSTRACT

The Mo content in UMo fuels influences the achievable Uranium densities and the parasitic absorption of the fuel. Furthermore, natural Molybdenum contains 15.9% of the isotope ^{95}Mo, a comparably strong absorber for thermal neutrons. The usage of Molybdenum that is depleted in this isotope reduces the parasitic absorption in the fuel.

In this paper, the influence of varying Mo contents and that of depleted Mo for a monolithic fuel plate designs for FRM II with 27% enrichment are discussed. For a constant fuel zone volume, higher Mo contents slightly increase the available neutron flux (+0.3% flux per +1% Mo) but notably decrease the available excess reactivity (-0.1% per +1% Mo), yielding shorter cycle lengths. The usage of depleted Mo decreases the neutron flux (-0.8%) but significantly increases the available excess reactivity (+1.0%). This excess reactivity can be used to change the fuel composition from U 8wt% Mo to the more irradiation stable U 10wt% Mo, shorten the fuel plates to regain flux and further decrease the enrichment to 25%

From an economic point of view, the use of enriched Mo complicates the fuel element production quality assurance and notably increases the costs associated with FE production.

1. Introduction

The “Arbeitsgruppe Hochdichte Brennstoffe” (Working group on high density fuels) of the Forschungs-Neutronenquelle Heinz Maier-Leibnitz (FRM II) is steadily publishing progress reports on the current status of the FRM II conversion and development stages of fuel element designs with increasing complexity [1, 2, 3, 4], step by step decreasing the enrichment to support the international non-proliferation efforts. Large progress has been made in the last years’ time, driving the required enrichment for acceptable operating conditions down to currently 30% for a dispersed and 27% for a monolithic solution [4].

FRM II has defined four conversion criteria, three regarding reactor performance and one regarding economic viability:

- Only marginal flux losses,
- Same cycle length (60d),
- No compromises regarding safety and
- Economic feasibility

The marginal flux loss is generally regarded as a loss of maximal 5%, however, as a concession regarding the overall feasibility towards the common goal of reducing the enrichment as far as reasonably possible, is doubled to maximal 10%.

Up to now, all calculations performed by TUM use a Molybdenum content in the UMo of 8wt% (short: U8Mo). From a neutronic point of view, a smaller Mo content is desirable, as less absorbers are present in the fuel which will increase the overall performance of the core.

Furthermore, less Mo in the fuel allows for higher Uranium densities. From the point of irradiation stability, fuels with higher Mo content have shown slightly superior irradiation behaviour regarding swelling [7, 8]. Furthermore, most knowledge regarding the production of monolithic fuel plates is available only for U10Mo.

In this paper, the question will be investigated how the Molybdenum content in the UMo affects the performance of possible new FRM II core designs. Here this dependency will exemplarily be analysed for the design with 27% enrichment presented at RRFM 2013 in St. Petersburg [5]. In addition, the impact of the usage of Molybdenum depleted in the strongest absorber ^{95}Mo is studied. Combining a change from U8Mo to U10Mo and using depleted Mo, it is possible to further decrease the enrichment to 25% without increasing losses.

2. Variation of Mo content in UMo

The data for the density of various UMo alloys is taken from the ANL U-Mo Fuels Handbook [6]. All calculations are made for a fresh core at the beginning of the cycle (BOC).

Material	Density	U density
U5Mo	18.0 g/cm³	17.1 g/cm³
U7.5Mo	17.6 g/cm³	16.3 g/cm³
U10Mo	17.2 g/cm³	15.5 g/cm³

a. Constant fuel volume

In the first step of the analysis, the total fuel volume of the monolithic meat is kept constant. A variation of the Mo content will therefore cause a difference in the Uranium loading of the core. The geometry of the core is unchanged.

Figure 1 shows the relative flux in the flux maximum in the D_2O tank. The flux is determined by averaging a cylinder of +/- 35cm around core mid-plane. As the rather strong Uranium absorber is replaced by the comparably weak absorbing Molybdenum, the flux slightly rises for increasing Mo content of the core. However, the thermal neutron flux depends not so strongly on the thermal absorption cross section in the core.

In contrast, the cycle length is significantly affected by the varying U content (Figure 2), yielding approximately 3% less excess reactivity for U10Mo and 4% more excess reactivity, i.e. longer cycles for U5Mo compared to U8Mo.[1] From the neutronic side, the excess reactivity is therefore the primary factor influencing the choice of the Mo content if the fuel volume is kept constant.

[1] The difference in the cycle length is a rough estimate based on an average reactivity consumption of $\Delta k=0.0008$ per day towards the end of the cycle.

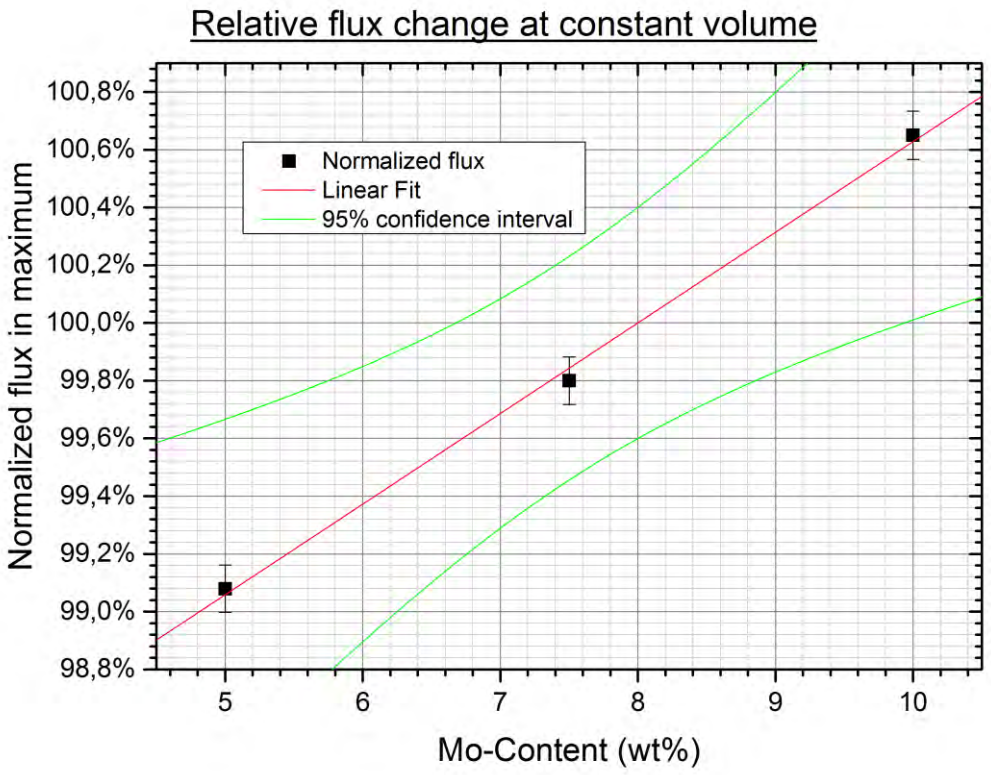


Figure 1: Relative flux change for a variation of the Mo content of the fuel with constant fuel volume. Normalised to U8Mo.

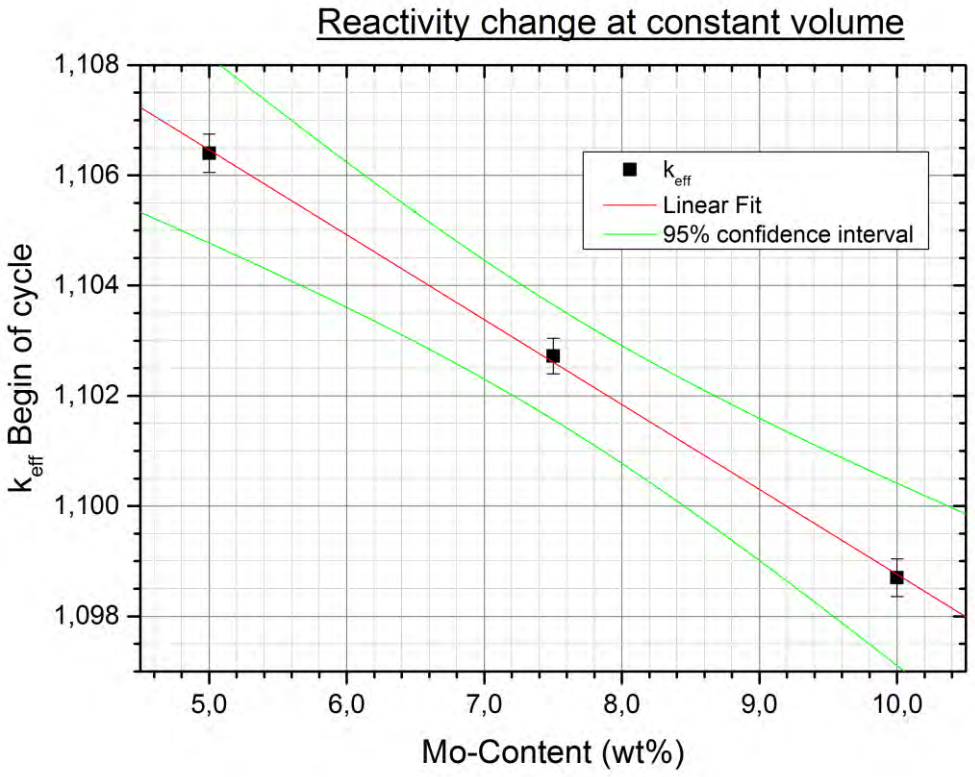


Figure 2: Change of the BOC reactivity for a variation of the Mo content of the fuel with constant fuel volume.

b. Constant Uranium mass

The second scenario covers the change in flux and reactivity if the total Uranium mass (47.5kg in the design with 27% enrichment [5]) in the core is kept constant while the Mo content is varied. This leads to a change of the total fuel volume, which here is taken into account by adjusting the length of the fuel plates.

Figure 3 shows the variation in the flux. The flux increases for a lower Mo content, as the core is more compact due to the shorter fuel plates and contains less absorbers.

The BOC reactivity is shown in Figure 4. It increases for higher Mo contents, as the ratio of Uranium to water in the active zone of the core is altered towards water for the longer plates. For U10Mo, the cycle length is approximately 2 days longer than for U8Mo, for U5Mo it is 4 days shorter. Compared with a total cycle length of 60 days for U8Mo, the reactor performance is again much more influenced by this excess reactivity than by the flux change.

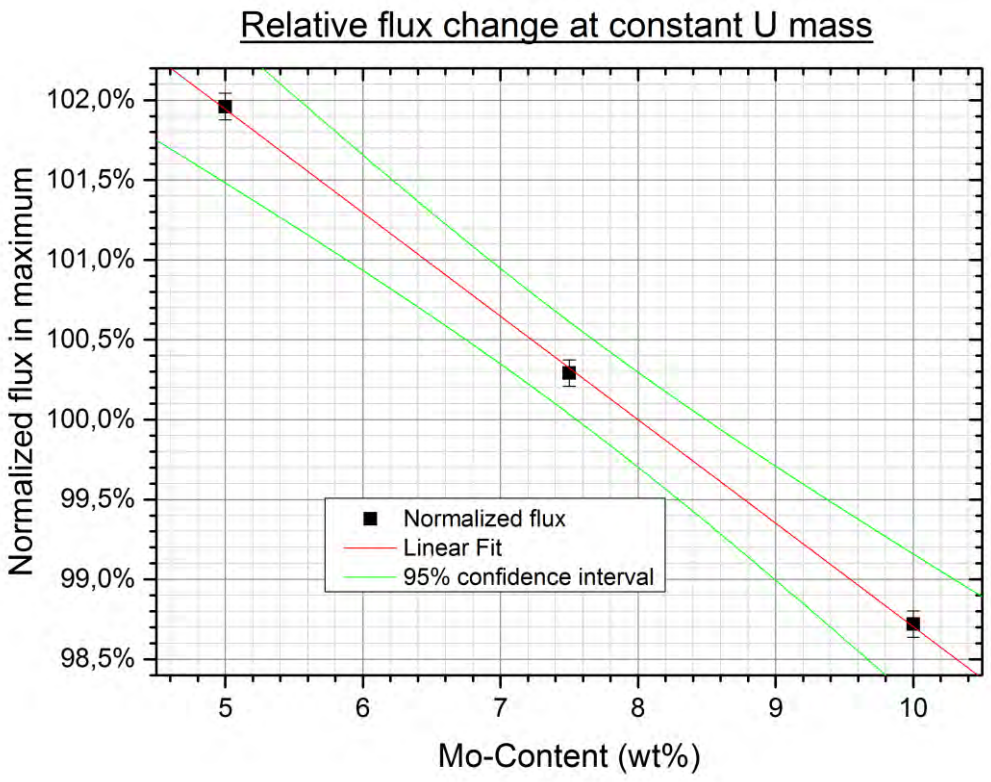


Figure 3: Relative flux change for a variation of the Mo content of the fuel with constant Uranium loading. Normalised to U8Mo.

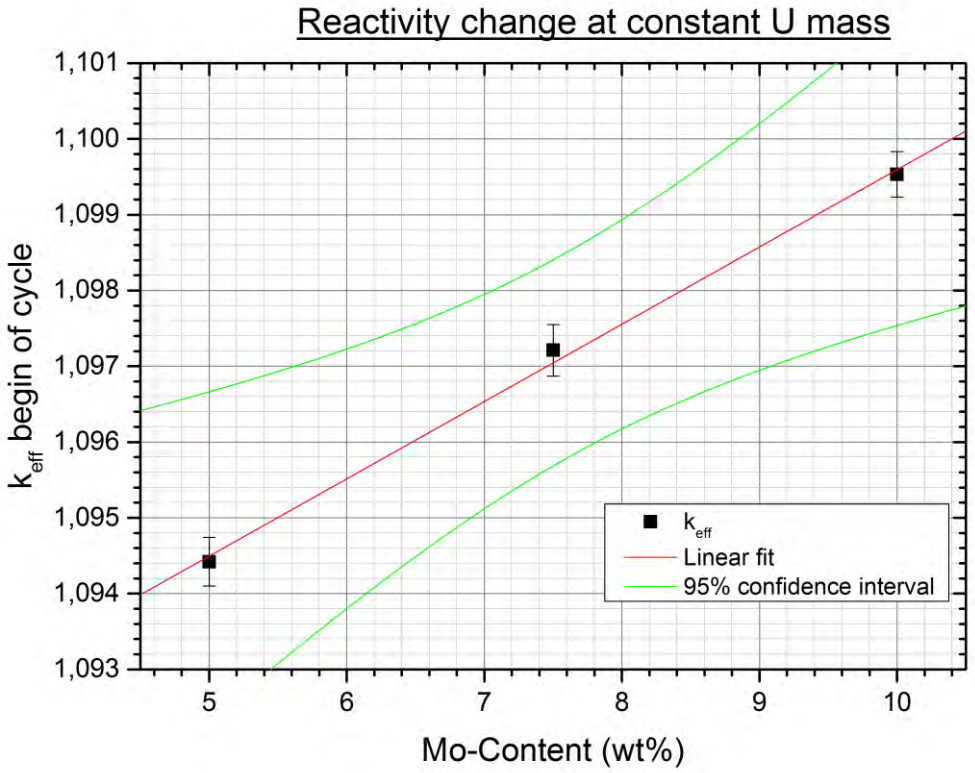


Figure 4: Change of the BOC reactivity for a variation of the Mo content of the fuel with constant Uranium loading.

3. Use of enriched / depleted Molybdenum

Natural Molybdenum contains 7 different stable isotopes, ^{92}Mo, ^{94}Mo, ^{95}Mo, ^{96}Mo, ^{97}Mo, ^{98}Mo and ^{100}Mo. Of these isotopes, ^{95}Mo is by far the strongest absorber with a thermal neutron absorption cross section of 13.4 barn and a natural abundance of 15.90%. For medical ^{99}Mo production, Molybdenum can be depleted in light isotopes (larger ^{98}Mo content) or enriched (smaller ^{98}Mo content). Table 1 shows the natural composition of Molybdenum and of two enriched / depleted sets produced by URENCO Netherlands.

Table 1: Isotopic abundance of different Molybdenum batches. Absorption cross sections are for 25.3 meV neutrons. Data was supplied by URENCO Netherlands.

	Low tail ("Depleted")	Natural	High tail ("Enriched")	Absorption XS
^{92}Mo	87.1%	14.77%	0.11%	0.06 barn
^{94}Mo	8.15%	9.23%	0.13%	0.02 barn
^{95}Mo	3.55%	15.90%	0.44%	13.4 barn
^{96}Mo	0.99%	16.68%	2.09%	0.5 barn
^{97}Mo	0.13%	9.56%	6.26%	2.5 barn
^{98}Mo	0.08%	24.19%	50.39%	0.14 barn
^{100}Mo	0.01%	9.67%	40.57%	0.19 barn

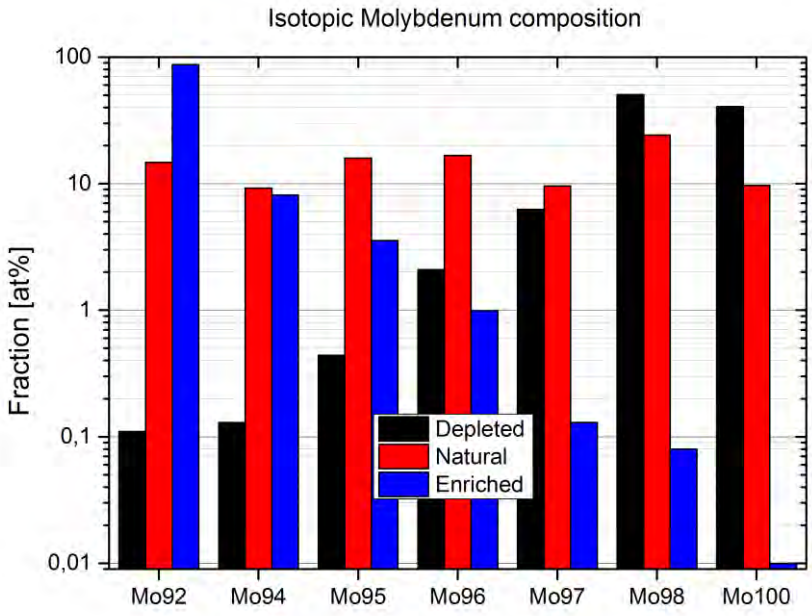


Figure 5: Isotopic composition of different Molybdenum batches. See Table 1. Data was supplied by URENCO Netherlands.

In the following, the use of enriched / depleted Molybdenum [9] will be studied for the U10Mo variant of the RRFM 2013 27%-core. This core is the original U8Mo core, only with replaced fuel at constant fuel volume. The weight densities of the UMo alloy using enriched / depleted Molybdenum are adjusted accordingly to keep the atom density constant.

Figure 6 shows the change in the thermal neutron flux in the flux maximum due to the use of enriched / depleted Molybdenum. No difference between depleted and enriched Molybdenum is observed. The change compared to natural Mo is in both cases -0.8%.

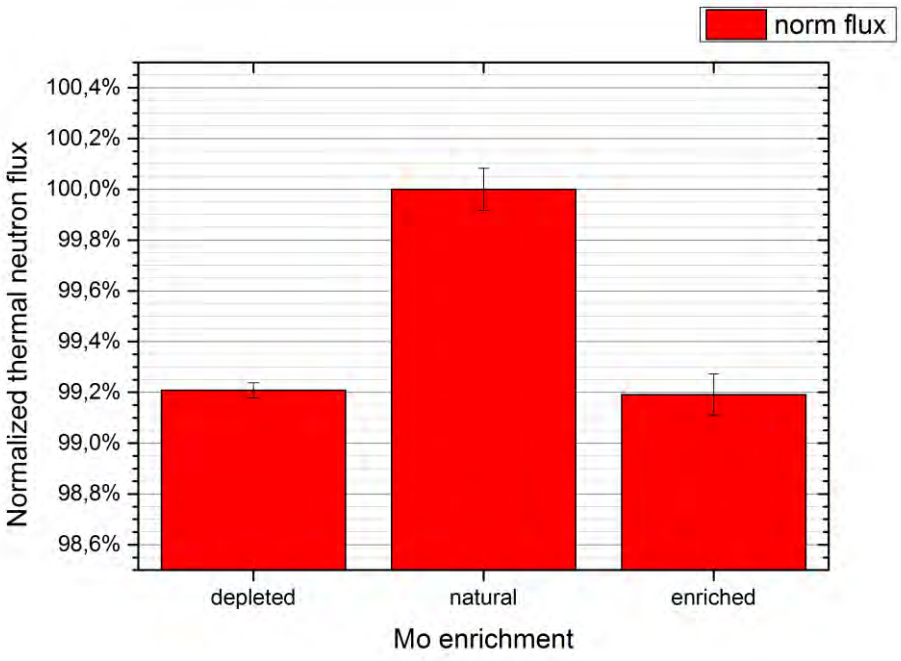


Figure 6: Changes in the neutron flux of the U10Mo core due to the use of enriched/depleted Molybdenum

Significant differences are visible in the excess reactivity (Figure 7) between enriched / depleted and natural Molybdenum. The use of enriched / depleted Molybdenum would lead to a gain of more than 10% excess reactivity, i.e. a longer cycle. This excess reactivity can in turn be invested in a shorter fuel element, increasing the flux slightly and therefore compensating flux losses caused by lower Uranium enrichments or higher Mo content of the fuel (U10Mo in US monolithic plates). The gain in excess reactivity can be explained by the change in the ratio of the fission cross section to the total absorption cross section of the fuel.

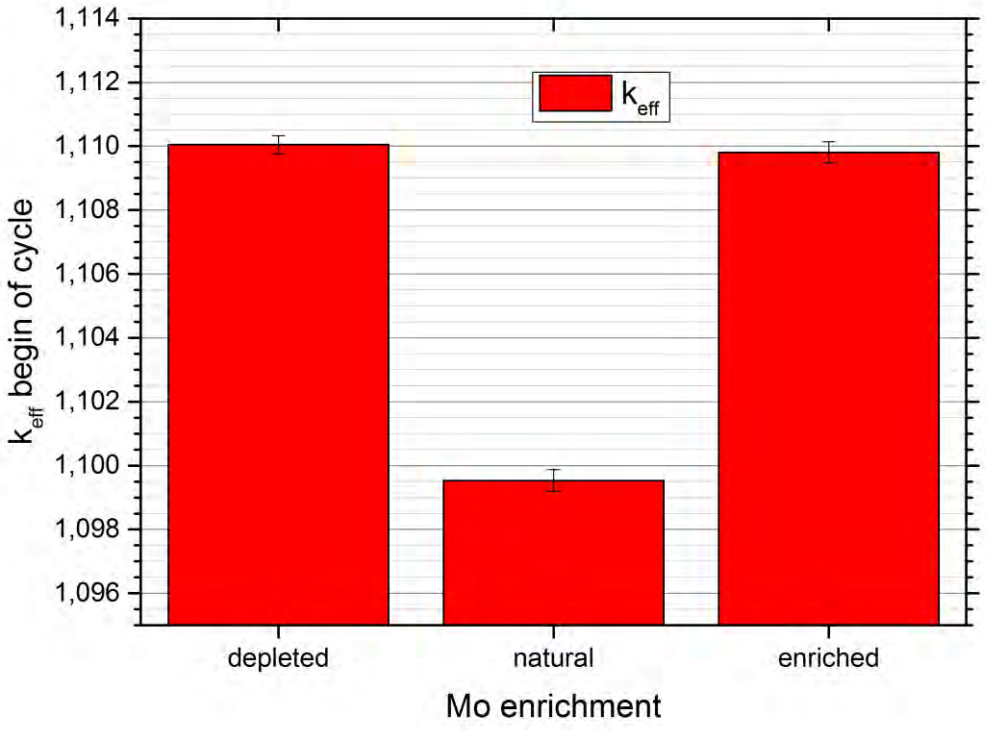


Figure 7: BOC reactivity and change in cycle length due to the use of enriched / depleted Molybdenum

Regarding economic aspects of using enriched / depleted Mo, two aspects have to be taken into account:

- Given current estimations for the price of enriched / depleted Mo, the needed amounts of Mo will significantly increase costs for the fuel element.
- Licensing and quality assurance processes will be complicated by the use of enriched / depleted Mo

4. Using depleted ^{95}Mo to further reduce the Uranium enrichment

Fuel element designs presented by FRM II so far are mainly limited by the three reactor performance conversion criteria defined in section 1. As discussed above, by the combination of the change from U8Mo to U10Mo and the usage of depleted Molybdenum the associated flux changes even out, but some additional excess reactivity is gained. This reactivity can be used to vary the length of the fuel plates and/or decrease the enrichment of the fuel. Again, a combination of both changes allows lowering the enrichment of the fuel while keeping the flux losses at the same level as in [5] and the cycle length at 60 days.

In the present case, the use of depleted Mo allows for a change from U8Mo to U10Mo and a reduction of the enrichment from 27% to 25%. The height-averaged thermal neutron flux is very much comparable (Figure 8). The same holds true for the thermal neutron fluxes at selected beam tubes (Figure 9).

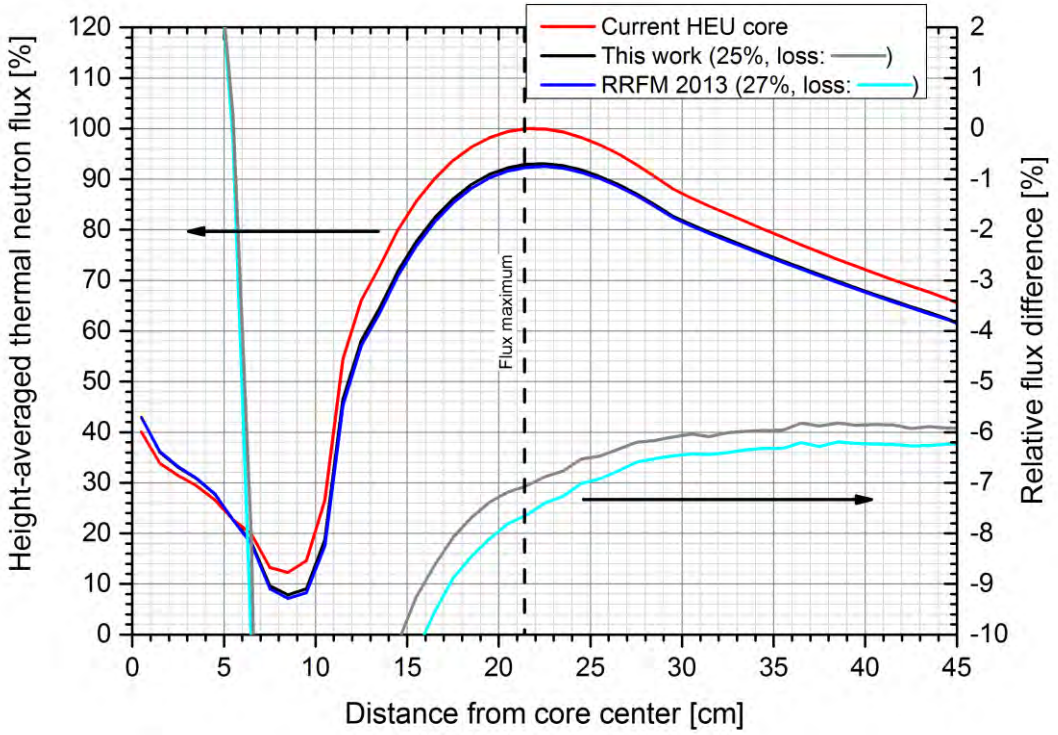


Figure 8: Height averaged flux losses for a reactor model with averaged built-in components. The actual losses at the instruments depend on the positions of the beam-tubes and can be higher. Losses in the point flux maximum are also notably higher. The blue and the black curve overlap strongly.

The thermal hydraulic parameters of the design are also very much comparable to that of the 27% design presented at RRFM 2013 [5]: Max. cladding surface heat flux 384 W/cm², max. cladding surface temperature 90.1°C. It has to be noted that the design presented here features the same aggressive optimisations as the 27% design from [5] and is therefore presented with the same caveats.

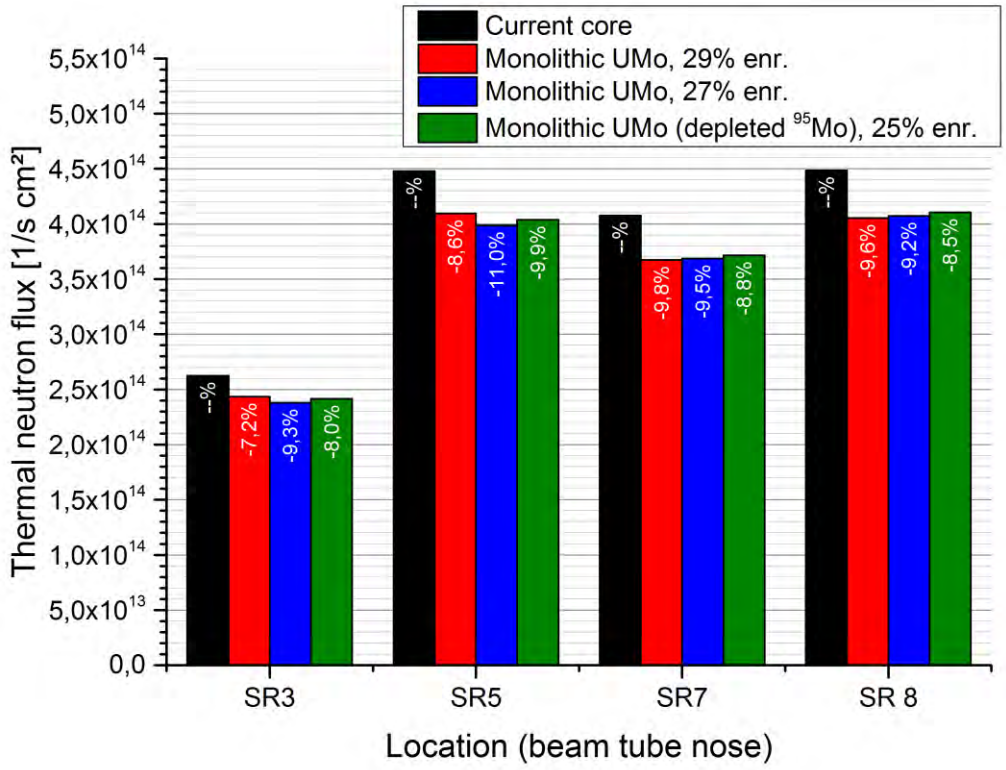


Figure 9: Comparison of expected flux losses in selected beam tubes. The 27% and 29% design were presented in [5].

5. Summary

A small variation of the Molybdenum content in the UMo alloy affects the thermal neutron flux only slightly, no matter if enriched, depleted or natural Mo is used and no matter if the fuel volume or the Uranium mass of the core is kept constant. However, the starting reactivity of the core and therefore the possible cycle length changes significantly. For the monolithic RRFM 2013 design (27% enriched), the use of depleted or enriched Mo would well compensate the losses in reactivity that would have to be accepted when changing from U8Mo to U10Mo. No difference was observed between enriched and depleted Molybdenum.

Combining the change from U8Mo to U10Mo and using depleted Mo, it is possible to further decrease the enrichment from 27% to 25% without differences in the expected flux levels. Again, it should be noted that economic and licensing aspects of the usage of depleted Mo have to be taken into account before the calculations presented here can be considered as a viable solution for FRM II.

Acknowledgements

The authors would like to thank Arjan Bos from URENCO Netherlands for the data on depleted Molybdenum-95 and the discussion on the economic aspects.

This work was supported by a combined grant (FRM0911) from the Bundesministerium für Bildung und Forschung (BMBF) and the Bayerisches Staatsministerium für Wissenschaft, Forschung und Kunst (StMWFK).

References

[1] A. Röhrmoser, W. Petry, N. Wieschalla, “Reduced Enrichment Program for the FRM II, Status 2004/05”, Proceedings of 9th International Topical Meeting on Research Reactor Fuel Management, RRFM, Budapest, 2005

[2] A. Röhrmoser, W. Petry, “Reduced enrichment program for FRM II, actual status & a principal study of monolithic fuel for FRM II”, 10th International Topical Meeting on Research Reactor Fuel Management, RRFM, Sofia, 2006

[3] H. Breitkreutz, “Neutronics and Thermal Hydraulics of High Density Cores for FRM II”, PhD thesis, Technische Universität München, Germany, 2011

[4] A. Röhrmoser, H. Breitkreutz, W. Petry, “Extended studies of FRM II core conversion with UMo dispersive fuel at a prolonged fuel element”, Proceedings of RRFM 2012, Prague, Czech Republic, 2012

[5] H. Breitkreutz, A. Röhrmoser, W. Petry, “Monolithic U8Mo based fuel element designs for FRM II”, Proceedings of RRFM 2013, St. Petersburg, Russia, 2013

[6] J. Rest et. al., “UMo fuels handbook”, ANL-09/31, November 2009

[7] D. A. Lopes, T. A. G. Restivo, R. G. Gomide, A. F. Padilha, “Processing window design for U alloys”, RRFM 2012

[8] Y. S. Kim, G. L. Hofman, J. S. Cheon, “Recrystallyzation and Swelling of U-Mo fuel during irradiation”, RRFM 2012

[9] K. Bakker et. al., “Using Molybdenum depleted in 95Mo in UMo fuel”, RERTR 2002

TEST PLAN FOR MINI PLATES IRRADIATION AND PIE FOR U-7MO FUEL QUALIFICATION

J.S.YIM, , Y.W.TAHK, J.Y.OH, H.J.KIM, B.H.LEE
Nuclear Fuel Design for Research Reactor, KAERI
zip305-353, 111 Daeduok Daero 989 Beon-gi, Yuseong-gu, Daejon, KOREA

J.M.PARK, Y.J.JEONG, K.H.LEE
Research Reactor Fuel Development, KAERI

ABSTRACT

In order to cope with global shortage of Mo-99 supplies and with growing demand of neutron transmutation doping, KJRR construction plan has been launched since April 2012 to provide self-sufficiency of domestic RI demand, and to enlarge Si doping capacity for power device market growth. Through comprehensive surveillance of the fuel in-reactor behavior, KAERI has selected the fuel meat of U-7%Mo/Al-5%Si for Mo contents more than 6% fuel showed a stable and good irradiation behavior in-reactor. As part of effort for fuel qualification of the KJRR fuel, three different mini-plate irradiation and PIE programs designated as HAMP (**HA**naro **M**ini-**P**late Irradiation)-X are planned to supplement the irradiation and PIE data to be obtained from a LTA irradiation and PIE at ATR. This paper describes the plan of HAMP irradiation test and PIE.

1.0 INTRODUCTION

In 2012, KAERI launched a project to construct a new research reactor, of which characteristics are listed in Table 1, in KiJang provincial district near Kori PWR complex. Based on a comprehensive surveillance [1-12] of the fuel similar U-Mo fuel to the KJRR(KiJang Research Reactor) fuel in-reactor behavior, KAERI have decided the fuel meat of U-7wt%Mo/Al-5wt%Si dispersion fuel with 8.0 g-U/cm3 to achieve more efficiency and higher performance than U3Si2 fuel.

Two different shapes of fuel assemblies, 16 standard fuel assemblies and 6 follower fuel assemblies shown in Figure 1 will be loaded in the core. Both FA consist 19 interior plates with uranium density of 8.0 g-U/cm3 and 2 exterior plates of 6.5 g-U/cm3[13].

Since the KJRR fuel will be the first of a kind fuel assembly for commercial utilization, it requires a qualification of the fuel by demonstrating the mechanical integrity, geometric stability, acceptable dimensional changes, and assurance that the performance of fuel meat and fuel assembly (FA) are stable and predictable during irradiation period.

KAERI has plans for licensing and qualification of the new fuel using 3 ways of data acquisition for relevant irradiation properties; 16 mini-plates irradiation in the High-flux Advanced Neutron Application Reactor (HANARO) and post-irradiation examinations (PIEs) in KAERI site, a lead test assembly (LTA) irradiation test at the Advanced Test Reactor (ATR) and PIEs in INL site, and using vast of available irradiation and PIE data obtained from plate wise irradiation and PIE program like as RERTR or European U-Mo development programs such as IRIS-3, IRIS-TUN, and E-FUTURES, etc.

Apart from the irradiation tests, the FA properties can be provided by an out-of-pile flow test and mechanical tests such as a vibration test to yield the vibrational characteristics of a fuel plate and an FA.

All test results will be integrated and compiled to issue a qualification report which demonstrates that the fuel design is adequate, manufacturing technology is acceptable and fuel performance is predictable under certain limits and condition in reactor operation.

As part of the fuel qualification program, three irradiation tests with mini-plates are scheduled to be performed at the HANARO reactor. HANARO located in KAERI site has been being operated successfully since 1995 with variety of neutron utilization facilities and irradiation holes under 30MW thermal power. The core configuration is shown in Figure 2. The maximum thermal neutron flux achievable in the central hole is 5 x 1014 n/cm2-s.
As the irradiation hole (OR-3, etc.) of the HANARO reactor is not sufficiently big to accommodate a full size KJRR fuel plate, mini-plate irradiation tests HAMP-1, 2, and 3 are planned. These mini-plate irradiation tests will provide basic irradiation data including the fuel behavior depending on the level fuel burnup, i.e. low burnup (about 40~45 % U235 depletion), fuel assembly average discharge burnup (about 65 %U235), and local maximum discharge burnup (about 85 % U235). The fuel plate integrity and fabrication robustness are to be verified through the irradiation test including post-irradiation examination (PIE). To assure the mechanical integrity of the fuel plates, the absence of fission product leakage and local deformation such as blisters or pillows will be demonstrated in addition to the identification of acceptable dimensional changes with respect to the design margins. These mini-plate irradiation data and properties will be added supplementary to the LTA test results.

Table 1 Main parameters of the KJRR[14]

Parameter	User Requirement	Design Result
Thermal Power	~ 20 MW	15 MW
Max. thermal neutron flux	> 3.0x1014 n/cm^{2}s	3.37x1014 n/cm^{2}s
Heat Flux Nominal/Peak (W/cm^2)	-	41.5/137
Operation day per year	~ 300 days	> 300 days
Excess reactivity at EOC	> 25 mk	27.6 mk
Reactor life	50 years	50 years
Average discharge burn-up	60~70 %U-235	64.6 %U-235
Cycle length	> 37.5 days	> 50 days
Shutdown margin	> 10 mk	1st : 22 mk, 2nd : 25 mk
Power defect	negative	-0.99 mk
Fission Mo production	2,000 Ci/week	2,300 Ci/week (6 targets)
NTD	150 ton/year	200 ton/year
Flux at HTS, PTS	HTS>1.0x10^{14} n/cm^{2}s PTS >1.0x10^{12} n/cm^{2}s	HTS >1.4x10^{13} n/cm^{2}s PTS >1.2x10^{12} n/cm^{2}s
Number of FA in the Core	-	22(16 standard, 6 follower)
Fuel consumption/year	-	12 EA

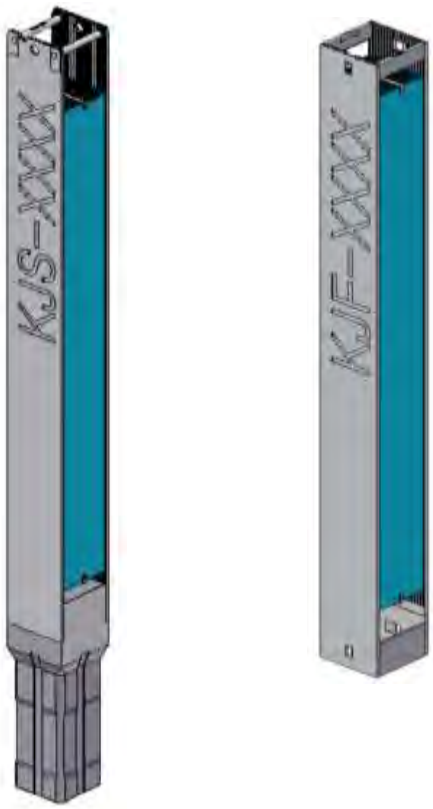


Figure 1 Standard and Follower FA for KJRR

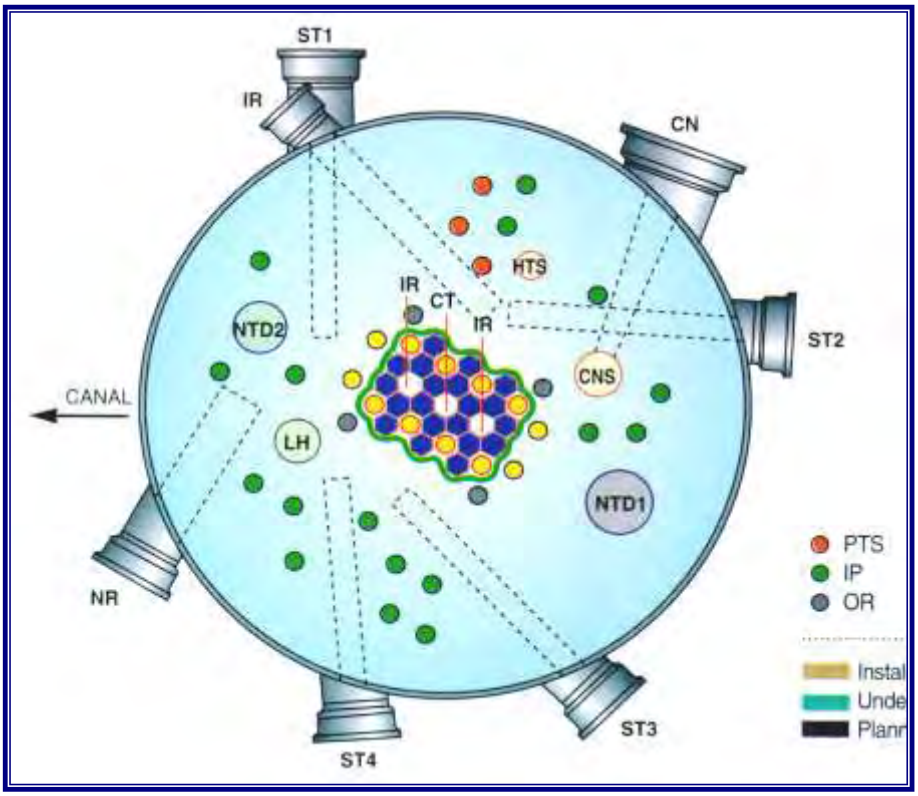


Figure 2 HANARO core configuration

2.0 HANARO IRRADIATION TESTS WITH MINI-PLATES AND PIES

Three times mini plate irradiation and PIE campaign for the total number of 16 mini-plates designated as HAMP-1, HAMP-2 and HAMP3 are planned. Among them HAMP-1 has already been started irradiation since the 28th January 2014.
The overall schedule for three series of mini-plate irradiation is shown in Figure 3. The detailed plan for each step of HAMP-1, 2 and 3 is described in the following subsection.

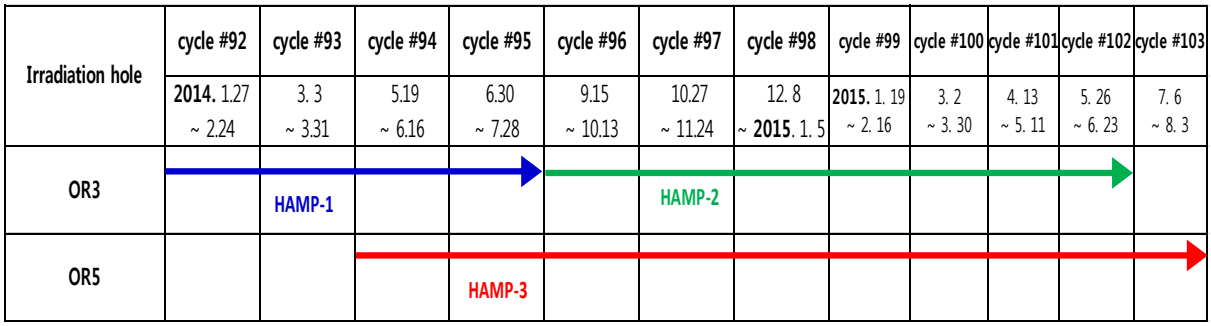


Figure 3 Schedule of fuel design, licensing, irradiation and ~~PIE~~(?)

2.1 HAMP-1 - THE 1ST MINI-PLATE IRRADIATION TEST AND PIE

HAMP-1 was originally scheduled to start from the middle of October 2013 to achieve a low burnup of about 25-35 %U235. However as a consequence of manufacturing delay of the mini plates, irradiation start was delayed from cycle #92 of HANARO and the target burnup was raised up to about 45% U235 depletion. The irradiation duration will be about 112 EFPD (4 cycles of HANARO operation. The mini-plates location in the capsule [15] and irradiation hole (OR-3) position for HAMP-1 in the HANARO core is shown in Figure 4. The irradiation capsule for HAMP-1 consists of 2 clusters and each cluster contains 4 mini-plates as shown in Figure 5. Each plate is to be inserted in the slots at both sides inside the cluster and a stopper will push the plate at its top to restrain its axial movement. If there is any defect in the fabrication, the cause and remedy can be assessed even at the low burnup irradiation. HAMP-1 has a feedback function for the development task and to confirm the fabrication process for the fuel plate of the fuel assembly.
After a cooling period of about 2-3 months, the PIE of the irradiated mini-plates will be performed at the IMEF (Irradiated Material Examination Facility in KAERI). Visual inspection, gamma scanning, density measurement of fuel plate, OM, cladding thickness measurement, oxide layer thickness measurement, blister threshold test, bending test and chemical analysis for burnup determination will be carried out. Since there will be limited number of irradiated plates, the number of samples are to be determined prudently later to obtain the most effective PIE results.
The irradiation conditions [16] can be summarized as follows:

- Irradiation hole : OR-3
- No. of mini-plates : 2 clusters x 4 mini-plates (total 8)
- Average heat flux of mini-plates at beginning of cycle: about 207 W/cm^2
- Local maximum heat flux : about 237 W/cm^2
- Irradiation duration : about 112 EFPD (4 operation cycles of HANARO from the 27th January, 2014, about 6 months of calendar days, including one and half month maintenance outage)
- Expected average burnup : about 45 % U235 depletion

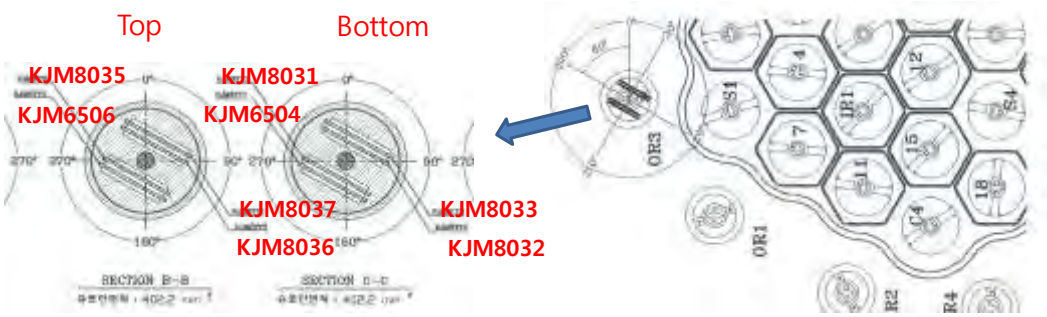


Figure 4 Fuel plate identification and OR-3 position in the HANARO core (1/4 section)

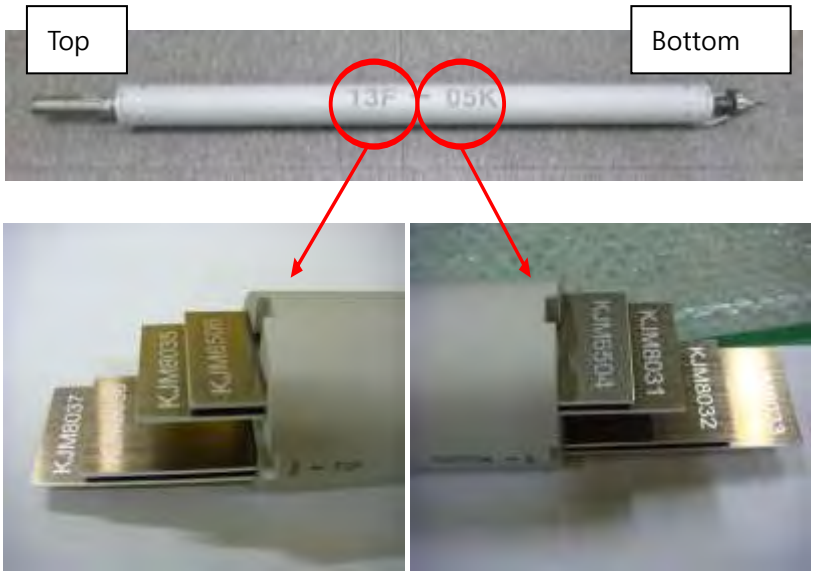


Figure 5 HAMP-1 Capsule and assemble the mini-plates (as of 22. Jan. 2014)

2.2 HAMP-2 - THE 2nd MINI-PLATE IRRADIATION TEST AND PIE

The target burnup of HAMP-2 is about 65%U235, which corresponds to the fuel assembly average discharge burnup of KJRR. The irradiation duration will be about 180 EFPD (7 operation cycles of HANARO, about 10 months of calendar days including 1.5 months maintenance outage). The irradiation capsule for HAMP-2 is expected to be loaded in the same irradiation hole (OR-3) after the HAMP-1 is finished. Thus, the starting date for HAMP-2 might be middle of September 2014, which depends on the completion of HAMP-1 irradiation in OR-3 and completion of the annual HANARO maintenance period.
Four mini-plates will be irradiated in HAMP-2. All other irradiation conditions such as heat flux and dimensions of a mini-plate are the same as HAMP-1. PIE of the HAMP-2 irradiation will commence after a cooling period of about 3 months. The PIE plan is almost the same as described in the HAMP-1 plan.
By successfully performing HAMP-2, the design and fabrication technology for the developed fuel will be verified up to the KJRR fuel assembly average discharge burnup.

2.3 HAMP-3 - THE 3rd MINI-PLATE IRRADIATION TEST AND PIE

HAMP-3 is scheduled to achieve a higher burnup than the local maximum discharge burnup

(about 85 %U-235) of the KJRR fuel assembly.
The width of a mini-plate of HAMP-3 is the same as HAMP-1 and HAMP-2, which is about half the width of a full-size plate. However, the length of a mini-plate of HAMP-3 is the same as that of a full-size plate for the fuel assembly. Thus, the mini-plate of HAMP-3 is called a full-length mini-plate. Four full length mini-plates will be irradiated in HAMP-3. The irradiation duration is expected to be about 250 EFPD (10 operation cycles of HANARO, about 16 months of calendar days including foreseeable 1.5 months maintenance outage). The capsule for HAMP-3 will be loaded in the irradiation hole, which is different from HAMP-2 because the irradiation should run in parallel with HAMP-2. The start date for HAMP-3 will be around middle of May 2014.
Although the irradiation hole for HAMP-3 has not yet been determined, OR-5 is tentatively expected to be used, neutron flux of which is lower than OR-3. Thus, the heat flux of the HAMP-3 would be lower than that of HAMP-1 and HAMP-2.
PIE of the HAMP-3 irradiation will commence in IMEF after a cooling period of about 6 months.
Nondestructive examination and destructive examination of the mini-plates will performed as listed in Table 2.

Table 2 Number of irradiated mini-plate specimen for PIE

Specimens and PIE			
	No. of irradiated plates	NDE (No. of Specimen)	DE (No. of Specimen)
HAMP-1	8	Visual inspection (8), Dimensional measurement (8), Density measurement (8), Gamma scanning (8)	Burnup determination by chemical analysis (4), OM (4), Oxide thickness (4), Blister test (2), 3-point bending test(2)
HAMP-2	4	Visual inspection (4), Dimensional measurement (4), Density measurement (4), Gamma scanning (4)	Burnup determination by chemical analysis (2), OM (2), Oxide thickness (2), Blister test (1), 3-point bending test(1)
HAMP-3	4	Visual inspection (4), Dimensional measurement (4), Density measurement (4), Gamma scanning (4)	Burnup determination by chemical analysis (2), OM (2), Oxide thickness (2), Blister test (1), 3-point bending test(1)

By successfully performing HAMP-3, the design robustness and fabrication technology for the developed fuel will be verified up to the local maximum peak burnup of the KJRR fuel design (85 %U-235). The results of HAMP-3 irradiation and PIE will supplement those of the LTA irradiation at ATR, and will be used as input data for the fuel qualification report also. Since the coolant chemistry (pH) of ATR is far different from that of KJRR, the cladding corrosion data of HAMP-1, HAMP-2, and HAMP-3 will be helpful in evaluation of the corrosion buildup of the KJRR fuel because the coolant chemistry of KJRR is designed to be similar with the HANARO conditions.

2.4 DIMENSION OF MINI-PLATE AND CAPSULE FOR HAMP TESTS

The mini-plates for HAMP-1 and HAMP-2 have a dimension of fuel meat length of 70±5 mm, fuel meat width of 25±1.8 mm, fuel meat thickness of 0.51±0.03 mm, fuel plate length of 130±0.5 mm, fuel plate width of 35±0.2 mm, and fuel plate thickness of 1.27±0.05 mm. The dimensions of mini-plates for HAMP-1, HAMP-2, and HAMP-3 are summarized in Table 1.

Table 3 Mini-plate dimension

(unit : mm)	HAMP-1	HAMP-2	HAMP-3
Fuel meat	0.51 x 25 x 70	0.51 x 25 x 70	0.51 x 25 x 600
Fuel plate	1.27 x 35 x 130	1.27 x 35 x 130	1.27 x 35 x 640
No. of Plate (8.0 g-U/cm^3)	6	4	4
No. of LDU Plate (6.5 g-U/cm^3)	2	0	0

The fuel meat will consist of an aluminum matrix dispersion of uranium 7 wt% molybdenum (U-7Mo) metallic alloy with a U235 enrichment of 19.75%. Two kinds of fuel meat with a uranium density of 8.0 g-U/cm^3 and low density uranium (LDU) of 6.5 g-U/cm^3 will be used for 19 inner plates and 2 outer plates of the KJRR fuel assembly, respectively. The matrix will also contain 5wt% silicon. Aluminum alloy 6061 will be used as the fuel cladding. Fabrication will be done by utilizing the hot roll bonding process to manufacture the fuel plates.
Six mini-plates among the total of eight mini-plates to be irradiated in HAMP-1 will consist of fuel meat with a uranium density of 8.0 g-U/cm^3. Two other mini-plates will consist of fuel meat with a uranium density of 6.5 g-U/cm^3 to simulate the outer fuel plates.
Four mini-plates among the total of four mini-plates to be irradiated in HAMP-2 will consist of fuel meat with a uranium density of 8.0 g-U/cm^3.

2.5 TEST REQUIREMENTS FOR HAMP TESTS & PIE

To ensure the fuel integrity and reactor safety during an irradiation test, the following test conditions and requirements for irradiation & PIE should be complied.

2.5.1 IRRADIATION TEST REQUIREMENTS

Irradiation Test requirements for the HAMP are summarized below;

- Coolant chemistry : pH 5.5 - 6.2
- Coolant inlet temperature in the channel (irradiation capsule) : < 35 ℃
- Coolant velocity in the channel : 11.65 (TBD) m/sec (For information, the upper limit of coolant velocity is about 16 m/sec corresponding to 2/3 of the critical velocity for flow induced vibration of the mini-plate.)
- Heat flux of mini-plate with a fuel meat uranium density of 8.0 g-U/cm^3 for HAMP-1 and HAMP-2 : avg. 207 W/cm^2, max. 237 W/cm^2
- Heat flux of mini-plate with a fuel meat uranium density of 6.5 g-U/cm^3 for HAMP-1 and HAMP-2 (TBD) : avg. 176 W/cm^2, max. 197 W/cm^2
- Heat flux of mini-plate for HAMP-3 : avg. 174 or 10% lower (TBD) W/cm^2, max. 212 (or 10% lower) W/cm^2

2.5.2 FUEL AND THERMAL HYDRAULIC DESIGN LIMIT AND REQUIREMENTS FOR IRRADIATION

Irradiation test requirements for fuel and thermal design limit of the HAMP are summarized below;

- The maximum fuel temperature for normal operation: 200 ℃
- The maximum fuel temperature for AOO : temporally 400 ℃
- Fuel plate thickness increase including swelling and cladding oxidation should not exceed 20% (temporally).
- The temperature drop across the corrosion layer of fuel cladding should not exceed 114°C
- The maximum surface temperature of the fuel cladding should be less than the saturation temperature at that position.

3.0 CURRENT STATUS AND FUTURE WORK

Fuel plate manufacturing equipment as well as FA assembling and inspection equipment has been installed in the HANARO fuel manufacturing building. Prior to fabrication of the mini plates for HAMPs, not only specification and drawings but also QA programs and procedures have been established. After safety analysis of the HAMP-1 irradiation in HANNARO, permission of the mini plate irradiation has been granted by safety committee of KAERI. The HAMP-1 capsule was inserted in the core on the 23th January of the Cycle number 92 and irradiation has been undergoing from the 27th January 2014.
Mini plates manufacturing for HAMP-2 and HAMP-3 is under progressing supposed to insert them in September for HAMP-2 and May for HAMP-3 in 2014, respectively.
Apart from the plates manufacturing, safety analysis of the HAMP-2 and HAMP-3 will be performed to obtain permission for the irradiation tests at HANARO.

4.0 CONCLUSIVE REMARKS

In order to overcome the shortage of domestic RI production in KOREA, KJRR construction project has been being progressing since April 2012. Through comprehensive surveillances of U-Mo fuel irradiation and PIE results, the fuel for the KJRR was selected to be U-7wt%Mo powder made by KAERI own manufacturing technology, known as a centrifugal atomization process, and dispersed in an aluminum matrix of 5wt%Si. Regarding the licensing and qualification of the fuel, 3 times irradiation tests with total 16 mini-plates and their PIE together with a LTA irradiation in ATR is planned and has been under progressing.

The HAMP tests will generate supplementary irradiation and PIE data to be used for the acquisition of licensing the fuel for the KJRR. An exact PIE plan will further be determined and the results of the HAMP PIE will help to clarify KJRR fuel behavior in the core, especially will produce valuable results of the oxidation build up on the fuel plate since the LTA in ATR will be irradiated at a different coolant pH value, much lower than the KJRR coolant condition.

After success the irradiation test of the KJRR fuel and being qualified, the U-7Mo fuel is expected hopefully to be used for fuel conversion from relevant power range of Research Reactors.

5.0 REFERENCES

[1] KAERI/RR-2359/2002, Final Research Report for the advance fuel development for RRs, C. K. KIM et al, 2002

[2] D. M. Perez, M. A. Lillo, G. S. Chang, G. A. Roth, N. E. Woolstenhulme, D. M. Wachs, RERTR-6 Irradiation Summary Report, Dec. 2011
[3] D. M. Perez, M.A. Lillo, G. S. Chang, G. A. Roth, N. E. Woolstenhulme, D. M. Wachs, RERTR-7 Irradiation Summary Report, Dec. 2011
[4] D. M. Perez, M.A. Lillo, G. S. Chang, G. A. Roth, N. E. Woolstenhulme, D. M. Wachs, RERTR-9 Irradiation Summary Report, May. 2011
[5] D. M. Perez, M.A. Lillo, G. S. Chang, G. A. Roth, N. E. Woolstenhulme, D. M. Wachs. AFIP-1 Irradiation Summary Report, May, 2011
[6] D. D. Keiser, Jr., D. M. Wachs, M. K. Meyer, A. B. Robinson, P. Medvedev, G. A. Moor, Microstructural Analysis of Irradiated U-Mo Fuel Plates : Recent Results, RERTR 2012
[7] A. B. Robonson, D. M. Wachs, D. E. Burkes, D. D. Keiser, US RERTR Fuel Development Post-Irradiation Examination Results, RERTR, 2008
[8] A. B .Robonson, D. M. Wachs, G. S. Chang, M. A. Lillo, Summary of 'AFIP' Full Sized Plate Irradiations in the Advanced Test Reactor, RRFM, 2010
[9] D. D. Keiser, Jr., A. B. Robinson, D. E. Janney, J. F. Jue, Results of Recent Microstructural Characterization of Irradiated U-Mo Dispersion Fuels with Al Alloy Matrices that Contain Si, 12th Annual Topical Meeting ogn Research Reactor Fuel Management, Mach, 2008
[10] G. L. Hofman, Y. S. KIM, H. J. Ryu, D. W. Wachs, M. R. Finlay, Resutls of Low Enriched U-Mo Dispersion Fuel miniplates from Irradiation Test, RERTR-6, RERTR 2006
[11] Leenaers, J. Van Eyken, S. Van den Berghe, E. Koonen, F. Charollais, P. Lemoine, Y. Calzavara, H. Guyon, C. Jarousse, B. Stepnik, D. Wachs, A. Robinson, LEONIDAS E-FUTURE : Results of the Destructive Analyses of the U(Mo)-Al(Si) Fuel Plates
[12] S. Van den Berghe, Y. Parthoens, F. Charollais, Y. S. Kim, A. Leenaers, E. Koonen, V. Kuzminiv, P. Lemoine, C. Jarousse, H. Guyon, D. Wachs, D. Keiser Jr., A. Robinson, J. Stevens, G. Hofman, Swelling of U(Mo)-Al(Si) Dispersion fuel under irradiation-Non-destructive analysis of the LEONIDAS E-Future plates, J. of Nuclear Material 430(2012) 246-258
[13] KJ-372-KN-416-001, Design specification of Standard and Follower Fuel assembly
[14] IGORR-2013, SI Wu, Status of the KJRR Construction Project, Daejeon, Oct. 2013
[15] HAN-IC-DW-13F-05K-ASS'Y, Rev. 0, "Irradiation Capsule for Mini-Plate Fuel", Korea Atomic Energy Research Institute.
[16] "Request for HANARO safety committee on HAMP-1 irradiation test", HAN-IC-CR-13-013 Sep., 2014 and "Meeting minutes on the 65th HANARO safety committee", HAN-SL-MN-1001-13-004, Oct., 2014.
[17] KJ-374-KN-416-001, Rev.0, "Design Specification of Mini Plate for HANARO Irradiation Test ", Korea Atomic Energy Research Institute.
[18] KJ-374-KN-192-001, Rev.0, "Mini Plate for HANARO Irradiation Test I,II ", Korea Atomic Energy Research Institute.
[19] KJ-374-KN-192-002, Rev.0, "Mini (Full Length) Plate for HANARO Irradiation Test III", Korea Atomic Energy Research Institute.
[20] KJ-372-KN-422-002, Fuel Design Report

RESULTS OF THE TRIAL OF LEAD TEST ASSEMBLIES IN THE WWR-K REACTOR*

F. ARINKIN, P. CHAKROV, L. CHEKUSHINA, SH. GIZATULIN,
S. KOLTOCHNIK, D. NAKIPOV, A. SHAIMERDENOV

The Institute of Nuclear Physics, Atomic Energy Committee, Ministry of Industry and New Technology,

1 Ibragimov str., 050032, Almaty – Republic of Kazakhstan

N. HANAN, P. GARNER AND J. ROGLANS-RIBAS

The Argonne National Laboratory,
9700 South Cass Av., Argonne, IL, 60439 - USA

ABSTRACT

As is known, in-reactor trial of a batch of lead test assemblies (LTA) is the last and the most important pre-fabrication stage. For the WWR-K reactor conversion to low-enriched fuel, eight-tube FAs with thin-walled FEs, 1.6mm thick, is proposed. Uranium density in fuel composition, UO_2-Al, is 2.8 g·cm^{-3}, meat is 0.7 mm thick.

In-reactor trial of three lead test assemblies was started in the WWR-K reactor core in March of 2011 and were completed after 480 days of reactor operation (23 operation cycles) in July of 2013. In two lead test assemblies the average burnup ≈60% was reached. Fortunate configuration of the core was chosen, which made it possible to carry out the trial faster.

Results of the accompanying calculations and controlled parameters of the trial are presented in the report.

INTRODUCTION

Today the points concerning provision of nonproliferation regime for fissile materials of high enrichment are vitally important. In particular, the activities related to provision of nonproliferation via conversion of the Kazakhstan research reactors, including critical assembly, to low enriched fuel are significant.

In the Kazakhstan Institute of Nuclear Physics (KINP), the WWR-K research reactor and critical assembly are being converted to the fuel enriched to 19.7% in isotope U-235. The studies performed at the KINP in a period of 2004 to 2008 [1-4] have made it possible to make a choice in favor of the fuel assemblies (FAs) containing thin-wall (thickness 1.6 mm) tubular fuel elements (FE seven having hexagonal cross section and the inner one - circular), named as the FA of the WWR-KN type. In March of 2011 in the WWR-K reactor trials of three lead test assemblies (LTA) of the WWR-KN type were started [5].

The trials were divided into three stages, related to achievement of pre-specified level of average burnup in LTAs (20, 40 and 60%). In course of the trials the following parameters were monitored: the LTA power, a level of radioactivity in coolant and the neutron flux density in irradiation device with LTAs. The trials were accompanied by calculations on determination of Uranium burnup, both in LTAs and all FAs in the core, as well as on optimization of refueling between operation cycles in view of provision of specified trial parameters.

Results of calculation of neutron-physical characteristics of the core with side beryllium reflector and the chosen low-enriched fuel composition and FA design have shown that, despite reduction of enrichment, reactor operational characteristics are improved.

* This work was supported by the U.S. Department of Energy

LTA LIFE TEST IN THE WWR-K REACTOR CORE

In compliance with the Kazakhstan regulatory documents in force, prior to a start of fabrication of new FAs, in-reactor trial of a batch of lead test assemblies against its design characteristics is mandatory. INP specialists jointly with specialists from the Argonne National Laboratory (USA) and NIKIET (RF) developed reasonable program of LTA trials and carried out substantiation of safety for LTA trials in the WWR-K reactor core, which includes analysis of the core steady states, thermal hydraulic calculations and analysis of potential transients. Jointly with the LTA developer (NIKIET), a decision was taken on trial of LTAs in the core with high-enriched fuel. Regulatory body issued permission for implementation of the trials. In February of 2011 in the Novosibirsk Chemical Concentrate Plant (NCCP) three LTA were manufactured, and in March of 2011 the LTAs life test in the WWR-K reactor core was started. The trials were assumed to be carried out in tree stages: on achieving average burnup in LTAs 20, 40 and 60%, with visual examination of one of LTAs after completion of each stage.

Following results of neutron-physical calculation of the WWR-K reactor core with low-enriched fuel, the power of the hottest FA comprises ≈360 kW. In view of provision of the same power level, we had to reduce the existing core, enhancing the specific power density in it. So, in the FAs from the outer circle of the core were replaced by 22 blocks of beryllium, which form side reflector. In addition, in the core center seven FAs were removed, and irradiation device, made of beryllium, was installed. The device made it possible to install three LTAs with the 68.3mm spacing and the assured 2-mm gap between the LTA - for coolant flow.

The core map for a start of trial (38 regular WWR-C-type FAs, 3 LTA inside beryllium device and 28 units of beryllium side reflector) and for an end of the trial (33 regular WWR-C-type FAs, 3 LTA and 38 units of beryllium side reflector) are presented in Figure 1 ((a) and (b) respectively).

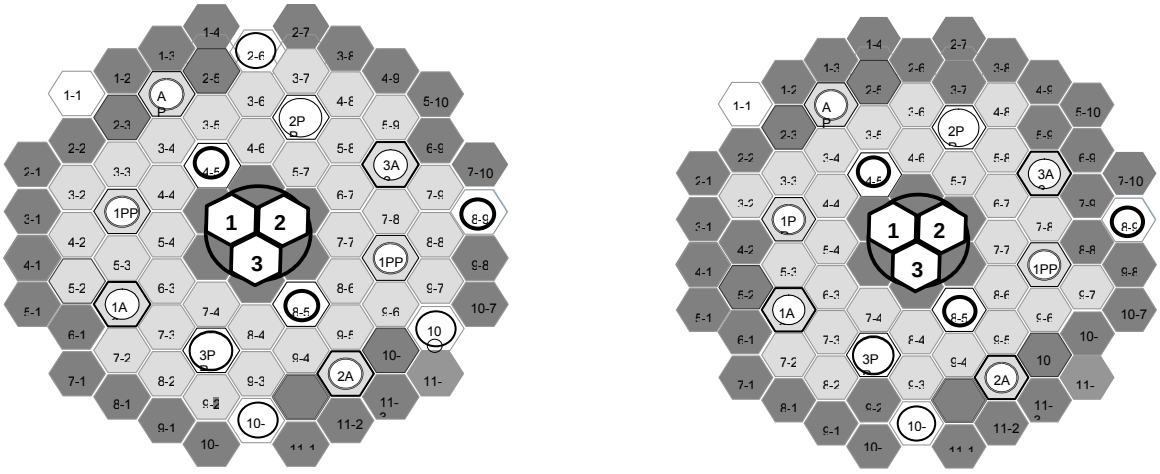


Fig.1. The WWR-K reactor core maps for LTA test (a) start and (b) end

The beryllium irradiation device was equipped by extra systems of monitoring of irradiation conditions. Two self-powered neutron detectors (SPND) with rhodium emitter were used to monitor the neutron flux density. Three thermocouples (chromel-alumel) were used for measuring of the coolant temperature (T_1) at the irradiation device entrance and (T_2, T_3) at exit. Figure 2 shows allocation of LTAs, temperature sensors and SPND in irradiation device.

Three thermocouples and SPND-1 were allocated in the channel 1 of irradiation device; SPND-2 was allocated in channel 2.

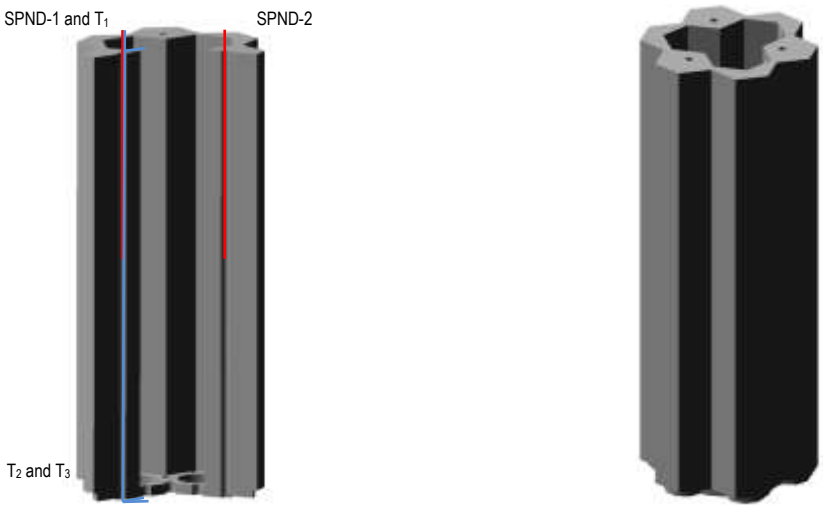


Fig.2. Schematic representation of irradiation device

Experimental support of the LTA trials was implemented by means of the information-measuring system (IMS), which provided operators and experimentalists with current values of the main parameters of the trial: temperatures at the irradiation device entrance and exit and SPND readings, which were recorded uninterruptedly.

Scientific support of in-reactor trials included:

- Calculation of values of the neutron flux density in irradiation device, the LTA generated power, reactor power and a level of radioactivity in coolant;
- Calculation of values of the burnup of Uranium-235 in LTAs and FAs of the core;
- Determination of optimal refueling between operation cycles - to provide prescribed parameters of the trials.

Stability of neutron field in irradiation device is illustrated by Figure 3, where readings of the SPND installed in irradiation device are given.

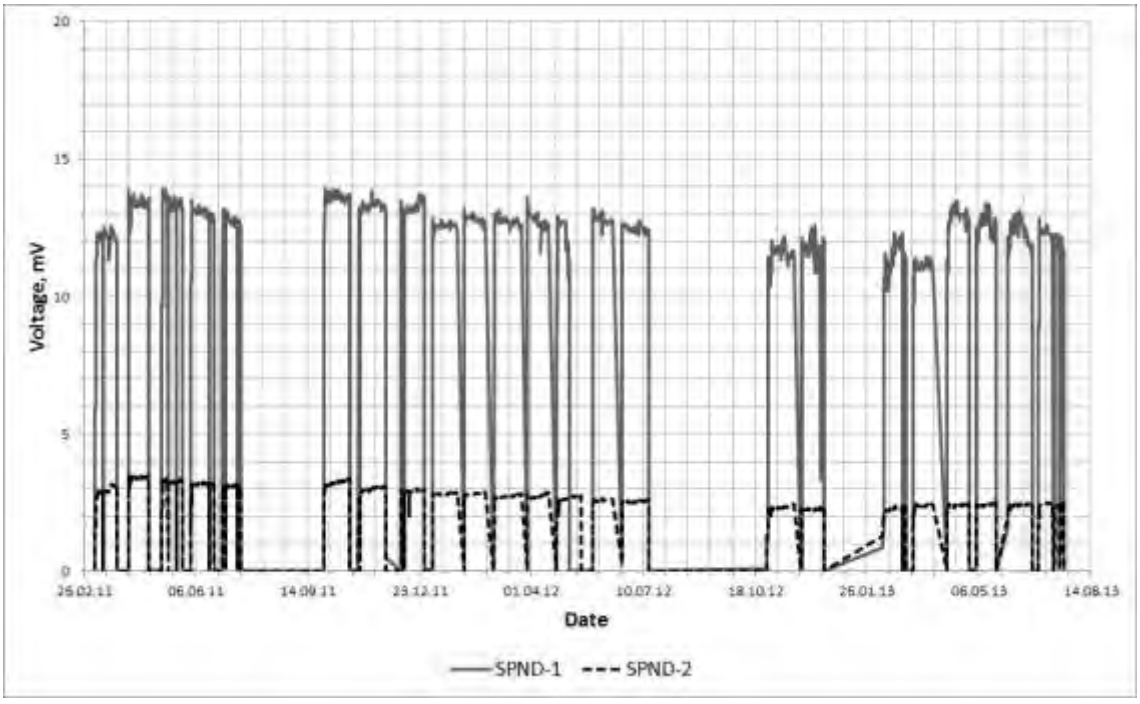


Fig. 3. Variation in SPND readings for period of the trials

Abrupt falls in the SPND readings within operation cycle are caused by actuation of emergency protection which happened, as a rule, in case of emergency loss of external power supply. Difference in readings of SPND-1 and SPND-2 is caused by its different load resistances.

With readings of thermocouples and values of coolant flow rate across LTA taken into consideration, the maximum power of three LTAs at a moment of start of the first operation cycle comprised 1054 kW, being in agreement with the relevant design value. (Uncertainty in power determination 10%.) The relevant calculated value is 1047 kW. The power of the hottest LTA comprised ≈360 kW, being in agreement with the design value of power for the hottest FA in LEU fuel core to a moment of the reactor energy startup.

Figure 4 shows variation in the net power of three LTAs (dashed line: result of calculation). The figure demonstrates good agreement between calculations and experiment.

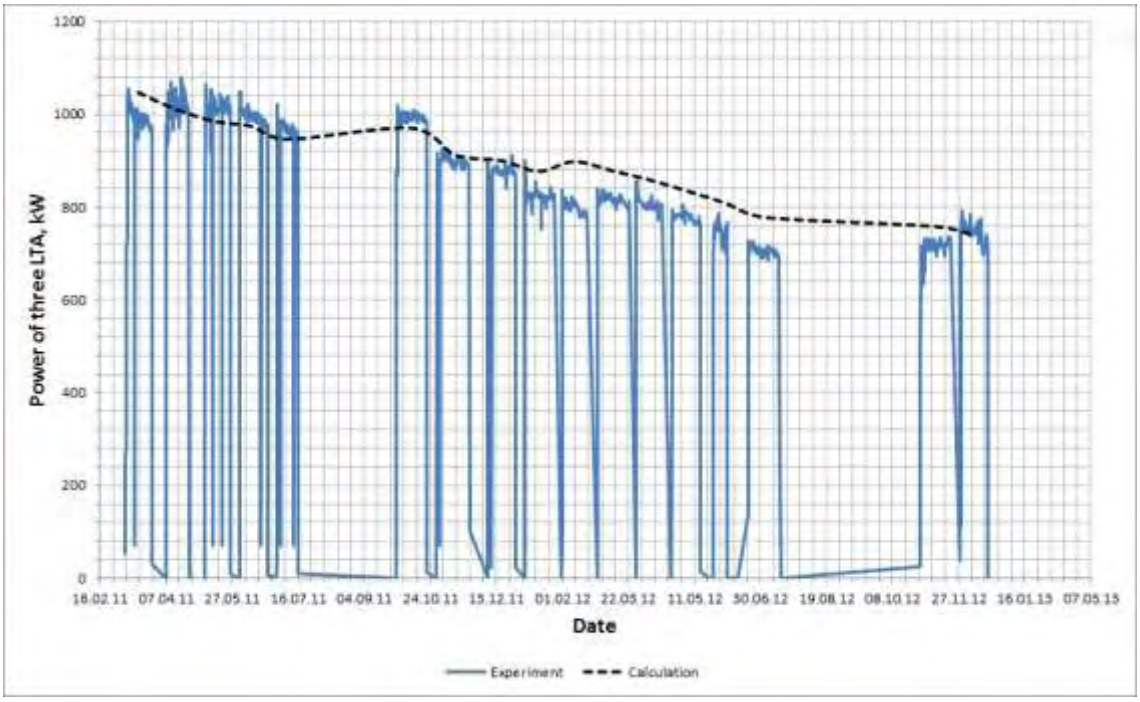


Fig 4. Temporal variation in the net power of three LTAs. Operation cycles 1 through 17.

Variation of the core excess reactivity versus time of reactor operation is shown in Figure 5.

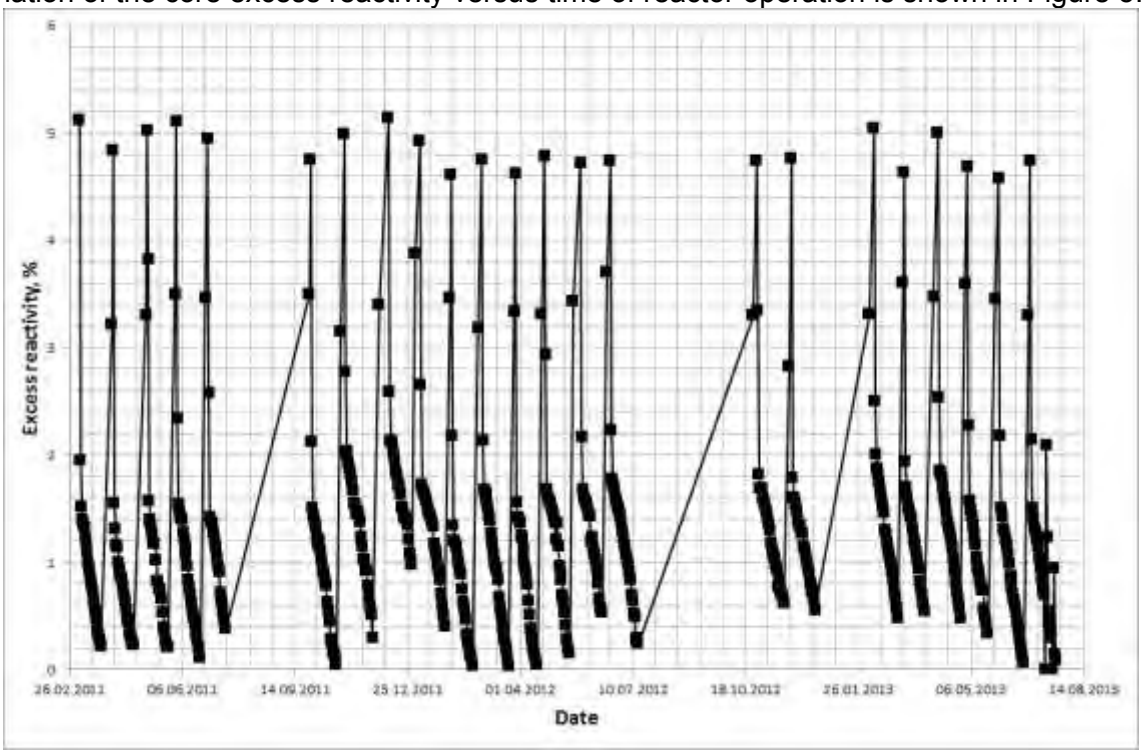


Figure 5. Temporal variation of the excess reactivity over 23 operation cycles of the trials

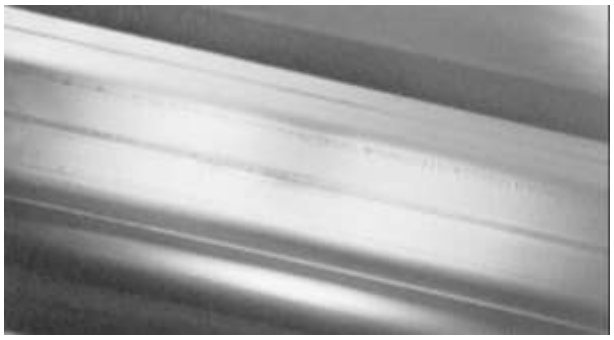
In view of control of integrity of LTA clad in course of the trials, primary-circuit water was sampled every day; the samples of water were analyzed against presence of cesium and other fission products. The found content of cesium in coolant does not exceed 500 Bq/l, which is the relevant background value for the WWR-K reactor (coolant quality norms (regulatory requirements) for fission product total activity is not more than 2.5 10^7 Bq/l).

Every operation cycle of LTA trials was accompanied by computational simulation by means of the computational 3D code MCU-REA [6] with calculation of optimum refueling in the core, determination of reactivity margin to a moment of the cycle start, variation in the excess reactivity over a cycle, calculation of fuel burnup in all FAs of the core, including LTAs.

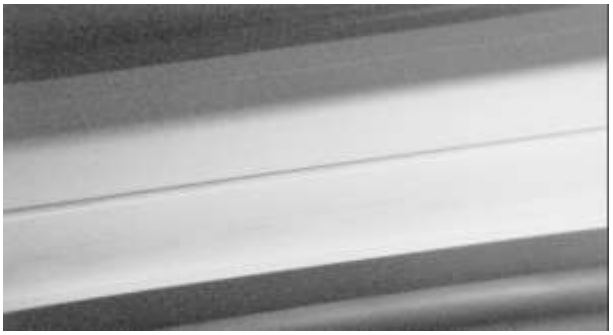
In the end of 2012, during operation cycle #17, an increase in the gas activity above the core mirror as well as an increase in the coolant activity by reference isotope Cesium-137 had occurred. The activity increase of this kind is a sign of loss of sealing in one of FAs in the core. On completing the 17-th cycle the trials were stopped. In January of 2013, all LTAs were removed from the core. Activity of the coolant passing through LTA was measured by immersion technique. Results of measurement pointed to leak in LTA1. A decision was taken on continuation of the trials with replacement of defective LTA by a similar new one. Leaked LTA was placed in wet storage for subsequent study of reasons for leaking. The trials were continued. To a moment of the trial stopping, burnup in LTA1 comprised 49.7%.

The net duration of the trials comprised 480 days; in LTA2 and LTA3 the achieved burnup comprised 59.7 and 60.3% respectively.

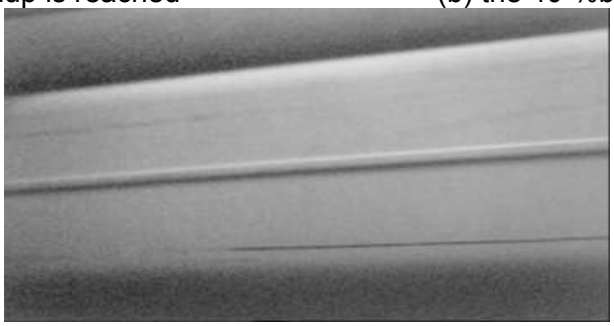
On completion of every stage of the trials flats of every LTA were examined visually. Results of visual examination are given in figure 6.



(a) the 20-% burnup is reached



(b) the 40-%burnup is reached



(c) the 60-% burnup is reached

Fig. 6. LTA 3. Central section over the height

ANALYSIS OF TEST RESULTS

Trials of the low-enriched VVR-KN LTAs in the WWR-K reactor were completed. Duration of the life test comprised 357 days for LTA1 and 480 days for LTA2 and LTA3. To an end of the test burnup of Uranium-235 reached 49.7% in LTA1, 59.7% in LTA2 and 60.3% in LTA3. Dynamics of burnup of Uranium-235 over the test is presented in figure 7.

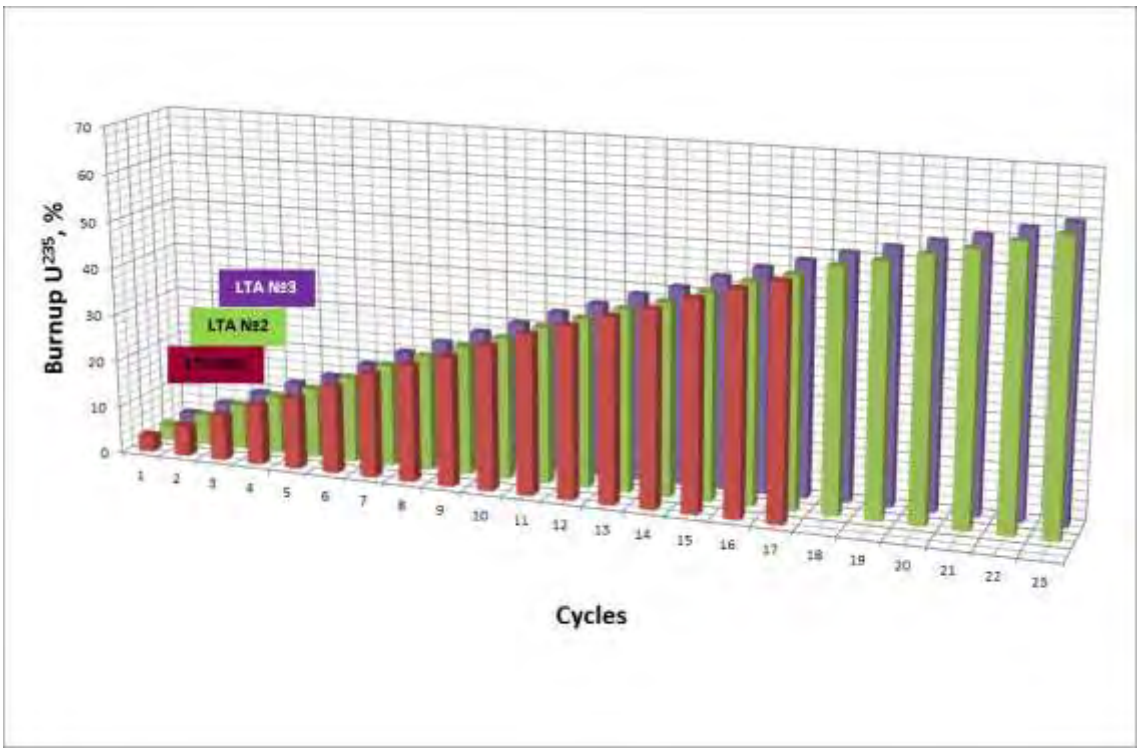


Figure 7. Dynamics of burnup of Uranium-235 in LTAs

As the figure shows, due to optimization of refueling in the core and enlarging of beryllium side reflector in course of the test, almost linear dependence of burnup on time was obtained. As a result, duration of the test was considerably diminished.

Figure 8 shows results of calculation of power versus time for every LTA over 23 operation cycles. Generated power comprised 106 MW·d for LTA1, 133 MW d for LTA2 and 135 MW·d for LTA3. Peaks on the curve correspond to moments of time when core sizes were reduced and/or beryllium side reflector was increased.

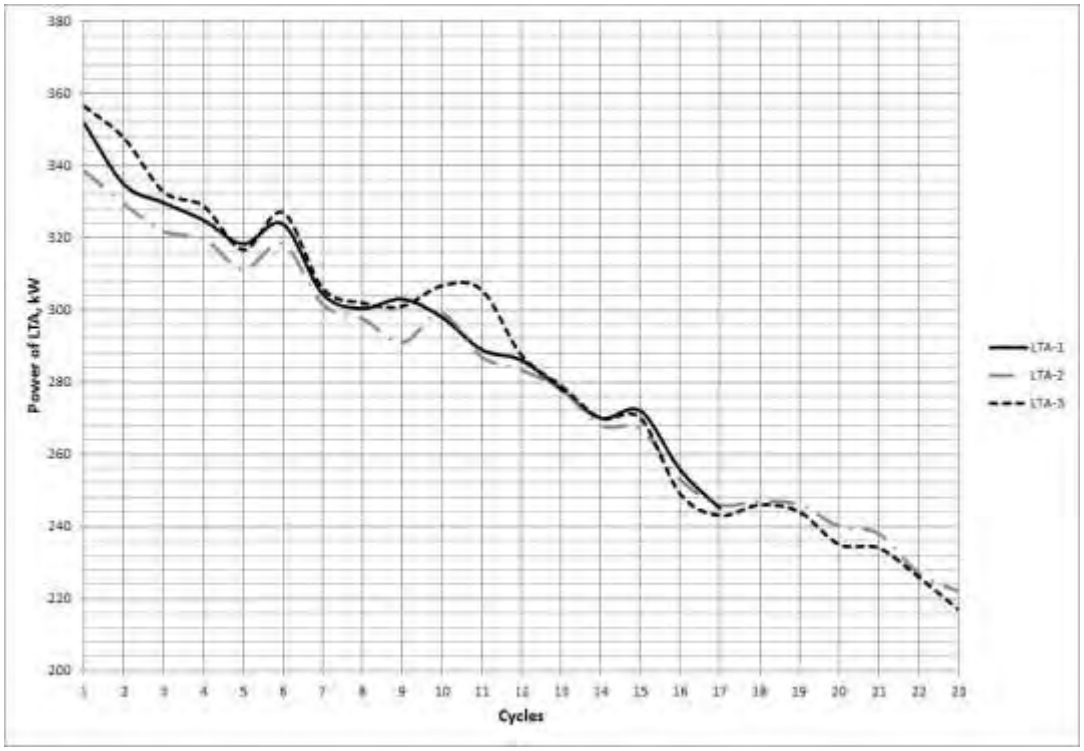


Figure 8. Dynamics of power change in every LTA

The measured levels of activity in primary-circuit water, as a whole, did not exceed the normal-operation limits, at the exception of the peak observed during the 17-th cycle, related to leaking in LTA1.

CONCLUSION

- Trials of the VVR-KN-type LTAs with low-enriched fuel were completed in the WWR-K reactor.
- Parameters of the performed trials are adequate to operational conditions for the hottest FA in the WWR-K reactor low-enriched core.
- Three LTAs operated successfully in the WWR-K reactor up to the 40-% burnup, confirming the manufacturing plant's guarantee.
- In one of LTAs, on reaching the burnup ~49%, signs of leaking were found. Trial of the LTA was finished. In two other LTAs the burnup nearly 60% was achieved without any signs of leaking.
- Preliminary post-irradiation examination of the LTAs burned to 60% was carried out. The study did not revealed any signs of leaking.
- The WWR-KN-type FAs are recognized as good for conversion of the WWR-K reactor.

REFERENCES

1. Arinkin F., Gizatulin, Sh., Zhotabaev Zh., Kadyrzhanov K., Koltochnik S., Chakrov P., Chekushina L. "Feasibility Study of the WWR-K Reactor" //RERTR-2004 International Meeting on Reduced Enrichment for Research and Test Reactors, Vienna, Austria, 7-12 November 2004 – P.5.
2. Arinkin F., Chakrov P., Chekushina L., Dobrikova I., Gizatulin Sh., Kadyrzhanov K., Koltochnik S., Nasonov V., Taliev A., Vatulin A., Zhotabaev Zh., Hanan N. Feasibility Analysis for Conversion of the WWR-K Reactor Using an Eight-Tube Uranium Dioxide Fuel Assembly // Abstract. Proceedings of the RERTR-2005 Meeting. – Boston, USA 6 to 10 November, 2005 - P.117
3. Arinkin F., Chakrov P., Chekushina L., Dobrikova I., Gizatulin Sh., Kadyrzhanov K., Koltochnik S., Nasonov V., Taliev A., Vatulin A., Zhotabaev Zh. Comparative Study of the WWR-K Reactor Using Low-Enriched U-Mo Fuel Pin- and Tube-Type // Abstract. Proceedings of the RERTR-2005 Meeting. – Boston, USA. 6 to 10 November, 2005. – P.122.
4. Arinkin F., Chakrov P., Chekushina L., Gizatulin Sh., Kadyrzhanov K., Kartashev E., Koltochnik S., Lukichev V., Nasonov V., Romanova N., Taliev A., Zhotabaev Zh. Characteristics of the WWR-R reactor core with low-enriched Uranium dioxide fuel // Proceedings of the RERTR 2006, – Cape Town, South Africa, October 29, 2006. – P.47.
5. F. Arinkin, P. Chakrov, L. Chekushina, Sh. Gizatulin, S. Koltochnik, D. Nakipov, A. Shaimerdenov, Zh. Zhotabaev, N. Hanan, P. Garner and J. Roglans-Ribas. Start of low-enriched fuel lead test assemblies in the WWR-K reactor core.// Proceeding of the RERTR-2011 International Meeting on Reduced Enrichment for Research and Test Reactors –Santiago, Chile, October 23, 2011 – P.82.
6. Code MCU-REA with the library of nuclear constants DLC/MCUDAT - 2.1. //Questions of Atomic Science and Engineering. Series «Physics of atomic reactors». Moscow. – 2001. – №3. – P.55-62 – in Russian.

LOW ENRICHMENT URANIUM FUEL ELEMENT DESIGNS WITH MONOLITHIC U-10MO FUEL AND UN-FINNED CLADDING FOR THE MIT RESEARCH REACTOR

E.H. WILSON, A. BERGERON, G. YESILYURT, F. E. DUNN, J.G. STEVENS
Argonne National Laboratory, 9700 S. Cass Avenue, Argonne, Illinois 60439

L.W. HU, T.H. NEWTON JR.
138 Albany Street, Massachusetts Institute of Technology, Cambridge, MA 02139

ABSTRACT

The Massachusetts Institute of Technology Reactor (MITR) is a university research reactor operating with highly-enriched uranium (HEU) finned plate-type fuel. This conversion study is to design a low-enriched uranium (LEU) fuel element that could safely replace the current 15-plate MITR HEU fuel element and maintain performance while requiring minimal, if any, changes to the reactor structures and systems. Prior LEU element design analyses have obtained equivalent performance and fuel cycle with an 18-plate element with 0.51 mm thick fuel and 0.25 mm cladding thickness (at the base of the fins). Recent manufacturing experience has led to a re-evaluation of the minimum cladding thickness. This study analyzed LEU fuel element designs to address three key design considerations: 1) increased cladding thickness to at least 0.3 mm for reliable fabrication; 2) remove longitudinal fins for simplified fabrication process; 3) incorporate plates with thinner fuel meat thickness to reduce power peaking in outer plates. The evaluation consists of neutronic and steady-state thermal hydraulic analyses and includes the impact of uncertainties due to fabrication tolerances. The designs were also required to maintain experimental and fuel cycle performance comparable to the current HEU reactor.

Fuel element design parameters investigated in this study include the number of plates, fuel thickness, cladding thickness, lower fuel loading in the outer plates, end channel size, and increased core coolant flow rate. Margin to onset of nucleate boiling (ONB) was calculated for each element design by statistically sampling the effect of tolerances and uncertainties for both all-fresh and depleted cores representative of MITR fuel management. In order to perform a whole core analysis, the limiting location for each design was determined by finding the element, channel, stripe, and axial with the minimum margin to ONB. Both fresh and depleted cores were analyzed in this manner. These calculations demonstrated an adequate fuel cycle at the 7 MW LEU power required to maintain experimental performance equivalent to 6 MW HEU operation. Six candidate LEU element designs with 0.3 mm thick un-finned cladding demonstrated sufficient margin to ONB provided core coolant flow rates can be increased by approximately 10-20%. A 19-plate element design where plates have 0.33, 0.43, and 0.64 mm thick fuel has been selected for further steady state, transient and accident safety analysis.

1. Introduction

Prior MITR LEU element design analyses with high-density monolithic alloy fuel have obtained equivalent flux performance and fuel cycle with an 18-plate element with 0.51 mm thick fuel and 0.25 mm cladding thickness (at the base of the fins). Whereas the prior MITR LEU design [1,2] was based upon cladding thickness of 0.25 mm, recent manufacturing development experience has led to a re-evaluation of the minimum cladding thickness for reliable fabrication. These core and element design activities were undertaken to determine if additional cladding thickness could be incorporated into an MITR LEU element. Removal of the fins would not only increase water-to-metal ratio in the core, but would improve economics by eliminating a fabrication step unique to MITR among U.S. high performance research reactors. In order to compensate for the loss of heat transfer area due to the removal of fins, an increased core coolant flow rate has been considered, and distinct fuel thicknesses were introduced in the outer plates of each element to limit heat flux peaking.

2. General Description of the Core

The MITR-II facility is currently licensed to operate at 6 MW thermal power. It is a hexagonal core containing 27 rhomboidal-shaped fuel locations in three radial layers (later referred to as rings A, B and C) as shown in . The 27 elements may be referred to with either the ring designation, or sequentially counting from element 1 (A-1) to 27 (C-15). Typically three of these positions (two in the A-ring and one in the B-ring) are filled with either an in-core experimental facility or a solid aluminum dummy (to reduce power peaking and increase shutdown margin).

The core is cooled by light water circulated upward through the core from bottom to top and is surrounded by a D_2O reflector. Boron impregnated stainless steel control blades are present at the periphery of the core at each side of the hexagon. The control blades have sufficient reactivity worth to shut down the reactor at any time. Each blade can be controlled independently but the 6 blades are typically banked for normal operation.

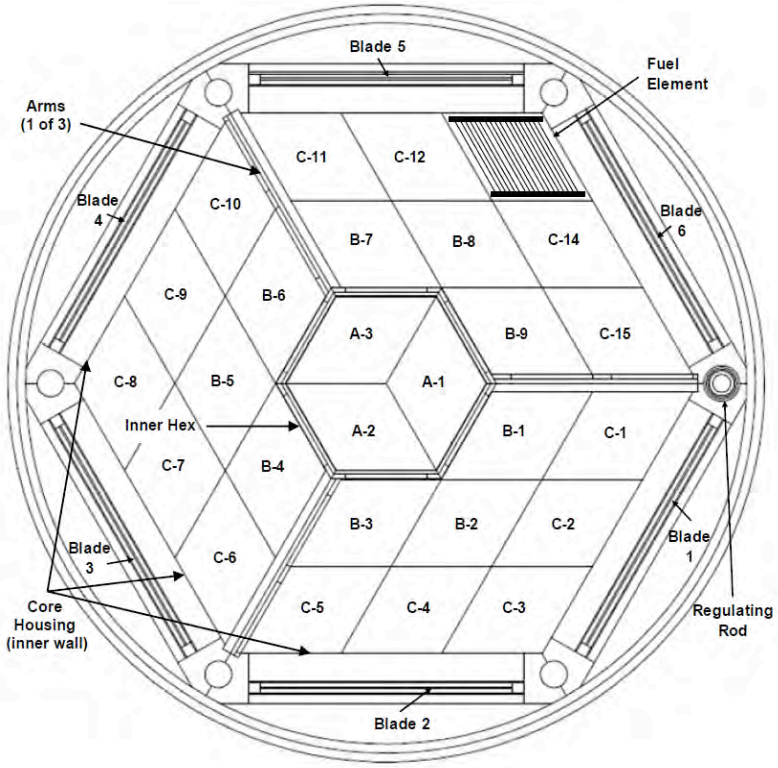


Figure 1. Layout of the MITR-II Reactor Core.

Several reentrant thimbles are installed inside the D_2O reflector, delivering thermal neutron flux to the beam ports outside the core region. Beyond the D_2O reflector, a secondary reflector of graphite exists in which several horizontal and vertical thermal neutron irradiation facilities are present. In addition, a fission converter facility is installed in the graphite reflector. This facility contains eleven partially spent MITR fuel elements for delivery of a beam of primarily epithermal neutrons to the medical facility for use in Boron Neutron Capture Therapy (BNCT).

3. ANALYSIS TOOLS AND METHODS

A number of neutronic models have been made for the MIT reactor. The Monte Carlo code MCNP has been used for many HEU and LEU core and experiment design studies. The basic reactor design and fuel structure has also been input into the MCNP-ORIGEN linkage code MCODE for fuel management and burnup evaluations [3]. Capabilities to study core and experimental loadings are very important for the MITR reactor since fuel loading is very adaptable to accommodate a wide range of in-core experimental facilities such as pressurized water loop, high temperature irradiation facility, fuel capsule experiment etc. MITR, which does not have a fixed core reloading pattern, uses flexible fuel management on an ongoing basis. In addition to the symmetric fuel element which can be rotated and/or flipped for efficient fuel utilization, MITR loads a variable core configuration in which an adjustable number of in-core experimental, dummy and fueled elements are arranged among the 27 core loading positions. Since there is no fixed core reloading, it is important to have

versatile fuel management capabilities integrated with neutronic modeling to evaluate potential LEU, and analogous HEU, cores series as well as for ongoing fuel management. Table 1 shows the arrangement of evenly distributed regions used for depletion and power shape calculations.

Table 1. Discretization of the LEU depletion zones and power regions used to generate representative depleted cores.

Regions	Geometry	Depletion	Power Shape
Plate Division	Each plate discrete	Each plate individual	Each plate individual
Fuel Axial Division	Continuous	6	18
Fuel Lateral Division	Continuous	1	4
Per LEU Core	-	864	31104

In order to readily screen candidates, all-fresh core depletion without fuel management was performed before selecting promising candidates to complete the more intensive fuel management modeling. In both fresh cores as well in cores with fuel management, the impacts on performance and thermal hydraulic safety margins have been analyzed using MCODE and by evaluating the margin to Onset of Nucleate Boiling (ONB) using the STAT7 code [4,5]. Fresh core results evaluated core power distributions throughout the whole core using MCNP and STAT7. The series of cores with fuel management have been evaluated at the beginning, Xe-equilibrium, and end of each core loading cycle.

Limiting Safety System Settings (LSSS) are based on ONB in the core. Uncertainties are accounted for in the analysis using Monte Carlo uncertainty propagation of the parameters influencing ONB. For design candidates, as in HEU, a 20% margin to the power at which the ONB is predicted was required. In these STAT7 analyses a 3-sigma confidence level (99.865%) of avoiding ONB was selected. All channels of an element are analyzed with a full three-dimensional core power profile, including end channels. Each element is analyzed in this manner so that a whole core analysis may identify the most limiting locations for each core configuration considered. It should be noted that margin to Critical Heat Flux (CHF) or Onset of Flow Instability (OFI) are not treated in these analyses because ONB is more limiting. A large margin to CHF has been previously demonstrated for MITR and will be later verified.

4 FRESH CORE DESIGN EVALUATIONS

4.1 Increasing Cladding Thickness by Removing the Fins

First, the effect of thicker (0.38 mm) un-finned cladding on the margin to ONB was assessed. Since in this case, the volume of aluminum cladding in the neutronic models with and without fins are identical, all neutronic related parameters are unaffected including performance (neutron flux and core lifetime), shutdown margin, and power distribution. However, margin to ONB (and other thermal-hydraulic margins) will be impacted by the change since the cooling surface area is reduced by removal of the fins. Consequently the limiting ONB power decreases substantially as shown in Table 2 with 5.01 MW well below the LSSS requirement of 8.4 MW (based on the 7 MW power required for equivalent experimental performance [5]). Note that the location of the minimum margin to ONB is designation numbers are **E**lement, **P**late, **S**tripe (1-4), **A**xial (from top, 1-18), **SU**rface of plate (on plate 1, surface 1 is the end channel).

Table 2. Limiting ONB power and Corresponding Location for Reference Configuration with and without Fins.

	Limiting ONB power	Location
Reference LEU with fins (MW)	9.71	E27P1S1Ax8SU1
Reference LEU no-fins (0.38 mm cladding) (MW)	5.01	E27P1S1Ax7SU1
Power Reduction from Fin Removal (%)	-48%	

4.2 Design Improvements to Increase ONB Power

The minimum margin to ONB occurs in the reference design in the end channel adjacent to the first plate located in a C-ring position. Accordingly the influence on the ONB margin of the end channel size relative to the others has been investigated. Increasing the end channel dimension is important, as seen in Figure 2, where the red point indicates the End Channel Ratio (ECR: ratio of end channel to interior channel dimension) of the prior reference design after removal of fins. Although increasing the ECR increases the ONB power, Figure 2 shows insufficient margin and so modifying the ECR cannot be the only design modification considered. In the following sections, the ECR has been set at 88% which leads to an improvement of 10% in the limiting ONB power. No significant impact on the other parameters (neutron flux, core lifetime, shutdown margins) has been observed by changing the ECR to 88%.

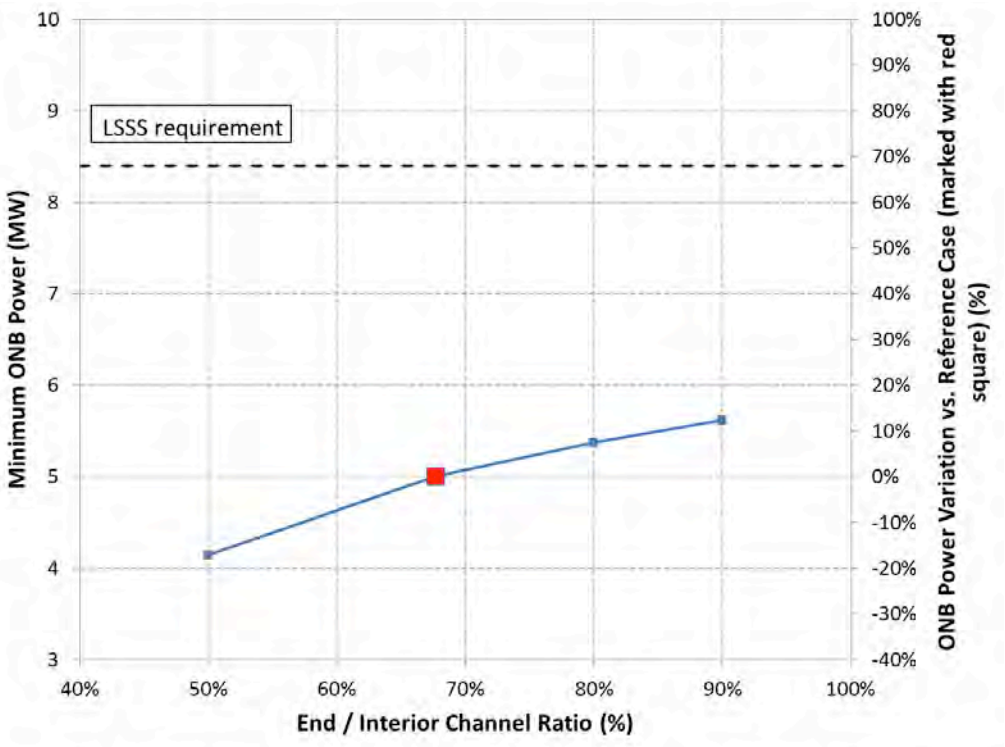


Figure 2. Limiting ONB Power vs. End Channel Ratio.

Since the limiting ONB power occurs on the edges of the element, the impact of a fuel meat thickness reduction in the outer plates, on both sides, of the element has also been considered. The ONB power can be increased by reducing power of the outer plates of the element which have been limiting in both fresh and depleted core designs analyzed previously [6,7]. Although the concept of flattening power profiles has been used throughout reactor design, implementing this into a core conversion is challenging due to the combination of competing effects. Although thinner plates aid

in reducing power peaking, they also degrade fuel lifetime. Since MITR loads into 3 radial rings and can rotate elements, plates on both sides of the element must be thinned for symmetry, which lowers overall fuel loading throughout the reactor in addition to the plates with power peaking immediately adjacent to the reflector. Additionally, the degree to which plates should be thinned cannot be predicted a priori without implementing representative fuel management capable of analyzing the power distributions found in depleted cores.

Pending fuel management calculations, four initial combinations of fuel meat reduction have been tested. In each case, the fuel thickness of 3 or 4 plates on each side of the element is reduced. For reasons of economy of fabrication it has been assumed as a constraint that there would be three distinct fuel foil thicknesses, and no more, in each element design. The thickness of all the plates is, however, kept constant. In other words, if a plate has a reduced fuel meat thickness, the cladding thickness increases accordingly in order to end up with the same plate thickness as the others. The selected combinations are presented in Table 3.

Table 3. Selected Combination of Fuel Meat Thickness Reduction.

Combination	**Fraction of nominal fuel meat thickness (%)**			
	1st plates	**2nd plates**	**3rd plates**	**4th plates**
A	45	60	60	100
B	55	70	70	100
C	50	50	70	70
D	60	60	80	80

In this section, the selected fuel meat reduction combinations have been tested with an element containing 18 plates, 0.38 mm cladding, no fins, ECR of 88%, matching the reference LEU design in other respects, and for a core flow of 2200 gpm. While an LSSS flow rate of 2200 gpm represents an increase from the current 1800 gpm, flow rates up to 2400 gpm have been demonstrated during pre-operational tests with the current pumps.

The selected combinations decrease the edge power significantly as illustrated in Figure 3 to Figure 7. These are based on the 7 MW LEU power required to maintain experimental performance equivalent to 6 MW HEU operation [5]. Figure 3 shows the axial heat flux profile obtained in element C-15, plate 1, stripe 1 for the reference configuration as well as for the four combinations tested. Maximum heat flux uncertainty is below 1% within one standard deviation. It is clear that the magnitude of the maximum heat flux decreases significantly with the fuel meat thickness reduction (from 25 to 35%, depending on the combination considered).

Figure 4 through Figure 7 show the heat flux profile by plate in element C-15, stripe 1, at the axial node 12 for the reference configuration as well as for combinations A, B, C and D. This location has been selected because it has been found to be limiting in previous analyses. The plots also show the corresponding fuel thickness, which is read on the right axis. These plots show clearly the power decrease on the edges and the power migration to the interior plates. Combination A has reduced the outer plate fuel thickness sufficiently to have the maximum power peak in the interior, full thickness, plates. However, the limiting plates are still observed to be in the thinned outer plates for combinations B, C, and D. The most appropriate level of thinning will need to be determined in concert with other factors such as core lifetime and ONB power for depleted cores operated over many cycles with representative fuel management.

The corresponding limiting ONB power obtained considering a flow rate of 2200 gpm and ECR of 88% are given in Table 4, where uncertainty on cycle length is estimated at ± 5 days. The four fuel

meat thickness reduction combinations give margin to ONB higher than the required 20% which show the effectiveness of the outer plate fuel meat reduction on improving core safety margins.

The core lifetime is however expected to decrease due to the significant decrease in uranium mass with the outer fuel meat reduction. Core lifetime calculations for the 4 fuel meat reduction combinations have been carried out at 7 MW with 24 elements. As expected the core lifetime drops substantially (from 25% to 40% depending on the combination considered) [5]. The core lifetimes of these designs are considered too short to be acceptable.

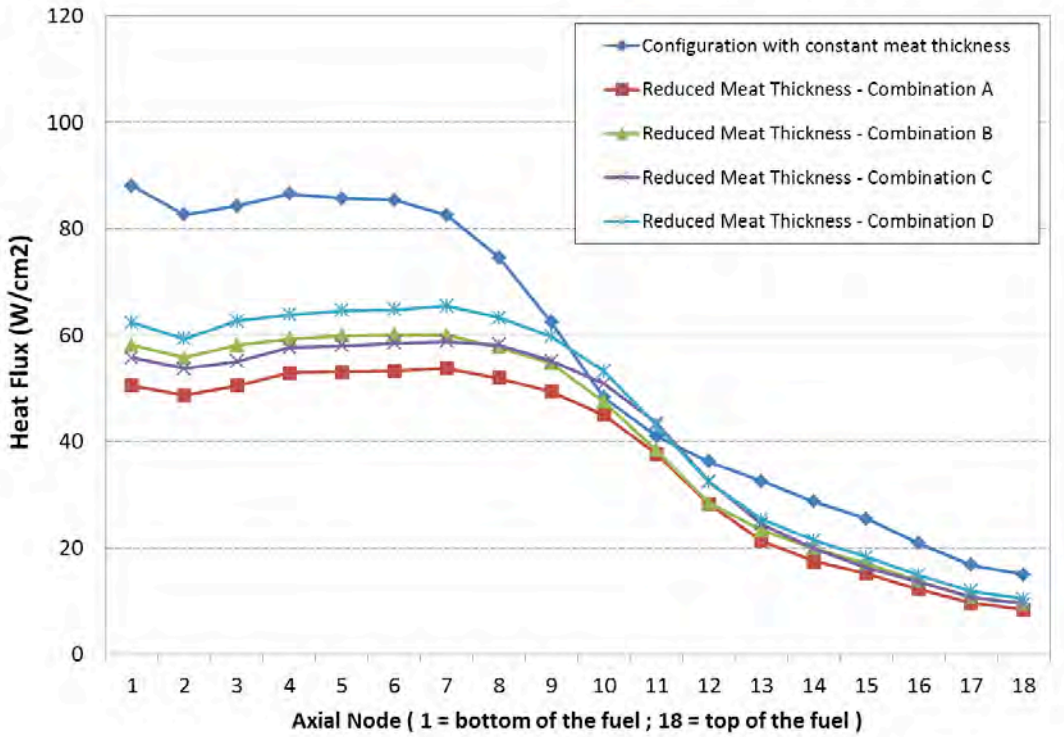


Figure 3. Axial Heat Flux Profile in Element C15, Plate 1, Stripe 1 for 7 MW 18-plates LEU Configuration for Various Reductions of Fuel Thickness.



Figure 4. Heat Flux Profile through the Plate in Element 27, Stripe 1, Axial Node 12 for Configuration with Constant Fuel Thickness and Reduced Fuel Thickness Combination A.

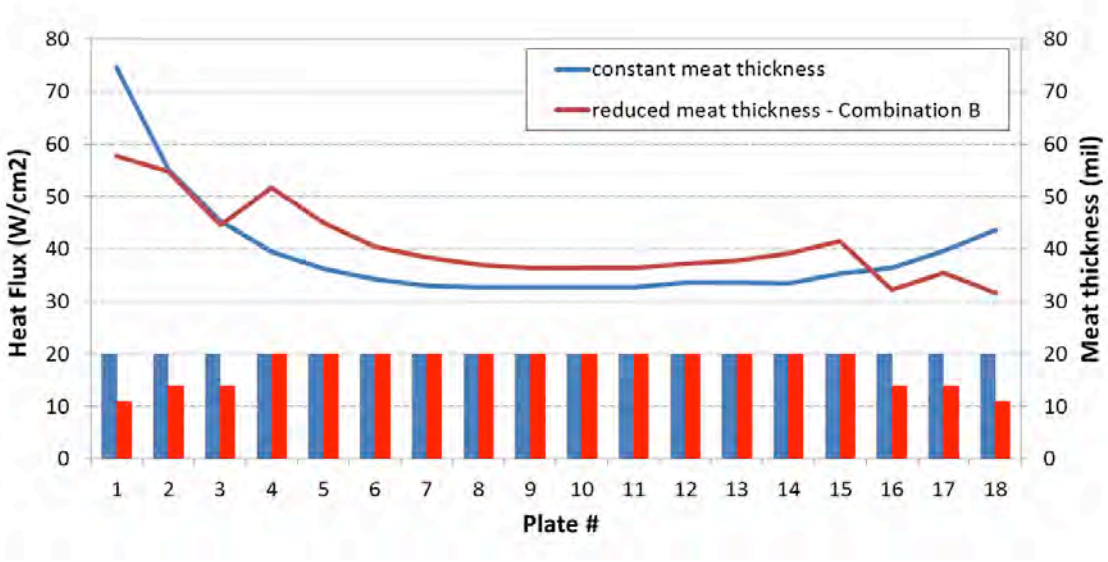


Figure 5. Heat Flux Profile through the Plate in Element 27, Stripe 1, Axial Node 12 for Configuration with Constant Fuel Thickness and Reduced Fuel Thickness Combination B.

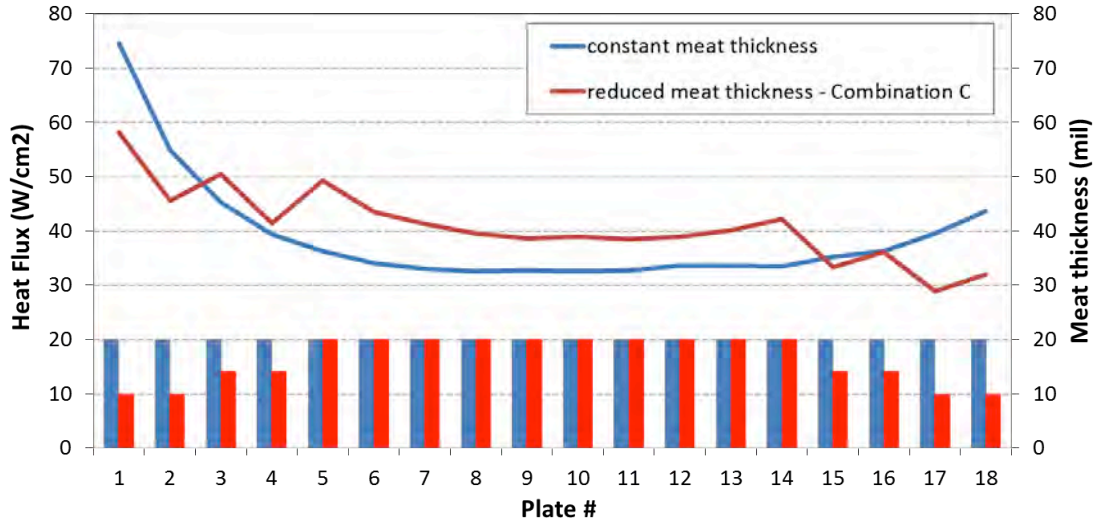


Figure 6. Heat Flux Profile through the Plate in Element 27, Stripe 1, Axial Node 12 for Configuration with Constant Fuel Thickness and Reduced Fuel Thickness Combination C.

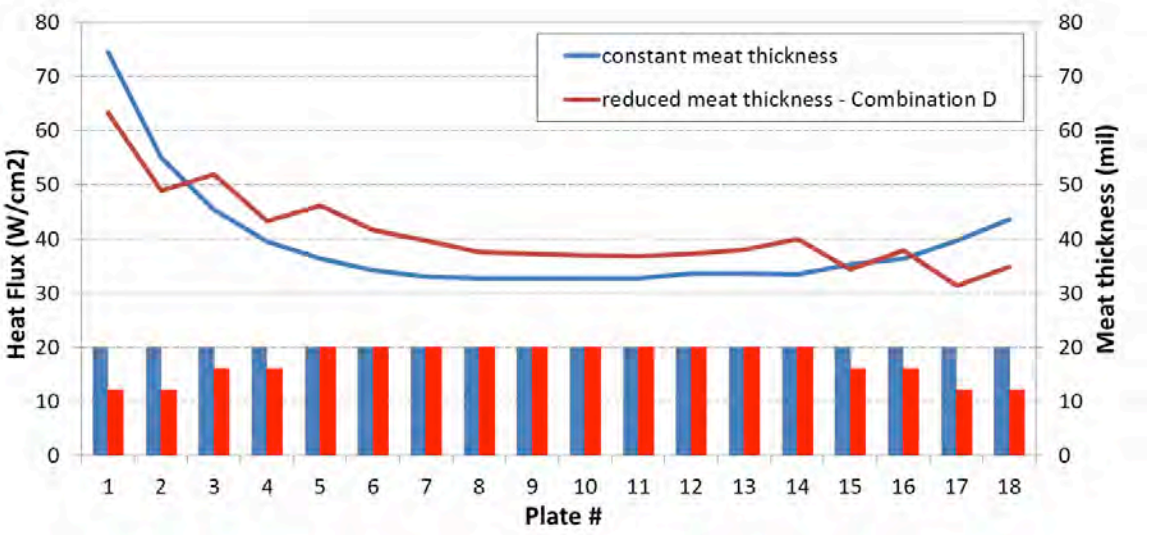


Figure 7. Heat Flux Profile through the Plate in Element 27, Stripe 1, Axial Node 12 for Configuration with Constant Fuel Thickness and Reduced Fuel Thickness Combination D.

Table 4. Limiting ONB Power for the Four Reduced Fuel Thickness Combinations with a Flow Rate of 2200 gpm (where >8.4 MW is required).

Configuration	Limiting ONB power (MW)	Location
LEU reference design except no fins, and ECR 88%	6.8	E27S1P1Ax8SU1
A	9.6	E13S4P15Ax9SU1
B	9.7	E27S1P1Ax8SU1
C	9.8	E14S4P14Ax9SU1
D	8.9	E27S1P1Ax8SU1

4.3 Design Options to Increase Cycle Length

In the previous section, different solutions have been explored to increase the margin to ONB of the LEU design without fins. The most efficient solution is a reduction of the fuel meat thickness, and hence heat flux, in the outer fuel plates of the element. While the distinct fuel meat thicknesses provide acceptable margin to ONB, the approach significantly penalizes the core lifetime. The following section describes the solutions that have been considered to increase the core lifetime of the reduced thickness fuel meat designs. Decreasing the cladding thickness from 0.38 mm will have the effect to increase the volume of water in the core which may increase the reactivity (if the coolant-to-heavy metal ratio becomes more favorable), and increase the cycle length. However there is a trade-off since, at a given flow rate, the coolant velocity would decrease, leading to a decrease of ONB margin.

Four reduced fuel meat thickness configurations have been tested with a nominal clad thickness reduced from 0.38 mm to 0.30 mm. Core lifetime and limiting ONB power are compared to the 0.38 mm clad configurations in Table 5. Acceptable configurations in terms of core rundown lifetime and limiting ONB power at 2200 gpm are highlighted in green. The favorable impact of the clad reduction on the core lifetime is significant since it leads to a lifetime increase of 30% to more than 60%, depending on the configuration considered. Two of the four configurations tested have core lifetime slightly exceeding that of the reference configuration (320 days). The impact on the ONB margin is a decrease of <14%. Designs with 0.30 mm cladding can be further considered.

Table 5. Core lifetime and limiting ONB Power obtained with the four reduced fuel meat configurations clad thicknesses.

Combination	Cladding 0.38 mm		Cladding 0.30 mm		Variation 0.30 vs. 0.38 mm cladding	
	Core lifetime (days)	Limiting ONB power (MW)	Core lifetime (days)	Limiting ONB power (MW)	Core lifetime (%)	Limiting ONB power (%)
A	230	9.6	300	8.29	+30.4%	-13.6%
B	235	9.7	330	8.77	+40.4%	-9.6%
C	195	9.8	285	8.77	+46.2%	-10.5%
D	205	8.9	330	8.95	+61.0%	+0.6%

The effect of a fuel meat thickness increase has also been explored. Additional uranium mass could increase the core lifetime but at the same time reduce the core coolant/fuel meat ratio. Consequently the reactivity of the core would decrease, which would reduce the core lifetime. But at a given coolant mass flow rate, that would also increase the coolant velocity and increase the ONB margin. In order to find an optimal solution design, options are considered here with nominal fuel meat thickness increased from 0.51 mm to 0.762 mm in increments of 0.13 mm.

4.4 Seeking the Best Combinations of Design Modifications with Fuel Management

Fresh cores without fuel management have been used to select more promising core design options in the analyses presented to this point. However, the performance of selected designs under representative depleted cores must also be considered. As further described in Reference [5], 36 candidate cores ranging from 17-19 plates, 0.51-0.762 mm thick fuel meat, and 4 combinations of fuel reduction were analyzed in all-fresh core configurations. This allowed down-selection of 11 designs which then underwent representative fuel management and performance analysis. The intent was to show that at every relevant cycle, the core lifetime, neutron flux performance and margin to ONB requirements are met. The evolution of these parameters during a shuffling scheme is difficult to predict since the core loading will vary at each cycle, mixing elements with various depleted elements with a few fresh elements. This is why an appropriate down-selection to the most promising design requires fuel management analyses. Note that the element design configuration name denotes the number of plates in the element, the fuel thickness reduction combination A, B, C, or D as described earlier, and the thickness of the interior full-thickness fuel (in 1/1000 of an inch).

Six designs remained promising after a 12 core series of fuel management calculations (analogous to HEU cores 179-190) and consideration of performance criteria including those shown in Table 6 [5]. It is noteworthy that some designs are limited by a fresh core configuration and others by a depleted core configuration (Core 189 BOC). Figure 8 shows the power shapes for promising design 19B25 at the most limiting point (lowest margin to ONB) in the 12 core series of fuel management. Note that for this design it is a fresh fuel element which provides the minimum margin to ONB. Table 6 quantifies the difference between this fresh element power peaking and the depleted element power peaking for each of the six designs. This illustrates the effect of the various combinations of reduced fuel meat thickness. The largest imbalance between fresh and depleted peaking (143%) is for the reference LEU design thus decreasing ONB margin overall for that design. Fresh element 10 was found to be limiting for all alternate designs except 19B30 where element 27 plate 1 adjacent to the reflector was most limiting (as was the case for the LEU reference design). Designs with values near 100% tended to have higher ONB margin, as was expected.

Table 6. Summary of Fresh and Depleted LEU Element Design Performance.

	LEU						
	Reference design	**18B25**	**18A30**	**19D20**	**19A25**	**19B25**	**19B30**
Geometry & uranium mass							
^{235}U mass per element (g)	831	910	1058	767	940	968	1169
plates per assembly	18	18	18	19	19	19	19
fins	Yes	No	No	No	No	No	No
plate thickness (mm)	1.02	1.24	1.37	1.12	1.24	1.24	1.37
1st fuel plates (mm)	0.508	0.33	0.33	0.30	0.28	0.33	0.41
2nd fuel plates (mm)		0.43	0.46	0.30	0.38	0.43	0.53
3rd fuel plates (mm)		0.43	0.46	0.41	0.38	0.43	0.53
4th fuel plates (mm)		0.64	0.76	0.41	0.64	0.64	0.76
other fuel plates (mm)		0.64	0.76	0.51	0.64	0.64	0.76
Limiting power to ONB for flow = 2200gpm (MW) (where >8.4 MW is required based on 20% margin to 7 MW LEU operating power)							
22 element fresh core	11.75	9.12	9.54	9.32	9.98	9.28	8.84
24 element fuel management	9.17	8.59	9.01	9.10	9.09	9.67	9.31

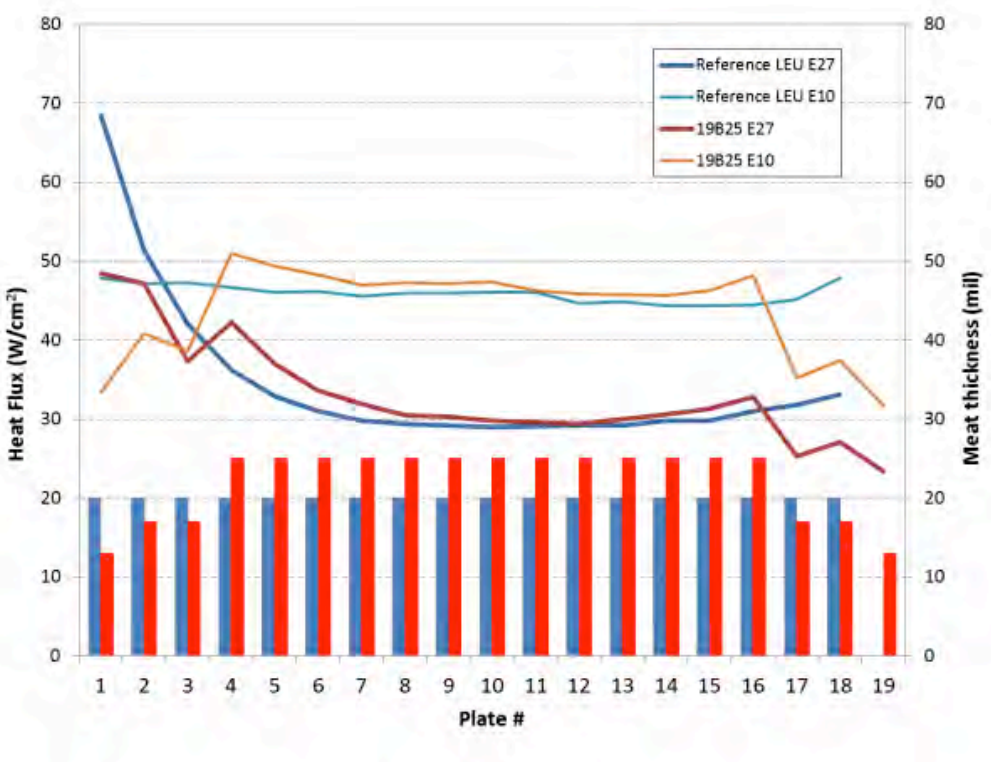


Figure 8. Core 189 BOC Heat Flux Profile by Plate for design 19B25 in both Element 10, Stripe 1, Axial Node 11 and Element 27, Stripe 1, Axial Node 11.

Table 7. Heat Flux in Plate 1 Stripe 1 of Element 27 of Core 189 EOC vs. Maximum Heat Flux in Core 189 BOC Element 10.

Axial 11	Reference LEU	18A30	18B25	19A25	19B25	19B30	19D20
Heat Flux Plate 1 Element 27 (W/cm^2)	68.5	47.4	47.3	43.4	48.5	54.2	48.3
Maximum all plates of Element 10 (W/cm^2) [a]	47.9	56.3	55.5	54.3	51.0	49.4	51.3
Heat Flux Plate 1 E27 vs. Max E10 all plates	143%	84%	85%	80%	95%	110%	94%

a. Fresh element 10 was found to be limiting for all alternate designs except 19B30 where element 27 plate 1 adjacent to the reflector was most limiting as was the case for the LEU reference design.

Figure 9 presents the estimated peak local fission density which was tabulated for all designs in support of the evaluation of fuel irradiation performance conditions, and design trade-offs. The size scale of the fission density estimation was based on the size region available which is relevant to thermal hydraulics for the safety basis (1 cm transverse by 3 cm axial). This data was also used in order to generate swelling in the channel in order to evaluate the effect on ONB margin. Swelling had no negative impact on ONB margin where a potentially minor improvement is due to the higher flow velocity and heat transfer coefficient [5].

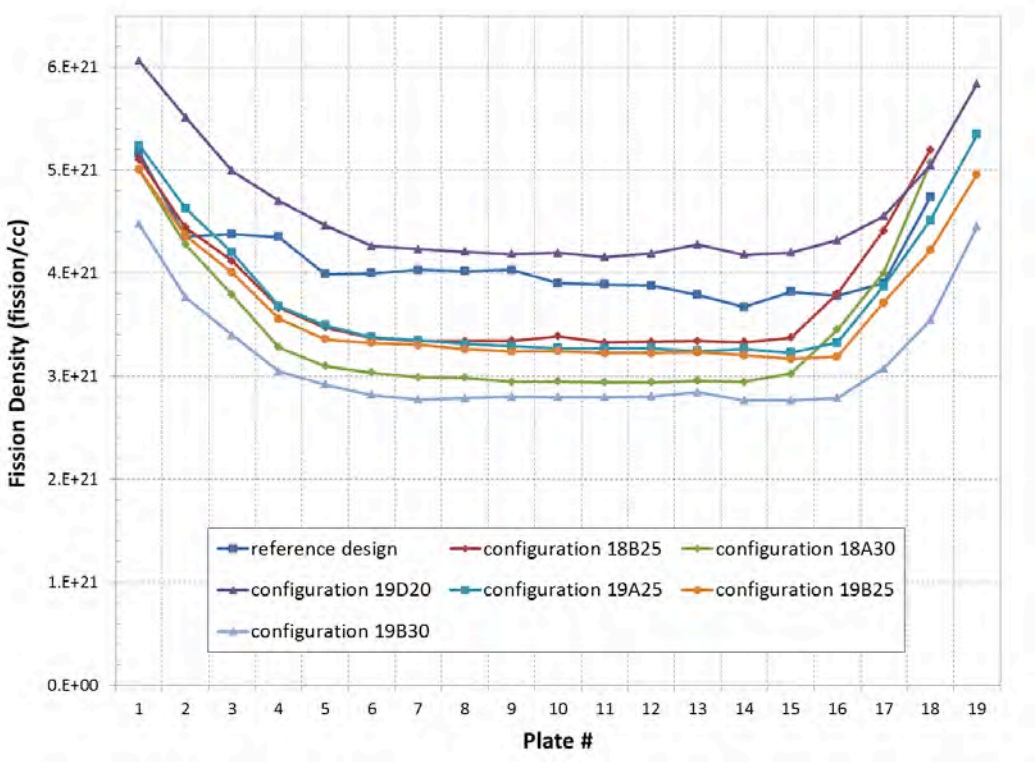


Figure 9. Maximum Fission Density by Plate.

5 SUMMARY

This study successfully re-designed the MITR LEU fuel element to address three key design considerations: 1) increase cladding thickness to at least 0.3 mm for reliable fabrication; 2) removal of longitudinal fins for a simplified fabrication process; 3) incorporate plates with thinner fuel meat thickness to reduce power peaking in outer plates. Many options were screened out based on fresh core performance metrics. After selecting the best candidates, fuel management calculations were performed, and six final designs demonstrated adequate fuel cycle including refueling on a quarterly, or less frequent, basis each year. The LEU power level of 7 MW maintains performance equivalent to 6 MW HEU operation. With the removal of fins, several design parameters were investigated in order to demonstrate sufficient margin to ONB, including the number of plates, a larger end channel, optimized fuel thickness combinations, cladding thickness and increased core flow rate. While the 10-20% increase in core coolant flow rate has been demonstrated during pre-operational tests with the current pumps, further evaluation is required.

Design 19B25 appears the most attractive, overall, since the analyses demonstrated the largest thermal hydraulic margin in fuel management calculations and hence the smallest increase in core flow would be required. Flux performance of 19B25 also matches HEU neutron flux levels within 2% by operating the LEU core at 7 MW. The 19B25 design contained 19 plates and full-thickness fuel meat of 0.64 mm in the interior plates of each element. The other five alternate designs demonstrated adequate, but significantly less, margin to ONB during the evaluation of fuel management. Complete safety analysis of the most promising LEU element design will be required to establish performance during all steady state and accident conditions.

The submitted manuscript has been created by UChicago Argonne, LLC, Operator of Argonne National Laboratory ("Argonne"). Argonne, a U.S. Department of Energy Office of Science laboratory, is operated under Contract No. DE-AC02-06CH11357. The U.S. Government retains for itself, and others acting on its behalf, a paid-up nonexclusive, irrevocable worldwide license in said article to reproduce, prepare derivative works, distribute copies to the public, and perform publicly and display publicly, by or on behalf of the Government. Work supported by US Department of Energy, Office of Global Threat Reduction, National Nuclear Security Administration (NNSA).

REFERENCES

[1] T. Newton, E. Pilat and M. Kazimi, "Development of a Low-Enriched-Uranium Core for the MIT Reactor," Nuclear Science and Engineering, 157: p. 264-279, (2007).

[2] L. Hu, K. Chiang, E.H. Wilson, F.E. Dunn, T.H. Newton, Jr., and J.G. Stevens, "Thermal Hydraulic Limits Analysis for LEU Fuel Conversion of the MIT Reactor," MITNRL-12-01, Massachusetts Institute of Technology, March 2012.

[3] Z. Xu, P. Hejzlar, and M. Kazimi, "MCODE, Version 2.2 - An MCNP-ORIGEN Depletion Program," Massachusetts Institute of Technology (2006).

[4] F. E. Dunn, L. Hu, K. Chiang, E. Wilson, T. H. Newton, Jr., and J.G. Stevens, "Calculations of LSSS Limits for Use of LEU Fuel in the MITR-II Reactor," Conf. of Am. Nucl. Soc., San Diego, California, November 2012.

[5] Bergeron, A. et. al., "Low Enriched Uranium Core Design for the Massachusetts Institute of Technology Reactor (MITR) with Un-finned 12 mil-thick Clad UMo Monolithic Fuel," ANL/GTRI/TM-13/15, Argonne National Laboratory, November 2013.

[6] N. Horelik, "Expanding and Optimizing Fuel Management and Data Analysis Capabilities of MCODE-FM in Support of MIT Research Reactor LEU Conversion," MS thesis, Massachusetts Institute of Technology, December, 2011.

[7] E.H. Wilson, N.E. Horelik, A. Bergeron, T.H. Newton, Jr., F. Dunn, L. Hu, J.G. Stevens, "Neutronic Modeling of the MIT Reactor LEU Conversion," Trans. Am. Nuclear Soc. 106, 1, 849-852 (2012).

EVALUATION OF U-10MO FOR THE CONVERSION OF KUCA DRY CORES

James A. Morman and Gerardo Aliberti
Argonne National Laboratory, 9700 S. Cass Ave, Argonne, IL, 60439 – USA

European Research Reactor Conference, RRFM
Ljubljana, Slovenia, March 30 – April 3, 2014

This work is sponsored by the U.S. Department of Energy
National Nuclear Security Administration Office of Global Threat Reduction (NA-21)

About Argonne National Laboratory
Argonne is a U.S. Department of Energy laboratory managed by UChicago Argonne, LLC under contract DE-AC02-06CH11357. The Laboratory's main facility is outside Chicago, at 9700 South Cass Avenue, Argonne, Illinois 60439. For information about Argonne and its pioneering science and technology programs, see www.anl.gov.

Disclaimer
This report was prepared as an account of work sponsored by an agency of the United States Government. Neither the United States Government nor any agency thereof, nor UChicago Argonne, LLC, nor any of their employees or officers, makes any warranty, express or implied, or assumes any legal liability or responsibility for the accuracy, completeness, or usefulness of any information, apparatus, product, or process disclosed, or represents that its use would not infringe privately owned rights. Reference herein to any specific commercial product, process, or service by trade name, trademark, manufacturer, or otherwise, does not necessarily constitute or imply its endorsement, recommendation, or favoring by the United States Government or any agency thereof. The views and opinions of document authors expressed herein do not necessarily state or reflect those of the United States Government or any agency thereof, Argonne National Laboratory, or UChicago Argonne, LLC.

EVALUATION OF U10MO FOR THE CONVERSION OF KUCA DRY CORES

James A. Morman and Gerardo Aliberti
Argonne National Laboratory, 9700 S. Cass Ave, Argonne, IL, 60439 – USA

ABSTRACT

The Kyoto University Critical Assembly currently uses combinations of highly enriched (93%) uranium-aluminum (HEU U-Al) alloy and polyethylene plates in the dry cores (A and B) to construct a variety of critical and subcritical configurations. One candidate fuel for conversion of these cores to low-enriched uranium (LEU) is U-10Mo. This paper presents the results of analyses that were done to evaluate the feasibility of using U-10Mo (19.75%) in the KUCA cores, and to study the reactivity effects of cladding the LEU fuel plates with aluminum. The reference HEU cores used to validate the calculational models are taken from a set of benchmark configurations provided by Kyoto University Research Reactor Institute staff.

The goal of the study was to determine if conversion to LEU fuel plates could maintain important system parameters (e.g., reactivity, spectra, core size). Comparative results are presented for core reactivity, reaction rate distributions and neutron spectra. While further study of the KUCA cores is necessary to compare power levels, reactivity coefficients and other performance parameters, none of the results presented here indicate any reason that the conversion of the KUCA dry cores to LEU cannot be performed successfully.

1. Introduction

The US Department of Energy (DOE) Global Threat Reduction Initiative (GTRI) research reactor conversion program is part of the global non-proliferation effort to minimize and, to the extent possible, eliminate the use of highly-enriched uranium (HEU) in civil nuclear applications by working to convert research reactors to the use of low-enriched uranium (LEU) fuel throughout the world. As part of this program the Kyoto University Research Reactor Institute (KURRI) and Argonne National Laboratory (Argonne) have established a collaboration to explore the feasibility of converting the Kyoto University Critical Assembly (KUCA) from HEU to LEU.

The KUCA consists of the solid-moderated and -reflected Type-A and Type-B cores, and the water-moderated and -reflected Type-C core. With the use of an external pulsed neutron generator, the Type-A core is also used to evaluate the Accelerator Driven Subcritical Reactor (ADSR) concept.

The present document describes results of the analyses carried out at Argonne on the KUCA Type-A cores using the ADSR benchmark assemblies for reference and model validation. With the HEU core analysis as a basis, feasibility studies on the conversion of the KUCA dry assemblies to the use of LEU, using both U-Al alloy and U-10Mo fuel plates were performed.

2. KUCA HEU Benchmark Analysis

2.1 Description of KUCA Benchmark Cores

Results of studies on two series of Type-A benchmark cores, each consisting of four configurations, have been reported by Pyeon *et al.* [1] as part of the KURRI ADSR research. A pulsed neutron generator is combined with the A-core for the purpose of injecting 14 MeV pulsed neutrons into the subcritical system. In some configurations, a neutron shield and a beam duct are installed in the reflector region. Figure 1 shows two representative HEU reference configurations with and without the beam duct and shield. Results from these HEU reference configurations are reported here as validation of the calculational models and for comparison to the LEU analyses.

The materials used in the KUCA cores are in the form of plates (coupons) or blocks, nominally 5.1-cm square (2-in. square), with thicknesses ranging between 0.16 cm (1/16 in.) and 5.1 cm (2 in.). The materials are stacked in vertical square aluminum tubes to achieve the desired composition and geometry and then inserted into the KUCA matrix (see Figure 2). These tubes are generally separated by 1-mm gap, with several gaps of 3 mm as shown in Figure 1. The reference fuel unit cell consists of one HEU U-Al plate, 0.16-cm (1/16-in.) thick, and two polyethylene plates 0.32-cm (1/8-in.) thick and 0.625-cm (1/4-in.) thick. Multiple unit cells are placed together to form the core region of each assembly. The functional height of the core is approximately 40 cm. The cores for the current study have polyethylene reflectors more than 50-cm long on either side of the fueled region as shown in Figures 2 and 3. To compensate for the tritium target not being located at the center of the core, a neutron shield and beam duct are installed in the polyethylene radial reflector region of some configurations (see Figure 1).

Sets of activation foils are positioned at relevant matrix positions, including (15, K) and at the tritium target for neutron spectrum measurements. An Indium wire, 1.5-mm diameter, is positioned in a gap within the matrix (between 16,J-W and 17,J-W) to measure reaction rates and indicate flux distributions.

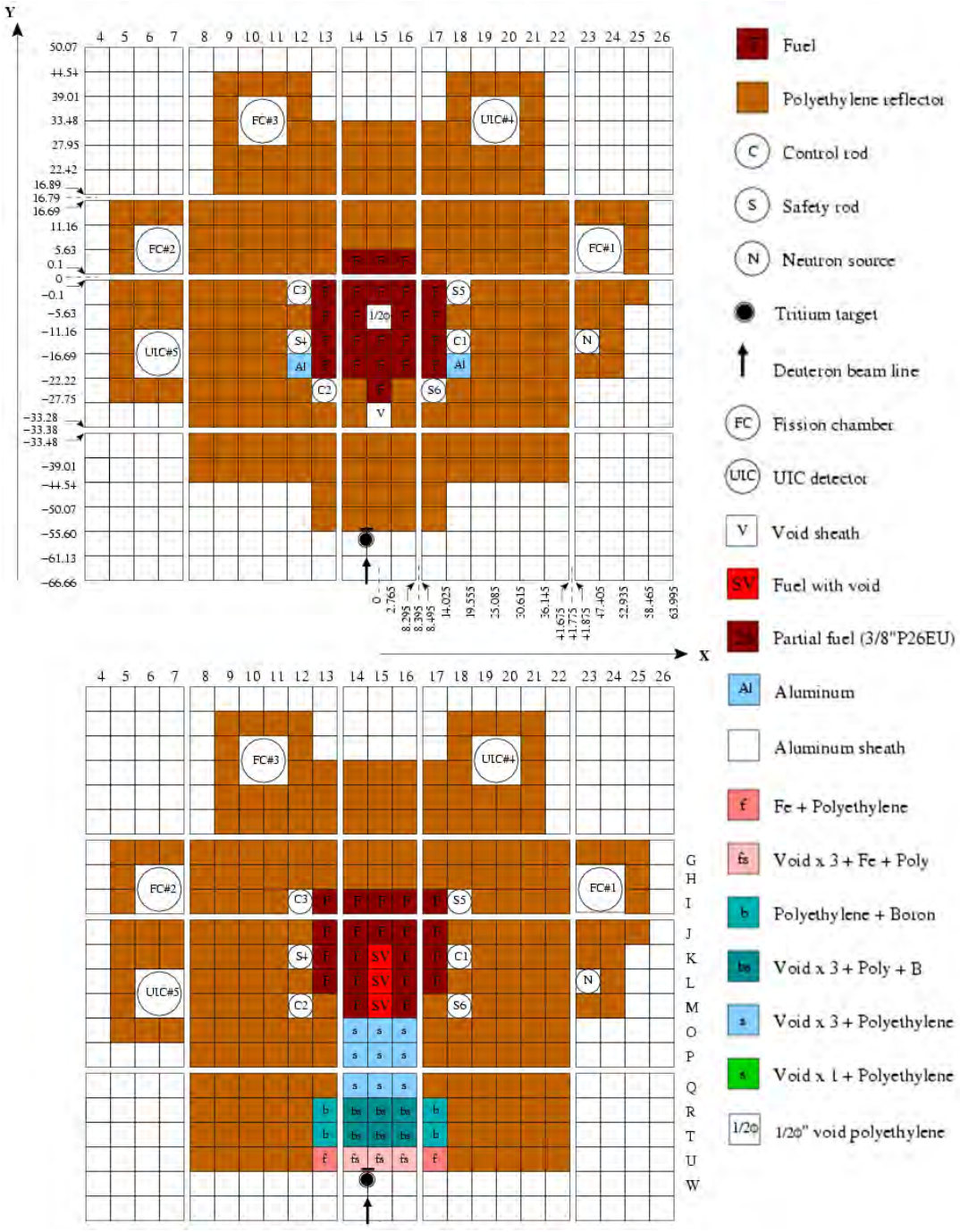


Figure 1. Representative HEU Benchmark Cores With (Lower Figure, Case II-3) and Without (Upper Figure, Case I-1) Neutron Shield and Beam Duct.

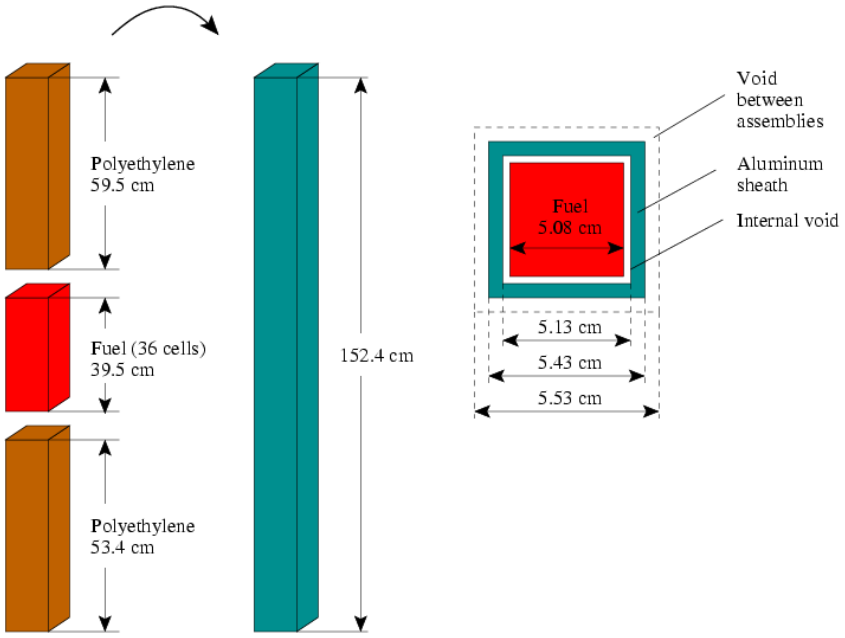


Figure 2. Typical KUCA Fuel Assembly.

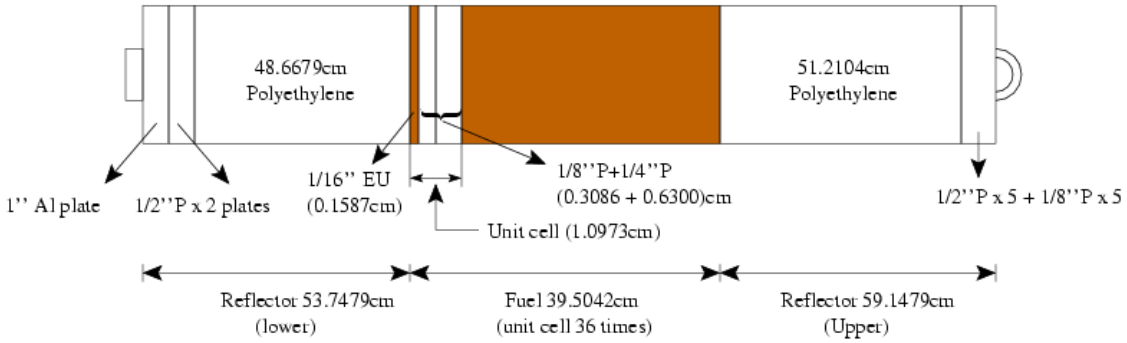


Figure 3. Detail View of Fuel Assembly "F".

2.2 HEU Benchmark Calculations

Calculations were performed using MCNP Version 5 with ENDF/B-VII.0 cross sections, plus several comparison calculations using other cross section sets. The MCNP models were developed by explicitly describing each fuel and polyethylene plate, Al sheaths, gaps, and each component of the control rods, safety rods and reactor structures. The HEU calculations serve to validate the MCNP models and establish any bias in the calculations.

For this initial feasibility study, calculations were concentrated on reactivity values, indium reaction rate distributions and neutron spectra. Comparison of HEU and LEU spectra provide one indication of the feasibility of conversion.

2.2.1 Excess Reactivity and Subcriticality

Reactivity calculations were performed with three different control rod configurations:

1. All control and safety rods fully withdrawn (excess reactivity configuration)
2. All safety rods completely withdrawn and all control rods fully inserted (subcritical configuration)
3. All safety rods completely withdrawn and control rods at the measured critical position (critical configuration).

The reactivity values obtained for each of the eight benchmark assemblies and reactivity configurations are presented in Table 1 together with the measured values.

Table 1. Calculated and Measured Reactivity Values [pcm].

Configuration	Rod Configuration	Measured	MCNP5
KUCA I-1	Excess Reactivity	+295 ± 21	746 ± 8
	Subcritical	-904 ± 63	-371 ± 8
	Critical	0 ±	446 ± 8
KUCA I-2	Excess Reactivity	+293 ± 21	695 ± 6
	Subcritical	-925 ± 65	-415 ± 6
	Critical	0 ±	422 ± 6
KUCA I-3	Excess Reactivity	+20 ± 1	445 ± 6
	Subcritical	-1171 ± 82	-616 ± 6
	Critical	0 ±	396 ± 6
KUCA I-4	Excess Reactivity	+296 ± 21	746 ± 6
	Subcritical	-907 ± 63	-368 ± 6
	Critical	0 ±	441 ± 6
KUCA II-1	Excess Reactivity	143 ± 10	776 ± 6
	Subcritical	-793 ± 56	-42 ± 6
	Critical	0 ±	641 ± 6
KUCA II-2	Excess Reactivity	246 ± 17	856 ± 6
	Subcritical	-677 ± 47	-18 ± 6
	Critical	0 ±	595 ± 6
KUCA II-3	Excess Reactivity	37 ± 3	564 ± 6
	Subcritical	-893 ± 63	-343 ± 6
	Critical	0 ±	507 ± 6
KUCA II-4	Excess Reactivity	232 ± 16	934 ± 6
	Subcritical	-702 ± 49	48 ± 6
	Critical	0 ±	714 ± 6

There is a consistent bias of approximately 400 - 500 pcm between the calculated (ENDF/B-VII.0) and measured results for all Series I configurations and approximately 500 - 700 pcm for all Series II configurations. It is important to note that configurations II-2, II-3 and II-4 have a set of foils (the exact location of which is not known) located in the void region of one of the central fuel assemblies and these have a reactivity effect of about 800 pcm.

In an attempt to determine the source of this bias, calculations were also performed with different data libraries (ENDF/B-VI.0, ENDF/B-VI.6, JEF3.1). The use of JEF3.1 and ENDF/B-VI.6 data lead to about the same results obtained with the ENDF/B-VII.0 library. With ENDF/B-VI.0 data the bias is about 200 pcm smaller than with the other libraries, but it

was concluded that the difference would not have a significant impact on the conclusions of this study.

2.2.2 Indium Reaction Rate Distributions

Indium reaction rate distributions were calculated along the core mid-plane to provide another parameter with which to compare the HEU and LEU cores. The calculated indium reaction rate distributions for the HEU models compare well with the measured ones [2], particularly in the fuel zone. In the reflector/shield region the calculations show a depression in the distributions that in some cases is not seen in the data. Results and Comparison to the LEU calculations are presented in Section 3.

2.2.3 Neutron Spectra Calculations

Flux spectra were calculated in 53 energy groups for the KUCA I-1 configurations using HEU fuel and LEU U-10Mo fuel with and without Al clad. Calculations were performed for the subcritical configuration. Flux spectra were determined at position A, (X,Y)=(8.395 cm; -2.6 cm), along the indium wire (see Figure 1) and in position B, in the fuel plate of the assembly (14,K) that is closest to the core midplane. Results are presented in Section 3 for the HEU core and for the LEU cases with and without Al cladding.

3. Conversion of the KUCA Cores from HEU to LEU

The primary purpose of the Argonne study was to evaluate the feasibility of converting the KUCA assemblies to the use of LEU. Two candidate fuels were considered, U-Al alloy and U-10Mo alloy. Comparisons with the HEU core characteristics are based on the benchmark core identified as KUCA I-1 (see Figure 1). Results presented in this section were partly included in Ref. 2.

In addition to a comparison of the reactivity values, the conversion from HEU to LEU was investigated through the analysis of flux spectra in relevant locations and reaction rate distributions.

3.1 Use of LEU U-Al Alloy Fuel

Calculations were initially performed with U-Al alloy plates having the enrichment reduced from 93% to 19.75%, which is typically used as reference value for LEU. However, even after adding 11 fuel assemblies, the calculated multiplication factor for the LEU configuration is as low as 0.63097 with a typical U-Al density of 0.65 g/cm^3. It was found that for the same fuel plate thickness, the uranium enrichment would need to be increased to 50% to obtain a multiplication factor comparable to the HEU reference core. The other options were to increase the thickness of the LEU fuel plates or to add more fuel assemblies to the core boundary. Because of the significant changes that would be needed to the basic fuel unit cell or the assembly boundary, no further consideration was given to using the U-Al LEU fuel.

3.2 Use of LEU U10Mo Fuel

The next obvious choice of LEU fuel, based on numerous previous conversions, is a high density fuel such as U-10Mo alloy. While this fuel can reduce the required fuel plate inventory and critical core volume, it can also significantly change the core spectrum and other core characteristics. Comparison to the HEU core characteristics provides data to help determine the feasibility of using U-10Mo LEU in the KUCA cores.

Conversion studies with U-10Mo fuel were performed primarily for the KUCA I-1 configuration. As a first attempt, the LEU model was created by replacing the 93% enriched U-Al plate by a 19.75% enriched U-10Mo plate with an alloy density of 17.02 g/cm^3.

3.2.1 Reactivity Calculations

Keeping the same thicknesses of fuel and polyethylene plates as in the HEU core unit cell, the calculated reactivity value of the KUCA I-1 subcritical configuration increased from -371 ± 8 pcm (high-enriched U-Al case) to 12341 ± 7 pcm (low-enriched U-10Mo case with same thickness as HEU plate) indicating that the use of nominal density U-10Mo plates would keep the LEU core subcritical only by significantly reducing the thickness of the fuel plates or the number of fuel assemblies. Consequently, two designs of LEU fuel plates were successively considered, in both cases by reducing the thickness of the U-10Mo foils so that the mass of U-235 be the same of the HEU U-Al plate (i.e. the thickness of the U-10Mo foils was reduced to 0.03 cm).

For the first design, no cladding is used on the U-10Mo foils. In order to preserve the total extension (i.e. 1.0973 cm) of the fuel unit cell, the thickness of the first polyethylene plate in the unit cell was increased from 0.3086 cm to 0.4364 cm.

The option to add Al clad to the U-10Mo foils was then considered first with the clad only on the flat surfaces of the LEU plate and then adding clad to the edges of the plate. In this case, the thickness of the U-10Mo plates is always fixed so that the U-235 mass in the fuel plate remains the same as in the U-Al HEU core. The thickness of the cladding is determined such that the thickness of the polyethylene plates also remains the same as in the U-Al HEU core.

For both designs of LEU U-10Mo KUCA I-1 configurations, calculations were performed in both excess- reactivity and subcritical configurations. Calculated reactivity values are presented in Table 2. For comparison, the reactivity of the HEU core is also given in Table 2. It is observed that by preserving the U235 mass, the LEU U-10Mo configuration gives smaller reactivity values due to the increased H/U volume ratio. Additionally, the use of Al clad has a negative reactivity effect of about 4000 pcm.

Table 2. Calculated and Measured Reactivity Values for the KUCA I-1 Configuration.

	Reactivity (pcm, using ENDF/B-VII.0 Data)		
Rod Configuration	**LEU U-10Mo Plate – No Clad**	**LEU U-10Mo Plate – With Clad**	**HEU U-Al Plate (measured)**
Excess Reactivity	98 ± 6	-3629 ± 6	746 ± 8
Subcritical	-792 ± 6	-4782 ± 6	-371 ± 8

3.2.2 Indium Reaction Rate Distributions

Figure 4 shows the reaction rate distributions for two of the HEU benchmark cores and the U-10Mo LEU configurations with and without the Al clad.

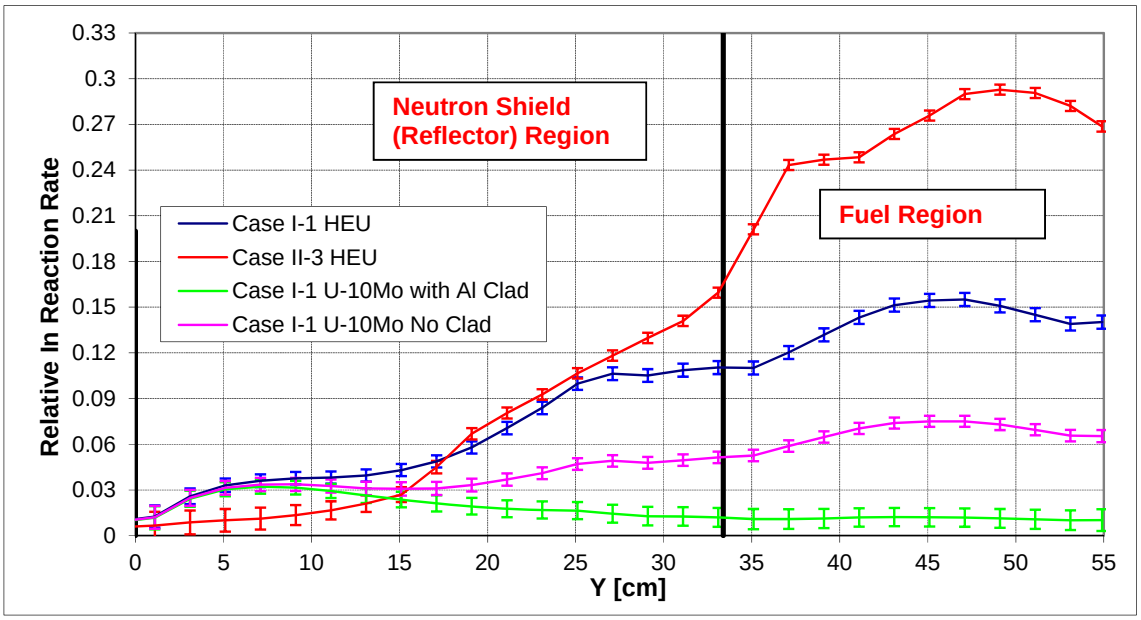


Figure 4. Calculated Relative Indium Absorption Rate Distributions.

The relative magnitudes of the curves are dependent of the fission source multiplication in the fuel plates, which is different for the HEU and LEU plates. While the general shapes of the HEU and LEU curves are similar, details within the distributions may indicate a mismatch between the HEU and LEU cores that requires further investigation.

3.2.3 Flux Spectra Calculations

Figure 5 shows a comparison of the flux spectra calculated in position B (near core center) in the HEU and LEU configurations, Similar to the previous KUCA configurations that have been analyzed, flux energy distributions in the core region show two peaks, one at high energy around 2 MeV and the other at lower energies around 0.1 eV. In both cases, with or without Al clad, the flux spectra in position B show enhanced peaks at 2 MeV and 0.1 eV and a decreased distribution in the range 3 - 300 eV.

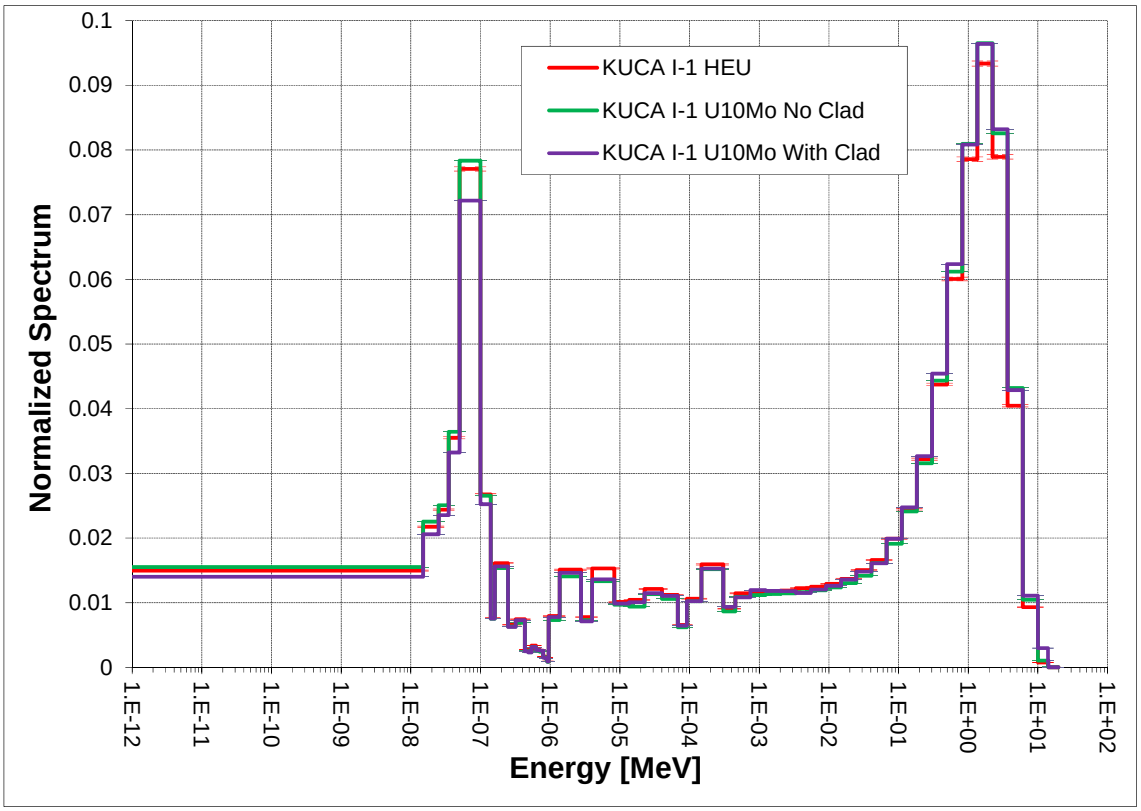


Figure 5. Flux Spectra at Position B of HEU and LEU KUCA I-1 Configurations.

4. Conclusions

The KUCA experiments were designed to establish measurement techniques for neutronic parameters in subcritical systems and to investigate the accuracy of the neutronic design of an ADSR. Due to the continuing interest in non-proliferation issues, new studies are being performed at KURRI to investigate the feasibility of converting the KUCA cores to the use of LEU fuel.

Calculations were performed with MCNP5 using ENDF/B-VII.0 nuclear data. The MCNP model was developed by explicitly describing all single plates, both for the polyethylene and the uranium.

Based on the benchmark specifications, reactivity calculations were performed with three different control rod configurations. The calculations show a consistent discrepancy between the calculated and experimental results of about 400 - 500 pcm for all KUCA configurations from Series I and of about 500 - 700 pcm for all KUCA configurations from Series II. It is however important to emphasize the fact that the foils located in the void region of the fuel assemblies “SV” of the KUCA configurations II-2, II-3 and II-4 have a reactivity effect of about 800 pcm. The use of different nuclear data libraries was shown to not have a significant impact on the discrepancies observed between the calculated and experimental results.

Indium rate distributions were calculated along the indium wire located at the core midplane with a (d,t) source in place. For the Series I and II configurations, the calculated indium rate distributions show reasonable agreement with the measurements in the shape of the

distribution, particularly in the fuel zone. In the reflector/shield region the calculations show a depression in the distributions that in some cases is not seen in the measurements.

Calculations were performed to evaluate the conversion of the KUCA “type A” cores from HEU to LEU using both U-Al and U-10Mo LEU fuel.

Besides the reactivity values, the feasibility studies on the conversion of the KUCA cores from HEU to LEU were also carried out with an extensive analysis of flux spectra and reaction rate distributions in relevant positions. While further study of the KUCA cores is necessary to compare power levels, reactivity coefficients and other performance parameters, none of the results presented here indicate any reason that the conversion of the KUCA dry cores to LEU cannot be performed successfully.

5. References

1. Cheol Ho Pyeon, Tsuyoshi Misawa, Hironobu Unesaki, Chihiro Ichihara and Kaichiro Mishima, “Research on Accelerator Driven Subcritical Reactor at Kyoto University Critical Assembly (KUCA),” AccApp'07, Pocatello, Idaho, July 29-August 2, 2007.
2. Gerardo Aliberti, Hironobu Unesaki and Cheol-Ho Pyeon, “Analysis of KUCA type-A Cores,” RERTR 2012, Warsaw, Poland, October 14-17, 2012.
3. Gerardo Aliberti, James A. Morman, John G. Stevens, Hironobu Unesaki and Cheol-Ho Pyeon, “On the Conversion of KUCA Type-A Cores from HEU to LEU Using U10Mo Foils,” ANS Winter Meeting, Washington, D.C., November 10-14, 2013.

THE NEWEST CASK DESIGN FOR INTERNATIONAL SHIPMENTS IN SUPPORT OF RESEARCH REACTOR AND LABORATORIES STAKEHOLDERS: TN-LC PACKAGE

N. GUIBERT
AREVA TN America
7135 Minstrel Way, Suite 300, Columbia, MD 21044 - USA

ABSTRACT

TN operates a comprehensive fleet of licensed packages for a wide spectrum of radioactive material shipments worldwide. Some of AREVA's licensed packages, such as the TN-106 or the TN-MTR are dedicated to the shipments of irradiated material or used fuel from research reactors. In order to respond to new shipment needs and to support future US domestic and international transports, AREVA TN America, the AREVA TN entity in the United States (US), is fabricating a new package, named the TN-LC. The TN-LC offers a specific and customized solution for unconventional research reactor and laboratory shipments. The TN-LC was granted a Nuclear Regulatory Commission (NRC) Certificate of Compliance (COC) license in December 2012 and is currently being manufactured. It will be available to support US domestic and international shipments by early 2015.

The TN-LC ("Long Cask") is a new type B(U)-F package that features a variety of basket designs that fit into the TN-LC cavity; thus it can accommodate used fuel from research reactors (Material Test Reactor (MTR), TRIGA, NRU/NRX, etc.), full length commercial fuel assemblies (Pressurized Water Reactor (PWR), Boiling Water Reactor (BWR)), irradiated pins (EPR™, Mixed Oxide (MOX), PWR, BWR) to support post irradiation examinations (PIE) or other irradiated contents. The package weighs 25 metric tons, thus is light enough to be used in many research reactors and laboratories. The TN-LC has been designed to allow versatile on-site operations and can be loaded and unloaded wet (underwater) or dry using a dry transfer system (DTS) or hot cell.

The TN-LC has been developed to meet the upmost recent International Atomic Energy Agency (IAEA) standards and safety requirement of the NRC and international regulators, and benefits of the recognized experience in the transport package design and fabrication of AREVA TN. Some of the most innovative technical improvements developed by the AREVA TN over the last years have been implemented in the package design and fabrication.

Because of the TN-LC operational flexibility, it can be used in commercial power plants as well as in research reactors and laboratories.

AREVA TN America handles nearly 800 shipments of radioactive material annually, and, with the TN-LC, now expects to expand its used fuel transport capabilities in the US and in the diverse worldwide market.

1. New Generation Transport Package for U.S. Domestic and International Shipments

The innovative TN-LC is a NRC licensed transport package designed to safely handle US domestic and international shipments of used commercial and research reactor fuel assemblies and irradiated material. It has been designed to meet the upmost safety standards from the IAEA and of the different competent authorities of the countries where the TN-LC is intended to be transported. It is already licensed in the US (Certificate of Compliance USA/9358/B(U)F-96) and is intended to be licensed in many countries around the world.

The TN-LC offers proven features, developed and tested in other packages that provide for increased safety, increased transport capabilities, and more efficient operations. These features are:

- Removable trunnions: The TN-LC trunnions are removable. They are put in place before the tilting operations and are removed before transport. The trunnions usually constitute a weakness in the structural behavior of transport packages especially during the drop test.

- Push-pull rod: a small lid has been put at the bottom of the cask. This lid is intended to allow the use of a shielded rod that will allow the loading or unloading operation of the payload when the package is connected to a hot cell. This feature is currently implemented and used on the TN-106 package.

- The TN-LC design authorizes the use of the TN® Vyal B resin as neutronic shielding. The TN® Vyal B resin is a high performance neutron shielding material that is resistant to fire (self-extinguishing). This resin provides improved shielding while keeping good thermal properties. For example, this resin is currently being installed on the EPR™ reactors among others.

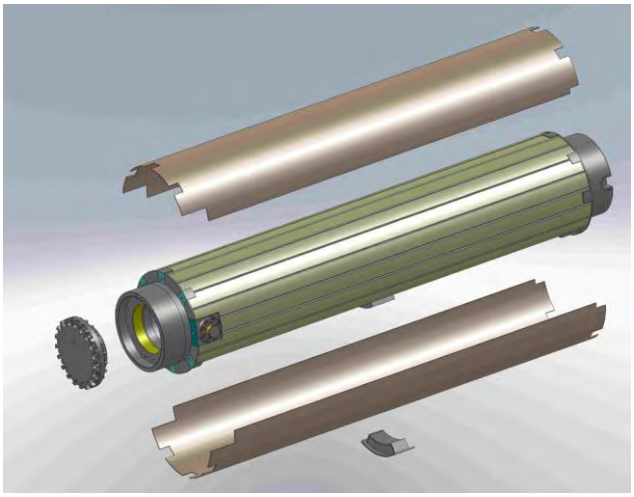


Figure 1 : TN-LC package design

2. Versatile Package Designed to Hold Different Contents

The TN-LC has the capacity to transport various types of fuel pins and assemblies, including commercial fuel assemblies (BWR, PWR), rods or pins (EPR™, MOX, PWR, BWR), and research reactor assemblies such as NRU/NRX, TRIGA elements, and MTR fuel assemblies.

To do so, four different internal arrangements called baskets have been designed to accommodate the different payloads in an optimal way:

- MTR basket : this basket is actually made of buckets that hold 3 assemblies each. One tier contains three buckets. With a maximum of six tiers, 54 MTR assemblies can be transported.

- TRIGA basket : This basket is available in different lengths to accommodate intact TRIGA elements of different sizes including TRIGA Fuel Follower Control rods. The basket has a capacity of 36 elements and up to five baskets can be loaded in the cask.

- NRU/NRX basket : This basket is composed of 2 “bucket baskets” that authorize the transfer of (13) intact or damaged NRU or NRX assemblies at a time with a dry transfer system

- 1FA basket : this basket can accommodate one intact full length fuel PWR or BWR assembly or pin cans that can accommodate up to (25) intact PWR, BWR, EPR™ or MOX fuel rods.

  Other baskets can also be designed to accommodate other transportation needs

3. Lighter and Longer Package With Higher Capacity

The TN-LC has the ability to handle longer fuel assemblies with an on-hook weight limit of 25 tons.

TN-LC Dimensions

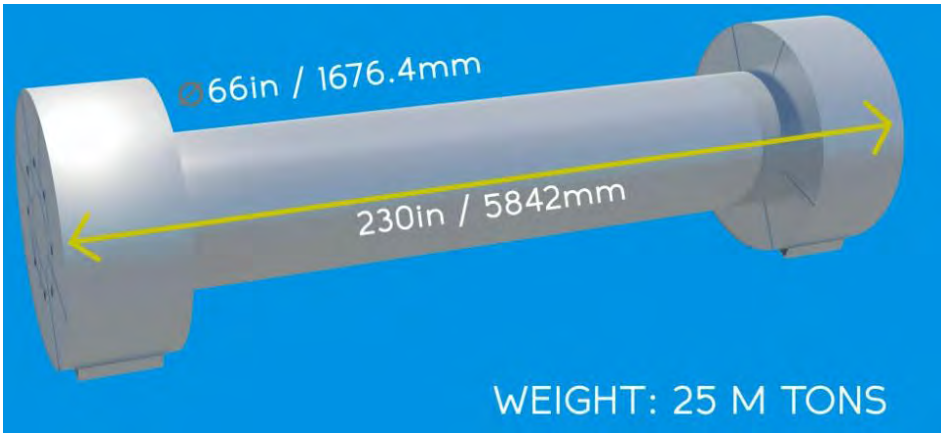


Figure 2 : TN-LC outer dimensions

Body dimensions :
Outer: 197.5 inches (5,017 mm) long by 44.5 inches (1,130 mm) diameter.
Inner: 182.5 inches (4,636 mm) long by 18.0 inches (457 mm) diameter.

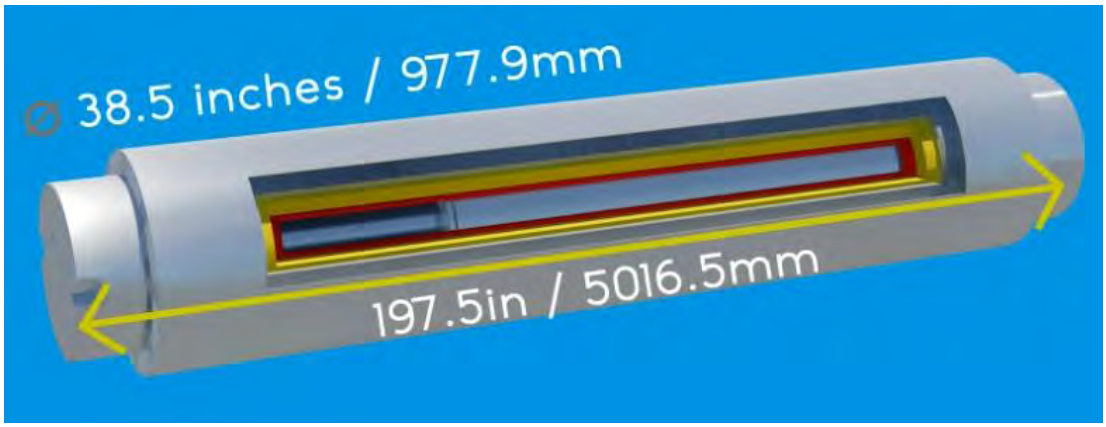


Figure 3 : TN-LC inner dimensions

TN-LC Capacity:
The TN-LC, designed with cavity dimensions that are longer and larger than what the market offers today, will accommodate large quantities of fuel assemblies. Higher transport capacity means more cost-effective transports. For each package, the maximum number of assemblies that can be shipped are:

- 1 PWR/BWR assembly
- 25 PWR/BWR/EPR™/MOX pins
- 26 NRU/NRX assemblies
- 54 MTR assemblies
- 180 TRIGA elements

4. Transport of High Burnup Fuel

The maximum burn-up authorized depends on the type of fuel and on the enrichment and cooling time of the fuel. As there is a wide range of contents, a lot of combinations are possible:

- For MTR fuel, the maximum enrichment is 94%, the maximum burn-up is 660 GWd/tU and minimum cooling time is 740 days.
- For PWR or BWR fuel assemblies, the maximum burn up is 62 GWd/tU
- For UO_2 fuel rods transported in the pin can, the maximum burn-up is 90 GWd/tU
- For EPR™ or MOX fuel rods transported in the pin can, the maximum burn up is 62 GWd/tU.

5. Flexible Operation Capabilities

With its 25 ton weight, the TN-LC complies with most commercial or research reactor site weight restrictions. The TN-LC is designed to be loaded or unloaded in the vertical or horizontal position and can be operated in wet or dry conditions, in fuel pools or hot cells. A dry transfer system is being developed allowing operation in sites with weight restrictions and shallow pools.

The TN-LC is a new generation of transport package for the safe transport of used fuel, designed to handle a large variety of contents for US domestic and international shipments, with flexible operation capabilities, for use in commercial and research reactor sites.

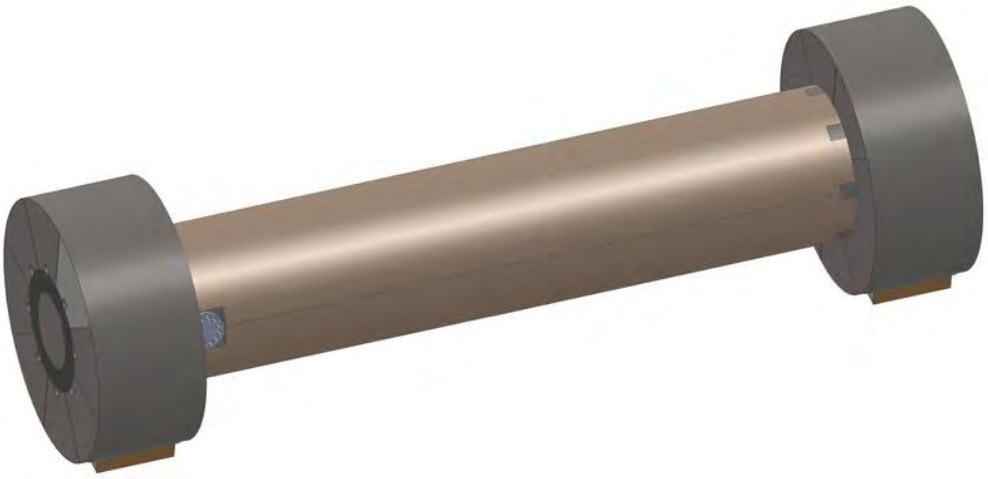


Figure 4 : TN-LC in transport configuration

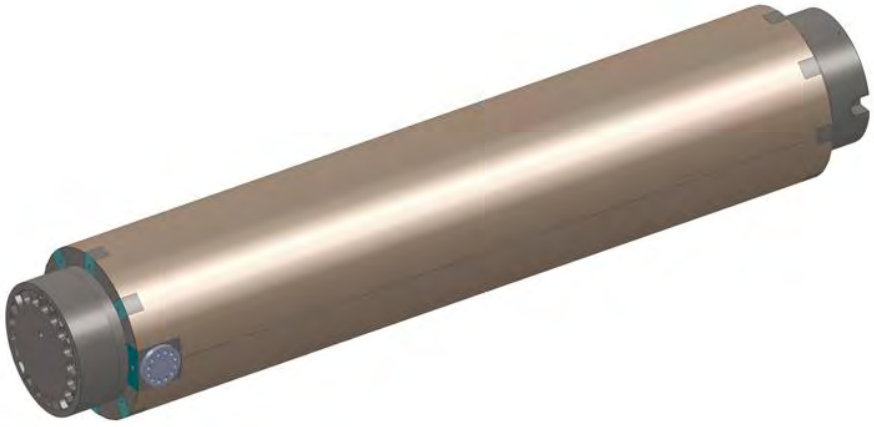


Figure 5 : TN-LC without the impact limiters

About AREVA

AREVA is the world leader in the back end of the nuclear fuel cycle with more than 48,000 employees around the world. As part of the AREVA Group, AREVA TN offers innovative solutions for the transportation and storage of nuclear materials for nuclear power plants and research reactors around the world. AREVA operates the largest fleet of transportation casks in the world and organizes more than 3,000 multi-model shipments of nuclear material each year; more than 70 shipments are in progress at any given time.

About AREVA TN America

AREVA TN America (previously named Transnuclear Inc.), a forward-thinking AREVA company, is a recognized leader in nuclear fuel and waste transportation and storage in North America. Dedicated to ensuring safe and error-free transportation and storage of fuel, the AREVA TN America team drives engineering innovation throughout the fuel cycle materials market.

RADIOACTIVE WASTE ANALYSIS OF RESEARCH REACTOR SPENT FUEL

R. KHAN, I. HUSSAIN, S. KHAN
Nuclear Engineering, Pakistan Institute of Engineering and Applied Sciences (PIEAS)
P.O. Nilore, 44000, Islamabad-Pakistan

A. MUHAMMAD
Nuclear Engineering Division, Pakistan Institute of Nuclear Science and Technology (PINSTECH), P.O. Nilore, 440001, Islamabad-Pakistan
Islamabad

T. STUMMER
Atominstitue, Vienna University of Technology
A-1020, Vienna, Austria

ABSTRACT

A sound knowledge of radiation safety parameters (radioactivity, surface dose rates and decay heat) is extremely important in safety assessments of the management of the radioactive waste. Specifically, the waste management community requires reliable information of these parameters in order to design the short and long term waste storage facilities. For this purpose, a hypothetical high level liquid waste generated from Pakistan Research Reactor-I (PARR-I) spent fuel. For this purpose, a spent fuel element of PARR-1 with 50% burn-up is selected and its relevant fuel composition is homogeneously mixed with water to form a high level liquid radioactive waste. The dose rates and decay heat profiles of radioactive waste storage are studied in this work. For this purpose, a cylinder of radius 54.19 cm and height 108.38 cm containing 1000 litres of water is assumed. From the material composition of spent fuel, five isotopes have been selected for this study. These isotopes (Cs-134, Ru-106, Cs-137, Pr-144, Nb-95) are homogeneously mixed with water to from a cylindrical high level liquid radioactive waste storage tank. The radioactive analysis of this hypothetical radioactive waste has been performed employing the combination of two radiation simulating codes ORIGEN2, MICROSHIELD and Monte Carlo radiation transport code MCNP5. The ORGIEN2 is used to simulate the radioactivity and its decay heat profile while MICROSHIELD code is aimed at radiation shielding and prediction of the surface dose rates along the height of the cylinder. The radiation simulating computer code MCNP5 is used to calculate the surface dose rate of radioactive waste tank. The five selected isotopes with their initial radioactivities exhibit an exponential decay. The surface dose rates, radioactivity and decay heat profile of the five selected isotopes are presented in this paper.

1 Introduction

In this research work, a spent fuel element of Pakistan Research Reactor (PARR-1) is selected for its radioactive analysis. The PARR-1 is a swimming pool type material testing research reactor (MTR), having a parallelepiped core comprising LEU (U3Si2-Al) fuel, containing 19.99% 235U. Demineralized light water is used as coolant and moderator. One side of the parallelepiped core is reflected by graphite, i.e. thermal column, while opposite side is reflected by a blend of graphite reflector elements and light water. The bottom side is reflected by a combination of aluminium and water. Rest of the three sides, i.e. top and two lateral sides, are reflected by light water only. PARR-1 core is designed to have negative coefficients of reactivity, a reflection of the fail-safe principle.. Fuel elements, control rods,

graphite reflector elements, water boxes for irradiation of samples and fission chambers with their guide tubes are assembled on a grid plate, having 54 holes arranged in 9×6 array, with a lattice pitch of 81.0×77.1 mm. PARR-1 core configuration shown in Figure1 comprising 24 standard fuel element (SFE) and 5 control fuel element (CFE) [1]. At PARR-1, five (Ag-In-Cd alloy) control rods are employed for reactor operating power level control and safe shut down in normal or any anticipated accidental condition. The PARR-1 core provides numerous irradiation facilities, which include water boxes, graphite thermal column, pneumatic rabbit tubes, beam port tubes, dry gamma cell, a bulk irradiation area and hot cell. Main specifications of PARR-1 are given in Table 1 [1].

A standard fuel element of PARR-1 is selected for its radioactive analysis. For this purpose, burn up calculations of the PARR-1 fuel element employing ORIGEN2 has been performed. The simulated results of one standard fuel element for (Cs-134, Ru-106, Cs-137, Pr-144, Nb-95) at 50 % burn up and zero decay time are given in Table 2. These isotopes are homogeneously mixed with water to form cylindrical high radioactive waste. The surface dose rates and decay heat profiles are calculated for radioactive waste using the combination of depletion computer code ORIGEN2, radiation shielding tool MICROSHIELD6 and Monte Carlo radiation transport code MCNP5. These softwares are well known and validated computer programs [2, 3, 4].
The ORIGEN2 is a one-group depletion and radioactive decay computer code which was developed by Oak Ridge National Laboratory (ORNL) [2]. The main utilization of ORIGEN2 is to calculate radionuclide composition, activity, decay heat and other related properties of nuclear materials. The materials most commonly characterized by ORIGEN2 include spent fuels, radioactive wastes (principally high-level waste), recovered elements (e.g., plutonium, uranium), mill tailings, uranium ore, and gaseous effluents streams (e.g., Nobel gases) etc.
The MICROSHIELD6 is used to evaluate surface dose of the container containing the radioactive waste [3]. It can be used to analyse the shielding and to estimate exposure from gamma radiation. This software helps in analysing shields, design of containers, assessing radiation exposure to the people and materials, selecting temporary shielding for maintenance work, inferring source strength from radiation measurements for waste disposal, reducing the exposure to people and materials, and teaching principles of radiation and shielding.
The MCNP5 is general purpose probabilistic radiation transport code used for radiation shielding, reactor core and criticality calculations [4]. This research work employs the JEFF3.1 nuclear cross section libraries.

Reactor type	**Swimming pool**
Nominal core power (MW)	10
Lattice pitch (mm)	81.0×77.11
Fuel material and enrichment	U3Si2-Al (19.99 % by wt)
Cladding material	Aluminum
Coolant/Moderator	Light water (H2O)
Coolant flow rate (m3/h)	950
Reflector	Light water and Graphite
Fuel element description	Straight plate MTR type fuel element
U235 contents per SFE (g)	290.0
U235 contents per fuel plate (g)	12.61
Control rods	Oval shaped 5 rods
Composition of control rods	80% Ag, 15% In, 5% Cd

Operational Modes	Manual and Automatic

Table 1: Main specifications of PARR-1 [1].

2 Models of the Radioactive Tank

2.1 MICROSHIELD Model

The cylindrical high level liquid radioactive waste storage tank of radius 54.19 mc and height 108.38 cm is simulated using radiation shielding design computer code MICROSHIELD6 to calculate the surface dose rate and decay heat profiles. The cylinder contains 1000 liters of water. The five radionuclides already mentioned are uniformly distributed in the waste tank. The surface dose rates have been calculated at five different pints at each 21 cm along the height of the tank. The MICROSHIELD model is presented in Figure 1.

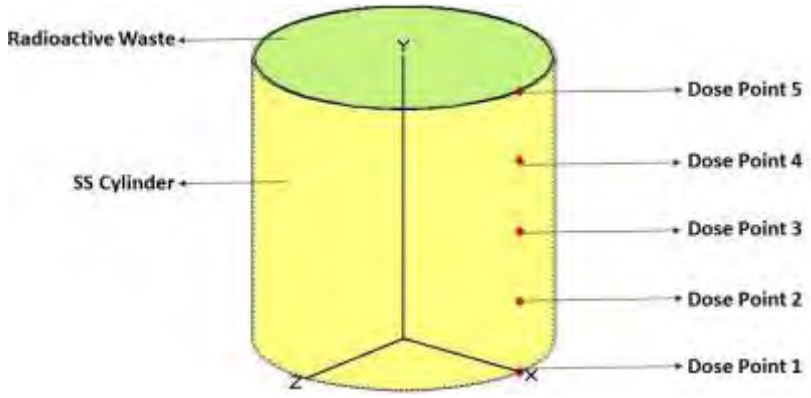


Fig. 1: MICROSHILD model of the radioactive waste storage tank.

2.2 MCNP Model

The MCNP model of the high radioactive waste cylindrical tank has been developed using nuclear cross section library JEFF3.1. The surface dose at each five points along the height of the waste tank is simulated using flux tally. The top and side view of the MCNP model has been shown in Figure 2.

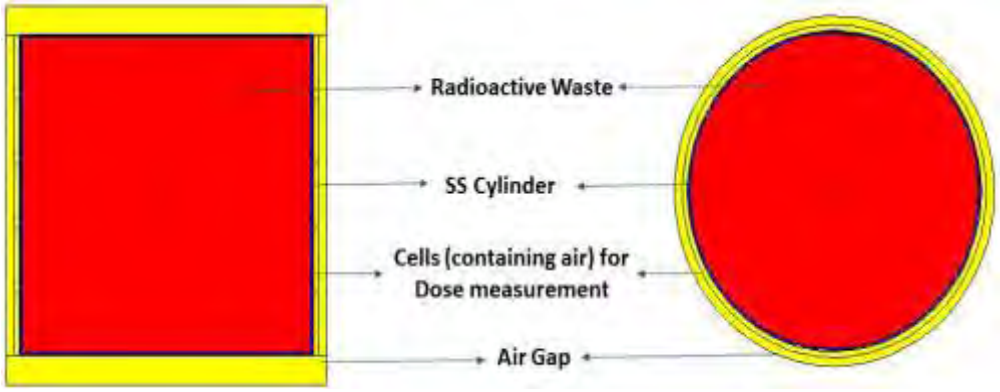


Fig. 2: The top and side view of the MCNP model of radioactive waste tank.

3 Results and Discussion

3.1 Surface Dose Rates

For the radioactive analysis of spent fuel, its consequent high level liquid radioactive waste, and material composition, a burned fuel element at 50% burned fuel element are simulated

using depletion code ORIGEN2. The results of one standard fuel element for (Cs-134, Ru-106, Cs-137, Pr-144, Nb-95) at 50 % burn up and zero decay time are given in Table 2.

Nuclides	Activity (Ci)
^{134}Cs	3.90E+02
^{106}Ru	7.33E+02
^{137}Cs	3.79E+02
^{144}Pr	8.93E+03
^{95}Nb	1.75E+04

Table 2: Radio activities (Ci) of nuclides at 50 % burnup of single LEU SFE.

The above mentioned isotopes are assumed to be uniformly distributed in the hypothetical radioactive waste tank. The surface dose rates at five different pints each at 21 cm along the height of the cylindrical waste storage are calculated using two different codes i.e. radiation shield design code MICROSHIELD6 and Monet Carlo radiation transport code MCNP5. The results from both techniques are compared in the Table no. 3 and Figure no. 3. The predicted results are quite symmetrical i.e. surface dose rate is maximum at the centre and decreases along the height. The percent difference between two different methodologies varies from 18.4 to 95 as given in Table 3. The main reason of these deviations could be the different nature of simulating methods and their nuclear data libraries. The computer code MICROSHIELD uses deterministic relations with set of attenuation coefficients and gamma interaction probabilities while MCNP applies probabilistic methods to solve radiation transport equation. MCNP5 uses JEFF3.1 nuclear data libraries which is different than MICROSHIELD6 data libraries

Dose point	MCNP dose rates (rad/hr)	MICROSHIELD dose rates (rad/hr)	%- difference
1	8.10E03	9.60E03	18.5
2	1.00E04	1.93E04	93.0
3	1.02E04	1.99E04	95.0
4	1.01E04	1.93E04	91.0
5	8.11E03	9.60E03	18.4

Table 3: surface dose rates Comparison along the height of the radioactive waste tank.

3.2 Radioactivity and decay heat profiles

The radioactivity and decay heat profiles of the selected isotopes are simulated using ORIGEN2 model. This code uses the PWR nuclear cross section library as there is no library for MTR type research reactor. The radioactivity and decay heat profiles of two isotopes i.e. Cs-134 and Cs-137 are presented in the Figure 4. The simulated profiles show good agreement with reference values [**5**].

.

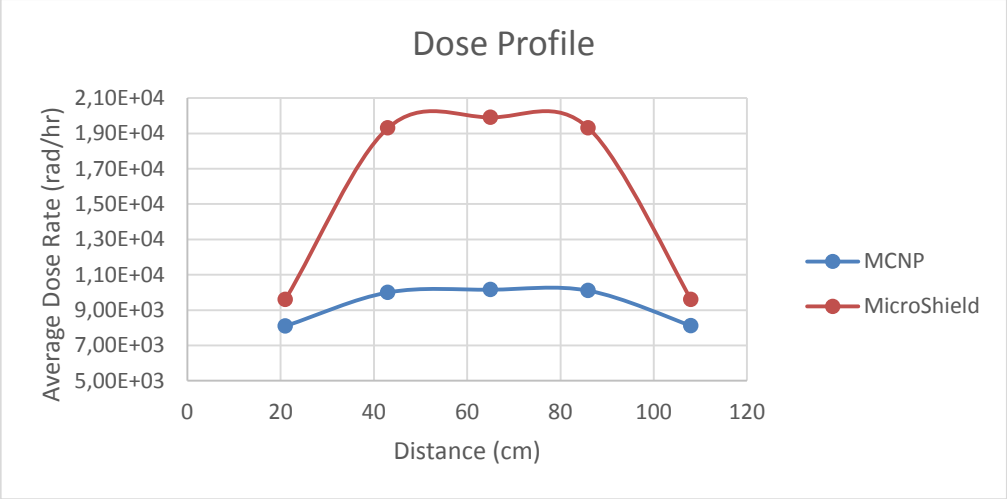


Fig. 3: Comparison of surface dose rates along the height of the radioactive waste tank.

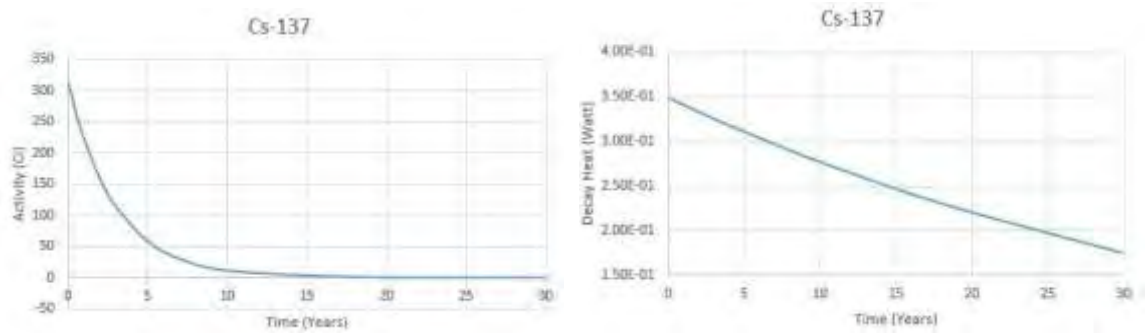


Figure 4: Radioactivity (Ci) and decay heat profiles of Cs-137.

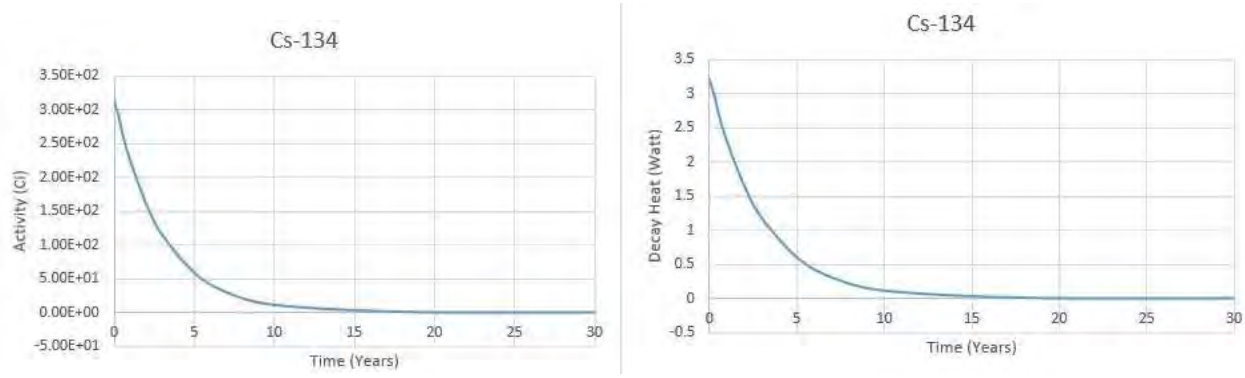


Figure 5: Radioactivity (Ci) and decay heat profiles of Cs-134.

4 Conclusion

The surface dose rates, decay heat profiles and radioactive decay of the selected isotopes in high level radioactive waste tank are studied using three different computer programs. These computer programs include radiation shielding tool MICROSHIELD6, nuclear depletion code ORIGEN2 and Monte Carlo radiation transport code MCNP5. A cylinder of radius 54.19 mc and height 108.38 containing 1000 litres of high active waste was assumed for its radioactivity, dose rate and decay heat study. The five radioisotopes (Cs^{134},

Ru^{106}, Cs^{137}, Pr^{144}, Nb^{95}) were considered as homogeneous mixture of water in waste storage tank. The comparison of estimated surface dose rates by two different methodologies is presented in this paper. The radioactivity and decay heat profiles of selected isotopes show good agreement with the literature.

REFERENCES

[1] Muhammad, A., Iqbal, M.,Mahmood, T., 2012. Burn-up effect on inherent safety parameters and reactivity insertion transient analysis of Pakistan Research Reactor-1. Progress in Nuclear Energy 58, 1-5.

[2] G.Croff, "ORIGEN2: A Versatile Computer Code for Calculating the Nuclide Compositions and Characteristics of Nuclear Materials," Nuclear Technology, 1983, vol. 62, pp. 335-352.

[3] Grove Engineering, MICROSHIELD shielding and dose assessment program, 2003.

[4] X-5 Monte Carlo Team, 2005, MCNP - A general Monte Carlo N-particle Transport code, Version 5, LA-UR-03-1987.

[5] Lamarsh, J.R, Introduction to Nuclear Engineering, Addison-Wesley, 1983. Grove Engineering, MICROSHIELD shielding and dose assessment program, 2003.

[6] INTERNATIONAL ATOMIC ENERGY AGENCY, "Classification of Radioactive Waste", SAFETY SERIES No. 111-G-1.1,1994. URL: www-pub.iaea.org/mtcd/publications/pdf/pub950e_web.pdf.

[7] INTERNATIONAL ATOMIC ENERGY AGENCY, "Classification of Radioactive Waste", General Safety Guide No. GSG-1,2009, URL: ww-pub.iaea.org/MTCD/publications/PDF/Pub1419_web.pdf.

[8] Herman Cember, Health Physics, McGraw-Hill, 1996.

[9] INTERNATIONAL ATOMIC ENERGY AGENCY,"Clearance levels for radionuclides in solid materials",Interim report for comment,1996, URL: www-pub.iaea.org/MTCD/publications/PDF/te_855_web.pdf.

C. E. MESSICK and J. J. GALAN
U.S.-Origin Nuclear Material Removal Program
U.S. Department of Energy, National Nuclear Security Administration
Office of Global Threat Reduction, Washington, D.C. 20585—United States of America

ABSTRACT

The United States (U.S.) Department of Energy (DOE) Global Threat Reduction Initiative's (GTRI) U.S.-Origin Nuclear Material Removal program, also known as the Foreign Research Reactor Spent Nuclear Fuel Acceptance Program (FRR SNF AP), was established by the U.S. Department of Energy in May 1996. The program's mission provides a disposition pathway for certain U.S. origin spent nuclear fuel and other weapons-grade nuclear material. The program will continue until May 2016 with an additional three year window for fuel cooldown and transportation. This paper provides an update on recent program accomplishments, current program initiatives and future activities.

1. Introduction

The National Nuclear Security Administration (NNSA) Global Threat Reduction Initiative's (GTRI) U.S.-Origin Nuclear Remove Program (Program), also known as the Foreign Research Reactor Spent Nuclear Fuel Acceptance Program (FRR SNF AP), supports permanent threat reduction by eliminating stockpiles of excess weapons-usable nuclear materials located at civilian sites throughout the world. GTRI has played a critical role in fulfilling commitments under the Joint Statement on Nuclear Security Cooperation agreed to by the U.S. and Russian presidents at Bratislava in 2005, and directly supports President Obama's commitment to secure all high priority nuclear materials worldwide within four years. This four-year effort successfully concluded at the end of 2013. To date, GTRI has repatriated 1,264 kilograms of highly enriched uranium (HEU) and 3714 kilograms of low enriched uranium (LEU) to the United States. This paper outlines the Program's history, various issues surrounding the Program's execution, and lessons learned from recent shipments that may affect foreign research reactor spent nuclear fuel (SNF) projects. In addition, the paper describes current GTRI efforts to advance the goals of the Program, highlighted by continuing efforts to work with foreign research reactors to ship eligible materials as early as possible.

Although the four-year effort has officially concluded and the Program was largely successful, more work remains ahead. As the Program approaches its termination date including the three-year window to allow fuel cooldown and transportation, GTRI is committed to working with all reactor operators or facilities with eligible HEU spent nuclear fuel or other eligible HEU materials to provide for safe removal and disposition activities. Additionally, GTRI is willing to work with reactor operators for acceptance of eligible LEU spent nuclear fuel.

2. Program History and Accomplishments

The Program, now in its eighteenth year, has successfully completed sixty-two (62) shipments to date, safely and securely. Thirty-two (32) countries have participated, returning a total of 9563 spent nuclear fuel elements to the U.S. for management at Department of Energy (DOE) sites in South Carolina, Tennessee and Idaho. Forty-eight (48) of the shipments contained aluminum-based SNF placed into storage at the Savannah River Site (SRS) in South Carolina. Ten shipments consisted of Training, Research, Isotope-General Atomics (TRIGA) type fuel placed into storage at the Idaho National Laboratory (INL). The

remaining four shipments were sent to the Y-12 National Security Complex because the fuel was fresh or slightly irradiated and eligible for receipt at that facility, enabling more efficient disposition. The most recent shipment, a joint shipment from Austria and Italy, was completed without incident, arriving at SRS on December 4th, 2012 (Austrian material) and INL on December 8, 2012 (Italian material). The Program is currently planning no shipments during the remainder of calendar year 2014 while the Savannah River Site receipt facilities are undergoing an outage for upgrades.

3. Contractual Requirements

3.1 Contract Implementation

DOE enters into a contract with each reactor operator who returns SNF to the U.S. If these reactor operators have not completed a contract extension or renewed their contract to allow shipments past 2009, the end of the original Program period, a new contract will be required to continue shipments. Reactor operators must contact the Program office to negotiate a new contract to authorize participation. Basic contract language has changed since the extension of the program. However, these contract language changes have no significant effect on the contract and shipping project implementation.

3.2 Public Disclosure of Shipment Information

It is very important that the contracting parties clearly understand all provisions in the contract. Contract requirements are usually described in detail prior to the first shipment. As time passes and personnel change, some understanding may be lost, so it is very important to review the contract and ask questions if there is any doubt about contractual obligations. Compliance with all contract requirements must be maintained.

One very important article in the contracts which has been misunderstood in the past covers public disclosure of shipping plans, shipment information or the individual details comprising such plans or information. Any such disclosure must comply with limitations required by U.S. Government regulations and IAEA Information Circulars, primarily the U.S. Code 10 CFR § 73.22(a)(2)(ii), 10 CFR § 73.21(b), and IAEA INFCIRC 225 Rev. 5. This means that information regarding dates and/or schedules, and any other information about the contents of the shipment, cannot be published or publicly released until 10 days after the shipment has arrived at its final destination in the U.S., unless permission is granted in advance in writing. Shipment information must only be revealed to those who have a legitimate need to know in order to support shipment activities. Information on security measures should never be publically released or published. Compliance with this contractual requirement is an important obligation to ensure safety and security for any shipment activity. DOE considers premature release of this information a violation of the contract. The inappropriate release of shipment information poses an unwarranted security risk and could make the shipment vulnerable to bad actors. It would also violate U.S. Nuclear Regulatory Commission (NRC) regulations under which all shipments are authorized. Further, The Convention on the Physical Protection of Nuclear Material, entered into by states which support the Program, requires that each state protect the confidentiality of this information. The ability to continue the Program is contingent upon our customers implementing the agreed upon information security requirements. As a result, the reactor operators should coordinate with participating organizations, governmental and nongovernmental, to ensure all persons and entities that receive shipment information understand they are affirmatively obligated to maintain confidentiality until the material arrives at its final destination.

An improper release of shipment information could affect DOE's decision to issue the "Authorization to Ship" which allows a shipment to depart a facility or reactor site. If the shipment is allowed to proceed, a heightened security posture or other mitigating actions

may be required, resulting in a delay. However, if the information release is deemed to create too large a risk, the Program can cancel the shipment altogether, pursuant to the excused performance section of the contract.

3.3 Revised Fee Policy

DOE is continuing to try to keep the reactor operator's cost to participate in the Program as low as possible, however, because of the increase in operational costs of receiving and managing SNF, on January 31, 2012 DOE issued the **Revised Fee Policy for Acceptance of Foreign Research Reactor Spent Nuclear Fuel From High-Income Economy Countries** (77 FR §4807). This was the first fee increase since the fee policy was established in 1996.

A synopsis of the revision:

- The first phase took effect January 31, 2012; and the fee for receipt of LEU fuel increased from no higher than $3,750 per kg of total mass to $5,625 USD per kg of total mass. The fee for SNF shipments containing HEU remains at no higher than $4,500 USD per kg of total mass.
- DOE also implemented a new minimum fee of $200,000 USD per shipment of any type and amount of eligible SNF to reflect a minimum cost of providing acceptance services, this fee took effect January 31, 2012.
- The fee for return of TRIGA fuel will be the same as that of aluminum based fuel.
- The second phase was automatically implemented on January 1, 2014 and the fee for the receipt of LEU fuel will increase from $5,625 USD per kg of total mass to $7,500 USD per kg of total mass and for HEU fuel, the fee for the receipt of HEU fuel will increase from no higher than $4,500 USD per kg of total mass to $6,750 USD per kg of total mass.
- The third phase will be implemented automatically on January 1, 2016, and the fee for the receipt of HEU fuel will increase from $6,750 per kg of total mass to $9,000 USD per kg of total mass.

In the case where a reactor operator already has a signed and executed contract, DOE intends to negotiate an equitable adjustment to the fee in accordance with this revised fee policy.

The current fees are based on the fee structure in effect as of January 1, 2014, but will increase again in 2016 for HEU fuel. Reactor operators and Program participants should carefully review the Revised Fee Policy to determine the effects of this revision. If you have any questions, please contact the Program office.

4. Focus on Advance Planning

GTRI focuses on the early planning and deliberate implementation of SNF shipments to the U.S. in support of worldwide nuclear nonproliferation efforts. Shipments involve many different logistical challenges and early planning mitigates the risk of unanticipated issues delaying a shipment schedule. The expiration of the program and the cooldown and shipping window is rapidly approaching. Any reactor operator considering participation in the Program should commence advance planning as soon as possible. The importance of communication and coordination with GTRI and the receiving site cannot be over-emphasized.

4.1 Shipment Scheduling

GTRI must clearly understand the intentions of all reactor operators so that shipment planning can be well integrated and supported. To ensure that shipments adhere to agreed-

upon schedules, it is imperative that the required fuel data be submitted as early as possible. This allows adequate time for the receiving site to perform necessary safety reviews and prepare for receipt and storage of the material. Early availability of this data is also essential for use in verifying transport package license requirements or providing sufficient time to submit a license amendment, when required. Budget limitations have been known to challenge implementation of shipping plans for our customers. Similarly, the DOE receiving facilities are facing ever increasing challenges in providing resources to receive material, particularly when shipping plans are not well known. It is anticipated that these funding challenges will continue to threaten DOE's receipt capability and capacity.

At the request of many foreign research reactors, the Program was extended in 2004 to allow time for further development of LEU fuels and planning for back end solutions in the fuel cycle. The extension was granted for the benefit of research reactors in justifiable need of relief. However, some foreign research reactors are now cancelling or rescheduling shipments to defer costs, which was not the intent of the extension. These delays negatively impact DOE's ability to maintain a regular schedule of operations and adequate resources for the receipt facilities. Thus, GTRI strongly encourages reactor operators to continue shipping as early as possible and maintain original schedules where possible. GTRI currently anticipates a large number of shipments near the end of the policy period. If too many shipments are deferred until the end of the policy period, DOE may be required to exercise its authority under the contracts to limit receipts to those specific customers it deems have the greatest need. This is particularly important to reactor operators that only have LEU fuel remaining and reactor operators that are limited in their selection of an appropriate transport package or cask. It is expected that some packages may have limited availability during these last few years of the Program.

4.2 Cask License Review

GTRI enjoys an excellent working relationship with the NRC and makes every effort to respect this relationship by ensuring that cask license applications are timely and complete. GTRI meets regularly with the NRC to discuss planned shipments and to forecast the support required to meet the needs of the Program and our customers. Because there are limited NRC resources for review of cask licenses, customers must ensure adequate time is available for the application preparation process, the NRC's review of the application, and final approval of cask licenses.

4.3 Insurance Issues

Insurance issues have recently become a recurring problem for reactor operators in high-income economy countries participating in joint shipments. The reactor operators are sometimes required to have overlapping insurance coverage with different requirements for minimum coverage. Reactor operators entering into a joint shipment can sometimes coordinate when obtaining nuclear liability insurance from the same pool or under a joint contract. It is important to plan early and determine how to provide the required coverage in the least expensive manner. Reactor operators should be conscious of this potential problem and budget for any added insurance costs that cannot be mitigated.

4.4 Title Transfer Location

Title transfer from the reactor operator and DOE is normally conducted at the U.S. port upon off-loading of the authorized material. The Secretary of Energy has authorized the NNSA Administrator to consider, on a case-by-case basis, whether it is in the best interest of the U.S. to take title to certain SNF and target material from reactors located in countries with high-income economies before it reaches the port of entry into the U.S. In order to be considered for title transfer at an earlier point, GTRI must provide the NNSA Administrator with sufficient evidence to prove the need exists to grant formal approval to accept title. In

these cases the title transfer location would be specified in the contract with the affected reactor operator. In order to extend the United States' Price-Anderson Amendment Act nuclear liability indemnification, DOE is also required to control and manage the carrier of the U.S. titled material.

5. Efforts to Improve and Accelerate

GTRI and reactor operators need to work together to schedule shipments as soon as possible to optimize shipment efficiency over the few remaining years of the Program. Countries interested in participating in the Program should express interest now so fuel and reactor facility assessments can be scheduled and shipment dates can be entered into the long-term forecast. Decreasing resources and coordination requirements with other government agencies could limit DOE's capability to support accelerated schedules, especially as the Program endpoint approaches. GTRI may not be able to accommodate a large number of requests at the end of the Program, particularly from geographically isolated regions.

5.1 Gap Material Acceptance

The Gap Materials Program is another GTRI program that facilitates the disposition of high risk, vulnerable nuclear material not covered by other removal efforts. GTRI's first priority in each case will be to find a viable commercial disposition pathway before considering sending the material to the U.S. The materials could include:

- U.S.-Origin spent or fresh nuclear fuel not covered by the existing U.S.-Origin fuel return program,
- Non-U.S.-Origin and non-Russian-Origin HEU materials, or
- Separated plutonium.

The NNSA Administrator approved a revised Record of Decision (74 FR 4173, January 23, 2009) permitting GTRI to transport up to one metric ton of HEU SNF (Gap Material SNF) from foreign research reactor locations to the U.S. and safely store this Gap material at a DOE site pending disposition. This Gap material must meet the following criteria to be eligible for return to the U.S.:

- The material must pose a threat to national security;
- The material must be susceptible to use in an improvised nuclear device;
- The material must present a high risk of terrorist threat;
- The material must have no other reasonable pathway to assure security from theft or diversion;
- The material must meet SRS River Site acceptance criteria; and
- There must be adequate storage capacity at SRS.

Since the Gap program began in 2006, GTRI has removed approximately 325 Kg of nuclear material from numerous countries around the world.

5.2 Material Disposition

The DOE Office of Environmental Management (DOE-EM), which previously managed the Program, is currently reviewing final disposition options for repatriated spent nuclear fuel. As originally intended in the DOE Programmatic Spent Nuclear Fuel Environmental Impact Statement and associated Records of Decision, GTRI currently transports all aluminum clad spent fuel to DOE's SRS for interim storage, while stainless steel fuel, such as TRIGA fuel, is transported to INL. However, INL is currently unable to receive TRIGA fuel with the possibility the prohibition will extend through the end of 2014 or longer. A small amount of unirradiated and very lightly irradiated fuel is sometimes shipped directly to the Y-12 National Nuclear Security Complex for easier disposition.

6. Conclusion

GTRI remains committed to supporting U.S. and international nonproliferation goals while helping the world benefit from the safe use of modern nuclear technology. The U.S.-Origin Nuclear Remove Program aims to accept all eligible HEU nuclear materials and strongly encourages reactor operators to work closely with technical points-of-contact to ensure shipping schedules are accurate and achievable. GTRI remains willing to accept LEU nuclear material as DOE facilities are able to support receiving this material. GTRI continues to support the needs of the foreign research reactor community and is always available to meet interested parties to discuss the Program.

PREPARATIONS FOR THE DECOMMISSIONING OF THE FINNISH TRIGA FIR 1 – SPENT FUEL BACK-END MANAGEMENT AND DISTRIBUTION OF THE UNSPENT FUEL

I. AUTERINEN, T. VIITANEN, A. RÄTY, S. HÄKKINEN, P. KOTILUOTO
VTT Technical Research Centre of Finland
Otakaari 3, FI-02044 VTT, Espoo – Finland

ABSTRACT

VTT Technical Research Centre of Finland as the licensee of the government owned FiR 1 TRIGA research reactor has decided to close down the FiR 1 reactor as soon as it is technically and legislatively possible. Currently an environmental impact assessment (EIA) of the decommissioning is conducted as a prerequisite for the application to the government for shutting down of the reactor. The current estimate is that the shutdown could take place at the earliest autumn 2015.

Studies are performed to support the assessment of the different options in the EIA process. For the spent fuel back-end preparation are made for the US-DOE Foreign Research Reactor Spent Nuclear Fuel Acceptance Program. Description of the fuel as required by DOE is worked on including fuel irradiation data and burnup calculations. Measurements are planned to verify the burnup calculations. For the domestic Finnish option in the Posiva repository for final disposal of spent nuclear fuel criticality calculations and other safety assessments have been performed. Risk assessment of the transport to and handling at the Posiva repository of the fuel is made. As the Posiva repository will accept the TRIGA fuel only later in the 2020's an intermediate storage solution is looked for.

Possibilities and solutions are investigated for arrangements to secure the unused TRIGA fuel at the FiR 1 to be used at other TRIGA research reactors.

1. Introduction

FiR 1 -reactor is a TRIGA Mark II type research reactor manufactured by General Atomics (San Diego, CA, USA). The FiR 1 started operation in 1962 and reactor power was increased in 1967 from 100 kW to 250 kW. The reactor instrumentation was renewed in 1982 and in 1996-1997 the reactor building was completely renovated and the ventilation and reactor cooling systems were replaced.

Boron Neutron Capture Therapy (BNCT) work has dominated the utilization of the reactor since late 1990's. The weekly schedule has allowed still three days for other purposes such as isotope production, neutron activation analysis as well as education and training [1]. The operating licence of the reactor was extended for the period 2011 to 2023 by the government of Finland in December 2011.

In June 2012 VTT Technical Research Centre of Finland as the licensee of the government owned FiR 1 TRIGA research reactor decided to close down the reactor as soon as it is technically and legislatively possible. Currently an environmental impact assessment of the decommissioning is conducted as a prerequisite for the application to the government for shutting down of the reactor. The current estimate is that the shutdown could take place at the earliest autumn 2015 [2]. To support the assessment of the different options in the EIA process various studies are performed and decommissioning procedures planned.

2. Issues raised during the preparation of the EIA programme

According to the Finnish Decree on Environmental Impact Assessment Procedure (713/2006) [3] nuclear power plants and other nuclear reactors, including the demolition or decommissioning of these plants and reactors, require an environmental impact assessment (EIA). The EIA coordinating authority is the Ministry of Employment and the Economy (TEM). The assessment is a prerequisite for the project to receive required permits.

The environmental impact assessment includes 1) the project description phase presenting evaluation methods and the project and its options, and 2) environmental impact assessment report as a summary description of the results of the assessment work, and 3), consultation of those parties whose circumstances or interests may be affected by the project and public hearings.

In the environmental impact assessment process the different options leading to final disposal of the spent nuclear fuel as well as the decommissioning waste are evaluated [2]. In November 2013 the Ministry of Employment and the Economy (TEM) as the EIA coordinating authority published the Environmental Impact Assessment Programme for the Decommissioning of the FiR 1 Research Reactor prepared by VTT and the Pöyry consulting and engineering company [2, 4]. TEM requested statements on the assessment programme from 22 authorities and three nuclear companies. The programme was also open for public opinion in a public hearing and on the website of TEM [5]. TEM received 19 statements and one written opinion by a private person [6]. Based on these TEM published the coordinating authority statement on the assessment programme in February 2014 [7]. TEM noted that the content of the programme covers the requirements of legislation and it has been dealt with to the satisfaction of the provisions of the legislation of the environmental impact assessment (EIA). It considered the EIA programme as essentially appropriate and comprehensive. The final environmental impact assessment (EIA) report should take into account the provisions made in the statements by TEM and the other authorities.

The Ministry of the Environment requested that the evaluation report should in addition describe as much as possible, how and under what circumstances spent nuclear fuel is handled and temporarily stored in the United States. Also a description of the plans for the US national final disposal of the spent fuel should be provided. On the basis of the information presented in the report alternative solutions for the management of FiR 1 spent nuclear fuel will be compared. This is possible only with sufficiently comprehensive and concrete information. On the basis of the information presented in the report it will be judged whether the safety requirements under section 7 (b) of the nuclear energy decree are met. It states that the treatment, storage and emplacement of spent nuclear fuel generated from operating a research reactor in Finland in a manner intended as permanent outside Finland can be justified for safety reasons, or for a significant financial or another cogent reason.

Other issues raised in the statements considered the technical and legislative problems in connection with the intermediate storage and back end for the decommissioning waste. The first final disposal facilities for the nuclear power plant decommissioning waste will start operation in Finland in the late 2020's and their planned licenses do not include aluminium or graphite which are specialities of a research reactor.

3. Fuel irradiation data and burn up calculations

Preparations are made for the US-DOE Foreign Research Reactor Spent Nuclear Fuel Acceptance Program. Description of the fuel as required by DOE is worked on including fuel irradiation data and burn up calculations. Measurements are planned to verify the burn up calculations.

The fuel inventory, decay heat and dose rate data has been produced by VTT using a calculation chain involving widely-used codes Serpent [8], MCNP [9] and ORIGEN [10].

3.1 Inventory Calculation with Serpent

The nuclide inventories are based on a rather detailed burnup calculation, performed in 2011 using a special version of the Monte Carlo Reactor Physics and Burnup Calculation Code Serpent 1 that was modified to allow changes in the fuel loading. [11]

The geometry model of Serpent calculation was based on blueprints of the reactor and accurate description of the fuel provided by the manufacturer. The level of detail was very high what comes to the reactor core and the graphite reflector surrounding the core, while the parts further away from the core were modelled more coarsely. All of the fuel in the model was at 400 K temperature, i.e. the feedback from fuel and moderator temperatures was not modelled in any way. The fuel loading history was based on history documents on the changes in the fuel loading patterns, and the power history was approximated using the yearly energy productions of the reactor. The extremely complex power history of the FiR 1 reactor was modelled very coarsely using one burn step for each year and, additionally, each change in the fuel loading. The neutron interaction, decay and fission yield data were JEFF-3.1.1 based.

In addition to the fuel inventories, rod-wise burnups, total activities and decay heat productions were taken from the Serpent calculation.

3.2 Inventory Calculation with ORIGEN

To provide a reference for the Serpent calculation and to provide additional parameters of the fuel, the inventory of an average, representative fuel rod was calculated also using inventory calculation code ORIGEN. In this calculation the neutron spectrum of a representative fuel rod was first calculated using MCNP [12] and the transmutation cross sections were weighed using this spectrum. The power history model was more detailed than in the Serpent calculation: the realistic power history was approximated using a model involving daily start-ups and shut-downs of the reactor. Also the vacation periods in the summer were taken into account in the power history model. The calculation was repeated for each fuel rod type in the reactor: Al-clad fuel rods, Stainless Steel (SS) clad fuel rods with 8.5 % uranium content and SS rods with 12 % fuel content.

The gamma source spectrum and the corresponding total activities for the average fuel rods, to be utilized in the dose rate calculations, were taken from the results of the ORIGEN calculation.

3.3 Dose Rate Calculation with MCNP

The dose rates of the representative fuel rods were calculated using MCNP. The gamma sources were taken from the ORIGEN calculations for representative rods of the three different fuel types. The gamma dose rate was estimated at one meter distance in air. The result was expressed in Sieverts per hour.

With this method the dose rates were obtained for the representative fuel rods. For all the spent fuel rods rod-wise values were estimated by scaling the dose rate of the representative fuel rod by the ratio of the total activity inventory of each rod (as calculated with Serpent) to the total activity of the representative rod (calculated with ORIGEN).

3.4 Summary of the calculated results

Variation in burnup, decay heat and radiation dose level can be seen in table 1. For the Al, 8m% U and SS 8m% U rods which all have been loaded into the core in the 1960's and have had a long service time the average burnup is about 20% of the U-235. 75% of the fuel rods were loaded into the core by the year 1971 during the university period of the reactor. Rest of the spent fuel rods have been taken into use by VTT.

During the yearly fuel inspection campaign late spring 2014 radiation dose and gamma spectroscopy for nuclide activity measurements are planned for to verify the burnup calculations. During the same campaign the DOE/INL team will perform a visual inspection of the fuel.

		Al, 8m% U	SS 8m% U	SS 12m% U
Element burnup (MW-days)	min	1.24	4.81	0.02
	average	4.88	6.55	3.20
	max	6.51	7.23	7.39
Element Burnup (% U-235)	min	4.13	15.34	0.05
	average	16.03	20.78	7.10
	max	21.32	22.90	16.31
Element Decay Heat (watts)	min	0.021	0.083	0.031
	average	0.122	0.179	0.149
	max	0.182	0.207	0.242
Element Radiation Dose Rate at 1 meter in air (Sv/hr)	min	0.004	0.007	0.004
	average	0.021	0.015	0.021
	max	0.031	0.018	0.036

Table 1. Minimum, average and maximum values for burnup, decay heat and radiation dose level calculated for the different types of TRIGA fuel elements used in FiR 1. The data is based on the operational history till end of year 2010 + 6 months of cooling.

4. Further studies on the handling options for the FiR 1 spent fuel

Previously criticality calculations and other safety assessments have been performed for the domestic Finnish option in the Posiva repository for final disposal of spent nuclear fuel [13]. Risk assessment of the transport to and handling at the Posiva repository of the fuel is made. As the Posiva repository will accept the TRIGA fuel only later in the 2020's an intermediate storage solution is looked for. Dry storage is an interesting option here.

5. Unused TRIGA fuel at the FiR 1

Possibilities and solutions are investigated for arrangements to secure the unused TRIGA fuel at the FiR 1 to be used at other TRIGA research reactors. This has been discussed within the Global TRIGA Research Reactor Network (GTRRN). There is interest among other TRIGAs especially for the 12m% U fuel. Distribution of the unused fuel will take place under the supervision of the Euratom Supply Agency.

References

1. Auterinen I, Salmenhaara S.E.J, The 250 kW FiR 1 TRIGA Research Reactor - International Role in Boron Neutron Capture Therapy (BNCT) and Regional Role in Isotope Production, Education and Training, Research Reactors: Safe Management and Effective Utilization - Proceedings of an international conference held in Sydney, Australia, 5-9 November 2007, Proceedings of an International Conference organized by the International Atomic Energy Agency (IAEA), IAEA-CN-156, 2008. http://www-pub.iaea.org/MTCD/publications/PDF/P1360_ICRR_2007_CD/datasets/I.H.%20Auterinen.html
2. Auterinen I, Rapid shutdown and decommissioning of the Finnish TRIGA FiR 1 – decisions and preparations, RRFM2013 transactions, pp. 354-359. http://www.euronuclear.org/meetings/rrfm2013/transactions/RRFM2013-transactions.pdf
3. Act (468/1994) and Decree (713/2006) on Environmental Impact Assessment Procedure. http://www.ymparisto.fi/download.asp?contentid=84193&lan=en
4. Decommissioning of the FiR 1 Research Reactor, Environmental Impact Assessment Programme, VTT and Pöyry PLC, October 2013. http://www.tem.fi/files/37879/FiR_1_YVA_ohjelma_final.pdf (in Finnish).
5. http://www.tem.fi/energia/ydinenergia/tutkimusreaktori_kaytostapoiston_yva/yva-ohjelma
6. http://www.tem.fi/energia/ydinenergia/tutkimusreaktori_kaytostapoiston_yva/yva-ohjelma/lausunnot_ja_mielipiteet
7. http://www.tem.fi/files/38760/YVA-ohjelma_teknologian_tutkimuskeskus_VTTn_tutkimusraktorin_kaystostapoistolle_yhteisviranomaisen_lausunto_7.2.2014.pdf
8. Serpent. Serpent website http://montecarlo.vtt.fi
9. X-5 Monte Carlo Team, MCNP—A general Monte Carlo N-particle transport code, version 5 volume I: MCNP overview and theory, Report No. LA-UR-03-1987, Los Alamos National Laboratory, New Mexico, 2003.
10. I.C. Gauld et al., Origen-S: A Scale System Module to Calculate Fuel Depletion, Actinide Transmutation, Fission Product Buildup and Decay, and Associated Radiation Source Terms, ORNL/TM-2005/39, version 6, Oak Ridge National Laboratory, 2011.
11. Viitanen T., Räty A., Calculating the nuclide inventory of FiR 1 TRIGA Mk-II reactor, VTT Report, VTT-R-05511-12 (2012).
12. Häkkinen S., Bromin aktivoituminen ja uusien polttoainesauvojen vaikutus FiR 1 – reaktorissa, VTT Report, VTT-R-02531-11 (2011).
13. Rantamäki K M, Criticality safety analysis of final disposal of TRIGA Mark II fuel in Finland, International Conference on Nuclear Criticality Safety ICNC2011.

DEPLETION / DECAY CHARACTERISTICS OF PARR-1 LEU FUEL

T. MAHMOOD, A. MUHAMMAD AND M. IQBAL
NED, PINSTECH
Nilore, Islamabad, Pakistan

Abstract

Pakistan Research Reactor-1 (PARR-1) has been fuelled by Low Enriched Uranium (LEU) Silicide fuel for last two decades with standard fuel element containing 290 grams of ^{235}U. In the current study, fuel burnup and decay calculations have been performed for the standard fuel element of PARR-1. Analysis has been carried out for the fuel element with maximum of 50% burnup by employing KORIGEN code. Spectral indices of PARR-1 have been utilized in this study. Calculations have been performed for the decay parameters including radioactivity, decay heat, and inventory of heavy metals. Variation of decay parameters per fuel element has been studied up to 100 years after shut down of the reactor. Analysis indicates that radioactivity of structural materials becomes less than 1 Curie after about 7 days of reactor shut down. Radioactivity of actinides approaches this value after about 100 years of decay. However, radioactivity of fission products remains more than 100 Curie even after 100 years of radioactive decay. Value of the decay heat for 50% burned fuel element at the time of discharge from core is about 55 kW. However, it drops to less than a Watt after 100 years of radioactive decay.

Introduction

When a reactor is operated at a certain power level, a gradual buildup of fission products takes place in fuel elements. After a certain irradiation time, fuel elements in the reactor contain highly radioactive fission products and actinides. Actinides include isotopes of U, Pu, Am etc. Fission products and actinides give rise to large amount of radioactivity and decay heat which cause problems in handling, transportation, reprocessing and storage of spent fuel elements. Keeping this in view, a study has been made to calculate the radioactivity and decay heat for fission products, actinides and light elements of Pakistan Research Reactor-1 (PARR-1). Inventory of actinides has also been determined at different burnup steps. This study has been performed for irradiation of standard fuel element of PARR-1 up to 50% burnup of initial inventory of ^{235}U.

PARR-1 is a pool type research reactor, using low enriched uranium (LEU) fuel, having reactor thermal power of 10 MW. PARR-1 core is totally reflected, i.e. reflected on all six sides. This core is reflected by graphite on two sides. Rest of the core sides are reflected by water. The coolant at PARR-1 is demineralized light water, and is available for natural convection as well as forced flow cooling. In forced flow cooling mode, coolant flow is gravity driven. The PARR-1 grid plate is made of 127 *mm* thick aluminum. It has 54 holes in 9×6 pattern with a lattice spacing of 81×77.11 *mm.* These holes accommodate the end fittings of the fuel elements. Equilibrium core configuration of PARR-1 consists of 29 standard fuel elements (SFE) and 5 control fuel elements (CFE). Each SFE contains 23 fuel plates while CFE contains 13 fuel plates. The control rod or control follower (water) has replaced space for 10 fuel plates in CFE. The reactivity control mechanism consists of five control rods of oval shape with material composition: 80% Ag, 15% In, and 5% Cd. Experimental facilities at PARR-1 include six beam tubes, one through tube, three pneumatic rabbit stations, gamma cell, hot cell, thermal column and three water boxes. The fuel material is uranium having 19.99% ^{235}U. This fuel is in the form of uranium silicide, i.e. U_3Si_2-Al. This fuel material is sandwiched between aluminum cladding, to form a single fuel plate [1]. SFE of PARR-1 along with unit cell selected for analysis is shown in Fig. 1.

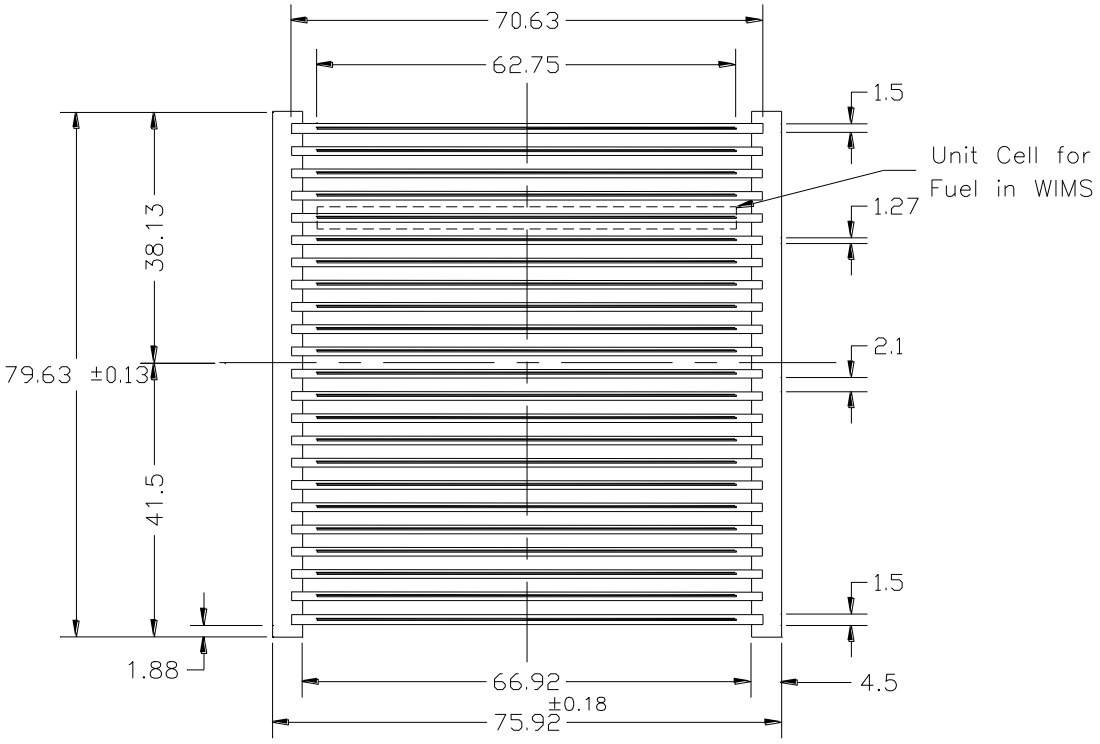


Fig. 1: Top View of the Standard Fuel Element of PARR-1 (All dimensions in mm)

Methodology

Three group average flux values utilized in the calculations of spectral indices were obtained by employing standard one dimensional computer code WIMSD/4 [2]. These values are used by KORIGEN [3] for computation of flux weighted averaging of 3-group cross-sections to one-group cross-sections. To perform calculations through WIMSD/4, unit cell selected is shown in Fig. 1. Due to symmetry of this unit cell, half unit cell modeled in WIMSD/4 is shown in Fig. 2.

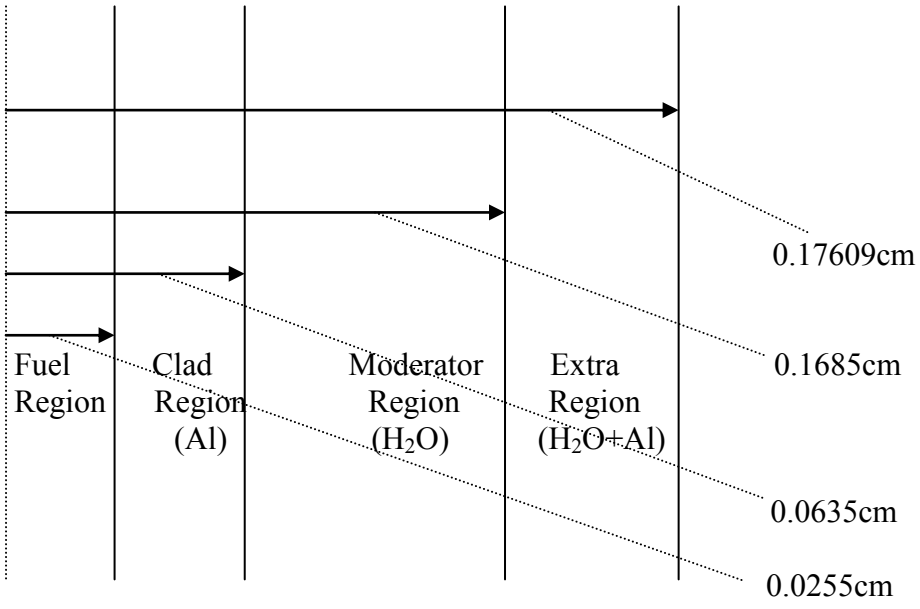


Fig. 2: Half Unit Cell Model Employed in WIMSD/4 for Fuel Meat of PARR-1

Depletion calculations have been performed employing KORIGEN code. Three spectral indices namely THERM, RES and FAST used in the KORIGEN code were evaluated for PARR-1 employing following standard relations [3]:

THERM = $(\pi\ T_0/4T)^{0.5}$ = Ratio of the neutron reaction rate for a 1/v absorber with a population of neutrons that has a Maxwell-Boltzmann distribution of energies at absolute temperature T, to the reaction rate with 2200 m/sec neutrons

RES = $\phi_{res} / \Delta U \phi_{th}$ = Ratio of the resonance flux per unit lethargy to the thermal neutron flux

FAST = $1.45\ \phi_{fast} / \phi_{th}$ = 1.45 times the ratio of flux above 1 Mev to the thermal neutron flux

Results and Discussion

Number density calculations were performed for the actual uranium silicide (U_3Si_2-Al) fuel of PARR-1. Applying these number densities and half unit cell model of Fig.2, three group average flux values were evaluated through WIMSD/4. Using these flux values and standard relations described in the Methodology section, following values of spectral indices were evaluated:

FAST = 1.9324
RES = 0.2129
THERM = 0.8540

Above mentioned values are close to the values as mentioned in the earlier work [4]. These values of spectral indices were accommodated in KORIGEN code for burnup calculations of the standard fuel element. Inventory of significant actinides is shown in Table 1 at three burnup steps. It can be seen that inventory of ^{234}U, ^{235}U and ^{238}U decreases by increasing burnup. However inventory of remaining actinides increases by increasing burnup of the fuel element.

Table 1: Actinides inventory (grams) at different burnup steps

% Burnup	0%	15%	30%	50%
U 234	4.86E-01	4.60E-01	4.31E-01	3.82E-01
U 235	2.90E+02	2.46E+02	2.05E+02	1.45E+02
U 236	0.00E+00	7.97E+00	1.54E+01	2.58E+01
U 237	0.00E+00	2.55E-02	6.40E-02	1.44E-01
U 238	1.16E+03	1.16E+03	1.16E+03	1.15E+03
U 239	0.00E+00	1.49E-03	1.73E-03	2.17E-03
NP237	0.00E+00	3.75E-02	1.79E-01	6.45E-01
NP238	0.00E+00	2.31E-04	1.41E-03	7.02E-03
NP239	0.00E+00	2.12E-01	2.47E-01	3.11E-01
PU238	0.00E+00	6.91E-04	8.07E-03	6.17E-02
PU239	0.00E+00	1.46E+00	2.53E+00	3.38E+00
PU240	0.00E+00	1.10E-01	4.16E-01	1.12E+00
PU241	0.00E+00	6.45E-03	4.95E-02	2.33E-01
PU242	0.00E+00	2.15E-04	3.78E-03	3.86E-02
AM241	0.00E+00	6.61E-06	9.62E-05	6.99E-04
AM242M	0.00E+00	5.58E-08	1.43E-06	1.49E-05

After achieving the maximum value of 50% burnup, radioactive decay characteristics up to 100 years of reactor shut down are shown in Fig.3. Value of 50% burnup corresponds to 118

MWD burnup of the standard fuel element. Behavior of light elements indicates that radioactivity of structural materials becomes less than 1 Curie after about 7 days of reactor shut down. Radioactivity of fission products reduces with the passage of time but remains more than 100 Curie even after 100 years of radioactive decay. However, Radioactivity of actinides approaches value of about 1 Curie after 100 years of decay. Investigation of this behavior of actinides reveals that main contribution to this decay is from decay of three isotopes namely ^{237}U, ^{238}Np and ^{239}Np during this period as shown in Fig. 4. Activity of remaining actinides remains insignificant as compared to these mentioned three isotopes up to 100 years of radioactive decay. Profile of decay heat for 50% burned fuel as shown in Fig. 5 reveals that decay heat at the time of discharge from core is about 55 kW. However, it drops to less than a Watt after 100 years of radioactive decay. This trend of decay heat for light elements, fission products and actinides follows the same profile as discussed for radioactive decay.

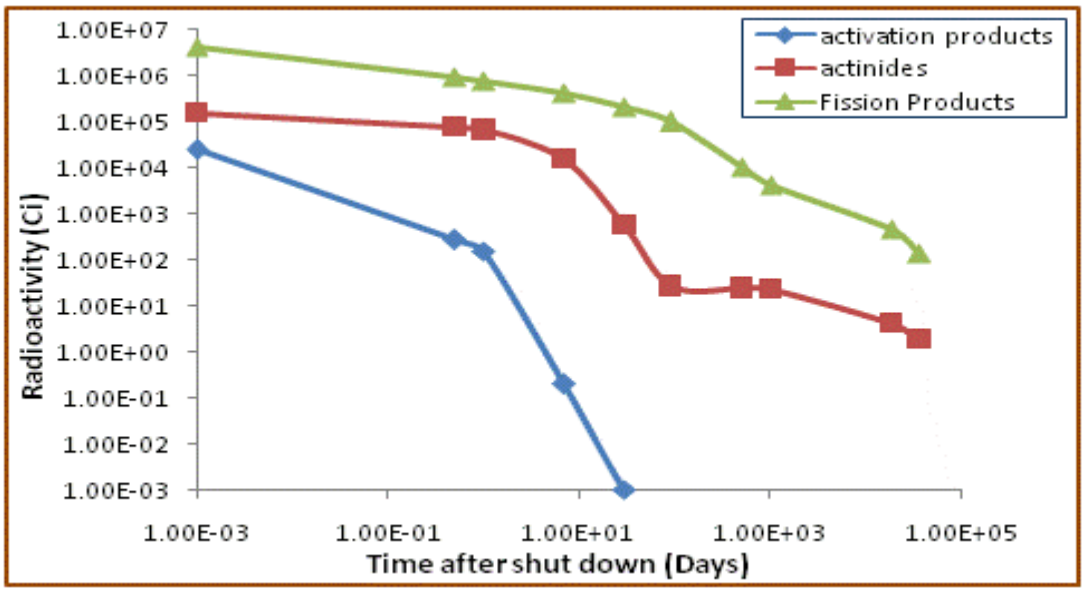


Fig 3: Radioactivity of Irradiated Fuel

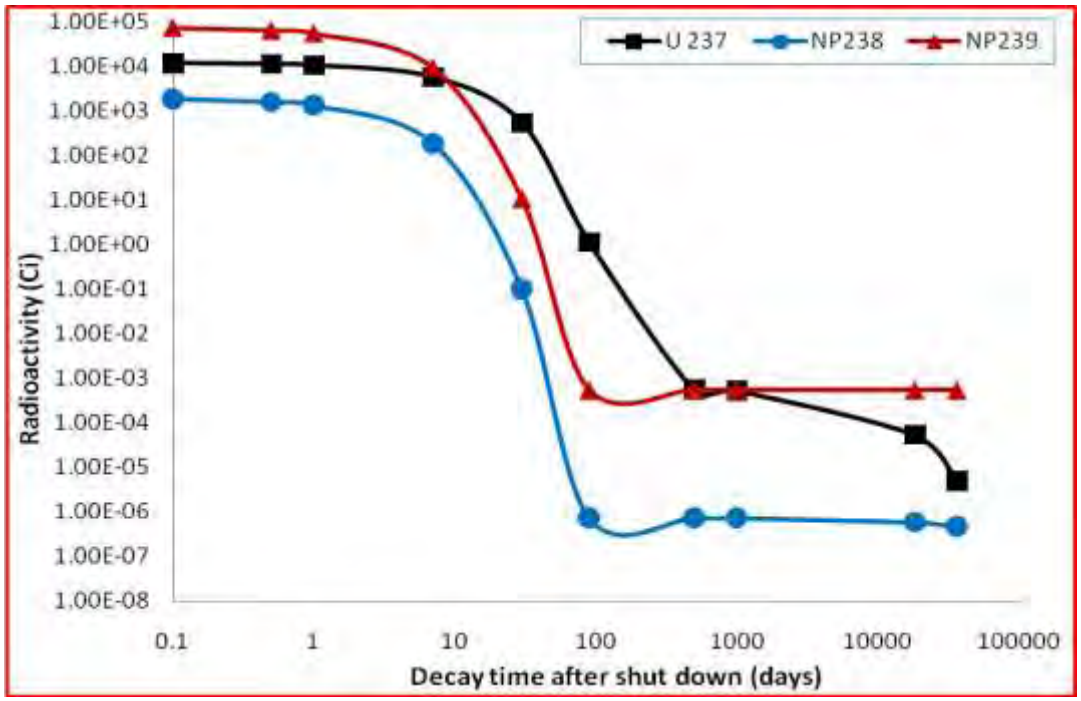


Fig 4: Radioactivity of significantly contributing actinides

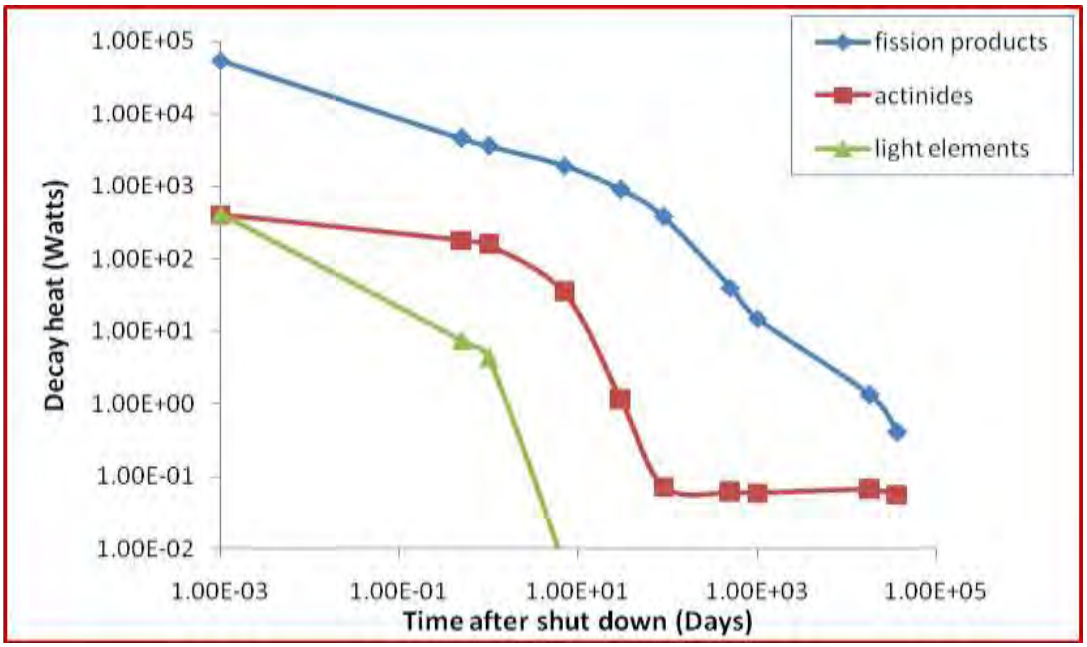


Fig 5: Decay heat profile of irradiated fuel

Conclusion

Main contribution to radioactivity and decay heat of the spent fuel element of PARR-1 up to 100 years of decay time of the fuel element is from fission products. After a few days of decay, contribution from light elements becomes negligible. However, although decay heat from actinides becomes less than a watt after about 30 days of reactor shut down, but more than 500 Ci of activity remains due to actinides after this time.

References

1. Final Safety Analysis Report (FSAR) of PARR-1, (2001).
2. J.R. Askew, F.J. Fayers and P. B. Kemshell, “A General Description of the Lattice Code WIMS”, Journal of the British Nuclear Engineering Society, (1966).
3. ‘‘KORIGEN’’ U. Fischer, H.W. Wiese Kernforschungszentrum Karlsruhe Institut Fuer Neutronenphysik Und Reaktortechnik.
4. Asif Salahuddin, M. Arshad “Isotopic Composition of Actinides and Fission Products in the Irradiated Fuel of the 10 MW low enriched PARR Reference Core” PINSTECH/NED-130 (1987).

AIR SHIPMENT OF SPENT NUCLEAR FUEL FROM THE BUDAPEST RESEARCH REACTOR

F. GAJDOS, I. VIDOVSZKY
Hungarian Academy of Sciences Centre for Energy Research
H1121 Budapest Konkoly T ut 29-33, Hungary

J. DEWES
Savannah River National Laboratory
Aiken, South Carolina USA

ABSTRACT

The shipment of spent nuclear fuel is usually done by a combination of rail, road or sea, as the high activity of the SNF needs heavy shielding. Air shipment has advantages, e.g. it is much faster than any other shipment and therefore minimizes the transit time as well as attention of the public. Up to now only very few and very special SNF shipments were done by air, as the available container (TUK6) had a very limited capacity. Recently Sosny developed a Type C overpack, the TUK-145/C, compliant with IAEA Standard TS-R-1 for the VPVR/M type Skoda container. The TUK-145/C was first used in Vietnam in July 2013 for a single cask. In October and November 2013 a total of six casks were successfully shipped from Hungary in three air shipments using the TUK-145/C. The present paper describes the details of these shipments and formulates the lessons learned.

Background

The Budapest Research Reactor, the first nuclear facility of Hungary has been in operation since 1959. The reactor used highly enriched Uranium (HEU) fuel for a long period of time (1966 - 2012), consequently the repatriation of the HEU SNF became a security issue. The first part of this spent fuel was taken back to Russia, i.e. to the country of origin in 2008 [1]. After this shipment had been completed, the conversion of the Budapest Research Reactor to low enriched Uranium (LEU) fuel was done. The conversion was completed in 2012; since November 2012 the reactor only uses LEU fuel. The remaining fresh HEU fuel was sent back to Russia in two shipments (2009 and 2012), and equivalent amount of fresh LEU fuel were delivered to Hungary in 2009 and 2013. The second and last SNF repatriation was foreseen for late 2013.

Preparations

The preparations for the second shipment started early 2011. The shortest and cheapest way from Budapest to Mayak facility (western Siberia) is certainly by rail via the Ukraine. However in 2008 the lack of a tri-lateral agreement between Russia, Ukraine

and Hungary on the transportation of nuclear material jeopardized this option. Since 2008 a lot of progress was achieved, but the agreement was still not ratified by the Parliament of the Ukraine. As the date of the ratification was unforeseeable the project management decided to look for other options that did not involve crossing the borders of the Ukraine.

Three options were considered. The first option was the one used in 2008, i.e. by rail to Koper, Slovenia and then by vessel to Murmansk and again on rail to Mayak. This option is obviously feasible, but requires a very long time due to the long sea route. The second option was similar to the first one, but was much shorter via rail through Slovakia and Poland, to the port of Gdynia. Gdynia to Murmansk by sea is less than half the way from Koper to Murmansk. The third option was rather non-conventional, using air shipment. This was made possible by the recent development by Sosny of a Type C overpack compliant with IAEA Standard TS-R-1 for the VPVR/M type Skoda container, the TUK-145/C. The three options were compared in a short study [2]. The conclusion of the study was to recommend air shipment, as the security benefit of its short duration offset slightly higher costs. It was also determined that the project risk of air transport was no higher than other modes of transportation.

The licenses and permits were granted in the usual way, similarly to the previous shipment. The TUK-145/C overpack was first used in Vietnam in July 2013. Watching this shipment gave valuable practice for the preparation of the Hungarian shipment. The manufacturing of the second overpack was finished in July 2013. Both overpacks arrived by air (using the AN-124 Antonov aircraft operated by the Volga-Dnepr aero-company) in August to Liszt Ferenc Airport in Budapest. The transport of the empty overpacks to the Budapest Research Reactor site was done during the night with the help of the police to minimize public attention. Loading of the spent fuel to the Skoda VPVR/M casks was performed in September 2013, similarly to the fuel loading in 2008.

The Shipments

The last fuel assemblies were removed from the reactor in November 2012. The radioactivity and heat load of the SNF was calculated for transport in October 2013. The calculations showed that neither the radioactivity nor the heat load would reach the limits given in the license of the VPVR/M cask. However it was decided to utilize six casks although the SNF could be loaded into five as well. This measure increased the margins to the limits. As only two overpacks were available, three shipments were needed to transport the six Skoda casks.

The first shipment started after midnight on October 7 from the site of the Budapest Research Reactor. It took about an hour to reach the airport. The loading of the filled overpacks to the airplane was similar to the unloading procedure and was finished well ahead of the scheduled departure time of the plane. The plane started in the early morning and arrived to Koltsovo airport in Yekaterinburg in the early afternoon local time. The flight was about four and half hours. At Koltsovo airport the title was transferred to the Russian partner. The rest of the route to the Mayak facility was covered on road.



Fig. 1. Placement of the Skoda cask into the overpack

The second and third shipments were similar to the first one, starting October 21 and November 4 respectively.



Fig. 2. Loading of the overpack into the aircraft

After the third shipment was completed, Hungary was declared to be free of HEU. The removal of the entire inventory of HEU from the country represents a substantial contribution to nuclear risk mitigation.

Lessons learned

Air shipments are possible if the amount of SNF is not too great. The greatest advantage of this type of shipment is that it is much faster than any other shipment mode and therefore minimizes the transit time as well as attention of the public. The transit time minimization is a goal itself, as it helps in optimal use of equipment and in keeping schedules. The attention of the public may have negative influence due to the special character of the transported material.

Disadvantages of the air shipment are the slightly higher price and the limited capacity of the airplane compared to train and sea vessel. In our case these disadvantages were not essential, as the price was only slightly higher, as mentioned earlier and three shipments could be realized easily within a month. However in cases where really large amounts have to be transported, the air shipment may not be feasible. In the Hungarian shipment in 2008 16 Skoda casks were transported, which would have required eight air shipments. Eight similar shipments would probably cause increased public attention and the costs could have been too high as well.

It is worth mentioning that the trilateral agreement between Russia, Ukraine and Hungary was ratified just days before the last shipment. This confirms that the decision was correct not to use this type of transport. In case we had been waiting for this ratification, the first shipment could have been started only recently and the Budapest Research Reactor would have had to be closed earlier because of a lack of spent fuel storage capacity.

References

1 J. Dewes, S. Tőzsér, I. Vidovszky: Lessons learned from the spent fuel shipment Budapest – Mayak, **ENS RRFM 2009 Transactions**, 13th International Topical Meeting on Research Reactor Fuel Management, Vienna, Austria, March 22-25, 2009, p1

2 J. Dewes, I. Vidovszky: Task 1 Shipment Initiation, Subtask 1.2 Project Authorization and Transport Concept, RRFR Internal Report, Budapest 2012

STATUS OF SILICIDE FUELS REPROCESSING AT LA HAGUE PLANT

C. EYSSERIC[(1)], A. JUVENELLE[(1)], N. REYNIER-TRONCHE[(1)],
JP. FERAUD[(2)], T. RANDRIAMANANTENA[(2)], D. ODE[(2)], B. LORRAIN[(2)]
[(1)]CEA, DEN/DRCP, [(2)]CEA, DEN/DTEC, SGCS
CEA Marcoule, – 30207 Bagnols sur Cèze Cedex – FRANCE

J.F. VALERY, X.DOMINGO
AREVA NC, Back-End Business Group
Tour AREVA - 1, Place Jean Millier – 92400 Courbevoie – FRANCE

ABSTRACT

U_3Si_2 fuel reprocessing qualification is currently ongoing at AREVA, with the same process at La Hague as the one for UAl fuel and to adapt it to the specific characteristics of silicide.

Since early 2000's, the research programs conducted through the collaboration between AREVA and CEA focused on the acquisition of U_3Si_2 dissolution data in nitric acid and especially on the Si behaviour and its possible impact on the AREVA reprocessing process steps: dissolution, centrifugation, Uranium and Plutonium extraction and fission products and fines vitrification.

The silicic acid $Si(OH)_4$ formed during dissolution polymerizes to yield hydrated silica gel; this gel may hamper the liquid/liquid extraction performance and induces a risk of equipment fouling.
The existing centrifugation step at the La Hague site for nuclear power plant UOx treatment is planned to be used in order to separate the silicide gel from the clarified solution which could then be managed in the separation process as for UAl fuel. The R&D program conducted by the CEA up to 2013 has finally demonstrated the ability of the centrifugation step to properly separate the silicide gel from the dissolution solution.

Based on CEA lab scale fruitful program, AREVA has started the industrial qualification phase to set up the silicide fuels reprocessing in La Hague UP3 T1B facility. The aim of this program is to get the approval from the French Safety Authority. With the ASN authorization, AREVA will be able to start industrial-scale U_3Si_2 fuel reprocessing.

AREVA has long experience in the industrial-scale treatment of RR UAl fuel. Over 23 tons of RR UAl type fuels have been reprocessed at AREVA's facilities in France, both in Marcoule and La Hague plants.
Currently, RR spent fuels reprocessing is conducted in the La Hague UP3 T1B facility.
In order to comply with its customers growing needs in terms of treatment capacity, AREVA is developing new RR spent fuel capacities in the La Hague UP2-800 facility. This new facility is planning to process both UAl and U_3Si_2 RR spent fuels.

1. Introduction

Since their creation, CEA and AREVA have been working together in the field of Research Reactors, especially regarding the back-end solutions for research and other spent fuels.
With the last decades development in RR spent fuel technologies, some RR operators (such as CEA) have chosen to use U_3Si_2 fuels in their reactor cores.

This paper introduces the past actions and remaining ones to be conducted by CEA and AREVA for U_3Si_2 fuels reprocessing at La Hague site: from lab-scale feasibility demonstration to industrial-scale reprocessing, including planning and capacities.

2. R&D program for the scientific and technical feasibility demonstration of the U_3Si_2 fuel reprocessing [1]

Previous R&D program had been performed by CEA in the field of Research and Test Reactor fuel reprocessing concerning fuel dispersed particles of UAl alloys surrounding into a specific aluminium alloy acting as the nuclear fuel cladding barrier. Based on this state of knowledge, the U_3Si_2 program have been carried out with the objective to specifically understand the chemical and physico-chemical behaviour of the silicon species during the main operations of the process: the nitric dissolution, the insoluble residues separation and conditioning in glass matrix and the liquid-liquid extractions dedicated to actinides and fission product recycling management. Complementing to basic chemical research, some technical aspects have been studied at laboratory scale in representative devices in order to find the better process implementation in the proven industrial technology and apparatus of the current La Hague reprocessing plants.

2.1. Behaviour of silicon at nitric acid dissolution step

The behaviour of silicon in the hot nitric acid had been explored with experimental acquisitions on three types of silicon forms: a first surrogate silica form focusing the study only on silicon behaviour, secondly on un-irradiated U_3Si_2 fuel with Al coating to compare the specific behaviour of the three main species: Si, U, Al and finally with irradiated U_3Si_2 fuel plates (cf. figure 1) including plutonium behaviour to confirm earlier conclusions.

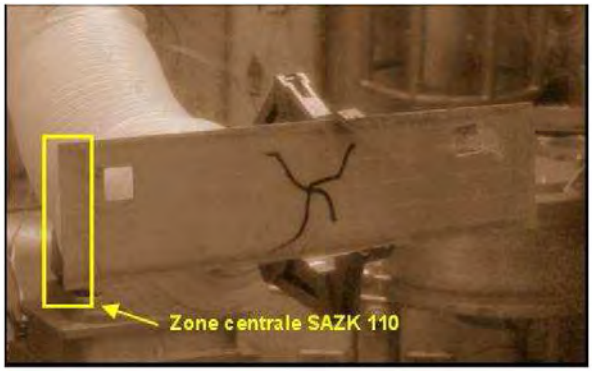


Figure 1: Photos of silicide irradiated fuel plates used in Atalante R&D facility in shielding cell C11/C12 for dissolution and liquid-liquid extraction studies

Apart from fluorhydric acid, the silicon is known to present very low solubility in most hot mineral acids. In nitric acid, silicon exists in its IV oxidation state, tetra-coordinated with oxygen atoms in the silicic acid form. This precursor evolves in a polymer form with formation of a colloidal gel. Typically, in 4-6M nitric acid at 90-100°C, the silicon solubility limit obtained is around 100 mg/L much lower than the excepted maximum silicon concentration around few g/L for the U_3Si_2 complete dissolution hypothesis. This data indicated the evidence that silicon has to be managed as a solid residue in a good accordance to the current La Hague residue management.

The CEA R&D have particularly studied the influence of chemical conditions (acidity, temperature, presence of others metal, duration at hot temperature) and the initial forms of the silicon (silica, U_3Si_2 compound, U-Si-Al alloy) on both the dissolution and polymerization kinetics and apparent solubility limits.

As an example, it was shown that the presence of aluminium in the nitric solution modifies the reactivity of silicon species, accelerates its polymerization and decreases its final solubility around 20-40 mg/L. Observations had shown that the final aspect of solid residue -dense hydrated silica particle or diffuse colloidal gel- depends on the initial Si solid form involved during the hot nitric dissolution. In optimized conditions, the silicon mass balance indicated that more than 98.6% of this element is present in solid phase, preferentially in the colloidal gel phase.

Furthermore, the behaviour of others expected soluble species as uranium, plutonium and aluminium had been checked during the solutionizing and polymerization consecutive steps. It was demonstrated that indeed the development of a oxide layer at the surface of the U_3Si_2 particles during the nitric attack, the merely-complete uranium and plutonium dissolution (> 99.2% measured for un-irradiated and irradiated silicide fuel) is achieved. No co-precipitation or co-driving have been observed and confirm the absence of irreversible interaction between silicon gel and others expected soluble species. The measured kinetics of uranium dissolution are very similar to the UAl experiment for which the limiting rate is dependent on the aluminium coating dissolution kinetics. In deduction, it will be expected to dissolve silicide RR in similar capacity as RR UAl.

2.2. Behaviour of the silicon in extractions steps

Generally, finely divided particles are not desired in liquid-liquid extraction apparatus because of their impact on emulsion stabilization and possible accumulation of crude at the aqueous-solvent interface. Particularly, the presence of more or less polymerized silicic acid is well-known to affect as well the first emulsion formation step and the coalescence one. However, these effects are not well understanding and the influencing parameters only partially quantified.

In the previous RR UAl R&D, the impact of traces of silicon was already investigated because of its presence as minor component of the aluminium alloy of the fuel particle coating. With respect to R&D results confirmed by the AREVA industrial know-how, a maximum silicon concentration was fixed for the clarified solution resulting from liquid-solid separation and provided to supply the liquid-liquid extraction part of the facility.

Because of the more important silicon quantity and its different speciation at higher concentration in the case of RR U_3Si_2, the CEA had carried on research in this field by contacting test of the nitric solution containing silicon with a current TBP 30% in TPH organic phase. In a first qualitative approach with surrogate silicic acid solution, it had observed that a fresh solution containing poorly polymerized silicic precursors, the delayed emulsion formation effect is stronger than when the polymerization time is longer showing that the very first small

silicic oligomer are the more influent. In the other way, the more advanced polymerized species still impact negatively the coalescence efficiency into the ultimate phase of the interface separation. To progress in better understanding and representativeness and because of the behaviour change of polymerized species as a solid residue, comparisons on decantation test were performed with the raw polymerized solutions resulting from un-irradiated silicide fuel and same solution after filtration with decreasing diameter porosities or after laboratory centrifugal separation. All the tests confirm the benefit of the solid separation on decantation test if the optimization conditions of dissolution are adapted to improve this separation efficiency and if this efficiency is effective in a large domain of particle size. Finally, this encouraging decantation results were verified with clarified solutions obtained by centrifugal lab device on the real irradiated silicide fuel dissolution solution.

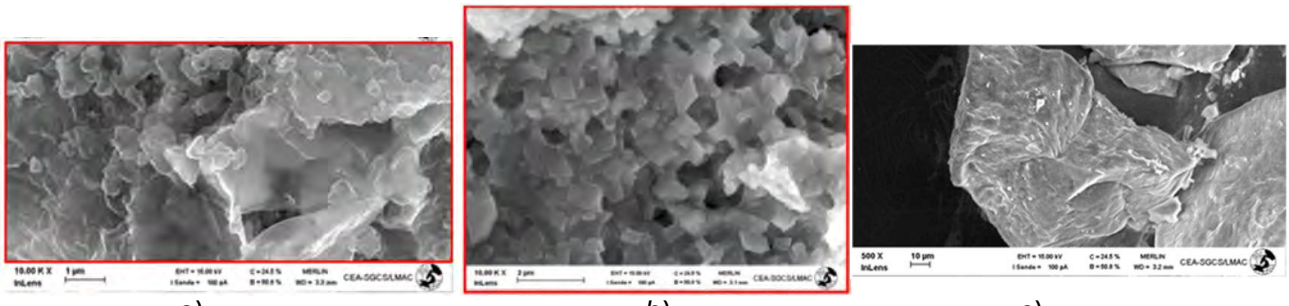
In conclusion of the whole laboratory experiment and industrial RTR UAl experience, it had been possible to specify the conditions required to guarantee that the silicon impact is negligible in the proven technology of the liquid-liquid extractions of La Hague plant.

2.3. Separation of silicon by centrifugation

As already mentioned, it was possible to demonstrate at laboratory scale and with respect to optimized process conditions that more than 98.6 % of the silicon including in silicide fuel evolved in colloidal phase.

Because of the atypical physico-chemical characteristics of the gel, CEA R&D had investigated the performance of the solid-liquid separation with representative surrogate silica gel and representative pilot-scale centrifugal equipment in order to confirm the feasibility to obtain a clarified solution with a residual silicon concentration under the maximum specification.

First, the extrapolation feasibility of the centrifugal pilot device (200 mm diameter) to the existing industrial equipment was checked. Its mechanical and dimension design allows to create the same accelerating field, same relative residence time (ratio of its volume capacity to input flowrate) and same maximal height of load such as the industrial one. Some measurement of residence time distribution of this pilot scale shows its good adequacy for direct extrapolation of pilot result. Secondly, the synthesis protocol of the representative surrogate gel from sodium silicate was consolidated. Some remarkable characterizations were done as the MEB photos represented observable structures in figure 2.



a) *b)* *c)*

Figure 2: MEB photos of different aspect of the silicon gel after centrifugation and drying for increasing silicon concentration - a) leafed aspect at lower concentration, b) nanometric cubic crystallite aggregate at intermediate concentration, c) massive and diffuse aspect at higher concentration

The most important parameter tested was the initial silicon concentration of the input solution. From the beginning of the supply to the almost total load of the bowl, the silicon leak remains constant and abruptly increases near the maximum bowl loading limit. Considering the four different silicon gel input concentrations tested, only the higher had revealed a residual silicon concentration of the clarified solutions upper to the fixed limit. These results allow extrapolating a convenient operating domain of the clarification with suitable efficiency of the existing equipment.

The resulting centrifuged gel (cf. photo figure 3) presents a Si concentration of about 20 g/L. Its humidity is high and the interstitial dissolution solution remaining into the gel is estimated more than 50 % of its total volume. However, the elimination of this residual dissolution solution can be very easily performed by one or successive rinsing operations. The achievement of efficient rinsing operations has been demonstrated with an inactive soluble tracer in pilot-scale tests but also with un-irradiated and irradiated fuel in laboratory-scale.



Figure 3: Example of the silicon massive gel collected into the bowl of the pilot-scale centrifugal equipment

2.4. Hydrodynamic aspect of the gel behaviour

From the dissolution to the residue storage, the process lines where gelatinous silicon species may be encountered represent a very large variety of apparatus with specific hydraulic behaviour in nominal operating conditions but also in transient period as their drainage and their transfer in pipe. In the other hand, the concentration of this gelatinous silicon form can varies from the initial concentration in the dissolution solution to the upper concentrated gel resulting from the centrifugal device loading and finally lower concentration due to the natural cake rinsing dilution or other simple dilution operating in classic industrial streams management. A lot of cases can be listed where the adequacy between the hydraulic forces and fluid flows and the physical properties of the gel have to be verified. CEA have realized some rheological measurement and numerical fluidic simulation.

As first example, the higher concentrated gel presents an elastic behaviour which is characteristic of a threshold fluid comparable to a solid. Anticipating corking problem, the pressure limit stress was determined to destructure and to fragment the compacted gel. In practice, for the draining operation of the concentrated cake into the centrifugal device, it has also been demonstrated that a designed nozzle which injects the draining solution with a ten lower order of magnitude of kinetic energy than the industrial one led to satisfactory recover of

the cake (more than 95 %). Other tests concerning the ageing of the concentrated gel fouling a steel vessel wall show a weak adhesion, the ageing fouling can be easily eliminated.

Moreover, the ×2 dilution of the concentrated gel improves significantly its rheology behaviour as an more classic rheofluidifying fluid with a viscosity about 50 times higher than water but acceptable for industrial utilization. The numerical simulation was performed in order to confirm the good suspending of dense particles in a pulsed vessel containing diluted silicon gel (cf. figure 4).

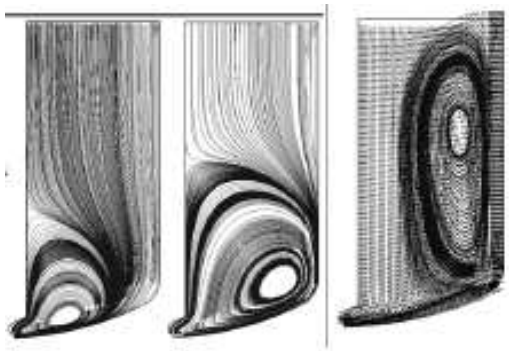


Figure 4: Example of calculated dynamic flows of the pulsed vessel containing diluted gel

Based on a very rich research and development program, the scientific feasibility of the silicide fuel treatment in existing equipment at La Hague plant has been demonstrated, the specific choice consisting in silicon management at the head of the process performing centrifugal separation of polymerized in solid and gelatinous form. In this goal, four complementary approaches were explored: i) basic chemical comprehension of major species : Si, Al, U, Pu, ii) original experiment in hot shielded cell with a representative irradiated silicide fuel plate in laboratory scale, iii) inactive experiment on pilot-scale equipment with qualified surrogate gel and iv) fluidic numerical simulation. It remains to transpose the optimized conditions and operating domains in the industrial environment with a qualification program and brings to final treatment authorization.

3. Industrial Qualification Program

Following the R&D results, an industrial qualification program has to be performed in order to ensure the scale 1 feasibility of the silicide treatment within the La Hague existing facilities.
This program aims to perform engineering studies in order to:

- take into account the process parameters coming from the R&D in the technical documents describing the industrial operating conditions,
- refine the actual production rhythm and annual capacity of treatment for silicide fuels,
- assess the impact of flows coming from silicide fuels treatment on the whole AREVA NC processing activities.

For example, the main issues to be tackled can be:

- the assessment of process flow dilutions due to the management of the silicide gel which have an impact on fission products concentration and vitrification processes,
- the qualification of the analyses referential due to new characterisation to be performed (new Si and Al analyses on others process flows, assessment of the impact of Si presence on current key process analyses…).

The global demonstration of the compliance of the process and related R&D results with La Hague technical and safety referential is then presented in a dedicated process book and qualification file. These documents will be the basis of the application file to be submitted to the French Safety Authority (ASN) in order to get the authorization for processing silicide fuels in AREVA La Hague plant.

AREVA is currently carrying out this engineering phase following the R&D. The completion of this phase and the application file to be submitted to the ASN are expected by the end of 2014.

All the studies performed by AREVA are based on a reference french silicide fuel to be processed in La Hague plant. Considering other silicide fuels, it will be necessary to check the characteristics deviation in comparison with this reference fuel in order to assess their process feasibility through their compliance with the process book, reprocessing rhythm capacity, and their related impacts on the whole reprocessing operations. The following non-exhaustive characteristics can be considered as key data to perform this assessment: geometry (diameter, length…), Si content, high content of element which can have a restrictive impact on the capacity (Mo or Mg content for instance), U content, initial enrichment.

According to silicide fuels specificities and/or if the characteristics deviation compared with the reference silicide fuels are significant; AREVA will have to tackle with dedicated studies even if the core process operations are similar (centrifugation to separate the Si prior to U & Pu exctraction).

Knowing such information as soon as possible for other silicide fuels will also allow AREVA to take into account these fuels at the earliest stage of the ASN application process, and consequently ease the reprocessing authorization agreement for these specific fuels.

The period from 2015 to the early 2017 is expected to be dedicated to:
- take into account the feedback of ASN prior to the authorization for the process operations,
- set the industrial conditions of the facilities prior to actual fuels processing operations.

By the completion of this overall process, and once the green light from the Authority is obtained, AREVA will be able to process UAl and U_3Si_2 fuels in an industrial scale, within the existing UP3 T1B facility.

<u>Note</u>: Concerning any new type of RR fuels (UMo fuels for instance), such qualification program following the prior R&D activities will have to be performed in order to get the dedicated process authorisation from the ASN.

The following timeline summarizes the considered planning that will conduct to industrial reprocessing of silicide fuel at AREVA La Hague plant.

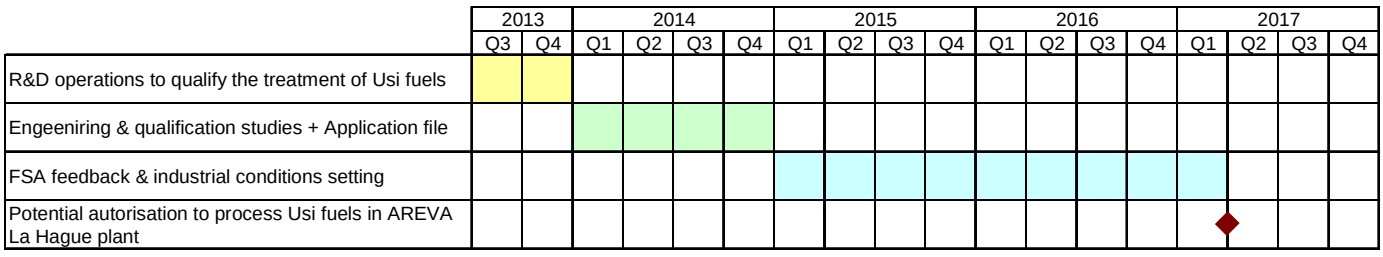


Figure 5: Program overview prior to process authorisation

4. Reprocessing capacity perspective in AREVA NC La Hague

AREVA has long experience in the industrial-scale reprocessing of RTR UAl fuel. As of end of 2013, more than 23 tonnes of U-Al type RTR fuels from 21 countries have been reprocessed at AREVA's facilities in France. At the Marcoule site, 18 tonnes have been reprocessed, and since 2005, more than 5 tonnes of U-Al type fuel have been successfully reprocessed at La Hague facility. These last fuels are also both French and foreign-origin elements: Belgian and Australian fuels.

Even though AREVA La Hague facilities were originally designed to reprocess irradiated UOx fuels (nuclear power plants fuel), the past experience illustrates AREVA ability to build and adapt new equipments, to industrialize new processes and to reprocess specific fuels in their already existing facilities.

Today, the AREVA capacity for RR spent fuel reprocessing is mainly limited by the aluminium concentration in the entire process.
First limitation is 35-40g aluminium/L after dissolution of the fuel elements in hot nitric solution, to manage the risk of precipitation into aluminium nitrate. The resulting solution is then blended with the solution coming from the dissolution of the UOx fuel.
The aluminium concentration bound also limits the reprocessing capacity at the very last stage of "vitrification": aluminium is here melted with the fission products and minor actinides into a stable, homogeneous and durable glass matrix. To ensure its stability, a precise aluminium concentration is required in the glass.

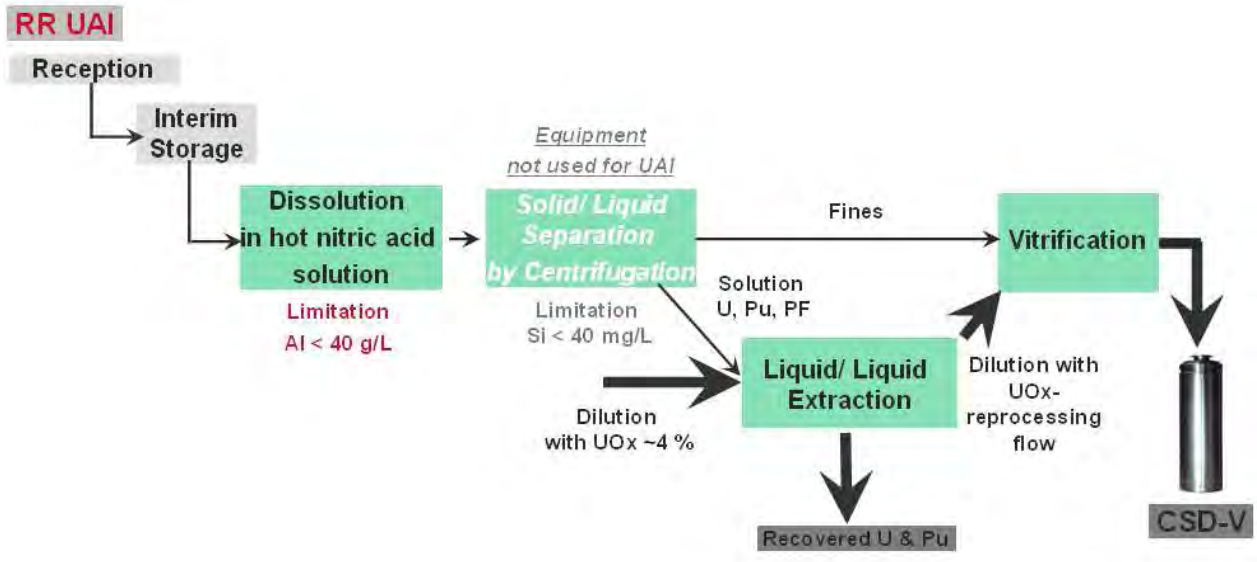


Figure 6: UAl SF reprocessing at La Hague: Current operations for UAl

Tomorrow, with the U_3Si_2 fuel reprocessing industrialization, the Si bound is also to be considered in the whole reprocessing process.

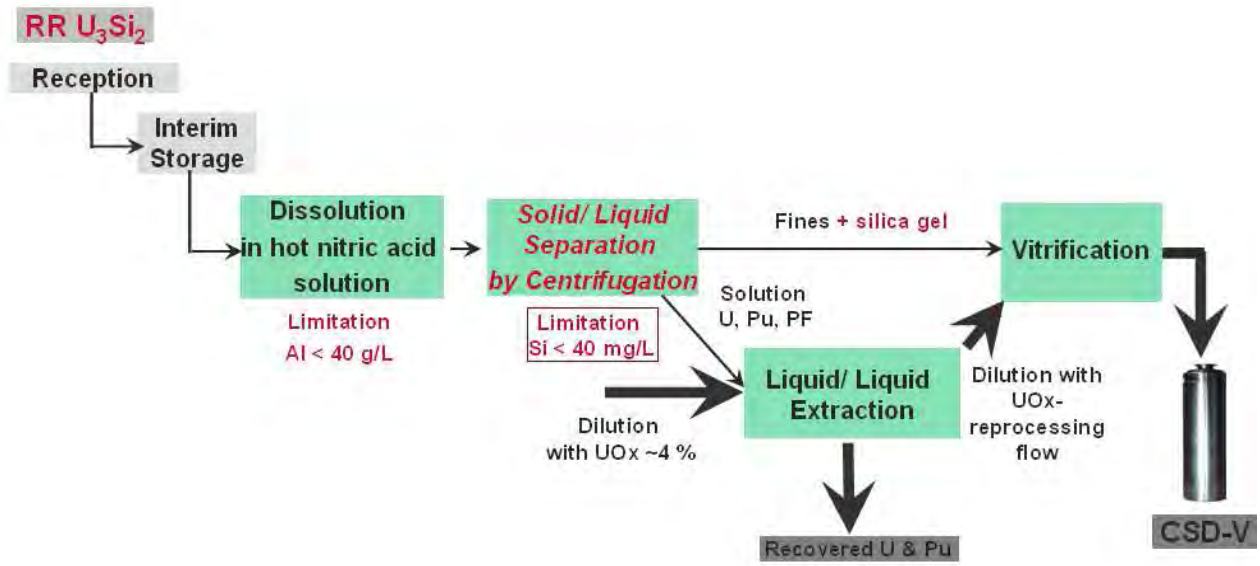


Figure 7: U_3Si_2 SF reprocessing at La Hague: Future operations

The former La Hague plant UP2-400 was designed to process 400 tHM/y of uranium oxide LWR used fuels. The two new plants UP2-800 and UP3 were erected in the 80's and 90's to reach a throughput of 1,600 tHM/y of uranium light water reactor used fuel.
The existing dissolution facility for RR spent fuel at La Hague: T1B, is located in the UP3 plant, and the RR reprocessing process benefits from the UP3 UOx dilution capacity for aluminium, and silicide in a near future.

To answer the increasing demand for RR spent fuel reprocessing, and to set up a new RR reprocessing capability at La Hague, it would be necessary to implement a new RR-dedicated reprocessing line in UP2-800 plant and then use UP2-800 "vitrification" unit capacity.
As part of a new installation project called TCP (French abbreviation for polyvalent fuel treatment: *Traitement des Combustibles Particuliers*), the RR spent fuel reprocessing capabilities at La Hague are planned to be increased in the 10 coming years.

This under-designing new facility is to provide polyvalent shearing and dissolution equipments for several types of RR spent fuel or exotic fuels, including UAl and U_3Si_2 fuels.
With the objective of optimizing safety and reprocessing capacity, the TCP design will be finalized according to AREVA's customers' needs and declared interests. Basic design is to be achieved late 2014, including scope of materials to be considered in the future installation. Detailed design studies will the start during year 2015.
The design is expected to be validated by the French Safety authority from year 2017.

5. Conclusion

AREVA is confident that U_3Si_2 spent fuel industrial reprocessing will be effective in a near future.
In order to precisely identify the cost associated with U_3Si_2 spent fuel reprocessing in its facilities, AREVA still need to apprehend and take into account the detailed impact of the standard silicide fuel reprocessing and specificities of new fuels in regards with the plants main flows and

capacities. This identification is to be made in year 2014, with the engineering and qualification studies.
As a long-term and reliable player, AREVA proposes to its current and future partners to join the U_3Si_2 spent fuel reprocessing qualification program, for a high-quality, sustainable and robust back-end solution for their spent fuels.

4. References

[1] L. Cheroux, Montpellier University Thesis, CEA-R-5964 report, 2001

AVAILABLE REPROCESSING AND RECYCLING SERVICES FOR RESEARCH REACTOR SPENT NUCLEAR FUEL (INTRODUCTION OF A NEW IAEA REPORT)

S. TOZSER, P. ADELFANG, E. BRADLEY
International Atomic Energy Agency,
PO Box 100, 1400 Vienna – Austria

M. BUDU
SOSNY Research and Development Company,
11 Derbenyovskaya Naberezhnaya, 115114 Moscow – Russian Federation

M. CHIGUER
AREVA
1 Place Jean Miller, 92084 Paris La Défense – France

ABSTRACT

International activities in the back-end of the research reactor (RR) fuel cycle have so far been dominated by the programmes of acceptance of highly-enriched uranium (HEU) spent nuclear fuel (SNF) by the country where it was originally enriched. These programmes will soon have achieved their goals and the SNF take-back programmes will cease. However, the needs of the nuclear community dictate that the majority of the research reactors continue to operate using low enriched uranium (LEU) fuel in order to meet the varied mission objectives. As a result, inventories of LEU SNF will continue to be created and the back-end solution of RR SNF remains a critical issue. In view of this fact, the IAEA, based on the experience gained during the decade of international cooperation in supporting the objectives of the HEU take-back programmes, will draw up a report presenting available reprocessing and recycling services for research reactor spent nuclear fuel. This paper gives an overview of the guiding document which will address all aspects of Reprocessing and Recycling Services for RR SNF, including an overview of solutions, decision making support, service suppliers, conditions (prerequisites, options, etc.), services offered by the managerial and logistics support providers with a focus on available transport packages and applicable transport modes.

1. Introduction

The international activities in the back-end management of RR nuclear fuel cycle have been dominated by the programmes of acceptance of RR SNF by the country where it was originally enriched. Two programmes were created under the Global Treat Reduction Initiative (GTRI) umbrella, for US-origin and Russian-origin fuel, and they had the major goal to eliminate the inventories of HEU fresh and spent nuclear fuel stored at the RR sites worldwide. However, these programmes will soon have achieved their goals. When there are no more HEU inventories at RRs and no commerce in HEU for RRs, the primary driver for the take-back programmes will cease resulting in their phase out.

The needs of the nuclear community dictate that the majority of the RRs continue to operate using LEU fuel in order to meet the various mission objectives, including science and research, education, isotope production, etc. As a result, inventories of LEU SNF will continue to be created during the RRs lifetime with no obvious path to its disposal. Countries

operating one or more RRs, especially those with no nuclear power programme, may have to choose either to create a national final disposition route for relatively small amounts of RR SNF or to permanently shut down their RRs before the termination of the HEU take-back programmes. Finding appropriate, sustainable and cost effective solutions for the back-end management of the fuel cycle is critical to the continued use of RRs in these countries.

Developing a geological repository for SNF and high level waste (HLW) is not an easy task. Only in a few advanced countries, great progress has been made towards its implementation, including Finland, the USA, Sweden, and France. The technology and costs involved for development and maintenance of a geological repository for hundreds of years make it difficult to afford for most countries, especially for countries with one or two RRs and no nuclear power programme. IAEA, NEA and OECD continue to support the nuclear community in developing geological repositories and their efforts are reflected in a wide range of available publications, including specific safety requirements, international conferences proceedings, joint research reports, guidelines etc.

The IAEA publication presented here [1] will address the available mature options for the management of the back-end RR fuel cycle. Thus emphasis is made on reprocessing and recycling, including regulatory framework, overview of solutions, decision making support, service suppliers' conditions (prerequisites, options, etc.), services offered by the managerial and logistics support providers, with a focus on available transport packages and applicable transport modes.

Industrial entities in two countries, France and Russia, offer international SNF management services on a commercial basis. These services can provide the basis for viable RR SNF management options, depending upon their scope, technical compatibility, applicable regulatory framework, sustainability criteria, cost and accessibility.

This paper summarizes the collection of information that will be included in the IAEA publication on available reprocessing and recycling services for RR SNF.

2. RR SNF Management in France

2.1. Reprocessing and Recycling

The reprocessing process as performed at the AREVA La Hague facility [2] is summarized in Fig 1. The RR fuel reprocessing technology of the La Hague facility includes the following steps:
A - The reception and cooling step: once the fuel is received at La Hague facility, it is placed in interim storage pools for cooling. This cooling or deactivation substantially decreases the radioactivity of the fission products.
B - The dissolution step: the fuel is introduced into the existing dissolver through a pit specially designed for RR spent fuel. The dissolution is realized in a hot nitric acid solution. At this step, the process is limited by the aluminium concentration to 35-40g aluminium/L, to manage the risk of precipitation into aluminium nitrate. The resulting solution is then blended with the solution coming from the dissolution of the UOx fuel (power reactor fuel).
C - The extraction step: Uranium and plutonium are extracted from the solution by a liquid-liquid extraction process. Several extraction cycles in pulsed columns, mixer-settler banks, or

centrifugal extractors are necessary to meet the end-product specifications. At the end of these cycles, the following solutions are generated:

- a solution specifically containing the uranium;
- a solution specifically containing the plutonium;
- a solution containing the fission products and the minor actinides.

This last solution is then “vitrified”, i.e. conditioned into a stable, homogeneous and durable glass matrix, and encased in a standard canister, “Vitrified Universal Canister” (UC-V)[1]. The UC-Vs are then stored in a specific storage facility at La Hague site for cooling.

D - Following a cooling storage period, the UC-Vs are returned to the customer country for interim storage prior to final disposal.

In order to comply with the customer country’s regulations and technical constraints, the waste can also be conditioned by other means.

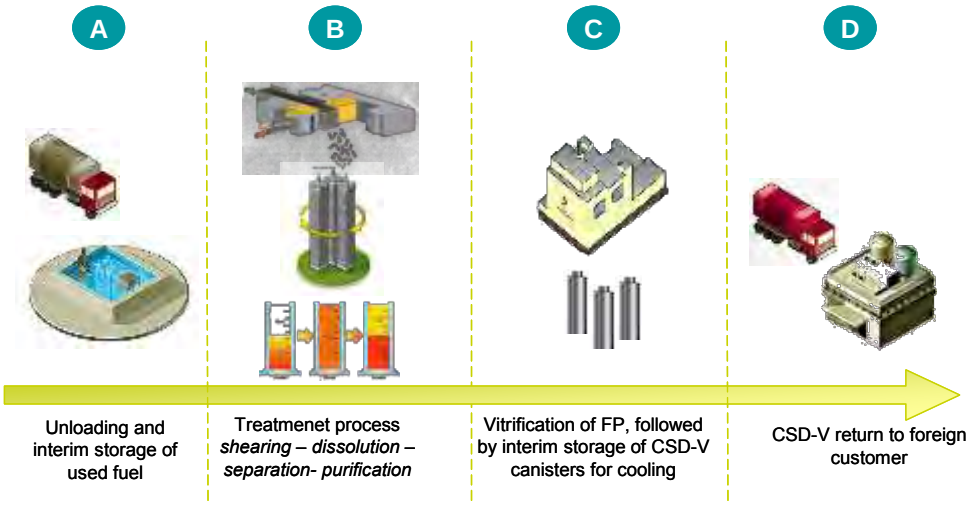


Fig 1. Schematic view of the research reactor fuel treatment process

2.2. Packages and Transport Modes

AREVA TN International, part of AREVA Logistics Business Unit, owns and operates a fleet of four TN™MTR casks (Fig. 2) whose design is based on IAEA regulations. Specific baskets have been developed for international shipments. Each cask can transport up to 68, 52 or 44 MTR radioactive elements, depending on the basket used and the SNF parameters. AREVA TN International can also propose several other types of casks which satisfy TS-R-1 IAEA 96 requirements (TN™MTR-RHF, TN-LC). A summary of the available packages and transport modes is presented in Table 1.

Package	Road	Railway	Water	Air
TN™MTR-68	Yes	Yes	Yes	No
TN™MTR-52, 52S, 52SV2	Yes	Yes	Yes	No
TN™MTR-44	Yes	Yes	Yes	No
TN™MTR- RHF	Yes	Yes	Yes	No
TN-LC	Yes	Yes	Yes	No

Tab 1: Packages and transport modes

[1] Conteneur Standard de Déchets Vitrifiés (CSD-V)

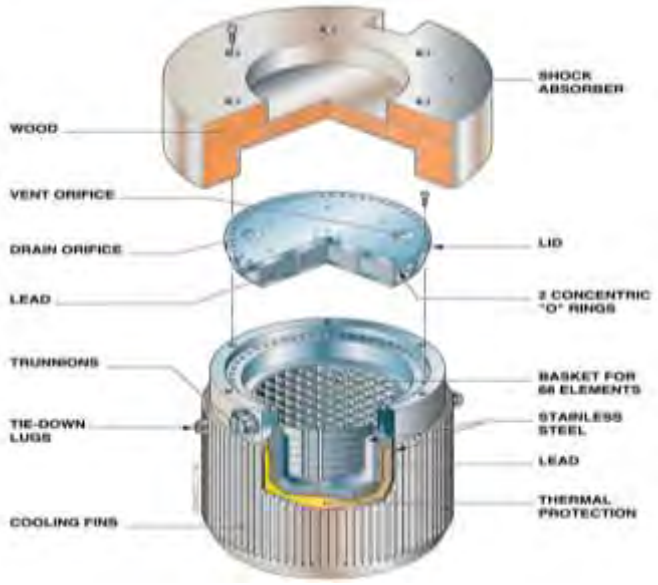


Fig 2. Artistic view of the TN™MTR Cask

Other packages, such as TN™-106 or TN™-17, can also be used depending on the customers' requirements and site constraints (e.g. existing lifting capacity, floor load limitation, special constraints etc.).

2.3. International Agreements and Licensing Summary

With the usual customer-supplier commercial and industrial relationship, the inter-governmental exchanges are to be very well considered in the whole project time frame. Except for the transportation and treatment authorization to be obtained after application to Safety Authorities, discussions for Intergovernmental Agreements (IGA) between the Governments of France and the corresponding country are to be set up. The Fig 3 bellow shows the typical schedule and main steps to be followed from first discussions and exchanges about a RR SNF management up to the effective contract signature.

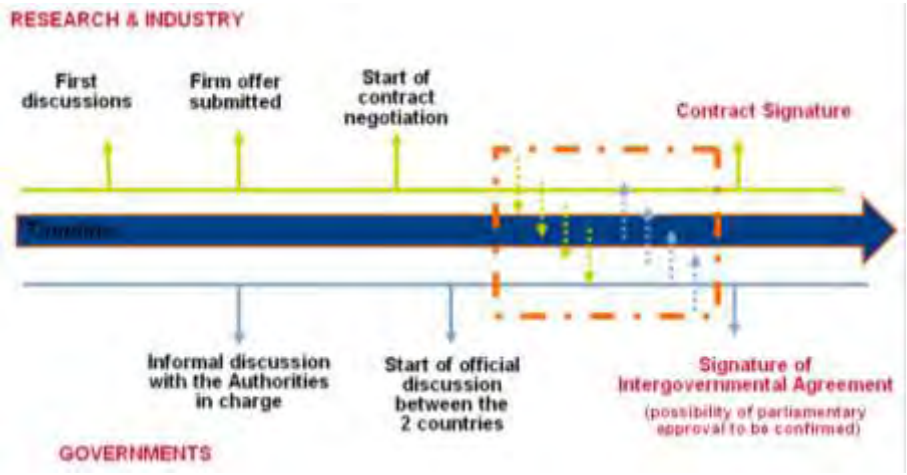


Fig 3. Typical schedule for a new RR used fuel recycling contract

This standard schedule is to be followed since 2006 French law on foreign radioactive waste management has been issued.

The IGA application is to feature three main types of information. Each of these steps is to be clearly developed in the final agreement:

- Project description: information on the material owner or related contractor (if different from the material owner), introduction of the main stakes for the owner or related contractor, location of the nuclear material, legal status and origin of the material, , the planned contractual structure for material treatment and recycling, the planned scope of collaboration between the parties;
- Acceptability of treatment: type and characteristics of material to be treated (design, total mass, mass of oxide and heavy metals, burn-up rate, cooling, initial enrichment, etc.), the material transportation (cask and transportation procedures to be realized);
- Schedule: quantities to be treated and timing, period of delivery of SNF from the customer to AREVA La Hague facility, periods of treatment, period of waste return, use/reuse of the recycled material, deadline for last return of waste.

The French approval certificates of AREVA transportation casks are regularly renewed in order for this equipment to be available for all RR SNF removal projects. Agreement extensions have to be obtained for each type of RR SNF to be transported in these casks. When needed, specific baskets can be designed and manufactured for RR SNF transportation.

Two main authorizations issued by the French Nuclear Safety Authority (ASN) are necessary in order to implement a reprocessing solution in France: transportation authorization and reception-reprocessing authorization at La Hague plant.

The AREVA reprocessing plant of La Hague has reception and reprocessing authorization for a wide range of known RR SNF. An extension of this authorization shall be obtained if the plant plans to receive new types of RR SNF. In addition, based on the past activities and experience in reprocessing various type of research and fast reactor spent fuel, AREVA has decided to launch the project of a new Polyvalent Fuel Treatment Facility (TCP[2]) at La Hague site. TCP will address various fuel specificities at the shearing and dissolution steps in order to answer varied customers' needs without hampering current La Hague reprocessing plant capacity. The new facility will substantially expand the reprocessing spectrum services of the La Hague plant.

3. RR SNF Management in Russia

3.1. Reprocessing and Recycling

At present, in Russia functions only one reprocessing facility – Mayak PA reprocessing plant RT-1, situated in Ozersk of the Chelyabinsk Region. The main distinctive feature of the plant RT-1 is a wide range of reprocessed fuel. SNF of power reactors (VVER-440 and BN-600), naval propulsion reactors, commercial-scale reactors and research reactors is reprocessed here. The distinctive features of the plant RT-1 technology are:

- Three multipurpose process lines allow not only reprocessing different fuel types on each of them, but implementing joint reprocessing of different SFAs.

[2] Traitement des Combustibles Particuliers

- Extraction of neptunium during SNF reprocessing is aimed at its separated storage and fabrication of radioisotopic products.
- Commercial output of regenerated uranium with targeted ^{235}U enrichment by means of mixing the uranium resulted from reprocessing different SNF.
- Separation of different elements from residual SNF solutions for fabrication of radioisotopic products (caesium, strontium, promethium, krypton, etc.).

The SNF, delivered to the plant, is placed into a cooling pool, where more than three meters of water above the fuel make a reliable biological shielding. The duration of RR fuel interim storage is up to 2 years before reprocessing. Safety of the SNF interim storage is ensured by highly efficient pool water purification system and radiation monitoring systems. The first stage of SNF reprocessing is to cut the SFAs into 60 mm pieces, load them into a batch-type dissolver, where the fuel is dissolved in nitric acid solution. Nitric-acid solution of fuel composition is clarified by filtering and then is reprocessed by the PUREX process. The PUREX process allows to extract and separate the valuable elements (uranium, plutonium, neptunium). The targeted products of SNF reprocessing are:

- uranyl nitrate melt, obtained from evaporation of nitric-acid solution of uranium;
- triuranium octoxide, obtained from precipitation by ammonia and subsequent roasting of the precipitate;
- plutonium dioxide, obtained from precipitation by oxalate and subsequent roasting of the precipitate.

Beside the mentioned targeted products, the plant process flow may provide full-scale extraction of neptunium and radioactive iodine. The needs of radioisotopic production require krypton (^{85}Kr), strontium (^{90}Sr), caesium (^{137}Cs), americium (^{241}Am), promethium (^{147}Pr) and other radionuclides to be separated from the spent fuel.

The safe management of radioactive waste is an important aspect of the plant RT-1 operation (Fig 4). The vitrification plant has been in operation since 1987. The principal objective of the vitrification plant is to include HLW and, partially, intermediary level waste (ILW), into the matrix of sodium aluminophosphate glass.



Fig 4. HLW treatment at Mayak PA

3.2. Packages and Transport Modes

The RR SNF can be shipped to the Russian Federation in certified transport packages. TUK-19, SKODA VPVR/M, TUK -145/C, Castor MTR2, TUK-128, TUK-135, TUK-32 (or TUK-18 cask similar to the latter) transport packages for RR SNF shipment operations have certificates in the Russian Federation (Table 2).

Package	Road	Railway	Water	Air
TUK-19	Yes	Yes	Yes	Yes
TUK-145/C[3]	Yes	Yes	Yes	Yes
SKODA VPVR/M	Yes	Yes	Yes	No
Castor MTR2	Yes	Yes	Yes	No
TUK-128	Yes	Yes	No	No
TUK-32 (or TUK-18)	Yes	No	No	No

Tab 2: Packages and transport modes

Over the past five years several air shipments of RR SNF to Russia were carried out due to the following advantages: the air shipment may help reaching difficult access places, improve the shipments schedule in big programs or when a limited fleet of transport packages can be used, assure better security in the cases of long routes and avoid dangerous goods transiting in the close proximity of communities or environmental protected zones [3]. For air transport of RR SNF TUK-19 casks have been certified as Type B(U) package and TUK-145/C as Type C package (Fig 5) [4].



a b c

Fig 5. a. TUK-19 casks in ISO container. b. Loading of ISO container on the board of AN-124-100 airplane. c. Loading of TUK-145/C cask on the board of AN-124-100 airplane.

3.3. International Agreements and Licensing Summary

The Federal Law No. 7-FL “On Environmental Protection” d/d January 10, 2002 extended the possibility for the Russian organizations to cooperate in the back-end nuclear fuel cycle services. The terms of SNF import are stipulated as follows:

- The SNF import is permitted for interim storage and/or reprocessing.
- The project shall undergo a state ecological expertise during which a general decrease of the radiation effects and enhancement of environmental safety, resulted from implementation of the project shall be justified.

[3] The TUK-145/C package represents a package-in-package design solution: the TUK-145/C accommodates the SKODA VPVR/M package converting with this the Type “B” package to Type “C”

- The basis for the import are international contracts of the Russian Federation.
- It is worth mentioning that the Law gives preference to the option of returning the radioactive waste resulting from reprocessing to the country of origin of the RR SNF.

The following project preparation procedure has been formed:

(1) Conclusion of an international contract on co-operation in SNF import (both of Russian and foreign origin) into the Russian Federation, which has the form of a government-to-government agreement with the foreign country. Two options are possible: radioactive waste (RW) return to the export country, or permanent disposition in the Russian Federation. To initiate an international contract, the authorized body of the export country has to send a corresponding letter to the State Atomic Energy Corporation Rosatom.

(2) Elaboration of the documentation for a Unified Project of SNF import. The Unified Project documentation is prepared in relation to the prospective conclusion of a Foreign Trade Contract (FTC) for operations with spent fuel assemblies subject to the state ecological expertise. These documents are elaborated and approved in compliance with the established requirements, including:

- FTC draft (containing the resulting finances for the Project implementation, and the expenses for the management of spent fuel assemblies and of products resulted from reprocessing, approved in the established order);
- special ecological programs, implemented out of the funds incoming from foreign trade operations with spent fuel assemblies;
- materials to justify general decrease of the risks of radiation impact and enhancement of environmental safety as result of the Unified Project implementation, as well as the timeframe of interim technological storage of spent fuel assemblies and reprocessing products, stipulated by the FTC;
- other materials to be submitted to the state ecological expertise assessment in compliance with the requirements of the Russian Federation legislation, including the conclusion of the Russian Federal Service for Environmental, Technological and Nuclear Supervision and the Ministry of Public Health of the Russian Federation.

Federal Centre for Nuclear and Radiation Safety (FCNRS) is authorized by the Government of the Russian Federation to sign FTCs for SNF imports.

The licensing procedure can be divided in three main steps:

- Package design approval;
- Shipment approval;
- Import/export license for nuclear commodities and technologies.

FCNRS prepares applications and obtains import licenses for SNF.

The certificate of approval for the package design and certificate of approval for shipment can be combined into one certificate of approval which can also contain the conditions for shipment of empty packages.

State Atomic Energy Corporation Rosatom, Department of Nuclear and Radiation Safety, Organization of Licensing and Approval Activities is responsible for issuing certificates of approval for package design and shipment.

4. Engineering Support, Management and Logistics Service Providers

Experience shown that engineering support is required during SNF preparation and shipment different stages:

(1) Decision preparatory phase: preparation of feasibility studies, selection of route, transport modes and packages, support in forming RR coalitions for cost and schedule optimization, development and licensing of new packages and transport means etc.
(2) Contracting: allows implementation of turnkey solutions providing project management of subcontractors, interface with authorities, schedule control, work implementation coordination etc.
(3) Licensing: according to [4] SNF is transported in Type B(U)F or C packages (for fissile materials) that require multilateral approval of certificates for package design and shipment, therefore engineering support is provided during licensing in the country of the Consignor, Consignee as well as in transit countries.
(4) RR Facility support in the shipment preparatory phase: during SNF inspection and acceptance by the reprocessing facility, development of spent fuel assemblies' loading technology in transport packages, Consignor's facility modifications for allowing the transport package handling, failed fuel repackaging etc.
(5) SNF shipment: carriers licensing, contracting and coordination, SNF loading in transport packages, preparation of shipment documents, technical escort of the shipment, interface between the Consignor, Consignee, carriers and different authorities during shipment etc.
(6) Post shipment activities: support during preparation, licensing and shipment of the HLW resulted from reprocessing back to the SNF originator country.

During many years of international cooperation lead by IAEA [5], US and Russian Governments for the implementation of the HEU take-back programmes, as well as of RR SNF commercial reprocessing and recycling services provided by France and Russia, worldwide service providers have worked together and developed experience in all above mentioned stages of SNF preparation and shipment.

AREVA TN has several decades of experience in the international transport of spent fuel by road, rail and sea, can rely on the collaboration of companies in the AREVA group and can offer efficient, reliable and safe solutions. AREVA TN's main activity is to design, manufacture and deploy packaging systems for nuclear material for both nuclear power plants and research reactors. AREVA TN has extensive experience under the U.S. Foreign Research Reactor Fuel Return Program with the transport of irradiated research reactor fuel elements (TRIGA, MTR, DIDO, etc.) to the Idaho National Lab and Savannah River Site in the USA from Japan, Denmark, Austria, Netherlands, Portugal, Taiwan, and Indonesia, shipments of LEU and HEU from the DOE/NNSA Y-12 site in Oak Ridge to France, and of fresh MTR and TRIGA fuel elements and radioisotope production targets from France to numerous countries, including the USA, Australia, Indonesia, The Netherlands, Sweden, Norway, Japan and South Africa. AREVA TN also transported nuclear fuel to AREVA's La Hague reprocessing plant from Australia, France, and Belgium. AREVA TN also has significant experience transporting irradiated targets, irradiated fuel pins, and irradiated hardware to hot cells and other research facilitates using the smaller TN-106 cask.
Beside its reprocessing and recycling activities, AREVA also provides comprehensive solutions for SNF management such as engineering work in developing waste storage and disposal equipment and facilities.

Sosny R&D Company's main activities are focused on research and development in the field of nuclear energy. Initially the company specialized in deliveries of irradiated SNF assemblies from Russian NPPs to Scientific Research Institute of Atomic Reactors - RIAR (Dimitrovgrad) for post-irradiation examinations, development of research equipment, SNF research and further analysis of the results. Later on Sosny R&D Company took part in the Russian Research Reactor Fuel Return (RRRFR) programme aimed to return research reactor fresh and irradiated fuel of Russian origin to the Russian Federation, participating in projects from Belarus, Bulgaria, Czech Republic, Germany, Hungary, Kazakhstan, Latvia, Libya, Poland, Romania, Serbia, Ukraine, Uzbekistan and Vietnam. Today Sosny R&D Company offers the following licensed services: development and supply of equipment for NPPs, RRs, subcritical assemblies, nuclear fuel cycle facilities and RW management facilities, destined for the production, reprocessing and transport of nuclear fuel and radioactive materials, research and engineering service provider to operators of facilities involving handling of nuclear materials and radioactive substances, transportation of nuclear materials and radioactive substances, development and certification of conveyances and packages (including foreign) in the Russian Federation, and those of Russian origin in other countries.

Different other contractors have proven international experience in different stages of SNF preparation and shipment: ÚJV Řež, a. s. (SKODA VPVR/M package services), SKODA a.s. (package development) and DMS s.r.o. (Class 7 dangerous goods shipment on public road) - Czech Republic, DAHER – NCS (package and shipment services) – Germany, J/S ASPOL-Baltic Corporation (SNF sea shipments) and Volga-Dnepr Airlines (fresh and spent nuclear fuel air shipments) – Russian Federation.

5. Conclusions

The upcoming IAEA Technical Report "Available Reprocessing and Recycling Options for Research Reactor Spent Nuclear Fuel" will contain a full set of guiding information on mature technologies and services for the back-end management of RR SNF that will help the RR community in finding and implementing available solutions, and so allowing the continued and safe operation of RRs in many countries.

REFERENCES

[1] DRAFT Technical Report "Available Reprocessing and Recycling Options for Research Reactor Spent Nuclear Fuel", IAEA, 2013.

[2] B.Stepnik, M.Grasse, D.Geslin, C.Jarousse, A.Tribout-Maurizi, F. Lefort-Mary "AREVA involvement in UMo fuel manufacturing and research test reactor fuel treatment", RRFM-2012, 18-22 March 2012, Prague, Czech Republic.

[3] M.E. Budu, D.V. Derganov, O.A. Savina, S.V. Komarov (Sosny R&D Company, Russia), S.D. Moses (ORNL, USA) "Perspectives For TUK-145/C Cask International Licensing and Further Utilization", PATRAM-2013, 18-23 August 2013, San Francisco, USA.

[4] IAEA Regulations for Safe Transport of Radioactive Materials, SSR-6, Vienna, 2012.

[5] Tozser, P. Adelfang, E Bradley: (IAEA): "A Decade of IAEA Cooperation with the RRRFR Programme", PATRAM-2013, 18-23 August 2013, San Francisco, USA.



Utilisation of Research Reactors

PRODUCTION OF RADIOISOTOPES FOR MEDICAL USE IN THE JULES HOROWITZ REACTOR

M. ANTONY*, J.-P. COULON, S. GAY, G. MARTIN

CEA, DEN, Cadarache,

F-13108 Saint Paul Lez Durance, France

*Corresponding author: muriel.antony@cea.fr

Abstract:

This paper describes the design studies of radioisotopes production facilities which are parts of the Jules Horowitz Reactor (JHR) under construction at the CEA (Commissariat à l'Energie Atomique et aux Energies Alternatives)/Cadarache center in France.

It focuses on the ^{99}Mo irradiation systems and associated equipments. The ^{99}Mo is produced by irradiation of uranium targets. JHR will contribute to the security of supply of medical radioisotopes, especially for the ^{99}Mo-^{99m}Tc.

It is scheduled that JHR will start producing radioisotopes at the beginning of reactor operation (providing completion of the qualification of the irradiation process).

To this end, a process of industrialization will start in 2014 for the construction of the ^{99}Mo production facilities (in-pile part, water loop and I&C systems).

1. Introduction

The production of molybdenum 99 (^{99}Mo), and its decay product, technetium 99m (^{99m}Tc), the most widely used medical radioisotope for diagnostic purposes, is important for public health. As a matter of fact, disruptions in the supply chain of these medical isotopes, which have half lives of 66 hours for ^{99}Mo and 6 hours for ^{99m}Tc, can lead to cancellations or delays in Department of Nuclear Medicine where this isotope is used as Single Photon Emission Computed Tomography (SPECT) tracer. Unfortunately, supply reliability has declined over the past decade, due to unexpected or extended shutdowns at the few ageing ^{99}Mo producing research reactors and processing facilities. These shutdowns have created global supply shortage. As an answer to minimize this risk for the next decades, the Jules Horowitz Reactor (JHR) under construction at the CEA Cadarache in France took into account as a new major challenge, the production of radioisotopes.

In this paper, we present an overview of JHR project, an update of the construction of the reactor and also the MOLY project. Then, we describe physics and technological studies undertaken, as well as the circuit's architecture and the nuclear safety issues. We also describe the chosen industrial policy to the device manufacturing. Finally, we conclude with the Jules Horowitz Reactor capacity for ^{99}Mo production.

2. Jules Horowitz Reactor Project

The Jules Horowitz Reactor (JHR) is a Material Testing Reactor currently under construction at the CEA (Commissariat à l'Energie Atomique et aux Energies Alternatives) Cadarache center in France. It will represent a major research infrastructure for scientific studies dealing with material and fuel behaviour under irradiation. The reactor will perform Research and Development programs for the optimization of the present generation of Nuclear Power Plants (NPPs), support the development of the next generation of NPPs and also offer irradiation possibilities for future reactors. The reactor will also be devoted to medical radioisotope production [R1] and [R2]. JHR will offer irradiation experimental capacities to study material and fuel behaviour under irradiation. JHR will be a flexible experimental infrastructure to meet industrial and public needs. It is designed to provide high neutron flux, to run highly instrumented experiments and to operate experimental devices with environmental conditions (pressure, temperature, flux, …) relevant for water reactors, or specific environments (eg. gas, sodium) related to other thermal or fast reactor concepts.
The construction of JHR is undergoing on and some major milestones were achieved like, for example the implementation of the dome on the top of the reactor building last December.



Fig 1. Artistic view of JHR (copyright CEA)



Fig 2. Overview of the implementation of the dome on the top of the reactor building (copyright CEA)

The next important milestone will be the commissioning of the reactor building's polar crane.

3. MOLY project

The objectives of the MOLY project are to be able to produce an annual volume of 25% of European needs on an average basis and up to 50% of European needs in peak production. The new facility will accommodate Low Enriched Uranium (LEU) targets. The objectives of the MOLY project became one of the major challenges at the beginning of JHR. For the business point of view, the project should set up long term agreements with industry. Then, our activities will strengthen the Mo-99 supply and the production of other radioisotopes within European network.
To answer to the industrial challenge, we decided to build an industrial project since 2011. An engineering team was structured. It was important to integrate different skills in the team to deal with numerous interfaces with the JHR construction and the development of the MOLY activities. The team is now consistent with the following tasks in different fields:

- Nuclear design: physics studies, nuclear safety, technological studies and (Instrumentation and Control) I&C systems. In this field, the iterative approach and the interfaces between skills are useful in order to converge into a final design ready to manufacture. It is the so called "pig tail" process;

- Nuclear manufacturing : manufacturing until factory acceptance as well as assembly on site
- Nuclear operating with tests, commissioning and normal operations;
- Project management;
- Business approach.

4. Studies

In 2010, first feasibility studies have been carried out [R3]. Since 2011 design studies were conducted in order to adapt to new objectives assigned and, from 2012, to the conversion of Uranium targets from High Enriched Uranium (HEU) to LEU. The references [R4] and [R5] present and summarize the existing studies. In the design area, iterations might be required for take into account new input data. This process which can be long has to be formalized by important milestones. In our case, we had:

- In late 2011, a review process on the preliminary definition studies with HEU targets
- In late 2012, a review process on the preliminary definition studies with LEU targets
- In late 2013, a review process on the detailed design studies and to validate the industrial policy for the manufacturing of the specified MOLY equipments

This year, the main goals will be to validate mechanical aspects with the use of mock up and the document edition to launch the manufacturing of the specified MOLY equipments.

4.1 Physics Studies

The MOLY irradiation devices will be located in the JHR beryllium reflector. In order to increase the JHR means of radioisotopes production, without decreasing the global experimental capacity, the design of the JHR reflector was redefined at the beginning of 2011. Consequently, the irradiation devices will be placed on movable systems in order to achieve the loading and unloading operations out of the neutron flux. Four locations are devoted to the ^{99}Mo production. The movable systems should be well interfaced with reactor structures. They should be very robust. The irradiation devices are connected by hoses to a dedicated cooling circuit.

Numerous physics calculations were performed. The main objective of neutronic calculations was to define the ^{99}Mo production performance of the uranium target in the environment of the reflector of the JHR. We had to take into account many input data:

- Target: enrichment in ^{235}U, shape, size, density …
- MOLY irradiation devices: material, shape, location…
- Interfaces with others equipments of the Jules Horowitz Reactor

In order to be able to compare our different results, we needed to define a parameter which was independent of the input data and representative of the performance we are finding out. We defined the following criteria: Curie of ^{99}Mo created/gram of initial ^{235}U.

As main result, we had shown that JHR will be able to produce ^{99}Mo with high level MOLY production rate, even with a lower than maximal expected power.

The thermo-hydraulics calculations are also an important issue of these studies. Calculations have been performed for both operational and nuclear safety purposes. They allowed us to check the heat removal from U targets and to define the main cooling circuit. The safety circuit was also defined in order to deal with accidental situations. The results of these calculations are also used for I&C system's definition.

We also performed thermo-mechanicals calculations on some equipment which are under this kind of constraints.

4.2 Nuclear Safety Studies

Nuclear Safety Studies are very important in the design phase of the MOLY facility. As already discussed, they were done in an iterative manner with the technical design.
Safety documents are produced:

- Safety options file and updates;
- Nuclear safety analysis of irradiation conditions;
- Nuclear safety analysis of operation conditions (without neutrons).

MOLY safety documents will be integrated, at the end of this year, in the general JHR licensing documentation (Safety Analysis Report, General Operating Rules…).
As required by the French Nuclear Safety Authority, stress tests (following Fukushima aspects) are studied as necessary on MOLY equipments.

4.3 MOLY Circuits Architecture

As described in [R6], the Jules Horowitz Reactor is designed to provide the largest possible experimental capacity possible with the largest flexibility. The MOLY production is an industrial process. Since both objectives should be compatible, it is needed to implement MOLY equipments in a dedicated location. It was decided to use the so called “REP cubicle” for the main part of the cooling system, located near the reactor pool. The figure 3 presents the schematic diagram of the MOLY circuits.
We have defined the main components for the electric power supplies (normal and emergency ones). The main principles for the MOLY Instrumentation and control system are determined. At last, the MOLY equipments in the dedicated cubicle and the implementation of electrical cabinets are defined. The MOLY equipments were defined and located in order to minimize the interfaces with those of the reactor and of the other test devices.

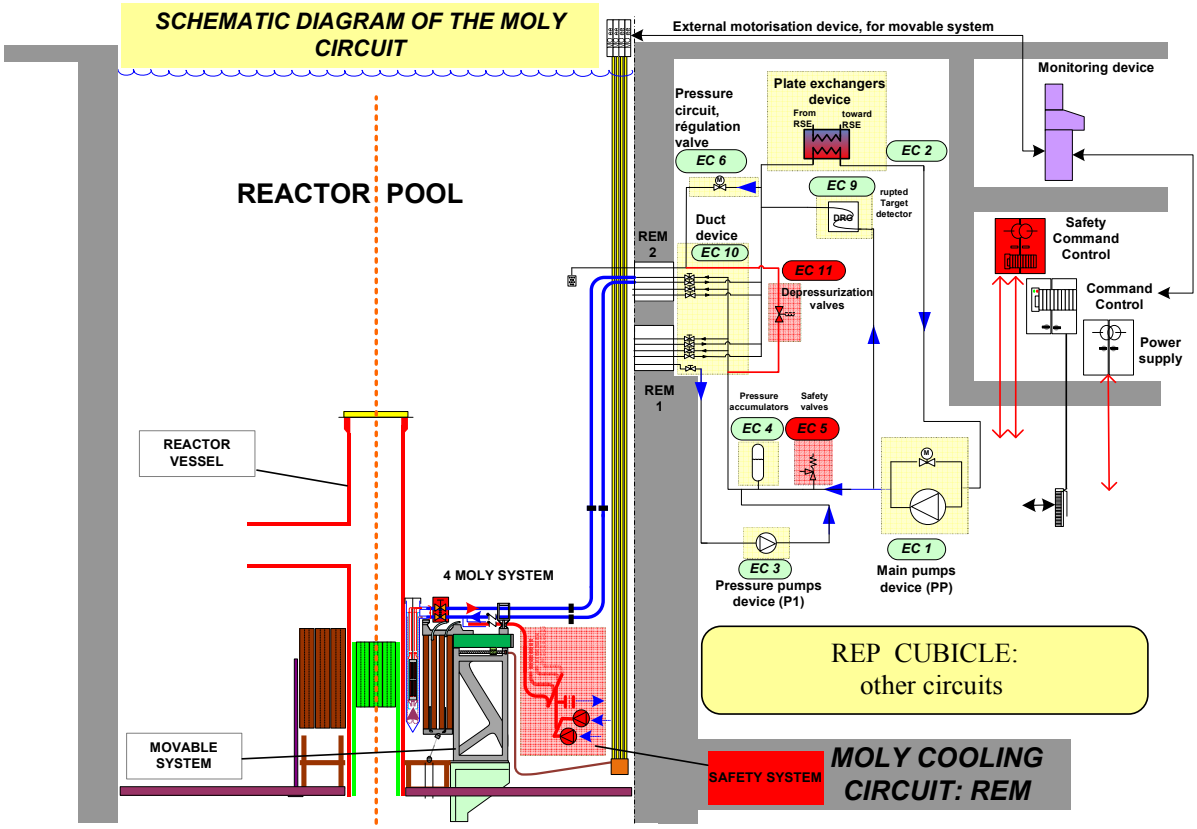


Fig 3 schematic diagram of the MOLY circuits (copyright CEA)

4.4 Technological Studies

In support to the physics studies, numerous technological studies have been carried out. For example, figure 4 presents the detailed design for the MOLY in pile part.

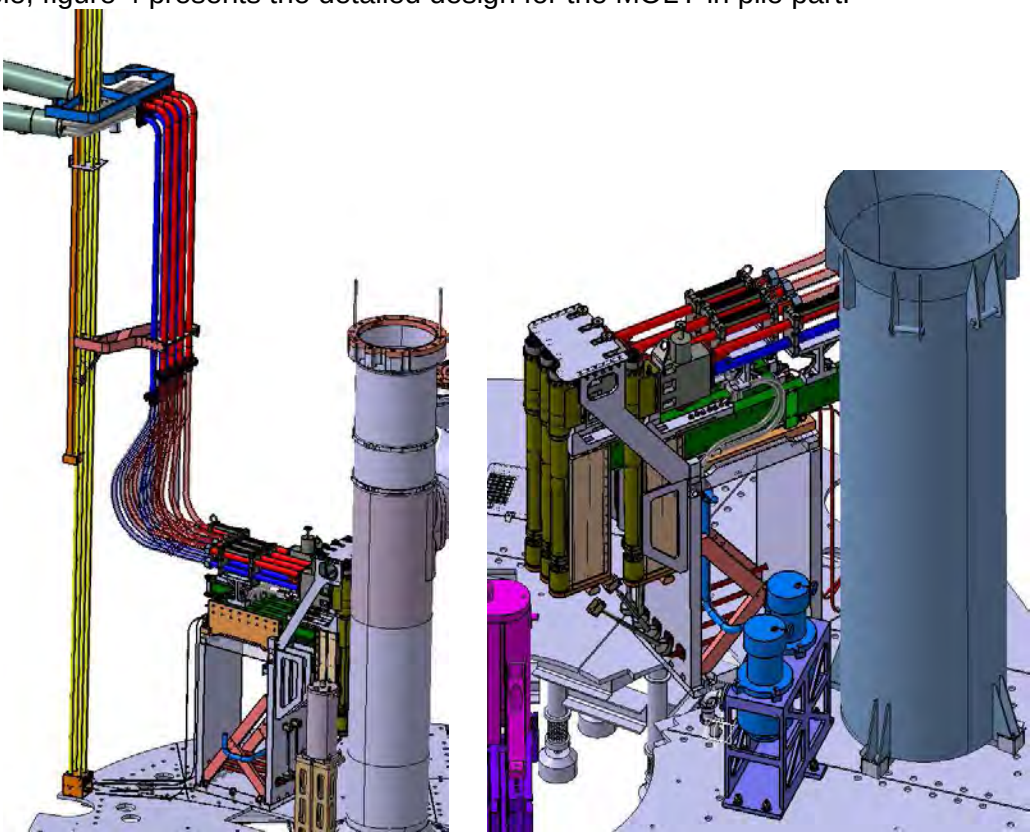


Fig 4 Detailed designs for the MOLY in pile part (copyright CEA)

Other more specific studies have been carried out on other equipments (irradiation devices, movable systems, pumps, flexible pipes, test materials, tools…). By 2014, a comprehensive plan for development of mock-ups is specified.

5. Industrial policy for the device manufacturing

In late 2013, a review process has validated the industrial policy for the MOLY device manufacturing.
This industrial policy will be based on 3 different contracts (see the Fig. 5):

- One for the in pile part of the device, including the movable system, the irradiation rigs, the flexible pipes up to the cubicle and the safety system
- One for the out of part of the device, including the cooling circuit in the cubicle, the I&C systems out of the cubicle and all the electric part.
- One for a contracting owner assistance for following the achievement and managing interfaces between Moly contracts and those of the JHR

All the documents to launch the manufacturing of the specified MOLY equipments will be written for the third trimester of 2014.
Thus, the contracting process may take place early 2015.

6. Conclusion

The construction of JHR is going on with more than 95 % contracts passed and 75% civil work progress. The target date for commissioning is by the end of the decade.
On MOLY aspects, studies are carried out in connection with the decision to irradiate LEU

targets. Studies have been focused on JHR ability to produce 25% of European needs on an average basis, and up to 50% in peak production. They showed us that we could achieve thermal neutron flux densities for an adequate production of ^{99}Mo. As announced in the OEDC-NEA High Level Group on the Security of Supply of Medical Radioisotopes (HLG-MR), JHR irradiation capacity will be the following:

- Annual operation : 220 days;
- Annual basic production : 500 LEU targets/year;
- Possibility to extend for limited periods;
- Weekly maximum capacity :
    - From 32 to 48 targets/week of production;
    - ^{99}Mo production level foreseen (6-days) : 2400 Ci/week of production
    - With the use of the outage reserve capacity (ORC) : until 4000Ci/week of production);
- Production flexibility according to customer's orders.

On MOLY project timeline, we can highlight the following points:

- Design studies for 99Mo irradiation systems based on LEU targets completed;
- Design assessment completed by a review at the end of 2013;
- Launch of the manufacturing process in 2015
- The irradiation tests of LEU targets are planned right after commissioning. In the general frame work of the reactor [R7], the MOLY project team is working on dedicated commissioning;
- First production will be reached after first phase of commissioning;

CEA is experienced in the ^{99}Mo supply chain, since operating for many years uranium target irradiations in OSIRIS (CEA Saclay). CEA is committed to remain a major actor of European network for sustainable ^{99}Mo long-term production, as well as for the other radioisotopes.
JHR should exhibit enhanced target capacity and significantly contribute to ^{99}Mo world market as soon as possible after JHR criticality. JHR is developing irradiation capacity for LEU targets and associated logistics in coordination with European fleet of reactors, to better ensure the back-up, and hence mitigate future risks of shortages.

7. References

[R1] Production of radioisotopes on the Jules Horowitz Reactor, IGORR 2013, JP Coulon and Al, CEA, France,

[R2] The Jules Horowitz Reactor: a new high performances Europeans MTR with modern experimental capacities : toward an international centre of excellence, RRFM 2012, G. Bignan and Al, CEA, France,

[R3] The Jules Horowitz Reactor MOLY system: Towards a concept proposal according a large molybdenum production capabilities, IGORR, September 19-24, 2010 Knoxville TN USA. S. Gaillot and Al, CEA,

[R4] Radioisotopes Production for Medical Use: Preliminary Design of the Jules Horowitz Reactor Facilities, RRFM - IGORR, March 18-22 2012 Prague, Czech Republic, J.P. Coulon and Al, CEA, France.

[R5] Radioisotopes Production for Medical Use: Jules Horowitz Reactor Facilities, ANS Winter Meeting & Nuclear Technology Expo, November 11-15 2012, San Diego, CA, USA, J.P. Coulon and Al, CEA, France.

[R6] Fuel and Material Irradiation Hosting Systems in the Jules Horowitz Reactor, IGORR, October 13-18, 2013, Daejon, Korea, C. Blandin and Al.

[R7] Jules Horowitz Reactor : Organisation for the Preparation of the Commissioning Phase and Normal Operation, IGORR, October 13-18, 2013, Daejon, Korea, J. Estrade and Al.

ADVANCED REACTOR PHYSISCS EXERCISES AT THE TRIGA MARK II REACTOR

L. SNOJ, S. RUPNIK, A. JAZBEC
Reactor physics division, Reactor Infrastructure Center, "Jožef Stefan" Institute
Jamovacesta 39, 1000 Ljubljana, Slovenia

ABSTRACT

Since the 1990s the Jožef Stefan Institute (JSI) TRIGA reactor has been extensively used for performing practical reactor physics exercises for future nuclear power plant operators, students of physics and nuclear engineering and for participants of various international training courses.
In 2012 we upgraded some of the existing and introduced some new exercises. The pulse mode operation exercise was upgraded by installation of new data acquisition system and development of new graphical user interface (GUI) by using LabVIEW software. The critical experiment exercise was upgraded by adding a new detector. Now we monitor neutron population with two independent fission chambers on different locations. Here as well new graphical user interface (GUI), by using LabVIEW software, was developed.
In the past the void reactivity coefficient exercise was performed by inserting Al tube into various positions in the reactor core and measuring the corresponding reactivity changes. In order to make the exercise more realistic, we installed a pneumatic system for generating air bubbles just below the core. The system consists of a system of valves, flow meters and Al tubes for conveying air under the core. The system is operated remotely by a computer running application in LabVIEW. The trainee can adjust the air pressure (proportional to the flow rate) and the location in the core at which the air bubbles are generated. The flow rate at individual locations is measured. The aim of the exercise is to measure reactivity changes versus flow rate and air bubble position.
The second new exercise was measurement of water activation. In this exercise we installed special system which pumps the water through the core at a constant flow rate to the reactor platform, where the water activity is measured with a portable GM tube and two spectrometers, a semiconducting HPGe and a scintillating LaBr. The purpose of the exercise is to measure the 16N and 19O gamma line intensity and dose rate versus reactor power. It can be seen that the relationship is linear. Similar system is used at the Krško NPP for primary coolant loop leakage detection.
The third new exercise, named in core flux mapping, was performed by measuring the axial fission rate distribution at various radial positions in the core. We used CEA – developed mini fission chambers and a special home developed system for moving the fission chamber in axial direction and measuring the count rate versus FC position. The moving system and the FC response were operated by LabVIEW software running on a portable computer.
In the paper we present the new exercises in more details, first results and plan for the future.

1. Introduction

The 250 kW TRIGA Mark II research reactor at the Jožef Stefan Institute (JSI) in Slovenia achieved first criticality on 31st May 1966 and since then the reactor has been playing important role in developing nuclear technology and safety culture in Slovenia. It is one of a few centres of modern technology in the country. Its international cooperation and reputation are important for promotion of JSI, Slovenian science and Slovenia in the world. The reactor has been mainly used for training and education of university students, future operators at Krško Nuclear power plant (NPP) as well as on-job training of staff working in public and

private institutions, isotope production, neutron activation analysis, beam applications, neutron radiography, testing and development of a digital reactivity meter, verification of computer codes and nuclear data, comprising primarily criticality calculations and neutron flux distribution studies[1]. In the past few years, it has been extensively used for irradiation of various components for the ATLAS detector in the European Organisation for Nuclear research (CERN). Due to good characterization of the irradiation channels the reactor has become a reference centre for neutron irradiation of detectors developed for the ATLAS experiment. In 2010 we established collaboration with CEA[2].

The reactor has been used in several international training courses, mostly organises by the NTC and the IAEA. In order to enhance utilisation of research reactors for educational purposes we established a coalition between Austria, Czech Republic and Hungary in the field of international trainings and education. The coalition is formalised within the Eastern European Research Reactor Initiative (EERRI), which was established with the support of the IAEA in 2008 [3].

Since then TRIGA Mark II research reactor has been extensively used for performing practical reactor physics exercises. Each year the reactor is used in regular laboratory exercises for graduate and post graduate students of physics and nuclear engineering. All NPP Krško reactor operators and other technical staff pass training courses on our TRIGA reactor and reactor has been also used in several international training courses, mostly organises bythe Nuclear Training Centre(NTC)[4] and the IAEA.In accordance with this many practical reactor physics exercises are performed each year. In 2012 a project, financially supported by the Krško NPP, was initiatedto upgrade some of the existing and to introduce some new exercises which are presented in more details below. In the paper the new practical exercises/experiments are described together with some results.



Figure 1:Students in the control room carrying out experiment at one of training courses.

2. Critical experiment

Critical experiment and study of subcritical multiplication is one of the basic experimentsin reactor physics.At the JSI TRIGA reactor critical experiment is performed in two different ways, either by adding fuel elements or by withdrawing control rods.Until recently the neutron population in the reactor was measured only by using the fission chamber that is part of the reactor instrumentation, the so called start-up channel. As the critical experiment should be performed with at least two independent neutron sensitive detectors, we installed the second fission chamber with autonomous electronic into one of the irradiation channels in the core. This allows us to demonstrate the dependence of 1/M curve shape versus detector position. Now we developed control and data acquisition software by using the LabVIEW software.This allows the trainee to control counting time of both fission chambers. In addition 1/M diagram is plotted and for each step the software automatically calculates reactivity required to reach criticality. In order to study reactor kinetics around criticality the software features a possibility of observing count rate versus time. The latter feature is especially convenient to study the level of criticality close to k =1 when criticality is estimated by inserting and withdrawing the neutron source. The graphical user interface (GUI) of the software is depicted in Figure 2.

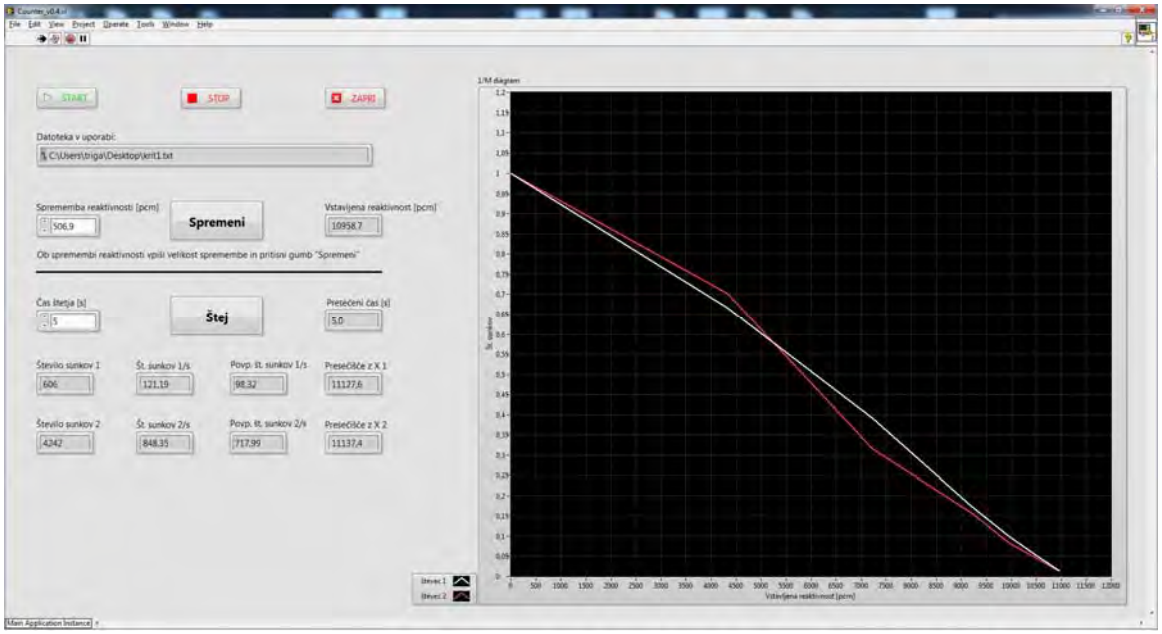


Figure 2: GUI of the software used for critical experiment.

3. Pulse experiment

The JSI TRIGA reactor features pulse rod, which is equipped with pneumatic mechanism that can shoot the pulse rod out of the core in a couple of ms.In pulse mode all control rods except the pulse one are completely withdrawn and the reactor is slightly subcritical. Then pulse rod is pneumatically shot out of reactor core till a predefined limit. This sudden increase in reactivity causes the reactor to go supercritical with a period of a few milliseconds. Reactor power sharply increases for a few decades and at the same time also the fuel temperature increases. Due to prompt negative temperature reactivity coefficient the reactivity is decreased and reactor shuts down. The full pulse length depends on inserted reactivity and is typically in the order of 100 ms (Figure 3). This experiment demonstrates inherent safety of the reactor and is very useful for verification of reactor kinetics models, such as Fuch Hansen adiabatic approximation [5].

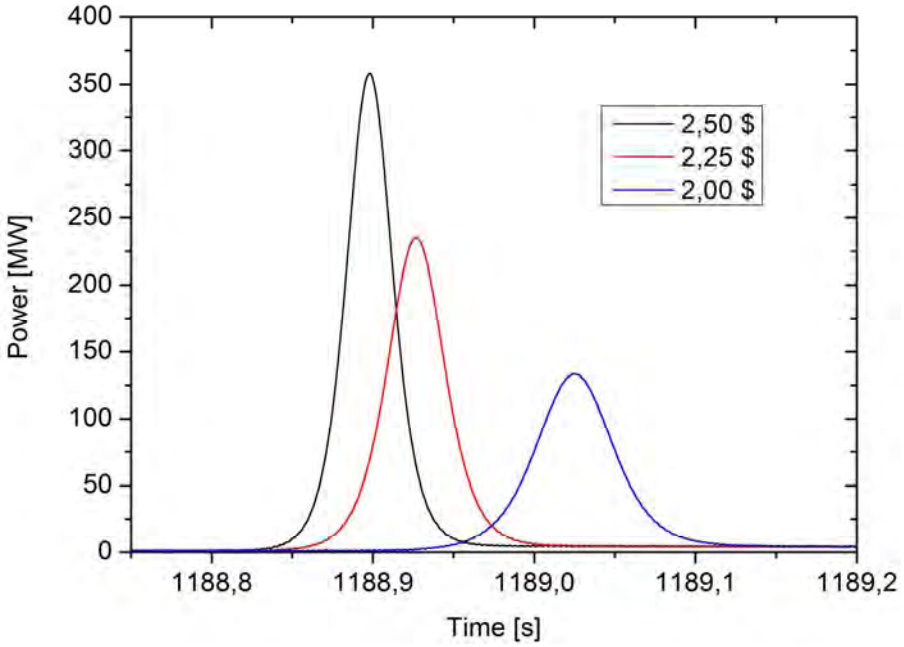


Figure 3: Three different pulses with inserted reactivity of 2,00 $, 2,25 $ and 2,50 $.

The data acquisition system that logs the signal on the pulse channel was upgraded and is now capable of very fast simultaneous sampling of reactor power and fuel temperature. The new software calculates basic parameters of a pulse such are peak power, peak temperature, released energy etc. immediately after the pulse. The TRIGA pulsing was also shot by using high definition and high speed cameras. The video clips are available at the JSI TRIGA webpage [6].

4. Void reactivity coefficient

Voids in nuclear reactor are usually formed as a result of primary coolant boiling and as such affect reactivity and thermo-hydraulic characteristics of the reactor. Consequently the void coefficient of reactivity is one of the key safety parameters in nuclear reactors.
At the JSI TRIGA reactor we used to "simulate" voids in the reactor by inserting small Al batons (6 m in diameter) at various places in the core and measured reactivity changes versus location and size of the void. The advantage of such approach is that the location and volume of the void is very well defined. The disadvantage, however, is that Al baton does not resemble bubbles and is not so illustrative.
Therefore we designed and made a system for simulating water boiling (generation of voids/bubbles) in the reactor. For this purpose we built a pneumatic system which generates air bubbles under the core. The system consists of controller, pressure regulators, valves, air flow meters, Al tubes and nozzles for producing air bubbles. Al tubes with nozzles are inserted in the reactor core on different radial locations so the nozzles are located just under the core. Each Al tube is individually connected to its own valve, choke and air flow meter so we can independently adjust and measure air flow through each individual tube. Alongside with the pneumatic system we developed LabVIEW application for controlling pneumatic system and acquiring data with implemented digital reactivity meter.

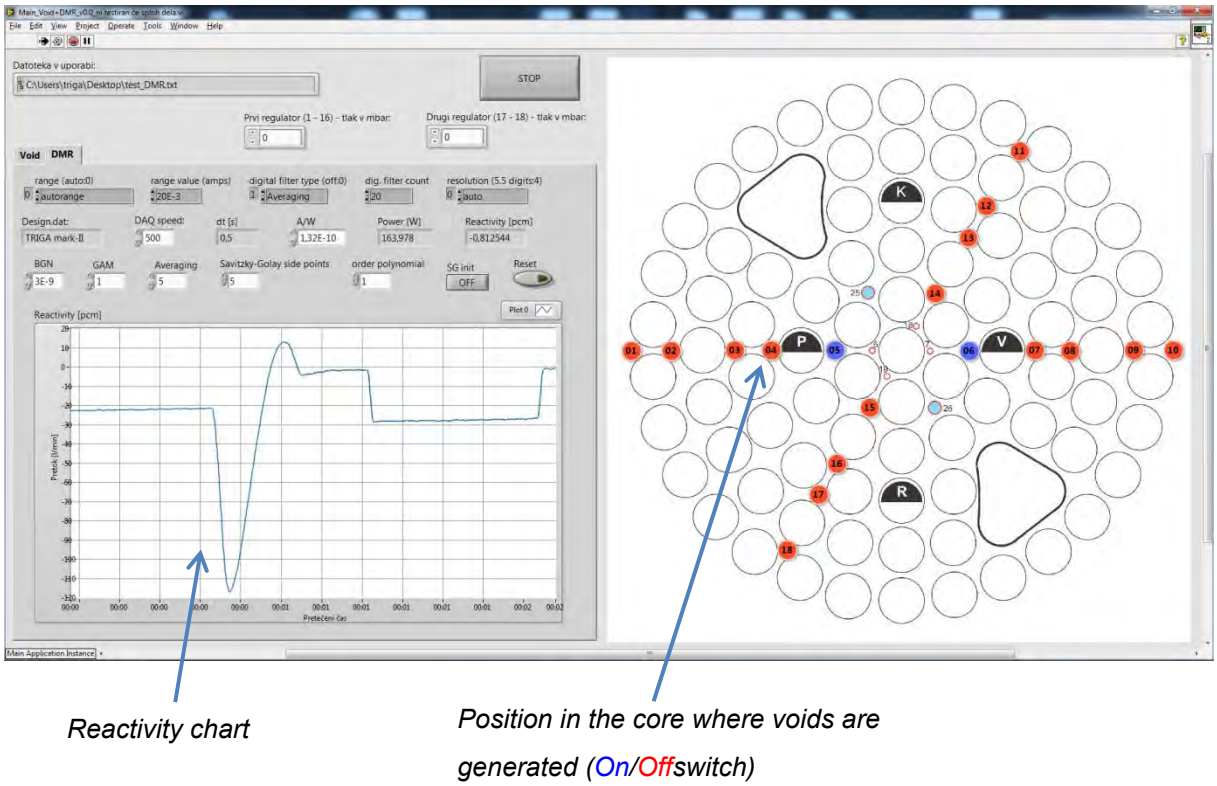


Figure 4: User interface of LabVIEW program developed to control voids generation and reactivity measurement. On the left there are reactivity measurements and on the right there is core scheme of our TRIGA reactor with positions where voids can be generated. By pressing on red circles we can turn on or off voids generation on that position. Airflow measurement tab is hidden on this picture.

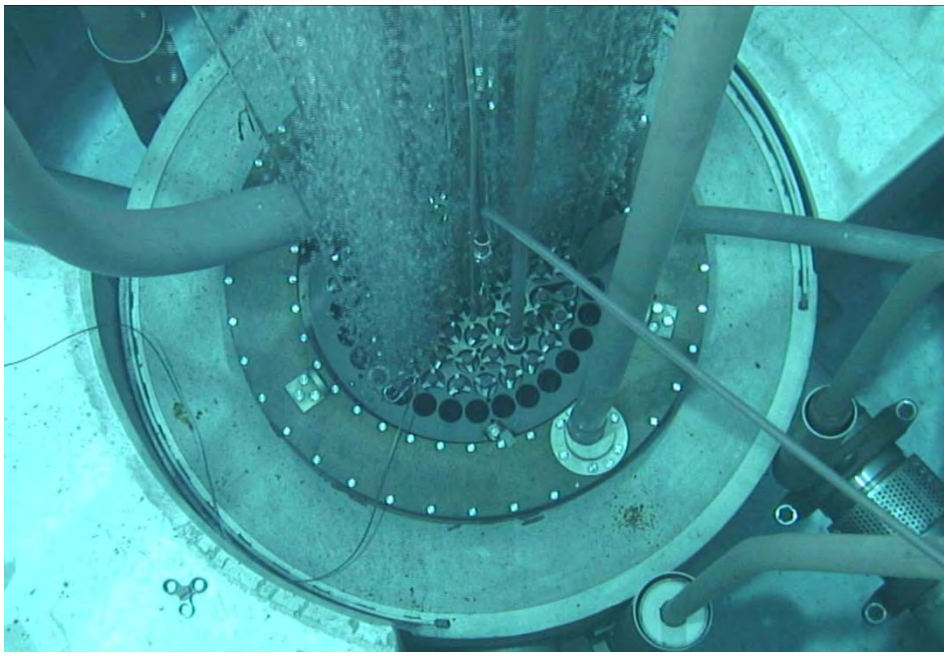


Figure 5: Simulation of water boiling in nuclear reactor. Air is fed just under the core where air bubbles (voids) are generated. Here air bubbles are generated across the reactor core.

By using the GUI in LabVIEW one can adjust air pressure and set location in the core where the voids are formed. By adjusting the air pressure the air flow rate and consequently volume

of the voids in reactor core is changed. Location of the voids is controlled by switching on or off each individual valve and thereby air flow through each individual tube. They are all controlled independently.

It is important to note that installation of this exercise was considered as temporary modification of the reactor. Hence a thorough safety screening and safety evaluation had to be performed prior to installation and is thoroughly described in [7].

The aim of the exercise is to measure reactivity changes versus flow rate and void position. Therefore a digital reactivity meter was integrated into the package. Dedicated software allows trainee to control the air flow, observe reactivity changes and acquire data all with one application. This way trainee can focus to reactor physics and not to the implementation of the exercise. Typical results are presented in Figure 6

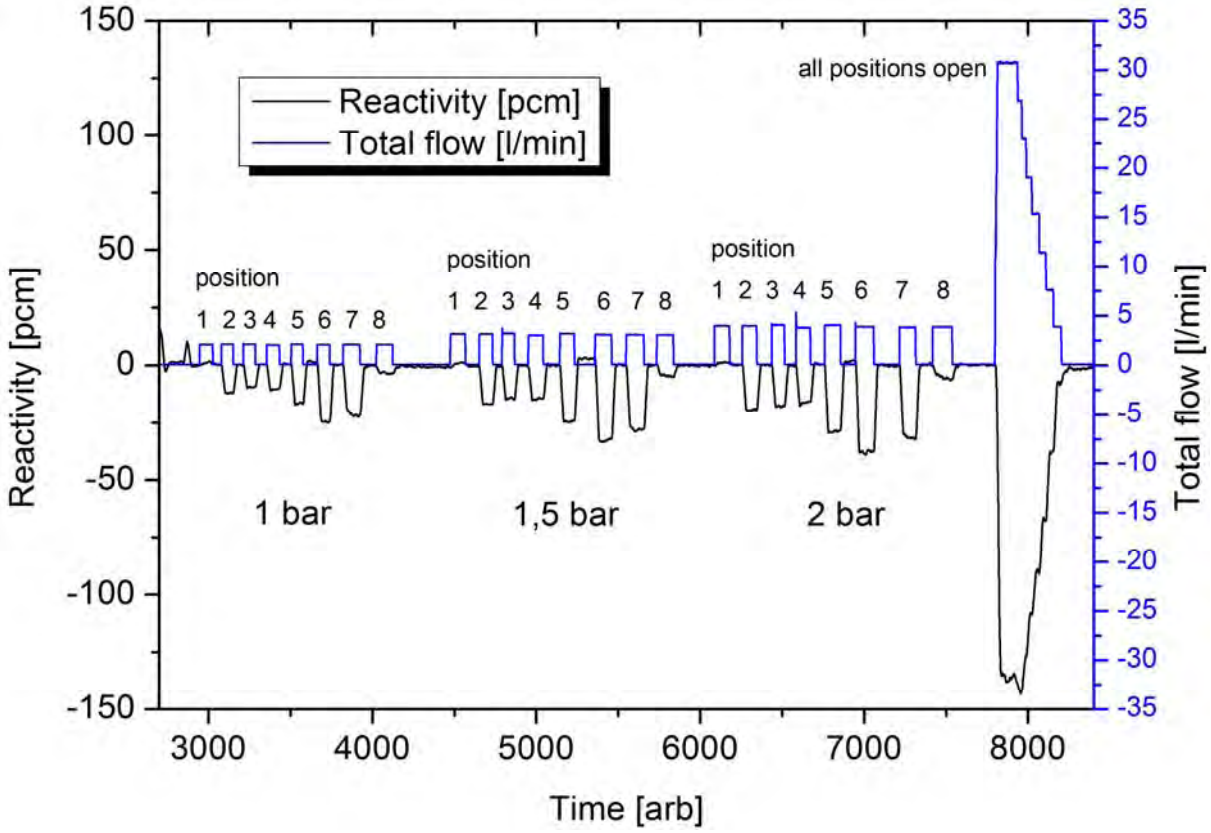


Figure 6: Reactivity changes at different flow rates and different void positions. Voids were triggered one after another on different positions across the reactor core. This was repeated 3 times at different flow rates and at the end voids were produced on all positions together and then switched off one by one.

5. Primar y water activation

Coolant in water cooled reactor gets activated by neutrons causing elevated dose rates in the vicinity of primary circuit, mostly due to ^{16}N, that emits gamma rays with relatively high energy (Table 1). The purpose of this practical exercise is to get familiar with methods for primary water activation measurements and to measure primary water activation versus reactor power level.

Table 1: The most important activation products in water.

nuclide	isotopic abundance	reaction (neutrons)	activation product	$t_{½}$	gamma ray energy
^{16}O	99,76	n,p (fast, E > 9 MeV)	^{16}N	7,13 s	6,129 MeV 7,117 MeV
^{18}O	0,20	n,γ (thermal)	^{19}O	26,9 s	0,197 MeV 1,357 MeV

The setup for this exercise is composed of a pump which pumps primary water through reactor core to reactor platform, where water activity is measured. Primary water is pumped below the core and is guided by the aluminium tube through the core to the platform at a constant flow rate, which can be adjusted. On the reactor platform primary water tube is fed through a lead shield where detectors are located, so the detectors measure only activation of primary water and not background radiation of working reactor. Water activity is measured with portable GM tube for measuring dose rate and two types of spectrometers, a semiconducting HPGe and a scintillating LaBr crystal. Signal from spectrometers is analysed with Amptek PX5 multichannel analyser and acquired with DppMCA software.

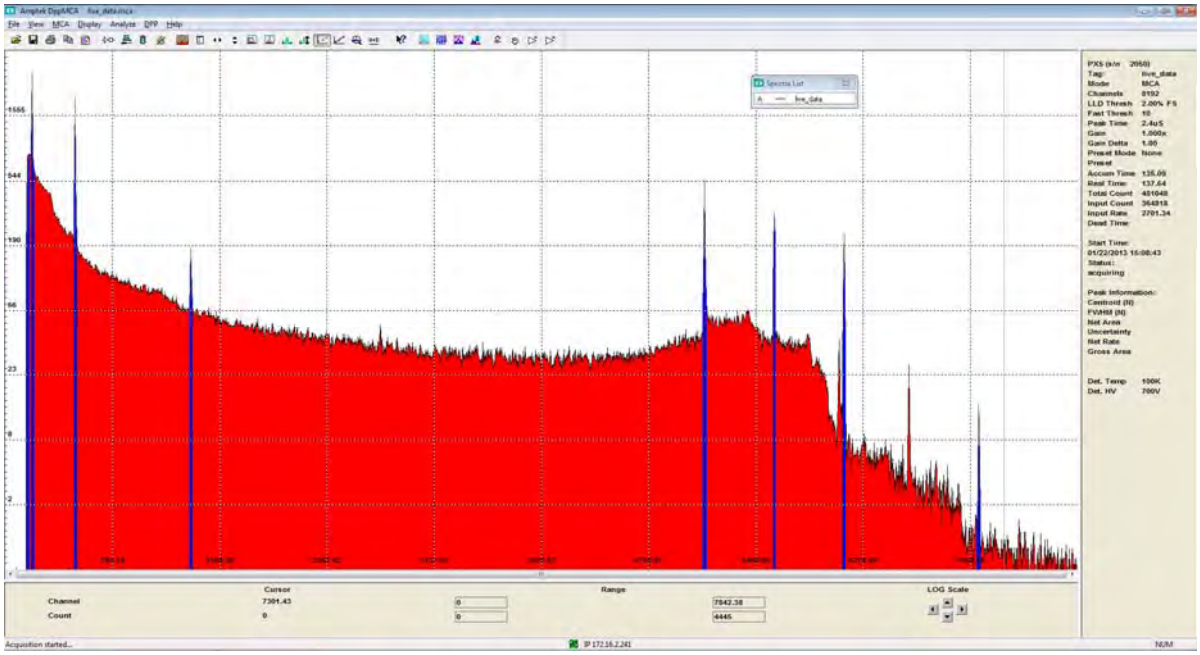


Figure 7:DppMCA software with spectrum of activated primary water, measured with HPGe spectrometer.

In the first part of the exercise the trainees learn how to calibrate the spectrometers with Cs source before the exercise and how to search the gamma line peaks. In the second part they monitor intensity of selected gamma lines corresponding to water activation products, versus reactor power level measured on the linear channel. In addition they monitor the dose rate. Some results are presented in Figure 8. It can be observed with naked eye that the relationship between the gamma line intensity and the reactor power level is not completely linear. One source of the discrepancy is the detector dead time correction, which currently has to be done separately.

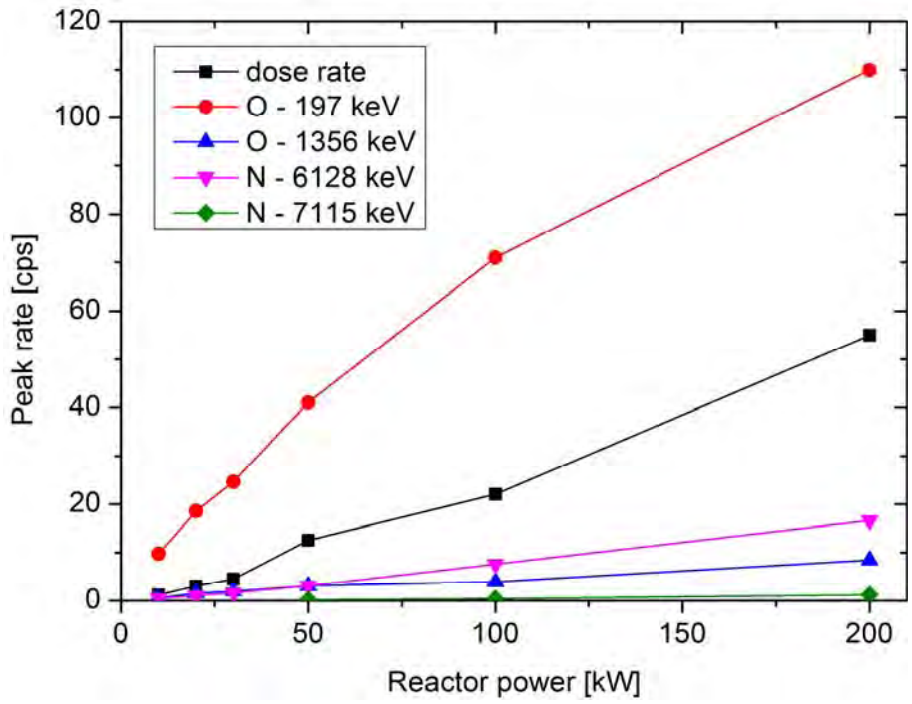


Figure 8: Relationship between line intensities (Peak rate) and reactor power for ^{19}O and ^{16}Ngamma lines measured with HPGe spectrometer and dose rate measured with portable GM tube.

Similar systems are used in nuclear power plants for detection of primary coolant leakage to secondary coolant loop. Hence such exercise is very useful for future power plant operators.

6. In core flux mapping

In core flux mapping at the nuclear power plant is performed regularly in order to verify the power profile calculations. As the in-core flux mapping system at the NPP is usually not suitable for training, we developed an analogous practical exercise. The aim of the exercise was to get familiar with the in-core flux mapping system and to get familiar with the axial power profile in a nuclear reactor. A special experimental set-up was made, in order to measure the axial fission rate profile in the reactor.
A fission chamber (FC) containing approximately 10 µg of 98.49 % enriched ^{235}U was used to perform axial measurements of the fission rate along the complete core height at various radial measurement positions shown in Figure 9.
The FCs were deployed into the reactor core by using a specially designed FC positioning system, composed of Al guide tubes, drive mechanism and data acquisition system. Figure 11 shows a schematic view of the system where FC integrated cable is also used for inserting and withdrawing the FCs into and out of the reactor core.
The FC position was regulated by a commercially available pneumatic drive consisting of a series of valves and pistons, all controlled by a microcontroller (Figure 10). The axial positioning was ensured by an incremental system which measures the FC position relative to the reference position at the end of the guide tube. The accuracy of the FC positioning system was ~ 0.1 mm and the repeatability of the FC position was within 0.3 mm.
Fission rate in the fission chamber was measured using Amptek PX5 MCA which was configured so that it generated 5 V TTL pulse for each detected fission. Response from fission chamber was measured by counting those digital pulses with NI-6356 DAQ and meantime accurate axial position was provided by incremental positioning encoder.

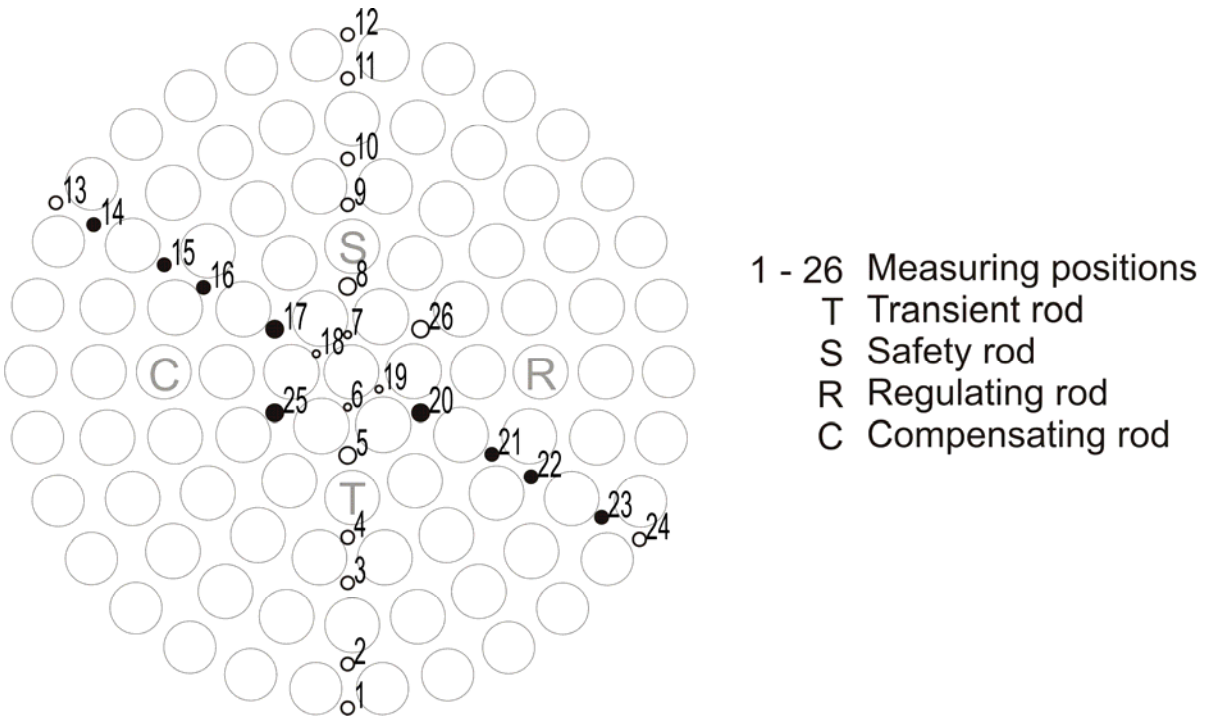


Figure 9: Measuring positions in upper supporting grid.

Dedicated software was developed in LabVIEW environment in order to control movement of fission chamber, adjust counting time and acquire data. Actual measurement of axial fission rate distribution is done by moving fission chamber in steps from the lower end stop, which is slightly below the core, to few centimetres above the core. On each step response from fission chamber and current position is recorded. Measurement of power profile can be done manually or automatically with adjustable axial resolution and speed.



Figure 10: Pneumatic system with fixed and moving jaw, which can move fission chamber in both directions. System is mounted above reactor pool. On the right we can see incremental positioning encoder which provides accurate axial position. System was developed and manufactured at the JSI.

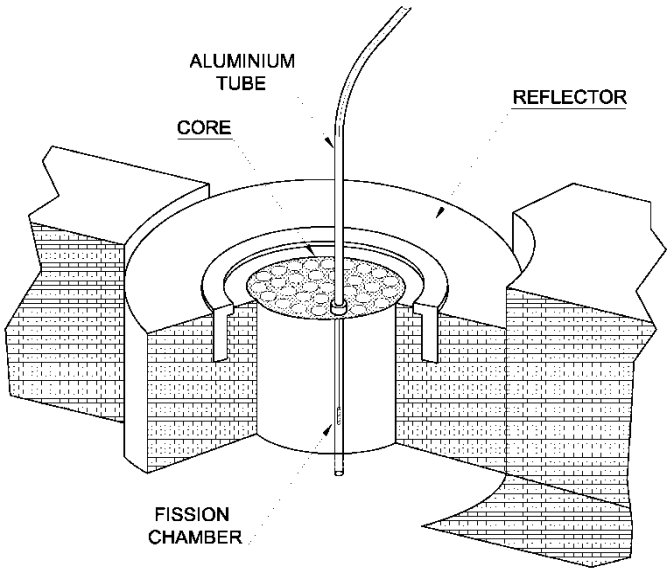


Figure 11: Schematic figure of the FC positioning system.

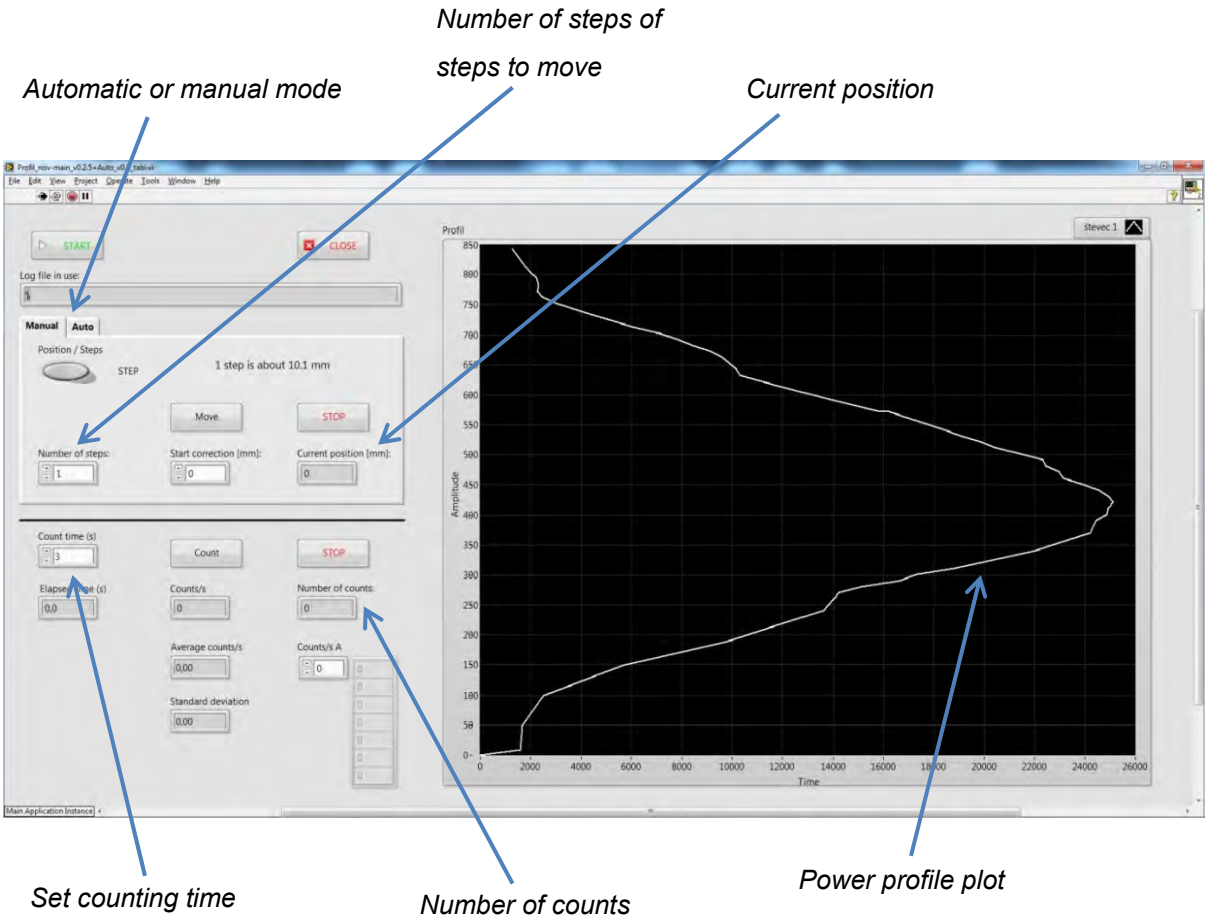


Figure 12: GUI of LabVIEW program developed to control movement of fission chamber, adjust counting time and acquire data. Profile on the right is actual axial power profile of our TRIGA Mark II reactor.

7. Conclusio ns

In the paper we presented some practical exercises that can be developed, manufactured and performed by a relatively small (4) team of reactor operators at a small research reactor like TRIGA with a reasonable budget. The development and improvement of all systems is still on going and is primarily based on the requirements of the users and trainees. The new and upgraded exercises were very well accepted among the trainees.

In the near future we will further improve the exercises in terms of simplifying the setup procedure and reducing the number of required components. Neutron count rate in critical experiment will be acquired by using Amptek PX5 MCA, similarly as in In core flux mapping exercise. Further we will develop LabVIEW acquisition software with which we will read measurement data from Amptek PX5 over the Ethernet. This will localize measurement equipment to one spot, reactor platform, and will allow students and trainees to perform exercises from the comfort of control room / classroom. Moreover this will allow performing exercises remotely from anywhere in the world.

Our new exercises are now updated to current technologies in terms of detection as well as in terms of data acquisition. Each exercise is relatively easy to setup and with further improvements will require minimum equipment. Hence any exercise could easily be implemented at any other similar reactor in the world.

With modern, educational and yet interesting exercises in the field of reactor physics and together with Nuclear Training Centre at the JSI we plan to become important regional centre for nuclear training and education.

8. References

[1] L. Snoj, B. Smodiš, “45 Years of TRIGA Mark II in Slovenia”, NENE 2011, Bovec, Slovenia, September 12-15, 2011, Nuclear Society of Slovenia

[2] L. Snoj, Ž. Štancar, V. Radulovič, M. Podvratnik, G. Žerovnik, A. Trkov, L. Barbot, C. Domergue, C. Destouches, "Experimental power density distribution benchmark in the TRIGA Mark II reactor", *PHYSOR 2012 – Advances in Reactor Physics – Linking Research, I ndustry, an d Educatio n*, Knoxville, Tennessee, USA, April 15-20, 2012, American Nuclear Society, on CD-ROM

[3] L. Snoj, L. Sklenka, J. Rataj, H. Boeck, Eastern Europe research reactor initiative nuclear education and training courses - current activities and future challenges. *PHYSOR 2012 – Advances in Reactor Physics – Linking Research, Industry, and Education*, Knoxville, Tennessee, USA, April 15-20, 2012, American Nuclear Society, on CD-ROM

[4] http://www.icjt.org/en/

[5] http://www.rcp.ijs.si/ric/pulse_operation.html

[6] http://www.rcp.ijs.si/ric/pulse-s.html

[7] A. Jazbec, D. Kavšek, L. Snoj, Analysis of a Void Reactivity Coefficient of the JSI TRIGA Mark II Reactor, Nuclear energy for new Europe 2013, Bled, Slovenija, September 9-12, 2013, Nuclear Society of Slovenia

MEASUREMENTS OF NEUTRON FLUX DISTRIBUTION AND ENERGY SPECTRUM IN THE HORIZONTAL BEAM TUBE AT THE TRIGA MARK II REACTOR VIENNA

M.CAGNAZZO, C.RAITH, T.STUMMER, M.VILLA, H.BÖCK
Atominstitut, Vienna University of Technology
Stadionallee 2, 1020 Wien, Austria

ABSTRACT

The core of the TRIGA Mark II research reactor at the Vienna University of Technology/Atominstitut has been recently fully refurbished with new fuel, slightly irradiated. Given this new core configuration, irradiation facilities need to be properly characterized in order to support future research activities. Aims of this work is to present the result of the measurements of neutron flux distribution and energy spectrum performed in one of the reactor horizontal tubes, applying a method based on a de-convolution technique of activated foils coupled with Monte Carlo code simulations (MCNP6). This method is very flexible and can be applied to characterize nuclear reactors that present a wide variability of core geometries, structural materials' compositions, fuel composition and neutron energy spectra. The method allows measuring both slow and fast neutron components proving as result a neutron spectrum in 620 energy groups. In the case of the measurements presented in this work, the absolute neutron flux was evaluated within accuracy within ±10%.

1. Introduction

The core of the TRIGA Mark II research reactor at the Atominstitut (ATI) of the Vienna University of Technology has been recently fully refurbished with new fuel elements, slightly irradiated. In this new core configuration, irradiation facilities need to be properly characterized in to order to support future research activities.
The characterization of the reactor is part of a PhD research project that will focus on the determination of both neutron fluxes distribution and energy spectrum by means of Monte Carlo calculations and direct measurements.
Aims of this work is to present the measurement of the neutron flux distribution and its energy spectrum performed in one horizontal beam tube (Beam Tube B) applying a method based on a de-convolution technique of activated foils coupled with Monte Carlo code simulation (MCNP6).

2. The TRIGA Mark II reactor

The TRIGA (Training Research and Isotope production General Atomics) MARK II reactor [2] is a pool-type research reactor moderated and cooled by light water.
The TRIGA Mark II at the Atominstitut is licensed for 250 kW steady state and up to 250 MW pulse operation. Recently the reactor was converted from a highly heterogeneous core which included HEU fuel elements to a full LEU core. As a result, the current core load consists out of 76 stainless steel clad zirconium-hydride fuel elements (8.5%-wt enriched 19.95%-wt in 235U), in a cylindrical geometry.
The TRIGA Mark II of ATI is equipped with various irradiation facilities inside and outside the reactor core. It incorporates facilities for neutron and gamma irradiation studies as well as for isotopes production, samples activation and students training.
The horizontal section of the reactor is shown in Figure 1[3] where the reactor core, the graphite reflector, the four horizontal beam tubes, the thermal column, the thermalizing column (that incorporate the neutron collimator), the reactor tank and the biological shield in concrete are displayed.
The four beam tubes (i.e. A, B, C and D) penetrate the biological shield and the aluminium tank reaching reactor reflector. These tubes provide both irradiation facilities for large specimen (up to 15 cm) in a region close to the core; and neutron beams and gamma radiation for experiments installed externally to the biological shielding.

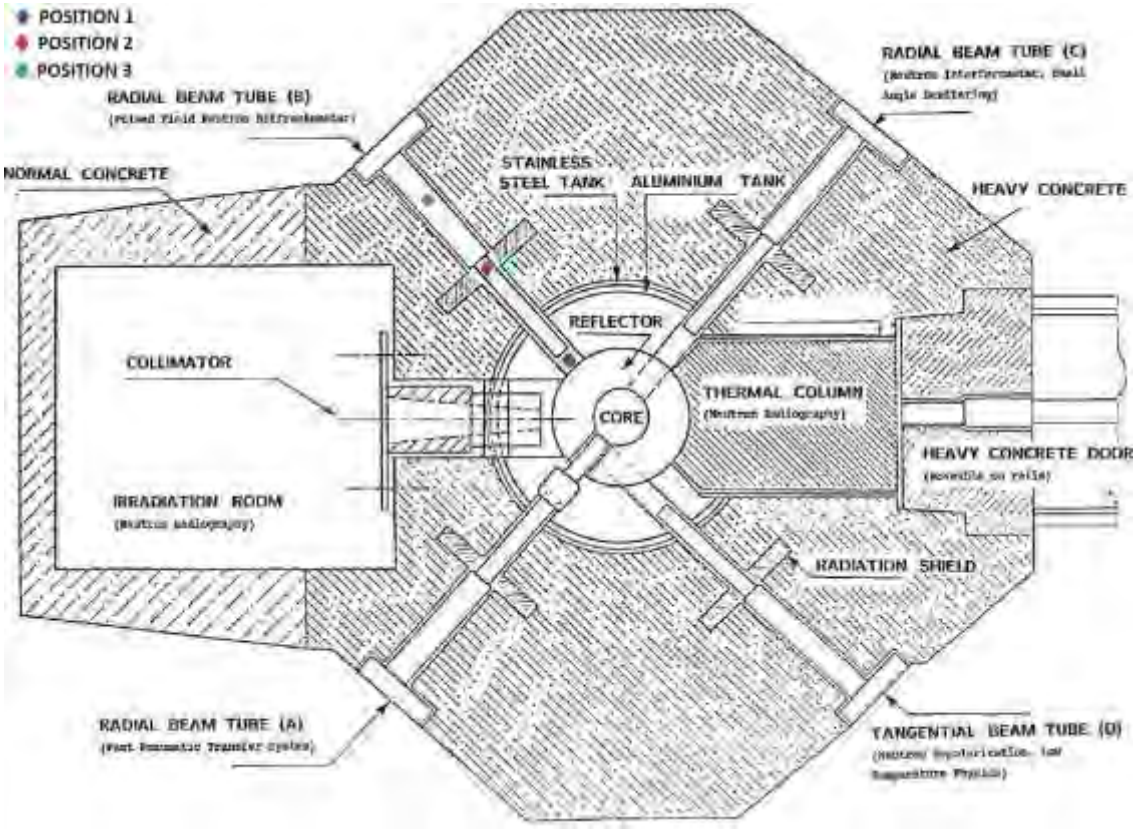


Figure 1: Horizontal section of TRIGA reactor at ATI

3. Experiment setting

At the TRIGA reactor at Atominstitut the horizontal beam tubes are all utilized for ongoing experiments. For this reason, the decision to start the reactor characterization from the Beam Tube B was due to the opportunity to perform foils irradiations during a special inspection of the beam tube. In this occasion, the Beam Tube B was opened and the collimator that normally lies inside, was extracted for inspection and verification.

It has to be pointed out that the setting of this experiment was strongly influenced by the limited time available for the irradiation of the foils and radiation protection constraints; i.e. few days of reactor availability in the described conditions and limitation of reactor power level. Due to these constrains it became necessary to schedule irradiations in only 3 positions along the beam tube and, for each position, all target foils had to be irradiated at the same time.

Accordingly, the irradiations time and the reactor power were set in order to optimize the measurement of the irradiated foils (activity, cooling-down time, counting time).

The irradiation positions were defined as in Table 1; the distances are taken from the graphite reflector and the location of the irradiation positions is shown by the markers in Figure 1.

The Figure 2 shows the irradiation device and its positioning inside the beam tube.

Irradiation position	Distance from reflector (cm)
Position 1	5
Position 2	125
Position 3	185

Table 1: irradiation positions for flux determination in Beam Tube B

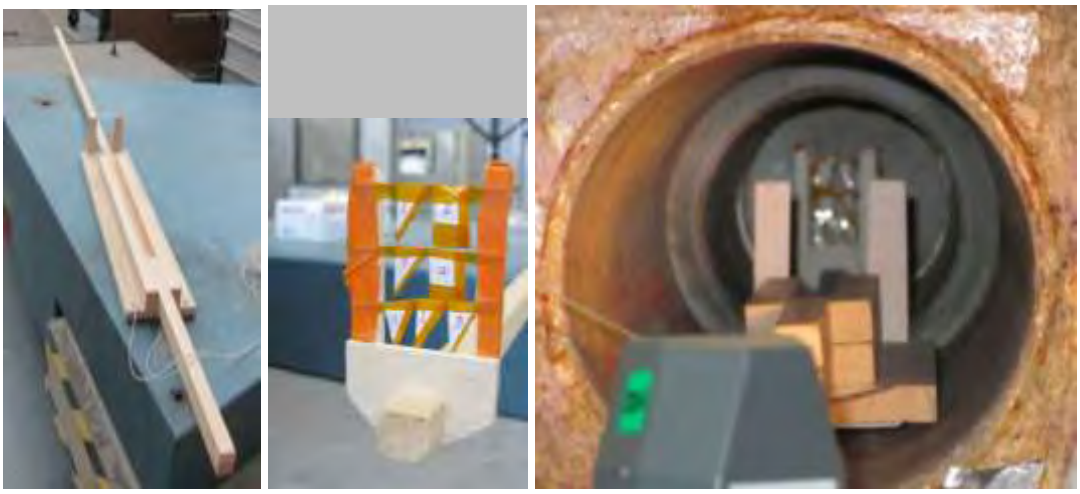


Figure 2: irradiation device used for foils irradiation in Beam Tube B and the positioning of the device inside the beam tube

3. Material Foils Selection and Irradiation

3.1 The SAND II code

The code SAND II [4] (Spectrum Analysis by Neutrons Detectors II) determines, applying a de-convolution method, the energy spectrum distribution and the absolute intensity of a neutron flux using as inputs the measured activities of infinitely diluted irradiated foils.
The calculation algorithm identifies a solution that meets some predefined criteria (e.g. maximum error or maximum number of iterations) through successive iterations starting from a *guess flux distribution* provided as "first approximation" input.
After a certain number of iterations, the solution is provided either in the form of differential flux, and in that of integral flux. As results are given in tabular form at 620 discrete energy intervals in the range between 10^{-10} and 18 MeV, the problem is essentially to solve for 621 unknowns in a system of *n* linear activity equations, where *n* is the number of foils used.
Since SAND II best approximated solution depends on the choice of the first approximation spectral form (guess flux), in this experiment the input guess flux utilized was calculated by means of a simulation of the TRIGA reactor performed using the Monte Carlo code MCNP6[1]. It is worthy to notice that SAND II best approximated solution is significantly dependent from the guess flux form (i.e. energy distribution) but almost independent from its absolute value.

3.2 Material Foils selection

In this work, to detect the thermal, epithermal and fast neutron spectrum components, a proper set of (n,γ), (n,α), (n, p) and (n, n^{l}) reactions with different activation thresholds have been selected for irradiations in the Beam Tube B, as shown in Table 2.
It should be pointed out that the selection of reaction presenting different thresholds values is also of primary importance in order to allow the SAND II code to reach a more reliable solution of the 621 equation system. This is because very different cross-sections contribute to reduce the indeterminacy of the system.

Element	(T-I)	θ% T-I	Reaction	E^{act}_{eff} (MeV)	σ_0 (barn)	$T_{1/2}$	Λ (sec^{-1})
Au	^{197}Au	100	$^{197}Au\ (n,\gamma)\ ^{198}Au$	--	98.8	2.7 d	$2.97 \cdot 10^{-6}$
Cu	^{63}Cu	69.1	$^{63}Cu\ (n,\gamma)\ ^{64}Cu$	--	4.5	12.7 h	$1.51 \cdot 10^{-5}$
Fe	^{54}Fe	5.84	$^{54}Fe\ (n,p)\ ^{54}Mn$	3.75	0.4	312.7 d	$2.56 \cdot 10^{-8}$
Ni	^{58}Ni	68.08	$^{58}Ni\ (n,p)\ ^{58}Co$	2.5	0.6	70.78 d	$1.13 \cdot 10^{-7}$
In	^{115}In	95.71	$^{115}In\ (n,n')\ ^{115}In^*$	1.65	0.35	4.36 h	$4.42 \cdot 10^{-5}$
Al	^{27}Al	100	$^{27}Al\ (n,p)\ ^{27}Mg$	5.30	$8 \cdot 10^{-2}$	9.46 min	$1.22 \cdot 10^{-3}$

Table 2: set of elements, isotopes and reactions used to perform the measurements in Beam Tube B.

4. Results

4.1 Activation results

Following the irradiations, for each foil the activity was measured by means of a coaxial closed-ended HPGe n-type (series C5020, CANBERRA) with 52.8% relative efficiency, 1.81 keV energy resolution at 1.33 MeV and Peak/Compton edge ratio equal to 73.6. The efficiency calibration of the detector was performed by means of a certified solid multi gamma calibration source (Type QCRB1186, Eckert&Ziegler) with dimension and geometry similar to the activated foils.
The values of measured specific activities per atom at the end of irradiation and extrapolated to saturation are listed in Table 3 for each material foil in the three irradiation positions.

Position 1		Position 2		Position 3	
Foil	**Activities (Bq/atom)**	**Foil**	**Activities (Bq/atom)**	**Foil**	**Activities (Bq/atom)**
AU	$(6.14\pm0.30)\cdot10^{-11}$	AU	$(2.70\pm0.13)\cdot10^{-13}$	AU	$(8.43\pm0.42)\cdot10^{-14}$
AU +CADMIUM	$(4.52\pm0.23)\cdot10^{-11}$	AU +CADMIUM	$(1.68\pm0.08)\cdot10^{-13}$	AU +CADMIUM	$(5.78\pm0.29)\cdot10^{-14}$
CU	$(1.22\pm0.06)\cdot10^{-12}$	CU	$(5.04\pm0.25)\cdot10^{-15}$	CU	$(1.18\pm0.06)\cdot10^{-15}$
AL	$(2.06\pm0.10)\cdot10^{-16}$	AL	$(6.11\pm0.30)\cdot10^{-18}$		
NI	$(6.20\pm0.31)\cdot10^{-15}$	NI	$(1.67\pm0.08)\cdot10^{-16}$		
FE	$(3.34\pm0.17)\cdot10^{-15}$	IN +CADMIUM	$(1.98\pm0.10)\cdot10^{-16}$		
IN +CADMIUM	$(8.09\pm0.40)\cdot10^{-15}$				

Table 3: measured specific activities per atom extrapolated to saturation for foils irradiated in Beam Tube B (Position 1, Position 2 and Position 3)

As SAND II code requires activities adjusted to infinite dilution of target nuclide, all input activities should be corrected for self-shielding effect. In this case, considering the specific reactions cross sections and the characteristic of the target foils, the only measurements that needed to be corrected for self-shielding were those related to Au foils activation and the correction was done according to the Westcott [5][6] theory.
Considering the optimization of cooling-down and counting time of the foils, statistical uncertainties of the measurements were evaluated for less than 3%. To investigate the systematic error several repeated measurements of an irradiated foil of gold were performed, every time repositioning the foil on the detector. The error was evaluated to less than 2% giving a total uncertainty of the gamma spectrometry measurements of about ± 5%.

4.2 Neutron energy spectrum results

The measured specific activities extrapolated to saturation have been used as input for the SAND II code in order to evaluate the neutron energy spectrum.
As from original data and drawings of the reactor was not clear if the Beam Tube B faces the graphite or a void in correspondence of the reflector, one of the purposes of this work was also to clarify this issue. For this reason, the SAND II code was run alternatively using two different input guess fluxes both generated by MCNP calculation: one guess flux was calculated considering the configuration facing graphite inside the reflector, the other facing a void volume inside the reflector. The considerable difference in the two Guess fluxes obtained by MCNP, did not affect the final results obtained by SAND II calculation; this result is considered a confirmation of the capability of SAND II code to build up the measured energy spectrum regardless of the absolute value and, partially, of the energy distribution of guess flux.

As results, the SAND II code provided the differential fluxes distributed over 621 energy values in the range between 10^{-10} and 18 MeV: Figure 3 and Figure 4 show respectively the Differential and Integral Flux in each of the 3 irradiation positions as provided by SAND II code.

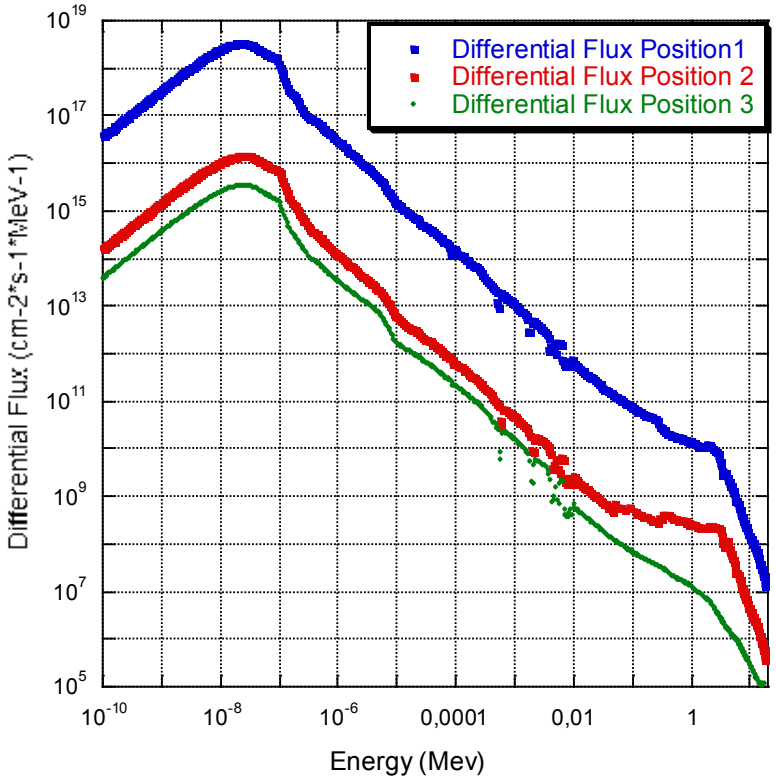


Figure 3: Measured Differential Flux in Beam Tube B (Position 1,2,3)

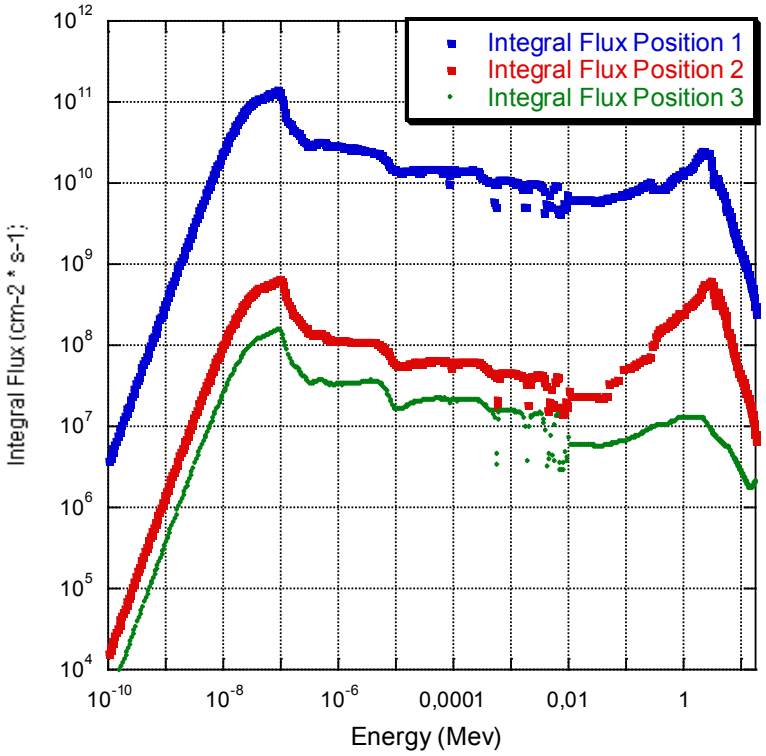


Figure 4: Measured Integral Flux in Beam Tube B (Position 1,2,3)

As the results are given by SAND in the form of very detailed differential energy spectrum, it is simple to calculate integral flux values over desired energy intervals. Thus, the Thermal (E<0.55 eV), Epithermal (0.55 eV < E < 100 keV) and Fast (E>100 keV) neutron flux is reported in Table 4.

	Total Flux (cm-2 *s-1)	**Thermal flux (<0.55eV)** (cm-2 *s-1)	**Epithermal Flux (0.55eV-100keV)** (cm-2 *s-1)	**Fast Flux (100KeV-18MeV)** (cm-2 *s-1)
Position 1	$(5.73\pm0.50)\cdot10^{11}$	$(3.28\pm0.30)\cdot10^{11}$	$(1.73\pm0.15)\cdot10^{11}$	$(7.28\pm0.70)\cdot10^{10}$
Position 2	$(3.13\pm0.30)\cdot10^{9}$	$(1.40\pm0.10)\cdot10^{9}$	$(7.11\pm0.70)\cdot10^{8}$	$(1.02\pm0.10)\cdot10^{9}$
Position 3	$(6.04\pm0.60)\cdot10^{8}$	$(3.39\pm0.30)\cdot10^{8}$	$(2.22\pm0.20)\cdot10^{8}$	$(4.43\pm0.40)\cdot10^{7}$

Table 4: Thermal (E<0.55 eV), Epithermal (0.55 eV < E < 100 keV) and Fast (E>100 keV) neutron flux in Beam Tube B

Considering the values obtained for the total Integral Flux in the 3 position, it was possible to build the best fit for the integral flux values along the Beam Tube B (Figure 5) and accordingly evaluate the integral flux in correspondence of various distances, such as (by extrapolation) at the beam port.
The estimated value of the total integral flux in correspondence of the beam port of Beam Tube B was of 1.76 • 10^8 s-1 • cm-2: this result, compared with historical data from other similar TRIGA reactors, indicates that, most likely, the Beam Tube B at TRIGA Vienna reactor faces the graphite in the reflector.
The uncertainties of the differential and integral neutron fluxes were evaluated taking into account the propagation of the uncertainties of the foils measurements in the SAND II de-convolution process; the uncertainties related to the determination of the weight of the foils (less than 1%); the thermal power calibration of the reactor performed according to specific procedure using certified instrumentation (about ± 3%). The uncertainties of the flux values resulted to be within ± 10%.

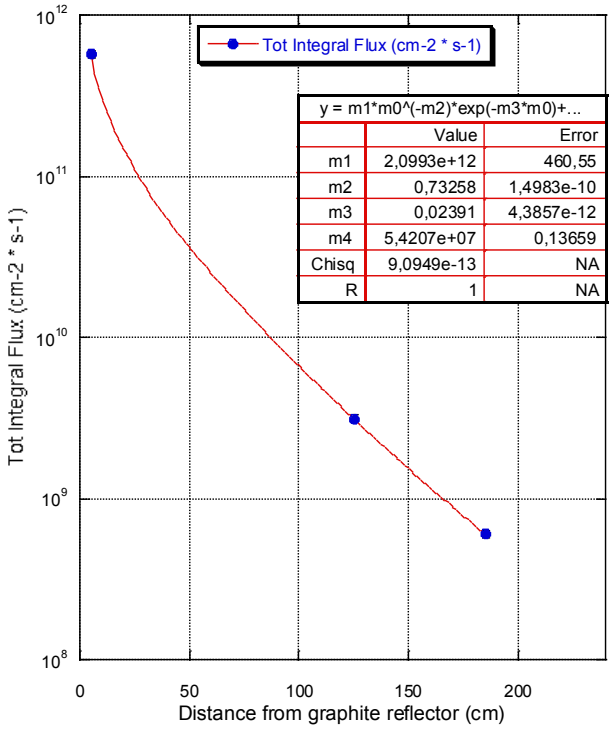


Figure 5: total integral flux behaviour along Beam Tube B

5. Conclusions

This work, through activity measurements of activated foils and consequent application of a de-convolution technique coupled with Monte Carlo calculations, allowed to determine the neutron flux distribution and the energy spectrum in one of the horizontal beam tubes (Beam Tube B) at the TRIGA reactor Vienna. The results are provided in the form of a very detailed energy spectrum (621 energetic intervals in the range between 10^{-10} and 18 MeV) and therefore it is possible to evaluate flux values for all desired energy intervals.
Moreover, the evaluation of flux distribution along the Beam Tube B, led to the indication that the Beam Tube B at TRIGA reactor Vienna presents the configuration design which faces the graphite in the reflector and not a void volume.
Finally, as this method is very flexible, in the near future it will be applied to characterize the reactor in different in-core and in tank irradiation position at the TRIGA reactor Vienna.

6. References

[1] MCNP6.1/MCNP5/MCNPX *Monte Carlo N–Particle Transport Code System Including MCNP6.1,MCNP5-1.60, MCNPX-2.7.0 and Data Libraries*, OAK RIDGE NATIONAL LABORATORY, August 2013;

[2] General Atomic (GA), March 1964, TRIGA Mark II Reactor General Specifications and Description. General Atomic Company, U.S.A.;

[3] R. Khan, June 2010, Neutronics Analysis of the TRIGA Mark II Research Reactor and its Experimental Facilities, PhD dissertation, Vienna University of Technology, Vienna, Austria;

[4] CCC-112 SAND II Neutron Flux Spectra Determination by Multiple Foil Activation - Iterative Method, Oak Ridge national Laboratory, 1994;

[5] Effective cross sections and cadmium ratios for the neutron spectra of thermal reactors, C.H. Westcott, A/C0NF.15/P/202 CANADA 26 May 1958;

[6] Messung von effektiven Neutronentemperaturen mit einem Neutronen-Kristallspektrometer am TRIGA Mark II-Reaktor, H. Rauch, Atomkernenergie, ATKE 10-22 (145-149), 1965;

CAPABILITIES AND CAPACITIES OF RESEARCH REACTORS FOR DEVELOPMENT OF MATERIALS AND FUELS FOR INNOVATIVE NUCLEAR ENERGY SYSTEMS. IAEA CATALOGUE UNDER DEVELOPMENT

M. KHOROSHEV*
A. BORIO, E. BRADLEY

Research Reactor Section, NEFW / NE
International Atomic Energy Agency
PO Box 100, Vienna, AUSTRIA

*Corresponding author: M.Khoroshev@iaea.org

ABSTRACT

For the development of new generation nuclear power reactors, such as those being developed within the framework of the Generation IV (GenIV) project and/or being considered in the International Atomic Energy Agency's (IAEA) International Project on Innovative Nuclear Reactors and Fuel Cycles (INPRO) or in national programmes of the IAEA Member States, maintaining and development of a sophisticated up-to-date experimental base is crucial. Research reactors represent one of the major parts of this experimental base. The special attention paid by the IAEA and the general public to research reactors is due to the fact that these facilities are quite expensive, and they are sensitive to non-proliferation and safety issues.

In support of the above-mentioned international and national efforts the IAEA is developing a comprehensive Catalogue on existing and future services that can be provided by existing and planned research reactors for innovative nuclear energy system and technology R&D. A broad range of research reactor applications will be covered in the Catalogue. Potential opportunities for research reactors and associated facilities to cover major areas of research reactor applications, focusing on the support that such reactors can provide for advanced materials and fuel development, is presented.

The users of the Catalogue will be governmental and private sector organizations responsible for the development and/or deployment of innovative nuclear energy systems, including designers, manufacturers, vendors, research institutions, academia and other organizations directly involved in the development of materials and fuels for nuclear energy industry.
Current status of the IAEA Catalogue (currently under development) on worldwide capabilities and capacities of research reactors for development of materials and fuels for innovative nuclear energy systems is presented in the paper.

1. Introduction

Despite having numerous uses, an important role of many research reactors remains focused on research and development of nuclear energy systems, i.e. nuclear reactors and their fuel cycles. Much of this R&D is generally viewed to be focused on advanced materials research and testing of advanced fuel and structural materials, studying actinides utilization and burn-out of long-lived fission products, and extension of fuel resources using thorium fuel options or fusion neutron sources, for example. Existing and planned research reactors have or will have capacities to perform a broad spectrum of R&D aimed at developing innovative power reactors like those being developed through the Generation IV International

Forum (GIF), in national programmes of the IAEA Member States and/or in the concepts of future nuclear energy system considered in the IAEA's INPRO project (International Project on Innovative Nuclear Reactors and Fuel Cycles). Looking beyond 2050, new high-performance research reactors might be used for the justification of an optimal option for fusion reactor arrangement, exploring options for combined systems with nuclear power plants (NPPs) and plants for hydrogen production and other technological processes.

2. Future research reactors versus R&D needs for innovative material testing

Many existing RRs have been in operation for 30 years or more – having supported the development of the first three generations of nuclear power plant technology. Such experimental capabilities must remain available to provide ongoing support and services until at least the middle of the current century and probably beyond.
In addition, to support innovative nuclear technologies, including fusion and advanced fuel cycles; high performance, highly reliable facilities with improved instrumentation capabilities are necessary to provide the required research and testing capabilities, and in particular, support advanced materials and fuel development.

At a technical meeting held in 2007 the following provisions regarding the R&D needs, which will have to be addressed by a new generation of research reactors were summarized:

- Flexibility (reactor core, test facilities and related ancillary facilities) is as important as continuously higher fluxes (water based RRs can provide this flexibility for Gen IV, fusion technologies and beyond),
- Provision for in-pile test loops and associated out of pile equipment in which test environments, relevant to various reactor coolants, pressure and temperatures can be maintained,
- Provision to manage safety related testing for existing and subsequent generation reactors can be performed,
- Provide for the development of resources (staff and technical capability) relevant to the next generation of reactor technology,
- Improved in-pile instrumentation,
- Capability to build and maintain basic nuclear knowledge and culture, including relationships with regulatory bodies and the general public, to establish confidence in advanced nuclear technologies,
- Fast flux facilities with at least 10 dpa/yr or 15dpa/yr for advanced materials research (fission and fusion),
- Ratio He/dpa (10 appm/dpa) to support some fusion materials research,
- Development of skills required to transform full scale component designs into experiments, conforming to the constraints of a given research facility, to obtain meaningful data on the behaviour of the component,
- State of the art post irradiation inspection, examination and characterization facilities – easily accessible from the reactor,
- To overcome transportation challenges between irradiation and examination – specific example being the use of neutron beams, associated with a different reactor, to perform post irradiation analyses,

A nuclear conglomerate, (campus, complex, centre, etc.) composed of multiple irradiation facilities (for example a high flux fast reactor, water cooled instrumented reactor, and high temperature reactor) and post-irradiation examination facilities (fuels and materials examinations including MA fuel) at the same site encompassing effective interfaces between the relevant facilities and their stakeholders can be one incarnation of future International Centres based on Research Reactors (ICERRs) for research reactor based technology development in support of innovative nuclear systems and advanced fuel cycles.

3. Existing and planned research reactors

As of November 2013, there were 246 operating research reactor facilities in the world. In addition, there were 20 research reactors in temporary shutdown mode, and 141 in long term shut down. Of the operational reactors, **51 are high capacity, operating at high power levels and offering a higher neutron flux.**

In recent years, the interest of the IAEA Member States in developing research reactor programmes has been steadily growing. Currently a number of Member States are in different stages of new research reactor projects. The majority of these Member States are building their first research reactor as their country's introduction to nuclear science and technology infrastructure.

Construction of new research reactors is on-going in France (Jules Horowitz Reactor and the RES reactor), in Jordan (JRTR), and in the Russian Federation (PIK reactor). Several Member States have formally planned to build new research reactors for specific experimental and commercial purposes; in particular, Argentina (RA-10), Belgium (MYRRHA), Brazil (RMB), the Netherlands (PALLAS), the Russian Federation (MBIR), the Republic of Korea (KJRR), India (HFRR and THRR), Saudi Arabia (low power research reactor - LPRR), South Africa (SAFARI-2).

However, the capacities of existing research reactors in IAEA Member States are frequently not fully utilized for several reasons, including issues of lack of funding, accessibility, information exchange, and intellectual property rights to name a few.

4. IAEA activities to increase utilization of research reactors

To assist under-utilized research reactors, the IAEA already recommends and helps in preparation of strategic and business plans. One opportunity to extend utilisation of RRs by interested stakeholders lies in the possibility of enhancing and extending the Research Reactors Database (RRDB). The RRDB maintained by the IAEA is well structured, it contains data on Data on 735 reactors in 58 countries (operational, shut down, decommissioned, planned, cancelled). The RRDB has a searchable interface with information on RRs all over the world. Data can be searched by name, country, operational status, power, utilization profile, applications etc. Extending the RRDB by including into it newly catalogued information supported by additional navigation options would serve as a complementary tool for planning of R&D programmes and other activities at RRs in the IAEA Member States on regional and international basis.

Furthermore, there are options to establish more topical coalitions of research reactors (currently there are 7 coalitions based on geographical principle and 3 based on topical joint activities and a new concept (under consideration) to establish International CEntres based on Research Reactors (ICERR), aiming to provide nuclear education programmes that offer direct experience of working in nuclear facilities and provide training opportunities. A concept of ICERR is being developed in consultation with international experts. The latest meeting on ICERR criteria was held 4-7 September 2013 in the IAEA.

These steps would help to increase utilization of some reactors and may avoid the need to build new reactors in the future which may be under-utilized.

5. Development of a Catalogue

Additional support of these IAEA activities is provided through the development of a comprehensive Catalogue on existing and future services, which can be provided by existing and planned RRs for development of materials and fuels for innovative nuclear energy systems. This activity was supported by the IAEA Technical Working Group on Research Reactors (TWG-RR) in April 2013.

The users of the Catalogue will be governmental and private sector organizations responsible for the development and/or deployment of innovative nuclear energy systems including designers, manufacturers, vendors, research institutions, academia and other organizations directly involved in the development of materials and fuels for nuclear energy industry.

In response to the letters requesting inputs to the Catalogue, which sent were to selected research reactors in the IAEA Member States, 46 inputs from 27 countries listed below were delivered to the IAEA secretariat:

Argentina: RA-10 Australia: OPAL Belgium: BR-2, MYRRHA Brazil: RMB China: CEFR, CARR Czech Republic: LVR-15 REZ Egypt: ETRR-2 France: OSIRIS, ISIS, ILL (HFR), ORPHEE, JHR Germany: BER-II, FRM II Hungary: BUDAPEST RES. REACTOR India: DHRUVA, HFRR Indonesia: RSG-GAS Italy: TAPIRO*, TRIGA RC-1* Japan: JMTR, JOYO	Kazakhstan: WWR-K, IGR Republic of Korea: HANARO The Netherlands: HFR, PALLAS Norway: HBWR Pakistan: PARR-1 Peru: RP-10 Poland: MARIA Romania: TRIGA II PITESTI - SS CORE* Russian Federation: IR-8, WWR-M, IVV-2M, MIR.M1, RBT-6, SM-3, BOR-60, BIGR, PIK Slovenia: TRIGA* Ukraine: WWR-M KIEV United States of America: ATR, HFIR, NBSR, MITR Uzbekistan: WWR-SM

*) Low power reactors related to R&D programmes will be presented in additional section of the catalogue

Currently the IAEA secretariat completes consultations with international experts who reviewed the inputs to the catalogue. Then the final draft of the technical document will be compiled.

The Catalogue will be published as an IAEA Technical document, and an extended electronic version will be made available for distribution in the IAEA Member States.

The following information can be found in the catalogue

- General information and technical data of a Research Reactor (RR) with a link to the IAEA RRDB
- Existing and prospective experimental facilities at RR including instrumentation devices.
  - General description of experimental and testing facilities
  - Loops for testing components of reactor core (fuel, control rods, structural materials, coolant technologies: lead, lead-bismuth, sodium, light and/or heavy water, molten salt, gas).
    - At steady state conditions
    - At transient conditions
    - At accident conditions
  - Experimental facilities for investigation of accidental conditions LOCA, LOFT, RIA, etc.
  - Facilities for investigation of corrosion of reactor materials.
  - Devices for capsule/ampule tests of materials in different environment, at wide range temperature and dose rates etc.
  - Devices for investigation of fuel and structural materials behaviour and characteristics (swelling, gas release, creep, long-term strength, relaxation resistance, etc.).

- Other facilities *(this section will be added only in the electronic version and it might include zero or low power facilities supporting innovative nuclear energy projects).*

- Related engineering and research infrastructure
  - Fresh and irradiated experimental material logistic
  - Hot cells, PIE facilities (radiochemistry facilities, SEM, TEM, X-Ray installations, gamma scanning, neutron beams facilities, etc.)
  - Capabilities to design and manufacture experimental devices and measurement systems including human resources development
- Recent achievements, some examples of R&D studies performed during the last 10 years (link to the list of recent publication is recommended)

6. Conclusion

Existing research reactors and their related ancillary facilities are fundamental to supporting existing nuclear power reactors and technologies, the manufacture of radioisotopes, training and education, and basic scientific research.

Much of R&D towards innovations in nuclear technologies is now focused on advanced materials research, studying actinides utilization and burn-out of long-lived fission products.

Publication of the Catalogue and the related update in the RRDB will foster wider access to existing RRs and thus ensure their increased utilization. It is foreseen that the Catalogue will serve as a supporting tool for the establishment of regional and international networking through RR coalitions and International Centres based on Research Reactors (ICERRs, a concept under development).

The next generation of RRs may include several large, multi-purpose reactors that serve as regional or topical centres of excellence; existing facilities could also be transformed for multilateral use. Such cooperation would lead to a reduction in the number of under-utilized facilities, as some older reactors are shut down and other, capable reactors serve a larger base of stakeholders.

Thermohydraulic design of the LORELEI experimental setup in JHR

M. Katz
NRCN, P.O.Box 9001 Beer Sheva, 84190, Israel

D. Gitelman , H. Shenha, Y. Weiss, A. Sasson
Rotem Ind., Mishor Yamin, D.N Arava 86800, Israel

D. Tarabelli, L. Ferry, C. Gonnier
French Atomic Energy Commission (CEA) – Cadarache Centre, France

Abstract

The LORELEI experimental setup in the Jules Horowitz Reactor (JHR) is dedicated for the study of fuel during a Loss of Coolant Accident (LOCA). During the experimental sequence the fuel sample experiences a transient neutron flux field, which generates representative power and cladding temperature field, simulating the thermo-mechanical behavior of the fuel and the clad during a LOCA accident. The challenge in the thermal design of the LORELEI test section is in finding a one closed capsule design, which will fulfill all experimental requirements by a balance between heat generation, heat losses and thermal inertia behavior. The study presented in this paper describes the preliminary design of the LORELEI test device, the models in use and its compliance to the required experimental protocol. The feasibility study of the preliminary design presents that the LORELEI design is promising to perform the LOCA type experiment.

1. Introduction

The LORELEI experimental setup in the Jules Horowitz Reactor (JHR) is dedicated for the study of fuel during a Loss of Coolant Accident (LOCA). The main objective of the LORELEI (Light-Water One-Rod Equipment for LOCA Experimental Investigation) is to study the thermal-mechanical behavior of fuel during such an accident and the fission products source term. In order to study those phenomena, the fuel sample will experience a transient neutron flux field, so that the Linear Heat Generation Rate (LHGR) in the fuel and temperature on the cladding and in the fuel, simulate the behavior of the fuel and the clad during a LOCA accident. In order to perform this transient variation, the experimental test section will be located on a moving device.

The transient sequence has four major features: An adiabatic heating of the fuel up to ballooning and burst occurrence, high temperature plateau which will promote clad oxidation, passive precooling by thermal inertia and heat losses and water re-flooding. In addition, a re-irradiation phase should be designed in order to generate the desired fission product inventory in the fuel. After the experiment, the fuel sample will be cooled before dismounting.

The challenge in the thermal design of the LORELEI test section is in finding a one closed capsule design, which will fulfill all experimental requirements by a balance between heat generation, heat losses and thermal inertia behavior. This design should be validated and verified to fill all safety and regulation requirements.

The study presented in this paper describes the preliminary design of the LORELEI test device, the models in use and its compliance to generate the required experimental protocol.

2. General description of the in-pile device

The in-pile device is made of a varied diameter double flask, closed by a device head. The double flask is made of stainless steel and serves as a pressure flask. The fuel sample is hold at the centerline of the device by a sample holder. A partition is installed in the flask which separates the volume to hot and cold channels. The partition additional function is as an instrumentation holder, where a peripheral heater is part of it. A schematic description of the in-pile device is presented in figure 1. The lower part of the device is in the flux zone therefore power is generated in its elements. The upper part is above the flux zone and is functioning as a heat exchanger where the power generated in the lower part (flux zone) is transferred to the cooling water surrounding the outer flask. The varied diameter shape has low gamma power generation volume (smaller diameter of the influx part) and high heat transfer area (larger diameter of the heat exchanger part).

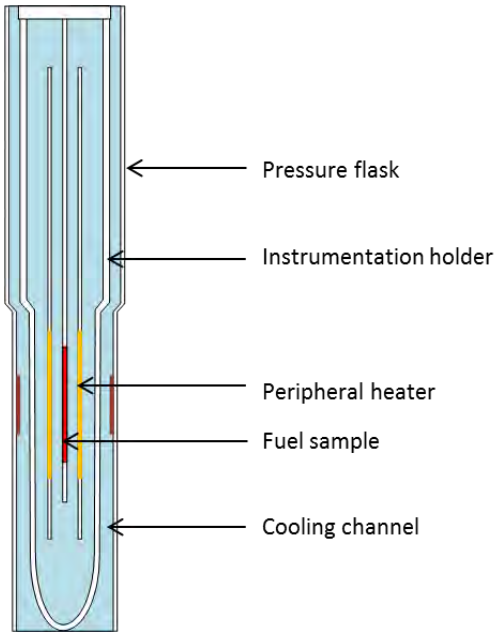


Fig 1. A schematic description of the LORELEI test device

3. Challenges in the thermal-hydraulic design

The LORELEI test device experiences non-uniform and intense neutron flux and gamma radiation due to its position in the reflector area. The gamma heating of the structure generates non-trivial thermal conditions, as can be seen in figure 2. The in-flux part of the device is heated where the heat generation at the hot spot on the side facing the core is about twice its value on the back side.

The non-uniform temperature field develops in the device is causing difficulties in the thermal-hydraulic design. Prior to the experiment, the fuel re-irradiates for several days in order to generate a representative fission products inventory. During re-irradiation, the fuel is cooled by thermosyphon flow. The heat generated in the fuel sample removed to the cooling water flowing in the cooling channel surrounding the outer flask. The gamma heat generation in the device structure is heating the cold channel water and the cold channel walls which induce opposed buoyancy forces. This phenomenon tends to generate instabilities and irregularities in the thermosyphon flow.

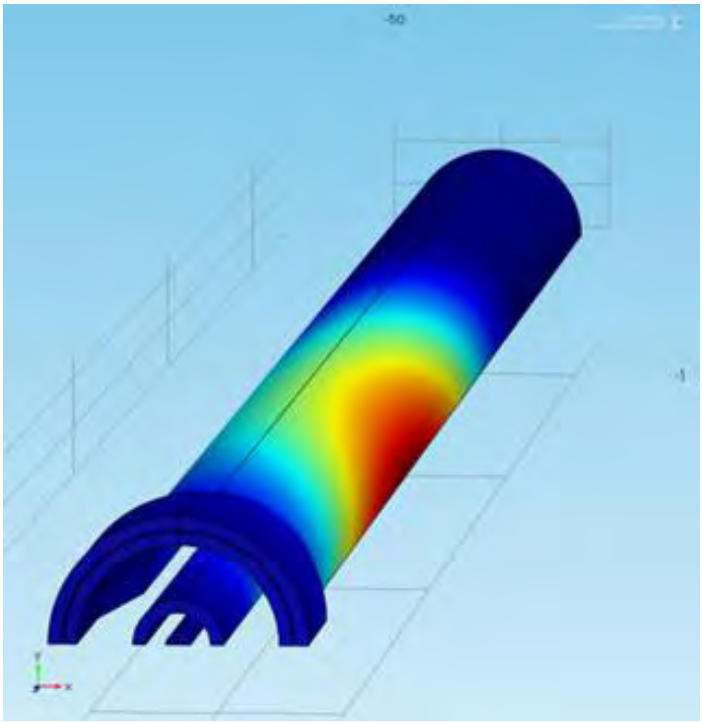


Fig 2. Non-uniform axial and azimuthal gamma heating distribution, in-flux zone

During the experimental sequence the device is empty from water and full with steam. The 3D gamma distribution which heats the structure non-uniformly, generate expansion forces which tend to bend the device. Such a bending can deform the channels and affect the heat transfer regime.
A second challenge in the design of the LORELEI test device is to prevent thermal escalation of the fuel cladding during the high temperature phases. The evolution of a thermal escalation is presented in figure 3. The clad is heated according to the device position. The Zirconium cladding is oxidized by the steam in an exothermal reaction. The reaction rate constants are strongly depends on the temperature. The power generated by the oxidation reaction tends to heat the cladding and increase the rate constant which in turn increases the reaction heat generation. The process can promote itself and lead to thermal escalation and fuel melting. The goal of the design is to present that the thermal escalation will not occur in any operational, incidental or accidental scenario.
The thermo-mechanical behavior is affected by different parameters such as the type of fuel and cladding, the fuel burn-up and the imposed thermal conditions. The thermo-mechanical process will be characterized experimentally by the ballooning strain level, fuel porosity and fuel relocation.

4. Models in use

The thermohydraulic design is based on CFD models and heat transfer models coupled to addition differential equation that represent different physics like the non-isothermal oxidation reaction. CFD calculations were performed by FLUENT and heat transfer calculations were performed by COMSOL Multyphysics. Because of the non-uniform axial and azimuthal power distribution of heat sources and in order to have complete picture of the flow and temperature fields, 3D geometry was used.
The system position was defined using a mathematical simulator (differential equation) of a PID controller that was implemented in the model. The PID controller calculates the position of the system (i.e. the power generated in the fuel sample and in the device components) that will generate the required clad temperature profile. Another simulator of a PID controller

was defined and implemented to operate a peripheral heater that generates adiabatic conditions for the fuel sample, during the adiabatic heating phase.

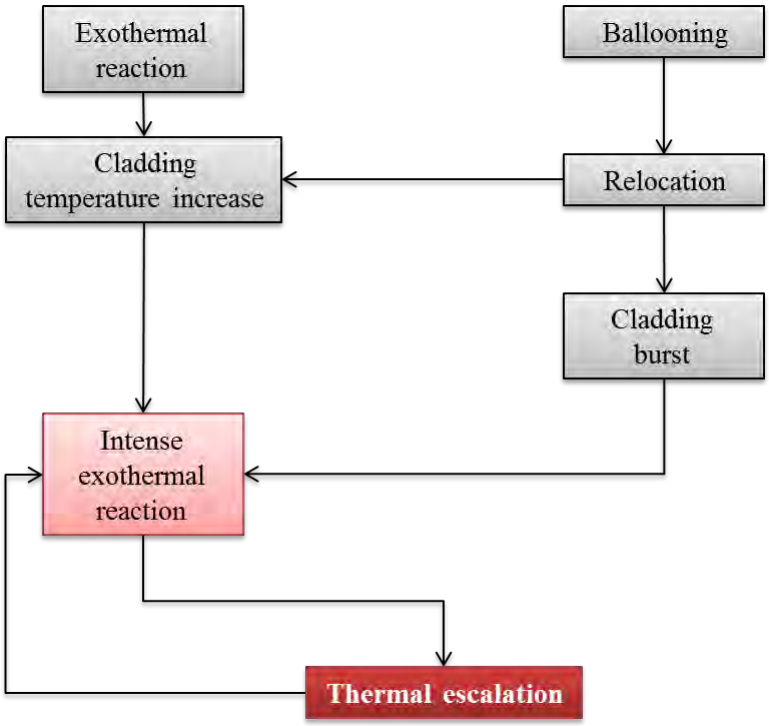


Fig 3. Thermal escalation evolution

5. Results

Figures 4 and 5 present the temperature and flow fields in the flask during re-irradiation. The high temperature of the device and the water in the side facing the core is clearly seen in figure 4. The hot water is flowing upward in the hot central channel, than it flows to the cold channel and transfer the heat to the outer cooling channel water in the pool. The water cools during its flow down but when it enters the flux zone they re-heat to its maximum temperature.

The streamlines formed due to the irregular temperature field can be seen in figure 5. The flow is in one direction in the hot channel but when it flows down in the cold channel, the stream coming up due to the outer wall buoyancy forces impinge with the stream coming down and most of the flow goes down at the back side of the device, where the temperatures are lower. The presented flow regime in complex and can't be predicted with 1D codes. Verification experiment will be needed in such a natural convective flow pattern.

Figure 6 present the feasibility to generate the desired temperature profile on the fuel sample cladding by the movement of the device. The red line represents position of the device along its channel in the reflector and the blue line represents and consequential cladding temperature. This calculation is based on the two mathematical PID controllers that were implemented in the COMSOL model and, was calibrated to generate the desirable cladding temperature.

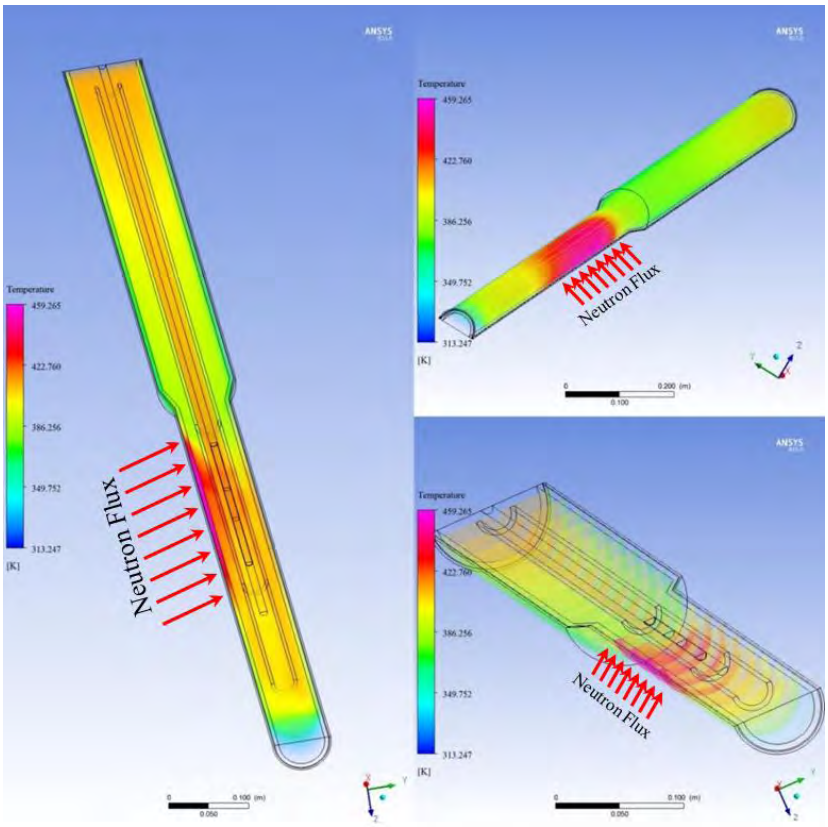


Fig 4. Temperature of the in-pile device during re-irradiation

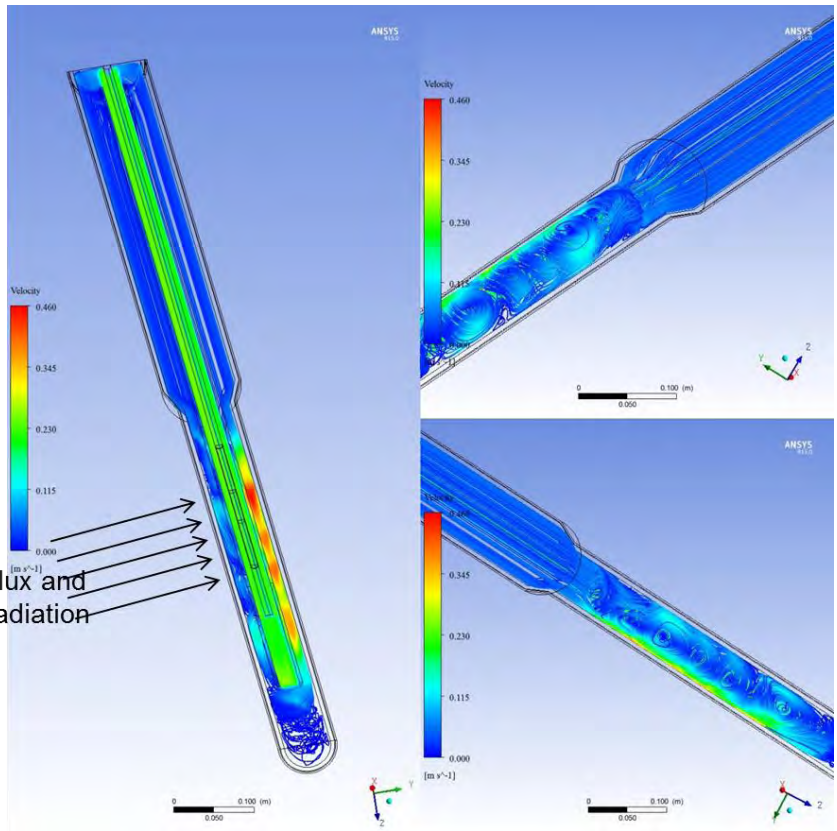


Fig 5. Stream lines in the in-pile device during re-irradiation

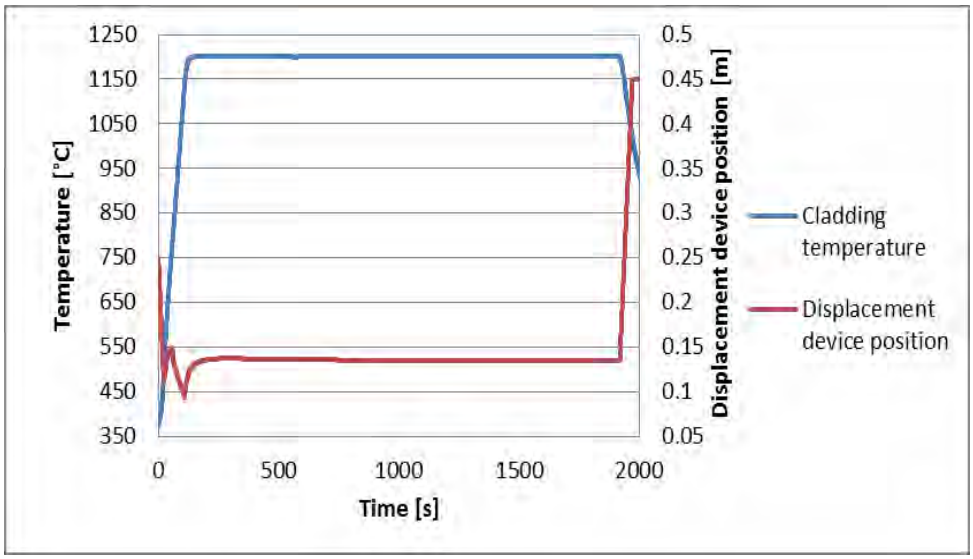


Fig 6. Displacement device position and cladding maximal temperature throughout the experimental sequence

Figure 7 presents a sensitivity study that calculates for a given displacement device location function (calculated for a most probable case), the deviation of the cladding hot spot from the required profile due to experimental uncertainties. It can be seen that the cladding temperature is far enough from the Zirconium melting temperature (safety limit).

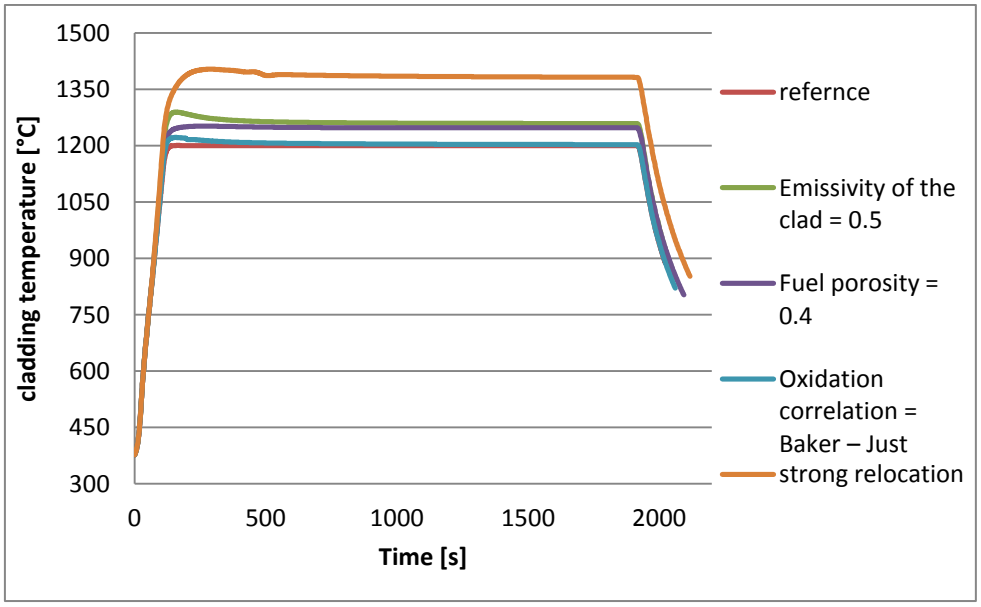


Fig 7. Cladding temperature profile due to various parameters

Figure 8 presents the post experiment cooling in which the ballooned fuel sample is cooled passively by thermosyphon flow. The low LHGR is enough to generate thermosyphon flow even with the higher hydraulic resistance that is an outcome of the balloon presence in the hot channel. The narrowing of the hot channel increases the water velocity and the heat transfer coefficients, which in turn improve the heat removal from the fuel and lower its temperature.

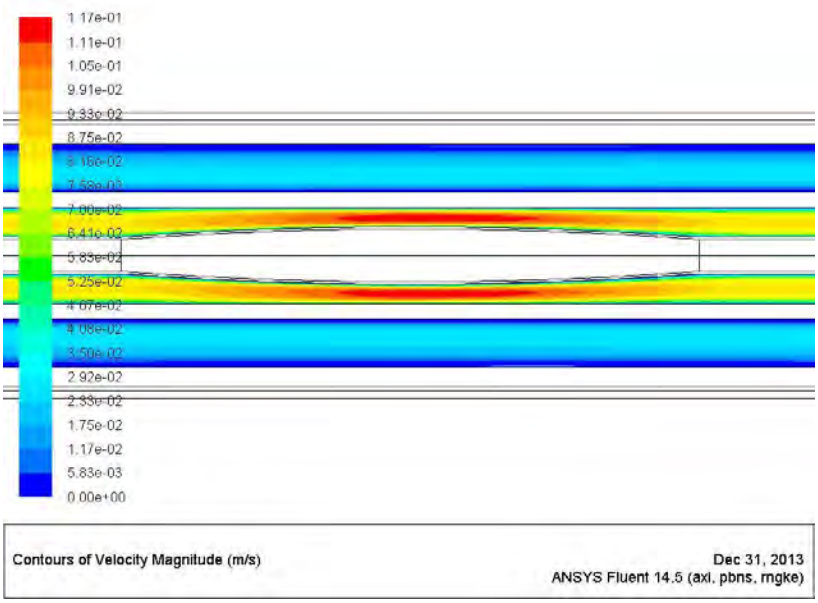


Fig 8. Velocity contours around ballooned fuel sample

6. Conclusions

This work presents numerical thermohydraulic study of the preliminary geometry of the LORELEI test device. The feasibility of the suggested geometry to generate the required conditions was presented. The difficulties in the design of the device as an outcome of the neutron and gamma radiation field were discussed. The flow regime in the re-irradiation phase will have to be studied deeply during the detailed design and the sensitivity of flow to geometrical, physical and operational parameters will be investigated. From the presented feasibility study of the preliminary design it seems that the LORELEI design is promising to perform the LOCA type experiment.

PRIMARILY POSITIVE PERCEPTIONS: A SURVEY OF RESEARCH REACTOR OPERATORS ON THE BENEFITS AND PITFALLS OF CONVERTING FROM HEU TO LEU

FERENC J.R. DALNOKI-VERESS
James Martin Center for Nonproliferation Studies (CNS)
Monterey Institute of International Studies (MIIS)
460 Pierce Street, Monterey, CA, 93940 - USA

ABSTRACT

This publication summarizes the results from a comprehensive survey of 33 operators whose research reactors have been converted from HEU fuel to LEU. The survey was conducted to determine the effect of conversion on fuel supply costs, security, understanding and utility of the reactor in order to provide other operators considering conversion with a better understanding of the conversion experience. It also sought to determine if the GTRI-Convert's (previously known as RERTR) principles of conversion (described in the report) had been adhered to in the process. Most of the questions in the survey had both a qualitative and a quantitative component. A key finding of the survey was that in many respects the perception of conversion by the operators appears to be overwhelmingly positive. Fewer than 8% of the reactor operators perceived that conversion led to even a "slight detriment" in the overall operation of their reactors. To be sure, some reactors did perceive some downsides to conversion. Yet operators overwhelmingly perceived any negative impacts to be outweighed by positive ones. Clearly, an important finding from this study is that the perception of an obligatory "flux penalty" often regarded as a serious obstacle to conversion is not determinative. The decision on conversion must be made by weighing multiple concerns such as the cost of fuel, fuel disposition, and effect on the uses of the reactor, training, education and outreach.

1. Motivation of the Study[1]

Over several decades, the United States has sought to minimize the use of weapons-usable highly enriched uranium (HEU) fuel in research reactors by converting such reactors to use non-weapons-usable low enriched uranium (LEU) fuel.[2] Over this period, under the Reduced Enrichment for Research and Test Reactor (GTRI-Convert) program coordinated through the National Nuclear Security Administration have converted (hereafter known as *conversion*) dozens of reactors to use less dangerous LEU fuel, but a number of reactor operators (hereafter *operators*) have resisted this change. Many in this group of hold-outs have raised concerns that switching to LEU fuels will reduce their reactors' capabilities, impeding research, the production of isotopes, and/or other significant activities. In order to better inform operators that are contemplating conversion, the aim of the present investigation is to determine what the experience of conversion has been for operators of research reactors of various types and fluxes and commercial ambitions. This paper presents the results of a survey of research reactor operators representing more than 30 research reactors that that have converted to LEU fuel in the past 40 years. This report is an

[1] A more detailed version of this publication is available at http://www.nonproliferation.org/
[2] The IAEA defines HEU as enriched uranium that contains equal to or greater than 20% U-235. The difference between the utilization of LEU (low enriched uranium is uranium that contains less that 20% U-235) and HEU is significant since highly enriched HEU can be directly used to produce a nuclear explosive device.

update of a similar study which focused on a small sample of recently converted reactors. [3] It was found in this study that the impact of conversion on the utility of the reactors was minimal. However, this was a small sample and was biased towards low neutron flux reactors. Therefore, it was determined that a more comprehensive study was required including a larger sample of reactors spanning low to high fluxes and a large range of reactor types.

1.1 GTRI-Convert Principles of Conversion

For conversion to be considered successful it must be done in a way that it does not "unduly burden the operators or negatively impact the facility." [4] For example, since lucrative applications such as isotope production and silicone neutron transmutation doping are done most efficiently at high flux research reactors, it is important that conversion be done in a way that maintains the necessary flux and does not impact commercial requirements.

The GTRI-Convert has outlined the following major requirements for successful conversion:

- Reactor with LEU core must have similar service lifetime as with HEU core
- Ensure ability of the reactor to perform its scientific mission is not significantly diminished
- Ensure conversion does not require major structural changes
- Ensure conversion can be done safely and that the LEU fuel meets all safety regulations
- Ensure the overall costs associated for conversion to LEU fuel does not increase the annual operating expenditure for the owner/operator.
- Coordinate with the fuel repatriation programs to establish the preferred time for conversion to LEU fuel. For more rapid or immediate conversions, the owner/operator may be compensated for the unused service lifetime of the repatriated HEU fuel.

To meet these goals the GTRI-Convert program has developed several different fuel types where the density of the uranium is increased to provide comparable neutron flux to that in the replaced HEU fuel. Most reactor fuels are composed of multiple chemical elements including uranium; the new LEU fuels compensate for their reduced level of enrichment by increasing the overall proportion of uranium in relation to other elements. That way, the total amount of uranium-235, is similar to the amount in the core before conversion. [5] Despite the progress made on conversions under the GTRI-Convert program, there are still operators, which currently use HEU fuels, *for which qualified LEU fuels are available* and have declined to change over. Among the arguments these operators have raised in opposing conversion is that switching to the alternative LEU fuels will reduce their reactors' capabilities, impeding research. This study has tested this argument by surveying reactor operators who represent research reactors that have converted in order to determine whether and in what ways utilization, fuel and security use and costs, and other activities have changed following their conversion. It is assumed that reactors that have not yet converted would have a similar experience to the converted reactors with comparable neutron fluxes and reactor types and these operators could use the results of this report as a guide to determine whether conversion is appropriate for their reactors.

2. Methodology

[3] F. Dalnoki-Veress, *Who Needs HEU Anyway? The Effect of Research Reactor Conversion on Reactor Usage*, GTRI-Convert Meeting, Lisbon, Portugal, Oct. 10-14, 2010.
[4] J. Roglans-Ribas, "Conversion of Research and Test Reactors to Low Enriched Uranium Fuel: Technical Overview and Program Status," www-pub.iaea.org/MTCD/publications/PDF/P1360_ICRR_2007_CD/Papers/J.%20Roglans-Ribas.pdf, accessed Aug 29 2010.
[5] In practice the total amount of U-235 is slightly higher in converted cores then the HEU cores they replaced.

Despite the concerns and difficulties associated with conversion, dozens of originally HEU-core research reactors have either been decommissioned or have successfully converted. The rate of reactor conversion has been steadily increasing since such programs began in the late 1970s, more recently averaging about two reactors per year. Of this set, the DOE identified a sample of 54 reactors from 30 different countries to be included in the present survey. [6] Thirty-three reactor operators responded to the survey–roughly a 60% acceptance ratio. [7]

2.1 Questionnaire Design

The questionnaire sent to all research reactor operators had 62 questions and was developed jointly between the DOE team responsible for reactor conversion and CNS. The purpose of the questionnaire was to determine if the principles of conversion have been adhered to and what the effect of conversion has been on fuel supply costs, security, understanding and utility of the reactor. Most of the questions in the survey have had both a qualitative and a quantitative component: the respondent was asked how a particular aspect of a reactor has been affected by conversion and then asked to rate the degree of impact of conversion on a 9-point Likert Scale, where the middle value of the scale represented 'no impact' on conversion and both extremes represent a very negative or a very positive experience. Note that in this report the term *positive* and *negative* will be used to indicate that conversion was beneficial or disadvantageous for a particular concern for research reactors. The value scale depends on the question asked. The ordinal, Likert scale is converted into a 9-point numerical scale which is used to do further quantitative analysis.

3. Survey Findings

3.1 Reactor Utilization

In this section operators were asked about their principal uses for their reactors. The reactor uses are similar to the ones discussed in IAEA-TECDOC-1234 which focused on applications of research reactors. [8] It was found that the majority of the reactors were primarily used for training and education (discussed in the next section), neutron activation analysis (NAA), followed by material research and isotope production. All of these uses may be affected by core conversion.

When operators were queried on how the top reactor use was affected by conversion, we found that about half of the reactors surveyed perceived little to no change due to reactor conversion. The other half of the reactors surveyed tended towards a positive perception of conversion for the top use chosen. Even medium (10^{13}-10^{14} neutron $cm^{-2}s^{-1}$) and high flux (>10^{14} neutron $cm^{-2}s^{-1}$) reactors, which included the greatest concentration of those who saw some negative effect, were about evenly split between those who saw a "very positive" impact from conversion on the reactors' top use and those who saw a "slightly negative" impact. See Figure 2 which is a scatter plot of reactor thermal neutron flux plotted against the perception of the reactor operators.

[6] The original list was comprised of 60 reactors, however, some of the reactors on this list had either not converted far enough in the past to make the analysis appropriate (no reactors after 2010 were used in the survey), or had planned to convert but was shut down before conversion or fuel was manufactured but the reactor was shut down before the fuel was loaded.

[7] Note that some of the data from the previous survey conducted in 2010 was also used in this survey since it overlapped with the reactors in the provided list.

[8] INTERNATIONAL ATOMIC ENERGY AGENCY, *The applications of research reactors*, IAEA-TECDOC-1234, Vienna (1999). http://www-pub.iaea.org/MTCD/publications/PDF/te_1234_prn.pdf

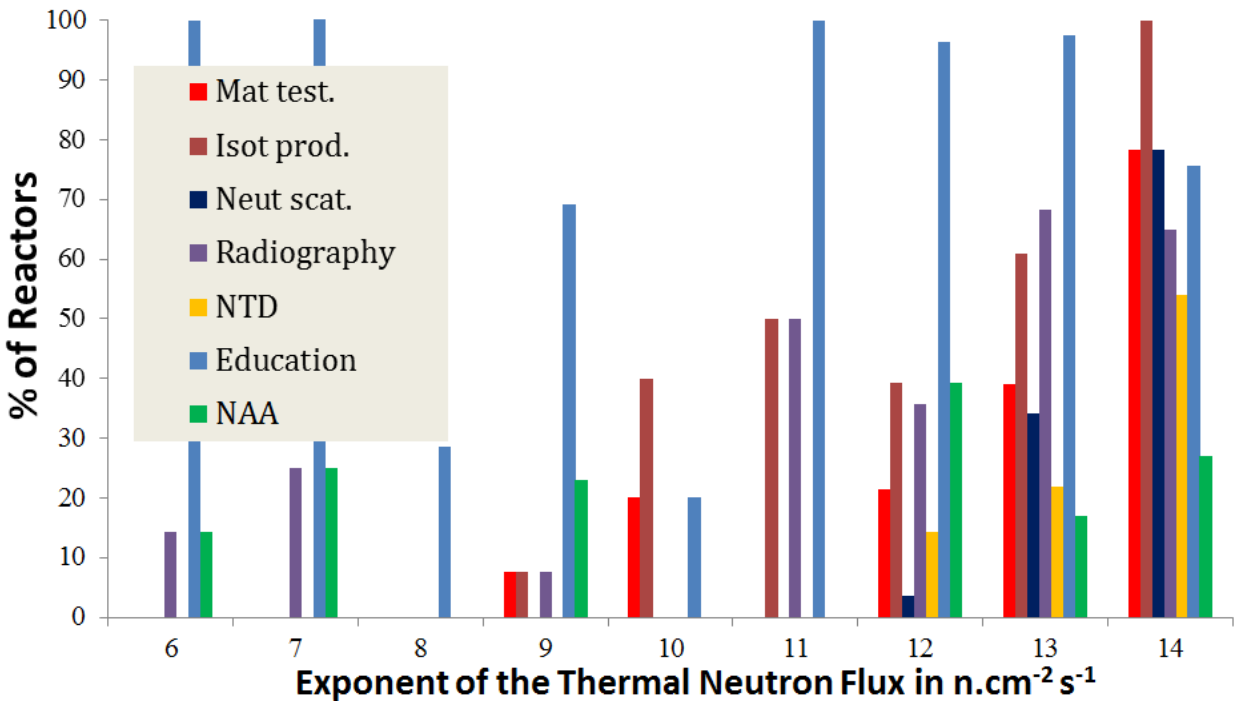


Figure 1: Graph of the proportion of reactors in database with the same maximum flux (represented as the log(flux) so that a flux of 10^{12} is represented as 12 on the abscissa) used for various purposes. All data is taken from the IAEA Research Reactor Database for reactors that are operational, temporarily shut down or are currently under construction. [9]

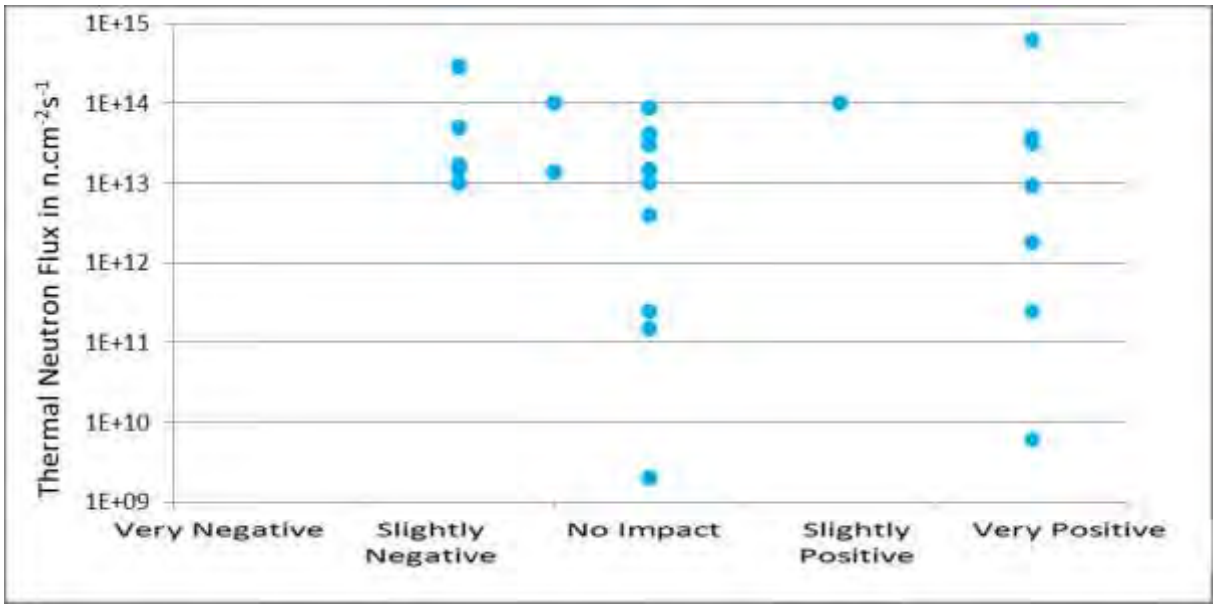


Figure 2: Scatter plot of the thermal neutron flux as a function of the Likert Scale Rating for how conversion affected the top reactor use. Notice that the reactors that perceived conversion as having a "slightly negative" way were principally high flux reactors. However, this is not universally true in the sense that some high flux reactors did not perceive that conversion had a negative impact on their top reactor uses.

Of those operators which saw a slightly negative impact, some reactors felt that reactor conversion from HEU to LEU "influenced the neutron spectra significantly. The fast flux

[9] The IAEA Research Reactor Database can be found at http://www-naweb.iaea.org/napc/physics/research_reactors/database/rr%20data%20base/datasets/foreword_home.html

decreased and the irradiation time for certain samples increased." This increased the time required to irradiate samples affecting commercial as well as collaborative research. For example, one reactor with a pneumatic transfer facility on the periphery of the core observed a decrease in flux of 1/3rd with higher reductions near the center and a thermal flux change in particular positions by as much as 25-40%. Another reactor reported that reconfiguration of the core has influenced their ability to conduct experiments because it became more cumbersome to access particular fuel assemblies. [10] Other high power reactors with commercial ambitions suffered a thermal neutron flux decrease ranging from 7%-10% from which they "could not recover the loss". One participant mentioned that since their reactor was already running at full capacity "we could not make up for the lower flux by higher utilization – we lost 10% flux without any possibility to make up for the loss".

As mentioned approximately ¼ of the operators felt that conversion was beneficial for their top reactor use. For example, while some reactors experienced a loss of flux others experienced an increase of flux of about 10%. This is because the reconfiguration of the reactor core allowed for more access to higher flux regions of the core, and in some reactors allowed for more reactor irradiation positions (one reactor reported an increase of 20% more capacity). In subsequent follow up interviews we questioned whether the flux change was different from the calculations before conversion and all of the operators suggested that the flux results corresponded to what was expected. Similar results were found when operators were queried on their second top use.

3.2 Education and Training

Every reactor, regardless of neutron flux, can be utilized for education and training, whether for public tours to introduce the concept of nuclear energy to the public or teaching students of diverse disciplines. In the present questionnaire we asked operators to rate their primary educational use for the reactor. Most of the reactors selected public tours and visits and teaching students in various fields as their top educational use. When operators were asked to rate on a Likert Scale how conversion has affected education and training, their response was overwhelmingly (65%) that there was hardly any. In addition, ¼ of the reactors saw a positive effect of conversion. For example, conversion was seen as "providing an additional talking point" during tours often of great interests to guests to the reactor and the "absence of weapons grade materials helped" reduce the perceived risk of the local population. A negative impression (<5% of reactor operators surveyed) was given by an operator who observed that the reduction of the flux required acquisition of equipment that were appropriate for dealing with lower counting rates. Many reactors recognized that from an educational point of view, conversion allowed students to get a "hands-on" experience with the reactor that they would not ordinarily get. One operator recognized that "studies associated with core conversion have provided an excellent real-world teaching tool for our students".

3.3 Fuel Use and Security Changes

In previous studies it was pointed out that most publications at the GTRI-Convert and RRFM conferences focus on the technical and safety issues related to conversion. [11] Hardly any studies specifically focus on the economic sustainability of the reactor, such as the fuel cost, change in cycle, spent fuel management etc. Conversion is expected to influence the costs

[10] According to J. Roglans of the GTRI-Convert program, these reductions and impacts are not typical; these could be some conversions that were done in less than ideal conditions of using adequate fuels, configurations, etc. For conversions performed under the auspices of the Program, it has always been left to the owner to make the decision as to whether the replacement of the fuel is acceptable (that is, of their ability to perform their mission is not significantly decreased).

[11] K. Alldred and N. Mote, Impact on fuel cycle costs of conversion to low enriched uranium fuels, RRFM 2008, March 2-5, 2008. http://www.euronuclear.org/meetings/rrfm2008/transactions/rrfm2008-session3.pdf (pg. 69-73)

especially of higher flux reactors where fabrication and disposal costs may change. Decisions made on conversion affect the economic viability and sustainability of the reactor.

Therefore, in this section we probe fuel accessibility and how the costs of fuel consumption, fuel assemblies and the change in the relative price of LEU compared to HEU were affected by conversion. Both cost and accessibility are treated as one issue because the same results were obtained on the Likert scale, and similar reasons were given to justify the results.

To determine if access to fuel was affected by conversion operators were asked to rate on a Likert Scale how much the acquisition and the cost of fuel changed before and after conversion. The majority of the reactors that do not routinely refuel selected the "not applicable (N/A)" option for both questions. This was for a variety of reasons but principally because reactors that do not routinely refuel have not needed to routinely pay for LEU fuel or for reactors that use little fuel such as for a zero power reactor. Technically, we could place the "N/A" population in the "No Change" column but there may be other reasons for reactor operators to choose "N/A". It is important to point out that not all reactor operators gave comments related to the costs of the fuel, since many operators chose "N/A" without giving explicit reasons.

When asked about the difficulty of acquiring LEU fuel, the majority of the reactors (55%) considered that there was little difference in both the acquisition and in the cost of the fuel. In some cases this was because the cost of fuel for the conversion was completely funded by the U.S Department of Energy (DOE). One of the reactors stated that "we neither required fuel on an annual basis nor did we pay for the conversion, the cost of the fuel was effectively neutral to the university." If we exclude the operators that chose "N/A" from the survey, 95% of reactor operators saw no change or at least an improvement in their ability to acquire fuel. This is not surprising because of the global norm towards minimization of HEU in the civilian sector is making it more and more difficult to obtain HEU fuel.

As a result of the conversion at least one of the national nuclear agency decided to start fabricating the fuel indigenously to support the reactors and the reactor operator reported that they perceived there to be a decrease in the overall cost of the fuel. [12] Several operators have also commented that access to fuel has Improved, because it is "easier to procure and to import LEU fuel" and easier to transport as well. This highlights the fact that additional security costs are associated with shipment of HEU compared to LEU. [13] One operator associated with a reactor that has a life-time core was pleased with conversion since the LEU core will ensure that the refueling will not be necessary for many more decades while the HEU core was already half-way through its life-cycle.

We also questioned reactor operators on how the total cost of fuel and cost of fuel assemblies have changed before and after conversion. We noticed that roughly 1/3rd of the reactor operators observed a slight improvement or saw no change in the price, 1/3rd of the operators chose "N/A" for a variety of reasons discussed earlier. However, the final 1/3rd of reactor operators reported an increase in the cost of fuel. In one case the operator claimed an increase as much as "4 times" the HEU fuel cost.

[12] Luis Olivares et al., Manufacture of Nuclear Fuel Elements in Chile (Fabricación de Combustible Nuclear en Chile), Workshop on "United Nations Framework Classification for Fossil Energy and Mineral Reserves and Resources–2009 (UNFC–2009) Applications in Uranium and Thorium resources: Focus on Comprehensive Extraction", Colegio de Ingenieros de Chile, 9 to 12 July 2013.

[13] This is because "An important feature of the CPPNM is its categorization of nuclear material by type and quantity for the purposes of applying physical protection levels" and physical protection rules differ for LEU and HEU. For more details see: IAEA, Management of high enriched uranium for peaceful purposes: Status and trends, TECDOC-1452, 2005. http://www-pub.iaea.org/mtcd/publications/pdf/te_1452_web.pdf.

Reasons given by these operators were an increase in the transportation costs, lower efficiency as well as higher utilization of the fuel than with LEU fuel, and because of the limited number of suppliers of LEU fuel. Note that there should not be a significant cost difference between LEU and HEU fuel fabrication costs when the same fabrication process is used (since LEU fuels require higher densities, fabrication is likely to generate more scrap and impact the cost somewhat). [14] However several reactors in the survey observed an increase of 2-4 times the fuel cost before conversion of the HEU fuel. A serious concern is that there are a limited number of suppliers of research reactor fuels so that the suppliers essentially have a monopoly.

It must be emphasized that it is not always easy to determine whether the reason for the difference in cost of fuel is because of conversion or as one operator observed because of "rapid changes in the international market prices for enriched uranium, the irregular and infrequent purchases of HEU fuel prior to conversion and, in certain cases, the commercial confidentiality of information". [15] In addition, the availability of HEU fuel would not be expected to have been assured even if the reactor had not converted. [16] So, it behooves the reader to be careful in interpreting the cost estimates.

3.4 How has the Process of Reactor Conversion Affected the Disposition of Spent Fuel Risks Posed by HEU and LEU Fuel

Disposition of spent nuclear fuel is a safety, security and proliferation concern both for research reactors and for nuclear power reactors. However, un-irradiated, and older irradiated HEU fuel used in dozens of research reactors around the world pose a more serious concern because depending on the uranium-235 enrichment it may be easily usable for a nuclear explosive device both for a state or non-state actor. It has been estimated that 1/3 of the world's Spent Nuclear Fuel (SNF) from Research Reactors is HEU.[17]

HEU poses a proliferation risk since as little as tens of kg of weapon grade U-235 could be used to construct a low yield nuclear device and if stolen, at the very least, could cause mass panic and disrupt the economy. The prevailing point of view has been that irradiated HEU fuel may offer some self-protection from theft in the sense that depending on the age of the fuel the dose received to a person stealing spent irradiated fuel assemblies may be fatal and this may be a deterrent to theft of spent fuel. However, for highly motivated individuals this dose is unlikely to be immediately incapacitating, a fact recognized in the fifth revision of INFCIRC-225. Furthermore, HEU that is not of weapons-grade can be re-enriched to weapons-grade and can then be used in a nuclear explosive device. Note that many of the licensed research reactors today are offline or shutdown and security of waste at these sites should not be neglected especially for HEU waste materials.

3.4.1 Research Reactor Repatriation Programs

Once nuclear fuel can no longer efficiently sustain a chain reaction the fuel is removed from the reactor and stored in spent fuel ponds. Therefore, during the time of reactor operation spent fuel has accumulated and has been stored where in some cases it may be vulnerable to theft or deliberate sabotage. Therefore, the United States and the Russian Federation

[14] Personal communication Jordi Roglans, Nuclear Engineering Division, Argonne National Laboratory Technical Director, International Reactor Conversion GTRI Convert Program.

[15] Note that while some of the operators may have interpreted the cost difference as being partly due to enrichment, the pricing of the raw material is not necessarily related to enrichment costs.

[16] Alldred and Mote, 2008.

[17] P. Adelfang and N. Ramamoorthy, "Nuclear Research Reactors: Seminar on Nuclear Science and Technology for Diplomats", IAEA, Vienna, Feb 6-8, 2007; C. D. Ferguson and T. C. Robinson, "An Analysis of the Technical and Political Dimensions of Highly Enriched Uranium in the Civilian and Naval Sectors," Nuclear Threat Initiative Report, March 2006 (unpublished), 60 pp. Also see P. Adelfang et. al, Spent Nuclear Fuel from Research Reactors: International Status and Perspectives, NATO Security through Science Series, Springer, 2007.

have instituted take-back programs where both fresh and spent HEU fuel are repatriated back to the country of origin. As of Oct 2012 the United States GTRI-Remove program (which is responsible for the the Foreign Research Reactor Spent Nuclear Fuel Acceptance Program (FRRSNF)) has repatriated 1255 kg of HEU to the United States. [18] Similarly the Russian Research Reactor Fuel Return Program (RRRFR) has successfully returned 1600 kg of fresh and spent HEU fuel as of Oct 2012 from countries that have reactors fueled by Russian fuels. [19] The purpose of these programs are to "eliminate the inventories of HEU by returning the spent fuel to the country where the fuel was originally enriched." [20]

3.4.2 Spent Fuel Disposition Before and After Conversion

When reactor operators in this survey were asked to rate on a Likert Scale whether fuel disposition had changed before and after conversion, one in two operators responded that there was no significant change in spent fuel disposition. Of the reactors that saw a change in the amount of fuel to be disposed, 1/4 of the reactor operators felt that they dealt with more spent fuel after conversion and 7% considered there to be a significant decrease in the amount of spent fuel. The response from the reactor operators to fuel disposition after conversion reflected the Likert scale results. Most operators considered to be indifferent or saw a positive change after reactor conversion in fuel disposition.

The reasons cited for a positive response were that after conversion there was enough space in spent fuel ponds to store the LEU fuel for decades into the future. This was especially true for reactor operators that had shipped the HEU fuel back to their point of origin which made vacant space available for LEU spent fuel assemblies. One reactor operator responded by stating that although the spent fuel disposition path is the same in the sense that they have the same issue with the problem of spent nuclear fuel they at least have an "increase in the time window".

3.5 How have the Physical Security Costs for the Site Changed After Reactor Conversion

It is expected that removal of fresh and spent HEU fuel would correspond to a decreased security cost associated with managing the fresh and spent fuels. However, more than 3/4 of the reactor operators surveyed saw no change in the security costs. In this case the reactor operators appeared not to change their physical protection after reactor conversion. Reactor operators that saw no change in their security costs also stated that small reactors burn very little fuel implying that significant core changes are done only every few years and there is no need to have a large stock of fresh fuel which would affect the security requirements. Twelve percent of reactor operators saw a decrease in security costs which were attributed to a smaller security system and less staff time required to perform security functions and maintain security systems. Another reason cited unrelated to conversion was decreased administrative costs associated with maintaining a security plan for HEU fuel. One reactor operator reported that there has been a significant increase in security costs not because of conversion but because of increased requirements on physical security of irradiated fuel due to the 4'th and 5'th revisions of INFCIRC 225. When operators were asked whether HEU still existed at their facility 88% said that it had been removed and 11% preferred not to answer.

---

[18] C.E. Messick and J.J. Galan, "Global Threat Reduction Initiative's U.S.-origin Nuclear Material Removal Program: 2012 Update," International Topical Meeting on Research Reactor Fuel Management (RRFM), Prague, Czech Republic, March 2012, www.euronuclear.org.

[19] S. Tozser, P. Adelfang, and E. Bradley, "Ten Years of IAEA Cooperation with the Russian Reactor Research Fuel Return Programme," paper presented at the 2012 RRFM conference in Prague, Czech Republic, March 2012, www.euronuclear.org.

[20] IAEA-TECDOC-1593: Return of Research Reactor Spent Fuel to the Country of Origin: Requirements for Technical and Administrative Preparations and National Experiences. Proceedings of a technical meeting held in Vienna, August 28-31, 2006. Vienna, Austria, July 2008.

3.6 Comprehensive View of Conversion

3.6.1 Net Benefits

Reactor operators were asked to rate on a Likert scale how they perceive the overall net benefit of reactor conversion given the security costs, public and safety concerns, maintenance responsibilities and other aspects of concern. Approximately 60% of the reactor operators perceived an overall slight or significant benefit to conversion while 30% saw no change and about 10% saw a slight detriment in conversion. Of the operators that commented, approximately half of the comments expressed that the greatest benefit was that public acceptance increased since the fuel poses less of a proliferation concern. It was an opportunity for the reactor operators to communicate with the local community about the benefits of a reactor. The second greatest benefit expressed by the operators was the decrease in security cost and the freeing up of space in the spent fuel pool essentially extending the life of the reactor. Finally, operators perceived an increase in safety of the reactor since a thorough safety analysis is required for operation of a converted reactor. Some smaller reactors also appreciated the financial support for personnel, equipment and training during the conversion process. The reactor operators that saw a slight detriment in conversion did not give a specific reason instead stated that there were no “technical benefits”.

4. Conclusions and Recommendations

This report summarizes the results from a comprehensive survey of 33 research reactor that have converted from HEU fuel to LEU. The survey aimed to cover all areas of conversion specifically where the perception of the consequence of conversion may have been an obstacle to conversion. The purpose of the survey is to determine if the principles of conversion have been adhered to and what the effect of conversion was on fuel supply costs, security, understanding and utility of the reactor. Most of the questions in the survey had both a qualitative and a quantitative component where the respondent was asked how a particular aspect of a reactor has been affected by conversion and then asked to rate the level of impact that conversion has had on a 9-point Likert Scale, where the middle value of the scale represents no impact on conversion and both extremes represent a very negative or a very positive experience with conversion. The value scale depends on the question asked. A key finding of the survey was that in many respects the perception of conversion by the operators appears to be overwhelmingly positive. Fewer than 8% of the reactor operators perceived that conversion led to even a “slight detriment” in the operation of their reactors (see Figure 3).

The survey found that the greatest benefit of conversion perceived by the reactor operators was that the public acceptance of reactors increased, since the reactor after conversion poses less of a proliferation concern. The operators recognized that this was an opportunity to communicate with the local community about the benefits and role of a nuclear reactor in society. The second greatest benefit expressed in comments made by the operators was the decrease in security cost and the freeing up of space in the spent fuel pool essentially extending the life of the reactor. Other positive perceptions on concerns of conversion are that less than 5% of reactor operators perceived a difficulty in acquiring fuel, a negative effect of conversion on teaching and education and on the modernization or understanding of the reactor. The decision on conversion must ultimately be made by weighing multiple concerns such as the cost of fuel, fuel disposition, and effect on the uses of the reactor, training, education and outreach.

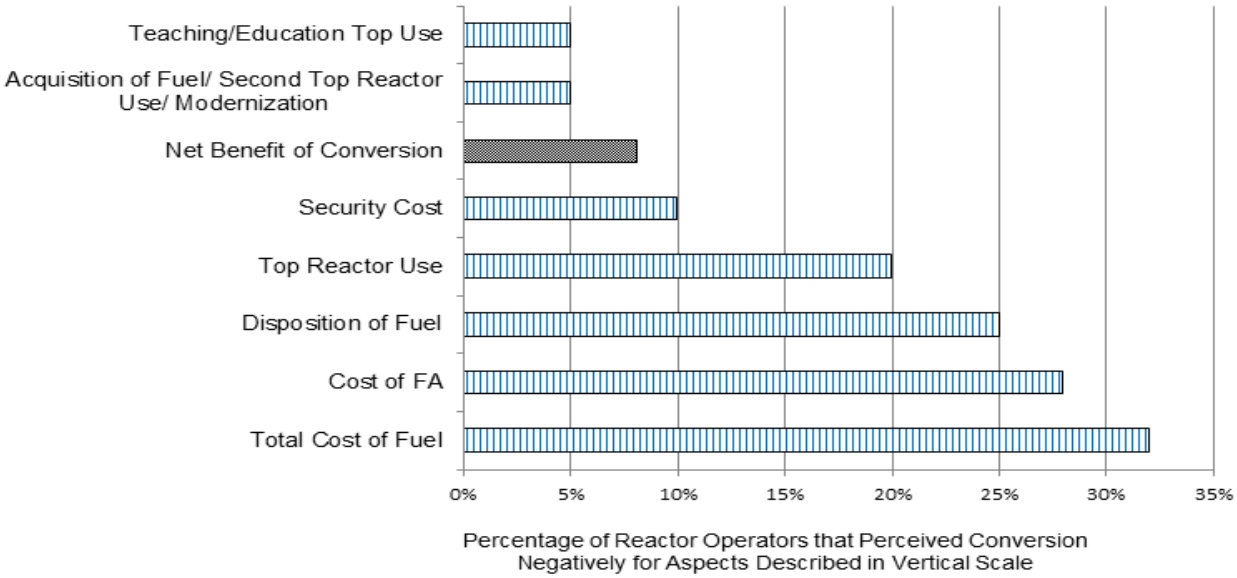


Figure 3: The percentage of operators that perceived conversion negatively with respect with specific aspects of reactor conversion discussed in this report. Also shown is the fraction of reactor operators that perceived the benefit of conversion negatively.

Acknowledgements

I would like to acknowledge the support of Christopher Landers, the Manager of the Reactor Conversion Program at the U.S. Department of Energy's National Nuclear Security Administration (DOE) and Jordi Roglans, Nuclear Engineering Division, Argonne National Laboratory Technical Director, International Reactor Conversion GTRI Convert Program. I would also like to acknowledge help from a variety of excellent graduate research assistants especially Sarah Norris and Miles Pomper for a final reading of the manuscript. Finally, I would like to thank dozens of reactor operators who have taken the time to be part of this study.

Limitations of this Study

This study has been conducted by contacting reactor operators of reactors that have been converted within the last fifty years. Many of the point of contacts provided by the DOE for the reactors were not active and we had to rely on local people to point us to the appropriate person. We did not verify independently whether the contacts suggested were the most appropriate for filling out the survey. We assume in this survey that the local personnel have the best knowledge of who should fill in the survey. Note also that with many of the reactors many decades have passed since conversion so there is a loss of institutional memory about the reactor since many of the operators have retired. Unfortunately, the survey is heavily biased towards Europe and North America since operators contacted in the Middle East and some in Asia did not participate in the survey. Finally, comments are voluntary so not all operators commented at all times it was requested. This means that the Likert scale quantitative data has higher statistics then the comments do.

EXPERIMENTAL PROGRAMS OUTLOOKS IN MTRS FOR SUPPORTING DEVELOPMENT OF SODIUM COOLED FAST REACTOR FUELS AND MATERIALS

M. PHELIP, M. PELLETIER, D. PARRAT
Fuel Research Department, CEA
Cadarache, F-13108 Saint-Paul-lez Durance - France

M. LE FLEM
Nuclear Material Department, CEA
Saclay, F- 91191 Gif-sur-Yvette - France

P. JAECKI
Reactor Studies Department, JHR Service, CEA
Cadarache, F-13108 Saint-Paul-lez Durance - France

ABSTRACT

The sodium-cooled fast reactor (SFR) concept is one of the four fast neutron concepts selected by the Generation IV International Forum (GIF). It has been chosen as the reference type in France, and benefits from a significant experience feedback from the previous French programs on experimental or commercial SFRs (Rapsodie, Phénix, Superphénix). In particular, the accumulated experience feedback in France on mixed oxide fuel (U, Pu)O_2 and austenistic steel cladding (cold-worked 15-15 Ti) demonstrated that this type of fuel element has an excellent behaviour up to high burnup fraction under normal operation and off-normal conditions, conducting to choose them as reference concept for starting of the ASTRID technological demonstrator.

For mid-term and long-term SFR fuel and material development, extension of fuel burnup and absorbers lifetime, minor actinides transmutation, Plutonium burning and improvement of safety margins are topics which will generate R&D needs on advanced fuel and structural materials to complete knowledge in term of in-pile behaviour under normal operation and to support safety demonstration. Selected new cladding materials are advanced austenitic steels, oxide dispersion strengthened steels (ODS steel) and SiC-SiC composites; in terms of innovative ceramic fuels, mixed carbide, mixed oxide of uranium and americium, mixed oxide high Pu content have to be considered.

Material test reactors (MTRs), in complementarity of the experimental capability of SFR reactors, despite their limitation to be representative in terms of fast neutron flux level and neutron spectrum, may participate actively to advanced SFR fuels qualification. Local adaptation of irradiation conditions can be implemented to activate at the right level phenomena and to control parameters governing fuel and cladding properties evolution, with the aim to provide relevant data for models. Potential opportunities for MTRs and associated facilities are presented in this paper, focused on dedicated experiments which could be carried out.

1. Introduction

The sodium-cooled fast reactor (SFR) concept is one of the four fast neutron concepts selected by the Generation IV International Forum (GIF). It has been chosen as the reference type in France, and benefits from a significant experience feedback from the previous French programs on experimental or commercial SFRs (Rapsodie, Phénix, Superphénix). In particular, the accumulated experience feedback in France on mixed oxide fuel (U, Pu)O_2 and austenistic steel cladding (cold-worked 15-15 Ti) demonstrated that this type of fuel element has an excellent behaviour up to high burnup fraction under normal operation and off-normal conditions, conducting to choose them as reference concept for starting of the ASTRID technological demonstrator.

For mid-term and long-term SFR advanced fuel and material development, the understanding of the physical and chemical phenomena induced by irradiation, the

characterization and the property measurement require neutron irradiations. Material test reactors (MTRs), in complementarity of the experimental capability of SFR reactors, despite their limitation to be representative in terms of fast neutron flux level and neutron spectrum, may participate to the knowledge improvement and the assessment of these new materials.

2. SFR fuel development and versatility of MTR to fulfil SFR fuel irradiation requirements

The development process of a SFR fuel product or material before using it at an industrial scale in a power reactor takes profit from a mix of knowledge:

- Experimental feedback gained during the previous operation of similar fuels in other SFR reactors (by plant operator or during post-irradiation surveillance programs),
- Use of qualified models to simulate the fuel product behavior for the new reactor operating conditions,
- Support of a limited experimental qualification program for confirming or improving (e. g. lower uncertainty, extension of validation domain for codes etc.) the above results and for gaining new results from specific tests not covered by existing knowledge (e.g. tests of totally new materials, new operating conditions, evolution of safety requirements etc.).

For implementing such an experimental program, several experimental infrastructures can be used to reproduce or to simulate irradiation effects of a SFR[1]:

- Gamma or X-ray sources to produce intense gamma fluxes at high energy,
- Electron or ion accelerators to simulate either the particles effect or the evolution of the material under neutron flux (ageing process) due to implantation of fission products,
- Fundamental research reactors (RRs), in which a small size sample is placed into an experimental chamber connected to a neutronic guide,
- Material test reactors (MTRs) and dedicated reactors (e.g. for safety tests) to irradiate a large scale experimental sample by neutron and gamma fluxes,
- Industrial reactors either at a prototypical or at a mature scale. In this case, the tested sample is a fuel product compatible with other standard products and irradiated in small number as “precursors”.

Only the two last types of infrastructures are capable to welcome large or instrumented specimens. Moreover, thanks to their design, the industrial reactors are the only ones which respect strictly all the environment parameters applied to the sample in normal conditions for which it is designed for (coolant thermal-hydraulics and chemistry, neutronic level and spectrum etc.). For this reason one could think that a progressive introduction of a new product, supported by results obtained thanks to “surveillance programs” regularly carried out during the life of the product thanks to post-irradiation examinations (PIEs), is the reference. However industrial facilities present some limitations when:

- The sample has to be tested beyond reactor operating limits (high dpa value or burn-up increase …) or with specific power time histories not compatible with reactor standard operation (cycling, soliciting transients, power ramps, verification of a safety criterion…),
- Specific environment parameters shall be applied (controlled stress, higher temperature or volumic power, neutronic spectrum, coolant chemistry…),
- Specific constraints or solicitation could induce a non-acceptable risk of sample integrity loss (geometrical change, rupture, clad failure),
- The sample aspect or properties observed or measured through PIEs are no more representative or cannot be transposed to the sample status during irradiation.

When these limitations are a real issue, an irradiation in MTR or a dedicated reactor is relevant to support the development process[2]. Moreover, two other MTR interests can be underlined:

- The possibility to integrate numerous instrumentation on the sample, for monitoring or quantifying effects of environment variation on its behavior. When it is technically

feasible this instrumentation is on-line (thermocouple, pressure gauge, LVDT, neutron detector etc.). If not, it plays the role of an integrator (e.g. neutron fluency or melting wire). Other on-line sensors monitor the environment of the sample. A lot of information is gained from this type of instrumentation (close sample behavior follow-up, identification of thresholds or non-reversible turn points). Then the sample is sent to hot cell laboratories for supplementary non-destructive and destructive examinations. This process represents a dramatic progress compared to previous "cook and look" irradiations, and new irradiation devices are designed to embark a lot of instrumentation and to transmit the various signals properly,

- The routine use of non-destructive examination (NDEs) on the sample and of specific analysis laboratories (mainly chemistry, fission product and activation laboratories) that can welcome and analyze fluids in contact with the sample. When these facilities are available in a MTR[3], a considerable improvement of the experiment scientific quality can be offered to the end-user, often with no specific handling (no supplementary risk for the sample) and a limited time consumption which doesn't jeopardize the experiment unfolding. NDE methods can be implemented during reactor shutdown period thanks to underwater benches on a sample still mounted on the sample-holder and connected. X-ray radiography and tomography, gamma scanning and tomography, or neutron radiography[4] are the most common techniques used in MTRs. At the end of the irradiation process, sample is unloaded from the device and disconnected from the sample-holder. Examinations are then performed in MTR fuel and material hot cells depending on the available equipment: visual inspection, metrology, Eddy currents, photon imaging and radiography etc.

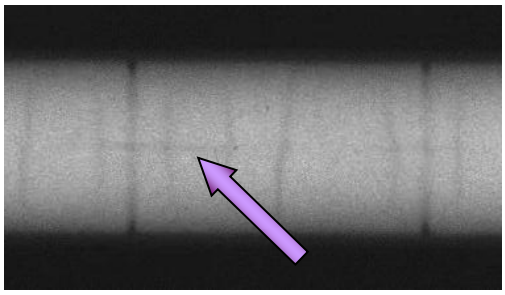


Figure 1: Example of NDE result – Neutron radiography - Central hole formation in a fuel pellet stack

3. SFR fuel R&D needs

3.1. Core Structure Material

The large feedback from previous French programs on SFRs allows selecting reference materials for the core components of ASTRID[5]. Concerning the fuel assembly, cold-worked 15-15Ti austenitic steels, exhibiting a large incubation dose before irradiation swelling will be used for the cladding tubes[6, 7] (and the spacer wire). The specification presently deals with the so-called AIM1 (Austenitic Improved Material #1) in which the cold-worked level (~20%) and the C, Mo, Ti, Si and P contents allow operating up to 130 dpa before reaching embrittlement.

Further R&D on future cladding materials is however needed to reach higher burn-ups and, consequently, a higher resistance to deformation under irradiation and at high temperature.

The improvement of austenitic steels with the aim to reach 150 dpa before embrittlement should be achieved by additional optimization of the Cr content, the swelling inhibitors (Ni) and the minor element amount (Si, P, B) to promote the annihilation of irradiation defects, the carbide precipitation and the dislocation pinning.

To achieve >150 dpa on the fuel cladding for commercial future SFRs, ferritic/martensitic steels reinforced by a nano-dispersion of oxides or carbides/nitride (ODS, CDS, NDS) should be the solution. Indeed, they combine outstanding dimension stability thanks to an

exceptional resistance to swelling and a very limited creep strain. 9-12Cr-ODS and 14Cr-ODS bars/tubes fabricated by CEA are being assessed: very good creep properties of CEA-ODS have been obtained[8] and recent characterizations after ion or neutron irradiations confirmed the stability of the microstructure and especially the stability of the nano-phases[9, 10]. The manufacture of tubes at an industrial scale and the understanding of the restricted intragranular plasticity[11] (resulting in almost no tertiary creep stage), would be the main challenge for their acceptability as cladding materials.

Many experiments conducted in Phénix have contributed to demonstrate the very good dimensional stability of the EM10 (Fe-9Cr/1Mo martensitic steel) up to 155 dpa[12, 13]. It will be used for the hexagonal wrapper tube in ASTRID and could also be envisaged for future SFRs. A revolutionary wrapper tube could be made of SiC/SiC[14] in order to ensure the dimension stability of the fuel assembly at higher temperature. Fabrication of SiC/SiC wrapper tube prototypes is being performed at CEA, benefiting from the advances experienced by CEA in the scope of the SiC/SiC cladding development for GFRs[15].

If the simulation of the damage can partially be reproduced by charged particles irradiations, only neutron irradiation combined with appropriate experiment duration are relevant to assess the material evolution. The irradiation needs of core materials have various purposes and requirements.

- First, an aim is the understanding of the physical and chemical phenomena induced by irradiation. This deals a basis R&D dedicated to accurately describing the mechanisms involved in the material evolution (modeling), and then, leading to proposal of improvements and optimizations.
- A second objective is to perform parametric studies in order to provide design rules to be implemented in the system design. The effects of parameters such as the temperature, the dose, the flux rate, the stress are addressed to assess the deformation, the change in mechanical properties, the corrosion kinetics, etc.
- This gives rise to another goal dealing with screening tests to select the most promising materials or design solution to be further qualified.
- Finally, the qualification requires to consider relevant prototypes (pins/assembly) and not only materials (samples).

For SFRs, the description of the evolution of the materials and of the corresponding component must be available from the very low doses (occurrence/nucleation of the phenomena) up to the target doses, i.e. >150 dpa (macroscopic evolution of the materials), even if the screening test may require only moderate irradiation level. The target temperature ranges from 400°C to 700°C and specific tests may be performed at higher temperature to reproduce an accidental scenario.

Regarding the materials, the AIM1 cladding and the EM10 wrapper tube may not need irradiation in MTR since there are well documented grades and since ASTRID is the opportunity to go on with the improvement of these grades.

The major needs concern the understanding of ODS behavior for commercial reactors: assessment of the deformation under flux and temperature, residual mechanical properties after irradiation (embrittlement), qualification of the welding process, etc., are necessary to update the design criteria (which may not be the same as AIM1 cladding) and to demonstrate the reliability of these steels. This involves irradiation of tube samples of various grades (chemical compositions, reinforcement amounts, fabrication routes), dedicated experiments and instrumented/experiment (thermal creep, irradiation creep), irradiation of pins prototypes (interaction with the fuel).

3.2. Fuel Material

The accumulated experience feedback in France on mixed oxide fuel (U, Pu)O_2 demonstrated that this type of fuel element has an excellent behaviour up to high burnup, conducting to choose them as reference concept for starting of the ASTRID technological demonstrator. It may not need irradiations in MTR, the readiness of the concept leading to envisage only confirmatory irradiations in SFR.

Further R&D on future fuel material is however needed to reach higher fuel burnup, to permit absorbers lifetime extension and to develop minor actinides transmutation and Plutonium burning fuels. The irradiation needs of these new materials aimed at improving the knowledge of the mechanisms involved in the material evolution under irradiation as a function of parameters such as the temperature, the burnup and the dose:

- Fuel fracture and relocation. The fracture behaviour of the fuel acts on the fuel temperature through its capacity to produce fuel fragments squeezed between pellet and the clad. This enhances fuel cladding contact, and thereby reduces the temperature drop in the gap.
- Fuel restructuring.
- Swelling and fission gas or Helium release.
- Fuel cladding chemical interaction, fuel and clad compatibility.
- Fuel behaviour in case of clad breach. Although the clad is the first safety barrier, previous reactor operation proved that cladding failures cannot be avoided.

In case of cladding failure of a mixed oxide fuel pin, the first event that occurs is the release of fission gases in the sodium coolant. The second stage is an ingress of the sodium inside the pin which may be followed by a chemical reaction between mixed oxide and sodium to form sodium urano-plutonate[16]: $3\ Na + MO_2 + O_2 \Leftrightarrow Na_3MO_4$. The reaction takes place first at the periphery of the pellets (see Figure 2) and requires an oxygen supply. As primary sodium is generally unpolluted (1 or 2 ppm of oxygen), mixed oxide fuel supplies the oxygen needed for the reaction. Consequently, the progress of this reaction depends on the quantity of oxygen that can be provided. The importance of the reaction increases with plutonium content and also with burnup.

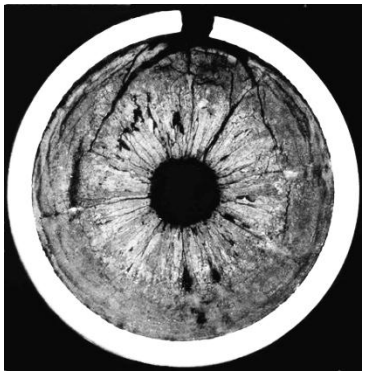


Figure 2: Macrograph of a failed Phenix fuel pin showing a wide layer of $Na_3(U, Pu)O_4$, an overheating of the centre fuel area and a large opening of the cladding

The volume expansion due to the reaction induces a strain in the cladding with the possibility of spreading the primary clad breach and releasing fission products and potentially fissile material in the coolant. This possible release depends upon the extent of the clad failure but also on the irradiation conditions. It was observed in the past, through the PHENIX feedback, that in many cases, there was no significant release of fissile material in the coolant. Nevertheless to better characterize this risk of pollution of the coolant, several programs were conducted in sodium loops such as in SILOE in France in the Thermopump facility (figure 3), mainly on PHENIX and SPX-1 irradiated fuel elements for various operating conditions representing the normal operating running[17, 18].

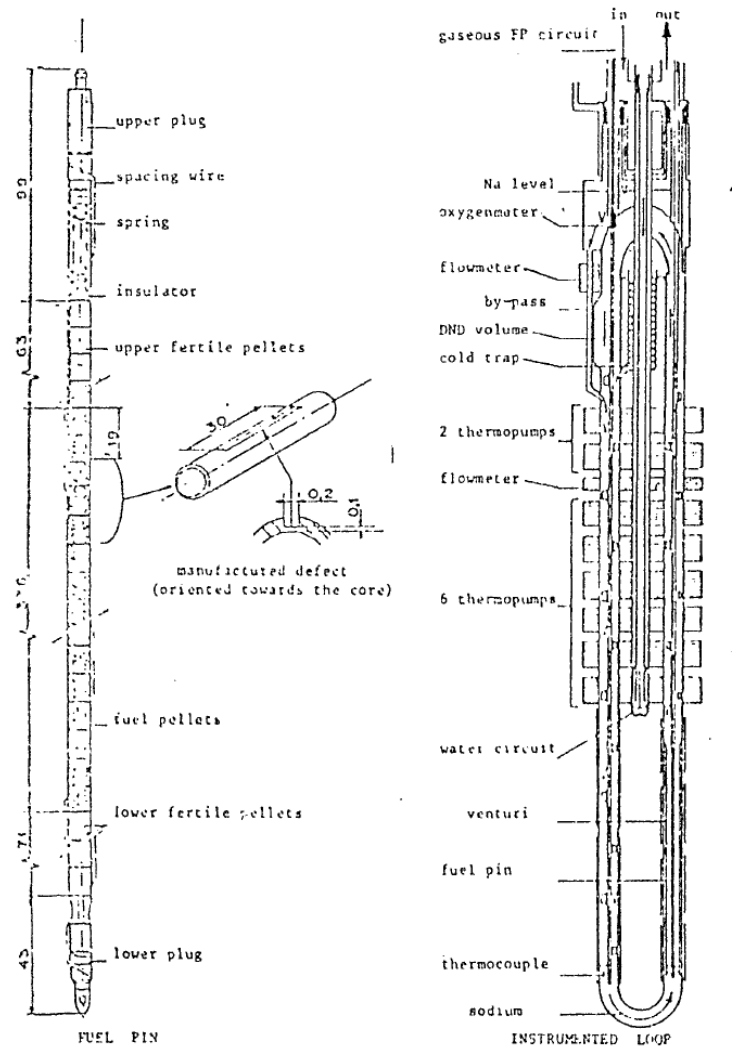


Fig. 1 : Fuel pin and instrumented loop of RS1

Figure 3: Example of fuel pin and instrumented irradiation loop

For new cladding material, or for fuel or burn-up which are not covered by previous programs, new experiments may be requested for demonstrating that the behaviour of fuel pin failures may be controlled in order to not downgrade the purity level of sodium coolant throughout the life of the reactor by radioactive nuclides.

4. Program Outlooks in MTRs

4.1. Introduction

The limitation to be representative in terms of fast neutron flux level and neutron spectrum leads to select type of experiments for which this limitation is acceptable:

- Separate effect experiment: this limitation may be an opportunity to accelerate or emphasize the phenomena.
- Semi integral experiment on fresh fuel for long term irradiations (“cooking”): exploratory irradiations for which the readiness level of the fuel is low enough to consider that this limitation is acceptable with regards to the expected results.
- Semi integral experiment on irradiated fuel for short irradiation run: the effect of this limitation on the fuel behaviour is limited, and moreover, these experiments are generally not compatible with SFR reactor operation.

The selected experiments are summarized in the following table:

Type	Material	Topic	Comments
Separate effect experiments Core material testing Fresh fuel	Cladding tube Wrapper tube $(U, Pu)O_2$, $(U, Pu, Am)O_2$, $(U, Am)O_2$ (U, Pu)C Absorber materials	Beginning of life phenomena (restructuring, relocation…) Pellet clad gap evolution Gas swelling and release	Improvement of knowledge : models and properties
Semi integral experiments on fresh fuel (small pins) "Cooking" of pin prototype	$(U, Pu, Am)O_2$ $(U, Am)O_2$ (U, Pu)C	Exploratory experiment: The low readiness of the product allows to use MTRs for a first assessment	MTR's interest: instrumentation (Thermocouple, pressure sensor…)
Semi integral experiments on irradiated fuel pins Power ramp Design to fail experiment	Irradiated fuel pins	Transient swelling, fuel creep, fission gas release, power to melt, clad integrity, clad failure evolution	Not compatible with reactor standard operation

Table 1: type of SFR fuel experiment which could be conducted in MTRs

The two next paragraphs are focused on irradiation experiments illustrating the table above which are on-going or in the phase of feasibility study.

4.2. Separate Effect Fuel Experiments

The capability for running heavy instrumented experiments and to fix or to control the local parameters (neutron flux and spectrum, temperature etc.) in an irradiation hosting system is a key feature of a MTR for supporting development and qualification of nuclear fuels and materials. As an example, in the Gen IV domain, a relevant application of MTRs is the possibility to perform separate effect fuel experiments on transmutation studies. For that aim, some experiments have been implemented or are in progress.

A possible concept for Am transmutation is the use of dedicated subassemblies in the blanket of a SFR core (Minor Actinide Bearing Blanket concept, or MABB)[19]. The typical fuel composition is $(U,Am)O_{2-x}$ with a 10-20% Am content. The production of Helium in power reactors conditions is quite large (expected about 7 mg He/cm^3 of initial fuel after 4100 EFPD), with moderate central fuel temperatures (700-1000 °C). The absence of relevant experimental irradiations and predictive models in these conditions leads to an uncertainty on the behavior of He (release, retention, effect on swelling leading to a possible fuel-cladding mechanical interaction…) in normal and transient conditions.

The MARIOS experiment in HFR[20] or the DIAMINO experiment in the OSIRIS reactor[21] have been designed to investigate He behaviour versus Am content, T, and fuel microstructure, for a base irradiation. Fuel sample is constituted by thin disks located between two thick disks of Molybdenum alloy, which allows a good homogeneity of the temperature during the irradiation[22]. This parameter is adjusted by a variable composition of a gas gap surrounding the fuel capsule.

The neutronic spectrum of a MTR differs markedly from a SFR and shall be adapted locally to the experiment objectives[23]. In the case of MABB fuel, the Am capture cross section in a thermal spectrum is very high, leading to an accelerated He production compared to the SFR reference case, and a higher power generation. However, this allows for an accelerated experimental irradiation (300 vs 1800 EFPD), as long as fission densities (representative of fuel matrix damage) are kept reasonably close to the power reactor reference case.

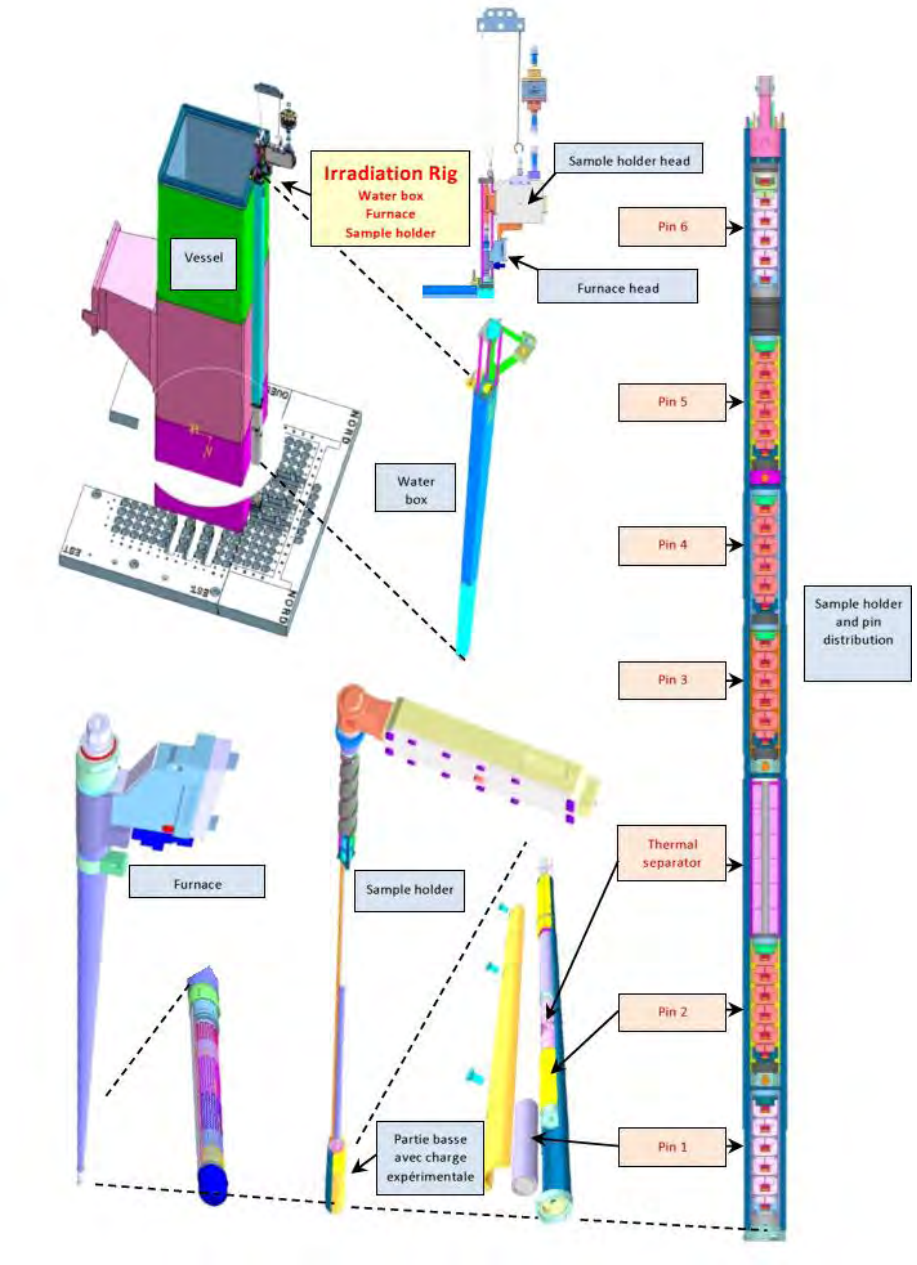


Figure 4: DIAMINO irradiation rig

4.3. Short irradiation run

MTR have been extensively used in the past so support SFR system development. In the French SFR program, most of the existing data concerning SFR fuel behaviour in power transients has been gained in the CABRI reactor, with a dominantly thermal spectrum.
Putting aside fast transients, it is possible to investigate the fuel pin behaviour during relatively slow power transients in a MTR (up to a few % of nominal power/s), up to the fuel melting temperature. This type of experiments, used in conjunction with existing data and

models, could be used if necessary in support to the safety case of an industrial reactor during postulated incidental conditions.

Such programs have been carried out in OSIRIS and HFR MTRs in the past[24, 25]
For new cladding grade or new type of fuel testing, this possibility is being investigated in the Jules Horowitz Reactor (JHR), currently under construction. The JHR will be equipped with up to 4 displacement systems installed in the Beryllium reflector, and used for instance to generate power ramps on a PWR fuel rod placed in an experimental irradiation loop[26]. Using these displacement systems and the design of a hosting system under development, a preliminary study showed that, from the neutronic point of view, it is possible to reach power to melt even on high burn-up pre-irradiated SFR pins.
Differences in neutron spectrum between a SFR and a MTR lead to a deviation on the fuel temperature radial profile. However this effect can partially compensated, for instance by adjusting cooling conditions, as previously done in CABRI for instance.

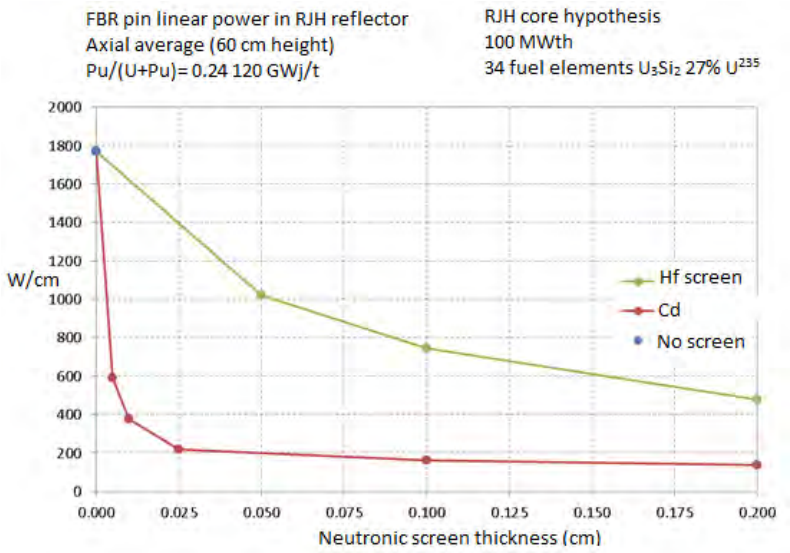


Figure 5: Maximum linear power in a prototypical FBR pin in the JHR reflector

5. Conclusion

The reference fuel materials envisaged for the core components of French fast reactor technological prototype (ASTRID) benefit from the large feedback from the French sodium cooled reactors and would not exhibit any strong issue, a dedicated program devoted to answer to the specificities of this core being on-going.
Further R&D on future advanced fuel materials is however needed to reach higher fuel burnup and absorbers lifetime and to develop minor actinides transmutation and/or plutonium burning fuels.

The MTR limitation to be representative in terms of fast neutron flux level and neutron spectrum leads to select type of experiments for which this limitation is not unacceptable:

- Separate effect experiment for property measurement or models improvement: this limitation may be on the contrary an opportunity to accelerate or emphasize the studied phenomena.
- Semi integral experiment on fresh fuel for long term irradiations (“cooking”): exploratory irradiations for which the readiness level of the fuel is low enough to consider that this limitation is acceptable with regards to the expected results.
- Semi integral experiment on irradiated fuel for short term irradiation: the effect of this limitation on the fuel behaviour is limited, and moreover, these experiments are generally not compatible with SFR reactor operation.

Some experiments are already on-going and others at the feasibility phase.

6. Reference

[1]Nuclear fuels and materials qualification programs in the European Jules Horowitz Material Test Reactor - D. Parrat, M. Tourasse, J.C. Brachet, G. Bignan, J.P. Chauvin, C. Gonnier

ANS-ENS-JNES LWR Fuel Performance Meeting – Topfuel 2013, 15-19 September 2013, Charlotte, North Carolina, USA

[2]Integrated Infrastructure Initiatives for Material Testing Reactors Innovations (MTR+ I3)

Final report - European Project FI6O 036440 – 01/10/2006 – 31/09/2009 - www.mtri3.eu

[3]Non-destructive examination benches and analysis laboratories in support to the experimental process in the Jules Horowitz Material Test Reactor - D. Parrat, P. Kotiluoto, T. Jäppinen, C. Roure, B. Cornu, B. Berthet, C. Gonnier, S. Gaillot -13th International Group On Research Reactors (IGORR 13), 19-23 September 2010, Knoxville, Tennessee, USA.

[4]The future underwater neutron imaging system of the Jules Horowitz MTR : an equipment improving the scientific quality of irradiation programs - D. Parrat, P. Guimbal, G. Le Guillou, E. Simon, L. Boucher - 15th International Group On Research Reactors (IGORR 15), 13-18 October, 2013, Daejeon, South Korea

[5]M. Le Flem, P. Gavoille, A. Courcelle, P. Olier, Y. de Carlan, M. Blat-Yrieix, P. Diano, « Status of the French R&D on ASTRID core materials », Proceedings of ICAPP 2014, Charlotte, USA, April 6-9, 2014

[6]J.L. Séran, V. Levy, P. Dubuisson, D. Gilbon, A. Maillard, A. Fissolo, H. Touron, R. Cauvin, A. Chalony, “Behavior Under Neutron Irradiation of the 15-15 Ti and EM 10 Steels Used as Standard Materials of the Phenix Fuel Subassembly,” Proc. of Effects of Radiation on Materials: 15th International Symposium, Nashville, Tenessee, USA (1992) 1209-1233.

[7]A. Maillard, H. Touron, J.M. Séran, A. Chalony, “Swelling and Irradiation Creep of Neutron-Irradiated 316Ti and 15-15Ti Steels,” Proc. of Effects of Radiation on Materials: 16th International Symposium, Aurora, Colorado, USA (1994) 824-837.

[8]B. Fournier, A. Steckmeyer, A.-L. Rouffie, J. Malaplate, J. Garnier, M. Ratti, P. Wident, L. Ziolek, I. Tournie, V. Rabeau, J.M. Gentzbittel, T. Kruml, I. Kubena, “Mechanical behaviour of ferritic ODS steels – Temperature dependency and anisotropy”, Journal of Nuclear Materials, vol. 430, 142-149 (2012)

[9]J. Ribis, S. Lozano-Perez, “Nano-cluster stability following neutron irradiation in MA957 oxide dispersion strengthened material”, Journal of Nuclear Materials, vol. 444, 314-322 (2014)

[10]M-L. Lescoat, J. Ribis, A. Gentils, O. Kaïtasov, Y. de Carlan, A. Legris, “In situ TEM study of the stability of nano-oxides in ODS steels under ion-irradiation”, Journal of Nuclear Materials, vol. 428, 176-182 (2012)

[11]M. Praud, F. Mompiou, J. Malaplate, D. Caillard, J. Garnier, A. Steckmeyer, B. Fournier, “Study of the deformation mechanisms in a Fe–14% Cr ODS alloy”, Journal of Nuclear Materials, vol. 428, 90-97 (2012

[12]P. Dubuisson, D. Gilbon, J.L. Séran, “Microstructural evolution of ferritic-martensitic steels irradiated in the fast breeder reactor Phénix,” Journal of Nuclear Materials, vol. 205, 178-189 (1993)

[13]J. Henry, CEA, to be published

[14]A. Ravenet, Body for a Nuclear Fuel Assembly, and Nuclear Fuel Assembly Comprising such a Body, Patent WO 2011/042406 A1, 14 April 2011, in French

[15]M. Zabiégo, C. Sauder, C. Lorette, P. Guédeney, Tube multicouche amélioré en matériau composite à matrice céramique, gaine de combustible nucléaire en résultant et procédés de fabrication associés, Patent submitted 1 August 2011, in French

[16]The fuel sodium interaction - M.A. MIGNANELLI and J. ROUAULT - Harwell AGT 010101/P8 (1990)

[17]Failure evolution in sodium loops. Results of the SILOE experimental program. - A. MATHIOT, J.P. HAIRION, H. PLITZ, P. WEIMAR and P. CECCHI - International Conference on Reliable Fuels For Liquid Metal Reactors Tucson (1986)

[18]Joint French German program to investigate continued LMFBR-Operation with detective fuel pins – P. Michaille, A. Chalony, F. Hairion, M. Pluchery, D. Rousseau, P. Vulliez, F. Gesterman, M. relic, H.

Kleykamp, H. Plitz, G. SCHMITZ, P. Weimar – Conférence international sur la sûreé des réacteurs à neutrons rapides – Lyon 19-23 juillet 1982.

[19]Development program on minor actinide-bearing blankets at CEA - J.M. Bonnerot et al. - 11th Information Exchange Meeting of Actinide and Fission Product Partitioning and Transmutation (IEMPT), 1-4 November 2010, San Francisco (USA)

[20]The results of irradiation experiment MARIOS on americium transmutation- E. D'Agata et al.- Annals of Nuclear Energy, 62 (2013) 40-49

[21]Americium-bearing blanket separate effect experiment: MARIOS and DIAMINO irradiations - S. Béjaoui, E. D'Agata, R. Hania, T. Lambert, S. Bendotti, C. Neyroud, N. Herlet, J.M. Bonnerot - Proceedings of the GLOBAL 2011 Conference, 11-16 December 2011, Makuhari (Japan)

[22]Thermomechanical simulation of the DIAMINO irradiation experiment using the LICOS fuel design code - S. Béjaoui, T. Helfer, E. Brunon, T. Lambert, S. Bendotti, C. Neyroud - Proceedings of the GLOBAL 2013 Conference, 29 September – 3 October 2013, Salt Lake City (USA) 2011

[23]Neutronics and photonics calculations in support to the design of the DIAMINO irradiation device in the OSIRIS reactor - A-C. Colombier, C. D'Aletto, L. Gaubert, S. Béjaoui, T. Lambert, J. Di Salvo, B. Pouchin, S. Bendotti, C. Neyroud - European Research Reactor Conference 2013 (RRFM 2013), 21-25 April 2013, St Petersburg (Russia)

[24]Ramp test facilities at HFR Petten, R. Hania, K. Baaker TopFuel 2013, Sept 15-19 2013, Charlotte NC, USA

[25]Presentation de la boucle BANJO (Osiris), J. Lalere, J. Rousseau, CEA CONF 1673, 1970, Kalrsruhe, Germany

[26]Fuel and material irradiation hosting systems in the Jules Horowitz reactor - C. Blandin, J. Estrade, C. Colin, T. Dousson, L. Ferry, J. Pierre, P. Roux, C. Gonnier - 15th International Group On Research Reactors (IGORR 15), 13-18 October, 2013, Daejeon, South Korea



New Research Reactor Projects

JULES HOROWITZ REACTOR: ORGANISATION FOR THE PREPARATION OF THE COMMISSIONING PHASE AND NORMAL OPERATION

J. ESTRADE, G. BIGNAN, J.L. FABRE,
O. MARCILLE, C. BLANDIN
French Alternative Energies end Atomic Energy Commission - Nuclear Energy Directorate
Cadarache Research Centre - France

Contact author: jerome.estrade@cea.fr

ABSTRACT

The Jules Horowitz Reactor (JHR) is a new modern Material Testing Reactor (MTR) currently under construction at CEA Cadarache research centre in the south of France. It will be a major research facility in support to the development and the qualification of materials and fuels under irradiation with sizes and environment conditions relevant for nuclear power plants in order to optimise and demonstrate safe operations of existing power reactors as well as to support future reactors design. It will represent also an important research infrastructure for scientific studies dealing with material and fuel behaviour under irradiation. The JHR will contribute also to secure the production of radioisotope for medical application. This is a key public health stake.

The construction of JHR is going-on with a foreseen operation by the end of this decade. Once in operation, the reactor will provide modern experimental capacity in support to R&D programs for the nuclear energy for the next 50 years.

In parallel to the facility construction, the preparation of the future staff and of the organisation to operate the reactor safely, reliably and efficiently is an important issue. CEA must also design and implement the first experimental devices for the start-up of the reactor. In this framework, many actions are in progress to elaborate:

- the staffing and the organisational structure for the commissioning test phases and also for normal operation,
- the documentation in support to the reactor operation (safety analysis report, general operating rules, procedures, instructions, …),
- the maintenance, in service and periodic test programs,
- staff training programs by using dedicated facilities (simulator,…),
- commissioning test programs for ensuring that the layout of systems and subcomponents is completed in accordance with the design requirements, the specification performances and the safety criteria,
- design and implementation of the first fleet of experimental devices in support to the commissioning test program and the future experimental programs.

These commissioning tests will also be helpful for transferring the knowledge on the installed systems to the operating group.

This paper gives the description of the main tasks to prepare the organisation for the commissioning and operation of the Jules Horowitz Reactor. This paper gives also an overview of the main experimental hosting systems, currently under design, that will be operational for the start up of the reactor or few years later.

1. Introduction

This paper provides a description of the organizational structure, responsibilities and main actions for the Jules Horowitz (JHR) Material Testing Reactor (MTR) commissioning and routine operation.
Its construction, started in 2007, is going-on with a foreseen operation by the end of this

decade. It will be operated by CEA, as an international user's facility on the CEA Cadarache site. The design of the reactor will provide modern experimental capacity in support to R&D programs for the nuclear energy for the next 50 years. It will also supply radio-isotopes used for medical applications.
JHR will be a modern MTR. It is a pool-type reactor; the maximum power will be 100 MWth. Its design allows a large experimental capability inside and outside the reactor core. Due to the high power density, the core primary circuit is slightly pressurized. Several equipments will be implemented in the reactor building and be used in support to the experimental programs (7 hot cells will allow the preparation and examination of test devices before and after irradiation, non-destructive examination benches (gamma spectrometry, X tomography, neutron imaging system) and specific laboratories (fission product lab, chemistry lab and dosimetry lab)).
In parallel to the construction of the reactor, the future staff training and the preparation of the organization, to operate the reactor safely, reliably and efficiently is a key item. In this framework, many actions are on-going to elaborate:

- the staffing and the organizational structure for the commissioning test phases and also for normal operation,
- the documentation in support to the reactor operation (safety analysis report, general operating rules, procedures, instructions, …),
- the maintenance, in service and periodic test programs,
- staff training programs by using dedicated facilities (simulator,…),
- commissioning test programs for ensuring that the layout of systems and subcomponents is completed in accordance with the design requirements, the specification performances and the safety criteria,.
- design and implementation of the first fleet of experimental devices in support to the commissioning test program and experimental program.

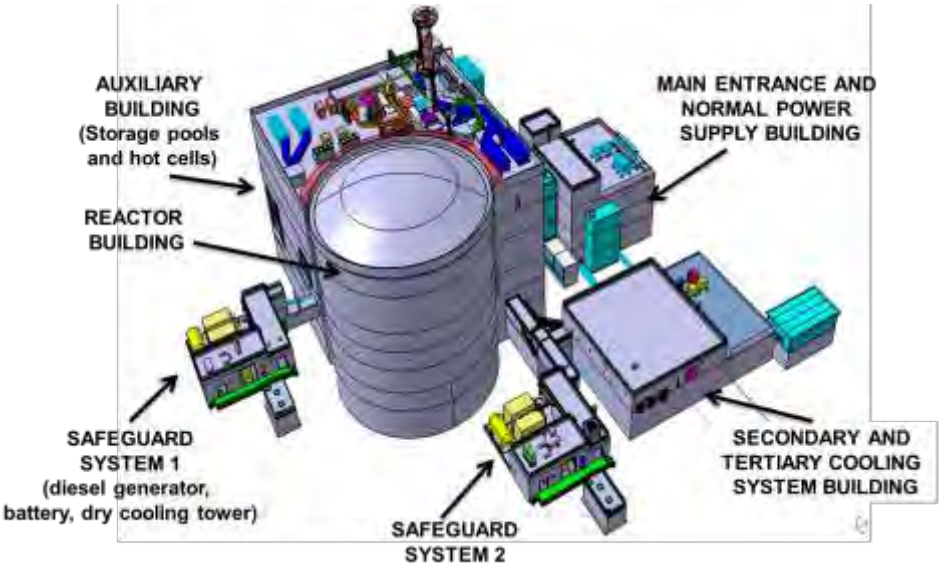


Fig.1 JHR Facility

2 Organization of the JHR project

The complexity of this unit, the organization of the JHR project and the safety requirements lead to a specific organization to prepare the facility commissioning. Concerning the organization of JHR project:

- The primary contractor, AREVA [12], has to design and to construct the future unit except the different equipments or systems in support to the experimental programs,
- CEA has :
    - to install and commission the experimental devices and equipments,

- to operate the reactor and the different system during the commissioning test phases and after during routine operation.

In 2010, a specific JHR section was set-up with 5 mains missions:

- Human Resources management to prepare the future operator,
- Setting-up of the operating referential (Safety Analysis Report, General Operating Rules…),
- Training and qualification of control room operator,
- Setting-up of the major contracts linked to the JHR operation (fuel assemblies, equipments, sub-contractors…),
- Design, manufacturing follow up, implementation and commissioning of the first fleet of experimental devices and associated equipments (nondestructive examination benches, laboratories…).

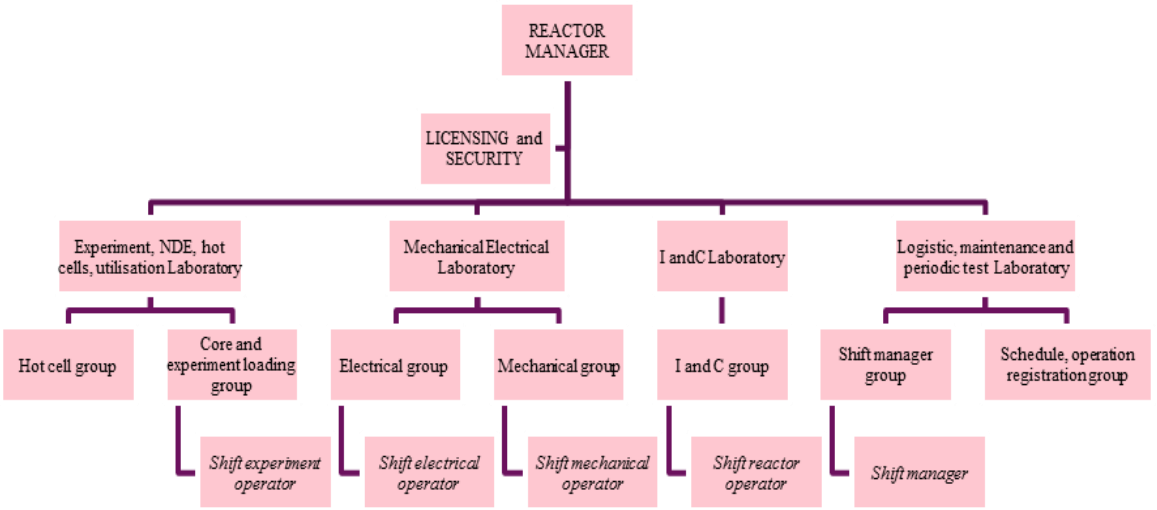
The future reactor operation and experimental systems operation staffs belong to this section to prepare the operation of the reactor and the nuclear auxiliaries as well as the integration of the test devices.These “mixed” staffs will contribute to enhance efficiency during this commissioning period but also for the future normal operation (existence of means shared between the operation and the experimental staffs to create a unique culture around the JHR).

3 Mains topics in preparation to start and operate JHR

3.1 Proposal of staffing and organizational structure

Based on the others research reactors feedback, the project of organization is also adapted to the reactor mission (neutrons for industry and medical application). This structure takes into account the future schedule of the reactor in operation and the maintenance and periodic test programs. The objective is to define clearly the responsibilities and the technical skills of each staff member (reactor manager, operation manager, shift manager and reactor operator) from the commissioning test phase to the normal operation.
JHR section and JHR project are also preparing the organization that will take place for the commissioning test program phase. The aim is to define the liability of each actor (main contractor, JHR project, future operator, contractors and sub-contractors).

For the future, an organization structure has been proposed and consists in two specific units: one to operate the reactor, the other one to conduct the experimental program.



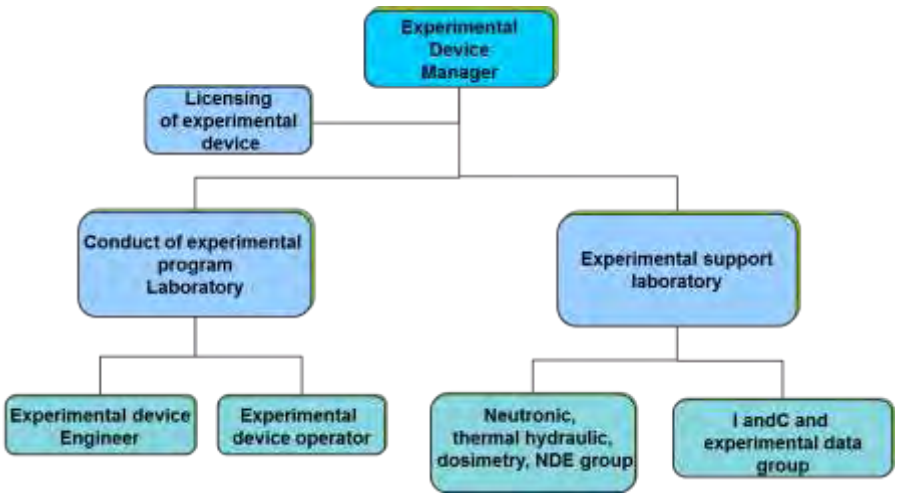


Fig 2. Organization structure to operate the reactor and to conduct the experimental program

3.2 Elaboration of the licensing and the operating documentation

3.2.1 Elaboration of the licensing documentation

Regarding the licensing documentation, CEA has to complete the project of Safety Analysis Report, provided by the primary contractor, with the test devices specifications (specific licensing document for each of them) and also with the largest possibilities of core configurations (number of fuel assemblies (34 to 37), enrichment (19.75 and 27% U235), thermal power (70 to 100 MWth)…) and the associated safety studies. For example, the PASSERELLE project is the safety report of the first « core » of the JHR (36 fuel assemblies, 19.75 % U235). The aim is to study the «best» loading of the core with a fuel

«consumption» optimization. It ensures the safety criteria and the core performances achievement.

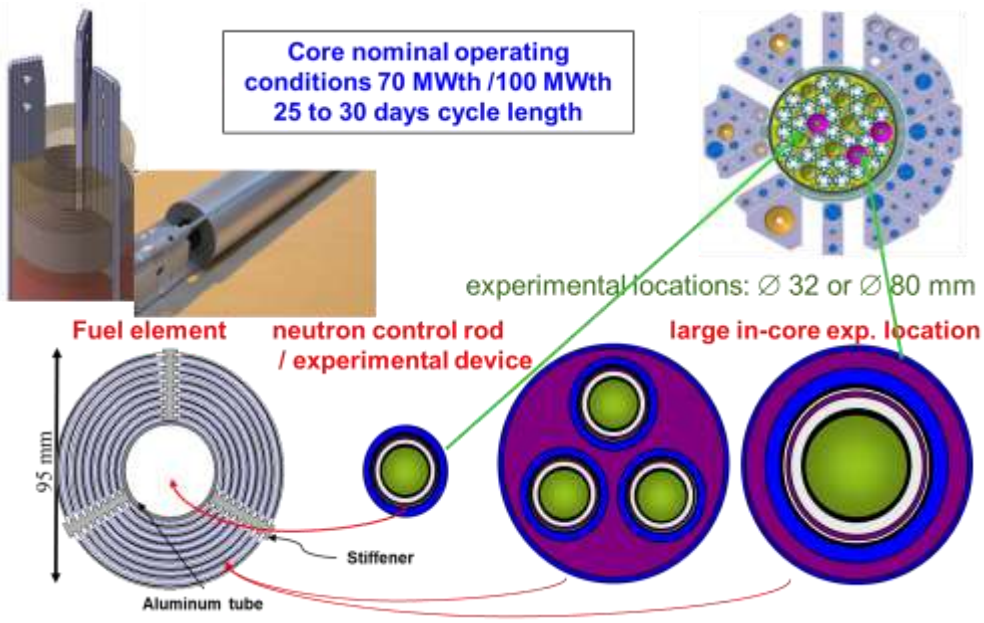


Fig 3. JHR core

This Safety Analysis Report is completed by General Operating Rules (description of reactor operations, strategy in case of incidental or accidental situations, periodic test and maintenance programs…).

3.2.2 Elaboration of the operating documentation

To elaborate the different documents in support to the commissioning test program and the future operation (routine operation), CEA has defined the operating documents structure based on the feedback of nuclear power plants, taking into account the specificities of experimental reactors. Three types of documents will be established:

- management and JHR safety and security referential documents (licensing),
- operating procedures (reactor and test devices),
- others activities (waste and nuclear materials management, transportation…).

JHR section is in support to the JHR project to follow the construction studies or the tests of the main utility equipments (primary pumps, the fuel handling machine, the hot cells equipments…) mainly for the operation and maintenance items. Through the documentation and the studies on going, the JHR section analyses the systems and the equipments to establish the maintenance and periodic test program but also begins to elaborate the reactor operating rules.

Approximately, 6000 documents will be mandatory to operate the reactor and the experimental hosting systems. Most of them will be validated during the commissioning test program, others by using the simulator (most of the incidental and accidental situations).

Operational procedures must provide direction and guidance to the reactor staff in the performance of operational activities, including the conduct of test devices but also for the technical and administrative support activities (training, waste management, human resources, nuclear materials management…). They are in accordance with the safety requirements.

Concerning the operating procedures, we have rules and instructions:

- the rules: these documents identify the requirements, the limit conditions to operate, the strategy to conduct the operation,
- the instructions: these documents are associated to the rules ; they provide step-by-step actions for accomplishing a specific task within that activity.

A specific item concerns the definition of the conduct strategy in incidental and accidental situations. The conduct strategy proposal, in incidental and/or accidental situations, is based on the feedback of the strategies applied in nuclear power plants, taking into account the specificities of experimental reactors and the specific design of the command control of JHR. All the incidental and accidental situations were identified; more than 200 Postulated Initiating Events (PIE), will be taken into account. The proposed strategy consists in separating the complex situations from the simple ones. For the complex situations, a document of «entrance to instruction » will allow:

- to confirm the expected automatic actions,
- to check the safety functions parameters,
- to realize a diagnosis with the aim of an orientation towards the adapted instruction.

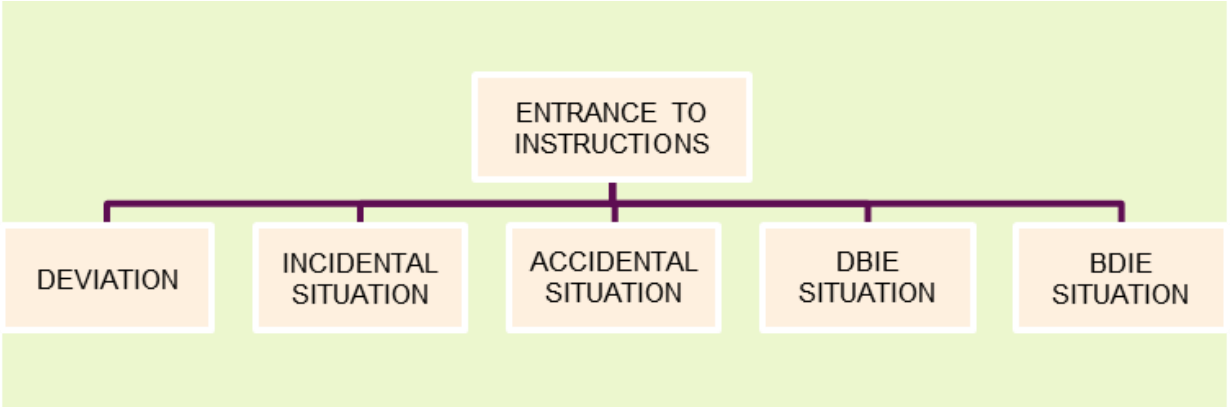


Fig 4. Conduct strategy in incidental and accidental situations

The orientation will be just a Deviation situation (D), an Incidental (I) or Accidental (A) situation or Design and Beyond Design Basis Accident (H and U) situations.

The sequence of events includes the actuation of the Safety Category 1 systems that control the process initiated by the Design Basis Initiating Events (DBIE). Where prompt reliable action is required to deal with DBIE, the reactor design includes the means to automatically initiate the operation of the necessary safety systems. This ensures that the three main safety functions, namely: reactor shutdown, core cooling, and radionuclides confinement remain fulfilled with a high degree of reliability. The design reduces operator actions as far as feasible, particularly for the period during and following an accident condition (within 30 minutes). This period is devoted to use «entrance to instructions».

Considering this first action to define the conduct strategy in incidental and accidental situations, the next step will be to elaborate the first procedure and perform the study to identify the best strategy. The final step will consist in validation by using a simulator.

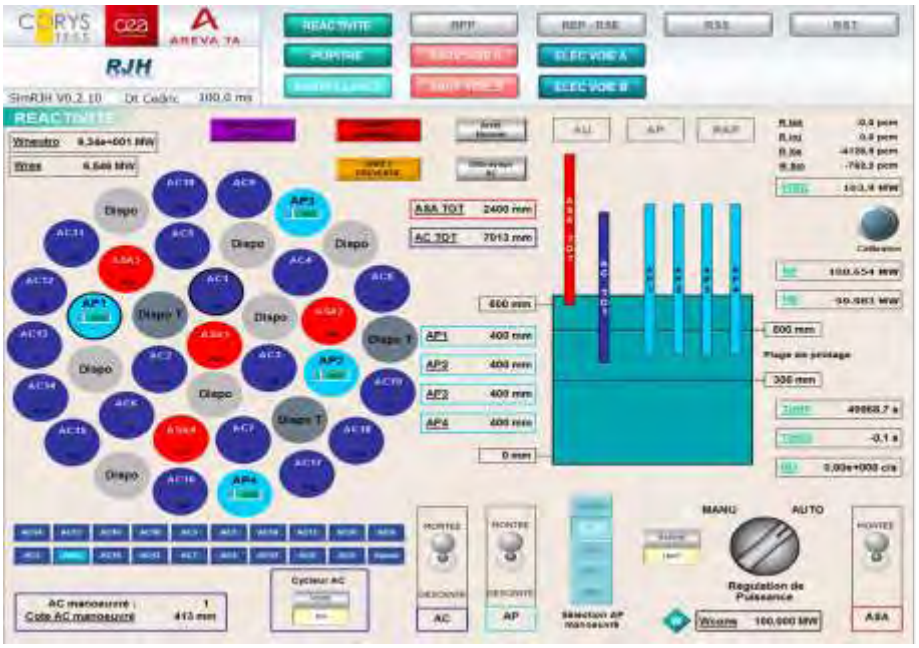


Fig 5. First version of the Simulator

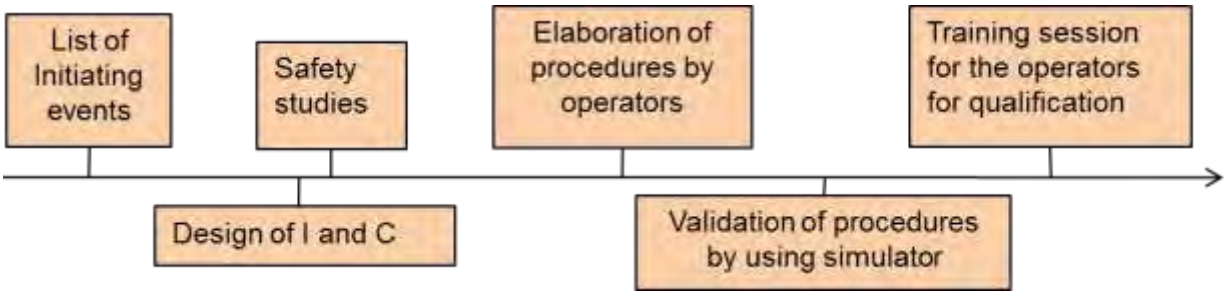


Fig 6. Logic of procedures establishment

3.3 Elaboration of the maintenance, in-service and periodic test programs,

After identifying the main Systems, Structures and Components (SSC), important to safety, a first inventory of maintenance, surveillance, inspection and testing activities has been performed. Taking into account the project of organization of the operator staff (number of operator and competences), an optimization of the maintenance plan has been proposed in three categories:

- the maintenance program which will be done by the operator,
- the maintenance program which will be done by a specific sub-contractor,
- the maintenance program which will be done by general sub-contractors managed by the Cadarache research center.

The objective of this categorization is also to optimize the maintenance subcontracting of a limited number of SSCs, to limit the risk of “external compromises” which would impact the reactor safety and the reliability.

This maintenance program should be reviewed since each contractor will send its own maintenance program strategy to confirm or modify the current project of maintenance plan. This part of activities has a huge impact on the reactor operation cost.

The in-service inspection and periodic test program will be in compliance with the requirements associated to the SSCs and depends on the different categories of classification (safety category 1 to 3). This program is adapted and optimized also with the schedule of the reactor in operation.

3.4 Elaboration of staff training program

As a basis of the future organizational structure, this training program for the future operators has been elaborated taking into account the feedback of similar worldwide nuclear facilities and the project of JHR organization structure. The strategy to establish this training plan was:

- to identify the different requirements for working in a nuclear unit (occupational health and safety, radiation protection, nuclear safety culture, waste management, nuclear materials management…),
- to identify the needs of competences for operating the reactor and the different circuits and establish the corresponding training program.

The training program preliminary inventory has identified approximately 130 different training courses. This program includes the JHR specificities. For the different phases of the project (commissioning test program, first start-up...) a schedule of the training sessions will be established in agreement with the actual annual recruitment of the reactor operation staff.



Fig 7. JHR Control room

3.5 Elaboration of commissioning test programs

The elaboration of the Commissioning Test Program consists to identify the needs of tests, instrumentation and/or calculations to verify the safety criteria and the performance of each Systems, Structure and Component (SSC) during the commissioning phases. The approach is a “step by step” one:

- Step 1: test assembly for each SSC,
- Step 2: functional test,
- Step 3: individual integration test,
- Step 4: global integration test.

Following some on-going studies (neutronic and thermal hydraulic calculations) specific devices/instrumentation, in support to the first core loading and the first start-up, will be developed. The aim is to check the JHR nominal performances and safety criteria (neutron and gamma detectors, temperature or flow sensors…).

The commissioning phases have been divided into stages:

- Stage A: test of the required SSC before fuel loading
- Stage B: fuel loading and approach to criticality tests
- Stage C: step by step power increase, and power tests.

These commissioning tests will also be helpful for transferring to the operating staff the knowledge on the installed systems.

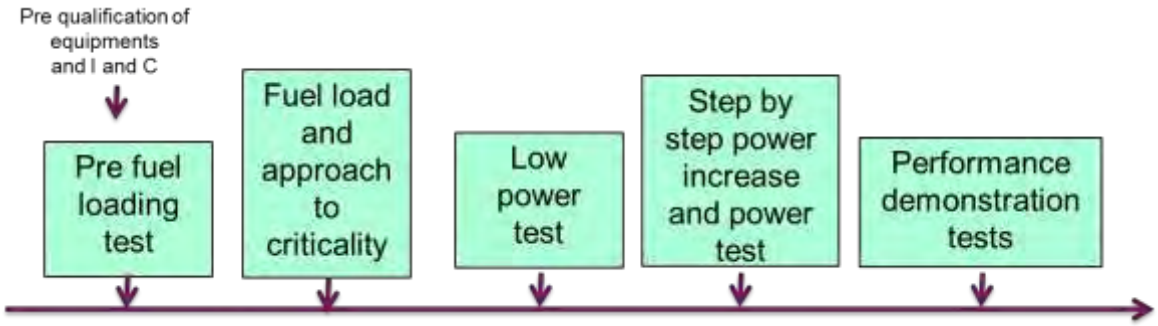


Fig 8. Different steps of the commissioning program

3.6 Design and implementation of the experimental device

CEA is developing a set of test devices that will be operational for the startup of the reactor or few years later. These experimental hosting systems will have to fulfil experimental needs concerning current NPP technologies (GEN II-III) and future reactors (GEN IV) as well.
Experimental programs could be related to either fuel basis properties acquisition, mastering of margins or improvement of fuel products (clad and pellet), in term of performance, safety, maximum burn up, innovative materials or extension of validation domain of fuel performance codes.
The main experimental hosting systems currently under design are:

- MADISON test device which will be available at the JHR start up, and will allow testing the comparative behavior of several instrumented fuel rods (between 1 to 8 rods of up to 60 cm fissile stack height) under NPP normal operating conditions (no clad failure expected).
- ADELINE test device which will be available for the JHR start up, and will allow testing a single experimental rod up to its operating limits. The fuel rod will be tested under conditions that correspond to off-normal situations with possible occurrence of a clad failure. The first version so called ADELINE “power ramps” will focus on the clad failure occurrence during one of these abnormal situations.
- LORELEI test device which will be available for the JHR start up and will allow testing a single rod under accidental situation that may lead to fuel damage. It will be able to reproduce all sequences of a LOCA-type transient, including the re-irradiation, the loss of coolant and the quenching phases, on a separate effect approach.

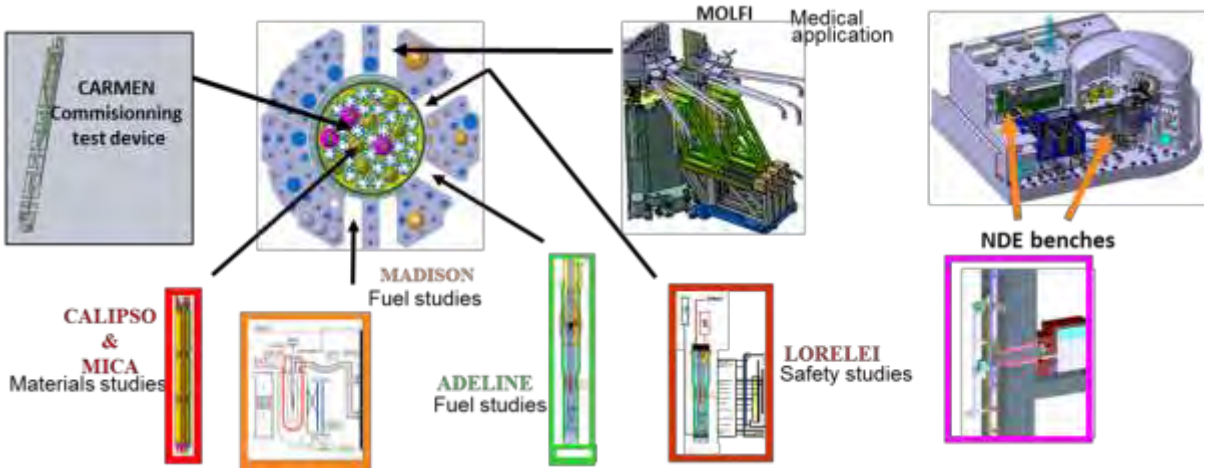


Fig 9. Set of test devices that will be operational for the startup of the reactor or few years later

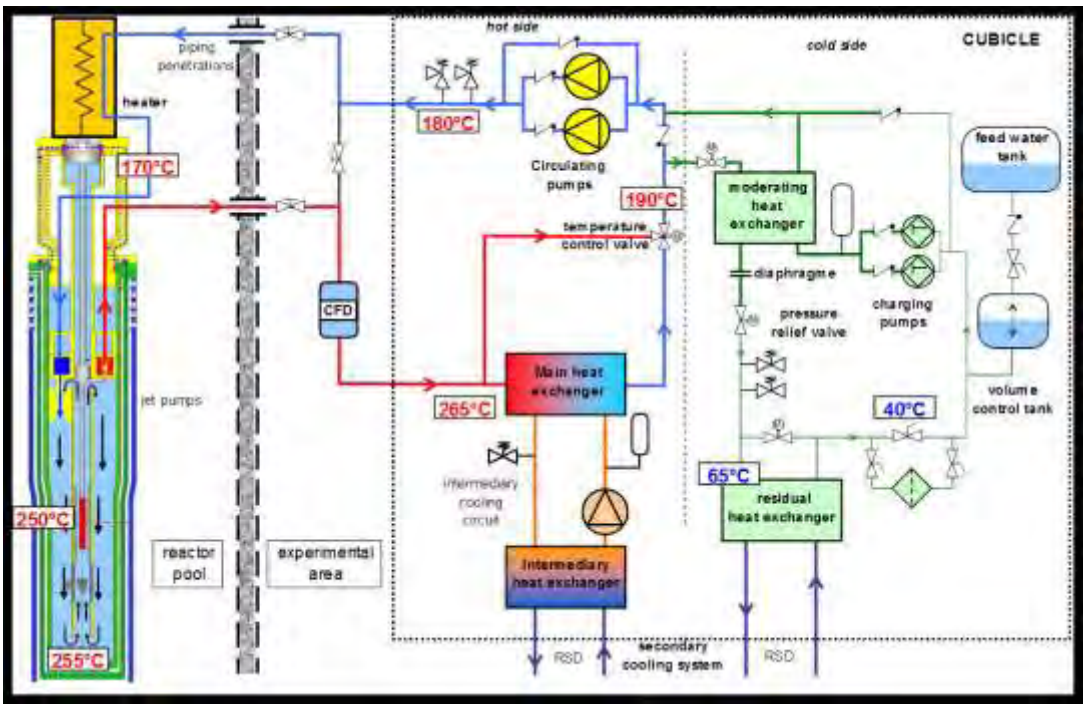


Fig 10. Schematic diagram of the ADELINE loop

These experimental devices dedicated to the fuel studies are completed by in-core and in reflector material test devices, corresponding to large ranges of irradiation conditions, in terms of temperature, neutron flux and neutron spectra. A special attention focuses on the improvement of the thermal stability and gradients in the interest zones of irradiated samples. Some specific devices will be described such as equipments designed to the qualification of reactor pressure vessel steels (OCCITANE test device), to the studies of creep-swelling of structural materials (MICA test device) or to the study of the stress corrosion cracking assisted by irradiation phenomena (CLOE test device: a corrosion loop with an accurate water chemistry monitoring for PWR or BWR requirements).

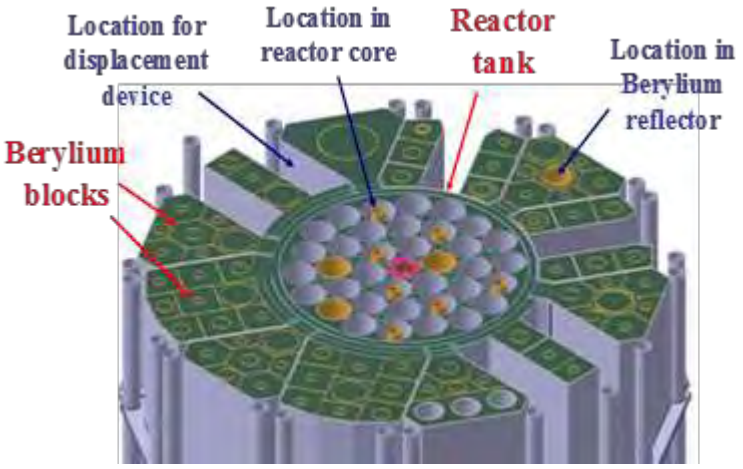


Fig 11. Schema of the JHR Block core

CEA has to design and implement the first fleet of test devices expected at the reactor start-up. JHR safety requirements are used also to design these experimental hosting systems. An important issue is the implementation of these test devices in the reactor: for each device, the

implementation in the reactor building is studied to identify, for example, the power supply and instrumentation and control cabinets needs and also the impact on the venting and effluents facility networks. The equipments in each experimental cubicle and the implementation of electrical cabinets are defined. The studies include also the use of hot cells, handling systems and temporary storage area. The JHR section uses the same “integrated system” (the CATIA software) as the primary contractor.

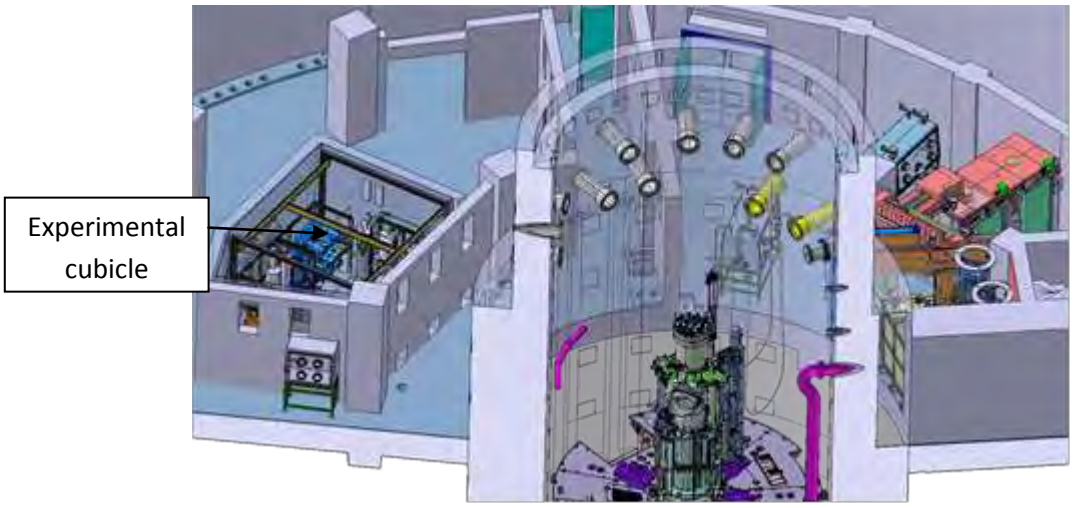


Fig 12. Layout of the experimental device in an experimental cubicle

4 Conclusion

The construction of JHR which started in 2007 is going-on with a first operation foreseen by the end of this decade. In parallel to the construction of the reactor, the preparation of the future staff and of the organization to operate the reactor safely, reliably and efficiently but also the design and realization of the first set of hosting device are important issues. This paper gives an overview of these actions to prepare the commissioning phases, the routine operation and the future experimental programs.



Fig 13. View of JHR site – December 2013

5 References

[1] The Green Paper, “Towards a European Energy Security Strategy”, published by the European Commission in November 2000

[2] FEUNMARR, Future European Union Needs in Material Research Reactors. 5th FP thematic network, Nov. 2001 – Oct 2002

[3] S. Gaillot and al.: “The Jules Horowitz Reactor Project - Experimental capabilities”. 10th IGORR conference, September 2005 – Gaithersburg Maryland, USA

[4] M. Boyard and al.: “The Jules Horowitz Reactor Project: JHR core and cooling design”. 10th IGORR conference, September 2005 – Gaithersburg Maryland, USA

[5] G. Bignan, D.Iracane, “The Jules Horowitz Reactor Project: A new High Performances European and International Material Testing Reactor for the 21st century”. Nuclear Energy International publication (NEI-Dec 2008)

[6] G. Bignan, D. Iracane, S. Loubière, C. Blandin, “Sustaining Material Testing Capacity in France: From OSIRIS to JHR”. 12th IGORR conference, October 2009 Beijing, China

[7] G.Bignan, P. Lemoine. X. Bravo, “The Jules Horowitz Reactor: A new European MTR (Material Testing Reactor) open to International collaboration: Description and Status”. RRFM 2011 Roma, Italy

[8] G. Bignan et al., “The Jules Horowitz Reactor: A new European MTR open to International collaboration”.13rd IGORR conference,September 2010, Knoxville ,TN –USA)

[9] G. Bignan et al.,”The Jules Horowitz Reactor: A new European MTR (Material Testing Reactor) open to International collaboration: Update Description and focus on the modern safety approach”. IAEA International Conference on Research Reactors: Safe Management and Effective Utilization, November 2011, Rabat, Morocco)

[10] J. Estrade and al., “The Jules Horowitz Reactor: a new high performances European MTR (Material Testing Reactor) with modern experimental capacities – Building an international user facility”. Research Reactor Fuel Management 2013, 21-25 April, 2013, St-Petersburg, Russia.

[11] C. Blandin and al., “LWR Fuel irradiation hosting systems in the Jules Horowitz Reactor”. LWR Fuel Performance Meeting 2013, 15-19 September 2013, Charlotte, NC, USA.

[12] H. Beaumont and al.:”The Jules Horowitz Reactor: Engineering Procurement Construction Management missions and Construction status”. 13th IGORR conference, October 2013, Daejeon - Corea.

RESEARCH REACTOR PROJECTS IN TUNISIA: CASE OF THE TUNISIAN SUBCRITICAL ASSEMBLY PROJECT

A. BEN ISMAÏL, W. DRIDI, M.A. NASRI, N. KAHLAOUI,
M. BEN ABDALLAH, N.REGUIGUI
Unité de Recherche UMTN-UR04CNSTN02, National Center of Nuclear Sciences and Technology, Sidi-Thabet Technopark 2020 Ariana Tunisia.

ABSTRACT

Several years ago, the National Centre of Nuclear Sciences and Technology (CNSTN) has conducted a feasibility study for the installation of its first research reactor. This reactor is intended to develop human resources for the future nuclear power programme, and to perform applied research and development in the nuclear field. The project was temporarily put on hold in 2010.

The CNSTN intends today to re-submit to the Government this same project of research reactor with an updated feasibility study including site reevaluation, and definition of the gaps in the necessary safety and technical infrastructure including the needs of human resources and adequate funding to support the operation and maintenance of the reactor.

In parallel with these efforts, CNSTN plans the installation of a subcritical assembly to support development of national human resources. The subcritical assembly will be extremely useful for carrying out research projects by scientists in order to provide them with a basic understanding of the main concepts relevant to nuclear reactors. Studies related to the site selection and to the technical characteristics of the facility, are currently in progress and almost finalised.

The state of the art and the detailed information, about the project of implementing a subcritical assembly in CNSTN, will be presented.

1. Introduction

A subcritical assembly is an outstanding example of a simplified low cost reactor which serves numerous purposes, including education, training, experimental research and providing practical experiences on the fundamental and applied physics of the fission process and of a nuclear reactor. Several facilities of subcritical assembly demonstrate today [1, 2] this wide list of applications. The implementation of a subcritical assembly in the CNSTN (National Center of Nuclear Sciences and Technology; a public institute belonging to the Ministry of High Education and Scientific Research), will serve as an efficient tool for educating and training students and for carrying out research projects by scientists in order to provide them with a basic understanding of the main concepts relevant to nuclear reactors. This facility is then selectively made available as a service to the community e.g. for industrial benefit and in particular to academic organisations as an institutional benefit.
The subcritical assembly project will contribute to the initiation of the first steps (including the enacting of new legislation and the establishment of competent and independent nuclear safety regulator) needed for the development of the Tunisian nuclear power programme and the related infrastructure.

The project of implementing the Tunisian subcritical assembly started in 2012. The project studies are currently focused on the finalization of the feasibility study and the bidding specifications. The design, construction and commissioning phases of the project are expected for 2016-2017.

This paper presents an overview of the study results already achieved under this project of Tunisia's first nuclear facility.

2. Facility description and foreseen applications

The subcritical assembly design and calculations are carried out in order to provide operators and users with an inherently safe tool, simple, reliable, easily operated with minimum operation and maintenance requirements. Parts of the subcritical assembly will be easily accessible for demonstration, inspection, and experimental purposes.

The subcritical assembly is planned to be light water moderated, and loaded with commercially available fuel; natural or low enriched Uranium (with maximum level of enrichment equal to 4%).
The effective multiplication factor (k_{eff}) will be less or equal to 0.90. The neutron emission rate, at an in core irradiation position, will be sufficiently high in order to ensure the expected applications listed below.
The subcritical assembly will be driven by an external neutron source, made with the combination of plutonium-beryllium (Pu-Be) or americium-beryllium (Am-Be). The neutron source will be driven, by a pneumatic control drive, into the reactor core. To shut down the reactor, the source will be driven back to its storage flask.

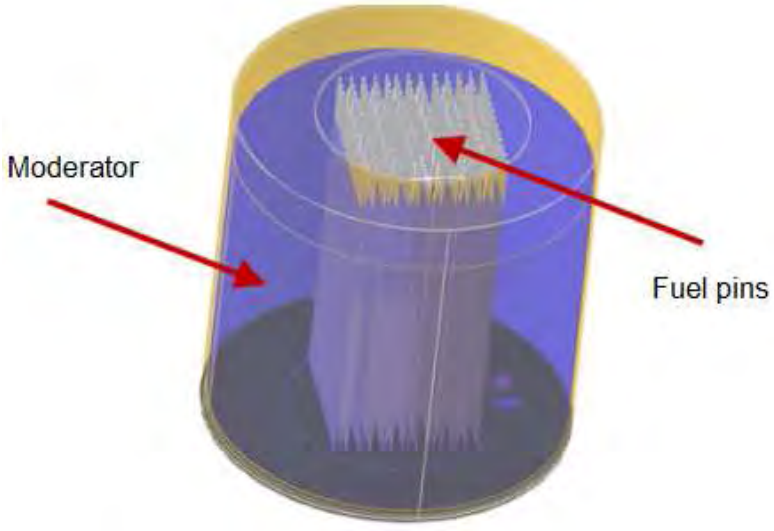


Fig.1 Preliminary model of the subcritical assembly,
showing the core in the water filled vessel

A wide list of nuclear experiments and measurements will be available, including: subcritical extrapolation experiment for fuel loading, source jerk experiment, Rossi-alpha measurement experiment, Feynman-alpha method measurement, neutron flux distribution (axial, radial and absolute) measurement, neutron energy spectrum measurement, neutron activation analysis (list of elements, that could be detected and analysed, will be established), and measurement of the neutron temperature.
An experiment of neutron source oscillating is also considered.

For the neutron activation analysis, at least one in core irradiation position will be implemented, in order to irradiate samples. The associated handling tools and suitable shielding, for the samples, are already seen.

3. Site characterization and infrastructure specifications

A number of studies for the site were conducted between 1993 and 1995 for the initial purpose of establishing the CNSTN and the associated construction of 2 MW nuclear research reactor. The study was further updated in 2000 by FRAMATOME ANP (now AREVA NP).
The study included the site characterization (topography, nearby installations and agricultural activities), geology, seismology (magnitude calculations within a radius of 10, 50 and 100 km, were performed), meteorological study (temperature and humidity), hydrology study (taking into account rain and floods), soil and biodiversity.
An update and validation of the site characteristics are being conducted. Their results will be included in the bid specifications, as they are essential for the design and safety analysis of the facility.



Fig.2 Layout of the proposed site for the subcritical assembly

An existing building (under construction) is already considered for the subcritical assembly implementation. The suitability of this site (location) is under evaluation, in order to identify important gaps and to define actions to address them.

For example, an extra shielding would be required for all walls (using probably concrete and, above the reactor hall, borated Polyethylene). This shielding will be calculated depending on the final design and configuration of the subcritical assembly.

The infrastructure will allow for : water supply and storage, water demineraliser unit, reservoir for collection and drainage of any water spillage within the rector hall, electric supply with uninterruptible power supply system, and special foundation (with extra protection) for the reactor vessel and operator platform.

Provision and requirements for safe and secure storage and radiation shielding, inside the reactor hall are already considered, both for the fuel (when uploaded) and for the external neutron source.

4. Modeling and optimisation

The development and application of advanced computational methods and tools for core modeling and optimization are ongoing. Benchmark exercises using two different Monte Carlo codes are expected.
The subcritical assembly reactor is being simulated using MCNP-5 [3] and GEANT4 [4] codes.

The MCNP-5 code, based on neutron transport theory, is used primarily for the simulation of nuclear processes, such as fission, but, also, has the capability to simulate particle interactions involving neutrons, photons, and electrons

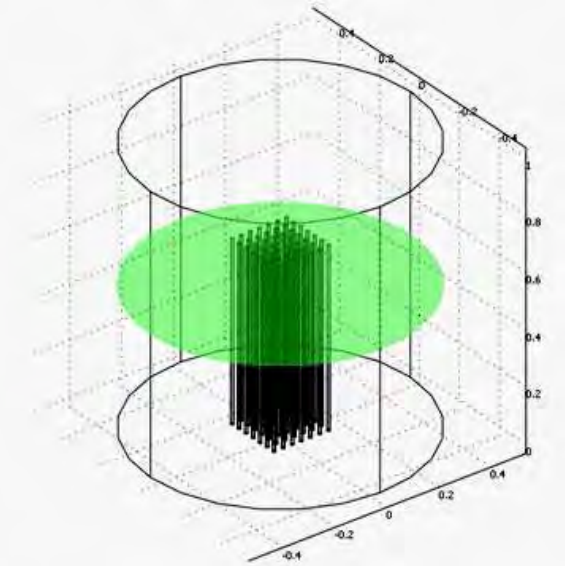


Fig.3 Monte Carlo modeling of the subcritical assembly reactor,
showing the core in the water filled vessel

GEANT4 is developed, revised and supported by an international collaboration from the high energy physics community. It is currently used to perform simulations of complex particle detectors. The version 10 of GEANT4 [5] supports event-level parallelism and becomes more accurate for the simulation of nuclear processes; Indeed, the neutron processes has been significantly improved, both for the cross section and the final-state modeling.

First results of criticality calculations, using these two Monte Carlo codes, are planned to be finalized within few months.

5. Conclusions

Important efforts, regarding the installation of the subcritical assembly, which is the first facility with nuclear material in the country, continue to be exerted. As the subcritical assembly project is planned as a preparatory step for installation of a new research reactor, a systematic approach, based on the IAEA safety standards and guidelines, in the development and implementation of this project, is applied.
Since the Tunisia's National Nuclear Safety Agency (NNSA) is currently under establishment, the implementation of the subcritical assembly project will be conducted according to the IAEA safety standards and guidelines.
However, a safety committee within CNSTN, independent from the project management, is being implemented, in order to perform independent safety reviews and assessments of the project phases and activities important to safety.
On the other hand, efforts are also exerted to ensure future integration of the subcritical assembly academic applications in national higher education curricula.

6. References

[1] J.L. Kloosterman, ‘Description of the Delphi subcritical assembly at Delft University of Technology.' Delft, (2003).

[2] N. Xoubi, ‘Design, Development and Installation of Jordan Subcritical Assembly’, Science and Technology of Nuclear Installations, vol. 2013 (2013).

[3] J.F. Briesmeister, ‘MCNP-A General Monte Carlo N-Particle Transport Code’, Los Alamos, (2000).

[4] S. Agostinelli et al., ‘Geant4: a simulation toolkit’, Nucl. Instrum. Methods Phys. Res. A. 506, 250 (2003).

[5] S. INCERTI et al, ‘The Geant4-DNA project’, Int. J. Model. Simul. Sci. Comput. 01, 157 (2010).

RMB: THE NEW BRAZILIAN MULTIPURPOSE RESEARCH REACTOR

J.A. PERROTTA, A.J. SOARES

Comissão Nacional de Energia Nuclear (CNEN)

Avenida Prof. Lineu Prestes 2242, 05508-000, Brazil

ABSTRACT

Brazil has four research reactors (RR) in operation: IEA-R1, a 5 MW pool type RR; IPR-R1, a 100 kW TRIGA type RR; ARGONAUTA, a 500 W Argonaut type RR, and IPEN/MB-01, a 100 W critical facility. The first three were constructed in the 50's and 60's, for teaching, training, and nuclear research, and for many years they were the basic infrastructure for the Brazilian nuclear developing program. The last, IPEN/MB-01, is the result of a national project developed specifically for qualification of reactor physics codes. Considering the relative low power of Brazilian research reactors, with exception of IEAR1, none of the other reactors are feasible for radioisotope production, and even IEA-R1 has a limited capacity. As a consequence, since long ago, 100% of the Mo-99 needed to attend Brazilian nuclear medicine services has been imported. Because of the high dependence on external supply, the international Moly-99 supply crisis that occurred in 2008/2009 affected significantly Brazilian nuclear medicine services, and as presented in previous IAEA events [1], in 2010 Brazilian government formalized the decision to build a new research reactor. The new reactor named RMB (Brazilian Multipurpose Reactor) will be a 30 MW open pool type reactor, using low enriched uranium fuel. The facility will be part of a new nuclear research centre, to be built about 100 kilometres from São Paulo city, in the southern part of Brazil. The new nuclear research centre will have several facilities, to use thermal and cold neutron beams; to produce radioisotopes; to perform neutron activation analysis; and to perform irradiations tests of materials and fuels of interest for the Brazilian nuclear program. An additional facility will be used to store, for at least 100 years, all the fuel used in the reactor. The paper describes the main characteristics of the new centre, emphasising the research reactor and giving a brief description of the laboratories that will be constructed, It also presents the status of the project.

1. Introduction

In 2009, pushed by the international Moly-99 supply crisis that occurred in 2008/2009, and that affected significantly the nuclear medicine services in the world, Brazilian government, decided to carry out a sustainability study, to decide about the feasibility to construct a new research reactor in the country. As demonstrated in reference [2], the result of the study, which was done following IAEA's recommendation presented on reference [3], was favourable to the construction of the new reactor, and Brazilian professionals started analysing its conceptual design.

In 2010, following recommendations of COBEN, a committee responsible for a bi-national cooperative agreement between Brazil and Argentina, a decision was taken to adopt, for the new research reactors of Brazil (RMB) and Argentina (RA10), a conceptual model based on INVAP designed OPAL research reactor, as a reference for radioisotope production and neutron beams utilization.

For the Brazilian RMB research reactor, in addition to radioisotope production and neutron beams utilization, two other requirements were established. The first one was the capability to test fuels and materials for the Brazilian nuclear program, and the second was the requirement to have, around the reactor building, the necessary infrastructure to allow the

interim storage, for at least 100 years, of all spent nuclear fuel used in the reactor. Details of these two characteristics will be given in the next sections.

2. Description of the reactor

RMB is a MTR open pool type reactor that uses beryllium and heavy water as reflector, and light water as moderator and cooling fluid. The power of the reactor is 30 MW, and its main requirements, established during the feasibility study, are: radioisotope production, to attend national demand beyond 2020; production of thermal and cold neutron beams for research and application in all areas; development of materials and nuclear fuels for the Brazilian nuclear program; neutron activation analysis; and silicon transmutation doping.
The core of the reactor is a 5 X 5 matrix, containing 23 MTR fuel elements, and leaving 2 positions available for materials irradiation tests. Each fuel element has 21 plates, with a meat made of low enriched (19,75%) Uranium Silicide-Aluminium dispersion (U_3Si_2-Al) clad with Aluminium. Dimensions of the fuel element are 80.5mm X 80.5mm X 1045mm, and meat dimensions are 0.61mm X 65mm X 615mm.
Three sides of the core are surrounded by a reflector vessel, filled with heavy water that acts as reflector for the neutrons produced in the core. The reflection on the fourth side is done with the utilization of removable beryllium blocks. These beryllium blocks are needed to allow RMB to be used as a tool for the Brazilian nuclear program. Figure 1 shows a top view of the reactor core and the reflector vessel.
The core is designed to have a cycle length of 28 days. To accomplish with this cycle, the fuel element is poisoned with Cadmium wires which are depleted together with the fuel element. Each fuel element has 42 Cadmium wires, which are placed on the fuel element alongside the fuel plates, one on each side of the plate. The Cadmium wires are 0.4 mm in diameter and 615 mm long. The core has also 6 independent Hafnium control plates, which move parallel to the fuel plates.

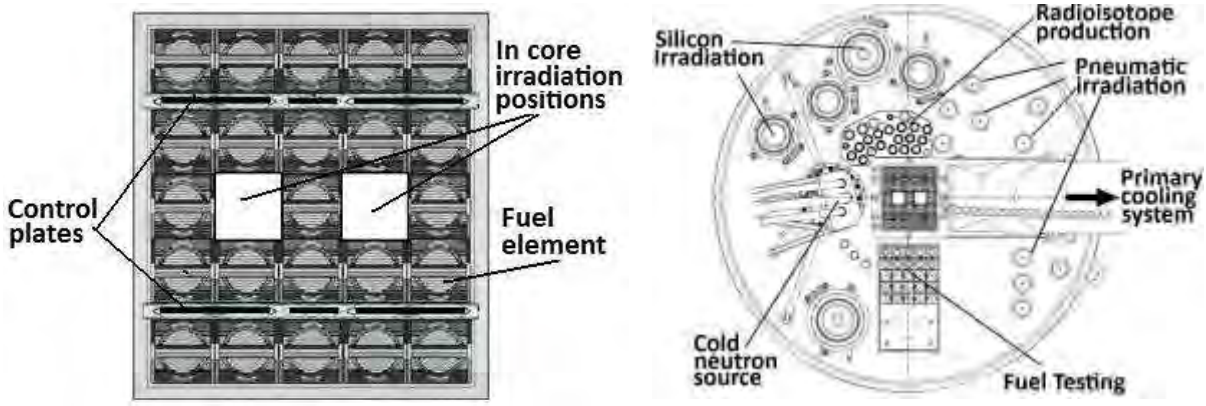


Fig 1. Top view of reactor core (left) and reflector vessel (right).

3. Reflector vessel

The reflector vessel is made of zircaloy, and it is installed in the bottom of the reactor pool, about 10.5 meters below water surface level. Filled with heavy water, it has an internal diameter equal to 2.6 meters and an internal height equal to 1.0 meter. It has 5 positions for neutron transmutation doping; 14 positions for pneumatic irradiation (9 with 3 vertical positions each and 5 with 2 vertical positions each); about 20 positions for bulk irradiation; one cold neutron source; 2 cold neutron beams; 2 thermal beams, 1 neutrongraphy beam and one position for fuel irradiation testing, where up to 2 rigs can be installed simultaneously. As explained before this fuel irradiation position constitutes one of the main differences between RMB and the reference reactor. The position has a 5 X 5 grid where beryllium blocks are placed to reflect the neutrons produced in the core when there is no fuel being tested. When used, the fuel irradiation position allows testing of fuel prototypes, simulating steady state and dynamic conditions (ramp tests and load following).

At least 10 of the bulk irradiation positions in the reflector vessel can be used to irradiate rigs with low enriched fuel miniplates, to produce Mo-99. Each rig is designed to produce, after 7 days irradiation, between 2400 and 3000 Ci of Mo-99, which will correspond to 400 and 500 Ci, respectively, after 6 days calibration.
On the lower part of the reflector vessel there is a skirt, whose interior is divided into two parts. The central part is used as water inlet for the primary reactor cooling system, and the outer section, between the central part and the wall of the skirt, is used as water outlet for the reactor pool cooling system. Figure 2 shows a perspective and a cutaway view of the reflector vessel.

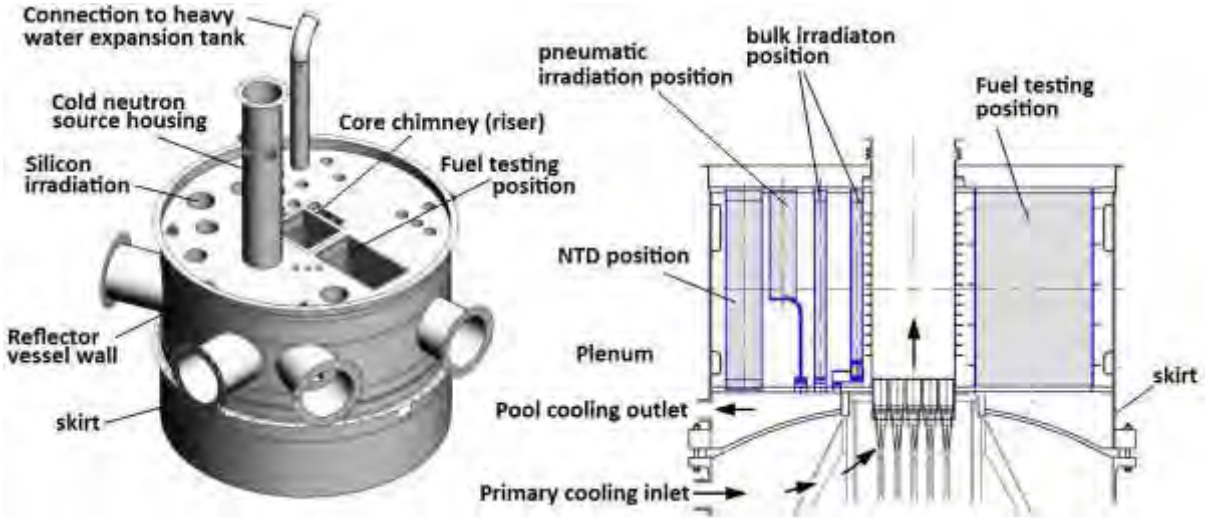


Fig 2. Perspective (left) and cutaway (right) views of the reflector vessel

4. Reactor and service pools

The reactor pool is a 5.1 meters diameter, 14 meters high cylindrical tank made of stainless steel, filled with water up to the 12.6 meters level. It houses the reflector vessel, a small spent fuel storage rack, with capacity to store up to 32 fuel elements; the bundles of tubes used for pneumatic irradiation; the internal piping that form the inlet and outlet of the primary and pool cooling systems; nuclear and process instrumentation; auxiliary support and mechanical structures, and the water inventory, required for the pool cooling system to perform its functions. The tank is embedded in a concrete block, anchored to the concrete by a set of reinforcement rings and clamps at the bottom. The bottom of the pool has 5 penetrations, one for the control plates driving mechanisms, and four for the heavy water system. One of the heavy water connections is used for drainage of the reflector vessel, two are used as inlet and outlet of the heavy water cooling system; and the forth connection is used as an alternative system to shut down the reactor. This connection has a set of valves that once open, removes about 50% of the heavy water in less than 15 seconds, assuring that the reactor is kept shutdown, even after returning to normal temperature.
Adjacent to the reactor pool there is the service pool, a 9.0 meters high rectangular stainless steel structure, with maximum water level equal to 7.6 meters. The service pool houses a spent fuel storage rack with capacity to 600 spent fuel elements, the equivalent to 10 years of operation; some containers specially designed to store damaged fuel assemblies; a basket for solid waste storage; a transport cask platform; a structure to store the reactor isolation gate; internal piping of the pool cooling system; pool lighting supports; and racks used for decay of materials irradiated in the reactor and that needs further processing, like Silicon, the miniplates for Mo-99 production, etc., The service pool also is the entrance of an elevator, which connects the service pool to a hot cell, named Moly Hot Cell, which is part of a system used to transfer the miniplates to a transport cask. The service pool is connected to the reactor pool by a transfer channel. The transfer channel, also made of stainless steel, has a 5.0 meters layer of water, which works as biological shielding when the spent fuel, or any material irradiated in the core, is transferred from the reactor pool to the service pool. A

sliding gate, when installed in a groove of the transfer channel, allows maintenance of one pool without the need to empty the other pool. Figure 2 shows a perspective view of the reactor and service pools.

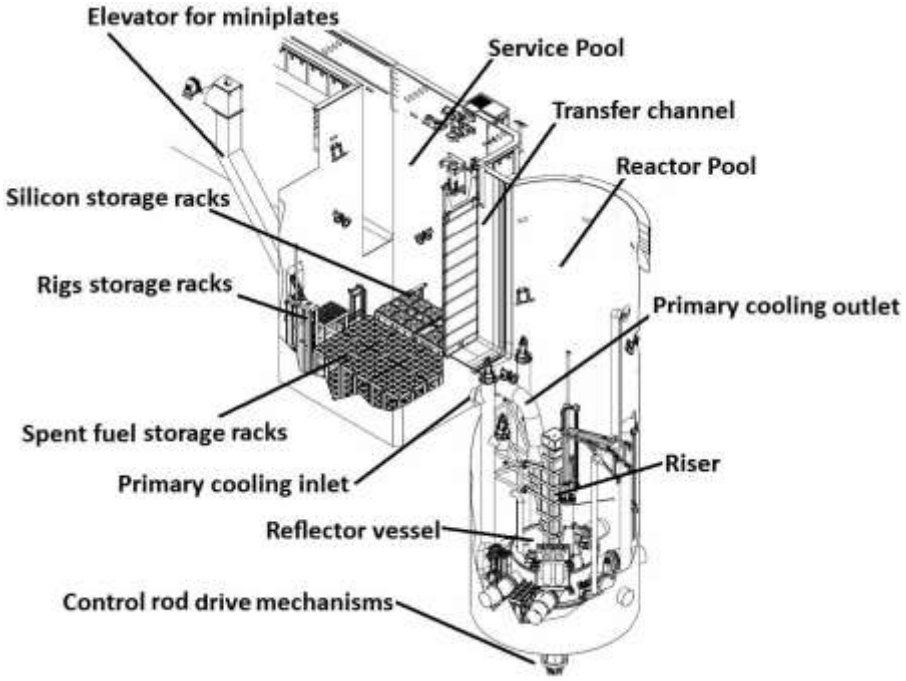


Fig 3. Perspective view of the reactor and service pools

5. Reactor and pools cooling systems

Light water is used for cooling the reactor core and the internals of the reactor and service pools. The water used in the reactor primary cooling system enters the reactor pool through two pipes installed about one meter below the transfer channel, and flows down to enter in the lower part of the reflector vessel, then flows upward through the reactor core, and through a riser installed on top of the reflector vessel, leaving the reactor pool through a single pipe also installed below the transfer channel, as shown in figure 3. The volume of water that flows through the core represents 90% or the total flow in primary cooling system. The other 10% comes from the top of the reactor pool. It enters the top of the raiser and flows down to the outlet piping. By using this design, all N-16 produced in the water, when it passes through the reactor core, goes directly to the N-16 decay tank, installed below the service pool.

The primary cooling system has 3 circuits. Each circuit has a pump, with inertia flywheel, and a plate type heat exchanger with capacity to remove 50% of the heat generated in the reactor core. One of the circuits remains in standby during normal operation.

In addition to the 10% of water that flows in the primary cooling system, the reactor pool has another equivalent volume of coolant that flows downward in the reactor pool, passes through the radioisotope production and silicon irradiation rigs, and enters a plenum between the primary cooling inlet region and the external wall of the skirt installed on the lower part of the reflector vessel, as shown in figure 2. The water leaves the plenum through a pipe that goes upward, leaving the reactor pool close to the transfer channel. The inlet and outlet pipes of both cooling systems, the primary cooling system and the pools cooling system, have siphon brake and flap valves on their top positions. The siphon brake valves are installed to prevent the accidental loss of water as a consequence of a siphon effect following the unlikely rupture of a pipe outside the pool, and the flap valves are installed to allow the establishment of the natural circulation process, to cool the reactor core, following the reactor shutdown.

A 1,5 m thick hot layer on top or the reactor and service pools, provides a non-activated stable water layer over the pools. It prevents active particles from reaching the surface of the

pools, reducing significantly the radiation dose to reactor operators. The hot layer temperature is 8 ºC higher than the pool water temperature.

6. Reactor control and shutdown systems

Six independent Hafnium control plates are used to control the fission process in the RMB research rector. Each control plate has an extension which has a magnetic disc at the end, and is driven by an independent mechanism installed in a sealed compartment below the reactor pool. The driving mechanism is based on a system known as “rack-pinion”, having on its extremity an electromagnetic assembly. When active, an electric current passes through the electromagnetic assembly and engages the magnetic disc, allowing the movement of the respective control plate. The movement is upwards for removal from the core, and downwards for insertion. Once the electric current is interrupted, the magnetic disc automatically disengages from the eelectromagnetic assembly, and the control plate falls by gravity. Compressed air, from a pneumatic cylinder, helps to accelerate the introduction of the control plate into the reactor core.
The negative reactivity inserted by any combination of five control plates is enough to keep the reactor shutdown, and if for some reason, following a “scram signal” it is detected that two control plates have not reached to bottom position, a second “scram signal” is generated. This second “scram signal” is used to open a series of valves that result in the removal of about 50% of the heavy water from the reflector vessel; quantity enough to assure keeping the reactor shutdown even when it returns to ambient temperature.

7. The spent fuel storage building

To comply with the requirement to allow the interim storage, for at least 100 years of all spent nuclear fuel used in the reactor; a building, named “Spent Fuel Storage Building”, was designed adjacent to the reactor building. This building, which can be accessed directly from the reactor building, will have two additional pools, one for temporary wet storage of the spent fuel used in the reactor, and the other for handling and dismantling rigs that were used for material and fuel irradiation tests.
The temporary spent fuel storage pool is a stainless steel structure, similar to the service pool. The pool has only three items, the spent fuel storage rack, the inlet piping from the pool cooling system, and the pool lighting system. The spent fuel storage rack has a capacity to store 1200 spent fuel elements, the equivalent to 20 years of reactor operation. In order to improve water distribution injection and water circulation through the fuel assemblies, the diffuser of the pool cooling system is placed below the storage rack. The pool cooling system has a derivation that is used to continuously purify the water, before it returns to the pool.
The handling and dismantling pool is also a stainless steel structure. It houses several racks, with capacity to store 4 in-core irradiation rigs, 2 used cold neutron sources, 1 fuel irradiation loop, and 2 isolation gates, one for the temporary storage pool and the other to isolate the pools from a “delivery transfer channel”, that connects the two pools with the service pool, located in the reactor building. The pool has also the pool lighting system, the piping of the cooling and purification system, and a transport cask platform, needed to receive a cask that will be used to transfer the spent fuel to a dry storage position. Figure 4 shows the temporary spent fuel storage pool and the handling and dismantling pool.
The two pools of the spent fuel storage building plus the reactor pool and the service pool, these last two located in the reactor building, form a stainless steel structure embedded in a concrete block, as shown in figure 5. Three hot cells located in the reactor building and one hot cell in the spent fuel storage building complement the concrete block.
According to the conceptual design of the spent fuel storage building, after 20 year of decay, the spent nuclear fuel shall be transferred from the storage pool to a dry storage position, located in the level -6,00 of the building. For this operation, a dual purpose cask (for transport and storage) is lowered in the transport cask platform, installed in the handling and dismantling pool. After being filled with spent fuel assemblies, the cask is taken to an area

where it will be properly dried, and then transferred to level -6,00 of the building, where 150 dual purpose casks can be stored for at least 100 years.

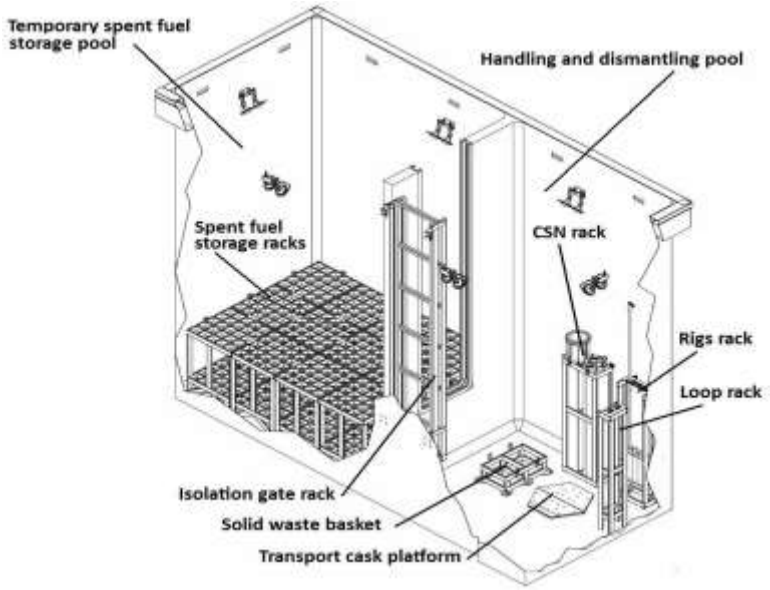


Fig 4. The temporary spent fuel storage and the handling and dismantling pools

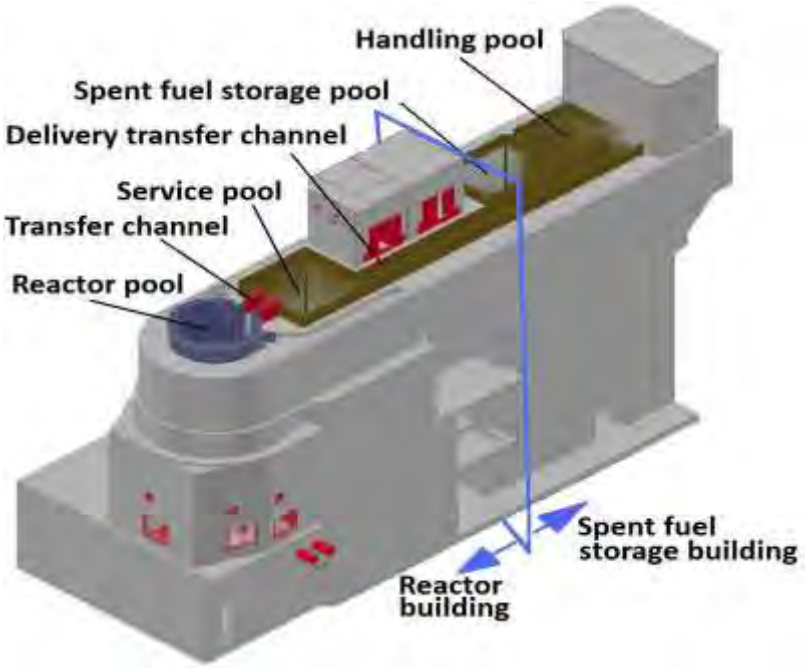


Fig 5. Pools embedded in the concrete block

A system comprising two ante cameras and two isolation gates, maintain the physical and environmental separation between the reactor and the spent fuel storage buildings.

8. The research and production nucleus

The reactor and spent fuel storage buildings are the centre of what is called the “research and production nucleus”, which includes a radioisotope production facility and three laboratories, one for research utilizing neutron beams, one for neutron activation analysis and the third one for post irradiation analysis of irradiated materials and nuclear fuels.
The radioisotope production facility will have two lines of hot cells, the first one for production of radioisotopes, like Mo-99 and I-131, and the second one for “sealed sources”, like Ir-192 and I-125, for industrial and medical applications. According to the established requirement,

it will have the capacity to produce radioisotopes and sealed sources to attend the national needs beyond 2020.
The neutron beams laboratory will have lines of thermal neutrons, for experiments like high resolution diffractometry, high intensity diffractometry, Laue diffractometry, residual stress diffractometry, and neutrongraphy; and lines of cold neutrons, for experiments like small angle neutron scattering (SANS), reflectometry, prompt gamma analysis and others that are under analysis.
The radiochemistry laboratory will have two pneumatic connections to receive long life irradiated samples, plus five pneumatic tubes connected directly to the reflector vessel, for cyclic irradiations of short life products and delayed neutron activation analysis.
The post irradiation laboratory is the facility that, together with the reactor, allows irradiation tests of materials and fuels needed for the Brazilian nuclear program.
Seven more facilities complement the research and production nucleus, the reactor auxiliary building, the cooling tower complex, the electrical supply and distribution building, a radioactive waste management facility, a workshop, an operator's support building, and a researcher's building. Figure 6 shows the main facilities of the research and production nucleus.

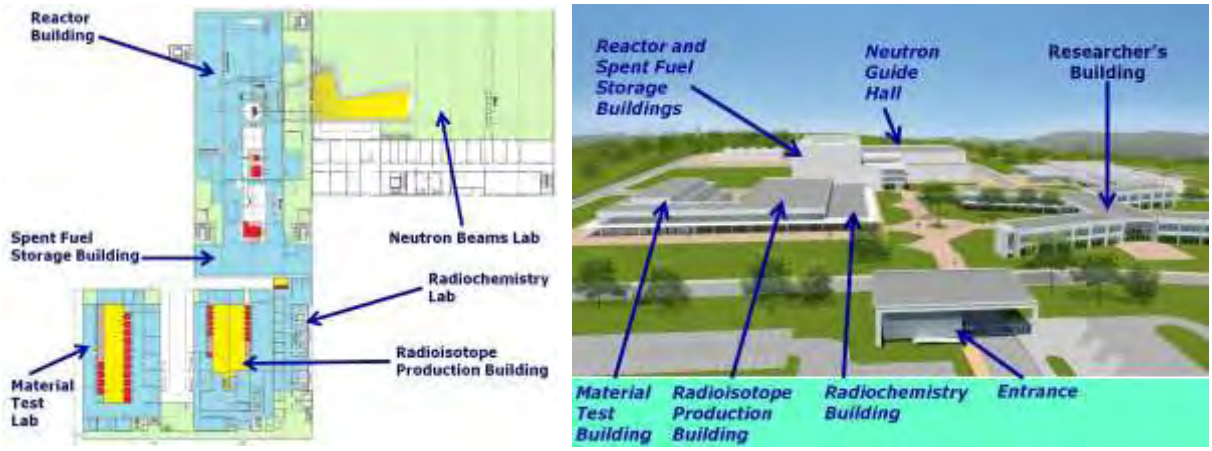


Fig 6. Plant (left) and perspective view (right) of the RMB research and production nucleus.

9. The RMB nuclear research and production centre

RMB is a new nuclear research and production centre that will be built in a city about 100 kilometres from Sao Paulo city, in the southern part of Brazil. The centre will have, in addition to the research and production nucleus, an administrative centre and an infrastructure centre to attend all the needs of the centre. The administrative centre will have a library, an administration building, a hotel, a restaurant, an ambulatory, and a training centre. The infrastructure centre will have a water treatment plant, a warehouse, a workshop, a facility for the fire brigade, a garage, a sewage treatment station, a chemical treatment plant, a meteorological station, the main gate, and the electrical substation. Shown in figure 7, RMB Centre has an area of about 2 millions square meters.

10. Status of the project

In 2011, the Ministry of Science Technology and Innovation allocated R$ 50 Mi (about US$ 25 Mi) for the conceptual and basic designs of the complex. It allowed, in 2012, the signature of a contract, with a Brazilian company, to develop the engineering work for the conceptual and basic design phases of all buildings and facilities of the centre, excluding the reactor and connected systems; and in 2013 the signature of the contract with INVAP for the work related to the preliminary engineering of the reactor and connected systems. Conclusion of both contracts is planned for the middle of 2014.
Also in 2012, a contract was signed, with a Brazilian company with tradition in environmental studies, to perform environmental and site studies. The report was finished by middle 2013,

allowing the starting of environmental and nuclear licensing processes, with presentation of site and local reports, requirements for first license. They were also the basis for the three public hearings, done in October 2013.



Fig 7. Artistic view of RMB nuclear research centre.

Site topography was already surveyed; geological sampling completed, and a meteorological tower was installed and it is operational since 2012.
Next steps are: conclusion of the basic and preliminary engineering, development of detailed design, manufacturing, construction, assembling and management. These phases will be carried out by national and international companies, and for these activities, a provision was made in the national budget, but not yet confirmed.
Total project remaining time span is estimated in 5 years after contract signature and subject to availability of funds.

11. References

[1] I. J. A. Perrotta, J. Obadia, “The RMB project development status”, on Proceedings of the 2011 International Conference on Research Reactors: Safe Management and Effective Utilization, held in Rabat, Morocco, 14-18 November 2011; International Atomic Energy Agency, Vienna, Austria (2012), available at: http://www-pub.iaea.org/MTCD/Publications/PDF/P1575_CD_web/datasets/abstracts/C6Perrotta.html

[2] I. J. Obadia, J. A. Perrotta, “A sustainability analysis of the Brazilian Multipurpose Reactor Project”, on Transaction of 14th International Topical Meeting on Research Reactor Fuel Management (RRFM-2010), held in Marrakesh, Morocco, 21-25 March 2010; European Nuclear Society, Brussels, Belgium (2010), ISBN 978-92-95064-10-2, available at: http://www.euronuclear.org/meetings/rrfm2010/transactions/RRFM2010-transactions-s6.pdf

[3] International Atomic Energy Agency, “Specific Considerations and Milestones for a Research Reactor Project”, Nuclear Energy Series NP-T-5.1, IAEA, Vienna, (2012), ISBN: 978–92–0–127610–0, Available at: - http://www-pub.iaea.org/MTCD/publications/PDF/Pub1549_web.pdf



Innovative Methods in Research Reactor Analysis and Design

ANALYSIS OF SMALL RESEARCH REACTOR WITH UMO FUEL USING MCNPX AND MULTI-GROUP NODAL DIFFUSION METHODS

MUSTAFA K. JARADAT, SALIH KHAFAJI
Research Reactor Department, Jordan Atomic Energy Commission
P. O. Box 70, Amman 11934, Jordan

CHANG JE PARK, BYUNGCHUL LEE
Reactor Core Design Division, Korea Atomic Energy Research Institute
1045 Daeduk-Daero, Yuseong-Gu, Daejeon, 305-353, Korea

ABSTRACT

Nodal diffusion method is used to study a 3 MW material testing reactor with a 3x3 fuel assembly arrangement fueled with UMo, and reflected with beryllium at all sides. The calculations also are performed by MCNPX code which was used as reference for the results of the 3D multi-group nodal diffusion code. Depletion calculations carried out using TRITON-NEWT system with the 3D multi-group nodal code and compared with MCNPX. TRITON-NEWT is a SCALE6 module which is used to obtain multi-group burnup dependent homogenized cross section needed for nodal code. The nodal code is used to study the neutronics parameters of the equilibrium core for UMo fuel and compare it with U_3Si_2 fuel to check the performance of the UMo fuel. The use of nodal diffusion theory for such a small core could present some difficulties but good results have been obtained and this code can be used for fuel management studies.

1. Introduction

UMo fuel is a promising candidate for a high performance research reactor and provides better fuel performance including an extended burnup and swelling resistance. Additionally, its relatively high uranium content provides high power density. However, when irradiating UMo fuel in the core, lots of pores are produced due to an extensive interaction between the UMo and Al matrix. The pore leads to an expansion of fuel meat and may result in a fuel failure after all. However, in terms of neutronics, the absorption cross section of Mo is much higher than that of Si, and thus a slightly high uranium density of UMo fuel is required to provide equivalent characteristics to U_3Si_2 fuel. It is also published that the core performance difference with silicide and moly fuel types is small. [1]
To review and make the neutronics characteristics of UMo fuel clear, a small 3 MW MTR core was proposed and depletion calculations have been carried out using MCNPX and using the multi-group nodal diffusion code.[2] First the results of the multi-group nodal code will be compared with MCNPX results. After that multi-group nodal code in combination with TRITON-NEWT system will be used for equilibrium core analysis of the MTR core for UMo fuel and compare it with U_3Si_2 fuel.[3][4]

2. MTR Core Description:

The assumed MTR core consists of 9 fuel assemblies of plate type fuel in 3x3 arrangements. Each assembly contains 21 fuel plates, the parameters of the fuel assembly is given in Table 1. It is reflected with beryllium at all sides except at top and bottom, and moderated with light water. The beryllium square block has side length of 77.2 mm. The thermal power of the reactor assumed to be 3 MW. The core is designed without considering control rods for the purpose of study.

Table 1 Specifications of the fuel assembly for a small research reactor

Meat thickness (mm)	0.51
Meat width of standard FA(mm)	62.1
Cladding thickness (mm)	0.38
Moderator channel thickness (mm)	2.35
Side plate thickness (mm)	4.8
Number of plates in standard FA	21
FA size (mm)	77.2 x 77.2 x 640

The assumed core is using LEU silicide fuel with U-density of 4.8 g/cc or uranium molly fuel with U-density of 5.0 g/cc. The enrichment of uranium is 19.75 wt% U-235, which is a typical value in research reactors. A description of the fuel materials is given in Table 2.

Table 2 Isotopic composition of U-7Mo and U_3Si_2 fuels

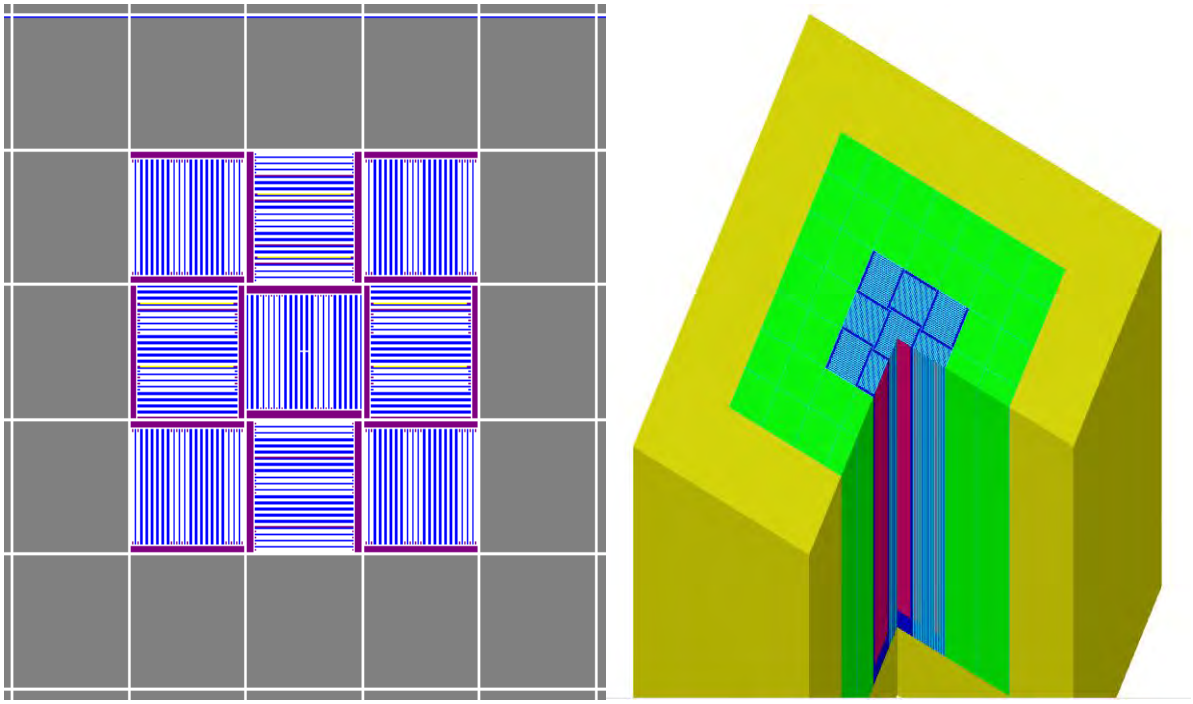
Isotope	**U_3Si_2 wt%**	**U-7Mo wt%**
U-234	1.163E-01	1.090E-01
U-235	1.454E+01	1.362E+01
U-236	1.621E-01	1.519E-01
U-238	5.881E+01	5.510E+01
Mo / Si	5.970E+00	5.203E+00
Al	2.040E+01	2.583E+01
Total	100	100
U density	4.8 gU/cc	5.0 gU/cc
Fuel Density	6.159 g/cc	7.234 g/cc
U-235 loading per FA (g)	403.52 g	420.34 g

The MCNPX model for the core describes the fuel assemblies by individual fuel plates. Each beryllium reflector element is modeled separately. Fig.1 gives a general view of the proposed core with fuel and reflector assemblies. In x-y-z directions the overall 3D model extends to 85x85x80 cm. The material composition of the fuel is given per fuel assembly. The burn-up dependent fuel composition is determined separately. The depletion of beryllium and the photo neutron production in beryllium have been neglected. For the calculations the ENDF/B-VII data library was used as distributed with the MCNPX-2.7 package.

3. UNM Code System:

UNM code is a multi-group 3D nodal diffusion code uses the unified nodal method (UNM) to solve 2G and MG neutron balance equation. This code was validated using well-known LWR

benchmark problems and also for the IAEA 10 MW MTR benchmark problem The code uses the homogenized cross sections generated by TRITON-NEWT system. This code will be used to perform research reactor calculations, the eigenvalue k_{eff}, thermal and fast flux distribution, and power distribution can be obtained from this code. [5] This code also can be used for reactor burnup or core follow calculations. Fig.2 shows the flow-chart diagram of the 3D UNM simulator.



(a) (b)

Figure 1 (a) Cross sectional view and (b) 3D model of the 3x3 core

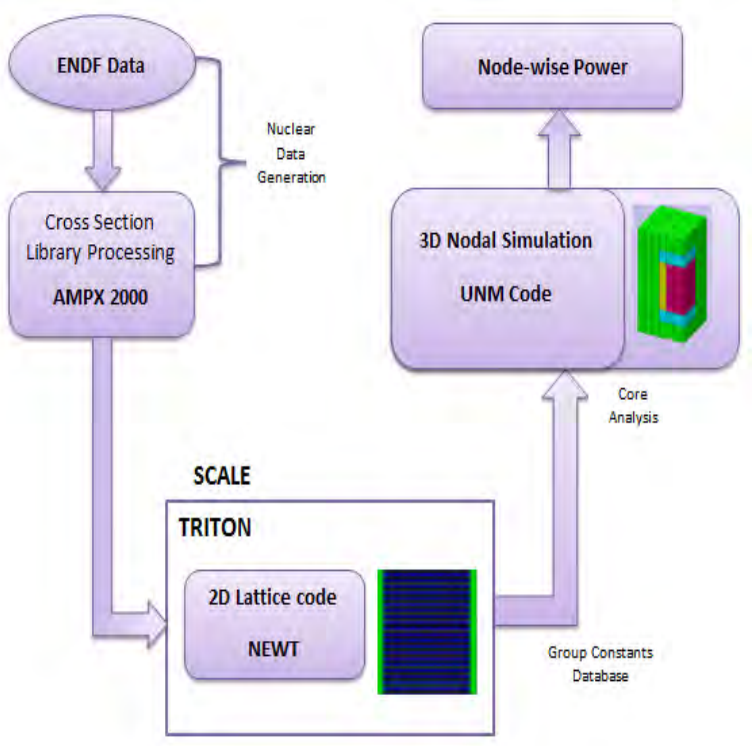


Figure 2 Reactor core analyses with 2D lattice code and 3D Nodal simulator

4. Depletion Calculations Results

Depletion calculations have been performed using MCNPX and nodal code with two types of fuel: U-7Mo and U_3Si_2. The MCNPX results were used as a reference for the results of the nodal code calculations with 2G and 6G. For the nodal code the average burnup of the core which was obtained from MCNPX was used to obtain cross sections from TRITON-NEWT system. So the fuel assemblies have the same burnup and equal the average burnup of the fuel assembly, this will help to obtain the cross sections easily. 250 days depletion was performed for MCNPX input with total 8 steps. The fuel and other materials temperature is 293 K was used for the calculations. The power density which was used to perform calculations for TRITON-NEWT system is 156.96 MW/MTU for U-7Mo and 163.15 MW/MTU for U_3Si_2. For MCNPX calculations the power which was used is 3 MW for both materials. The dependence of k_{eff} on the burnup of the assemblies is shown in Fig.3, the results of nodal calculations with 2G and 6G are shown with the MCNPX results for comparison.

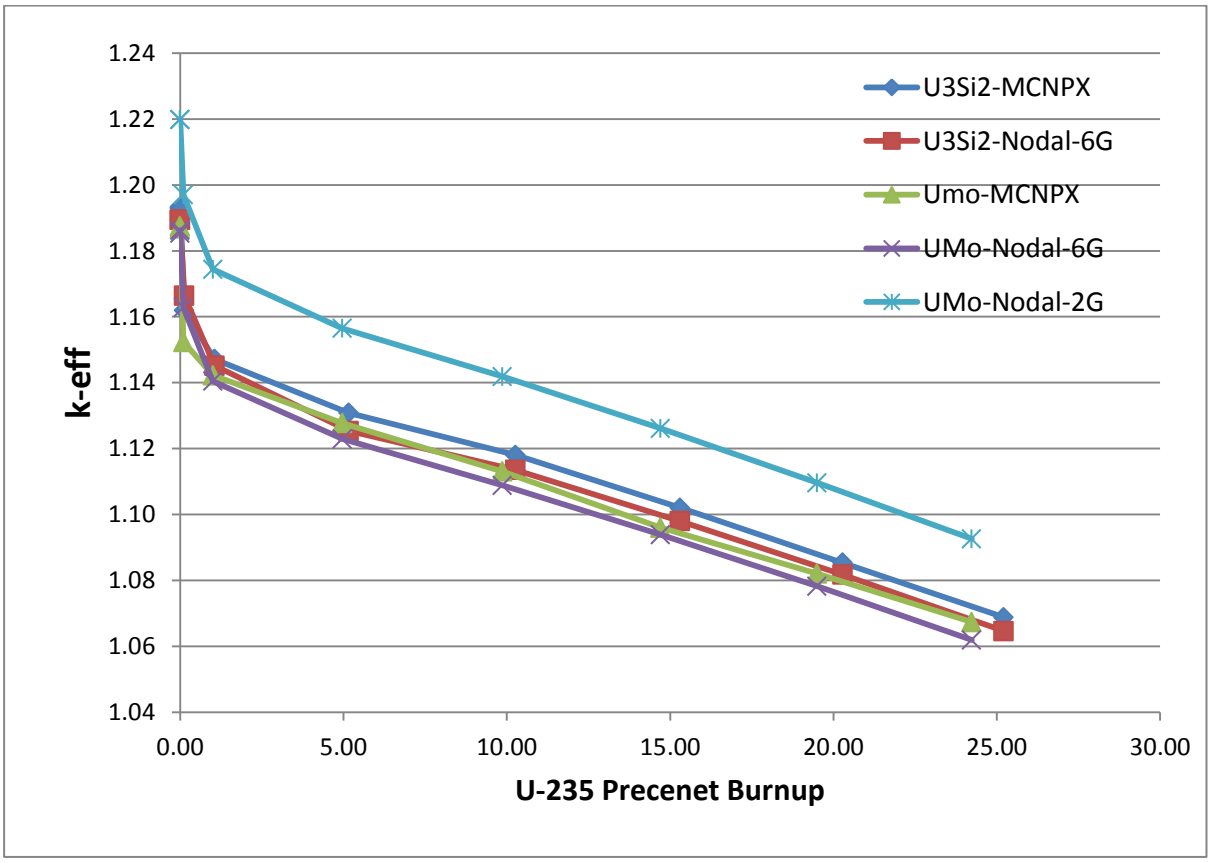


Figure 3 The change of k_{eff} with percent U-235 burnup for different fuel material

As expected, the depletion behavior is similar for all cases. The reactivity difference between U_3Si_2 and U-7Mo fuels is less than 5 mk. The U3Si2 fuel provides a slightly higher reactivity due to less uranium loading even if the fuels are irradiated with similar power density. For the 2G calculations the results were higher than the MCNPX results by 30 mk but for the 6G case the results were higher by 5 mk. The 6G calculation provides slightly higher results than MCNPX results; this is due to the effect of the uniform burnup which was applied to nodal calculations.

5. Equilibrium Core Analysis

An equilibrium core for a specific core configuration can be obtained by reloading and burning the core repeatedly until equilibrium conditions are reached. When equilibrium conditions are in place the reload pattern and the cycle operating length converge, resulting in the BOC U-235 mass distribution being constant after every reload. Equilibrium core

calculations may also be performed for different core configurations in order to determine the long-term fuel economy for optimal reactor performance. Equilibrium core studies also determine the most appropriate core layout that will provide high thermal fluxes while operating within an envelope of the safety and fuel constraints of the reactor core. [6]
Feasibility study of the U-7Mo fuel performance was done by analyzing equilibrium core and compare with U_3Si_2 fuel for the present reactor core configuration using nodal code. A depletion calculation has been carried out for the 3 MW MTR to obtain the neutronics parameters at the equilibrium core such as discharge burnup and power peaking factors. 18 cycles were considered with cycle length is fixed as 70 days, and one fuel is assumed to be replaced at every cycle. The cycle length was chosen so that at the end of cycle either excess reactivity was higher 20 mk, either maximum burnup of one fuel has reached the value 60% after 9 cycles.
Burnup distributions of the core in MWD/MTU were obtained as a result cycle-by-cycle form TRITON-NEWT system and the assembly power distribution obtained from nodal code for each assembly at BOC. The power distribution is then assumed constant over the burnup step. Using the burnup of each fuel assembly the burnup dependent cross sections can be obtained by linear interpolation for the cross sections obtained from TRITON-NEWT system.
The equilibrium core is searched for the 3 MW MTR core using the fuel management scheme through nodal calculations. The transmutation of beryllium is not considered, it is assumed to have a very little effect on core reactivity. Fig.4 shows the fuel management scheme of the 3 MW MTR.

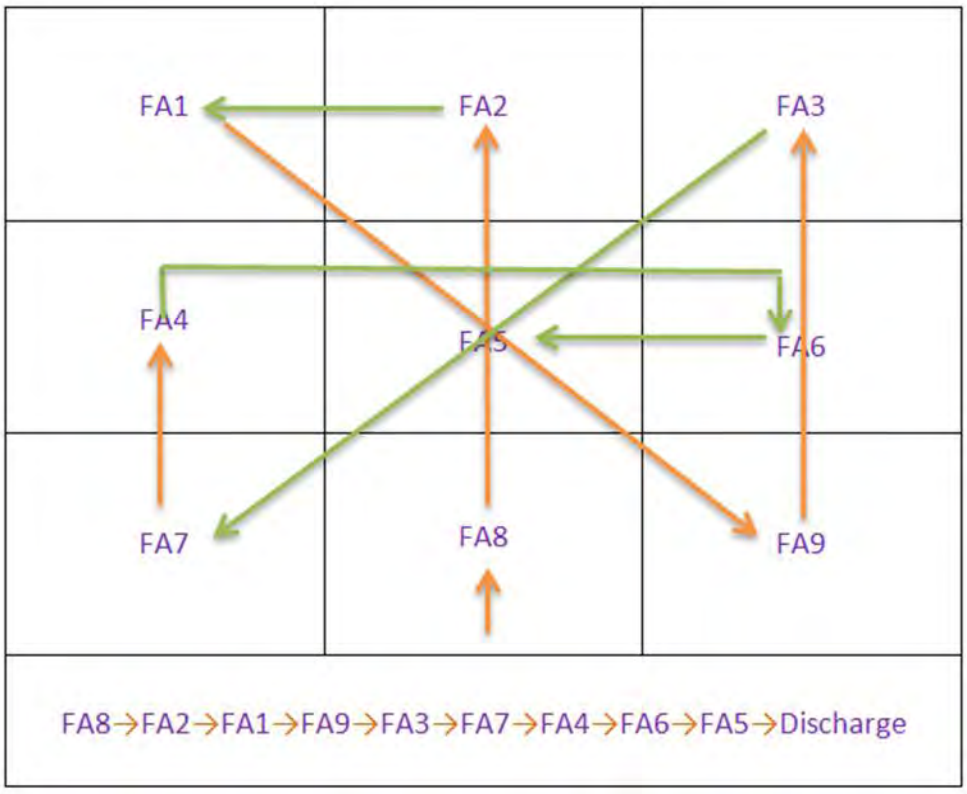


Figure 4 Fuel management scheme for the 3MW core

One fuel assembly is reloaded for one cycle and the most burned fuel assembly is discharged and all other fuel assemblies are reshuffled. The calculations were done for U_3Si_2 core and for U-7Mo for same cycle length and same refueling scheme to compare the fuel material performance. Only 6G nodal diffusion code will be used to make this study since it was seen from the previous section that it was sufficient to perform calculations and because shuffling and refueling cannot be done with MCNPX.
Several calculations were done for both fuel materials and important parameters were compared like k_{eff} for each cycle, power distribution, power peaking factors, fast and thermal

flux values, and burnup distribution for each cycle. Fig.5 shows the change of k_{eff} with 18 cycles for BOC case. It can be observed from the k_{eff} curve is become saturated after cycle 11. For equilibrium core the excess reactivity on BOC about 50 mk and at EOC 20 mk.

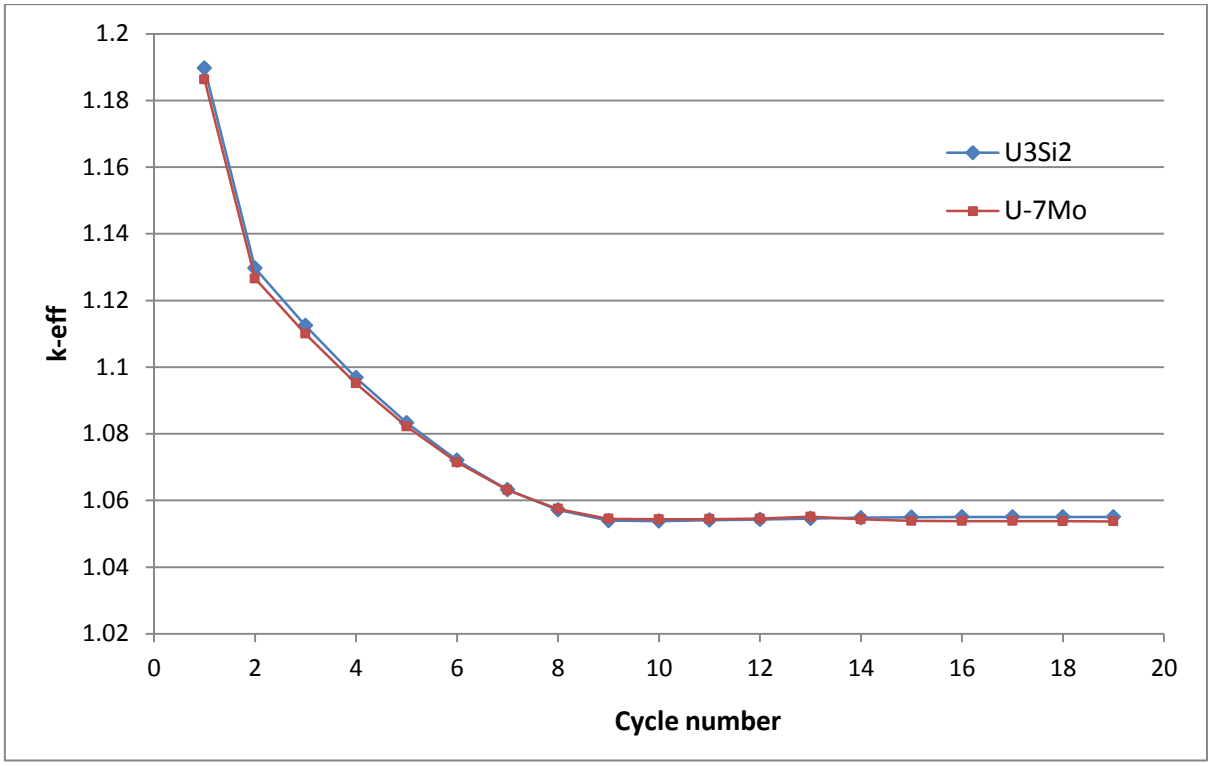


Figure 5 The change of k_{eff} with cycle number for both materials

For the power distribution and power peaking factors also it was calculated using nodal code since each assembly is divided into multiple meshes in the axial direction, so that the power peaking factors can be determined easily from this code. The power peaking factors are the link between the nuclear and thermal-hydraulics analysis of the reactor core as they define maximum power released locally in the core. For the present core the total power peaking factors were calculated for equilibrium core, it was for both fuel materials 1.52 at BOC case, also the power distribution was similar. Fig.6 shows the power distribution and the power peaking factor of each fuel assembly for both fuel materials.

CYC18 BOC		
FA1 0.3734 1.45	FA2 0.3026 1.42	FA3 0.3315 1.31
FA4 0.3670 1.16	FA5 0.2471 0.94	FA6 0.3927 1.08
FA7 0.3414 1.27	FA8 0.2834 1.52	FA9 0.3609 1.39

FA ID
PA (MW)
Fq

EOC		
FA1 0.3794 1.47	FA2 0.3772 1.46	FA3 0.3455 1.33
FA4 0.3001 1.15	FA5 0.2462 0.93	FA6 0.2769 1.05
FA7 0.3281 1.26	FA8 0.3869 1.50	FA9 0.3596 1.39

(a)

CYC18 BOC		
FA1 0.3726 1.44	FA2 0.3000 1.41	FA3 0.3331 1.32
FA4 0.3649 1.15	FA5 0.2513 0.95	FA6 0.3910 1.08
FA7 0.3422 1.28	FA8 0.2840 1.52	FA9 0.3609 1.39

FA ID
PA (MW)
Fq

EOC		
FA1 0.3729 1.47	FA2 0.3046 1.45	FA3 0.3331 1.33
FA4 0.3651 1.14	FA5 0.2487 0.95	FA6 0.3911 1.06
FA7 0.3420 1.27	FA8 0.2818 1.49	FA9 0.3607 1.39

(b)

Figure 6 power distribution and the power peaking factors of equilibrium core for (a) U_3Si_2 fuel and (b) U-7Mo fuel.

The burnup distribution of the U-235 for the equilibrium core is given in Fig.7. For U_3Si_2 in BOC case the average burnup was 27.92% (45.32 GWD/MTU), for EOC case the average burnup was 34.73% (56.74GWD/MTU). The discharge burnup was 61.26% (102.78GWD/MTU). For U-7Mo in BOC case the average burnup was 27.26% (44.21 GWD/MTU). For EOC case the average burnup was 33.81% (55.20 GWD/MTU). The discharge burnup was 59.11% (98.92 GWD/MTU).

CYC18 BOC		
FA1 12.83 20.08	FA2 6.25 9.71	FA3 28.34 45.22
FA4 42.00 68.26	FA5 56.68 94.31	FA6 49.19 80.84
FA7 35.16 56.58	FA8 0.00 0.00	FA9 20.81 32.87
Average	FA ID Bu% GWD	 27.92 45.32

EOC		
FA1 20.81 32.87	FA2 12.83 20.08	FA3 35.16 56.58
FA4 49.19 80.84	FA5 61.26 102.78	FA6 56.67 94.30
FA7 42.02 68.28	FA8 6.25 9.71	FA9 28.35 45.23
Average	FA ID Bu% GWD	 34.73 56.74

(a)

CYC18 BOC		
FA1 12.43 19.39	FA2 6.12 9.45	FA3 27.39 43.66
FA4 42.35 68.95	FA5 54.59 90.64	FA6 48.41 79.56
FA7 33.91 54.51	FA8 0.00 0.00	FA9 20.13 31.73
Average	FA ID Bu% GWD	 27.26 44.21

EOC		
FA1 20.09 31.67	FA2 12.40 19.34	FA3 33.98 54.64
FA4 49.22 80.98	FA5 59.11 98.92	FA6 55.58 92.45
FA7 40.52 65.79	FA8 6.06 9.36	FA9 27.37 43.63
Average	FA ID Bu% GWD	 33.81 55.20

(b)

Figure 7 U-235 burnup distribution for (a) U_3Si_2 fuel (b) U-7Mo.

Finally to summarize the results of previous study for both fuel materials, table 3 gives the most important results calculated. This study which was done to make feasibility study of the U-7Mo for reactor fuel, although the mass of the uranium loaded into the core and the density for U-7Mo was higher than for U_3Si_2 but keff value for the U-7Mo was lower. Also the discharge burnup was lower for U-7Mo than for the U_3Si_2 but these differences is not that much and it may be related to the absorption cross section of the Mo which is higher than Si.

Table 3 Summarized results for both fuel materials for equilibrium core calculations

Parameter	U_3Si_2	U-7Mo
U density	4.8 gU/cc	5.0 gU/cc
Fuel Density	6.159 g/cc	7.234 g/cc
Mass of U-235 per fresh fuel assembly	403.52 g	420.34 g
Mass of U loaded into the fresh core	18.388 Kg	19.155 Kg
Cycle length	70 days	70 days
Number of cycles to reach equilibrium core	18	18
k_{eff} at BOC of the equilibrium core	1.05505	1.05377
k_{eff} at EOC of the equilibrium core	1.02241	1.02251
Power Peaking factor for equilibrium core	1.52	1.52
Average U-235 burnup at BOC of equilibrium core	27.92% (45.32 GWD/MTU)	27.26% (44.21 GWD/MTU)
Average U-235 burnup at EOC of equilibrium core	34.73% (56.74GWD/MTU)	33.81% (55.20 GWD/MTU)
Discharge burnup	61.26% (102.78GWD/MTU)	59.11% (98.92 GWD/MTU)
Maximum average thermal flux for BOC	5.73E+13	5.63E+13
Maximum average fast flux for BOC	4.05E+13	4.04E+13

6. Conclusions

A 3 MW reactor was proposed to apply depletion calculation using nodal methods and MCNPX. 2G and 6G nodal calculations were compared with MCNPX reference results for the same geometry, 2G and 6G burnup dependent cross sections also generated using TRITON-NEWT system. The calculations were done for fresh and after 250 days of irradiation. The results for 2G case were higher than MCNPX results with 30 mk difference, while 6G results were almost same as MCNPX with 5 mk difference, so it was used for equilibrium core analysis.

A fesibilty study was made to check the neutronics parameters of the U-7Mo fuel and compare it with U_3Si_2 values for fresh and equilibrium cores using the same core configuration and same cycle length which is 70 days. It was assumed that the equilibrium core will be achieved after 18 cycles. Both fuel materials have similar uranium density while the U-7Mo fuel density is higher than U_3Si_2 fuel. For this part the eigenvalue, flux, power distribution, power peaking factors, and burnup distribution were compared for fresh and equilibrium core for both fuel materials.

It was seen that the neutronics parameters of the U-7Mo fuel was similar to the U_3Si_2 of almost same uranium density ,and since U-7Mo can be used with a higher density so a higher amount of uranium can be loaded in a fuel assembly which means a longer cycle length can be achieved.

Finally multi-group nodal methods can be used for fast core calculations and it can be used for fuel management studies which cannot be done in MCNPX.

References

1. C.J. Park, B. Lee, “Lattice Characteristics and Activity Analysis of U_3Si_2 And UMo Plate Type Fuel Assemblies with Scale6 Code”. International Meeting on Reduced Enrichment for Research and Test Reactors, Warsaw, Poland, October 14-17, 2012.
2. Denise B. Pelowitz, editor, 2011, “MCNPX™ USER’S MANUAL Version 2.7.0.
3. M.D. DeHart, TRITON: A Two-Dimensional Transport and Depletion Module for Characterization of Spent Nuclear Fuel, ORNL/TM-2005/39, Ver.6, Oak Ridge National Laboratory (2009).
4. M.D. DeHart, NEWT: A New Transport Algorithm for Two-Dimensional Discrete Ordinates Analysis in Non-Orthogonal Geometries, ORNL/TM-2005/39, Ver.6, Vol. II, Sec. F21, Oak Ridge National Laboratory, 2009.
5. M. K. Jaradat, L. M. Alawneh, C. J. Park, B. Lee, “Application of Nonlinear Nodal Diffusion Method for a Small Research Reactor”, Annals of Nuclear Energy, Vol 66, pp 20–30, 2014.
6. C. Phillips. “Investigation into different core configurations of the safari-1 research reactor”, Master of Science in Engineering at the Potchefstroom campus of the North West University, 2007.

CALCULATION OF KINETIC PARAMETERS OF THE JSI TRIGA REACTOR WITH TRIPOLI 4 AND MCNP

R. HENRY
Reactor engineering division R4, Jožef Stefan Institut
Jamova 39, SI-1000 Ljubljana, Slovenia

L. SNOJ, I. LENGAR
Reactor physics division F8, Jožef Stefan Institut
Jamova 39, SI-1000 Ljubljana, Slovenia

ABSTRACT

Monte Carlo transport codes enable very accurate calculations of most important reactor kinetic parameters such as effective delayed neutron fraction β_{eff} and mean neutron generation time Λ. New methods have been implemented to calculate those parameters in only one run. We used two different codes to calculate β_{eff} and Λ for various realistic and hypothetical TRIGA Mark II core configurations with different types and amount of fuel. Values obtained with MCNP and TRIPOLI are very similar. It can be observed that the effective delayed neutron fraction strongly depends on the number of fuel elements in the core or on the core size. E.g., for 12 wt. % uranium standard fuel with 20 % enrichment, βeff varies from 800pcm for a small core (31 fuel rods) to 710pcm for a full core (91 fuel rods). It is interesting to note that calculated value of βeff strongly depends also on the delayed neutron nuclear data set used in calculations. The prompt neutron life-time mainly depends on the amount (due to either content or enrichment) of ^{235}U as it is approximately inversely proportional to the average absorption cross-section of the fuel. E.g., it varies from 28 μs for 30 wt. % uranium content fuelled core to 48 μs for 8.5 wt. % uranium content LEU fuelled core. Description of the calculation method codes comparison and detailed results are presented in the paper.

1. Introduction

The most important parameters in reactor kinetics are the effective delayed neutron fraction βeff and mean neutron generation time, Λ. In research reactors (e.g. TRIGA) these parameters are usually provided by the manufacturer in the design phase and are not calculated for various core conditions. For example, the recommended value of βeff for the TRIGA Mark II by General Atomic is ~720 pcm and the recommended mean neutron generation time for 12 wt. % standard fuel reflected by water is 32 μs [1]. As the reactor kinetic parameters strongly depend on the fuel type and core configuration, it is very important to take this into account especially when performing changes in core configuration.

It is very difficult to measure βeff and Λ separately (only their ratio, βeff/Λ, can easily be measured), hence these parameters have usually been calculated. Keepin provided the theoretical foundations for such calculations [2], however, related to deterministic transport equation. His approach requires calculation of flux and its adjoint function as a weighting function. The method is very difficult to apply as it requires detailed multigroup transport calculations. Also, it cannot be applied in continuous-energy Monte Carlo codes [3].

In TRIGA type research reactors the reactor core configuration can be changed within several minutes. In fact the reactor core configuration does change several times per year or

even a month (depending on the usage and type of experiments) in order to meet the demands of the experiments. The type of fuel elements used in the core depends on the availability of the fuel and on the recommendations of international community. Therefore it is necessary to calculate kinetic parameters after every major change in core configuration.

L. Snoj and al. calculate βeff and Λ for various realistic and hypothetical annular 250 kW TRIGA Mark II at IJS cores with different types and amount of fuel [4] using MCNP5 [5]. Since at that point no experiment, in which the kinetic parameters were measured have been performed.

The only validation was comparison of theoretical models and experimental pulse mode operation by using the calculated kinetic parameters and comparison of calculated kinetic parameters with values provided by the manufacturer. As the calculations were performed with one code only, it was decided to use another Monte Carlo neutron transport code and to repeat the procedure. TRIPOLI-4 [6] is a general purpose radiation transport code. It uses the Monte Carlo method to simulate neutron and photon transport in three-dimensional geometries. TRIPOLI and MCNP are both well established Monte Carlo neutron transport codes with nevertheless some small differences [7]. Estimator used to determine kinetic parameter are also different and express the growing interest for calculating kinetic parameter with Monte Carlo code in the last years [8,9].Moreover, TRIPOLI and MCNP do not have the same approach for modelling the unresolved resonance region especially for inelastic scattering reaction. While MCNP is directly using probabilities tables to compute the given cross section, TRIPOLI is first generating “statistical” resonance which will be applied to calculate cross section.

After a brief presentation and validation on the model built with TRIPOLI, βeff (computed from different estimators) behaviour will be study for different core configuration (size, fuel type) and for different nuclear data libraries.

2. Criticality benchmark model

As the calculation of βeff is strongly connected with the criticality calculations, it was decided to firstly compare MCNP and TRIPOLI in criticality calculations. The TRIGA criticality benchmark from the ICSBEP handbook [10] was used for this purpose. Two critical core configuration (denoted as core 132 and core 133) were analysed. They are presented schematically in figure 1.

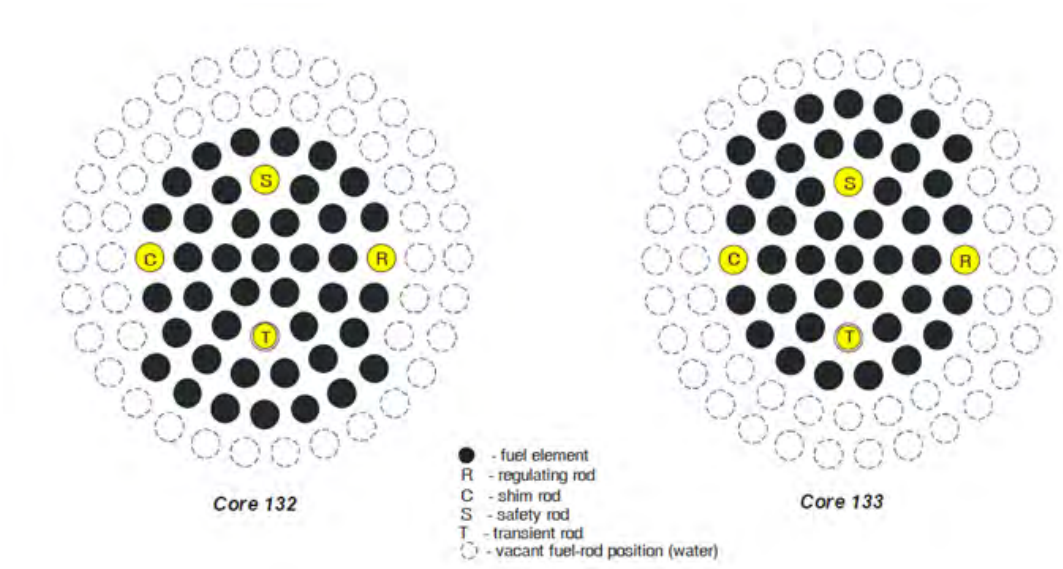


Figure 1: Configurations of the benchmark cores, top view.

The effective multiplication factor of the benchmark model is different from the experimental one due to geometry simplifications and uncertainties in the material and geometrical data of the benchmark model [10]. The differences in k_{eff} between the simplified "benchmark" model and the full model are presented in Table 1:

	Experimental k_{eff}	Benchmark-model k_{eff}
core 132	0.99865 ± 0.00015	1.0006 ± 0.0056
core 133	1.00310 ± 0.00015	1.0046 ± 0.0056

Table 1: Experimental and Benchmark-model k_{eff} with their uncertainties (measurement for experimental value and material for Benchmark-model value)

The computational model of the benchmark core is commonly simplified. Simplifications of the geometry were done by simplifying the surroundings of the core such that the k_{eff} was not affected significantly. The simplifications are done mainly to avoid complex modelling which has a minor or negligible effect on k_{eff}. The fuel element was modelled exactly, meaning that Zr rod, stainless steel cladding, air gaps and Mo supporting disc were modelled explicitly. The supporting grid, graphite reflector with rotary groove and central irradiation channel in the core were also explicitly modelled. The following structures were omitted or simplified:

- irradiation channels in the reflector,
- graphite of the thermalizing and thermal column,
- end caps of fuel and control rods,
- source element
- Al cladding of the groove in the graphite reflector.

TRIPOLI benchmarks model are visualised in figure 2

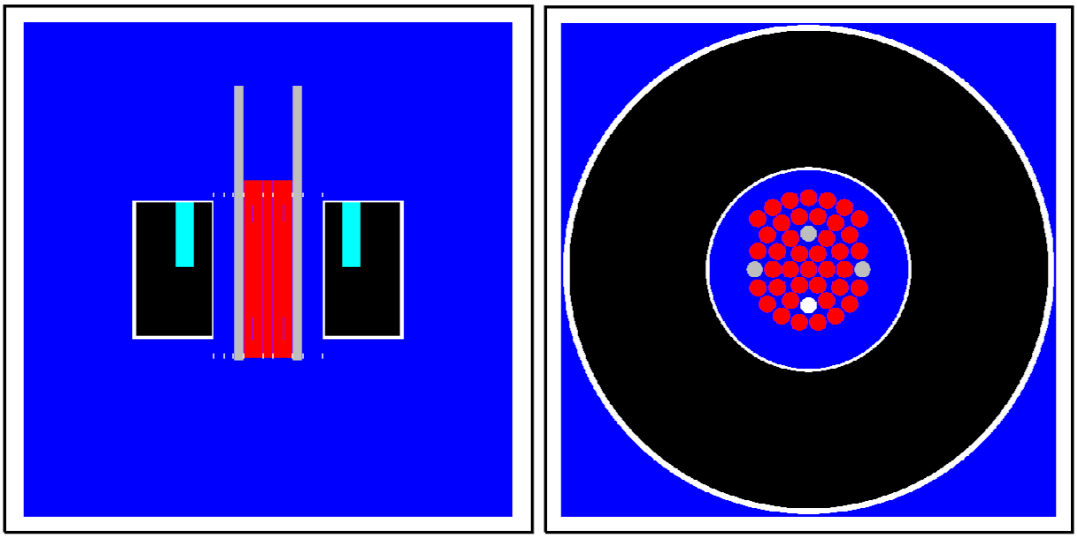


Figure 2: Side and top view of the TRIPOLI Computational model

All the calculations presented in this paper use the version 4.8 of the code. ENDF/B-VI.6, ENDF/B-VII.0 and JEFF-3.1 cross-section libraries were used. Criticality calculations were performed for 1000 batches of 10^5 neutrons each. The code discards the first few batches (5 on averages) in order to achieve convergence of the fission sources. TRIPOLI calculations (denoted by C) of k_{eff} were compared against experimental (denoted by E) and MCNP v 5.1.40 values to detect eventual discrepancies. Results are summarises in Table 2 and 3:

library\code	TRIPOLI	MCNP	C/E-1(TRIPOLI) in pcm	C/E-1(MCNP) in pcm
ENDF/B-VI.6	1.00081±0.00037	1.00010±0.00008	21	-50
ENDF/B-VII.0	1.00617±0.00028	1.00588±0.00008	557	528
JEFF-3.1	1.00168±0.00037	1.00193±0.00008	108	133

Table 2: Calculated values of the benchmark k_{eff} using different cross-section libraries for the core 132

library\code	TRIPOLI	MCNP	C/E-1(TRIPOLI) in pcm	C/E-1(MCNP) in pcm
ENDF/B-VI.6	1.00508±0.00037	1.00358±0.00008	48	-102
ENDF/B-VII.0	1.00986±0.00010	1.01071±0.00019	524	608
JEFF-3.1	1.00556±0.00010	1.00648±0.00025	96	187

Table 3: Calculated values of the benchmark k_{eff} using different cross-section libraries for the core 133

A very good agreement can be seen between values computed either by MCNP or TRIPOLI. Largest differences between codes are 150 pcm and in general difference remain under 100 pcm whereas for a same code, nuclear data set may bring up to 500 pcm of difference. In a nutshell, it has been shown that both codes can well reproduce the criticality benchmark experiment.

3. Kinetic parameters calculation

Each core studied from now were very similar to the one used for benchmark evaluation of TRIGA Mark II reactor, the main difference being in control rod position and number of fuel rods. Zero power and no-xenon conditions were assumed. In order to observe βeff and *Λ* resulting purely from differences in fuel composition and core size and not from other perturbations (e.g. empty positions, irradiation channels, etc.) the core was made as uniform as possible by replacing the empty positions and irradiation channels with fuel rods. All fuel rods in the core were considered to be fresh.

Three different nuclear data libraries were used in our calculations; ENDF/B-VI, ENDF/B-VII and JEFF 3.1. First calculations for kinetics parameters were performed with MCNP5 version 1.40 by using the so called prompt method that requires two runs [4]. In MCNP5 v 1.60 a new methods was introduced that allows calculation of adjoint weighted kinetic parameters in one runs only. [11, 12, 13].In the new version of TRIPOLI the effective delayed neutron fraction βeff calculation has been improved [3]. Instead of running twice (prompt method) to obtain βeff with a relative important variance, two new methods to estimate βeff with different approximations in simulation have been implemented into the TRIPOLI-4 continuous energy run. The first method based on the contribution from the prompt fission neutrons and the second method based on the contribution from the delayed neutrons. First approach is an improved one of the Bretscher's prompt method [9] and second one was proposed by Nauchi and Kameyama [10] allowing also direct calculation of Λ. Geometry and material modelling in TRIPOLI was done identically as in MCNP so discrepancies observed will only result from calculation algorithm specificities of each code.

To sum up we have four different βeff estimators. Two are based on the prompt method which approximate $\beta\mathrm{eff}$ with the ratio of multiplication factor with (k) and without (kp) delayed neutron (Eq. 1)

$$\beta\mathrm{eff} = 1 - \frac{\mathrm{kp}}{\mathrm{k}} \qquad (1)$$

This will be referred to as prompt method.

When MCNP needs two runs (one for each keff) TRIPOLI with one small approximation, βeff is approximated by Eq. 2.

$$\beta\mathrm{eff} = \frac{\mathrm{Npd}}{\mathrm{Npp+Npd}} \qquad (2)$$

Where Npp is the averaged value of prompt neutrons produced by the prompt neutrons of previous generation, and Npd is the average value of prompt neutrons produced by the delayed neutrons of previous generation.

The second estimator from TRIPOLI is based on the Nauchi method (Eq. 3) and allows calculation of βeff and Λ in only one run.

$$\beta\mathrm{eff} = \frac{\mathrm{Npd+Ndd}}{\mathrm{keff}} \qquad (3)$$

MCNP version 5. 1.60 features calculation of adjoint-weighted reactor kinetic parameters. The method is thoroughly described in [14] and is based on methods proposed by Meulekamp and van der Marck [12, 13]. This will be referred to as adjoint weighted method.

4. Discussion and results
4.1 Uranium content effect

First βeff was calculated for four critical TRIGA cores (Fig 3.), each containing different type of fuel elements [8]. Fuel elements had standard dimensions of outer and inner diameter being respectively 3.645 and 0.635 cm and an active length of 38.1 cm only the fuel composition change (Tab 4). The calculated values of βeff for various realistic and hypothetical TRIGA Mark II cores containing different types of fuel elements are presented in Table 5.

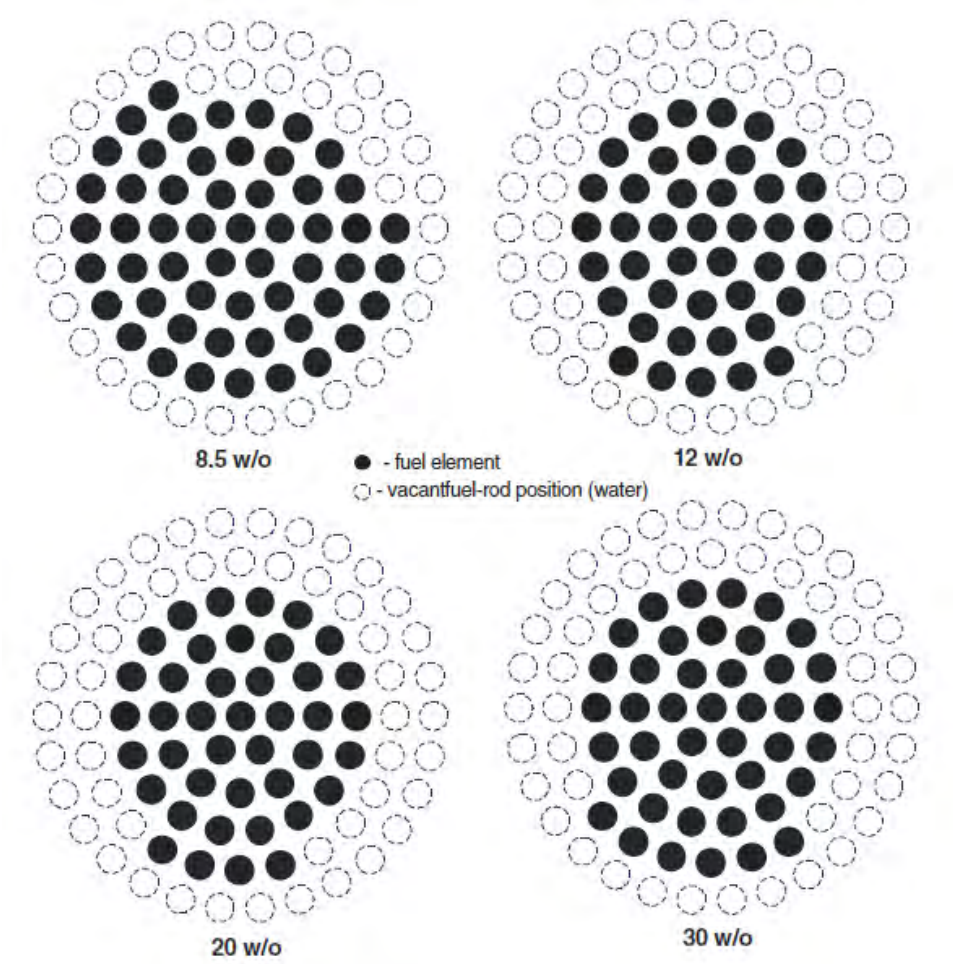


Fig 3. Configurations of the core, top view

Fuel rod (FR) name	8.5FR	12FR	20FR	30FR
U concentration (w/o)	8.5	12	20	30
U-ZrH mass(g)	2235	2318	2462	2500
U enrichment (%)	20	20	20	20
H:Zr	1.6	1.6	1.6	1.6
^{235}U mass(g)	38	55.6	99	150
Er concentration (w/o)	0	0	0.44	0.6

Tab 4: Fuel rods compositions

The number of rods was adjusted in order for each configuration to be close to criticality. Calculations were performed with the ENDFB VII cross section library. 1000 batches of 10^5 neutrons were performed with discarding of a few batches (less than 10) to obtain a well distributed neutron sources. Table 5 displays the calculated keff, βeff and Λ for both codes. A very good agreement between both codes can be observed.

	TRIPOLI			MCNP	
Fuel	β PROMPT(pcm)	β NAUCHI(pcm)	Λ(μs)	β PROMPT(pcm)	Λ(μs)
8.5wo	734±3	734±4	48.3±0.1	749±11	47.7±0.2
12wo	748±4	749±4	43.0±0.05	749±11	42.0±0.3
20wo	745±4	740±4	32.4±0.07	769±13	31.9±0.3
30wo	747±4	746±4	29.4±0.1	777±13	28.1±0.4

Tab 5: Calculated kinetic parameters of cores containing different fuel type. The uncertainties correspond to statistical uncertainties of the Monte Carlo calculations

We can observe that βeff does not depend significantly on the fuel type. This is expected as the cores with different fuel types are practically of the same size; A, B, C and D rings (Fig 3. and 4.) are completely full and E ring is only partially filled with fuel elements. The core size impact on βeff was also investigated.

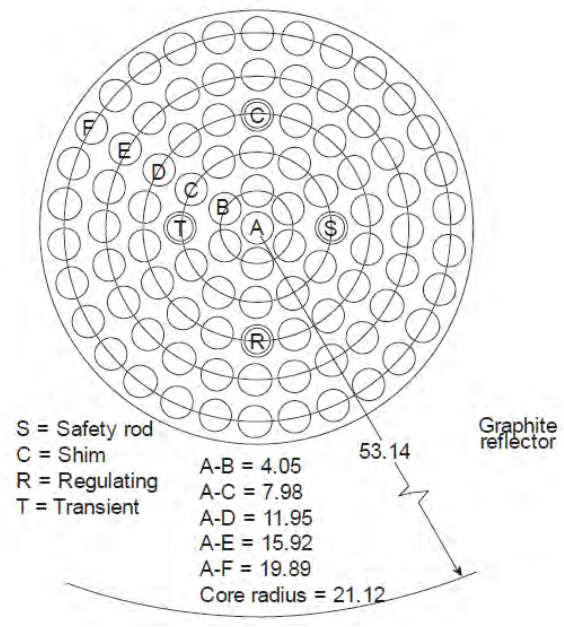


Fig 4. Core Configuration with Rod Locations Labelled by rings

The mean generation time varies from 28 μs to 50 μs for 30 wt. % or 8.5 wt. % fuels, respectively. It can be observed that the mean generation time decreases with increasing U 235 content. If we plot the mean generation time versus inverse ^{235}U atom density in the fuel, we can observe that mean generation time is approximately linearly proportional to inverse U 235 atom density

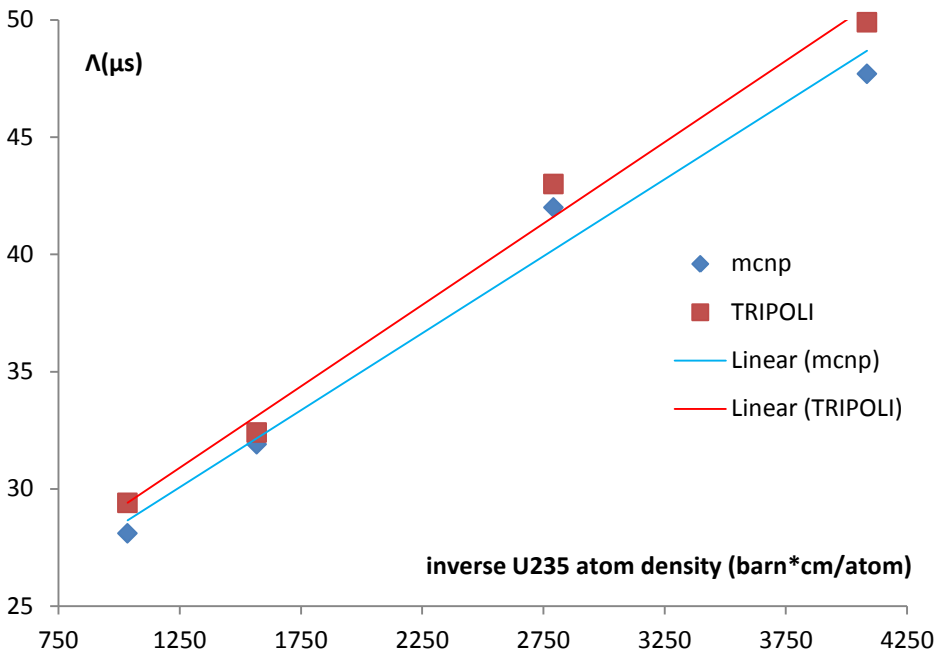


Fig 3. Λ in function of inverse U 235 atom density

4.2 Core size effect

In order to investigate the effect of the core size on βeff, we modelled several different cores, differing in number of fuel elements (12FR). In the first core A, B and C rings were completely filled with fuel elements. In the second, third and fourth cores fuel elements in D, E and F ring were successively added, respectively. The calculated values of βeff are presented in Table 6. Once again values obtained agree well. One can observe the strong correlation between βeff and the core size: the bigger the core, the smaller is βeff. The result is expected as the delayed neutrons are born with lower energies and are more effective in inducing fission in systems with larger leakage.

code	TRIPOLI		MCNP
method	PROMPT	NAUCHI	PROMPT
C	801±5	802±5	806±14
D	759±5	756±5	774±11
E	723±4	725±4	762±10
F	712±4	708±5	718±10

Tab 6: βeff values (in pcm) of cores uniformly filled to the denoted ring

Last but not least part of our work was to investigate the nuclear data library effect on kinetics parameters

4.3 Cross section library effect

The effect of nuclear data library on the calculated value of βeff was investigated for the ''benchmark core 132'' [6] (Fig 1.), filled with 12 FR fuel only. The results are presented in Table 7. We can see that the calculated value of βeff strongly depends on the nuclear data library used. The main differences are in delayed neutron data, as can be seen in Table 9 presenting the delayed neutron fractions from different cross-section libraries. Anyway once again both codes agreed with a maximum relative error smaller than 4%.

code	TRIPOLI		MCNP	
method	β PROMPT(pcm)	β NAUCHI(pcm)	β PROMPT(pcm)	β ADJOINT-WEIGHED(pcm)
ENDF/B-VI	792±4	791±4	796±12	818±15
ENDF/B-VII	745±4	746±4	752±12	744±14
JEFF-3.1	771±4	766±5	799±12	768±12

Tab 6: βeff values (in pcm) of cores uniformly filled to the denoted ring

	ENDF/B-VI	ENDF/B-VII	JEFF-3.1
vd	0.01670	0.01585	0.01620
v	2.43670	2.43670	2.43620
β	0.00685	0.00650	0.00665

Tab 8 Delayed neutron yields (v_d), average number of neutrons released per fission (v) and delayed neutron fraction (β) from thermal fission in ^{235}U

4 Conclusion

Computational model of the TRIGA criticality benchmark model was built with TRIPOLI. The calculated effective multiplication factor computed with TRIPOLI differs from the one calculated by MCNP for less than 0.1% (100pcm). The largest differences in calculated k_{eff} arise due to use of different nuclear data libraries, where discrepancies are on the order of 0.15 to 0.5 %) in k_{eff}. The reactor kinetic parameters were calculated by using two codes, four methods and three nuclear data libraries. It was observed that the differences in calculated kinetic parameters arise mainly due to nuclear data libraries but no due to methods or codes. In addition it was found that prompt neutron generation time Λ strongly depends on the fuel type (Uranium content) and that βeff depend more on the core size (leakage). However large differences between βeff values arise also from differences in delayed neutron data.

5 Acknowledgement

I gratefully acknowledge Anže Jazbec for providing me data and Gašper Žerovnik for help considering fruitful discussions and explanations.

6 References

[1] Simnad, M.T., Foushee, F.C., West, G.B., 1976. Fuel elements for pulsed TRIGA_research reactors. Nuclear Technology 28, 31

[2] Keepin G.R., Wimett T.F., Zeigler R. K., 1957, Delayed neutrons from Fissionable Isotopes of Uranium, Plutonium and Thorium, Physical review, vol. 107. No. 4, August 15, pp. 1044.

[3] Lee Y.K., Hugot F.X. Calculation of the effective delayed neutron fraction by TRIPOLI-4 code for IPEN/MB-01 research reactor

[4] Luka Snoj, Andrej Kavčič, Gašper Žerovnik, Matjaž Ravnik, Calculation of kinetic parameters for mixed TRIGA cores with Monte Carlo , Annals of Nuclear Energy, 37 (2) 2010.

[5] X-5 Monte Carlo Team, 2004. MCNP – A general Monte Carlo N-Particle Transport Code, Version 5, LA-UR-03-1987.

[6] Petit O., Hugot F.X., Lee Y.K., Jouane C., Mazzolo A., TRIPOLI-4 version 4 user guide

[7] MacFarlane R.E., Blomquist R.M., Cullen D.E., Lent E., Sublet J.C., A Code comparison Study for the Bigten Critical Assembly, LA-UR-08-4668.

[8] M. M. Bretscher, "Evaluation of Reactor Kinetic Parameters Without the Need for Perturbation Codes," Int. Meeting on RERTR, WY, USA, Oct. 5-10, (1997).

[9] Y. Nauchi, T. Kameyama, "Proposal for Direct Calculation of Kinetic Parameters βeff and Λ Based on Continuous Energy Monte Carlo Method," J. Nucl. Sci. Technol. 42, 503, (2005).

[10] Jeraj R. and Ravnik M., TRIGA Mark II reactor: U(20) - Zirconium Hydride fuel rods in water with graphite reflector, IEU-COMP-THERM-003, International Handbook of Evaluated Critical Safety Benchmark Experiments, Organization for Economic Cooperation and Development - Nuclear Energy Agency

[11] Anže Jazbec, Luka Snoj, Calculation of kinetic parameters using MCNP5 version 1.60, IJS Report IJS-DP-10945, 2012

[12] Klein Meulekamp, R. and van der Marck, S.C., 2004. Delayed neutrons, NRG, Petten, 20571/04.57372/P

[13] Klein Meulekamp, R. and van der Marck, S.C., 2006. Calculating the effective Delayed Neutron Fraction with Monte Carlo, Nuclear science and engineering, vol. 152, pp.142-148.

[14] Forrest Brown, Brian Kiedrowski, Jeffrey Bull, "MCNP5-1.60 Release Notes", LA-UR-10-06235 (2010).

NEUTRONIC AND THERMAL HYDRAULIC CHARACTERISTICS OF U-MO FUEL MINI PLATES IRRADIATED IN HANARO REACTOR

DAESEONG JO, HAKSUNG KIM, CHUL GYO SEO, HEETAEK CHAE
Korea Atomic Energy Research Institute, 1045 Daedeok-Daero, Yuseong-Gu, 305-353, Daejeon, Republic of Korea

ABSTRACT

Neutronic and thermal hydraulic analyses of U-Mo mini plates irradiated in the HANARO reactor were performed to investigate the heat production and cooling capacity. The LEU fuel was loaded with 6.5~8 gU/cc U-7Mo, and irradiated at OR-3 irradiation hole in the HANARO reactor. The heat generation was estimated regarding four different CAR (Control Absorber Rod) elevations i.e., 350 mm, 450 mm, 550 mm, and 650 mm. The irradiation capsule containing eight mini plates was modeled using the MCNP code to evaluate heat generation of each plate. Thermal hydraulic analyses were performed using the TMAP code to ensure the fuel integrity for limited accidents i.e., RIA (Reactivity Insertion Accident) and LRA (Locked Rotor Accident). For RIA, the reactor power can be increased up to 131% of Full Power. For LRA, the flow rate can be decreases up to 56% of Full Flow. As a result, the minimum DNB ratio for RIA and LRA is 1.96 and 2.10, respectively.

1. Introduction

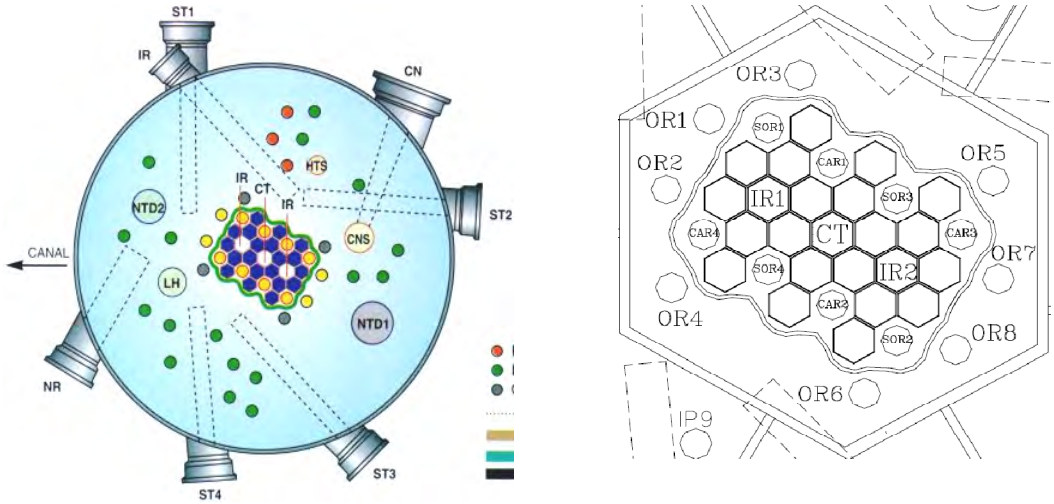
The Reduced Enrichment of Research and Test Reactor (RERTR) program was launched in 1978 to develop nuclear technologies to convert research and test reactors from the use of fuels and targets containing Highly Enriched Uranium (HEU, ≥ 20% U^{235}) to the use of Low Enriched Uranium (LEU, ≤ 20% U^{235}). The RERTR program converted over 40 research and test reactors from the use of HEU to the use of LEU. However, some of reactors, which require a very high power density, have not been converted since suitable LEU fuel is not currently available for the reactors. For example, the MITR-II reactor at MIT is a 5MW tank-type reactor uses 93% enriched HEU with a density of approx. 1.6 g-U/cc [1]. When 1.5 g-U/cc HEU is converted to LEU, a LEU uranium density higher than 7.5 g-U/cc is required to be the equilibrant amount of U^{235}. Development efforts to achieve high uranium density of LEU have been put by many international institutes and countries. The international RERTR fuels working group including Argentina, Canada, France, Korea, Russia, and United States was established to develop, qualify, and license high density LEU fuel. This program is mainly engaged with U-Mo dispersion fuel with densities from 6 to 8 g-U/cc and U-Mo monolithic fuel with densities as high as 16 g-U/cc [2]. The Advanced Test Reactor (ATR) at the Idaho National Laboratory (INL) tested U-Mo alloys with at least 6 wt.% Mo at low irradiation temperature to relatively high burn up. The results (RERTR-1 and 2) showed that U-Mo alloys exhibited better behavior such as low and stable swelling as compared with current used uranium silicide fuels. The new RERTR irradiation test (RERTR-3) was performed in the ATR to obtain irradiation performance data on a series of high density U-Mo alloy dispersion fuels. The mini plates irradiated in RERTR-4 and 5 contained atomized fuel particle supplied by Korea Atomic Energy Research Institute (KAERI). The composition of the fuel alloys ranged from 6 wt % to 10 wt % Mo, and the fuel meat contained 6 and 8 g-U/cc. The mini plates in these tests were 100 mm long, 25 mm wide, and

1.40 mm thick. Three MTR fuel plates loaded U-Mo fuel with densities up to 8 g-U/cc were irradiated in the OSIRIS reactor at CEA. The result showed that there was uniform density of fission gas bubble inside the fuel meat. After early irradiation tests, the modified matrix dispersion fuels including 0.2 wt % Si, 2 wt % Si, and 5 wt % Si were irradiated in the ATR. The result showed that at least 2 wt % Si into the fuel meat matrix substantially reduced the amount of interaction layer formation. Irradiation tests of U-Mo fuel in the HANARO reactor were performed to investigate the effects of fuel particle size and composition within KOMO program [3,4]. The fuel density irradiated was 4.5 and 5.0 g-U/cc, and the fuel type was pin type.

Since Korea has a plan to build a new research reactor with the use of U-Mo fuel, KAERI plans to perform irradiation tests with U-Mo mini-plates in the HANARO reactor. In the present study, neutronic and thermal hydraulic characteristics of U-Mo alloy fuel plates irradiated in the HANARO reactor were numerically investigated. Nuclear physics calculations to obtain heat fluxes of the mini plates in the axial direction were carried out using the MCNP code, and thermal hydraulics calculations to estimate thermal margins were carried out using the TMAP code. The composition of U-Mo fuel used in the present study was selected based on their early irradiation tests in the HANARO reactor. Thermal margins were estimated based on the mini plate, which had the maximum power. For normal operation, the channel flow had been calculated based on the core pressure drop of the HANARO reactor. For abnormal conditions, thermal margins such as minimum ONB temperature margin and DNBR were evaluated with a reactor power increased by 60% and a flow rate decreased by 40%.

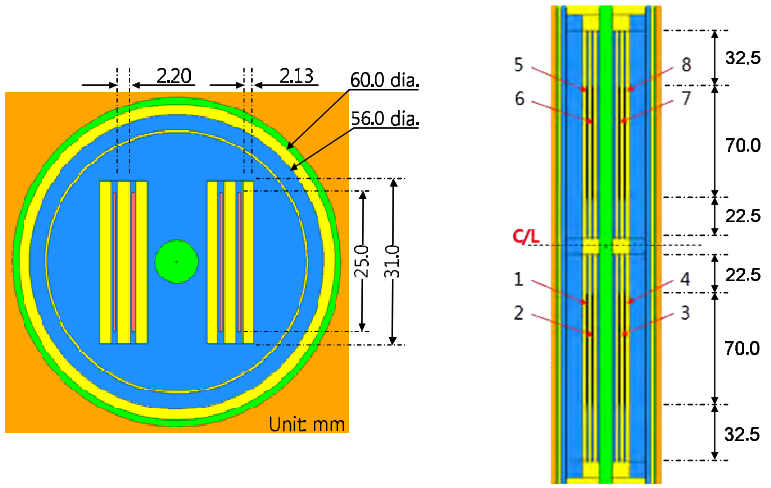
2. HANARO reactor and irradiation target

HANARO (**H**igh-flux **A**dvanced **N**eutron **A**pplication **R**eact**O**r) reactor is a light water cooled and heavy water reflected research reactor designed to operate at a nominal power of 30 MW thermal [5]. During normal operation, the core is cooled by forced upward flow through two pumps. During reactor shutdown, the core is cooled by natural convection through flap valves. The core, shown in Fig.1(a), consists of the inner core, the outer core, and the reflector region. The inner core has 23 hexagonal and 8 circular flow channels. Except for 3 hexagonal channels indicated as CT, IR1, and IR2, 20 hexagonal channels are loaded with a hexagonal fuel bundle, which has 36 fuel elements. 8 circular channels are loaded with a circular fuel bundle, which has 18 fuel elements. Each circular fuel bundle is surrounded by 4.5 mm thick cylindrical neutron absorber made of natural Hafnium. Four of them are used to control the reactor power during normal operation, and four of them are used to shutdown the reactor for emergency. In Fig.1(b), the control rods are indicated as CAR1, CAR2, CAR3, and CAR4. The shutoff rods are indicated as SOR1, SOR2, SOR3, and SOR4. The outer core has 8 circular channels numbering from OR1 to OR8. The four circular channels (OR1, OR2, OR7, and OR8) are loaded with circular fuel bundles with 18 fuel elements, and the other 4 circular channels are reserved for irradiation tests. The irradiation target of U-Mo mini plates is irradiated in OR3. OR3 has a fast neutron of 2.01×10^{13} n/cm^2/sec and a thermal neutron of 3.30×10^{14} n/cm^2/sec [6]. The fuel has a thickness of 0.51 mm, a width of 25.0 mm, and a length of 70.0 mm. As shown in Fig.2(a) and (b), the fuel plates are stacked to load total eight fuel plates. Since the flow direction is upward, the fuel plates loaded to the lower stack are numbered from 1 through 4, and the fuel plates loaded to the upper stack are numbered from 5 through 8. Each stack has 2 inner channels and 4 outer channels. The thickness of the inner channel is 2.20 mm, and the thickness of the outer channel is 2.13 mm.



(a) (b)

Figure 1 HANARO reactor: (a) core configuration and (b) locations of irradiation sites



(a) (b)

Figure 2 Mini plate fuel assembly: (a) cross sectional view, and (b) longitudinal view

3. Neutronic analyses

Fig.3 shows the mini fuel plates irradiated at OR3, which has a fast neutron of 2.01×10^{13} n/cm^2/sec and a thermal neutron of 3.30×10^{14} n/cm^2/sec. The fuel loaded at plate 2, 3, 4, 6, 7, and 8 is 8.0 gU/cc U-7Mo, and its density is 9.98 g/cc. The fuel loaded at plate 1 and 5 is 6.5 gU/cc, and its density is 8.11 g/cc. Neutronic calculations were carried out using the MCNP code, and the equilibrium core was modeled with various Control Absorber Rod (CAR) locations. Four control rod locations were considered for the present neutronic analyses: 350 mm, 450 mm, 550 mm, and 650 mm. In the case of 350 mm, the control rod is ejected 350 mm away from the bottom of the core. Fig.5 shows the heat fluxes with different control rod locations. For all of the cases, the plate 1 and 5 loaded with 6.5 gU/cc resulted in heat flux approx. 15% lower than that with 8.0 gU/cc. Also, the plate 4 and 8 located closest to the core resulted in the maximum heat flux. The maximum heat fluxes are 2.36E02 W/cm^2 with CAR at 350 mm, 2.37E02 W/cm^2 with CAR at 450 mm, 2.34E02 W/cm^2 with CAR at 550 mm, and 2.38E02 W/cm^2 with CAR at 650 mm. With the CAR at 350 mm, the lower stack releases more power than the upper stack, but the upper stack releases more power than the lower stack with the CAR at 650 mm.

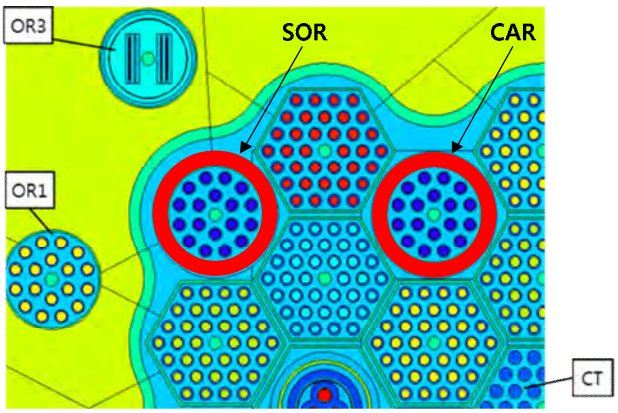


Figure 3 Mini fuel plates loading in HANARO reactor (MCNP model)

4. Thermal hydraulic analyses

Since the maximum flow rate through the irradiation site OR3 at the HANARO reactor is limited to 12.7 kg/s, the flow rate through the mini fuel plates needs to be evaluated before irradiation. If the flow rate through the target is higher than 12.7 kg/s, it reduces the core flow rate through fuel elements, which may cause a safety issue. The eight mini fuel plates are stacked to the irradiation target assembly shown in Fig.2(a). This irradiation target assembly was tested at the out-pile test facility to measure the total flow rate through the target. Since the core pressure drop of the HANARO reactor is 209 kPa, the pressure drop indicated as DP1 in Fig.4 must be 209 kPa. The flow rate through the irradiation target was measured to be 6.38 kg/s. This flow rate consists of the flow rate through 6 fuel cooling channels and the flow rate through the 2 mm thick annulus gap between the irradiation site hole and irradiation target assembly. To obtain the flow rate through the annulus gap, the pressure drop indicated as DP2 was measured. The distance of the pressure measurement points was 650 mm, and the pressure drop was measured to be 15 kPa. Based on the pressure drop, the flow rate through the 2 mm thick annulus gap was estimated as 1.14 kg/s. At this flow rate, the flow velocity through the annulus gap is approx. 3.14 m/s. Then, the flow rate through the fuel cooling channels are 5.24 kg/s, and the flow velocity is approx. 13.18 m/s.

From the neutronic calculations, the maximum power was released from plate 4 for the lower stack, and plate 8 for the upper stack. Fig.5 shows the comparison of the axial power distributions of plate 4 and 8 regarding CAR locations. As shown, the power distribution given as the CAR location of 650 mm was chosen for thermal hydraulic analysis for the lower stack, and the power distribution given as the CAR location of 350 mm was chosen for thermal hydraulic analysis for the upper stack. During normal operation, the flow direction is upward and the pressure drop through the lower and upper stacks is approx. 209 kPa. Since the outlet of the core is located 10 m below the pool top surface, the outlet pressure as 2.0 bar is the reference pressure. For the lower stack, the inlet temperature is the pool temperature (36 ^{o}C), but the inlet temperature of the upper stack is the outlet temperature of the lower stack. The thermal margin analysis results summarized in Table 1 show that there is no boiling occurred during normal operation since the ONB temperature margin is positive. The thermal margin analysis results during limited accidents such as RIA and LRA summarized in Tables 2 and 3. For both accidents, the fuel integrity is maintained since the minimum DNB ratio is higher than 1.50.

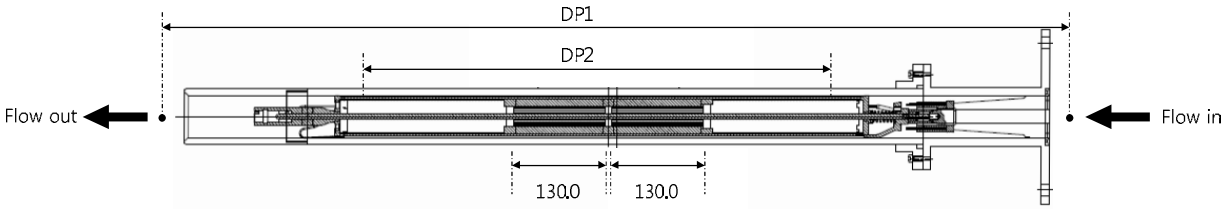
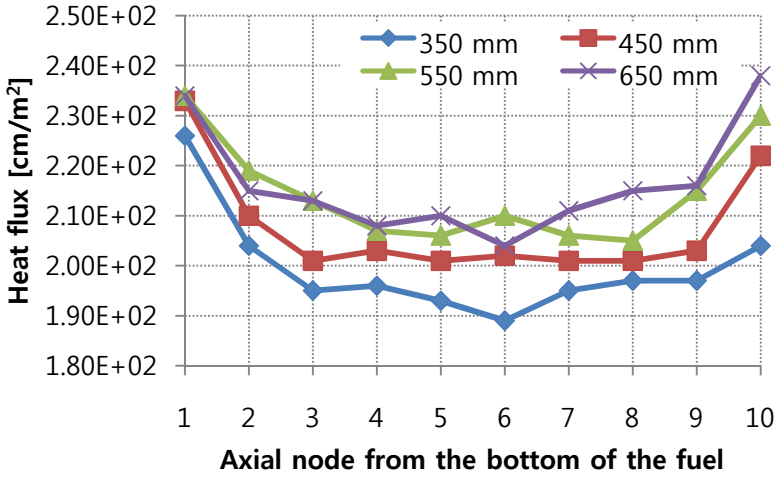
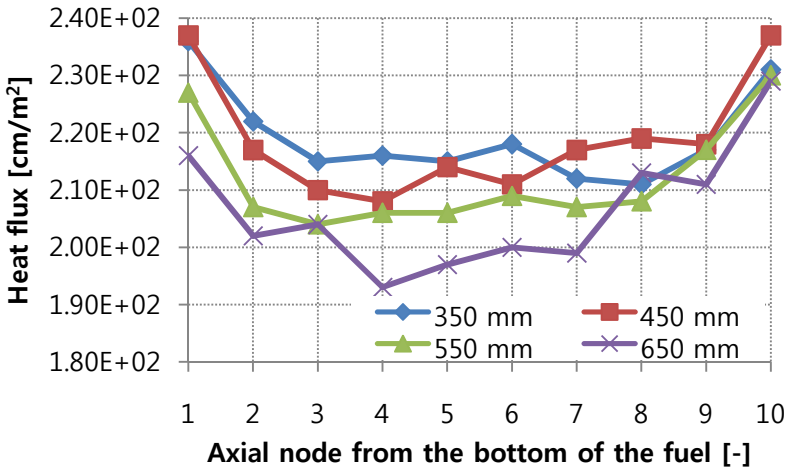


Figure 4 Out-pile test facility of the irradiation target



(a)



(b)

Figure 5 Axial power distributions: (a) plate-4 and (b) plate-8

Table 1 Thermal margin analysis results for normal operation

	Plate-4	Plate-8
Inlet temperature [^{o}C]	36.0	39.0
Reference pressure [bar]	3.0	2.0
Inlet velocity [m/s]	13.18	13.18
Average heat flux [kW/m^2]	2214.0	2174.0
Pressure at the fuel channel inlet [bar]	3.85	2.90
Pressure at the fuel channel outlet [bar]	3.25	2.30
DP through fuel cooling channel [kPa]	59.0	58.2
DP through irradiated target [kPa]	105.4	103.4
Max coolant temperature [^{o}C]	39.0	41.9
Max wall temperature [^{o}C]	113.0	114.4
Max fuel temperature [^{o}C]	177.3	178.9
Minimum ONB temperature margin [^{o}C]	41.8	31.8
MDNBR [-]	2.64	2.58

Table 2 Thermal margin analysis results for RIA

Power [%]	Max. $T_{coolant}$		Max. T_{fuel}		Minimum ONB		Minimum DNBR	
	Plate-4	Plate-8	Plate-4	Plate-8	Plate-4	Plate-8	Plate-4	Plate-8
100	39.0	41.9	177.3	178.9	41.8	31.8	2.64	2.58
131	39.9	43.7	220.5	221.9	18.5	8.8	2.01	1.96

Table 3 Thermal margin analysis results for LRA

Flow [%]	Max. $T_{coolant}$		Max. T_{fuel}		Minimum ONB		Minimum DNBR	
	Plate-4	Plate-8	Plate-4	Plate-8	Plate-4	Plate-8	Plate-4	Plate-8
100	39.0	41.9	177.3	178.9	41.8	31.8	2.64	2.58
56	41.3	46.5	221.5	222.4	-14.9	-19.3	2.17	2.10

4. Conclusions

Neutronic and thermal hydraulic analyses of U-Mo mini plates irradiated in the HANARO reactor were performed to investigate the heat production and cooling capacity. The heat production of the mini plates were evaluated regarding various CAR locations. The total number of the mini plates was eight, and four plates were stacked each. For the lower stack, the maximum heat production was resulted from the plate-4, and the maximum heat production was resulted from the plate-8 for the upper stack. From the out-pile test, the flow rate through the irradiation target was measured to be 6.38 kg/s. During normal operation, there is no boiling since the minimum ONB temperature margin is positive. During the limited accidents such as RIA and LRA, the fuel integrity is maintained since the minimum DNB ratio is higher than 1.50. As a result of the thermal hydraulic analyses, U-Mo mini fuel plates irradiated in the irradiation site OR3 at the HANARO reactor have a sufficient cooling capacity.

References

[1] Matos, J.E., LEU conversion status of U.S. research reactors September 1996. International Meeting on RERTR, Seoul, Korea, Oct. 7-10, 1996.

[2] Lemoine, P., Wachs, D., 2007. High density fuel development for research reactors. INL/CON-07-12889.

[3] Kim, C.K., Kim, K.H., Park, J.M., Ryu, H.J., Lee, Y.S., Lee, D.B., Oh, S.J., Chae, H.T., Seo, C.G., Lee, C.S., Progress on KOMO-3 irradiation test for various U-Mo dispersion and monolithic fuel to overcome interaction problem in U-Mo/Al dispersion fuel. Proc. of the 27th RERTR meeting, Boston, USA, Nov. 6-10, 2005

[4] Ryu, H.J., Kim, Y.S., Park, J.M., Chae, H.T., Kim, C.K., 2008. Performance evaluation of U-Mo/Al dispersion fuel by considering a fuel-matrix interaction. Nuclear Engineering and Technology 40, 409-418.

[5] Han, G.Y., Ha, K.S., 2002. Modifications and assessment of RELAP5/MOD3.2 for HANARO thermal-hydraulic safety analyses. Journal of the Korean Nuclear Society 34, 455-467.

[6] Lee, Y.S., Choi, M.H., Kang, Y.H., 2001. Thermal and mechanical characteristics of an instrumented capsule for a material irradiation test. Nuclear Engineering and Design 205, 205-212.

A 3D Thermo-Mechanical model to predict ballooning and burst behavior of Zircaloy-4 fuel cladding during LOCA transients in LWR employing commercial numerical simulation software

E. LANDAU,

Department of Nuclear Engineering, Ben Gurion University
P.O.B. 653 Beer-Sheva 8410501 Israel

M. SZANTO, Y. WEISS

Engineering and Computational Mechanics center, Rotem Industries LTD.
Mishor Yamin, D.N Arava 86800 Israel

ABSTRACT

A 3D Numerical code for the simulation of Zircalloy type nuclear fuel cladding during LOCA transients is proposed, based on the commercial numerical simulation software SIMULIA ABAQUS©, the algorithm for the material thermo-mechanical behavior relies on several known sources for material properties and constitutive behavior, and is implemented into ABAQUS© through the use of Fortran programmed coupled user subroutines. The Abaqus/Explicit solver is chosen to better facilitate the fast ballooning near cladding burst, and relies on the VUMAT subroutine along with several other utility and secondary routines to provide the Elasto-Viscoplastic Thermo-Mechanical relations. The model results were compared with the HALDEN IFA650.2 [1] [2] calibration experiment for as-received un-irradiated cladding and the FRAPTRAN1.4 [3] code. The comparison for the ballooning shape, rupture time and temperature, and max diametric expansion of the cladding show good agreement with the HALDEN experiment under current assumptions and is within reasonable error. While the IFA650.2 experiment allows only the assumption of axisymmetric loading, the full 3D nature of the model will enables more in-depth parametric analysis of the phenomena and the parameters affecting it for more complicated loading scenarios. The current model is still in development stages and does not facilitate thermo-hydraulics or fuel performance and interactions at this time. The ultimate goal is to calibrate and validate the model with coupled thermo-hydraulics and fuel performance codes during the planned LORELEI single rod LOCA experiments in the French JHR reactor.

1. INTRODUCTION

Modeling of nuclear fuel cladding behavior during a Loss of Coolant accident (LOCA) is a principal requirement in reactor safety analysis, most former safety criteria were obtained from experiments during the 1970's, conducted mainly with fresh fuels. Changes in modern fuel design, introduction of new cladding materials and motivation towards higher burn-ups have generated a need to re-examine safety criteria and their continued validity.

This led to the growing development of both experiments and simulations meant to address this need. The Halden IFA-650 [1] series of experiments for example, beginning in the early 2000's have clearly shown that existing criteria and experimental data were insufficient for the growing demand for higher burn-ups.

Several codes for reactor core and fuel rod analysis exist nowadays, such as FRAPTRAN1.4 [3] or RELAP5-3D [4]. These are tailor-made codes, designed to predict general core behavior and fuel performance, and while they are also used in predicting core components behavior during accident conditions, including those of cladding ballooning and failure with good accuracy, they contain several limitations on modeling the full transient cladding thermo mechanical phenomena. Limitations such as mechanical models being one dimensional or in axisymmetric geometries only, relying mostly on analytical models therefore having further restricting assumptions in return for accuracy, etc. These limitations disable the full simulation of several important aspects, such as modeling full 3D azimuthal behavior for example.

The objective of the current work is to develop a comprehensive numerical model for predicting zircalloy cladding thermo mechanical behavior during a LOCA. The model will eventually predict full cladding ballooning and burst behavior followed by fuel relocation, for fuel rods that can be subjected to 3D distributed flux. The model is fully three dimensional and is created using the commercial FEM numerical simulation software ABAQUS© applying coupled user subroutines to describe the complex material behavior during the process.

The target model will eventually display wide simulation capabilities regarding thermo-mechanical phenomenon, and will grow into including multi physics couplings such as fluid-structure interactions, all relying on well tested commercial software. These capabilities will enable conducting computation on complex geometries as well as coupling to various physical phenomena. In addition, in contrary with most tailor made codes, the ABAQUS© interface is user friendly and affords a high level of pre and post processing capabilities, as well as being widely available.

An additional aim is to eventually validate and calibrate the model during the upcoming LORELEI single rod LOCA experiments in the French JHR reactor.

2. BASIC CODE DEVELOPMENT

Due to the highly dynamic nature of the ballooning behavior near cladding burst, the Abaqus/Explicit dynamics solver was chosen, since the explicit method does not require convergence during every solution iteration (which is difficult to achieve properly during rapid deformations), but instead relies on stability by using very small time increments determined using a courant form criteria.
The main challenge in this case is modeling the material complex thermo-mechanical behavior, since it is composed of several inner-dependent variables and phenomena.
To achieve this, the current model utilizes the Abaqus/Explicit VUMAT user type subroutine to describe the Thermal Elasto-Viscoplastic material behavior, as well as several other secondary routines used to calculate the various parameters, properties, and boundary conditions variations during the process. The VUMAT subroutine essentially relates the change in the element strain to the change in stress, where the Abaqus solver solves the equations of equilibrium as shown in basic schematics in Figure 1.

The VUMAT subroutine also includes the effects of Cladding Oxidation, Cold Work, and Irradiation damages, as well as material anisotropy, annealing, CREEP, thermal expansion, Failure and several others. The Constitutive material model was composed from several external sources providing Zircalloy thermo-mechanical material libraries and properties which include MATPRO [4], FRAPCON3.4 [5], and FRAPTRAN1.4 [3], as well as several other literature sources. The code allows the user to choose which of the abovementioned material libraries to implement for several key relations in the constitutive model, and also includes several other input parameters for calibration purposes.

The primary relation used by most sources to account for Tensile strength, Yield strength and strain is shown in equation 1.

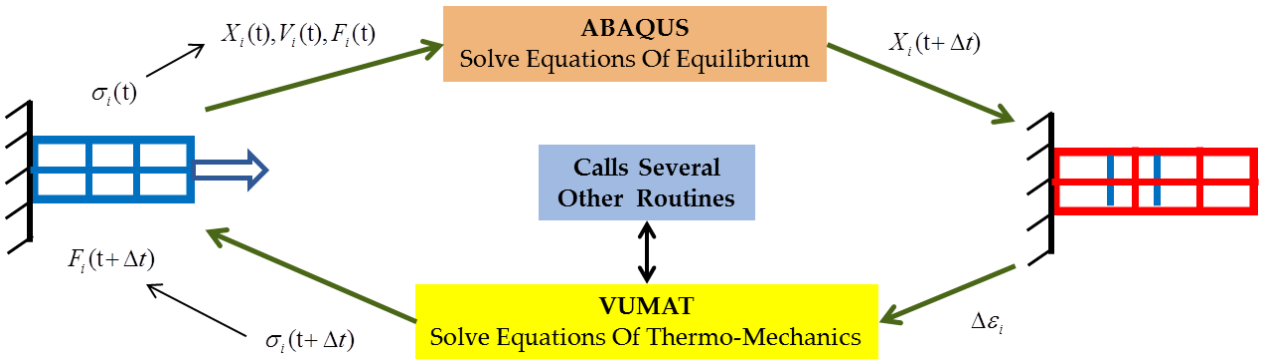


Figure 1. Schematics of VUMAT subroutine in the Abaqus/Explicit Solver

(1) $$\sigma = K\varepsilon^n \left(\frac{\dot{\varepsilon}}{10^{-s}}\right)^m$$

Where

σ = *True Effective Stress* [*Pa*]
K = *Strength Factor* [*Pa*]
$\dot{\varepsilon}$ = *Strain Rate* [*unitless*]
m = *Strain Rate Sensitivity Constant* [*unitless*]
ε = *True Effective Strain* [*unitless*]
m = *Strain Hardening Exponent* [*unitless*]

K, n, and m from equation 1 are correlated with respect to Temperature, irradiation, oxidation, Cold Work, and Zircalloy material type.

The BALON2 [6] model which is implemented in the FRAPTRAN1.4 [3] code, as well as in RELAP5 [4], to account for cladding shape during ballooning, uses a time integration form of equation 1 while assuming constant stress over the time increment to account for the faster visco-plastic deformation once a certain instability strain has been passed, the form of this integration is shown in equation 2.

(2) $$\varepsilon_f = \left[\left(\frac{n}{m}+1\right)10^{-3}\left(\frac{\sigma}{K}\right)^{1/m}\Delta t + \varepsilon_i^{\left(\frac{n}{m}+1\right)}\right]^{\frac{m}{n+m}}$$

In the current model, VUMAT performs newton iterations to better predict the effective strain increment with varying stress, but can also implement equation 2 for this purpose by user request. The VUMAT algorithm then returns the plastic stress-strain relation using incremental visco-plasticity theory and HILL anisotropy.
The equilibrium equations translating the stress-strain relation into actual deformation shapes and resulting stress are solved by the Abaqus FEM solver.
This method does not require assumptions such as axisymmetric loading or deformation of the cladding, treating the cladding as "Thin-Wall" and assuming constant stress, strain and temperature through cladding thickness, or neglecting of bending stress and strains.

Failure criteria are also adopted and compared from different sources, the BALON2 [6] uses an algorithm to predict the evolution of max azimuthal temperature difference and its effect is implemented through the failure criteria. In a full 3D model the azimuthal temperature distribution is implemented directly into the problems boundary conditions, therefore the Failure criteria are taken to be dependent only on the element temperature, oxidation, cold work and irradiation depending on which criteria is utilized.

All chosen criteria are checked during the simulation, and burst is either determined by the first criteria to reach failure or chosen specifically by the user, this enables comparing several criteria for each scenario. Most failure criteria employ a correlation for the engineering hoop stress, though this sometimes results in very large strains at failure, In FRAPTRAN1.4 [3] this is addressed through the use of a second empirical criterion on the engineering hoop strain which yields reliable results.

The VUMAT subroutine was pre-tested on several simplified cases and single element simulations to verify consistency of the subroutine results, Figure 2 displays typical behavior from a single element tensile model of the equivalent and yield stress values over time where a constant tensile load is implemented with a temperature increase over time at a rate of about 8(°C/s) beginning at 220°C. The mechanical properties decrease as the temperature increases, and when yielding occurs under constant stress the increasing plastic strain rate increases the Yield stress to the equivalent stress value, this causes exponentially increasing deformation rates, and eventually Necking/Ballooning and Failure.

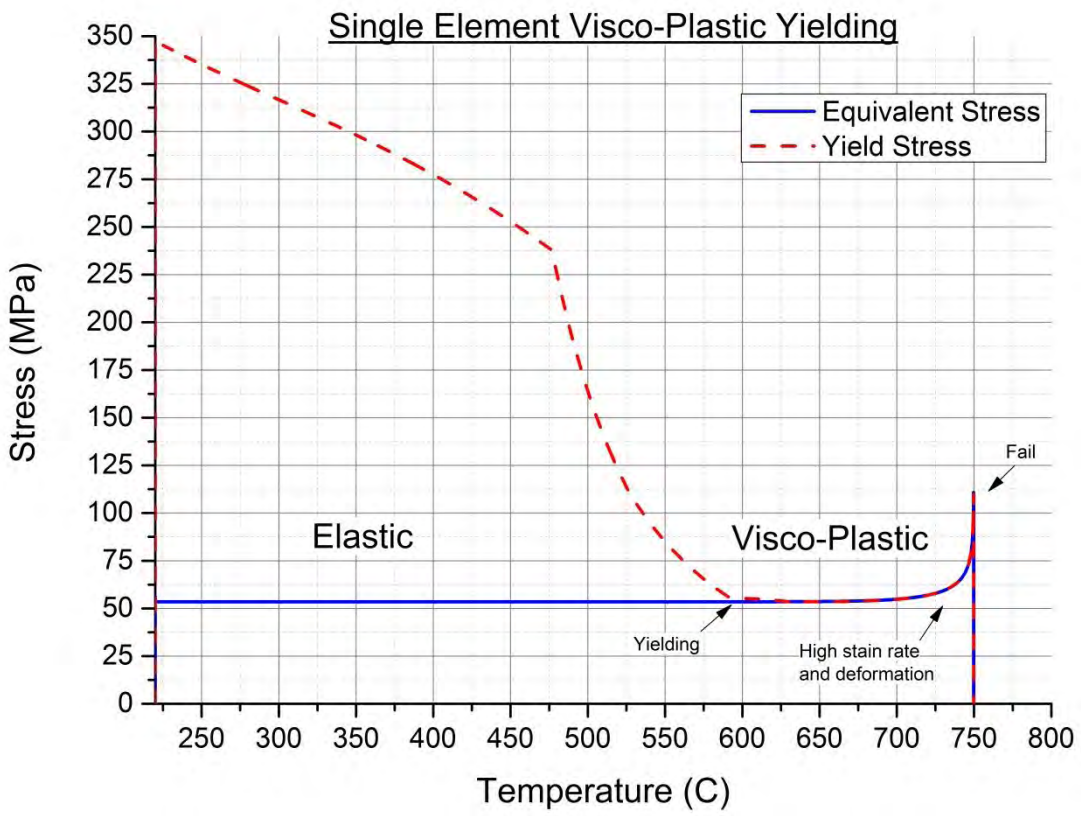
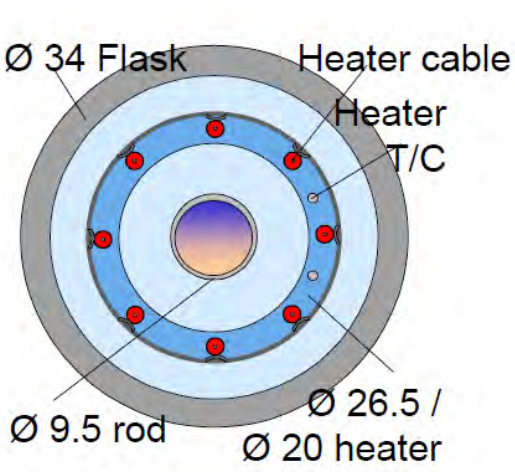


Figure 3. Zircalloy Visco-Plastic behavior under constant load and Temperature increase

3. PRELIMINARY MODEL RESULTS

At this stage, the full model is still in development though a preliminary version for the cladding alone during the accident has been mostly completed and model performance was compared to available experimental data for initial validation.
The Preliminary results were compared with the chosen benchmark experiment and licensing code overview data from the HALDEN IFA650.2 [1] [2] experiment for as-received cladding, originally meant for calibration before testing with higher burn-up fuels. Figure 3 describes the IFA650.2 [1] [2] applicable and available initial experimental setup data by which the comparison was performed (Figure from external source [7]).



Cladding	IFA650.2 Data
Material	Zircalloy-4
Outer Diameter	9.5[mm]
Wall Thickness	0.57[mm]
Initial Outer surface Oxide Layer Thickness	--
Initial Hydrogen content	--
Fuel Rod	**IFA650.2 Data**
Burn-up [MWd/kgU]	0 (Fresh Fuel)
Active Length	500[mm]
Total length of test rod	1040[mm]
Radial Pellet-Clad Gap	0.035[mm]
Fabrication Temperature	25˚C

Figure 3. Halden IFA650.2 [1] [7] experiment data for cladding geometry and user inputs.

At this stage the model does not yet calculate all boundary conditions independently, and so the axial temperature distribution and variation for this comparison was averaged from the IFA650.2 thermocouple measurements and Power distribution under the assumption that the temperature distribution is roughly equivalent to the power distribution which is given as roughly sinusoidal with a peak to average ratio of about 1.06 with the highest value at the center of the rod height.

Table 1 displays the primary values calculated by the current model version as compared with the HALDEN IFA650.2 available experimental data [1] and the FRAPTRAN1.4 [3] calculations, Figures 4 and 5 display exemplary visualization of model results.

Test/Parameter	IFA650.2 Experiment [1]	FRAPTRAN Calculations [1]	Abaqus/Explicit 3D with VUMAT	Deviation from Experiment [%]
Rapture Temperature [˚C]	800	773 , 806	793	1
Max. diameter expansion near burst [%]	90	82 , 76	79	12
Time to Rupture after start of Blowdown [s]	99	75.8 , 81.2	96	3
Internal Pressure at Rupture [MPa]	5.6	5.7 , 5.8	5.8	3.5
Axial Location of Rupture (center) [mm]	212.5	225	239	12.5

Table 1. Comparable Results (at Rupture point)

The hoop strain values vary quite significantly between the cladding inner and outer diameter, as can be inferred from Figure 4 where the inner diameter max engineering hoop strain is above 90% while the outer diameter max value is 79%, this is of course due to the cladding "thinning" from 0.57mm wall thickness to about 35mm wall thickness at the balloon center.

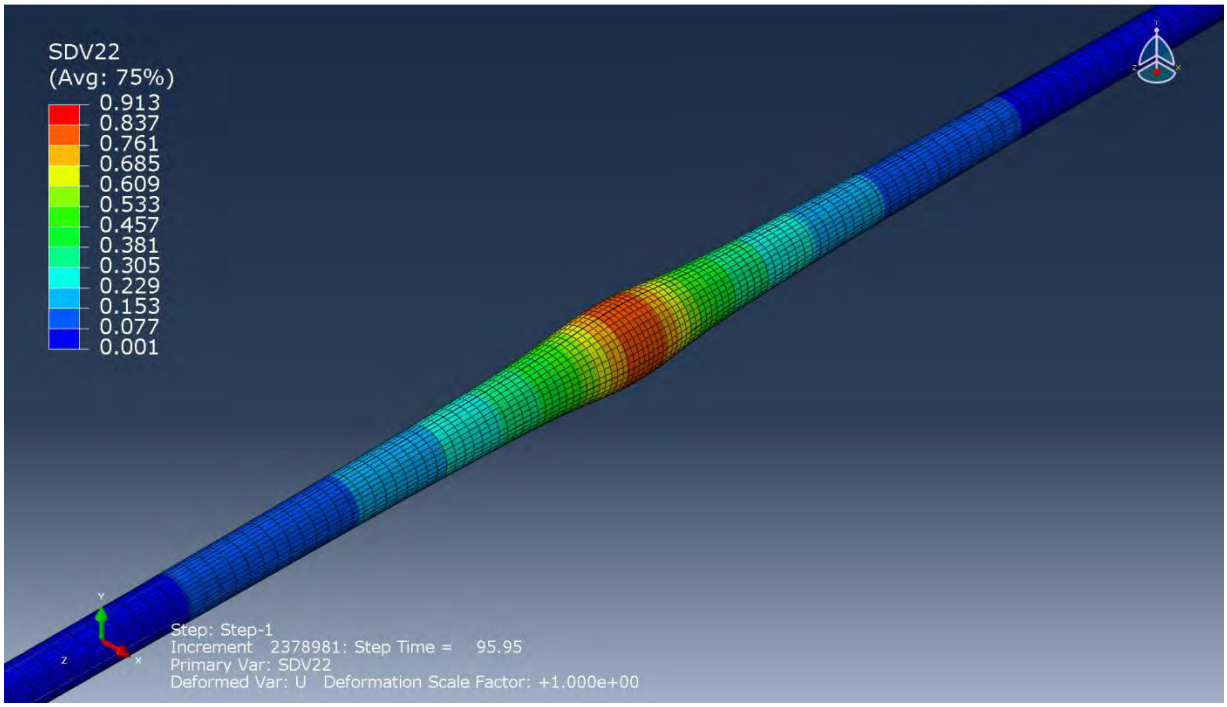


Figure 4. Engineering Hoop strain contours near cladding failure from an isometric view.

An example of the failure criteria on the engineering hoop strain is displayed in Figure 5 as the subtraction of the engineering hoop strain from the failure criteria strain value in eq. 3.

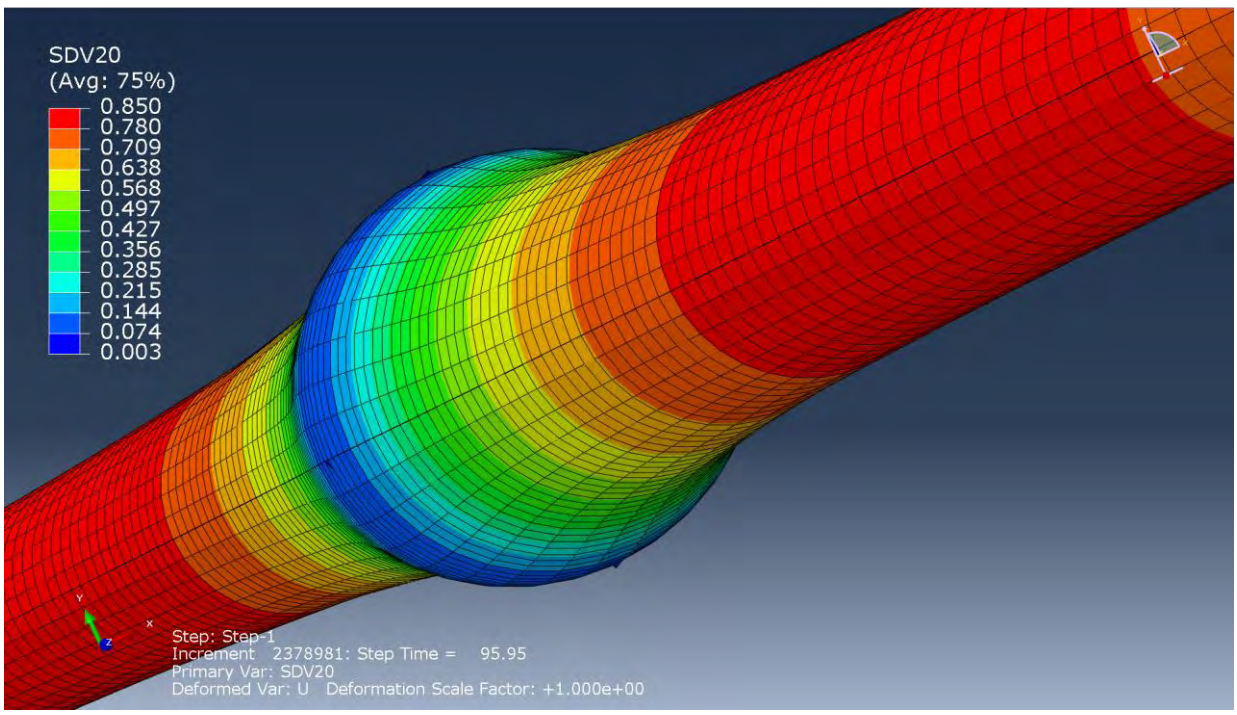


Figure 5. Failure criteria contours, FRAPTRAN1.4 [3] empirical criteria for hoop strain

An example of the failure criteria on the engineering hoop strain is displayed in Figure 5 as the subtraction of the engineering hoop strain from the failure criteria strain value in eq. 3.

(3) $SDV20 = \varepsilon_{fail}(T) - \varepsilon_{\theta}$ so that failure is introduced for $SDV20 < 0$

The ballooning stage shown in Figure 5 is at high strain rates of over $10^{-1}(1/s)$ meaning failure will occur immediately.

Figure 6 displays a graphic comparison of Ballooning shape at burst (Data from [1]), it is important to note that the comparison is a rough one, since the IFA650.2 experimental measurement of the post burst external diameter is approximated and is interpolated from the post-rupture shape after the full accident duration including reflooding and quenching, while the VUMAT data displayed in Figure 6 is taken for the first appearance of rupture. The axial location of the rupture is mostly affected by the axial temperature distribution, which was roughly approximated for this case using the thermocouple readings positioned at 100mm and 400mm from the fuel stack lower end.

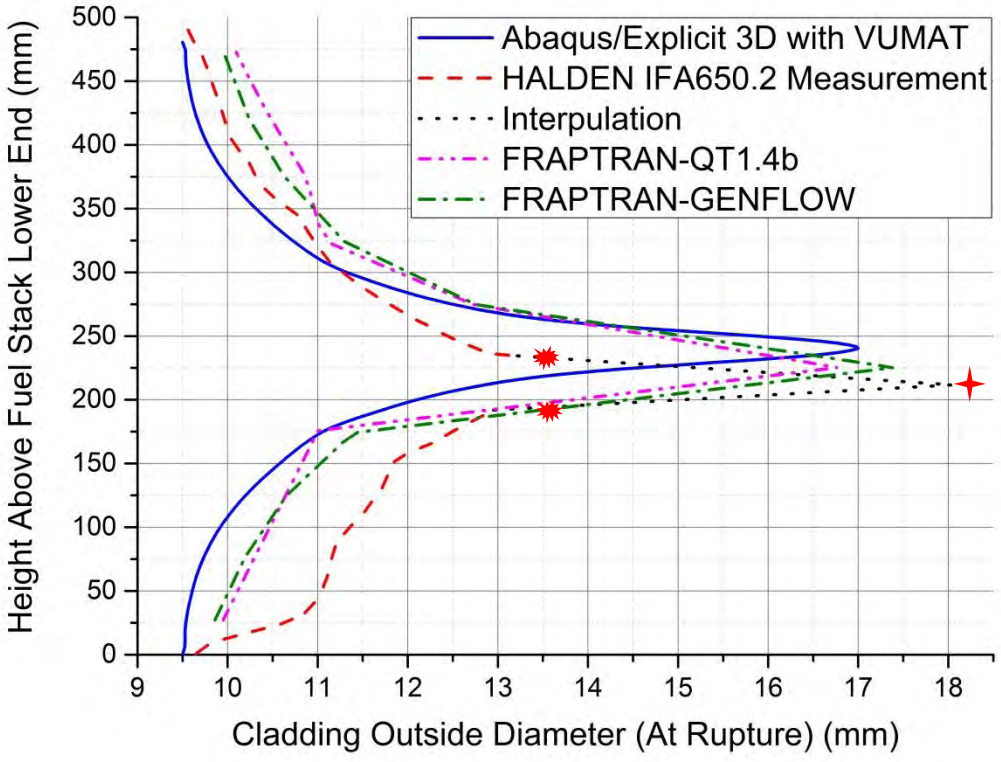


Figure 6. Cladding ballooning shape over effective (heated) length

Preliminary results are in good agreement with available data, and it can be seen that the visco-plastic yielding implemented into Abaqus/Explicit 3D for the private case of axisymmetric loading is in agreement with other codes relying on the same material properties libraries.

The LORELEI Project single rod LOCA experiments in the French JHR reactor, currently in design stages, will better serve to calibrate and validate the model proposed in this paper and with it, performing of further in-depth parametric study of the various factors affecting this complex problem.

4. Summary

- A comprehensive 3D model for clad ballooning and burst behavior prediction was proposed, relying on commercial FEM software with coupled user subroutines.

- Current model displayed here is still in development stages, but preliminary results were compared to the simplified case of the IFA650.2 HALDEN Experiment for as-received cladding and show good agreement with the experimental data for current conditions.

- Shown here are only some key comparable parameters, many more variables are tracked during the simulation and are available for a more in-depth full 3D analysis of the problem.

- Amongst Several significant advantages in using an advanced commercial numerical simulations software such as ABAQUS© is the far simpler and better detailed post-processing abilities.

References

[1] Tero Manngård, Ali Massih, Jan-Olof Stengård(VTT), "Evaluation of the Halden IFA-650 loss-of-coolant accident experiments 2, 3 and 4," Quantum Technologies AB, Uppsala, Sweden, 2012.

[2] Tero Manngård, Lars Olof Jernkvist, Ali R. Massih, "Evaluation of Loss-of-Coolant Accident Simulation Tests with the Fuel Rod Analysis Code FRAPTRAN-1.4," Quantum Technologies AB, Uppsala, 2011.

[3] K.J. Geelhood, W.G. Luscher, C.E. Beyer, "FRAPTRAN 1.4: A Computer Code for Oxide Fuel Rods," U.S NRC, Pacific Northwest National Laboratory, 2011.

[4] Code Development Team,, SCDAP/RELAP5-3D© CODE MANUAL, Idaho National Engineering and Enviromental Laboratory, 2003.

[5] K.J. Geelhood, W.G. Luscher, C.E. Beyer, "FRAPCON-3.4: A Computer Code for the Calculation of Steady-State Thermal-Mechanical Behavior of Oxide Fuel Rods for High Burnup," Pacific Northwest National Laboratory, Richland, 2011.

[6] D. L. Hagrman, "ZIRCALOY CLADDING SHAPE AT FAILURE (BALON2)," Idaho National Engineering Laboratory, 1981.

[7] Stengård, J-O., Miettinen, J., Kelppe, S., *LOCA Test Simulation with FRAPTRAN-GENFLO,* SAFIR2010 –Interim Seminar VTT TECHNICAL RESEARCH CENTRE OF FINLAND, 2009.

MEASUREMENT AND CHARACTERIZATION OF THE INTEGRAL AND FAST NEUTRON FLUX DISTRIBUTION IN THE TRIGA MARK II REACTOR CORE.

D. CHIESA, M. CLEMENZA, M. NASTASI, S. POZZI,
E. PREVITALI, G. SCIONTI, M. SISTI
Physics Department "G. Occhialini" and INFN section of the University of Milano-Bicocca
Piazza della Scienza 3, 20126, Milano, Italy

M. PRATA, A. SALVINI
Applied Nuclear Energy Laboratory (L.E.N.A.) and INFN section of the University of Pavia
Via G. Aselli 41, 27100 Pavia – Italy

ABSTRACT

The neutron flux distribution in the TRIGA Mark II reactor core installed at the Applied Nuclear Energy Laboratory (L.E.N.A.) of the Pavia University was measured through the neutron activation technique, irradiating Al-Co samples in different positions among the fuel elements. The fast and integral fluxes were simultaneously measured in the same positions analyzing the $^{27}Al(n,\alpha)^{24}Na$ threshold reaction and the (n,γ) activation of ^{59}Co, respectively. This measurement was used as experimental benchmark for validating the MCNP reactor model, which was recently upgraded to the present configuration through the burnup analysis of each fuel element.

1. Introduction

TRIGA reactor description The TRIGA (Training Research and Isotope production General Atomics) Mark II is a pool-type reactor cooled and partly moderated by light water, with the fuel consisting of a uniform mixture of uranium (8%wt, enriched at 20%wt in ^{235}U) and zirconium hydride, which provides neutron moderation inside the fuel itself. The TRIGA Mark II reactor installed at the University of Pavia is licensed for operating at 250 kW power in steady state.

The core shape is a right cylinder 44.6 cm in diameter, delimited by two aluminium grid plates (64.8 cm vertically spaced) which provide accurate spacing between the fuel elements. Both grids have 90 symmetric holes distributed along 6 concentric rings labelled from A to F, which hold 1, 6, 12, 18, 24 and 30 locations, respectively. These locations are filled with fuel elements (FEs), graphite (*dummy*) elements, three control rods (named SHIM, REGULATING and TRANSIENT and located in C3, E21 and D10, respectively), the neutron source and two irradiation facilities (the *Central Thimble* in A1 and the *Rabbit Channel* in F24). In order to perform neutron activation or other measurements within the water filling the volumes between the fuel elements, 16 holes of diameter 8 mm are drilled in the upper grid at different distances from the center of the core (Fig. 1).

A 30 cm thick radial graphite reflector surrounds the core while the axial reflector is provided by the fuel element itself in which two graphite cylinders are located at the ends of the rod. Light water in the reactor tank also has the effect of a reflector (about 46 cm in the radial direction and 60 cm minimum in the axial downward direction).

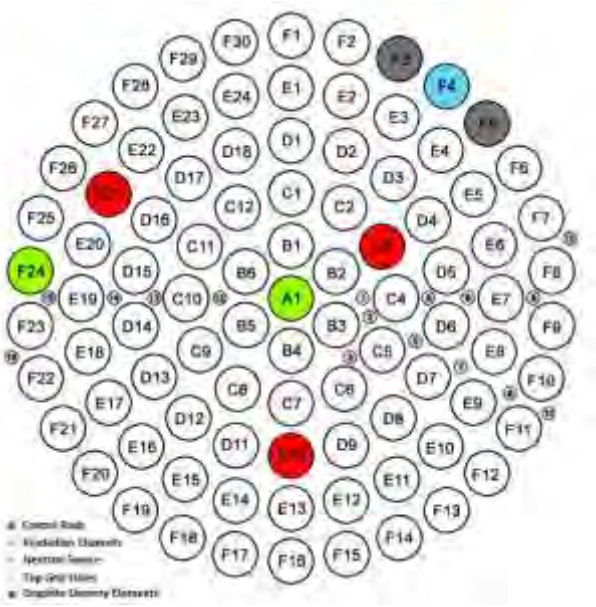


Fig. 1: The core scheme with the positions of the top grid holes.

Flux measurement by neutron activation The neutron activation technique for the evaluation of the flux consists in irradiating some samples with a known amount of elements and then measuring the *activation rate* R, i.e. the number of radioisotopes that each second are created by neutron-induced reactions. The following equation describes the relation between the neutron flux (φ) and the activation rate:

$$R = \mathcal{N} \int \sigma(E)\varphi(E)dE$$

where $\mathcal{N}$ represents the number of precursor isotopes in the irradiated sample and $\sigma(E)$ is the activation cross section. The *effective cross section* (σ_{eff}, i.e. the mean value of the cross section weighted for the neutron energetic distribution) can be introduced to calculate the flux intensity: $\Phi \equiv \int \varphi(E)dE$.

$$\sigma_{eff} = \frac{\int \sigma(E)\varphi(E)dE}{\int \varphi(E)dE} \qquad \Phi = \frac{R}{\mathcal{N}\,\sigma_{eff}}$$

The effective cross section depends on the neutron spectrum distribution, which can vary in the different core positions. For this purpose, we decided to exploit the MCNP [1] model of the TRIGA reactor, which was developed in the recent years [2, 3] and that can be considered a reliable tool for simulating the neutron flux spectrum [4, 5].

The radioisotopes produced through neutron activation usually decay β^- with simultaneous emission of γ-rays, which can be measured to assess the sample activity and, from this, R. If the isotope after the first decay is stable, the differential equation that describes the time evolution of the radioisotope production during the irradiation is:

$$dN = Rdt - N\lambda dt$$

where λ is the decay constant and N the number of radioisotopes in the sample. After the irradiation, the activity of the sample is described by the following law:

$$A(t) = R\left(1 - e^{-\lambda t_{irr}}\right)e^{-\lambda t}$$

where t_{irr} is the irradiation time. Finally, if the measurement of a sample starts after a time t_{wait} and lasts a time t_{meas}, the number of decays that occur is expected to be on average:

$$n_{dec} = \frac{R}{\lambda}\left(1 - e^{-\lambda t_{irr}}\right)e^{-\lambda t_{wait}}\left(1 - e^{-\lambda t_{meas}}\right)$$

Gamma-ray spectroscopy with High Purity Germanium (HPGe) detectors allows to evaluate n_{dec} once the detection efficiency is known for each γ-ray emitted by the radioisotopes.
In order to evaluate the efficiency, we decided to exploit a Monte Carlo tool, based on the GEANT4 code [6], for its accuracy and flexibility in simulating the particle transportation and detection. The Monte Carlo output provides a simulated γ-ray detector spectrum for a fixed number of decay events (n_{sim}) in the simulated source. In this way, the efficiency can be evaluated for each γ-ray of interest as the ratio between the photopeak counts in the simulated spectra (C_{sim}) and n_{sim}. Then, the number of decays (n_{dec}) can be calculated for each γ line observed in the experimental spectra through the following relation:

$$n_{dec} = \frac{C_{meas}}{C_{sim}} n_{sim}$$

where C_{meas} are the photopeak counts in the recorded spectra.

2. Experimental measurements

In order to map the neutron flux distribution, aluminium-cobalt wires (Al 99.9% - Co 0.1%) were chosen as samples to be irradiated in different core positions corresponding to the holes of the upper grid.
The fast flux component was evaluated through the analysis of the ~4MeV threshold reaction $^{27}Al(n,\alpha)^{24}Na$, while the integral flux was determined from the (n, γ) activation of ^{59}Co. In this way, it has been possible to simultaneously measure the fast and the integral fluxes in the same positions, providing the opportunity to perform interesting comparative analyses.
The Al-Co wires (1 mm in diameter and ~15 mm long) were looped on dedicated supporting rods which can be inserted in the upper grid holes and can host up to 11 samples 5 cm apart from each other. In this way, an overall length of 50 cm is covered, allowing to map the neutron flux in correspondence with the active fuel region and part of the FE axial reflectors (Fig. 2).

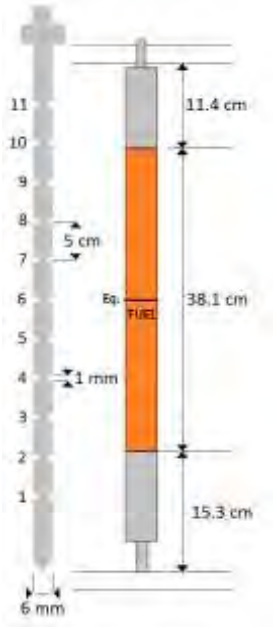


Fig. 2: Schematic drawing (not to scale) of the supporting rod position respect to the FEs.

Two identical supporting rods, made of nuclear aluminum, were manufactured so as to perform the irradiations in two holes at the same time. Due to the relatively short ^{24}Na half-life (14.96 h) and the waiting time required to handle the supporting rods after the irradiation (at least 5 days), we decided not to map more than two holes at a time, otherwise it would have been difficult to measure the ^{24}Na activity in all irradiated samples. For this reason, 6 irradiation campaigns were performed so as to measure the neutron flux in correspondence with 12 upper grid holes (Tab. 1). In order to minimize possible systematic effects, the control rods were kept in similar positions (with the TRANS and the SHIM completely withdrawn), and the power track was recorded to determine the effective irradiation time at full-power condition (250 kW).
Moreover, in order to check that the flux intensity was equally reproduced in the different irradiations, Al-Co *monitor samples* were positioned in the Lazy Susan facility, which is located within the radial graphite reflector. Analyzing the ^{60}Co specific saturation activity (*SSA*, equal to the activation rate per unit mass of precursor isotope) in the monitor samples, we can state that the flux intensity was actually the same within the uncertainty bandwidth (Fig. 3). For this reason, to compare the results concerning different irradiations, the data have been normalized to the average monitor's specific saturation activities and their errors have been appropriately estimated including the monitor's uncertainty component.
The activation rates of aluminum and cobalt were evaluated through γ-ray ray spectroscopy measurements performed with the "*GePoz*" HPGe detector installed at the Radioactivity Laboratory of Milano-Bicocca University. Thanks to the well configuration of this detector, the geometric efficiency is maximized and the sample placement can be easily reproduced in the

different measurements. As previously mentioned, the detection efficiency was determined through GEANT4 Monte Carlo simulations.
For each observed γ line, we calculated the activation rate and the corresponding uncertainty, which was evaluated by combining the statistical errors in the measurement and in the simulation, plus a 5% error to keep into account the accuracy of the Monte Carlo model of the "*GePoz*" detector [7]. Thanks to the possibility of analyzing three γ lines of ^{60}Co (1173 keV, 1332 keV and the sum peak at 2505 keV) and two γ lines of ^{24}Na (1368 keV and 2754 keV), the corresponding activation rates were finally estimated as the weighted average of the different results obtained from each observed γ line. In this way, the experimental relative errors associated with R resulted about 4% for ^{60}Co and between 4.5% and 7.5% for ^{24}Na.

Irr. #	Date	Time	t_{irr} (s)	Holes
1	23/05/2013	11:27	3624	12
2	23/05/2013	15:58	4859	13
3	29/05/2013	15:13	4999	1 & 14
4	21/06/2013	12:02	7232	10 & 16
5	26/06/2013	15:09	4786	4 & 8
6	02/07/2013	11:28	4989	3 & 6
7	09/07/2013	11:08	4816	5 & 9

Tab. 1: List of the irradiation performed in the different core positions with the corresponding dates and durations.

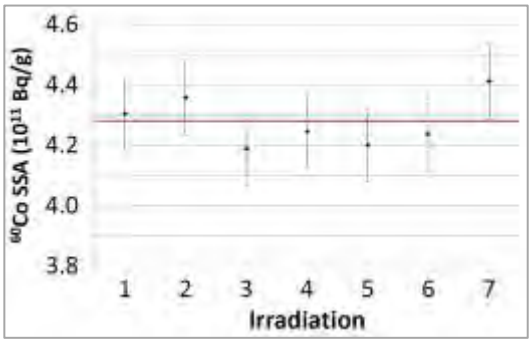


Fig. 3: Specific saturation activity of ^{60}Co measured in the monitor samples irradiated in the Lazy Susan facility. The average value is shown through the red line.

3. Fast flux analysis

Firstly, we present the data of the fast flux component, whose energy threshold was fixed at 4 MeV, according to the cross section of the ^{27}Al(n,α)^{24}Na reaction. The effective cross section was evaluated assuming that the fast flux spectrum has an exponential energy dependence: $e^{-\alpha E}$ with α = 0.65, as obtained by fitting the MCNP spectrum simulated in the Central Thimble. It is reasonable to assume that this energy dependence does not significantly vary within the core, because it depends primarily on the spectrum of prompt neutrons by fission. For this reason, the same effective cross section value (8.4 mb) can be used for all irradiation positions.
The fast flux vertical profiles obtained for each irradiation position are presented in Fig. 4. The data concerning holes which are located at the same distance from the center of the core are drawn on the same graphs.
The fast flux data referring to the peripheral positions are always symmetric respect to the center of the fuel active region (position 0 cm) with two exceptions: the holes #3 in ring B and the hole #13 in ring C. Since these two profiles appear shifted downward respect to the others, we can reasonably assume that the supporting rods were not fully inserted in the core during the irradiations. If this is the case, the experimental data would refer to positions which are few centimeters higher, thus resulting compatible with the other profiles.
In general, it is interesting to note that the fast flux is also symmetric in the radial direction: in fact, comparing the data acquired in the same rings, the profiles are always overlapping except for the outer ring (F). The reason why such large difference was recorded between the data of holes #10 and #16 is not easy to identify and further measurements would be required to investigate this aspect; however, it should be noted that the Rabbit Channel is not far from the hole #16 and its presence could lead to a lower fast flux because a reduced number of fission reactions occur in that core region.
Finally, the measured data show that the fast flux decreases with a relatively high gradient when moving towards the peripheral core regions: in fact, in the vertical profiles, there is a

ratio around 1:10 between the data at ±25 cm and the ones at the center, while in the radial direction a decrease by a factor ~2.5 is recorded between the data of ring B and F.

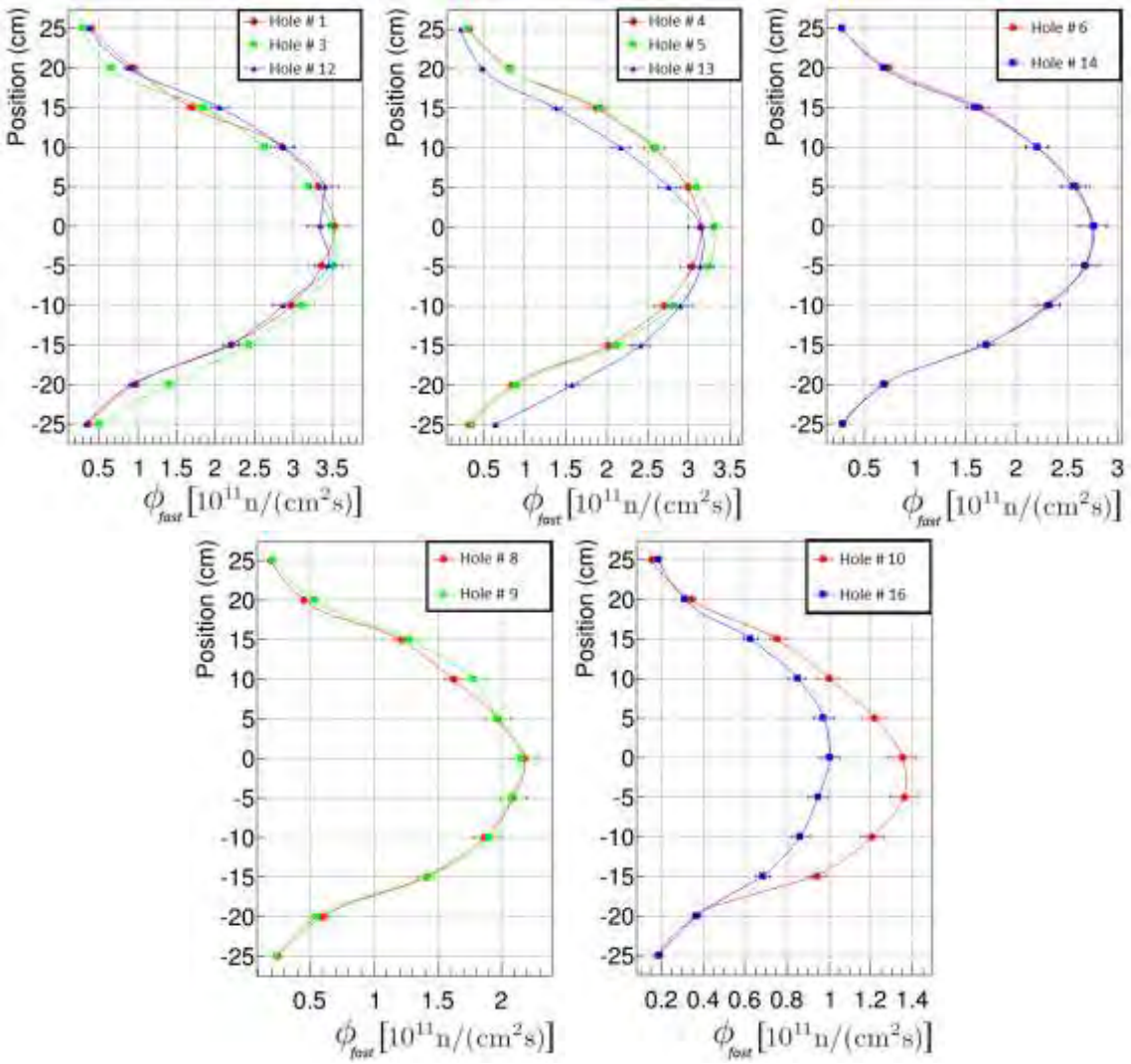


Fig. 4: Vertical profiles of the fast flux measured in the holes at different distances from the center of the core (rings).

4. Integral flux analysis

The measurement of the integral flux was performed by analyzing the (n,γ) reaction on ^{59}Co, which is mainly induced by thermal and epithermal neutrons. In this case, it is interesting to firstly analyze the graphs referring to the ^{60}Co *SSA* in the different irradiation positions. Looking at Fig. 5, it will be noted that the profiles are not as symmetric as those obtained for fast neutrons. Irregular patterns are also observed in the peripheral positions outside the fuel active region (which extends between ±19 cm). In particular, in some holes of rings E and F, the activation rates at ±15 cm resulted lower than those at ±20 cm.

These experimental findings can be explained by considering that the neutron spectrum varies within the core. In particular, the fraction of thermal neutrons over the total flux increases in the peripheral core regions and, as a consequence, the effective cross section is higher. Therefore, for evaluating the integral flux, it is not possible to use the same σ_{eff} value for all the irradiation positions, otherwise we would obtain incorrect flux profiles characterized by the same irregular patterns observed in the *SSA* graphs.

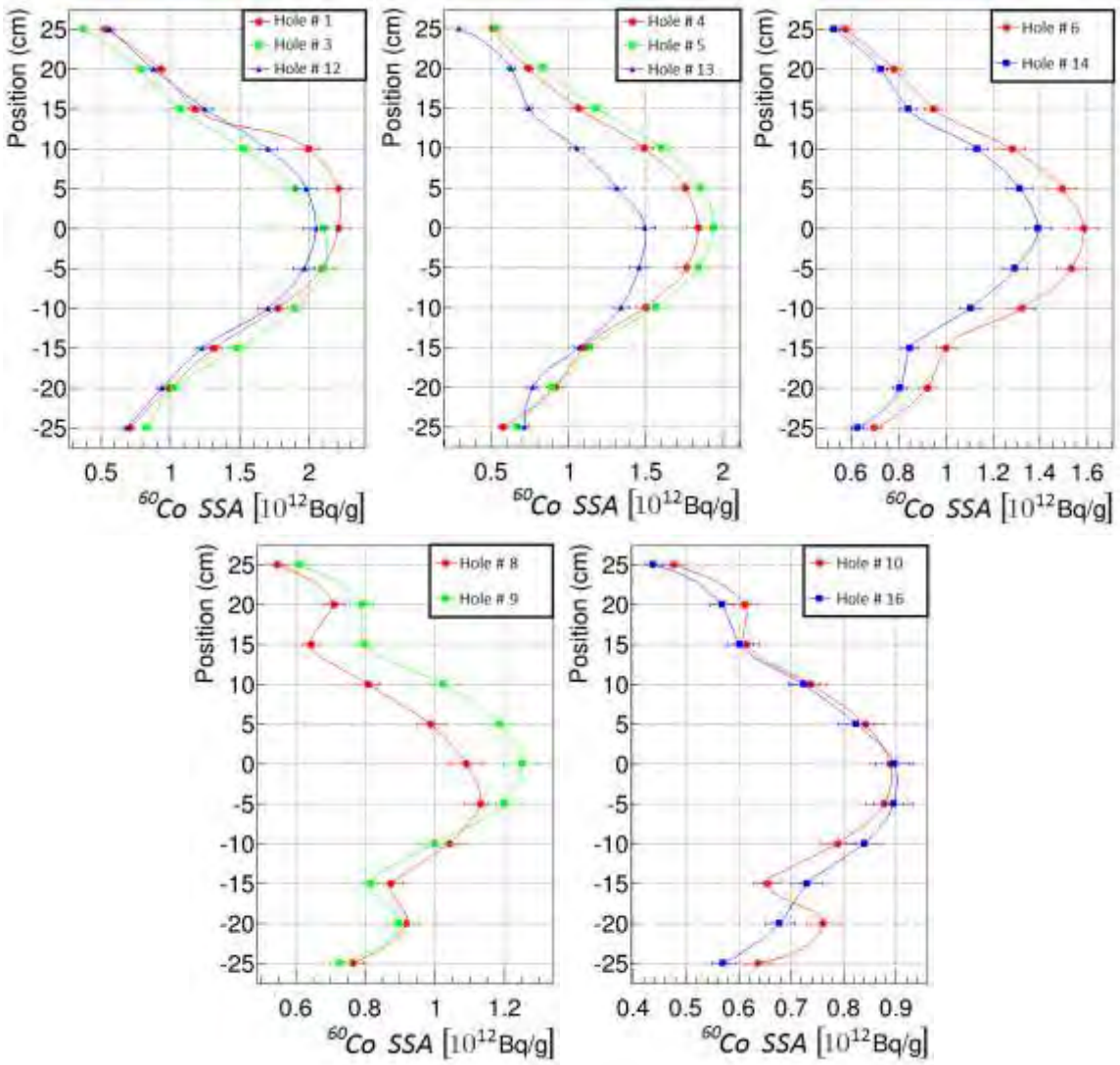


Fig. 5: *Vertical profiles of the ^{60}Co SSA measured in the different holes and rings.*

For this reason, the MCNP reactor model was exploited to evaluate the neutron spectra and calculate the corresponding effective cross sections in all irradiation positions. The σ_{eff} values obtained for the case of hole #16 are shown in Fig. 6, where differences up to a factor 2 are recorded between the central and the peripheral positions.

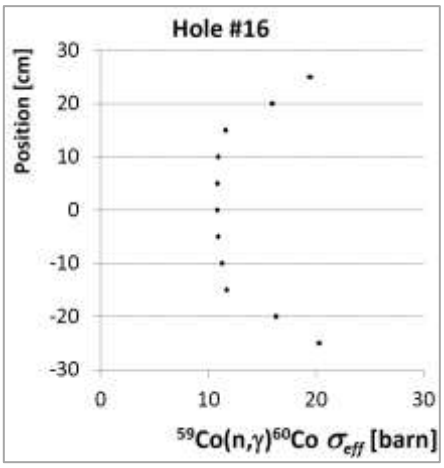


Fig. 6: The σ_{eff} of (n,g) reaction on ^{59}Co evaluated in the different irradiation positions of hole #16.

The integral flux values were then calculated with the effective cross sections evaluated point by point and the results are presented in Fig. 7. As expected, the integral fluxes are characterized by decreasing intensities while moving towards the peripheral regions and the irregular patterns are no longer present. With respect to the fast flux, these profiles have a lower gradient: in fact, comparing the data at the ends and at the center of the vertical profiles, we observe a ratio of about 1:3 in the outer rings and 1:5 in the inner ones. Moreover, in the radial direction the flux data in the different rings are nearly constant at ±25cm and their ratio does not exceed

2.5 at position 0 cm. The data of the holes #3 and #13 appear again as shifted downward, in line with the observations concerning the corresponding fast flux profiles, thus supporting the hypothesis that in those cases the samples were not correctly positioned in the core.
Analyzing the integral flux profiles referring to holes at the same distance from the center, no significant differences are observed in the case of Ring F, in which the fast fluxes resulted asymmetric in the opposite holes. The interpretation of these findings is not straightforward and further experimental tests would be needed to check the repeatability of this measurement, in order to exclude possible systematic errors related to the position of the supporting rod in the holes of ring F.
On the contrary, some differences are recorded in the rings C, D and E. In particular, it is interesting to note that the corresponding fast flux profiles are completely overlapped, meaning that these asymmetries regard the thermal and epithermal neutron flux component only.
These experimental observations can be explained by considering the peculiar geometry of an experimental reactor such as the TRIGA Mar II, equipped with a graphite reflector which is not totally symmetric, because it hosts the Lazy Susan facility and the penetrating and tangential irradiation channels. Since the reflector acts mainly on thermal neutrons, this would account the fact that these differences are observed in the integral flux profiles only.
Moreover, the different fuel burnup can locally influence the distribution of the thermal neutrons, which are particularly susceptible to be captured by the poisons that have accumulated over time in the fuel elements.

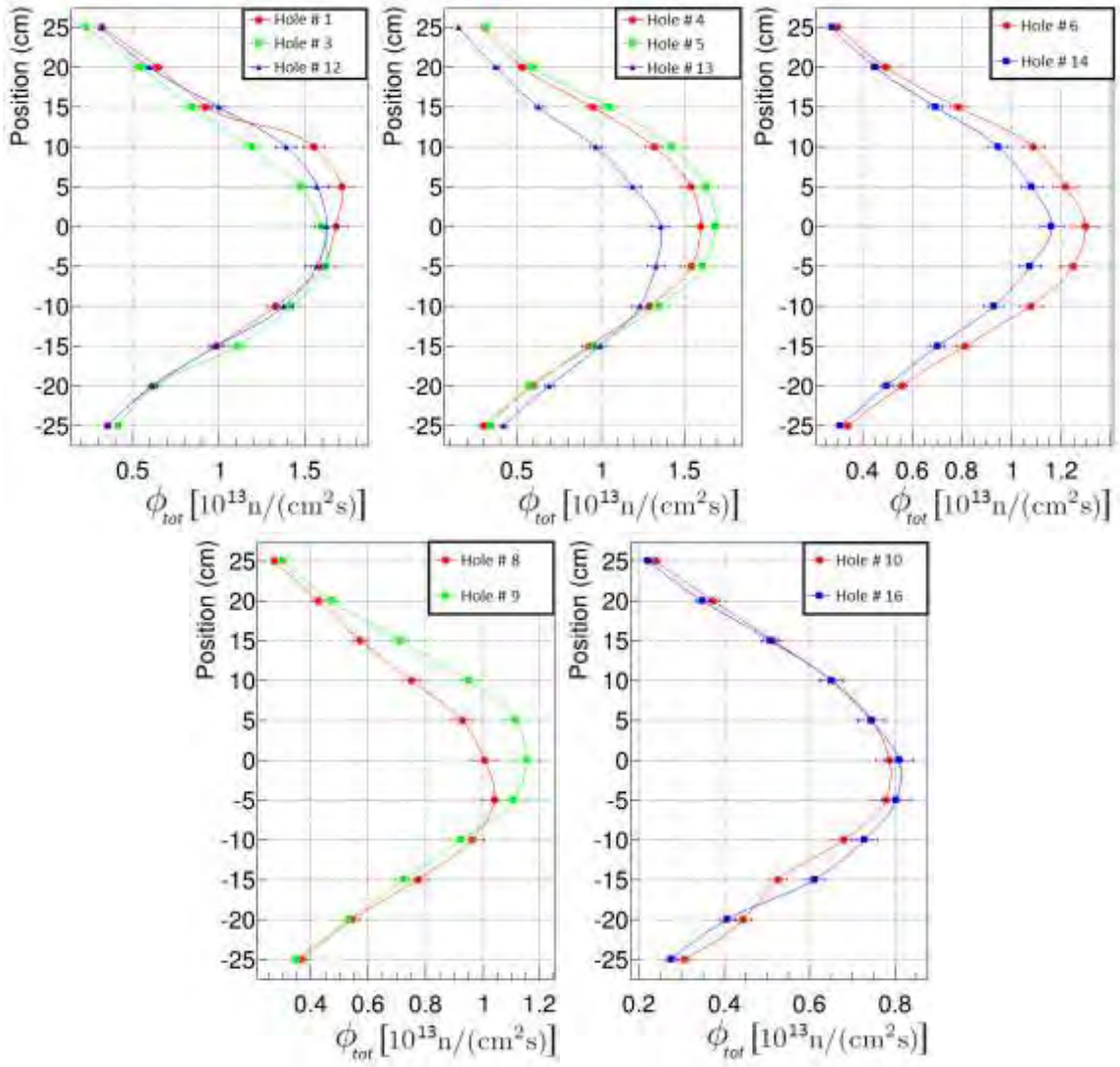


Fig. 7: Vertical profiles of the integral flux measured in the different holes and rings.

5. Integral and fast flux distribution map

The experimental data referring to the positions sampled on the diagonal of the core[1] were then interpolated to create 2-dimensional maps of the integral and fast fluxes.
Looking at Fig. 8, the symmetry characterizing the fast flux is even more evident than before; the only place in which asymmetry is observed is around the -11 cm horizontal position, which corresponds to the hole #13, affected by systematic error. Since the fast flux is strictly connected with fission density, this map provides at the same time some information about the power distribution in the core.
On the other hand, the integral flux map exhibits an interesting asymmetry: in fact, we observe that the flux below the fuel active region is higher than that measured in the corresponding upper positions. This observation can be related with the fact that water and graphite below the fuel are colder and, as a consequence, their moderating and reflecting power is higher.

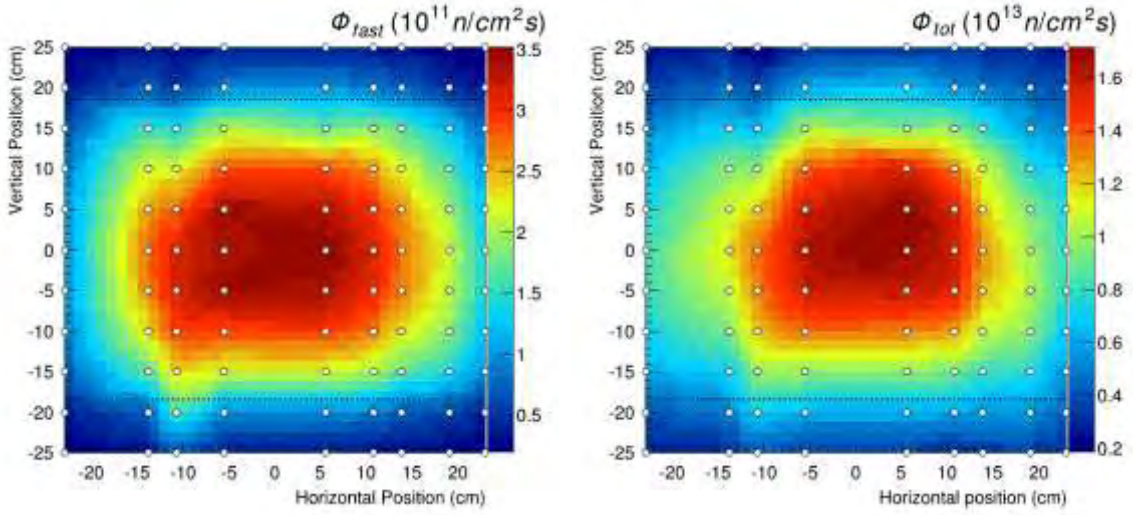


Fig. 8: The 2-dimensional maps of the fast (left) and integral (right) fluxes. The white points correspond to the sampled positions; the fuel active region is between the dotted lines.

6. Benchmark analysis of the MCNP simulation model

The experimental data of the integral flux distribution were then used as a benchmark to validate the MCNP model referring to the reactor configuration of July 2013. Particularly, we checked the model capability to correctly simulate the flux intensity in the different irradiation positions.
The neutron flux data obtained from the simulations were normalized to the total number of neutrons which are produced per unit time in the reactor when it operates at 250 kW (1.96×10^{16} neutrons/second).
The benchmark analysis results are presented in Fig. 9: in general, a good agreement is observed between the experimental and Monte Carlo data in all irradiation positions.
Particularly, a very good agreement is obtained for the holes number 6, 9 and 12, whose data all agree within 8%, which corresponds to $\sim 2\sigma$ range, taking into account that the experimental uncertainties are equal to about 4%.
In the holes number 5, 8 and 14, larger differences are observed: in the first two cases, a small positioning error seems to affect the results, while some mismatch is recorded in the central positions of hole #14. Anyway, in these data sets, the maximum difference between each couple of data is within ~20%, that can be considered an acceptable error for the Monte Carlo simulation of a complex system such as the TRIGA reactor core.

[1] See holes numbering scheme in Fig. 1 (holes #10 and #16 were also included).

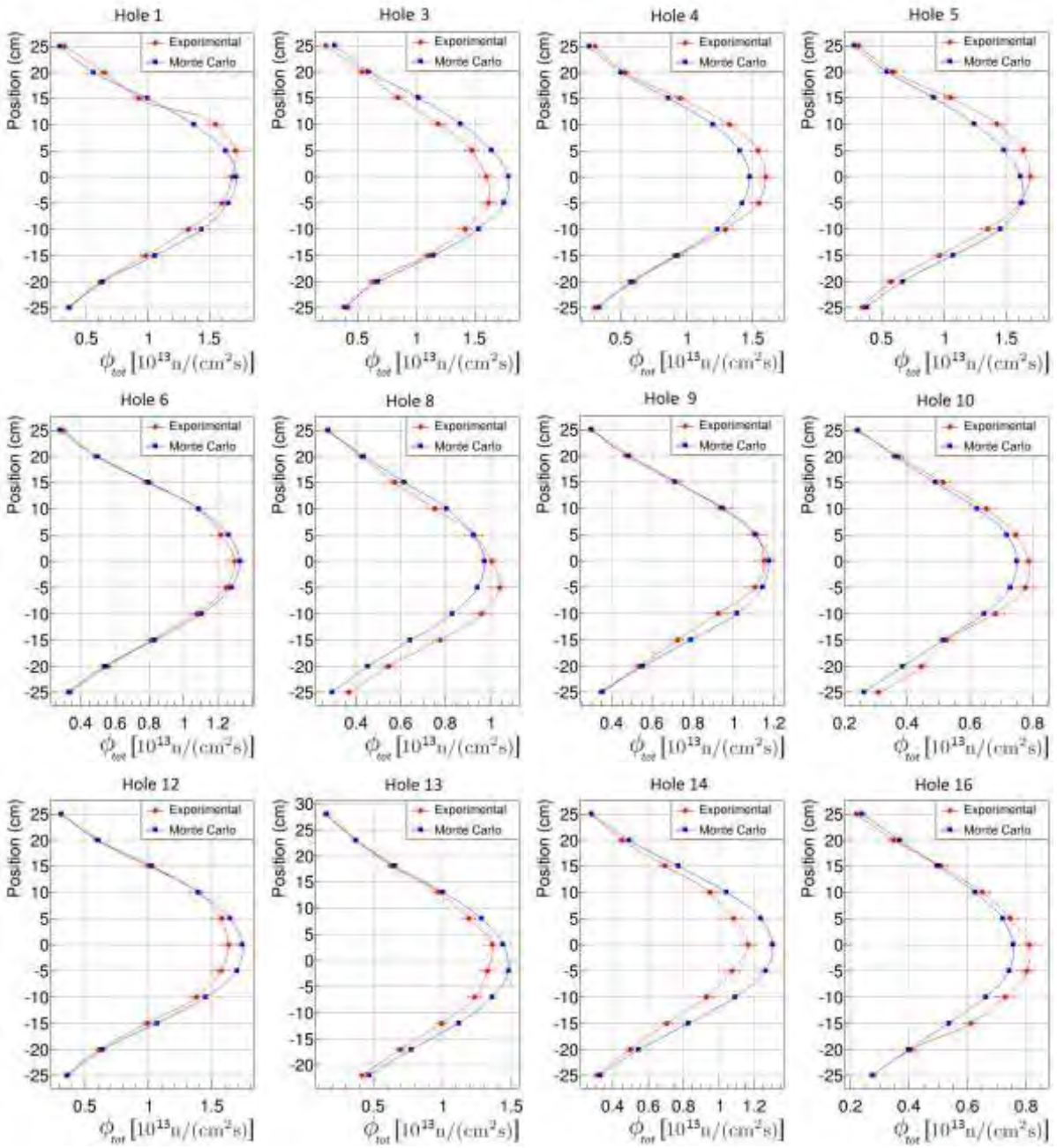


Fig. 9: Comparison between the experimental and the simulated vertical distributions of the integral neutron flux.

Concerning the holes number 3 and 13, we have to consider the systematic positioning error which was highlighted by the analysis of the fast flux profiles. In the case of hole 13, affected by a larger displacement (about 3 cm), we decided to run the Monte Carlo simulation so as to evaluate the neutron fluxes in the corresponding positions translated by 3 cm. With this correction, a good agreement is obtained between the experimental and the simulation data, confirming the reliability of our interpretation.

Finally, in the remaining data sets, differences up to $\sim 3\sigma$ are recorded for some data referring to the peripheral positions, while a better agreement characterize the data corresponding to the active fuel length in the range ±15 cm.

7. Conclusions

The results of this analysis show that the adopted experimental technique, based on the neutron activation of Al-Co samples, allows to simultaneously measure the integral and the fast fluxes in the same positions, providing the opportunity to perform interesting comparative analyses.
Particularly, it was shown that the fast flux component is characterized by a symmetric distribution, reflecting the symmetry of the fuel elements disposition and power distribution. For this reason, the fast flux profiles are also suitable to identify possible systematic errors due to sample positioning.
On the other hand, the integral flux (whose evaluation is dominated by the thermal and epithermal component) exhibits asymmetries, especially in the peripheral core regions. In this respect, it is important to underline the role of the MCNP simulations: in fact, their utilization has proved to be fundamental for a correct interpretation of the activation rate data, taking into account the higher thermalization in the positions corresponding to the axial graphite reflectors.
Finally, since a good agreement was found between the experimental data and the simulation results, we can state that the MCNP reactor model is able to correctly simulate not only the spatial profile of the flux distribution, but also its absolute intensity.
In conclusion, this analysis proves that the MCNP model of the TRIGA Mark II reactor of the University of Pavia, developed in the recent years, is a reliable and powerful tool for a fully comprehensive description of the neutron flux and reaction rates in the core.

References

[1] X-5 Monte Carlo Team, *MCNP - A General Monte Carlo N-Particle Transport Code, Version 5*. Los Alamos National Laboratory, 2008.

[2] A. Borio di Tigliole and *et al.*, "Benchmark evaluation of reactor critical parameters and neutron fluxes distributions at zero power for the TRIGA Mark II reactor of the University of Pavia using the Monte Carlo code MCNP," *Progress in Nuclear Energy*, vol. 52, pp. 494-502, 2010.

[3] D. Alloni and *et al.*, "Final characterization of the first critical configuration for the TRIGA Mark II Reactor of the University of Pavia using the Monte Carlo code MCNP", *accepted for publication in Progress in Nuclear Energy*.

[4] D. Chiesa, E. Previtali, and M. Sisti, "Bayesian statistics applied to neutron activation data for reactor flux spectrum analysis", *accepted for publication in Annals of Nuclear Energy*.

[5] D. Chiesa, E. Previtali, and M. Sisti, "Bayesian statistical analysis applied to NAA data for neutron flux spectrum determination", *accepted for publication in Nuclear Data Sheets*.

[6] S. Agostinelli and et al., "Geant4: A simulation toolkit," *Nucl. Instr. Meth. A*, vol. 506, pp. 250-303, 2003.

[7] A. Borio di Tigliole and *et al.*, "TRIGA reactor absolute neutron flux measurement using activated isotopes", *Progress in Nuclear Energy*, vol. 70, pp. 249-255, January 2014.

EXPERIMENTAL STUDY OF THERMOSIPHON CIRCULATION OF WATER TROUGH TRISNGLE ROD BUNDLE

Y. AHARON(1) , I. HOCHBAUM(1)

(1) – NRCN , P.O.B. 9001, Beer – Sheva, Israel

ABSTRACT

An experimental study of natural circulation has been performed for a water flow in a uniformly heated vertical three rods bundle. The rods were 12 mm in diameter and 1000 mm in length and they located inside a 32 mm ID tube. The experiments conducted under a various values of channel power up to 5 kW and three channel flow resistance values. All the experiments conducted in atmospheric pressure and simulating a normal operation or Loss of Flow Accident in a research reactor or small power reactor in accident conditions.

During the experiments the water and rods temperatures were measured for calculation of the flow rate and the convective heat transfer coefficient inside the channel. A simple model, based on the conservation equations was written and compared with the experimental results. A good agreement was achieved in the flow rate prediction and the rods temperatures.

1. Intrudaction

In many research reactors the reactor can operate under either forced or natural convection modes. Under forced convection, the primary cooling system removes the heat generated in the reactor core through a heat exchanger to the secondary cooling system, which releases this thermal energy through the cooling tower to the atmosphere. Under natural convection operating mode, the generated nuclear power imply heats up the pool water, and is ultimately dissipated through the pool surface to the containment atmosphere. Hence, the large pool provides a heat sink for the energy generated within the core. The pool surface is open to the containment atmosphere, where thermal energy exchange via evaporation and convection heat transfer can occur.

In case of loss of primary flow under forced convection operating mode (Loss of Flow Accident - LOFA) the natural convection flapper valve opens automatically leading to natural circulation in the reactor core. Whereas under natural convection operating mode, the flapper valve remains open during all the process. In both cases, the natural circulation flow ensure safe reactor core cooling by natural convection and all decay heat can be absorbed completely by the large water inventory of the reactor pool with no need for further external cooling. This mechanism of natural circulation is used also for low power operation of the core or for zero power research reactors like the Canadian SLOWPOKE research reactor [1].

In the last three decades small integral PWR are also design without a main circulation pumps and the coolant flow is driven by natural circulation like the REX-10 [2]. Those reactors are working in a higher pressure comparing to research reactors. That high pressure provides a higher working temperatures and a higher moving force for the natural circulation.

Researches on natural circulation and passive cooling of nuclear reactors and developing of integrated PWRs which basically working on natural circulating cooling were encouraged after the last nuclear accident in Fokushima which was a result of electrical supply failure due to the Tzunami and Loss of Flow Accident.

Safety aspect of the reactor design is the cooling capacity in natural circulation mechanism. The natural circulation cooling capacity of a research reactor is determined by the temperature margin at ONB, which ensures a large margin from any boiling crises.

Usually, the natural circulation cooling capacity of a research reactor is investigated by numerical simulation using commercial codes like RELAP5, TRAC and THYDE-W and so on

[3]-[4]. Those commercial codes are usually developed for NPP and they need many corrections to be used in research reactors due to the complicated geometrical and different structure of the core in the research reactor. That problem makes the prediction of the numerical simulation be unreliable.

The most common fuel geometry in research reactors is the plates geometry and validation experiments are usually conducted for that geometry [5]. Fuel rods geometry is used usually in NPP but it can also be found in few research and low power reactors like the HANARO and SLOWPOK 2 and also in Zero Power Reactors [6] which their normal operation cooling mode is natural circulation (like the 20 kW SLOWPOK-2 research reactor). A research on natural circulation on hexagonal and square rod bundles was published also in [7] and [8]. Those researches were conducted for accurate prediction of heat transfer coefficient in rod bundles at low Reynolds Number (Re<1000) in design and operation of open pool type research reactors such as the Annular Core Research Reactor (ACRR) of Sandia National Lab. (SNL) and other TRIGA type reactors. The natural circulation data in [7] indicated that rod spacing only slightly affects the heat transfer, and Nu increased proportionally to $Ra^{0.25}$ as follows:

$$Nu = 0.272 Ra^{*0.25} \quad (1)$$

Where Ra* is Rayleigh number based on the heat flux and the hydraulic diameter as a characteristic length. In another publication [9] experiments were conducted in natural convection with rod bundle in both sides of the loop (the cold side and the hot side). Empirical correlations for the average Nusselt number have been developed as well as for the frictional resistances of the loop. The proposed correlation for natural circulation and mix convection are equations (2) and (3) respectively as follows:

$$Nu = 0.024 Gr^{*0.42} \Pr^{0.43} \quad (2)$$

$$Nu = 0.00091 \left(\frac{Gr^*}{\mathrm{Re}} \right)^{0.8} Gr^{*0.176} \Pr^{0.43} \quad (3)$$

Where Re is the Reynolds number based on the average velocity in the bundle and the hydraulic diameter, as a characteristic length. Gr* is modified Grashof number based on the heat flux and the hydraulic diameter. The analysis of the effective flow resistance parameter R indicates that a plot of RA_f^2 versus 1/Re would be a straight line of the form:

$$RA_f^{\,2} = C_R/\mathrm{Re} + K_T A_f^{\,2} \quad (4)$$

Where A_f is the cross-sectional flow area and Re is the Reynolds number of the circulating fluid in the source leg (the hot rod bundle). The constant C_R is composed of the individual friction factors for each loop component, and K_T is the total form loss coefficient for flow in the loop. Analysis of the data that was done in [9] indicates a slope of C_R = 8050 and $K_T A_f^2$= 1.467. The intercept is nearly zero, indicating that the effect of form losses in the loop is negligible in comparison with the frictional losses. The experiments in [9] included also a comparison between the heat transfer coefficient in the rod bundle with and without spacer grids. It was reported that the hydraulic affect of the spacer grids on the flow resistance was negligible in natural circulation mode.

The purpose of this study is to present a simple model for calculation of a natural circulation loop and to investigate the prediction accuracy of various correlations in simple rod bundle natural circulation.

2. Experimental equipment and procedure

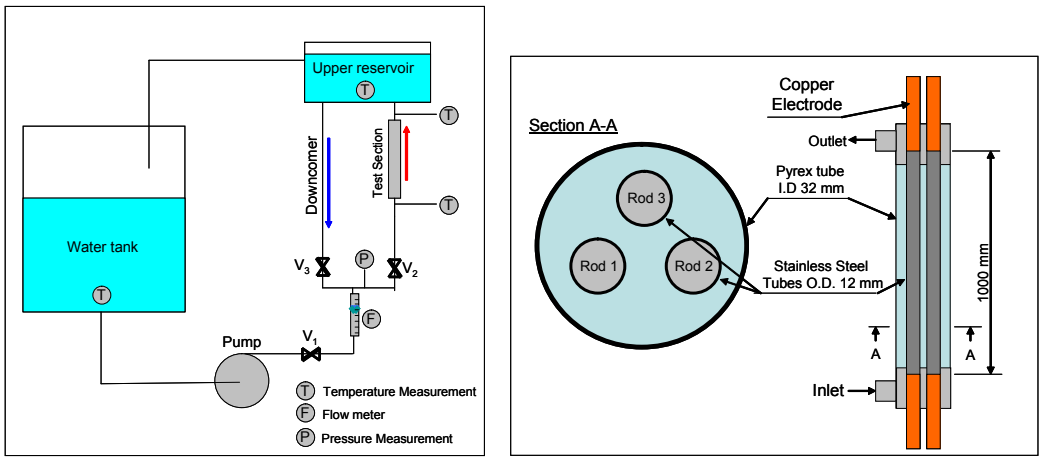
The test loop is presented in figure 1(a). The loop consists of test section, upper reservoir, water tank and circulating pump. Two valves (V2 and V3) are locating along the natural circulation loop to control the flow loop friction losses. Flow-meter is located at the outlet of the pump to measure the flow rate from the pump in the calibration experiments as will be describe in the next paragraph. Thermocouples were located at the inlet and the exit of the

test section and also in the upper reservoir and in the water tank. Pressure was measured at inlet of the loop branches for the calibration measurements.

The test section was made up of three 12- mm OD, stainless steel tube which located inside a Pyrex tube 32 ID. The heating tubes were arrange in triangle arrangement with p/d= 1.17 where p is the pitch between the rods center and d is the rod diameter. Copper electrodes were silver soldered to each end of the stainless steel tubes. The length of the heated zone was 1000 mm as shown in Figure 1(b). Thermocouples were attached to the outside surface of two heating rods (rod 1 and 2) in various locations to measure the heaters wall temperatures. The temperature measurement location in each rod is presented in table 1. The test section was heated electrically by a low voltage D.C power supply of 15 V and 5000 A. The power of the test section was measured by measuring the voltage and the current through the test section. The current was measured by using a calibrated shunt which located in serial with the test section.

Table 1: Temperature measuring location from the bottom of the heating zone in rod #1 and #2 (in mm)

Rod 1	Rod 2
60	
300	300
495	
685	685
945	945



(a) (b)

Figure 1: The test loop (a) and the test section (b)

2.1 Calibration measurements

In the calibration measurements, water was circulated through the two branches of the loop (separately) by the pump and the pressure drop of each branch was measured in a various flow rates. The total pressure drop of the loop (by assuming that the flow direction is not influences the flow resistance) was the sum of the pressure drop of the two branches. Three positions of valve V2 were used for three values of flow resistance of the loop while V3 is used in open position in the three cases of flow resistance.

2.2 Natural circulation experiments

At the calibrated position of valve V2 where V3 is entirely open, power applied to the test section in few nominal power levels between 2-6 kW. In each power step the heaters and the water temperatures were measured after reaching a steady state conditions. The experiments were conducted in the same procedure for each flow resistance which was

regulated by changing the position of V_2 and calibrated as described in the previous paragraph.

3. Results and analysis

3.1 Calibration results

Three values of flow resistance were calibrated in the calibration experiments and used in the natural experiments. The flow resistance of the loop was defined as follows:

$$K = \frac{\Delta p}{\dot{V}^2} \quad (5)$$

Where Δp is the measured pressure drop in forced flow and $\dot{V}$ is the flow rate. Figure 2 presents the measured pressure drop vs. the flow rate in square power ($\dot{V}^2$) for the three flow resistance cases: K1, K2 and K3 where K1 is the case when the valve V2 is also entirely open. The plot K-0 presents the measured value of the downcomer branch with V3 open. The slope of a linear regression of the experimental values (which is also presented in the figure) is the flow resistance value (K) of the measured branch. As can be seen, the flow resistance of the downcomer branch is almost negligible. The total flow resistance coefficient of the loop is the sum of the bundle branch coefficient for each case and the downcomer branch. That sum is almost the value of the bundle branch coefficient.

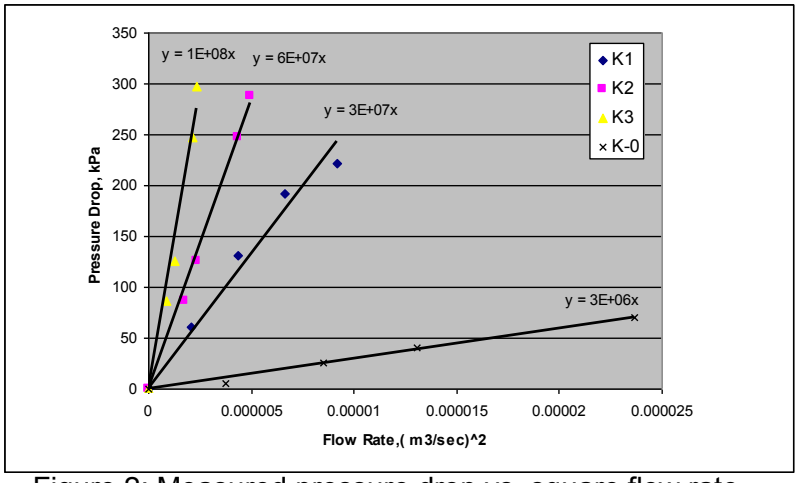


Figure 2: Measured pressure drop vs. square flow rate

3.2 Natural circulation modeling and experiments results

Modeling of a natural circulating in the loop based on a balance between the friction losses along the loop due to the flow rate ($\Delta p_{tot,f}$) and the moving force (pressure drop) due to the density decreased by the heating of the water which causing buoyancy force ($\Delta p_{tot,b}$).

$$\Delta p_{tot,f} = \Delta p_{tot,b} \quad (6)$$

In each zone, the friction losses were calculated as follow.

For the longitudinal friction losses: (7)

$$\Delta p_{L,i} = \left(f \frac{L}{D_H} \rho \frac{\mathrm{v}^2}{2} \right)_i$$

And for local friction losses: (8)

$$\Delta p_{loc,i} = \left(K_f \rho \frac{\mathrm{v}^2}{2} \right)_i$$

The friction coefficient f in eq. 7 was taken according to the Reynolds number in the calculated zone. In case of natural circulation the Reynolds number is usually in the range of laminar flow regime. In this case the friction coefficient f is calculated as follow: (8) $f = C/\mathrm{Re}$

where C depends on the channel geometry. For the local friction losses the available value of the constant K_f is usually for developed turbulent flow. Use of those values in the model over predicts the flow rate in the channel which yields a lower temperature gradient along the heated zone. That problem was also reported by [10] which used the RELAP-5 code for calculation of

natural circulation in a loop. In that work, the form loss coefficients in the junctions were chosen large enough to obtain the correct mass flow. In the same manner, in the present work the longitudinal friction losses were calculated by using eq. 4 and 6 and in eq. 5 the value of the coefficient K_f was calculated by using the following relationship which was recommended by W. Hooper [11]:

$$K_i = \frac{K_r}{\mathrm{Re}} + K_{\infty,i}\left(1 + \frac{1}{D_i}\right) \quad (9)$$

In this Equation $K_{\infty,i}$ is the "classic" K for the i^{th} tubes fitting in the fully turbulent flow regime, D_i is the fitting diameter (in inchs) and K_r is a constant which was adopted to get the flow rate and the temperature gradient along the heated zone as follows:

$$\Delta T_i = T_{in} + \frac{q_i}{\dot{m} Cp} \quad (10)$$

Where T_{in} is the inlet temperature to the calculated zone, q_i is the heating power which supply to the water along the calculated zone, $\dot{m}$ and C_p are the mass flow rate and the heat capacity of the coolant, respectively. The velocity v in each zone is calculated from the mass flow rate and the cross section of the calculated channel.

The moving force (buoyancy pressure drop) is depending on the mass flow rate of the coolant, the heating power of each zone and the inlet and outlet level of the calculated zone as follow:

$$\Delta p_{b,i} = g \Delta z \left(\rho_{\inf} - \rho_i\right) \quad (11)$$

Where Δz is the elevation difference between the inlet and the exit of the channel, ρ_{inf} is a reference water density and ρ_i is the average density value of the water in the calculated zone. The density value in each zone is varying with the coolant temperature. That value was calculated by using a curve fitting of the density vs. temperature of the water. The water temperature gradient in each zone (ΔT_i) was calculated from the energy equation (eq. 10). In case of heating zone (along the rod bundle) the average temperature was calculated between the inlet and the outlet temperature and the average density was calculated from the density function with that temperature.

Based on eq. 6-11 the flow rate in the loop in various channel power values was calculated. The outlet temperature from the heated zone was calculated by using the calculated flow rate, the channel power and the measured inlet temperature (eq. 10).

Comparison between measured and calculated outlet temperatures for the flow resistance case K2 is presented in Fig. 3. The agreement between the experimental results and the calculated values was achieved by using K_r=13300 in eq. 9.

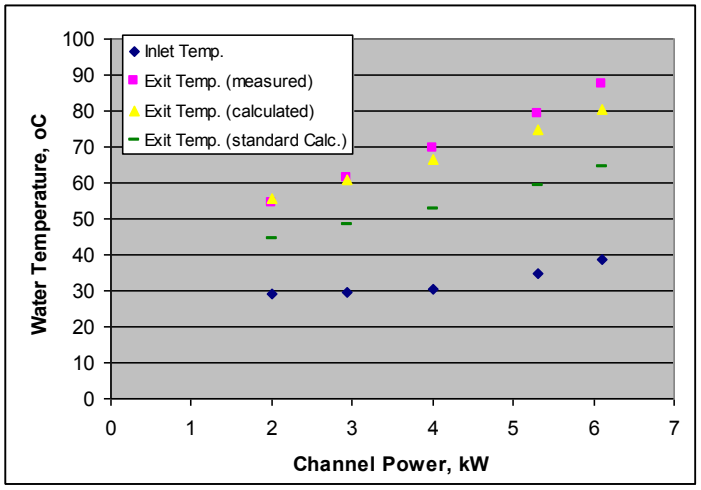
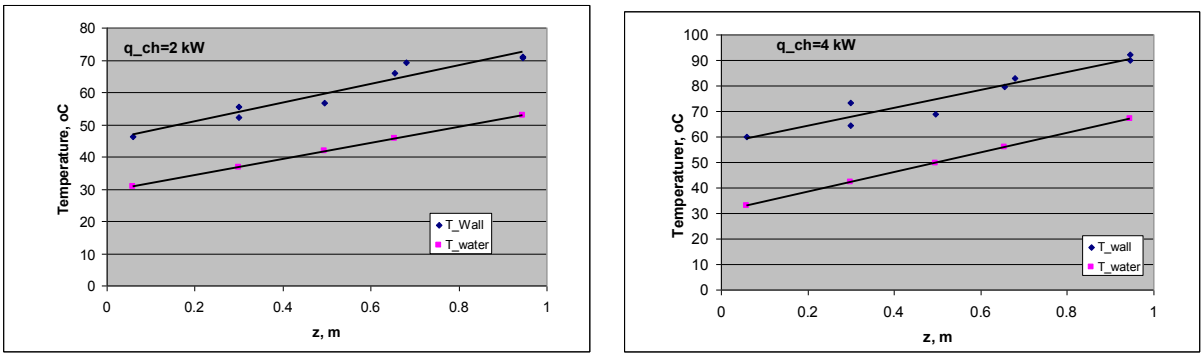


Figure 3: Comparison between measured and calculated water temperature in various channel power

For comparison, exit calculated temperatures with standard local resistance coefficient values (from engineering tables) are also presented in Fig. 3. It can be seen that in this case the model over predicts the flow rate in the loop and causing an under prediction of the water temperature in the heated channel.

The local measured wall temperatures at five axial locations corresponding to the locations of the wall thermocouples (table 1) are presented in Figure 4 (a) and (b) for channel power of 2 and 4 kW respectively. In the figures the water bulk temperature is also presented based on the inlet and outlet measured water temperatures and the assumption of no heat losses along the channel. From a linear regression of the wall temperature measured values it can be seen that there is a small scattering of the measured values. It can also be seen that the linear regression lines of the wall temperatures and the water calculated values are almost parallel which means that the thermal developing zone at the inlet of the channel is very small and it can be assumed that all the measurements are in a developed zone.



(a) (b)

Figure 4: Local measured wall and calculated water temperatures for channel power of 2 kW (a) and 4 kW (b)

Evaluation of the wall temperature was done based on eq. 1, 2 and 3 for natural and mix convection from references [7] and [9]. The water temperature was calculated based on the inlet and the outlet measured temperatures and the assumption of linear temperature distribution along the channel (constant water heat capacity and no heat losses). Comparison of the measured and calculated values based on various correlations is presented in Fig. 5. The experimental results are for channel power of 2 and 4 kW.

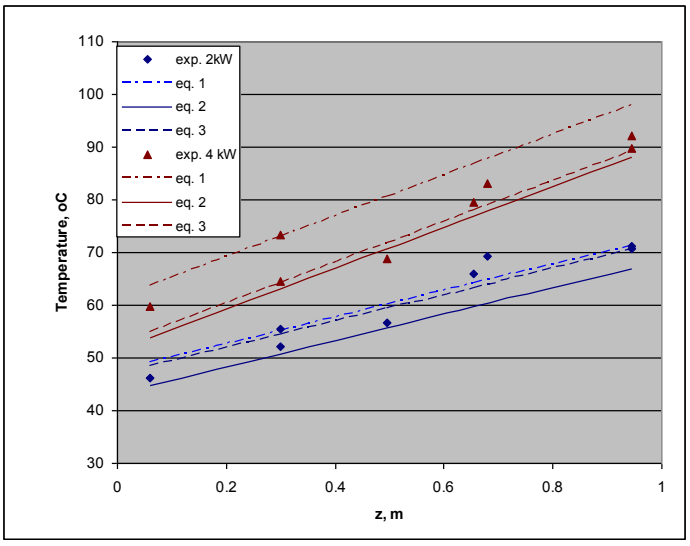


Figure 5: Comparison between measured and calculated wall temperatures based on various correlations

As can be seen in Figure 5, the power channel range influences the prediction quality of the three correlations that was used for comparison. In channel power of 2 kW the best the wall temperature was achieved with eq. 1 and 3. In channel power of 4 kW, the best prediction was achieved by eq. 1 and 3. Explanation of that behavior may be due to the channel power and geometries that those correlation were based on which were different from the present work.

Conclusions

The model which was presented in this paper for calculation of the flow rate in the natural circulation loop based on a modification of the local friction losses constant values. Standard values of those constants from engineering tables are usually for fully developed turbulent flow. In the present work the modification is required because of the low Reynolds number in the loop in case of natural circulation. In this flow regime the local friction constant becomes much higher than the fully developed turbulent value. That means that without that modification the model over predicts the flow rates in the loop. That over prediction leads to lower temperatures along the heated zone and lower heaters predicted temperatures.

The prediction quality of the correlations which were used in this work is varied with the channel power as was presented in Fig. 5. That variation may be due to the fact that those correlations were developed for other rod bundle geometries and power channel. Generalization of those correlations for other geometries needs some modifications.

References

1. R. E. Kay, P. D. Stevens – Guille, J. W. Hilborn, R. E. Jervis, SLOWPOKE: A New Low – Cost Laboratory Reactor, Int. J. Applied Radiation and Isotops, V. 24, pp. 509-518, 1973
2. Y. G. Lee, G. C. Park, Assessment of TAPINS and TASS/SMR Cods and Application to Overpower Transient in REX – 10, Nucl. Eng. Design 263, pp. 269-307, 2013
3. C. Park, M. Tanimoto, T. Imaizumi, M. Miyauch, M. Ito, M. Kaminga, Preliminary Accident Analysis for a Conceptual Design of a 10 MW Multi-purpose Research Reactor, Japan Atomic Energy Agency, JAEA – Technology 2012 – 039, 2013.
4. H. T. Chae, C. Park, H. Kim, B. J. Jun, J. B. Lee, On the Natural Convection Cooling in HANARO; Experiment and RELAP5/KMRR Simulation, Proceedings of NURETH 8th, pp. 1809-1814, 1997
5. J. Zhang, X. Z. Shen, Y. Fujihara, T. Sano, Y. Takahashi, K. Oono, A. Nakamori, N. Maruyama, K. Hasegawa, T. Tsuchiyama, K. Minami, K. Okumura, T. Yamamoto and K. Nakajima, Experimental Investigation on Natural Circulation Capacity of Kyoto University Research Reacror, NURETH15-125, Pisa, Italy, 2013
6. G. R. Dimmick, P. E. Bindner, V. Chatoorgoon, J. R. Schenk, R. Sollychin, Thermal Hydraulics R&D for SLOWPOKE Heating Reactor, Nucl. Eng. Design, 122, pp. 425-434, 1990
7. S. H. Kim, M. S. El-Genk, Heat Transfer Experiments for Low Flow of Water in Rod Bundles, Int. J. Heat Mass Transfer, vol. 32, pp. 1321-1336, 1989
8. M. S. El-Genk, B. Su, Z. Guo, Experimental Study of Forced Combined and Natural convection of Water in Vertical Nine Rod WITH Square Lattice, Int. J. Heat Mass Transfer, vol. 36, pp. 2359-2374, 1993
9. K. P. Hallinan, R. Viskanta, Heat Transfer from a Vertical Tube Bundle under Natural Circulation Conditions, Int. J. Heat and Fluid Flow, vol. 6, pp. 256-264, 1985
10. J. Hyvarinen, H. Kalli, T. Kervinen, RELAP 5 Assessment with REWER-III Natural Circulation Experiments, NURETH – 4, Vol. 1, pp 510-515, 1989
11. W. Hooper, Chem. Eng, Aug 24, p. 97, 1981

FUEL BURNUP MODELIZATION WITH THE MONTE CARLO CODE MCNP5 AND CORE RECONFIGURATION PREDICTION FOR THE TRIGA MARK II REACTOR AT THE UNIVERSITY OF PAVIA

D. CHIESA, M. CLEMENZA, S. POZZI, E. PREVITALI, M. SISTI
Physics Department "G. Occhialini" and INFN section of the University of Milano-Bicocca
Piazza della Scienza 3, 20126, Milano, Italy

D. ALLONI, S. MANERA, M. PRATA, A. SALVINI
Applied Nuclear Energy Laboratory (L.E.N.A.) and INFN section of the University of Pavia
Via G. Aselli 41, 27100 Pavia – Italy

A. CAMMI, A. SARTORI, M. ZANETTI
Energy Department of Polytechnic University of Milan
Via Lambruschini 4, 20156 Milan – Italy

ABSTRACT

A time evolution model was developed to study fuel burnup for the TRIGA Mark II reactor at the University of Pavia. The results obtained by this model were used to predict the effects of a complete core reconfiguration and the accuracy of this prediction was tested experimentally. The Monte Carlo code MCNP5 was used to reproduce system behaviour and to analyze neutron fluxes in the reactor core. Before the evolution analysis, the model was validated by reproducing experimental data from 1965, year in which the reactor reached its first criticality. The results showed good accuracy for both low and high power configurations. The software that took care of time evolution, completely designed in-house, used the neutron fluxes obtained by the Monte Carlo simulations to evaluate material consumption. This software was developed specifically to keep into account some features that differentiate experimental reactors from commercial reactors, such as the daily on/off cycle and long fuel lifetime; these effects could not be neglected to properly account for neutron poison accumulation. The model was used to evaluate the effects of 58 years of reactor operation and to predict several possible new configurations for the reactor core: the objective was to remove some of the fuel elements from the core and to obtain a substantial increase in the Core Excess value. The evaluation of fuel burnup and the reconfiguration results are presented in this paper.

1. Introduction

The TRIGA Mark II Reactor at the Applied Nuclear Energy Laboratory (L.E.N.A.) of the University of Pavia is a pool type reactor with a nominal power output of 250 kW. It was brought to its first criticality in 1965 and since then it was used for several scientific activities, such as radioisotope production, material analysis via neutron activation and reactor physics studies.

The reactor core is shaped as a right cylinder and contains 90 slots, distributed over 5 concentric rings; they can contain either fuel elements, graphite (*dummy*) elements, control rods or irradiation channels. The fuel consists of a uniform mixture of uranium (8% wt., enriched 20% wt. in ^{235}U), zirconium (91% wt.) and hydrogen (1% wt.). At the moment, the core contains two types of fuel elements, having respectively an aluminium (102-type) or stainless steel (104-type) cladding. System reactivity is governed by three control rods, named Shim, Regulating and Transient; the first two contain boron carbide, while the latter is filled with boron enriched graphite.

To fully characterize the reactor critical parameters a Monte Carlo code was developed, based on the MCNP5 [1] code. This code was chosen thanks to its general geometry

modelling capabilities, correct representation of transport effects and continuous-energy cross section treatment. The model has been thoroughly tested by reproducing the experimental results obtained in 1965, during the operations that followed the reactor first startup[2]. The analysis included the evaluation of the k_{eff} value in several reactor configurations both at low power (~10 W) [3][4] and full power (250 kW), reproduction of control rods calibration curves [4] and neutron flux evaluation in different irradiation facilities [5][6][7]. In this initial configuration (Fig.1) all the fuel elements were new, so they didn't contain significant amounts of neutron poison.

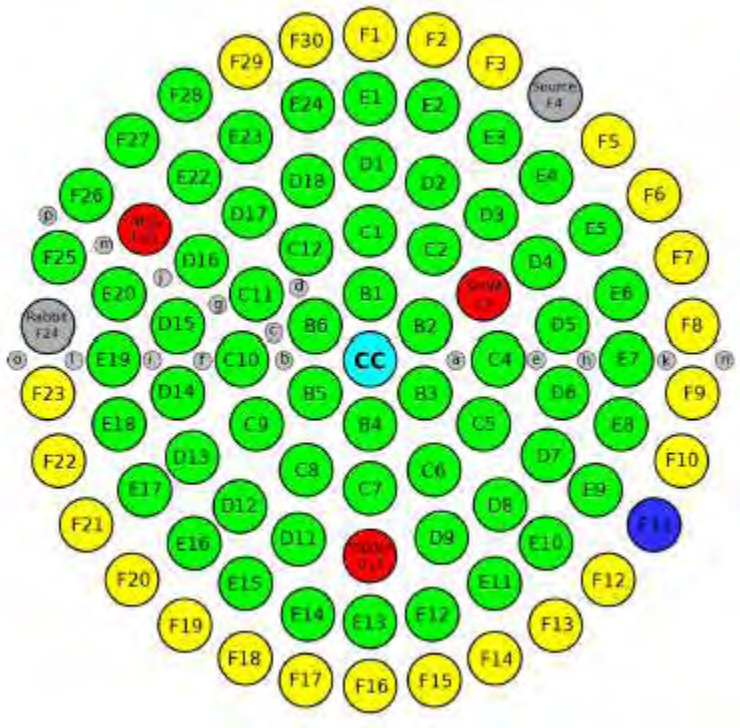


Fig. 1: Core configuration in 1965. Fuel rods are represented in green, graphite rods in yellow, control rods in red, irradiation channels in gray and an empty channel in blue. CC = central irradiation channel (or central thimble).

2. Fuel burnup analysis

The fuel burnup analysis is an essential component in the development of a complete simulation model for a nuclear reactor, since fuel consumption and neutron poison buildup significantly affect the reactivity value and system behaviour. This kind of analysis is also important to evaluate the fuel cycle and to determine the amount of long-lived radioactive waste which is produced in a reactor.

In order to adapt the MCNP model for simulating the current configuration of the TRIGA Mark II reactor, a time evolution software was developed to evaluate the condition of each fuel element. The historical data of reactor operating time and all the adopted core configurations were combined with the information about in-core neutron flux, derived from MCNP simulations, to reproduce the material aging through about 48 years. This software was completely developed in-house to take into account some features that differentiate experimental reactors from those used for power production, such as the daily ON/OFF cycle and the long fuel lifetime; these effects are, in fact, not negligible to properly account for neutron poison accumulation in this kind of system.

2.1 Burnup calculation strategy

The simulation model for the fuel burnup is based on the solution of a coupled set of differential equations, describing the concentrations of various isotopes in the fuel elements. The main processes that we considered for the modelled isotopes were fission, neutron

capture and radioactive decay. The isotopic concentration $n_j(t)$ of a fission product species *j*, characterized by λ_j decay constant and σ_a^j neutron absorption cross section, evolves in time following this generic formula[8]:

$$\frac{dn_j}{dt} = \gamma_j \Sigma_f \Phi + \sum_i \left(\lambda^{(i\to j)} + \sigma^{(i\to j)}\Phi\right) n_j - \left(\lambda^j + \sigma_a^j \Phi\right) n_j, \quad (1)$$

where γ_j is the fission yield of isotope *j*, Σ_f is the macroscopic cross section of the fissioned nucleus, Φ is the integral neutron flux intensity; $\lambda^{(i\to j)}$ and $\sigma^{(i\to j)}$ are associated with isotope *i*, which may produce isotope *j* either by radioactive decay or neutron capture. In this equation, all cross sections are intended as effective, to take into account the reaction rate dependence on the flux shape. The time evolution of the elements belonging to the original fuel composition (U, Zr and H) or produced exclusively through neutron capture are still described by Eq.1 by setting the fission yield value γ_j equal to 0.

Equation 1 can be integrated to determine fuel composition changes over its lifetime; in order to carry out this calculation, however, the time dependence of the neutron flux must be known. To overcome this issue, the 48 year period is divided in several time intervals in which the neutron flux distribution is assumed to vary negligibly. For the TRIGA Mark II reactor, we found that the time scale for significant flux changes is greater than the maximum operation time elapsed between two core reconfigurations (~3500 hours). For this reason, we carried out our calculation using 27 time steps, one for each core reconfiguration occurred between 1965 and 2013.
The time evolution of the fuel elements was then evaluated by iterating the following procedure over all the time steps:

1. an MCNP simulation with the full power reactor model is run to determine the neutron flux distribution in the fuel elements;
2. the effective cross sections of the isotopes of interest are calculated by combining the flux spectra, coming from MCNP, and the ENDF/B-VII cross section data libraries;
3. the data about neutron fluxes, fission yields, cross sections, radioactive decay chains and reactor operating time are combined to calculate, by solving Eq.1, the new isotopic composition of the fuel elements;
4. a new MCNP input file is prepared, where the fuel elements are upgraded with the new isotopic composition and repositioned in the reactor core, according to the new configuration.

The poison accumulation and fuel evolution were calculated by applying some approximations, which were essential to simplify the problem solution.

- Each fuel element was divided in 5 axial sections, to account for the uneven distribution of the neutron flux over the vertical axis. Configurations with more axial sections were tested, but the results were found to be compatible and therefore we chose to model just 5 sections, to save computational time.
- A restricted set of fission products and trans-uranium isotopes was simulated (see Tab.1); we selected isotopes that, according to an initial, rough resolution of Eq.1, would impact the k_{eff} value in a non-negligible way.
- Each time step was divided in sub-intervals, to account for the reactor daily ON/OFF cycle; since the complete reconstruction of the real cycles was impractical, we chose 6 hour sub-intervals for the ON condition and we calculated the duration of the OFF sub-steps to match the real time difference between the two reconfiguration dates.
- The calculation for ^{135}Xe was carried out separately, due to its large daily variations;

its average concentration was estimated by considering a typical week in which the reactor operates 6 hours a day, from Monday to Friday.

Fission Products						Trans-Uranium
^{83}Kr	^{102}Ru	^{131}Xe	^{145}Nd	^{152}Sm		^{236}U
^{95}Nb	^{103}Rh	^{133}Cs	^{147}Pm	^{153}Sm		^{239}Pu
^{95}Mo	^{105}Rh	^{135}Cs	^{147}Sm	^{153}Eu		^{240}Pu
^{97}Mo	^{105}Pd	^{139}La	^{149}Sm	^{155}Eu		^{241}Pu
^{99}Tc	^{113}Cd	^{141}Pr	^{150}Sm	^{155}Gd		^{241}Am
^{101}Ru	^{129}I	^{143}Nd	^{151}Sm	^{157}Gd		

Tab. 1: List of the fission products and trans-uranium elements included in the burnup calculation

2.2 Fuel evolution results

In order to analyze the burnup calculation results, we plotted the concentration of the different isotopes as a function of the total reactor operating time. As an example, we report some of these plots in Fig.2, regarding a fuel element that has been inside the reactor core from 1965 to 2013, in different locations. The average neutron flux in the central fuel element section is also reported in red.

We chose to show a set of representative isotopes, characterized by different, peculiar behaviours.

- The fissile isotopes ^{235}U and ^{239}Pu; while the first one is burned and its concentration decreases in time, ^{239}Pu is steadily produced by capture reactions on ^{238}U.
- ^{133}Cs, a fission product which does not reach saturation and exhibits a linear trend as a function of the reactor operating time.
- ^{149}Sm, a fission product with a high neutron capture cross section, which reaches saturation; the saturation level changes over time due to the decreasing total neutron flux on the fuel element.
- ^{155}Eu and ^{155}Gd, whose evolution is correlated because ^{155}Gd is produced by the decay of ^{155}Eu (4.75y half life).

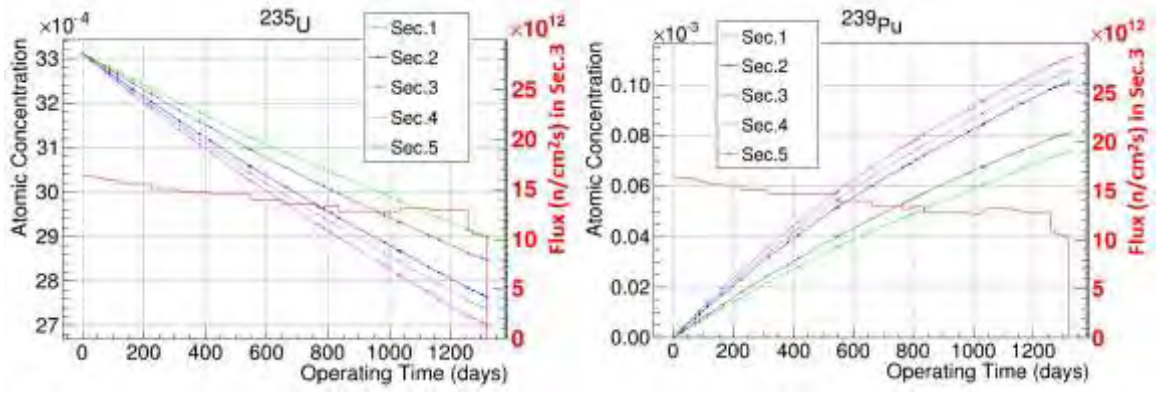


Fig.2: Time evolution of some atomic concentrations in the 5 sections of a fuel element. The integral neutron flux in the central section is represented in red. The horizontal axis represents the net reactor operating time at full power.

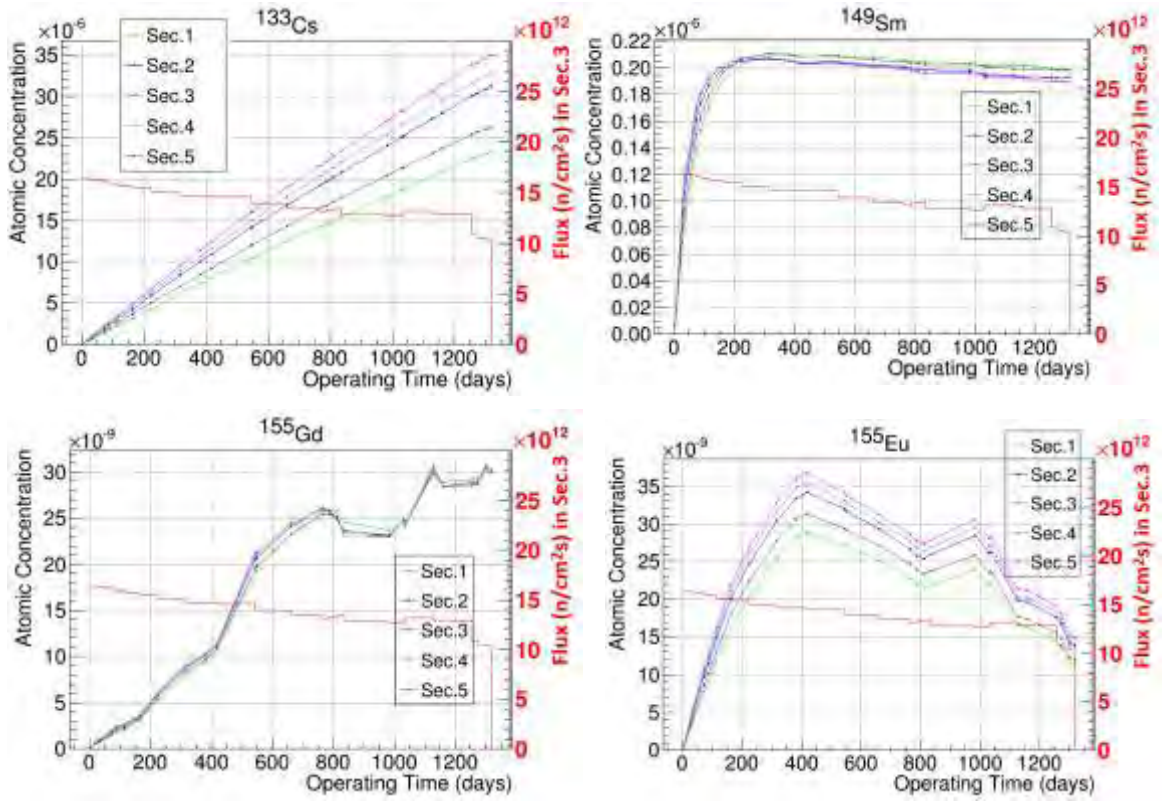


Fig.2: Cont.

The case of ^{155}Eu and ^{155}Gd is particularly interesting: their concentration depends not only on the reactor operating time, but also on the OFF time, during which the decay of ^{155}Eu continues to occur. Since the ratio between ON and OFF time varies over the years, ^{155}Eu concentration doesn't reach a stable value. Without the inclusion of the OFF time evaluation in our model, it would have been impossible to correctly calculate the concentration of these isotopes and, therefore, the final k_{eff} value would have been incorrect.

3. Analysis of the updated Monte Carlo Model

In order to check the MCNP model response to the fuel composition changes, we analyzed the variation of the k_{eff} value over the years, following each core reconfiguration.

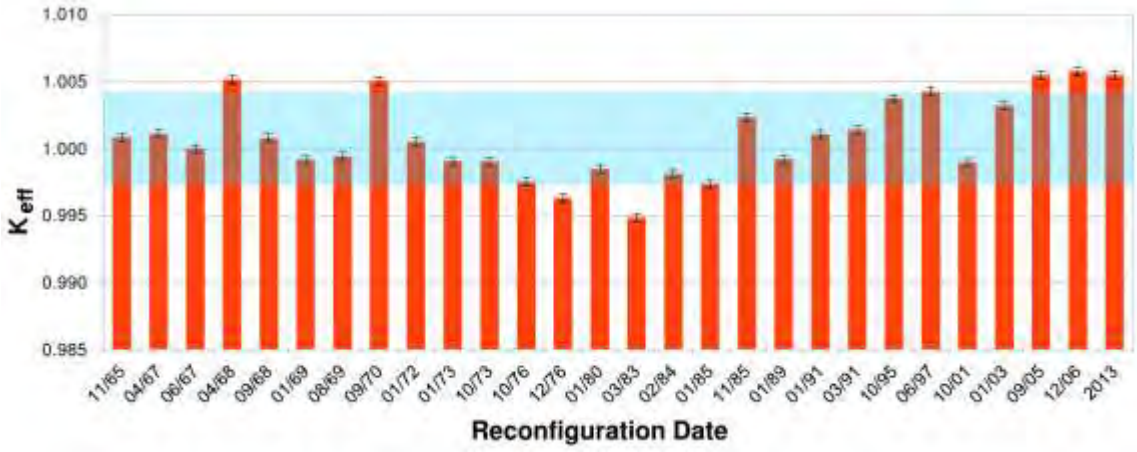


Fig. 3: k_{eff} values obtained by the Monte Carlo simulations at each time step. The shadowed area corresponds to the ±1σ range from the average value, σ being the standard deviation of the results. The reported error comes from the statistical component only.

For each simulation, the control rods were positioned as to reproduce the first full power criticality following the reconfiguration. The results are shown in Fig.3: all the results are within ±0.005 with respect to the expected value, k_{eff} = 1. By calculating the average value and the standard deviation of the results, we obtain k_{eff} = 1.00067±0.00291, which is in good agreement with the expected value.
Taking into account the fact that this calculation was performed over a period of 48 years, the analysis confirms that the fuel aging was simulated with good accuracy. We do not observe any particular trend in the results, which could have been linked to an over or underestimation of fuel aging. The fluctuations that affect our data are most probably due to imprecise information in the historical data and to the error associated with our calculations, which has not been completely evaluated yet.

3.1 Low power benchmark

As a further benchmark, we checked the ability of the updated Monte Carlo model to reproduce the system reactivity at low power; in this way, the thermal effects that greatly affect the full power measurements of k_{eff} can be neglected.
At first, a simulation was performed with the control rods in the positions recorded during a low power (~1.5W) criticality measurement dated 9 September 2013. The result we obtained was

$$k_{eff} = 1.00117 \pm 0.00025 \text{ (stat.)} \pm 0.00180 \text{ (syst.)}$$

as opposed to the expected value k_{eff} = 1. The systematic component comes from the uncertainty in material composition in the original reactor configuration, in 1965[4], and doesn't yet contain the contributions due to the burnup calculations.
As a second test, we reproduced the Regulating control rod calibration curve, obtained experimentally in July 2013. The results of this test are shown in Fig.4. To conform with the experimental data format, the control rod positions are expressed in steps (with each step≈0.05 cm) and the reactivity in pcm:

$$1\,pcm = 10^5 \times \frac{\left(k_{eff} - 1\right)}{k_{eff}}. \qquad (2)$$

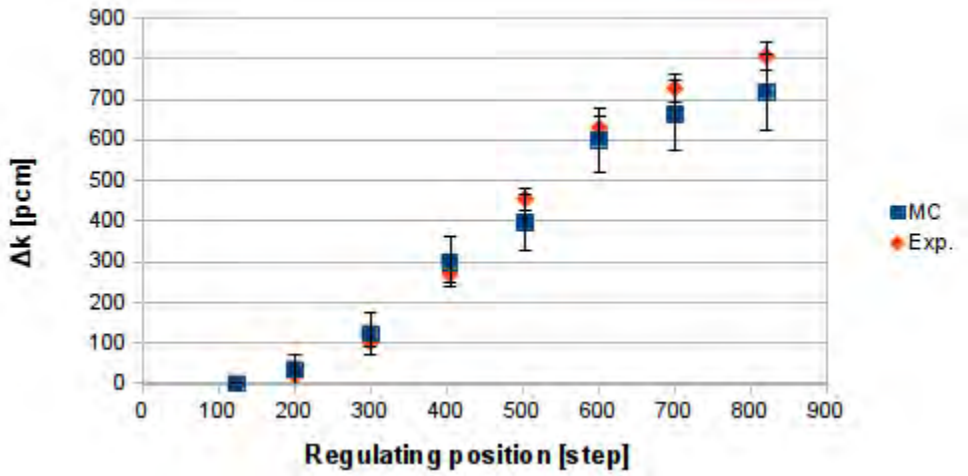


Fig. 4: Comparison between experimental and Monte Carlo calibration curve for the Regulating control rod, referring to the 9 September 2013 configuration. The error bars are associated to the statistical component only.

Both tests show a very good agreement between experimental results and Monte Carlo simulations: the calibration curve is reproduced with great accuracy and the low power simulation, when we consider the systematic error component, leads to results compatible with the expected values.

4. Core reconfiguration

The updated simulation model of the TRIGA reactor, whose reliability was demonstrated through the benchmark analysis, was then exploited to identify a new optimized core configuration, with the aim of increasing system reactivity while decreasing the total number of fuel elements in the system.

An important parameter to be considered for this kind of analysis is the Core Excess (CE), defined as the system reactivity which would be obtained if all the control rods were completely withdrawn from the core. The Core Excess value should be high enough to compensate for the reactivity losses due to thermal effects and ^{135}Xe poisoning.

On 9 September 2013, the Core Excess was evaluated both at low (~10 W) and full (250 kW) power; the measurement was performed on a Monday, to avoid the influence of the ^{135}Xe accumulated over the previous week. The results we obtained were CE_{low}=1504 pcm and CE_{high}=314 pcm; these low values were particularly alarming, since the ^{135}Xe accumulated in just one day of operation would be enough to render the reactor inoperable at full power the morning after. To solve this situation, a core reconfiguration was needed in order to increase the reactor CE by at least 300 pcm. For this purpose, we exploited the MCNP model with the fuel burnup calculation extended up to September 2013: new configurations, ensuring a higher CE and requiring less fuel elements in the reactor core, were simulated and analyzed.

The general idea behind the choice of those configurations was that the fuel elements with the highest content of fissile material left were to be put in the innermost region of the core, where the neutron flux is higher. To help us identify which fuel elements were best suited for this positioning, we defined a *Burnup Index* (*B.I.*) as follows:

$$B.I.(t) = \frac{1}{n_{235}(0)}\left[n_{235}(0) - \left(n_{235}(t) + n_{239}(t) \times \frac{\sigma_{235}^{f}}{\sigma_{239}^{f}} \right) \right] \tag{3}$$

where σ_{235}^{f} is the fission cross section for ^{235}U, σ_{239}^{f} the fission cross section for ^{239}Pu, $n_{235}(t)$ and $n_{239}(t)$ are the concentrations of ^{235}U and ^{239}Pu at time t. With this index, we keep into account not only the consumption of the original fissile isotope, but also the accumulation of ^{239}Pu over time, whose effect has been determined to be significant.

The new core configuration, chosen to comply with the reactor safety requests and technical prescriptions, contains 80 fuel elements, as opposed to the 83 elements in the 9 September 2013 configuration. The comparison between the two configurations is reported in Fig.5, along with the Burnup Index scale.

The reactivity gain predicted by the MCNP simulations was of 416±37 pcm, leading to a Core Excess value at low power of 1920±37 pcm. Right after the reconfiguration, that took place on 25 September 2013, an experimental measurement of the CE was performed, in order to check the outcome of the procedure. The new experimental CE resulted equal to 1851±22 pcm, which is a value compatible within 2σ of the CE predicted by the Monte Carlo simulations. The final reactivity increase, equal to 325±22 pcm, was completely satisfactory and proved that the model had successfully reproduced the fuel evolution over the reactor lifetime.

To further verify the effectiveness of our model, we simulated a set of critical reactor configurations, obtained during the operations that followed the reconfiguration by positioning the Shim and Regulating control rods in 11 different ways. The expected result in these configurations k_{eff} = 1; the simulation results are shown in Fig. 6.

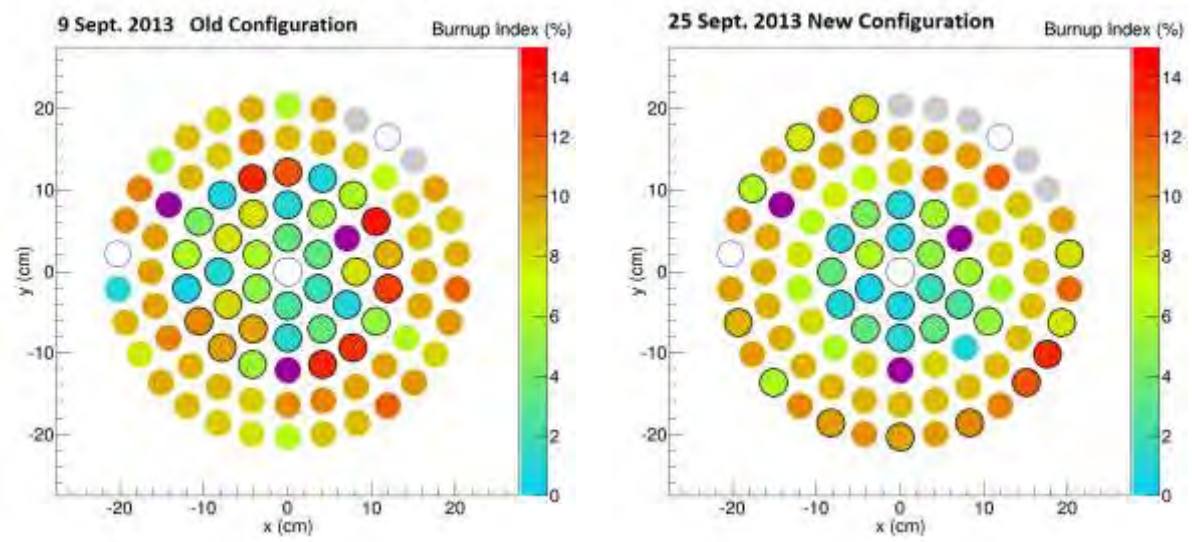
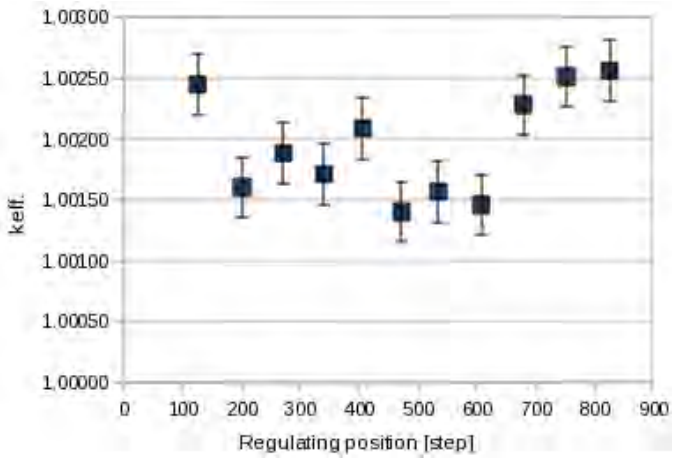


Fig.5: Comparison between the old and new core configurations. Control rods are in purple, graphite rods in gray. Fuel elements with a black border have a stainless steel cladding, while the others have an aluminium one.



Reg. [step]	Shim [step]	k_{eff} ± 0.00025
126	477	1.00245
201	460	1.00160
271	447	1.00188
340	432	1.00171
406	406	1.00209
472	379	1.00140
534	353	1.00157
608	313	1.00146
679	295	1.00228
752	278	1.00251
826	262	1.00256

Fig.6: Set of critical reactor configurations, obtained after the core reconfiguration.

The average k_{eff} value obtained by the simulations was k_{eff} = 1.00196±0.00043; while this result is not compatible with the expected value of 1, it is worth noting that this offset is compatible with that affecting the reactivity simulations prior to the reconfiguration (paragraph 3.1). Since the same considerations apply to the systematic error evaluation, this result can be considered in good agreement with the experimental data.

5. Conclusions

An improved MCNP model for the TRIGA Mark II reactor has been developed, in which the effects of fuel aging has been simulated.

The effectiveness of the time evolution model was tested in multiple ways. The time profile of the k_{eff} value over the 48 years of operation shows no particular trend, indicating that no significant over- or underestimation of fuel burnup took place; the average k_{eff} value over this time period, equal to 1.00067±0.00291, was compatible with the expected value of 1. The Regulating control rod calibration curve, measured on July 2013, was reproduced completely

and with good accuracy. A low power system configuration, dating 9 September 2013, was simulated and led to results that, considering the systematic error component, are compatible with the experimental values.
Once the effectiveness of the simulation model was proven, its results were used as a tool to predict the effect of a core reconfiguration on the Core Excess value. The CE predicted by the model was compatible, within 2σ, with the value obtained by experimental measurements; moreover, the net CE increase following the reconfiguration was completely satisfactory and will allow the reactor to operate at full power for several more years.

References

[1] X-5 Monte Carlo Team, "*MCNP – A General Monte Carlo N-Particle Transport Code, Version 5*", Los Alamos National Laboratory, 2008.

[2] A.Cambieri, F.Cingoli, S.Meloni and E.Orvini, "*Il reattore TRIGA Mark II da 250 kW, pulsato, dell'Università di Pavia. Rapporto finale sulle prove nucleari*", tech.rep., University of Pavia, L.E.N.A., 1965.

[3] A.Borio di Tigliole, A.Cammi, M.Clemenza, V.Memoli, L.Pattavina and E.Previtali, "*Benchmark evaluation of reactor critical parameters and neutron fluxes distributions at zero power for the TRIGA Mark II reactor at the University of Pavia using the Monte Carlo code MCNP*", Progress in Nuclear Energy, vol. 52, pp. 494-502.

[4] D.Alloni, A.Borio di Tigliole, A.Cammi, D.Chiesa, M.Clemenza, G.Magrotti, L.Pattavina, S.Pozzi, M.Prata, E.Previtali, A.Salvini, A.Sartori and M.Sisti, "*Final characterization of the first critical configuration for the TRIGA Mark II Reactor of the University of Pavia using the Monte Carlo code MCNP*", accepted for publication in Progress in Nuclear Energy.

[5] A.Borio di Tigliole, A.Cammi, D.Chiesa, M.Clemenza, S.Manera, M.Nastasi, L.Pattavina, R.Ponciroli, S.Pozzi, M.Prata and E.Previtali, "*TRIGA reactor absolute neutron flux measurement using activated isotopes*", Progress in Nuclear Energy, vol. 70, pp. 249-255.

[6] D.Chiesa, E.Previtali and M.Sisti, "*Bayesian statistical analysis applied to NAA data for neutron flux spectrum determination*", accepted for publication in Nuclear Data Sheets.

[7] D.Chiesa, E.Previtali and M.Sisti, "*Bayesian statistics applied to neutron activation data for reactor flux spectrum analysis*", accepted for publication in Annals of Nuclear Energy

[8] W.M.Stacey, *Nuclear Reactor Physics*, WILEY-VCH Verlacg GmbH & Co. KgaA, 2007.

REVERSAL OF OFI AND CHF IN RESEARCH REACTORS: APPLICATION TO THE BR2 HEU AND LEU CORES

M. KALIMULLAH, A.P. OLSON, E. E. FELDMAN, B. DIONNE
GTRI Program, Nuclear Engineering Division, Argonne National Laboratory, 9700 S. Cass Avenue, Argonne IL 60439 – USA

S. KALCHEVA, G. VAN DEN BRANDEN, AND E. KOONEN
SCK•CEN, BR2 Reactor Department Boeretang, 2400 Mol – Belgium

ABSTRACT

This paper presents an assessment of the OFI-CHF reversal for the BR2 HEU and the LEU cores analyzed in the conversion feasibility study. The LEU fuel is currently under development. Two methodologies are used: (1) a scoping methodology developed for US research reactors and (2) a detailed thermal-hydraulic analysis using PLTEMP/ANL. For BR2, CHF is most-limiting regarding peak heat flux for higher mass flow rates, in excess of about 100% of nominal flow. Conversely, OFI is most-limiting regarding peak heat flux for mass flow rates less than about 100% of nominal flow. This applies to HEU and to LEU fuels. It is concluded that, relative to OFI versus CHF, there is very little difference between the safety performances of HEU versus that of LEU fuels under steady-state operating conditions. Both methodologies are in good agreement.

1. Introduction

BR2 is a water-cooled reactor moderated by water and beryllium. Fig 1 shows its physical arrangement. The beryllium is a matrix of hexagonal prisms each having a central bore that contains either a fuel assembly (FA), a control rod, an experimental device, or a plug. The core is located inside an aluminum pressure vessel, and at nominal conditions, the channel exit pressure is 10.3 bars while the inlet water temperature varies from 30 to 40°C. Normally, the coolant flows from the top of the core to the bottom with an average speed of 10.4 m/s in the FAs. The current maximum heat flux allowed for routine operation (470 W/cm^2) is based on an experimental heat flux value* that preserves large margins to boiling crisis (essentially no boiling) during a loss-of-flow/loss-of-pressure (LOF/LOP) event. That maximum nominal heat flux is generally compared to the heat flux at which Onset of Nucleate Boiling (ONB) occurs.

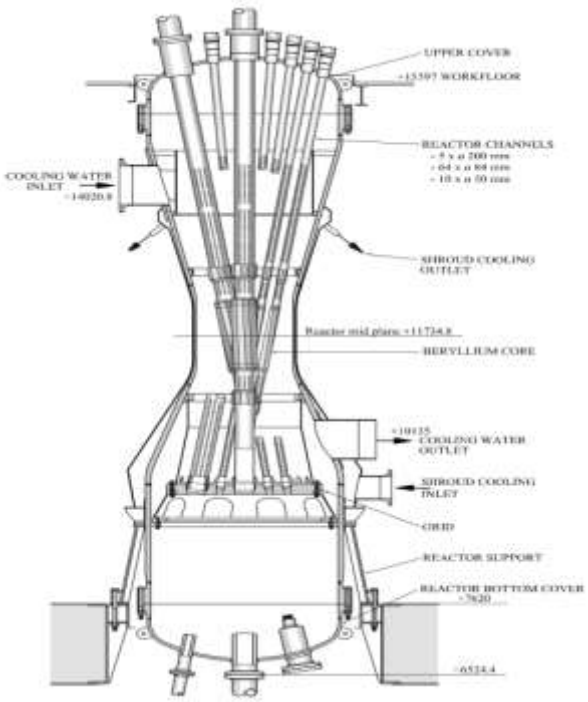


Fig 1. BR2 Reactor Schematic

In order to quantify the thermal-hydraulic safety margins, the heat fluxes at which onset of flow instability (OFI) and critical heat flux (CHF) occur are calculated. During the analysis of

* Based on LOF/LOP tests performed in 1963, the limit was set to 430 W/cm^2. Currently, a permanent deviation for a heat flux up to 470 W/cm² is authorized.

BR2 for conversion from highly-enriched uranium (HEU, ≥20% enrichment) fuel to low-enriched uranium (LEU) fuel, the following questions arise: (1) Does CHF occur *before* or *after* OFI? (2) Does LEU fuel perform as well as HEU fuel relative to OFI and to CHF? (3) How do the above criteria compare to the heat flux at ONB?

To address these questions, two approaches were used to study the behavior of the BR2 core with respect to ONB, OFI and CHF. The first approach is based on the use of OFI-CHF reversal diagrams developed for US research reactors [1]. This methodology is useful to perform scoping studies as it requires minimal computations. Since the use of OFI-CHF reversal diagrams cannot replace the detailed thermal-hydraulic analysis that is required to evaluate safety margins, a series of calculations were also performed using the PLTEMP/ANL [2] models developed for the thermal-hydraulics feasibility study [3].

Section 2 presents general considerations that are useful to provide a background of the OFI-CHF reversal phenomenon and the evaluations presented in this paper. Sections 3 and 4 present the scoping and detailed analyses of the CHF-OFI reversal in BR2.

2. General Considerations on CHF and OFI

The occurrence of CHF before bubble detachment (i.e., OSV) was observed in high-speed (20000 frames/s) cinematographic study of bubbles in subcooled nucleate boiling of water and its approach to CHF by Gunther [4, 5] and Celata et al. [6]. A more detailed discussion of CHF mechanisms during boiling with high subcooling to high quality and in different flow patterns is presented in Ref. [1].

The onset of static flow instability (OFI) is defined as the minimum ΔP point on the plot of ΔP versus flow rate of subcooled boiling liquid in a heated channel. OFI is caused by lack of a hydraulic equilibrium point (on the ΔP versus flow plot) between the ΔP demanded by the heated channel and the ΔP supplied by the pump. In the feasibility study, OFI was evaluated using the Whittle & Forgan (W&F) correlation [7]. To further verify the applicability and reliability of the W&F correlation, it was compared to the Saha-Zuber (S&Z) correlation [8]. Technically, the S&Z correlation predicts the onset of significant void (OSV), i.e., onset of bubble departure from the heated wall, which is generally considered a precursor to OFI. However, these phenomena occur sufficiently close to each other that the S&Z correlation has been quite successful in predicting various experimental data for OSV and OFI [7]. More details about the comparison of these correlations are provided in Ref. [1] but the overall conclusion is that there is a close agreement between the two prediction methods. The W&F correlation was selected because it has been extensively used for conversion analyses and has been shown to reproduce experimental data well [9].

In this work, the critical heat flux (CHF), i.e., the maximum heat flux that can be transferred from the heated wall to the coolant, is evaluated using the Groeneveld 2006 CHF Table [10] extended to higher mass flux as described in Ref. [11]. In that work, the applicability and reliability of the extended Groeneveld 2006 CHF Table was evaluated by comparing it with the Hall-Mudawar Inlet Conditions correlation [12] over a mass flux range of 1000 to 30000 kg/m^2-s for 216 combinations of heated lengths, exit pressures, heated diameters, and inlet temperatures. There was a close agreement between the two correlations. The extended Groeneveld Table was selected because it is also applicable to saturated CHF (exit quality ≥ 0).

3. Scoping Evaluation of OFI-CHF Reversal in BR2

The methodology presented in Ref. [1] can be used to scope whether a research reactor is OFI-limited or CHF-limited based on five characteristics of its coolant channel: (1) heated length, (2) heated diameter, (3) inlet temperature, (4) exit pressure, and (5) mass flux. The channel conditions are compared to OFI-CHF reversal diagrams, i.e., diagrams showing the

mass flux at which OFI and CHF intersect as a function of exit pressure for a fixed heated length, and a given set of heated diameters, and inlet temperatures. The point of intersection is called the reversal point with the corresponding mass flux and heat flux referred to as the reversal mass flux (G_{rev}) and reversal heat flux (q_{rev}). The intersection is referred to as the reversal because the OFI heat flux is smaller than the CHF for mass fluxes $G < G_{rev}$ whereas for mass fluxes $G > G_{rev}$ the CHF is smaller than the OFI heat flux. This means that the channel is OFI-limited for $G < G_{rev}$ and CHF-limited for $G > G_{rev}$, i.e., a reversal in the roles of OFI and CHF occurs at the intersection. It is important to note that, in Ref. [1], the scoping methodology results were shown to agree with the results of detailed thermal-hydraulic analyses performed by different responsible organizations for five US reactors.

At ANL, the Whittle & Forgan correlation is generally used with a default η of 32.5 (based on work by INTERATOM [13]) which produces a bounding estimate of OFI. An ANL statistical analysis [2] of the experimental data showed that this value is more conservative than the value of 31.09 needed to attain a 95% confidence interval that 95% of the rectangular channel OFI data measured by future experiments will not result in a value of η exceeding 31.09. However, to perform a fair comparison with the Groeneveld CHF predictions (considered a "best-estimate" evaluation), the OFI calculations performed in this paper used η=24.93 which, according to the statistical analysis presented in Ref. [2], produces a "best estimate" of the heat flux at which OFI occurs.

To use the reversal diagram, one has to determine[†] if the reversal point is located above (CHF-limited) or below (OFI-limited) the reversal line. Fig 2 shows a reversal diagram made using η=24.93 specifically for the BR-2 heated length of 0.762 m. Using the BR-2 exit pressure of 10.3 bar and mass flux of 10344 kg/m^2-s (100% of nominal flow), the reactor is represented in Fig 2 by a black point which is above the orange reversal curve applicable to the reactor. This implies that BR-2 is CHF-limited at 100% of nominal flow.

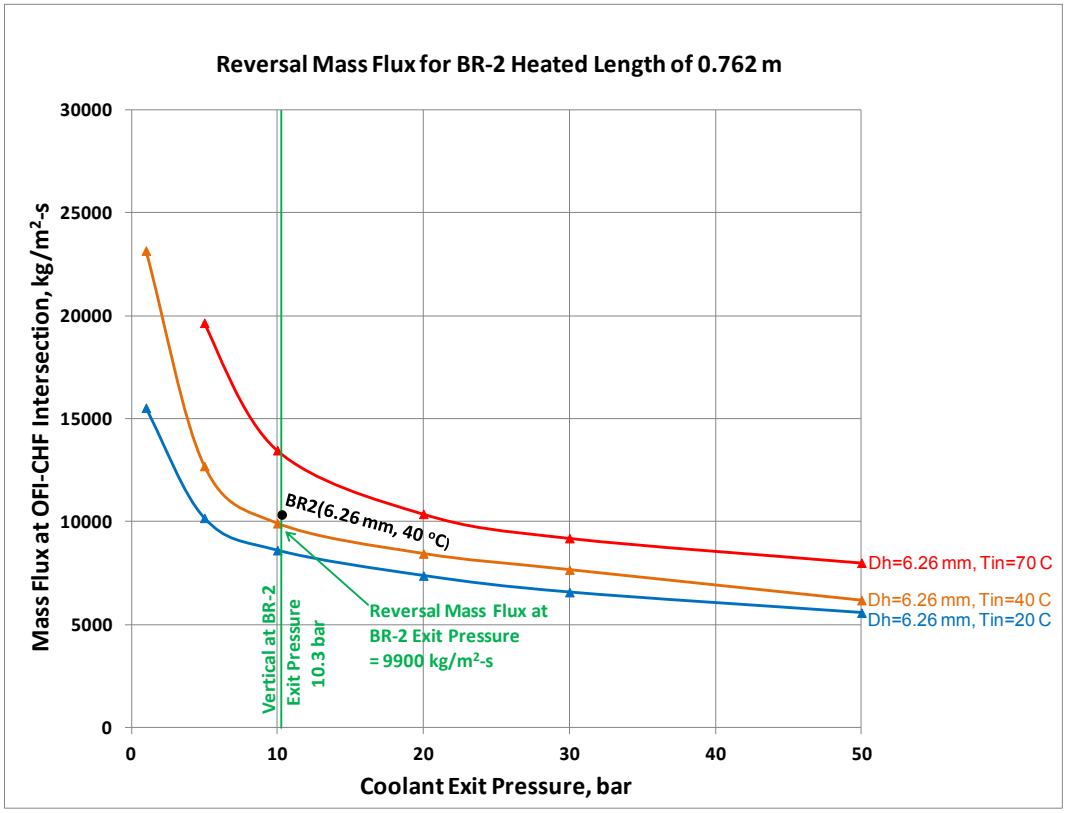


Fig 2. Reversal Diagram Using η=24.93 for 0.762 m Heated Length: Mass Flux at OFI-CHF Intersection.

[†] Using the channel heated length and diameter, inlet temperature, exit pressure, and mass flux.

As another application of the reversal diagrams, one can obtain the heat flux[‡] at which OFI occurs (q_{OFI}) at any flow rate using the reversal mass flux (G_{rev}) obtained from Fig 2. This is performed by multiplying the reversal heat flux (q_{rev}, see Fig 3) by the ratio of the mass flux of interest (G) to the reversal mass flux as shown in Eq (1).

$$q_{OFI} = q_{rev} \times \frac{G}{G_{rev}} \tag{1}$$

The peak heat flux at which OFI occurs can then be obtained by multiplying the value of q_{OFI} from Eq (1) by the plate power axial peak-to-average ratio.

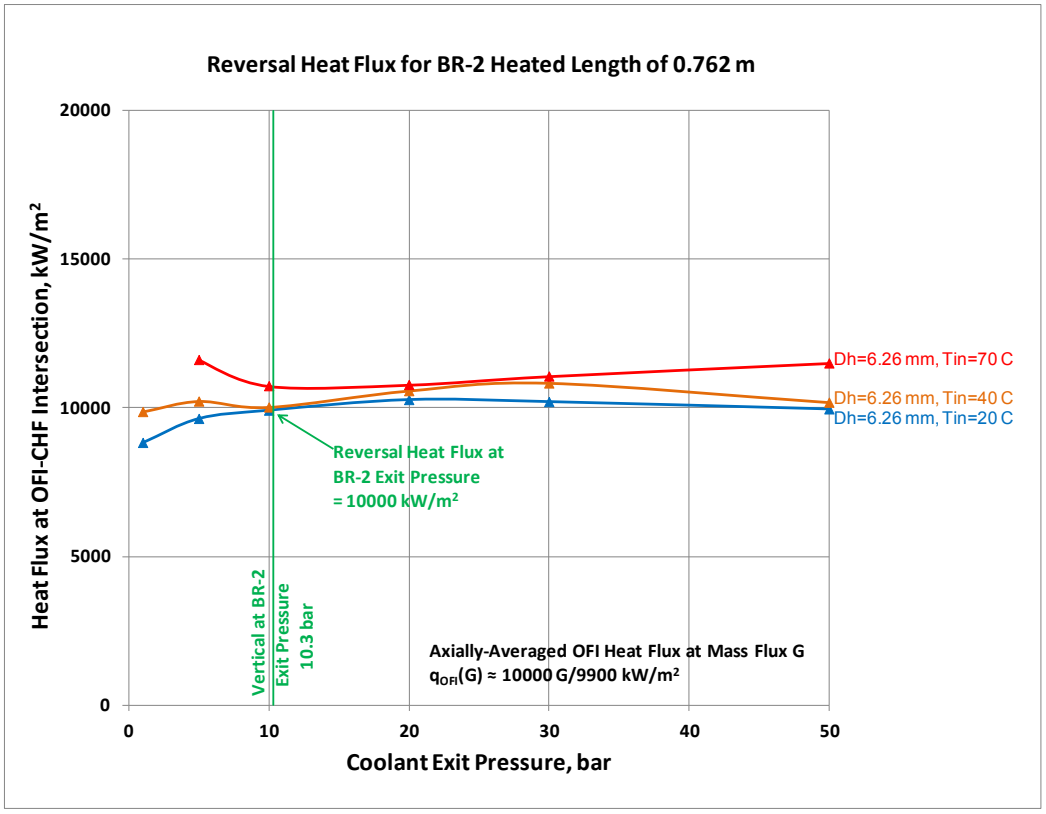


Fig 3. Reversal Diagram Using η=24.93 for 0.762 m Heated Length: Heat Flux at OFI-CHF Intersection.

Using the reversal mass flux (G_{rev}=9900 kg/m^2-s) and heat flux (q_{rev}=10000 kW/m^2) obtained for BR2-specifc conditions (G=10344 kg/m^2-s), the estimated plate-averaged OFI heat flux is found to be 1044.8 W/cm^2 (10448 kW/m^2). Using the same peak-to-average ratio (1.4312) assumed in the detailed analysis presented in Section 4, the estimated peak heat flux at OFI is 1045 x 1.4312, i.e., 1495 W/cm^2. This value will be used for comparison with the detailed methodology.

Two comments about the scoping methodology should be made:

(1) The development of reversal diagrams used best-estimate values of CHF and OFI heat flux. Regulatory requirements such as CHF ratio ≥ 2.0 can be applied after the reversal diagram is obtained.

(2) The effect of uncertainties in coolant mass flux and channel exit pressure, if available, may be accounted for by plotting a rectangle (rather than a point) to represent a coolant channel. However, these uncertainties require a complete thermal-hydraulic analysis, and therefore are not usually available for scoping calculation.

[‡] Under the flat power profile assumption used in the generation of the reversal diagrams.

4. Detailed Analysis of OFI-CHF Reversal in BR2

A BR2 fuel assembly, shown in cross section in Fig 4, is composed of six concentric “tubes” with a central aluminum plug. Each “tube” is made of three curved plates (fuel meat clad in aluminum) separated by stiffeners. The current fuel uses UAl_x (~1.3 gU/cm^3) with B_4C and Sm_2O_3 (burnable absorbers) dispersed in an aluminum matrix. All the dimensions of the proposed LEU FA are unchanged but its fuel meat consists of U8Mo (7.5 gU/cm^3) dispersed in an aluminum matrix (this fuel is still under development) with, as burnable absorbers, 36 Cd wires located in the stiffeners. In the BR2 core, the FAs can be loaded according to different configurations based on operational requirements (reactivity, neutron flux levels in experiments, etc.).

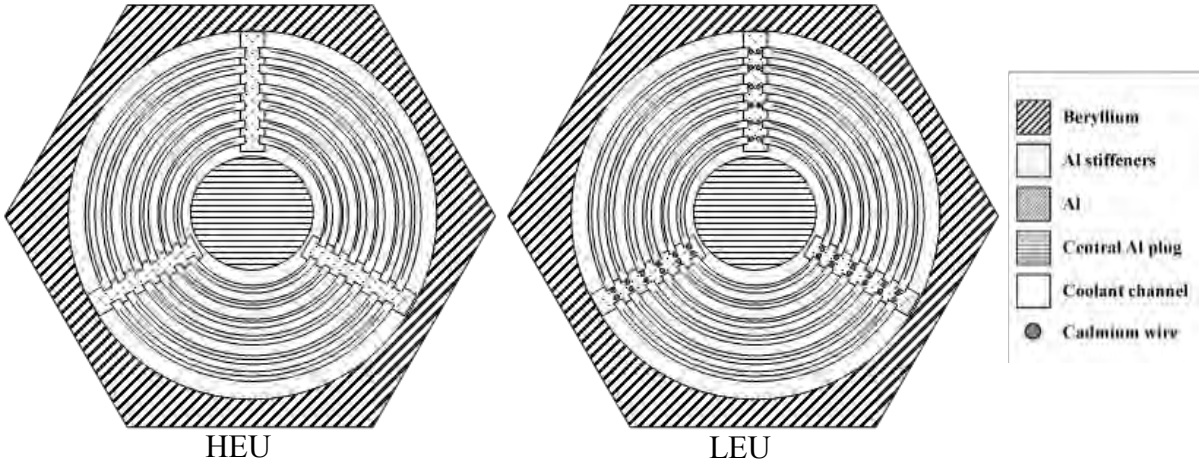


Fig 4. BR2 current HEU and proposed LEU Fuel Assemblies - Horizontal Cross-Section

Therefore, for analyzing the BR2 core conversion, HEU and LEU representative cores [14] were developed to reflect the expected core configuration (location and burnup of FAs, Be matrix isotopic compositions, number and locations of experimental devices, etc.) at the time of the conversion.

4.1. Analysis Procedure

The hot fuel assembly was modeled in the steady-state thermal-hydraulics code PLTEMP/ANL as 18 fuel plates and 21 heated coolant channels. All the plates and channels of a single sector are thermally coupled in the radial direction. Heat conduction is not modeled in the azimuthal and axial directions within a plate. The central plug, the stiffeners, and the beryllium are modeled as adiabatic boundary conditions. The detailed power shape information was obtained from MCNPX [15] 3D models of the BR2 representative HEU and LEU cores. This information was supplied to PLTEMP/ANL in order to determine various key parameters such as the peak heat flux at which the CHF ratio (CHFR) becomes unity, or the OFI ratio (OFIR) becomes unity, i.e., when CHF and OFI occurs

A modified Dittus-Boelter (DB-M) single-phase heat transfer correlation was used in the feasibility study and again in this work. The modification is a correction factor for coolant viscosity based on the ratio of the viscosities at the bulk and wall temperatures [16]. The DB-M correlation was selected after a comparison with different correlations and computational fluid dynamics calculations [17]. The detailed analysis uses the same CHF and OFI correlations used for the scoping study (see Section 3). The ONB heat flux was evaluated using the Bergles and Rohsenow correlation [18].

PLTEMP/ANL was used to first search for the pressure drop at which a desired mass flow rate (kg/s) is attained. This step determined the flow solution in all coolant channels. Next, a

search was performed for either CHFR=1, OFIR=1, or Onset of Nucleate Boiling Ratio (ONBR) of 1.

4.2. Results

Fig 5 shows the predicted peak heat flux in the HEU core at which ONBR=1, OFIR=1, and CHFR=1 occur for a wide range of flow rates in the turbulent region (> 2.4% of nominal flow rate). It can be observed that there is a cross-over of the OFI and CHF curves at a mass flow rate of about 100% of nominal flow. This result is consistent with the scoping study conclusion presented in Section 3. The predicted peak heat flux at which OFI occurs (1500 W/cm^2) is also in good agreement with the value obtained from the scoping study (1495 W/cm^2).

Fig 6 shows the predicted peak heat flux in the LEU core at which ONBR=1, OFIR=1, and CHFR=1 occur for a wide range of flow rates in the turbulent region (> 2.4% of nominal flow rate). As with the HEU core, a cross-over of the OFI and CHF curves at a mass flow rate of about 100% of nominal flow can be observed for the LEU core.

It is interesting to note that the OFIR heat flux ratios for η=24.93 relative to η=32.5 are all 1.051 as the mass flow rate ranges from 160% of nominal flow down to 10% of nominal flow. This means that increasing η to 32.5 reduces the peak heat flux by less than 5.1% while increasing the confidence interval that the flow is stable from 50% to 95%.

For mass flow rates less than about 15%, it is not possible for the PLTEMP/ANL code to find the heat flux at which CHFR=1 because the fluid solution is no longer single-phase. Using the saturation temperature of the coolant (about 185°C), a solution can be found for the CHFR that corresponds to a desired mass flow rate, by running the code using the option to search for peak water temperature. That solution for 10% mass flow rate is: P=1.060 MW, peak heat flux=200.1 W/cm^2, and CHFR=3.45.

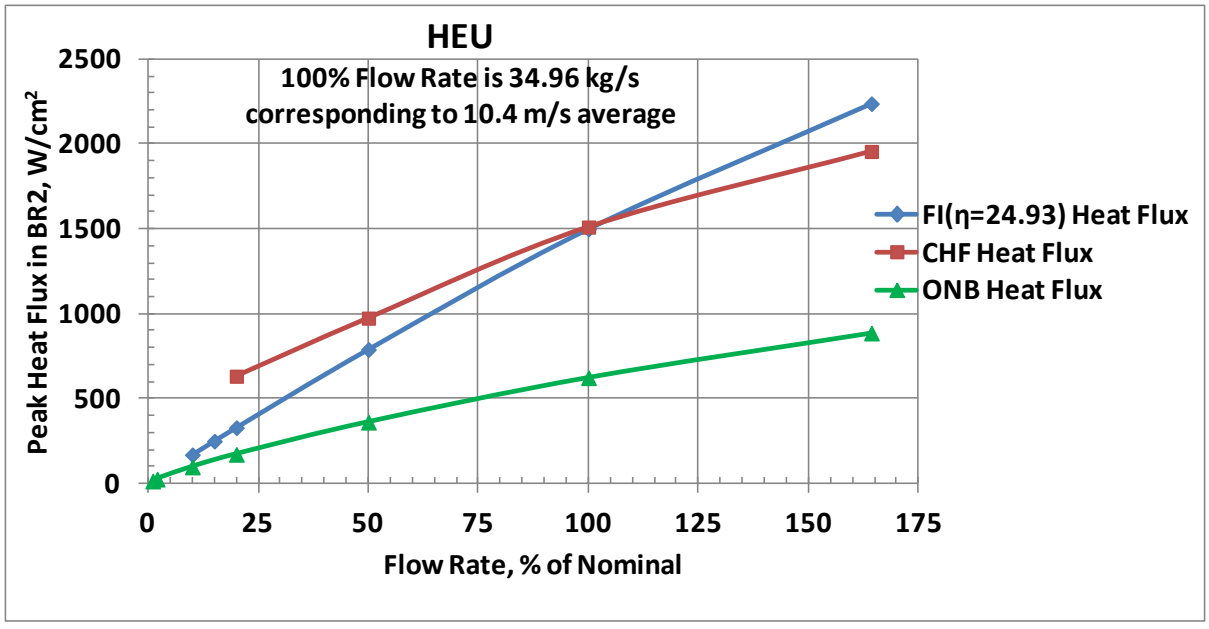


Fig 5. Comparison for HEU of Heat Flux Required for OFIR=1 and for CHFR=1. The heat flux at ONBR=1 is also shown.

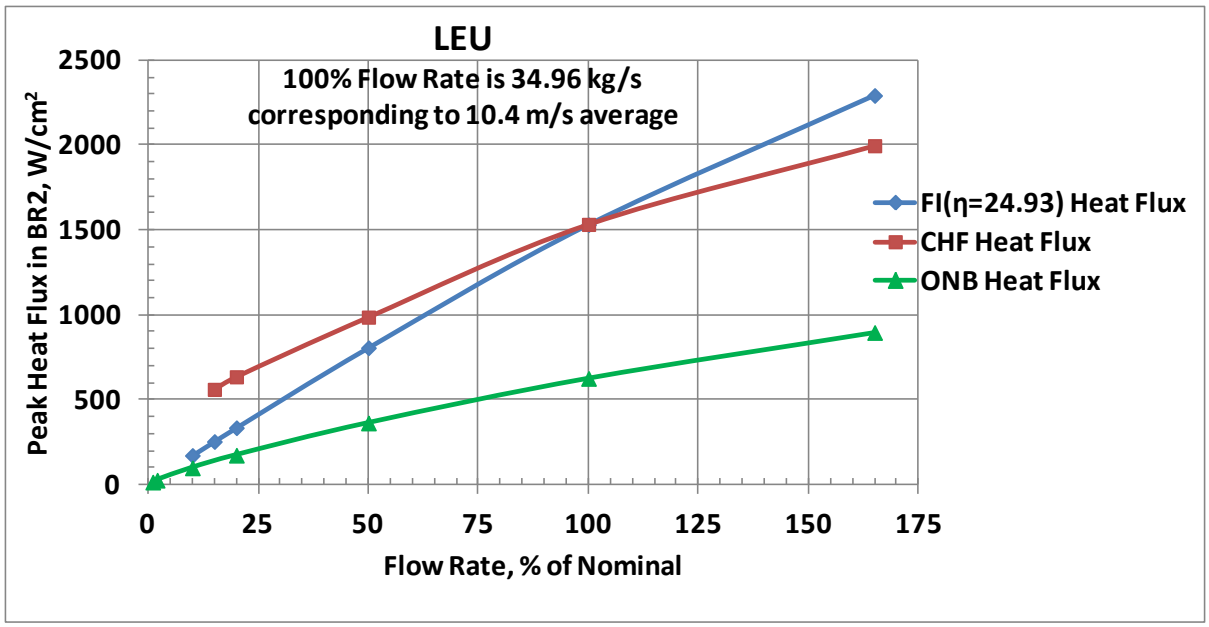


Fig 6. Comparison for LEU of Heat Flux Required for OFIR=1 and for CHFR=1. The heat flux at ONBR=1 is also shown.

Even though BR2 operates well below ONB during routine operation, it is useful to look at "CHF safety margin" defined as ratio of the heat flux at CHFR=1 to the heat flux at ONBR=1. Fig 7 shows that the margin between CHF and ONB is larger than 2 for all flow rates relevant to BR2. It can also be observed that this ratio is essentially the same for the HEU and LEU cores (within 1%). This is consistent with the behavior of ONB and OFI reported in the feasibility study [3, 13], i.e. that no significant differences between the HEU and LEU cores were observed for those quantities. This equality shows that there is very little difference between the "safety margins" of a pure HEU core versus that of a pure LEU core under steady-state operating conditions.

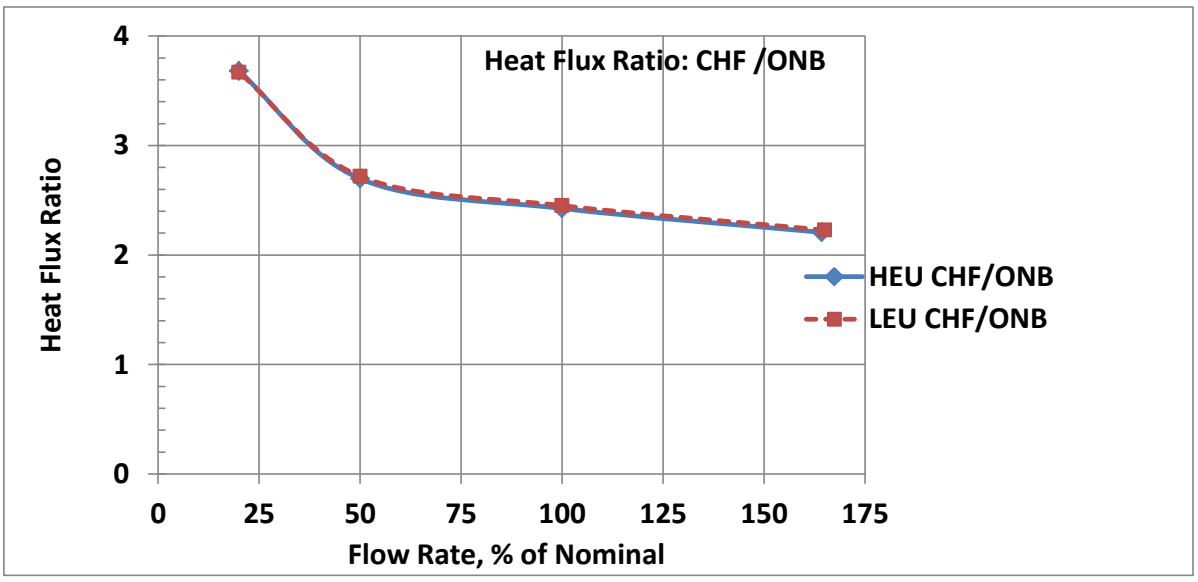


Fig 7. Comparison of the Ratio of Heat Flux at CHFR=1 to that at ONBR=1

5. Summary and Conclusions

Based on the comparison of the ONB heat flux, OFI heat flux and CHF, the safety limits imposed by OFI and CHF are found to cross over in a consistent manner, in the parametric range studied. The cross over is consistent with the experimental evidence shown in Refs [4, 5, 6].

A BR2-specific OFI-CHF reversal diagram showing the mass flux at the intersection of OFI heat flux and CHF (called the reversal mass flux) is created as a function of exit pressure, for a given heated length, with heated diameter and inlet temperature as parameters. Within the accuracy of the scoping methodology, the diagram shows that a BR2 coolant channel at 100% of nominal flow is CHF-limited. Since reversal diagrams are only recommended for scoping studies, a detailed thermal-hydraulic analysis was performed.

For BR2, CHF is most-limiting regarding peak heat flux for higher mass flow rates, in excess of about 100% of nominal. Conversely, FI is most-limiting regarding peak heat flux for mass flow rates less than about 100% of nominal. This applies to LEU and to HEU fuels. It is concluded that, relative to OFI versus CHF, there is very little difference between the safety performances of HEU versus LEU fuel under steady-state operating conditions.

The scoping methodology and the detailed analysis are also in good agreement with respect to the heat flux at which the OFI-CHF reversal occurs (scoping study: 1495 W/cm^2, detailed analysis: 1500 W/cm^2).

6. Acknowledgement

This work was sponsored by the U.S. Department of Energy, National Nuclear Safety Administration (NNSA) Office of Global Threat Reduction (NA-21).

7. References

1. M. Kalimullah, A. P. Olson, E. E. Feldman, and J. E. Matos, “Reversal of OFI and CHF in Research Reactors Operating at 1 to 50 bar,” ANL/GTRI/TM-13/14, Version 1.0, Argonne National Laboratory, Argonne, IL, USA (September 15, 2013).
2. A. P. Olson and M. Kalimullah, “A User’s Guide to the PLTEMP/ANL Code,” ANL/RERTR/TM-11-22, Version 4.1, Argonne National Laboratory, Argonne, IL, USA (November 15, 2011).
3. A. P. Olson, B. Dionne, J. Stevens, S. Kalcheva, G Van den Branden, and E. Koonen, "Steady-State Thermal-Hydraulics Feasibility Study for the Conversion of the BR2 Reactor to LEU," ANL/RERTR/TM-11-45, Argonne National Laboratory, Argonne, IL, USA (November 15 2011).
4. F. C. Gunther, “Photographic Study of Surface-Boiling Heat Transfer to Water with Forced Convection,” Progress Report No. 4-75, Jet Propulsion Laboratory, California Institute of Technology, Pasadena, California, USA (1950).
5. F. C. Gunther, “Photographic Study of Surface-Boiling Heat Transfer to Water with Forced Convection,” Transactions of ASME, Vol. 73, pp. 11 5-123 (February 1951).
6. G. P. Celata, M. Cumo, A. Mariani, and G. Zummo, “Burnout in Subcooled Flow Boiling of Water, A Visual Experimental Study,” Intern. Journal of Thermal Sciences, Vol. 39, pp. 896-908 (2000).
7. R. H. Whittle and R. Forgan, “A Correlation for the Minima in the Pressure Drop vs. Flow Rate Curves for Subcooled Water Flow in Narrow Heated Channels,” Nuclear Eng. and Design, Vol. 6, pp. 89-99 (1967).
8. P. Saha and N. Zuber, “Point of Net Vapor Generation and Vapor Void Fraction in Subcooled Boiling,” Proc. of 5th Intern. Heat Transfer Conf., Vol. 4, Tokyo, pp. 175-179 (1974).
9. E. E. Feldman, "Comparison of the PLTEMP Code Flow Instability Predictions with Measurements Made with Electrically Heated Channels for the Advanced Test Reactor," ANL/RERTR/TM-11-23, Argonne National Laboratory, Argonne, IL, USA (June 9, 2011).

10. D. C. Groeneveld, J. Q. Shan, A. Z. Vasic, L. K. H. Leung, A. Durmayaz, J. Yang, S. C. Cheng, and A. Tanase, “The 2006 CHF Look-up Table,” Nucl. Eng. and Design, Vol. 237, pp. 1909-1922 (2007).
11. M. Kalimullah, E. E. Feldman, A. P. Olson, B. Dionne, J. G. Stevens, and J. E. Matos, “An Evaluation of Subcooled CHF Correlations and Databases for Research Reactors Operating at 1 to 50 bar Pressure,” RERTR 2012, 34th Intern. Meeting on Reduced Enrichment for Research and Test Reactors, Warsaw, Poland (October 14-17, 2012).
12. D. D. Hall and I. Mudawar, “Critical Heat Flux for Water Flow in Tubes – II. Subcooled CHF Correlations,” Intern. J. Heat and Mass Transfer, Vol. 43, pp. 2605-2640 (2000).
13. INTERATOM, on behalf of the Minister of Research and Technology of the Federal Republic of Germany, Appendix A-1 of IAEA-TECDOC-643, “Research Reactor Core Conversion Guidebook,” Vol. 2: Analysis (Appendices A-F), International Atomic Energy Agency, Vienna, (April 1992).
14. S. Kalcheva, E. Koonen, V. Kuzminov, G. Van den Branden, E. Sikik, A. P. Olson, B. Dionne, “Feasibility Report: Conversion from HEU to LEU fuel of the BR2 Reactor,” BLG-R-5439, SCK•CEN, (2012).
15. MCNPX, Version 2.7.E, John S. Hendricks, Mike Fensin et al., LA-UR-11-0150, Los Alamos National Laboratory, Los Alamos, NM, USA, (March, 2011).
16. J. P. Harnet and T.F. Irvine, Jr, Editors, "Advances in Heat Transfer," Vol. 6, Academic Press, New York, 1970.
17. Constantine P. Tzanos, Heat Transfer Predictions by Turbulence Models and Heat Transfer Correlations, Trans. ANS 105, American Nuclear Society (November 2011).
18. A.E. Bergles and W.M. Rohsenow, “The Determination of Forced-Convection Surface-Boiling Heat Transfer,” J. Heat of Transfer, Vol. 86, pp. 365–372 (1964).

STATUS AND CALL FOR PROJECT PROPOSALS RELATED TO THE NEW IAEA CRP ON "BENCHMARKS AGAINST EXPERIMENTAL DATA ON FUEL BURNUP AND MATERIAL ACTIVATION"

N.D. PELD[(1)], D. RIDIKAS[(2)]*, A. BORIO[(1)], W. KENNEDY[(3)]

(1) Research Reactor Section, NEFW-NE
(2) Physics Section, NAPC-NA
(3) Research Reactor Safety Section, NSNI-NS

International Atomic Energy Agency
Vienna International Centre, PO Box 100, Vienna, AUSTRIA

*Corresponding author: D.Ridikas@iaea.org

ABSTRACT

The IAEA is in the process of developing a Coordinated Research Project for the term 2014–2017 titled "Innovative Methods in Research Reactor Analysis: Benchmarks against Experimental Data on Fuel Burn-up and Material Activation." The new project will be a follow up to the already terminated Coordinated Research Project 1496 on "Innovative Methods in Research Reactor Analysis: Benchmark against Experimental Data on Neutronics and Thermal-hydraulic Computational Methods and Tools for Operation and Safety Analysis of Research Reactors", which was jointly conducted and equally funded by NSNI, NEFW and NAPC (2008-2012). The new project was recommended by the participants of the previous project and by the Technical Working Group on Research Reactors during its meetings in 2012 and 2013. The new Coordinated Research Project will collect the available experimental data on fuel burn-up and material/target activation and assess the computational methods and tools used in the related analysis for research reactors (RRs). The expected research outputs of the new project are:

- An IAEA experimental database on fuel burn-up and material/target activation;
- An IAEA Technical Document comparing the experimental data with the computational results and describing the work developed by each individual group, including any innovative methods applied in the analysis;
- An executive summary that identifies remaining open issues for future R&D activities and indicates a possible role for the IAEA in the area of innovative methods in research reactor analysis.

1. Introduction

In order to encourage cooperation and foster exchange of information in the area of numerical analysis for improving research reactor design, operation, utilization and safety, a Coordinated Research Project (CRP) comparing neutronics and thermal-hydraulic methods against experimental data was conducted in 2008–2012 [1]. Experimental data from 9 research reactors of various designs and power ratings were collected and used to verify the efficacy of theoretical results and evaluate various codes and modelling tools. These results and subsequent conclusions are described in a forthcoming IAEA Technical Report Series No. 480 (2014) in the form of a CD-ROM containing descriptions of the experiments and a database of experimental data [2].

The 2nd publication (IAEA TECDOC Series, presently in final editing) will provide practical information and examples of benchmarking studies done by the participants of the CRP and be complementary to the experimental database mentioned above. This document will be helpful to improve operational performance, utilization and safety of research reactors.
In some cases, a disparity between the experimental data and neutronics/thermal-hydraulic analysis was identified, and additionally the CRP participants acknowledged a critical need to continue work in benchmarking fuel burn-up and irradiation data. Therefore, in agreement with the members of the IAEA Technical Working Group on Research Reactors, this subsequent CRP was proposed and will begin in 2014.

3. Objectives and description of the new CRP

The scope of the new CRP is to collect available experimental data and assess the computational methods and tools used for fuel burn-up calculations and material/target activation in research reactor analysis. The expected research output of the CRP will be, among others:

- A database on specific experimental results on fuel burn-up and material/target activation;
- An IAEA Technical Document comparing the experimental data and the computational results, including descriptions of the work performed by each individual research group;
- Identification of remaining open issues for future R&D activities and indication of a possible role for the IAEA in the area of innovative methods in research reactor analysis.

3. Preparatory work for the new CRP

In preparation for the new CRP, the IAEA conducted a specific survey of Member States that operate research reactors in order to collect preliminary information on (1) the existing experimental data on fuel burn-up and material/target activation, (2) presently used computational methods and tools, and (3) willingness to participate and share available data with others. The first three questions dealt with what kind of fuel and irradiation experiments are performed and whether data from these experiments is available. The final three attempted to determine the level of completeness of the data, the types of codes used for analysis and the willingness to participate in the CRP. Table 1 provides the IAEA questionnaire.

4. Preliminary analysis of the survey

Replies were received from close to 30 institutions world-wide, again representing different types of reactors (Miniature Neutron Source Reactor, TRIGA, Material Test Reactor, etc.) and power ratings ranging from 30 kW to 30 MW. More than half of the research reactor facilities replied positively and confirmed their readiness to provide their valuable data to other participants in the CRP.

The survey responses indicated that 10 responders perform or performed experimental analyses and measurements for fuel burn-up calculations and 19 perform or performed experimental analyses and measurements on irradiated unspecified materials/targets. Most of these affirmed that some data is available to the research group or the public, and thus these may be considered to form the core participants of the research project. Among the codes cited by these operating organizations were MCNP, SCALE/ORIGEN, CINDER-90, FISSPACT, MCB and some others, and most indicated the use of gamma spectroscopy to obtain data on fuel burn-up and characteristics of irradiated materials and targets. Therefore, the survey responses indicate that the potential research group as a whole already possesses the basic components to establish a valuable database for comparison of burn-up and irradiation data with computational results.

TABLE 1. IAEA questionnaire on the available experimental data and modelling tools relevant to research reactor fuel burn-up and material/target activation.

<table>
<tr><td colspan="2">1. Do you perform any type of experimental analysis/measurements <u>for fuel burn-up at your RR facility</u>? (e.g., gamma spectroscopy, radiochemical analysis, neutron imaging, dose measurements, etc.)</td></tr>
<tr><td>□ Yes
□ No</td><td>If yes, please provide your scheme/methods below
• …
• …
• …</td></tr>
<tr><td colspan="2">2. Do you perform any type of experimental analysis/measurements <u>for irradiated materials/targets at your RR facility</u>? (e.g., gamma spectroscopy of radioisotope production targets, radiochemical analysis, dose measurements, etc.)</td></tr>
<tr><td>□ Yes
□ No</td><td>If yes, please provide your scheme/methods below
• …
• …
• …</td></tr>
<tr><td colspan="2">3. Is your data under (1) and (2) available for sharing within the CRP or with the public?
□ Yes, public availability (e.g. through published reports/articles)
□ Yes, but only within the IAEA CRP
□ No</td></tr>
<tr><td colspan="2">4. Do you have all the input parameters required for benchmarking your experimental data under (1) and (2) for sharing within the CRP or with the public? (e.g., irradiation history in terms of power/flux/time, initial fuel/target composition, detailed neutron flux/energy profiles either calculated or experimental, etc.)</td></tr>
<tr><td>□ Yes, public availability
□ Yes, but only within the IAEA CRP
□ No</td><td>If yes, please provide the list of these parameters:
• …
• …
• …</td></tr>
<tr><td colspan="2">5. What are the fuel burn-up or material evolution/activation codes you employ at your facility? Please provide their name/type and duration they have been in use at your institution (e.g. MCB – Monte Carlo Burn-up, CINDER90, ORIGEN-2, burn-up capability within MCNP5, etc.)
• …
• …
• …</td></tr>
<tr><td colspan="2">6. In case this new CRP is approved, are you interested to participate?
□ Yes, as an experimental data provider
□ Yes, as a participant in benchmarking exercises
□ Yes, for both as above
□ No</td></tr>
</table>

4. Initial activities of the CRP and dates

The IAEA has already planned a dedicated Consultancy Meeting from 24 to 28 March 2014 in Vienna in order to

- Review the analysis of the preliminary survey;
- Propose the structure of a burn-up/activation database;
- Draft design of a new CRP and plan related follow up actions;
- Prepare meeting report, including conclusions and recommendations.

The CRP proposal will be submitted for the approval in April 2014, and the call for research contract proposal is expected to be announced before summer 2014 [3].

The first Research Coordination Meeting (project kick-off) of this new CRP (2014-2017) is tentatively scheduled for December 2014.

References

[1] INTERNATIONAL ATOMIC ENERGY AGENCY, IAEA CRP 1496, http://www-naweb.iaea.org/napc/physics/research_reactors/crps/crp.html (last updated in March 2014).

[2] INTERNATIONAL ATOMIC ENERGY AGENCY, Research Reactor Benchmarking Database: Facility Specification & Experimental Data, IAEA Technical Reports Series No 480, IAEA, Vienna (2014) in print.

[3] INTERNATIONAL ATOMIC ENERGY AGENCY, Coordinated Research Activities, http://cra.iaea.org/cra/index.html

MODELING THE CLADDING-OXIDE GROWTH AND ITS EFFECTS ON THE THERMO-MECHANICAL PERFORMANCE OF THE FUEL PLATES IN THE E-FUTURE-1 EXPERIMENT

A.M. TENTNER, A. BERGERON, Y.S. KIM, J.G. STEVENS
Nuclear Engineering Division
Argonne National Laboratory, 9700 S. Cass Ave., Argonne IL 60439 – USA

S. VAN DEN BERGHE[1], V. KUZMINOV[2]
1 - Institute for Nuclear Materials Science, Microstructural and Non-Destructive Analyses
2 - BR2 Reactor Department
SCK•CEN, Boeretang 200, B-2400 Mol - Belgium

ABSTRACT

The growth of an oxide layer with low thermal conductivity on the surface of the fuel plates used in research reactors can have a significant impact on the maximum fuel temperature reached during the irradiation cycle. Existing oxide growth models were generally developed using plate surface temperatures obtained from traditional one-dimensional fluid dynamics calculations. As detailed oxide thickness measurements become available from the E-FUTURE experiments and 3-D multi-physics analyses of these experiments provide more accurate temperature distributions, it is possible and necessary to refine and validate the oxide growth models in the context of these 3-D analyses. A Computational Fluid Dynamics (CFD) model based on the STAR-CD code and a Fuel Behavior (FB) model for the simulation of UMo dispersion named SIMDIF are used at Argonne National Laboratory (ANL) for the multi-physics analysis of the E-FUTURE-1 fuel irradiation experiment conducted in the BR2 reactor at SCK•CEN in Belgium. The oxide thickness calculated in a multi-physics simulation of the E-FUTURE-1 experiment is compared with the corresponding oxide thickness measured during post-irradiation destructive and non-destructive examinations. An improved representation of the oxide growth rate is proposed which is shown to improve the agreement between the measured and calculated oxide thickness results. The effects of the oxide layer growth on the fuel meat temperature during the E-FUTURE-1 experiment are examined. The validation of the oxide formation models in conjunction with the 3-D multi-physics E-FUTURE-1 simulation is part of the overall validation of the 3-D multi-physics models which can help improve our understanding of the LEU fuel behavior in the RHF reactor and other LEU research reactors.

1. Introduction

The effort to develop dispersed UMo LEU fuel elements with densities up to 7.5 - 8.5 gU/cm³ is currently focused on the qualification of LEU fuel elements at high heat-fluxes for use in the BR2, RHF, and future JHR high flux reactors [1]. The high-heat-flux irradiation test named E-FUTURE-1, consisting of 4 full-size flat plates in a dedicated irradiation basket, started in March 2010 and was completed in October 2010 in the BR2 reactor at SCK-CEN. The plates containing dispersed UMo in an Al-Si matrix were irradiated at heat fluxes up to 470 W/cm^2 at BOL. The non-destructive and destructive measurements of the fuel plates

provided valuable information about the fuel plate behavior during irradiation which is now being used to guide the development of analytical models. The non-destructive examination of the fuel elements showed significant plate swelling and oxide film formation, and the destructive examination confirmed the oxide film formation and showed substantial changes in the fuel structure. The integrated Computational Fluid Dynamics (CFD) and Fuel Behavior (FB) model [2] developed at ANL with the goal of providing a predictive fuel performance tool was used to simulate the E-FUTURE-1 experiment. The experimentally measured changes in the fuel plate dimensions and fuel composition were compared with the corresponding calculated results in [3]. Good agreement between the calculated results and measured data was obtained for the fuel meat composition and fuel plate swelling, with the exception of the blister locations. Some discrepancies were also noted between the calculated and measured oxide layer thickness in the blister regions. In this paper we describe recent enhancements of the oxide growth model used in the multi-physics E-FUTURE-1 simulation which lead to improved prediction of the oxide layer thickness in the blister regions and evaluate the impact of the oxide layer growth on the fuel plate response during irradiation.

2. The E-FUTURE-1 Experiment and the Power History

The E-FUTURE-1 irradiation test was designed to allow the selection of the best combination of parameters for the LEU UMo in terms of Si content and thermal treatment . It consisted of irradiating four full size flat fuel plates contained in a specially designed basket in the BR2 reactor at high heat fluxes and then in assessing their performance parameters through non-destructive and destructive post-irradiation examinations. A schematic cross-section through the fuel basket and cross-sections through the fuel plate are shown in Figures 1 and 2, respectively. The coolant flow enters at the top of the irradiation basket with a nominal temperature of 38 C and flows downward between the fuel plates, exiting at the bottom of the basket. A thicker Al plate installed at the center of the coolant channel, parallel to the fuel plates provides additional rigidity, as shown in Figure 1.

The E-FUTURE plates are full size, high density, flat fuel plates made of dispersed UMo in Al-Si matrix (8 gU/cm^3, 19.7 % ^{235}U enrichment) with two different cladding types (AG3-NET as used in BR2 and AlFeNi as used in RHF). An important parameter specified for the E-FUTURE fuel plate was the Si content in Al matrix required to stabilize the interaction layer formed between the UMo and the Al matrix. Two Si contents (4 and 6 wt%) were chosen for the E-FUTURE test plates.

The power history experienced by the E-FUTURE plates during irradiation in the BR2 reactor is an important input of the coupled CFD-FB simulations. The E-FUTURE power history was obtained from neutronic calculations of each BR2 operating cycle, based on the actual operating history of BR2 (power and control rods positions versus time during irradiation) and on the actual loading scheme of the fuel and uranium fission targets in the reactor core during each cycle [2]. The irradiation of the E-FUTURE basket in BR2 continued for three cycles during which the fuel burn-up and power changed significantly. The calculated spatial power distributions were provided to the CFD-FB simulation for the beginning, middle, and for the end of each cycle.

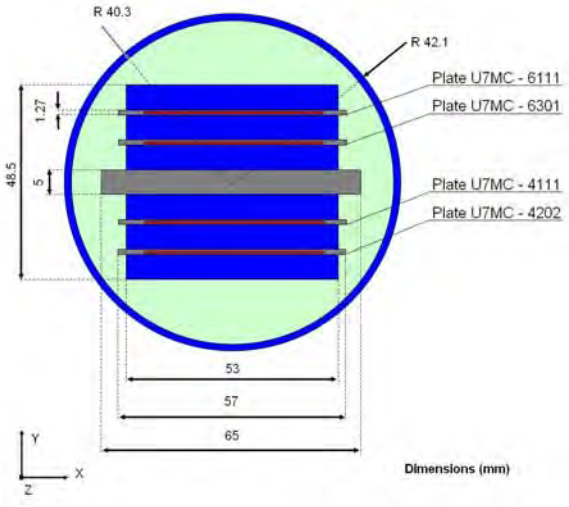


Figure 1 Cross section of the E-FUTURE basket with four U7Mo fuel plates

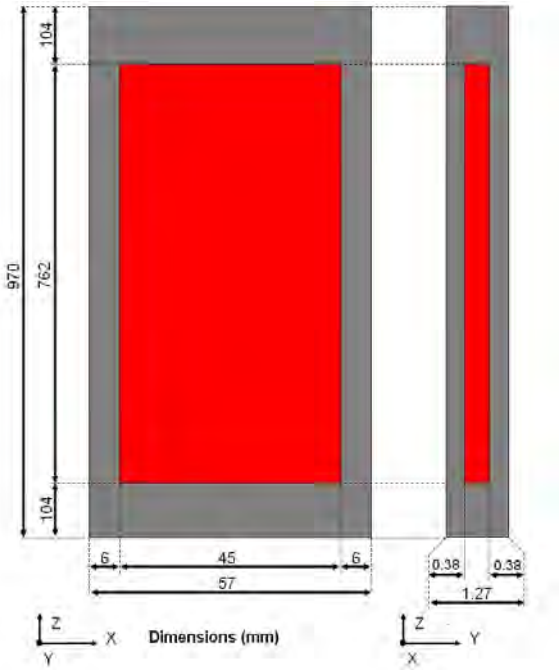


Figure 2 E-FUTURE fuel plate and fuel meat dimensions

3. The Integrated CFD-FB Model of the E-FUTURE-1 Experiment

3.1 The CFD Model

The CFD model, based on the commercial Star-CD code, describes the irradiation basket, containing the four fuel plates and the coolant channels. The initial model geometry is the original geometry of the fuel plates before irradiation illustrated in Figure 2. The thickness of the fuel meat and cladding can change during the irradiation, as described in Section 5 below. The CFD model includes conjugate heat transfer, calculating both the thermal-hydraulic conditions of the coolant and the temperatures in the solid fuel plates and basket. The power generation in the fuel plates at a specified time during the irradiation cycle is based on the results of neutronic calculations performed for that time.

This fluid mesh is unequally spaced, with the cell thickness decreasing near the cladding surface, to ensure an adequate y^+ value. A non-uniform mesh has also been used in the fuel meat region, in order to capture the sharp temperature gradients and local temperature peaks that develop in the fuel meat near the boundaries with the non-fuel cladding regions [2]. The model allows mesh deformations in the direction normal to the fuel plate surface, describing the geometry changes due to fuel plate swelling and oxide formation during irradiation.

3.2 The Fuel Behavior Model SIMDIF

The fuel behavior (FB) model SIMDIF (Simulation of Dispersed Fuel), evaluates the changes in the geometry and thermo-mechanical properties of the fuel "meat" and cladding of the four full size fuel plates during irradiation. In order to get an accurate spatial solution, SIMDIF used the same mesh in the fuel region of the plates as the CFD model mesh. The plate faces are also meshed like the CFD model in order to allow an accurate information exchange between the FB and CFD models at the coolant – cladding interface. SIMDIF

describes the sequence of phenomena that occur in the fuel plate during irradiation including: a) oxide layer growth, b) fuel particle swelling, c) interaction layer (IL) growth, d) fission gas generation, e) fuel plate swelling due to fission gas pressure, f) fuel meat porosity changes, and g) fuel meat conductivity changes. These models have been described in [2] and [3]. The extended oxide layer growth model and the effect of the oxide layer on the fuel plate response are discussed in Section 5 below.

3.3 Coupling of the CFD and FB Models

To capture the interactions between the fuel mechanics and thermal-hydraulic effects during the E-FUTURE experiment, each of the three irradiation cycles was divided into two discrete time intervals, resulting in six time intervals as shown in Table 1. For each time interval, a CFD calculation is performed at the beginning of the interval, using the most current fuel plate geometry, fuel meat conductivity, and oxide layer thickness. An additional CFD calculation is then performed at the mid-point of the time interval, using a power generation distribution obtained by averaging the beginning- and end-of-interval power distributions. This calculation determines the mid-interval fuel meat temperatures and plate-coolant interface temperatures which are then provided to the FB model. Using this information, the FB model calculates the changes in the fuel conductivity, fuel meat swelling, and cladding oxide growth during the time interval. This information is sent back to the CFD model, which uses the information received from the FB model to change the fuel plate and coolant channel geometry, and then calculates the new thermal-hydraulic conditions at the end of the time interval. More details about the coupling between the CFD and FB models can be found in [2].

Table 1 Time intervals for the E-FUTURE experiment simulation

Interval number	Irradiation cycle	Interval limits	Maximum ^{235}U BU [%]
1	310	day 1 (BOC) - day 7	10
2	310	day 8 - day 26 (EOC)	31
3	410	day 1 (BOC) - day 7	39
4	410	day 8 - day 28 (EOC)	55
5	510	day 1 (BOC) - day 10	64
6	510	day 11 - day 20 (EOC)	71

4. Post-test Oxide Growth Measured Results

4.1 Non-destructive Analysis Oxide Growth Results

The non-destructive PIE of the E-FUTURE plates at SCK•CEN was performed with the BONAPARTE measurement bench [4, 5]. Non-destructive analyses included oxide thickness and plate thickness measurements over the entire plate surface. Oxide thickness measurements are based on the eddy current principle. For the measurements on the E-FUTURE fuel plates, a measurement grid of 5×1 mm was adopted, with measurement points every 1mm in the longitudinal plate direction. A line scan was performed every 5mm in the transversal plate direction. Detailed scans, using a 1x1 mm² grid were recorded in the blistered areas of each fuel plate. The results show the presence of a thicker oxide layer as well as significant local swelling at the highest burnup locations of the fuel plates. The non-destructive oxide thickness at the location of destructive analysis cuts described in Section 4.2 are presented in Section 5.1.3 below. The oxide thicknesses in the blister areas are considered less reliable, because of the sensitivity of the eddy current technique to defects in the substrate material. When these values are different from the destructive oxide

measurements, the destructive results were used to guide the oxide growth model calibration.

4.2 Destructive Analysis Oxide Growth Results

In the destructive examinations, samples were cut from each of the 4 E-FUTURE fuel plates to assess microstructure evolution, particularly interaction layer formation and fission product distribution by microscopy and spectroscopy. The location of the samples is shown in Figure 3. Destructive analyses also allowed measurement of the oxide thickness values which are compared with the corresponding values determined in the non-destructive PIE and with the values calculated in the multi-physics simulation of the experiment in Section 5.1.3 below. The results of the destructive analysis were reported in [6].

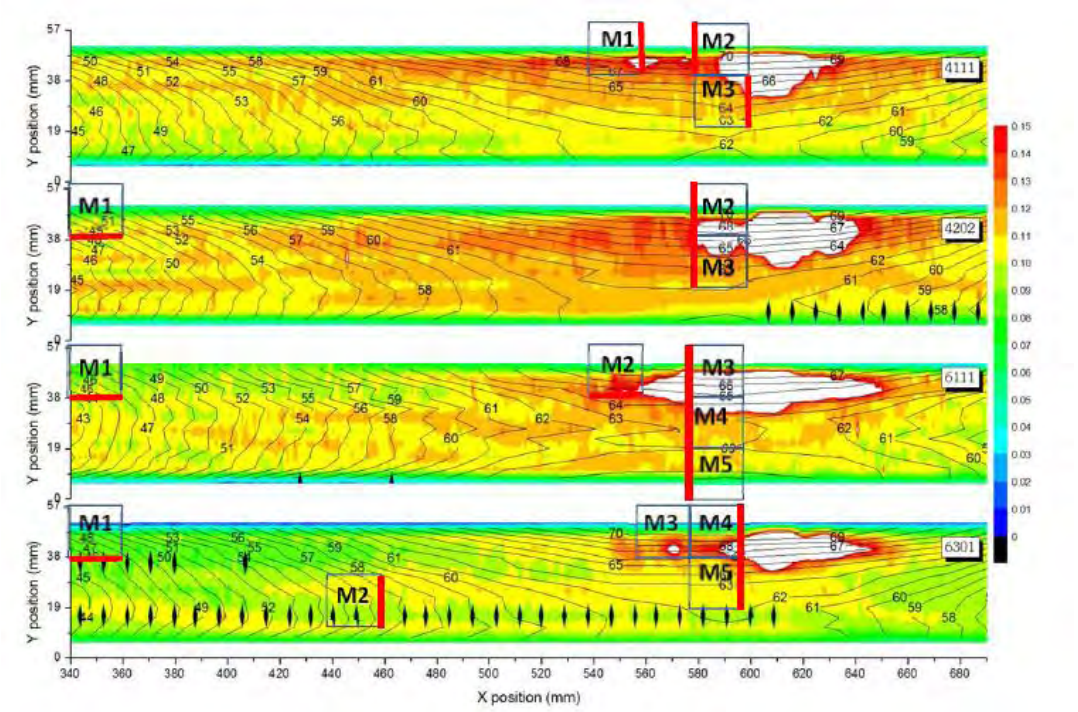


Figure 3 Cutting scheme for the E-FUTURE-1 plates. The color scheme is adapted to show the blistered areas, which have a Swelling-to-Burnup ratio greater than 0.15. The polishing planes are indicated in red [6].

5. Results of Coupled CFD-FB Simulations

This section describes the recent oxide growth modeling changes implemented in SIMDIF with the goal of providing an enhanced description of the changes that occur during the irradiation in the fuel plate in general, and in the thickness of the oxide layer and cladding temperature in particular. The calculated oxide layer thickness is compared with the corresponding measured results of non-destructive and destructive post-test analyses in Section 5.1 and the effect of the oxide growth on the fuel plate behavior during irradiation is discussed in Section 5.2.

5.1 Validation of the extended Oxide Layer Growth Model

In this section we present the changes introduced in the original oxide model and compare the E-FUTURE-1 measured oxide layer thickness with the results calculated with the extended oxide growth model and with those obtained with the original model.

5.1.1 The original Oxide Layer Growth Model

The water-side oxide growth kinetics for Al cladding of research reactor fuel plates has been described in previous SIMDIF analyses [2, 3] using a model similar to that proposed by Kim et al 0. The model comprises a series of equations empirically fitted to measured data. The kinetics equation describing the oxide growth on the aluminum alloy surface is given by:

$$x = \left[{x_0}^{p+1} + (p+1)\, k\, \Delta t \right]^{\frac{1}{p+1}} \tag{1}$$

where x_0 is the film thickness at time zero in μm, p is the rate law power, k the rate function and Δt is the time step in hours. The rate law power p is dependent on oxide dissolution in the water, so it is given by a function of coolant pH and temperature. The rate law power p is given by:

$$\mathrm{p} = 0.12 + 9.22 \exp\left(-\frac{\mathrm{C_s}}{6.82 \times 10^{-9}} \right) \tag{2}$$

and C_s is expressed by:

$$\mathrm{C_s} = \exp\left[-\left(-13.79 - \frac{1211.16}{\mathrm{T_{x/w}}} \right) \left(0.041\mathrm{H}^2 - 0.41\mathrm{H} - 0.07 \right) \right] \tag{3}$$

where $T_{x/w}$ is the temperature at the oxide-water interface and H is pH of the coolant.
The rate function k is expressed by an empirical formula:

$$k = 0.9 \times 10^3 \exp\left(\frac{-3800}{T_{x/w} + C_k \frac{q\,x}{\lambda}} \right) \tag{4}$$

where C_k is a fitting constant dependent on the coolant flow rate, q is the heat flux in the oxide, x is the oxide thickness and λ is the oxide thermal conductivity. The new oxide thickness is calculated using Eq. (1) with time steps Δt=24 h and the value of x at the end of the previous time step is used in Eq. (4) to avoid iteration.

The oxide thickness calculated with this model in the E-FUTURE-1 in the multi-physics analyses described in [3] is compared with the destructive and non-destructive oxide thickness measurements in Figures 4-7. These figures show that the original oxide model tends to under-predict the oxide layer thickness, particularly in the high temperature regions of the plates.

5.1.2 Oxide Film Growth Model Enhancements

In order to improve the agreement between the calculated oxide thickness and the corresponding measured data the original oxide growth model has been modified using the assumption that, when cracks develop in the oxide layer, the temperature that drives the oxide growth is the temperature in the oxide cracks $T_{x/crack}$ rather than the temperature at oxide-water interface $T_{x/w.}$ The oxide-crack temperature is used in both Equations (3) and (4), which become:

$$C_s = \exp\left[-\left(-13.79 - \frac{1211.16}{T_{x/crack}} \right) \left(0.041H^2 - 0.41H - 0.07 \right) \right] \tag{5}$$

$$k = 0.9 \times 10^3 \exp\left(\frac{-3800}{T_{x/crack}}\right) \quad (6)$$

The temperature $T_{x/crack}$ is calculated as follows:

$$T_{x/crack} = T_{x/w} + F\frac{qx}{\lambda} \quad (7)$$

where F is a fraction between 0 and 1, so that the temperature $T_{x/crack}$ lies between the temperature at oxide-water interface $T_{x/w}$ and the temperature at the oxide-substrate interface. The fraction F is calculated as:

$$F = \begin{cases} 0 & if\ x < x_{min} \\ (x - x_{min})/(x_{max} - x_{min}) & if\ x_{min} \leq x \leq x_{max} \\ 1 & if\ x > x_{max} \end{cases} \quad (8)$$

The oxide thickness results presented in this paper were obtained with x_{min} = 0.10 and x_{max} = 0.25. When the oxide thickness is below x_{min} the effect of the oxide layer cracks is assumed negligible and the temperature that governs the growth of the oxide layer is the temperature at the oxide-water interface. When the oxide thickness is above x_{max} the cracks are assumed to span the entire oxide layer and the temperature that governs the growth of the oxide layer is the temperature at the oxide-substrate interface.

5.1.3 Evaluation of the Oxide Layer Growth Model results

To evaluate the performance of the oxide growth model, a full simulation of the E-FUTURE-1 experiment was performed using the extended oxide growth model, in addition to the simulation performed earlier with the original oxide growth model [3]. The oxide thickness calculated with the original oxide growth model and the extended model were compared with experimental results of destructive and non-destructive oxide layer measurements for the cut locations identified in Figure 3. The results for selected cut locations - one for each plate - are shown in Figures 4 through 7. These figures also provide a comparison of the destructive and non-destructive measured results. Although these measured results agree reasonably well, occasionally differences between the destructive and non-destructive measured oxide thickness are observed. When this is the case the authors assume that the destructive measurement results are more reliable than the non-destructive results.

As illustrated in Figures 4 through 7, the original oxide growth model - referred to as OxMod-1 in the legend - consistently under-predicts the measured thickness of the oxide layer, particularly in the high-temperature regions where the calculated oxide thickness can be 10-15 µm lower than the corresponding measured value. The oxide thickness calculated with the extended oxide model - referred to as OxMod-2 in the legend - shows substantially improved agreement with the measured data. The results calculated with the extended oxide model show a more pronounced increase in the oxide thickness in the high-temperature regions of the plate, in agreement with the experimental observations. An analysis of the extended model indicates that the improved predictions are primarily due to the use of the temperature $T_{x/crack}$ in Equation 5, while the change in Equation 6 has a small effect on the calculated oxide results

.

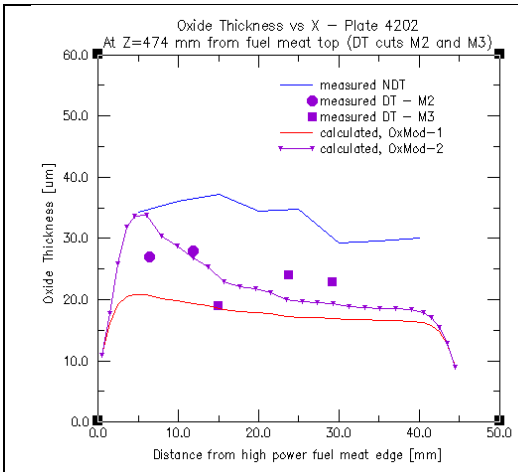


Figure 4 Oxide thickness for plate 4202, at z=474 mm from the fuel meat top

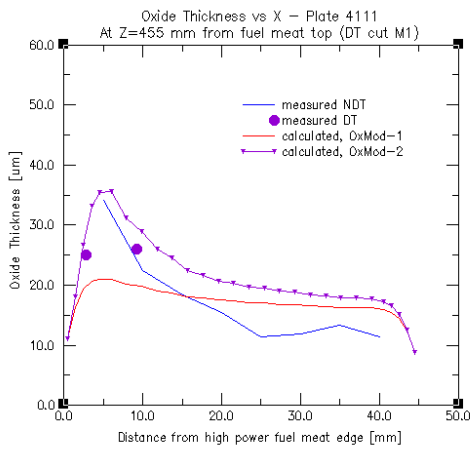


Figure 5 Oxide thickness for plate 4111, at z=455 mm from the fuel meat top

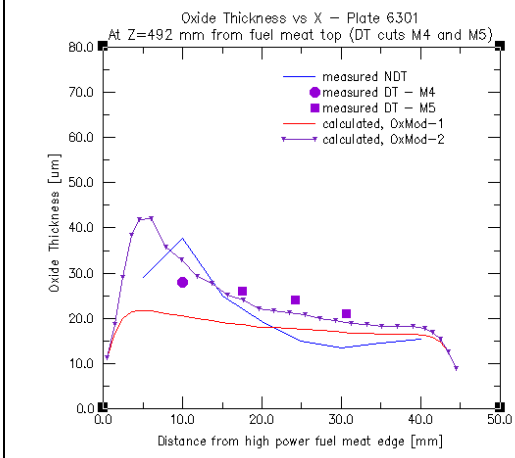


Figure 6 Oxide thickness for plate 6301, at z=492 mm from the fuel meat top

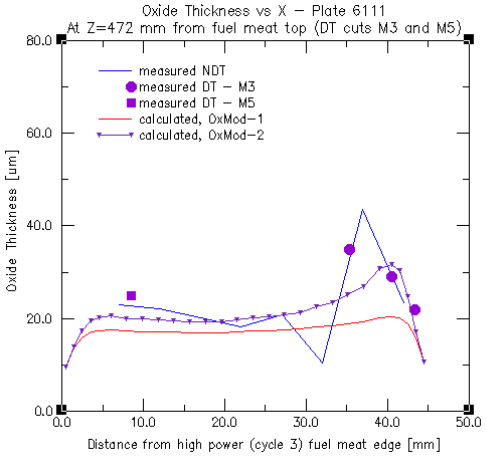


Figure 7 Oxide thickness for plate 6111, at z=472 mm from the fuel meat top

5.2 Effect of Oxide Layer Growth on Fuel Plate Thermo-Mechanical Response

The growth of the oxide layer affects both the local cladding and fuel temperatures. The higher oxide thickness observed in the high temperature region of the plates leads to higher fuel temperatures and higher pressures in the fuel meat. It also causes an increase in the local cladding temperature, which leads to a decreased cladding yield strength and creep strength. The combination of higher fuel meat pressures and reduced cladding creep strength can lead to faster cladding creep, potentially favoring the formation of the local blisters observed in the E-FUTURE-1 experiment. To quantify the effect of the oxide growth on the fuel plate response, the results of a coupled CFD-FB simulation of the E-FUTURE-1 experiment using the enhanced oxide growth model were compared with the corresponding results obtained with the original oxide growth model. The improved prediction of the oxide fuel thickness for the plates 4111 and 6301 illustrated in Figures 4 and 5 leads increases in the maximum fuel meat temperatures of approximately 20 K for plate 4111 and 16 K for plate 6301 during the first half of the third irradiation cycle, as shown in Figures 8 and 9 respectively. The cladding temperatures at the location of maximum cladding swelling increase by approximately 20 K for both plates 4111 and 6301 at approximately the same time in the irradiation cycle, as shown in Figures 10 and 11 respectively.

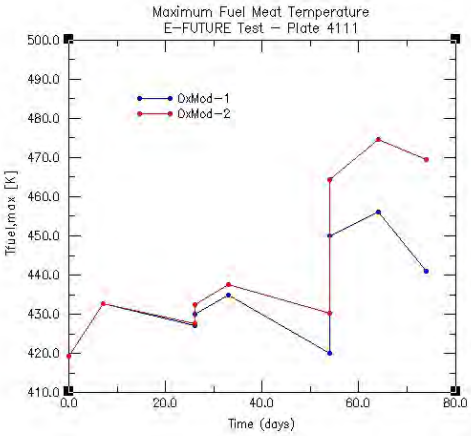


Figure 8 Maximum fuel meat temperature history for plate 4111

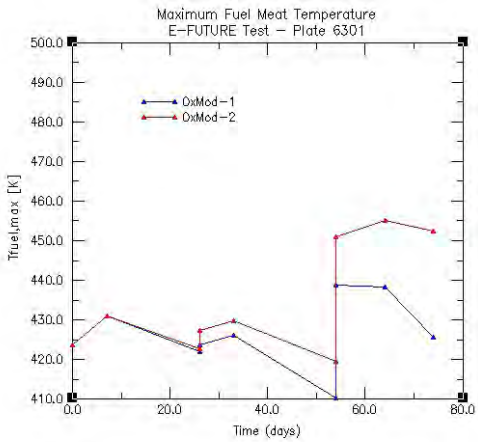


Figure 9 Maximum fuel meat temperature history for plate 6301

Several fuel behavior models are currently evaluated at ANL in order to understand the mechanisms that lead to the fuel plate pillowing and blister formation observed in the E-FUTURE experiment. These models range from detailed microscopic models describing the behavior of the fuel particles [8] to macroscopic models that explore the interactions between the fuel meat irradiation effects and the coolant and cladding thermal-hydraulic conditions [2]. The SIMDIF fuel behavior model which was used in this analysis describes the degradation of the cladding mechanical properties induced by oxide growth and higher temperatures, and the effect of the increasing pressure exerted by the fission gas in the fuel meat interaction layer on this weakened cladding. The increased fuel meat temperature leads to increased fission gas pressures, while the increased cladding temperature leads to decreased cladding strength, both effects favoring increased local swelling of the fuel plate. The simulation results indicate that the higher cladding temperatures have an important effect, when we account for the fact that aluminum alloys can exhibit a significant decrease of the creep strength as the cladding temperatures approach and exceed 50% of the cladding melting temperature. Several aluminum alloys are shown in [9] to exhibit a significant decrease of the creep strength at temperatures higher than 395 K.

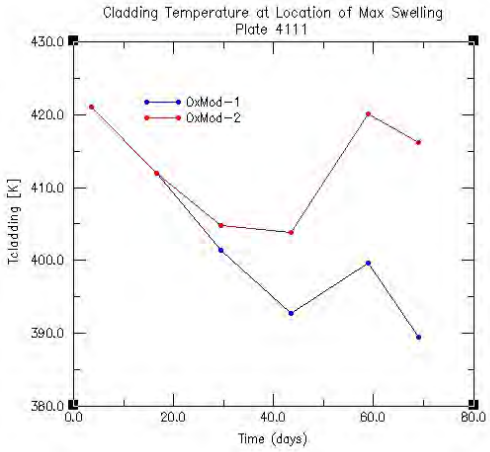


Figure 10 Cladding temperature history at the location of maximum swelling for plate 4111

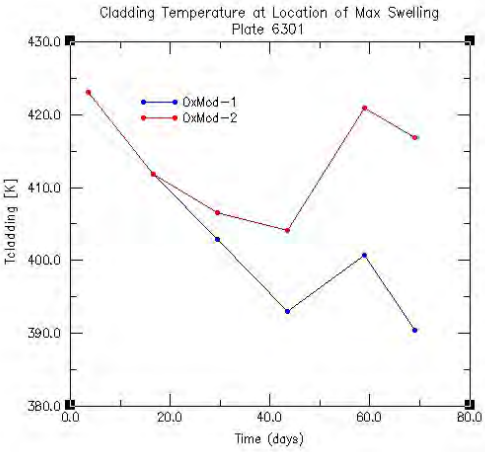


Figure 11 Cladding temperature history at the location of maximum swelling for plate 6301

As shown in Figures 10 and 11, the calculated maximum cladding temperature during the third irradiation cycle, when a large fraction of the matrix has been consumed and significant

fission gas pressures are present, is well above 400 K when the enhanced oxide growth model is used, whereas it remains below 400 K with the original oxide growth model. Figure 14 shows the calculated plate 6301 swelling at the end of the irradiation at 10 mm from the high power edge, when the plate deformation is calculated with the plate swelling model described in [3], which considers the cladding yield strength but does not include creep effects. In this simulation, the use of the enhanced oxide growth model leads to increased plate swelling in the region of the observed blister, but the predicted swelling increase is limited and remains well below the observed blister deformation.

The SIMDIF plate deformation model has been recently extended to include a simplified cladding creep model. For cladding temperatures below Tclad=395 K this model assumes that the creep effects are negligible and the plate deformation is calculated as described in [3], accounting for the fuel particle swelling and interaction layer growth and using the cladding yield strength to contain the fission gas pressure in the interaction layer fission gas bubbles. At temperatures above 395 K the creep strength decreases rapidly to values lower than the yield strength and the cladding creep strength replaces the yield strength in the procedure described in [3]. The underlying assumption is that the creep becomes fast enough to allow the forces acting on the cladding to reach an equilibrium condition during the irradiation time step considered, i.e. to cause cladding deformation until the stress due to interaction-layer fission gas pressure is equal to or lower than the creep strength. The 395K threshold value is based on [9] but it is acknowledged that it does not necessarily correspond to the E-FUTURE cladding properties. This value will be modified when more accurate cladding data becomes available.

Figure 13 shows the plate 6301 swelling results calculated with the extended plate deformation model, which includes the simplified cladding creep model. The swelling predicted when using the original oxide growth model increases only modestly in the blister region, because the cladding temperatures remain generally below the temperature where the creep effects become significant, as shown in Figure 12. The use of the enhanced oxide growth model leads higher cladding temperatures, with some temperatures well above 395 K, where the cladding deformation predicted by the cladding creep model accelerates. The creep effects lead to a significant swelling increase in the blister region, comparable with the measured plate swelling as shown in Figure 13.

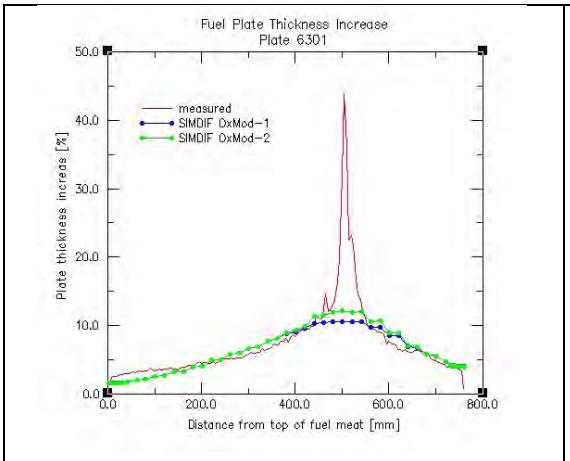


Figure 12 Fuel plate 6301 swelling calculated with a model without creep effects [3]

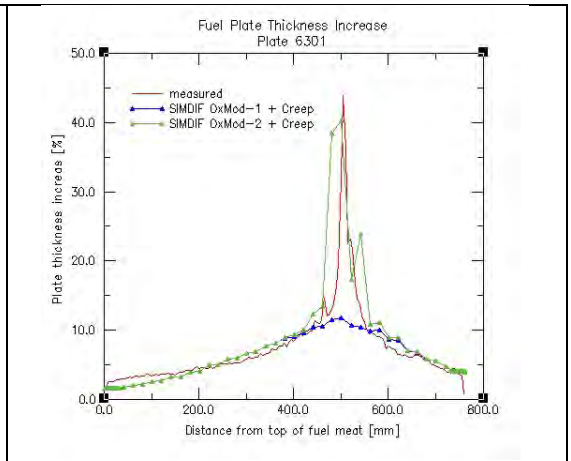


Figure 13 Fuel plate 6301 swelling calculated with a model that includes creep effects

6. Conclusions

The performance of the oxide layer growth model was evaluated in the context of a coupled CFD-FB analysis of the E-FUTURE-1 experiment. Modeling enhancements for the original

oxide layer growth model are proposed which are shown to improve significantly the agreement between the E-FUTURE-1 measured and calculated oxide thickness results. The effects of the oxide layer on the fuel meat and cladding temperatures and the fuel plate swelling during the E-FUTURE-1 experiment were examined. It was shown that the more accurate modeling of the oxide layer growth leads to the prediction of higher cladding and fuel temperatures in the E-FUTURE1 experiment and can affect the prediction of the plate swelling and blister formation when the cladding creep effects are considered. Using a simple creep model the observed fuel plate deformation could be modeled as a combined result of the weakened cladding and the high fission gas pressure in the fuel meat. The high fission gas pressure itself is due to the combination of high fuel meat temperatures and the release of large amounts of fission gas associated with the continuous interaction layer formation. The validation of the oxide formation models in the context of 3-D multi-physics experiment analyses is part of the overall validation of the 3-D multi-physics models which can help improve our understanding of the LEU fuel behavior in the RHF reactor and other LEU research reactors.

7. References

[1] F. Frery et al., “LEONIDAS U(Mo) Dispersion Fuel Qualification Program: Progress and Prospects,” Proceedings of the 32nd International Meeting on Reduced Enrichment for Research and Test Reactors, Lisbon, Portugal, October 10-14, 2010.

[2] A.M. Tentner, A. Bergeron, Y.S. Kim, G.L. Hofman, J.G. Stevens, "An Integrated Computational Fluid Dynamics and Fuel Mechanics Model for the Analysis of the E-FUTURE Fuel Irradiation Experiment", Proceedings of the 33rd International Meeting on Reduced Enrichment for Research and Test Reactors, Santiago, Chile, October 23-27, 2011.

[3] A.M. Tentner, A. Bergeron, Y.S. Kim, G.L. Hofman, J.G. Stevens, S. Van den Berghe, V. Kuzminov, "Multi-Physics Simulation of the E-FUTURE-1 Fuel Irradiation Experiment", Proceedings of the 34th International Meeting on Reduced Enrichment for Research and Test Reactors, Warsaw, Poland, October 14-17, 2012.

[4] S. Van den Berghe, Y. Parthoens, F. Charollais, Y. S. Kim, A. Leenaers, E. Koonen, V. Kuzminov, P. Lemoine, C. Jarousse, H. Guyon, D. Wachs, D. Keiser Jr, A. Robinson, J. Stevens and G. Hofman, Journal Of Nuclear Materials 430 (1-3), 2012.

[5] S. Van den Berghe, A. Leenaers and Y. Parthoens in: Proceedings of the International Meeting On Reduced Enrichment For Research And Test Reactors (RERTR), Santiago, Chile, October 2011.

[6] A. Leenaers, J. Van Eyken, S. Van den Berghe, E. Koonen, F. Charollais, P. Lemoine, Y. Calzavara, H. Guyon, C. Jarousse, B. Stepnik, D. Wachs and A. Robinson in: Proceedings of the International Conference on Research Reactor Fuel Management (RRFM), Prague, Czech Republic, October 2012.

[7] Y.S. Kim, G.L Hofman, A.B. Robinson, J.L. Snelgrove, N. Hanan, "Oxidation of aluminum alloy cladding for research and test reactor fuel", J. Nucl. Materials, Vol. 378 (2008) p 220

[8] B. Ye, Y.S. Kim, J. Rest, G. Hofman, “Modeling of U-MO Fuel Swelling to High Burnup”, this conference

[9] D.M. Royster, "Tensile Properties and Creep Strength of three Aluminum Alloys Exposed up to 25,000 hours at 200 F to 400 F", NASA technical Note NASA TN D-5010, Washington, D.C., January 1969

The submitted manuscript has been created by UChicago Argonne, LLC, Operator of Argonne National Laboratory (“Argonne”). Argonne, a U.S. Department of Energy Office of Science laboratory, is operated under Contract No. DE-AC02-06CH11357. The U.S. Government retains for itself, and others acting on its behalf, a paid-up nonexclusive, irrevocable worldwide license in said article to reproduce, prepare derivative works, distribute copies to the public, and perform publicly and display publicly, by or on behalf of the Government. Work supported by US Department of Energy, Office of Global Threat Reduction, National Nuclear Security Administration (NNSA).

MULTI-CHANNEL THERMAL HYDRAULIC ANALYSIS OF PLATE TYPE RESEARCH REACTOR

MOHAMMAD A. ALBATI[1*], OMAR SH. AL-YAHIA[1], SALIH ALKHAFAJI,

Jordan Atomic Energy Commission (JAEC), AMMAN, JORDAN

Daeseong Jo[2]

[2]*Korea Atomic Energy Research Institute, 1045 Daeduk-Daero, Dukjin-Dong, Yuseong-Gu, Daejeon, 305-353, Republic of Korea*

[*]*Corresponding author: mohammed_bate3@yahoo.com*

ABSTRACT

An introduction of the multi-channel systems is introduced. The geometry of the multi-channel systems is described. The basic conditions used in the multi-channel analysis are introduced. The methodology of the multi-channels analysis is explained. An explanation of the different iterations used in the analysis is described. A description of the methodology used in the calculation of the temperature profiles of a multi-plate system is introduced. A multi-channels Thermal hydraulic analysis code is developed using the MATLAB programing software. A verification of the mass and energy conservation equation models and the basic conditions applied to the multi-channel analysis is conducted through the run of multiple test cases. The code is used to calculate the mass flow distribution and the temperature profile radially and axially for the China Advanced Research Reactor (CARR). The code results are validated against the results of (Tian et al., 2005). The developed code is applied to a 5 MW MTR reactor and the results for the mass flow distributions and temperature profiles are validated against the PLTEMP V3.7 code. A conclusion and suggestion for future work is introduced.

Keywords: TMAP, COOLOD-N2, thermal margin, forced convection, natural convection, research reactor

1.0 Introduction

Research reactors are nuclear reactors that are used primarily as a neutron source. These neutrons are utilized for many applications such as neutron transmutation doping (NTD), radioisotope production, material testing, and research and education. Research reactors are used all around the world. There are around 764 research reactors around the world from which 246 are operational, 5 under construction, and 8 planned .Research reactors are simpler than power reactors and operate at lower pressure and temperatures than power reactors. Although the fuel needed in the research reactor is less than power reactor, the uranium enrichment is much higher and in these days is limited to 20 percent enrichment as stated by the U.S. Department of energy in its program that was initiated to develop the means to convert research reactor from the use of highly enriched uranium to the low enriched uranium. This program was then called the Reduced Enrichment Research and Test Reactor (RERTR) project. There are many types of Fuel that are used in research reactors such as MTR type, TRIGA type, VVR, and many others. The most common type of fuel is MTR type. Almost 25% of the operational reactors around the world (65 research reactors) use the MTR type fuel, which constitutes the largest percent of the different fuel types used in research reactors (IAEA, 2009). The thermal power generated in research reactors have a very wide range starting from almost Zero power to the highest power of 250 MW in the ATR reactor in the United States (IAEA, 2009). The research reactor produces neutrons by uranium fission process. Each fission process produces about 200 MeV of energy. Most of This energy is carried out by fission products as kinetic energy and the rest goes as neutron or radiation energy. This energy is transferred to a heat form generated in the fuel and then transferred through cladding to the coolant. In the design process of research reactors, many limitations control the way of design. One of the most important steps in the design of research reactors is to ensure their safety against nuclear and thermal hydraulics margins. The insurance of reactor safety against these limits is very important to prevent any failure in the fuel plate that can lead to a release of radioactive materials into the environment. These limitations are divided into nuclear limitations and thermal limitations. The nuclear limitations includes reactivity control, power density, etc. the thermal limitations includes fuel, cladding, and coolant temperatures, along with many safety limiting parameters such as Onset of Nucleate Boiling (ONB), Onset of Flow Instability (OFI), and Departure from Nucleate Boiling (DNB). In general, computer codes are used to evaluate the thermal hydraulic margins of research reactors, but unfortunately most of the developed and commercialized codes are originally designed for power reactors such as RELAP and RETRAN. Although more recent versions of these codes include modifications capable of simulating the operational conditions of research reactors, the use of these codes requires a lot of effort in the input preparation and program simulation. For this reason, many attempts had been made to develop simpler thermal hydraulics codes to design, license, and evaluate the performance of research reactors under various conditions. For example, JAERI (Japan Atomic Energy Research Institute) developed COOLOD-N2, which was applied to evaluate the steady state thermal hydraulic analyses for JRR-3. In 2011, KAERI (Korea Atomic Energy Research Institute) developed a computer code, TMAP, to evaluate the thermal hydraulic margins of a plate type fuel research reactor. Although there are many computer codes, they cannot be directly applied to a newly designed research reactor owing to the unique features of the research reactor or the different methodology adopted by the regulatory body. Most of these designed thermal hydraulic codes are used for single channel analysis, in which the mass flow rate and heat flux are provided as input parameters. In single channel codes, it is assumed that the heat generated in a fuel plate is distributed equally to the two adjacent channels. This assumption may not be true for the case where different cooling conditions exist on the two sides of the fuel plate. In some cases, the mass flow distribution and the heat distribution between the different types of flow paths in the reactor should be calculated rather than assumed.

Most of these are designed for single channel analysis, in which the mass flow rate and heat flux are provided as input parameters. The following study is conducted to develop a thermal hydraulic code that is capable of calculating the mass flow distribution between different flow paths in parallel with each other and connected to a shared upper and lower plenum. The code is also capable of calculating the coolant, cladding, and fuel temperature profiles radially and axially.

2.0 Geometry model

The geometry of the parallel coolant mass flow paths are shown in Figure II-1. The system is composed of (***np***) number of parallel flow paths that is connected only at the upper and lower plenums. It is assumed that each flow path is composed of different axial regions. Each axial region in a flow path has its own, geometry and properties. There are two main types of flow paths which are:

1. Heated flow paths (Fuel assemblies).
2. Un-heated flow paths (different types of bypasses).

In the heated flow paths there is a parallel fuel plates, and so more calculation efforts are needed to obtain the mass flow distribution in the flow channels parallel to the fuel plates. Figure II-2 shows the geometrical model for single fuel assembly which is considered as single flow path in the system shown in Figure II-1. The fuel assembly is composed of different axial regions. Each region has its own shape and dimensions. Axial Regions are numbered from ***J=1*** to ***J=nr*** including the region between fuel plates. The pressure drop in the fuel assembly is the sum of the pressure drops in each of the axial regions.

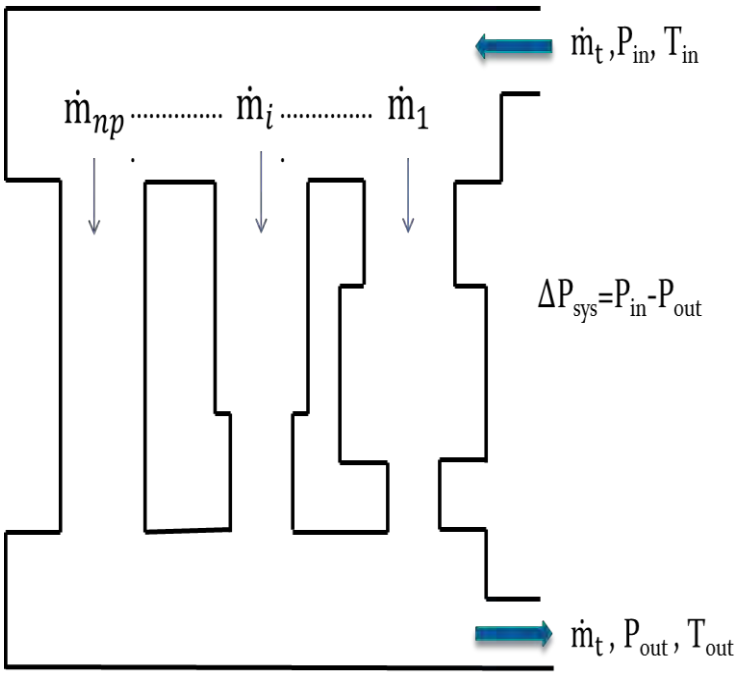


Figure 1: Parallel flow paths system.

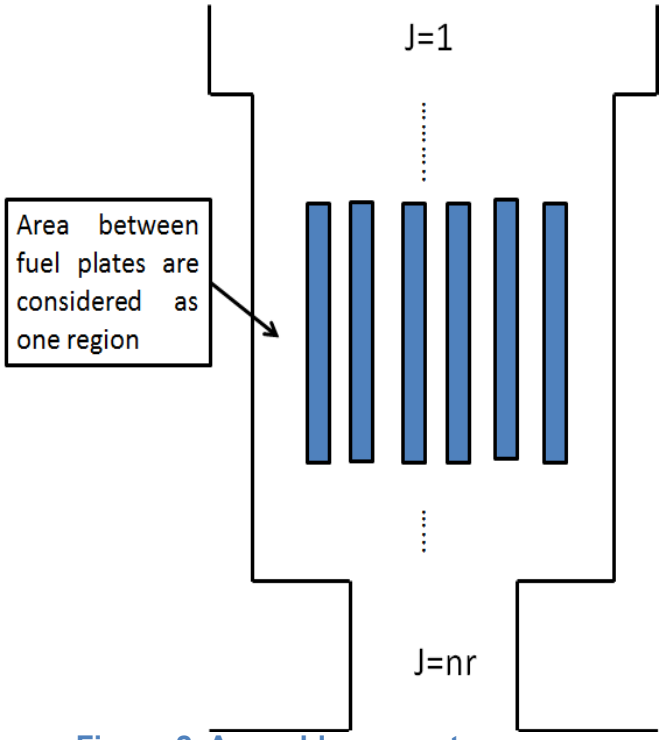


Figure 2: Assembly geometry.

3.0 Governing equations:

In this section, the general governing equations for mass, momentum, and energy are introduced. The assumptions used in the derivation of the final version of these equations are described.

3.1 Mass conservation equation:

The mass conservation equation (continuity equation) is

$$\frac{\partial \rho}{\partial t} + \frac{\partial}{\partial z}(G) = 0$$

Where ρ is the coolant density in kg/m^3, G is the coolant mass flux in $kg/m^2.s$, t is time in s, and z is the axial location in m. Assuming steady state conditions, the equation reduces to

$$\frac{\partial}{\partial z}(G) = 0$$

Integrating along the axial length of the channel and multiply by the constant flow area yields

$$G * A_{flow} = Constant$$

This constant is the mass flow where $G * A_{flow} = \dot{m}$.

3.2 Momentum equation

The momentum equation is

$$\frac{\partial G}{\partial t}+\frac{\partial}{\partial z}\left(\frac{G^2}{\rho}\right)=-\frac{\partial p}{\partial z}-\frac{f\,G\,|G|}{2D_h\rho}-\rho g\cos\theta$$

Where G is the coolant mass flux in *kg/m².s*, t is the time in *s*, z is the axial location in *m*, ρ is the coolant density in *kg/m³*, p is the pressure in *kg/m.s²* (*Pascal*), f is the dimensionless friction factor, D_h is the hydraulic diameter in *m*, g is the gravity acceleration in *m/s²*, θ is the angle from the vertical position ($\theta = 0$) for vertical channels. Assuming steady state condition yields to

$$\frac{\partial}{\partial z}\left(\frac{G^2}{\rho}\right)=-\frac{\partial p}{\partial z}-\frac{f\,G\,|G|}{2D_h\rho}-\rho g\cos\theta$$

Assuming a vertical channel (θ=0) of length L, and integrating yields to the total pressure drop in the channel as

$$\Delta p=\int_0^L \rho g\,dz+\int_0^L\left(\frac{f\,G\,|G|}{2D_h\rho}\right)dz+\sum\left(\frac{K\,G\,|G|}{2\rho}\right)dz+G^2\left(\frac{1}{\rho(L)}-\frac{1}{\rho(0)}\right)$$

3.3 Energy equation

The energy equation used in the analysis is

$$\dot{m}C_p\frac{dT}{dz}=q''*P_h$$

Where $\dot{m}$ is the mass flow rate in *kg/s*, C_p is the specific heat of coolant in *kJ/kg.°C*, T is the temperature in *°C*, *z* is the axial length in *m*, q'' is the heat flux in *kW* ,and P_h is the heated perimeter in *m*.

4.0 Analysis methodology:

4.1 Multi-Channels basic applied condition:

In this section, a description of the two main conditions that should be satisfied in the analyses of Multi-channel systems is described. These two conditions are used in the multi-channel thermal hydraulic codes to obtain the mass flow distribution in the system. The two conditions are:

1. Equal pressure drop in all flow paths.
2. Conservation of the total mass flow rate.

Pressure drop condition

Since the parallel flow paths are connected to the shared upper and lower plenums, they all share the same coolant pressures at the inlet and outlet. This means that all the flow paths shares the same amount of pressure drop given as

$$\Delta P_1=\Delta P_2=\Delta P_3=\ldots..=\Delta P_i=\cdots..=\Delta P_N=P_{in}-P_{out}$$

Where ΔP_i is the total pressure drop through the i-th flow path, P_{in} is the inlet pressure to the system (shared for all flow paths), P_{out} is the outlet pressure to the system (shared for all flow paths).

Conservation of the total mass flow rate

The total mass flow rate is equal to the summation of all the flow rates in the different flow paths. This provides us with

$$\dot{m}_t = \sum_i \dot{m}_i$$

Where $\dot{m}_t$ is the total mass flow rate in the system in *kg/s* and $\dot{m}_i$ is the mass flow rate in the i-th flow path in *kg/s*.

4.2 Calculation methodology:

The calculation methodology of the thermal hydraulic analysis is summarized by the following three main functions:

1. Iteration on pressure drop.
2. Iteration on mass flow (subroutine FLOW).
3. Solution of the multi-plate temperature profile.

Each of the previous main functions is explained separately.

4.2.1 Iteration on pressure drop

In this section the solution procedure to obtain the mass flow distribution is described. The inputs needed for the calculations are the total mass flow rate, the inlet pressure and temperature to the system, the geometry of all the flow paths, and the heat generation in each flow path. The unknowns are:

1. The mass flow rates distribution in the system.
2. Pressure drop through the system.

The known parameters are:

1. Total mass flow rate.
2. Inlet pressure and temperature to the system.
3. Geometry of all flow paths.
4. Heat generation in each fuel plate.

Iteration on the pressure drop in the system is the main body of calculation procedure, and it is the outer iteration of the calculation code.

4.2.2 Iteration mass flow rate (subroutine FLOW)

The subroutine **FLOW** is used to calculate the mass flow in a single flow path for a given pressure drop. The known variables are:

1. Pressure drop in the flow path (from the pressure drop iteration).
2. Geometry of the flow path.
3. Heating condition of the flow path.

The unknown variable is the mass flow rate in the flow path. There are two procedures used in subroutine flow depending on the heating condition of the flow path:

1. Procedure for the un-heated flow path (different types of bypasses).
2. Procedure for the heated flow path (fuel assemblies).

4.2.3 Multi-plate temperature profile solution:

In The single channel thermal hydraulic analysis, it is always assumed that the heat is distributed symmetrically from the fuel plate to the two adjacent channels and that the maximum fuel temperature is located in the middle of fuel plate thickness. This assumption is valid only for the case where exact cooling conditions are applied to the two sides of the fuel plate. In some cases the cooling conditions from the two sides differ from each other. This happens if a different channels thickness and so different mass flow rates exists on both sides of the fuel plate. In this analysis, it is assumed that each channel have different flow area and wetted perimeter and also it is assumed that each fuel plate have different dimensions, thicknesses, and heat generation rates. First, a differentiation of the heat and energy transfer equations is conducted on a system composed of only two plates and 3 channels. Then the solution is extended to a system composed of N plates separated by N+1 Channels. The description of the solution requires a large amount of explanation and derivation so it was dismissed in this paper.

5.0 Results:

The China Advanced Research Reactor (CARR) is located at the china institute of atomic energy. It is multi-purposes research reactor used for neutron scattering measurements, radioisotope production, neutron transmutation doping, etc. the CARR is a tank in pool reactor with nuclear power of 60 MW. Slightly pressurized light water is used as the primary coolant. The top of the reactor core is located 16 m below the surface of the pool. The core is about 0.85 m in height and 0.451 m in diameter. Under the normal operation of CARR, the coolant is pumped to flow through the cold leg, downward through the active core, then through the decay tank, the hot leg, the heat exchanger, and re-circulated to the main pump (Tian et al., 2005).
In 2005, a thermal hydraulic study is conducted on the CARR by (Tian et al., 2005). In the study, the whole reactor core is analysed to find the mass flow distribution in reactor assemblies, and the temperature profile of coolant, cladding, and fuel in each fuel element. In the following sections, the CARR reactor is analysed using the developed Multi-Channel Code. And the results are compared and verified against the results shown by (Tian et al., 2005).

Design parameters of CARR:

The main design parameters of CARR are shown in Table 1. The core is composed of 17 standard fuel assemblies and 4 follower fuel assemblies. Each standard fuel assembly is composed of 20 fuel plates separated by 21 coolant channels. All the standard fuel assemblies have the same geometry. All the fuel plates in the standard fuel assembly have the same shape and geometry. The channels in the assemblies vary in thicknesses and are symmetrical around the centre channel. The channels thickness variations are shown in Figure 3 (Xian et. al) below. As can be seen, there are 5 different channel thicknesses. In the code, the channels are numbered from left to right starting from 1 to 21 as shown in Figure 4. The geometry of fuel plates and coolant channels are summarized in Table 2

Table 5: Main design parameters of CARR.

Design parameters	Input
Core diameter (m)	0.399
Core height (m)	0.85
Elevation of reactor pool water surface (m)	13.2
Core inlet temperature (°C)	35
Core inlet pressure	0.89
Core nuclear power (MW)	60
Core thermal power (MW)	56.4
Mass flow rate in primary loop (kg/s)	600
Number of standard fuel assembly	17
Number of follower fuel assembly	4
Type of fuel elements	Plate

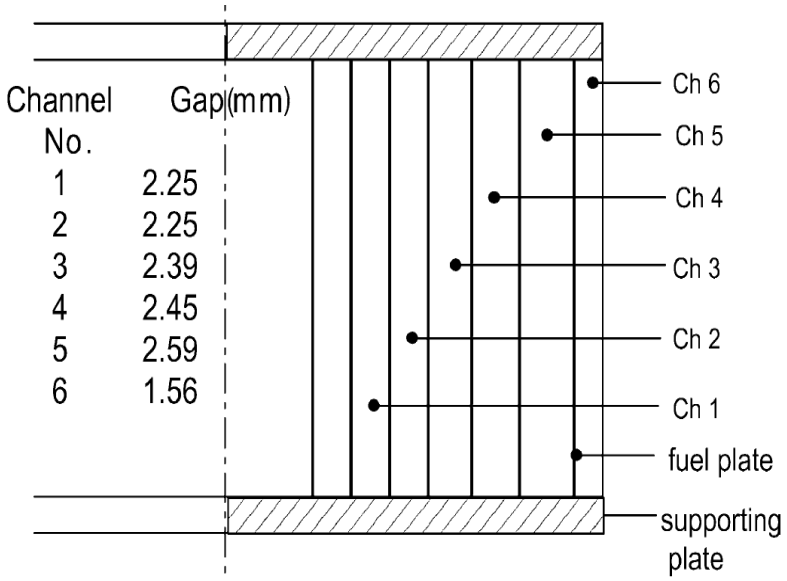


Figure 3: Detailed structure of CARR standard assembly.

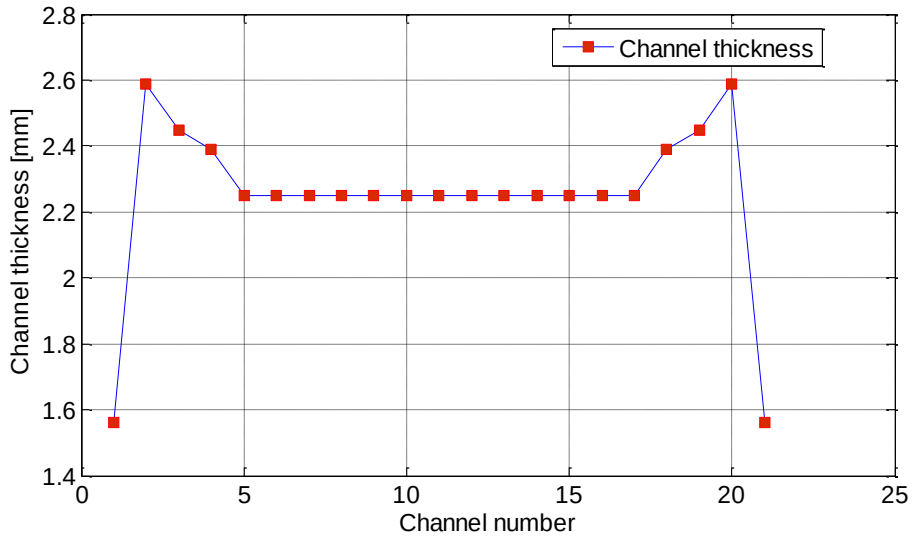


Figure 4: Channels thickness variation of the standard fuel assembly.

Table 2: Fuel plate and coolant channels geometries.

Geometry parameter	Input
Fuel plate	
Fuel thickness[mm]	0.6
Fuel width [mm]	61.6
Fuel length [mm]	850
Cladding thickness [mm]	0.38
Fuel thermal conductivity [W/m.oC]	32
Cladding thermal conductivity	180
Coolant Channel	
Channel width [mm]	71
Channel thickness [mm]	Figure 4
Channel length [mm]	880

The power distribution in the fuel assemblies is represented by the radial power peaking factor distribution that is shown in Figure 5. The power generated in one assembly is assumed to be distributed equally between the different fuel plates in the assembly. The axial length of the active core is divided into 17 control volumes. Each control volume has its axial weighted power factor. The axial weighted power distribution used in the analysis is shown in Figure 6.

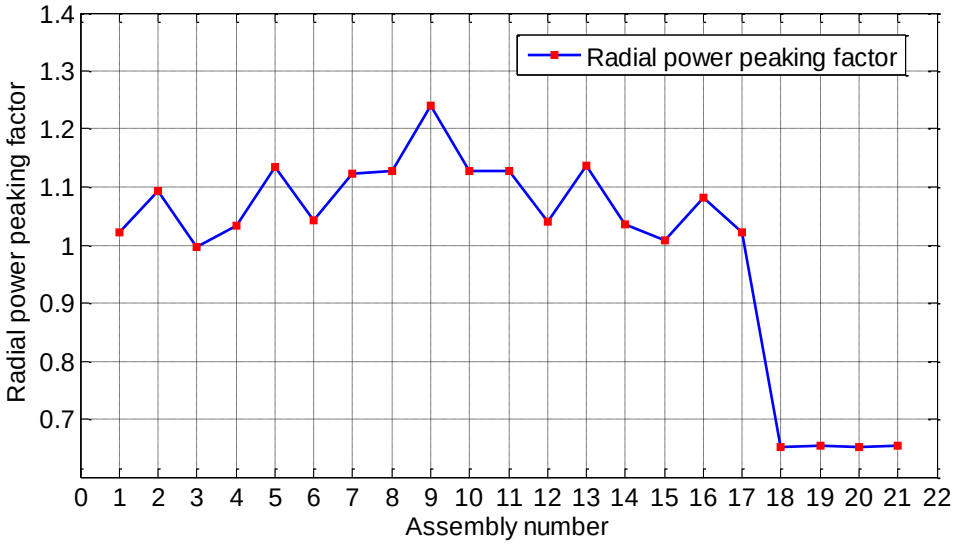


Figure 5: Radial power peaking factor distribution.

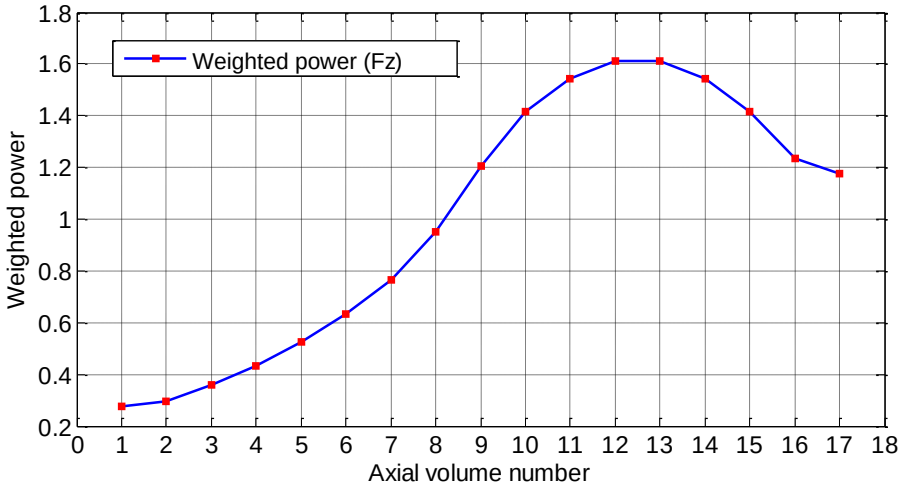


Figure 6: Axial weighted power distribution.

The results of thermal hydraulic analysis of CARR show a good agreement between the developed code and the results published by (Tian et al., 2005). The mass flow distribution in the standard fuel assemblies is shown in Figure 7. The results shows a good agreement with a maximum relative error of 0.3% which could be neglected. As can be seen from Figure 7, the assembly mass flow rates distribution follows the same trend in both results. The assembly with the highest power generation requires more mass flow rate in order to keep the same pressure drop. This phenomenon is studied in detail and the reason is found to be the effect of temperature on the density and viscosity of water. As it is already described the pressure drop is calculated using The Equation below

$$\Delta \mathrm{P}_{friction} = \frac{1}{2}\rho V^2 \frac{fL}{D_h}$$

The friction factor used is calculated as

$$f = 0.316 Re^{-0.25}$$

Where Re is given by

$$Re = \frac{\rho V D}{\mu}$$

And the velocity V is given by

$$V = \frac{\dot{m}}{\rho A}$$

This gives the following equation for pressure drop

$$\Delta P_{friction} = \left(\frac{0.316}{2}\right)\left(\frac{{D_h}^{-1.25} L}{A^{1.75}}\right)\left(\frac{\mu^{0.25}}{\rho}\right)\dot{m}$$

The first and second terms on the right hand side are independent of heat flux, and only the third term in parentheses is to be studied. The change in μ , ρ, and $\frac{\mu^{0.25}}{\rho}$ with temperature is shown in Figures 7, 8, and 9 respectively. As can be seen from Figures 7 to 9, the effect of increasing the heat flux is to decrease the value of ($\mu^{0.25}/\rho$), which in turn decreases the frictional pressure drop and so the total pressure drop.

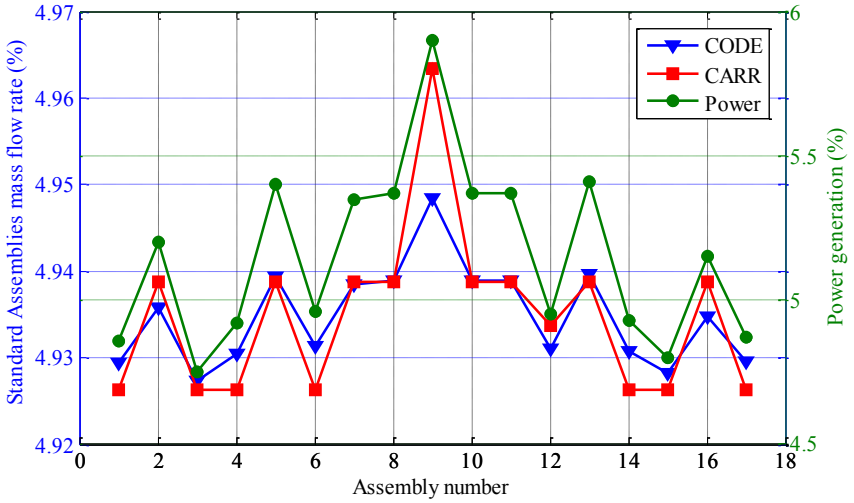


Figure 7: Assemblies Mass flow rate distribution.

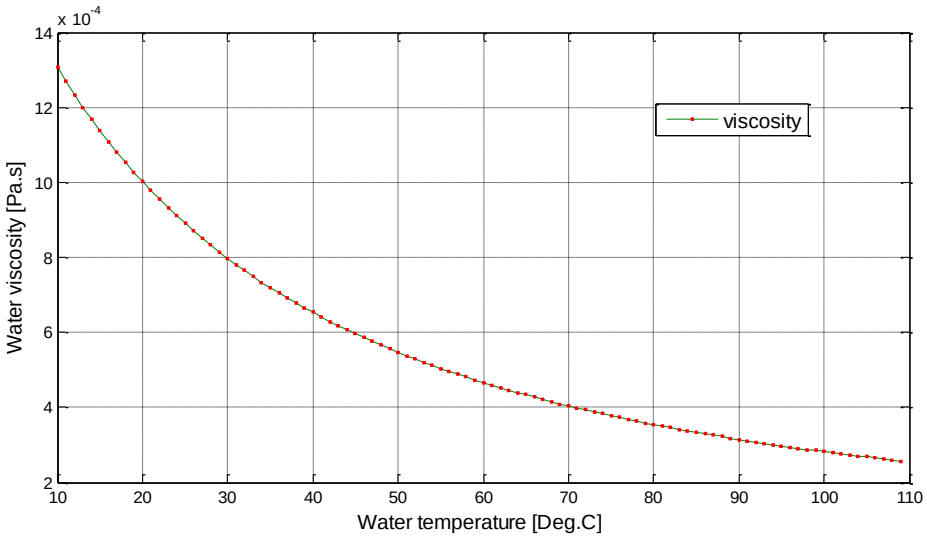


Figure 5-1: The change in water viscosity μ with temperature under a fixed pressure of 0.17 MPa.

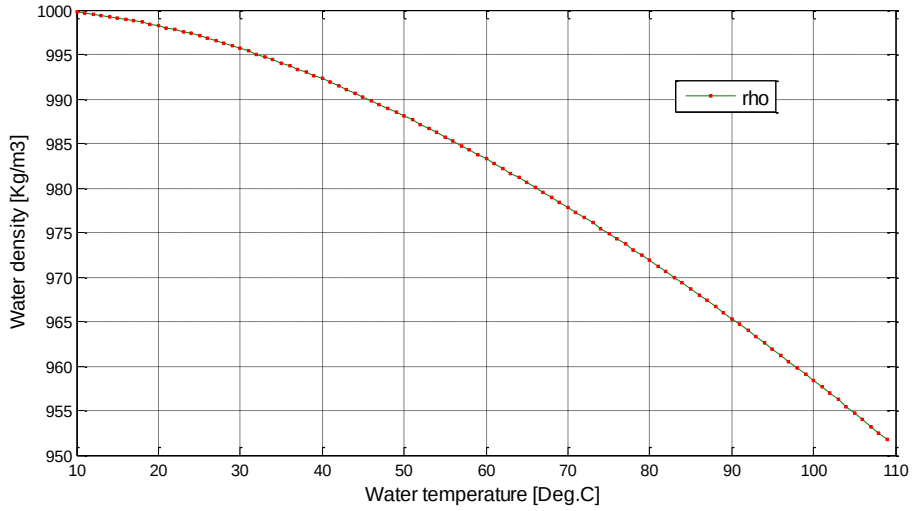


Figure 8: The change in water density $\boldsymbol{\rho}$ with temperature under a fixed pressure of 0.17 MPa.

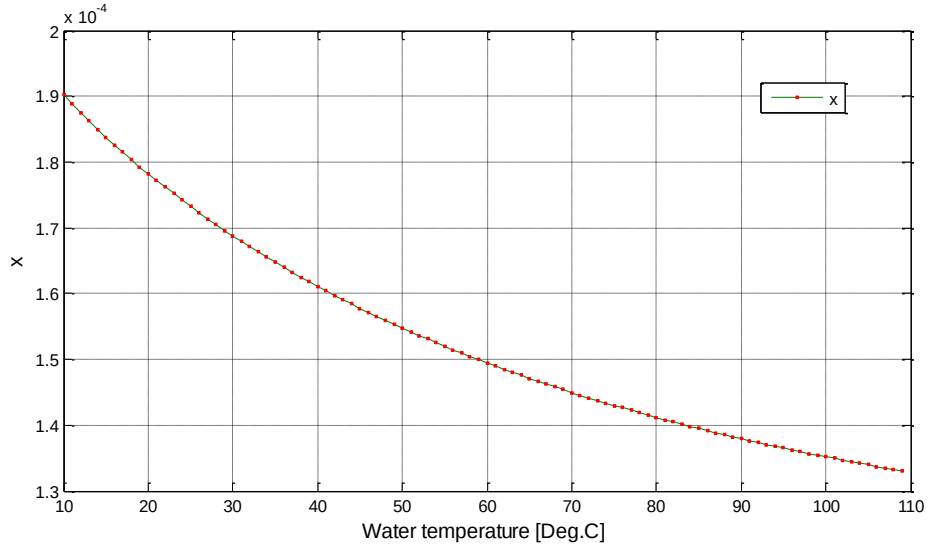


Figure 9: The change in $\boldsymbol{x = \frac{\mu^{0.25}}{\rho}}$ with temperature under a fixed pressure of 0.17 MPa.

The channels mass flow distribution is shown in Figure 10 below. As can be seen, the results show a good agreement. The maximum error in the channels flow rates is calculated to be 3.7%.

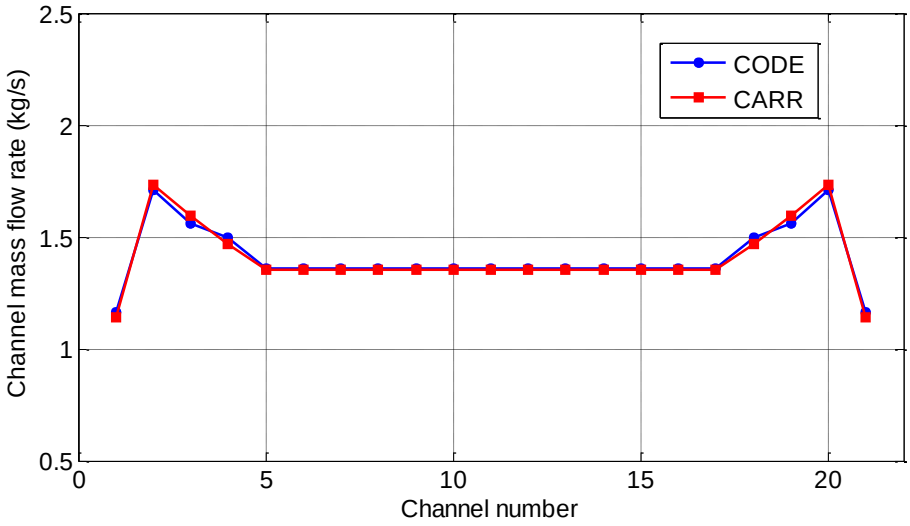


Figure 10: Channels mass flow distribution in the hot assembly (Assembly No.9).

The axial coolant temperature profiles in Channels types numbered from 1 to 6 are shown in Figure 11 below. Figure 12 shows the zoom out view for channels 1 and 2. The coolant channels outlet temperatures for all the 21 channels (numbered 1 to 21 starting from left to right) of the hot assembly in CARR reactor are shown in Figure 13. The maximum difference is 0.7 °C.

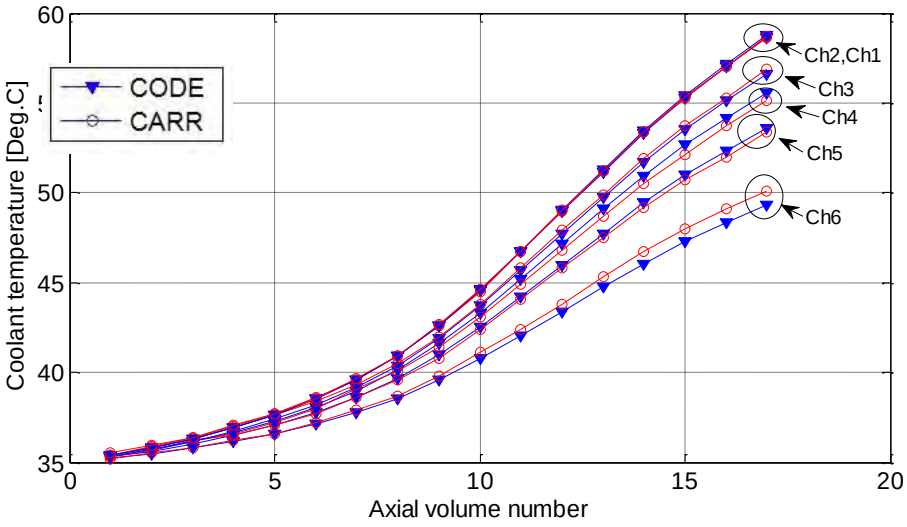


Figure 11: Axial coolant temperature profile along the hot assembly for channels 1 to 6.

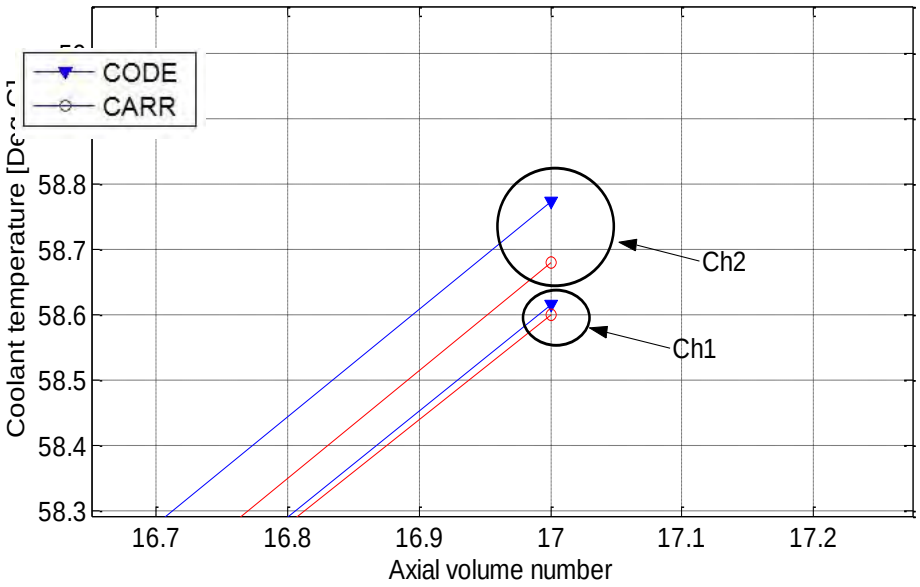


Figure 12: Zoom out of Figure III-11 around channels 1 and 2.

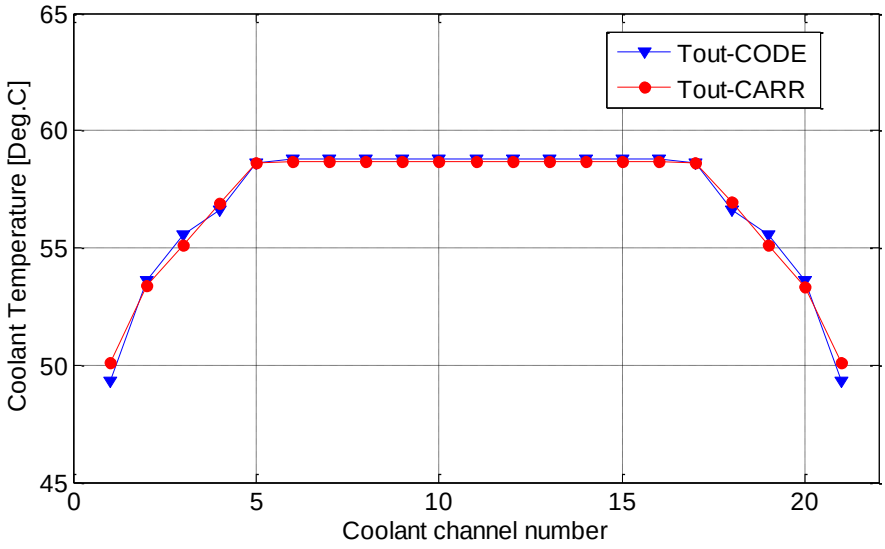


Figure 13: Channels coolant outlet temperatures in the hot assembly in CARR.

As can be seen from Figures 10 to 13, the mass flow rates and coolant temperature shows a very good agreement.



Research Reactor Operations and Maintenance

CORROSION BEHAVIOR FOR CARBON STEEL IN RSG-GAS SECONDARY WATER COOLANT

Geni Rina Sunaryo*, Muhammad Imam Santoso and Anni Rahmat
Center for Nuclear Reactor Saety and Technology (PTKRN-BATAN), Bldg. 80, Puspiptek Area, Serpong, Tangerang, 15310, INDONESIA.
**Email : genirina@batan.go.id*

ABSTRACT

Cupon analyses for carbon steel that has been used for secondary cooling pipes of RSG-GAS was done. The material is designed as series of disc that has been strung vertically and horizontally for understanding homogeny, crevice and galvanic corrosion. The immersing into raw water and cooling tower ponds have been done for four years. Visually and metallography observation toward materials, and periodically water analysis have been done. From the results, it is known that the corrosion for all those three mechanism occurred with different color for both two different water chemistry environment, raw water and secondary cooling water. Reddish corrosion appeared for raw water environment and slightly greyish red for secondary water cooling. Those three corrosion mechanism occurred for carbon steel. The crevice corrosion occurred severely for carbon steel. Galvanic corrosion also can be seen clearly for carbon steel but not for the stainless steel as pair. Homogen corrosion also occurred. For two similar cupons that have been coincided as crevice, shows interesting differences between surface surrounded by free water cooling and surface coincided with similar or different material. More pitting corrosion observed on the material surface contacted freely with secondary cooling water. This mechanism also happened for carbon steel that being strung as galvanic pair with stainless steel.

Keywords : *Carbon steel*, homogeny corrosion, galvanic corrosion, crevice corrosion, visual, metallography

INTRODUCTION

Research Reactor (RR) GA Siwabessy is the biggest RR in Indonesia with a power of 30 MW. It has been operating for about 28 years old. This research reactor is having two cooling systems, primary and secondary. In the purpose to maintaining the primary structure integrity as long as designed life, the demineralized water is being applied as a primary cooling system. However, the raw water coming from PUSPIPTEK the tap water is being used for the secondary system. The treatment applied for the secondary cooling water depositing method, and no further process. Stainless Steel and aluminium are the material used in the primary system, and carbon steel is the most material used for secondary system. Therefore, to suppressing the corrosion rate, the inhibitor is being added in a certain concentration. The anti microbe and anti scaling also are being added to suppress the scaling formation and microbial growth that may induce the microbial induce corrosion. The inhibitor, anti scale and anti microbe solution concentration applied into the secondary water are recommended by the company. However, the actual scientific understanding that backgrounding the recommended concentration has not yet been understood. Therefore, some research activities have been started in the objective related.

In the previous study, the preliminary result from corrosion surveillance for RSG GAS secondary cooling water has been reported. The corrosion tendency has been monitored visually and it has a close relation with the water chemistry management.

In this paper, the following results will be reported after four years exposuring into RSG GAS cooling water system.

METHOLOGY

Carbon steel and stainless steel materil are used for this experiemnts. Those material is being cut as CD model with the hole inside. The cupons have set up into three different series as uniform, crevice and galvanic. Horizontally and vertically series are made. Every couples are immersed into raw water pool and secondary cooling water pool. For four years

The quality of water is analysed through the parameter of pH, conductivity, Sulphate ions, phosphate ions, silica, free Chlor, total chlor, total Fe, Zinc and Calcium. The analyse methods applied are pH-meter, UV-Viss sphetrophotometer and titration.

Cupons are visually observed by using camera and the corrosion products by using XRD and microscopic camera.

RESULTS AND DISCUSSION

The water chemistry allowed numbers for raw water and secondary cooling water of RSG GAS research reactor is shown in Table 1. The periodically analyses numbers are on that range.

Table 1. The water chemistry quality allowed numbers for raw water and secondary cooling water of RSG-GAS.

Parameter	*Raw water*	*Cooling tower*
Ca as CaCO3 (ppm)	34	280
Cl- (ppm)	7.1	177.5
Total Hardness (ppm)	40	480
Silica (ppm)		
SO_4^{2-} (ppm)	67.8	320
Zn^{2-} (ppm)		> 0.3
Fe total (ppm)	1	1
Conductivity (S/cm)	150	maks 1500
pH	7 - 7.5	6.5 - 8

The conductivity for secondary cooling water is very high due to the chemicals added into the water for preventing scale, corrosion and bacteri growing. The fluctuation range for that conductivity is very severe, and it has att

The cupons that have been immersed into raw water and secondary cooling water are shown in Figure 1.



Figure 1. Coupons for four years immersing into raw water and secondary cooling tower.

The cupons that has been immersed into the raw water gives very orange deposites that covering whole the cupons surface, especially for crbon steel. The cupons that has been immersed into the secondary coolong water show less orange deposites. It can be understood that the water chemistry give a significant effect on corrosion process. The raw water environment shows a worse corrosion effect than the treated secondary cooling water that has been added by chemicals for suppressing corrosion, bacteria and scaling process (right one).

The visually image for the uniform corrosion for both horizontally and vertically position of coupons after being immersed into the raw water are shown in Figure 2.

	Horizontally	Vertically
raw water		
secondary cooling water		

Figure 2. The cupon's surface from uniform corrosion horizontally and vertically position's immersing under raw water and secondary cooling water.

It is clear that the raw water gives lot of orange deposites which is coming from the corrosion products. There is no significant different on the image of corrosion products between horizontally and vertically positions. Compare with this raw water immersing results, the cupons that have been immersed into secondary cooling water gives less numbers of orange deposites. The crevice inner surface is shown in Figure 3.



Figure 3. The crevice inner surface from carbon steel and carbon steel.

The galvanic corrosion between carbon steel and aluminum magnesium under raw water is shown in Figure 4.



Figure 4. The galvanic corrosion between carbon steel (left) and stainless steel.

The galvanic corrosion occurs on the carbon steel material and almost nothing on the stailess steel surfave. The orange color appear on the stainless steel surface is only deposites which is coming from the corrosion products from carbon steel. By wrapping it with paper tissue has cleanedthe surface of the stainless steel surface.

CONCLUSION

It can be concluded that the water chemistry hold as a main role that initiate the corrosion process. Different water chemistry will give a different products that can be distinguished easily by the change of color.

From the XRD analyses, it is known that the $FeCl_3$, Fe_3O_4, $Fe_2(SO_4)_3$, Fe_2O_3, $FeSO_4$, $FeCl_2$, FeS, $Fe(OH)_3$, and FeO compounds are formed. The corrosion mechanism happened in this experiments based on the continuously process between corosion products with the following and available corrosive ion exist in the water. The macro structure changes on the surface makes an intergranular profile on its micro structure because of the corrosion that caused by the weak potential on the crystal edge.

REFFERENCES

[1] “Secondary Cooling Water Quality Management for Multi Purpose Reactor 30MW GA Siwabessy Indonesia”, RRFM-Rome, 2011.

[2] ”Analisis Kandungan Mikroba di Pendingin Sekunder RSG-GAS 30MW”, Prosiding seminar PTAPB, Yogyakarta, 2011.

[3] Aplikasi Program *Corrosion Surveillance* untuk kolam penyimpan reaktor RSG-GAS, TKPFN-seminar, Surabaya 2010.

[4] GENI RINA SUNARYO. SRIYONO. DIYAH ERLIANA, International Conference on Research Reactors: Safe Management and Effective Utilization, Sydney, Australia, 5-9 November 2007, “Water Chemistry Surveillance for Multi Purpose Reactor 30 MW GA Siwabessy, Indonesia”.

[5] “Pengaruh senyawa antimikroba terhadap Laju Korosi Pipa Baja Karbon”, skripsi S1, Herry Sander Pranoto, STTN, 2011.

[6] Karliana, Itjeu dan Sunaryo, GR. 2008. ”Karakterisasi Mikroba dalam Air Pendingin Sekunder RSG-GAS”. Serpong : PTRKN-BATAN.

COMPARISON OF MEASURED AND CALCULATED INTEGRAL AND DIFFERENTIAL REACTIVITY WORTH OF CONTROL RODS IN A TRIGA REACTOR

VID MERLJAK, IGOR LENGAR, ANDREJ TRKOV
Reactor physics department, "Jožef Stefan" Institute
Jamova cesta 39, 1000 Ljubljana - Slovenia

ABSTRACT

At the TRIGA Mark II research reactor of the "Jožef Stefan" Institute the chain reaction is controlled by four control rods. Their integral and differential reactivity worth curves are commonly measured by the rod-swap and the rod-insertion methods. A comparison of the experimentally measured values with those obtained from numerical simulation by the Monte Carlo method is performed with differences analysed and uncertainties estimated. It was found that the simulation of the rod-swap method gives qualitatively and quantitatively adequate results, while the simulation of the rod-insertion method is less accurate. The deviation between the experiment and simulation for the latter method is found to be due to simplifications in the computational method used. Special care was devoted to the determination of the error in the current computational model of the reactor since experimental measurements revealed insufficient knowledge of the reactor's control system.

1. Introduction

Knowledge of the integral and differential control rod worth is essential to ensure safe nuclear reactor operation. Numerical methods and computational codes are nowadays indispensable tools in reactor engineering. Since the latter are validated against extensive set of existing benchmark experiments, much is left dependent on the quality of the numerical model used. Comparison of calculated data to physical experiment is thus needed.

1.1. Brief description of the reactor

"Jožef Stefan" Institute's (JSI) TRIGA Mark II reactor is a 250 kW pool-type research reactor capable of operation in both normal and pulse mode. Its core holds 91 main positions for fuel elements, control rods, irradiation channels, neutron source etc. arranged into six concentrical rings (Figure 1). Reactivity is controlled using four control rods, three of them – namely Safety (S), Shim (C) and Regulating (R) – being of the fuel-follower type, and the Transient (T) rod being of the air-follower type.

1.2. Inverse point kinetics equation and DMR

Time evolution of the neutron population and the delayed neutron precursors' concentrations in a sizeable nuclear reactor is adequately described by the point kinetics equations, especially in the asymptotic regime. In reverse, reactivity can be calculated by solving the inverse kinetics equation

$$\rho(t) = \frac{\Lambda}{T(t)}\frac{dT}{dt} + \sum_{i=1}^{I}\left[\frac{\beta_i}{T(t)}e^{-\lambda_i t}\int_0^t \frac{dT}{dt'}e^{\lambda_i t'}dt'\right] - \Lambda\frac{Q(t)}{T(t)} \qquad (1)$$

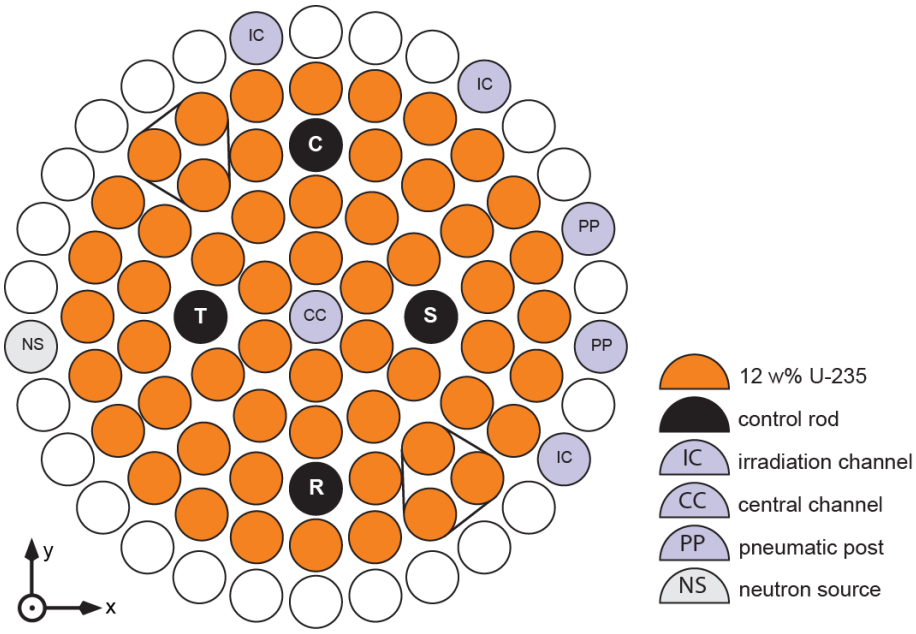


Figure 1: Reactor core configuration during measurements. Labels T, S, R and C stand for Transient, Safety, Regulating and Shim control rod respectively. Blank (i.e. empty) positions are filled with water.

where $T(t)$ is the neutron amplitude function, β_i and λ_i are the delayed neutron fraction and decay constant, respectively, for i-th group of precursors, $Q(t)$ is the neutron source strength and Λ is the (prompt) neutron lifetime. Following this equation the reactivity values were obtained using JSI's own developed Digital Reactivity Meter (DMR) system DMR-043 [1] for measurements with both the rod-insertion and rod-swap method.

1.3. The rod-insertion method

The rod-insertion method's [2, 3] great advantages are speed and its simplicity to perform. Following this method of control rod worth measurement one has just to insert the control rod continuously into the reactor core and measure the neutron flux (e.g. from an ionisation cell). No reactivity compensation is needed as the method relies heavily on the DMR's ability to satisfactorily account for the source term Q. Integral and differential rod worth are then calculated off-line from the stored neutron flux signal and corrected for background noise [4].

It should be noted, that during a continuous insertion of a control rod, the spatial distributions of prompt and of delayed neutrons change with time in a manner where the latter distribution is somewhat trailing behind the former. This is due to the finite decay rates of the delayed neutron precursor concentrations. As the inverse kinetics equation (Eq. 1) originates from the *point* kinetic representation of the reactor, this effect is currently measured but unaccounted for (an additional correction factor could be devised).

2. Measurements and calculation

The experimental values were obtained in June 2013 using two different measuring methods – the rod-swap method and the rod-insertion method. The integral and differential worth curves were obtained for the regulating and shim rod (rod-swap) and for all four control rods (rod-insertion). The course of actions during the rod-swap method was slightly altered in a manner that as far as it was possible there were only the measured and reference control rods present in the reactor core. Figure 2 provides a comprehensive explanation of this change in the normal procedure. In each position of the control rods, reactor core configuration was kept still and value of the reactivity was read when the asymptotic regime was established.

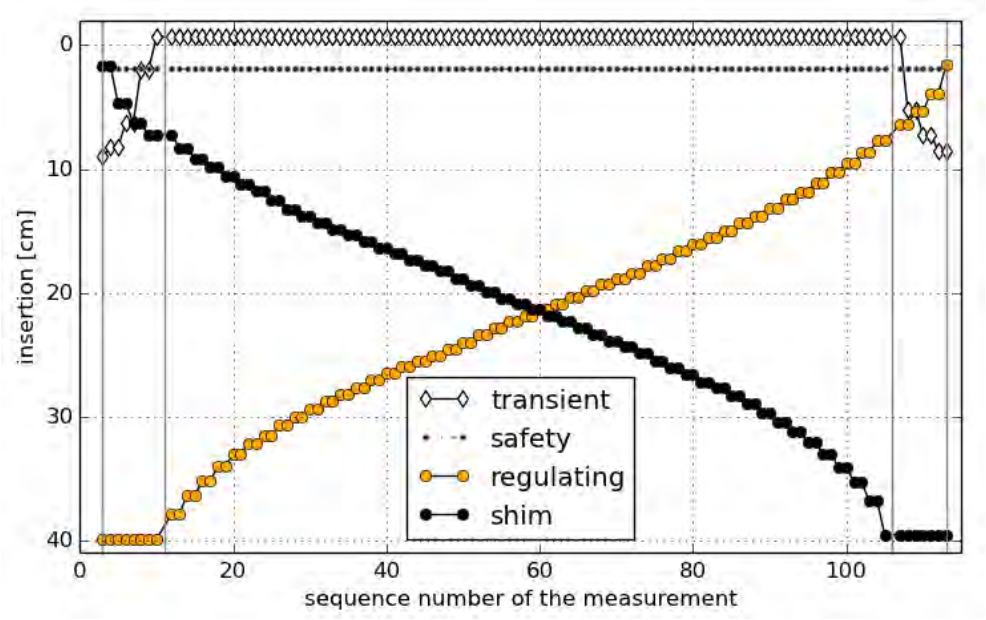


Figure 2: Insertion depths of control rods during the rod-swap method. When the position is not changing for more than 3 measurements, the rod is in its extreme position (rods have different initial and final insertion depths). The x-axis is in the measurement-number "scale", rather than in time scale.

Calculations of k_{eff} were performed using Monte Carlo code *MCNP5 1.40* [5] and for it an existing numerical model of the reactor was used. Simulation of the rod-swap method is straightforward: the control rod positions in the model simply have to match the experimental setup. This was done so to the best of our knowledge (see subsection 2.1). Simulation of the rod-insertion method suffers from the fact that *MCNP5 1.40* cannot simulate time dependent geometry. This is equivalent to say that the delayed neutron decay constants, λ_i, are all set to zero. Consequently for the rod-insertion method a proper comparison of the measured and calculated values cannot be made. Nevertheless, a qualitative comparison is informative. The values of k_{eff} were hence calculated only for 36 equidistant insertion depths.

2.1. Additional measurements

Preliminary results showed a significant discrepancy while comparing the measured and calculated values for the transient rod. The measurements using the rod-insertion method indicated that its integral reactivity worth is negligible for up to nearly 10 per cent of full insertion length. This led to a hypothesis that transient rod starts few centimetres above the core and so that inside each pair of points compared the measured and calculated values actually corresponded to non-equal insertion depths. Thus a reassessment of reactor core geometry was needed.

One could assume that during the construction of the reactor care was taken to adjust control rod positions and length of their travel, so that the fuel-follower and neutron absorber would align with the active core in fully withdrawn and in fully inserted state respectively. We now measured the characteristic initial insertion and total length of travel for all control rods. Not only have we proven that the starting position of the transient rod lies high above the active core, the initial positions of all other rods had to be corrected too. The total length of travel for the transient rod was found to be more than 3.5 cm longer than previously assumed!

As shown in Figure 3, the fuel-follower/absorber does not align with the active core neither in fully withdrawn (case "a") nor in fully inserted state (case "b"). This, of course, does not (!) pose a threat to safe reactor operation as criticality can be re-established by simple adjustment of control rods. For accurate simulations however knowledge of control rod positioning is crucial.

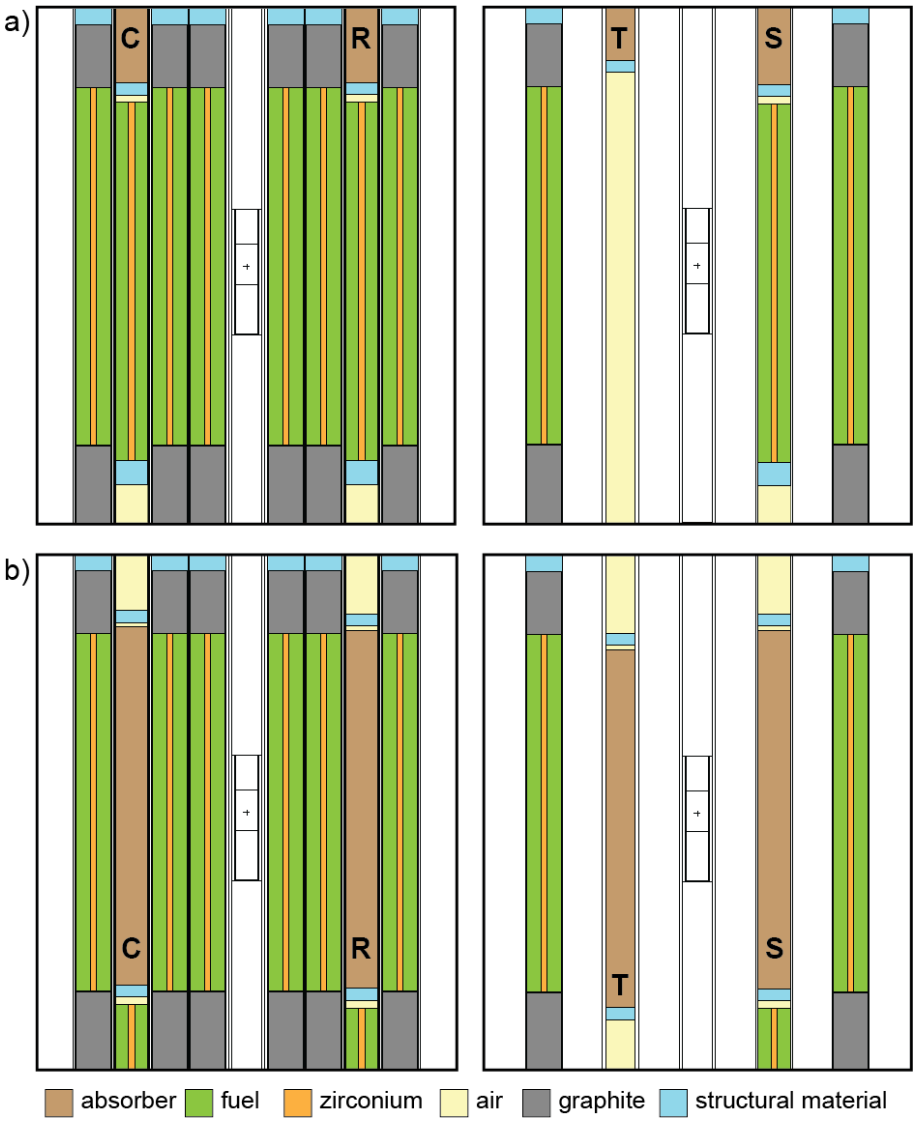


Figure 3: a) Initial and **b)** final insertion depths of all four control rods relative to the active core. The yz (on the left) and xz (right) plane of the numerical model are represented.

The new values for initial and final insertion depth meant that integral and differential curves had to be updated, i.e. curve shrinking/stretching due to total length of travel, horizontal displacement due to initial insertion and vertical displacement to ensure that the integral worth curve starts at $0\ pcm$ (see also Figure 7).

3. Results and discussion

Results are presented in Figures 4 - 7, where low position values ('step' or 'cm' inserted) mean almost extracted control rod, and vice versa. Integral worth is herein presented as an absolute value of negative reactivity available for insertion with the control rod from fully withdrawn state to the chosen position. The uncertainties plotted include only uncertainties of/and related to position and reactivity (i.e. exclude contributions of temperature gradients, numerical model geometry simplifications etc.).

Calculated and measured integral curves show very good agreement for the rod-swap method, but progressive underestimation towards full insertion for the rod-insertion method. Around the middle of the core height the simulation of the rod-swap method (blue) yields higher values than measurements (red), and slightly lower values at the end of the travel. The former can be

explained by the fact, that numerical model uses axially homogenised fuel regions and even assumes fresh fuel in fuel-follower control rods. In reality, the fuel has a cosine-shaped burnup and has burnt a little further than the modelled one. In simulation the control rods are thus inserted into higher neutron flux than in reality, yielding higher reactivity worth.

Let the total reactivity worth of a certain control rod (e.g. rod "Y") be labelled as W_Y and the relative difference between the measured and calculated values of W_Y as ΔW_Y. Table 1 then gives ΔW_Y for all observed cases. Simulation of the rod-swap method is adequate, while this (with an exception for the S rod) cannot be said for the simulation of the rod-insertion method.

ΔW_Y [a]	R	C	T	S
rod-swap	-1.85 %	-1.09 %	/ [b]	/ [b]
rod-insertion	-11.0 %	-10.3 %	-7.6 %	-0.4 %

(a) For control rod Y it holds $\Delta W_Y = (calculated - measured)/measured$.
(b) Rod-swap was not performed for control rods T and S.

Table 1: Relative difference between calculated and measured total control rod reactivity worth $\boldsymbol{W_Y}$.

Since the measured value of W_Y for the rod-swap method is numerically reproduced with only 1.85 % underestimation, the areas under the differential curves in Figure 5 are comparable. We see that the differential worth curve for calculation (blue) is uniformly shifted toward lower positions in regard to measurements (red). This again is a consequence of the axial homogeneity of the modelled fuel. The differential worth uncertainties are considerable (especially since the regulating (R) rod has only the smallest axial position uncertainty of all control rods), but could be reduced if fewer measurements along z-axis were made. The emphasis was on frequent sampling of integral worth though.

In Figure 6 an absolute difference between measured and calculated integral worth curves for rod-swap method is given point by point, and referred to as the "mismatch". Uncertainty of these integral worths, and hence of the "mismatch", is normally a monotone rising function of insertion depth (as governed by the rod-swap sequence), but is here overridden by the contribution of linear interpolation needed after the true insertion depths were determined. Note that the mismatch uncertainty does not exceed $35\ pcm$, as the Monte Carlo simulations were run long enough to reduce the statistical error of k_{eff} for each single core configuration down to $\pm 2\ pcm$. This on the other side results in lowering the percentage match of the integral worth curves as given by Table 2. The first point of integral curve is left out of this statistics because it is zero by definition.

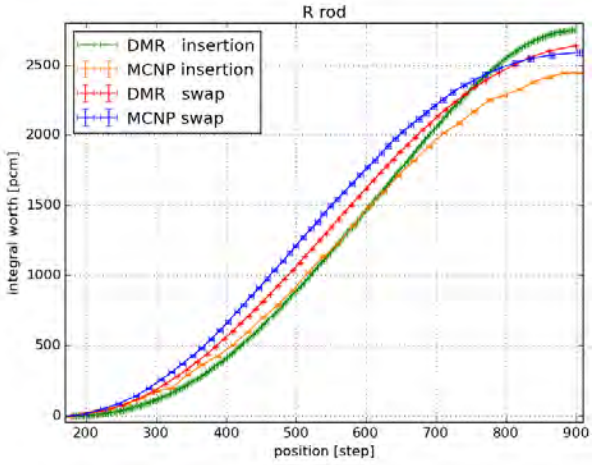


Figure 4: Integral worth curve for R rod. The calculated values for the rod-insertion method progressively underestimate the measured ones.

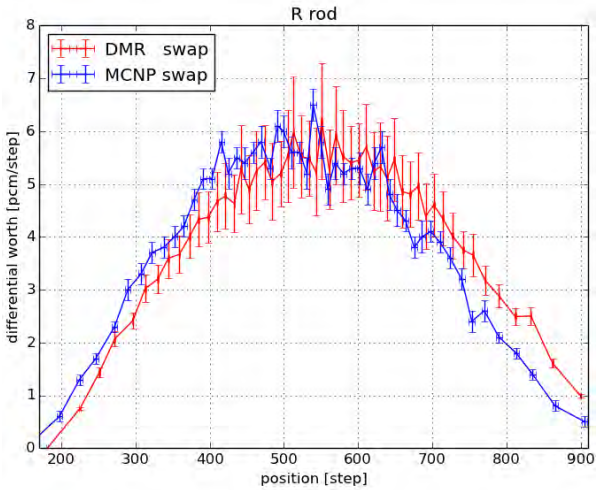


Figure 5: Differential worth curve for R rod and the rod-swap method.

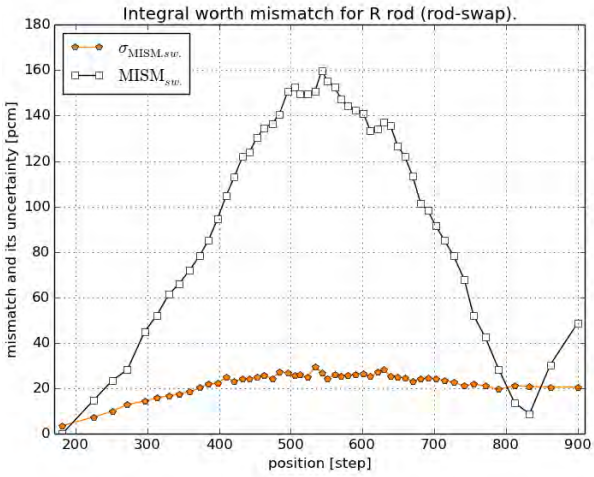


Figure 6: Absolute difference between measured and calculated integral – "mismatch" (for R rod and the rod-swap method). In a statistical sense the calculation is considered to reasonably agree with measurements when mismatch falls under its $\mathbf{1}\boldsymbol{\sigma}$ uncertainty.

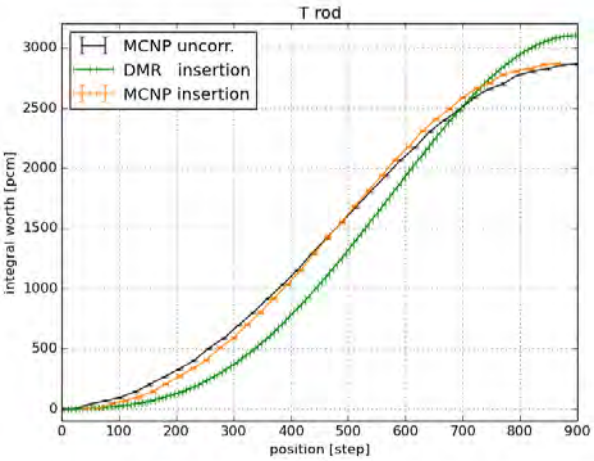


Figure 7: Integral worth curve for T rod. Curve uncorrected for initial insertion depth and total travel length is also plotted.

percentage match	R	C
$1\,\sigma$	3.9 %	10.0 %
$2\,\sigma$	7.8 %	84.0 %

Table 2: Percentage match for the integral curves following the rod-swap method.

Lastly the calculated integral worth of the transient (T) rod is compared to the values measured by the rod-insertion method (Figure 7). As a reference, calculated curve with uncorrected insertion depths is also plotted (black line). The correction of initial and final insertion depths yields some improvement, but the calculated curve still differ significantly from the measured one. It is suggested that some other source of error remains unaccounted for. It could be possible that the inner axial position of the transient rod absorber material relative to the cladding is inconsistent with blueprints available (e.g. in Ref. [6]). A neutron radiograph image of the transient rod is proposed.

Extensive report on the work done can also be found in Ref. [7].

4. Conclusion

In general, the results show that rod-swap method can be simulated adequately, while simulations of rod-insertion method can be used only as a quick reference. This difference is mainly due to insufficient physics model of the simulation code, which (with the version of code used) does not allow the delayed neutrons to have different spatial distribution than that of the prompt neutrons.

An important side-products of the comparison described in this paper are findings of inconsistency regarding the transient rod integral worth. This led to additional measurements and ultimately to corrections in numerical model of the reactor. It can be thus seen, that periodical comparison of calculations to actual experimental data could improve research efficiency.

5. References

[1] A. Trkov, “Digital Reactivity Meter DMR-043, Part A - Theory and Methods,” IJS-DP-5238, "Jožef Stefan" Institute, 2004.

[2] B. Glumac and G. Škraba, “Rod Insertion Method for Rod Worth Measurement,” in *IAEA Technical Committee Meeting on Operational Safety Experience of Two-loop Pressurized Water Reactors*, Bled, May 30 - June 3 1988, IAEA-650 (1989), pp. 280–297.

[3] A. Trkov, M. Ravnik, H. Wimmer, B. Glumac and H. Böck, “Application of the rod-insertion method for control rod worth measurements in research reactors,” *Kerntechnik,* vol. 60, pp. 255-261, 1995.

[4] I. Lengar, A. Trkov, M. Kromar and L. Snoj, “Digital meter of reactivity for use during zero-power physics tests at the Krško NPP (Uporaba digitalnega merilnika reaktivnosti pri zagonskih testih na ničelni moči v NE Krško),” *Journal Of Energy Technology - JET,* vol. 5, pp. 13-26, 2012.

[5] X-5 Monte Carlo Team, “MCNP — A General Monte Carlo N-Particle Transport Code, Version 5, LA-UR-03-1987,” Los Alamos National Laboratory, 2003.

[6] R. Jeraj and M. Ravnik, “TRIGA Mark II reactor: U(20) - Zirconium Hydride fuel rods in water with graphite reflector, IEU-COMP-THERM-003,” *NEA/NSC/DOC(95)03,* 1999.

[7] V. Merljak, “Primerjava merjenih in izračunanih integralnih in diferencialnih vrednosti reaktivnosti kontrolnih palic v reaktorji TRIGA (Comparison of measured and calculated integral and differential reactivity worth of control rods in a TRIGA reactor),” University of Ljubljana, Faculty of Mathematics and Physics, 2013.

RESEARCH ACTIVITIES IN BATAN FOR THE BURNUP MEASUREMENT OF SILICIDE FUEL

T.M. SEMBIRING
Centre for Nuclear Reactor Technology and Safety, National Nuclear Energy Agency (BATAN)
Kawasan PUSPIPTEK Gd. No. 80, Serpong, Tangerang Selatan 15310 - Indonesia

ABSTRACT

The research activities in BATAN for fuel burn-up measurement have been carried out in the Center for Multipurpose Reactor (CMR) and the Center for Nuclear Fuel Technology (CNFT). The activities are very important for establishing the technology to fabricate silicide fuel for the core conversion program in the RSG-GAS reactor. The irradiation of silicide fuel elements (MTR plate type) and the development of in-core fuel management code were carried out in the CMR. However, the experimental burn-up of the irradiated silicide fuel was carried out in the CNFT. The first activity is the development of the in-core fuel management code. The code is based on the few-group neutron diffusion method. The second activity is the irradiation of the silicide fuel element for several cycles to get a burn-up level of approximately 50% loss of U235. The irradiation has been carried out in the oxide cores. Among 21 plates, two plates, center and outer part, were dismantled in the hot cell. The third activity is the burn-up measurement based on the nondestructive method. The plates were gamma scanned, independently, using a gamma-ray spectroscopy. The Cs-134/Cs-137 activity ratio was selected and measured to obtain the axial distribution of relative burn-up. Finally the calculation results were compared with the experimental results. An excellent agreement between the calculated and measured values of the activity ratio was confirmed.

1. Introduction

Core conversion program in RSG-GAS reactor was started from oxcide (U_3O_8-Al) to silicide (U_3Si_2-Al) fuel with higher uranium density. For the core conversion, BATAN decided that the silicide fuels supplied to the RSG-GAS reactor were all in-house manufactured. The core conversion was started using the same uranium density of oxide fuel with 2.96 gU/cc. Since the fuel fabrication in BATAN was no license for manufacturing the silicide fuel so some research activities were carried out, such as cold test, hot test (irradiation) and post irradiation examination (PIE), for two full scale of silicide fuel elements with uranium density of 2.96 gU/cc.

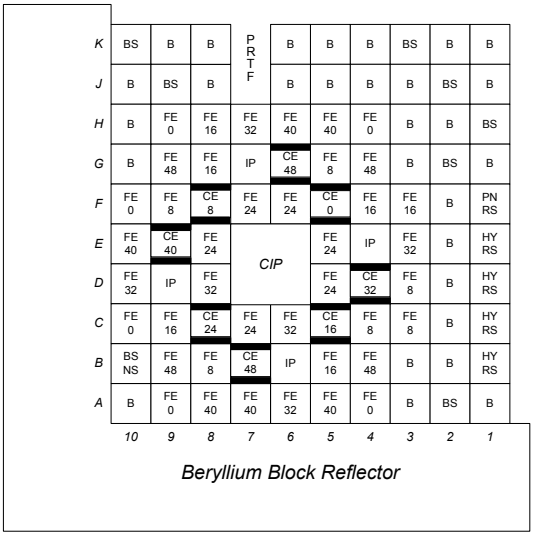
Since the target of RSG-GAS core conversion is to use the higher uranium density of silicide fuel, so the in-core fuel management code has to be developed [1]. It is decided that the code is developed based on the multi-group neutron diffusion method with 2-dimension X-Y geometry model. This paper showed the research activities related to the irradiation program, burn-up measurement using non-destructive method and the development of the in-core fuel management code for RSG-GAS reactor. The accuracy of the code is also described.

2. Fuel irradiation history

The silicide fuel elements, RISIE-1 and RISIE-2, were irradiated in the several core cycles as shown in Table 1. The fuel elements were expected to reach a burn-up level of approximately 50% (loss of ^{235}U). Fig 1 shows the core configuration of RSG-GAS reactor. The fuel elements stayed in the core for 924 days with the total shutdown of 278 days.

Core	Core Grid Position		MWD
	RISIE-1	RISIE-2	
IV	A-6	D-3	572.8
V	A-6	D-3	688.7
VI	B-5	C-4	726.4
VII	F-7	E-5	755.6
VIII	H-7	A-6	672.5
IX	H-6	E-10	782.2

Tab 1: The irradiation history of the silicide fuels



Note: BE = Beryllium Element;BS = Beryllium Element with plug;CIP/IP = Irradiation Position; PNRS/HYRS = Pneumatic/ Hydraulic Rabbit System;

Fig 1: Equilibrium core configuration of RSG-GAS reactor with burn-up (% of ^{235}U loss) in the second rows [2]

3. Burn-up Measurements

The burn-up of silicide fuel of RISIE-2 was measured by the gamma-ray spectroscopy measurements [3]. Two plates among 21 plates were selected to determine the burn-up, plate number 12 and number 20. The HPGe detector was used to measure the axial gamma-ray profiles. The counting time of 1800 s and the gamma energy peaks of 605 keV and 662 keV for Cs-134 and Cs-137, respectively, were chosen to obtain the gamma energy spectra for positions [3]. The activity ratio of Cs-134 and Cs-137 were used for the burn-up analysis. Fig 2 shows the hot cell facility where used for the gamma-ray spectroscopy experiments.



Fig 2: The hot cell facility [3]

4. Burn-up analysis

The burn-up analysis is carried out by using the 2-dimensional in-core fuel management code based on the multi-group neutron diffusion code. The in-core fuel management code, Batan-FUEL, has been developed for establishing the new equilibrium core of RSG-GAS multipurpose reactor using silicide fuel with higher fuel loading [4]. Currently the code is used for the routine in-core management of RSG-GAS reactor. The Batan-FUEL code has also several unique features such as the capability to search automatically an equilibrium core without performing lengthy and time consuming transient cores.

Based on the irradiation data, such as irradiation time, core grid position and the calculated radial power peaking factor, the depletion analysis is carried out by using the SRAC2006 code system based on the JENDL-3.3 nuclear data library [5]. The code was chosen since the depletion analysis has Cs-134 and Cs-137 nuclides then the calculation activity ratio can be compared with the experimental results.

Table 2 shows the burn-up verification results between calculation and experimental results. The calculation Cs134/Cs-137 activity ratio is 6.1% and 1.6% higher compared with the experimental results for plate number 12 and 20, respectively. As known, the calculation result is the average burn-up and the experimental results were obtained by averaging the axial activity ratio with 4^{th} polynomial fitting. Table 2 also shows that the calculation burn-up using Batan-FUEL code is 0.6% lower compared with the SRAC2006 result.

Parameters	Calculation (C)		Experimental (E)	
	SRAC2006	Batan-FUEL	Plate number 12	Plate number 20
Average burn-up (% loss ^{235}U)	50.60	50.31	-	-
Average Cs-134/Cs-137 activity ratio	0.502	-	0.473	0.494
C/E for average Cs-134/Cs-137 activity ratio	-	-	1.06	1.02

Tab 2: The comparison of calculation and experimental result for average burn-up

5. Conclusions

The developed in-core fuel management code, Batan-FUEL, gives a very good agreement with the SRAC2006 code system result in the calculation of average burn-up with the difference of 0.6%. Since the SRAC2006 code system gives a good agreement with the experimental results, so the Batan-FUEL code can be used as the in-core fuel management code for the RSG-GAS, routinely.

References

[1] LIEM, P.H., *et al.*, "*Fuel Management Strategy for the New Equilibrium Silicide Core Design of RSG GAS (MPR-30)*", Nuclear Engineering and Design **180**, p. 207–219 (1998).

[2] BATAN, "*MPR-30 Safety Analysis Report*" , Rev. 7, Jakarta (1987).

[3] LIEM, P.H., *et al.*, "*Nondestructive Burn-up Verification by Gamma-ray Spectroscopy of LEU Silicide Fuel Plates Irradiated in the RSG GAS Multipurpose Reactor*", Annals of Nuclear Energy **56**, p. 57–65 (2013).

[4] P.H. Liem, "BATAN-FUEL: A general in-core fuel management code," *Atom Indonesia* **22(2)**, p. 67-80 (1996).

[5] Okumura, K., et al.,"SRAC2006: a comprehensive neutronics calculation code system" , JAEA-Data/Code 2007-004 (2007)

IMPACT OF HEU TO LEU FUEL CONVERSION ON THE LIFETIME AND EFFICACY OF THE UNIVERSITY OF MISSOURI RESEARCH REACTOR BERYLLIUM REFLECTOR

J.L. Saddler, N.J. Peters, J.C. McKibben and L.P. Foyto
Reactor and Facilities Operations, University of Missouri-Columbia Research Reactor
1513 Research Park Drive, Columbia, Missouri, 65211 – U.S.A.

ABSTRACT

In accordance with the mission of the Global Threat Reduction Initiative (GTRI) program of maintaining the current capabilities of research and test reactors after converting them from highly-enriched uranium (HEU) fuel to low-enriched uranium (LEU) U-10Mo monolithic fuel, studies must be performed to ensure that the reactor core performance will not be challenged in any way. While detailed work has been completed that predicts core neutronic and thermal-hydraulic behavior, the impact of a fuel conversion has not yet been studied to any level of detail for various critical components other than the reactor core for the University of Missouri-Columbia Research Reactor (MURR). In particular, there are limitations on the specialized beryllium sleeve used as the primary neutron reflector, which is replaced at every 26,000 megawatts days (MWd) of operation with HEU fuel operating at 10 MW. This is to avoid the eventual stress-fracture failure due to thermal stresses from gamma heating and swelling from gas production, in addition to the performance degradation seen as a corresponding loss in core reactivity due to lithium-6 poisoning and swelling. The replacement cycle, which will change with LEU operations at 12 MW, is being determined. Preliminary investigations using MURR MCNP models, coupled with ORIGEN depletion simulations that compare the HEU and LEU cores, have predicted differences in the gamma heating distribution, gas production rates and core reactivity changes concerning the beryllium as a function of MWd. Results from this work indicate that for an end-of-cycle beryllium reflector at MURR, the changes at the peak-flux region of production, when converting from HEU to LEU fuel, are a 21.5% decrease in gamma heating and an 11% increase in gas swelling. Using the results reported here, a systematic approach to predict beryllium performance and failure point as a function of MWd is being developed.

1. Introduction

In keeping with the mission of the Global Threat Reduction Initiative (GTRI) program of maintaining the current capabilities of research and test reactors after converting them from highly-enriched uranium (HEU) to low-enriched uranium (LEU) fuel, studies must be performed to ensure that reactor performance will not be notably altered by fuel conversion. While detailed work has been completed which predicts core neutronic and thermal-hydraulic behavior, the impact of a fuel conversion has not yet been studied to any level of detail for various critical components of the University of Missouri-Columbia Research Reactor (MURR). In particular, MURR requires a beryllium reflector specifically designed and fabricated as a primary neutron reflector in order to provide a critical core and desired power distributions. The choice of using beryllium as a neutron reflector has advantageous qualities which include having one of the highest atom number densities (i.e., a relatively large scattering cross-section) and a very small neutron absorption cross-section. Though not as efficient, beryllium is also a neutron multiplier due to its small ^{9}Be (n_f, 2n) 2 ^{4}He and ^{9}Be (γ, n) 2 ^{4}He cross-sections which increases core reactivity.

1.1 Limits on the Lifetime of Beryllium

The limitation of using a beryllium reflector in a high power density research reactor like MURR is that it has to be routinely replaced. The beryllium reflector replacements are performed because of the continually increasing internal strain that develops based on operating history, which could result in fracture if the yield point is reached. The strain of thermal stress from radiation heating combined with the strain caused by three different reactions that transmute beryllium atoms into either two or three smaller atoms causes this failure. When combined with the radiation heating strain, transmutation of the beryllium slowly increases the swelling strain until the yield point is reached.

Two of the transmutation reactions of beryllium are ^{9}Be (n_f, 2n) 2 ^{4}He and ^{9}Be (γ, n) 2 ^{4}He, which help provide additional reactivity for the reactor. The third reaction is ^{9}Be (n_f, α) ^{6}He. The ^{6}He quickly decays to ^{6}Li, a strong thermal neutron absorber that can quickly capture a neutron and divide into helium and tritium, which decays to ^{3}He. As a result, the concentration of ^{4}He and ^{3}He or ^{3}H steadily increases in the beryllium matrix during operation. Below is this (n, α) reaction followed by the associated reaction chain and cycle with pertinent cross-sections and decay times:

$n_f + {}^{9}Be \rightarrow {}^{6}He + {}^{4}He$	$\sigma_{n,\alpha} \approx 0.05$ barns
${}^{6}He \rightarrow {}^{6}Li + \beta^-$	$t_{1/2} = 0.8$ seconds
$n + {}^{6}Li \rightarrow {}^{4}He + {}^{3}H$	$\sigma \approx 838$ barns
${}^{3}H \rightarrow {}^{3}He + \beta^-$	$t_{1/2} = 12.5$ years
$n + {}^{3}He \rightarrow {}^{3}H + p$	$\sigma \approx 4900$ barns

The above reactions result in: $n_f + {}^{9}Be \rightarrow {}^{4}He + {}^{4}He + [{}^{3}H \text{ and } {}^{3}He]$

The two reactions on the fourth and fifth lines above show the cyclic portion of the reaction: ^{3}H decays to ^{3}He which has a large neutron capture cross-section that facilitates the conversion back to ^{3}H while the reactor is operating. Overall, the net fast neutron reaction with ^{9}Be will result in three helium atoms and a hydrogen (tritium) atom. Over time, the three ^{9}Be reactions slowly produce swelling within the beryllium reflector, which increases the tensile stresses. The tensile stresses are also increased while operating because of the gamma heating within the beryllium. This radiation heating results in a peak temperature inside the beryllium with lower temperatures on the outer surfaces where the pool coolant absorbs the heat. The higher the radiation energy deposition inside the beryllium, the higher the temperature gradient required to provide the necessary heat transfer out of the beryllium.

1.2 Description of the MURR Beryllium Reflector

The MURR beryllium reflector is a cylindrical sleeve located around the outer reactor pressure vessel at the height that contains the reactor core. The reflector, made of S-200FH grade beryllium, is 37 inches (94 cm) tall with a 9-inch (22.9 cm) tall aluminum skirt that overlaps a little less than the bottom 2 inches (5.1 cm) of the beryllium. The beryllium outer diameter is 19 inches (48.3 cm) and the sleeve thickness is 2.71 inches (6.9 cm). Five grooves are machined on the inside surface which allow spacers to be inserted which help maintain a uniform, approximately ½-inch (1.3 cm) wide circular water gap between the reflector and outer reactor pressure vessel for the five control blades to travel in.

2. MURR Beryllium Lifetime

2.1 Heating and Swelling-Induced Stresses – Highly-Enriched Uranium Fuel

Since thermal stress is proportional to reactor power level and transmutation swelling-induced stress is proportional to the fast neutron fluence, the failure of the beryllium reflector from fracture will occur when the combination of these two stresses reach the yield point

while the reactor is operating. In the case of MURR, the first beryllium reflector actually fractured in place when these combined stresses reached that yield point. It was eventually replaced in October 1981. Based on this experience and modeling of the MURR in the 1980's using a neutron diffusion code, the MURR beryllium reflector has been replaced approximately every 26,000 megawatt-days (MWd) of reactor operation. Since 1977, the reactor has operated at 10 MW for 90% of the available time each year, so based on this operating schedule the beryllium reflector has been replaced approximately every eight years.

The MURR MCNP-ORIGEN simulations and MCNP models were used to tally separately the following processes in the beryllium reflector: the transmutation of beryllium into helium and tritium gases and the deposition of neutron energy, and the capture and prompt-fission gammas from the core. The delayed-fission gamma contribution was included based on a scaled value of the energy of the prompt-fission gammas. The heating sources were summed to give the total energy deposited. The beryllium reflector modeling used mesh intervals that divided the reflector into three cylindrical rings with five axial zones (or divisions). The parts per million (ppm) productions of helium and tritium and the radiation heating in the beryllium were calculated for each mesh interval for operating with either the HEU core or the proposed LEU core.

Table 1 and Figure 1 and Table 2 and Figure 2 provide the helium and tritium gas concentrations in ppm and heating densities in watts/cm^3 in the beryllium, respectively, for a core with HEU fuel operating at 10 MW for 90% of the time for eight years.

	Division 1 (top)	Division 2	Division 3 (peak)	Division 4	Division 5 (bottom)
Inner Ring	2.81E+02	1.18E+03	1.53E+03	1.01E+03	1.79E+02
Middle Ring	1.79E+02	6.85E+02	8.89E+02	6.40E+02	1.15E+02
Outer Ring	1.14E+02	4.00E+02	5.24E+02	3.50E+02	7.54E+01

Table 1: Helium and tritium concentration in beryllium at 8 years - HEU core (in ppm)

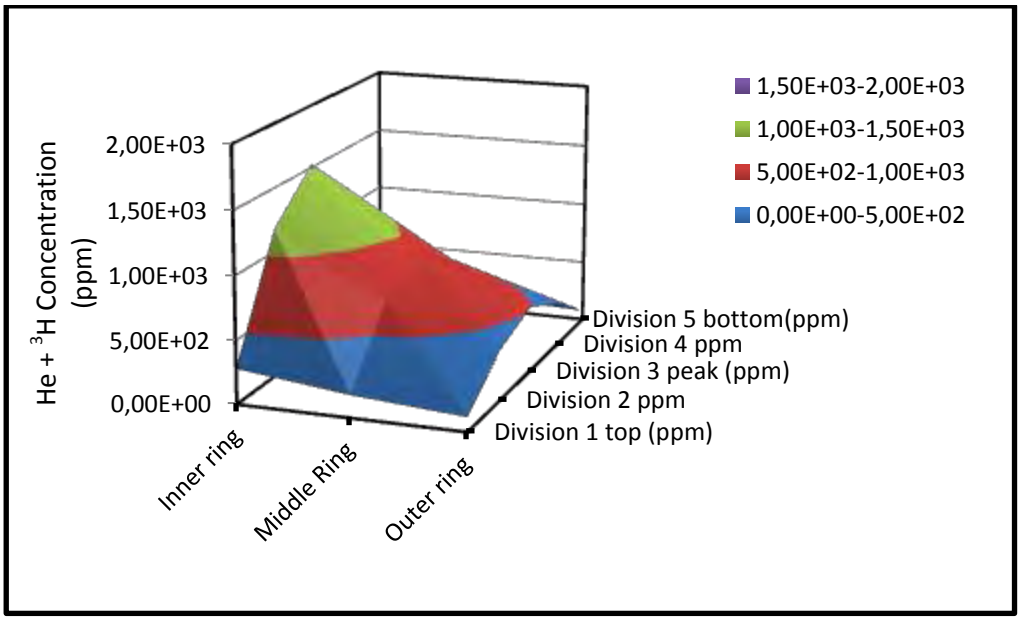


Figure 1. Helium and tritium concentration profile in beryllium at 8 years - HEU core

	Division 1 (top)	Division 2	Division 3 (peak)	Division 4	Division 5 (bottom)
Inner Ring	1.06E+00	3.62E+00	4.65E+00	3.05E+00	6.19E-01
Middle Ring	8.40E-01	2.56E+00	3.31E+00	2.62E+00	5.07E-01
Outer Ring	6.47E-01	1.79E+00	2.32E+00	1.55E+00	4.09E-01

Table 2: Total gamma energy deposition in beryllium at 8 years - HEU core (in watts/cm^3)

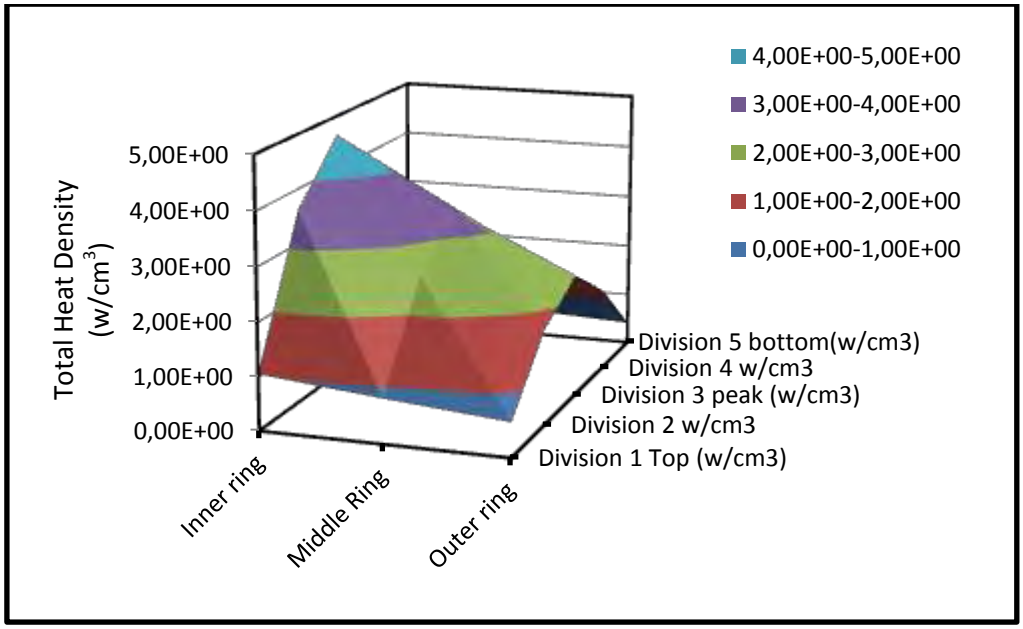


Figure 2. Total gamma energy deposition profile in beryllium at 8 years - HEU core

2.2 Heating and Swelling-Induced Stresses – Low-Enriched Uranium Fuel

With the projected conversion from UAl_x HEU to U-10Mo LEU fuel, the fast flux will still be nearly proportional to reactor power level and the total gamma energy per fission will increase slightly. However, the fuel element changes that will alter the power distribution within the core can change the fast flux levels in the beryllium. Yet, the approximate order of magnitude increase in the mass of uranium loaded in the core will reduce the gamma heating departing the core region and reaching the beryllium and producing the corresponding thermal stress. With no change in total power, this would increase the amount of MWd a beryllium reflector can be operated with LEU fuel as compared to HEU.

The LEU core values are based on operating at 12 MW for 90% of the time for eight years. Table 3 and Figure 3 and Table 4 and Figure 4 provide the helium and tritium gas concentrations in ppm and heating densities in watts/cm^3 in the beryllium for an LEU core, respectively.

	Division 1 (top)	Division 2	Division 3 (peak)	Division 4	Division 5 (bottom)
Inner Ring	2.99E+02	1.30E+03	1.69E+03	1.09E+03	1.74E+02
Middle Ring	1.92E+02	7.50E+02	9.83E+02	6.40E+02	1.15E+02
Outer Ring	1.22E+02	4.37E+02	5.78E+02	3.79E+02	7.59E+01

Table 3: Helium and tritium concentration in beryllium at 8 years - LEU Core (in ppm)

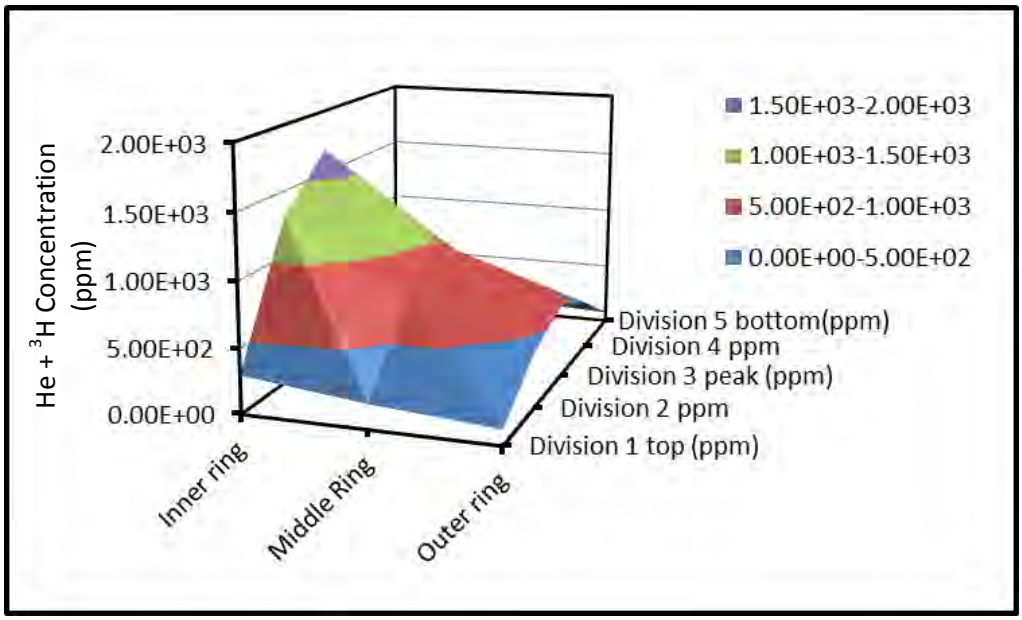


Figure 3. Helium and tritium concentration profile in beryllium at 8 years - LEU core

	Division 1 (top)	Division 2	Division 3 (peak)	Division 4	Division 5 (bottom)
Inner Ring	7.87E-01	2.82E+00	3.63E+00	2.32E+00	4.19E-01
Middle Ring	6.17E-01	1.98E+00	2.56E+00	1.66E+00	3.40E-01
Outer Ring	4.66E-01	1.37E+00	1.77E+00	1.17E+00	2.64E-01

Table 4: Total gamma energy deposition in beryllium at 8 years - LEU core (in watts/cm^3)

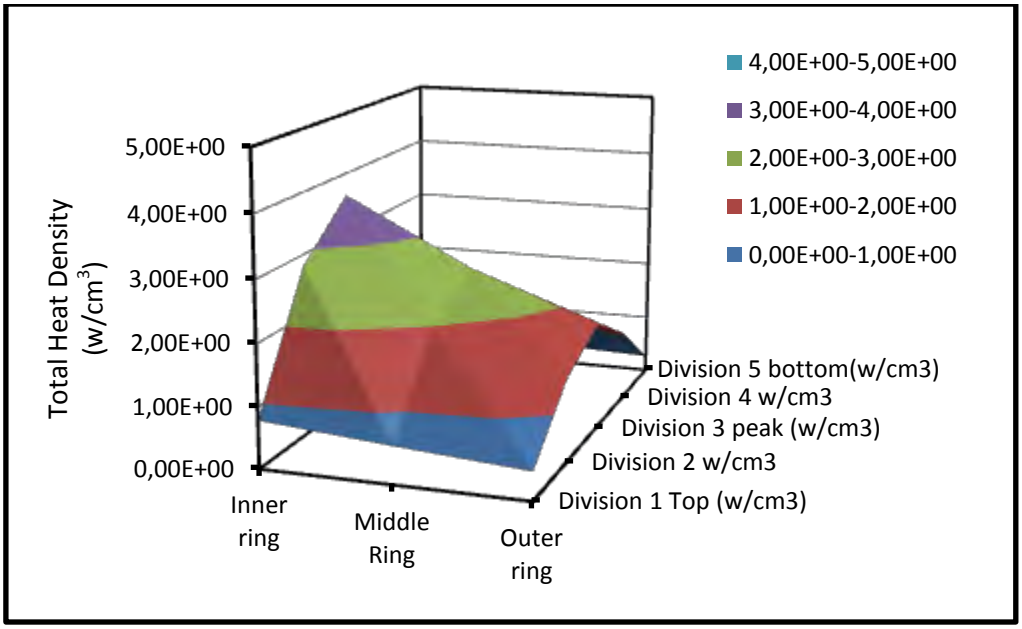


Figure 4. Total gamma energy deposition profile in beryllium at 8 years - LEU core

3. Swelling Prediction and Performance Degradation

3.1 Swelling Predictions from Gas Production Profiles

Swelling was predicted in the MCNP beryllium reflector model using mesh intervals of three cylindrical rings each having five axial divisions. Since the calculated ppm production of each gas nuclide (^{3}He, ^{4}He and ^{3}H) from the ^{9}Be transmutation in each mesh interval is different, the corresponding amount of swelling is also expected to vary proportionally. This

way, the peak swelling is expected to occur in the mesh interval where the peak gas production is. It is assumed that both the peak swelling and peak gas production mesh also contains the peak fast flux (i.e., neutron in the energy range > 0.1 MeV) in the beryllium. Figure 5 shows the MCNP calculated fast flux profile for the current HEU core beryllium reflector. The peak flux is observed to occur in the axial section 3 of the innermost radial mesh. In comparison, the peak fast flux difference for the LEU core is shown to be ~10% greater than the current HEU core.

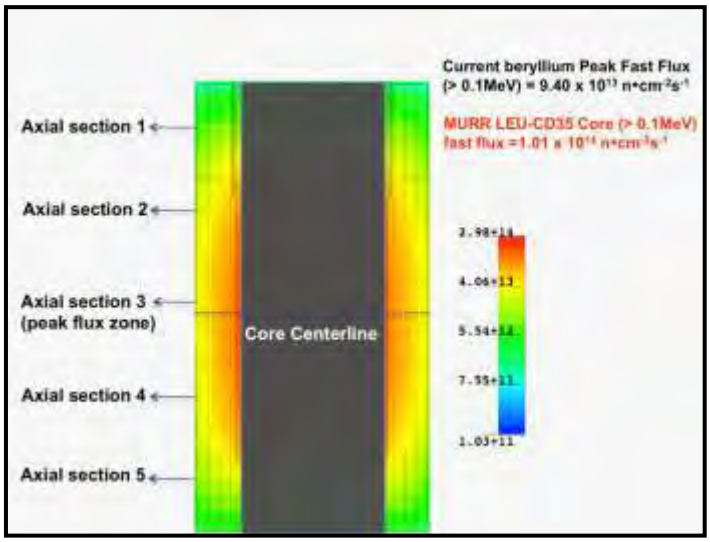


Figure 5. MCNP calculated fast flux profile for the beryllium reflector - HEU core

Normalizing the gas production at the peak flux zone to one (1), the gas production in any other mesh can then be written as a ratio, which is a fraction of peak gas production. This way, the peak mesh can be given an arbitrary swelling value as a percentage, which when multiplied by the gas production ratios in every mesh establishes a swelling profile over the entire beryllium sleeve. Since a direct correlation between gas production and swelling (in terms of change of the volume ratio **Δ**V/V) in beryllium has not been documented, to include the dimensional changes in the beryllium due to swelling in the MCNP model a simplified approached was used; the swelling in each mesh was assumed to change in the radial dimensions only. Particularly, for the inner radial meshes, the increase in volume occurred towards the center of the core; for the outer radial meshes the increase in volume occurred outwards from the core. An additional assumption for the middle radial meshes was made where two-thirds of the volume increase occurred towards the center of the core and a third occurred outwards from the core. This assumption was based on the calculated gas production profile where the production increases non-linearly and peaks on the inner surface of the beryllium towards the core center.

The radial dimensional change of each axial zone for the inner surface ($\mathbf{\Delta s_{in}}$) of the beryllium after a period of operation is approximated as $\mathbf{\Delta s_{in} = \Delta r_{in} + 2/3\Delta r_{mid}}$, where $\mathbf{\Delta r_{in}}$ and $\mathbf{\Delta r_{mid}}$ are the changes in the inner radii of the inner and middle meshes, respectively. Similarly, the radial dimensional changes of each axial zone for the outer surface ($\mathbf{\Delta s_{out}}$) of the beryllium is approximated as $\mathbf{\Delta s_{out} = \Delta r_{out} + 1/3\Delta r_{mid}}$, where $\mathbf{\Delta r_{out}}$ is the radial change of the outer mesh.

For the current HEU core, a peak swelling rate was arbitrarily selected at 0.25% per year which cumulatively equates to 2.0% of swelling, and an average beryllium sleeve swelling of 0.72% at 26,000 MWd. Based on this selection, the peak inward growth (towards the core) of the beryllium reflector after 26,000 MWd was calculated to be 0.048 inches (1.219 mm) and the peak outwards growth of the reflector was calculated to be 0.037 inches (0.940 mm) after 26,000 MWd. Figure 6 shows the growth of the inner and outer beryllium surfaces with the HEU core at 10MW after 26,000 MWd.

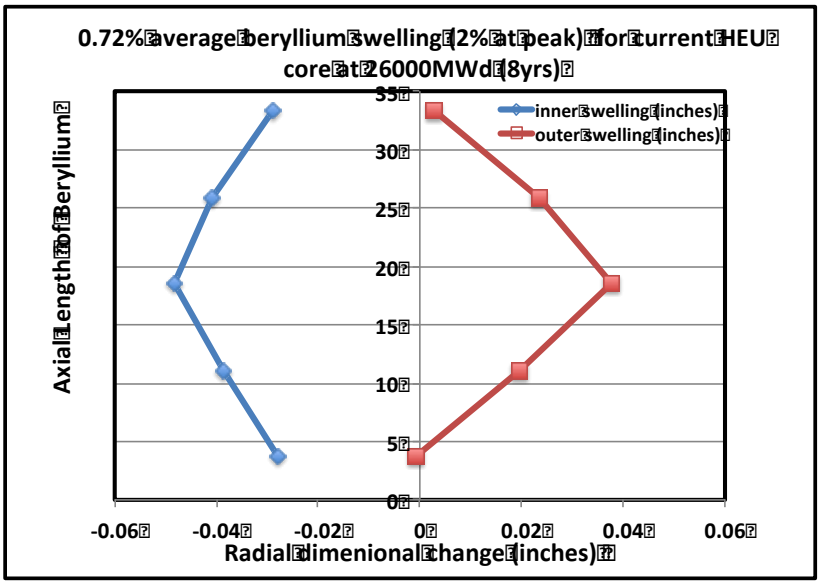


Figure 6. Predicted growth of the inner and outer beryllium surfaces after 26,000 MWd - HEU core

Figure 7 provides a comparison of calculated and measured growth of a MURR beryllium reflector that had approximately 26,000 MWd of operation. A measurement fixture, consisting of a baseplate, an upper structure, and a potentiometer carriage, was used to measure 8 radial positions; data was taken every 2 inches (5.08 cm) of axial downward travel. Measurements were then offset by 1 inch (2.45 cm) and data was taken every 2 inches (5.08 cm) of upward axial travel. This provided data points for every inch (2.54 cm) axially for each of the 8 radial positions.

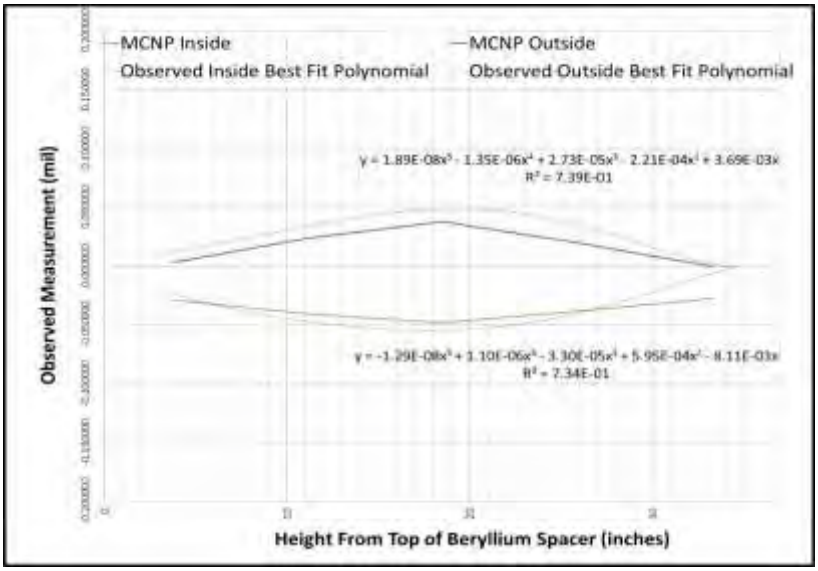


Figure 7. Comparison of calculated and measured growth of a MURR beryllium reflector - HEU core

At each measurement node, carriage motion was stopped to collect several samples. The digital data was taken at a rate of 10 samples per second. A stop of greater than 10 seconds provided a minimum data set of 100 samples per node. After all data was collected, the data from each node was consolidated into two sets, inside and outside, each averaged radially. To do this, all data that was collected while the potentiometers were translated between nodes, was removed so that all that was left was the desired data taken at each node. Then

an average value was generated from all the samples at each node. The eight nodes for each axial location were averaged giving two data sets, inside and outside, each averaged radially.

To account for any misalignment in the measurement rig linear rails, the data was geometrically adjusted by translating the data such that one endpoint was fixed at a value of 0. A data deviation slope line was then calculated by using only the first and last measurement nodes. Using the slope, the entire data set was rotated so both the first and last measurement nodes were fixed at 0. This rotation was accomplished with vector matrices. To account for the racking effect noticed in the upward and downward travel measurements, an Excel curve fit was applied to both the inside and outside data sets. These equations are shown on the graph.

3.2 Impact of Transmutation and Performance Degradation

The impact of beryllium transmutation, which causes swelling and poisoning, is seen in the results from complex MCNP MURR core simulations used to predict the current estimated critical positions (ECP); the inclusion of a more detailed beryllium reflector model is shown to increase the accuracy of the ECP predictions. The MWds on the currently operating beryllium is ~26,000. Therefore, the details of the current beryllium model include the predicted transmuted nuclides, density and dimensional changes at 26,000 MWd specific to each mesh. The effects of these details are shown in Figure 8, which is a plot of the percent deviation of the predicted ECP from the actual critical rod heights over a non-consecutive nine-week period. After week three, the improvements in the ECP predictions, after adding the most appropriate beryllium burnout details along with the calculated swelling at eight years, are quite noticeable; i.e. moving from a biased of a -1.2% deviation to a ±0.25% deviation.

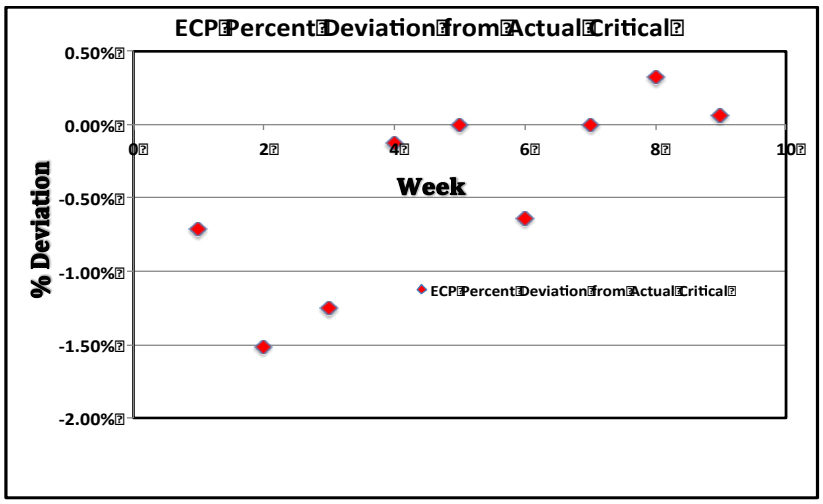


Figure 8. Plot of the % deviation of the predicted ECP from the actual critical rod heights - 9 week period

Degradation in the beryllium performance as the MWd increase will primarily manifest itself as a loss in core excess reactivity. The loss in excess reactivity is primarily due to the following: (1) the presence of the neutron poisons ^{6}Li and ^{3}He, and (2) swelling due gas buildup which decreases the macroscopic scattering cross-section of beryllium. In the case of the neutron poison ^{6}Li and ^{3}He with thermal capture cross-sections of 900 and 4900 barns, respectively, ^{6}Li achieves an equilibrium value within 5,000 MWd while the much less produced ^{3}He steadily increases with MWd. In the interest of an HEU to LEU fuel conversion, a study was done using a series of MCNP KCODE calculations to understand

how the beryllium performance differs with increasing power for the two MURR core configurations.

With the HEU core at 10 MW and the LEU core at 12 MW, both operating at 90% of the available time over eight years, a basis was set for comparison. The excess reactivity loss (-**Δ**k/k) was computed for a fresh beryllium model, a beryllium model with 90% full-power operation at 4 years, and a beryllium model with 90% full-power operation at 8 years for both the current HEU and the proposed LEU core configurations. The peak swelling in the beryllium model for the HEU core was maintained at 0.25% per year. However, since the gas production is ~11% higher for the LEU core, the peak swelling in its beryllium model was proportionally increased to 0.278% per year. Figure 9 shows a plot of the core excess reactivity loss comparison between the HEU and LEU cores.

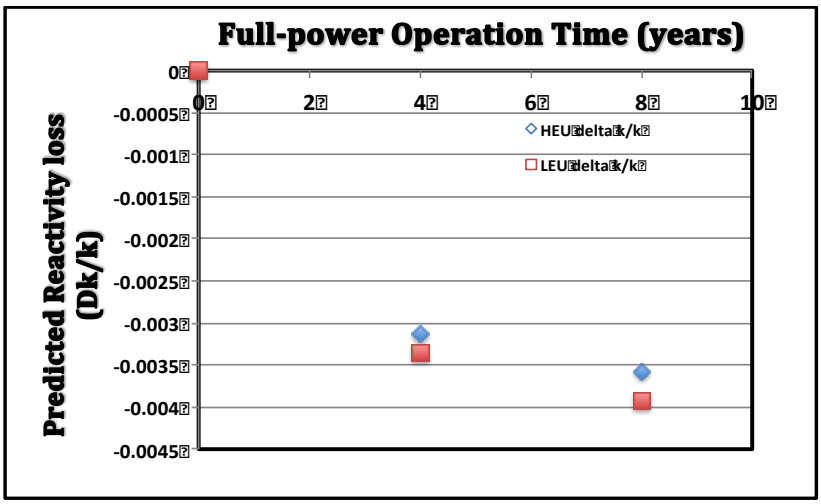


Figure 9. Plot of the core excess reactivity loss comparison between the HEU and LEU cores

It is observed that the rate of reactivity loss generally increases with MWds sharply within the first four years then decreases significantly over the following four years. This can be attributed to the equilibrium production of ^{6}Li well within the first four years. However, the LEU core shows an increasingly larger excess reactivity loss approximately 10% greater at eight (8) years, then the HEU core. This is not surprising since with its increase in fast flux, the neutron poisons and swelling is predicted to increase which contributes to decreasing the beryllium efficiency as a neutron reflector.

4. CONCLUSION

With the current operating schedule of 90% of the available time (151 hours/week) at 10 MW with an HEU core, the beryllium reflector is replaced approximately every eight years. Modeling this same operating schedule using MCNP-ORIGEN burnup simulation, it was determined that the peak gas production region has an average concentration of 1,530 ppm (0.153%). Additionally, in the peak region the average heating rate is 4.65 watts/cm^3. Using this same operating schedule (151 hours/week) with the proposed LEU core at 12 MW for an eight year period, the average concentration in the peak gas production region increases to 1,690 ppm (0.169%), which is 10.5% greater than the HEU core. However, for the LEU core, the average heating rate in the peak region is reduced to 3.63 watts/cm^3, which is 24% less than the HEU core.

In 1962 for the preliminary design of the beryllium reflector, Internuclear Company calculated a maximum thermal stress of 16,690 psi as compared to the assumed beryllium's yield stress

of 27,000 psi [Ref. 1]. The preliminary design had an inner diameter of 13.175 inches (84.9998 cm) and outer diameter of 19.095 inches (123.193 cm). The final and current design has an inner diameter of 13.675 inches (88.226 cm) and outer diameter of 19.095 inches (123.193 cm), which should produce a slightly reduced maximum thermal stress as compared to the original design data. A 7.03% reduction in the volume of the beryllium when comparing the preliminary design to the current design results in a decrease in the amount of heat transferred out of the beryllium and 8.4% less distance between the two heat transfer surfaces. The current design also has a 1.55% increase in the heat transfer surface area because of the larger diameter of the inner surface. These should combine to provide a slight reduction in the maximum thermal stress.

A simple approach to estimating the lifetime of the beryllium with an LEU core at 12 MW as compared to an HEU core at 10 MW is using their respective predicted energy deposition and helium/tritium gas production in the beryllium reflector. If the 1962 Design Data values of a beryllium yield stress of 27,000 psi and a maximum thermal stress of 16,690 psi are used for a beryllium reflector operating at 10 MW with HEU fuel, then the stress from the transmutation of beryllium into helium and hydrogen gas had to be equal to or greater than 10,310 psi to crack the first MURR beryllium reflector, assuming that the yield stress stayed constant.

Using the gamma heating rates at core center line, the difference in heating rates between the inner and outer rings with an HEU core operating at 10 MW and for a LEU core operating at 12 MW are 2.33 watts/cm^3 and 1.86 watts/cm^3, respectively. If the thermal stress is proportional to the heating difference, then the maximum thermal stress would be reduced from 16,690 psi to approximately 13,320 psi. This would increase the allowable stress for the transmutation of beryllium into helium and hydrogen gas from 10,310 psi for the HEU core to 13,680 psi for the LEU core. Assuming the stress from the transmutation of beryllium is proportional to the difference in the gas production rate at core centerline multiplied by the number of years operating at full power:

Conversion factor =
Maximum stress limit / (difference in gas production per year x years' operating)

10.25 psi/ppm = 10,310 psi / (125.75 ppm/yr x 8 years)

Therefore, the number of years the LEU core could operate before the maximum stress limit is reached could be approximated by:

Years' operating =
Maximum stress limit / (Conversion factor x difference in gas production per year)

9.6 years = 13,677 psi / (10.25 psi/ppm x 139 ppm/yr)

If the assumptions in this approximation are valid, then the decrease in gamma heating of the beryllium reflector with an LEU core at 12 MW should compensate for its higher gas production rate and not reduce the beryllium reflector operating lifetime. However, it is anticipated that a more rigorous beryllium lifetime analysis to yield better predictions can be accomplished by working with the material science expertise within the GTRI High Performance Research Reactor Working Group.

5. REFERENCES

[1] "Missouri University Research Reactor Design Data, Volume I," Internuclear Company, Clayton, Missouri, September 28, 1962.

DEVELOPMENT OF REACTOR INFORMATION SYSTEM AT JSI TRIGA MARK II REACTOR

ANŽE JAZBEC, LUKA SNOJ, BORUT SMODIŠ
Reactor Infrastructure Centre, "Jožef Stefan" Institute
Jamova cesta 39, 1000 Ljubljana, Slovenia

ABSTRACT

Slovenian TRIGA reactor is almost 50 years old. To ensure safe operation, every component should be under a strict supervision. Most of them were replaced or refurbished during the maintenance program. Some components are replaced due to ageing and others are replaced due to existence of better or more reliable technology.

In the last 50 years, the development in the field of electronics and communication was enormous. To make the operation of the reactor safer, easier and better, often completely new systems are added.

In 2007 the wastewater handling system was refurbished. A decision was made, to digitalize it. After the renovation, operators are able to observe important parameters like water levels and its activity remotely from the reactor control room. Beside that, alarm levels were set and the system automatically warns the staff when a certain parameters exceeded its limit.

Three years later, system was expanded. A new ventilation system was installed inside reactor hall and control room. Since then, system allows not just observing the process, but also to control some parameters. Today, we can turn on the ventilation system, set air temperatures, under and overpressures. In case of emergency, system goes automatically into isolation mode. In 2012 similar ventilation system was also installed in hot cell facility.

In near future, we will go one step further. Reactor primary and secondary cooling loop will be equipped with ultrasonic flow rate monitors and thermometers and connected to the current system. Beside that, a leakage detection system will also be installed.

1. Introduction

One of the main goals of reactor operation is to operate safely. Components and system of nuclear reactor have to be constantly under strict supervision. Often new components are added in order to improve nuclear safety.

In the beginning, when the reactor started to operate in the 1960s, only the most important data on reactor status were send to control room. Today, when the communication technology improved, it is easier and easier to send data at different locations. The idea is, to set a system, where reactor operator will have a remote access to control and supervise all processes directly or indirectly connected to reactor operation. That would come very convenient in case of emergency, when access to some facilities would be dangerous or blocked. Beside that, system is constantly monitoring parameters like activity of wastewater, level of water inside wastewater tank, under pressure inside reactor hall or in hot cell, leakage of water etc. In case of exceeded alarm level, system warns operator and manages processes e.g. shuts down the reactor, ventilation system, pumps etc.

2. Wastewater system

Wastewater system is designed to collect potentially radioactive or chemically dangerous waters from the reactor building, hot cell facility and different laboratories. In case that system does not operate correctly, all activities in mentioned facilities would be stopped. System is set in the basement of a nearby building (Fig. 1). A decision was made, to renovate the system, digitalize important components and improve reactor safety.

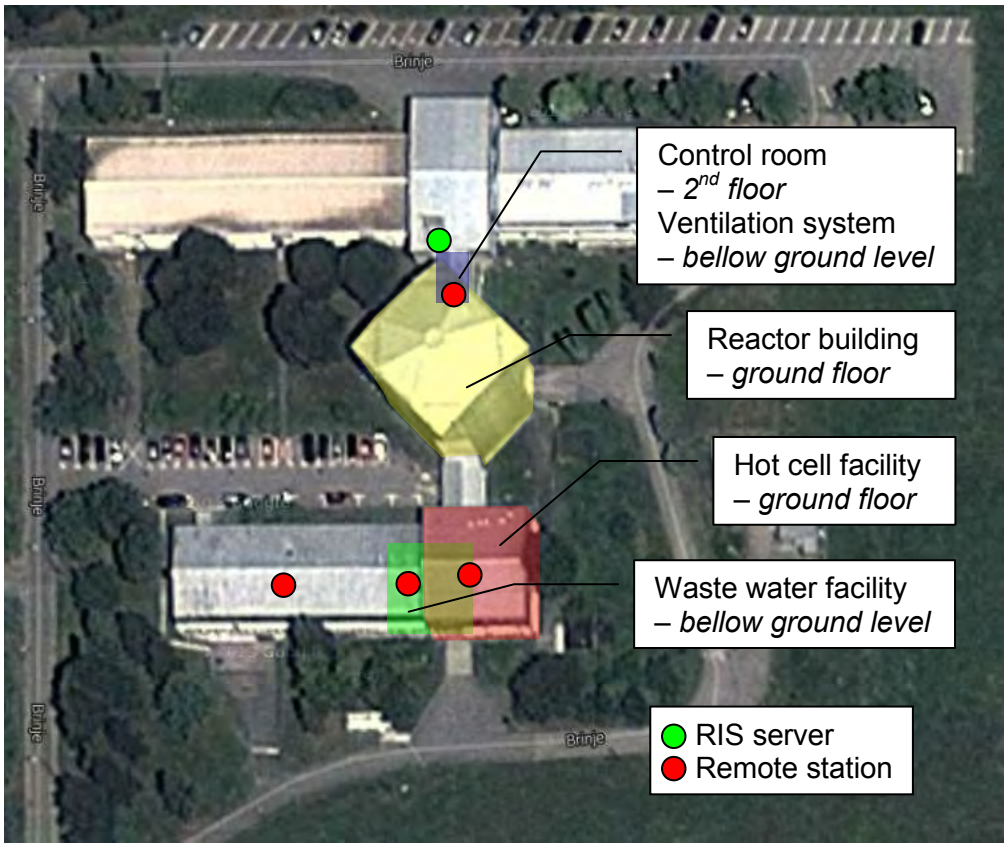


Fig. 1: Reactor buildings layout at JSI Reactor Centre. Marked are current locations of remote stations server of the Reactor information system [2].

The old system allowed some human errors. The pumps could be started in case of blank conditions e.g. closed valves. Furthermore, wastewater could be released in case of too high activity.

All these disadvantages were eliminated with the new communication system. Furthermore, start/stop of different routines can be performed on site or remotely. Alarms and events are archived. Alarms are set for parameters like increased activity of wastewater, increased inflow of wastewater tanks, high level inside tanks, failure of pump etc. Some alarms are connected with light warnings. All measured data are stored so their history trends can be later analysed.

To achieve such operability, multiple valves and pumps were equipped with sensors which signal weather the valve is open and weather the pump is in operation. Water tanks were equipped with level meters. Activity of water is also measured using old detector that was connected to the system.

Hardware was installed in the basement, where the system was already set. A connection was established with remote computer which was installed in the office of radiation protection group.

Software was provided by external company, who has a lot of experience with SCADA systems. Graphical user interface (GUI) of the system is presented in Fig. 2.

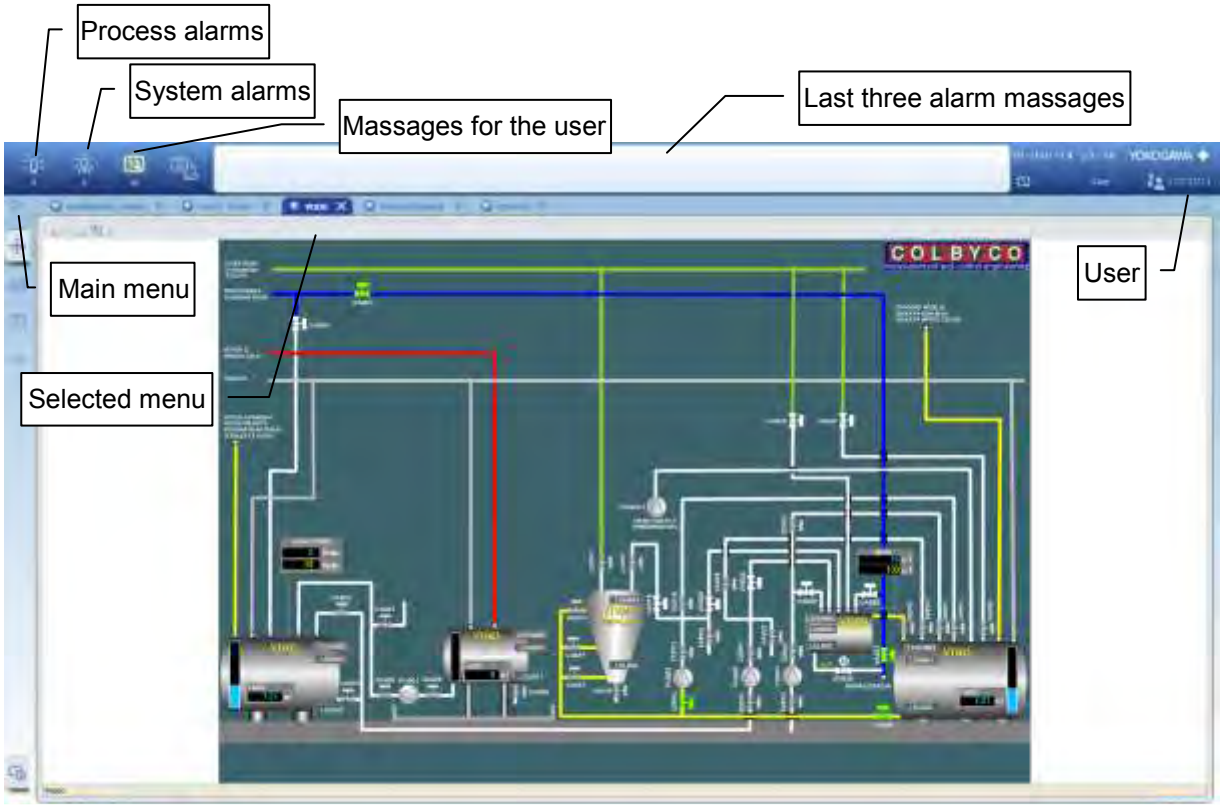


Fig. 2: Graphical user interface with selected wastewater menu.

GUI allows user to monitor which valves are open, which pumps are in operation, water levels in each tank and volume of water inside, activity of the wastewater and which department is currently producing wastewater. Routines like releasing wastewater into environment are automated. Before the routine starts, the sample of water is taken and is measured by radiation protection group. Wastewater goes than in sedimentation tank, where system measures activity again. In case of too high activity, water is not released [1].

3. Ventilation system

Ventilation system is important component of each reactor facility. In case of contaminated air inside reactor building, ventilation system should prevent an exhaust of air into the environment. During the normal operation, a slight under-pressure (~20 Pa) is kept inside reactor hall and a slight over-pressure (~10 Pa) is kept inside control room to prevent that potentially contaminated air would enter control room or be released into environment without being filtered. Beside that, our ventilation system is connected to the argon system, which is ventilating beam tubes during reactor operation. It is important to note that in all safety analyses related to the JSI TRIGA reactor the ventilation system is not taken into account and is considered inoperative.

It is located in the same level as reactor basement, 2 stories below control room (Fig. 1).

In 2010, ventilation system was renovated due to ageing. A decision was made, to install similar process controller as in wastewater facility. That would assure better reliability of the system and operators would have better overview of the process.

Additional pressure and temperature sensors were installed. All doors were equipped with sensors that monitor their status (open / closed). Flow meter was installed inside outlet duct of ventilation and argon system. Existing activity meter of outlet air was connected to the system. The remote unit to control the system was installed inside reactor control room. The

inlet air is cooled by the water from water tower, so there was installed a water level meter. To make the system redundant, processor, process communication and power supply were made redundant.

All measured data are archived and can be manually processed later by operators. At this stage, control unit of wastewater and ventilation system were connected into a single control system. Operators can set desired temperatures, under pressure inside hall and inside argon system. Recirculation mode can be turned on to improve energy efficiency when the reactor is not in operation. The GUI of the system overview is presented in Fig. 3. In case of insufficient under pressure, operator can quickly check if any doors are open.

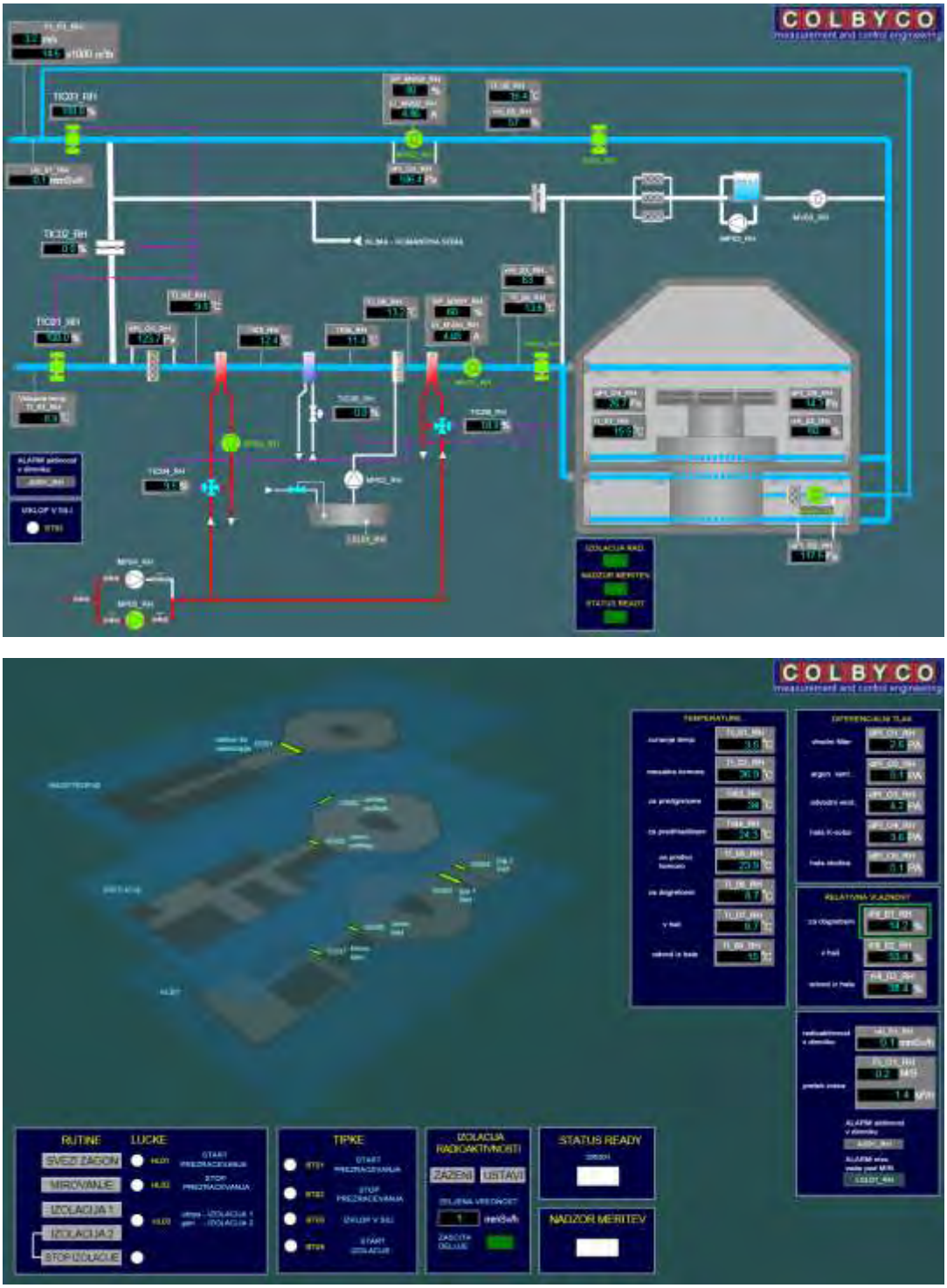


Fig. 3: User interface of ventilation system. Ventilation menu (top) and ventilation control menu (bottom).

System can also prevent some human errors. Reactor cannot be started if the under pressure is not sufficient and if argon system is not in operation. In case of failure, system can shut down the reactor. In case of high dose alarm in chimney or environment, isolation mode is turned on – air from the hall is released through HEPA filters, no inlet air is provided and consequently, reactor is shut down.

4. Hot cell facility

In 2012, similar ventilation system was installed in hot cell and connected to the existing controller system. At that time, system grew so much; we were able to rename it into "Reactor Information System" (RIS). Hot cell facility consists of three rooms (A, B and C) which are connected by hallway. Actual hot cell and four hoods are located in room A, room B is a service room. Low radioactive samples are measured and analysed in room C, where is all necessary equipment.

A completely new ventilation system was acquired. Temperature, pressure difference and air humidity sensors were installed in each room. Doors were equipped by sensors that indicate weather they are closed or not. If one of the doors is open for more than a minute, a red light at the hallway starts to blink. In case that door is not closed in the following minute, a siren will warn staff to close the door (Fig. 4).

The highest over-pressure is kept in hallway; a bit lower pressure is kept inside room A, B and C and the lowest pressure is kept inside hot cell and different hoods, where radioactive materials are handled. Pressure differences are small (~Pa). Air from the hoods and cell is released into environment through HEPA filters.

Hot cell facility is located in nearby building; therefore we installed another remote control station inside hallway. Operator can set desired temperatures and set desired under-pressures inside hoods. Ventilation of the hot cell is constantly turned on. All these parameters can also be controlled from the reactor control room. All remote units were connected to the system server, which was installed near control room.

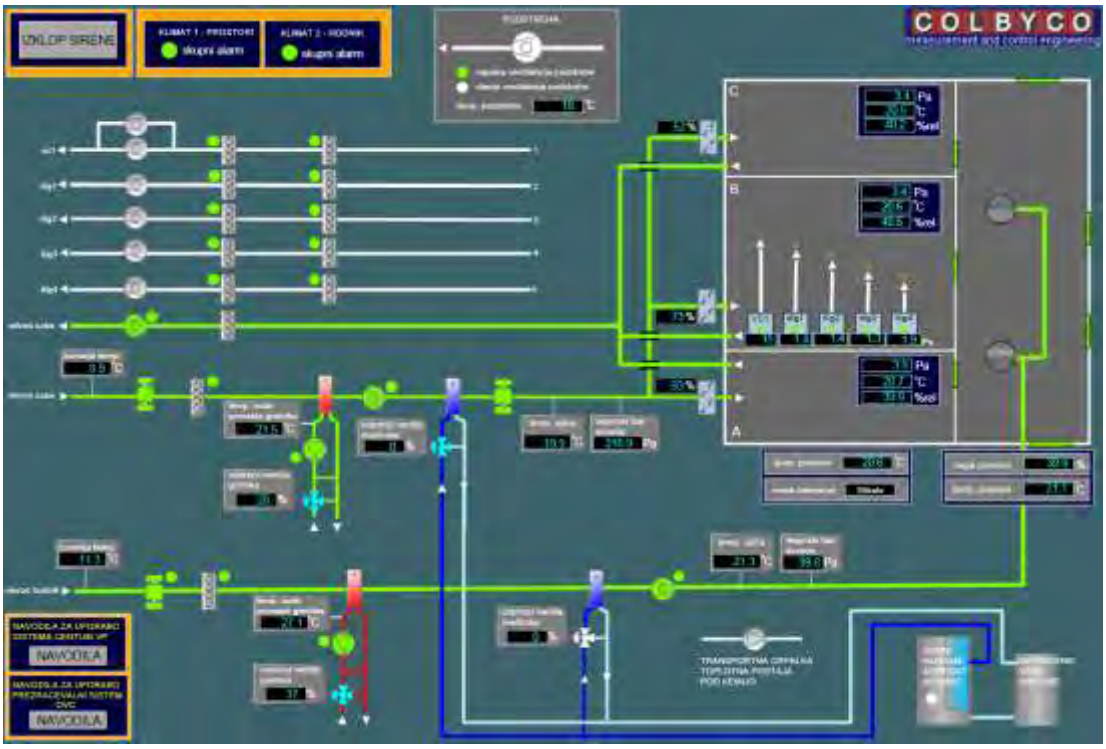


Fig. 4: User interface of the hot cell facility ventilation. In the upper right side of the figure, one can see the floor plan of the hot cell facility.

5. Paperless recorder

In 2012, we installed a paperless recorder (Fig. 5) in our radiation instrumentation unit inside control room. It collects data from 8 detectors of radiation. If one of parameters exceeds alarm level, it warns operators. Beside that, all data are archived. It is also collecting some data from reactor control board like water temperatures in primary loop, water flow in secondary loop, water level inside reactor tank, temperature of the fuel, activity of primary and secondary loop. Currently, we are still in the phase of testing the equipment. So far, no negative experience occurred therefore we are planning to connect the recorder with RIS. That would expand its usability and make reactor processes more connected. Eventually, RIS will be able to take the role of existing alarm central that alert operators in case some parameters are close or even beyond operating limits. As a consequence of exceeded limit, reactor scrams.



Fig. 5: Paperless recorder.

6. Fire alarm

In 2013 a completely new fire protection system was installed in all buildings at reactor centre. A connection between RIS and fire alarm was made. In case of fire in buildings that are connected with the reactor, RIS would stop ventilation system inside reactor hall, control room and inside hot cell facility to prevent the spreading of fire. As a consequence of turned off ventilation, reactor would scram.

7. Future work

In 2014, water leakage system will be installed inside reactor hall. Sensors that detect water will be placed inside all beam tubes, inside dry chamber and inside thermal column. Additional sensors will be placed in reactor basement. There is already a 30 m^3 empty storage below the basement level, which is painted with the watertight paint. Storage is covered with concrete block where holes were drilled through which will enter water in case of flood (Fig. 6).

One of the most important processes according to the reactor operation is cooling the reactor core. We are planning to digitalize that process as well. From the installation point of view, that stage will not be challenging. Temperature sensors and flow meters need to be installed. Water pumps should be equipped with sensors and some process will be automated e.g. refilling the reactor tank with reserve demineralised water. Reactor primary pump will be equipped by frequency regulator and the flow of primary coolant will be adjustable. That would allow circulating water at low speed during reactor shutdown which would prevent growth of cyanobacteria inside reactor tank.

Beside that, additional water level meter will be installed inside reactor tank and inside spent fuel storage, which does not have any sensor now. Some valves will be just digitalized, more important ones will also be motorized – e.g. ones required to refill reactor tank.

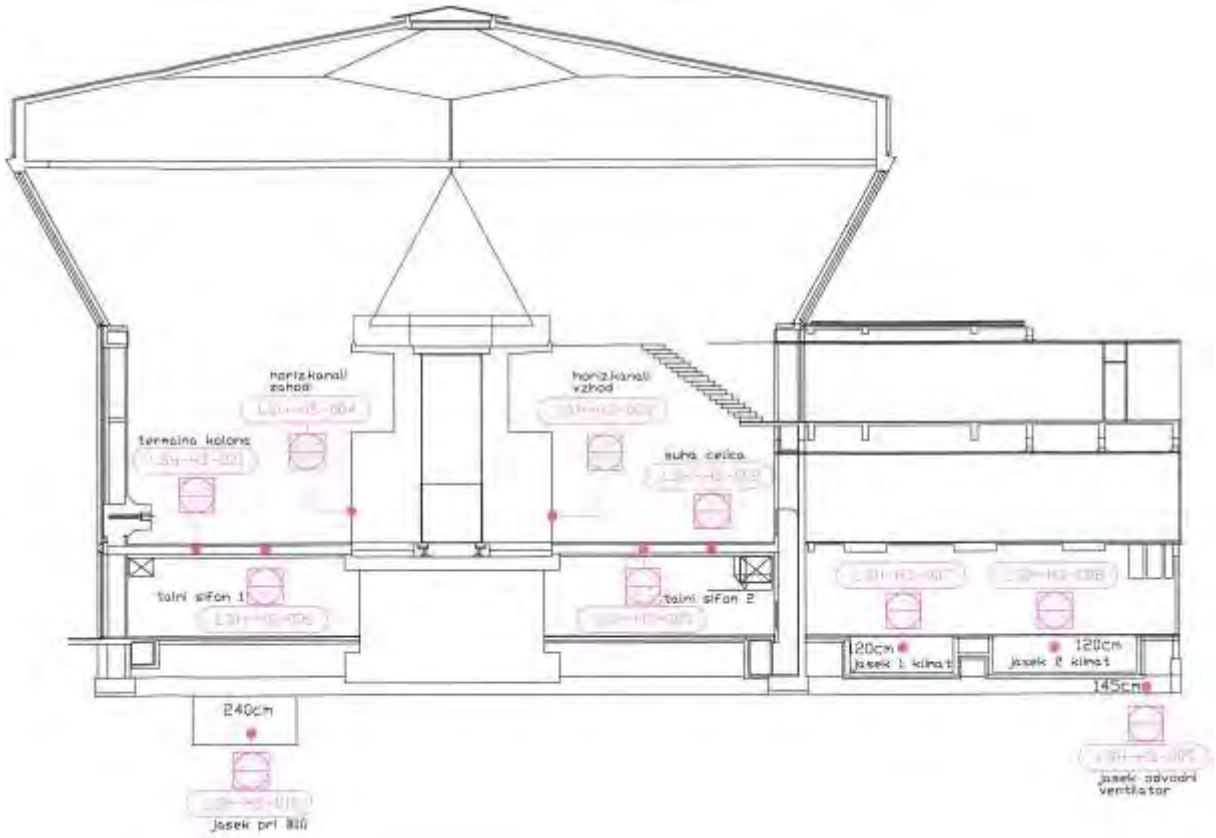


Fig. 6: Locations of the leakage detection sensors inside reactor building.

8. Conclusion

The system we are installing is unique and designed especially for our reactor. Due to small team of operators, we decided to hire external company, which developed software to control processes. Hiring external company could be one of the major drawbacks of such system. If there are problems, possibly we do not know how to solve them. To overcome the problem, the same external company is responsible for tech support and usually it takes less than one day to resolve the problem.

To sum up, the process controller system or RIS is reliable, easy to operate and cheap to maintain. The system prevents some human errors; in case that observed parameters exceeds limits it alarms staff. Furthermore, all data are collected and archived at one place.

9. References

[1] G. Pregl et al., Varnostno poročilo za reaktor TRIGA Mark II v Podgorici, IJS Delovno Poročilo, IJS-DP-5823, Revision 3, 1992 (*Safety Assessment Report*).

[2] JSI Reactor Centre, Map. Google Maps, Google, Web. February 2014.

REACTIVITY MEASUREMENTS AT THE TRIGA REACTOR USING SIGNAL FROM MULTIPLE FISSION CELLS

IGOR LENGAR, VID MERLJAK
Reactor physics department, "Jožef Stefan" Institute
Jamova cesta 39, 1000 Ljubljana - Slovenia

ABSTRACT

A digital meter of reactivity (DMR) is applied for the measurements of physical parameters of the reactor cores of the TRIGA reactor and in the Nuclear power plant Krško (NEK). The DMR used uncompensated ionization cells in order to obtain the neutron flux signal in the past. At the TRIGA reactor only one ionization cell is currently used for flux measurements. During the insertion of one control rod the neutron flux distribution is significantly altered affecting the flux measurements of inserting different control rods. The problem is presently solved by assigning a correction factor to each control rod what introduces an additional uncertainty.
In the present paper the implementation of four fission cells for reactivity measurements is presented. In this way determining the correct gamma background and its subtraction, performed by DMR algorithms, becomes less important as previously by using ionisation chambers. The larger number of detectors also reduces the flux redistribution effects on the signal during individual control rod movements.

1. Introduction

The control rod worth in research reactors and power plants can be determined by different methods [1,2]. In this paper the rod-insertion method, which is particularly convenient because it is very quick and simple to perform, is studied. The principle of the rod-insertion method is to start from a critical reactor operating at low power and to measure the time-dependent reactivity change while a control rod is inserted into the core with the drive mechanism at normal speed. By analyzing the flux trace using six-group point-kinetics equations, not only the total rod worth but also the differential and the integral control rod worth curves are obtained.
During the rod-insertion measurement the flux may drop by several orders of magnitude. The analysis is performed by transferring the data to a digital reactivity meter (DMR) consisting of a high-quality electrometer to monitor the neutron flux signal and a computer using special software for analysis of the signal.

2. Neutron flux depression factor

Control rods are large neutron absorbers and have a large impact on the neutron flux spatial distribution. In the TRIGA research reactor of the "Jožef Stefan" Institute (JSI) four control rods are employed [3]. The flux in the core is frequently presented as $\Phi(\mathbf{r},t)=T(t)\cdot S(\mathbf{r},t)$ [4] (it is a standard derivation and will not be repeated here). The neutron flux amplitude term $T(t)$ in the point kinetics equation [4] is representative of the integral neutron flux. This quantity cannot be measured directly. Generally we measure the neutron flux $\Phi(\mathbf{r},t)$ at one or more points outside the core and assume that the signal is proportional to the integral of the flux in the core. This assumption is acceptable if the relative change in $S(\mathbf{r},t)$ is negligible during the measurement. Otherwise, a correction on $T(t)$ due to the flux redistribution is necessary. The correction depends on the positions of the control rods and of the detector. An ionization chamber neutron detector measures essentially the flux of neutrons thermalized in the vicinity of the detector. The thermal flux for a core in which a control rod in the vicinity of the detector is inserted is much lower at the detector location and correspondingly higher at a location far from the inserted rod and the detector, compared to the unrodded core assuming that the flux distributions are normalized to unit fission neutron density in the core, which is assumed proportional to the neutron amplitude function $T(t)$. The two flux distributions therefore correspond to the same $T(t)$, but the measured flux values, $T_m(t)$ at the detector locations are different. To reconstruct $T(t)$ from the measured $T_m(t)$ (neglecting the proportionality constant) when an arbitrary rod Y is being inserted into the core, the following correction can be introduced [5]:

$$\boldsymbol{T(t)=\frac{T_m(t)}{1+(f_Y-1)g(l)}}$$

The parameter f_Y is called the flux depression factor for rod Y; it represents the required correction factor for the neutron flux radial redistribution. The function $g(1)$ is the interpolation function for the correction factor between the fully withdrawn (g = 0) and the fully inserted (g = 1) control rod positions and takes into account the actual axial control rod position dependence of the redistribution effect. The parameters F_Y and F_0 correspond to the thermal neutron flux for the rodded and the unrodded core at the location of the detector, respectively. They can be obtained easily from calculations. The flux depression factor for rod Y, f_Y, is obtained as the ratio of F_Y/F_0. In the rod-insertion method the control rod is inserted uniformly with the drive mechanism, therefore a linear transformation can be performed between the time t and the inserted depth 1 during rod travel. The interpolation function $g(t)$ is assumed proportional to the reactivity worth of the inserted part of rod Y during the measurement:

$$\boldsymbol{g(t)=\frac{1}{W_Y}\rho(t)}$$

where W_Y is the total rod Y integral worth. This assumption is based on experience and supported by measurements [5].

The measurements, presented in the paper, were performed on a particular core configuration of the TRIGA reactor of the "Jožef Stefan" Institute, which is presented in Figure 1. The flux depression factors for the four control rods for this core configuration were calculated [5] and are presented in Table 1.

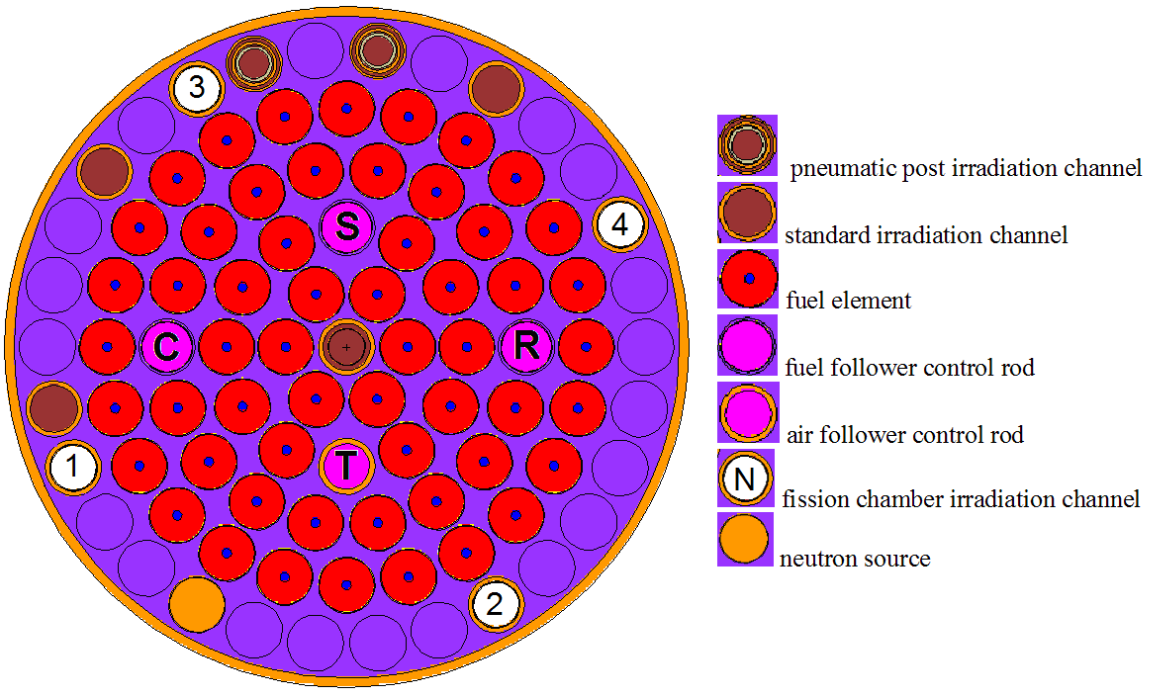


Fig 1: TRIGA core configuration. The control rods are labeled as (T) transient, (R) regulating, (C) shim, (S) safety. The ionization chamber is located behind the reflector (both are not visible in the figure) on the left side of the core. The Fission chambers are numbered.

Tab 1: Flux depression factors (TRIGA) [5]:

transient	(T)	1.025
regulating	(R)	1.116
shim	(C)	0.858
safety	(S)	0.975

By using the signal from the ionization chamber and the rod insertion method, which algorithms employ the point kinetic equations only, the redistribution of the flux has to be taken into account by using the above redistribution factors. The exact algorithm is complicated, in the first approximation this is done by multiplying the point kinetic result by the appropriate factor (Tab 1) for a specific control rod.

3. Using signal from mulitple fission cells

The drawback of using a signal from one ionization chamber is the necessary calculation of the flux form factors, which can be dependent also on core configuration. For this reason, in the frame of this work, the rod insertion measurements were performed by using four fission chambers instead; they were located symmetrically around the core (numbered in Figure 1). By using the average signal from all four fission chambers the difference of the signal from the average flux in the core is reduced with respect to the case of measuring the flux at only one location.

The differential values of the control rods were measured and calculated with the rod-insertion method by using signals from both described sources – a) signal from one ionization chamber or b) signal from four fission cells, located symmetrically around the core. Both results were compared in order to evaluate the new technique.

The differential control rod curves for the shim control rod (C) rod, measured and calculated by the rod insertion method for the four individual fission cells, are presented in Figure 2. On the figure the average curve by using the combined signal from all fission cells is also presented. The individual integral values are given in Table 2.

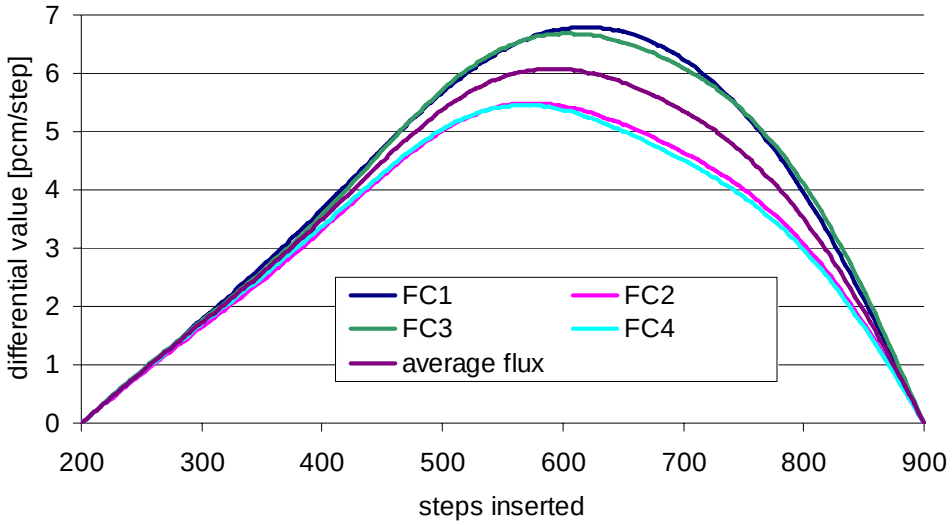


Fig 2: The differential control rod curves for the shim rod, measured and calculated by the rod insertion method for the four individual fission cells, and the curve by using the combined (average) signal from all fission cells.

Using four symmetrically positioned fission cells reduces the need for the flux form factor usage. The integral control rod worth can, however, still be determined from signals from individual fission cells.

Tab 2: Integral values for the transient rod as obtained by using individual fission cells and the combined signal from all fission cells.

	integral value of the shim rod (pcm)
Fission cell 1	2872
Fission cell 2	2367
Fission cell 3	2869
Fission cell 4	2362
combined (avereged) signal	2617

The value obtained with the ionization chamber, located behind the reflector and with the usage of the flux form factor amounts for the shim rod to 2707 pcm.
It can be seen from Figure 3 and the last table that the location of the fission cell with respect to the measured control rod is of crucial importance for the correct integral value; the two fission cells which are on the same side of the reactor as the measured shim rod and experience an excessive large change in neutron flux and hence a too large value of the calculated integral value, whereas for the other two cells, located on the far side of the pulse rod, the situation is reversed.

The comparison of the integral values in Table 2 shows, that the value obtained by using the combined signal from all fission cells is closer to the value obtained in the standard way with the use of the flux form factor than any of the individual values from the fission cells. Introducing the measurement with multiple fission chambers thus enables quick

measurements of the integral and differential value without having to calculate the flux form factor, which is configuration specific.

It should be noted, that further analyses of the work should focus on calculation of the individual flux form factors for all four of the fission cells.

4. Measurement Background / Noise

In case of the rod insertion measurements with one uncompensated ionization chamber, which has been the practice up to now, the value of the gamma background is substantial; since the reactor becomes highly subcritical during the measurement the background is often a few times larger than the signal due to the neutron flux – hence the background noise and exact determination of the background also become important. In case of measurements with fission cells the gamma background is much less important due to their insensitivity to gammas. Figure 3 displays a typical calculation of reactivity with the DMR for the two cases of obtaining the signal from an ionization chamber or fission cells.

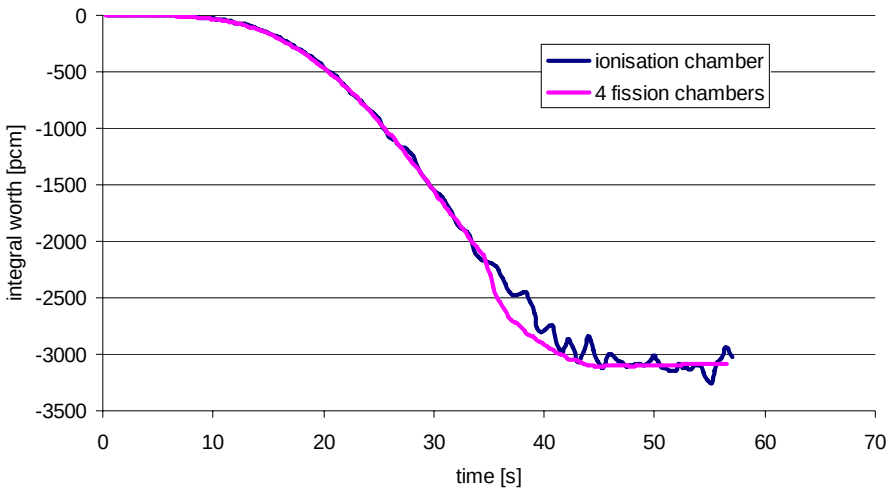


Fig 3: A typical calculation of the reactivity with the DMR for the two cases of obtaining the signal from ionization chambers or fission cells. The larger noise in the former measurement is visible.

As can be seen from Figure 3 the noise due to the fluctuation in the gamma background is greatly reduced by using the signal from fission cells and reflected in a smaller noise in the reactivity signal. This of course improves the accuracy of results and also enables their easier automatic evaluation.

5. Conclusions

The rod insertion method for measuring integral and differential worth of control rods using a digital meter of reactivity was extended by collecting the signal from four fission cells rather than the usual signal source from a single uncompensated ionization chamber. In this way the correct gamma background determination and subtraction, performed by DMR algorithms, became less important. The larger number of detectors was also found to reduce

the flux redistribution effects on the signal during individual control rod movements. Four fission cells, symmetrically positioned around the reactor core, were found to be a suitable configuration for control rod measurements using the rod insertion method, in which case the usage of flux redistribution factors is reduced or banished.

References

[1] J. Shaw, Reactor Operation. Pergamon Press, New York 1969.

[2] V. Merljak, I. Lengar, A. Trkov, *Comparison of Measured and CalculatedIntegral and Differential Reactivity Worth of Control Rods in a TRIGA Reactor*, this proceedings

[3] R. Jeraj, M. Ravnik, *TRIGA Mark II reactor: U(20) - Zirconium Hydride fuel rods in water with graphite reflector, IEU-COMP-THERM-003*, Nuclear Energy Agency, NEA/NSC/DOC(95)03, Paris 1999.

[4] J.J. Duderstadt, L.J. Hamilton, *Nuclear Reactor Analysis*, John Wiley & Sons, (1976).

[5] A. Trkov, M. Ravnik, H. Wirnmer, B. Glumac, H. Böck, H, *Application of the rod-insertion method for control rod worth measurements in research reactors*, Kerntechnik 60, 1995, pp 255–261.

[6] I. Lengar, A. Trkov, M. Kromar and L. Snoj, *Digital meter of reactivity for use during zero-power physics tests at the Krško NPP* (Uporaba digitalnega merilnika reaktivnosti pri zagonskih testih na ničelni moči v NE Krško),” *Journal Of Energy Technology - JET,* vol. 5, pp. 13-26, 2012.

FUEL MANAGEMENT AT ENEA TRIGA RC-1 REACTOR

L.FALCONI, M.CARTA, M.PALOMBA, M.SEPIELLI
Technical Unit for Nuclear Fission Technologies and Facilities, and Nuclear Material Management,ENEA
Via Anguillarese 301, 00123 S.Maria di Galeria

ABSTRACT
TRIGA Mark II reactor of ENEA's Casaccia Research Centre (in Italy named RC-1) reached first criticality in 1960. The reactor core was realized with 61 standard TRIGA fuel elements, aluminium cladded. In this condition, the reactor was operated until August 1965 at a steady state power level of 100 kW. In the summer of 1965, a program to increase the reactor power to 1 MW was established. The new criticality was reached in July 1967, after significant plant modifications, in order both to adapt the reactor to the new operative circumstances (including safety requirements) and to extend reactor flexibility in the widest research areas. The first configuration at 1 MW was obtained with 76 standard TRIGA fuel elements stainless steel cladded. The RC-1 Reactor is still operating and during these years, many fuel elements were used. In this paper we describe the facility, the infrastructures available for fresh and spent fuel storage and the operative experience accumulated during these years in the management of RC-1 nuclear fuel. In particular will be described also the last core configuration management, the control rod calibration, burn-up evaluation and spent fuel management and shipment. Also the actual situation of fresh fuel needs and availability will be focused.

1. TRIGA RC-1 Research reactor [1]

RC-1 is a thermal pool reactor, based on the General Atomic TRIGA Mark II reactor design, actually operating at the thermal power of 1Mw. The core, composed of 111 standard TRIGA fuel elements, is contained in an aluminium vessel, seven meters deep, filled with demineralised water. A cylindrical graphite structure around the core is the lateral reflector of the reactor. The biological shield is provided by concrete with an average thickness of 2.2 meters. The water inside the vessel provide first biological shield, neutron moderator and cooling mean. Thermal power is removed from the core by natural convection, and exchanged with the environment through two thermoydraulic loops, coupled by two heat exchangers and two cooling towers. The horizontal section of the core with graphite surrounding the core, a detail of the core with fuel elements, control rods and graphite dummies elements are shown in Fig 1. In Fig 2 the horizontal and vertical section of the reactor are shown, together with 3D section of the reactor with neutron channels.

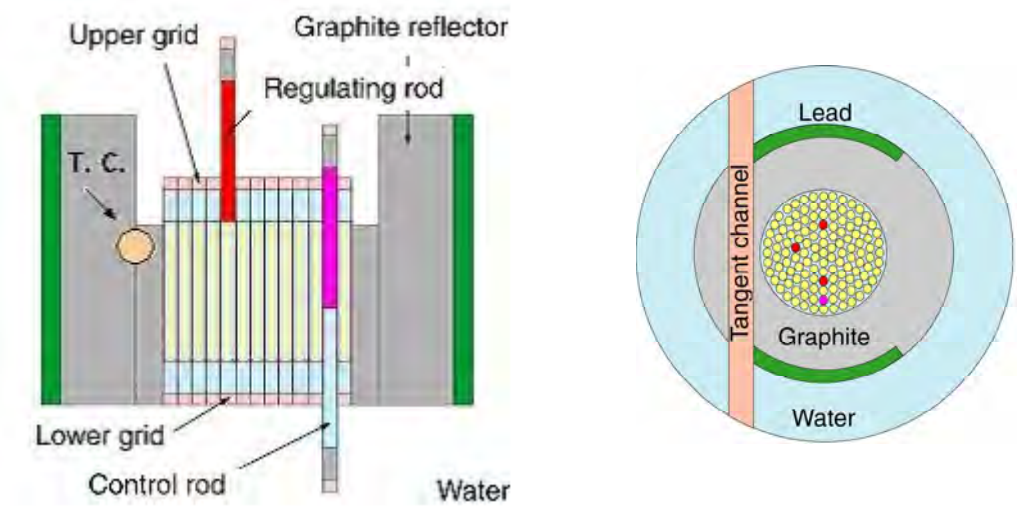


Fig 1 Vertical section of the core and standard configuration

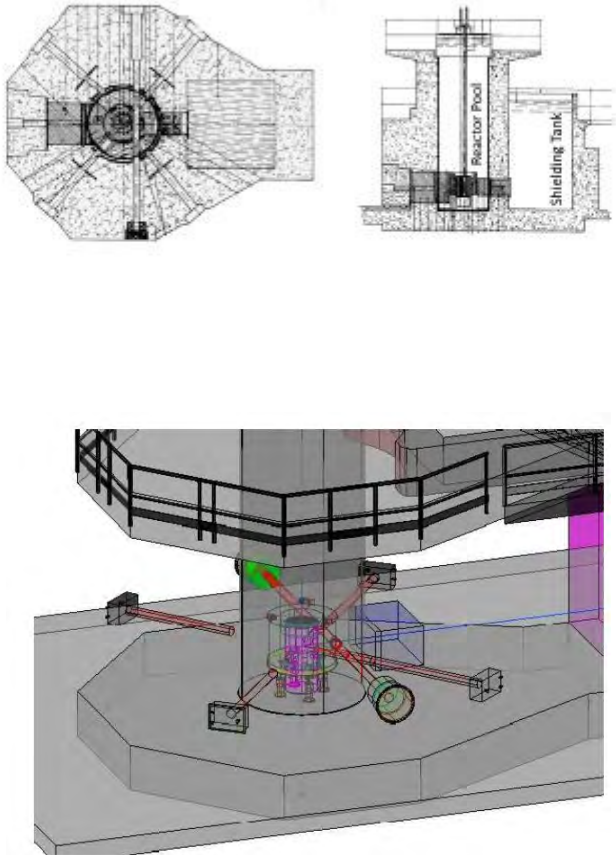


Fig 2 Horizontal and vertical section of RC-1 research reactor and neutron channels

The reactor is controlled by four boron carbide rods: three, stainless steel cladded, are *fuel followed* type (two shims and the safety rods) whereas the last, aluminium cladded, is the regulation rod.
The reactor is monitored by a starting channel, two wide range linear channels and one safety channel. One logarithmic channel operates between 10 W and 10 MW. Three X, γ monitors , two monitors for α and β contamination, and one for gaseous contamination of the air extracted from reactor hall and radiochemical lab ensure a complete information about the radiological situation on the plant and relative laboratories.
In Fig 2 it's possible to identify the experimental channels used for neutron extraction. Other irradiation facilities are the Lazy Susan, the pneumatic transfer system and the central thimble. In Tab 1 are summarized the neutron flux available for irradiation facilities at RC-1.[1][2]

Description	Neutron flux($ncm^{-2}s^{-1}$)
Lazy Susan	$2.00\ 10^{12}$
Pneumatic transfer system(rabbit)	$1.25\ 10^{13}$
Central channel	$2.68\ 10^{13}$
Thermal column collimator	$\sim 1\ 10^{6}$
Tangential piercing channel	$\sim 1\ 10^{8}$

Tab 1 Neutron flux available at RC-1 irradiation facilities

The RC-1 core, surrounded by a graphite reflector, consists of a lattice of TRIGA stainless steel standard fuel elements, graphite dummies elements, control and regulating rods. There are 127 channels on the upper grid plate available for these core components and the grid itself is divided into seven concentric rings. One channel houses the start up source (Am-Be) while two fixed channels are available for irradiation (central channel and *rabbit*).
The TRIGA fuel elements ,cylindrical shaped and stainless steel cladded (AISI 304 - thickness 0.5 mm) consists of a ternary alloy of H-Zr-U. The Uranium is 20% enriched in ^{235}U, and represents the 8.5%wt of the total fuel weight. Two graphite cylinders at the top and the bottom of the fuel rod ensure the upper and lower neutron reflection. The fuel element is provided externally with two fittings in order to allow the remote movements and the correct placements into the grid plates. Fig 3 shows the fuel elements details. [1][2]

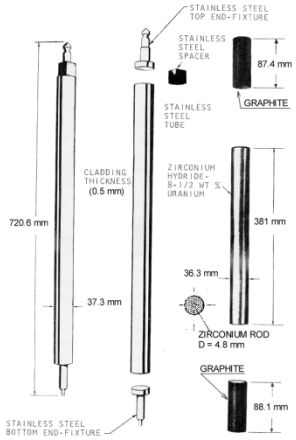


Fig 3 Fuel element details

The metallurgic alloy's stability is related to a variation of the total number of atoms less than 1%: The ternary mixture ensures that also in case of total burn up of ^{235}U present the total atom variation is 0.7%. Another feature regards the prescription that forces the removal of elements from the core if their burn up is higher than 35%: this is a condition linked to the U-

ZR-H lattice properties. From the point of view of the utilization, the reactor is mainly utilized for training, flux measurement and irradiation of neutron detectors.

2. Fuel and spent fuel management facilities at RC-1[1]

The spent fuel or, more in general, fuel rods can be stored in various facilities of RC-1: the racks into the reactor pool tank (Fig. 4), the stainless steel pits in the reactor building (Fig.5) and the external storage pool (Fig. 6). All the reactor storage facilities are wet type. The first type of storage consists of three racks each with twelve position : they are 3 meter deep in the reactor pool so that fuel can be stored, also for several month, in order to allow fission product decay. This facility is used in case of load/unload/configuration's change operations on the core. The second facility consist of five stainless steel pits located in the ground of the reactor all. The total capacity is of 95 elements. Each pit houses one circular rack three meters deep in the reactor building floor. Each pit is filled with demineralised water. The last storage facility is located out of the reactor building and consists of racks contained into a pool three meters deep. The total capacity is of 290 elements. This storage facility is totally "clean": it has never been used. The shielded tank near the reactor pool, as shown in Fig.2, has been licensed for temporary use as fuel storage: this is the case of fuel transfer that occured on the plant in 1999.[3] In this case the total capacity of the rack is of 144 elements.



Fig 4 Reactor pool storage rack

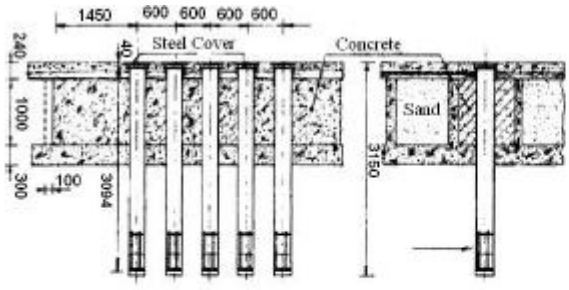


Fig 5 Spent fuel storage pits

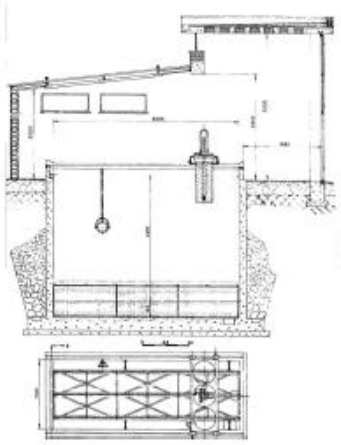


Fig 6 External pool storage

Element Id	Facility and position	Burn up(%)
SS 3848	Pit1C01	32,52
SS 3966	Pit1C02	33,86
SS 3843	Pit1C03	32,70
SS 3942	Pit1C04	33,71
SS 3846	Pit1C05	33,18
SS 3842	Pit1C06	33,18
SS 3844	Pit1C07	32,70
SS 3841	Pit1C08	34,77
SS 4032	Pit1C09	34,77
SS 3954	Pit1C10	34,77
SS 4045	Pit1C11	34,92
SS 3971	Pit1C12	33,85
SS10001	Pit2C06	0
SS10036	Pit2C02	0
SS10037	Pit2C04	0
SS10656	Pit2C03	0
SS10657	Pit2C01	0
SS10658	Pit2C05	0
ST10924	Ras3p01	0

Tab 2 Pits utilization

In Tab 2 the pit's racks actually utilized: it's to be noted that some positions are used for fresh fuel storage (Highlighted in red). One position (Rasp3p01)) is relative to rack into the fresh fuel storage. This facility is not described in the previous section: it's a rack of 114 elements located in the reactor building. It's used just for fresh fuel.

3. Core configuration management

Since March 2012 the TRIGA RC-1 operates with core configuration labelled 260. Previous configuration, labelled 250, has been analyzed highlighting fuel burn-up , ^{235}U consumption and total Pu production, other the mean energy production for each element, so to decide how to change core configuration. In January 2006 the core configuration 250, shown in Fig 1, begins to operate providing , until the 12th of March 2012, about 508 MWD of energy. Fig. 7 shows the burn up into each ring distinguishing single element (that is every position into the core). Exact evaluation and daily operations indicate that the reactivity excess value wasn't sufficient (it should be 4.9 % Δk/k [1]) to ensure weekly program for irradiation and forced to start a core reconfiguration driven by the analysis shown in Fig. 7. Histograms provide an intuitive description of burn up distribution into the core. It's useful to group elements by ring and identify elements with a burn up between 25% and 35 %: by prescription burn up, either of a fuel element either of the fuel followed control rod, cannot be higher than 35%. It's to be noted the high burn up value of elements in ring B, the inner one.

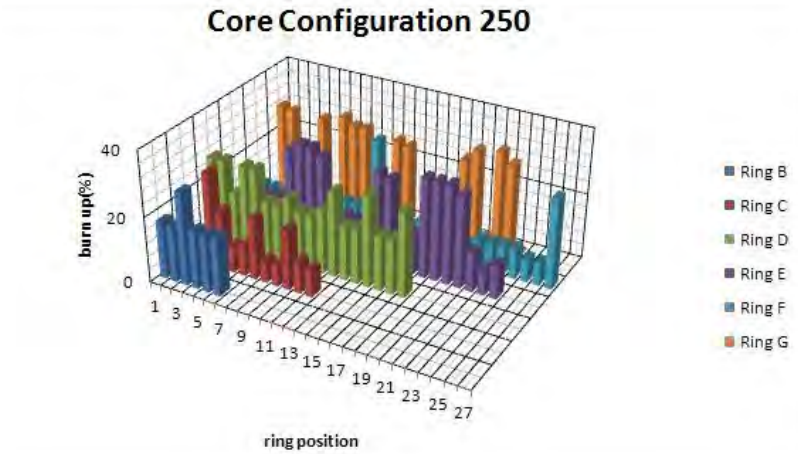


Fig 7 Fuel elements burn up in function of fuel ring position

The core management is based on a fuel element position change so that low burned elements are placed in the inner rings. High burned elements should replace the changed one in the outer ring: fresh fuel occupy inner position, with higher flux values (Fig 8). The result of such permutation in fuel's position is described in the following Table 1.

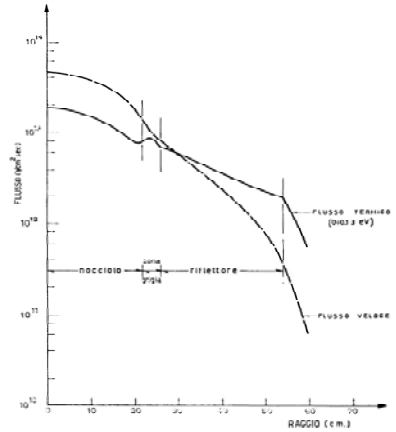


Fig 8 Thermal and fast neutron flux in the RC-1 Core

Practically we start from element in B1 position removing, putting it into the pool rack (Fig. 4) and substituting with one element in the outer ring (G10). Following permutations depends on place left empty. Changes goes on until we reach a configuration ensuring the right amount of reactivity excess. Check on the critical configuration at low power will confirm us the opportunity to adopt the specific configuration, throw an estimate of the excess core reactivity. Fuel element movement requires the use of the racks in the reactor pool for temporary storage.

	CONFIGURATION 250		CONFIGURATION 260
element Id	ring position	burn up(%)	ring position
SS 7208	G10	0.43	B01
SS 9999	G34	0.44	B04
SS 9669	F06	6.13	C12
SS 9526	F02	7.15	D17
SS 9516	F18	9.04	E10
SS 8934	E03	11.97	E20
SS 9489	E10	12.14	F02
SS 9673	C12	8.35	E03
SS 8928	D17	16.82	F06
SS 9491	B04	17.80	F18
SS 8936	B01	17.51	G34
SS 8545	G33	27.46	G10
SS 6633	E20	30.45	G33

Tab 3 Fuel element position changes

The effectiveness of this procedure, in the specific case of RC-1 and its operating history, can be put in evidence by the relative few changes necessary to obtain a new core configuration.

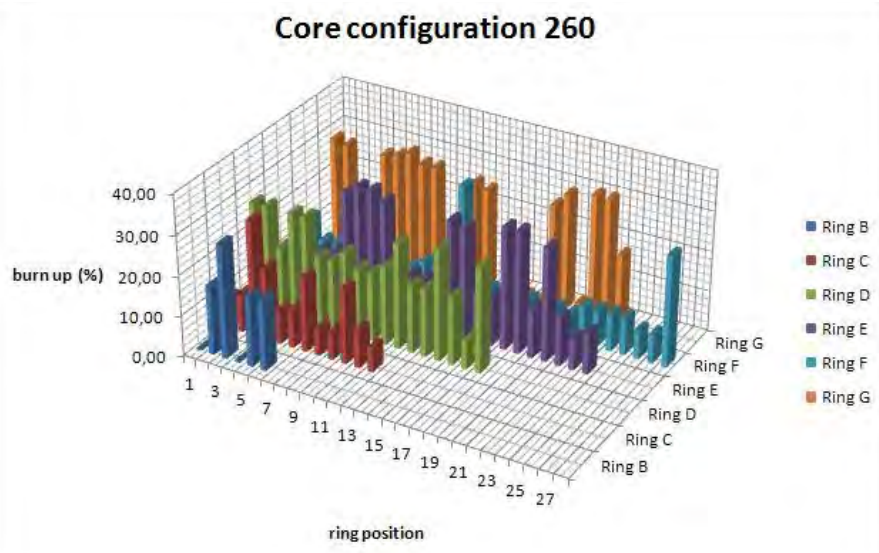


Fig 9 fuel element for ring position after core configuration change

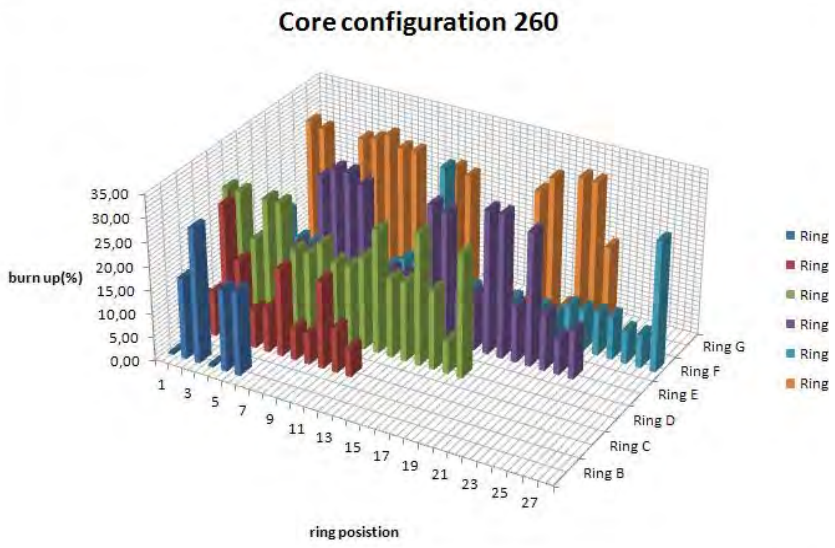


Fig 10 Fuel element as a function of ring position (situation updated to 31-12-2013)

Fig. 8 and Fig. 9 demonstrate that RC-1 core configuration 260 is characterized by few MWD produced. More in detail, Tab 4 describes the composition of fuel elements and the relative burn up and energy produced. The actual isotope composition is relative to the end of 2013 and is referred to Fig.9.

		Initial isotope composition(gr)		Burn up(%)	Produced energy (MWD)	Actual isotope composition		
		^{235}U	^{238}U			^{235}U	^{238}U	Pu
Fuel still in the core	Total	4170	16858	N.A.	3.48	3533	16795	62
	Average per element	37.57	151.87	0.14	0.03	31.8	151.3	0.56
Fuel stored in pits	Total	449	1811		121	297	1796	15
	Average per element	37.42	150.92	33.7	10.10	24.79	149.69	1.22

Tab 4 Parameter of RC-1 fuel elements

RC-1 operation relative to configuration 260 (April 2012- December 2013) is limited to 3.48 MWD produced. This activity has been analyzed in Fig 10 for the last two years. Fig 11 and Fig 12 represent the total reactor operating time divided by specific activity.

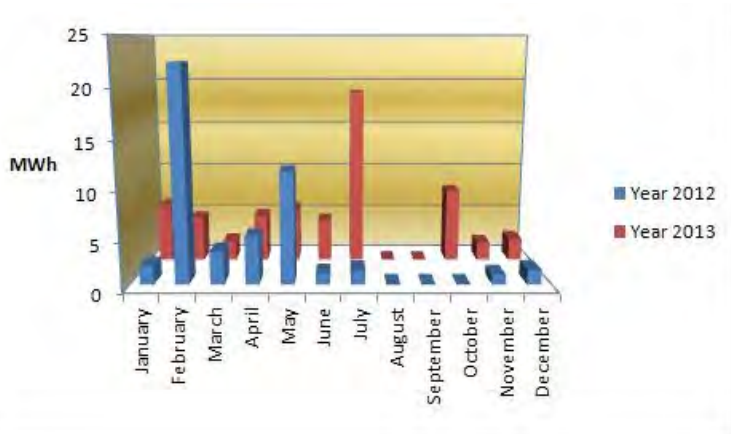


Fig 11 Energy production during 2012/2013

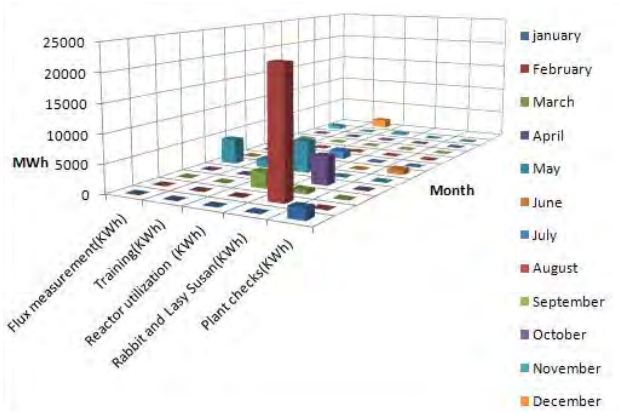


Fig 12 Reactor utilization during 2012

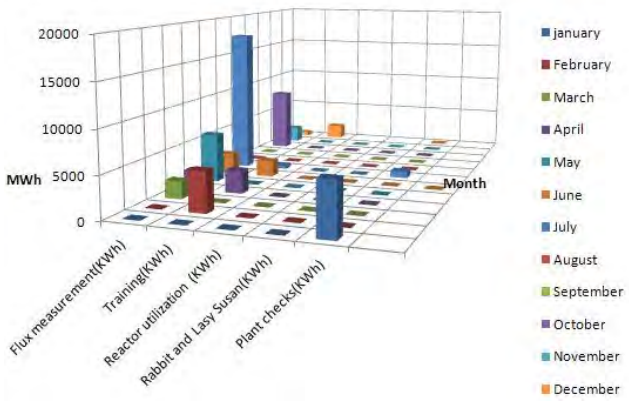


Fig 13 Reactor utilization during 2013

During 2013 an increasing in flux measurement and training hours occurred, while hour dedicated to reactor utilization by universities or industries for material irradiation had a stop.
Training continues to hold an important role in reactor activity. The increasing operating time dedicated to flux measurement indicates the aim to give the reactor RC-1 a clear 'identity card' so that it can be correctly understood by stakeholders. It's a necessary internal activity because data on flux and dose rate regarding RC-1 facilities date back to more than 20 years and completeness is not ensured. Plant checks, that is all activities requested to ensure calibration and prescription verification, are always an important activity.

4. Conclusions

During 2014 the reactor RC-1 will be utilized for training of students on specific topics related to reactor. Flux measurements will continue in order to obtain a detailed map of the reactor flux in all the experimental facilities. This is very important for utilization of RC-1 by the industry especially for material irradiation. The last activity is also supported by MCNP calculation in order to confirm experimental data and improve staff capabilities.
The actual fuel management is sufficient to ensure a long term operation of RC-1. There is no need for immediate refuelling of the core and the actual store capacity of pits and wet storage are more than sufficient for the future activity planned for the reactor. Italy has no National Long-Term Nuclear Waste Site yet and there are also no indications about decommissioning the reactor before 2016 when the USA Foreign Research Reactor Spent Nuclear Fuel (FRRSNF) acceptance programme ends.
For this reason Triga RC-1 (and Italy in general) is strongly interested in the continuation (or renewal) of USA - FRRSNF policy.

5. References

[1] DI PALO, L. I RC-1 Reattore 1MW – progetto definitivo e rapporto di sicurezza , CNEN Centro Studi Nucleari Casaccia , 1966
[2] Dipartimento FPN, ENEA , Manuale di Operazione del reattore RC-1 1MW, C.R. Casaccia
[3] M. PALOMBA, R. ROSA The Management of TRIGA spent fuel ENEA RC-1 research Reactor - Management and Storage of Research Reactor Spent Nuclear Fuel – Proceedings of a Technical Meeting held in Thurso, United Kingdom, 19–22 October 2009 - IAEA 2013
[4] M.CARTA Re-examination of the fuel burn up level of the TRIGA RC-1 Casaccia Reactor ENEA Technical Report

THE RESULTS OF REPLACEMENT OF THE PUMPS IN PRIMARY FUEL CHANNEL COOLING CIRCUIT IN MARIA REACTOR

G. KRZYSZTOSZEK, K. PYTEL
Department of Nuclear Energy, National Centre for Nuclear Research
A. Sołtana 7, 05-400 Otwock – Poland

ABSTRACT

The research reactor MARIA is operated at the National Centre for Nuclear Research. The multipurpose high flux research reactor MARIA is a water and beryllium moderated reactor of a pool type with graphite reflector and pressurized channels containing concentric tube assemblies of fuel elements.
In September 2012 was launched MARIA reactor conversion from HEU fuel to LEU fuel based on fuel fabricated by AREVA-CERCA. Within the period October 2012 – August 2014 it is anticipated to change in a systematic way the spent fuel elements of the HEU type for the LEU fuel elements. New fuel elements of CERCA type are to be characterized among other things by larger hydraulic resistances in relation to the MR fuel type used so far. To maintain the reactor parameters it was needed to increase cooling water flow in the individual fuel channel by around 25-30% . Bearing this is mind the replacement of primary cooling pumps has been done within the period June-August 2013 and we achieved the results which enable for full core conversion in MARIA reactor.

1. Introduction

The high flux research reactor MARIA is a water and beryllium moderated reactor of a pool type with graphite reflector and pressurized channels containing concentric tube assemblies of fuel channels.
In the framework of the Reduced Enrichment for Research and Test Reactors (RERTR) in National Centre for Nuclear Research there has been led from 2005 the works over conversion program from HEU to LEU.
In view of reduction of enrichment under assumption for preserving to maximum extent the physical parameters of the reactor it was proposed to use the silicide fuel (U_3Si_2) with uranium density of 4.8 g/cm^3, which substantially surpassed the uranium density of oxide fuel (UO_2), to be 2.8 g/cm^3. The silicide fuel to be proposed has been proved up to very high levels of burnups and has been widely used in more than twenty research reactors in the world.
The fuel assemblies for MARIA reactor differ from hitherto being applied fuel elements U_3Si_2 (fuel plates) in the world. To use the new fuel type in MARIA reactor it was required to carry out the validation of the new fuel elements in MARIA reactor. Supplier of the silicide fuel is the French company Areva (CERCA Romans). The main point of the certification procedure for the new fuel for MARIA reactor was to perform the irradiation of two test fuel subassemblies (LTA, Lead Test Assemblies) under normal operation conditions of the reactor [1].
In September 2012 started the MARIA reactor conversion process from HEU (MR) to LEU (MC) fuel. Until now about 60% of reactor core was converted from HEU to LEU fuel and full core conversion is predicted till the end of August 2014.

2. Modernization of the fuel channel cooling circuit

2.1. Main assumptions for modernization of the fuel channel cooling circuit

In 2009 the MARIA reactor conversion program on low enriched fuel was extended to upgrading of the pump system in the fuel channel cooling circuit. Considering the thermal and hydraulic characteristics of the core with full core conversion we have agreed with ANL specialists the necessity for replacement of the currently used primary coolant pumps for the new more powerful ones.
One of the necessary conditions to proceeding the conversion of MARIA reactor core for low enriched MC fuel is to provide the flow rate on the level of 30 m^3/h through the channel of the core containing 25 fuel channels under higher by around 25% pressure drop in fuel channel.
The necessity to replace the pump facilities has consequences to consider the mode for the shutdown and emergency cooling. In the present system for that goal the main pumps operating at half rated revolutions are being used which is ensured by using the two-speed motors. This kind of solution – beyond certain profits (minimalization of number of facilities, reliability and effectiveness to be confirmed by experience gained for many years) – it also possess faults of which the major one is based on the fact that the intensity of flow rate in the shutdown regime substantially exceeds the level to be needed for reactor core cooling after shutdown.
The above arguments incline to chargé the shutdown task and emergency reactor cooling task to a separate shutdown pumps system with parameters to be matched to the real needs to be arisen from the course of reactor power shutdown. This system includes three parallels branches of the shutdown assemblies. Each loop is equipped with isolation gate valves at inlet and outlet of the pump, a check valve at inlet and outlet of the pump, a check valve at pump outlet and a bypass ensuring to maintain normal coolant flow through the pump under the locked check valve at pump outlet.

2.2 The characteristics of the new fuel channel cooling circuit.

Bearing in mind these assumptions on order of the IAE a conceptual project of upgrading the fuel channel cooling circuit for MARIA reactor has been developed [2]. Schematic design of the fuel channel cooling system after upgrading is shown in Table 1.

Parameter	Pumps	
	Main units	Shutdown units
Number of installed assemblies	4	3
Number of operating assemblies	2	2
Flow rate [m^3/h]	400	70
Pressure head [H_2O m.col.]	128	12
Demand of power supply [kW]	170	3.1
Motor power [kW]	200	4

Tab 1: Parameters of the pump assemblies of the MARIA reactor fuel channel cooling circuit to be upgraded.

During the normal operation of the system there are operating two main pumps and two residual power pumps. The remaining pump assemblies are in reserve. Cooling capacity of the two main pumps (of 800 m^3/h) provides to cool the reactor containing the 25 MC fuel channels. The residual power pumps during the normal reactor operation time provide the coolant circulation only through the bypass pipingThe start-up of the main pump is performed by the operator, however, the two main pumps are to be setting in power each one from another transformer. The main pumps are to be in motion in turn. Then the operator puts into operation the shutdown pumps to be supplied from the emergency power source. The main pumps operate in automatics with the valve gates installed behind each main pump. When the main pump is disengaged the gate valve behind the pump is closed. Setting the pump in

motion causes an opening of the gate valves up to full opening. Disconnection of the main pump brings about to close the gate valve in automatic mode.
Forwards the normal operation conditions of the cooling system is to be included reactor shutdown cooling to be realized by means of residual power pumps. Disconnection of the main primary pumps after reactor scram causes a reduction of pressure in the pressure header of the circuit and when the pressure difference between the pressure and suction headers of the main pumps will reach the pressure head of the shutdown pump the water from the pressure ferrule of the shutdown pump flows to the delivery collector of the reactor cooling system ensuring the cooling of the fuel channels.

3. Safety analysis for modernization of the cooling circuit

Modernization of the cooling circuit for the reactor fuel channels does not cause any changes within the scope of safety analyses at the steady states, because all parameters (power, coolant flow rate, temperature) remain to be unchanged with regards to the terms described in [1] and [4]. However, it is necessary to verify the analyses for unsteady states associated with triggering of the cooling mode from the main into the shutdown one for which an extreme case refers to the total loss of the basic power supply for the motors of main circulation pumps. The course of this process will undergo a change due to that:

- the characteristics of the coastdown for the main pumps (various moments of inertia of the pumps assemblies);
- the magnitude of the target flow rate in the shutdown cooling mode.

Among reactor unsteady states to be analyzed in connection with conversion of the core from MR fuel on MC fuel of significant importance are those states in which the specifics of MC fuel, i.e. the terms for heat exchange and balance of fission products activity is manifested. It is also necessary to take into account the modification of the fuel channels' cooling circuit. Due to that the verification of analyses is needed for the following groups of unsteady states:

- Decay of coolant flow rate in the channel circuit.
- Blocking of flow rate through the LTA fuel channel and in a consequence its burnout.
- Loss of tightness of the fuel channel cooling circuit.
- Insertion of the positive reactivity and relevant to this matter the changes of power during reactor start-up and at operation on full power.

In work [3] there are included the analyses for unsteady state after decay of power supply in the main pumps (Wafapomp) after their modernization for both types of fuel and for two options of the residual cooling: two or one shutdown pump is on. Beyond the following assumptions there were taken into consideration:

- catalogue inertia of Wafapomp assemblies,
- maximum number of fuel channels in the core – 25 (conservative approach),
- coolant flow rate for the MR fuel - 25 m^3/h, whereas for the MC fuel – 30 m^3/h,
- water temperature at the inlet to the channel – 45°C,
- water pressure at the inlet to the channel – 1.7 MPa,
- rated power of the fuel channel – 1.8 MW,
- accident signal after pressure drop to the level 1.4 MPa,
- water flow rates through the stabilizer and the filter branch – 30 m^3/h i 2.5 m^3/h.

In Fig. 1 are presented the calculation results in the form of time-dependent courses of changes of the following parameters [4]:

- coolant flow rate through the channel with accounting for the total flow rate and the flow to be induced by the operation of residual power pumps,
- fuel channel power (total and the component to be added by the residual power after shutdown),
- maximum cladding temperature of the fuel element (in the MR fuel it is related to the inner cladding of the third fuel tube and in the MC fuel – to the 6^{th} fuel),

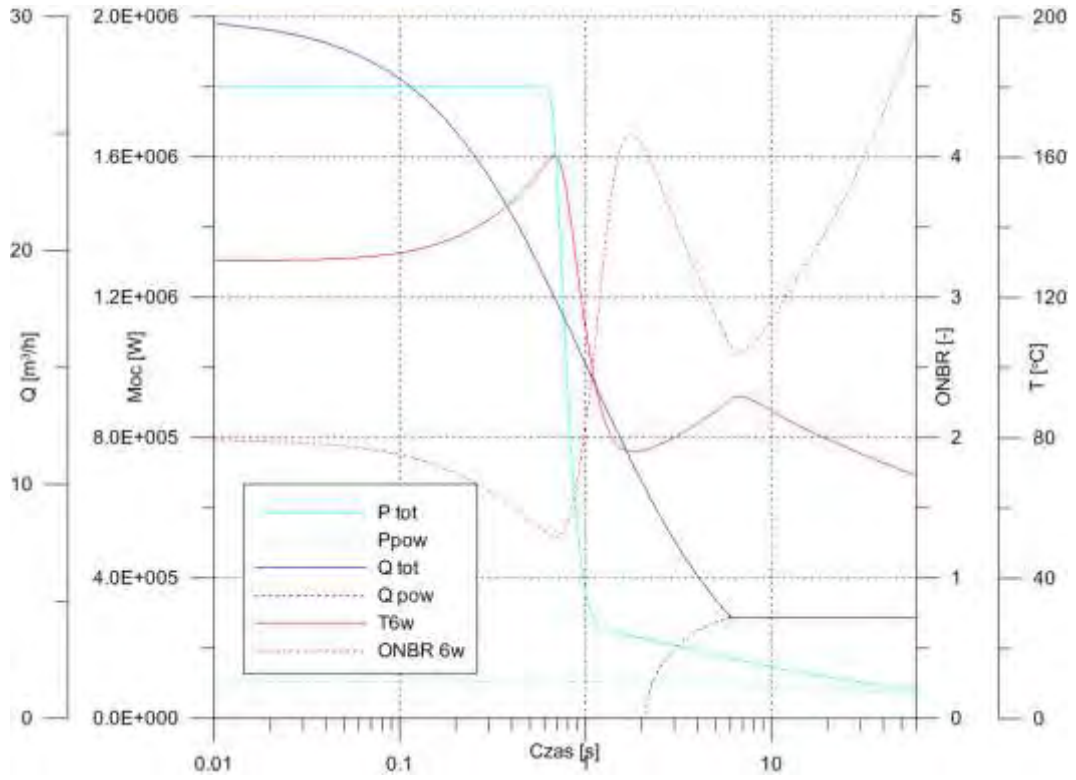


Fig 1. Residual cooling after reactor shudown – 25 MC FA. – 2 reactor shutdown pumps

4. Installing of the pumps and equipments.

The fabricator and supplier of primary and shutdown pumps was the factory GRUPA POWEN WAFAPOMP SA located in Warsaw, PL. Simultaneously POWEN-WAFAPOMP is a contractor responsible for the delivery of the remained hardware to be mounted in the installation.
The final protocol for the ultimate acceptance of installation and the transfer to the operation was signed on 27.08.2013.
The primary and shutdown pumps were delivered into the construction site at the end of QI. 2013. The delivery included the hardware as follows:

1. Four primary pump assemblies of the 12A32-P7 type,
2. Three shutdown pump assemblies of the 8A20P type.

The fittings, cables I&C devices, construction materials were delivered earlier.
The installation work could only be launched in June 2013 because the reactor had to operate due to the molybdenum production obligation.
The installation work has been developing in accruing rate from the onset of project realization. At first it have been removed the existing components of hardware like old primary pumps, fittings, parts of piping, measuring works and miscellaneous. Next the assembling work has been distributed among different industrial branches such as: technological and thermal and machines branch, building and constructing branch, electric and I&C branch.
Finally during August 22÷25, 2013 the 72 hours trial was launched.

5. Develop the instrumentation and control system for the new pumps

Control system and diagnostics of pumps for the fuel channel cooling circuit carries out the functions as follows:

- Controls the operation of the main pumps, the wedge valves as well as shutdown pumps of the fuel channels' circuit furnishing the logics ensuring the safety of reactor operation,

- Collects, processes, records and displays on the monitor screen Fig. 2. the data informing on pump' operation run, i.e.:
    - temperature of pumps' and engine's bearings,
    - vibration levels of pumps and bearings,
    - powers and currents to be consumed by engines,
    - flow rates of the shutdown pumps,
    - other facility signals;
- informs over pressure drop or lowering of the barrier liquid,
- generates over alarms to inform on abnormalities of pumps or measuring systems,
- produces an emergency signal or warning signals to be transmitted to the SAIA system.

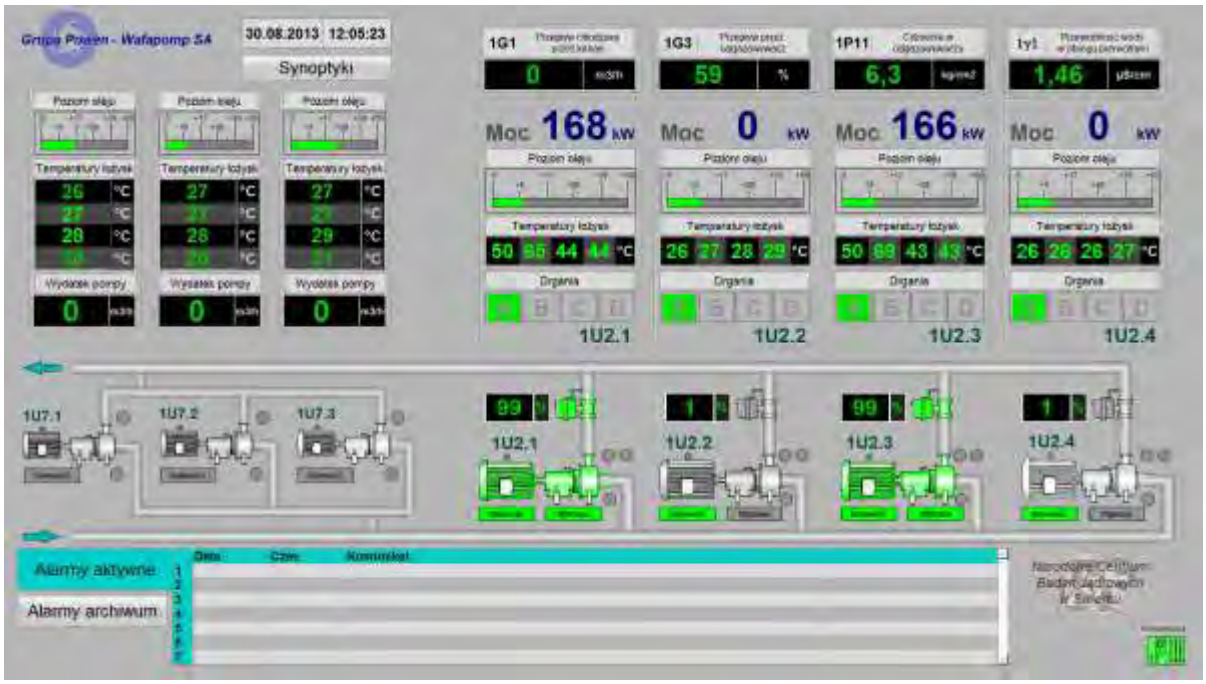


Fig 2. Head side of the control system and pumps' diagnostics of the fuel channel circuit.

6. Parameters of the fuel channels' cooling circuit.

After obtaining an approval from the Regulatory Body on September 9, 2013 the reactor has been set into operation and currently it is mainly being used to producing the radioisotopes, in particulary Mo-99. There were installed 12 fuel channels of LEU type and 12 fuel channels of HEU type in configuration shown in Fig. 3.

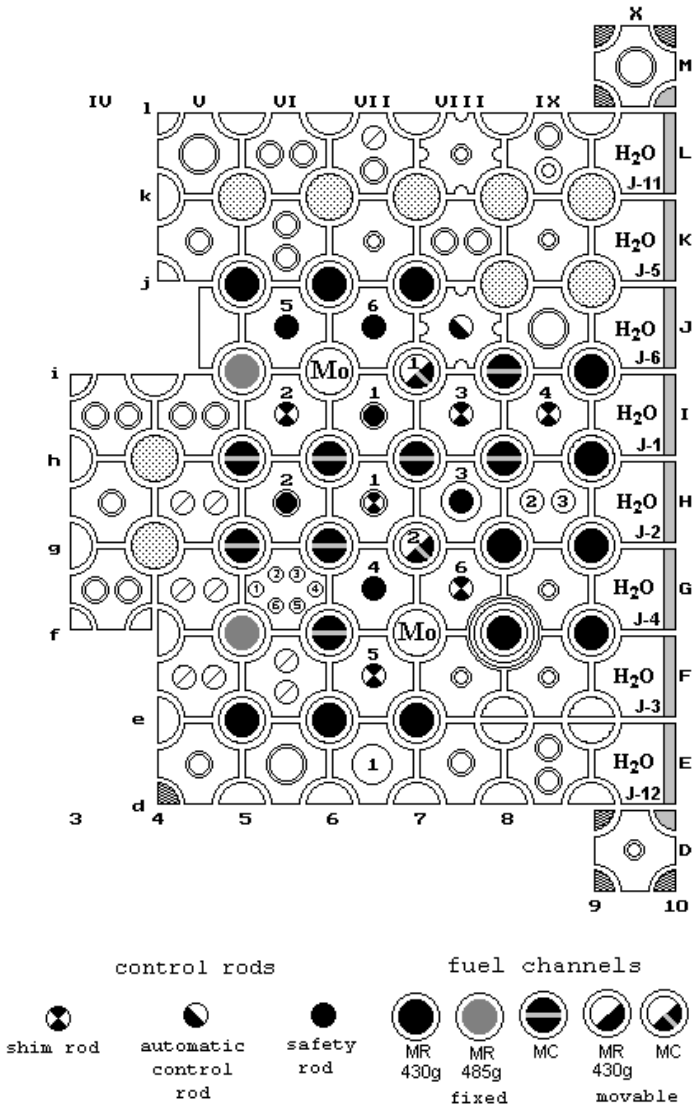


Fig 3. Reactor MARIA core configuration

The reactor operated on power ca. 23MW (19MW – the power being removed by the fuel channels' cooling circuit; 4 MW the power being removed by the pool cooling circuit).
The basic parameters of fuel channels' cooling circuit were as follows:

- Total flow rate – 695 m^3/h
- Temperature at the reactor inlet – 42,5 °C
- Temperature at the reactor output – 66,8 °C
- Pressure in the recator outlet – 1,7 MPa
- Coolant flow rate through the fuel channel – 30 m^3 /h.

The achieved parameter in the fuel channels' cooling circuit make possible to pursue the process of reactor conversion from the highly enriched fuel of the HEU type into the fuel of LEU type.
In comply with program of reactor operation in Q.IV 2013 and 2014 it is anticipated to complete the MARIA reactor conversion in August 2014.

7. Conclusion

The trial tests of the pumps and fittings have been successfully performed and based on the acceptance monitoring all the hardware associated with modification of fuel channel cooling system the President of National Atomic Energy issued the first permit to pursue the reactor

operation for the three isotope production cycles. On completing the trial isotope production cycle the NCBJ was obliged to transmit the post execution documentation over the primary pumps' modification of MARIA reactor fuel channels' cooling circuit to the Regulatory Body. Besides it should also be delivered the verified Annex for the Safety Analyses Report supplemented by all changes associated with primary pumps' modification. After acceptance of this documentation President of National Atomic Energy Agency issued the final permit for further reactor operation.

References

[1] Annex 2009/1 to ERB MARIA reactor. Irradiation testing of MC fuel. June 2009.
[2] Technical Description 1 18914_01. ENERGOPROJECT®-WARSZAWA.2011
[3] W. Mieleszczenko: Preliminary analysis of main circulation pumps shutdown consequences after loss of the basic electrical supply and post-shutdown cooling model for MARIA reactor fuel elements cooling circuit after modernization, Raport B-12/2012.
[4] Operational Safety Report of MARIA Reactor, 2009.



Safety and Security of Research Reactors

TRANSIENT ANALYSIS OF THE IR-8 REACTOR MIXED LOADINGS DURING CONVERSION FROM HEU TO LEU

V. NASONOV, Y. PESNYA, A. SIDORENKO
National Research Centre «Kurchatov Institute» (NRC KI)
1, Akademika Kurchatova Sq., 123182 Moscow - Russia

N. HANAN, P. GARNER
Argonne National Laboratory (ANL)
Building 208, 9700 South Cass Avenue, Argonne, IL 60439-4842 - United States

ABSTRACT

As a part of studies related to conversion of the IR-8 research reactor to Low Enriched Uranium (LEU) fuel NRC “Kurchatov Institute” with support from ANL is performing transient analysis of the IR-8 reactor mixed HEU-LEU loadings. Analysis of possible accidents is carried out using a new version of the PARET/ANL code specially created for cases with different types of fuel in the core. This paper includes the results of calculations for equilibrium HEU and LEU cores and for mixed HEU-LEU core of the following postulated pre-emergency accidents: spontaneous withdrawal of one of the most effective CPS rods, unplanned insertion of positive reactivity during reloading, influence from experiments and experimental facilities.

1. Introduction

As a part of studies related to conversion of the IR-8 research reactor to Low Enriched Uranium (LEU) fuel NRC “Kurchatov Institute” with support from ANL has made an calculation estimation of the reactor safety during conversion to LEU fuel. This article includes the results for analysis of accidents with positive reactivity insertion (RIA) at the IR-8 reactor during conversion from HEU to LEU for starting equilibrium loading with HEU, mixed HEU-LEU loading and for equilibrium loading with LEU fuel. RIA calculations were carry out using the new version of the PARET/ANL code [1], in which the opportunity of analysis reactor loadings with different types of fuel was added.

2. Description of analyzed loadings and initial data

To analyze the consequences of accidents with the insertion of positive reactivity at the IR-8 reactor during conversion from HEU to LEU the equilibrium loading AZ09 [2], mixed loading HLEU05 [3], consisted of 8 FAs with HEU and 8 FAs with LEU, and also the equilibrium loading 37M [4] with LEU were considered. During previously performed calculations using MCU-PTR code [5], implements the Monte-Carlo method, all necessary neutronic and thermal-hydraulic parameters of this loadings required for estimation with PARET/ANL code were obtained. Values of fuel burnup and FA’s power (Fig. 1), and also the detailed power density distribution per height and azimuth for each FA allowed to determine the most heat-stressed sector of FA. For the loading AZ09 (HEU-EC) the most heat-stressed FA #E13 located in 3-2 cell. For the loading HLEU05 (MIX) the most heat-stressed FA # E16 with HEU located in 2-4 cell, the most heat-stressed FA # M05 with LEU located in 3-2 cell. For the loading # 37M (LEU-EC) the most heat-stressed FA # AD13 located in 3-2 cell.

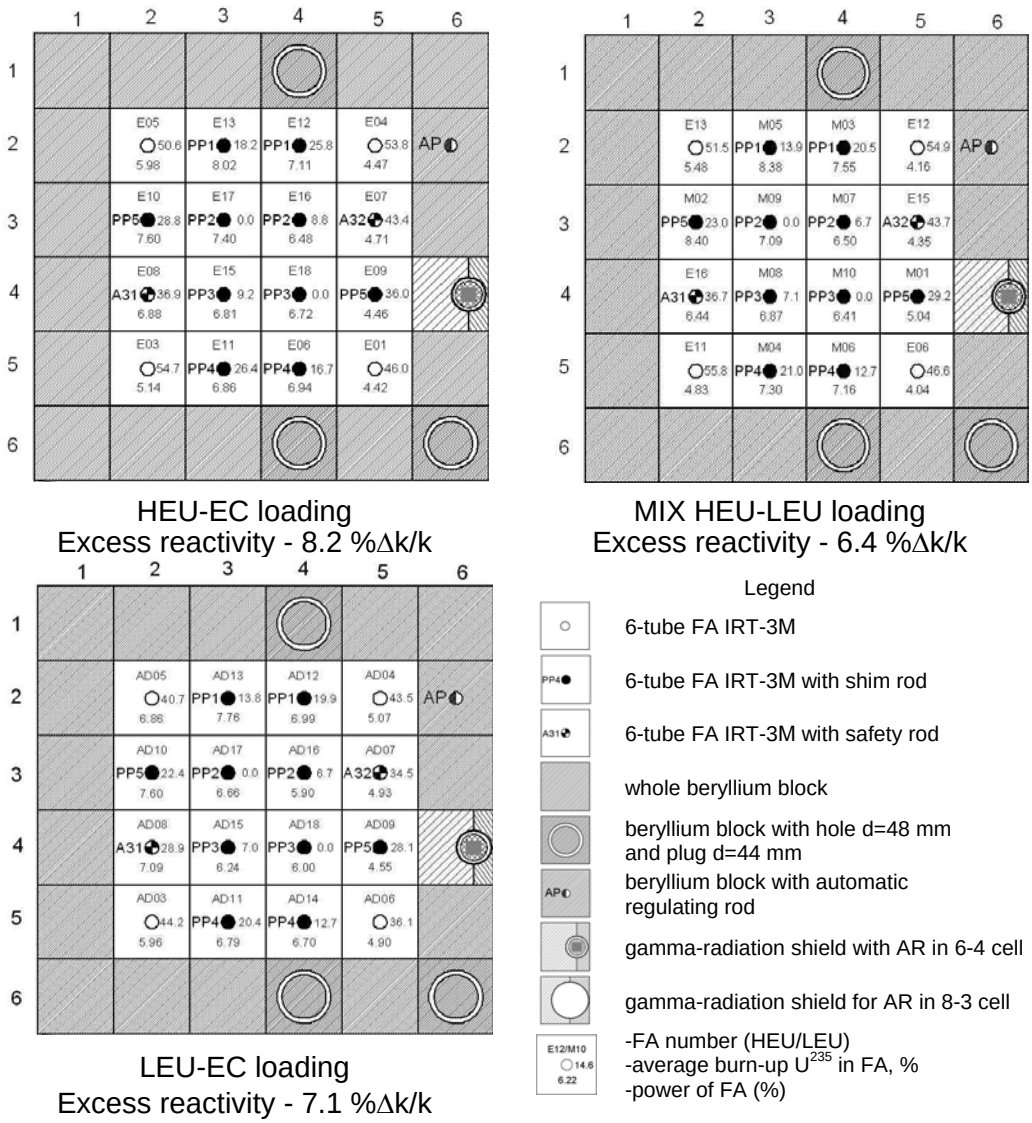


Fig 1. Burnup of ^{235}U and FAs power for HEU and LEU loadings (BOC)

Also for analyzed loadings using the MCU-PTR code integral and differential characteristics of CPS rods [2], reactivity coefficients and parameters of neutron kinetic (Table 1) were obtained.

Parameter	Loading		
	HEU-EC	MIX	LEU-EC
Fuel temperature (Doppler), $/K	-0.00013	-0.0024(HEU-LEU) -0.00012(HEU) -0.0022(LEU)	-0.0032
Coolant temperature, $/K	-0.0157	-0.013(HEU-LEU) -0.004(HEU) -0.009(LEU)	-0.012
Coolant density, $/%	-0.37	-0.41(HEU-LEU) -0.10(HEU) -0.31(LEU)	-0.43
Prompt neutron generation time (Λ), μs	81	74	67
Effective delayed neutron fraction (β_{eff})	0.00764	0.00752	0.00740

Tab 1: The reactivity coefficients, prompt neutron generation time and effective delayed neutron fraction

At the IR-8 reactor at the emergency system response all CPS rods are falling in the core by gravity. Fig. 2A shows integral characteristics of shim and safety rods of IR-8 reactor in critical state at the emergency system response. It was assumed in calculations that rods fall under its own weight with a constant acceleration, i.e. the negative reactivity insertion is not linearly. (Fig. 2B).

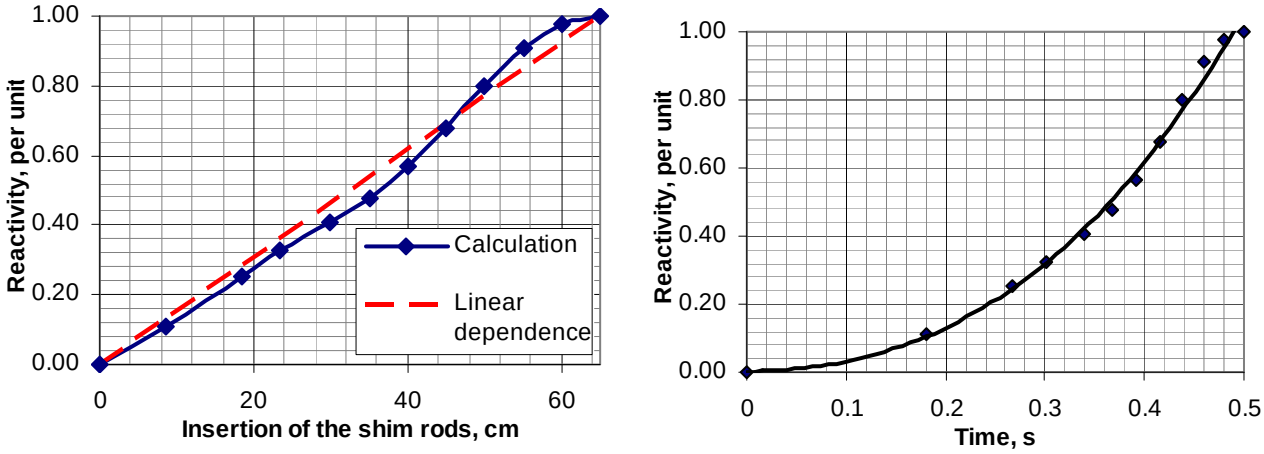


Fig. 2. Integral characteristics of shim and safety rods of IR-8 reactor at the emergency system response

RIA calculations were performed with the following conditions:

- Coolant temperature at the core inlet T=50 °C.
- Coolant pressure at the core inlet P= $1.90 \cdot 10^5$ Pa.
- Coolant pressure at the core outlet P= $1.74 \cdot 10^5$ Pa.
- Mass flux in the most stressed FA channel (between 1-st and 2-nd FE) W_m=2175 kg/s·m^2.
- Fraction of heat generated in fuel is 0.9.
- Scram signal delay – 0.3 s.
- Time of falling CPS rods – 0.5 s.
- Overpower trip setting equals 20%.
- Period trip setting equals 10 s.

3. Spontaneous withdrawal of one most effective group of CPS control rods

Spontaneous withdrawal of one most effective CPS member consisting of two absorber rods is possible, for example, when sticking two groups of relay or sintering of two transistors being in the drive control circuit. Figure 3 and Table 2 show the calculated for loadings HEU-EC, MIX, LEU-EC changes in the reactor power, maximum clad temperature and coolant temperature at the core outlet which can be achieved as a result of spontaneous withdrawal of two shim rods until the scram by the signal of 20% power level excess. It was assumed in the PARET/ANL code calculations that the input rate of positive reactivity is 0.07 $/s (allowable input rate of positive reactivity), although, in fact, in the IR-8 reactor does not exceed ~0.03 $/s. Positive reactivity insertion equals 8.9 $ (HEU-EC), 7.9 $ (MIX), 7.7 $ (LEU-EC). Full reactivity worth of CPS rods falling from critical state are 20.9 $ (HEU-EC), 21.1 $ (MIX), 19.4 $ (LEU-EC).

Obtainer results allow to make a conclusion that in this case the departure of nucleate boiling (DNB) will not appear and FEs damage will not occur because the margins to the critical heat flux are ~4.2 (HEU-EC), ~3.8 (MIX), ~4.2 (LEU-EC).

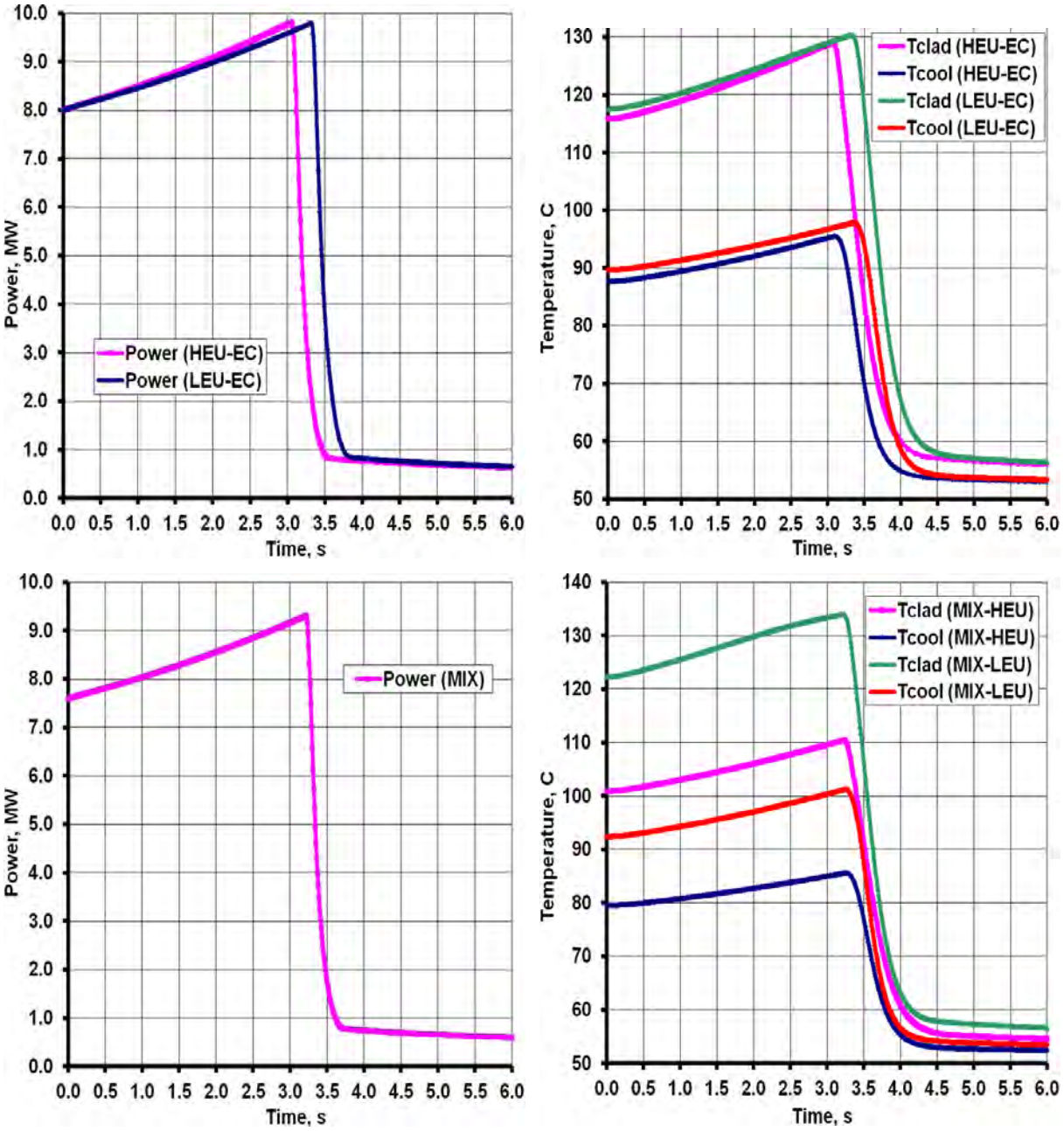


Fig. 3. Reactor power, peak cladding surface temperature and the peak coolant exit temperature at spontaneous withdrawal of one most effective group of CPS control rods

Loading	Reactor power, MW		Peak cladding surface temperature, °C		Peak coolant exit temperature, °C	
	Steady state	Max	Steady state	Max	Steady state	Max
HEU-EC	8.0	9.8	116	129	88	96
MIX	7.6	9.3	122 (LEU)	134 (LEU)	92(LEU)	101 (LEU)
LEU-EC	8.0	9.8	118	130	90	98

Tab 2: Calculation results of the spontaneous withdrawal of one most effective of CPS control rods consequences

4. Unplanned insertion of positive reactivity during reloading

Calculations of the reactor power change in time were carried out for the case when as a result of series personnel mistakes during the loading of FA into the core in critical state the device failure appears and FA falls into the core.
It was assumed in the calculations that the reactor is in critical state with power of 5 kW and in the regime of natural convection, overpower trip setting for this case equals 16 kW level. Time of FA falling in the core is 0.5 s. Maximum reactivity worth of FA equals 4.6 $ (HEU-EC), 3.5 $ (MIX), 3.3 $ (LEU-EC). Negative reactivity, inserted into the core by emergency protection signal (with allowance for two safety rods failure) equals 22.1 $ (HEU-EC), 18.2 $ (MIX), 17.3 $ (LEU-EC).
The results of the calculations of FA falling into the core subsequences at the period scram are presented in Fig. 4.

As it seen, the reactor power is increasing from 5 kW up to 88 kW for HEU-EC, 32 kW for MIX and up to 29 kW for LEU-EC. This accident does not lead to a significant change of temperature parameters. Due to increasing of natural convection level the increasing of cladding surface temperature is not occur and therefore the departure of nucleate boiling (DNB) will not appear and FEs damage will not take place.

5. Influence (reactivity insertion) from experiments and experimental facilities

According to Radiation Safety Standards at the reactor operation on power the insertion of positive reactivity less than $0.3\beta_{eff}$ is allowed. It was assumed that in this case tool failure occurs and experimental device falls into the core. Changes in reactor power were calculated under the following: inserted positive reactivity equals 0.3 $, full time of positive reactivity insertion is 0.5 s. Negative reactivity inserted into the reactor at the emergency protection signal equals: 20.9 $ (HEU-EC), 21.1 $ (MIX), 19.4 (LEU-EC).

The calculated changes of reactor power, peak cladding temperature and the coolant temperature by insertion of positive reactivity and scram by the overpower protection system are shown in Fig. 5 and Tab 3.

Loading	Reactor power, MW		Peak cladding surface temperature, °C		Peak coolant exit temperature, °C	
	Steady state	Max	Steady state	Max	Steady state	Max
HEU-EC	8.0	10.6	116	131	88	97
MIX	7.6	9.9	122 (LEU)	135 (LEU)	92(LEU)	103 (LEU)
LEU-EC	8.0	10.3	118	132	90	99

Tab 3: Calculation results of the unplanned positive reactivity insertion during experiments consequences

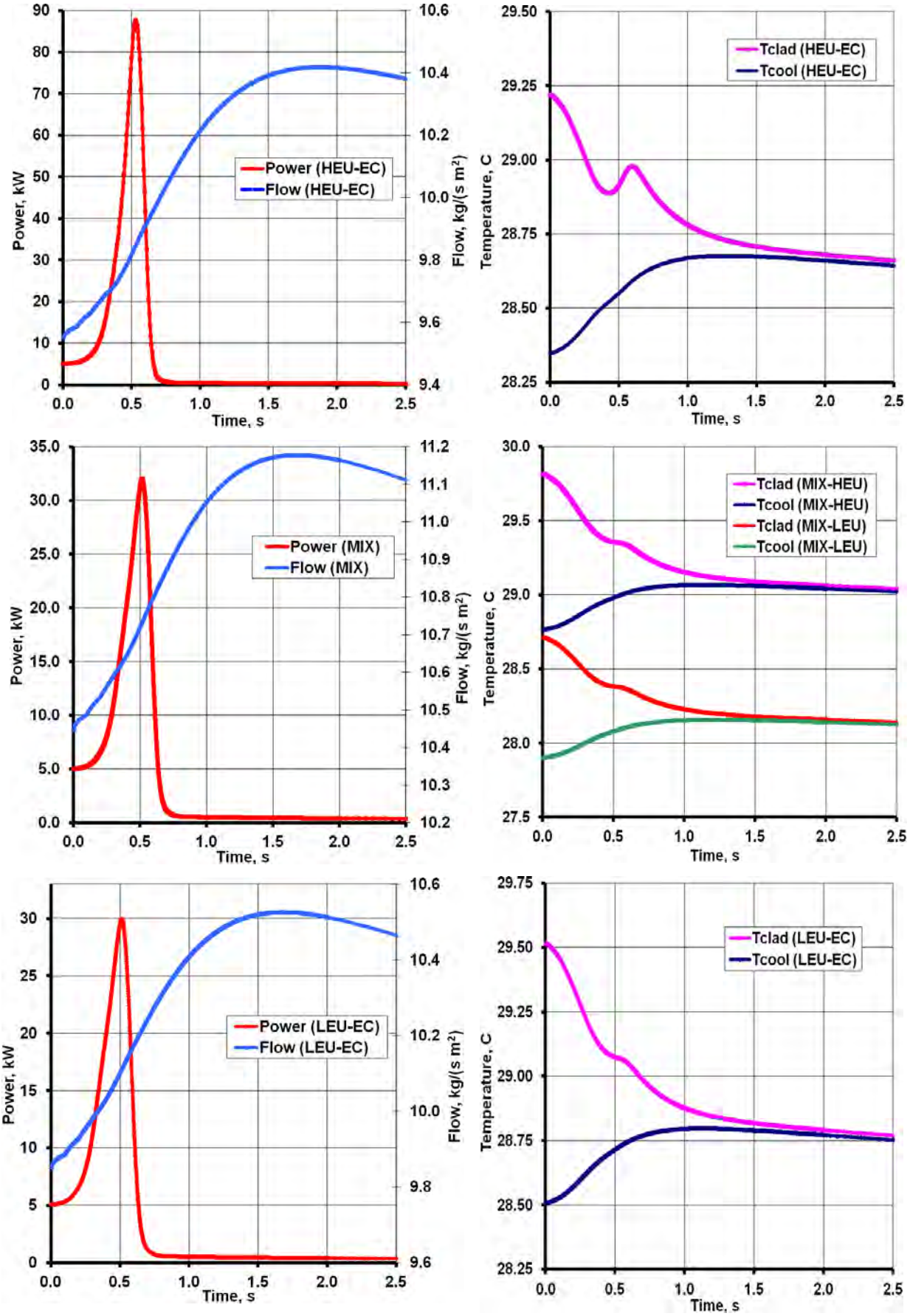


Fig. 4. Reactor power, coolant mass flux, peak cladding temperature and coolant temperature at FA falling into the core and occurring the period scram.

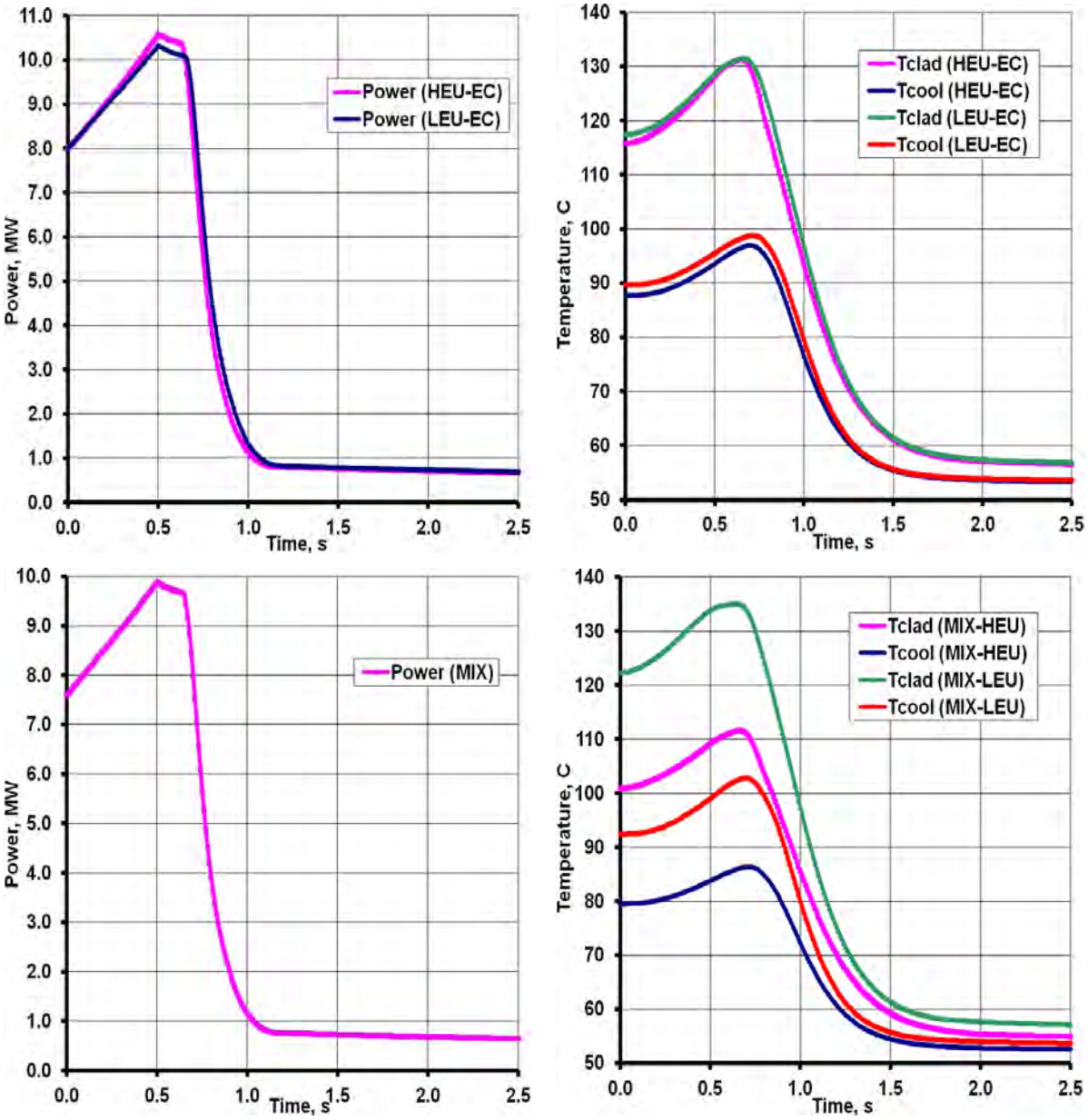


Fig. 5. Reactor power, peak cladding temperature and coolant temperature at reactivity insertion during an experimental device fall into the core

The graphs show that at the moment when positive reactivity fully inserted the reactor power reaches its maximum and then until the beginning of control rods falling gradually decreases under the influence of temperature reactivity effects. Analysis of results allow to make a conclusion that in this case the departure of nucleate boiling (DNB) will not appear and FEs damage will not occur because the margins to the critical heat flux are ~4.0 (HEU-EC), ~3,6 (MIX), ~4.1 (LEU-EC).

Conclusions

Analysis of accidents with positive reactivity insertion (RIA) at the IR-8 reactor during conversion from HEU to LEU for equilibrium HEU and LEU loadings and also for the mixed loading showed that the calculated coolant temperature reaches a value of not more than 103 °C, which does not exceed the saturation temperature of 119 °C at a pressure in the core $1.9 \cdot 10^5$ Pa. Cladding temperature only briefly (in first second) can reach values up to ~135 °C. The mixed HEU-LEU and full LEU core results are very similar to the HEU core results with exception of FA drop at critical.

Analysis of the consequences of accident shows that fuel elements damage in the conversion of IR-8 reactor to LEU fuel in the considered situations will not happen.

References

[1] A.P. Olson, A Users Guide to the PARET/ANL Code Version 7.6 beta_130417, Argonne National Laboratory, 2013.

[2] D. Erak, V. Nasonov, Y. Pesnya, A. Taliev, Y. Dubovskiy, A. Sidorenko (NRC KI), N. A. Hanan, P. L. Garner (ANL). Plan and preliminary calculations for IR-8 reactor during conversion to LEU fuel. Report on International Meeting “Research Reactor Fuel Management”- RRFM-2013. Saint Petersburg, Russian Federation, April 21 – 25, 2013.

[3] D. Erak, V. Nasonov, A. Taliev, Y. Pesnya, A. Sidorenko. Progress in assess safety of the IR-8 reactor during conversion to LEU fuel. Report on International Meeting “Research Reactor Fuel Management”- RRFM-2014. Ljubljana, Slovenia, March 30 – April 3, 2014

[4] D. Erak, V. Nasonov, Y. Pesnya. State of work on calculation feasibility of the IR-8 reactor conversion to LEU fuel. Proceedings of the 2012 International Meeting on RERTR. Warsaw, Poland, October 14-17, 2012.

[5] N.I. Alexeev, E.A. Gomin, S.V. Marin, V.A. Nasonov, D.A. Shkarovsky. MCU-PTR Code for Precision Calculation of Pool and Tank Types Research Reactors. - Atomic Energy, vol. 109, is. 3, 2010, p. 123-129.

Acknowledgment: This work was supported by the U.S. Department of Energy, National Nuclear Security Administration, Office of Defense Nuclear Nonproliferation, under contract DE-AC02-06CH11357.

PROGRESS IN ASSESS SAFETY OF THE IR-8 REACTOR DURING CONVERSION TO LEU FUEL

D. ERAK; V. NASONOV; A. TALIEV; Y. PESNYA; A. SIDORENKO;
Y. DUBOVSKIY; V. PAVLENKO, L. SMIRNOV; V. DANICHEV
National Research Centre «Kurchatov Institute
1, Akademika Kurchatova Sq., Moscow, 123182, Russia

ABSTRACT

As a part of the RERTR program NRC KI is performing the Studies to Establish the Feasibility of Converting the IR-8 Research Reactor to LEU Fuel with financial support from U.S. Department of Energy. In 2012 year the work to Assess Safety of IR-8 Reactor during Conversion to LEU Fuel has been begun. Currently the radiation safety analysis for the IR-8 reactor during normal operation and possible accidents was finished. The calculation of the radionuclides release and radiation dose to the population in the vicinity of the reactor has been performed. As a next step in assessing safety of the IR-8 reactor during conversion NRC KI began the analysis of postulated accidents.

1. Introduction

After finishing the feasibility studies of the IR-8 research reactor conversion to LEU fuel [1] NRC “Kurchatov Institute” under the RERTR program began to evaluate the IR-8 reactor safety during conversion to LEU [2, 3].

2. Tasks for assessing the safety of the IR-8 reactor during conversion to LEU

Currently the studies to assess safety of IR-8 reactor during conversion to LEU fuel are continued. These studies include implementation of the following tasks.

Neutronic and thermal-hydraulic calculations

(a) calculations of the main neutronic and thermal-hydraulic parameters for the equilibrium loading of the core with HEU; (b) calculations of the main neutronic, reactivity and thermal-hydraulic parameters for different loadings of the core during conversion form HEU to LEU.

Radiation safety

(a) calculations of gaseous radioactive emissions into the environment during normal operation; (b) analysis of the possible effects of the IR-8 reactor radiation to the population; (c) calculate accidental release of iodine radionuclides in the environment associated with the melting of a FA.

Analysis of possible accidents

Analysis is to be performed for various transients (RIA, LOFA and LOCA), including design basis and beyond design basis as required by the Regulatory Body (RTN). The list of initiating events is made on the basis of the existing SAR of IR-8 reactor for the HEU fuel, and the recommendations for research reactor safety of the IAEA.

3. Neutronic and thermal-hydraulic calculations

For neutron-physical calculations the MCU-PTR code with database MDBPT50 was used [4]. The MCU-PTR code with database MDBPT50 is certified by the Scientific and Technical Center for Nuclear and Radiation Safety of the RF Federal Environment, Engineering and Nuclear Supervision Service for calculation neutronic characteristics of the IR-8 research reactor taking into account fuel burn-up, absorber burn-up in control rods, beryllium reflector poisoning and control rods insertion. For steady-state thermal-hydraulic calculations used the ASTRA code [5].

3.1. Initial loading of the equilibrium core consisting of HEU

Taking the BOEC #35 [2] as a starting loading, calculations for eight equilibrium cycles with the reactor core consisting of HEU in the regime of partial reloading of 2 FAs with new calculating model were carried out using MCU-PTR code. On the results of the neutronic and thermal-hydraulic calculations of equilibrium loadings of the reactor in the regime of partial reloading the characteristics (neutron, thermal hydraulic and reactivity) of equilibrium core with HEU (AZ09 loading), which was chosen as a starting point for reactor conversion to LEU (Figure 1) .

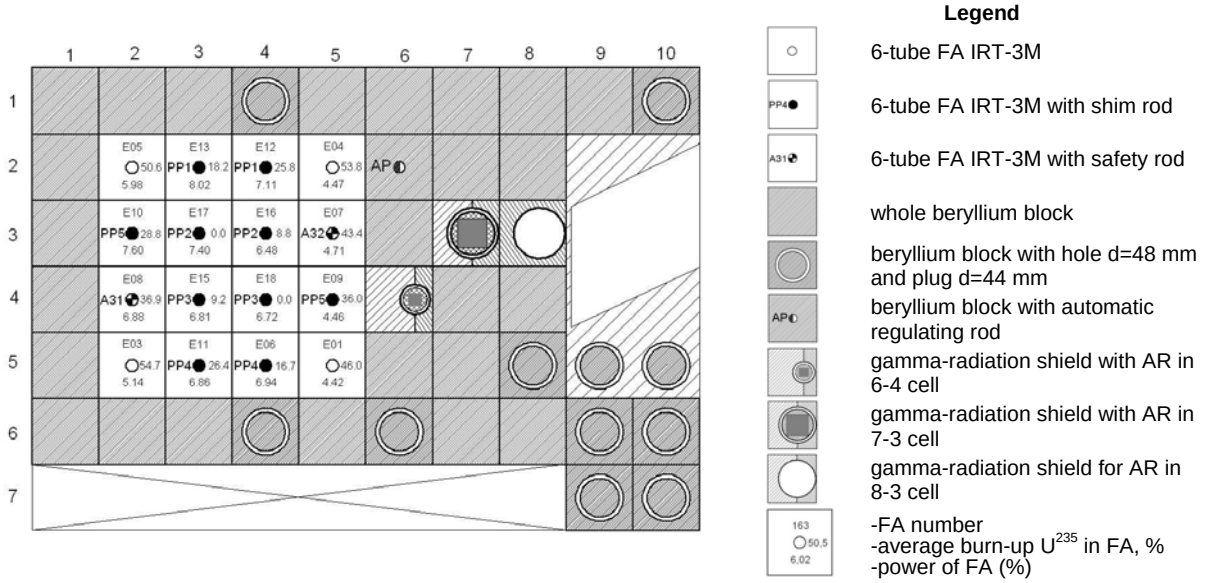


Fig 1. The values of fuel burnup and FAs power for the loading with HEU (BOEC)

3.2. Loadings of the core during conversion from HEU to LEU

Conversion of the core from 16 FAs with HEU to LEU is to be carried out in 8 transitional cycles replacing two FAs in each cycle. Calculations of the fuel burnup in FAs and excess reactivity were performed for transitional loadings from HEU to LEU (# HLEU01, # HLEU02, # HLEU03, # HLEU04, # HLEU05, # HLEU06, # HLEU07) and first loading with LEU (# LEU08).

The thermal-hydraulic analysis was performed for four mixed loadings and the first loading with LEU in steady state. It was obtained that for mixed loadings # HLEU01, # HLEU03 and # HLEU05 reactor power should be limited to the value of 7.0, 7.5 and 7.6 MW accordingly. The safety margin to onset nucleate boiling (ONB) for these power levels exceeds the minimum allowed value of 1.4. The carried-out analysis for loading # HLEU07, first loading with LEU and the equilibrium loading of the core with LEU showed that operation of the IR-8 reactor with power of 8 MW is allowable.

For four mixed loadings # HLEU01, # HLEU03, # HLEU05, # HLEU07, for the first loading with LEU (Figure 2) and for the equilibrium loading of the core with LEU (Figure 3) the main neutronic and reactivity characteristics were calculated.

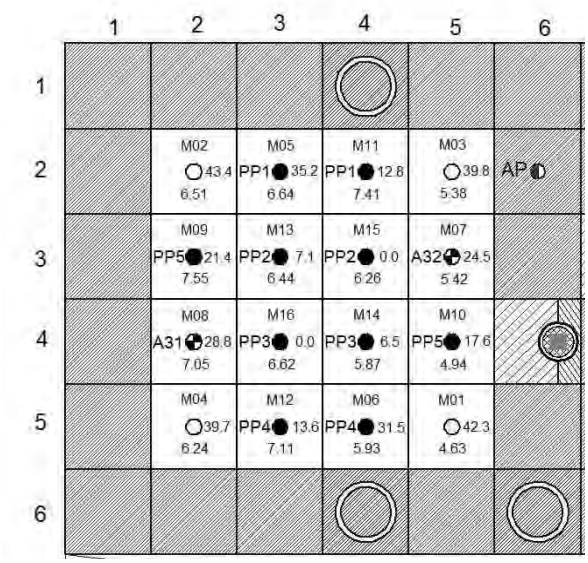


Fig 2. The values of fuel burnup and FAs power for the first loading with LEU (BOC)

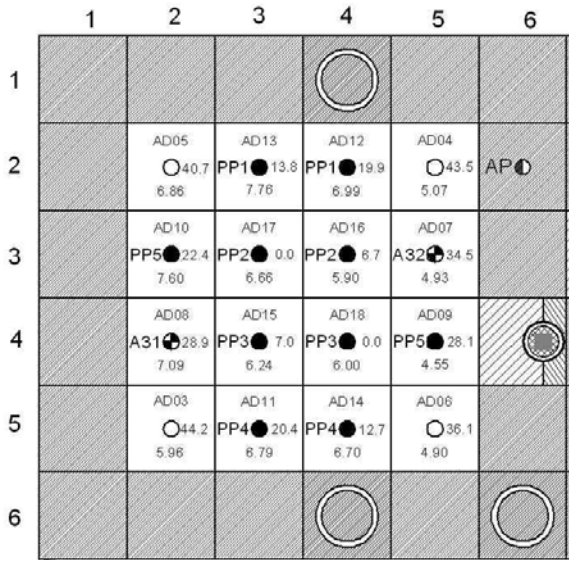


Fig 3. The values of fuel burnup and FAs power for FAs with LEU (BOEC)

4. Radiation safety

For calculations of fission product activity the MCU-PTR code was used. To evaluate the radiation situation and the expected irradiation to the population at long radioactive releases into the atmosphere a certified NUCLIDE code is used. To calculate the radiation environment and the expected exposure of the population in the short-term release of radioactive substances into the atmosphere certified calculation program NUCLIDE - ACCIDENT is used. NUCLIDE and NUCLIDE - ACCIDENT codes are parts of GARANT-UNIVERSAL software package [6-9] for calculations of atmospheric air pollution by radioactive substances.

At normal operation of the IR-8 reactor the radiation doses to the population due to external and internal exposures, even at the nearest border of the NRC "KI" vicinity will not exceed the value of 10^{-2} mSv/yr, which is essentially lower than allowable value.

The calculation results of radiation consequences of the accident showed that total annual individual dose to the population living in the vicinity of IR-8 reactor will not exceed the value of 0.32 mSv/yr, which is essentially lower than allowable value equal to 1 mSv/yr. Therefore no additional protective actions are required.

From the analysis of radiation effects at normal operation and accidents it follows that conversion from HEU to LEU fuel will not lead to decrease in the radiation safety of the reactor.

5. Analysis of possible accidents

For transient analysis the PARET/ANL Version 7.6 [10] code was used. Calculation analysis of the unbalanced rod position situation, criticality of “fresh” and spent FAs with HEU and LEU fuel in the fuel storage of the IR-8 reactor and FAs efficiency calculations were performed using the MCU-PTR code. The analysis of radiation consequences of the accidents was performed for initial loading of the core with HEU, four mixed loadings HEU-LEU, the first loading with LEU and for the equilibrium loading with LEU.

5.1. Analysis of the consequences of pre-emergency accidents

The list of considered initiating accidents for the analysis of the consequences of pre-emergency conditions includes:

1. Spontaneous withdrawal of one most effective CPS rod.
2. Failure of primary pumps due to loss of electrical power

3. Unplanned insertion of positive reactivity during reloading.
4. Loss of the normal electrical power supply.
5. Unbalanced rods position.
6. Cold water insertion into the pool.
7. Influence from experiments and experimental facilities; i.e. reactivity insertion from unplanned movement of experiments.

Analysis of the obtained results showed that calculated coolant temperature in considered situations reaches the value not above 103 °C, which does not exceed the saturation temperature equal to 119 °C at pressure of $1{,}9 \cdot 10^5$ Pa in the core. The cladding temperature shortly (in first second) can reach up to ~135 °C.

Except the case of FA drop at the reloading, the results for mixed HEU-LEU loadings and loadings with LEU are very similar to the results for loading with HEU.

5.2. Analysis of the consequences of design basis accidents (DBA)

The list of considered initiating accidents for the analysis of the consequences of design basis accidents includes:

1. Criticality of “fresh” and spent FAs in the fuel storage.
2. Failure of FE cladding in the core.
3. Full instantaneous blockage of the coolant flow in a FA.
4. Primary coolant flow reduction.

It was obtained that condition of K_{eff} <0.95 at the storage of "fresh" and spent FAs with HEU and LEU fuel in the IR-8 reactor is fulfilled. Based on the calculation results and taking into account the regulations the safety of "fresh" and spent FAs with HEU and LEU fuel storage in the storage pool and temporary storage cells of the IR-8 reactor.

The results of FE damage calculation showed that radiation consequences of HEU or LEU FE cladding failure will be noticeable against activity of the fission products which have got in the coolant due to the surface FE cladding contamination by uranium, at the total area more than 20 cm^2. Thus sensitivity of control methods of fission product activity levels in the coolant and in ventilated air from underdeck space allows to define existence of FEs with cladding failure. At excess of admissible level of activity in the circulation circuit of the coolant the reactor shuts down automatically and cladding failure monitoring is carried out.

The calculation results of radiation consequences of the accident showed that at blockage of coolant flow through a FA with LEU, doses to the personnel on the territory of the NRC KI and to the population living in the vicinity of IR-8 reactor will be similar to the same accident with HEU. The total annual individual dose to the population living in the vicinity of IR-8 reactor is essentially lower than allowable value equal to 1 mSv/yr.

The calculation analysis of the IR-8 reactor primary coolant flow reduction showed that departure from nucleate boiling (DNB) will not occur, because the margin to critical heat flux is not less than 4.7. A short-term boiling on the surface is possible, because the temperature of FE claddings in the "hot spot" during first seconds is close to the temperature of ONB. Consequently, in case of the primary coolant flow reduction, even without shim and safety rods insertion into the core the FE damage will not occur.

CONCLUSIONS

From the performed transient analysis (RIA and LOFA) it follows that FE damage during the conversion from HEU to LEU fuel in considered situations will not occur.

The storage of "fresh" and spent FAs with HEU and LEU in the storage pool and temporary storage cells of the IR-8 reactor is safe.

The calculation results of radiation consequences during normal operation of the IR-8 reactor and considered accidents showed that conversion from HEU to LEU fuel will not lead to decrease in the radiation safety of the reactor and additional protective actions are required.

Currently the safety analysis of the IR-8 reactor during conversion to LEU is continued for beyond design basis accidents (BDBA).

Acknowledgements

Authors would like to thanks colleagues from ANL Jordi Roglans-Ribas, Nelson A. Hanan and Patrick L. Garner for expert assistance and analytical support during the works on the calculated justification of the IR-8 reactor safety during conversion to LEU fuel.

References

1. D. Erak, V. Nasonov, Y. Pesnya. State of work on calculation feasibility of the IR-8 reactor conversion to LEU fuel. Proceedings of the 2012 International Meeting on RERTR. Warsaw, Poland, October 14-17, 2012.
2. D. Erak, V. Nasonov, Y. Pesnya, A. Taliev, Y. Dubovskiy, A. Sidorenko (NRC “KI”, RF), N. A. Hanan, P. L. Garner(ANL, USA). Plan and preliminary calculations for IR-8 reactor during conversion to LEU fuel. Report on International Meeting “Research Reactor Fuel Management”- RRFM-2013. Saint Petersburg, Russian Federation, April 21 – 25, 2013.
3. D. Erak, V. Nasonov, Y. Pesnya, A. Taliev, Y. Dubovskiy. Calculations for the IR-8 reactor conversion to LEU fuel. Report on International Meeting “Research Reactor Fuel Management”- RRFM-2012. Prague, Czech Republic, March 18-22, 2012.
4. N.I. Alexeev, E.A. Gomin, S.V. Marin, V.A. Nasonov, D.A. Shkarovsky. MCU-PTR Code for Precision Calculation of Pool and Tank Types Research Reactors. - Atomic Energy, vol. 109, is. 3, 2010, p. 123-129.
5. A.V. Taliev. Modernized ASTRA code for thermal calculation of research reactor FAs consisting from tubular coaxial fuel elements. Preprint IAE-6405/5, Moscow, 2006.
6. http://www.ecoguild.ru/docs/2007garantstatya.htm
7. http://garant.hut.ru/programs/nuklid.html
8. http://www.ecoguild.ru/members/garant2011.htm
9. http://www.ecoguild.ru/docs/2009garant.htm
10. A.P. Olson, A Users Guide to the PARET/ANL Code Version 7.6 beta_130417, Argonne National Laboratory, 2013.

SAFETY ANALYSIS FOR CONVERSION OF IRT MEPHI RESEARCH REACTOR TO LEU FUEL

V.P. ALFEROV, E.F. KRYUCHKOV, M.V. SHCHUROVSKAYA
National Research Nuclear University MEPhI
31 Kashirskoe shosse, 115409 Moscow – Russia

N.A. HANAN, P.L. GARNER, D. KONTOGEORGAKOS
Nuclear Engineering Division, Argonne National Laboratory,
9700 Cass Avenue, 60439 Argonne, Illinois – USA

ABSTRACT

Safety analysis for conversion of 2.5 MW pool type research reactor IRT MEPhI of the National Research Nuclear University MEPhI was jointly performed with the GTRI Program at Argonne National Laboratory. This paper presents the results of the designed accidents caused by the reactivity insertion, loss of electrical power supply, blockage of the cross section of the primary circuit pipe and one of two primary pumps shutdown. The transient analysis was performed using the PARET (v7.5) code. Some of the transients were also performed with the RELAP5/MOD3.3 code for comparison with PARET.

1. Introduction

The feasibility studies of converting IRT MEPhI research reactor to low-enriched uranium (LEU) fuel were completed in November 2011 [1]. For feasibility studies tube-type fuel assembly (FA) IRT-3M with U9%Mo-Al fuel (enrichment of 19.7%) was chosen as a LEU fuel. The analysis sufficient to determine that conversion from HEU to LEU fuel is technically feasible was performed. The next step was to perform the safety analyses to show that LEU fueled reactor satisfies all safety requirements. Safety analysis for the conversion was completed in July 2013. Now the work on completion of Safety Analysis Report (SAR) for the IRT MEPhI reactor with LEU fuel required for the approval by regulatory bodies is being performed.

Four representative transients are analyzed in this paper: one reactivity insertion accident (RIA) and three loss-of-flow accidents (LOFA). Design accidents are analyzed (accidents with realization of safety systems function).

2. Input parameters for transient analysis

Calculations were performed for the operational (current) high-enriched uranium (HEU) core (16 fuel assemblies), the proposed initial LEU core (12 fresh fuel assemblies) and the proposed operational LEU core (16 fuel assemblies).

Initial data for transient analysis are presented in Table 1.

T **This work was supported by the U.S. Department of Energy, National Nuclear Security Administration, Office of Defense Nuclear Nonproliferation, under contract DE-AC02-06CH11357.**

.

Table 1: Input parameters for transient analysis

Parameter	Value
Normal operating power, MW	2.5
Coolant flow direction	up-down
Coolant inlet temperature, °C	45
Core pressure drop, Pa (2 primary circuit pumps)	$9 \cdot 10^3$
Core pressure drop, Pa (1 primary circuit pump)	$2.2 \cdot 10^3$
Coolant pressure at core outlet, Pa	$1.55 \cdot 10^5$
Coolant density, kg/m^3	993
Coolant mass velocity, kg/(m^2·s)	1390
Fuel thermal conductivity, W/(m·K)	170/120/120*
Cladding thermal conductivity, W/(m·K)	175
Fuel heat capacity, J/(kg·K)	750/310/310*
Cladding heat capacity, J/(kg·K)	900
Peak-to-average power density	3.16/2.69/2.95*
Over-power trip point, %	120
Delay time before scram rods start in after trip, s	0.2
Time of linear shutdown reactivity insertion, s	0.8
Shutdown reactivity worth, $	-13.4/-15.8/-12.1*

* – HEU operational core /LEU initial core /LEU operational core.

Kinetic parameters and reactivity feedback coefficients used in transient calculations are presented in Table 2.

Table 2: Kinetic parameters and reactivity coefficients

Parameter	Core		
	HEU - operational	LEU - initial	LEU - operational
Effective delayed neutron fraction, β_{eff}	0.00771 $\pm 2 \cdot 10^{-4}$	0.00798 $\pm 1 \cdot 10^{-4}$	0.00767 $\pm 2 \cdot 10^{-4}$
Prompt neutron generation time Λ, μs	68	53	57
Reactivity coefficients:			
Moderator temperature (300-400K), $\Delta\rho/\Delta T$, %/K	-1.33e-2 $\pm 2 \cdot 10^{-4}$	-8.0e-3 $\pm 2 \cdot 10^{-4}$	-8.4e-3 $\pm 2 \cdot 10^{-4}$
Fuel temperature (294-400K), $\Delta\rho/\Delta T$, %/K	-	-2.2e-3 $\pm 2 \cdot 10^{-4}$	-2.1e-3 $\pm 2 \cdot 10^{-4}$
Moderator density (void) (0-5%), $\Delta\rho/\Delta\alpha$, %/%	-0.27 $\pm 4 \cdot 10^{-3}$	-0.39 $\pm 4 \cdot 10^{-3}$	-0.31 $\pm 4 \cdot 10^{-3}$

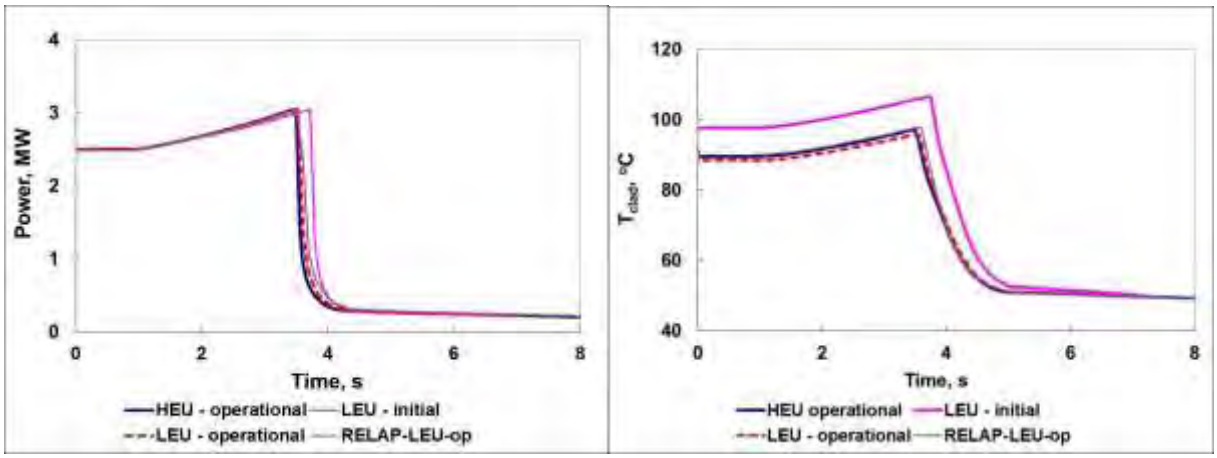
3. Transient analysis

All transient calculations were performed using PARET 7.5 code [2]. In this analysis, the hottest fuel tube was modeled, along with the rest of the core modeled as the average channel; i.e. two channels were used in the PARET model. PARET transient calculations were performed with following heat transfer correlations:
- Single-Phase Correlation IONEP=4 (Russian);
- Two-Phase Nucleate Boiling Correlation ITWOP=1 (McAdams);
- Transient Two-Phase Scheme IMODE=1 (transition model);
- DNB and Flow Instability Correlations ICHF=0 (original DNB).

Also in all transients a one second steady state is included at the beginning of the simulation. For comparison, two transient calculations (one RIA and one LOFA) were also performed using RELAP5/MOD3.3 code [3].

3.1. Uncontrolled withdrawal of control rods from critical state at nominal power level

The transient is assumed to be initiated by the upwards movement of shim rods from their critical position to the fully withdrawn position. Positive reactivity insertion rate is assumed to be 0.07$/s for all HEU and LEU cores.



(a) **(b)**

Figure 1: HEU and LEU cores PARET and RELAP results for shim rods withdrawal transient; (a) - power, (b) - peak clad surface temperature.

In PARET calculations (which are the curves having no code name in legend in figure), peak clad surface temperature during the transient is less than 107°C for operational HEU and LEU cores. Peak clad surface temperature for initial LEU core is ~10°C higher than for operational LEU and HEU cores because of higher power density due to less number of fuel assemblies. The time of peak power and trip time are approximately the same for all cores since the process finishes before the reactivity feedbacks have time to bring influence. Results for the operational LEU core from RELAP are essentially identical to the PARET results.

3.2. Loss of the offsite electricity supply (LOFA#1)

The accident occurs because of loss of the offsite electricity supply. When devices of core pressure drop measurement lose electricity supply a signal of these devices decreases to zero immediately (0.02 s) and the system in 0.02 s generates scram signal “Loss of electricity supply”. Coolant flow and pressure in primary circuit and core pressure drop decrease by exponential law $e^{-t/\tau}$ with decay constant $\tau \sim 0.1$ s. Reserve pumps with independent electricity supply are not provided. In accordance with exponential law $e^{-t/\tau}$ (τ= 0.1 s) coolant flow after 0.02 s decreases to 90%. By setting in transient calculation low flow trip point of 90% scram action in loss of the electricity supply accident can be modeled. Scram rods have to start in after 0.22 s (0.02 s +0.2 s) from the beginning of the accident.

In the analysis of this and other LOFA it is assumed that core pressure drop decreases to zero over 1 second. Such a rapid flow decay is explained by using the ejector in the cooling circuit. In this case the decrease of core pressure drop occurs immediately after the shutdown of primary circuit pumps engines. It can be explained by the following reasons:

- The use of the ejector in cooling circuit enables to ensure the flow rate through the core three times larger than the flow rate of primary circuit pumps. Therefore when the ejector scheme is used the primary circuit pumps with lower power can be used in comparison with direct cooling system (for the same core pressure drop). The inertia of the pumps with lower power is less and their decay time is less.
- The ejector works up to some level of water flow which inputs through its nozzle. When supplied water flow decreases to some level the ejector does not work.

The calculated results for HEU and LEU cores are shown in Figure 2.

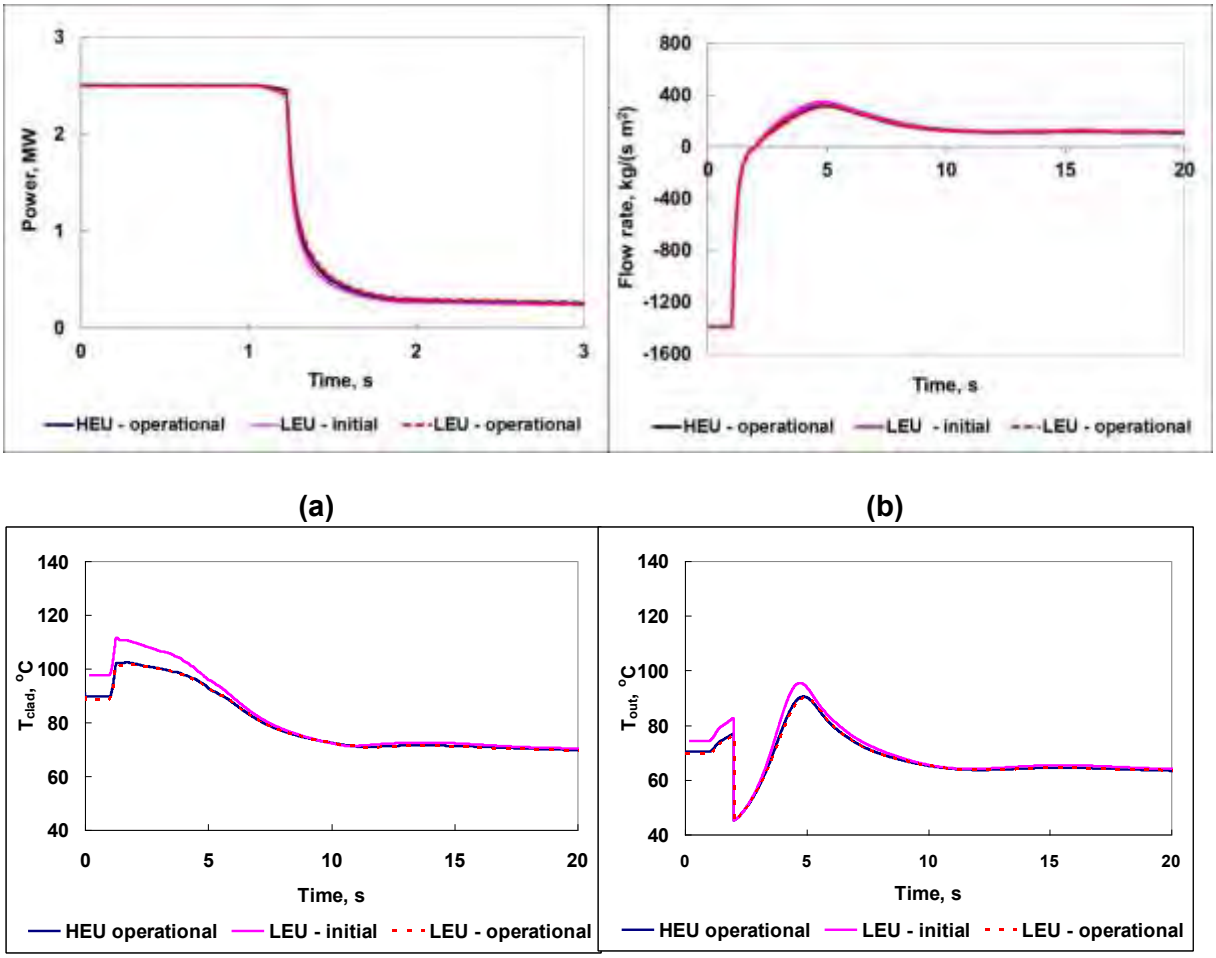


Figure 2: HEU and LEU cores PARET results for the electricity supply loss transient; (a) - power, (b) – mass flow rate, (c) - peak clad surface temperature; (d) - coolant outlet temperature

Flow reversal occurs over 1 s after the accident start for all the cores. It can be seen in Figure 2(d) as a sudden change in outlet temperature of the coolant since outlet and inlet coolant temperatures trade places in calculation.

Peak clad surface temperature during the transient is less than 112°C for operational HEU and LEU cores. Peak clad surface temperature for initial LEU core is ~10°C higher than for operational LEU and HEU cores because of higher power density due to less number of fuel assemblies. The time of peak clad surface temperature is approximately the same for the operational cores, for the initial LEU core the peak clad surface temperature occurs 0.4 s earlier.

3.3. One of two primary pumps shutdown (LOFA#2)

After one of two primary pumps shutdown core pressure drop decreases from 9 kPa to 2.2 kPa in accordance with the law:

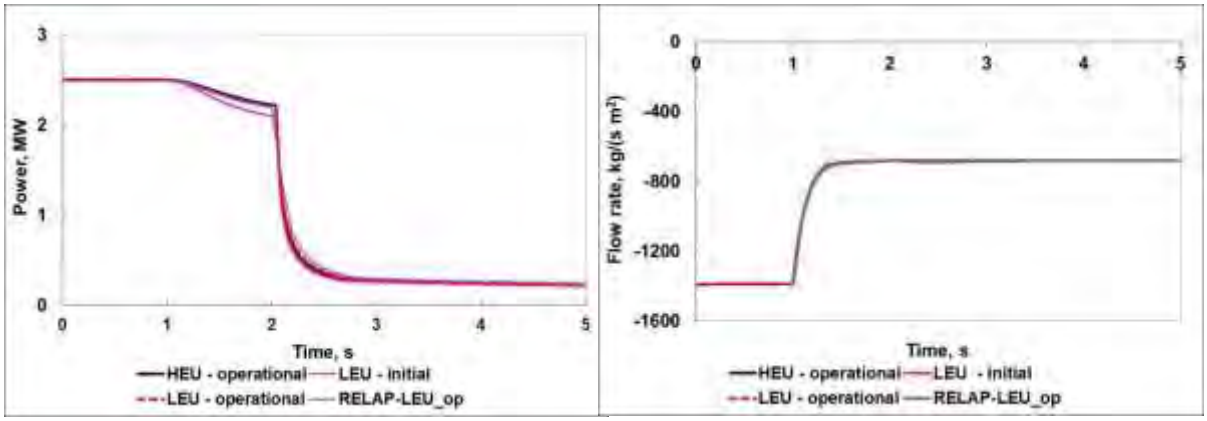
$\Delta P(t)=9\cdot e^{-t/\tau} + 2.2\cdot(1-\cdot e^{-t/\tau})$, kPa ($\tau$= 0.1 s)

Because of pressure drop indicator lag effect the signal of pressure drop measurement device decreases with decay constant $\tau\sim$ 0.3 s:

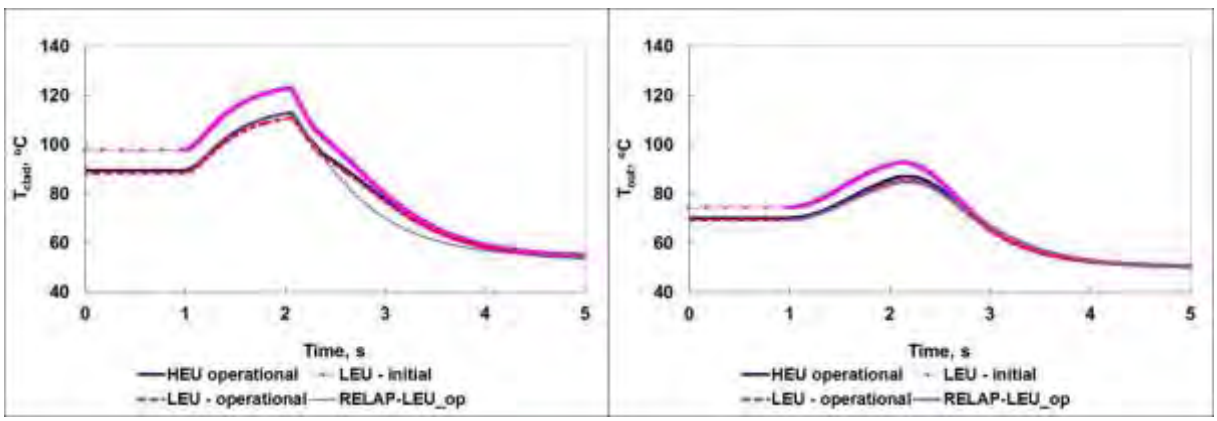
$\Delta P_d(t)=9\cdot e^{-t/\tau} + 2.2\cdot(1-\cdot e^{-t/\tau})$, kPa ($\tau$= 0.3 s).

When reactor operates at nominal power level fluctuations (±1 kPa) of measured pressure drop indicator signal are observed. Therefore instead of low flow trip point the following scheme is used. The scram at core pressure drop reducing operates as follows: using measured core pressure drop the system defines allowable power level according to the diagram of allowable power vs measured core pressure drop (this diagram is incorporated in I&C system logic). After that the system chooses minimum value between the allowable power level and current set power N_{set} (which was set by operator earlier) and sets new value of N_{set} equal to this minimum value. If current measured power is more than 1.2 N_{set} then scram operates due to power exceeding. That is, when reactor operates at 2.5 MW, core pressure drop reducing less than 2.6 kPa leads to scram since set power N_{set} becomes less than 2.08 MW and scram trip point becomes less than 2.5 MW (=1.2·2.08 MW).

So, scram operates at core pressure drop device signal of 2.6 kPa (flow of 54% at 0.28 s). “Real” core pressure drop at this moment is less than 2.6 kPa. In calculation it can be taken into account by using delay time equal to the difference between the moments when “real” core pressure drop and device signal is 2.6 kPa. The delay time is 0.56 s. This delay time should be added to time delay of scram which is 0.2 s. So scram rods have to start in after 1.04 s (0.28 s+0.56 s+0.2 s) from the beginning of the accident.



(a) **(b)**



(c) **(d)**

Figure 3: HEU and LEU cores PARET and RELAP results for the one of two primary pumps shutdown transient; (a) - power, (b) – mass flow rate, (c) - peak clad surface temperature, (d) - coolant outlet temperature.

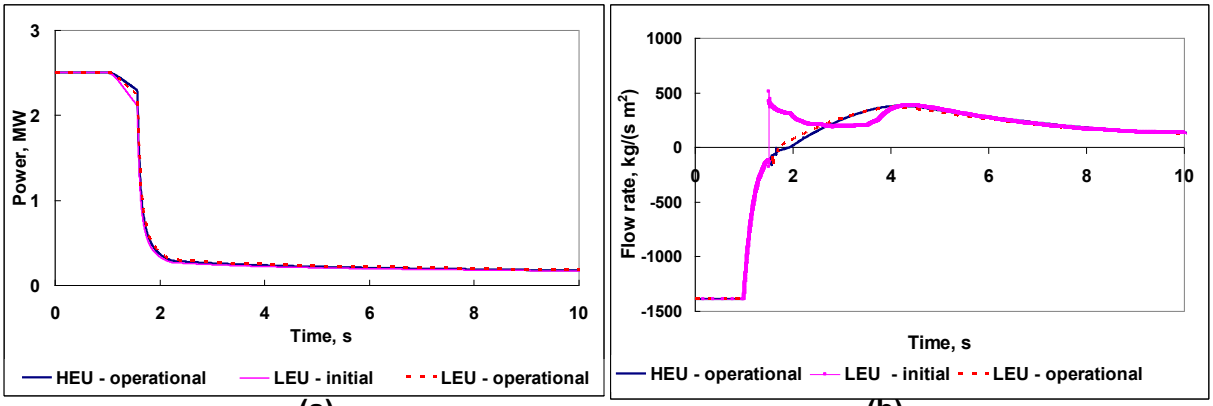
In PARET calculations (Figure 3), peak clad surface temperature during the transient is less than 113°C for the operational HEU and LEU cores. Peak clad surface temperature for initial LEU core is ~10°C higher than for operational LEU and HEU cores. Results for the operational LEU core from RELAP are essentially identical to the PARET results.

3.4. Blockage of the cross section of the primary circuit pipe (LOFA#3)

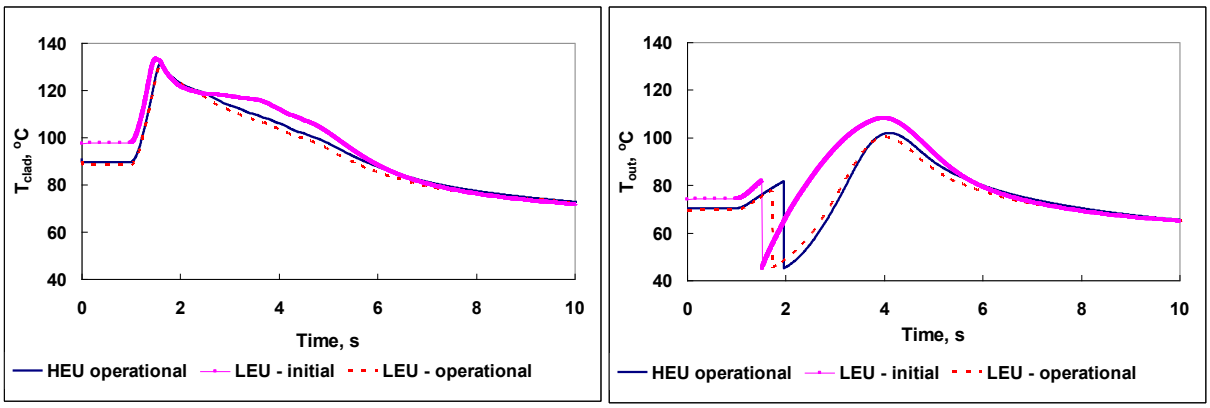
Possible cause of this accident is primary circuit pipe valves rupture. It is assumed that the fragments of destructed valve result in the instantaneous full blockage of the cross section of the primary circuit pipe. The probability of this event is very low. It is considered as the most severe designed accident.

Core pressure drop function versus time for this case is the same as for the case of loss of offsite electricity supply but scram operates later. In this case system generates scram signal due to core pressure drop decrease. This signal occurs later than scram signal “Loss of electricity supply”.

Similarly to one of two primary pumps shutdown, low flow trip point is set according to the “real” process. Delay time equal to the difference between the moments when “real” core pressure drop and device signal is 2.6 kPa is used. The delay time is 0.25 s. This delay time should be added to delay time of scram which is 0.2 s. So scram rods have to start in after 0.57 s (0.12 s+0.25 s+0.2 s) from the beginning of the accident.



(a) (b)



(c) (d)

Figure 4: HEU and LEU cores PARET results for the blockage of the cross section of the primary circuit pipe transient; (a) - power, (b) – mass flow rate, (c) - peak clad surface temperature, (d) - coolant outlet temperature.

Flow reversal occurs over 1 s after the accident start for HEU operational core, over 0.7 s for LEU operational core and over 0.5 s for LEU initial core (Figure 4(b)).

Peak clad surface temperature during the transient is less than 133°C and higher than the temperature for onset of nucleate boiling for HEU and LEU cores.

4. Conclusions

Table 3 presents the summary of the results of considered design accidents calculation for IRT MEPhI reactor with HEU and LEU fuel.

Table 3: Main results of design accidents calculation

Transient	Core	T_{clad}^{max}, °C	T_f^{max}, °C	T_{out}^{max}, °C
RIA#1*	HEU – operational	97.3	98.5	74.8
	LEU – initial	106.6	108.2	79.7
	LEU - operational	95.9	97.1	73.9
LOFA#1	HEU – operational	102.4	102.5	90.2
	LEU – initial	111.6	112.1	95.3
	LEU - operational	101.8	101.9	90.0
LOFA#2	HEU – operational	112.8	113.7	87.2
	LEU – initial	122.8	123.8	92.6
	LEU - operational	110.8	111.6	85.6
LOFA#3	HEU – operational	131.1	131.9	102
	LEU – initial	133.3	134.3	108
	LEU - operational	130.2	131.0	99.7

*- RIA#1 - uncontrolled withdrawal of control rods from critical state at nominal power level; LOFA#1 - loss of electrical power supply; LOFA#2 - one of two primary pumps shutdown; LOFA#3 - blockage of the cross section of the primary circuit pipe.

Comparison of the operational HEU and LEU cores shows that the peak clad surface temperature and the coolant outlet temperature are almost identical. For the initial LEU core the peak cladding surface temperature and the coolant outlet temperature are higher than for operational LEU and HEU cores because of higher power density due to less number of fuel assemblies. For the analyzed protected transients the difference in the reactivity feedbacks and kinetic parameters between the different cores has no time to bring influence and the behavior of all considered cores is very close. The differences in the fuel meat thermal conductivity have not a significant impact on the obtained results. The thermal conductivity of the LEU fuel meat in the initial LEU core was varied from 20 to 120 W/m·K. In changing the thermal conductivity from 20 to 120 W/m·K the peak fuel temperature decreased by 2% from 108°C to 106°C and the peak clad temperature increased by less than 0.1°C.

Results calculated for operational LEU core using RELAP are essentially identical to those calculated using PARET.

All of the peak clad surface temperatures computed for analyzed transients for HEU and LEU cores are far below the melting temperature of the cladding (~585°C).

REFERENCES

[1] V. Alferov, E. Kryuchkov, M. Shchurovskaya «Feasibility Studies for LEU Conversion of the IRT MEPhI Reactor Using U-Mo Tubular Fuel». Proceedings of the 33rd International Meeting on Reduced Enrichment for Research and Test Reactors RERTR 2011. Santiago, Chile, October 23-27, 2011.

[2] C. F. Obenchain, PARET— A Program for the Analysis of Reactor Transients, AEC Research and Development Report, Reactor Technology, IDO-17282, Phillips Petroleum Company, Idaho, January 1969. Also A. P. Olson, A Users Guide to the PARET/ANL Code, ANL/RERTR/TM-11-38 Version 7.5, Argonne National Laboratory, Argonne, Illinois, August 14 2012.

[3] RELAP5/MOD3.3 Code Manual, NUREG/CR-5535 Rev.1 (multiple volumes), Information Systems Laboratories, Rockville, Maryland and Idaho Falls, Idaho, December, 2001.

TRANSIENT ANALYSIS BEHAVIOR FOR THE JRTR RESEARCH REACTOR UNDER LOSS OF ELECTRICAL POWER ACCIDENT

O.S.AL-YAHIA, S.ALKHAFAJI, M.A.Albati
Jordan Atomic Energy Commission
Amman 70 (11934) Jordan

D.JO
Korea Atomic Energy Research Institute
1045 Daeduk-Daero, Dukjin-Dong, Yuseong-Gu, Daejeon, 305-353, Republic of Korea

ABSTRACT

Modeling and simulation for the Jordan Research and Training Reactor (JRTR) during Loss of Electric Power (LOEP) is performed in this work. Loss of Flow Accident (LOFA) is analyzed as a consequence of LOEP. During the 5 MWth normal operation, the cooling mode is downward forced convection and upward natural circulation during shutdown and training mode operation. The natural circulation is generated through flap valves. A coupled neutronic and thermal hydraulic model is developed to analyze the reactor behavior under the transient operation mode. The flap valves opening time is determined based on the pressure drop across the core. The evolution of the reactor parameters in hot and average assembly was investigated in this analysis. The flow inversion phenomenon is taken into consideration in the present study. It was found that, the flow inversion occurs earlier in the hot channel than in an average channel. Two fuel temperature peaks and two bulk temperature peaks occur during the reactor transient in the hot and average assembly. The evolution of the reactor parameters in the average assembly is investigated. However, the general behavior of the reactor during LOEP is similar to the average channel behavior. The movement of hotspot location during flow inversion is investigated.

1. Introduction

JRTR is a 5 MW multi-purpose open pool plate type fuel research reactor. Most of the plate type fuel reactors undergo the downward cooling mode during normal operation and upward flows during shutdown and training mode via natural circulation. Loss of normal electric power (LOEP) is a suggested event that can occur due to either electric load conditions such as overload in the system buses or natural & environmental conditions, like flood, storm, earthquake, tsunami, etc. Loss of flow accident (LOFA) is the main consequence of LOEP accident. However, when a LOFA occurs, the flow direction will be converted from downward to upward flow, this phenomenon is called *"flow inversion"* [1].

After the initiating event of LOEP, the reactor is tripped by the insertion of the control rods and the secondary shutdown rods. The decay heat power is removed by slowing down the coolant which is induced by the inertia force of the pumps flywheel, as well as the natural circulation flow after flow inversion through the flap valves. The flap valves open passively by their weight as the pressure difference across them becomes below 1.5 kPa. When the flap valves open, cold water in the pool inflows into the exit pipe and sucked away to the PCS line with the core flow. Therefore, the flow rate through the reactor core is further reduced. After flow inversion, the pool water inflow to the outlet pipe and a natural circulation through the flap valves is established.

2. Reactor description

The reactor contains 18 fuel assemblies that consist of flat fuel plates. Each fuel assembly has 21 fuel plates. The fuel meat is Uranium Silicide U_3Si_2 with enrichment for the equilibrium core of 19.75 w/o. The schematic drawing for the reactor assembly is shown in Fig.1. The fuel plates are assembled one after another with small gap between each of them, where the coolant flows. Each fuel assembly has many coolant channels, as shown in Fig.1-c.

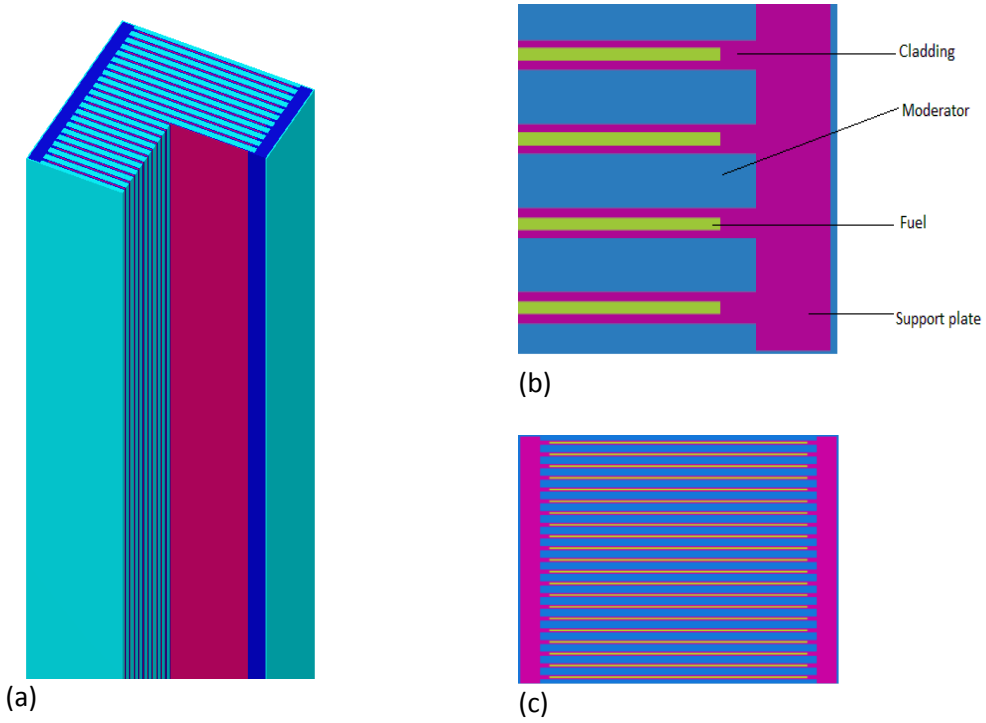


Fig 1. Reactor fuel assembly

The reactor core is located in a large water pool in which it has an adequate water inventory to ensure the reactor cooling during accidents; such as LOFA. The reactor structure is composed of the outlet plenum, grid plate, upper guide structure (UGS), screen, outlet pipes, and flap valves for the natural convection cooling mode. Fig.2 shows the reactor schematic diagram and the flow path for the cooling modes, in downward and upward direction. The

thermal hydraulic design bases of the reactor structure provides a flow path of primary coolant for the removal of heat deposited in the core components. The thermal hydraulic design variables under the forced convection cooling at steady state are shown in Table 1. However, the major design parameters used in this analysis are listed in Table 2. Also it summarizes the specifications of the reactor. The total and axial power peaking factors of the core were considered in the analysis.

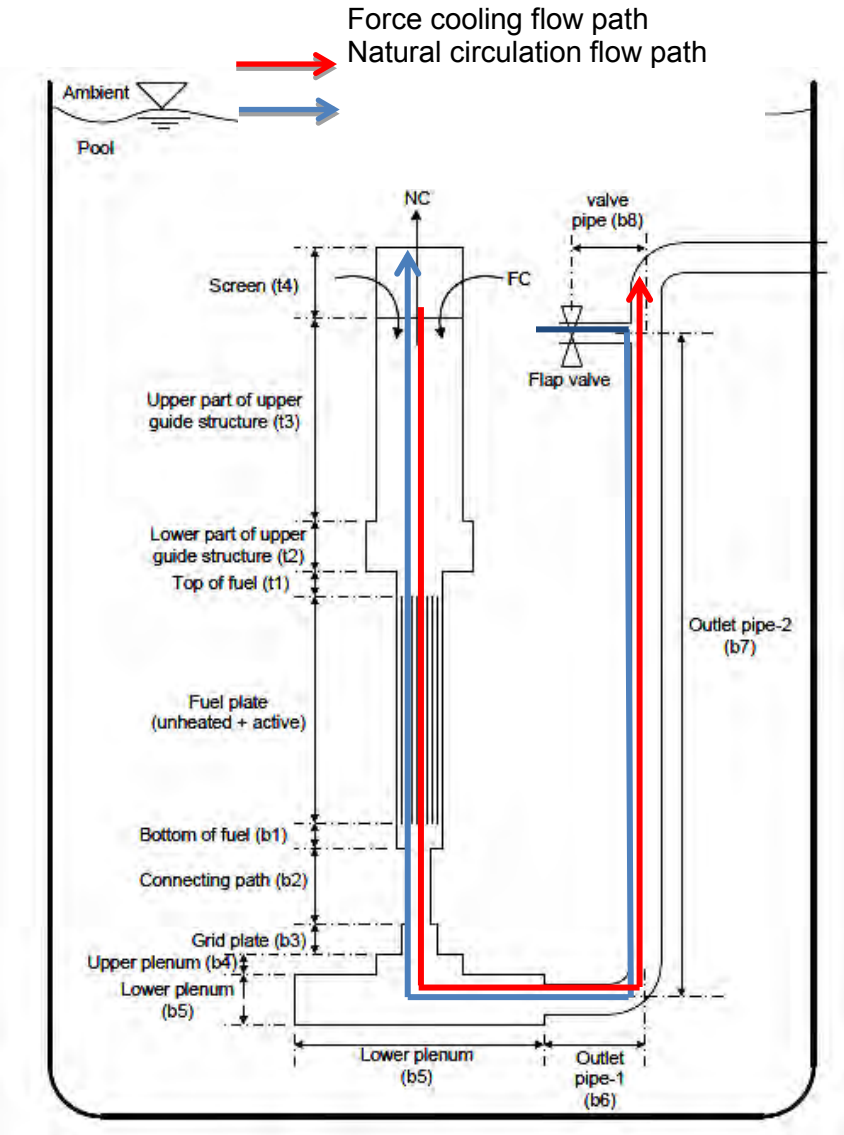


Fig 2. Reactor schematic drawing

Tab 1: Thermal hydraulic design variables

Design variables at normal operation	**Value**
Core Power (MW)	5.0
Core inlet coolant temperature (^{o}C)	37.0
Core flow rate (kg/s)	170.0
Core inlet pressure (MPa)	0.18
Average core flow velocity (m/s)	2.5

Tab 2: Reactor core specification

Geometry Data	
Number of fuel assembly	18
Number of plates per FA	21
Fuel plate height (mm)	680
Fuel thickness (mm)	0.51
Fuel width (mm)	62.1
Cladding thickness (mm)	0. 38
Channel width (mm)	66.6
Channel thickness (mm)	2.25
Core peaking factors	
Total power peaking factor	3
Radial peaking factor, F_R	2.48
Axial peaking factor, F_Z	1.21

3. Analysis Method

A neutron kinetic and thermal hydraulic coupling model is adopted to investigate the reactor transient behavior under LOEP. However, point kinetic equations with six precursor groups were used to calculate the reactor power. A one dimensional spatial dependent model was adopted for a sub-cooled liquid flowing through a single rectangular channel heated from both sides. *AL-Yahia et.al* described the coupling model in detail [2]. They used the model to simulate the IAEA 10 MW benchmark problem to investigate the flow inversion during fast and slow LOFA. However, the general behavior of these types of reactors under LOFA accident is the same, whereas the downward flow rate decreases with time and then the flow reverses to the upward direction.

In the IAEA benchmark problem, the return flow path is not specified, but in the present study the effect of the return flow path on the reactor parameters as well as the flow inversion period is taken into consideration. All reactor structures are simulated in this study including UGS, plenum, and natural circulation valves. The additional structures introduce more friction, which reduces the flow velocity after flow inversion [3]. On the other hand, the mass flow rate through the channel is determined in terms of a balance between driving forces (flywheel inertia) and prevention forces (friction and buoyancy force), and expressed as [2];

Before flow inversion:

$$v(t) = v_{cs}(t) - \int \frac{\Delta\rho}{\rho_p} g dt \tag{1}$$

After flow inversion:

$$\frac{dv}{dt} = -\frac{1}{2}\frac{f}{D_h}\left(\frac{\rho_i}{\rho_p}\right)|v|v - \frac{\Delta\rho}{\rho_p} g \tag{2}$$

When the flap valves open before flow inversion, the pump coast-down flow rate is shared between the core and the inflowing cold water through the flap valves. The mass flow rate through the core and the mass flow rate through the flap valves must be equal to the pump mass flow rate. Also the pressure drop across the core must be equal to the pressure drop across the flap valves. In order to determine the mass flow rate through the core and through the flap valves, an iterative method is used between the following equations:

$$\dot{m}_{core} + \dot{m}_{flap} = \dot{m}_{pump} \tag{3}$$

$$dP_{core} = dP_{flap} \tag{4}$$

where dP_{core} and dP_{flap} are the pressure drop across the core and across the flap valves, respectively.

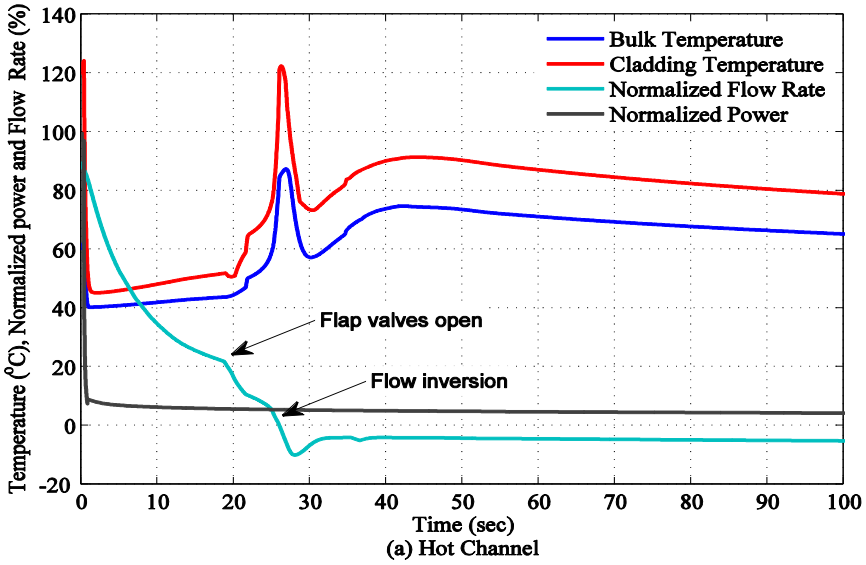
The cladding surface temperature was calculated by different packages of single-phase convective heat transfer correlations for narrow rectangular channel [4]. Implicit finite volume method was used to solve the conduction equation to obtain the temperature distribution in the fuel and cladding region [2].

4. Results and Discussion

Before LOEP initiation, the reactor power is considered to be 120% of the nominal power. Fig.3 shows the transient behavior of the reactor after LOEP in the hot and average channels. Generally, the core behavior during LOEP is the same as the average channel transient. The evolution of the maximum cladding temperature and the maximum bulk temperature is shown. After the initiating event, the flow rate decreases directly in conjugation with the reactor trip, which has delay time around 0.280 sec. Initially, the reactor power, flow rate, and maximum cladding and coolant temperature drop simultaneously, causing the first cladding and coolant temperature peaks [2]. In the hot channel, the first temperature peaks are 124.4^{o}C and 62.46 ^{o}C for the cladding and coolant, respectively. While decreasing in the flow rate the flap valves open after around 19 sec. Therefore, the flow rate through the reactor core is further reduced. Then the core temperature increases again. The increase of the buoyancy force in the channel leads to flow reversal.

At the start time of the flow inversion, the hot slug moves backward in upward direction, and the maximum coolant temperature keeps increasing until it is ejected from the core, which results in the second temperature peaks. Then the flow rate decreases due to decreasing the buoyancy force, which leads to increase in the coolant temperature again. This feedback explains why there is a coolant temperature oscillation after the second temperature peak [2].

Fig.4 shows the effect of buoyancy on the flow velocity in the hot and average channels during LOEP. The difference between the actual flow and pump coast down is grater in the hot channel than in the average channel. Because of this, the flow inversion in the hot channel occurs earlier than in the average channel [2]. The flow inversion in the hot channel occurs at approx. 26 sec, while in the average channel the flow inversion occurs after around 35 sec. Table 3 summarizes the analysis results for hot and average channels.



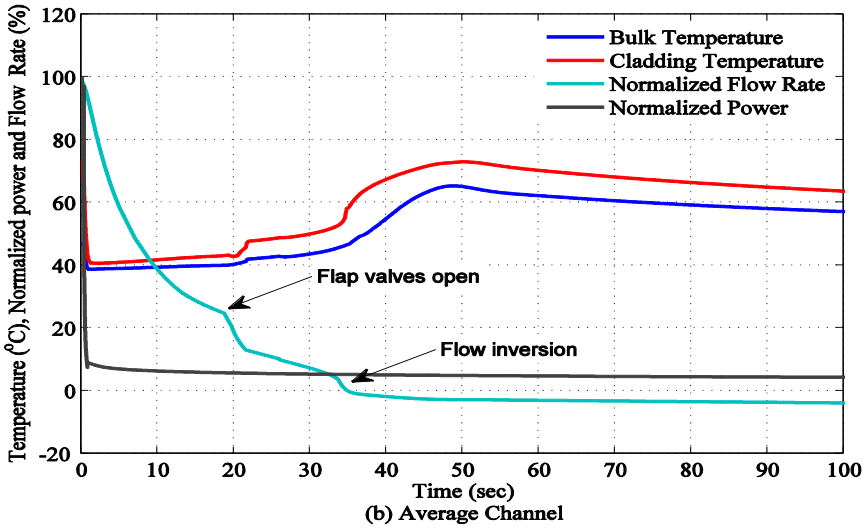


Fig 3. Transient behavior of the reactor during LOEP

Tab 3: Consequences of LOFA due to loss of electric power

Description	Hot Channel	Avg.Channel
Reactor power at scram (MW)	4.8615	4.8615
(sec)	(0.2829)	(0.2829)
1st cladding temperature peak	124.4 °C	73.11°C
(sec)	(0.2901)	(0.2891)
1st coolant temperature peak	62.46 °C	46.98 °C
(sec)	(0.2983)	(0.2911)
Flap vale opens (sec)	18.8	18.8
Flow inversion (sec)	25.97	35.04
2nd cladding temperature peak	122.6 °C	73.06 °C
(sec)	(26.12)	(46.97)
2nd coolant temperature peak	87.53 °C	65.41 °C
(sec)	(26.80)	(48.87)

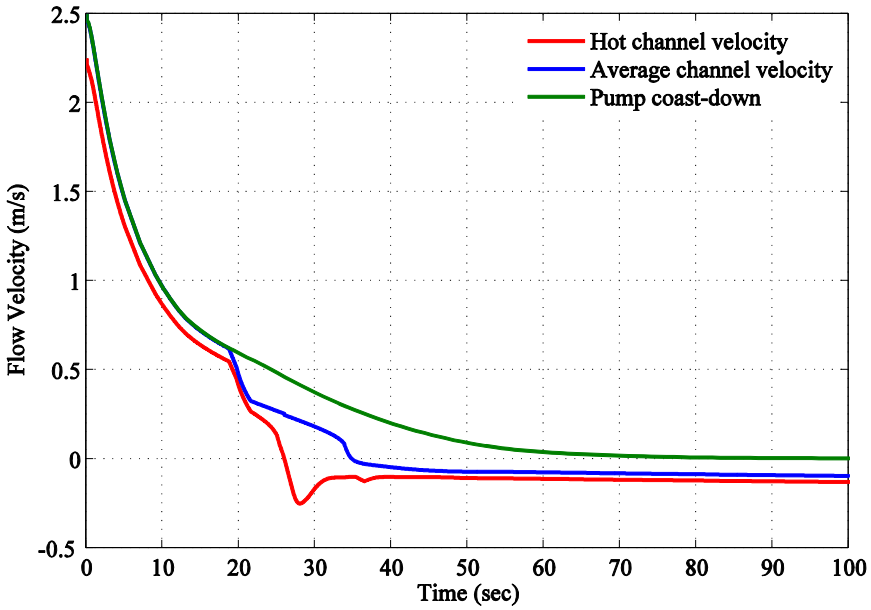


Fig 4. Core channels flow velocity

Fig.5 shows the inlet and outlet coolant temperature for the hot and average channel. When the hot channel flow reverses, the coolant inlet temperature is the outlet temperature of the average and bypass channels as shown in Fig.5. With more decreasing in the core flow rate, the buoyancy force dominants enough to resist the downward flow and reverse the flow direction to the upward direction. After flow inversion, the core inlet temperature will be the same as the core outlet temperature before flow inversion, because there is a lot of hot coolant already existing in the return flow path; lower part of fuel, grid plate, plenum, and outlet pipe.

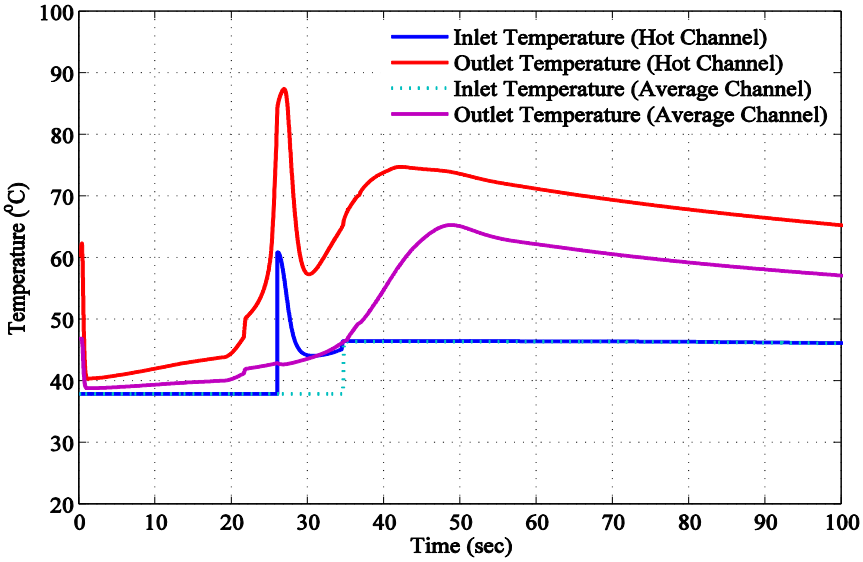


Fig **Error! No text of specified style in document.**. Coolant Temperatures during LOEP

Conclusion

A 5 MW open pool plate type fuel research reactor flow inversion is analyzed in the present work during loss of electric power accident. LOFA is one of the LOEP consequences. The reactor trip signal is trigged at time 0.0 sec, but the reactor scram occurs with delay time about 0.28 sec. With a decrease in the flow rate, the pressure across the flap valves decreases. After 19 sec, the flap valves open, in which the pressure drop through the core is 1.5 kPa. Two cladding temperature peaks and two bulk temperature peaks occured during the reactor transient in the hot and average assembly. For the hot channel, the first temperature peaks are 124.4 ^{o}C and 62.46 ^{o}C for fuel and coolant, respectively. The second fuel temperature peak is 122.6 ^{o}C, and the second bulk temperature peak is 87.53 ^{o}C. For the average channel, the first temperature peaks are 73.11 ^{o}C and 46.98 ^{o}C for fuel and coolant, respectively. The second fuel temperature peak is 73.06 ^{o}C, and the second bulk temperature peak is 65.41 ^{o}C. However, the reactor general behavior during LOEP is similar to the average channel behavior. The core flow inversion occurs around 35 sec. On the other hand, the flow inversion occurs at around 26 sec in the hot assembly.

References

[1] R.S Smith, W.L. Woodruff, .Thermal-hydraulic aspects of flow inversion in a research reactor. International meeting on Reduced Enrichment for Research and Test Reactor, Gatlinburg, Tennessee, November 1986.

[2] Al-Yahia, O.S., Albati ,M.A., Park, J., Chae, H., Jo, D., 2013. Transient thermal Hydraulic analysis of the IAEA 10 MW MTR reactor during loss of flow accident to investigate the flow inversion. Annals of nuclear energy 62, 144-152.

[3] Jo, D., Park, S., Park, J., Chae, H., Lee, B., 2012. Cooling capacity of plate type research reactors during natural convective cooling mode. Progress in Nuclear Energy 56, 37–42.

[4] Jo, D., Al-Yahia, O.S., Altamimi, R.M., Park, J., Chae, H., (2014), Experimental investigation of convective heat transfer in a narrow rectangular channel for upward and downward flows. Nuclear Engineering and Technology (in print).


RRFM
EUROPEAN RESEARCH REACTOR CONFERENCE 2014
Ljubljana
30 March -3 April 2014
SLOVENIA

Poster

STUDY OF METHODS FOR PHASE CHARACTERIZATION IN INTERMETALLIC UAl_x

G. CONTUBIA, R. H. L. GARCIA, A. M. SALIBA-SILVA, E. F. URANO DE CARVALHO, M. DURAZZO

Nuclear and Energy Research Institute IPEN-CNEN/SP
Av. Professor Lineu Prestes 2242, 05508-000, São Paulo, SP - Brazil

ABSTRACT

The UAl_x is an intermetallic compound used in the manufacture of irradiation targets for molybdenum-99 production. The fissionable uranium-235 is presented in the form of intermetallic UAl_x powder, which is dispersed in an aluminum matrix. This paper aims at studying methods for phase characterization of the intermetallic. The index x identifies the phase composition of the compound, usually a mixture of UAl_2, UAl_3 and UAl_4. The phase composition was quantified in the UAl_x powder and UAl_x-Al dispersion by means of image analysis and x-ray diffraction, applying the Rietiveld method. Both methods allowed the quantification of the presented phases. The results from the two methods differed from each other with respect to the concentration determination. Possible error sources are discussed in this paper. The quantification method based on x-ray diffraction showed potential to be applied to the RMB Project for phase quantification in UAl_x-Al dispersion targets, which is required by specification.

1. Introduction

Every year the world demands more than 30 million medical imaging procedures that use technetium-99m radioisotope (Tc^{99m}), which correspond to approximately 80% of all nuclear medicine diagnoses. [1] This radiopharmaceutical product derives from the radioactive decay of molybdenum-99 (Mo^{99}), which is commercially produced in research reactors by irradiation targets that contain uranium-235. However, continuous supplying of Mo^{99} has decreased over the last decade, mainly due to shutdowns that have occurred in the main research reactors that produce radioisotopes [2]. To deal with this scenario, Brazil has decided to build up a multipurpose reactor which among other functions will irradiate uranium targets to produce enough Mo-99 to meet domestic demand.

There are currently two technologies available to produce uranium targets. One is based on metallic uranium thin foils [3] and the other one is based on a uranium-aluminum alloy dispersed in an aluminum matrix [4].

The binary system, uranium and aluminum, forms a phase diagram which shows the existence of intermetallic compounds consisting of three phases, UAl_2, UAl_3 and UAl_4. The mixture of these phases is known in the literature as UAl_x [5]. Because of its experience acquired over the years in the manufacturing technology based on dispersion fuels, IPEN has decided to adopt this technology for fabricating UAl_x-Al dispersion targets for future Mo^{99} production in Brazil.

Characterizing the phase composition in UAl_x powder used as raw material for target fabrication is important because the maximum uranium concentration depends on the phase composition presented in the starting powder. Furthermore, it is important to mention that the UAl_3 and UAl_4 are more easily dissolved in alkaline solutions than the UAl_2, which defines,

ultimately, the radiochemical processing throughput after the irradiation [6]. So, the presence of UAl_2 in the UAl_x-Al dispersions target also must be quantified.

This paper aims at investigating methods to quantify the phases present in UAl_x powder and UAl_x-Al dispersions. Two possible methods were investigated: image analysis and x-ray diffraction.

2. Materials and Methods

The intermetallic was prepared from a mixture of metallic uranium and metallic aluminum metal in stoichiometric proportions to obtain UAl_2 (81.5 wt% U). The starting materials were charged into a zirconium crucible and melted using a 15 kW induction furnace. Prior the melting, the furnace was purged with argon after vacuum of 2.6×10^{-3} mbar. The UAl_x ingot was ground in a mortar under argon atmosphere.

A mixture of aluminum and UAl_x powders corresponding to 50 and 45 vol% respectively has been pressed to form the target meet, which is called briquette. It contains UAl_x particles dispersed in an aluminum matrix. The particle size distribution of the UAl_x powder in the briquette was 80 wt% of 44 to 150 μm particles and 20 wt% of particles smaller than 44 μm.

The roll billet consists of a picture frame, two cover and a briquette. These components were assembled and joined by Tungsten Inert Gas (TIG) welding and then rolled to form the targets, according to the picture-frame technique [7-9]. Prior the rolling operation, the briquettes were degassed at 250 °C for 3 hours under vacuum of 0.8×10^{-3} mbar. The assemblies were hot-rolled at 450 °C in four rolling passes. The final specified thickness for the target was reached with two cold-rolling passes. Table 1 shows the typical rolling scheme adopted to manufacture UAl_x-Al dispersion targets.

Target Number	Thickness (mm) (assembly starting thickness= 9.23 mm)					
	P1 (hot)	P2 (hot)	P3 (hot)	P4 (hot)	P5 (cold)	P6 (cold)
1	5.90	→ withdrawn for analysis (WA)				
2	5.98	3.91	→ WA			
3	6.03	3.90	2.66	→ WA		
4	6.00	3.90	2.65	1.77	→ WA	
5	6.02	3.89	2.64	1.77	1.63	→ WA
6	5.99	3.90	2.64	1.75	1.64	1.52

P = rolling pass

Tab 1: Typical rolling scheme to manufacture UAl_x-Al dispersions targets

X-ray diffraction data were collected from samples of polished briquettes and rolled target meats by a Rigaku Multiflex diffractometer, operating with Cu-Kα radiation at 40 kV and 20 mA, with a scan of 0.02° and for 8 s counts. The reference information was obtained from the ICDD files 58195, 58196 and 24233. The crystalline phases were quantified using the Rietiveld method with GSAS for data refinement.

The phase composition was also quantified by studying the microstructure of briquettes and rolled meats through scanning electron microscopy (backscattered electron image) and energy dispersive spectroscopy. A Philips XL30 microscope was used. Image analysis was used for quantifying the phases by using the software Omnimet Enterprise Buehler.

3. Results and Discussion

Figure 1 show a scanning electron micrograph of the cross section of a UAl_x-Al briquette, where the UAl_x particles are homogeneously dispersed in the aluminum matrix. Because of the atomic number contrast obtained from the backscattered electrons, which is sensitive to the composition, it was possible to observe three shades of gray, which indicate the existence of three phases.

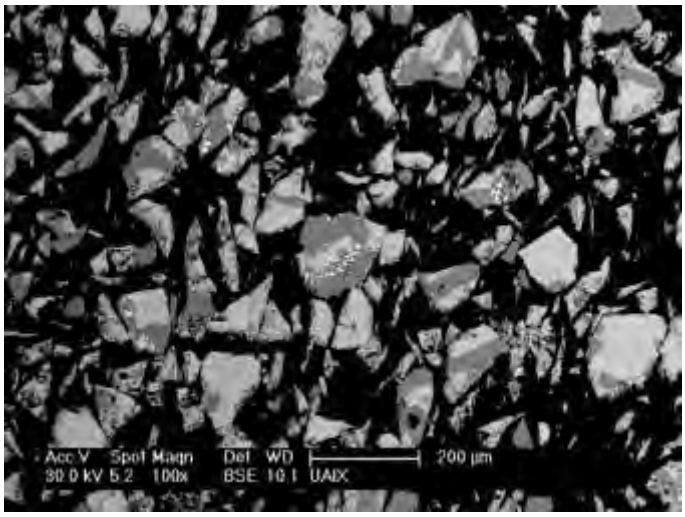


Fig 1. Scanning electron micrograph from a UAl_x-Al briquette cross-section illustrating the dispersion and the phases presented (backscattered electrons)

EDS analysis (Figure 2) were used to quantify the levels of uranium and aluminum in the three phases. Region 1 (lighter gray tone, almost white) showed a composition of 99.0 wt% U and 1.0 wt% Al. As discussed later, this phase was identified by X-ray diffraction as UO. The grayscale observed on region 2 corresponded to the concentration of 82.5 wt% uranium and 17.5 wt% aluminum, while the darker gray tone related to the region 3 showed a composition of 76.6 wt% U and 23.4 wt% Al. Based on the stoichiometric composition, the compositions of the regions 2 and 3 characterize the UAl_2 and UAl_3, respectively.

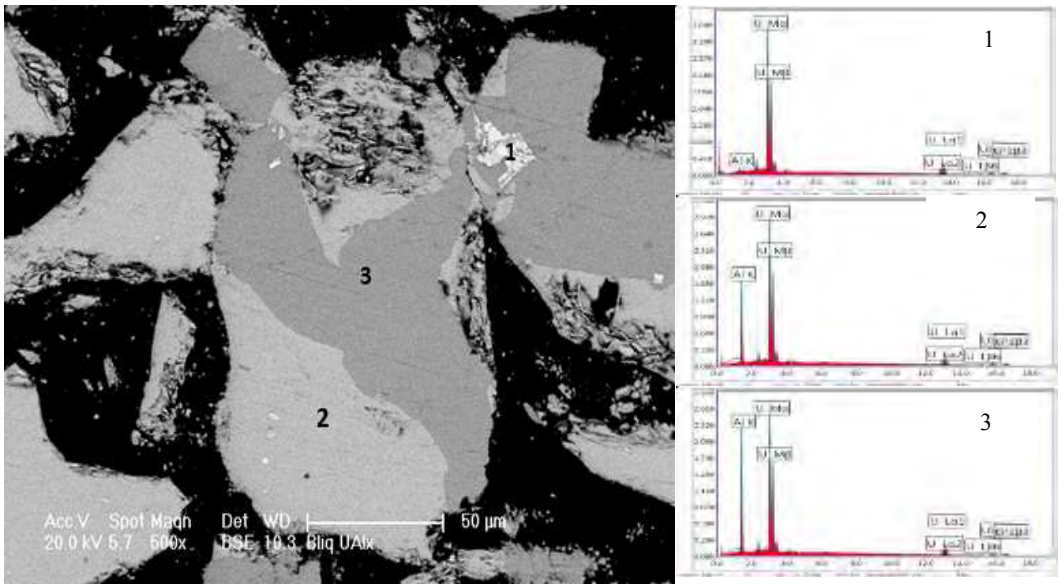


Fig 2. Scanning electron micrograph and EDS analysis of the regions designated by 1, 2 and 3. The compositions of regions 2 and 3 indicate the presence of UAl_2 and UAl_3, respectively (backscattered electrons)

The volumetric fractions of the three phases present were determined by using image analysis. Eight images were analyzed. Figure 3 shows a typical image that was analyzed. The cyan color (light blue) was used to identify the UAl_2 phase, the yellow color was used to identify the UAl_3 phase and the dark blue color was used to identify the denser phase of UO. The red color was used to identify the aluminum matrix.

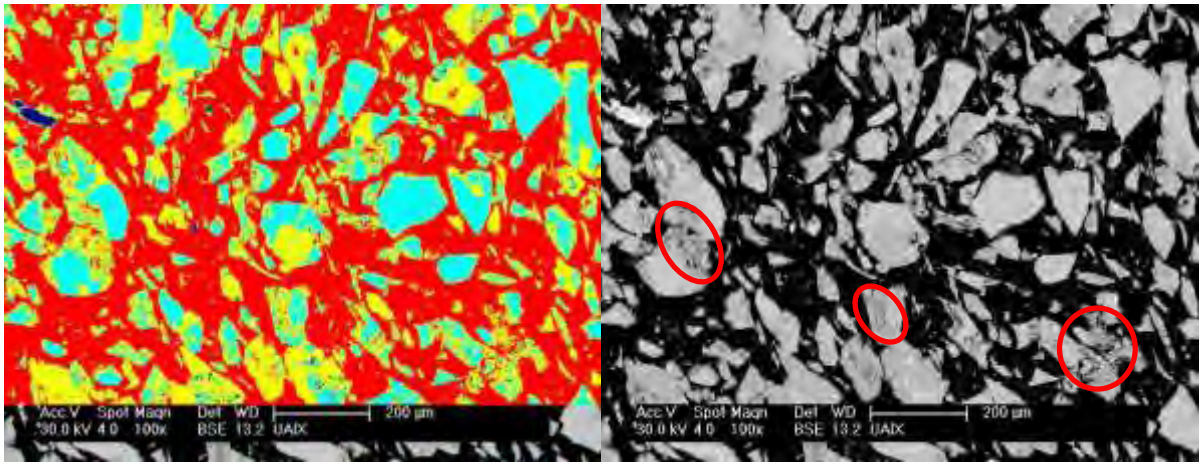


Fig 3. Left, image processed by the image analyze. Right, unprocessed image

The red circles in Figure 3 (right) illustrate regions where fragmentation of UAl_2 (fragile phase) can be observed. The fragments of fragmented UAl_2 particles present a dark shade of gray that is confused with the shade of gray of UAl_3 particles. This is an important source of error, as discussed below.

The phase quantitation by image analysis resulted in 42.6 wt% for UAl_2, 56.26 wt% for UAl_3 and 1.2 wt% for UO. Chemical analysis determined the uranium content in the powder as 80.74 wt%, with a uranium loss of 0.76 wt% compared to the nominal uranium content of the starting composition of the charge of fusion (81.50 wt%). This loss can be attributed to the oxidation of uranium alloy during the melting process to form UO.

Considering that the uranium content was determined by chemical analysis and neglecting the presence of the oxidized phase remaining in the sample, from the U-Al equilibrium diagram [5] the expected phase composition in the powder would be about 89.4 wt% for the UAl_2 and 10.6 wt% for UAl_3. The composition resulted from the image analysis shows underestimated values for the UAl_2 concentration. This result can be explained by the fragmentation of the fragile UAl_2 particles, which occurs when pressing and rolling the UAl_x-Al dispersion. Differences in height (porosity) in the regions of fragmentation cause fewer backscattered electrons reaching the detector, which decrease the brightness in these regions and result in a darker shade of gray on the edges of the UAl_2 particles and fragments thereof. This darker shade of gray in the image is confused by the image analyzer as UAl_3, as illustrated by the regions marked with red circles in Figure 3. The image analyzer distinguishes the edges of the UAl_2 particles and its fragments as UAl_3. Thus, the processed image leads to a concentration underestimated for the UAl_2 fraction and overestimated for the UAl_3 fraction. This effect does not occur with the UAl_3 particles due to its greater ductility [7].

The phase composition obtained by X-ray diffraction for the same UAl_x-Al briquette analyzed by image analysis is presented in Figure 4, which shows the experimental and calculated diffraction pattern by Rietveld method. The value of $\chi 2$ resulting from the simulation was 66, showing a reasonable agreement between the experimental and the theoretical values.
As mentioned before, the compositional analysis of the phases obtained by SEM-EDS indicated the existence of UAl_2, UAl_3 and a third phase rich in uranium (lighter gray tone, almost white, region 1 in Figure 2). This observation was confirmed by X-ray diffraction,

which shows that the uranium-rich phase is UO. The results for the phase measurement from the Rietveld method showed 85.4 wt% for UAl_2, 11.4 wt% for UAl_3 and 3.2 wt% for UO.

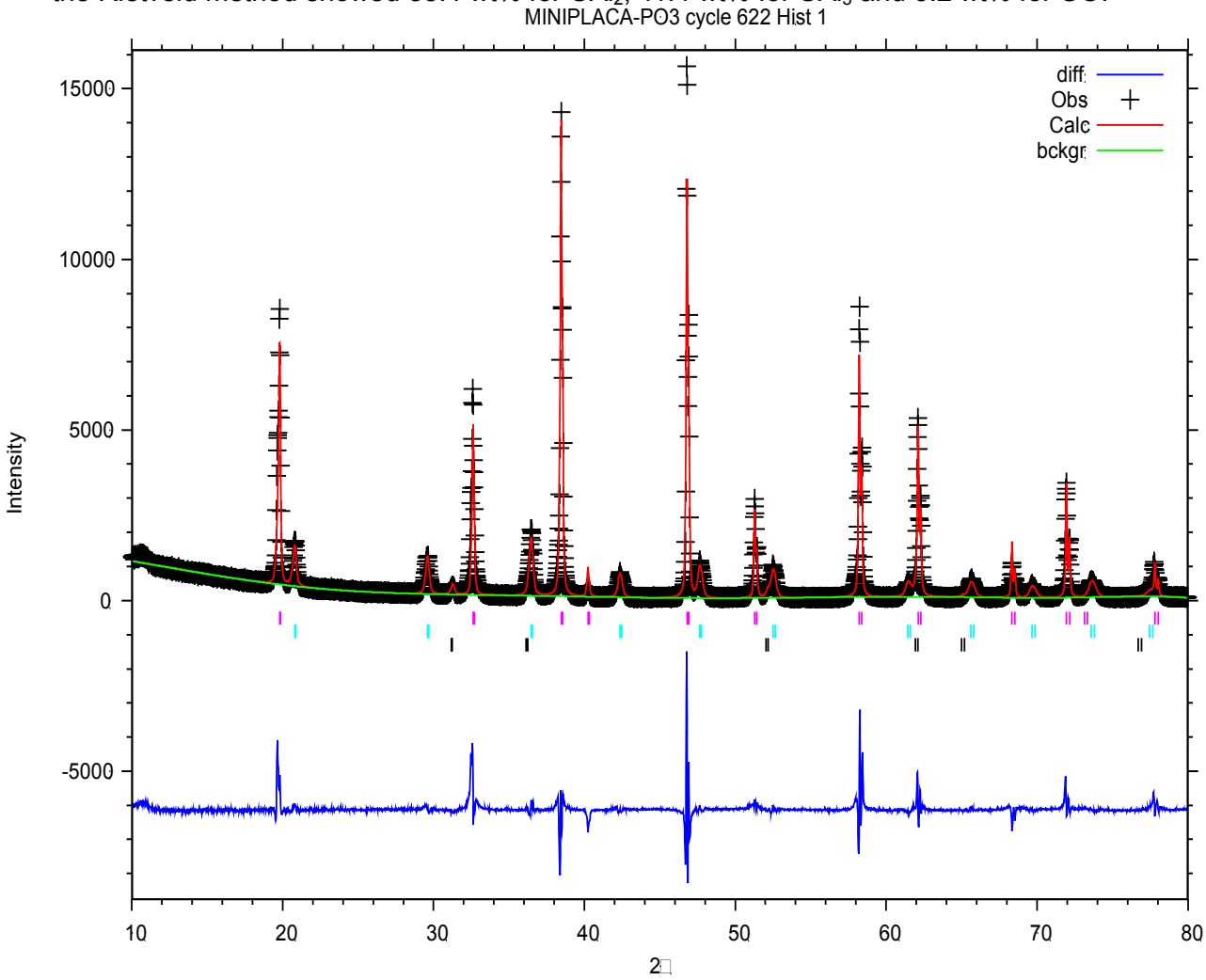


Fig 4. Experimental and calculated diffractograms for the UAl_x powder. The peaks marked with purple bars are from UAl_2, cyan bars from UAl_3 and black bars from UO

By Analyzing the results, it can be observed that they who? are extremely different with respect to the phase quantification. Table 2 summarizes the results obtained by image analysis and X-ray diffraction with Rietiveld refinement.

Phase	Rietiveld	Image Analysis	Expected Composition (chemical analysis)
UAl_2	85.4	42.6	89.4
UAl_3	11.4	56.2	10.6
UO	3.2	1.2	0

Tab 2: Results for phase quantitation in UAl_x powder (wt%)

The UAl_2 content determined from Rietiveld refinement is below the one expected according to the chemical analysis. This indicates low fit between the experimental and calculated data by the method, which could be attributed to the impossibility of rotating the sample during the X-ray diffraction analysis, since it was not possible to use the "spinner" during the analysis to avoid preferred orientation. Anyway, the approximation can be considered good, with a deviation of around 5 %.

In order to verify the feasibility of the method for following the phase composition during the UAl_x-Al dispersion target manufacturing process, core samples were analyzed by the x-ray diffraction with Rietveld refinement after each rolling pass, as showed in Table 1. The aim was to follow the phase composition evolution during the rolling process for target fabrication. This aspect is important, since the maximum UAl_2 phase concentration presented in the target must be determined by specification request. Polished specimens of the targets meat were analyzed by X-ray diffraction applying Rietveld refinement. The results are presented in Table 3.

Figure 5 presents the phase composition evolution inside the target meat during the target manufacturing process. After the first hot-rolling pass occurs remarkable transformation of UAl_2 to UAl_3 due to the solid state reaction with aluminum from the dispersion matrix. This reaction results from the heat treatment performed before the first hot-rolling (1 hour at 450 ^oC). In the subsequent hot-rolling passes does not occurs significant transformation, keeping the composition stable, within the error of the Rietveld method. After the last hot-rolling pass a new thermal treatment is accomplished with duration of 1 hour at 450 ^oC (blister test). The objective of this new heat treatment is to verify the bonding quality. After this new heat treatment, a significant transformation from UAl_2 to UAl_3 and the starting UAl_4 formation occur again, which is formed by the reaction of UAl3 with the aluminum matrix of the dispersion. The oxide concentration keeps unchanged within the error of the method.

Rolling Pass	UAl_2	UAl_3	UAl_4	UO
Briquette	85.4	11.4	0	3.2
P1 (hot)	74.3	24.3	0	1.4
P2 (hot)	71.7	27.2	0	1.1
P3 (hot)	75.5	22.7	0	1.8
P4 (hot)	73.1	24.7	0	2.2
P5 (cold)	47.6	47.1	4.6	0.7
P6 (cold)	48.1	45.6	5.3	1.0

Tab 3: Results for phase quantitation in UAl_x target meats (wt%)

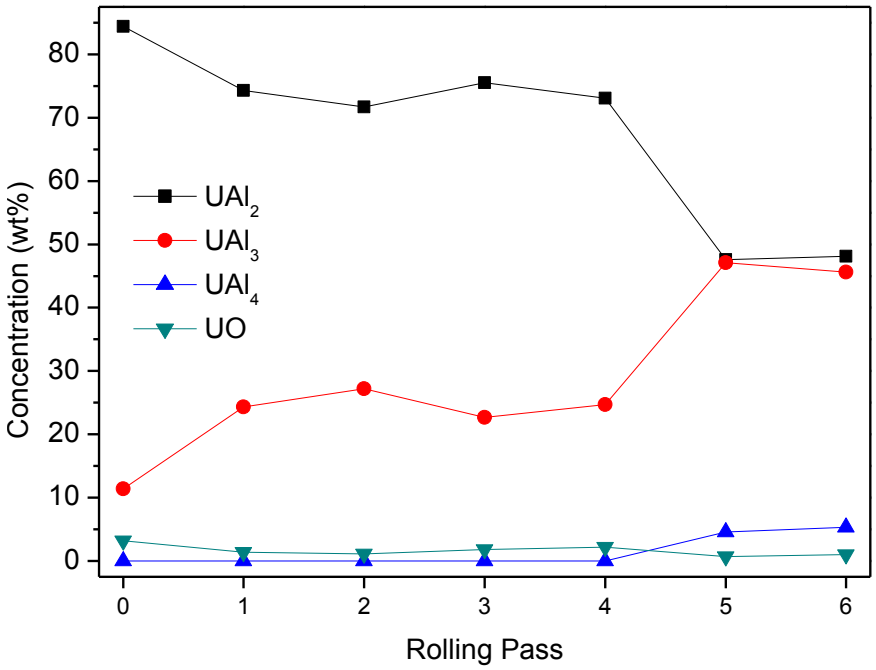


Fig 5. Phase composition evolution during the target manufacturing process

4. Conclusions

Two possible methods for phase quantification in dispersion based UAlx-Al irradiation targets were successfully studied. The method based on scanning electron microscopy and image analysis proved to be inapplicable due to some errors related to the fragmentation of UAl_2 particles. The method based on X-ray diffraction with Rietveld refinement proved to be applicable, with an estimated error of 5 %. By applying this method, it was possible to follow the evolution of the phase composition during the target manufacturing process. However, additional work on these methods is necessary to determine the error of the method.

Acknowledgments

The authors are grateful to FAPESP and CNPq for the research grants (2011/13849-9 and 471008/2011-7) provided for this work.

5. References

1. "A Supply and Demand Update of the Molybdenum-99 Market-2012," http://www.oecd-nea.org/med-radio/#docs (2012).
2. "The Supply of Medical Radioisotopes: the Path to Reliability," http://www.oecd-nea.org/med-radio/#docs (2011).
3. Briyatmoko, B.; Guswardani, B; Purwanta, S.; Permania, S.; Basiran, D.; Kartaman, M. "Indonesia's current status for conversion of Mo-99 production to LEU fission," *Proceeding of International Meeting on Reduced Enrichment for Research and Test Reactors*, Prague, Czech Republic, September 23–27, 2007. http://www.rertr.anl.gov/RERTR29/Abstracts/S6-1_Briyatmoko.html
4. Kohut, C.; Fuente, M.; Echenique, P.; Podesta, D.; Adelfang, P. "Targets development of low enrichment for production of Mo99 for fission," *Proceeding of International Meeting on Reduced Enrichment for Research and Test Reactors*, Las Vegas, Nevada, October 1-6, 2000. http://www.rertr.anl.gov/Web2000/Title-Name-Abstract/Fuente00.html
5. Bramfitt, B. L.; Leighly H. P. Jr. "A Metallographic Study of Solidification and Segregation in Cast Aluminum-Uranium Alloys," *Metallography*, **I**, pp. 165-193 (l968).
6. Cols, H. J.; Cristini, P. R.; Manzini, A. C. "Mo – 99 from low-enriched uranium," *Proceeding of International Meeting on Reduced Enrichment for Research and Test Reactors*, Las Vegas, Nevada, October 1-6, 2000. http://www.rertr.anl.gov/Web2000/Title-Name-Abstract/Cristi00.html
7. Cunningham, J. E.; Boyle, E. J. "MTR-Type fuel elements,". *Proceeding of the International Conference on Peaceful Uses of Atomic Energy*, Geneva, 8-20 August. 1955. Vol. 9: Reactor technology and chemical processing, pp.203-207 (1956).
8. Durazzo, M.; Urano de Carvalho, E. F.; Saliba Silva, A. M.; Souza, J. A. B.; Riella, H. G. "Current status of U_3Si_2 fuel elements fabrication in Brazil," *Proceeding of International Meeting on Reduced Enrichment for Research and Test Reactors*, Prague, Czech Republic, September 23–27, 2007. http://www.rertr.anl.gov/RERTR29/Abstracts/S11-8_Durazzo.html
9. Durazzo, M.; Urano de Carvalho, E. F.; Saliba Silva, A. M.; Souza, J. A. B.; Riella, H. G. "Fabricação de elementos combustíveis a base de U_3Si_2 no Brasil," *Rev. Bras.Pesq.Des.*, **Vol. 9**, **n. 1**, pp.18-26 (2007).

Benchmark Criticality Experiments for Uranium-Water Heterogeneous Configurations with Low Enrichment UZrCN Fuel

S.N. Sikorin, S.G. Mandzik, S.A. Polazau, T.K. Hryharovich, I.S. Soltan,
Y.V. Damarad, Y.A. Palahina
Joint Institute for Power and Nuclear Research – Sosny,
99 Academic Krasin Street, 220109 Minsk, Belarus

Y. Gohar, A. Talamo, Z. Zhong
Nuclear Engineering Division
Argonne National Laboratory,
9700 South Cass Avenue, Argonne, IL 60439, USA

I. Bolshinsky
Idaho National Laboratory,
2525 Fremont Ave, Idaho Falls, ID 83401, USA

Sh.T. Tukhvatulin, R.Kh. Zhalilov, V.Yu. Vishnevsky, I.D. Daragan
Scientific Research Institute Scientific Industrial Association "LUCH",
24 Zheleznodorozhnaya Street, 142100 Podolsk, Russia

ABSTRACT

Benchmark criticality experiments of uranium-water heterogeneous configurations with low enriched uranium (LEU) nuclear fuel were performed using "Giacint" critical facility of the Joint Institute for Power and Nuclear Research – Sosny (JIPNR–Sosny) of National Academy Science of Belarus. The fuel rod pitch is 18, 32, or 47 mm with a triangular grid. The criticality conditions were obtained by adjusting the liquid moderator height of the configurations. The fuel was designed and produced by the Scientific Research Institute Scientific Industrial Association "LUCH" (SRI SIA "LUCH") under the Russian Research Reactor Fuel Return (RRRFR) Program of the U.S. Department of Energy. The fuel material uranium-zirconium-carbon nitride $U_{0,9}Zr_{0,1}C_xN_{1-x}$ has U-235 enrichment of 19.75%. The fuel material density is ≥12 g/cm^3; the porosity is <12%. The uranium metal density is >10.5 g/cm^3. The total fuel rod length is 620 mm, and the active fuel length is 500 mm. The outer fuel rod diameter is 12 mm, and the fuel material diameter is 10.7 mm. The clad material is stainless steel or niobium. The Argonne National Laboratory (ANL) and the JIPNR-Sosny have been collaborating on analyzing the experimental results obtained from these benchmark experiments by developing detailed calculation models and performing simulations for the different experiments. The sensitivity of the obtained results for the material specifications and the modeling details were examined. The analyses used the MCNP and MCUFREE computer programs. This paper presents the obtained experimental and analytical results.

1. Introduction

The Belarusian-Russian-American cooperation on conversion of nuclear fuel from research reactors included the delivery to the Joint Institute for Power and Nuclear Research – Sosny (JIPNR–Sosny) of National Academy Science of Belarus of new fresh low enriched uranium (LEU) nuclear fuel for the “Giacint” critical facility.
This nuclear fuel, developed and fabricated in the SRI SIA “LUCH”, represents uranium-zirconium-carbon nitride UZrCN with U-235 enrichment of 19.75% [1].
The JIPNR–Sosny of National Academy Science of Belarus, together with the Argonne National Laboratory (ANL) of the USA, developed a program of benchmark experiments in order to investigate critical parameters of pure uranium-water grids with the said LEU nuclear fuel. The “Giacint” critical facility was used to test eight critical assembly configurations with different levels of the water moderator and three pitches of fuel rod arrangements in the triangular grids (18, 32 and 47 mm). The known material composition and a simple geometry of the said critical assemblies made it possible to build analytical models for the MCNP [2, 3] and MCUFREE [4] codes and compare the experimental results and calculated data.
This report includes experimental data on the criticality of uranium-water multiplication systems with cores based on the above fuel rods and the analytical results on the criticality of such multiplication systems using the MCNP and MCUFREE codes in order identify the possibilities of using such results as benchmark data on criticality.

2. Fuel rods based on uranium-zirconium-carbon nitride

The fuel rod based on uranium-zirconium-carbon nitride UZrCN (type 20 or 20.1) (Fig. 1) includes a fuel core, a clad and end parts. The fuel rod clad is 12 mm in outer diameter with the 0.6 mm wall thickness. The fuel core comprises tablets 10.7 mm in diameter and 14.7 mm in height from uranium-zirconium-carbon nitride $U_{0,9}Zr_{0,1}C_XN_{1-X}$. The core density is 12.0 g/cm^3, with the U-235 enrichment of 19.75%. The U-235 mass in the fuel rod is 96.6 g. The gaseous He spacing between the fuel rod tablets and the fuel rod clad has the pressure ~0.11 MPs. The total core height is 500 mm. The total fuel rod length is 620 mm. The fuel rod is tightly sealed by welding the upper and lower plugs to the clad. The clad and end parts of fuel rods, type 20, are made from stainless steel, and of fuel rods, type 20.1, from niobium alloy.

3. “Giacint” critical facility

The “Giacint” critical facility includes: a critical assembly, a control and protection system, a hydraulic system, a temporary (working) storage of nuclear fuel, radioactive materials and radioactive waste, etc. The “Giacint” critical facility is versatile and can be used for research of critical assemblies with liquid or solid moderator or without moderator. Fuel rods and fuel cassettes are available, containing uranium-235 of different enrichment (10, 21, 36, 75 and 90%), as well as cassettes and reflector units (based on zirconium hydride, beryllium, polyethylene, stainless steel, etc.) and controls (rods and plates) of the control and protection system (based on europium oxide, boron carbide (*inter alia*, with up to 85% enrichment by boron-10), cadmium, etc.).

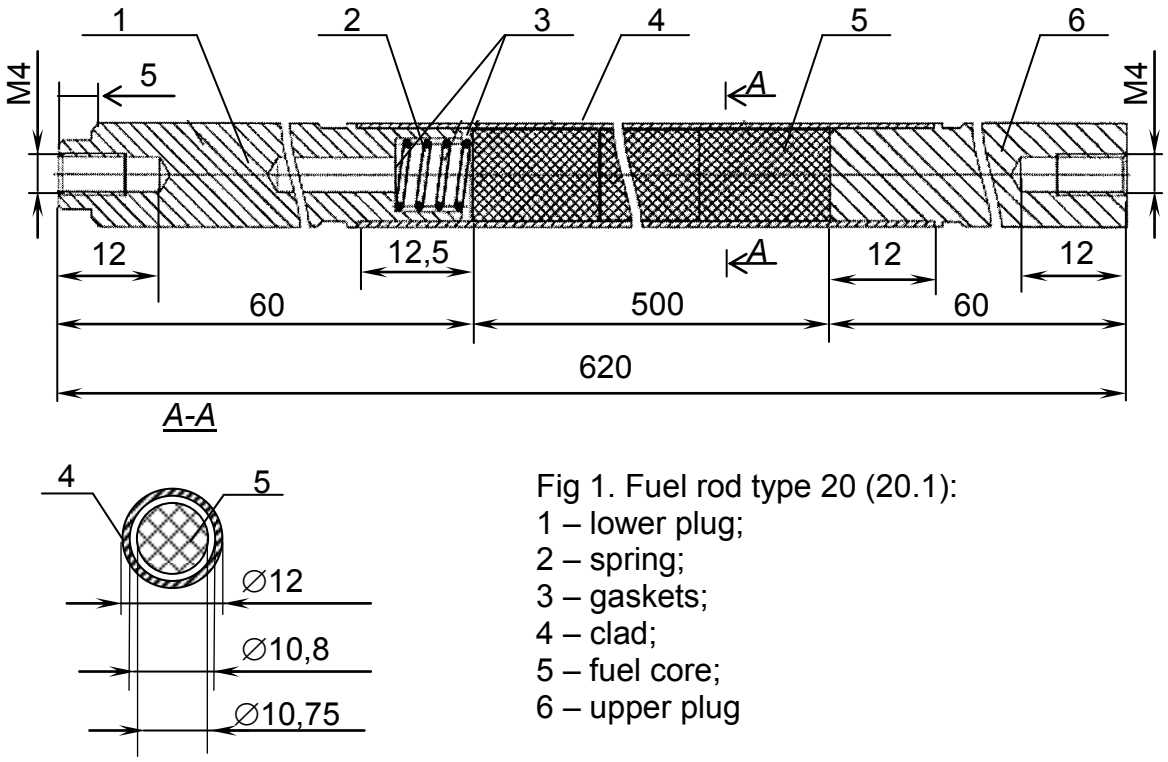


Fig 1. Fuel rod type 20 (20.1):
1 – lower plug;
2 – spring;
3 – gaskets;
4 – clad;
5 – fuel core;
6 – upper plug

4. Uranium-water critical assemblies

Each of the three studies uranium-water critical assemblies represents a homogeneous grid (18, 32 or 47 mm pitch) of fuel rods, containing uranium-zirconium-carbon nitride UZrCN with 19.75% U-235 in a steel (type 20 fuel rods) or niobium (type 20.1 fuel rods) clad, with water moderator and reflector. The critical assembly (see Fig. 2) is a thermal “open tank” critical assembly, comprising the core, the side reflector, the upper and lower end reflectors, and the controls of the control and protection system (CPS).

The critical assembly with water moderator is located in the critical assembly’s tank, which represents a welded stainless steel structure 2020 mm high and 1810 mm in diameter. The tank has a top flange to fix the aluminum hoods of the neutron detectors. The core of the critical assembly comprises fuel rods, types 20 or 20 and 20.1, which are fixed in the spacing hexagonal grids from 10-mm aluminum with holes arranged in the hexagonal grid with the pitch of 18 mm (critical assembly B-20-1), 32 mm (critical assembly B-20-2) or 47 mm (critical assembly B-20-3) and supported by the hexagonal plate from stainless steel, 16 mm thick, with holes for the control and protection system’s controls. A hexagonal upper plate from 16-mm stainless steel is arranged above the fuel rod pitch; the plate also has holes arranged in the hexagonal grid with the pitch equal to the pitch of holes in the spacing grids. The spacing grids are arranged along the upper (bottom of the grid) and lower (top of the grid) edges of the core. The support plate is arranged ~800 mm from the bottom of the critical assembly’s tank.

The side water reflector has tight hoods, around the core, with neutron detectors of the control and protection system, which are fixed to the flange of the critical assembly's tank.

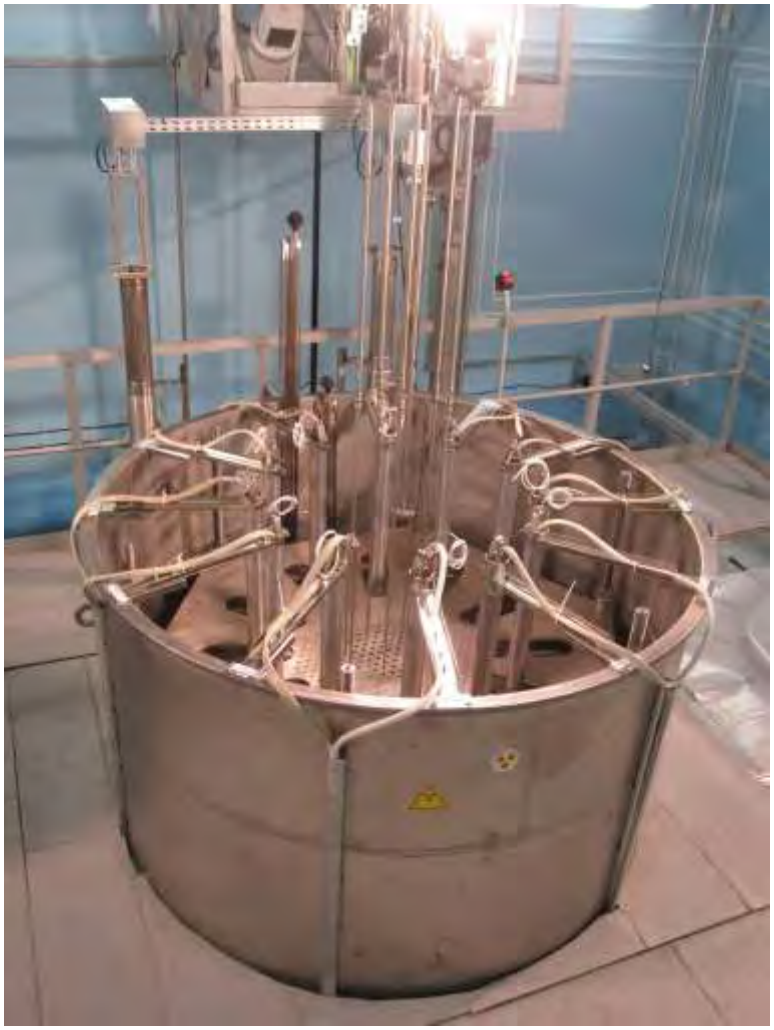


Fig 2. Critical assembly with water moderator

The critical assembly includes six control and protection system's controls; three controls are in the core and others in the reflector. The control and protection system's controls in the core contain composite rods formed by the fuel rod type 20 and the absorber element rigidly interconnected via the adaptor. The critical assembly reactivity decreases by moving the fuel rods downwards from the core and moving the absorber elements in their place. The control and protection system's controls located in the side reflector represent clusters of two composite rods, represented by the organic glass tip and the absorber element rigidly interconnected via the adaptor. In this case, the critical assembly reactivity decreases by moving the organic glass tips downwards from the side reflector and moving the absorber elements in their place.

The absorber element is a cylindrical clad from stainless steel of 12 mm diameter and 1 mm walls, filled with natural density boron carbide powder (~1.3 g/cm^3) to 500 mm height. The absorber element is tightly sealed by welding the upper and lower 60-mm long stainless steel plugs to the clad. The total stainless steel length is 620 mm.

Thus, when the control and protection system's controls are moved out from the core and the side reflector, the critical assembly represents the so-called "pure" (i.e. without absorbers) grid of fuel rods in the water moderator.

The "Giacint" critical facility was used to make experiments on the criticality of three uranium-water critical assemblies B-20-1, B-20-2 and B-20-3 with different critical loads. The critical assemblies represented pure grids of fuel rods, type 20, or type 20 and 20.1. The criticality was assured by the level of the moderator in the critical assembly. Table 1 presents characteristics of the critical assemblies.

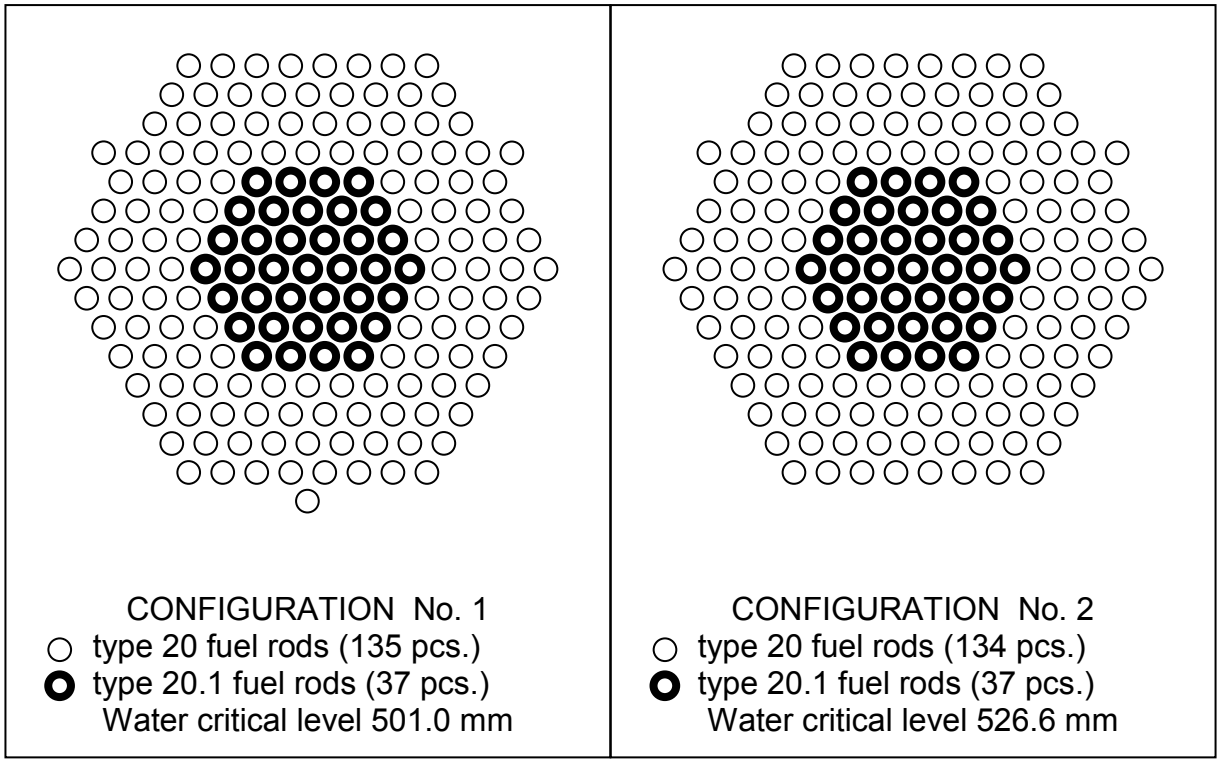


Fig 3. Critical configurations of critical assembly B-20-1

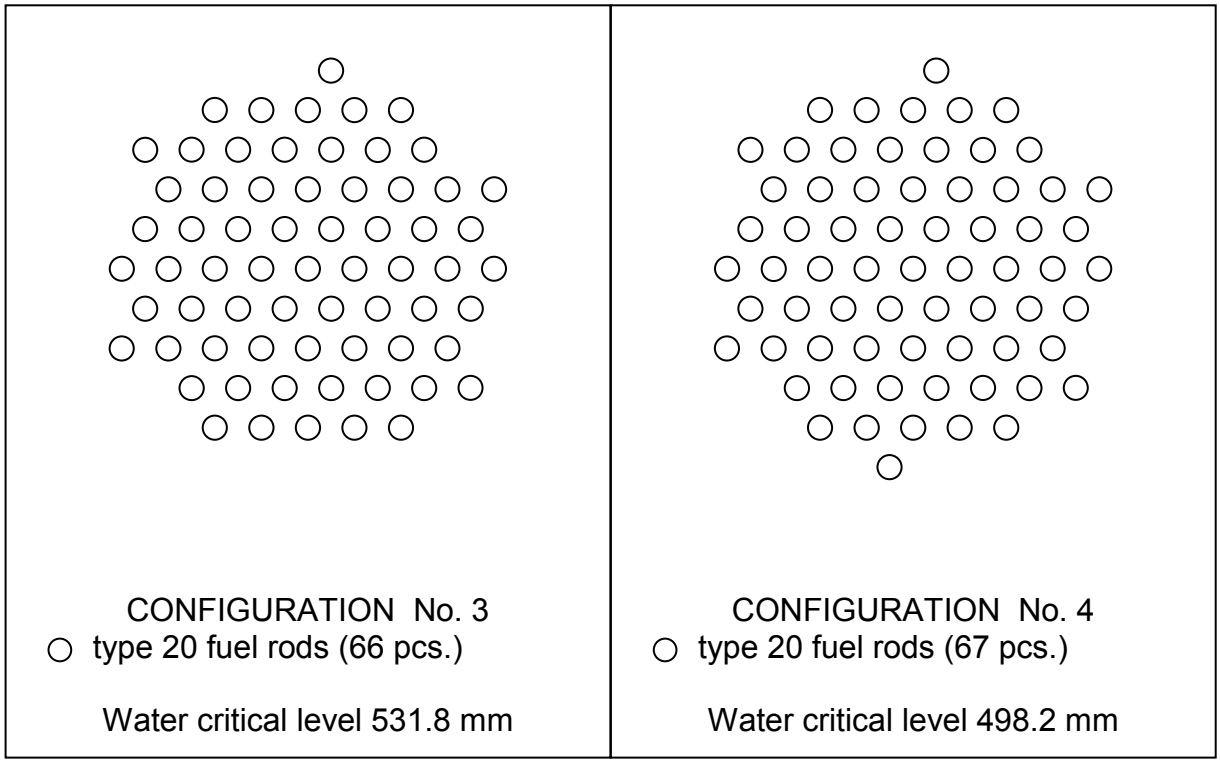


Fig 4. Critical configurations of critical assembly B-20-2

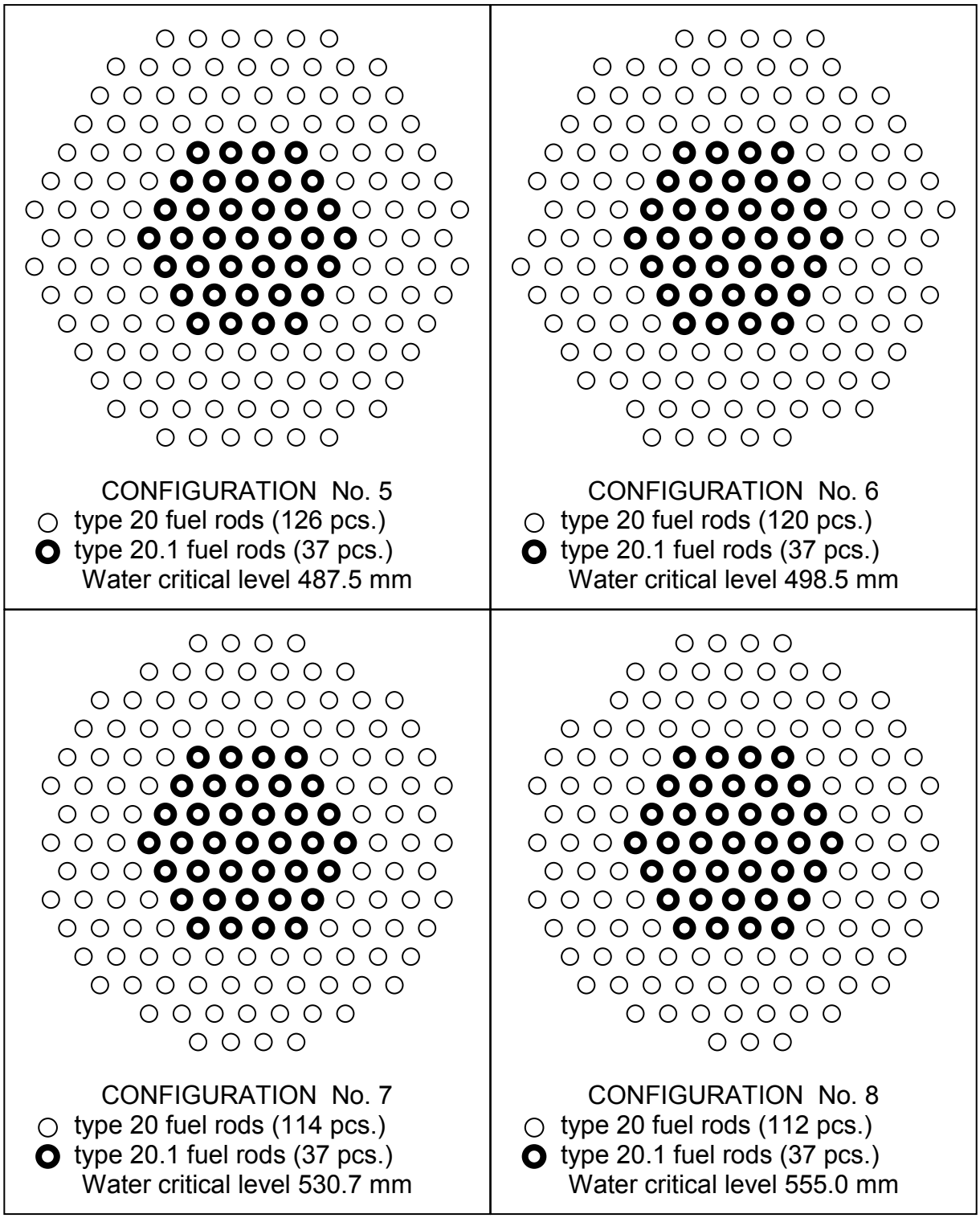


Fig 5. Critical configurations of critical assembly B-20-3

Tab 1. Critical assembly characteristics

Critical assembly No.	Confi-guration	Grid pitch, mm	Fuel rods type 20, pcs.	Fuel rods type 20.1, pcs.	Water critical level*, mm	Water temperature, °C
B-20-1	1	18.0±0.1	135	37	501.0±1.0	20.6±0.1
	2		134	37	526.6±1.0	20.6±0.1
B-20-2	3	32.0±0.1	66	-	531.8±1.0	16.5±0.1
	4		67	-	498.2±1.0	11.8±0.1
B-20-3	5	47.0±0.1	126	37	487.5±1.0	18.9±0.1
	6		120	37	498.5±1.0	19.4±0.1
	7		114	37	530.7±1.0	19.4±0.1
	8		112	37	555.0±1.0	19.6±0.1

* — the level was measured from the core bottom.

5. Calculation results

For the estimation of experimental results, analytical models for each critical assembly have been constructed by using two program codes MCNP and MCUFREE. Calculations of K_{eff} were made by the method of Monte-Carlo using: 1) versions MCNP-4C and libraries of nuclear data ENDF-B/V and ENDF-B/VI (the calculations were made in JIPNR-Sosny); 2) versions MCNP-6.1 and libraries of nuclear data ENDF/B-VII.1 [5] (the calculations were made in ANL) and 3) MCUFREE code (the calculations were made in JIPNR-Sosny). The results of calculations are presented in Table 2.

Tab 2. Calculation results of K_{eff} for uranium-water critical assemblies

Critical assembly No.	Confi-guration No.	K_{eff}			
		MCNP-4C (ENDF/B-V)	MCNP-4C (ENDF/B-VI)	MCNP-6.1 (ENDF/B- VII.1)	MCUFREE
B-20-1	1	0.99584±8	0.99650±8	-	1.0052±4
	2	0.99621±8	0.99653±8	-	1.0037±6
B-20-2	3	1.00034±17	0.99819±17	1.00097±4	0.9974±12
	4	1.00547±18	1.00268±18	1.00170±4	1.0008±16
B-20-3	5	0.99682±16	0.99485±16	1.00375±4	1.0008±13
	6	0.99594±15	0.99375±15	1.00275±4	0.9994±11
	7	0.99592±16	0.99407±15	1.00287±2	0.9911±13
	8	0.99587±15	0.99381±16	1.00270±2	0.9898±13

From Table 2, it can be seen that the analytical and experimental data received for described above uranium-water critical assemblies match very well within the value of experimental and analytical errors.

6. Conclusions

The results of the analysis of experimental data and analytical calculations for uranium-water critical assemblies with 19.75 % enrichment UZrCN fuel rods give the possibility to conclude that these results on criticality (critical loadings) can be used as benchmark criticality data.

7. References

1. Dyakov E., Blank V. Uranium Carbonitride Compounds – Fuel for Promising Compact Nuclear Reactors / Proceeding of Space Nuclear Conference 2007, Boston, Massachusetts, 24-28 June 2007.
2. ”MCNP – A General Monte Carlo N-Particle Transport Code, Version 4C,” Ed. J. F. Briesmeister, Report LNL, LA-13709-M, 2000.
3. D.B. Pelowitz et al., MCNP6 User Manual, version 1, Los Alamos National Laboratory, LA-CP-13-00634, 2013.
4. The application and instructions to users for MCUFREE code of Monte Carlo nuclear reactor characteristics calculation / Edited by D. Shkarovsky, M., 146 p. http://mcuproject.ru/museum/lvmvant/lvmvant07.pdf.
5. M.B. Chadvick et al., ”ENDF/B-VII.1 Nuclear Data for Science and Technology Cross Sections, Covariances, Fission Product Yields and Decay Data”, Nuclear Data Sheets 112/12, 2011.

PASSIVE RESIDUAL HEAT REMOVAL SYSTEM OF AN OPEN-POOL TYPE RESEARCH REACTOR USING GRAVITY CORE COOLING TANK

K.Y. LEE, D.Y. CHI, S.H. KIM, K.W. SEO, J. YOON
Fluid System Design Division, Korea Atomic Energy Research Institute
Daedeok-daero 989-111, Yuseong-gu, 305-353, Daejeon, Korea

ABSTRACT

A research reactor is cooled by a primary cooling system during normal operation. After a normal or abnormal shut-down, the decay heat of the core is removed by a natural circulation through flap valves to the reactor pool after the primary cooling pump is turned off. That is, the flap valves installed on the pipe of the primary cooling system inside the pool are designed to be passively opened, when the flowrate of the system is reduced. In an open-pool type research reactor, however, the primary cooling system can be designed to have a downward flow inside the core during normal operation because of the plate type fuel geometry. This means that there is a flow inversion inside the core from the downward flow by the inertia force of the primary coolant to the upward flow by the natural circulation when the pump is turned off. To delay the flow inversion time, a flywheel is installed in a shaft of the pump to have larger inertia force. However, the inertia force by the flywheel is not sufficient to remove the residual heat for a high power research reactor. Thus, a passive system with a Gravity Core Cooling Tank (GCCT) is developed to remove the residual heat. The GCCT is an additional small pool next to the reactor pool, and there is a piping system connecting two pools. Before the pump starts up, the water level of the GCCT is same as that of the reactor pool. During the pump operation, the water in the GCCT is moved into the reactor pool because of the pump suction head. Here, a hydraulic static head generated by the water level difference between the two pools is equivalent to a pressure drop through the core. After the pump stops, the potential head generates a downward flow inside the core by moving the water from the reactor pool to the GCCT, and removes the residual heat. When the water levels of the two pools are the same again, the core flow has an inversion of the flow direction, and natural circulation is developed through the flap valves.

1. Introduction

Research reactors are generally divided into a Tank-in-pool type and an Open-pool type. An Open-pool type research reactor has a benefit in the points of reactor usage such as isotope production because the top of the core is opened. In an open-pool type research reactor, the decay heat of the core is transferred into the reactor pool by a natural circulation through the flap valves after the Primary Cooling Pump (PCP) is turned off. That is, the flap valves installed on the pipe of the Primary Cooling System (PCS) inside the reactor pool are designed to be passively opened, when the flowrate of the PCS is reduced below the design limit. If the core flow is in an upward direction during PCP operation, the transition from a forced convection to a natural convection will be natural, and worry about the core damage will be very small. However, there is a recent trend to use a plate type fuel, and a core downward flow is considered because it is benefit to install plate type fuel in the core. In this case, a flow inversion from a downward to upward flow in the core is generated after the PCP is turned off. If this phenomenon is introduced within a high heat flux region of residual heat, the fuel fails instantly due to zero flow. Therefore, the core downward flow should be sufficiently maintained until the residual heat is in a low heat flux region.
In a small power research reactor, inertia generated by a flywheel of the PCP can maintain a downward flow shortly and resolve the problem of a flow inversion. However, a high power research reactor more than 10 MW should have an additional method to have a longer downward flow until a low heat flux. Usually, other research reactors have selected an active residual heat removal system as a safety class. In this case, it is difficult to design

and operate an active system pump because its operating point is various according to the operation conditions of a PCP. In addition, the system should have two trains separately considering the redundancy and diversity, and safety class UPS (Uninterruptible Power Supply) or EDG (Emergency Diesel Generator) considering a loss of electric power accident.
Recently, the consumption of a radioactive isotope is increased for cancer diagnosis. However, isotope production research reactors existing in the world are deteriorated and have low efficiency. Therefore, there are several plans to construct new research reactors for isotope production including the KJRR (KIJANG Research Reactor) of South Korea. The work place to replace fuels and isotope targets is at the top of the reactor pool, and replacement works are difficult and take several days because of the heat waves by natural convection in the decay heat removal process. Thus, it is necessary to maintain a downward flow in the core with a low flowrate for the decay heat and heat wave removal.

2. Passive residual heat removal system using GCCT

A passive residual heat removal system for an open-pool type research reactor was developed using a Gravity Core Cooling Tank (GCCT), as shown in Figure 1. The GCCT beside a reactor pool is a small tank opened to the air with atmospheric pressure. A Residual Heat Removal Pipe (RHRP) is connected to a lower plenum of the Reactor Structure Assembly (RSA) and bottom of the GCCT. Thus, cooling water passing the core can flow to the GCCT through the RHRP to remove core decay heat.
Additionally, a Pool Water Cooling and Purification System (PWCPS) was designed to improve the safety and usability of the research reactor, as shown in Figure 1. A PWCPS consists of a pump, a flow control valve, a heat exchanger, a filter, an ion exchanger, and related pipes. A Decay Wall (DW) is installed to separate a discharge area from the RHRP and a suction area of the pump because cooling water passing the core has a very high radiation level. Namely, cooling water discharged from the RHRP stays for a sufficiently long time inside the GCCT before entering the PWCPS to decay out N-16, which has a high radiation level but short half-life time. As a result, cooling water inside the PWCPS has a low radiation level, and the design of PWCPS is easy and cheap.
Here, the reactor pool, GCCT, and RHRP shall be designed as the safety class, but the PWCPS will be a non-safety class because it is not related with reactor safety directly.

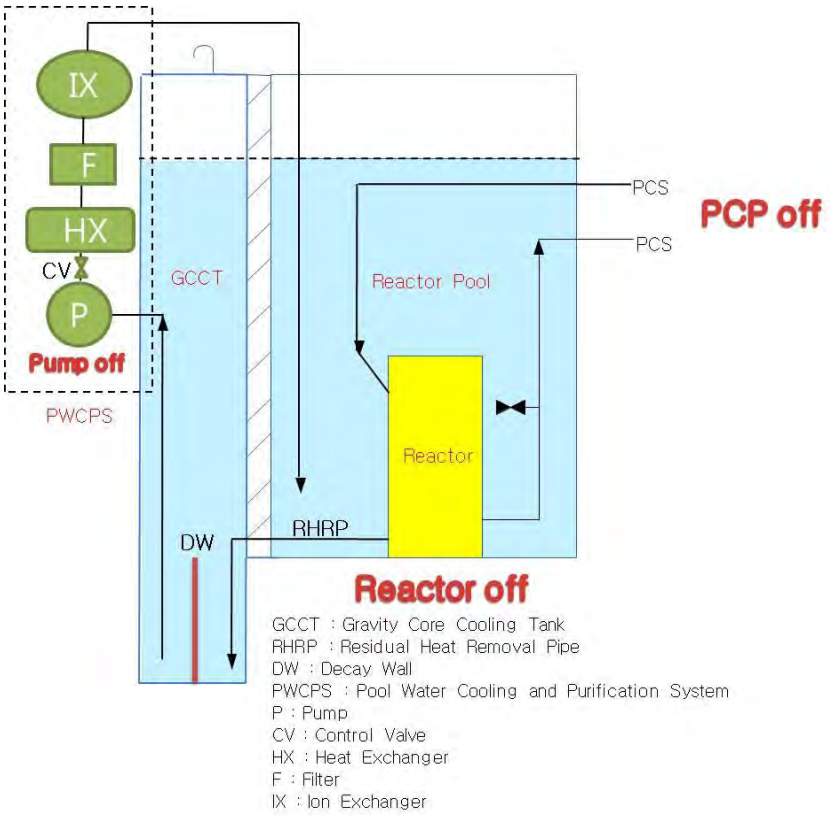


Fig 1. Schematic diagram of PRHRS using GCCT

3. Operation

3.1 PCS operation

Figure 1 shows the status of a reactor off, PCP off and PWCPS pump off of an open-pool type research reactor. The reactor pool and GCCT have the same pool water levels because cooling water can move freely through the RHRP between the two pools.
After the PCP is turned on, the water level of the GCCT gradually decreases because some water moves from the GCCT to the reactor pool through the RHRP. An increase of the reactor pool water level is small because the surface area of the reactor pool is much larger than that of GCCT. Finally, two pools have a water level difference, as shown in Figure 2, and the flow of cooling water through the RHRP is stopped. Here, the hydrostatic head by the water level difference is the same as the pressure drop through the core.

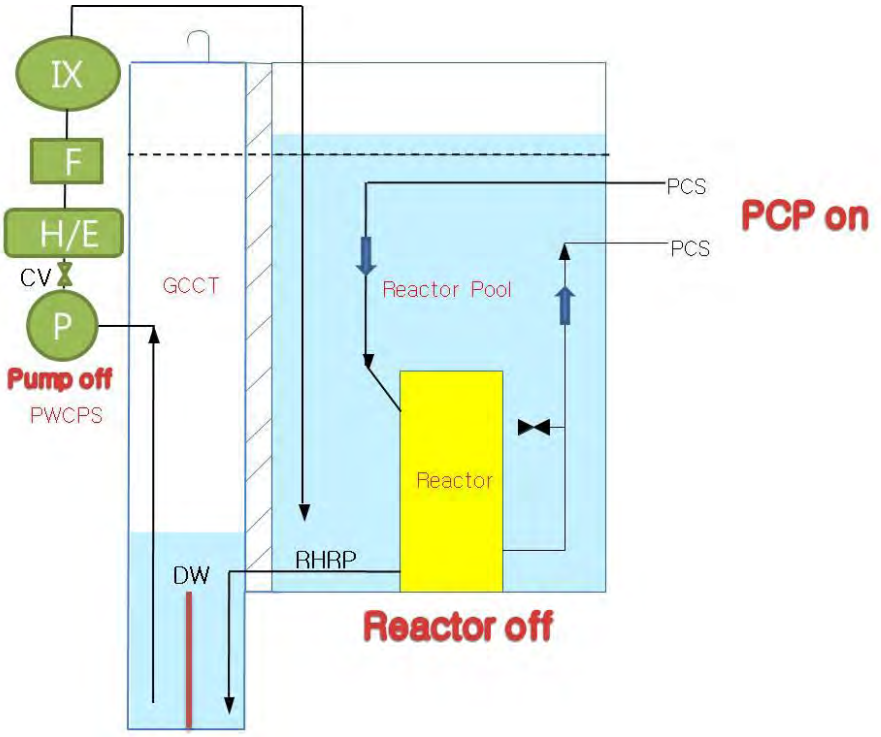


Fig 2. PCS operation

3.2 Normal power operation condition

PWCPS is turned on after the PCS, reactor pool, and GCCT are in stable operation conditions. Cooling water flows in the PWCPS from the GCCT, and is discharged into the reactor pool after passing the pump, heat exchanger, filter, and ion exchanger of the PWCPS. Some reactor pool water is suctioned into the reactor through the top opening of the RSA, mixed with PCS water, and passed the core. Some of the heated cooling water at the lower plenum of the RSA moves into the GCCT through RHRP. After PWCPS is stable with the balanced mass flowrates, the reactor shall start a power operation. A flow diagram is shown in Figure 3 for normal power operation conditions.
When PCS water is discharged into the RSA, some PCS water will be released into the reactor pool through the top opening of the RSA due to collisions between flows and structures. It will generate some flow in the upper section of the reactor pool above the reactor, and this flow will make the radiation material moved on the surface of the reactor pool. In this case, reactor operation will be impossible because of a high pool top surface radiation limit. However, the suction flow of the reactor pool water through the top opening of the RSA blocks the released PCS flow, and the pool top surface radiation level is low. In addition, an extra purification system for a PCS is not required because the purified water from a PWCPS is mixed with PCS water.

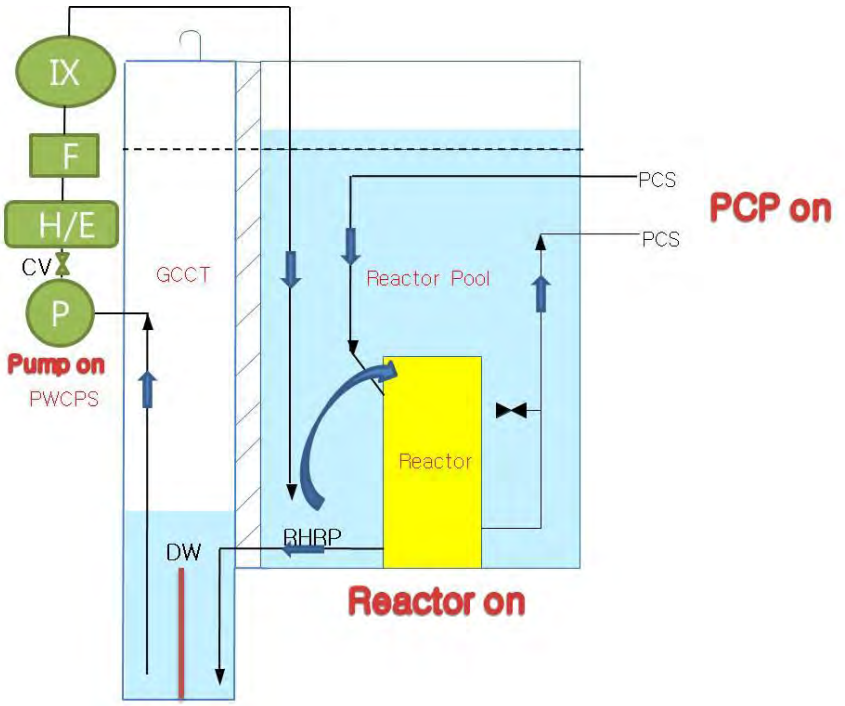


Fig 3. Reactor operation

3.3 Normal shut-down condition

Figure 4 shows the pool water level and flow when nuclear fuel or targets for isotope production are changed after a reactor normal shut-down. The PCP is turned off after the reactor is shut-down, and the core differential pressure is decreased. Then, some reactor pool water moves through the core and RHRP, and the core decay heat is removed. Finally, the reactor pool and GCCT have the same water levels. Because PWCPS is still in operation, the core downward flow is continually maintained. It can remove the core decay heat and heat waves actively. Here, a check valve shall be installed in the PCS pipe to protect backflow and to confirm that the RHRP flow is identical with the core downward flow. In addition, a flow control valve is designed at the downstream of the PWCPS pump due to water level changes in GCCT.

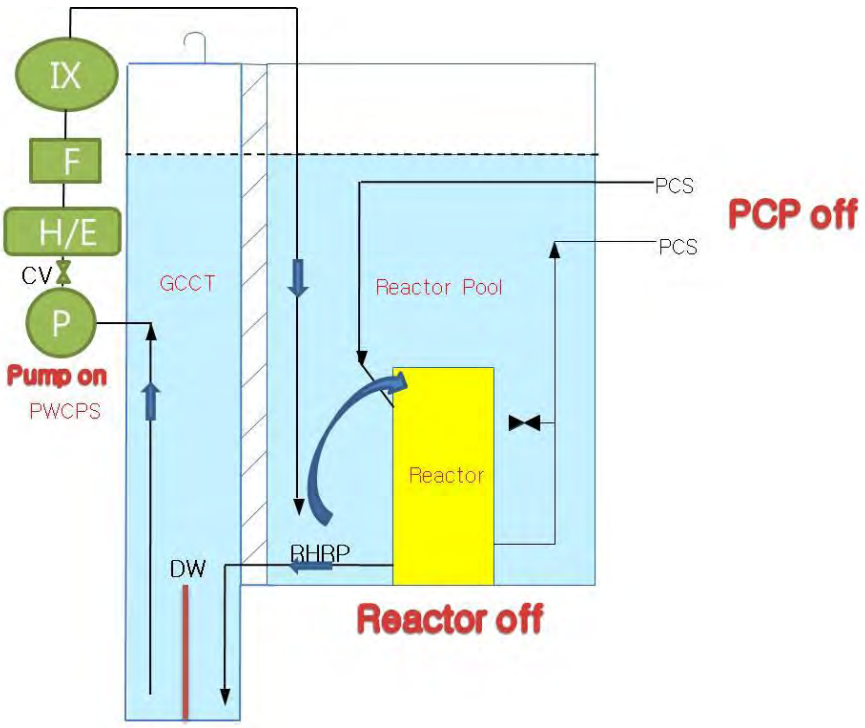


Fig 4. Reactor normal shut-down

3.4 Reactor accident condition

Under reactor accident conditions, the reactor is shut-down, and the PCP is quickly turned off. Even though PWCPS can remove the core decay heat, this system shall be neglected for the safety analysis because it is a non-safety class. The water level difference between the reactor pool and GCCT maintains core downward flow naturally, as shown in Figure 5, and the flow stops when two pool levels are equal. Then, a flap valve on the PCS pipe inside the reactor pool is automatically opened by gravity force. The decay heat is removed by natural circulation through the flap valve, lower plenum, and the core to the pool. It is important to decide the sizes of GCCT and RHRP considering a decay heat curve and a natural circulation performance.

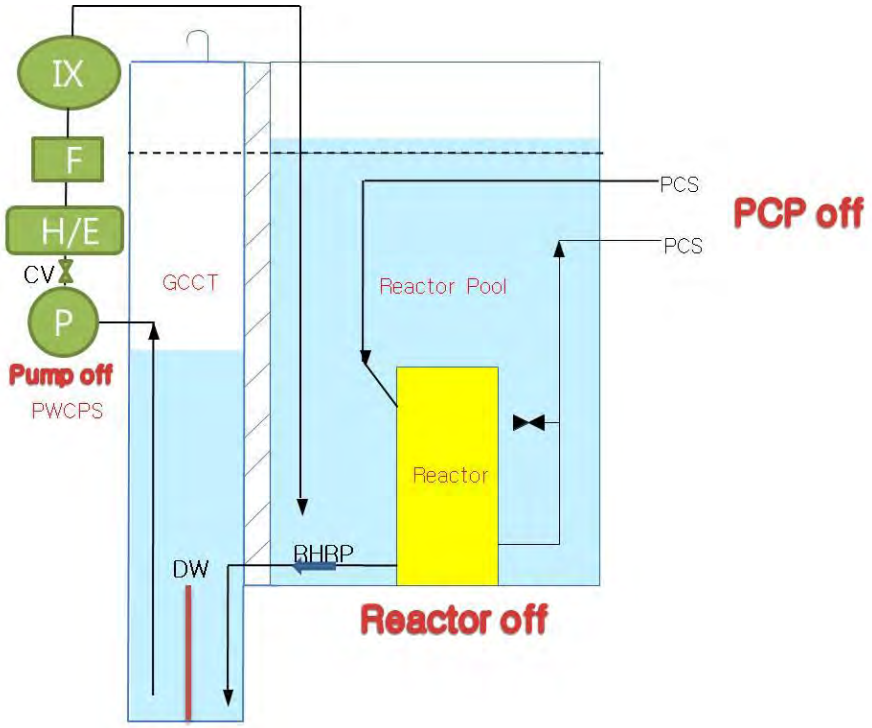


Fig 5. Reactor accident

4. Preliminary design

An open-pool research reactor was preliminarily designed in this paper. It has 15 MW of thermal power, a 20 m^2 reactor pool area, a 30 m^2 service pool area, and 11 m water levels under normal power operation conditions. Normally, the pool gate between the reactor pool and service pool was opened. The flowrate of PCS was 550 kg/s, and the pressure drop through the core was 110 kPa. During reactor normal operation, the rector pool and service pool therefore had an 11 m water level, and the GCCT had a 0 m water level.

After the reactor shut-down, 8% of full power was considered as a decay heat of the core, and was 1200 kW. To consider the hot channel effect, we assumed that the required heat removal capacity was double, i.e., 2400 kW. In addition, we assumed that the inlet coolant temperature was 40 ℃, and it was heated as saturated liquid at the outlet of the core with 120 ℃. The specific heat was assumed to be 4.2 kJ/kg·℃. Then, the required flowrate was 7.14 kg/s from the heat balance. The decay heat was decreased to 4% and 2% of full power after about 200 and 2000 seconds, respectively. Of course, the required flowrate was 1.78 kg/s for 2% decay heat removal. A natural circulation flow can beremoved at this level of decay heat, and the flow reversal from downward to upward at the core may then be permitted.

At first, a flywheel with 150 kg· m^2 inertia was considered in the PCP for the initial cooling of the core after a reactor shut-down. A coast down flow by the flywheel is shown in Figure 6. It was enough to maintain the downward flow to remove the core decay heat until approximately 130 seconds.

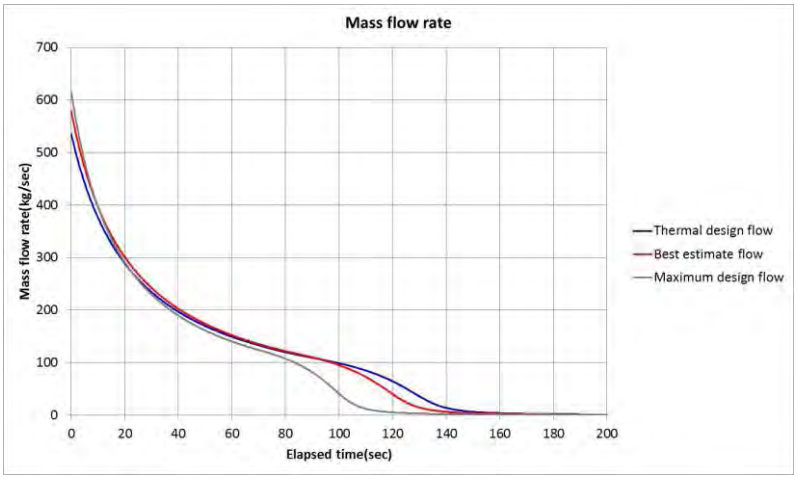


Fig 6. Coast down flow by PCP flywheel

From the Bernoulli equation, the velocity at the RHRP was dependent on the root of the water level difference, and the flowrate through the RHRP was the pipe diameter multiplied with the velocity. The reactor pool water level gradually decreased and the GCCT water level increased. The flow disappeared when the two water levels were the same. Figures 7 and 8 show the flowrate from the reactor pool to the GCCT along with their water levels. The flowrate was decreased linearly, but it was higher than 1.78 kg/s until 1990 seconds. The flow stopped at 2200 seconds, and the final water levels were identically 10.6 m. The GCCT may be capable of applying an intermediate cooling method.
For long-term cooling, the flap valve will be opened at around 2000 seconds after a reactor shut-down to generate natural circulation.

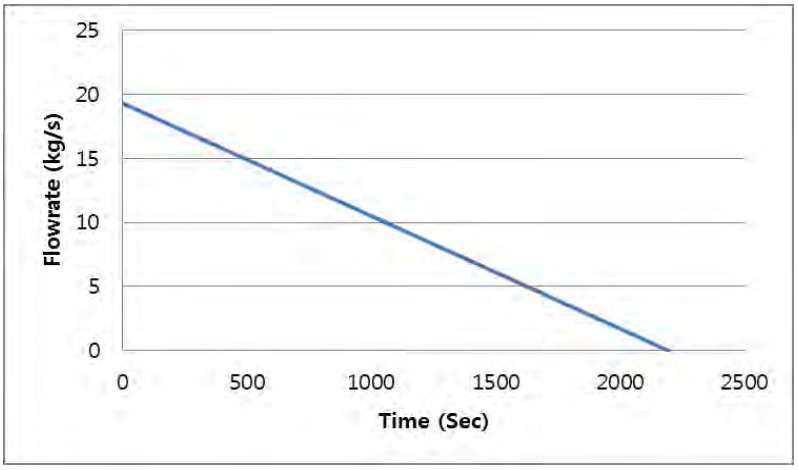


Fig 7. Flowrate through the RHRP

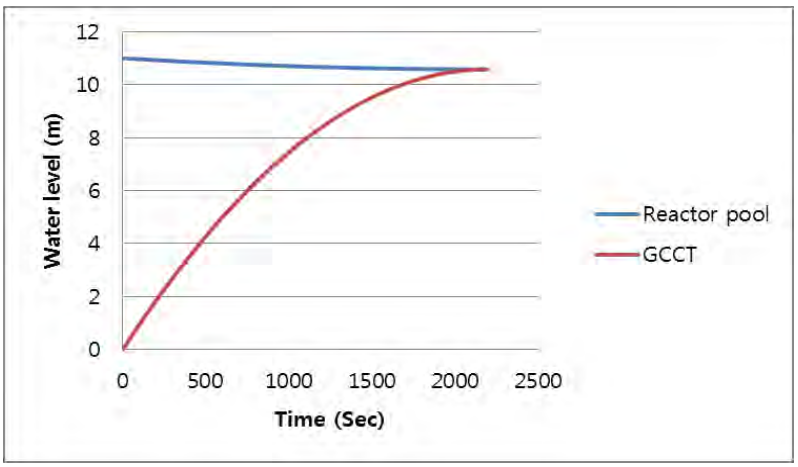


Fig 8. Water levels of reactor pool and GCCT

5. Conclusion

A Gravity Core Cooling Tank (GCCT) beside the reactor pool with a Residual Heat Removal Pipe (RHRP) connecting two pools was developed and designed preliminarily as a passive residual heat removal system for an open-pool type research reactor. The GCCT can remove the decay heat of the core with the flywheel of the Primary Cooling Pump (PCP) and the flap valve in reactor accident situations. It is very simple to design and cheap to construct. Additionally, a non-safety, but active residual heat removal system is applied with the GCCT. It is a Pool Water Cooling and Purification System (PWCPS). It can improve the usability of the research reactor by removing the thermal waves, and purify the reactor pool, the Primary Cooling System (PCS), and the GCCT. Moreover, it can reduce the pool top radiation level.

6. References

[1] Sonntag, Borgnakke, Van Wylen, “Fundamentals of Thermodynamics”, fifth edition, 1998
[2] Munson, B.R., Young, D.F., and Okiishi T.H., “ Fundamentals of fluid mechanics”, fourth edition, 1990

SERPENT CODE SIMULATION OF IPR-R1 TRIGA REACTOR

V.V. ARAÚJO SILVA, S.P. MEIRELES, A.A.C. SANTOS, D.CAMPOLINA, A.Z. MESQUITA

{vitors, spm, aacs, campolina, amir}@cdtn.br
Serviço de Tecnologia de Reatores, CDTN/CNEN
Av. Antônio Carlos 6627, CEP 31270-901, Belo Horizonte, MG - Brazil

ABSTRACT

There are many different reasons to perform a neutronic simulation of a research reactor. The main one is to determine its neutron flux distribution and effective multiplication factor. With this information, it is possible to obtain other important parameters of reactor's operation, like reactivity coefficients or power distribution. One of the most used tools to perform nuclear simulations is Monte Carlo based codes. The IPR-R1 TRIGA Mark I reactor, located at the Centro de Desenvolvimento da Tecnologia Nuclear, in Belo Horizonte, Brazil, is operating for more than fifty years and was successfully simulated before. However, new techniques and methods used in nuclear reactors analysis make a further simulation inevitable. In this work we present the neutronic simulation of IPR-R1 TRIGA reactor using Serpent 2.1.16. Serpent is a Monte Carlo code aimed to nuclear reactor analysis coded in modern C language distributed with source code. The neutronic modeling and simulation presented in this work are part of a bigger project, which aims to couple this neutronics simulation with a thermal-hydraulics simulation carried using a Computational Fluid Dynamics (CFD) code called OpenFOAM. In this seminal work the focus in this very first part: the neutronics simulation of IPR-R1 TRIGA reactor. The neutronic parameters obtained from this simulation are compared to MCNP simulation results at the same conditions.

1. Introduction

The TRIGA IPR-R1 Reactor is in operation since 1961 at the Centro de Desenvolvimento da Tecnologia Nuclear (CDTN). After more than fifty years of operation, even considering the operation books and reports, the precise nuclear fuel composition is unknown. Among the many reasons to try to obtain this information, are the individual fuel composition, control rods calibration, precise power calculations and also a radioisotopes inventory for decommissioning. The Monte Carlo simulation carried in this work alone is expected to be part of a multi-physics simulation, completed by the CFD simulation of the fluid flow in TRIGA IPR-R1 reactor. The coupled calculations will, in turn serve as sources for other future tasks, including fuel safety assessment for decommissioning plan.

1.2. Serpent code

Some characteristics of Serpent code make it the best choice for the overall simulation plan for TRIGA IPR-R1 reactor. Distributed with source code and with an active community of users, Serpent allows relatively simply modeling and its second version – Serpent 2 - is under active development. Moreover, this new version have functions aiming external coupling with thermal-hydraulics [1], matching the needs of the project to which this work is the first part.

2. Objectives

The main objective in this work is to simulate the TRIGA IPR-R1 reactor using Serpent 2 under usual operational conditions and validate the results against former MCNP simulations [2].

3. Methodology

The methodology consists in simulate the TRIGA IPR-R1 reactor operating at 250 kW. The two types of fuels existent in the core were modeled, being one type made of aluminum and another one made of stainless steel. The structural differences among the two fuel types are minimal as is their composition. Whenever, their composition modeling is based on the values defined and used in the MCNP modeling [2] and the same assumptions about the samarium discs existent in the aluminum fuel were extended to the present model. Figure 1 shows core elements, where aluminum elements are depicted in yellow while, four stainless steel in clear orange, neutron source in pink, control rods in green, central tube in clear blue and graphite elements in gray.

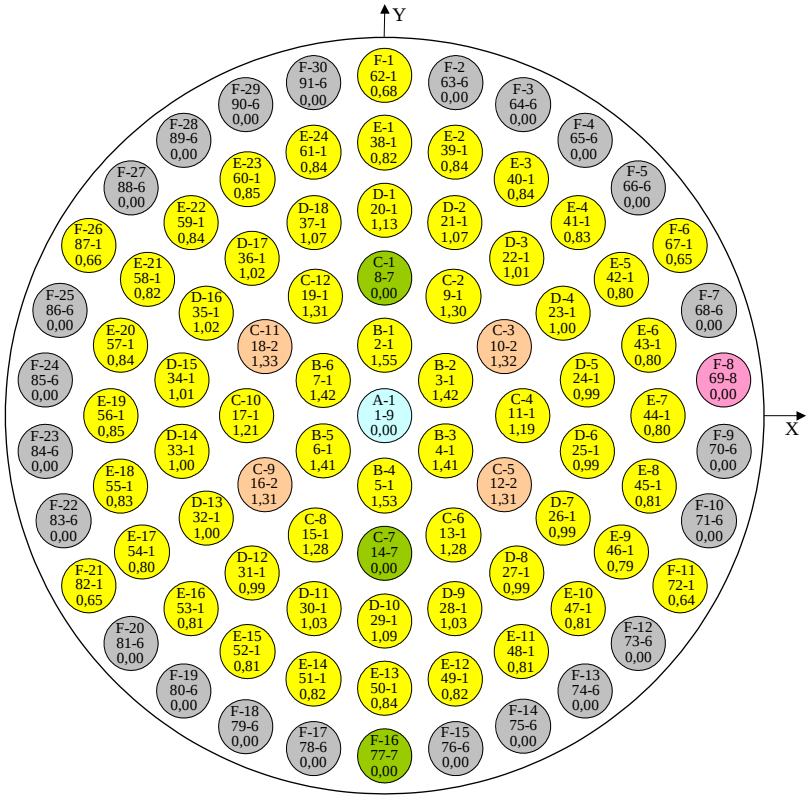


Figure 1 – Element distribution of TRIGA IPR-R1 reactor.

Along with the core, the pool, the water tank and the irradiation channel were modeled in the Serpent. Figure 2 shows the upper view of TRIGA IPR-R1 reactor modeled in Serpent while Figure 3 shows the same model from a different angle.

All the simulations were carried in parallel in a AMD Phenom II X4 B97 Processor 2.2 GHz computer (4 cores) and the average time for simulations is about 4 hours.

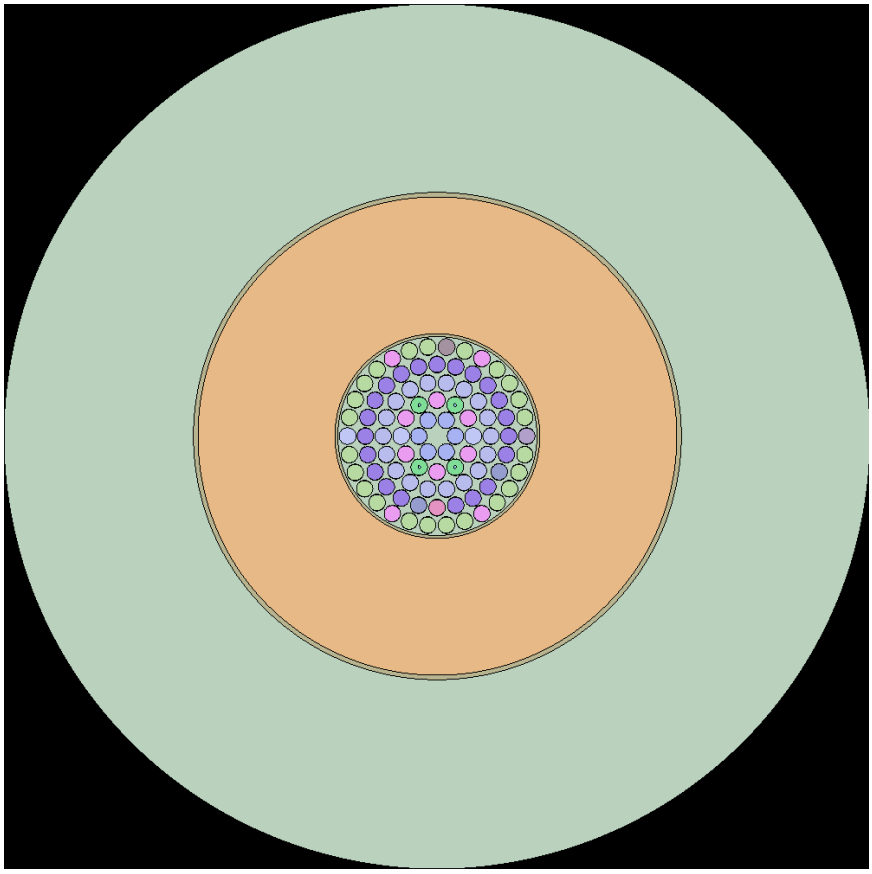


Figure 2 – Top view of TRIGA IPR-R1 reactor modeled in Serpent.

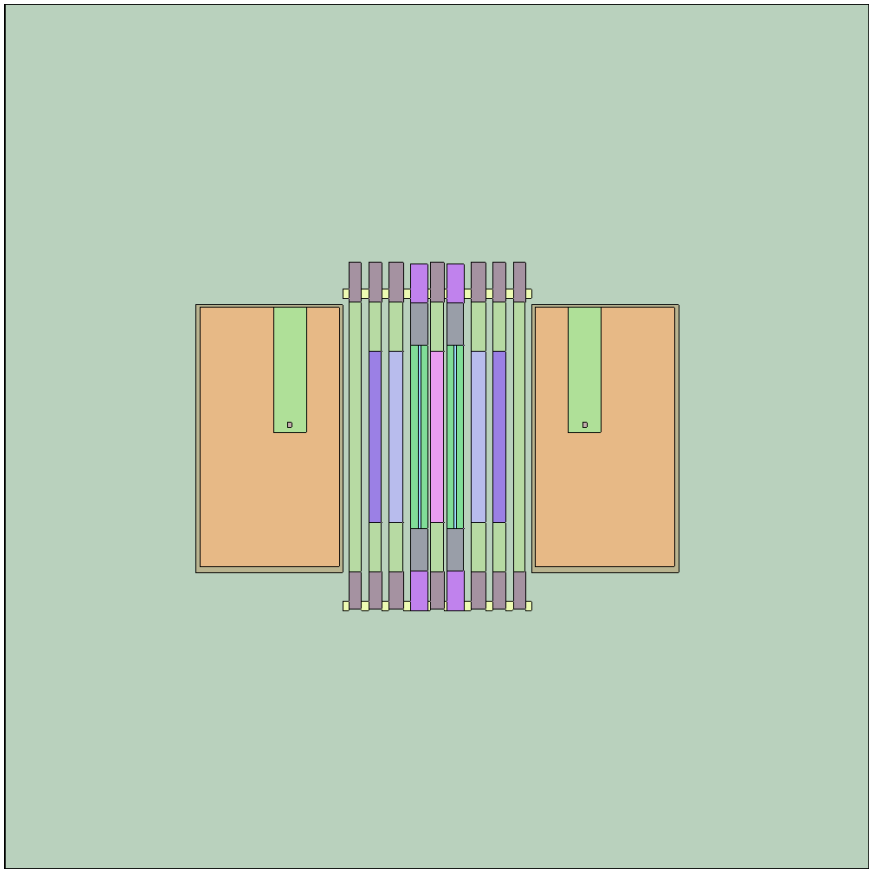


Figure 3 – Side view of TRIGA IPR-R1 reactor modeled in Serpent.

3.1 Cross-sections

The cross-section files provided with Serpent version 1.1.7 (which are used in Serpent 2.1.17) has marked “problematic tables” for some nuclides [3]. Unfortunately, *zirconium hydride*, which is an important constituent of TRIGA IPR-R1 fuel elements, has its constituents nuclides marked as “problematic” for all libraries supplied with Serpent. In order to overcome this issue, MCNP cross-section libraries were used instead after being converted to Serpent format using Serpent utility `xsdirconvert.pl`.

The simulation was performed using all available libraries and the results compared. Another set of simulations was carried to verify the influence of *zirconium hydride* in the results. There is an interesting work where the impact of the amount of *zirconium hydride* over the multiplication factor is evaluated [4], which makes mandatory the use of well defined cross-sections for TRIGA IPR-R1 reliable simulation.

The results were evaluated only in therms of K_{eff}.

4. Results

There is only a slightly difference for the effective multiplication factor when used different cross-section libraries. In table one are the results for all available libraries when simulation run with Serpent 2.1.16.

Table 1: Multiplication factor obtained using different cross-section libraries

Library	K_{eff}	Standard deviation
ENDF-6.8	1.05633	0.00022
ENDF-7	1.0571	0.00022
JEF-2.2	1.062645	0.00022
JEFF-3.1	1.056665	0.00022
JEF-3.1.1	1.0569125	0.00022

The small difference for K_{eff} considering different libraries shows that they can be used interchangeably for this simulation, exception for JEF-2.2 library which presents higher value. However, even for it the difference for others is less than 1% of the multiplication factor.

The next set of simulations were ran both in Serpent 2.1.17 and MCNP4B, with presence and absence os *zirconium hydride*. In the cases where it is not present, *zirconium hydride* was replaced in the model by aluminum. The results for these four simulations are presented in Table 2.

Table 2: Multiplication factor for simulations in Serpent and MCNP

Keff±σ	*with zirconium hydride*	
Code	Yes	No
Serpent	0.95564 ± 0.00027	1.03778 ± 0.00022
MCNP	1.01855 ± 0.00078	1.04157 ± 0.00039

All simulations presented in Table 2 were carried using MCNP cross-section libraries. They show an important difference between calculations considering and not considering the

zirconium hydride cross-sections. The difference is about 2100 pcm for MCNP and about 3700 pcm for Serpent.

The results obtained by Serpent are slightly different for those obtained using MCNP. Although a 4% difference for K_{eff} cannot be neglected, is important to recall that this is the first attempt of this group to carry simulations using Serpent. This is the reason for some slightly simplifications in the TRIGA IPR-R1 modeled in Serpent compared to the MCNP model, which could have led to the differences in results obtained.

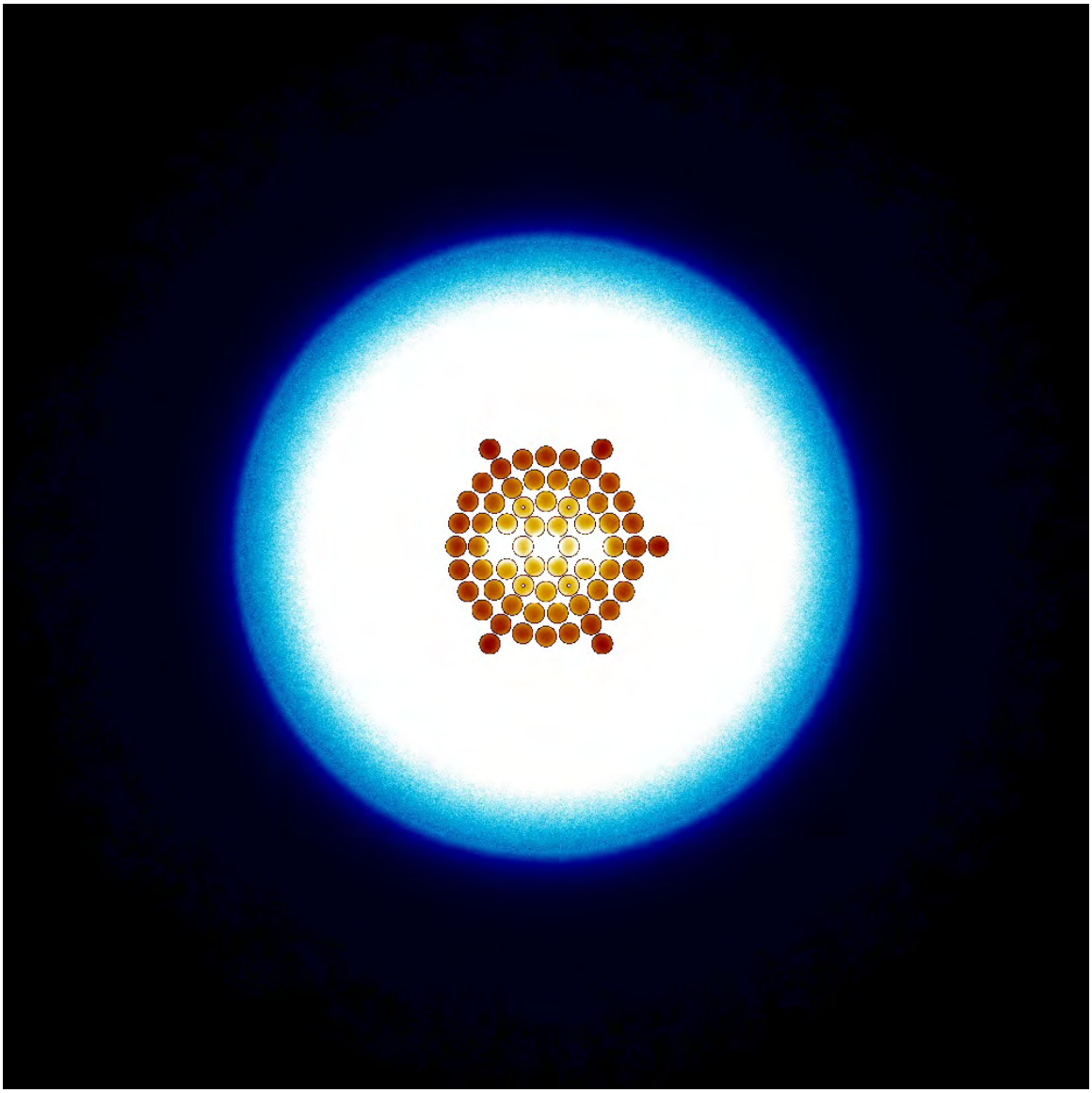


Figure 4 – Top view of TRIGA IPR-R1 reactor power spectrum.

That said, there is another issue with the Serpent simulation including *zirconium hydride*, which is the sub-critical value for the K_{eff}. This means the reactor would not sustain the nuclear chain reactor in this case, which is clearly wrong. Posterior simulations using Serpent 2.1.17 gave a very different value for $K_{eff} = 1.0158 \pm 0.0003$. This value is closer to the results obtained running MCNP. However, since the simulations were carried in different machines at different times, further investigations must be done before a final conclusion since the information about changes on Serpent does not present any bug fix directly related to the effective neutron multiplication factor.

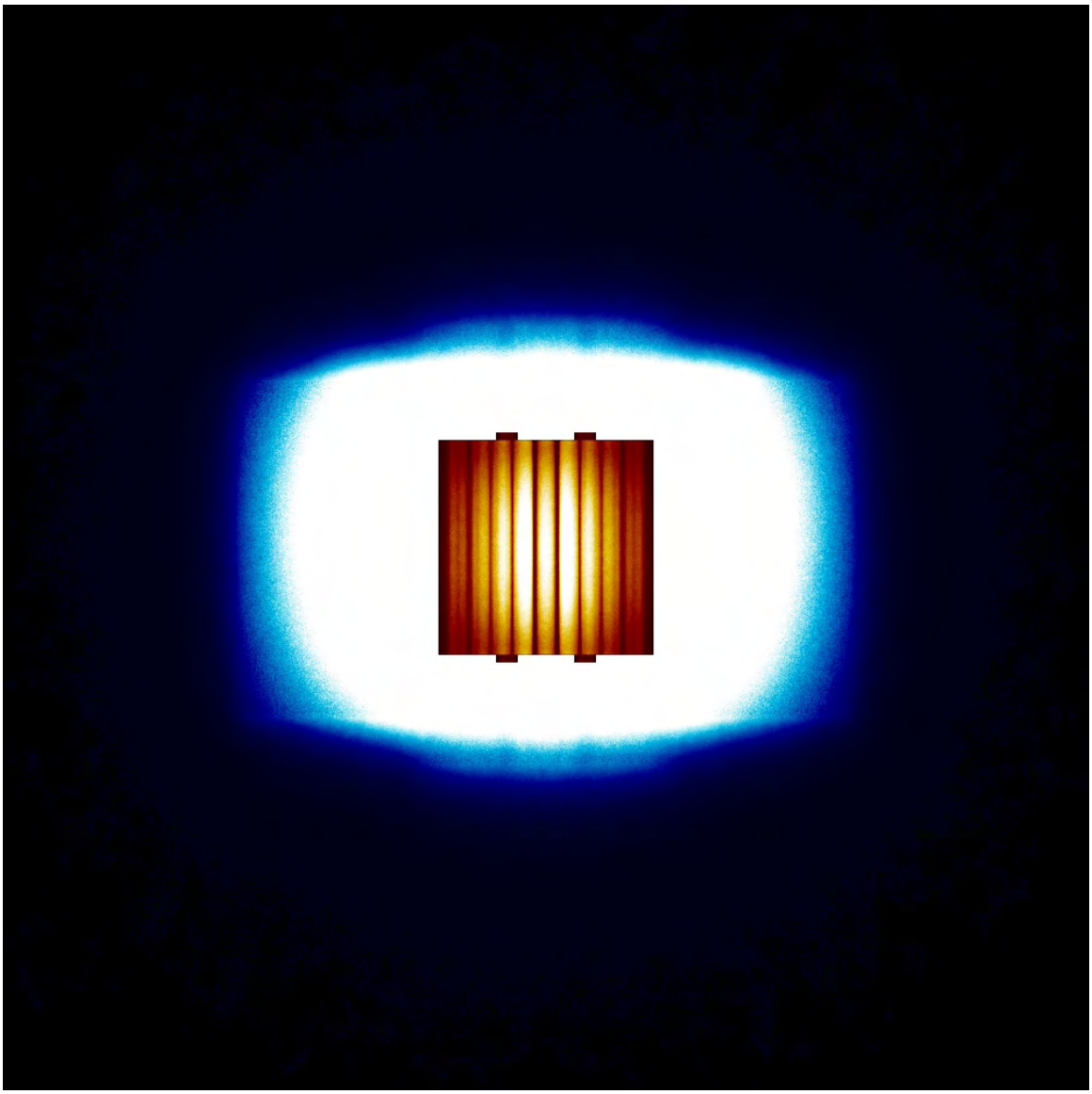


Figure 5 – Side view of TRIGA IPR-R1 reactor power spectrum.

Figures 4 and 5 show the power distribution in TRIGA IPR-R1 reactor in a simulation with 10,000 neutrons population per cycle.

5. Conclusions

The results obtained using Serpent for TRIGA IPR-R1 simulations are encouraging. The problems found are important, specially the sub-critical K_{eff}, but there is space for improvements in the model. The evident one is to have a better generation of cross-sections for *zirconium hydride.* It is worth mention that this first simulation using Serpent is expected to be one part of a multi-physics calculation involving a Computational Fluid Dynamics (CFD) tool. The new version of Serpent, Serpent2, has built-in structures aimed to simplify geometry sharing with external codes and its ability of calculating reactor time constants [5], both useful characteristics for coupling with CFD.

6. Future work

The immediate work consists in improving the simulation including *zirconium hydride.* Since it is an important structure in TRIGA IPR-R1 fuel rods, no simulation without considering its effects on the neutron flux would be completely reliable. The next step is to couple Serpent, in this case Serpent2, to a CFD tool aimed to calculate the thermal-hydraulics behavior of TRIGA IPR-R1. This results will be validated with experimental data [6].

7. Acknowledgments

Authors would like to thank Centro de Desenvolvimento da Tecnologia Nuclear – CDTN/CNEN - for paying RRFM 2014 conference registration fees and CAPES and CNPq respectively for the “sanduíche” and Ph.D scolarships for two of the authors.

8. References

[1] LEPPÄNEN, J. **Modeling of Nonuniform Density Distributions in the Serpent 2 Monte Carlo Code .** Nuclear Science and Engineering, number 174, (318-325), 2013.

[2] DALLE, H. M. **Simulação do reator TRIGA IPR-R1 utilizando métodos de transporte por Monte Carlo.** Ph.D thesis. Faculdade de Engenharia Química da Universidade Estadual de Campinas, Campinas, SP, 2005. (Portuguese)

[3] LEPPÄNEN, J. and VIITANEN, T. **Cross-section libraries for Serpent 1.1.7.** Documentation, October 22, 2013.

[4] BESS, J. D. Et al. **Fresh-Core Reload of the Neutron Radiography (NRAD) Reactor with Uranium(20)-Erbium-Zirconium-Hydride Fuel .** Idaho National Laboratory (INL), INL/EXT-10-19486. March 2013.

[5] LEPPÄNEN, J. et al. **Calculation of effective point kinetics parameters in the Serpent 2 Monte Carlo code.** Annals of Nuclear Energy, volume 65, pages 272-279. March 2014.

[6] MESQUITA, A. Z. **Investigação experimental da distribuição de temperaturas no reator nuclear de pesquisa TRIGA IPR-R1**. Ph.D Thesis. Faculdade de Engenharia Química da Universidade Estadual de Campinas, Campinas, SP, 2005. (Portuguese)

ASSESSMENT OF GLOBAL UNCERTAINTY WITH 5-MW POOL-TYPE RESEARCH REACTOR

SOO-BEEN YUM, SU-KI PARK, YOUNG-JONG CHUNG
Safety Analysis Group, Korea Atomic Energy Research Institute,
989-111 Daedeokdaero, Yuseong, Daejeon, 305-353, Republic of Korea

ABSTRACT

Best estimate plus uncertainty (BEPU) is the promising approach to the safety analysis of nuclear power plant (NPP), and the uncertainty calculation is the most interesting concern for it. BEPU takes global uncertainty assessment for the parameters and secures safety margin and reactor effectiveness, whereas previous uncertainty analyses consider each parameter separately. Reactivity induced accident (RIA) of a 5MW open-pool type research reactor was selected as a sample problem for BEPU uncertainty assessment. We assumed one control rod withdrawal with maximum speed for the analysis. Significant contributors to the reactor safety are identified and ranked, and then input sets are sampled. By using RELAP5/MOD3.3 (or MARS developed by KAERI), 124 times of calculation were performed for the uncertainty evaluation, which is required for 3rd order Wilk's formula to achieve 95%/95% tolerance level. MOSAIQUE software developed by KAERI was used for automated sampling of uncertainty parameters, global uncertainty calculation, and post processing of calculated variables. We calculated the fuel centerline temperature (FCT) and the critical heat flux ratio (CHFR) and also presented the overall uncertainty bands of the variables.

1. Introduction

1.1 Objective

US NRC revised regulations in 1989, such that BEPU is able to replace previous conservative approach to reactor safety analyses. Following the new regulation, ATUCHA unit 2 in Argentina recently obtained operating license with the final safety analysis report using BEPU approach. These 2 examples show the global trends for safety analysis which are changing slowly from conservative analysis to BEPU. Figure 1 shows the comparison of a safety parameter calculated by different analysis methodologies. BEPU estimates safety parameters more realistically comparing to those by conservative analyses, reducing excessive conservatism in safety analysis and increasing margin in reactor operation.

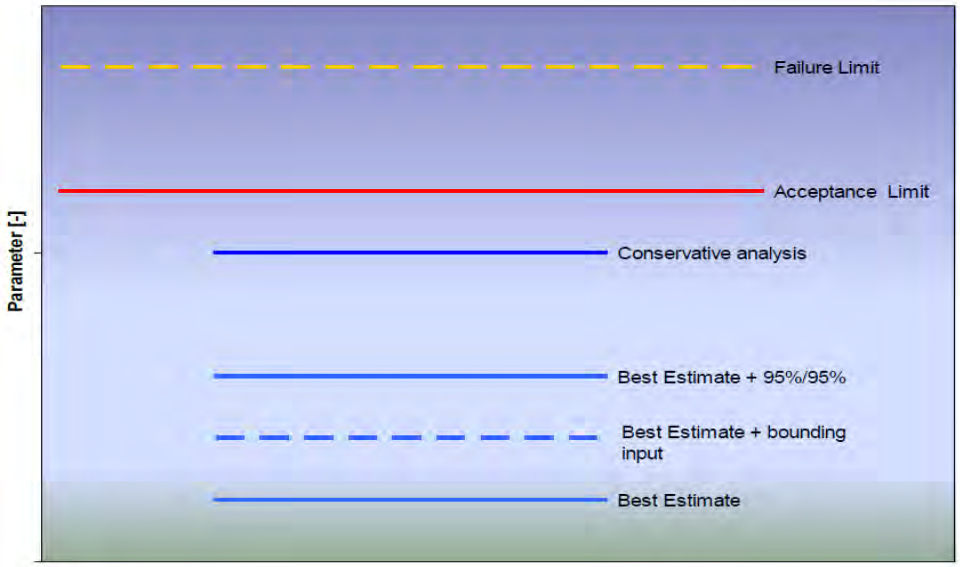


Fig 1 Comparison of different analysis methodologies

Following these international trends, we introduced the BEPU safety analysis for reactivity induced accident of 5-MW pool-type research reactor. The core safety parameters and the input variables affecting the parameters are selected first, and the overall uncertainties of the safety parameter are calculated following non-parametric uncertainty analysis. Then, the safety parameters including uncertainties are presented and the importance of each variable is ranked by sensitivity analyses.

1.2 MOSAIQUE

MOSAIQUE (Module for SAmpling Input and Quantifying Estimator) software is developed in KAERI to perform probabilistic uncertainty analysis of computerized simulation models [1]. The software provides automated sampling, calculation and post processing, therefore reduces a lot of time and effort required to perform BEPU analysis.
MOSAIQUE has three main functions: (1) Sampling of input variables, (2) Calculating global uncertainties of safety parameters, (3) Post processing of uncertainty bands of safety parameters and sensitivity of input variables.

1.3 Reactivity induced accident

For BEPU uncertainty assessment, RIA of a 5-MW open pool-type research reactor is selected as a sample problem. The scenario is the accident that one control rod is withdrawn with its maximum speed due to an operator error. Maximum reactivity insertion rate is assumed to be 0.282mk/s in this scenario. The safety parameters investigated are maximum fuel centerline temperature (MFCT) and minimum critical heat flux ratio (MCHFR)

2. Uncertainty assessment

2.1 Input variable selection

PIRT (Phenomena identification and ranking table) is a main performs at the stage of identify and rank phenomena in BEPU. As main thermal-hydraulic phenomena are selected and ranked at this stage, this is the most important step throughout the all steps. Table 1 shows the input thermal hydraulic phenomena and the related variables during RIA.

Phenomenon	Concerning variables
Operating condition	Initial core power, Pool inlet temperature, Mass flow rate, Pool level
Fuel data	Fuel corrosion layer, Engineering hot channel factor
Correlation	Critical heat flux correlation coefficient, Heat transfer coefficient

Tab 1: PIRT for RIA

All variables are assumed as having normal distributions. The characteristics of each input variables are described below.
1) Initial core power: Initial core power affects the trip time and also affects the maximum power when the trip occurs. The uncertainty of initial core power is ±3.81%.
2) Pool inlet temperature: Pool inlet temperature is the initial temperature of the coolant before coming into the core. It is controlled by changing the heat transfer area of the primary heat exchangers. The uncertainty of pool inlet temperature is ±0.61^{o}C.
3) Mass flow rate: Mass flow rate determines the cooling capability of reactor core. It is controlled by the primary coolant pump head. The uncertainty of mass flow rate is ±2.3%.
4) Pool level: Pool level determines the core pressure, which is related to the saturation temperature of core coolant. The uncertainty of pool level is ±0.02m.
5) Fuel corrosion layer: The corrosion layer on the fuel cladding has low conductivity less than 2W/m·K. The fuel corrosion layer is a thermal insulator between the coolant and the fuel cladding and meat, affecting the fuel temperature. The uncertainty of fuel corrosion thickness is assumed as ±50%.
6) Engineering hot channel factor: Engineering hot channel factor (HCF) is multiplied to the core heat flux to compensate for the fuel meat fabrication tolerances. HCF is originated from U235 homogeneity, U235 loading per plate and the thickness and width uncertainties of fuel meat. U235 homogeneity is tolerance on how well the U235 is mixed with the ingredients that

are in the fuel meat. U235 loading per plate is a tolerance on the weight of U235 that is to go into a plate. The combined uncertainty of HCF considering 2 factors is ±19%.
7) CHF correlation: Sudo-Kaminaga CHF [2] correlation developed for the plate type fuel channel is used for estimating the CHF during accidents. During RIA, the core flow is downward and the correlation in this situation is explained in equation (1).

$$q''_{CHF} = \frac{A}{A_H} \Delta T_{sub} |G| \quad (1)$$

(A: flow area, A_H: heated area, ΔT_{sub}: subcooling, G: mass flux)
The uncertainty of this correlation is ±33%. The CHF correlation is controlled by multiplying a factor corresponding to the uncertainty.
8) Heat transfer correlation: Dittus-boelter correlation [3] in RELAP5 is used to calculate the heat transfer coefficient since the coolant is single phase during RIA. The uncertainty of this correlation especially for liquid is ±12.75% [4].

Number	Models/Parameters	Range	Distribution
1	Initial core power	0.96~1.04	Normal
2	Pool inlet temperature	±0.61°C	Normal
3	Mass flow rate	0.98~1.02	Normal
4	Pool level	±0.02m	Normal
5	Fuel corrosion layer	0.50~1.50	Normal
6	Engineering hot channel factor	0.81~1.19	Normal
7	CHF correlation	0.67~1.33	Normal
8	Heat transfer correlation	0.87~1.13	Normal

Tab 1: Uncertainty parameters for RIA

2.2 Non-parametric uncertainty calculation

Non-parametric uncertainty calculation is statistical technique and the required number of code run is independent of the number of input variables. Equation (2) shows the Wilk's formula [5] which decides the number of code run required for certain percentile value with certain confidence level. Table 2 shows the number of code runs, to estimate 95% probability value with 95% confidence level, which is 95%/95% tolerance limit. The table also shows the analytical confidence level calculated from the formula.

$$\beta \le 1 - \sum_{j=n-p+1}^{n} \binom{N}{j} \gamma^j (1-\gamma)^{N-j} \quad (2)$$

(γ: probability, ß: confidence level, N: number of sample, p: order of Wilk's formula)

Order	Number of code runs	Analytical confidence (%)
1	59	95.1505
2	93	95.0024
3	124	95.0470
4	153	95.0555
5	181	95.0837

Tab 2: Wilk's formula

124 set of input variables were sampled and the same number of code runs were performed following 3rd order Wilk's formula. The input sets were automatically sampled by MOSAIQUE with Latin-Hypercube Sampling method. The safety parameters, FCT and CHFR, were then calculated by RELAP5/MOD3.3 with the inputs.

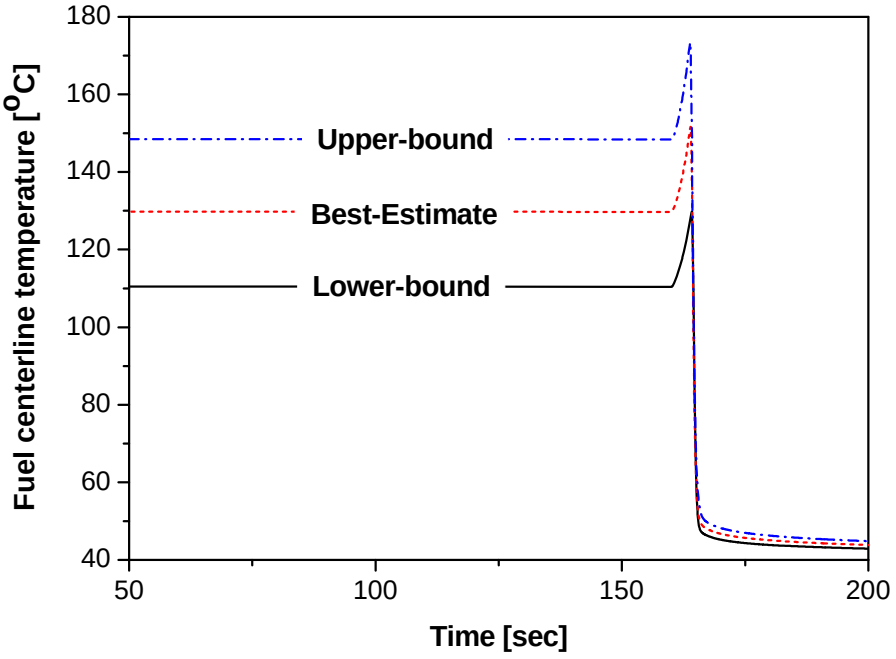


Fig 3. FCT with uncertainty during the accident

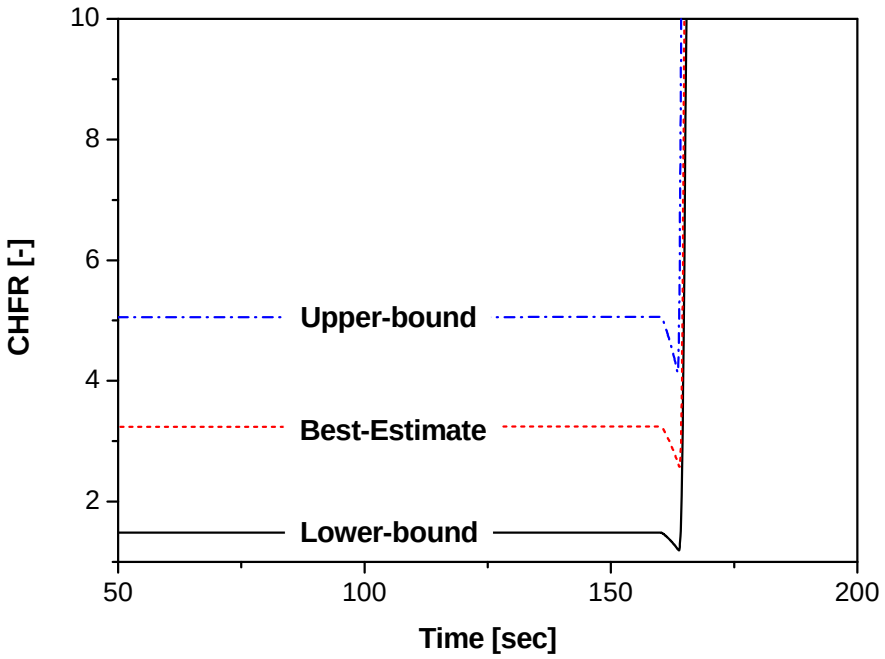


Fig 4. CHFR with uncertainty during the accident

2.3 Calculating overall uncertainties

FCT and CHFR can be expressed as below.

$$FCT_{Final} = FCT_{95/95} + Bias$$
$$CHFR_{Final} = CHFR_{95/95} + Bias \quad (3)$$

$FCT_{95/95}$ and $CHFR_{95/95}$ mean the 95%/95% values of FCT and CHFR estimated from the analyses, by selecting the 3rd largest FCT and the 3rd smallest CHFR among the calculated results. The $FCT_{95/95}$ is 169.3°C and $CHFR_{95/95}$ is 1.68. The bias stems from the scale effect

and separate/integral effect test is assumed to be 0 in this analysis.

2.4 Uncertainty analysis

Figure 2 and Figure 3 show the FCT and the CHFR including uncertainties during the accident. The upper 5% values and lower 5% values with 95% confidence level are presented. Here, the 95%/95% limit of FCT is upper 5% value, and that of CHFR is lower 5% value. The upper and lower uncertainties of FCT are +17.5^{o}C and -16.4^{o}C from the best estimate value, and those of CHFR is +1.3 and -0.88.

Output uncertainty parameter		Lower uncertainty bound	Reference calculation value	Upper uncertainty bound
FCT	^{o}C	135.4	151.8	169.3
CHFR	-	1.68	2.56	3.86

Tab 3: Lower and upper bound of FCT and CHFR

2.5 Sensitivity analysis

The meaning of sensitivity analysis is to evaluate of impact of each uncertainty parameter on the parameter of interest. The importance of input variables on the safety parameters is represented quantitatively by Pearson's correlation coefficient [6]. Pearson's correlation coefficient shows the relationship between two quantities and shown in Equation (4).

$$Pearson = corr(X,Y) = \frac{\mathrm{cov}(X,Y)}{\sigma_X \sigma_Y} = \frac{E\left[(X-\mu_X)(Y-\mu_Y)\right]}{\sigma_X \sigma_Y} \quad (4)$$

(X,Y: variable, μ_X, μ_Y: expected value, σ_X, σ_Y: standard deviation)

The Pearson correlation is +1 in the case of a perfect direct linear relationship, -1 in the case of a perfect inverse linear relationship and some value between -1 and 1 in all other cases, being a measure of linear dependence between the variables. Larger absolute value of Pearson correlation coefficient means stronger dependency between the variables. Figure 4 and Figure 5 shows the Pearson correlation coefficient between the input variables and the safety parameters. The followings are the main findings from the figures.

1) Fig 4 shows that the MFCT increases as the corrosion thickness increases and heat transfer coefficient decreases whereas the other parameters do not show distinct dependence on the MFCT
2) Fig 5 shows that the MCHFR increases as pool level and CHF correlation coefficient increases and HCF decreases whereas the other parameters do not show distinct dependence on the MCHFR.
3) If the initial core power becomes smaller, the time taken to reach the trip signal becomes longer. It makes the power logarithm rate to be higher at the time trip signal occurs and the power logarithm rate is a standard of judgment for power variation. Therefore, power at the time trip signal occurs becomes higher and it makes FCT become higher while makes CHF become smaller. But the uncertainty span for initial power assumed in this analysis is narrow, the effect of power was not showed up.
4) Since corrosion layer acts as a thermal insulator between the coolant and the fuel cladding and meat, MFCT is proportional to the thickness of corrosion layer. Accordingly, strong positive correlation exists between them.
5) Although the pool level causes small variation on the core pressure due to the small uncertainty, the pool level and the MCHFR shows unignorable relationship. However, the relationship is caused by the characteristics of random sampling, and has no rational bases.
6) Since the heat transfer coefficient is in inverse proportion to temperature difference between fuel and coolant, strong negative correlation is found between heat transfer coefficient and MFCT.
7) Since the hot channel factor and CHF correlation coefficient compensate the heat flux directly, it shows clear influences to the MCHFR.

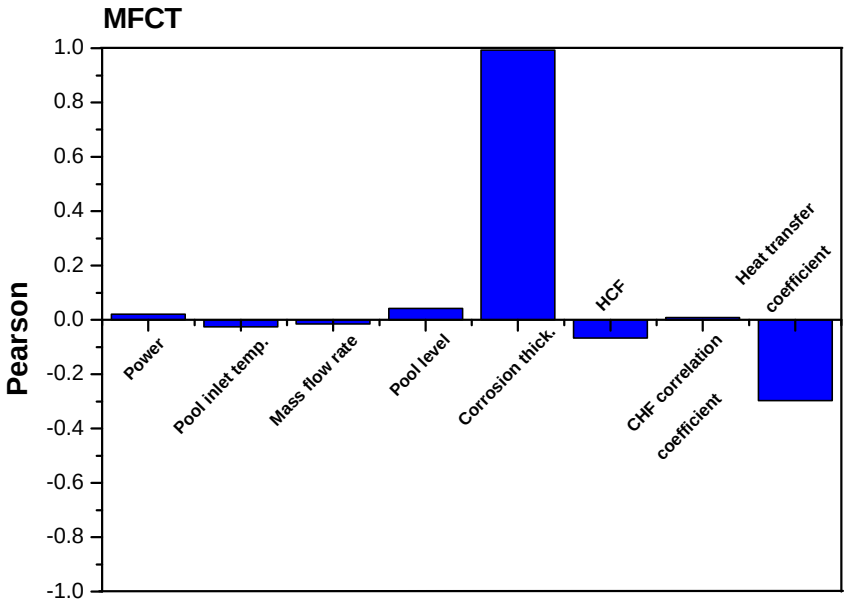


Fig 5. Pearson correlation coefficient vs. input variables for fuel centerline temperature

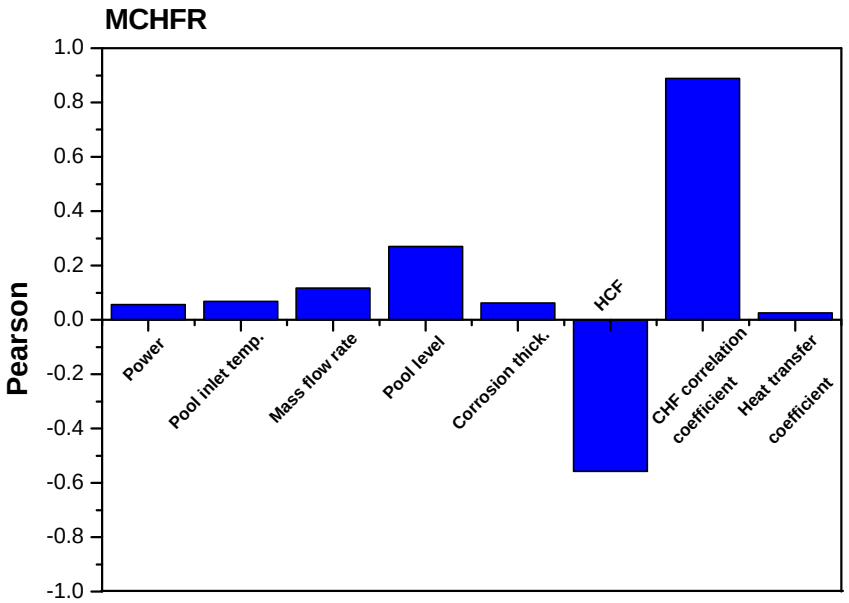


Fig 6. Pearson correlation coefficient vs. input variables for critical heat flux ratio

3. Conclusions

A BEPU methodology was applied to the reactivity induced accident of 5-MW pool-type research reactor. Important phenomena of the accident were identified and key input variables for each phenomenon were identified. 124 sets input variables are sampled and the same numbers of code runs were performed to evaluate the uncertainty of the key safety parameters, FCT and CHFR. The uncertainty ranges of FCT and CHFR were presented with $FCT_{95/95}$ and $CHFR_{95/95}$ values. The importance of each input variables on the safety parameters were then analyzed by sensitivity analyses. The procedures and the results in

this paper show the applicability of BEPU safety analysis on a research reactor.

References

[1] H.G.Lim, et al., 2011. MOSAIQUE-A network based software for probabilistic uncertainty analysis of computerized simulation models. Nuclear Engineering and Design 241, 1776-1784.
[2] Sudo, Y. and Kaminaga, M., 1993. A New CHF Correlation Scheme Proposed for Vertical Rectangular Channels Heated From Both Sides in Nuclear Research Reactors, Journal of Heat Transfer 115, 426-434.
[3] F. W. Dittus, et al., 1985. Heat Transfer in Automobile Radiators of the Tabular Type, Heat and Mass Transfer 12, 3-22.
[4] Korea Institute of Nuclear Safety, Improvement of the ECCS Best Estimate Methodology and Assessment of LOFT L2-5 Experiment, KINS/RR-279, 42.
[5] Nutt, W.T. and Wallis, G.B., 2004, Evaluation of nuclear safety from the output of computer codes in the presence of uncertainties, Rel. Eng. Sys. Saf. 83.57-77.
[6] Lehmann, E.L., 1975, Nonparametrics, Statistical Methods Based on Ranks, Holden-Day, Inc, California, USA.

BIOLOGICAL SHIELDING CALCULATIONS AND DESIGN FOR THE SCWR-FQT TEST LOOP AT THE LVR-15 REACTOR

J. ŠOLTÉS, A. VOJÁČEK, M RŮŽIČKOVÁ, O. FRÝBORT
Reactors Services Section, Research Centre Rez Ltd.,
Husinec - Rez 130, 250 68 Rez, Czech Republic

ABSTRACT

The SCWR-FQT is a joint European-Chinese project aiming to design and licensing of a supercritical in-pile fuel qualification test loop at the site of the LVR-15 reactor operated by the Research Centre Rez. One of the key issues for the facility is radiation protection. The technology parts of the loop (including the active primary circuit components) are designed to be located in a new building adjacent to the reactor hall, currently under construction. As the operational staff is expected in the experimental hall during the facility operation, high biological shielding demands would be necessary for the active facility components to get reasonably low dose rate values around the facility components. In addition, the primary pipelines connecting the active channel of the loop with the other circuit components would require shielding as well. As the loop cooling is provided by supercritical water, nitrogen-16 as the most prominent water activation product will be the limiting radioactive source for the shielding design under operational conditions. Additionally, corrosion products cumulating on the primary circuit filters were considered as sources. For all of the calculations necessary for the shielding design the Monte-Carlo particle transport code MCNPX was used. More options for the shielding material were considered in the simulation, resulting into lead being the most appropriate variant. After the shielding design for operational conditions, an accident scenario involving the release of fission products from the disintegrated fuel elements and contamination of the primary circuit components was also subject of study.

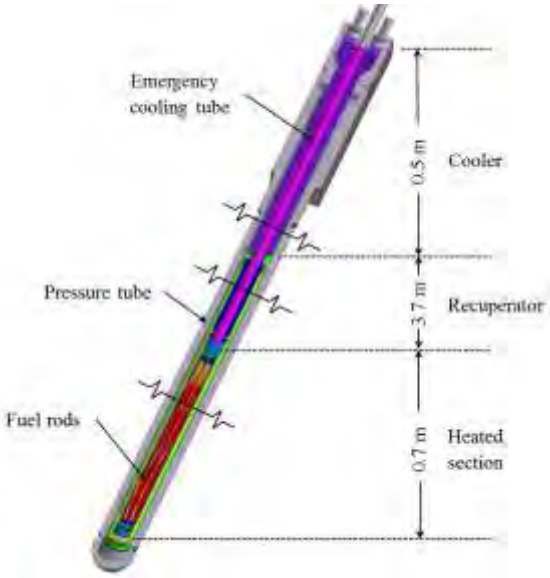
1. Introduction

In the framework of the The Generation IV International Forum several different reactor type concepts are subjects of studies. One of the studies involves the Supercritical-Water Cooled Reactor (SCWR) concept. Between 2006 – 2010 joint efforts of 13 consortium partners from 8 Euratom member states lead to the concept design of a 1000 MWe reactor entitled the High Performance Light Water Reactor [1].

In order to understand material behaviour under supercritical water conditions as well as the thermo-hydraulics an in-pile fuel qualification test loop is under development at the site of the LVR-15 research reactor in Rez, Czech Republic. The loop is known as the SCWR-FQT (Supercritical Water Reactor – Fuel Qualification Test) and is currently in its final design stages.

One of the key components of the loop is the active channel - Fig. 1 containing four UO_2 fuel rods, inserted into the reactor's active core in place of a fuel assembly (Fig. **1**2 – position D3). Besides the active channel the primary circuit of the loop will be assembled of several other components comprising the main circulation pump, heat exchangers, coolers, a pressurizer, and others. Due to the limited space available inside the reactor building most of these components will be located in a new built adjacent experimental hall. As the coolant supercritical water flowing through the primary circuit undergoes activation, all the primary components will require biological shielding as presence of operational staff may be

expected near the circuit components or the pipelines connecting the active channel with the remaining components.



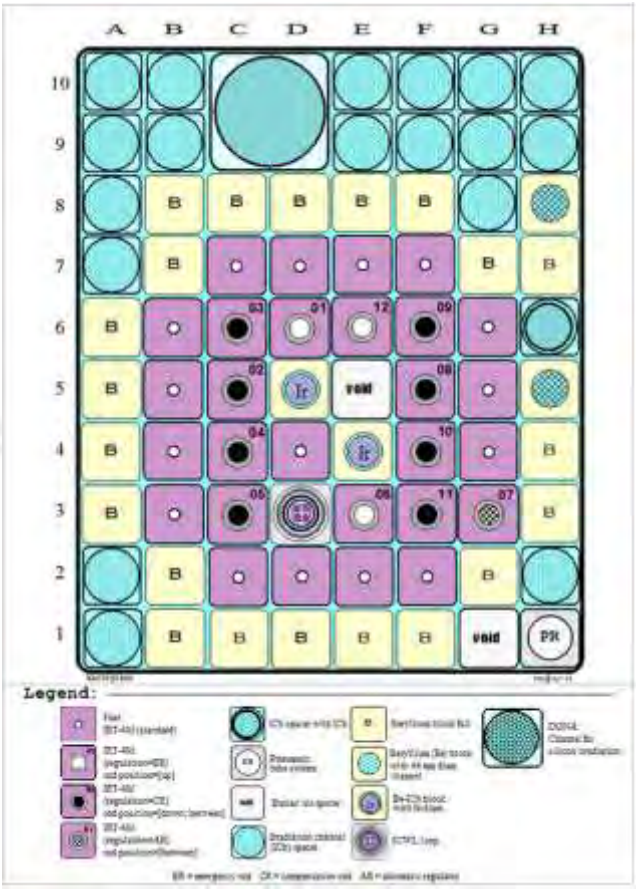


Fig. 1 Active channel design [2] Fig. 2 LVR-15 core with the SCWR-FQT loop

For purposes of shielding design, several calculations have been made using the Monte Carlo method implemented by the MCNPX 2.7.0 transportation code. As shielding of the active channel is provided by the reactor itself the calculations were focused on the shielding design of the so called primary block containing the circulation pump, pressuriszer, heat exchangers, coolers and filters, and around the pipeline tracking connecting the active channel with the primary block (Fig. 3).

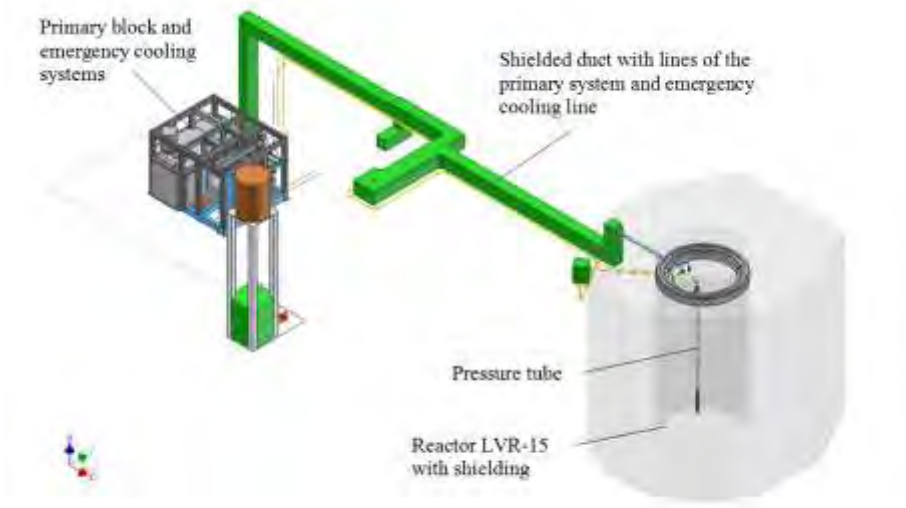


Fig. 3 SCWR-FQT loop components installation [3]

2. Source term definition

In order to realize the shielding design for the primary circuit, the cooling supercritical water activity has to be determined first. The water activity is caused due to the presence of water activation products and activated corrosion impurities. As long as we have no experience with SCWR-loop operation, we are unable to estimate the amount of specific radio-isotopes in the water. Therefore, we based our calculations on a distribution of radio-isotopes as it is present in typical pressure-water or boiling-water loop of a reactor.

The most dominant isotope contributing to the activity of the cooling water is N-16, a product of the (n,p) reaction realized on the water's O-16 nuclei. Having a short half-life of 7.1 s, as opposed to the other contained isotopes, its activity stays still dominant in relation to the other isotopes for a period of several half-lives. The activity values of the activated corrosion products and F-18 (another water activation product) are negligible small. With respect to the mentioned facts, it is possible to reduce the problem just to the calculation of the activity caused by N-16, and cover the left over isotopes by a safety margin of 5 % of the base N-16 activity at the exit at the reactor's active core.

To calculate the N-16 activity in the cooling supercritical water it is possible to use a proposed MCNP LVR-15 reactor active core model with the SCW FQT-loop installed. Cross-section of this active core configuration and a vertical cut of the loop's fuel section are shown on schematics in Fig. 4. As seen from this figure the cooling supercritical water through the facility is horizontally divided into more sectors. This was done to simulate the varying temperatures and densities of the flowing cooling supercritical water along FQT channel, as long as these parameters have influence on the neutron interaction with matter.

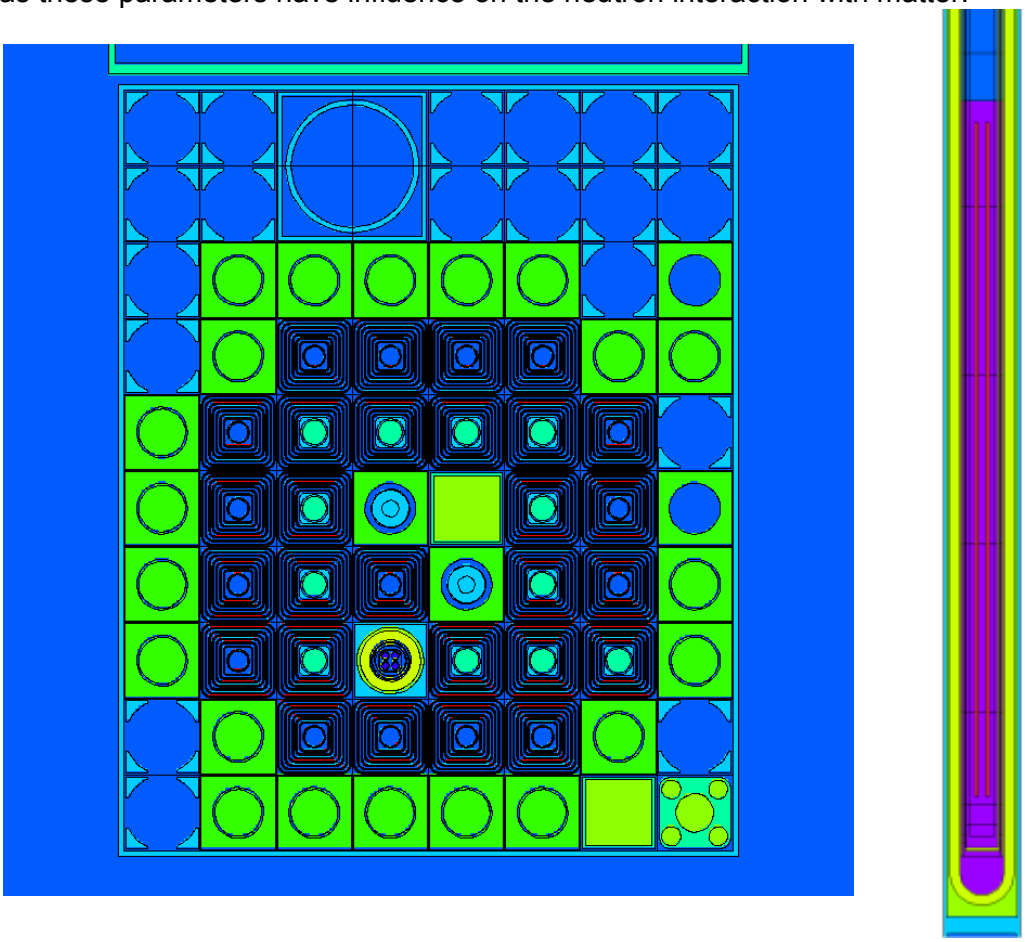


Fig. 4 LVR-15 active core model with SCWR-FQT loop's active channel installed (left) and the active channel model (right)

It is important to mention that the O-16(n,p)N-16 has a threshold energy of 10 MeV. Therefore, only interactions with fast fission neutrons can lead to N-16 production. The percentage of the neutrons with energies exceeding 10 MeV, which is still low, significantly falls with the rising distance from the fuel. So the N-16 production in supercritical water segments distant from the fuel elements is negligible. Therefore, only supercritical water segments along the height of the fuel element have been taken into account in the N-16 production calculations. These segments are marked purple in Fig. 4 (fuel elements are marked red).

MCNP allows calculating the reaction rate (1/s/cm^3) of a certain reaction. Knowing the production rate of N-16 in the cooling supercritical water and the average time the calculated supercritical water segment is flowing along the height of the fuel elements, allows us to calculate the supercritical water activity per volume unit at the exit of the . Knowing the densities in each calculated water segment allows expressing the activity per a mass unit.

The calculated average activity at the fuel element region exit is 1.7 MBq/cm^3 which can be expressed per a mass unit as 3.49 MBq/g.

However, for the for the primary block components N-16 is not the only limiting factor. It plays a significant role only in the first stages of the facility operation. Later long living corrosion products may become the dominant radioactive inventory. Based on experience with operating other test loops a cumulative long-living corrosion product inventory after two years of operation was estimated for the calculation (Tab. 1). The activity of the corrosion products exceeds the ^{16}N by 25 times, thus, rising the shielding demands. However, the majority of the corrosion product can be removed using the ion-exchanger filters, therefore, in the final project the whole shielding may be designed for ^{16}N and only the ion filters would require extra shielding in order to shield the long-living cumulated corrosion products.

Tab. 1 Corrosion products inventory estimate after two years of operation

Corrosion product	**Activity [Bq]**
^{51}Cr	7.2E+09
^{54}Mn	6.9E+07
^{55}Fe	6.9E+08
^{59}Fe	1.03E+08
^{58}Co	2.90E+10
^{60}Co	3.51E+10
^{59}Ni	2.37E+06
^{63}Ni	3.65E+08
^{65}Zn	7.82E+09
Total	*8.01E+10*

The last case considered in the calculations was the primary circuit under accident conditions. In this scenario the fission product and minor actinides inventory from the fuel elements was considered as the radioactive source for the primary circuit. As a proposal for a possible accident condition scenario, the failure of one fuel pin was chosen. In this scenario the actinides and fission product release can be estimated by applying the CORSOR-O recommended release rate model [4] onto the calculated inventory. The fission products and actinides inventory was calculated using the tier 2 BURN card v the MCNP code. In this calculation the same model was used as for the ^{16}N activity calculation. A list of the prominent radioisotopes and their corresponding activities can be found in Tab. 2. The inventory was calculated after 20 reactor cycles (2 years of standard reactor operation) reflecting, thus, the end stage of the loop operation.

Tab. 2 Gamma emitting actinides and fission products after 2 year of operation with the CORSOR-O recommended release rate model coefficients (used for the radioactive source calculation for accident conditions prediction).

Isotope	Mass (g)	Activity (Bq)	Coef.	Isotope	Mass (g)	Activity (Bq)	Coef.	Isotope	Mass (g)	Activity (Bq)	Coef.
^{82}Se	2.58E-02	2.99E-08	-	^{135}Xe	1.78E-04	1.68E+13	1	^{154}Eu	1.40E-02	1.40E+11	
^{85}Kr	2.07E-02	3.01E+11	1	^{134}Cs	8.46E-02	4.05E+12		^{155}Eu	3.46E-03	6.31E+10	0.1
^{86}Rb	3.18E-05	9.59E+10	-	^{136}Cs	4.60E-04	1.24E+12	1	^{156}Eu	2.22E-03	4.54E+12	
^{91}Y	6.24E-02	5.67E+13	-	^{137}Cs	8.38E-01	2.70E+12		^{157}Eu	1.05E-05	5.13E+11	
^{95}Zr	8.34E-02	6.63E+13	2E-04	^{133}Ba	7.67E-08	7.25E+05	0.2	^{153}Gd	9.48E-07	1.24E+08	-
^{94}Nb	1.43E-06	9.90E+03	-	^{140}Ba	2.63E-02	7.12E+13		^{160}Tb	1.67E-05	6.97E+09	-
^{95}Nb	4.41E-02	6.42E+13		^{138}La	8.46E-06	7.73E-03	2E-04	^{232}Th	3.08E-07	1.25E-03	
^{99}Mo	4.51E-03	8.01E+13	-	^{140}La	3.48E-03	7.15E+13		^{234}U	2.65E-03	6.11E+05	
^{103}Ru	3.36E-02	4.01E+13	0.02	^{139}Ce	3.37E-06	8.51E+08		^{235}U	2.02E+01	1.61E+06	
^{105}Ru	9.39E-05	2.34E+13		^{141}Ce	5.90E-02	6.23E+13	0.002	^{236}U	4.96E+00	1.19E+07	6E-04
^{105}Rh	6.37E-04	1.99E+13	-	^{143}Ce	3.01E-03	7.40E+13		^{237}U	9.71E-03	2.93E+13	
^{111}Ag	1.46E-04	8.55E+11	0.4	^{144}Ce	3.73E-01	4.40E+13		^{238}U	1.85E+02	2.30E+06	
^{123}Sn	7.40E-05	2.25E+10		^{142}Pr	5.05E-05	2.16E+12	-	^{239}U	2.40E-04	2.98E+14	
^{125}Sn	4.82E-05	1.93E+11	0.4	^{144}Nd	5.47E-01	2.40E-02		^{236}Np	1.09E-06	5.33E+02	
^{126}Sn	8.43E-03	8.86E+06		^{145}Nd	5.04E-01	7.67E-04	-	^{237}Np	2.55E-01	6.65E+06	-
^{124}Sb	2.13E-05	1.38E+10		^{147}Nd	8.69E-03	2.60E+13		^{238}Np	1.32E-03	1.26E+13	
^{125}Sb	3.89E-03	1.51E+11	0.5	^{147}Pm	1.22E-01	4.19E+12		^{239}Np	3.46E-02	2.97E+14	
^{126}Sb	1.05E-05	3.25E+10		^{148}Pm	7.13E-04	4.34E+12	-	^{236}Pu	1.15E-07	2.22E+06	
^{132}Te	5.17E-03	5.81E+13	0.8	^{149}Pm	1.30E-03	1.91E+13		^{237}Pu	1.97E-07	8.87E+07	
^{129}I	7.38E-02	4.82E+05		^{151}Pm	2.35E-04	6.35E+12		^{238}Pu	6.47E-02	4.10E+10	
^{130}I	6.28E-06	4.54E+11	0.8	^{149}Sm	1.88E-03	8.36E-05		^{239}Pu	1.59E+00	3.65E+09	2E-05
^{131}I	8.08E-03	3.71E+13		^{151}Sm	8.00E-03	7.79E+09	-	^{240}Pu	3.74E-01	3.14E+09	
^{135}I	6.34E-04	8.29E+13		^{153}Sm	1.01E-03	1.65E+13		^{241}Pu	2.94E-01	1.12E+12	
^{133}Xe	1.23E-02	8.54E+13	1	^{152}Eu	4.58E-06	2.99E+07	0.1	^{242}Pu	5.68E-02	8.31E+06	

3. Primary pipeline shielding

Prior to these calculations, a shielding pre-design has been proposed around the primary pipelines leading out of the reactor's concrete shielding. A 10 cm thick wall in each direction had been proposed for the shielding purposes. A horizontal cross-section of this proposal is shown in Fig. 5. For the purposes of dose rate calculations in MCNP, models of pipeline shielding segments have been created around the red marked locations in the figure.

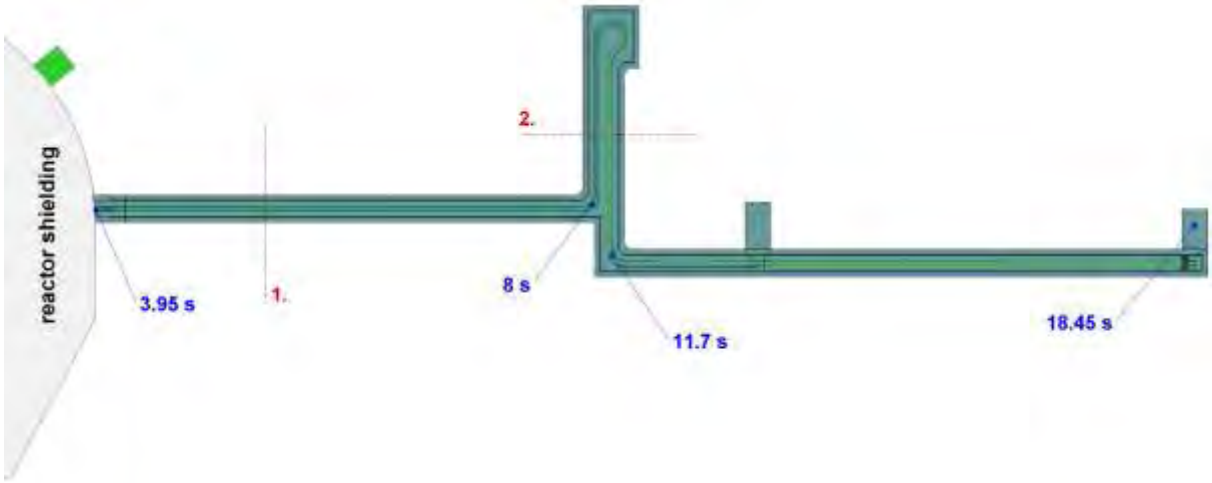


Fig. 5 Primary pipeline tracing and shielding pre-design, cross-section

Lead and steel were considered as shielding materials. Various thicknesses have been considered in the calculations. The dose rate values have been calculated on the surface of the shielding and in 1 m distances in each case.

To minimize the dose rate increment in the reactor hall, a condition has been set that the dose rate values on the surface shouldn't exceed the value of 100 μSv/h. This value is acceptable with respect to the decrease in dose rate values in the distances of 1 and 2 m from the shielding.

Calculation results show that the minimal shielding thickness of the steel shielding should not be less than 13 cm and in the case of a lead shielding not less than 6 cm. It is also possible to use the advantages of both shielding materials. A combination of a 4 cm inner layer of lead and a 5 cm outer layer of steel would be sufficient to satisfy the condition of 100 μSv/h at the shielding surface. This can also be achieved by choosing a 3 cm inner lead layer and a 8 cm outer steel layer.

The resulting dose rates at 1m and 2m distance for the proposed shielding materials and thicknesses on the shielding surface at segment 1 are listed in Tab. 3. Similar calculations have been made for the pipeline at segment 2. The calculated dose rates at segment 2 are all lower than at segment 1.

Tab. 3 Calculated dose rates at segment 1 for different shielding options

Shielding thickness and material	Dose rate [μSv/h]		
	Shielding surface	1 m distance	2 m distance
13 cm Fe	73.8	8.85	2.64
6 cm Pb	90.5	8.52	3.22
4 cm Pb + 5 cm Fe	71.5	7.39	2.05
3 cm Pb + 8 cm Fe	61.5	6.45	2.06

4. Primary block components shielding

Besides the shielding calculations for the primary pipeline tracking several calculations were realized for the shielding requirements of the primary circuit components. As these are going to be located outside the reactor hall in a new built experimental hall, the need for lowering the dose rates is even higher than for the primary pipes.

As the primary circuit of the SCWR-FQT facility consist of numerous components, which are assembled in a block, it would be unreasonably time-consuming to model all of them in the radiological calculation. Therefore, only the most prominent components were chosen to represent the primary circuit in the model. The final model used for the simulations included the pressurizer, the main circulation pump, two heat exchangers, two water coolers, one air cooler, two ion exchangers and two mechanical filters. The listed components were considered as representative in the approximation to reflect the radiological situation of the primary circuit. The pipelines connecting the components were not considered in the model as the volume of the primary water flowing through them is negligible compared to the volumes of the listed components.

Additionally to the primary circuit shielding, the necessity of a shielding for several components of the measurement circuit located outside the primary circuit block was discussed as well. These included two pumps and a de-aerating tank.

Due to the need for reducing the difficulty of the MCNP simulation a representative approximation of the selected components was necessary. Therefore, all components in the model containing the primary water were represented by cylinders of equal volume with wall thicknesses corresponding to the minimal wall thickness of the approximated component. The chosen approach sufficiently reflects the radiation situation in the primary circuit and

offers a conservative basis for later calculations. The primary circuit components and their approximations in the MCNP model are shown in Fig. 6.

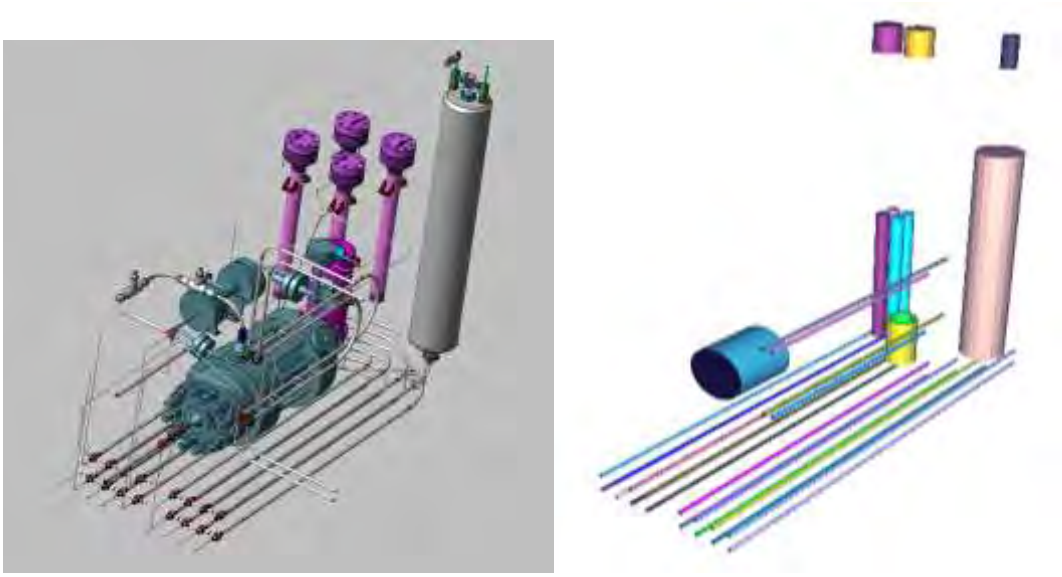


Fig. 6 All SCWR-FQT primary circuit components (left) and their approximative representations in the MCNP model (right)

All the primary circuit components and the three additional measurement circuit components were placed inside a shielding box with various thicknesses. Lead and stainless steel were considered as shielding materials for the box. After the first series of calculations the shielding box model was redesigned to correspond with the shielding pre-design from the project phase (Fig. 7 – left). Additionally, a smaller shielding box was introduced for the measurement circuit components. Only lead was considered as shielding material in the final calculation (model in Fig. 7 – right) as the steel shielding dimensions proved to be over-sized from early stage calculations.

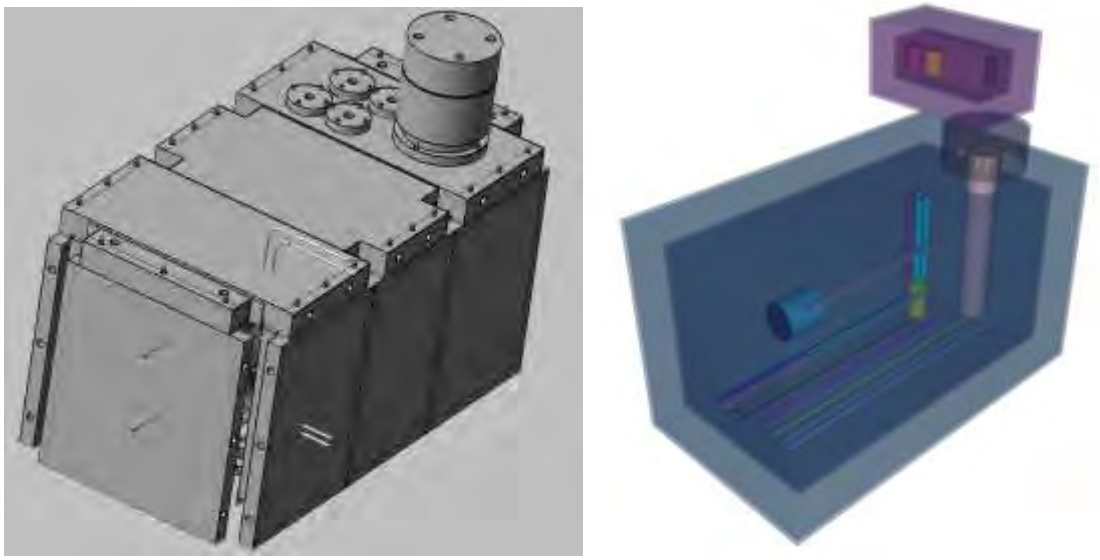


Fig. 7 Shielding box pre-design (left) and the later MCNP shielding model (right)

The shielding calculation was realized for two different radioactive sources in the primary circuit. The first series of calculations, reflecting normal operational conditions, was carried out using nitrogen-16, the major primary water activation product, as the only radioactive source in the primary water in all components. The expected nitrogen activity was calculated in the previous studies on the demands for the primary circuit pipeline tracking. The calculated N-16 activity in the active channel reaches a value of 3.4e+07 Bq/g. Knowing the flux rate in the circuit, the pipeline distances between the components and their values the overall N-16 activity of 3.2e+09 Bq in the primary circuit was calculated. Additionally a source term covering the cumulating corrosion product activities was placed inside the filters.

The second series, reflecting potential accident conditions, was based on the fission products and actinides inventories listed in Tab. 2. For each element its release rate coefficient was taken into account. As a proposal for a possible accident scenario, the failure of one fuel pin was chosen in the late stages of the loop operation (after two years).

Based on preliminary conservative calculations and respecting the limited space available around the primary circuit components, attempts were made to optimize the required shielding dimensions by reducing the thickness of the shielding box and add extra shielding layers to the ion-exchange filters (accumulation of corrosion products) and the main circulation pump (contains over 93 % of the total N-16 activity in the primary circuit). These attempts resulted into the design of a lead box with a thickness of 10 cm around the entire primary circuit, a smaller 10 cm thick lead box for the measurement circuit pumps and de-aerating tank and a 7 cm thick box around the ion-exchange filters. As the space limitations around the main circulation pump do not allow installation of a larger additional shielding segment, three options were considered: the main circulation pump without additional shielding, with a 2 cm lead layer and a 4 cm lead layer. The source term used in the calculation comprised the N-16 activity distribution in the entire primary circuit and the corrosion products located in the ion-exchange filters. Additionally, an estimate of the accident conditions of a single fuel pin failure was realized. The results are shown in Tab. 4.

Tab. 4 Primary circuit components shielding optimization variants

Shielding thickness				Dose rates values [µSv/h]			
Primary block	Measurement components box	Ion filters	Main circulation pump	Operational conditions		Accident conditions	
				surface	1 m distance	surface	1 m distance
10 cm	10 cm	7 cm	0 cm	22.5	4.1	9300	1900
10 cm	10 cm	7 cm	2 cm	11.1	1.9	3500	850
10 cm	10 cm	7 cm	4 cm	4.8	1.3	1450	570

5. Conclusion

MCNP calculations have shown that a satisfactory solution for the primary circuit shielding assuring safe operation would be a lead shielding with a thickness of 10 cm around the entire primary circuit and certain measurement circuit components, an additional shielding thickness of 7 cm around the ion-exchange filters to reduce the radiation impact of the accumulated corrosion products, and an extra shielding of at least 2 cm around the main circulation pump (the dominant ^{16}N activity component). The pipelines connecting the reactor with the primary block would require at least a 6 cm thick lead layer.
Such shielding design can be expected to reduce the radiation impact of minor fission product and actinides releases as well; however, it may prove insufficient in case of large releases under accidental conditions. For this case a permanent monitoring of the cooling water activity is necessary to clearly identify minor releases which will lead to the loop shut-

down. Thus, heavy contamination of the primary circuit components caused by large releases may be avoided.

6. References

[1] T. Schulenberg, J. Starflinger, P. Marsault, D. Bittermann, C. Maraczy, E. Laurien, A. T. Lycklama, H. Anglart, M. Andreani, M. Ruzickova, L. Heikinheimo; „European supercritical water cooled reaktor“; FISA 2009, Prague, Czech Republic.

[2] M. Raqué, A. Vojacek, P. Hajek, T. Schulenberg; „Design and 1D Analysis of the Safety Systéme for the SCWR Fuel Qualification Test“; NUTHOS-9, Kaohsiung, Taiwan (2012).

[3] T. Schulenberg, A. Vojacek, T. Zeiger, M. Raqué; „Risk and Safety Analyse of an SCWR Fuel Qualification Test Loop“; ISSCWR-6, Shenzhen, Guangdong, China (2013).

[4] R.A. Lorentz, M.F. Osborne; A Summary of ORNL Fission Product Release Tests with Recommended Release Rates and Diffusion Coefficients, (NUREG/CR-6261, ORNL/TM-12801); Oak Ridge National Laboratory (1995)

UTILIZATION OF A UNIVERSITY REACTOR FOR PUBLIC ACCEPTANCE

MYUNG HYUN KIM
Reactor Research & Education Center, Kyung Hee University
1732 Deogyeong-daero, Giheung-gu,Yongin-si, Gyeonggi-do, 446-701 - Rep. of Korea

ABSTRACT

AGN-201K is a university reactor in Kyung Hee University(KHU) mainly used for student education as training short course as well as academic course for senior-level. After the Fukushima accident, public concern on radiation hazard has been increased beyond rational level at a neighboring country. It was found that AGN-201K be the perfect tool for interaction with general public. It is very safe to operate with general participants because it is adapted to the very low power. However, radiation level is reasonably high to detect and shield for practice. KHU has an Regional Radiation Monitoring Post where environmental radiation level at Suwon city is continuously measured. In this facility, radiation level at soil, rain, and local agricultural products were measured and reported to the national monitoring headquarter.

A new mission of reactor research and education center of KHU has been tried from last summer. Facilities were opened for high school students and teachers for their science camps during summer & winter. A special public acceptance program named as experience camp for understanding the nuclear power and radiation was held 6 times for the last one-year period. Even though number of attendee was limited and small, feedback from participants was hot and positive enough to make professors be ready to sacrifice their personal time.

1. Introduction

Aftermath of Fukushima accident at March 2011 has never been disappeared and sometimes grown in socio-political aspect and also in public awareness. Sensitivity on radioactive material release to the pacific ocean is still very high in the Rep. of Korea as a neighboring country. From the summer of 2013, public fear to the radioactivity in sea product increased suddenly because of internet gossip and interest of mass media. Destination of many tourist from Korea was changed from Japan to the other countries because of distracting rumors and public fear against unknown source of hazard. Many people refused to eat fish only because there is a small chance to be contaminated. Government try to revive fish market before sinking and distrust. Under the strong attack of anti-nuclear activist through internet, it was found some facts in public domain after Fukushima.

- People tend to rely on internet information rather than expert's opinions shown on major media.
- People now know radioactivity unit better than before, but still are confused with them.
- People do not know well about radiation dose from our living environment, such as background radiation, radiation dose during medical diagnosis, etc.
- Young school students do not have good information database on internet. They can find many booklet from anti-nuclear parties and emotional information on internet.
- Nuclear issues are not special topics of stakeholders anymore. They are now popular topics for discussion either in social subject class or in science subject class.
- There has been no technical interaction between nuclear society and school teachers in Korea. Most of activities done were lectures and tours designed for a few hours.

An operating body of a university reactor, AGN-201K in Kyung Hee University(KHU) was established as the Reactor Research and Education Center(RREC) in 2008. Since then, RREC opened one-week short course for reactor experiment; 34 times to 349 participants from 9 Korean universities and 2 oversea universities. This mission must be the main role of RREC and participants will be increased continuously and expanded to overseas.

It was found that conditions of RREC is perfect for the public education and a feasibility of experience camp for school teachers was tested for the year of 2013 with government funding. RREC proposed this new project based on the following benefits.

- Maximum permitted power level of AGN-201K is 10 watt with corresponding thermal flux at the beam port is about $1.0X10^8$ #/cm^2-sec. It is quite low for research but high enough to measure neutrons and gammas inside and outside of reactor. Because of low radiation level, students can access near to the reactor closer compared to most of research reactors in institutes.
- After the refurbishment on the reactor facility, safety measures were enhanced with many monitoring devices. Installation of many detectors give more information through modern digital consoles.
- A new digital operation console was installed side by side in parallel to the original safety console used by licensed operators. Students can actually manipulate two control rods at the digital console under the supervision of operators at the analog console. This gives good experience what is reactor operation and how reactor is protected against accidents.
- KHU has a government designated center; regional environmental radiation monitoring center with radioactivity measurement post. This center has high-end accurate equipment to measure environmental radioactivity from samples of soil, rain, air-dust and agricultural food products. This center is a place to experience real environmental radiation.
- RREC do not operate a reactor for 24 hours. Reactor is operated only for the special missions and classes. Therefore, time and space of RREC can be used for general public without difficulties.
- The best partner for interaction with school teachers must be professors in university. Many documentary works and safeguard procedures are more flexible in university reactors compared to research reactors in national labs.

The test classes in Year 2013 were provided successfully even though participation of teachers were asked on voluntary base. Three camps were opened in July and September for teachers. The same class was provided to high school students in August by the request of Pyeonghae High School. The second year project is now on the way in Year 2014. In this year, official training credits are given to participants because this camp was accepted as registered classes for teachers by local educational board. 39 teachers visited in January for 2 camps. The followings in this paper explains in detail about what kinds of classes are given and feedbacks from teachers.

2. Facility Features for Nuclear Experience Camp

2.1 Reactor in RREC

AGN-201K reactor is one of two research reactors in Rep. of Korea in use. 30 MWt HANARO is the main research reactor used in many purpose with high performance records. One more research reactor is ready to be constructed at Kijang for a dedicated isotope production reactor as well as a multi-purpose research reactor. Because of low flux, AGN-201K cannot be used as a backup facility to HANARO, but can be used for a platform as a research and training facility for university. A extensive refurbishment was done during the period of 2004 through 2007. Components for I&C and safety features was repaired and added in order to comply with standing safety regulations and rules. [1] The second refurbishment was done

during 2010-2012 for the enhancement of safety and safeguards. Many sets of neutron detectors were added and connected to the operating console. CCTVs and entrance check points were installed with hand-foot monitors. Two more sets of gamma and neutron area detectors were also installed for the safety check. Improvement of reactivity meters was also done for better experimental conditions.[2]

This reactor is ideal for student experiments also for the experimental class for general public. First of all, this reactor is absolutely safe as a zero power reactor. This is free from risk of excursion at any case. Margin to core melt is almost infinite and there is no way to make fuel hot because of small excess reactivity with high thermal feedback. Under any kinds of mistake in operation, reactor cannot go into danger in reactivity matter. Only risk from reactor is radiation exposure and release of radioactive material. If there is no mechanical impact from outside, all radioactive material can be confined in a sealed reactor tank because there will be no pressure change in this reactor. Radiation exposure is the only measure to be monitored and controlled during experiment. From this point of view, reactor is adaptable to the students and public.

The second unique feature of this reactor is dual console in parallel. One original analog console was refurbished with new cables and parts. This console should be touched by licensed operator only by the law. However, the second console is an additional console plugged in analog console. All control action can be override by operator in analog console. Therefore digital console can be given to students and public without safety violation. Therefore this reactor is the only reactor which student who are not licensed can touch to.

2.2. Environmental Radiation Monitoring Center

There are 14 regional environmental radiation monitoring center in Rep. of Korea. One of them in KHU is monitoring radiation near Suwon province. In this center has two facility, one is the sampling post at the hill top to collect air dust and rain. The other is the center with measurement lab and sample preparation lab. In this center regularly, samples from soil and agricultural products were collected regularly at the various spot. Radiation from sensitive radioisotopes was measured semiconductor detectors and multichannel NIMs. The records were reported to the regulatory body, Korea Institute of Nuclear Safety. This facility can be used for students for education. The experience for the measurement of environmental radiation from Cs and I is very helpful for student in understanding of radiation hazard from Fukushima and Chernobyl. The purpose of this facility in public education is to make the understand some facts.

- Environmental radiation is monitored constantly all around the country. There is no chance to be irradiated without knowing.
- The number of specific radioactivity should be compared carefully with MPC in air or in water under the regulations. Most number shown in media is actually very low enough values.
- There is very low possibility of food contamination within a short period time, specially by radioactive material release at Fukushima.

3. Purpose of Classes in Experience Camp

This camp is designed for school teachers as a knowledge transfer about nuclear power and radiation. It is different from lectures which is usually done at a huge hall. Those lectures are given to more than 100 audiences with well prepared slides and movies by the specialist or renowned scholars. This may be the most efficient way to communicate with public. However, it may not be good enough to make audience have confidence in the transferred knowledge. This camp is named as Nuclear Experience Class for School Teachers. This is a small group camp for three days with boarding at the university dormitory. There are 6 classes with practice session and lectured and guided 4 professors. Maximum number of

participants was limited 20 and they are divided into two groups in order to make all teachers practice one by one individually. This may be inefficient way in the aspect of expenses and number of trainee. The structure and contents of classes are shown in Table 1.

Class	Lecture	Experiment
1	Nuclear Power & Radiation	Radiation Detection & Shielding
2	Environmental Radiation in Our Life	Radioactivity Measurement
3	Reactor Operation and Safety Protection	Reactor Operation
4	Nuclear Safety & Radwaste Treatment	Group Discussion
5	Practice of Neutron Radiography	
6	Panel Discussion on Selected Nuclear Issues	

Tab 1: Structure of nuclear experience camp

At the first day, ice breaking and introduction is given. Before the classes, education for radiation safety rules is given as a legal procedure for admission permit. Following class#1 is the introductory class teaching the fundamentals of nuclear engineering; principles of nuclear force and radioactive decay, characteristics of radiation, source of fission energy, meaning of power, measurement of radiation. The first experiment is provided for each small group to detect gamma and neutron counts from different detectors, at the different locations and at the different power levels. The purpose of this set of class is to teach the following facts.

- We can detect gammas everywhere even reactor power is off.
- Detected counts and dose is changing with big variation at every second as a background level.
- Some small-sized detectors(specially pocket dosimeters) are not reliable.
- Efficient shielding can be provided with distance and barriers even at the high power level.
- We cannot differentiate external dose from internal dose with detectors.

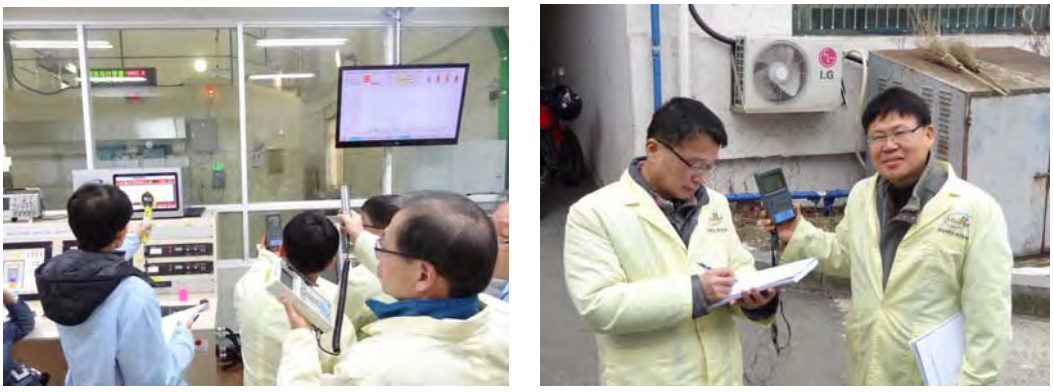


Fig 1. Experiment for gamma & neutron detection



Fig 2. Visit to sampling post for environmental R.I.

At the second day, two or three classes are given. The second class is the measurement of environmental radioactivity from prepared samples. Lecture is given for the understanding of radiation dose from daily life, hospital, work place and nuclear power plants. The purpose of this class is clear just like the followings.

- Legal limit of 1 mSv/yr for public is quite low enough and very low dose is not a source of health hazard.
- Background radioactivity for each isotope is not easy to be detected and they are varying with high variation.
- Sometimes radiation from our daily life is quite high in hospital. However, it is still far less than the hazard level.
- We can control the internal dose.



Fig 3. Measurement of radioactivity from environmental samples

The third class at the second day is reactor operation. This is a real fun for participants because they can move control rod and control a reactor to be critical. At the lecture, meaning of power and criticality is introduced. Principles of reactor operation and safety shutdown is the key issue for this class. The purpose of this class is to convince them that reactor cannot be in danger like a bomb at any time.




Fig 4. Reactor operation experiment

Additional class can be given for neutron radiography. There is a competition game among small groups for the prize. Picture by neuron transmission is shown to them and asked to find what were the targets for each images.

At the third day, two discussion sessions are given without experiments. The first session is for the social issues about choice of national energy including renewable energy, choice of radioactive waste treatment including LLW disposal, site selection for HLW repository, and reprocessing issues and proliferation. Scope of discussion is quite broad and very practical for teachers.

At the last discussion session, a small group of 4 persons should select a discussion issue from 7 candidates. One and half hour is given for group discussion for the final consensus of each group. As a final activity of camp, leaders of each group should present their position declaration about the raised issue without further discussion.




Fig 5. Group discussion & final presentation

4. Achievements and Results

The following table shows the record of 5 nuclear experience camps for teachers and one camp for high school students during the last one year. First two camps at July 2013 was the test camp with voluntary participants with limited advertisement. From the 4th camp, camp was advertised as an official credit course for teachers and there was many applicants exceeding maximum number of 20. Up to now, teachers near to the nuclear power plant sites were invited with priority for the first two. For the third camp, science teacher group in suburbs of Seoul participated as a group voluntarily. 4th and 5th camp was designed for science teachers in the metropolitan Seoul & Pusan. For the coming summer of 2014, invitation will be done for the other local province.

	Education Period	Participants	Number of Trainee
1	July 23-25, 2013	School Teachers (JeonNam, GwangJu, GyeongJu)	11
2	July 25-27, 2013	School Teachers (GwangJu, JeonNam, UlJin)	13
*	Aug. 28-29, 2013	High School Students (PyeongHae Nuclear Maister)	30
3	Sep. 14-15, 2013	School Teachers (GyeongGi)	28
4	Jan. 6-8, 2014	School Teachers (Seoul, Pusan, Incheon)	19
5	Jan. 9-11, 2014	School Teachers (Seoul, Pusan, Incheon)	20
		Total	121

Tab 2: Record of participants for the last one year

	Excellent	Good	Average	Bad	Very Bad
Course Contents	82%	18%	-	-	-
Quality of Education	82%	18%	-	-	-
Attitude of Activity Involvement	67%	33%	-	-	-
Applicability of Knowledge	79%	21%	-	-	-
Value of Education Data	64%	28%	8%		

Tab 3: Satisfaction data of participants

The table 3 shows the results of questionnaire for teachers. Satisfaction level for the course was very high in both contents and quality. They evaluated that 67% participated willingly and actively with interest and the others participated with interest. Most of participants evaluated educational materials will help their career as teachers at the school for students. Overall satisfaction level was high for the facility, system, food, and housing, etc.

References

[1] Myung-Hyun Kim, "Reactor Upgrade of AGN-201 in KHU, Korea," Research Reactor Fuel Management(RRFM-2008), Hamburg, Germany, March 2-6, 2008.

[2] Myung Hyun Kim, "Utilization of AGN-201K for Education and Research in Korea," Research Reactor Fuel Management (RRFM-2011), Rome, Italy, March 20-24, 2011.

[3] Aerojet General Nucleonics, “Educational Experiments Utilizing The AGN-201 Nuclear Reactor," AGN REPORT No.16, AGN, January, 1957.

INTERDIFFUSION STUDY BETWEEN A U7wt%Mo ALLOY AND ZIRCALOY-4

K. ARALDI CARDOSO[1], E. F. URANO DE CARVALHO[1],
M. DURAZZO[1] , H. G. RIELLA[2],

[1] *Nuclear Fuel Center, Nuclear and Energy Research Institute - IPEN/CNEN-SP.*
Av. Prof. Lineu Prestes, 2242 CEP 05508-900, São Paulo/SP.
[2] *Chemical Engineering Department, Santa Catarina Federal University, Florianópolis, Brasil.*

ABSTRACT

The United States Reduced Enrichment for Research and Test Reactors Program (RERTR) is tasked with the development of a fuel type that will allow conversion to low enriched uranium (LEU) of the world's research reactors that are currently fueled by uranium enriched to more than 20% U^{235} (HEU). These efforts have led to U-Mo alloy dispersion fuel and monolithic fuel. While the U-Mo dispersion fuel achieves uranium loadings around 8 gU/cm^3, the use of monolithic fuel can achieve fuel meat loading around 16 gU/cm^3 for the U-7wt%Mo alloy. The monolithic fuel consists of a single metallic fuel region cladded with aluminum. However, the U-Mo alloy interacts chemically with the aluminum cladding under irradiation. This interaction has been subject of research, because the formed layer decreases substantially the thermal conductivity of the fuel, which results in an undesirable temperature increase. The interaction forms a large number of ternary U-Al-Mo phases that can cause swelling of the fuel plates. Because of this undesirable interaction between the U-Mo meat and the aluminum cladding, a new alternative has been studied to eliminate this problem by replacing the aluminum cladding by Zircaloy-4, which has apparently better compatibility with the alloy U-Mo. In this work the interdiffusion between the U-7wt%Mo alloy and Zircaloy-4 has been studied. The study was conducted through heat treatment under inert atmosphere. The interdiffusion was preliminarily evaluated by Scanning Electron Microscopy (SEM). An interpenetration of around 270 μm was measured after 100 h heat treatment at 950°C.

1. Introduction

Researchers have been seeking a new and better alternative for manufacturing of nuclear fuel plates with low-enriched uranium. In this work, it was decided to employ monolithic material for development of mini plates. The U-Mo alloys have been studied in the recent years due to the fact that the alloy has high uranium loading capacity and specially can stabilize the gamma phase (γ) of Uranium. The introduction of molybdenum as an alloying element in uranium promotes the retention of the metastable phase in a wide temperature range, permitting a safer operation of the reactor. The stability of this alloy prevents phase transformations resulting from thermal cycling, suffered by the fuel elements during neutron irradiation [1]. The percentage of molybdenum used was 7% in weight (≈15,5% atomic), which according to the U-Mo phase diagram shown in the Figure 1 [2], ensures the stability of the gamma phase of uranium.

Because of its properties in the nuclear industry, Zircaloy was employed as a cladding. One of the main characteristics of this alloy is the low neutron capture, which justifies its importance and use in the nuclear industry. Furthermore, the Zircalloy-4 is characterized by complex structure of precipitates, which are known to play an important role in the macroscopic properties, i.e. strength, ductility, stiffness, strain rate sensitivity and resistance of the material to corrosion [3].

According to the Mo-U-Zr ternary diagram, various compounds are expected to be found through the interdiffusion layer that is formed [4,5]. As stated in the work of K. Huang et al, multiple phases including αU, Mo_2Zr, Zr solid solution, γUZr, and UZr_2 were observed at the

interface of U-Mo with Zr [5]. In their work, A. B. Robinson et al, reported that the interaction products formed between U-Mo fuel and Zr are apparently stable during the irradiation process [6].

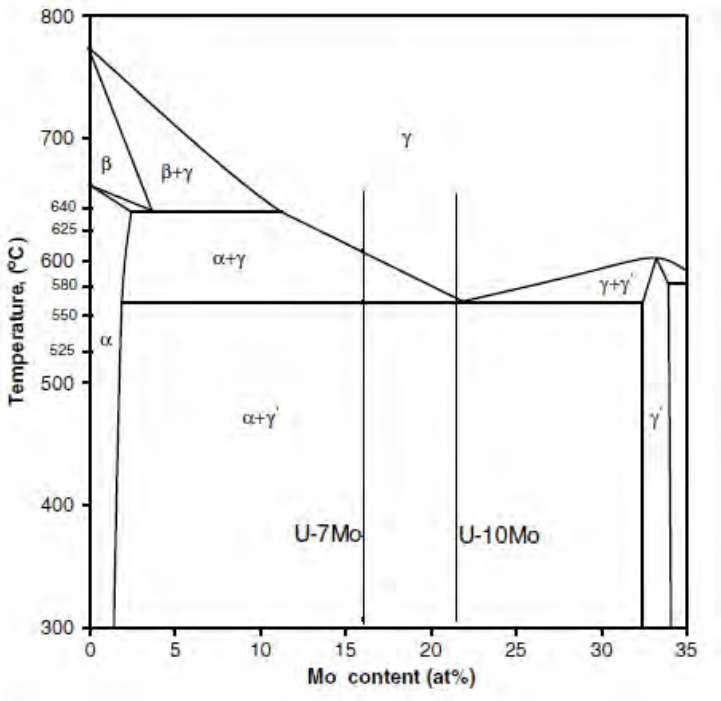


Figure 1 - U-Mo Phase Diagram. [3]

This work is focused in the study of the interdiffusion that occurs between the core material of the fuel and the cladding. The interdiffusion was preliminarily studied by observation of the interaction region between U-Mo and Zircaloy 4 with SEM.

2. Materials and Methods

The sample was prepared according the picture frame technique, employing U-7wt%Mo alloy as the fuel and Zry-4 as the cladding material. These components were assembled and TIG welded at the external borders. After that, the was hot-rolled at 800ºC with one pass just to pull over and ensure good contact between the U-Mo alloy and the Ziecaloy-4. The heat treatment was carried out at 950 ± 5 °C for 100 hours in a stainless steel retort (AISI 310) that was placed in a tubular furnace with programmable temperature. Argon was used to protect the sample from oxidation, flowing at 1L/min at a pressure of 1.5 kgf/cm². The cooling of the stainless steel retort was carried out removing it from the furnace and exposing to the ambient. Argon flow was maintained during the cooling. The sample was cut around the core and mounted in rapid polymerization resin, and afterwards, polished. Finally, the microstructure of the sample was analyzed by Scanning Electron Microscopy (SEM) equipped with x-ray energy dispersive spectroscopy (XEDS). The interface region was observed and evaluated.

3. Results and Discussions

Figure 2 shows the interdiffusion zone, where atoms from the U-Mo alloy diffused in the ZRY-4 region. This interdiffusion layer is approximately 270 μm width. The shades of gray show the gradient of uranium concentration from U-Mo alloy region into the ZRY-4 region. Due to the atomic number contrast, we can observe the shades of light gray near the UMo/ZRY-4 interface (uranium rich region), which becomes darker as uranium is diluted toward the ZRY-4 region.

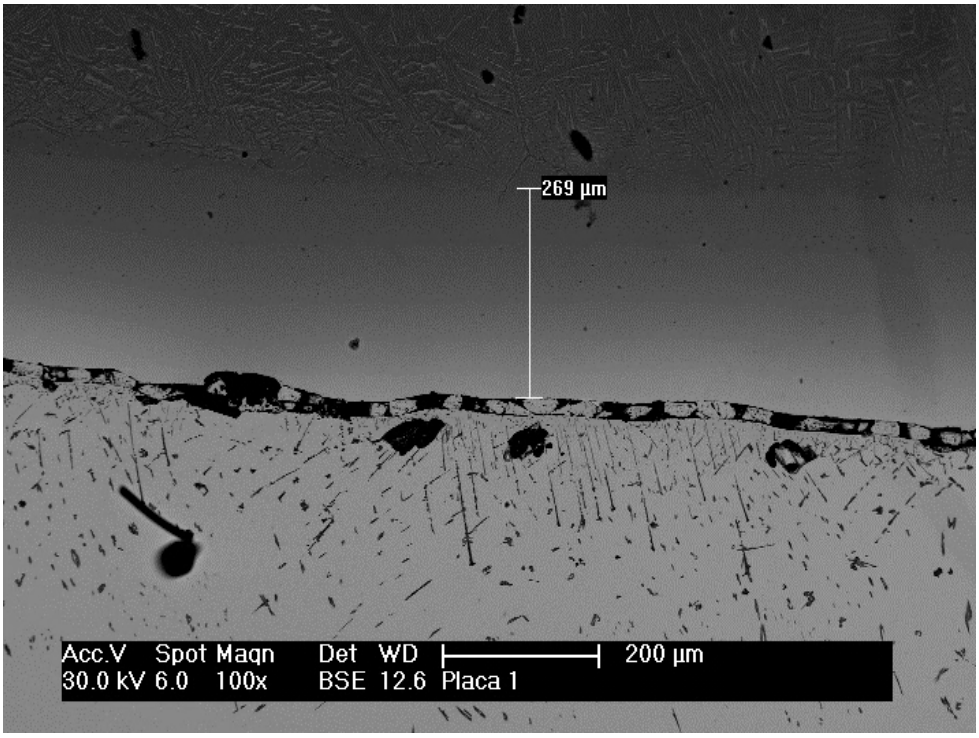


Figure 2 – Backscattered electron micrograph of the interdiffusion layer.

Figure 3 shows the micrograph and elemental mapping in the interface region (images from Field Electron Gun Microscopy - FEG). We see the formation of two bands in the interdiffusion zone, a lighter, near the interface UMo/ZRY-4 on the ZRY-4 side, and other darker. The lighter is clearly outlined and is the layer where occurred a marked diffusion of atoms from the U-Mo side. In the darker band, the diffusion of these atoms starts to decrease and there is a higher Zr concentration.

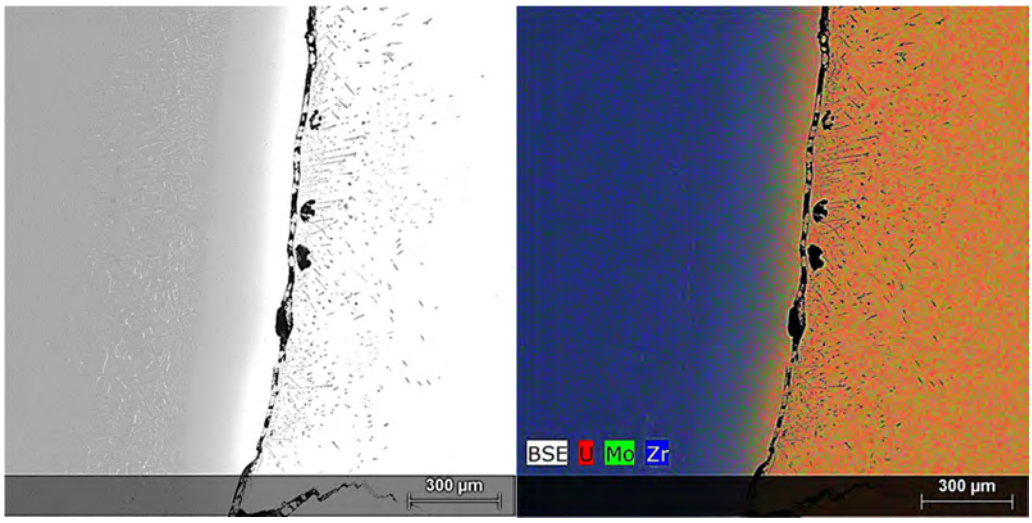


Figure 3 - FEG image of interdiffusion layer and elemental mapping.

From figures 2 and 3 it can be seen precipitates on the U-Mo alloy side. According to the elementary mapping analysis, the precipitates have been identified as almost pure Zr. Huang et al [5] also found these precipitates and reported on his work as a Zr-rich phase, which is composed by more than 95 at.% Zr and a small portion of U and Mo. According to the author, this tiny Zr-rich precipitate should be the αZr formed during the quenching. The U-Zr solid solution decomposed into eutectoidally αZr and Mo_2Zr upon cooling. The Mo_2Zr phase

was not found in this study and the precipitates formed along the interface were identified as a Zr rich phase.
In Figure 4 it´s possible to better visualize the Zr-rich phase formed in the U-Mo alloy side. The blue features correspond to almost pure zirconium.

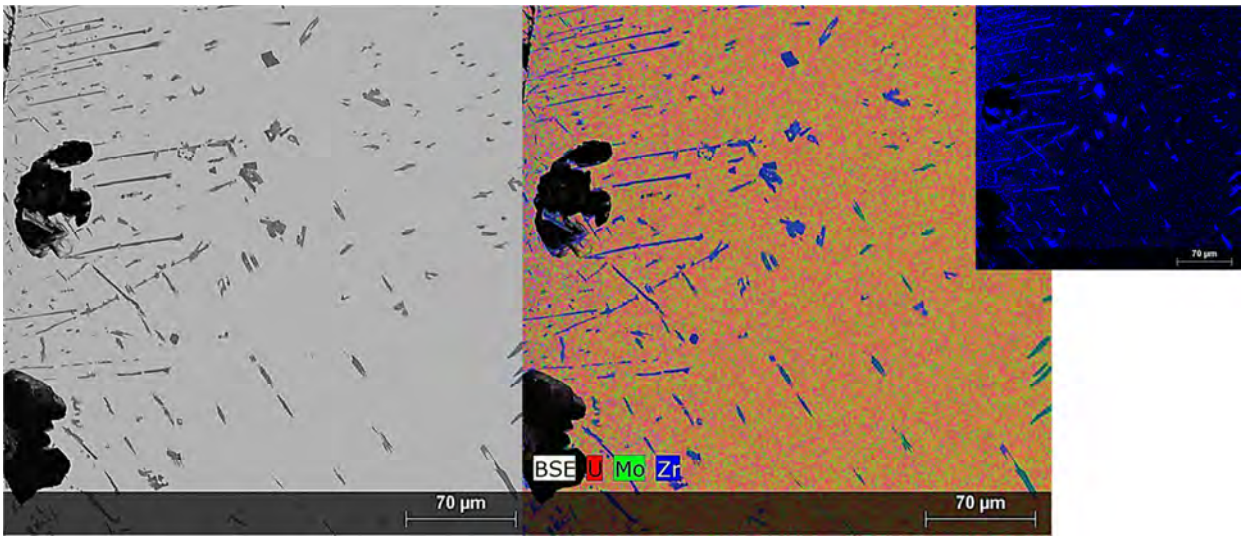
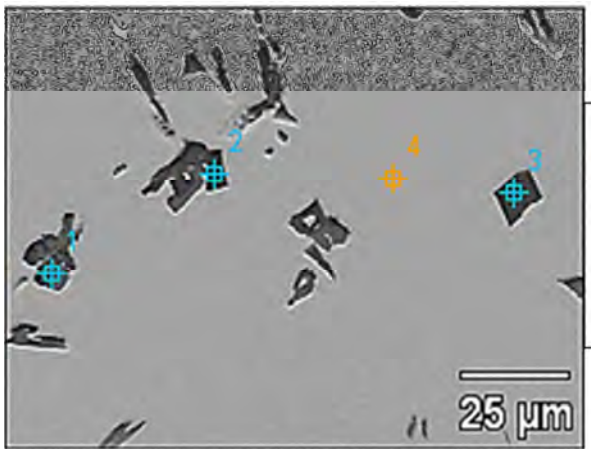


Figure 4 - FEG image of the Zr rich phase formed on the U-Mo side and elemental mapping.

Semi-quantitative XEDS was also carried out at four points inside the blue features showed in figure 4. Figure 5 presents the obtained results. The semi-quantitative analysis confirms that the precipitates are a Zr-rich phase. This observation agrees with the result reported by Huang et al.



Point	Zr	Mo	U
1	100.00	0	0
2	88.13	0	11.87
3	96.96	0	3.04
4	1.81	5.38	92.81

Figure 5 - XEDS analysis of dark precipitates.

The phenomena occurring in the interdiffusion zone are indicated in Figure 6. There is indication that the Kirkendall effect occurs in the U-Mo side due to pore formation on this region, which indicates that uranium atoms diffuse more rapidly in ZRY-4. This explains the lighter interdiffusion region on the ZRY-4 side, which contains a high U concentration.
On the side of Zircaloy-4 the microstructure known as Widmanstätten was formed. Zirconium in solid state undergoes an allotropic transformation from the low temperature hexagonal closed-packed (hcp) α-phase to body-centered cubic (bcc) β-phase at 865ºC. On cooling, the transformation is either bainitic or martensitic depending on the cooling rate, with a strong epitaxy of the α-platelets in the former β grains. Quenching Zircaloy from β-phase in moderate cooling rates produces two variants of Widmanstätten structure, namely, the basketweave and the parallel-plate structure [7]. This microstructure is most visible near the

diffusion layer, because in this region the cooling rate was lower, creating conditions for the microstructure to develop.

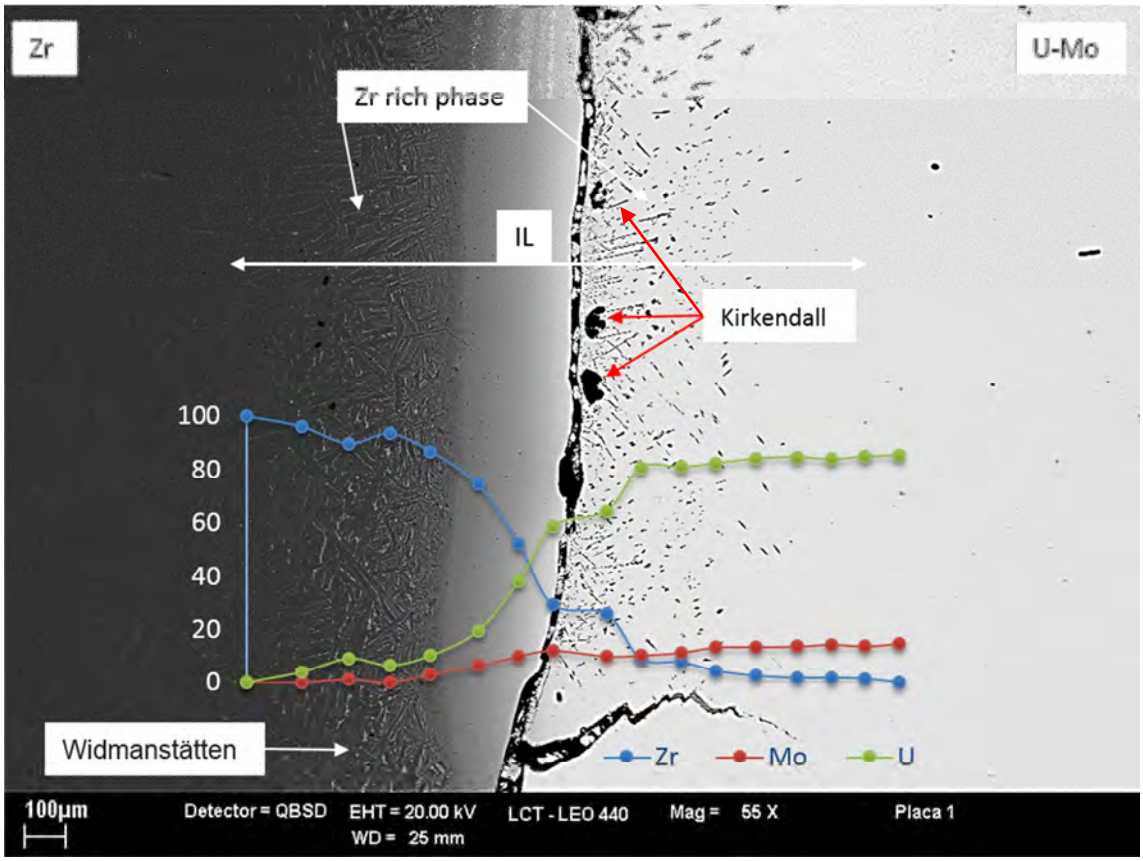


Figure 6 – Backscattered electron micrograph and concentration profile from Zr vs. U-Mo.

As already mentioned, a XEDS semi-quantitative analysis was performed on interdiffusion zone. In Figure 6 was presented a preliminary concentration profile constructed with the results. It is observed that there is a decrease in the Zr concentration in the interdiffusion layer due to diffusion of atoms of U in this region. More studies should be conducted to obtain more reliable results.

4. Conclusions

Diffusional interaction between Zry4 - U7wt%Mo alloy has been studied in the temperature of 950ºC for 100 h. A rich Zr phase and the Kirkendall effect has been found at the interface.

Based on the results obtained in these preliminary analyzes, it was concluded that there is an intense diffusion of uranium atoms within the ZRY-4 alloy. The interdiffusion layer of 270 µm confirms the severe interdiffusion.

Additional analysis must be performed to characterize the precipitates formed during the diffusion process on the U-Mo alloy side.

References

[1] Martins, I.C (2010). Estudos microestruturais sobre interações químicas na liga U-Mo com Al. Dissertação [Mestrado] – Instituto de Pesquisas Energéticas e Nucleares – IPEN/USP.

[2] J. Park, H. Ryo, S. Oh, D. Lee, C. Kim, Y. Kim, G. Hofman - Effect of Si and Zr on the interdiffusion of U-MO alloy an Al – Journal of Nuclear Materials, 2008, 374. P 422-430.

[3] H. Paul, M. Darrieulat, N. Vanderesse, L. Litynska, M. Miszczyk – Microstructure of Warm Worked Zircalloy-4 - Archives of Metallurgy and Materials. Vol. 55, 2010.

[4] B. Picchetti, L. Lemos, M. Lopez – Diffusion Couples of UMo/Zry in Different Conditions – RRFM 2013 – Saint Petersburg – Russia

[5] K. Huang, Y. Park, D.D. Keiser Jr, Y.H. Sohn – Interdiffusion Between Zr Diffusion Barrier and U-Mo Alloy – Journal of Phase Equilibria and Diffusion., Vol. 33, Nº 6, 2012.

[6] A.B. Robinson, D.M. Wachs, D.E. Burkers, and D.D. Keiser, US RERTR Fuel Development Post Irradiation Examination Results, *Proceedings of the 30th International Meeting on Reduced Enrichment for Research and Test Reactors (RERTR), Washington, DC, 2008.*

[7] A. R. Massih, L.O. Jernkvist – Transformation Kinects of Alloys Under Non-isothermal Conditions – Materials Science, 2009.

IRRADIATION TEST CONDITIONS OF U-7MO DISPERSION FUEL FOR KJRR FUEL QUALIFICATION

Y.W. TAHK*, J.Y. OH, B.H. LEE, H.J. KIM, J.S. YIM
Fuel Design, Korea Atomic Energy Research Institute, 111, Daedeok-daero 989 beon-gil, Yuseong-gu, Daejeon 305-353 – Korea

J.M. PARK
Research Reactor Fuel Development, Korea Atomic Energy Research Institute, 111, Daedeok-daero 989 beon-gil, Yuseong-gu, Daejeon 305-353 – Korea

*Corresponding author: ywtahk@kaeri.re.kr

ABSTRACT

KiJang research reactor (KJRR) adopts U-7wt%Mo / Al-5wt%Si dispersion fuel with 8.0 gU/cm^3 to achieve more efficiency and higher performance than conventional silicide fuel. KAERI has planned mini-plate wise and fuel assembly wise irradiation tests for the qualification of the new fuel; 16 mini-plates irradiation in the High-flux Advanced Neutron Application Reactor (HANARO) at KAERI and a fuel assembly irradiation test at the Advanced Test Reactor (ATR) in the USA. Regarding the qualification, the irradiation conditions for the KJRR fuel qualification were compared with those of irradiation programs of RERTR and European U-Mo development programs. To perform successfully the irradiation tests without any concern, the effects of main irradiation parameters such as peak and average heat flux, fission power density, peak fission density and peak fuel temperature during the irradiation have been touched. The results of preliminary evaluation show that the mini-plate irradiation tests and the fuel assembly irradiation test are expected to be performed with integrity of the new fuel.

1. Introduction

For the qualification of U-7Mo dispersion fuel, KAERI has planned a series of mini-plates irradiation test in the High-flux Advanced Neutron Application Reactor (HANARO) in KAERI and a FA irradiation test at the Advanced Test Reactor (ATR) in Idaho National Laboratory.
Three **HA**NARO **M**ini-**P**late Irradiation tests (HAMP-1, 2, and 3) with total 16 mini-plates will provide basic irradiation data including the fuel behavior depending on the fuel burnup, i.e. low burnup (about 45 %U235 depletion), fuel assembly average discharge burnup (about 65 %U235), and local maximum discharge burnup (about 85 %U235). The fuel assembly irradiation test at ATR (KJRR-FAI) is to be performed in the North East Flux Trap (NEFT) of ATR to achieve maximum 85% local burnup goal.
U-7Mo dispersion fuel for KJRR has an aluminum-5 wt.% silicon matrix to minimize the growth of the interaction layer (IL) between the U-Mo fuel particle and the matrix [1-3]. The fuel meat consists of an Al-5wt.%Si alloy matrix dispersion of uranium 7 wt.% molybdenum (U-7Mo) metallic alloy with a U235 enrichment of 19.75%. Aluminum alloy 6061 is used as the fuel cladding.
The irradiation test conditions for the KJRR fuel were compared with those of AFIP-1 and IRIS-3 with similar medium high heat flux using the U-7Mo dispersion fuel with silicon added

matrix. The preliminary fuel performance evaluation results such as peak fuel temperature and peak plate swelling during the irradiation were also compared.

2. Irradiation test conditions

2.1 Mini-plate irradiation test condition

The mini-plates for HAMP-1 and HAMP-2 have a nominal dimension of fuel meat length of 70 mm, fuel meat width of 25 mm, fuel meat thickness of 0.51 mm, fuel plate length of 130 mm, fuel plate width of 35 mm, and fuel plate thickness of 1.27 mm.
The width of a mini-plate of HAMP-3 is the same as in HAMP-1 and HAMP-2, which is about half the width of a full-size plate. However, the length of a mini-plate of HAMP-3 is the same as that of a full-size plate for the fuel assembly. Four full-length mini-plates will be irradiated in HAMP-3.
The irradiation capsule for HAMP-1 consists of 2 clusters and each cluster contains 4 mini-plates as shown in Fig. 1. Six mini-plates among the total of eight mini-plates to be irradiated in HAMP-1 will consist of fuel meat with a uranium density of 8.0 g-U/cm^3. Two other mini-plates will consist of fuel meat with the same uranium density of 6.5 g-U/cm^3 as the outer fuel plates of the fuel assembly for the equilibrium core of the KJRR. However, a fuel performance evaluation will be focused on mini-plates of 8.0 g-U/cm^3, which show a higher heat flux.

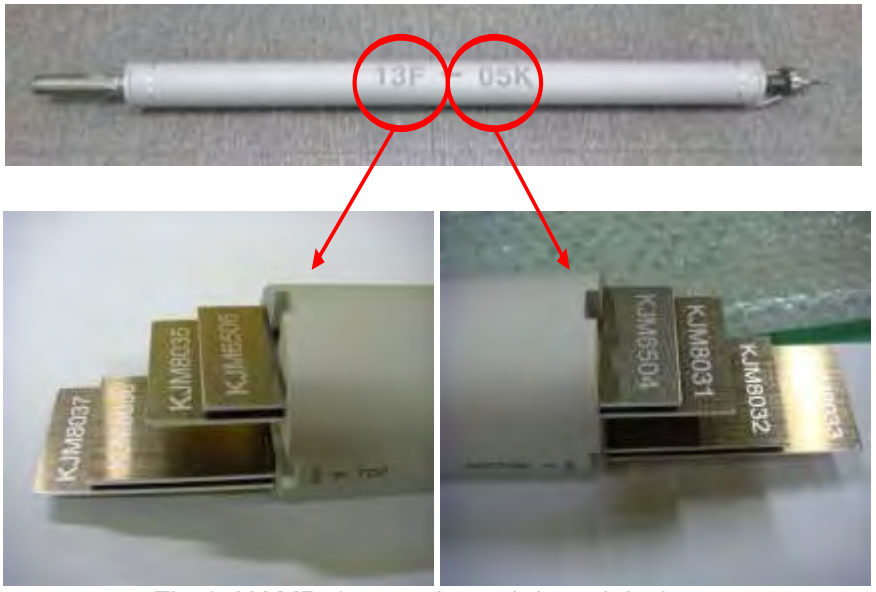


Fig 1. HAMP-1 capsule and the mini-plates

The irradiation capsules for two sequential HAMP-1 and HAMP-2 tests are to be loaded in the irradiation hole (OR-3) with an upward coolant flow in the HANARO core. The capsule for HAMP-3 will be loaded in the irradiation hole, which is different from HAMP-2 because the irradiation should run in parallel with HAMP-2. OR-5 is tentatively expected to be used as the irradiation hole for HAMP-3, the neutron flux of which is lower than OR-3. Thus, the heat flux of the HAMP-3 in OR-5 would be about 90% compared with that in OR-3. However, a fuel performance evaluation for HAMP-3 was performed based on the heat flux of OR-3, conservatively. The heat flux profiles of mini-plates were obtained from the MCNP code calculations [4].

The irradiation conditions for HAMP-1, 2, 3 and KJRR-FAI are summarized in Table 1.

Parameter	HAMP-1 and 2	HAMP-3	FA irradiation (KJRR-FAI)
U-235 enrichment	19.75 ± 0.2 wt%		
Number of mini-plate or full-size plate (uranium density of fuel meat)	10 (8.0 g-U/cm^3) 2 (6.5 g-U/cm^3)	4 (8.0 g-U/cm^3)	19 (8.0 g-U/cm^3) 2 (6.5 g-U/cm^3)
Fuel meat dimension (mm) (thickness x width x length)	0.51 x 25 x 70	0.51 x 25 x 600	0.51 x 62 x 600
Fuel plate dimension (mm) (thickness x width x length)	1.27 x 35 x 130	1.27 x 35 x 640	1.27 x 70.7 x 640
Cladding thickness (mm)	0.38		
Target burn up (U235 depletion %)	Avg. 45 % (HAMP-1) Avg. 65 % (HAMP-2)	Local maximum 85~90%	Local maximum ~ 85 %
Average heat flux at beginning of cycle (BOC), (W/cm^2)	207 (mini-plate #4)	173	160 (plate #20)
Local maximum heat flux (W/cm^2)	237 (mini-plate #4)	212	183 (plate #20)
Flow rate of fuel channel (m/s)	11.65	11.65	7.2
Water gap between mini-plates or full-size plate (mm)	2.13~2.20	2.13~2.20	2.35
Irradiation Test Date	Jan.~July.2014 (HAMP-1) Sep.2014~Jun.2015 (HAMP-2)	May.2014~Oct.2015	Feb.2015~Jan.2016

Tab 1: Irradiation test conditions of mini-plate and fuel assembly

2.2 Fuel assembly irradiation test condition

Two kinds of fuel meat with a uranium density of 8.0 and 6.5 g-U/cm^3 will be used for 19 inner plates and 2 outer plates of the KJRR fuel assembly, respectively. The matrix will also contain 5 wt.% silicon. Aluminum alloy 6061 will be used as the fuel cladding material. Twenty-one fuel plates will be assembled into a fuel assembly by swaging in the grooves of the side plates as shown in Fig. 2.

The North East Flux Trap (NEFT) in the ATR is expected to be used for the irradiation of KJRR test fuel assembly [5]. To achieve maximum 85% local burnup goal with a heat flux of less than 200 W/cm^2, the fuel assembly will be irradiated at a North East Lobe operating powers of 21 MW for 100 days followed by an additional 150 days with slightly higher test operating powers of 23 MW.

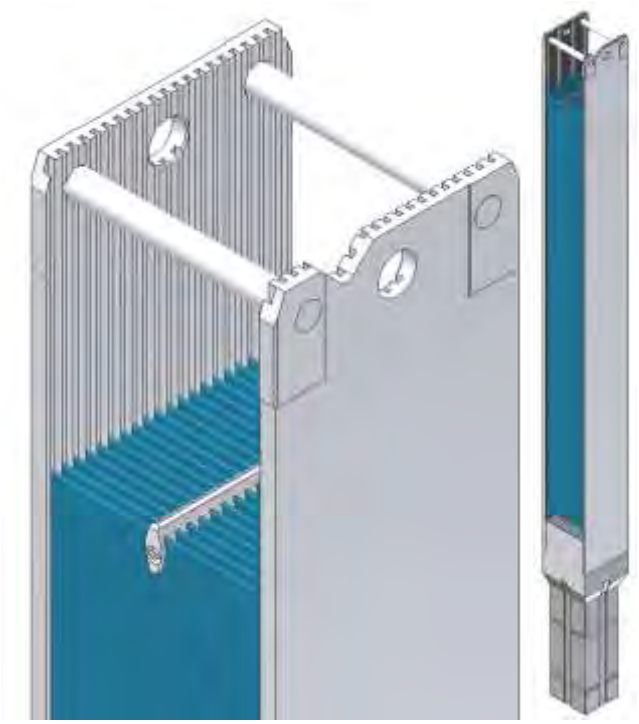


Fig 2. KJRR test fuel assembly

3. Fuel performance evaluation of mini-plate irradiation test

The fuel center temperature have been evaluated taking into account the influence of fuel meat swelling, fuel particle-matrix interaction layer growth, and boehmite corrosion layer growth on the cladding surface.
Fig. 3 (a) and (b) show the fuel peak temperature as a function of burnup for the mini-plate tests. The maximum peak fuel temperature is about 155~156 °C at a burnup of around 17~18 % U235 depletion. Up to a maximum burnup, the fuel temperature shall be kept below the design limit of 200°C for the irradiation test.
The boehmite corrosion layer thickness was evaluated upto the maximum burnup. The maximum boehmite layer thickness and maximum temperature difference across the boehmite layer are predicted to be about 27~33 μm and 24~31 ℃, respectively.
The irradiation swelling also needs to be checked for the maintenance of the proper channel gap. The swelling correlation of U-Mo fuel is composed of two parts: solid fission products swelling and gas bubble swelling [6,7].

$(\Delta V/V_0)$ total (%) = $(\Delta V/V_0)_g + (\Delta V/V_0)_s$

The solid fission product swelling is a linear function of burnup (or fission density).

$(\Delta V/V_0)_s$ (%) = $4.0\times10^{-21} f_d$, where f_d is the fission density in fissions/cm^3.

The gas bubble swelling has different rates depending on the fission density.

$(\Delta V/V_0)_g$ (%) = $1.0\times10^{-21} f_d$, for $f_d \le 3\times10^{21}$ fissions/cm^3

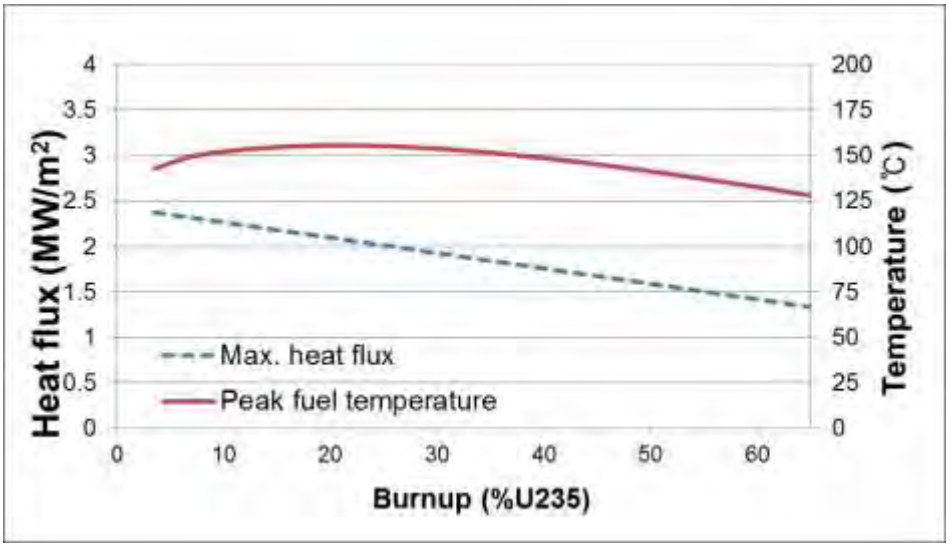
$(\Delta V/V_0)_g$ (%) = $3.0+2.3\times10^{-21}(f_d - 3\times10^{21}) + 0.33\times10^{-42}(f_d - 3\times10^{21})^2$, for $f_d > 3\times10^{21}$ fissions/cm^3

Additionally fuel meat volume will be increased 1~1.2 % at the maximum burnup for HAMP-1, HAMP-2, and HAMP-3 by interaction layer formation between the U-Mo fuel particle and the matrix.

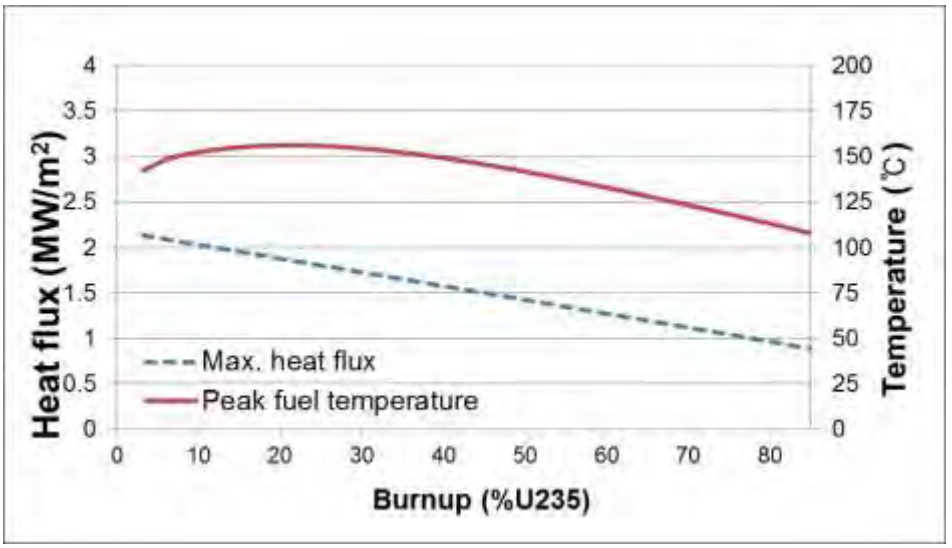
As shown in Fig. 4, the calculated values of the fuel meat swelling for HAMP-1, HAMP-2, and HAMP-3 are about 10%, 16%, and 22%, respectively. The swelling of a mini-plate occurs almost totally in the thickness direction. Thus, the maximum thickness increase of the fuel meat of HAMP-3 is transferred to the mini-plate thickness increase of about 110~122 μm.

Conclusively, the substantial swelling caused by interactions between fuel particles and aluminum matrix is prevented by limiting the maximum temperature below 200°C for all normal irradiation conditions. The local peak narrowing of the channel gaps by fuel swelling

and boehmite layer of dual surfaces of a mini-plate is less than 9% of the initial channel gap.



(a) HAMP-1 and HAMP-2



(b) HAMP-3

Fig 3. Fuel center temperature as function of burnup for mini-plate irradiation

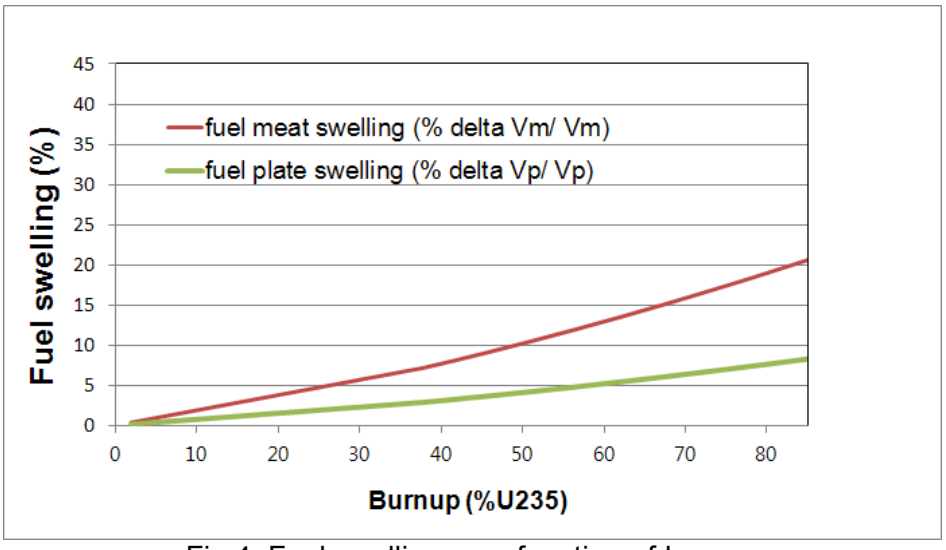
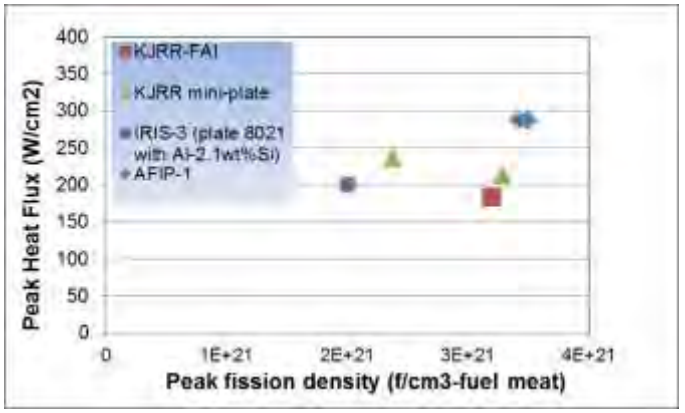


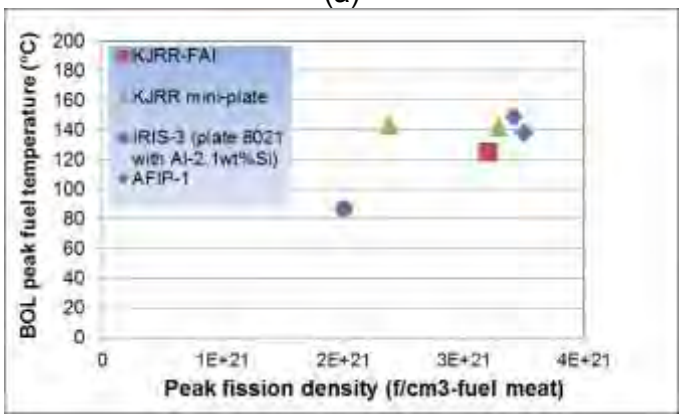
Fig 4. Fuel swelling as a function of burnup

4. Comparison of peak fuel temperature and fuel swelling

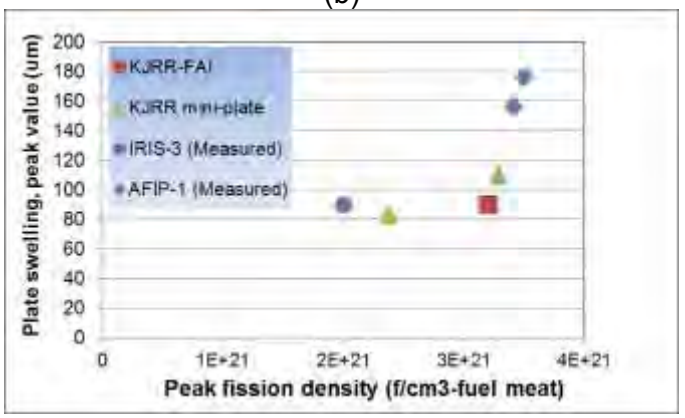
Table 2 summarizes the irradiation evaluation results of the KJRR fuel mini-plate and fuel assembly and those of AFIP-1 and IRIS-3 with similar medium high heat flux [8,9]. The preliminary evaluations of the KJRR fuel assembly irradiation test were performed by INL using PLATE model and ABAQUS simulations [5].
Although two full-size plates in AFIP-1 used the fuel meat with a uranium density of 8.8 g-U/cm^3, the other condition for U-7Mo dispersion fuel were very similar with KJRR fuel. One plate in AFIP-1 test adopted 2wt.%Si added aluminum matrix and the other plate adopted Al-4043 alloy for the matrix. In the case of IRIS-3, 8021 plate of U-7Mo dispersion fuel with 2.1 wt.% silicon added aluminum matrix was chosen for the comparison.
Fig. 5 (a) shows the comparison of peak heat flux vs. peak fission density of fuel meat for the irradiation tests. Fig. 5 (b) and (c) show the preliminary evaluated results of peak fuel temperature and plate swelling vs. peak fission density for KJRR fuel test and the evaluated and measured results for AFIP-1 test [8] and IRIS-3 test [9]. All the evaluated values of peak fission density, peak fuel temperature and peak plate swelling for KJRR fuel test came within the range of AFIP-1 test results.



(a)



(b)



(c)

Fig 5. (a) peak heat flux, (b) peak fuel temperature and (c) peak plate swelling of the irradiation tests (peak fission density of fuel meat was used for the x-axis).

	KJRR HAMP-1,2	KJRR HAMP-3	KJRR FAI [5]	AFIP-1		IRIS-3
Plate ID	KJM#4 (8033)	#1	Plate #20	1T2	1B5	8021
uranium density of fuel meat (gU/cm^3)	8	8	8	8.8	8.8	8
wt%Si in Al matrix	5	5	5	2	5	2.1
BU (% U235 Depletion)	65	85~90	85	79	78	59.3
Peak fission density (f/cm^3-fuel meat)	2.38E+21	3.2~3.4E+21	3.20E+21	3.5E+21	3.42E+21	2E+21
Peak Heat Flux (W/cm^2)	237	212	183	286	287	201
Fission Power Density (kW/cm^3-fuel meat)	~ 9.3	~ 8.4	~ 7.2	~ 11.2	~ 11.3	~ 7.9
Corrosion layer (um)	27	32~33	32			
Peak Swelling (um)	83	110~122	90	176	156	90
BOL peak fuel temperature (°C)	143	142	125	137.5	148.8	87
Maximum fuel temperature (°C) (w/ interaction layer formation and boehmite corrosion)	155	156	134			92

Tab 2: Evaluation results of KJRR irradiation test, AFIP-1 test and IRIS-3 test

5. Conclusion

The maximum fuel temperatures for the irradiation condition of KJRR fuel irradiation tests are evaluated to be about 155°C for mini-plate test and about 134°C for fuel assembly test and, which are far below the preset limit of 200°C on the rapid swelling by reaction between fuel particles and the matrix. The calculated temperature difference between the inside and outside of the boehmite layer is in the range a maximum of 24~31 °C and far below the spallation criterion. The local peak narrowing of the channel gaps by fuel swelling and corrosion layer of dual surfaces of a fuel plate is estimated to be less than 9% of the initial channel gap. All the evaluated peak values of fission density, fuel temperature and fuel swelling for KJRR fuel test are within the range of full-size plate test results of AFIP-1. The fuel integrity and fabrication robustness of KJRR fuel are to be verified through the irradiation test and post-irradiation examination.
By successfully performing the mini-plate irradiation tests at HANARO and the FA irradiation test at ATR, the U-Mo fuel design and manufacturing technology of KAERI are expected to be qualified for KJRR, which is the first research reactor powered by U-Mo fuel.

6. References

[1] G. L. Hofman et al., RERTR 2006, Capetown, South African, Oct. 29-Nov. 2, 2006.
[2] G. L. Hofman et al., RRFM 2007, Lyon, France, Mar. 11-15, 2007.
[3] A. Leenaers al., RRFM 2008, Hamburg, Germany, Mar. 2-5, 2008.
[4] Chul-Gyo Seo, Haksung Kim, Daeseong Jo, "Heat flux evaluation of U-Mo mini-plate Irradiation in the HANARO core", KAERI internal document
[5] N.E. Woolstenhulme, R.B. Nielson, D.B. Chapman, J.W. Nielsen, P.E. Murray, D.S. Crawford and S.D. Snow, “KJRR-FAI Status Report of Conceptual Design Activities”, INL External Report INL/EXT-13-30857, December 2013.
[6] J. Rest, Y.S. Kim, G.L. Hofman, M.K. Meyer, and S.L. Hayes, “U-Mo Fuels Handbook”, ANL-09/31, 2009
[7] Y.S. Kim, G.L. Hofman, J. Nucl. Mater. vol.419, p.291, 2011.
[8] D. D. Keiser et al., "Microstructural Analysis Of Irradiated U-Mo Fuel Plates: Recent Results". RRFM 2012, Prague, Czech Republic, 18-22 March 2012
[9] M. Ripert et al.,"Synthetic Review of the IRIS3 Experiment", RRFM 2011, Rome, Italy, 20-24 March 2011

INFLUENCE OF THERMAL ANNEALING ON THE SPECIFIC HEAT CAPACITY OF DIFFERENT DISPERSION U-(7-8)WT%MO FUELS

C.REITER[1], H. BREITKREUTZ[1], T.K. HUBER[1], T. ZWEIFEL[1,2], W. PETRY[1]

[1)] *Forschungs-Neutronenquelle Heinz Maier-Leibnitz, FRM II*
Technische Universität München, Lichtenbergstr. 1, 85747 Garching, Germany
[2)] *Also at CEA / DEN / DEC – F-13108 St. Paul-lez-Durances CEDEX - FRANCE*

ABSTRACT

For safe reactor operation and conception, the knowledge of the thermal properties of the reactor fuel is mandatory. So, the specific heat capacity of dispersion U-(7-8)wt%Mo has been investigated in this paper. Therefore, samples with two different powder types, atomized and ground, have been analysed.
During irradiation, U-Mo fuels are known to grow a so called interdiffusion layer (IDL), which consists of different uranium-aluminium compounds. Instead of in-pile irradiation, it is possible to form a similar IDL by thermal annealing. This way it is possible to measure the influence of thermal annealing on the specific heat capacity of these powder samples. Electron microscopy images are used to observe the macro structural changes during thermal annealing.

1. Introduction

The Forschungs-Neutronenquelle Heinz Maier-Leibnitz (FRM II) is actively participating in the world-wide efforts to reduce proliferation risks in the civil nuclear fuel cycle by minimizing the use of HEU. Its activities comprise, among others, the analysis of new high density fuels, core designs and fabrication methods. One part of these activities is the determination of the thermo-physical properties of promising candidates for a future fuel. Currently, uranium molybdenum alloys (U-Mo, 7-12 wt%Mo) are considered to be the most promising solution for a conversion fuel. For the dispersion type of this fuel, two different kinds of U-Mo powder can be used: ground powder and atomized powder.

One of the major challenges in the development of this fuel is the formation of a so called interdiffusion layer (IDL) during irradiation. This layer consists of different uranium-aluminium compounds (UAl_2, UAl_3, UAl_4) [1,2]. For the fuel to reach its desired performance, the growth of this layer has to be limited. One way to achieve this, is by adding silicon to the matrix in order to slow down the growth of these compounds [3,4]. In this paper, two different powder types are examined: ground and atomized U-(7-8)wt%Mo powder. Two samples of each powder type have been investigated: one with a pure Al matrix and one with an Al-(2.1wt%Si)-matrix.

Additionally, an IDL was grown out-of pile by thermal annealing [8] in these samples to quantify the influence of the heat treatment on the specific heat capacity. Scanning electron microscope (SEM) investigations were performed to observe possible changes of the sample macroscopic structure, i.e. due to a growing IDL, after thermal annealing.

2. Experimental Methods and Materials

2.1. Sample Preparation

Measurements on atomized powder samples were carried out on IRIS 4 U-7wt%Mo fuel samples [5], while those on ground powder used IRIS TUM U-8wt%Mo samples [3]. For each powder type, two samples were selected, one without addition of silicon to the matrix and one with addition of 2.1wt% silicon, respectively. In Table 1 all relevant data for the used samples is listed.

Sample ID	Powder type	Matrix type	U-density [gU/cm³]	Al-percentage [vol %]
IRIS TUM 8003	Ground U-8Mo	Pure Al	8.5	41.5
IRIS TUM 8502	Ground U-8Mo	Al with 2.1 wt.% Si	8.3	41.3
IRIS 4 UMo/Al	Atomized U-7Mo	Pure Al	7.9	49.1
IRIS 4 UMo/Al(Si)	Atomized U-7Mo	Al with 2.1 wt.% Si	7.3	49.8

Table 1: Overview of used fuel samples.

For the temperature treatment, the samples were wrapped into a zirconium foil and annealed in a tube furnace. The zirconium serves as an oxygen getter and prevents an oxidation of the samples. Furthermore, the tube was evacuated and successively filled with argon inert gas to minimize the remaining amount of oxygen. After these precautions, the samples themselves were put from the cool storage area to the hot center of the furnace to start the heating process. During the heat treatment the temperature of the samples was controlled with a K-type thermocouple being in contact with the samples. Each sample was annealed at 475°C for a total of 15 hours. Every 5 hours, a measurement of the specific heat capacity was performed to check for possible changes. An exemplary (2 x 2) mm² part of the sample was cut for SEM/EDX to observe the IDL growth.

2.2. Determination of the specific heat capacity by using a Differential Scanning Calorimeter (DSC)

To determine the specific heat capacity, a differential scanning calorimeter DSC 8500 by Perkin Elmer, was used. This instrument consists of two spatially separated furnaces; each furnace with its own heater-sensor-pair (see Figure 1). First, the same amount of heating power is given to both furnaces, but due to the specific heat capacity of the sample, the furnace with containing the sample will heat up slowlier than the empty reference furnace. Hence, the different temperatures are balanced by increasing the heating power of the furnace with the sample inside. The difference in the required heating power for both furnaces is the so called “heat flow”. This heat flow is proportional to the specific heat capacity of the sample.

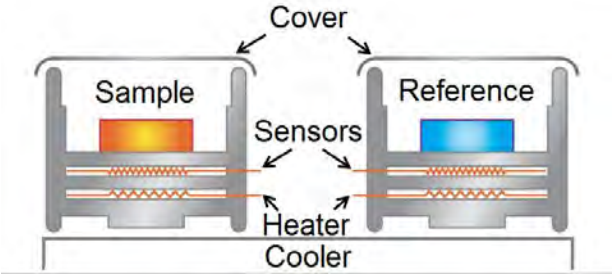


Figure 1: Schematic setup of a differential scanning calorimeter [10].

In this work, the “three curves method” [7] was used. This method requires three different measurements: a baseline, a reference and a sample measurement. For the determination of the baseline which quantifies differences that appear due to imperfections of the furnaces and the aluminum pans, both furnaces were filled with an empty aluminum pan. The reference measurement ensures a more precise heat flow calibration. Here, an ASTM standard sapphire [6] was used as reference material.

As described in [7], the specific heat capacity c is calculated using

$$c(T) = \frac{[\Phi_s(T) - \Phi_b(T)] * m_r}{[\Phi_r(T) - \Phi_b(T)] * m_s} * c_r(T)$$

where Φ_i is the corresponding heat flow of the baseline (b), reference (r) and sample (s), while m_r is the mass of the used reference, m_s is the mass of the sample and $c_r(T)$ is the specific heat capacity of the reference material for each temperature T.

The functionality of the used differential scanning calorimeter has been proven by comparing the measured sapphire values with those provided by ASTM. The deviations were found to be smaller than 1% and the results were well reproducible.

Changes of the form or macroscopic structure of a sample, i.e. separation of the matrix from the U-Mo grains or cracks, change the measured heat flow as well. So it is possible to visualize these changes with a differential scanning calorimeter.

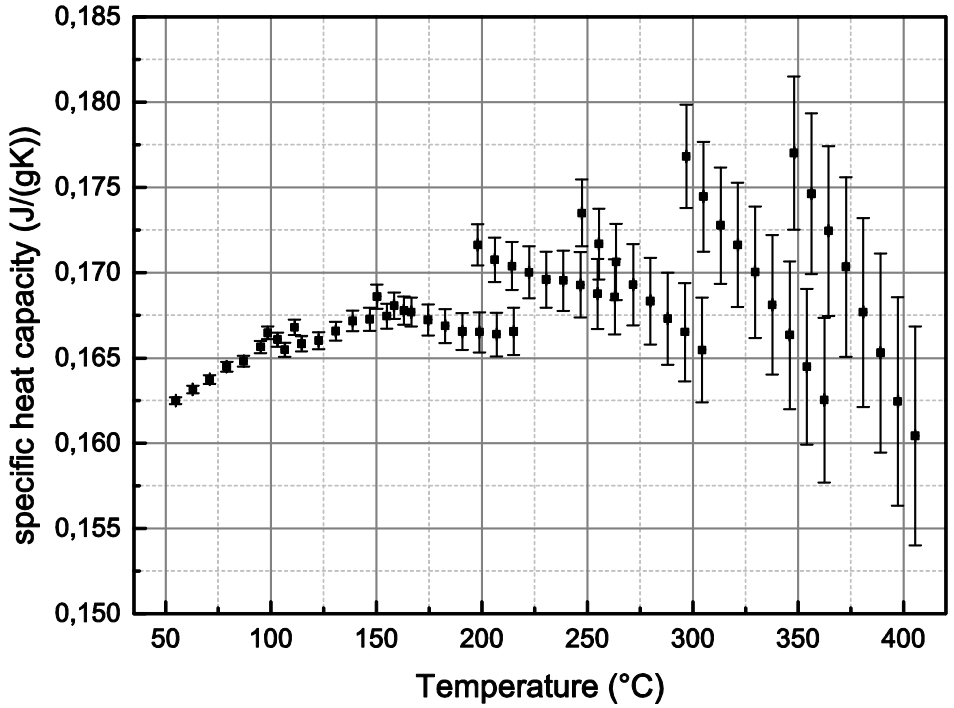


Figure 2: Measurement of the specific heat capacity of an IRIS-TUM sample, which has broken in two pieces at about 150°C.

Figure 2 shows a measurement of a sample, which broke during the heating process. The drastic change of the heat flow when the sample broke is clearly visible.

3. Results

As mentioned before, after every 5 hours of annealing, a part of each sample was cut and characterized by SEM/EDX to verify the IDL growth.

3.1. SEM/EDX analysis on IDL growth during thermal treatment

Figure 3 shows according SEM-images of annealed ground powder fuel, while Figure 4 shows annealed atomized powder fuel. The black areas represent the aluminum matrix, the bright grey areas correspond to the UMo grains and the dark grey areas are the possible IDL. To confirm this, EDX scans in some promising areas (red boxes) were made.

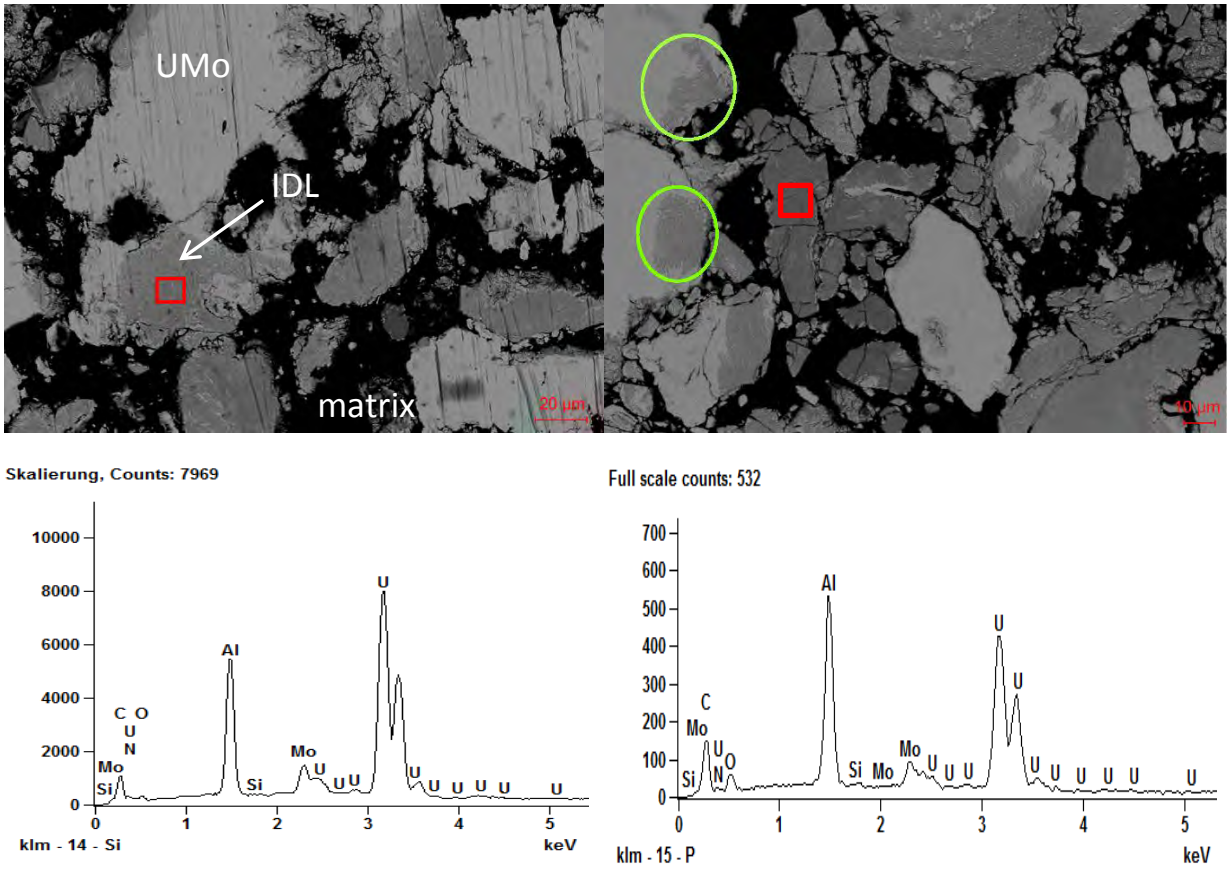


Figure 3: SEM images of the ground powder UMo/Al (IRIS TUM 8003) sample after 10 (upper-left) and 15 hours (upper-right) annealing time with corresponding EDX scan. EDX scans for (lower-left) the 10 hour case and (lower-right) for the 15 hour case. The regions of the obtained EDX scans are highlighted by a red box in (upper-left) and (upper-right). Green circles indicate regions of dendrite crystal growth.

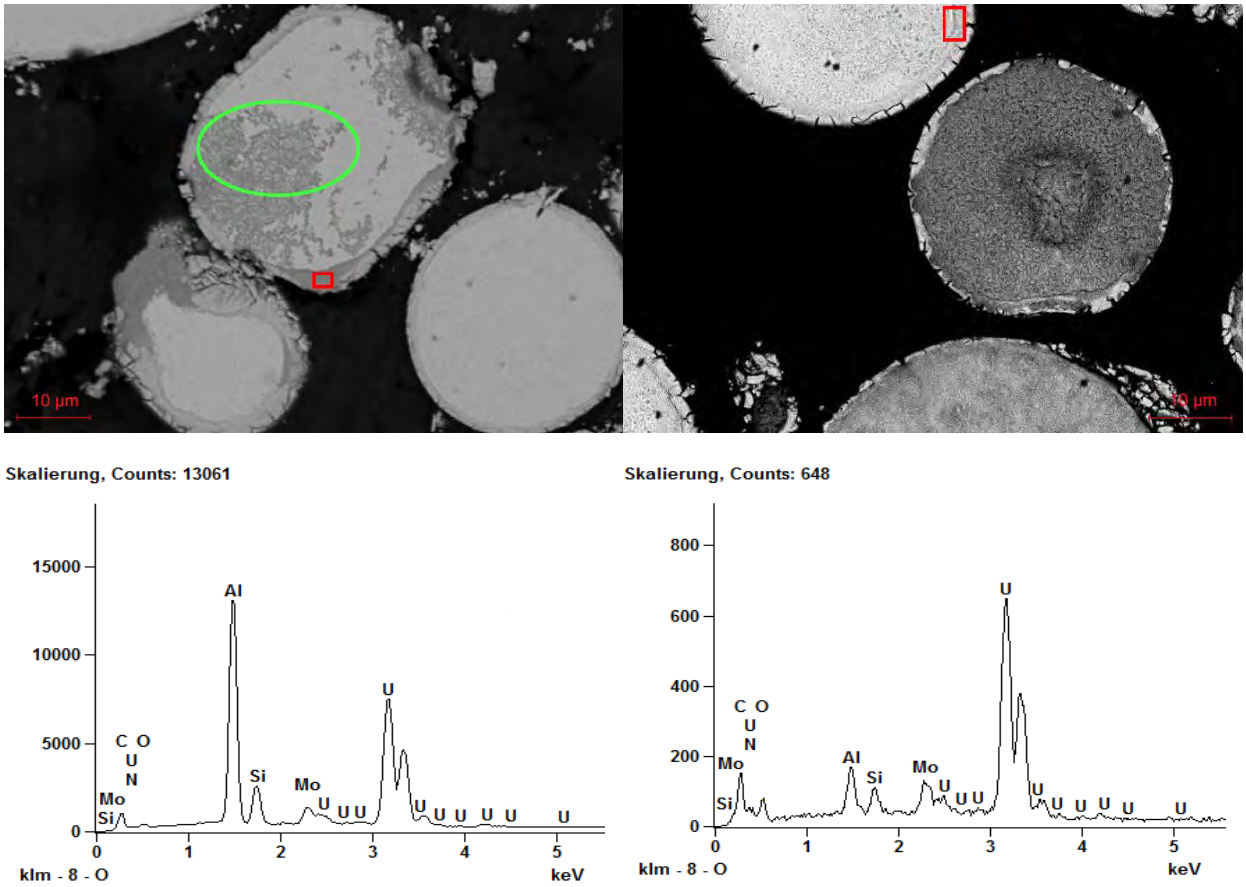


Figure 4: SEM pictures of the IRIS 4 UMo/Al(Si) sample after 10 (upper-left) and 15 hours (upper-right) annealing time with corresponding EDX scan. Because of the fabrication process of IRIS 4, the oxide layer around the U-Mo particles are visible. The EDX analysis (lower-left) and (lower-right) shows an IDL growth in the red boxes. Also an enrichment of silicon is noticeable in those areas. Again in the green circle typical dendritical structures are visible.

After each 5 hour annealing step, the samples were analyzed with a SEM. EDX scans clearly show that in the investigated regions (i.e. red boxes) there was a build-up of different uranium aluminum compounds, i.e. an IDL. As expected, the amount of IDL increases with increasing thermal treatment time[5]. However, it was not possible to really quantify the amount of IDL from the images, as the chosen sample snippets were not large enough to collect sufficient information. For this reason, the evolution of the specific heat capacity could only be calculated with respect to the annealing time but not on the more desirable IDL volume fraction.

3.2. Effects of the thermal treatment on the specific heat capacity

After each annealing step, the specific heat capacity was measured and compared with the values of the fresh, non-annealed sample. Table 2 summarizes the calculated values for 100°C, which is the fuel operating temperature of many research reactors.

	IRIS TUM			IRIS 4		
	ID ground	Annealing time [h]	C_p(100°C) [J/(gK)]	**ID atomized**	Annealing time [h]	C_p(100°C) [J/(gK)]
Pure Al	**8003**	0	0,218	**UMo/Al**	0	0,260
		5	0,227		5	0,250
		10	0,204		10	0,257
		15	0,226		15	0,258
With Si	**8502**	0	0,228	**UMo/Al(Si)**	0	0,251
		5	0,231		5	0,256
		10	0,232		10	0,254
		15	0,224		15	0,251

Table 2: Calculated values for C_p at 100°C for each sample after the 5 hours stepwise annealing times. A reference value is given for the non-annealed case. The uncertainty of the measured values is less than 1%.

The uncertainties of these measured values are dominated by statistical variations but in total less than 1%. The specific heat capacity varies in the range between 2% and 10%, but seemingly there is no correlation between these values and the annealing time (see Figure 5).

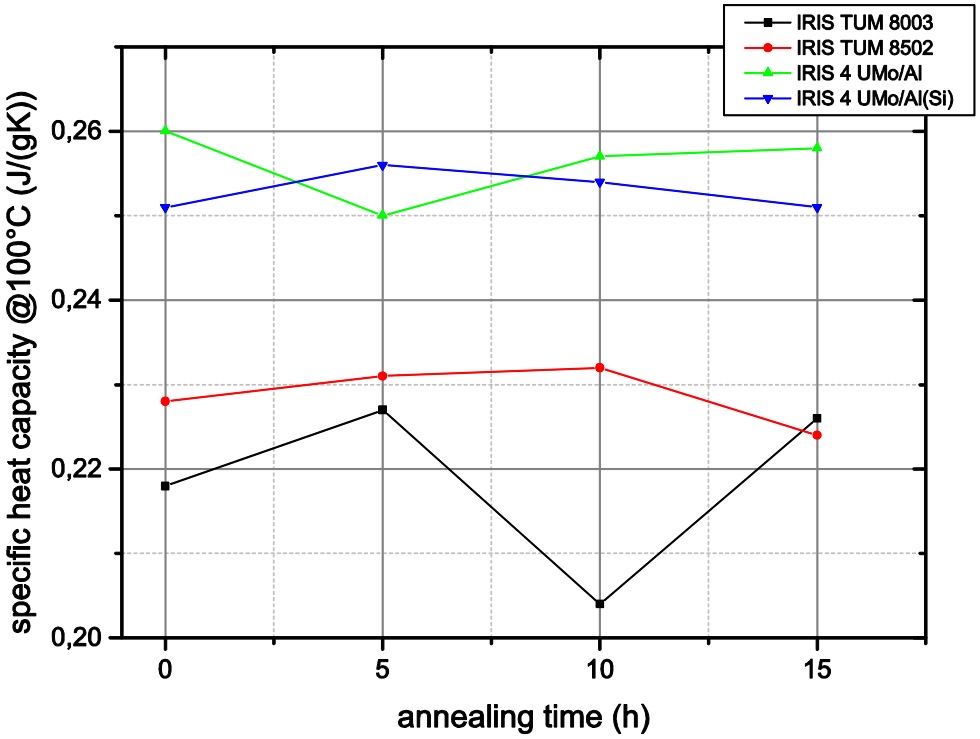


Figure 5: Specific heat capacity of different dispersed fuels at 100°C plotted against the annealing time.

A possible explanation for this behavior could be that during the thermal treatment, two effects occur, both influencing the specific heat capacity. On the one hand the material composition changes due to the formation of the interdiffusion layer, on the other hand the macrostructure of the matrix changes due to thermal effects. The variations in the measurement result of the ground powder samples were much larger than the variations of the atomized powder samples. The non-monotonic behavior of the curves (see figure 5) does not seem to follow an obvious pattern that could directly be attributed to the IDL growth. More information on the IDL amount and the structural changes would be mandatory to rate their influence on these measurements.

Figure 6 and 7 show a plot of the specific heat capacity of the annealed samples relative to the as-fabricated samples in the full measured temperature range from 20C to 300C.

It is assumed that a higher/increasing IDL amount has a systematic impact on c_p. c_p should either increase or decrease with increasing IDL volume. However the macro structural changes in the sample seem to predominate the change of the specific heat capacity caused by the IDL.

Because of the regular grain shape of the atomized powder, the suspected structural changes are considered to have less influence than those influenced by the highly irregular shape of the ground powder. This is a possible explanation for the differing amplitude of the fluctuations in the curves of ground and atomized powder samples.

A malfunction of the used differential scanning calorimeter is unlikely as the results of the verification measurements with sapphire showed very good accordance with the literature values.

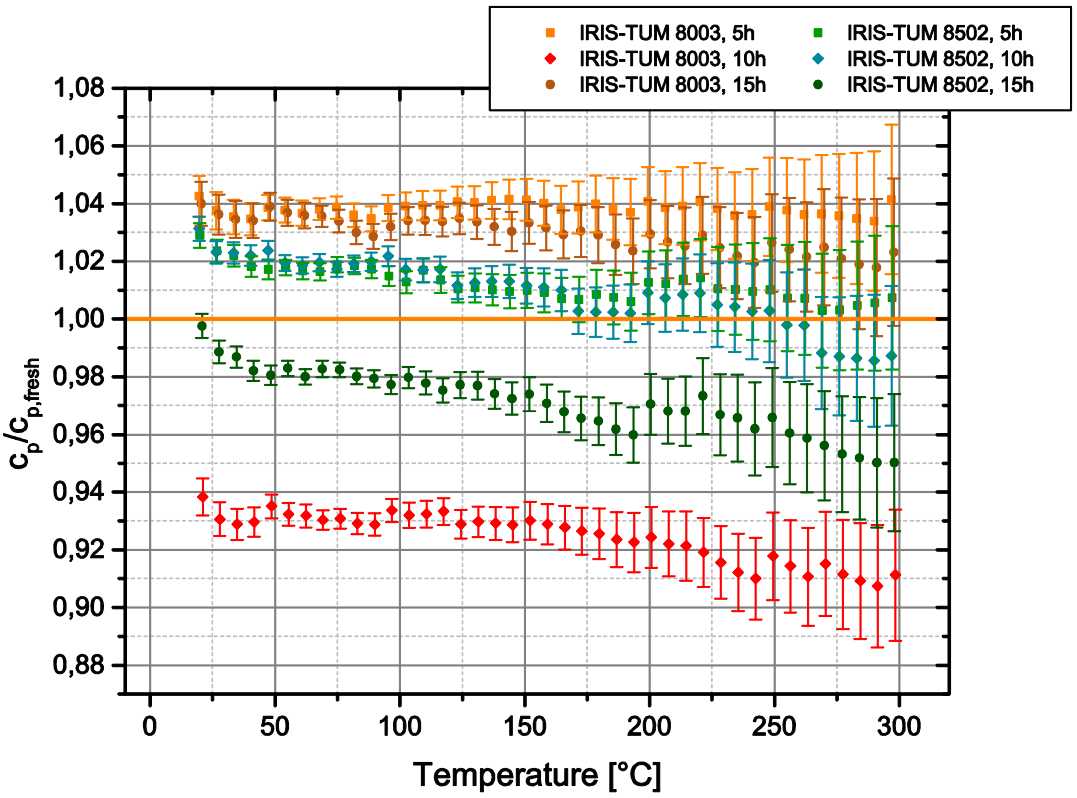


Figure 6: Relative change of the specific heat capacity of ground powder samples with increasing annealing time as a function of the temperature

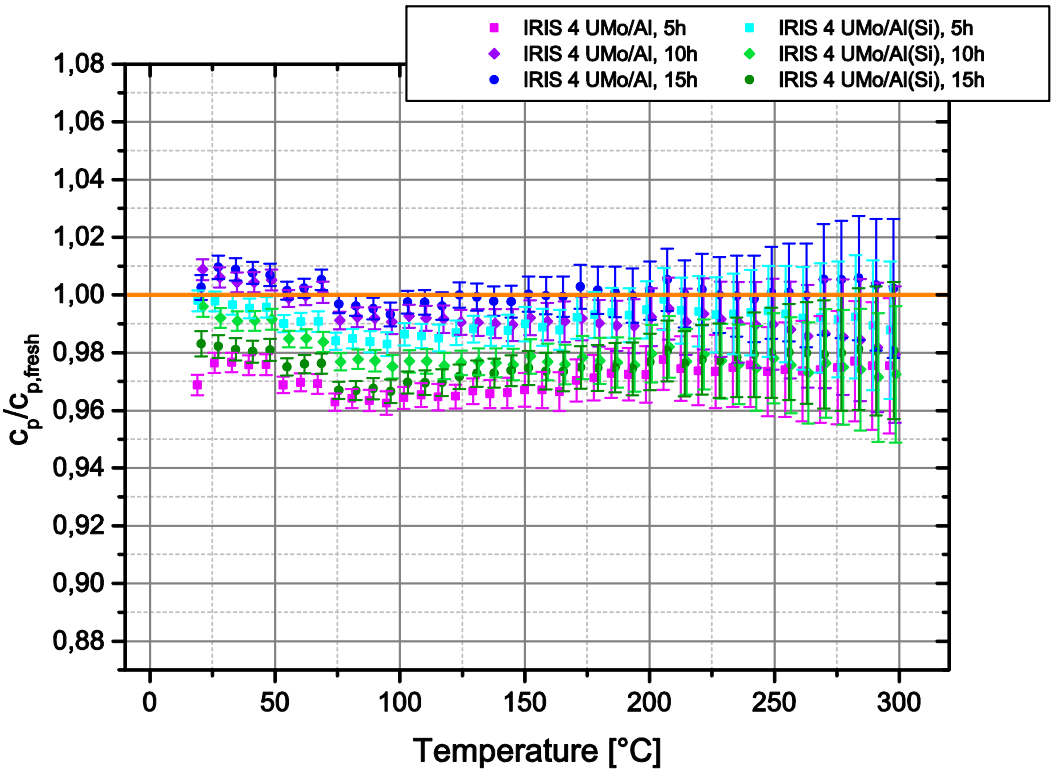


Figure 7: Relative change of the specific heat capacity of atomized powder samples with increasing annealing time as a function of the temperature

4. Summary

Within the given error margins, no change of the specific heat capacity when annealing dispersion fuel to temperatures above 475°C can be determined with the necessary certainty. No specific pattern can be identified in the dependence on the annealing time. It is therefore well possible that the according variations are not induced by the growing IDL, but rather from changes of the macroscopic structure or form of the samples. Because of the more regular shape of the atomized fuel particles, the structural changes in the IRIS 4 samples have less impact on the specific heat capacity than those in the ground powder of the IRIS TUM samples.

5. Acknowledgements

This work was supported by a combined grant (FRM0911) from the Bundesministerium für Bildung und Forschung (BMBF) and the Bayerisches Staatsministerium für Wissenschaft, Forschung und Kunst (StMWFK).

The authors want to thank CEA and AREVA CERCA for providing the samples.

The measurements of the specific heat capacity have been performed at Materials Science Lab of Heinz Maier-Leibnitz Zentrum (MLZ), Technische Universität München (TUM).

References

[1] Colon K., Sears D., *Neutron powder diffraction of UMo fuel irradiated to 60 at% ^{235}U burnup,* Proceedings of the 11th RRFM 2007, Lyon, 2007

[2] Meyer M.K., *Metallographic analysis of irradiated RERTR-3 fuel test specimens,* RERTR 2000, Las Vegas, 2000

[3] Leenaers A., et.al., *Irradiation behavior of ground U(Mo) fuel with and without Si added to the matrix,* Journal of Nuclear Materials, 412: 41-52, 2011

[4] Leenaers A., et.al., *Microstructural evolution of U(Mo)‑Al(Si) dispersion fuel under irradiation ‑ Destructive analyses of the LEONIDAS E-FUTURE plates,* Journal of Nuclear Materials**,** 441: 439-448, 2013

[5] Ripert M., et al., *Results of the IRIS 4 Irradiation in OSIRIS Reactor: Oxidized U-Mo particles dispersed in Al (with 0 or 2.1%Si).* RERTR 2009, Peking, China, 2009.

[6] ASTM International, *Standard Test Method for Determining Specific Heat Capacity by Differential Scanning Calorimetry*.

[7] Höhne G.W.H., el al., *Differential Scanning Calorimetry*, Springer Verlag, 1996

[8] Palancher H., et al., *Evidence for the presence of U-Mo-Al ternary compounds in the U-Mo/Al interaction layer grown by thermal annealing: a coupled micro X-ray diffraction an micro X-ray absorption spectroscopy study*, Journal of Applied Crystallography, 40:1064–1075, 2007.

[9] Huber S., *Thermische Eigenschaften von Polymernanokompositen*. Bachelorarbeit, Technische Universität München, 2013.

INSPECTION SYSTEM OF U-MO PLATE FUEL USING X-RAY TESTING AND ULTRASONIC TESTING METHOD

Y.S. LEE, K.H. LEE, C.M. SIM, Y.J. JEONG, H.I. LEE, J.M. PARK

Research Reactor Fuel Development, Korea Atomic Energy Research Institute.
989-111 Daedeok-daero, Yuseong-gu, 305-353, Daejeon-Korea

ABSTRACT

During fabrication of a high density U-Mo dispersion fuel, quality control is very important to secure the integrity of fuel elements. To check the integrity of the fuel elements, non-destructive testing methods such as x-ray radiography and ultrasonic testing methods are applied. In KAERI we have been developing NDT methods to check the homogeneity of high density U-Mo fuel meat using x-ray linear scanner and to check the integrity of welding area of the fuel assembly using x-ray 3D computer tomography. To check the cladding thickness of the fuel plate, a scanning microscope ultrasonic technique is applied. In this paper we introduce the testing results and non-destructive testing system for U-Mo plate fuel in KAERI.

1. Introduction

In KAERI, plate fuel fabrication lines and quality control system for the U-Mo plate fuel have been developed. During fabrication of a high density U-Mo dispersion fuel plate, quality control is very important to secure the integrity of fuel element. One of the quality control items is homogeneity of the uranium distribution in the fuel plate. To check the homogeneity, the conventional method has been the use of an x-ray radiography using film [1]. KAERI has established digital x-ray radiography system to inspect the homogeneity of the plate type dispersion U-Mo using x-ray scanner and to check the integrity of welding area of a fuel assembly using 3D CT computer tomography. Conventional x-ray method using film for those was time consuming job. The digital radiography method is fast and easy to evaluate the homogeneity from the x-ray image.

For the cladding thickness measurement, a scanning microscope ultrasonic technique is applied.

In this paper, we introduce x-ray and ultrasonic inspection method for the U-7Mo dispersion fuel plate and welding area of the fuel assembly.

2. Homogeneity measurement using x-ray linear scanner

The liner scanner system for the homogeneity of the mixture of the U-7Mo particles and Al particles consists of an x-ray generator, x-ray line scan detector, digital image processer software, and display monitor.

For the verification of the homogeneity measurement procedure, a comparison between the results of conventional film methods and the results of digital x-ray methods using linear scanner had to be done. The results of film methods was gotten from a simulated fuel plate fabricated in ANL, which was made of stainless steel powder mixed with aluminium powder instead of U-Mo powder. The dimension of the simulated plate is about 600 mm in length, 100 mm in width, and 1.27 mm in thickness. The fuel meat thickness of the mixture is 0.5 mm. The simulated fuel plate is made with a mixture of stainless steel powder and Al powder by rolling. The step wedge has 6 steps of which thickness are 0.05, 0.1, 0.15, 0.2, 0.25, and 0.3 mm respectively [2].

By using the simulated plate, the homogeneity of the mixture using liner scanner following the ANL/RERTR/TM-15 procedure [2] was inspected. For the inspection of homogeneity, measuring the gray value of an x-ray image with digital radiography software was introduced instead of measuring the film density with a densitometer which has been used conventionally.

Conventional method of the density measurement for the homogeneity of the plate is to measure the film density with a densitometer whose spot diameter is 2 ~ 3 mm. To make it equivalent for the 3 mm diameter spot size, mean gray values in 3 x 3 mm square area for the fuel meat area and for the step wedge were taken.

The average gray value reading for each step of the wedge is plotted on the ordinate vs. the step wedge thickness on the vertical on a graph as shown in Fig. 1. The gray value variations through the longitudinal direction of the fuel meat region are shown in Fig. 2. The average, maximum and minimum values of the equivalent thickness of the simulated fuel plate are 0.21 mm, 0.24 mm(+14.2%), 0.18mm(-14.0%). The equivalent thickness for the fuel meat should be 0.2 mm.

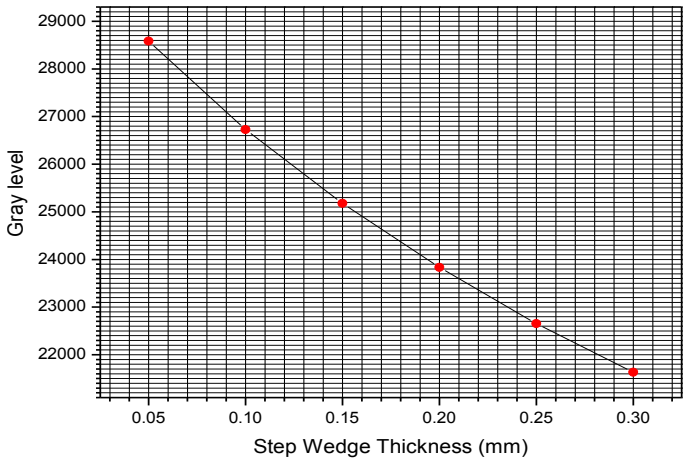


Fig. 1 Calibration curve for the measurement of equivalent thickness for the stainless steel foil step wedge.

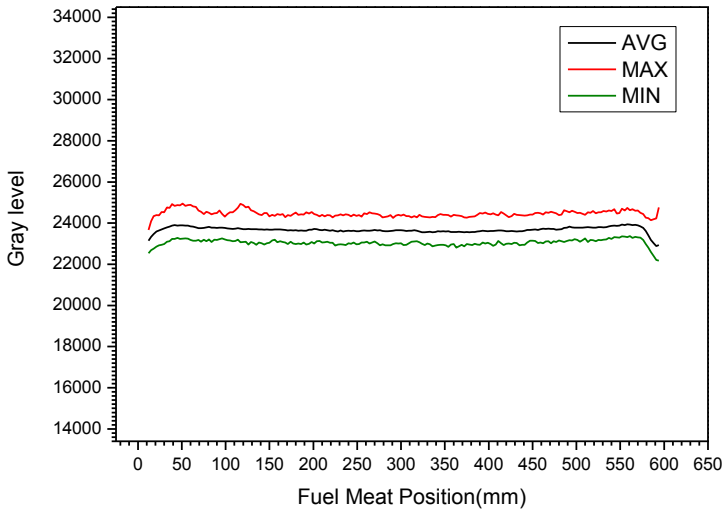


Fig. 2 The gray value distribution on the simulated fuel meat region

In KAERI, mini-plates of U-7Mo/Al-5Si dispersion fuels for the irradiation test in HANARO research reactor have been fabricated, and performed non-destructive test following the quality assurance procedures. The dimension of mini-plate was 75 mm in length, 28 mm in width and 1.27 mm in thickness. The dimension of fuel meat was 65 mm in length, 23 mm in width and 0.51 mm in thickness. The cross cut SEM image of mini-plate of U-7Mo/Al-5Si is shown in Fig.3

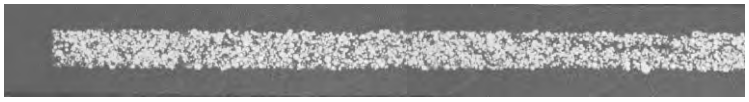


Fig. 3 Cross cut SEM image of mini-plate of U-7Mo/Al-5Si

The x-ray image for the homogeneity of mini-plate was taken under the condition of 140 kV, 3mA. The step wedge for the U-7Mo high density fuel was made of U-56wt%Zr, and has 6 steps whose thickness are 0.47, 0.67, 0.8, 0.95, 1.16, 1.4 mm respectivelly.

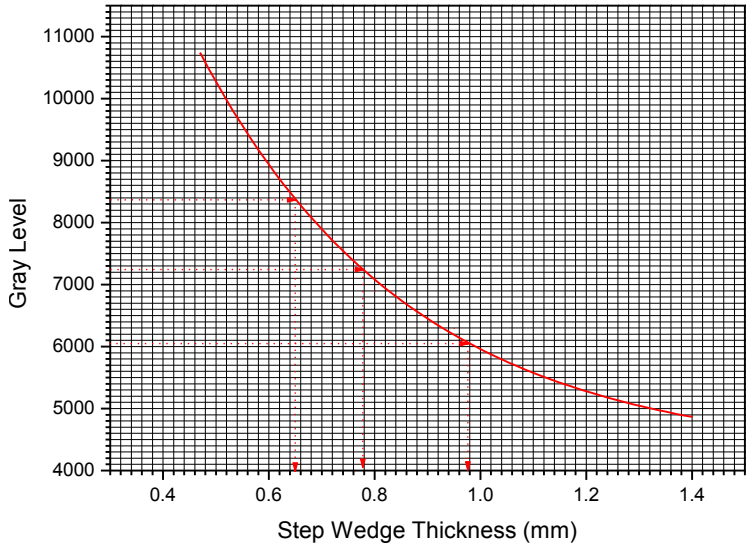


Fig. 4 Calibration curve for the measurement of equivalent thickness for the U-Zr step wedge.

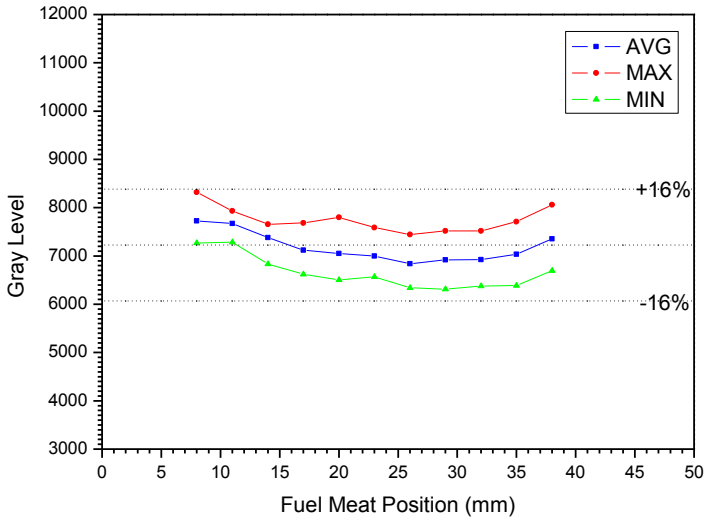


Fig. 5 The gray value distribution on the mini-plate fuel meat region

The homogeneity of mini-plate of U-7Mo/Al-5Si was measured as shown in Fig. 5. The result shows that the distribution of uranium particle is in allowable limitations of criteria.

3. 3D CT computer tomography for welding area of fuel assembly

The micro 3D x-ray CT system for the welding area of the fuel assembly consists of an x-ray generator, 8x8 inch digital image panel, CT processing software and VG studio software.

There are two welding area of the fuel assembly, one of which is between the fuel box and end fitting and the other is between the side plate and fixing bar. The x-ray 3D image for the welding area was taken under the condition of 200 kV and 0.2mA.

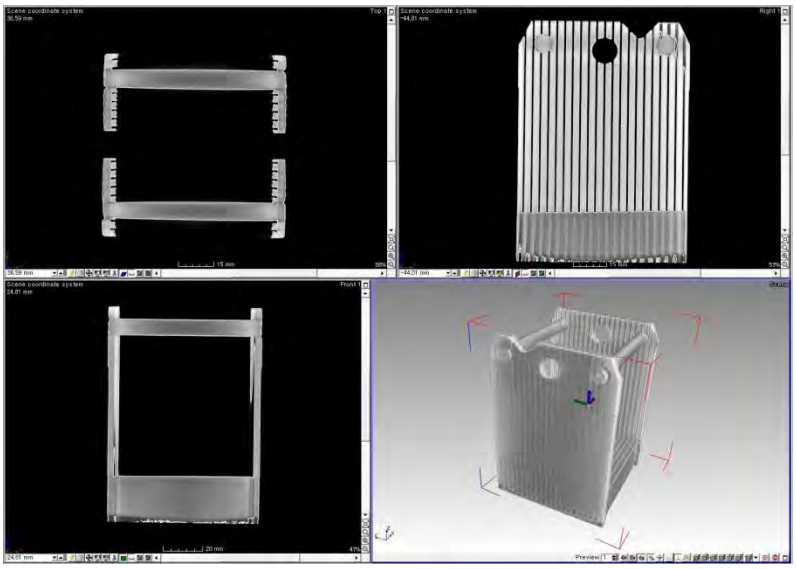


Fig. 6 The 3D image of x-ray CT for welding area between fixing bar and side plate

Small porosities inside the welding area could be easily detected through the 3D CT x-ray system.

4. Ultrasonic System

The scanning microscope ultrasonic system consists of 3 channel data acquisition, 4 axis servo motor with 5 μm resolution, pulser-receiver, transducer as shown in Fig. 7. The cladding thickness of U-Mo fuel plate was measured .The thickness measurement result for the standard specimen is shown in Fig. 8. UT signal of de-bonding area is checked by using this system as shown in Fig. 9.

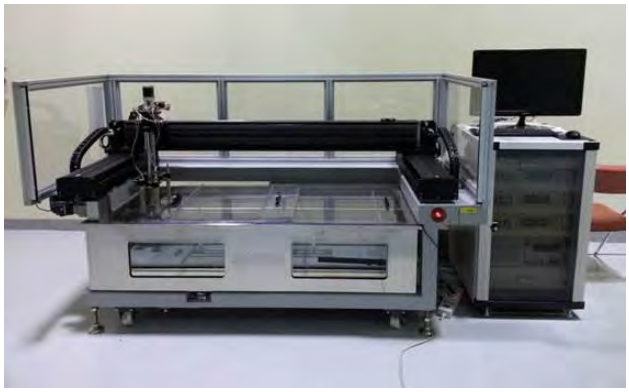
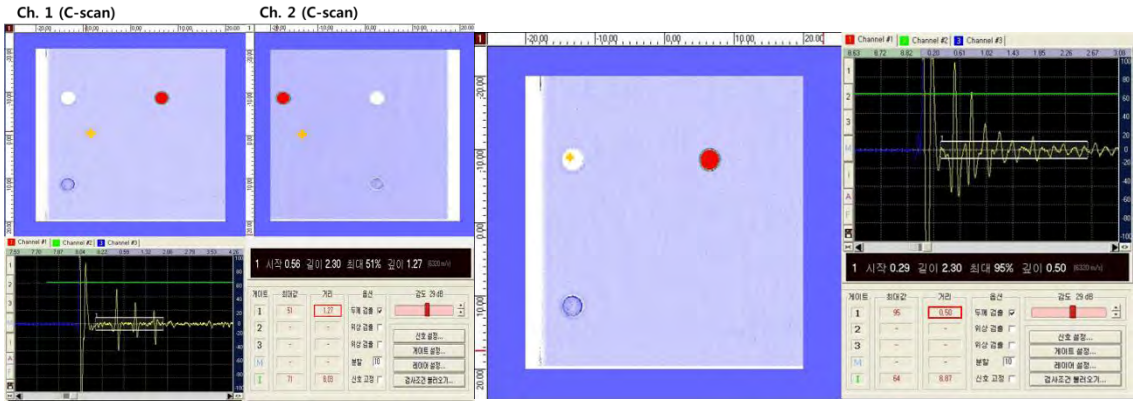


Fig. 7 Scanning Microscope Ultrasonic system for plate fuel



(t=1.27 mm) (t= 0.5 mm)

Fig. 8 Ultrasonic signals of the standard specimen



Fig. 9 Ultrasonic signals for the de-bonding area (right upper position) of full length plate fuel

5. Conclusions

In this paper, non-destructive inspection systems for the plate-type high density U-Mo dispersion fuel being developed in KAERI are introduced. The liner scanner system for the homogeneity of the mixture of the U-7Mo particles and Al particles was verified by comparing the results of conventional film methods and it showed the almost exact equivalent thickness for the simulated fuel plate. It could successfully be measured the homogeneity of mini-plate for irradiation test in HANARO. Using 3D x-ray CT system, small porosities inside the welding area could be easily detected and visualized 3 dimensionally. The scanning microscope ultrasonic system could measure the cladding thickness of the fuel plate and de-bonding area.

References

[1] F.B.J. FERRUFINO, et al, "Quantitative Determination of Uranium Homogeneity Distribution in MTR Fuel Type Plates", RRFM2011.
[2] Y.S. Lee, et al, "A Measurement of Homogeneity of Simulated Research Fuel Plate using Real Time X-ray", RRFM2012.
[3] T.C. Wiencek, "Summary Report on Fuel Development and Miniplate Fabrication for the RERTR program 1978 to 1990", 1995. 8, ANL.

IMPROVED POWER MEASUREMENTS AT THE JSI TRIGA REACTOR IN LJUBLJANA USING MULTIPLE DETECTORS

G. ŽEROVNIK, L. SNOJ, A. TRKOV
Reactor Physics Department, Jožef Stefan Institute
Jamova cesta 19, SI-1000 Ljubljana

L. BARBOT, D. FOURMENTEL, J.-F. VILLARD
Instrumentation, Sensors and Dosimetry Laboratory, CEA, DEN, DER,
Cadarache, F-13108 St-Paul-Lez-Durance

February 28, 2014

ABSTRACT

The aim of the current bilateral project between CEA Cadarache and JSI is to improve the accuracy of the online thermal power monitoring at the JSI TRIGA reactor. In the paper, calculational and experimental power calibration methods using fission chambers are described. The focus is on the use of multiple detectors in combination with pre-calculated and pre-measured control-rod-position-dependent correction factors to improve the reactor power reading. The system will be implemented and tested at the JSI TRIGA reactor in 2014.

1 Introduction

Within the bilateral collaboration between the CEA Cadarache and the JSI we will analyze and improve the accuracy of the power reading at the JSI TRIGA reactor by implementing a new system of measuring neutron flux at two to four different positions in the reactor core at the same time. Currently, the reactor online power reading is taken from a linear channel signal coming from a single ionization chamber located outside the reactor core. It is assumed that the reactor power is proportional to the detector signal. However, this is only true for a constant core configuration. For example, by simply shuffling control rods while maintaining criticality the spatial neutron flux distribution can be changed significantly, thereby changing the power reading as well.

Preliminary calculations with the Monte Carlo neutron transport code MCNP-5 [1] show that the ratio between the power level and the neutron flux at the position of the detector as a function of the control rod position typically varies for 10-15 %. In extreme cases the ratio can vary as much as 30 % [2]! However, the spatial integral of the power-to-flux in the reactor core remains unchanged. Therefore, by clever placing of multiple flux detectors at different positions in the core the variation of the power-to-flux ratio can be averaged out. The positioning of the detectors will be optimized during the course of the collaboration to minimize the deviation from the signal-power proportionality thereby improving the reactor power reading.

During normal operation, only two control rods – regulating and compensating – are used. Other two control rods – safety and transient – are always fully withdrawn. Therefore, the regulating and compensating rods induce an axial symmetry within the core. Preliminary calculations confirm the symmetry and show that it is sufficient to place two fission chambers close to the centre of the reactor core in the plane perpendicular to the line connecting the regulating and compensating rods.

First measurements confirmed the results obtained by preliminary calculations. Further measurements and comparison with calculations will be performed in 2014.

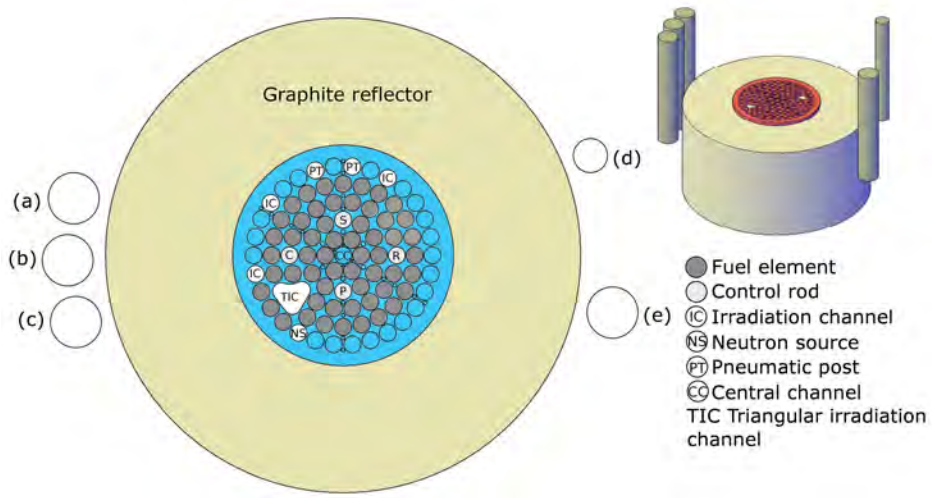


Figure 1: Reactor core configuration with current neutron detector locations: safety (a), pulse (b), logarithmic (c), start-up (d) and linear channel (e). Control rods are denoted as safety (S), transient (P), compensating (C) and regulating (R) [2].

2 Short description of the JSI TRIGA reactor

TRIGA Mark II at the JSI is a pool type nuclear research reactor with a maximum steady-state power of 250 kW [3]. The reactor core is cooled by natural water convection.

Reactor power is monitored with five independent neutron detectors, covering different power ranges from source level (mW) to pulse operation (GW). They are all located on the outer side of a graphite reflector surrounding the reactor core. The detector signals make up the so called starting, linear, logarithmic, safety and pulse channels. The linear, logarithmic and safety channels are used for neutron power monitoring or neutron flux measurements during continuous reactor operation, i.e. up to 300 kW. These detectors are positioned inside separate instrumentation chambers (aluminium tubes) measuring 67.3 cm in height with outer diameter 11.4 cm. The detectors are located at the bottom of the instrumentation chambers, i.e. approximately from -7.95 cm to +25.7 cm around the core mid plane. The current reactor core configuration with detector locations is depicted in Fig. 1.

As shown in Fig. 2, there are 90 positions in the reactor core available for fuel elements, control rods, irradiation channels, etc., including two larger openings in the D-E rings. In the metal grid above the reactor core, there are 26 additional small holes, i.e. measuring positions, enabling access from the water above the core. For example, fission chambers can be inserted in any of these positions to measure the neutron flux at any axial position in the reactor core.

2.1 Computational model of the reactor

A detailed geometrical MCNP model [4] of the JSI TRIGA reactor was developed in order to accurately calculate physical parameters of the TRIGA reactor. Our model is based on the criticality benchmark model [5], which is thoroughly described in International Handbook of Evaluated Criticality Safety Experiments [6]. Such simplified model can be used in calculations of effective multiplication factor (k_{eff}) [3], power peaking factors [7], reactor kinetic or other integral parameters.

In the criticality benchmark model of the TRIGA core [5], simplification of the geometry is done by neglecting some details of the surroundings of the core to an extent that does not affect k_{eff} significantly. Although the omitted structures do not have significant effect on k_{eff} , they do affect neutron flux profile, especially in the carrousel facility in the graphite reflector. For accurate calculation of the detector response (as well as other applications, e.g. calculation of the reaction rate distributions in irradiation channels [4]), the criticality benchmark model has been supplemented by adding the following components:

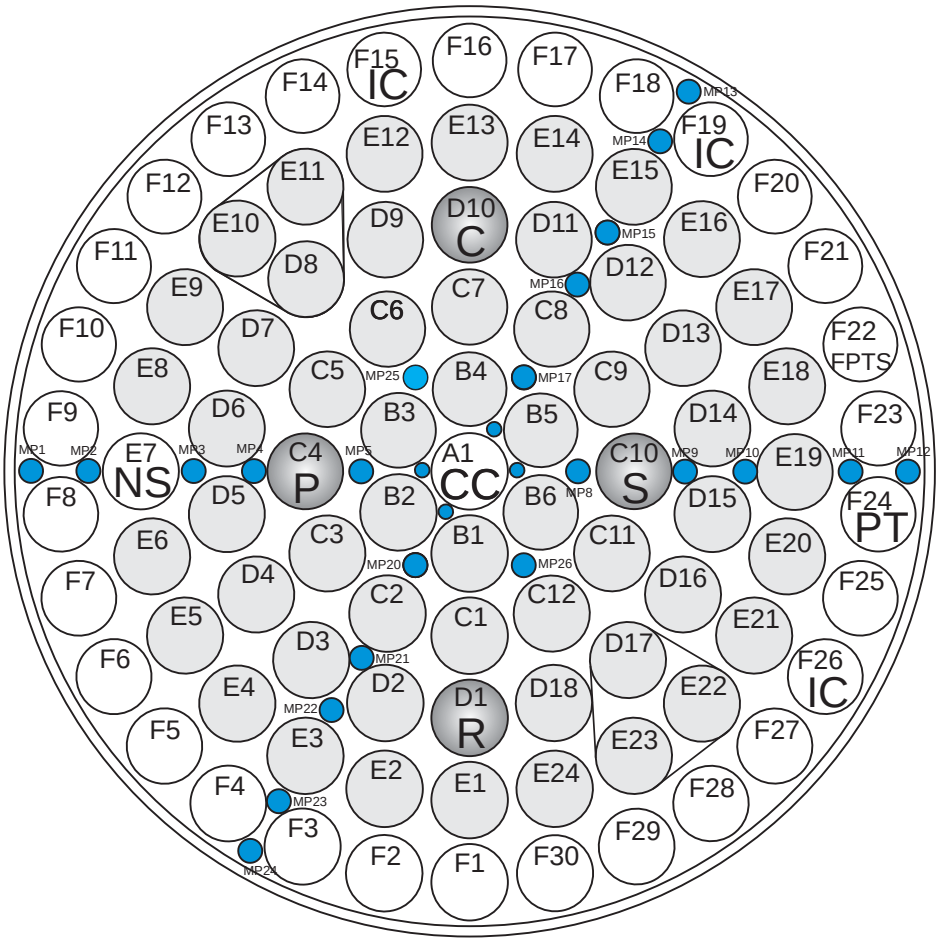


Figure 2: Positions (A-F) in the reactor core including the small upper grid openings (MP) for in-core measurements.

- irradiation channels in the core,
- graphite of the thermalizing and thermal column,
- carrousel with explicitly modeled irradiation tubes,
- neutron source element,
- triangular irradiation channel,
- radial and tangential beam ports,
- neutron detectors outside the graphite reflector.

3 Thermal power measurements at the JSI TRIGA reactor

In MCNP, the calculated neutron flux ϕ_{MC} is normalized per source particle. The absolute value of the neutron flux in the reactor ϕ is proportional to the thermal power P_{th} assuming no changes in spatial distribution. The relationship between the Monte Carlo calculated and 'real' fluxes is [8]:

$$\phi = K\phi_{MC}, \qquad K = \frac{P_{th}\bar{\nu}}{w_f k_{eff}}, \tag{1}$$

where w_f is average recoverable energy release per fission, and $\bar{\nu}$ average number of neutrons per fission.

On the other hand, the thermal power P_{th} can be expressed as

$$P_{th} = \int_V \Sigma_f \phi w_f \mathrm{d}V, \tag{2}$$

where Σ_f is the macroscopic fission cross section and the integration is over the entire volume V of the fuel regions. Assuming constant spatial flux distribution

$$P_{th} \propto \phi(\vec{r}) \tag{3}$$

at any chosen position $\vec{r}$.

3.1 Calorimetric method

In non-zero-power research reactors and power reactors, the calorimetric method (or heat balance method), whereby the coolant temperature increase as a function of time is measured in steady-state conditions, is the most common method for determining the thermal power output of the reactor core [9]. The calorimetric method is relatively accurate but impractical for monitoring the instantaneous reactor power level, particularly during transients. Therefore during normal operation, the reactor power is usually monitored by neutron detector(s), pre-calibrated by the calorimetric method.

According to the recommendations of the manufacturer (General Atomics), optimal accuracy of the calorimetric method at the JSI TRIGA reactor can be achieved under the following conditions [9]:

- Coolant water, concrete, and air temperature should not differ significantly.
- The reactor should operate at constant power with primary cooling system switched off.

Then, the reactor power P_{th} depends only on the temperature rise rate [9]:

$$P_{th} = Q\frac{\Delta T}{\Delta t}. \tag{4}$$

The heat capacity constant Q can be either calculated or determined for example by comparison with a control experiment with insertion of a heat source in the water pool with well-known thermal power. The heat capacity constant for the JSI TRIGA reactor was experimentally determined to be 19.05 kWh/K [9].

Using the calorimetric method, both the thermal power P_{th} and flux at detector location $\phi(\vec{r})$ in (3) are measured simultaneously, thereby experimentally determining the ratio between both at a chosen detector position. Linear relationship between power and flux at certain position is assumed as any conditions, and the measured ratio is adopted as default constant to multiply the online measured flux to produce the reactor power signal.

The reactor power in research reactors is usually calibrated with accuracy of around 10 %, however the deviations at different conditions can be as large as 30 % [9].

3.2 Absolute power calibration by fission chambers

Complementary to the macro-scale (thermodynamic) approach of the calorimetric method, the power calibration problem can be tackled from the micro-scale (nuclear reaction) side.

Fission chambers can be used to measure the magnitude of the neutron flux via fission rate:

$$R = \int \phi(E) \sum_i N_i \sigma_{f,i}(E) \mathrm{d}E, \tag{5}$$

where N_i is the number of nuclei i in the fission chamber and $\sigma_{f,i}(E)$ is the corresponding microscopic fission cross section. The measured reaction rates can be directly compared to the Monte Carlo calculated reaction rates:

$$R_{MC} = \int \phi_{MC}(E) \sum_i N_i \sigma_{f,i}(E) \mathrm{d}E. \tag{6}$$

Assuming the measured and calculated spectra are in agreement, it follows:

$$\frac{R}{R_{MC}} = \frac{\phi}{\phi_{MC}} = K = \frac{P_{th}\bar{\nu}}{w_f k_{eff}}, \tag{7}$$

wherefrom the thermal power P_{th} of the reactor can trivially be obtained [2]. However, in order to ensure reliability and sufficient accuracy of the estimate for the constant K and consequently the thermal power, the fission rate R must be measured at a large number of positions in the reactor core.

Albeit much more complicated, the absolute power calibration is significantly more accurate compared to the calorimetric method. By minimization of uncertainties, e.g. in the isotopic composition and mass of the fissile material in fission chambers, the accuracy of this calibration method can be within a few percent. Furthermore, the method can be used in combination with validation of the reactor computational model, as e.g. already done at the JSI TRIGA reactor [10, 11].

3.3 Multiple detectors

Depending on the location in the reactor core, responses of a pair of detectors to control rod movement can be in opposite directions [2]. In principle, using multiple detectors the variations of the flux form factors due to control rod movement can be averaged out to some extent.

Below, several methods how to improve the averaging are proposed.

3.3.1 Average detector signal

When having n detectors at disposal, taking the average of the signal from all detectors

$$P_{th} = \frac{1}{n}\sum_{i=1}^{n} C_i\phi_i, \tag{8}$$

as the power signal is the simplest solution. C_i and ϕ_i are the power/flux proportionality constants and measured fluxes for detector locations i, respectively.

3.3.2 Optimization of the correction factors

The pre-measured constants C_i are valid at certain fixed conditions. However, during the operation of the reactor, the conditions may change significantly, therefore the constants C_i might not be optimal. Additional correction factor can be introduced via:

$$P_{th} = \sum_i a_i C_i \phi_i. \tag{9}$$

a_i are constant pre-calculated correction factors, which can in principle differ for different detectors due to various asymmetries.

To get the most out of the detector signals ϕ_i, a multi-variable optimization is to be undertaken. Additionally to the constants a_i, axial, radial, and azimuthal positions of the detectors can be optimized to minimize the deviation of the (9) from the "real" power.

In order to mathematically formalize the optimization problem, a cost function f has to be defined. A possible example would be to minimize

$$f = \sum_i a_i C_i \int_{h_{min}}^{H} \phi_i(x, h_{C,c}(x), H, H)\mathrm{d}x - P, \tag{10}$$

where h_{min} is the critical position of the regulating rod with other rods fully withdrawn, H is the fully withdrawn position, ϕ_i is the calculated detector response, written as a function of the regulating, compensating, safety, transient rod, respectively, $h_{C,c}(x)$ is the critical position of the compensating rod with regulating rod at position x while other rods fully withdrawn, and P is the calculated reactor power.

Thus, the cost function f in (10) reflects the assumption that the reactor is critical, transient and safety rods fully withdrawn, while there is no information on the position of the regulating

and compensating rods. Using this relatively simple cost function, the power monitoring would be optimized for operation at constant power with equilibrium xenon concentration, only.

Nevertheless, the computational and especially post-processing requirements to minimize f are immense. First, a long (to reduce the statistical error) MCNP calculation for each position of the control rods would have to be run. Enough positions would have to be taken into account to ensure sufficient control rod position resolution. Between the calculations, interpolation should be used. In each individual MCNP run, several reaction rate tallies to estimate ϕ_i as a function of axial, radial and azimuthal position would have to be introduced.

Next, for each (plausible) positioning of the detectors i, the cost function f would have to be minimized. Finally, the constants a_i and positions of the detector corresponding to the global minimum of f would be adopted and implemented in the reactor power electronic online monitoring system.

Even if all that would be performed, an uncertainty of supposedly order of at least a percent would still be present due to the limitations of the computational model and nuclear data.

3.3.3 Position-dependent correction factors

Due to the complexity of the above-described optimization problem, an alternative approach is proposed and will be implemented.

The formula in (9) is generalized to:

$$P_{th} = \sum_i a_i(z_R, z_C) C_i \phi_i, \tag{11}$$

where the correction factors a_i now depend on the axial position z_R and z_C of the regulating and compensating rod, respectively. Here it is assumed that during normal reactor operation the safety and transient rods are always fully withdrawn. For chosen positions of the fission chamber detectors i, the factors a_i can be determined by calculating the detector response as a function of the control rod positions using the MCNP model of the reactor.

Compared to the optimization of the correction factor, the method of using the position-dependent correction factors is more straight-forward, however it requires online capturing of the control rod position, calculation of the correction factor via (11), and displaying of the corrected thermal power. Currently, the control rod position and thermal power signals are not connected. The new system will be tested at the JSI TRIGA reactor in near-term future.

4 Results

Since during normal operation, two control rods – safety and transient - are always fully withdrawn, the partially inserted regulating (R) and compensating (C) rods induce an axial symmetry within the core (Fig. 2). Preliminary calculations confirm the symmetry and show that it is sufficient to place two fission chambers close to the centre of the reactor core in the plane perpendicular to the line connecting the regulating and compensating rods. For maximization of the detector response, positions MP5 and MP8 have been chosen.

Axial distributions of the fission reaction rates were measured using CEA manufactured fission chambers at the measuring positions MP5 and MP8 in the JSI TRIGA reactor core for different position of the compensating and regulating control rods (safety and transient were always fully withdrawn).

Fig. 3 shows the axial fission rate distribution in measuring positions MP5 and MP8 for fully withdrawn compensating rod and regulating rod at the critical position (around step 580). The agreement between the calculated and measured distributions is generally very good, some problems arrive only in the vicinity of the safety rod (near position MP8), presumably due to unknown concentration of boron in the safety rod stainless steel cladding.

As the next step we tried to reproduce the fission rates as a function of control rod position at a fixed position of the fission chamber in MP5 and MP8 axial heights with minimum variation have been chosen. Due to relatively small differences in variations compared to the uncertainties axial position close to the center of the active fuel region ($z = 8$ mm) has been adopted. The comparison is shown in Fig. 4. While during measurements the reactor thermal power signal was kept as constant as possible,

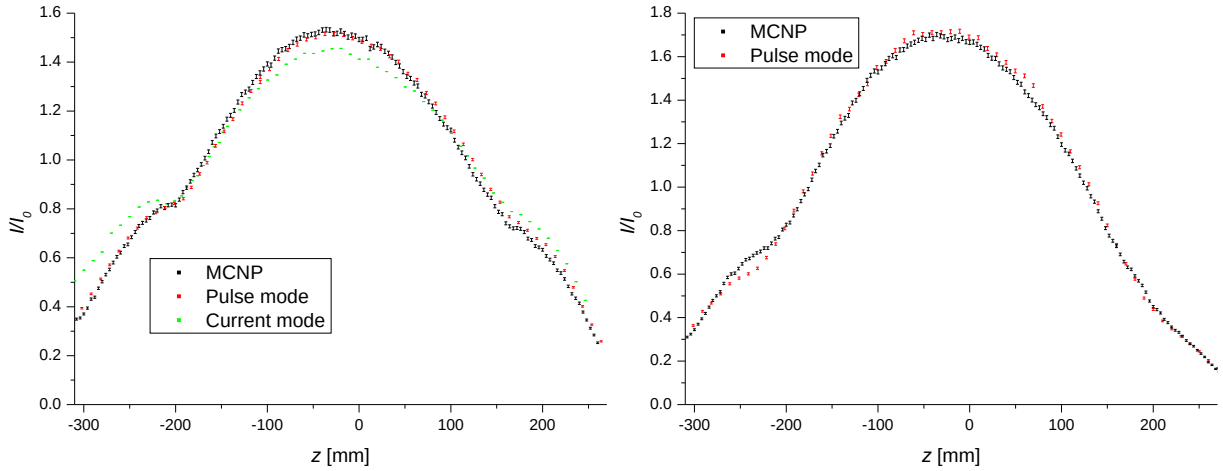


Figure 3: Relative ^{235}U fission rates as a function of axial position z of the fission chamber in measuring positions MP5 (left) and MP8 (right). In MP5, the measurements were performed both in current and pulse mode of the fission chamber. The discrepancy of the current mode is due to a significant contribution of photons to the measured current.

the real power has been changing slightly due to neutron flux redistribution. Therefore, both the measured and calculated reaction rates in Fig. 4 were normalized to the thermal neutron flux at the position of the ionization chamber which is used for reactor online power monitoring. The calculated and measured fission chamber response distributions are in good agreement, with variations due to control rod movement within ±2 % for MP5 and within ±1 % for MP8. which is hardly significant with respect to the experimental (pulse mode) and calculational (MCNP) statistical uncertainties. Therefore, the method with the position-dependent correction factors (Section 3.3.3) might not be necessary in combination with fission chamber measurements in the reactor core, however it would provide a significant improvement for the correction of the signal from the existing online power monitoring system with ionization chamber located outside the reflector.

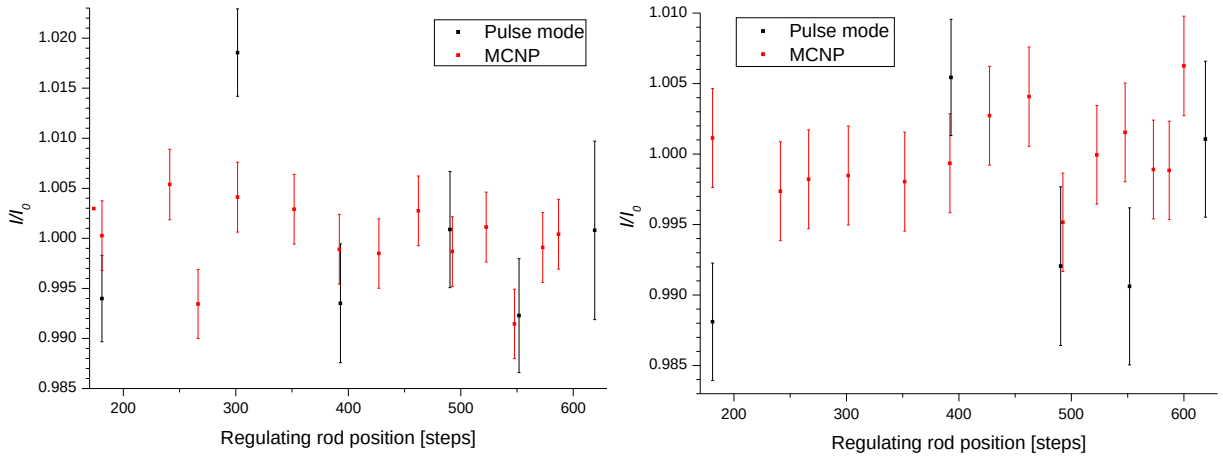


Figure 4: Response of the ^{235}U fission chamber as a function of the regulating rod position in measuring positions MP5 (left) and MP8 (right) at height $z = 8$ mm. Compensating rod was at zero power critical position, with transient and safety rod fully withdrawn.

5 Conclusion

Currently, the JSI TRIGA reactor online power signal is determined from a single neutron flux detector located outside the reactor core. Flux-power proportionality is assumed regardless the reactor conditions, while the absolute power calibration relies on the calorimetric method. The accuracy of the online power monitoring can be improved significantly using multiple detectors and correction factors, which primarily depend on the control rod positions. Such system will be tested at the JSI TRIGA reactor in the course of the ongoing bilateral project with CEA Cadarache. First results show good agreement between the predicted and measured reaction rate distributions and confirm the feasibility of the implementation of the improved monitoring system.

Acknowledgment

The research is funded by the bilateral project "Experimental verification of neutron flux form factors and Qualification of a new wide range multichannel neutron instrumentation" between the Slovenian Research Agency (ARRS) and Commissariat à l'énergie atomique et aux énergies alternatives (CEA).

References

[1] X-5 Monte Carlo Team, MCNP - A general Monte Carlo N-particle Transport code, Version 5, LA-UR-03-1987, 2003.

[2] M. Podvratnik, L. Snoj, A. Trkov and G. Žerovnik, "Calculations to Support Absolute Thermal Power Calibration of the Slovenian TRIGA Mark II Reactor," in *Proc. Int. Conf. Nuclear Energy for New Europe 2011,* Bovec, Slovenia, 2011, pp. 408.1-408.9.

[3] R. Jeraj, T. Žagar and M. Ravnik. (2002, Mar.) Monte Carlo Simulation of the TRIGA Mark II Benchmark Experiment with Burned Fuel. *Nucl. Technology.* Vol. 137, pp. 169-180.

[4] L. Snoj, A. Trkov, R. Jaćimović, P. Rogan, G. Žerovnik and M. Ravnik. (2011, Jan.) Analysis of neutron flux distribution for the validation of computational methods for the optimization of research reactor utilization. *Appl. Radiat. Isotopes.* Vol. 69, pp. 136-141. Available: *http://dx.doi.org/10.1016/j.apradiso.2010.08.019*

[5] M. Ravnik and R. Jeraj. (2003, Sept.) Research reactor benchmarks. *Nucl. Sci. Eng.* Vol. 145, pp. 145-152.

[6] *International Handbook of Evaluated Critical Safety Benchmark Experiments*, Organization for Economic Cooperation and Development - Nuclear Energy Agency, NEA/NSC/DOC(95)03, Paris, published on DVD, ISBN 978-92-64-99054-8.

[7] L. Snoj and M. Ravnik. (2008, Sept.) Power peakings in mixed TRIGA cores. *Nucl. Eng. Design.* Vol. 238, Issue 9, pp. 2473-2479. Available: *http://dx.doi.org/10.1016/j.nucengdes.2008.02.005*

[8] L. Snoj and M. Ravnik, "Calculation of power density with MCNP in TRIGA reactor," in *Proc. Int. Conf. Nuclear Energy for New Europe 2006,* Portorož, Slovenia, 2006, pp. 109.1-109.6.

[9] T. Žagar, M. Ravnik, and A. Peršič, "Analysis of TRIGA Reactor Thermal Power Calibration Method," in *Proc. Int. Conf. Nuclear Energy in Central Europe '99,* Portorož, Slovenia, 1999, pp. 91-98.

[10] L. Snoj, Ž. Štancar, V. Radulović, M. Podvratnik, G. Žerovnik, A. Trkov, L. Barbot, C. Domergue, and C. Destouches, "Experimental power density distribution benchmark in the TRIGA Mark II reactor," in *Proc. Int. Conf. PHYSOR 2012, Advances in reactor physics,* Knoxville, TN, USA, 2012, Vol. 4., pp. 3500-3514.

[11] L. Barbot, C. Domergue, S. Bréaud, C. Destouches, J.-F. Villard, L. Snoj, Ž. Štancar, V. Radulović, and A. Trkov, "Neutron Field Characterization of Irradiation Locations Applied to the Slovenian TRIGA Reactor," to be presented at *Int. Conf. Advancements in Nuclear Instrumentation Measurement Methods and their Application (ANIMMA) 2013,* Marseille, France, 2013, to be published.

[12] A. Trkov, M. Ravnik, H. Wimmer, B. Glumac, and H. Böck. (1995) Application of the rod-insertion method for control rod worth measurements in research reactors. *Kerntechnik.* Vol. 60, Issue 5-6, pp. 255-261.

Coated U(Mo) Fuel: As-Fabricated Microstructures

by

D. Keiser, Jr[1], E. Perez[1], A. Leenaers[2], S. Van den Berghe[2], and T. Wiencek[3]

[1]Idaho National Laboratory

[2]SCK CEN

[3]Argonne National Laboratory

Corresponding Author Contact Information:
Dennis D. Keiser, Jr.
Idaho National Laboratory
P.O. Box 1625
Idaho Falls, ID, 83415-6146 U.S.A.
Phone: 1 (208) 533-7298
Fax: 1 (208) 533-7863
E-mail: Dennis.Keiser@inl.gov

For Publication in the Proceedings of the *Research Reactor Fuel Managment Conference*

(March 30-April 3, 2014 in Ljubljana, Slovenia)

This manuscript has not been published elsewhere
and has not been submitted simultaneously for publication elsewhere.

COATED U(MO) FUEL: AS-FABRICATED MICROSTRUCTURES

D. KEISER, JR.[1], E. PEREZ[1], A. LEENAERS[2], S. VAN DEN BERGHE[2], T. WIENCEK[3]

[1]*Nuclear Fuels and Materials Division, Idaho National Laboratory*
P. O. Box 1625, Idaho Falls, Idaho 83403 USA

[2]*SCK CEN*
Boeretang 200, B02400 Mol, Belgium

[3]*Argonne National Laboratory*
9700 S. Cass Ave. Argonne, Illinois, 60439 USA

ABSTRACT

As part of the development of low-enriched uranium fuels, fuel plates have recently been tested in the BR-2 reactor as part of the SELENIUM experiment. These fuel plates contained fuel particles with either Si or ZrN thin film coating (up to 1 μm thickness) around the U-7Mo fuel particles. In order to best understand irradiation performance, it is important to determine the starting microstructure that can be observed in as-fabricated fuel plates. To this end, detailed microstructural characterization was performed on ZrN and Si-coated U-7Mo powder in samples taken from AA6061-clad fuel plates fabricated at 500˚C. Of interest was the condition of the thin film coatings after fabrication at a relatively high temperature. Both scanning electron microscopy and transmission electron microscopy were employed. The ZrN thin film coating was observed to consist of columns comprised of very fine ZrN grains. Relatively large amounts of porosity could be found in some areas of the thin film, along with an enrichment of oxygen around each of the the ZrN columns. In the case of the pure Si thin film coating sample, a (U,Mo,Al,Si) interaction layer was observed around the U-7Mo particles. Apparently, the Si reacted with the U-7Mo and Al matrix during fuel plate fabrication at 500˚C to form this layer. The microstructure of the formed layer is very similar to those that form in U-7Mo versus Al-Si alloy diffusion couples annealed at higher temperatures and as-fabricated U-7Mo dispersion fuel plates with Al-Si alloy matrix fabricated at 500˚C.

1. Introduction

The High Performance Research Reactor Fuel Development (HPRRFD) program, also known as the Reduced Enrichment for Research and Test Reactor (RERTR) program, is developing low-enriched uranium (LEU) fuels for application in research reactors. [1] U-Mo alloy dispersion fuel is one type of fuel that is being developed. [2] In order to eliminate a deleterious fuel/matrix interaction that occurs during fabrication and irradiation, a diffusion barrier is being evaluated for deposition on the U-Mo fuel particles before the coated fuel particles are used for fuel plate fabrication. [3] Zirconium-mononitride (ZrN) is a possible candidate diffusion barrier material. ZrN is a IV-B transition metal nitride with a face centered cubic (FCC) crystal structure (NaCl structure) that is known for its extremely high hardness (4510 kg/mm) and high melting temperature (2950˚C). It has a density of 7.09 g/cc, a thermal expansion coefficient of 7.24 x 10^{-6}/˚C, and a lattice parameter of 4.58 angstroms. As a IV-B transition metal nitride, ZrN can be produced as a thin film that, besides having a high hardness and melting point, also exhibits chemical stability, corrosion resistance, low resistivity and low coefficient of friction. Overall, the

transition metal nitrides are very attractive compounds because of their excellent mechanical, thermal, electical, and catalytic properties. [4] The IV-B transition metal nitrides have been investigated as diffusion barriers in metallization schemes, superlattice constituents, field emitters, electrical contacts to III-V semi-conductors, Josephson junctions, and cryogenic thermometers. [5] ZrN specificallly has been used for many industrial applications, including hard coatings, diffusion barriers in semiconductor technologies, optical applications for heat mirrors, and decorative coatings. [4]

In addition to ZrN, Si is being investigated as a diffusion barrier material, based on the experience performing irradiation experiments with dispersion fuel plates that contain Si additions to the matrix. [6]

Microstructural characterization using synchrotron radiation has been performed on ZrN coating that was deposited using the STEPS&DRUMS process. [7] The samples that were characterized were cylindrical compacts that were fabricated using U-7Mo fuel particles coated with ZrN (using the STEPS&DRUMS process) and Al powder. These samples were characerized after they had been annealed at 340˚C for 130 days, 450˚C for 4 hours, or 550˚C for 2 and 4 hours. ZrN was detected in the samples (about 1.2 wt.%), but considering the 1-µm overall thickness and density of about 7.3 g/cm^3, the detected amount was considered to be lower than expected. Overall, the ZrN was observed to be heavily textured with a strong relation to the U-Mo grains on with the ZrN was deposited. The development of some U-Mo particle oxidation was observed. Almost no U-Mo/Al matrix interaction was observed overall. EPMA and SEM have also been employed to characterize annealed compact samples that contained ZrN-coated U-7Mo and Al powder, along with samples from actual as-fabricated fuel plates. [6] The results of this work showed that no U-7Mo/Al interaction occurred during sample testing, except for the as-fabricated samples that were subsequently heated at 550˚C for 2 and 4 hours. Some damage of the ZrN coating was observed due to the fuel plate fabrication process.

Irradiation experiments using ions and neutrons have been performed on samples from as-fabricated fuel that contain U-7Mo particles coated with 1-µm-thick ZrN. For the ion irradiation experiments, 80 MeV iodine ions were used to simulate in-reactor behavior. [8]. It was observed that in locations where cracks were present in the ZrN, extensive interaction occurred between the U-7Mo and Al matrix. Howerver, where the ZrN coating was intact, no interaction was observed. To test the irradiation performance of ZrN coating using neutrons, a reactor test was performed using an Al matrix pin-type fuel and U-9Mo powders coated with 2 to 3-µm-thick ZrN using a process that was different than STEPS&DRUMS. [9] It was observed that for burnups up to 60 and 84% no U-9Mo/Al interaction occurred for locations where the ZrN coating was intact. Another reactor experiment that was performed used plate-type fuel and U-7Mo particles coated with 1-µm-thick ZrN using STEPS&DRUMS, and it was performed in the BR-2 reactor as part of the SELENIUM (Surface Engineering of Low ENriched Uranium-Molybdenum) test. [6, 10,11] The initial NDE results that have been reported for this irradiation showed that the plates with ZrN-coated or Si-coated U-7Mo plates did not exhibit fuel plate blistering.

In order to further the understanding of the effectiveness of using a thin 1-µm-thick ZrN or 800-nm-thick Si thin film as a diffusion barrier to eliminate U-7Mo/matrix interaction, where the thin film is deposited on U-7Mo particles using a STEPS&DRUMS process, it is beneficial to utilize multiple microstrucural characterization techniques, including TEM. Detailed microstructural information, particularly at a low length scale, can help in determining the effects of irradiation during subsequent reactor testing. To this end, U-7Mo fuel particles with a 1-µm-thick ZrN and 800-nm-thick Si coating, deposited using the same barrel coating system as those that were

tested in the SELENIUM reactor test, have been characterized using scanning electron microscopy (SEM) and transmission electron microscopy (TEM). The samples for characterization were produced from fuel plates with Al-6061 (AA6061) cladding that were fabricated at 500˚C. These plates had been fabricated to complete a reactor experiment named RERTR-11A, but this test did not get irradiated. The main difference between the ZrN and Si coatings discussed in this paper and those that were irradiated in SELENIUM is that the SELENIUM plates were fabricated at a temperature no higher than 450˚C. [8] It is benefical to characterize samples from fuel plates fabricated at a higher temperature to investigate the effect of the relatively high temperature fabrication process on the ZrN and Si coating. This paper discusses the results of the microstructural characterization that was performed and identifies some microstructural characteristics that could be changed in order to possibly improve the performance of the thin film diffusion barriers during irradiation.

2. Experimental

A 1-µm-thick ZrN thin film and 800-nm-thick thin film were applied to the U-7Mo powders by personnel at the Studiecentrum voor Kernenergie, Centre de l'Energie Nucléaire (SCK CEN) in Belgium. The STEPS&DRUMS system described earlier was employed to complete the process. The following are the steps of operation that were used for depositing the ZrN: (1) attach a high-purity Zr target; (2) operate the source a power of 800 W; (3) pump down the reactor to around 10^{-6} mbar; (4) admit high-purity Ar gas into the chamber at a rate of 80 cc per minute; (5) add high purity nitrogen at a rate of 6 cc per minute, while reducing the Ar flow to 76 cc; and (6) rotate the drum at around 2 to 5 rotations per minute. The total sputter time can be up to 7 hours. For depositing Si, nitrogen was not admitted into the system. [6]

A U-Mo dispersion fuel plate was fabricated for ultimate destructive examination using ZrN-coated U-7Mo particles following standard steps. [7] In short, the ZrN-coated U-7Mo fuel powder received from SCK CEN was blended with Al powder, where the major impurities were 0.09 wt.% Fe and 0.03 wt.% Si, and pressed into a compact. The compact was placed in an AA6061 picture frame, sandwiched between AA6061 cover-plates, roll-bonded to final thickness, and sheared to final plate length. The final fuel loading of the fuel plate was 8 grams U/cm^3.

From the as-fabricated fuel plate, transverse and longitudinal cross sections were sliced using a slow-speed saw. The cross sections were mounted in epoxy, metallographically polished, and then characterized at the Microscopy and Characterization Suite (MaCS), Center for Advanced Energy Studies (CAES) at INL. A scanning electron microscope (SEM) was used to produce both secondary electron images (SEIs) and backscattered electron images (BEIs) of the microstructure. Compositional analysis was performed using energy dispersive spectroscopy (EDS). Samples were produced for transmission electron microscopy (TEM) using a focused ion beam (FIB) insitu lift out (INLO) technique. The TEM analysis was performed in a FEI Tecnai G2 F30 STEM equipped with a high-angle annular dark field (HAADF) detector. For each specimen, both low- and high magnification Bright Field (BF) and HAADF STEM images were collected for bulk and detailed analysis. Selected area and convergent beam diffraction patterns (SAED and CBED) were collected and indexed to crystallographically identify the phase constituents. Standard TEM Bright Field (BF) micrographs were produced to characterize the microstructure. HAADF micrographs were used to identify compositional contrast. EDS was employed to determine phase composition.

3. Results and Discussion

3. 1 ZrN-Coated U-7Mo

3. 1.1 Scanning Electron Microscopy

SEM images of the microstructure observed for the archive plates with ZrN-coated U–7Mo particles are presented in Figure 1. A uniform distribution of the fuel particles is observed with some dog-boning at the end of the fuel zone. The higher magnification image in Figure 1b shows the presence of a distinctive interface in the ZrN coating that could be distinguished better with subsequent TEM analysis. The arrows in Figure 1c identify fine particulate present in the Al matrix. Much of the particulate appears to be ZrN overspray that was not sieved out before the coated U–7Mo was used to make fuel plates. Figure 2 shows where the FIB was used to expose the ZrN a depth into the sample for a fuel particle, when looking at the polished surface, looked like it had fractured ZrN coating. It can be seen that a gap is present at the ZrN/Al interface, suggesting that there was not good bonding between the ZrN and Al in this area. Also the ZrN looks cracked at the surface, but is found to be intact when the FIB is employed to “trench” into the sample. This suggests that the fracturing of the ZrN for this particle may be due to sample preparation.

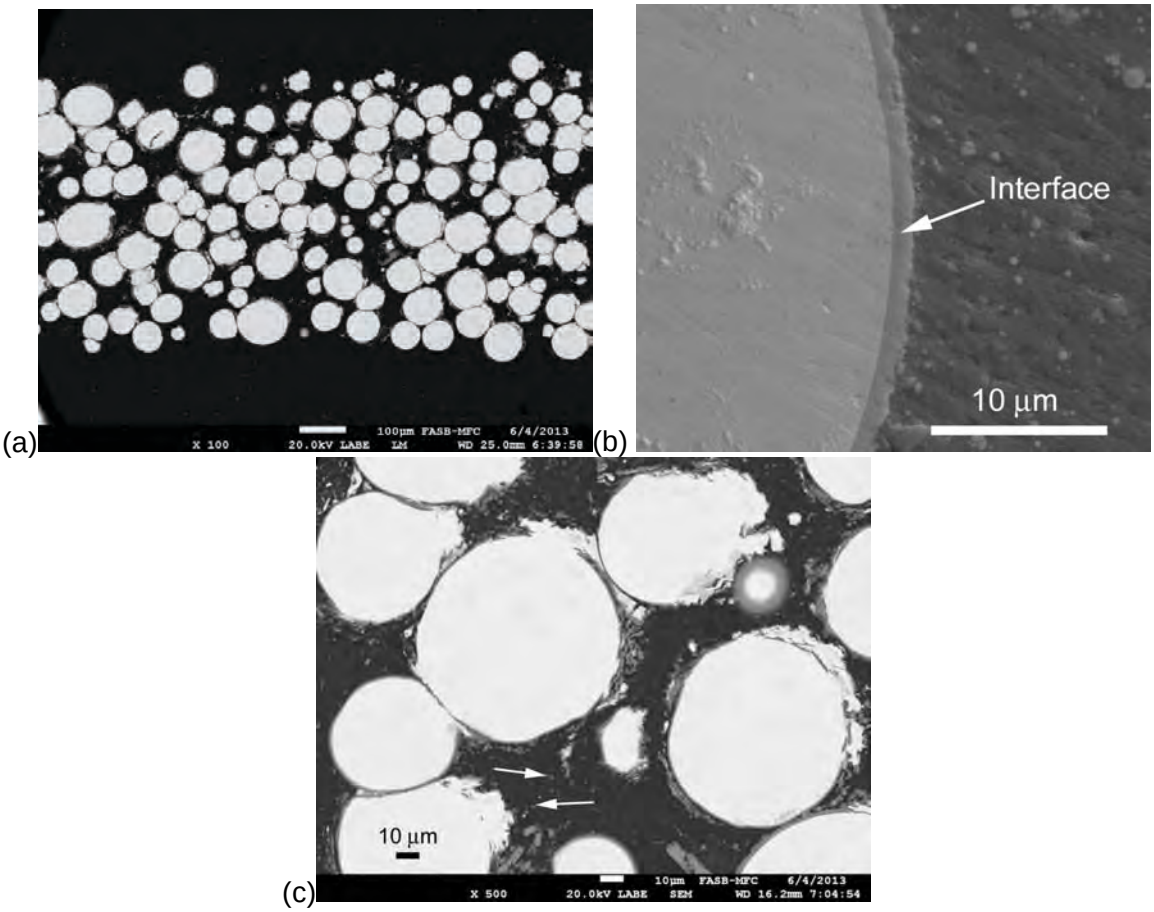


Figure 1. BEIs of the microstructure observed for the fuel plate with ZrN-coated fuel particles (a,c), and (b,d) expose transverse and longitudinal cross sections, respectively.

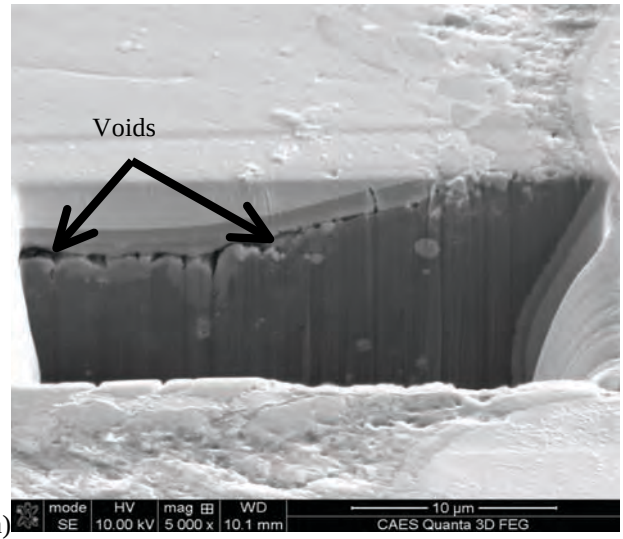
(a) 

Figure 2. SEM image of region where a FIB was used to generate a trench that extended into the sample and exposed the ZrN/Al interface for a particle that looked fractured when looking at the polished surface.

3.1.2 Transmission Electron Microscopy

Five FIB samples were produced from regions with uniform ZrN thin film. Four of the produced samples were oriented parallel to the growth direction of the thin film (see Figure 3). The fifth sample was oriented perpendicular to the growth direction (see Figure 7). A TEM HAADF micrograph showing a representative microstructure for the different longitudinal cross-section ZrN FIB samples is presented in Figure 4. For the thin film, columns of ZrN are observed through the thickness, and some cracks were also observed (not shown). The first layer (layer 1 in Figure 4b), nearest the U–7Mo, has finer columnar features as compared to the thicker second layer (towards the Al matrix) that has larger columns. Layer 2 typically has more porosity vis-à-vis layer 1. Based on EDS analysis, more oxygen was present in the ZrN closer to the Al matrix. SAED patterns that were generated from the low and high-oxygen regions showed that the layer is comprised of ZrN (cF8), and it is very fine grained.

The quailty of bonding at both the U-7Mo/ZrN and ZN/Al interfaces was investigated. As shown in Figure 5, an interaction zone seemed to be present at the U-7Mo/ZrN interface that was comprised of different precipitate phases (appear to contain high levels of oxygen and nitrogen), and at the ZrN/Al interface (see Figure 6) porosity could be observed and little evidence of any interaction zone. Gaps could also be observed at this interface. Precipitates were observed along Al grain boundaries at some ZrN/Al interface locations. Further characterization will be required to determine if these precipitates are due to interaction between the ZrN and Al. The precipitates were typically very small, making definitive phase identification difficult. Many precipitates in the Al matrix seemed to be ZrN overspray or (Fe, Si)-containing phases (from impurities in the original Al powder).

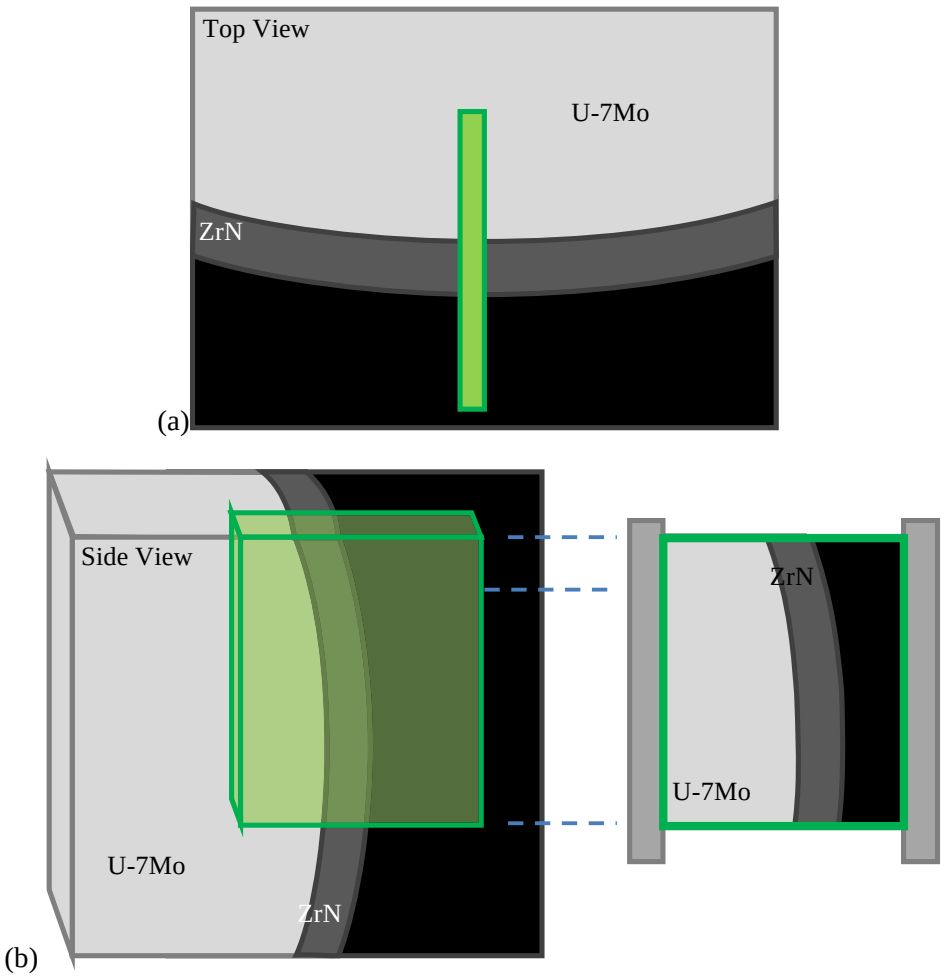


Figure 3. Schematic diagrams showing (a) a top view and (b) a side view of a location where a FIB sample is sliced through the ZrN to capture an orientation that exposes the microstructure parallel to the growth direction.

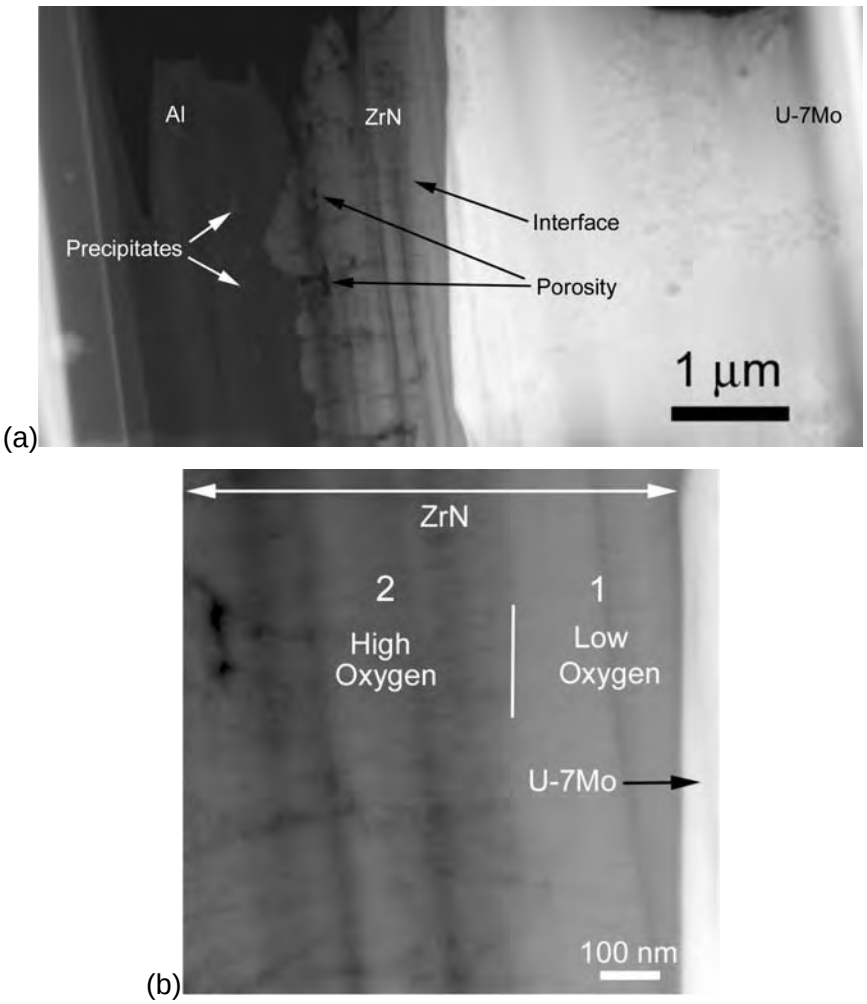


Figure 4. TEM micrograph showing a representative ZrN microstructure that was observed in the four FIB samples oriented in the growth direction.

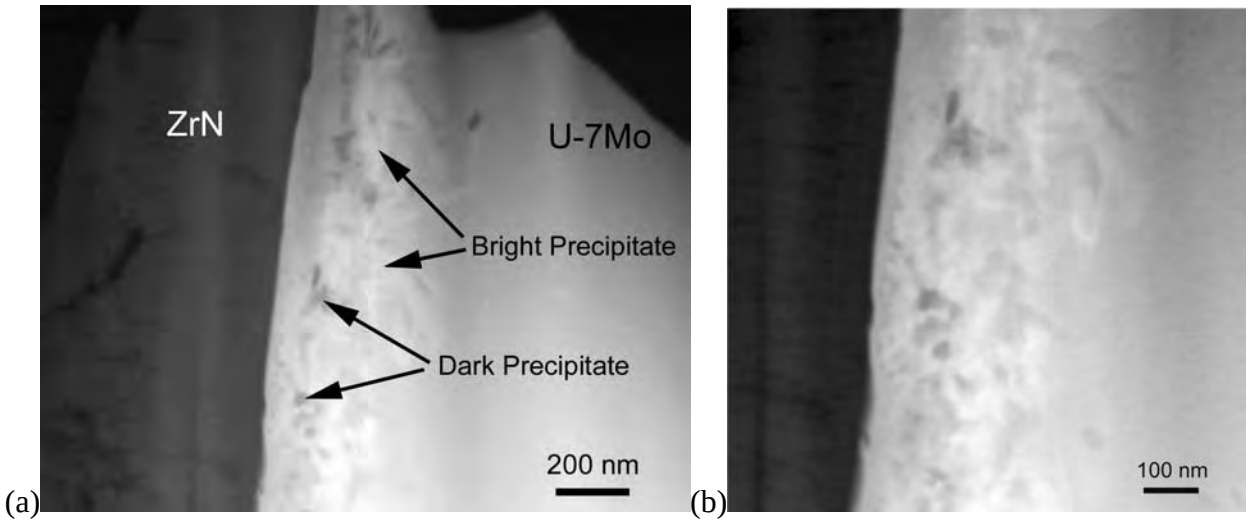


Figure 5. High-magnification TEM images (a,b) showing the presence of an interaction layer between the U–7Mo and ZrN. Dark and bright contrast phases constitute the layer.

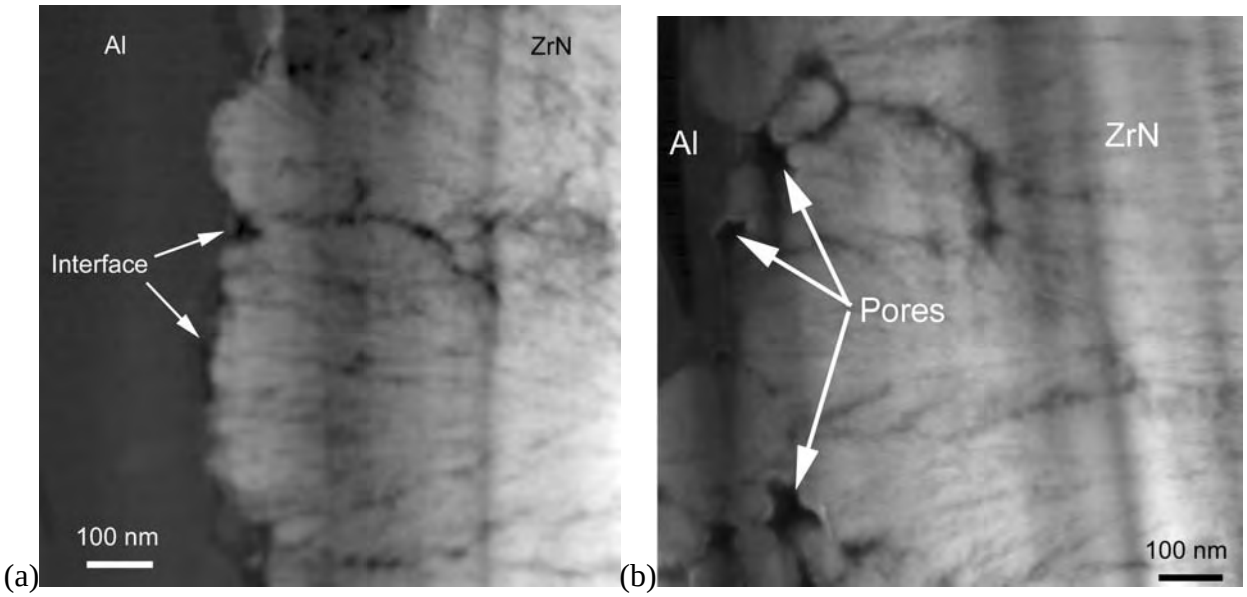


Figure 6. High-magnification TEM images (a-c) showing the presence of pores at the Al/ZrN interface.

One sample was produced oriented perpendicular to the growth direction of the ZrN (see Figure 7). This sample captured a transverse cross section of the columnar ZrN microstructure. Figure 8 shows HAADF and bright field TEM images of the microstructure that was observed. The grains within the ZrN columns are tens of nanometers in size. The results of EDS analysis indicate the interfaces between the ZrN columns (columnar boundaries) were enriched in zirconium, oxygen and, possibly, aluminum. Negligible oxygen was observed within the individual ZrN grains. Bright field TEM micrographs were also produced that showed the presence of a crystal lattice at a ZrN column boundary that may be Zr-oxide. Limited open voids are observed at the boundaries of the different ZrN columns.

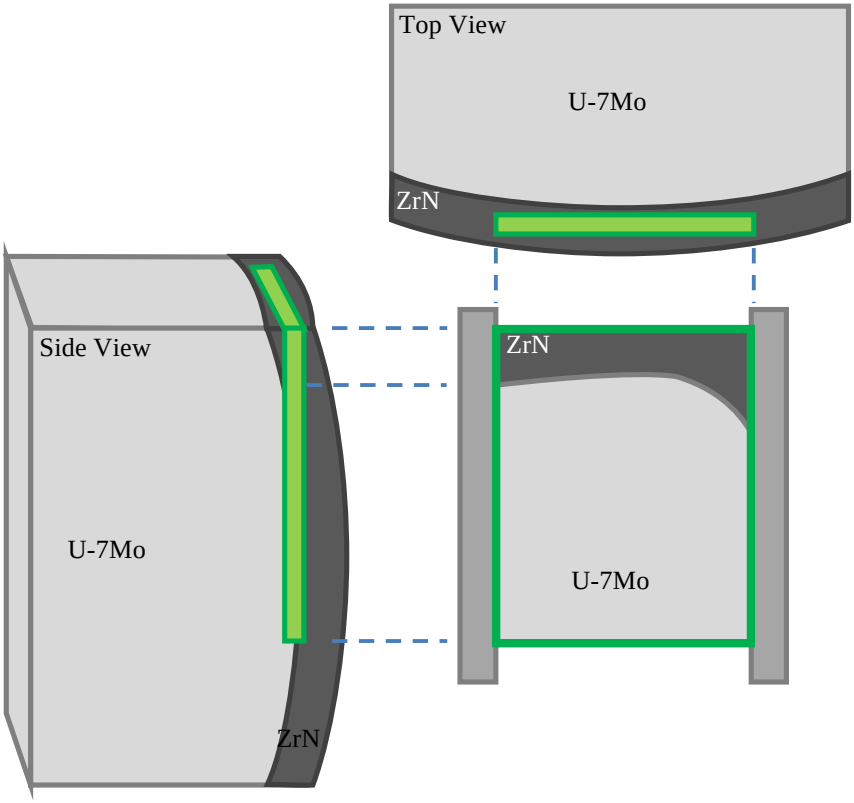
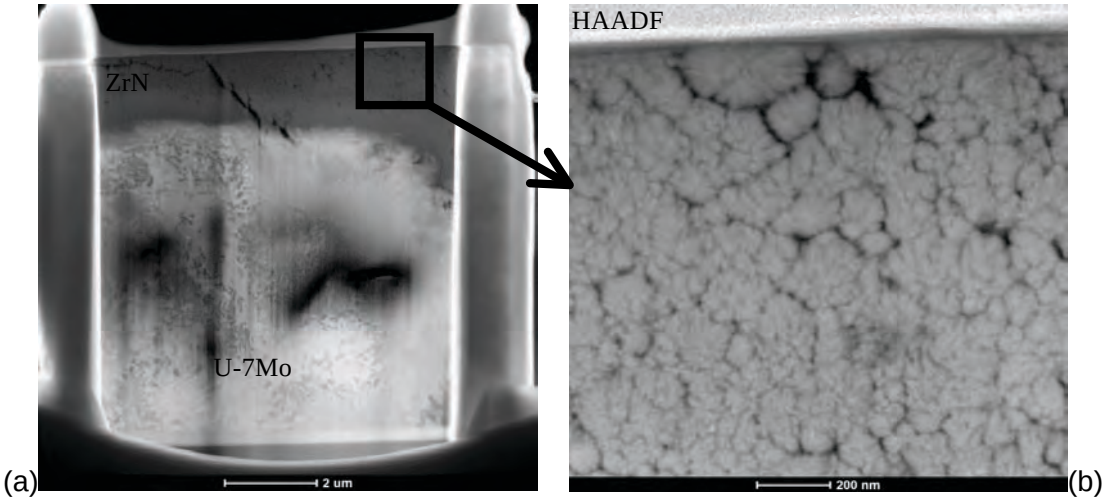
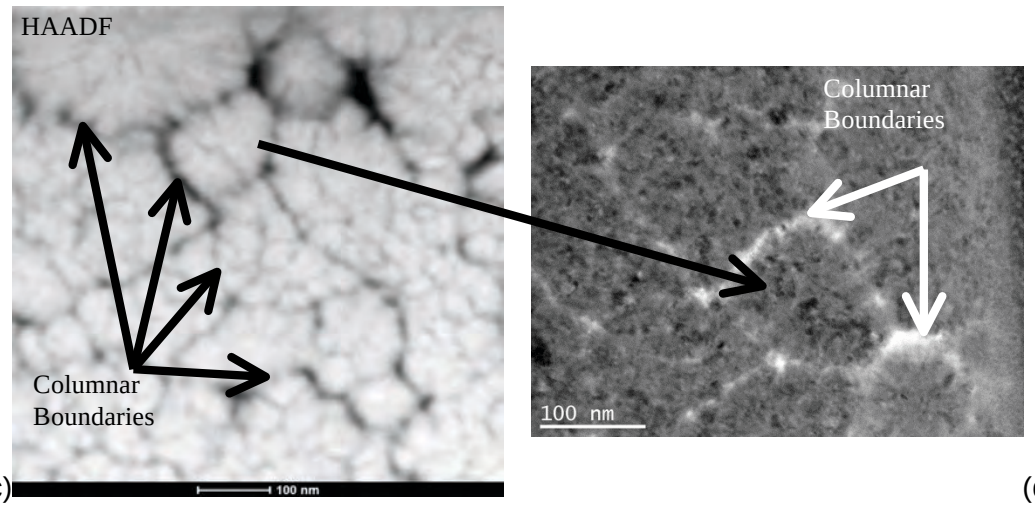


Figure 7. Schematic diagrams showing top and side views of the location where a FIB sample is sliced through near the U-7Mo/ZrN interface to capture a sample with an orientation that exposes the microstructure parallel to the “substrate” and perpendicular to the ZrN growth direction.



(a) (b)

.



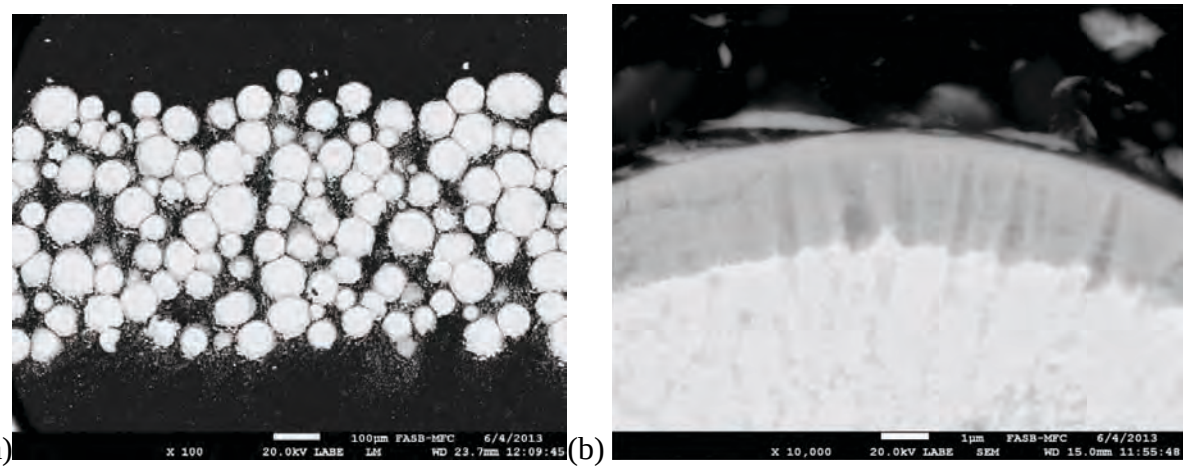
(c) (d)

Figure 8. HAADF TEM micrographs (a-c) showing the microstructure observed for a sample oriented perpendicular to the ZrN growth direction. (d) is a bright field image of the microstructure. The bright contrast regions in (d) have been shown by EDS to be enriched in oxygen.

3.2 Si-Coated U-7Mo

3.2.1 Scanning Electron Microscopy

A low-magnification SEM image of the microstructure observed for the archive plates with Si-coated U–7Mo particles is presented in Figure 9, along with a higher magnifcation image of the Si-rich layer around a fuel particle. A uniform distribution of the fuel particles is observed in the fuel meat, along with a fine particulate in the Al matrix that appears to be Si overspray that was not sieved out before the coated U–7Mo was used to make fuel plates. The Si x-ray map shown in Figure 10 indicates that the layer present around the fuel particles was enriched in Si.



(a) (b)

Figure 9. BEI (a) of the microstructure observed for the fuel plate with Si-coated fuel particles. The U-7Mo is white, the Al matrix is black, and the Si coating is medium contrast, and the fine particles in the matrix are Si overspray. (b) is a higher magnifcation BEI of the Si-rich layer present around a fuel particle.

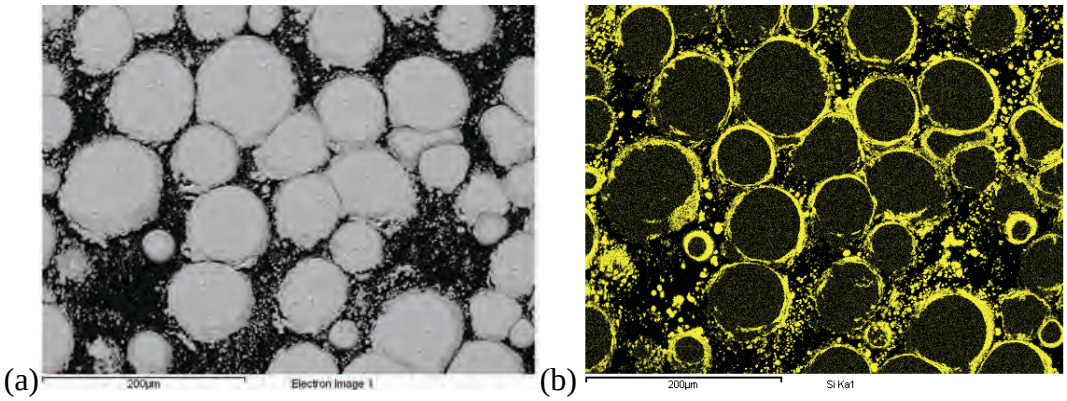


Figure 10. SEI (a) and Si WDS x-ray map (b). The layers around the U-7Mo particles are enriched in Si, and fine Si-rich particulate is present in the Al matrix.

3.2.2 Transmission Electron Microscopy

Figure 11 shows SEM images of the microstructure near where a FIB sample was produced for TEM analysis, along with the exact location where the FIB sample was produced. Figure 11d shows a TEM HAADF micrograph generated from the FIB sample.

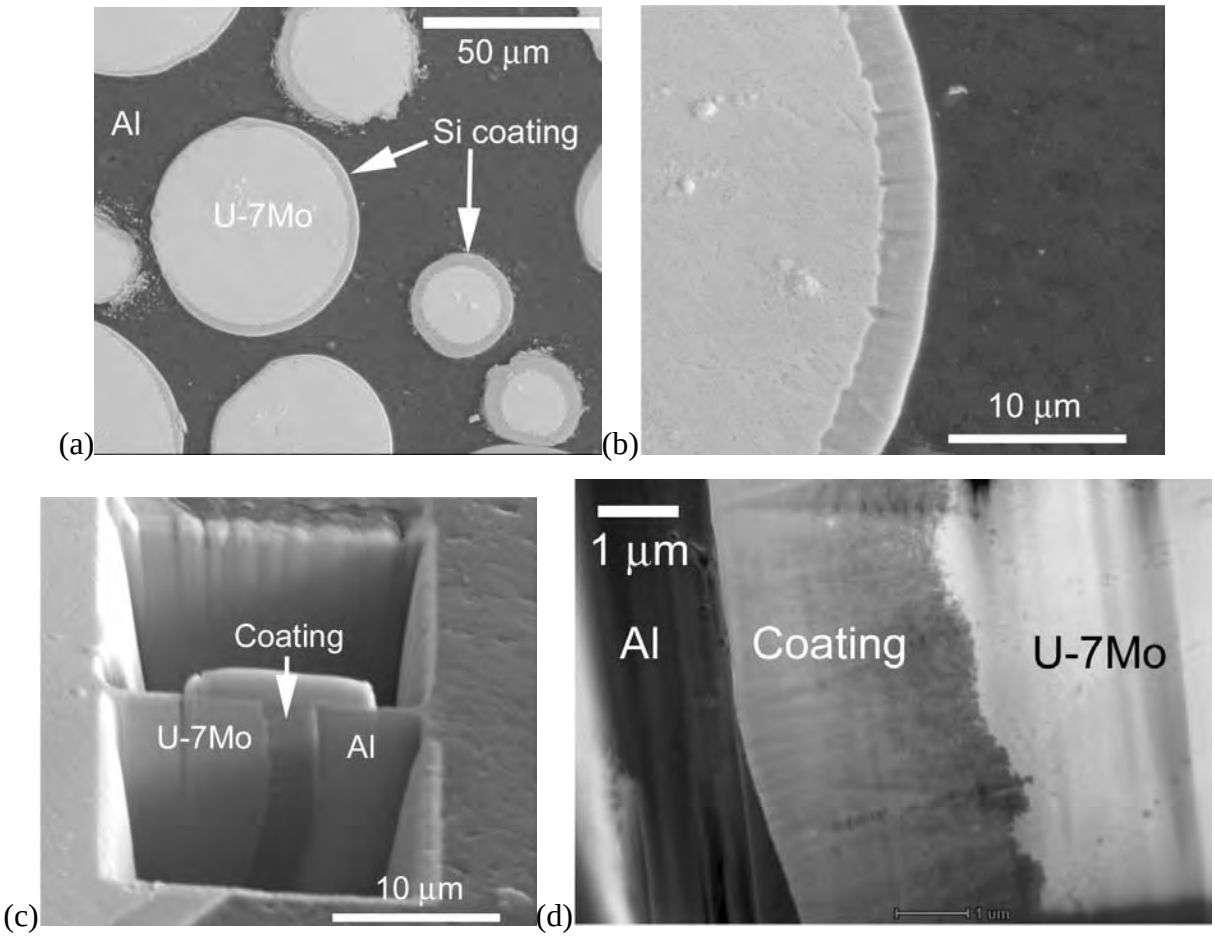


Figure 11. BEIs (a,b) of the layer observed around the fuel particles. (c) is a BEI of a FIB sample that captures the coating layer, and (d) is a HAADF micrograph of the observed microstructure in the FIB sample.

Figure 12 shows a high magnification TEM image of the layer present around a fuel particle. This layer has become an interaction layer that contains U, Mo, Al, and Si. Within this layer, three phases appear to be present: Al-rich, Si-rich, and another (U, Mo, Al, Si) phase. It is of interest to see if there is any evidence of the original pure Si phase within the coating layer. Based on generated linescans, U, Mo, Al, and Si was observed throughout the thickness of the layer, and no unreacted layer of pure Si could be observed.

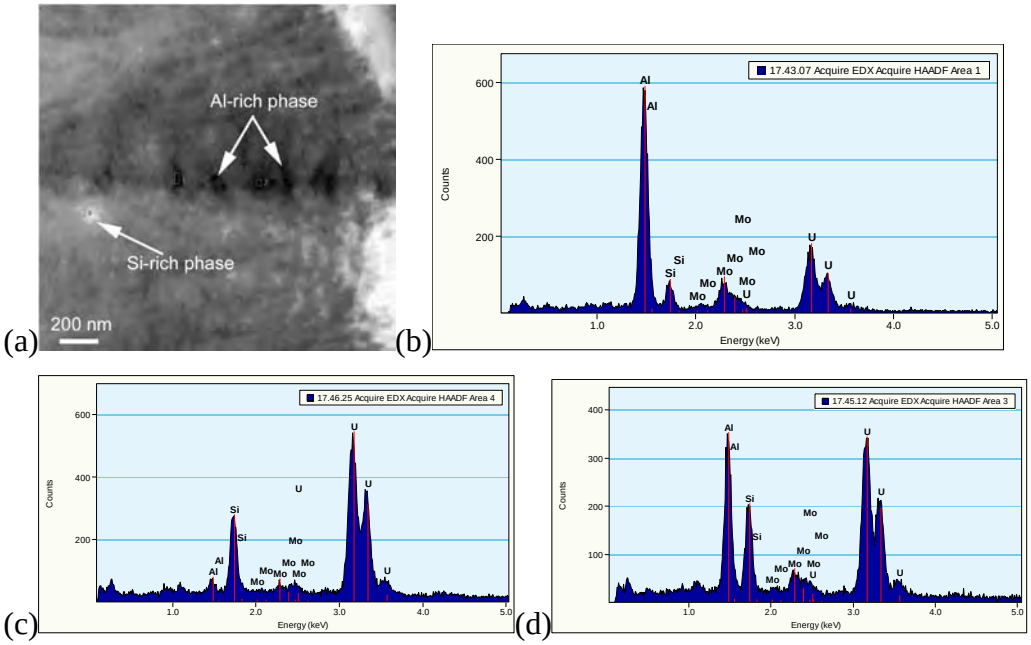


Figure 12. HAADF micrograph (a) showing Al-rich and Si-rich phase locations in the interaction layer. The bulk of the layer are (U,Mo,Al,Si) phases. EDS spectra are shown for the (b) Al-rich, (c) Si-rich, and (d) (U,Mo,Al,Si) phases.

Selected area electron diffraction patterns were generated from different locations in the interaction layer, and Figure 13 shows an example. It was observed that, based on the ring pattern, many fine grains are observed in the layer. By comparing the microstructure and SAED patterns reported for U-Mo/Al-Si diffusion couple samples [12] (see Figure 13b and 13d) with that for the interaction layer characterized in this study (Figure 13a and 13c), it appears that during fuel plate fabrication the original pure Si coating has reacted with U–7Mo and Al to form the same kind of layer that could form if U–7Mo interacted with an Al-Si matrix in a diffusion couple or as-fabricated fuel plate.

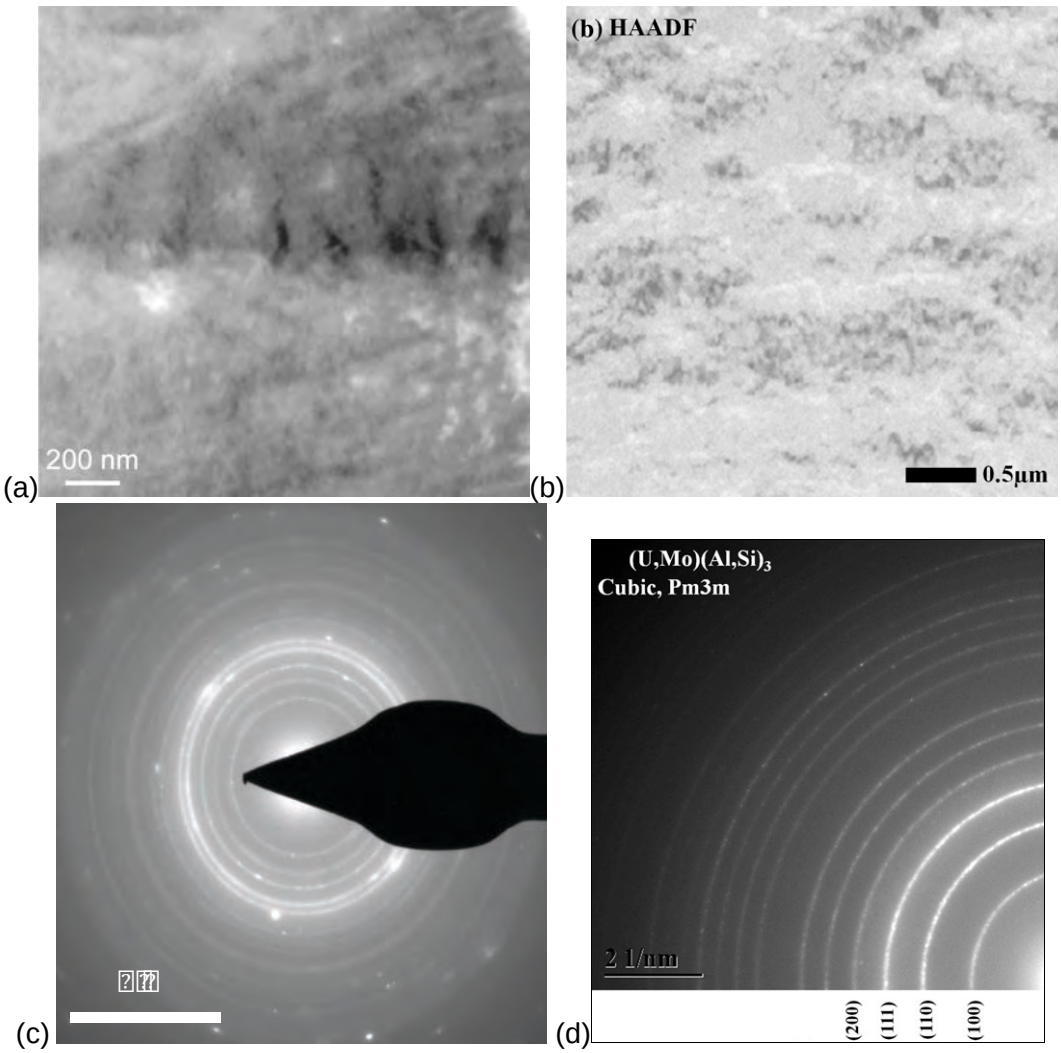


Figure 13. HAADF micrographs showing the layer in the (a) Si-coated sample and (b) a U–Mo/Al-Si diffusion couple interaction layer. SAED patterns are shown for (c) the Si-coated sample and (d) a U–Mo/Al-Si diffusion couple interaction layer. Great similarity is observed.

4. Summary

Based on the results of microsctructural characterization of a 1-µm-thick ZrN thin film in fuel plates manufactured at 500˚C, the following is considered to be the main observations about the thin film microstructure: (1) Porosity is observed in the ZrN thin film, and the regions with the highest porosity are located nearest the Al matrix; (2) During the PVD coating process, the ZrN thin film appears to nucleate on the surface of the U–Mo particles and then grows as columns through the one-micron thickness. The first ~200 nm of the coating has finer microstructural features than the final 800 nm, which shows coarser, “feathery” features; (3) the ZrN thin film does not exhibit bulk interaction with the Al, but some Zr or N diffusion may occur into the Al matrix along grain boundaries;. (4) Based on contrast variation and EDS compositional analysis, the ZrN grain boundaries extending from the Al side to the U-7Mo side may contain something other than Zr and N (possibly Al or oxygen); (5) A narrow interaction zone is present at the U-7Mo/ZrN interface either formed during the STEPS&DRUMS coating process and/or during fuel plate fabrication, and (6) Based on ring patterns observed in SAED patterns generated from the ZrN, many fine grains (tens of nanometers in size) constitute the layer, resulting in the presence of a relatively large amount of grain boundaries that could serve as fast diffusion paths.

However, it is possible that the presence of impurities on these boundaries could impede grain-boundary diffusion.

In terms of ways to potentially improve the irradiation performance of a ZrN thin film diffusion barrier, it may be beneficial for the layer to be of higher density, to have larger grains, to contain less oxygen, and to have better contact at the ZrN/Al interface. Less porosity in the ZrN may help provide more mitigation of the transport of gaseous fission products through the film; larger grains in the thin film would reduce the grain boundary area availbe for relatively fast diffusion; less oxygen in the thin film would mean that more of the material is comprised of the radiation stable ZrN phase; and, finally, better adhesion at the ZrN/Al interface during fabrication may reduce the amount of debonding at this interface that may occur during irradiation.

For the sample with Si-coated U-7Mo particles, the original, pure-Si coating interacted with the U-7Mo and Al matrix during fabrication at 500˚C to form a (U, Mo, Al, Si) interaction layer. This layer is very similar in morphology and composition to the interaction layer that develops in U-7Mo vs Al-Si alloy diffusion couples and in U–7Mo dispersion fuel where the Al-Si matrix interacts with the U-7Mo during fabrication. Based on the observation of the presence of a (U,Mo,Al,Si) interaction layer, a fuel plate that contains Si-coating applied to the U-7Mo particles should conceivably exhibit irradiation performance that is similar to what is observed for fuel plates with uncoated U-7Mo fuel particles and Al-Si alloy matrix.

Acknowledgments

This work was supported by the U.S. Department of Energy, Office of Nuclear Materials Threat Reduction (NA-212), National Nuclear Security Administration, under DOE-NE Idaho Operations Office Contract DE-AC07-05ID14517.

References

[1]. J. L. Snelgrove, G. L. Hofman, M. K. Meyer, C. L. Trybus, and T. C. Wiencek, Nucl. Engr. And Design 178 (1997) 119-126.
[2] D. D. Keiser, Jr., S. L. Hayes, M. K. Meyer, and C. R. Clark, *JOM* 55(9) (2003) 55-58.
[3]. S. Van den Berghe, A. Leenaers, and C. Detavernier, in: Proc. of the International Meeting on Reduced Enrichment for Research and Test Reactors, Warsaw, Poland, October 9-12, 2012.
[4]. Akash Singh, P. Kuppusami, Shabana Khan, C. Sudha, R. Thirumurugesan, R. Ramaseshan, R. Divakar, E. Mohandas, and S. Dash, Applied Surface Science 280 (2013) 117-123.
[5]. David Ross McGregor, Jr., “Growth Optimization and Characterization of Reactively Sputtered ZrN Thin Films for III-V Buffer Layer Applications", Master of Science Thesis, North Carolina State (2002).
[6]. A. Leenaers, S. Van den Berghe, and C. Detavemier, J. Nucl. Mater. 440 (2013) 220-228.
[7]. T. Zweifel, H. Palancher, A. Leenaers, A. Bonnin, R. Tucoulou, S. Van Den Bergen, R. Jungwirth, F. Charollais, and W. Petry, J. Nucl. Mater. 442 (2013) 124-132.
[8] R. Jungwirth, T. Zweifel, H.Y. Chiang, W. Petry, S. Van den Berghe, A. Leenaers, J. Nucl. Mater. 434 (2013) 296–302.
[9]. A. Izhutov, V. Alexandrov, A. Novosyolov, V. Starkov, A. Sheldyakov, V. Shishin, V. Iakovlev, I. Dobrikova, A. Vatulin, G. Kulakov, V. Suprun, in: Proc. of the International Meeting on Reduced Enrichment for Research and Test Reactors (RERTR), Lisbon, 2010.
[10]. S. Van den Berghe, A. Leenaers, and C. Detavernier, in: Proc. of RRFM 2010, Marrakech, Morocco, March 21-25, 2010.
[11] S. Van den Berghe, Y. Parthoens, G. Cornelis, A. Leenaers, E. Koonen, V. Kuzminov, C. Detavernier, J. Nucl. Mater. 442 (1023) 60-68.
[12] E.Perez, Y.H. Sohn, D.D. Keiser, Jr., *Met. Trans. A* 44 (2013), 584–595.

THERMAL DESIGN OF THE LORELEI TEST DEVICE USING COMSOL MULTIPHYSICS INVERSE SOLUTION

H. SHENHA, D. GITELMAN, A.SASSON, Y. WEISS
Rotem Ind., Mishor Yamin, D.N Arava 86800, Israel

M. KATZ, I. PREKER, M. ARBEL-HADDAD
NRCN, P.O.Box 9001 Beer Sheva, 84190, Israel

L. FERRY
French Atomic Energy Commission (CEA) – Cadarache Centre, France

ABSTRACT

This work presents a COMSOL multiphysics model that was developed to simulate the LORELEI experimental sequence, in the dry phases. The in-pile test device is installed on a displacement device located in the pool water channel through the Beryllium reflector. The movement of the device in the flux zone generates power in the fuel sample. The goal is to generate a desirable temperature profile representing a typical cladding temperature evolution during LOCA accident, to reproduce the typical thermo mechanical behavior of the clad.
A numerical simulation of heat transfer is coupled with first order differential equations that represent the cladding oxidation reaction. PID controllers were numerically implemented within an axi-symmetric geometry, to minimize the number of iterative procedures and evaluate possible control rules. The work presents part of the feasibility study in the preliminary design phase of the LORELEI test device, to generate a LOCA type transient.

1. Introduction

The LORELEI (Light-Water One-Rod Equipment for LOCA Experimental Investigation) test device in the Jules Horowitz Reactor (JHR) is dedicated to study cladding thermo-mechanical behavior during Loss of Coolant Accident (LOCA) in power reactors. By using a displacement device, the fuel sample moves in the neutron flux field. Gamma radiation generates heat in the structure according to the device location. Figure 1 presents schematically the cladding temperature variation throughout the experimental sequence which simulates some specific thermal conditions as in a real LOCA scenario:

- An adiabatic heating of the cladding up to ballooning and burst occurrence
- High temperature plateau which will promote clad oxidation
- Passive precooling and water quenching

The design of the LORELEI test device should be able to produce this temperature variation profile by moving the experimental setup on a displacement device in the flux field.
This study presents the development of a transient numerical model that calculates, for a given geometry, the device position that will generate the desired cladding temperature profile. The thermal analysis of the LORELEI test device was performed by the COMSOL Multiphysics software. The model takes into account parameters that affect and represent the thermo-mechanical behavior such as the cladding oxidation reaction, ballooning strain level, fuel porosity, initial oxidation thickness and fuel relocation. The range of these parameters will affect the cladding temperature and the goal of the design is to present that thermal escalation will not occur in any scenario.

The model is a parametric model that allows us to investigate these random behavior effects. The exothermal reaction of the Zirconium cladding that occurs in the environment of steam is major phenomenon that may cause thermal escalation. The reaction rate is strongly depended on the cladding temperature and the surface area that is exposed to steam. During the experimental sequence the clad is expected to burst in the range between 700 and 900°C. At this time, the inner cladding surface is exposed to steam and the amount of Zirconium reacting with steam increases. The cladding temperature continues to increase up to the plateau phase which contributes to increase the exothermal reaction rate. The power generated by the oxidation reaction is heating the cladding, causing additional increase of the reaction rate. This self-enhancing phenomenon can initiate thermal escalation. The thermal design of the LORELEI test device should demonstrate a prevention of thermal escalation during the experimental sequence, in normal operation and in accidental scenarios.

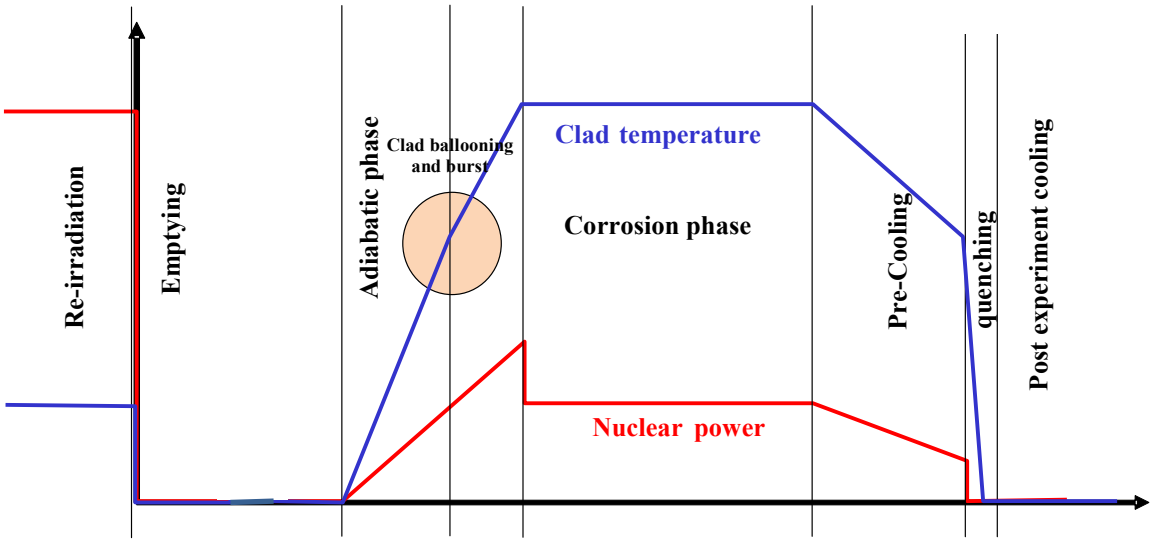


Fig 1. The LORELEI experimental sequence

2. The numerical model

A 2D axi-symmetric, heat transfer model coupled with first order differential equations was developed in COMSOL Multiphysics software. The power generated by the oxidation reaction of the Zirconium cladding during the thermal sequence has been defined as a first order differential equation and coupled to the temperature variation in the model (instead of coupling chemical reaction). The reaction rate constant, K_p, is given in equation 1 and the amount of Zirconium reacted, w, is given in equation 2[1]:

(1) $$K_p = A \exp\left(\frac{-E_a}{RT}\right)$$

(2) $$w^2 = K_p \cdot t$$

where A is the Arrhenius constant, E_a the activation energy, R the universal gas constant, T the cladding temperature and t is the time. A non-isothermal model was applied that solves the amount of Zirconium reacted at each time step according to the cladding temperature.
The power generated in the reaction, Q, is given in equation 3:

(3) $$Q = \frac{\Delta H \times \Delta w \times S}{\delta t}$$

where ΔH is the enthalpy of reaction, Δw the amount of Zirconium reacted at the current time step, S the surface area and δt the time step.
The values of the pre-exponential factor A and the activation energies for the oxidation of zirconium and zircaloy alloys (Zircaloy-2 and zircaloy-4) were determined experimentally by several research groups. This study focused on the conservative values of Baker and Just and the more realistic values of Cathcart and Pawel. Table presents the values published for the temperature range relevant to LOCA scenarios by the two groups.

Table 1: Constants for Arrhenius equation of zirconium oxidation reaction

Research group	Alloy type	Temperature range [K]	A [(mgZr/cm2)2/s]	Ea [J/mol]
Baker-Just [2]	zirconium	1273-2125	333*105	190,465
Cathcart-Pawel [2]	Zircaloy-4	1273-1773	29.32*105	167,190

The system position was defined using a mathematical simulator (differential equation) of a PID controller that was implemented in the model. The PID controller calculates the position of the system (i.e. the power generated in the fuel sample and in the device components) that will generate the required clad temperature profile. Another simulator of a PID controller was defined and implemented to operate a peripheral heater that generates adiabatic conditions for the fuel sample, during the adiabatic heating phase.

3. Results

Figure 2 presents the resulted maximum cladding temperature change in time (at the hot spot, in blue line) and the corresponding position of the displacement device (in red line). The hot spot temperature variation in time is similar to the required profile according to the experimental objectives and the displacement device position throughout the experimental phases is in its range of motion.

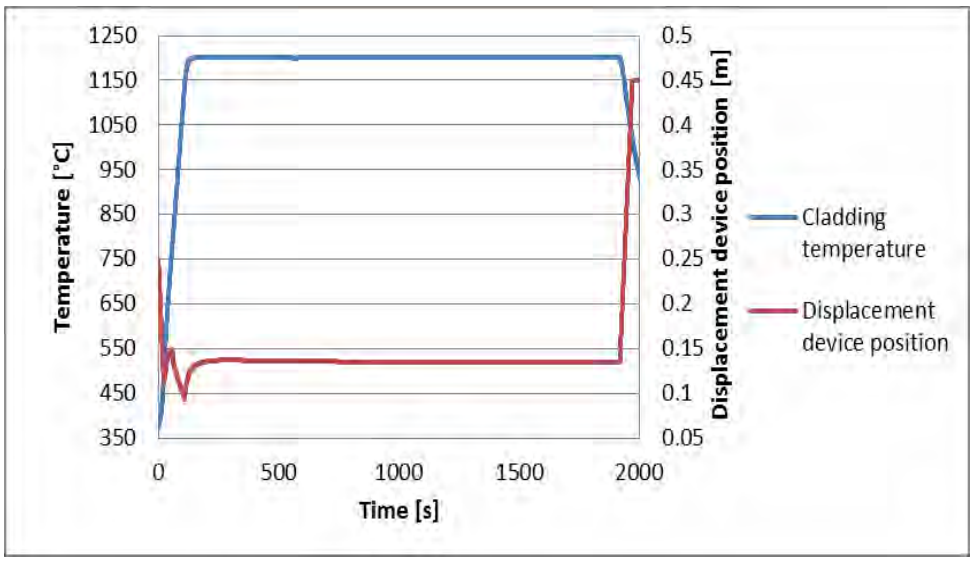


Fig 2. Displacement device position and cladding maximal temperature throughout the experimental sequence

Figures 3 and 4 presents a sensitivity study that calculates for a given displacement device location function (calculated for a most probable case), the deviation of the hot spot from the required profile due to experimental uncertainties. It can be seen that the cladding temperature is far enough from the Zirconium melting temperature (safety limit).

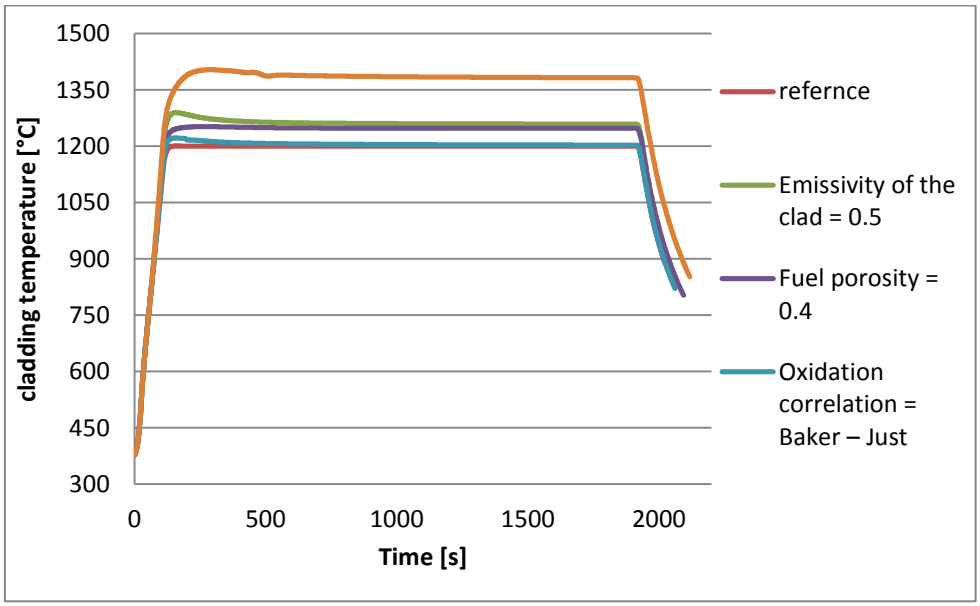


Fig 3. Cladding temperature profile due to various parameters

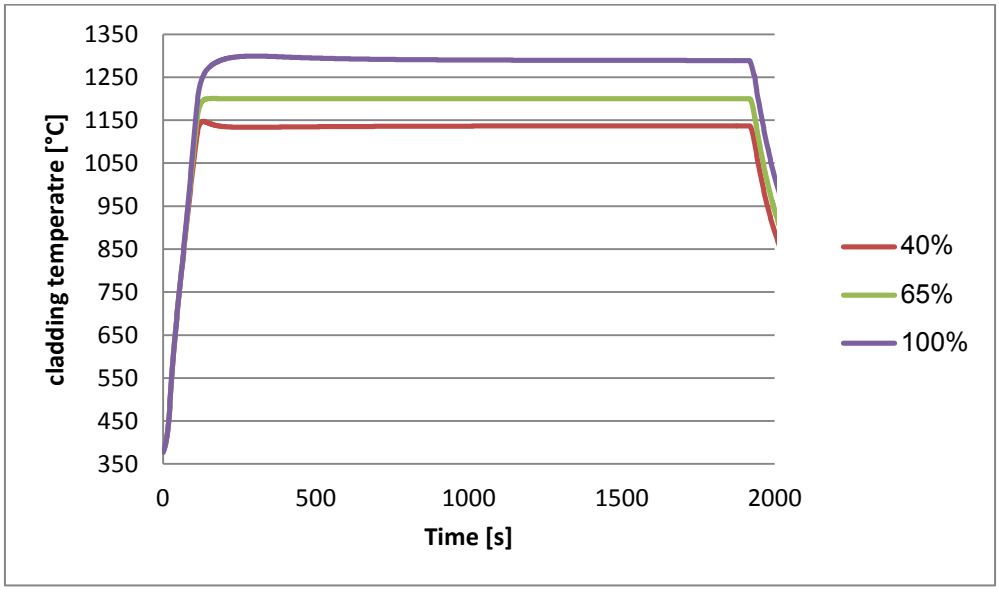


Fig 4. Cladding temperature profile due to different strain levels

4. CONCLUSIONS

According to this study, the conceptual design of the LORELEI test device has the ability to generate the required conditions in all experimental phases. The current design is robust and ensures safety in critical abnormal scenarios.

The sensitivity of the device temperature to several uncertainties and unexpected phenomena was defined with a coupled COMSOL model. A method to control the experiment without direct measurement of the temperature on the clad was suggested.

REFERENCES

1. D. G.Cacuci (Editor), Handbook of Nuclear Engineering, Springer 1st edition, 2010
2. Nuclear Fuel Behavior in Loss-of-Coolant Accident (LOCA) Conditions, State of the Art Report, OECD, 2009

NUMERICAL SIMULATION OF A SINGLE-PHASE CLOSED-LOOP THERMO-SIPHON IN LORELEI TEST DEVICE

D. GITELMAN, H. SHENHA, A. SASSON, Y. WEISS
Rotem Ind
Mishor Yamin, D.N Arava - Israel

M. KATZ
NRCN
P.O.Box 9001 Beer Sheva, 84190 - Israel

CH. GONNIER, D. TARABELLI
French Atomic Energy Commission (CEA)
Cadarache Centre - France

ABSTRACT

This work presents an investigation of a single-phase thermo-siphon flow in the LORELEI test device, as part of the conceptual design and optimization study. A Numerical simulation of the conjugated turbulent natural convection and heat transfer within a 3D geometry was performed by FLUENT. The numerical model includes a non-uniform axial and azimuthal distribution of heat generation in the device structure, due to gamma heating. The study presents irregular flow field where circulations occurs in the water cold channel due to strong apposed buoyancy forces.

1. INTRODUCTION

The LORELEI experimental setup in the Jules Horowitz Reactor (JHR)[1] is dedicated for the study of fuel during a Loss of Coolant Accident (LOCA). The main objective of the LORELEI[2] (Light-Water One-Rod Equipment for LOCA Experimental Investigation) test device is to study the thermal-mechanical behavior of fuel during a LOCA accident and to produce a short half-life fission products to characterize the potential source term. In order to study those phenomena, the fuel sample will experience a transient neutron flux field, which in turn will generate a Linear Heat Generation Rate (LHGR) and determine the temperature of the fuel and its cladding, simulating the behavior of the fuel and the cladding during a LOCA accident. In order to reproduce a LOCA-type transient sequence presented in Figure 1, the experimental test device will be mounted on a displacement device located in a dedicated water channel through the Beryllium reflector.
The displacement device moves the test device in the flux field in order to generate a representing LHGR in the fuel or temperature of its cladding.
The LOCA-type transient sequence has four major features:

- An adiabatic heating of the fuel up to the ballooning and burst occurrence.
- High temperature plateau which will promote clad oxidation.
- Passive precooling by thermal inertia.
- Water re-flooding and quenching.

The challenge in the thermo-hydraulic design of the LORELEI test section is in defining a one closed water capsule design that can operate as a thermo-siphon at re-irradiation phase and also can reproduce all LOCA-type transient sequence phases. A thermo-siphon at re-irradiation phase should be able to remove nominal power with uncertainty operation margin of 3.3. The complexity of the flow field in the LORELEI test device, as a closed-loop thermo-siphon, is due to the opposing forces in the device - buoyancy forces and natural convection

flow generated (mainly) by the fuel power in the hot channel, opposed by buoyancy forces generated by non-uniform gamma power generated in the device structure. This thermo-hydraulic design should be validated and verified to fill all safety and regulation requirements.

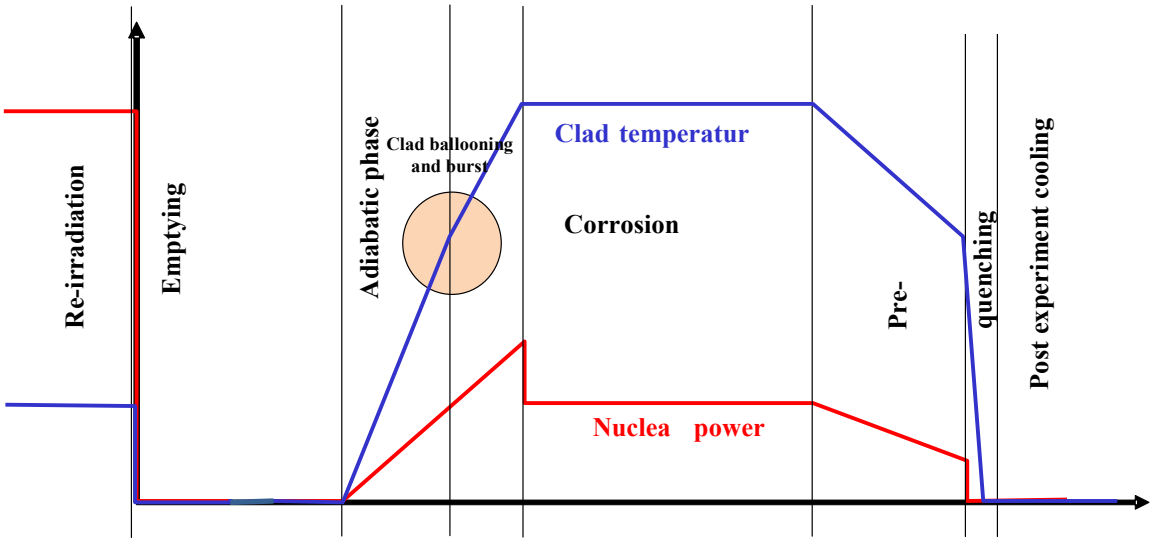


Fig 1. LOCA-type transient sequence

As a first stage, an average 2D axisymmetric model was studied and compared with a 1D CATHARE analysis. Modeling of a 3D power distribution in the system, generated by gamma heating, presents a very complex flow field due to the asymmetric opposed buoyancy forces.

2. NUMERICAL MODEL

The numerical calculations were performed by FLUENT, commercial CFD software. As a consequence of a non-uniform axial and azimuthal distribution of heat sources shown in Figure 2 and in order to have complete view of the flow, 3D geometry was used.

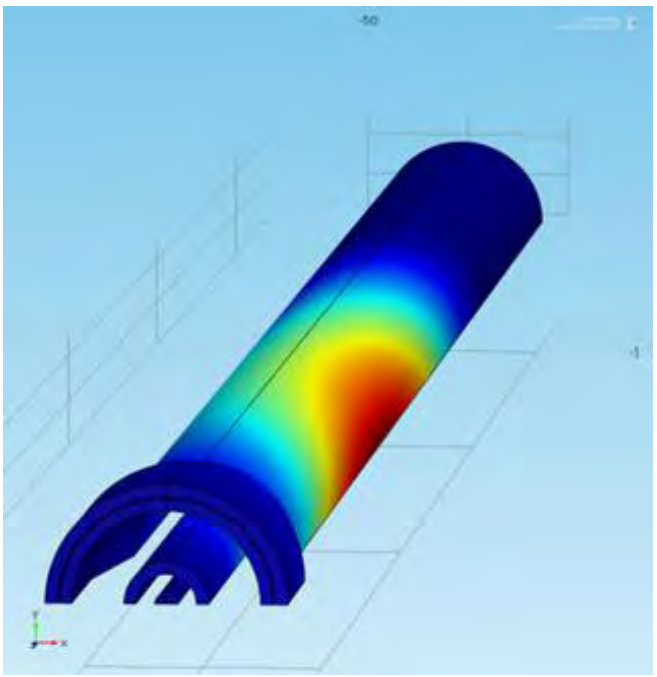


Fig 2. Non-uniform axial and azimuthal gamma heating distribution

A primarily nuclear heating calculation of LORELEI device performed by CEA showed that there is axial middle plane symmetry of heating sources generated by gamma radiation. Therefore, only one half of the experimental capsule body was simulated. The device geometry is shown in Figure 3.

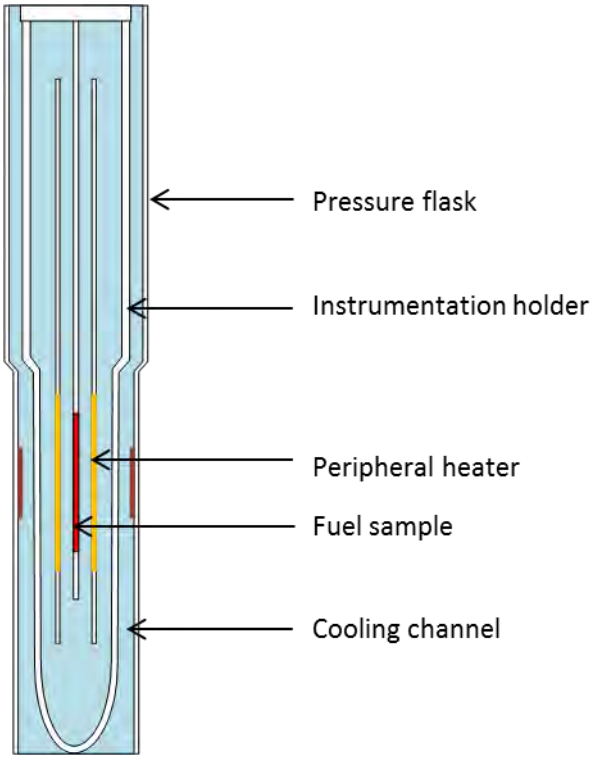


Fig 3. Schematic description of the LORELEI in-pile device

Hexahedron (bricks) mesh method was chosen in order to line up with the flow direction and with the wall easily and also for its better solution accuracy. Results of different mesh size models were compared in order to insure solution mesh independence. The final mesh which consists of about 1.5M elements is shown in Figure 4.

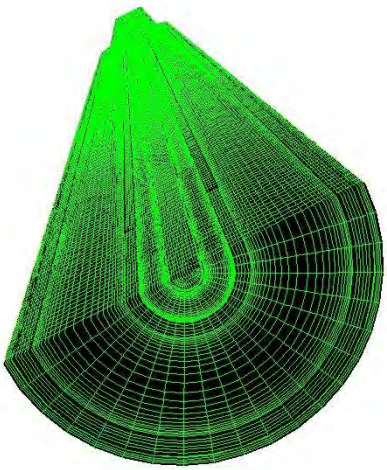


Fig 4. Numerical mesh in a 3D model, 1.5M elements

Conjugated turbulent natural convection and heat transfer was solved. The pressure of the system was set to 70 bars, which is the nominal pressure of the re-irradiation phase. Due to the lack of experimental results of similar problems in the literature, the results of three different RANS turbulent models (k-epsilon, k-omega and k-omega SST) were compered. Figure 5 presents a comparison of the results, streamlines colored according to the velocity magnitude. It can be seen that for all models the flow field has the same pattern. There is a slight difference in mass flow rate and water maximum temperature summarized in Tab 1. Those are major parameters that indicate device ability to passively remove generated heat.

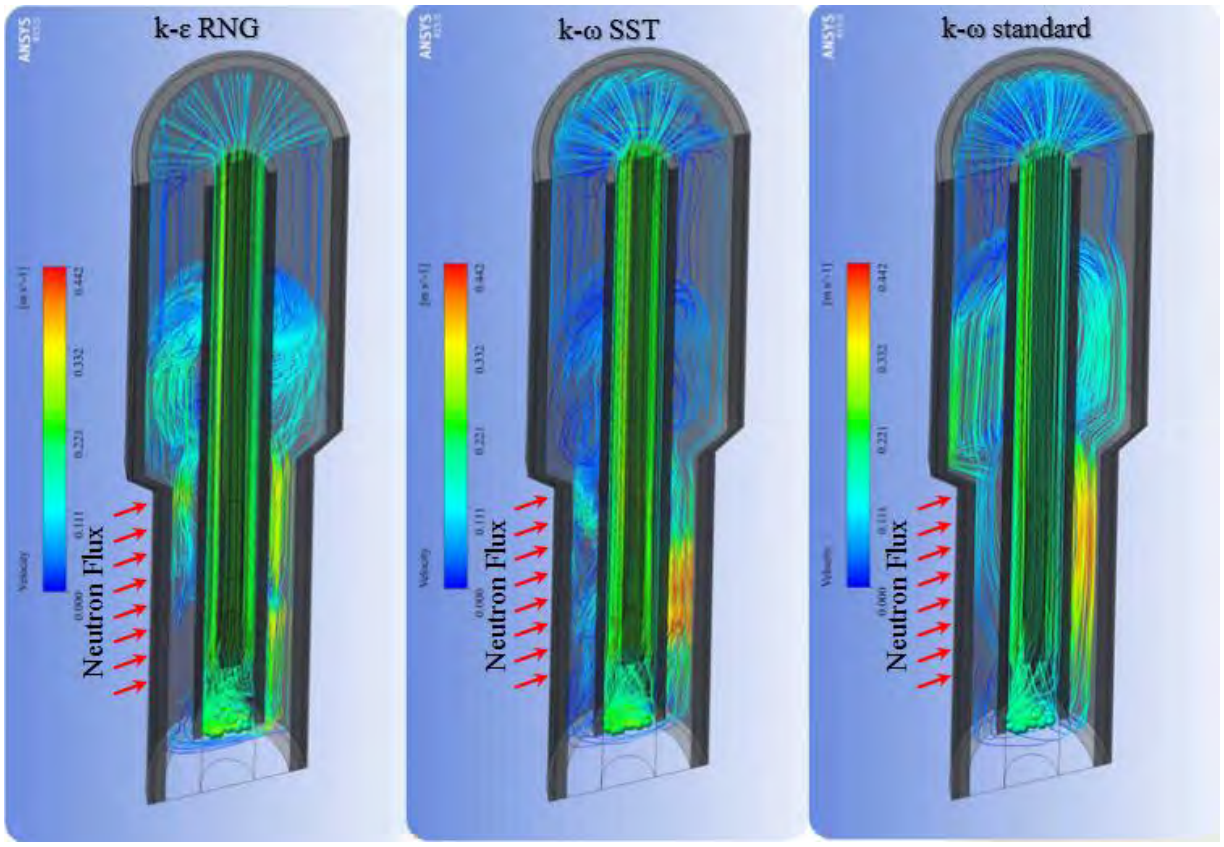


Fig 5. Velocity stream lines for different turbulence models

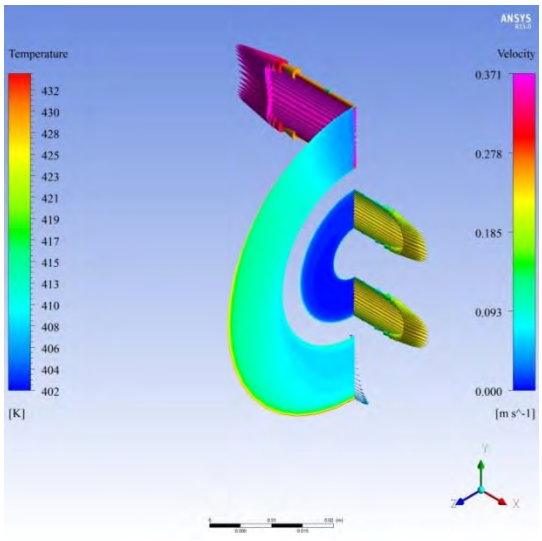
	k-ε RNG	k-ω standard	k-ω SST
Mass flow rate [kg/s]	0.08	0.071	0.08
Maximum water temperature [°C]	166	176	182

Tab 1: Mass flow rate and maximum water temperature for nominal power conditions

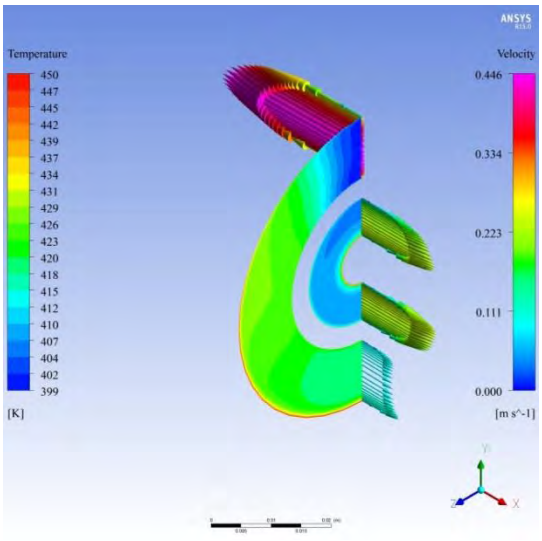
A k-ε turbulence RNG model with enhanced wall treatment was chosen, as a viscous model for the flow, for its lower need in computational resources during solving stage. Validation experiments are needed to indicate which model has better predictions.

3. RESULTS

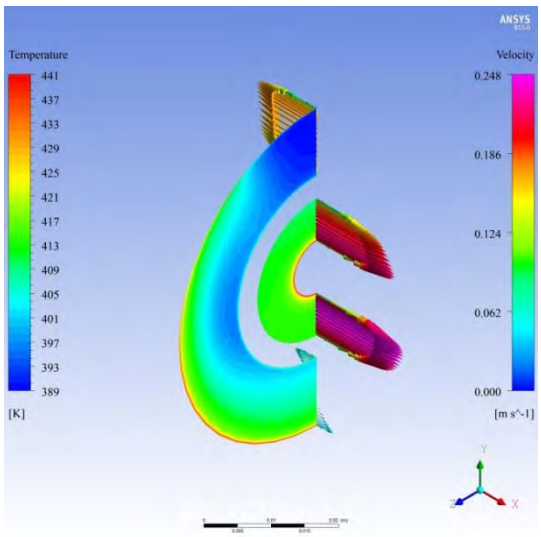
The simulation shows that at the influx part of the inner flask there is an azimuthal temperature distribution as a result of the azimuthal gamma heating distribution. This thermal azimuthal distribution generates local circulations in the flow field. Figure 6 presents temperature and velocity radial and azimuthal distributions in the water channels at the fuel rod's inlet, center and outlet cross sections, respectively.



a. Fuel bottom end cross section



b. Fuel middle cross section



c. Fuel top end cross section

Fig 6. Velocity vectors and temperature contours at different cross sections

4. CONCLUSIONS

In this study, a heat removal ability of the device was verified. The thermosyphon flow in the LORELEI test device during the re-irradiation phase was analyzed. The strong gamma radiation field surrounding the test section generates non-uniform gamma power in the structure. The consequent flow field is irregular where circulations occur in the cold channel due to strong buoyancy forces. In order to improve the flow field, the balance between buoyancy forces and friction losses should be changed. Benchmark experiment must be performed in order to define proper turbulence model for numerical simulation.

REFERENCES

[1] Estrade J. et al, The Jules Horowitz Reactor: a new performance European MTR (Material Testing Reactor) with modern experimental capacities – Building an international user facility. Research Reactor Fuel Management 2013. 21-25 April, St-Petersburg, Russia, (2013).

[2] Gonnier C. et al, Fuel and material irradiation hosting systems in the Jules Horowitz Reactor. Joint IGORR 2013 & IAEA Technical Meeting, 13-18 October, DCC, Daejeon, Korea, (2013).

Fission-induced Creep of U-Mo/Al Dispersion Fuel Meat

Yeon Soo KIM
Argonne National Laboratory
9700 S. Cass Ave, Argonne, IL 60439 – USA

G.Y. JEONG, D-S SOHN
Ulsan National Institute of Science and Technology
50 UNIST-gil, Eonyang-eup, Ulju-gun, Ulsan 689-798 – Republic of Korea

ABSTRACT

Post-irradiation U-Mo/Al dispersion plates showed fuel meat relocation away from the plate transverse end toward the transverse center region and, as a result, fuel meat thickness was additionally increased in a region between the plate transverse end and the center. This phenomenon is attributed to the fission-induced creep of fuel meat. By this mechanism, the stresses generated by the meat swelling at the fuel-meat-transverse end are effectively relieved. An ABAQUS finite element method has been used to simulate this fuel behavior in the plate-transverse-end regions. The objectives of this study are to confirm that the fuel microstructural evolution was indeed caused by the creep of fuel meat and to obtain the creep-rate constant for the IL and Al.

1. INTRODUCTION

U-Mo dispersion in Al, designated as U-Mo/Al, showed meat mass relocation away from the fuel edge close to the rail region, a similar phenomenon observed in a foil fuel [1]. U-Mo particle deformation and sintering with neighboring U-Mo particles were also observed.

In dispersion fuel meat, fuel particle swelling induced by fission products has to be accommodated by the plastic deformation of the more ductile aluminum matrix and newly forming interaction layers (ILs) between the U-Mo particles and Al. It is plausible to that, if the fuel particles move, the Al matrix and IL should both also move. The local stress state is much more complex in a dispersion fuel meat than in a fuel foil, and there must be local adjustments in the neighboring fuel particles, the matrix, and IL. Nonetheless, the overriding direction of the movement of the U-Mo particle, Al matrix and IL at a given spot should be the same as observed in a monolithic fuel [1].

To analyze creep in a U-Mo/Al dispersion fuel, creep behaviors of U-Mo, Al matrix and IL must all be treated. In the monolithic fuel case, fuel swelling is a result of fission product accumulation and fission gas bubble formation. In a dispersion fuel case, fuel swelling occurs by fission product accumulation and fission gas bubble formation, and simultaneously fuel is consumed by interaction layer growth. Therefore, the volume change of U-Mo before-and-after irradiation yields smaller fuel swelling than the measured in a monolithic fuel with the same burnup. In a dispersion fuel case, the loss in fuel swelling is compensated by the volume expansion by IL growth. Hence, fuel meat swelling in a dispersion U-Mo/Al plate corresponds to fuel foil swelling in a monolithic fuel plate.

For the present work, we measured meat volume swelling for two plates: One with a pure Al matrix, the other with a Si addition in the matrix. The burnup-dependent meat swelling is

expressed as a function of burnup. The calculated meat volume is compared with the measured at EOL.

ABAQUS finite element analysis (FEA) was performed using the assumption that mass relocation in the fuel meat is caused by only the continuous phase, a homogenized medium that is composed of U-Mo, Al and IL, given by burnup-dependent functions. By comparing with the measured meat volume, the creep rates for Al and IL were iteratively found. In addition, another objective of the work was to show using ABAQUS FEA that creep and mass relocation of the U-Mo/Al dispersion meat can be simulated.

2. EXPERIMENTAL

The miniplates analyzed for this work are summarized in **Table 1**. Plate A used a LEU powder and Plate B used a HEU (~44.4% U-235) powder. The dimensions are 100 (axial) x 25 (transverse) x 1.4 (thickness) mm, and the meat dimensions are 82 x 19 x 0.64 mm. Plate B was loaded in the irradiation vehicle in such a way that one of the transverse ends was closer to the ATR core, so higher power and burnup prevailed at the end. Thereby a power peaking occurs at the closer-to-ATR-core end. Plate A, however, was flipped sideways between cycles to have more uniform power and burnup in the width (transverse) direction. The test plates were sectioned at the axial center plane and metallography was performed on one of the exposed transverse cross sections. Fuel meat thicknesses were measured at an interval of 0.5 mm for both plates. Calculated temperatures at the meat-width-and-axial center are shown in **Fig. 1**.

Table 1 Summary of irradiated test parameters of plates included in the analysis

Plate ID	Fuel Type	Meat U density (gU/cm^3)	Enrichment (% U-235)	Average particle size (μm)	Time (EFPd)	Average BU (% LEU Eq.)	x (mm)
A	U-10Mo/Al	6	19.5	70	257	78	2.5
B	U-7Mo/Al-5Si	8	44.4	50	98	64	2.0

x is distance between the location of the peak plate thickness and the meat edge.

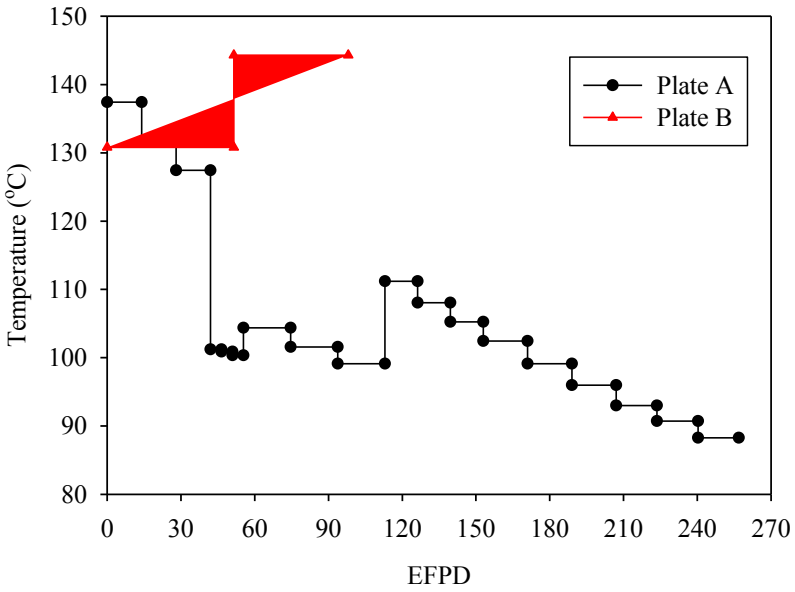


Fig. 1 Temperatures at meat center for Plate A and Plate B.

3. MEAT SWELLING MODELING

The fuel meat volume changes according to fuel particle swelling by fission products, IL growth, and fuel particle and Al consumption by IL growth. Fuel meat swelling at the meat transversal and axial center as a function of fission density was calculated as shown in **Fig. 2**. The comparison of the EOL volume fractions of the U-Mo, IL, and Al with the measured values from PIE shows the accuracy of the modeling.

Although substantial fuel swelling occurs, the change of fuel volume is small (~20%) due to simultaneous consumption by IL growth and more importantly porosity in the meat was excluded in the calculation.

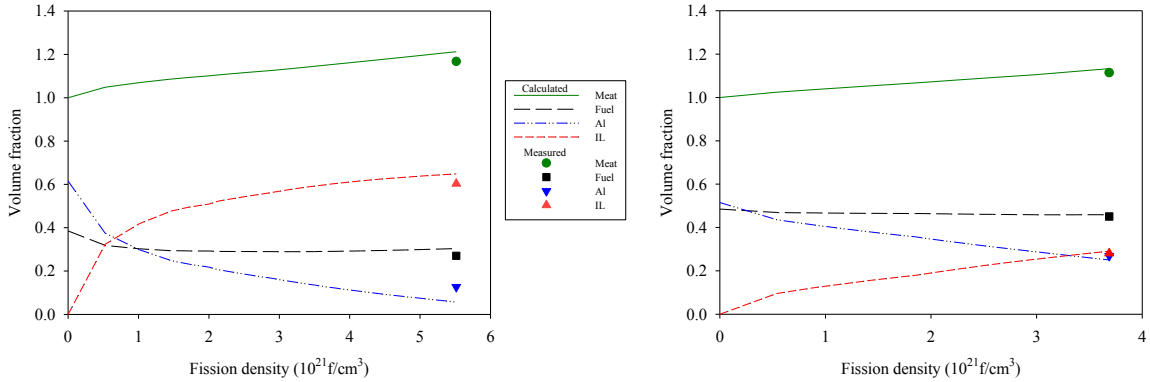


Fig. 2 Calculated meat swelling evolution as a function of fission density at meat width and axial center location for Plate A and Plate B. Changes of volume fractions for U-Mo, Al matrix, and IL are also shown and the EOL values are compared with measured data.

The calculated EOL meat swelling without considering creep and mass relocation is compared with the measured at locations with an interval of 0.5 mm in the width direction (**Fig. 3**).

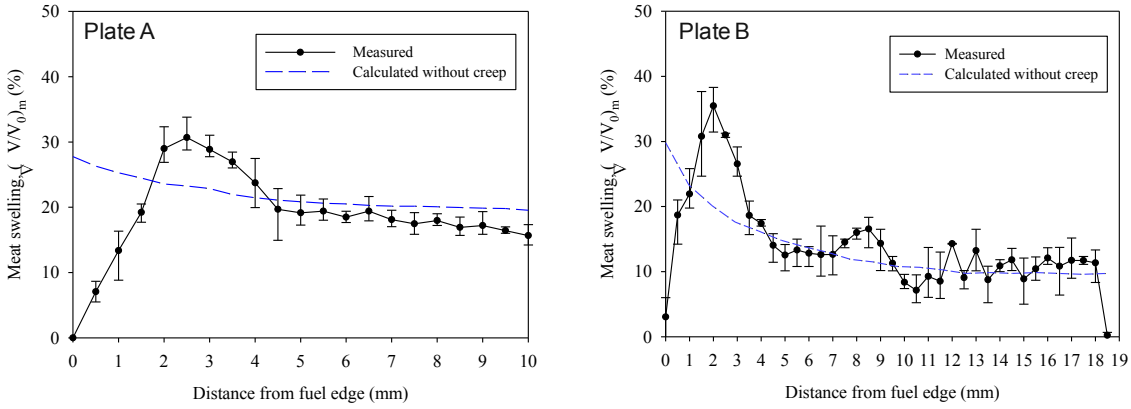


Fig. 3 Comparison of the calculated meat swelling with the measured as a function of distance from meat edge.

4. ABAQUS SIMULATION

Fission-induced creep of U-Mo is available in the literature [1]. Ref. [1] dealt with plates of a monolithic U-Mo foil directly encapsulated in an Al alloy cladding in plate geometry and employed the following equation for U-Mo creep

$$\dot{\varepsilon}_c = A\sigma\dot{f} \tag{10}$$

where $\dot{\varepsilon}_c$ is the equivalent creep strain rate (s^{-1}), A the creep rate coefficient (cm^3/MPa), σ the equivalent stress (MPa), and $\dot{f}$ the fission rate (fissions/cm^3-s).

For the monolithic U-Mo case, U-Mo is the continuous phase. Hence, U-Mo undergoes creep and, as a result, produces mass relocation. However, for a typical U-Mo/Al case, in which the fuel volume fraction is smaller than the combined volume fraction of Al and IL, the Al matrix and IL combined are the continuous phase and U-Mo particles are isolated in the matrix and IL. Hence, the creep in the Al and IL results in mass relocation while the U-Mo particles remain mostly inactive in regard to mass relocation. To simplify ABAQUS simulation, the Al matrix and IL are treated as a single phase by giving an averaged creep rate coefficient. The creep rate coefficient in Eq.(10) is modified by

$$A = v_{Al} A_{Al} + v_{IL} A_{IL} \tag{11}$$

where v are the volume fractions and A the creep rate constants. Notice that the contribution by U-Mo is assumed negligible.

The total meat swelling (i.e. fission induced swelling of fuel particle, volume expansion due to IL growth, fuel and Al matrix volume consumption due to IL growth) is given by Eq. (2).

The meat true strain is derived from the meat swelling as follows:

$$\varepsilon_{true} = \ln\left[1 + \left(\frac{\Delta V}{V_0}\right)_m\right] \tag{12}$$

Table 2 summarizes material properties used for ABAQUS simulations.

Table 2 Summary of material properties and calculation scheme in ABAQUS simulation

	Al 6061 Cladding	U-Mo Fuel particle	Ref.
Poisson's ratio	0.34	0.34	[1]
Young's modulus (GPa)	66	85	[1]
Yield strength (MPa)	280 MPa (irradiation hardening)	-	[1]
Creep rate coefficient (10^{-25} cm^3/MPa)	-	500	[1]

The ABAQUS simulation result for the meat swelling is compared with the measured in **Fig. 4**. The best results were obtained when the creep rate coefficient for Al matrix was set $100x10^{-25}$ cm^3/MPa and that for IL $250x10^{-25}$ cm^3/MPa. It appeared that the addition of Si did not change the creep rate of IL and Al matrix. These creep rate coefficients are considered effective values fitted for the test results. Therefore, a more detailed simulation including the effect of the presence of U-Mo particles is necessary to obtain more realistic data.

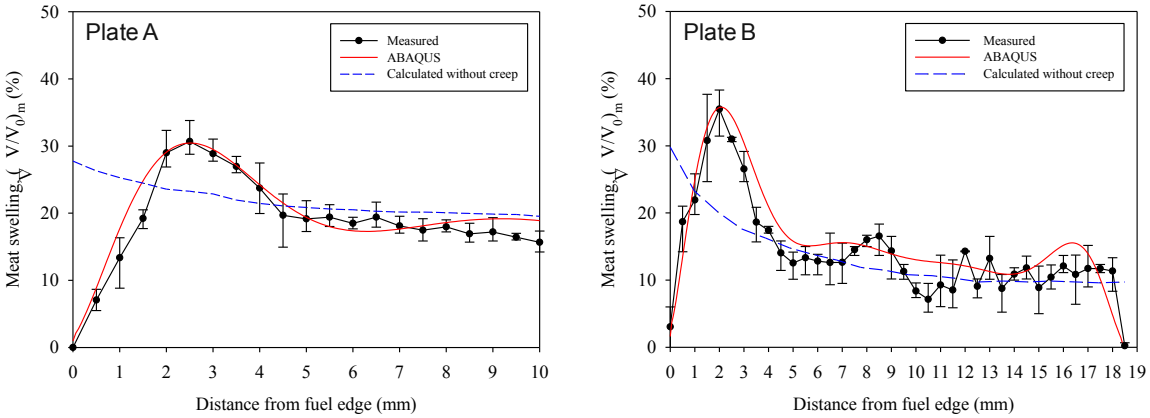


Fig. 4 ABAQUS simulation result for meat swelling compared with the measured. The calculated meat swelling without considering creep and mass relocation is also given for comparison. The best simulation were obtained when the creep rate coefficients were set 100×10^{-25} cm^3/MPa for Al matrix and 250×10^{-25} cm^3/Mpa for IL.

5. CONCLUSIONS

The fuel meat swelling of two U-Mo/Al dispersion fuel plates was modeled. One is of a pure Al matrix and the other with 5% Si addition. The model considers U-Mo fuel particle swelling and volume expansion by IL growth subtracted by fuel and Al volume consumption by IL.

The meat swelling model was used to calculate meat swelling and the result is inputted for ABAQUS finite element analysis (FEA) simulation. In our modeling, only the continuous phase, Al matrix and IL combined, was allowed to undergo creep. The best ABAQUS FEA was produced when the creep rate coefficient was set 250×10^{-25} cm^3/MPa for IL, and 100×10^{-25} cm^3/MPa for Al. These creep rate coefficients are considered effective values fit for the test results. Therefore, a more detailed simulation including the effect of the presence of U-Mo particles is necessary to obtain realistic data.

ACKNOWLEDGMENT

The authors are grateful to Dr. J.S. Cheon of KAERI for his help with ABAQUS simulation. The test plate data were obtained in the US GTRI-CONVERT program. The submitted manuscript has been created by the UChicago Argonne, LCC as Operator of Argonne National Laboratory under Contract No.DE-AC-02-06CH11357 between UChicago Argonne, LLC and the US Department of Energy. The UNIST contribution in this work was supported by the National Research Foundation of Korea (NRF) grant funded by the Korean government (Ministry of Education, Science and Technology) (No. 2011-0031771).

REFERENCES

[1] Yeon Soo Kim, G.L. Hofman, J.S. Cheon, A.B. Robinson, D.M. Wachs, J. Nucl. Mater., 437 (2013) 37.

Concept of the LORELEI test device for LOCA experiment in the JHR reactor

M. Szanto, N. Moran, A. Azulay, O. Mileguir, Y. Weiss

Rotem Industries LTD
Mishor Yamin, D.N Arava 86800 Israel

L. Ferry

French Atomic Energy Commission (CEA)
Cadarache Centre, France

Abstract

In JHR material testing reactor, which is currently under construction, one significant experimental device is the LORELEI testing device. The objective is to examine the LOCA sequence influence on: thermo-mechanical behavior of the fuel clad, possible fuel relocation, corrosion at high temperature, oxidation, hydriding and resulted clad embrittlement. The current presentation describes the approach applied defining the concept of the device, using high-level design combined with computational and experimental tools.

Introduction

Modeling of nuclear fuel cladding behavior during a Loss of Coolant accident (LOCA) is a principal requirement in reactor safety analysis. Former safety criteria were obtained from experiments during the 1970's, conducted mainly with fresh fuels. Changes in modern fuel design, introduction of new cladding materials and motivation towards higher burn-ups have generated a need to re-examine safety criteria and their continued validity. This led to the growing development of both experiments and simulations meant to address this need. The Halden IFA-650 [1] series of experiments for example, beginning in the early 2000's have clearly shown that existing criteria and experimental data are insufficient for the growing demand for higher burn-ups.

In JHR material testing reactor, which is currently under construction, one significant experimental device is the LORELEI testing device. The objective is to examine the LOCA sequence influence on: thermo-mechanical behavior of the fuel clad, possible fuel relocation, corrosion at high temperature, oxidation, hydriding and resulted clad embrittlement. The device is a single rod closed loop system built inside a special pressure flask and placed on a displacement device inside a defined channel in the reflector. Several operational constrains on the device, as required by the reactor operational philosophy, resulted quite a few challenges in

the design. Constrains as: pre experimental re-irradiation phase under thermo-syphonic flow, application of active insulation to simulate the surrounding fuel, application of tensile force during refolding simulation, controlling the experiment with non-direct temperature measurement, etc. requires sophisticated solutions. The main objective of the conceptual design was to remove the uncertainties of those challenging requirements. The current presentation describes the approach applied defining the concept of the device, using sophisticated design combined with computational and experimental tools.

Objectives:

The objective of the LORELEI testing device is to simulate thermo-mechanical behaviour of one LWR rod in the following aspects:

- Ballooning and clad burst with possible fuel relocation inside and outside the rod.
- Corrosion at high temperature, oxidation, hydriding and resulting clad
- Embrittlement.
- Quenching and post-quench behaviour (mechanical strength).
- Radiological consequences : FP source term.

Motivations:

- Testing of new cladding material.
- New fuel (UO2, MOX, additives,..).
- High Burn-Up effect on the cladding material (corrosion and hydriding due to normal operation).
- Investigation of LOCA phenomenology (fuel relocation, possible coupling between fuel and clad behaviour, etc.).

The LOCA sequence realization is according to the plot in Fig. 1.

The experimental device that accomplishes the sequence in Fig. 1 is under development in ROTEM industries. The conceptual design is shown in figure 2.

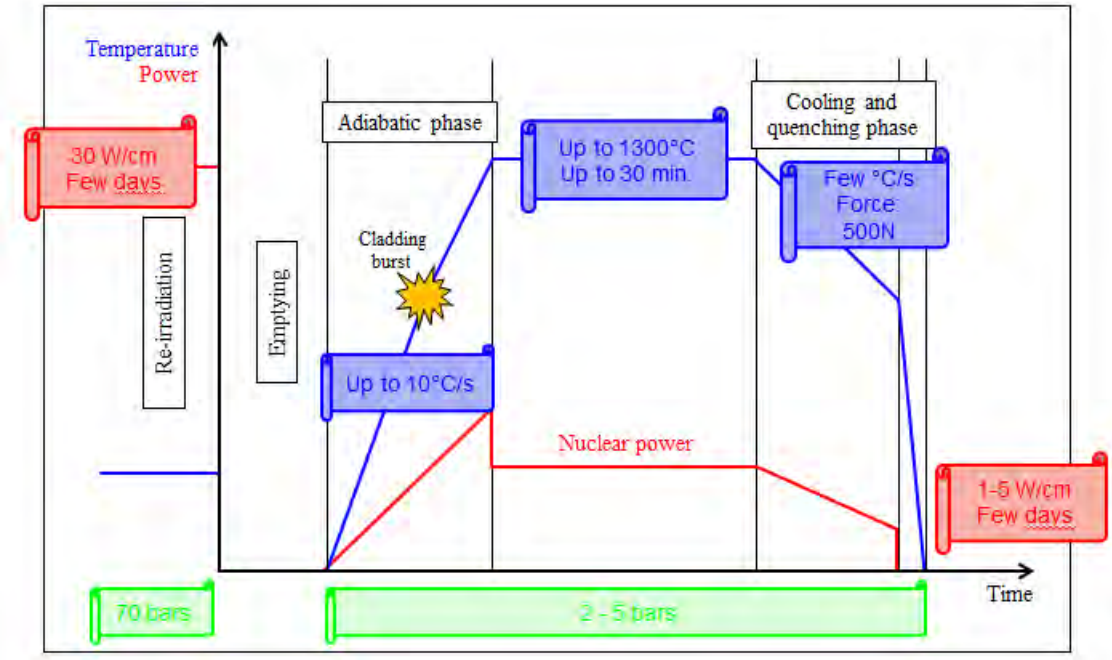
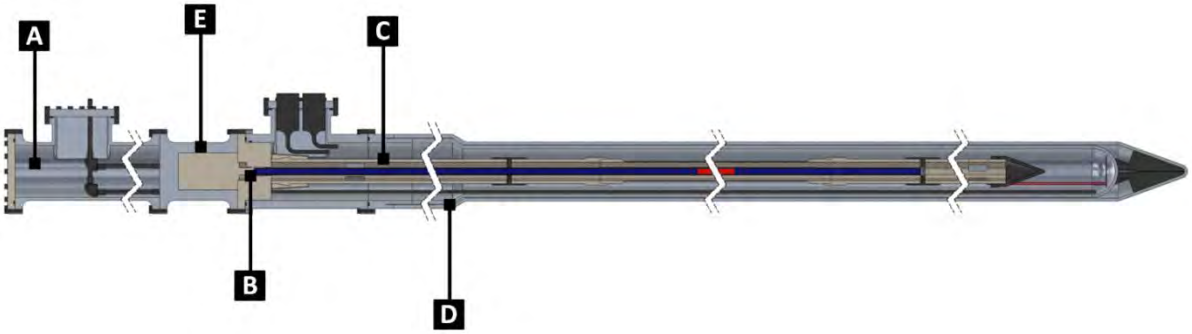


Figure 1: The sequence of the LOCA test.



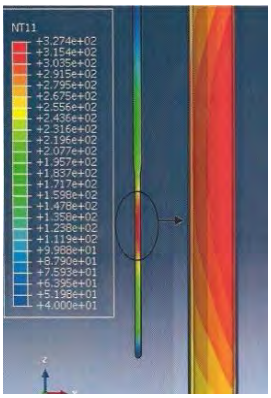
A - Extension that consists of all the on device instrumentations such as valves, filters, etc.
B - Sample holder (B). **C** - Instrumentation holder.
D - Pressure flasks. **E** - Device heads.

Figure 2: Conceptual design of the experimental device.

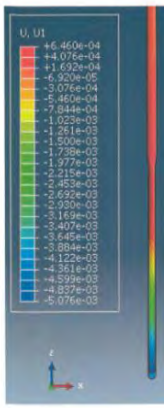
Challenges in the mechanical design

Among the major challenges in the roadmap toward the design are:

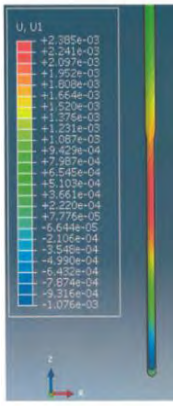
- Controlling flask distortion resulted by azimuthal temperature distribution due to non symmetrical Gamma radiation heating. As shown in figure 3, different boundary conditions have been simulated to see the impact on the perpendicular distortion.



Azimuthal temperature distribution



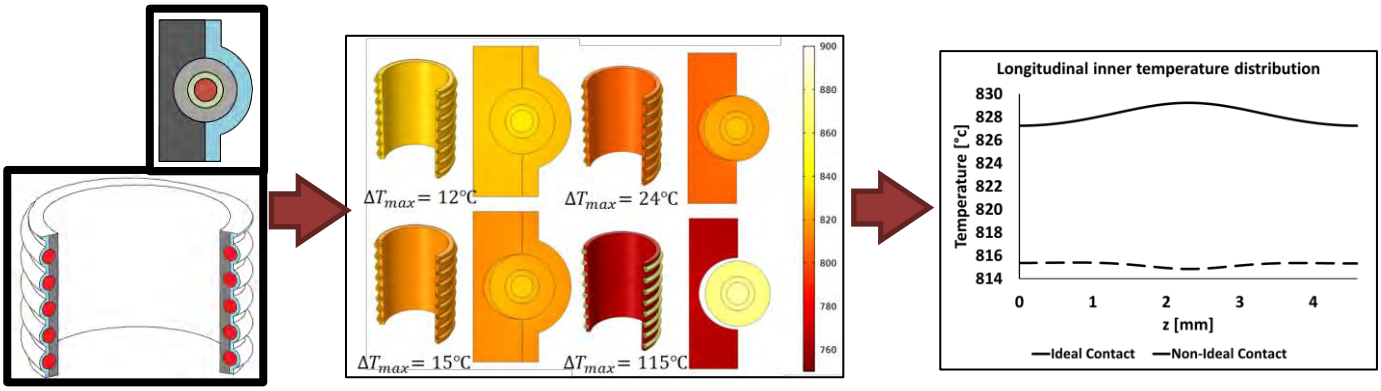
Free at the bottom



Fixed at the bottom

Figure 3: Numerical analysis of the flasks distortion.

- Development of a high temperature (~900 ^{o}C) very high power density, peripheral heating element (10-20 Kw in a ~ 60 cm long ~ 25 mm inner and 31 mm outer diameter hollow cylinder). The heating element, serves as an active insulation, simulates the effect of the fuel rods surrounding the test rod, by creating an adiabatic thermal condition.
  The development based on a distinctive idea supported by numerical computations. To validate the design, a prototype was build and tested. The above described process is shown in figure 4.



Concept and Design

Computational backup

Testing

Resulted final product



Figure 4: Development process of the high power density heating element.

Additional challenges in the mechanical development and design are:

- Realization of a thermo-syphonic heat removal system,
- Non-direct temperature measurement,
- Assembly in a hot cell
- Compliance with nuclear safety regulation.
- Safety oriented design: reliability in the measurements, inherent prevention of temperature escalation, double walled flask and piping in order to detect leakage, emptying and re-flooding in short time, etc.

Summery

- The conceptual design of a single rod out of core LOCA sequence test loop was shown
- The project involves multi-disciplinary subjects, such as Mechanical engineering, Thermo-dynamics, nuclear physics, Material engineering
- Technical challenges of the loop development were presented.

Reference:

1. Tero Manngård, Ali Massih, Jan-Olof Stengård(VTT), "Evaluation of the Halden IFA-650 loss-of-coolant accident experiments 2, 3 and 4," Quantum Technologies AB, Uppsala, Sweden, 2012.

DEVELOPMENT OF U(Mo) DISPERSION FUEL MINIPLATES WITH Al(Si) MATRIX. MICROSTRUCTURAL CHARACTERIZATION.

M. MIRANDOU [(1)*], S. ARICÓ [(1,2)], S. BALART [(1)] AND J. FABRO [(3)]

(1) Gerencia Materiales, Gerencia de Área Energía Nuclear.
(2) Instituto de Tecnología "Jorge Sabato", Universidad Nacional de General San Martín.
(3) Departamento Elementos Combustibles para Reactores de Investigación (ECRI), Gerencia de Ciclo del Combustible Nuclear (GCCN)

Comisión Nacional de Energía Atómica (CNEA), Avda. Gral. Paz 1499, B1650KNA, San Martín, Buenos Aires, Argentina.

***corresponding author e-mail**: mirandou@cnea.gov.ar

ABSTRACT

The development of U(Mo) dispersion fuel miniplates with Al(Si) matrix has been re-started at ECRI facility (CNEA) in 2011. The principal aim of this development is to obtain an interaction layer surrounding all the U(Mo) particles as a consequence of fabrication process. This interaction layer is expected to be uniform in width and formed by the Si containing phases. Miniplate meats studied in this work were made with U-7wt%Mo atomized particles dispersed in two different matrices: a mixture of pure Al and Si particles or a mixture of pure Al and atomized Al(Si) eutectic alloy being 4wt% the global amount of Si in both matrices.

Results are presented focusing on: interaction layer formation, evolution during fabrication process and characterization of final products, occasional formation of oxide layers surrounding U(Mo) particles, evolution during fabrication process and its influence on the formation of the interaction layer. Characterization was performed by OM, SEM, WDS and XRD.

1. Introduction

In the last decade a significant international effort has been dedicated to qualify U(Mo) alloy as high uranium density fuel to be used in the conversion of high flux research reactors. This conversion is needed to fulfill the reduction in U enrichment proposed by international non-proliferation agreements [1].

The addition of 7 to 10 wt % Mo to form the U(Mo) alloy is used to retain in metastable condition, at room temperature, γU phase (cI2) (stable at temperatures over 772 ºC, [2]) which performs well under irradiation [3]. A dispersion fuel element consists in U-alloy particles dispersed in a heat conducting matrix usually Al. Nevertheless when U(Mo) particles are used as fuel and pure Al as matrix, important failures appear during irradiation which conduct to break-away swelling [4, 5]. Pos-irradiation experiments have shown a significant interaction layer (IL) grown by interdiffusion between U(Mo) particles and the Al matrix which has been proved to be predominantly amorphous. This is an important factor in these failures because fission gases can migrate easily through it and accumulate at the fuel/matrix interface causing a severe weakening of the mechanical strength of the fuel plate [6, 7].

To solve this problem, the addition of Si to the Al matrix arose, among others, as one of the most promising solution. This led to a big amount of out of pile investigation which have proved the migration of Si to the IL (and concentration) due to the affinity between U and Si [8, 9, 10, 11]. To qualify U(Mo) fuel elements, Si added to Al is being evaluated through several in pile experiments. These experiments using this modified matrix have shown the positive effect of Si but has not provided, yet, reliable evidence to allow qualification of U(Mo) fuel for high flux research reactors [12,

13]. Fresh analysis of the fuel elements that performed well under irradiation demonstrated that good irradiation behavior is correlated with the formation during fabrication of a proper IL around the U(Mo) particles [14, 15]. However, very recent investigations have shown that, after fabrication process, IL forms only on part of U(Mo) surface particles and have revealed that, during irradiation, Si has a positive effect only at those locations where a Si rich layer was formed on the particle during plate manufacturing [13].

Other attempt to solve this problem is to provide the U(Mo) particles with an intentional covering previous to miniplate fabrication. This layer has the aim to prevent interdiffusion between U(Mo) particles and pure Al matrix during fabrication process as well as irradiation. Positive post irradiation results have been obtained when 600 nm Si and 1000 nm ZrN coatings are used [16, 17].

In 2012, a systematic and careful study have been initiated in CNEA – Argentina, to determine how to obtain the better IL characteristics (uniformity, composition, phases that form it, width, etc) with the lesser modifications to the fabrication process and the smallest amount of Si added to the matrix. It is supported by the experience gather from out of pile investigation of diffusion couples U(Mo)/Al and U(Mo)/Al(Si) performed since 2003 [8, 9, 18] that is now applied to the characterization of dispersion miniplates made by ECRI facility (Departamento ECRI, GCCN, CNEA).

In this work the results of the characterization of the meats of miniplates which are made with atomized U-7wt%Mo dispersed in Al-2wt%Si and Al-4wt%Si are presented. The principal aim is to obtain an IL, formed by Si-rich phases, that completely surrounds U(Mo) particles. Samples were taken at three different stages of the fabrication process to study the influence of the different fabrication steps on the morphology, concentration and phases that form the meat. Special attention was given to distribution of Si in the matrix; IL characteristics as uniformity, chemical composition, width and phases present in it. Partial transformation of U(Mo) particles was taken into account during characterization. Besides, one miniplate without Si was made as reference to observe clearer the Si effects if any.

2. Experimental procedure

Depleted U-7wt%Mo alloy (U-7Mo) as atomized particles provided by KAERI were used as fuel alloy, size ranging from 75 to 125 μm. Two different kinds of Al-Si matrices were used: one was prepared by mixing, at different ratios, pure Al (38 μm) and pure Si (25 μm) powders to reach Al-2wt%Si (Al-2Si) and Al-4wt%Si (Al-4Si). The other one was obtained by mixing pure Al particles with of eutectic Al-Si alloy particles (which Si concentration is 12 wt%) in order to obtain Al-4wt%Si as matrix global concentration (Al-4Si_E). In this last case, Si is present in the matrix as 1-2 μm pure Si precipitates. Also a pure Al matrix (Al) was used as reference.

Fuel particles and matrices were mixed and cold pressed to obtain 7 gU/cm^3 compacts which are positioned in an Al 6061 frame and TIG welded to Al 6061 covers with open corners (from now on *open welded - OW*) or full welded (from now on *FW*).

Hot rolling at 500 ºC up to 82 % reduction is used to obtain final size followed by a heat treatment of 1 h at 500 ºC and cold rolled. After hot rolling, one miniplate for each kind of Al-Si matrix was separated to be studied in the *as rolled* condition (from now on *AR*) and be compared to *full fabricated* condition (from now on *FF*). Besides, two compacts (one with Al-2Si matrix and the other with Al-4Si matrix) were specially fabricated to be studied as starting point (from now on *C*). TABLE 1 summarizes identification and characteristics of the miniplates studied in this work.

Samples were cut from each miniplate and characterized by optical microscopy (OM-Olympus BX60M), scanning electron microscopy (SEM –Philips SEM 515, and FEI QUANTA 200), energy dispersive spectroscopy (EDS-EDAX Phoenix 3.2), wave length dispersive spectroscopy (WDS – CAMECA SX50) against U, Mo, Al, and Si standards and X-Ray diffraction (XRD- Philips PW 3710 with Co *kα* radiation and PANalytical-Empyrean with Cu *kα* radiation). Crystal structures identification and the estimation of lattice parameters were obtained by direct comparison between theoretical spectrum of each phase with the experimental spectra using POWDERCELL software [19].

TABLE 1. Identification of the miniplates.

Identification	***Matrix***	***Step of fabrication process***	***Welding***
Al-FF-OW	Pure Al	Full fabricated	Open welded
2Si-C	Al-2Si	Compact	-
2Si-AR-OW	Al-2Si	As rolled	Open welded
2Si-FF-OW	Al-2Si	Full fabricated	
4Si-C	Al-4Si	Compact	-
4Si-AR-OW	Al-4Si	As rolled	Open welded
4Si-FF-OW	Al-4Si	Full fabricated	
$4Si_E$-AR-OW	Al-$4Si_E$	As rolled	
$4Si_E$-FF-OW	Al-$4Si_E$	Full fabricated	
4Si-AR-FW	Al-4Si	As rolled	Full welded
4Si-FF-FW	Al-4Si	Full fabricated	
$4Si_E$-AR-FW	Al-$4Si_E$	As rolled	
$4Si_E$-FF-FW	Al-$4Si_E$	Full fabricated	

Characterization of *open welded* set of miniplates was focused on the influence of the different fabrication steps on the morphology, concentration and phases that form the meat (i.e. U(Mo) particles, Al-Si matrices and IL) together with distribution of Si in relation with the amount of Si in the matrix. On the other hand characterization of *full welded* set of miniplates was focused on a deeper analysis of IL together with the comparison between two different ways to incorporate 4%Si to the matrix (i.e. pure Si or eutectic Al-Si alloy particles).

3. Results and Discussion

3.1 Characterization of open welded miniplates

3.1.1 Changes observed on U(Mo) particles

To study U-7Mo particles in the as received condition, a representative sample of them were stuck on a double-sided tape to perform XRD being γU and O_2U the identified phases. As there is no evidence of αU phase, cellular reaction of γU is ruled out.

Low percentage of U-7Mo particles showed low fraction of cellular reaction on samples 2Si-AR-OW, 4Si-AR-OW and $4Si_E$-AR-OW after hot rolling (500ºC). Due to final thermal treatment (500ºC-1h) the percentage of particles with any fraction of cellular reaction as well as the fraction itself on each individual particle, evidence significant growth.

After the hot rolling process U-7Mo particles developed an oxide layer (OL) with different characteristics according the relative position of the particles in the meat: *peripheral particles* or *inner particles*. This difference in oxidation was observed on all the samples independently of the amount of Si in the matrix. To clarify the idea of *peripheral or inner* U-7Mo particles, Figure 1 is presented to represent all the miniplates.

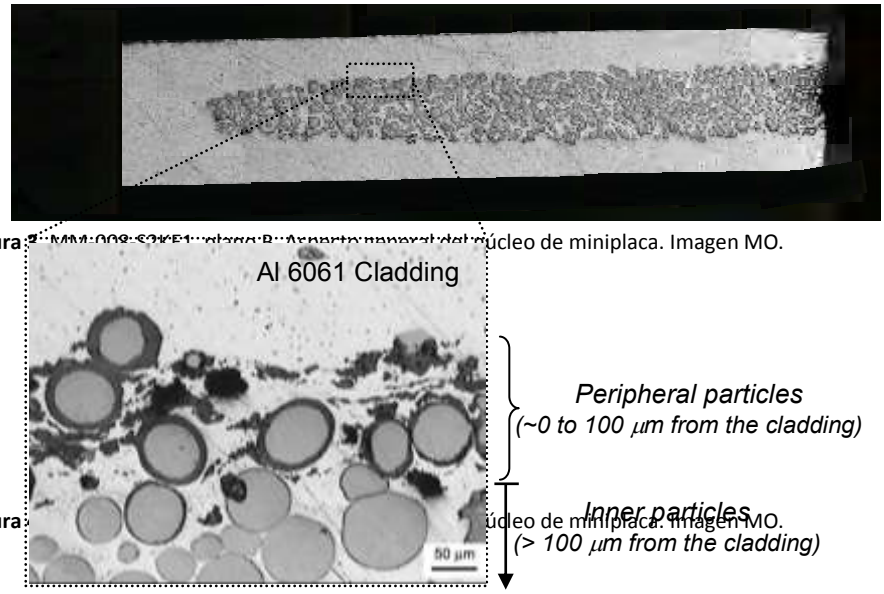


Figura 2: MM-009-S2YF1-plaqa B: Aspecto general del núcleo de miniplaca. Imagen MO.

Figura 3: MM-009-S2YF1-plaqa B: Detalle del núcleo de miniplaca. Imagen MO.

Figure 1 Classification in peripheral or inner U(Mo) particles according to its distance to the cladding. MO.

Figure 2 shows U-7Mo particles at three different stages during fabrication process: after compact fabrication, after hot rolling and full fabricated. As it can be seen in Figure 2a, after compact fabrication UO_2 oxide layer identified by DRX is very narrow, lesser than 1 μm, and cannot be optically observed. However after hot rolling process an important OL developed surrounding U-7Mo particles which can be easily observed, Figures 2b and 2c.

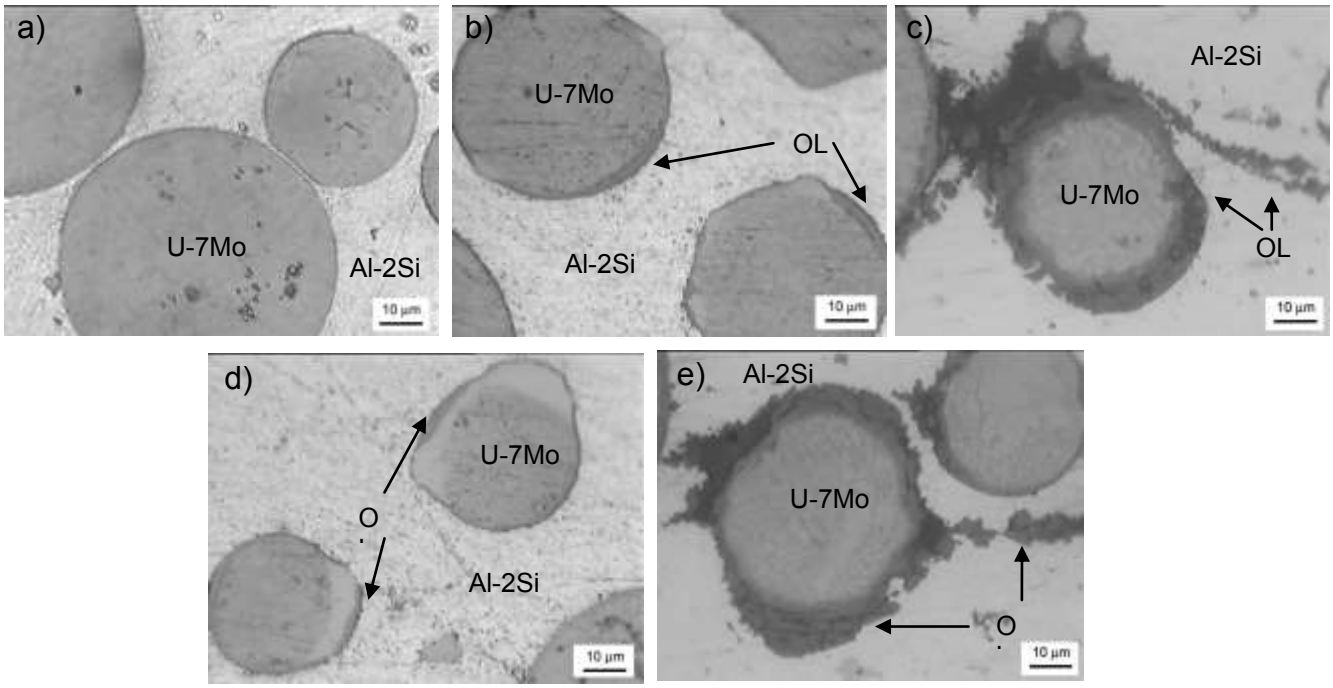


Figure 2. Superficial oxidation on U-7Mo particles during fabrication process. a) Compact 2Si-C, b) Miniplate 2Si-AR-OW, inner particles, c) Miniplate 2Si-AR-OW, peripheral particles d) Miniplate 2Si-FF-OW, inner particles, e) Miniplate 2Si-FF-OW, peripheral particles. – OM

On *peripheral particles*, this OL is 10 to 20 μm width approximately, covers U-7Mo surface completely and, as it is very fragile, is very cracked and small pieces of it are found stuck in the matrix following hot rolling direction (Figure 2c). On the other hand for *inner particles* the OL is 1 to 3 μm width approximately and does not cover U-7Mo particle surface completely (Figure 2b).

Comparing Figures 2b with 2d and Figures 2c with 2e no evolution of the OL due to final thermal treatment is observed. This means that its growth occurs only during hot rolling.

3.1.2. Changes observed on Al-Si matrices

After compacts fabrication careful observations were done to evaluate Si particles distribution on samples 2Si-C and 4Si-C. A homogenous distribution without Si conglomerates was observed.

After full fabrication, some Si particles still remained undissolved on both samples 2Si-FF-OW and 4Si-FF-OW. Concerning sample $4Si_E$-FF-OW, almost no Si precipitates were found in the Al-Si matrix.

To evaluate homogeneity in Si distribution when 2 wt%Si or 4 wt%Si are added to the matrix, point to point concentration measurements were performed in the matrix zone of 2Si-FF-OW and 4Si-FF-OW samples. More than one hundreds points were randomly collected from each sample avoiding pure Si particles. To be sure that only matrix information was being evaluated, those points which U+Mo concentration was greater than 0.1 at% were ruled out. Si concentration values were plotted on bar-graphs to be easily compared, Figure 3.

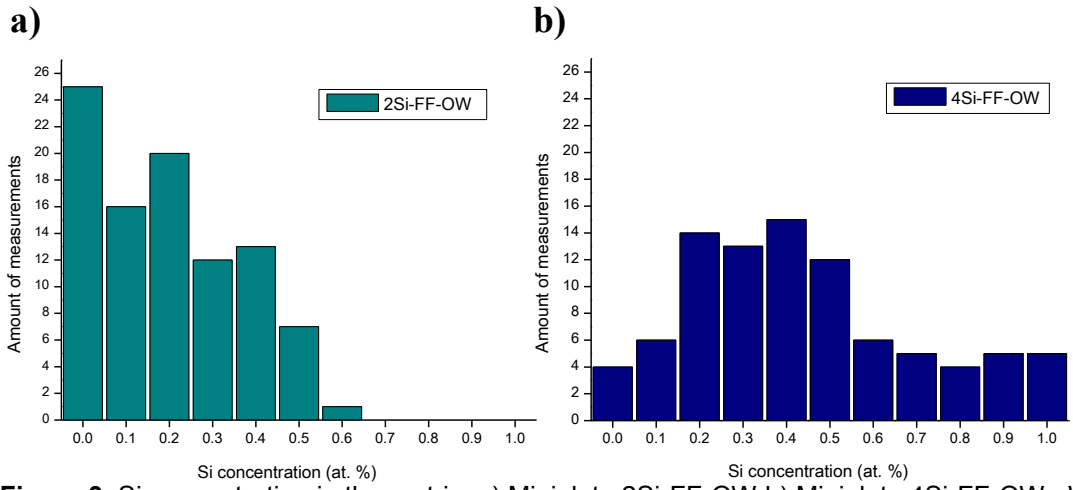


Figure 3. Si concentration in the matrix. a) Miniplate 2Si-FF-OW b) Miniplate 4Si-FF-OW - WDS.

As it can be easily observed, Si distribution in the matrix is much better in miniplate 4Si-FF-OW than in 2Si-FF-OW. Concerning 2Si-FF-OW miniplate, two relevant things should be remarked: from the first bar in the figure, 25% of the matrix does not contain Si and from the first three bars, 75% of the matrix has a Si concentration in the range 0-0.2 at%. On the other hand, for 4Si-FF-OW only 0.5% of the matrix does not contain Si and values in the range 0.2-0.5 at% were obtained on 75% of the matrix. According to this data Si distribution in 2Si-FF-OW matrix is not good enough considering that the more uniform the distribution is, the better Si will reach U(Mo) particles to form the IL.

3.1.3. Interaction layer formation, growth and characterization

After hot rolling process (AR condition) a very narrow IL (width < 2 μm) grew due to interdiffusion on a small fraction of U-7Mo surfaces ***only on inner particles***. It is located between the OL and the particle and coincides spatially with cracks or thinning on the OL, Figure 4a. When comparing miniplates 2Si-AR-OW with 4Si-AR-OW or $4Si_E$-AR-OW it can be suggested that more U(Mo) particles developed located IL when 4%Si is added to the matrix being this IL slightly thicker.

An important evolution of the IL was observed as a consequence of the final thermal treatment. Localized IL developed on almost all the inner U(Mo) particles being some of them covered on their whole surface with a noticeable evolution in thickness, Figures 2d and 4b. As it was previously mentioned, formation of IL is closely linked to cracks or thinning on OL. This correlates with the fact that the oxide layer acts as a barrier against the IL formation. This assertion is reinforced by the fact that no IL at all was observed on peripheral particles which developed the thick oxide layer previously depicted (Figure 2c).

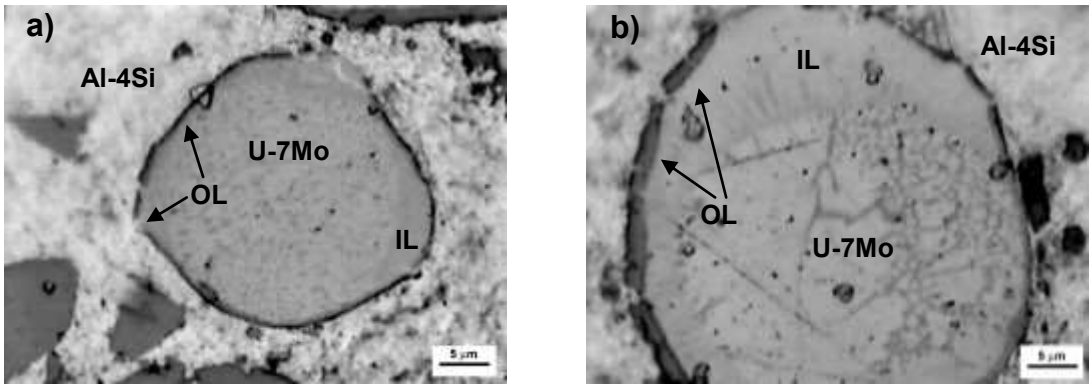


Figure 4. IL grown by interdiffusion due to fabrication process. a) Miniplate 4Si-AR-OW, inner particle, b) Miniplate 4Si-FF-OW, inner particle - OM.

On miniplate Al-FF-OW (pure Al as matrix) only a very low percentage of U-7Mo particles developed an IL after the whole fabrication process. This IL is much thicker than the one on miniplates with Al-Si matrices consuming, in some cases, the U-7Mo particle almost completely. All the particles on which IL is formed showed a high percentage of γU(Mo) phase cellular reaction, Figure 5.

It is important to remark that, as γU(Mo) phase cellular reaction depends on time at temperature, the four miniplates that went through the whole fabrication process (Al-FF-OW, 2Si-FF-OW, 4Si-FF-OW and 4Si_E-FF-OW) showed very similar global percentage of transformed phase. However, when Si is present in the matrix, IL does not grow abruptly consuming U-7Mo reacted particle. Moreover, careful observations with optical and scanning microscopes on these three samples allow the conclusion that no important differences in IL thicknesses were observed when comparing particles with and without γU(Mo) phase cellular reaction.

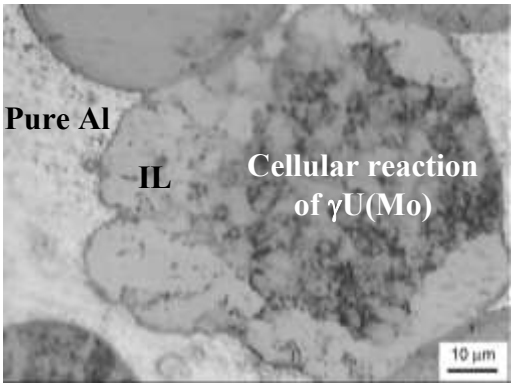


Figure 5. Miniplate Al-FF-OW. General aspect of IL formed only on particles with a high percentage of γU(Mo) phase cellular reaction. OM.

XRD technique was used to find the crystalline structure of the phases that form samples 2Si-FF-OW and 4Si-FF-OW. Spectra obtained for both samples, Figure 6, are very similar concerning angular

position of the peaks which means that same crystalline structures are expected for both samples. γU and αU phases from the U-7Mo particles, O_2U and OU phases from the OL, Al and Si phases from the matrices were identified for both of them. It is important to notice that αU and OU were not identified on as received U-7Mo particles. This is in good agreement with the oxidation and γU phase cellular reaction observed on the particles due to fabrication process. Concerning the IL, crystalline structure corresponding to $U(Al,Si)_3$ phase was clearly identified with a lattice parameter *a* ~ 4.20 Å for both samples. By the use of the correlation between lattice parameter and Si concentration in this phase proposed by Dwigth [20], the amount of Si in this phase is 28 %at approximately.

From the seven phases identified in these spectra only peaks corresponding to $U(Al,Si)_3$ phase are marked with black dots in Figure 6 for clarity. Also a set of four peaks, that were not associated to any of the seven phases previously mentioned, was marked with arrows. From all the known aluminides, silicides, ternary U-Mo-Al and ternary U-Al-Si phases, theoretical spectrum of Si_2U, Si_5U_3 and $Al_2Si_3U_3$ are the ones that match better with some of these four peaks.

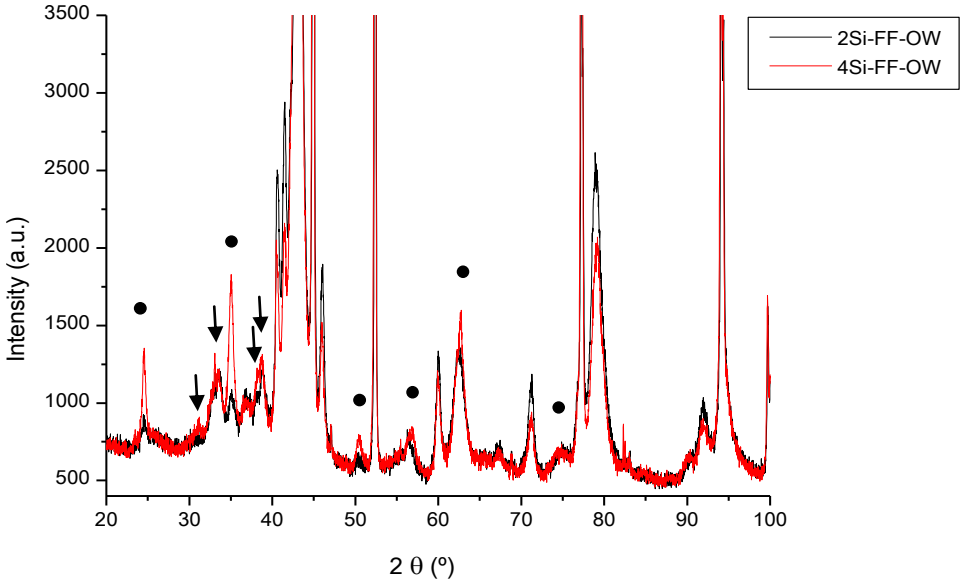


Figure 6 Spectra obtained for both samples 2Si-FF-OW and 4Si-FF-OW. Black dots correspond to $U(Al,Si)_3$ and arrows correspond to unidentified peaks- XRD.

Point to point concentration measurements were performed on miniplates 2Si-FF-OW and 4Si-FF-OW and data is represented in pseudoternary Gibbs triangles (U+Mo)-Al-Si, Figure 7. On miniplate 2Si-FF-OW a set of different 1μm step line scans were done on several particles in radial direction starting on the matrix, crossing the whole IL and ending inside U-7Mo particle, Figure 7a. On 4Si-FF-OW miniplate a set of individual measurements conveniently positioned inside IL were performed, Figure 7b. On both Figures relevant phases are indicated to correlate WDS results with XRD ones.

On both samples Si concentration inside IL is much higher than the original nominal Si concentration in the matrices. An important density of point, situated around $U(Al,Si)_3$ phase with ~ 25-30 at% Si, not only confirmed the existence of this phase (already identified by XRD) but shows that this is the majority one. On both Figures it can be observed a set of points with higher Si concentration than 30 at% Si which evidences that IL is formed, at least, by a second phase. The dispersion observed on these points does not allow the confirmation of any in particular but does not reject Si_2U, Si_5U_3 or $Al_2Si_3U_3$ proposed by XRD.

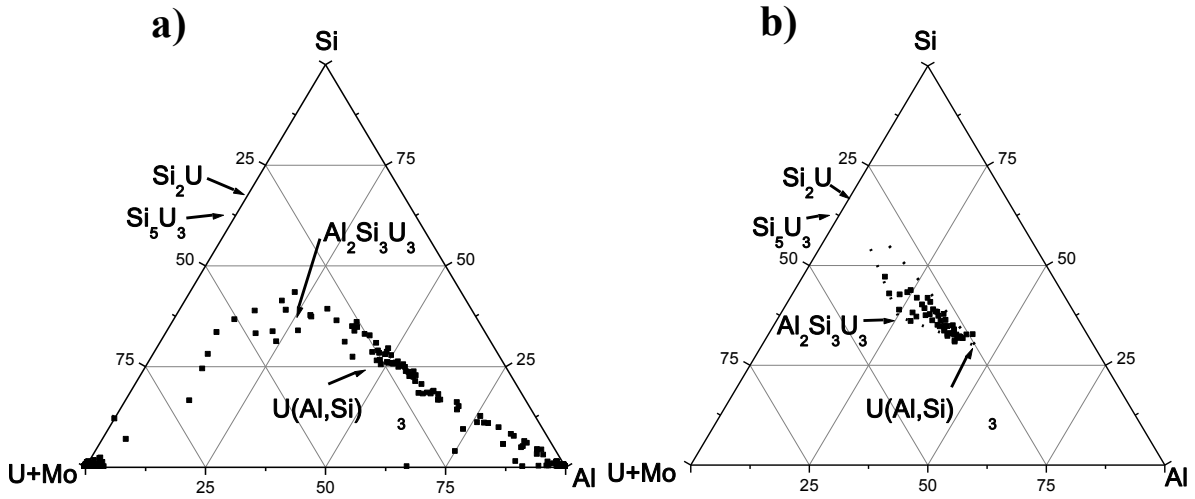


Figure 7. Point to point concentration measurements. a) 2Si-FF-OW miniplate, b) 4Si-FF-OW miniplate – WDS

3.2. Full welded miniplates.

3.2.1. Oxide layer formation

Representative micrographs of peripheral and inner particles of full welded miniplates in the as rolled condition are shown in 4Si-AR-FW and $4Si_E$-AR-FW.

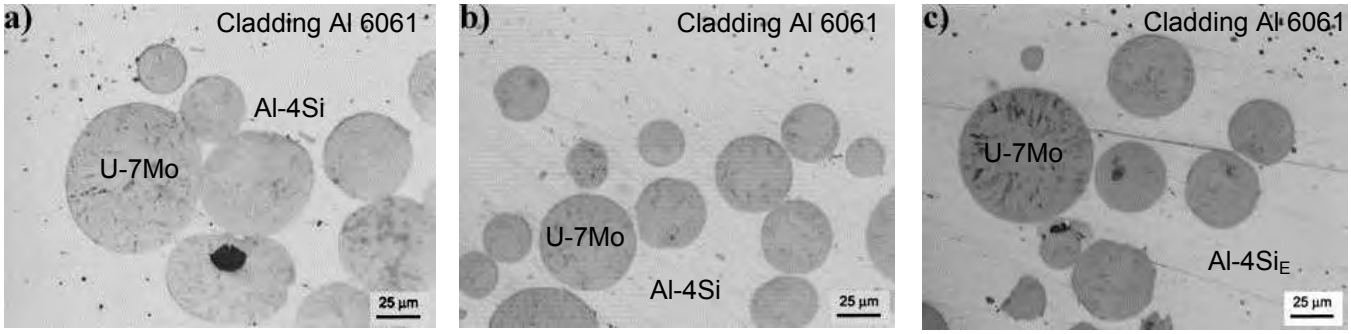


Figure 8. Absence of oxidation on peripheral U-7Mo particles after hot rolling on full welded miniplate. a) and b) Miniplate 4Si-AR-FW, c) Miniplate $4Si_E$-AR-FW. – OM.

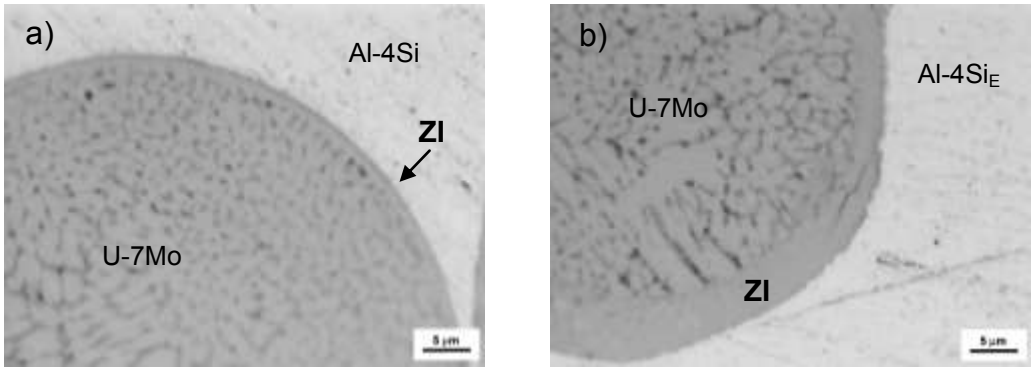


Figure 9. Absence of oxidation on inner U-7Mo particles after hot rolling on full welded miniplates. a) Miniplate 4Si-AR-FW, b) Miniplate $4Si_E$-AR-FW. – OM.

It is very noticeable that neither peripheral particles nor inner ones developed oxide layer surrounding them. (For comparison see Figures 2b and 2c). In this case the absence of the OL allow the formation of an interaction layer that completely surrounds U(Mo) particles all along the meat.

No changes were observed when comparing AR miniplates with FF ones which reinforces the results presented in section 3.1.1 in which it was shown that OL forms and grows during hot rolling.

3.2.2. Comparison between both ways of incorporating 4%Si to the matrix: pure Si or eutectic Al-Si alloy particles.

Same concentration of Si (4wt%) was incorporated to the matrix in two different ways: as pure Si particles or by the use of the eutectic Al-Si alloy in which Si is present as very small pure Si precipitates. The aim of this comparison is focused on establish any difference concerning Si migration to form IL. According to results presented in Section 3.2.1 only FW samples will be considered to avoid possible effects of OL formation in OW miniplates.

After hot rolling, remaining Si in the matrices was found in the form of particles in 4Si-AR-FW or as groups of precipitates (eutectic regions) in $4Si_E$-AR-FW, Figure 10.

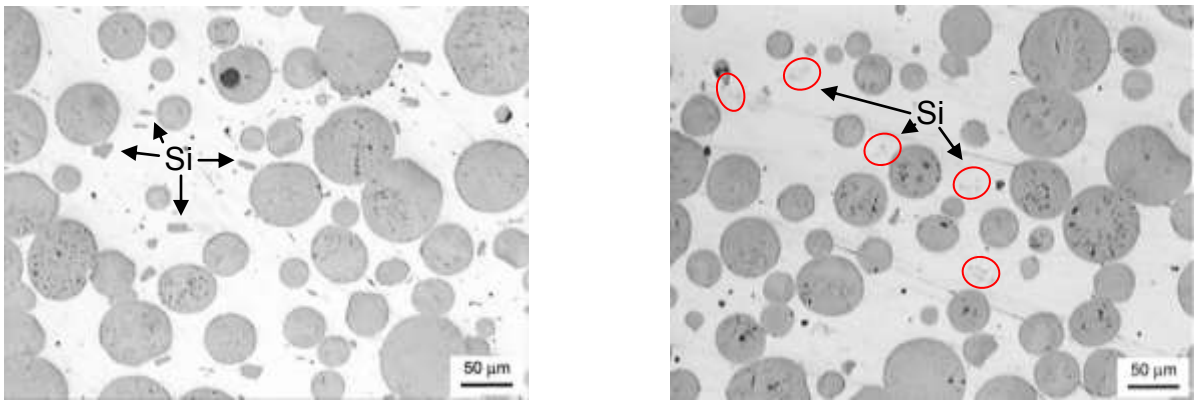


Figure 10. Remaining Si in the Al-Si matrix. a) Miniplate 4Si-AR-FW, b) Miniplate $4Si_E$-AR-FW. – OM.

After final thermal treatment miniplates 4Si-FF-FW and $4Si_E$-FF-FW showed differences in their matrices concerning Si present in them. Some pure Si particles were still clearly found in 4Si-FF-FW miniplate randomly distributed in the whole meat. However only a few groups of Si precipitates were found in $4Si_E$-FF-FW located only in the matrix close to the cladding. Figure 11 is representative of the general aspect of the meat for both miniplates.

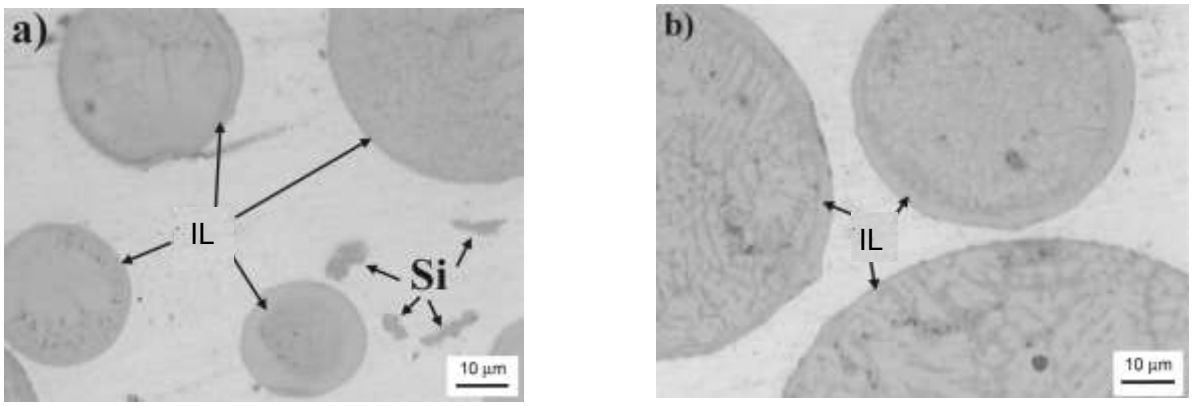


Figure 11. Remaining Si in the Al-Si matrix. a) Miniplate 4Si-FF-FW, b) Miniplate $4Si_E$-FF-FW. – OM.

From this result it is inferred that when Si is incorporated to the matrix in the form of precipitates (eutectic alloy) it dissolves and reaches IL more efficiently.

3.2.3. Interaction layer characterization.

After hot rolling the miniplates 4Si-AR-FW and $4Si_E$-AR-FW developed a very narrow IL which showed an important growing during thermal treatment. At the end of fabrication process almost all U(Mo) particles were completely covered by an IL which looks homogenous in thickness (dark gray in Figure 12). The IL developed even between very close particles as shown in detail in Figure 12c.

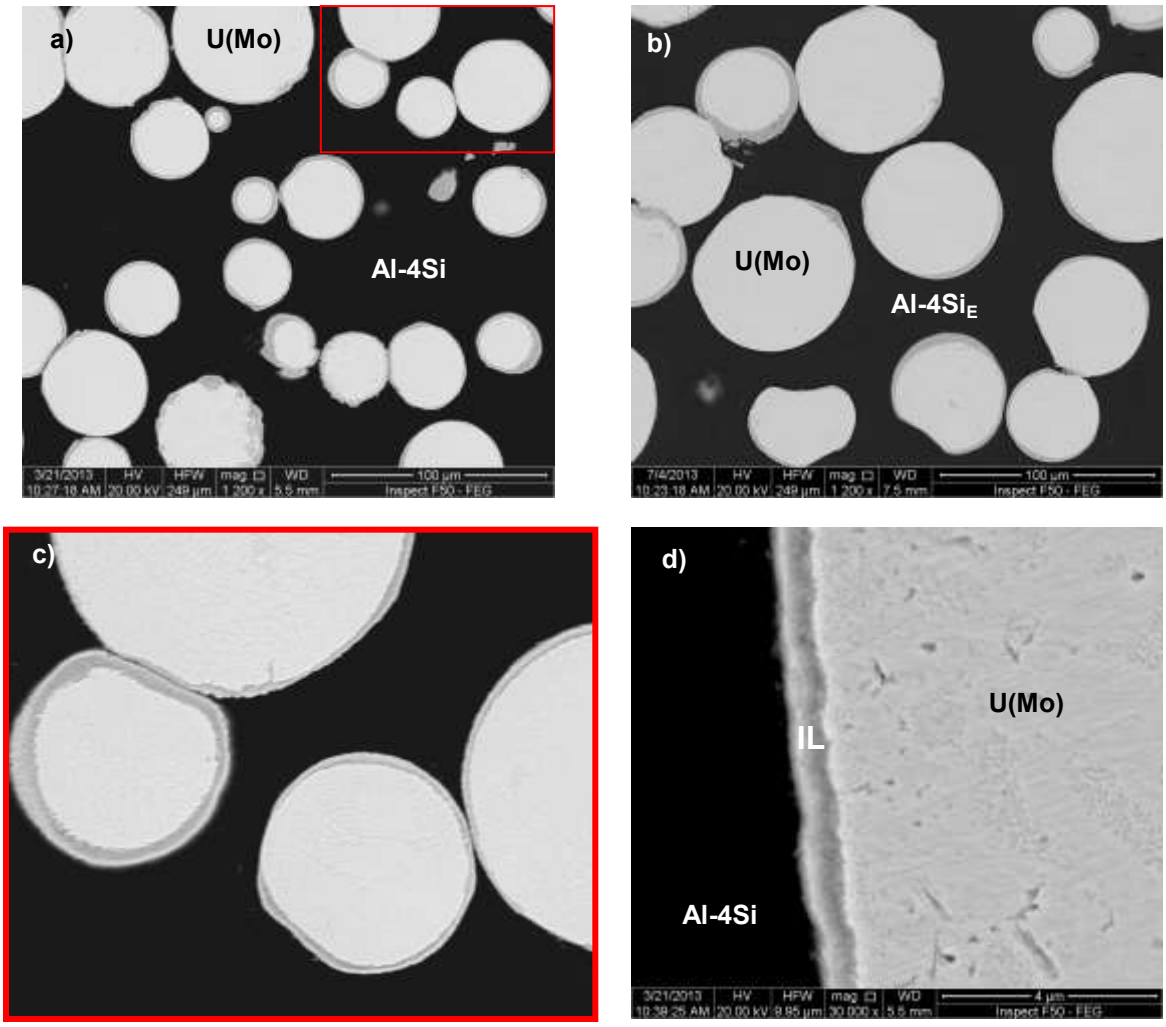


Figure 12. Full welded miniplates. U(Mo) particles completely covered by an IL of homogenous thickness. a), c) and d) Miniplate 4Si-FF-FW, b) Miniplate $4Si_E$-FF-FW. – SEM.

To obtain IL real thickness, only equatorial cuts of the particles have to be considered. However sample preparation (i.e. polishing) exposes different cuts of the particles which, in some cases, enlarge IL overestimating its value. To have a real estimation only 100 μm (or higher) particles were carefully observed resulting the IL thickness between 0.5 - 2 μm (see Figure 12d).

In section 3.1.2 it was shown that IL is formed by Si-rich phases. Taking advantage of this characteristic X-ray mapping was performed on samples 4Si-FF-FW and $4Si_E$-FF-FW using Si Kα radiation to evidence IL formation around almost all U(Mo) particles, Figure 13. A very small amount of U(Mo) particles as the one shown in Figure 13 e) were found to be not completely covered by IL which

is very clear on X-ray map image, Figure 13 f). Although it represents only a low percentage of particles, longer final thermal treatments are under study nowadays in order to improve this.

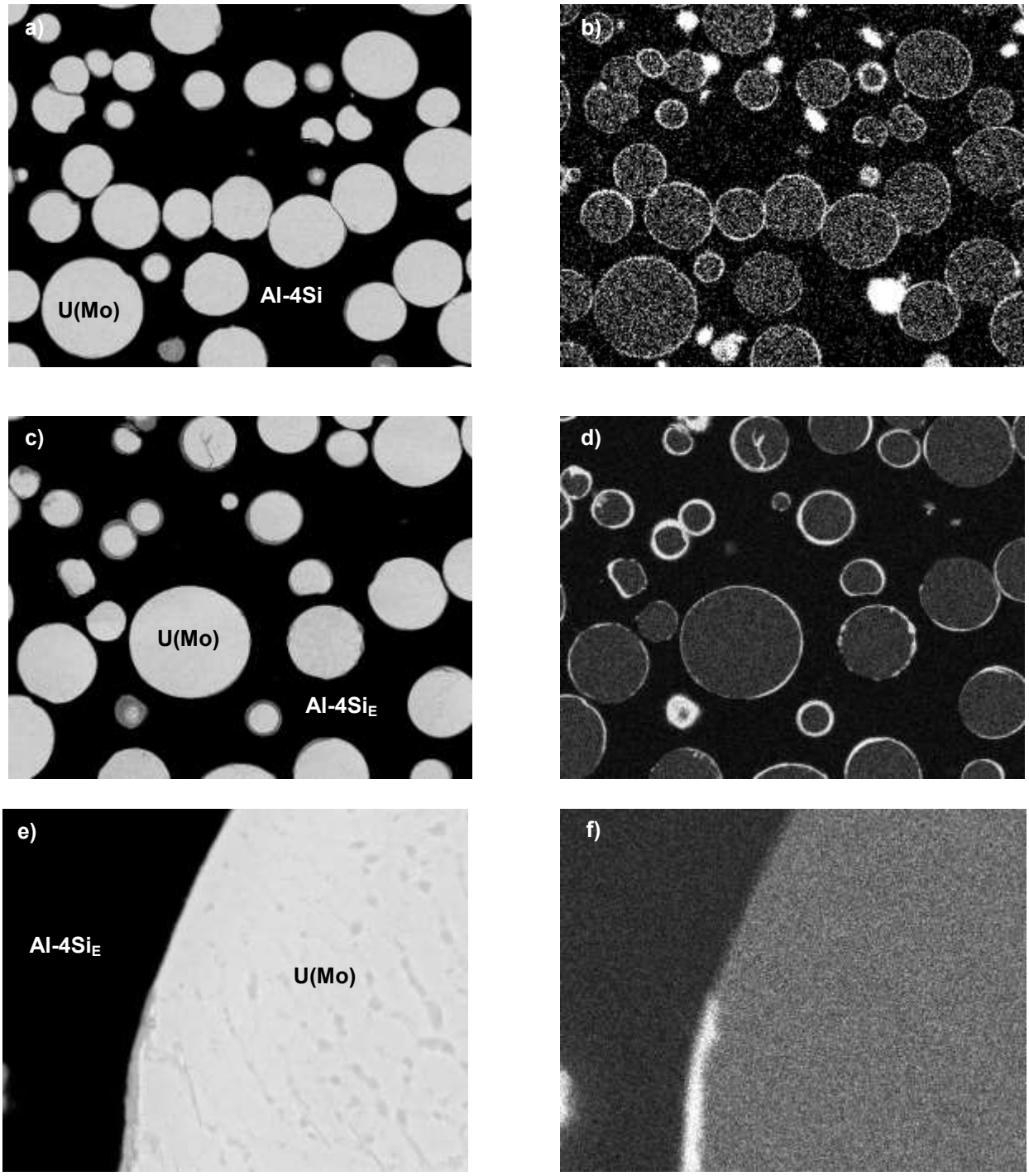


Figure 13. Si X-ray mapping. a) and b) Miniplate 4Si-FF-FW, c), d), e) and f) Miniplate 4Si$_E$-FF-FW. SEM - EDS.

XRD was used to identify crystalline structure of the phases that form the whole meat for both full welded miniplates 4Si-FF-FW and 4Si$_E$-FF-FW. Both spectra are presented together in Figure 14 for easy comparison and phases from the IL are only indicated for clarity. Concerning initial components of the meat, γU, αU and O_2U phases from the U-7Mo particles together with Al phase from the matrices were identified for both miniplates. Si phase was only identified for miniplate 4Si-FF-FW (its

principal reflection is marked with an arrow in Figure 14a) which is in good agreement with the absence of Si precipitates mentioned in Section 3.2.2. Concerning IL, same phases as in open welded miniplates were tested in this case (i.e. $U(Al,Si)_3$, Si_2U, Si_5U_3 and $Al_2Si_3U_3$). Among them, $U(Al,Si)_3$ was clearly identified with lattice parameter *a* ~ 4.20 Å (~28 %at Si according to Dwigth [20]) meaning that IL is mainly formed by it. Crystalline structure corresponding to $Al_2Si_3U_3$ was not identified meanwhile a deeper analysis was needed to clarify the possible presence of Si_2U and/ or Si_5U_3. With this objective two new spectra were performed on miniplate $4Si_E$-FF-FW. For both of them very narrow angular ranges were selected avoiding reflections from U, Al or Si phases. First spectrum, Figure 14b, includes reflection (001) from USi_2 phase and (001) from U_3Si_5 phase and the second one, Figure 14c, includes reflection (200) from USi_2 phase which is very near to reflection (211) from UO_2. As all these reflections are very low intensity ones, long exposure time was used to force them to become evident if they are really present in the IL.

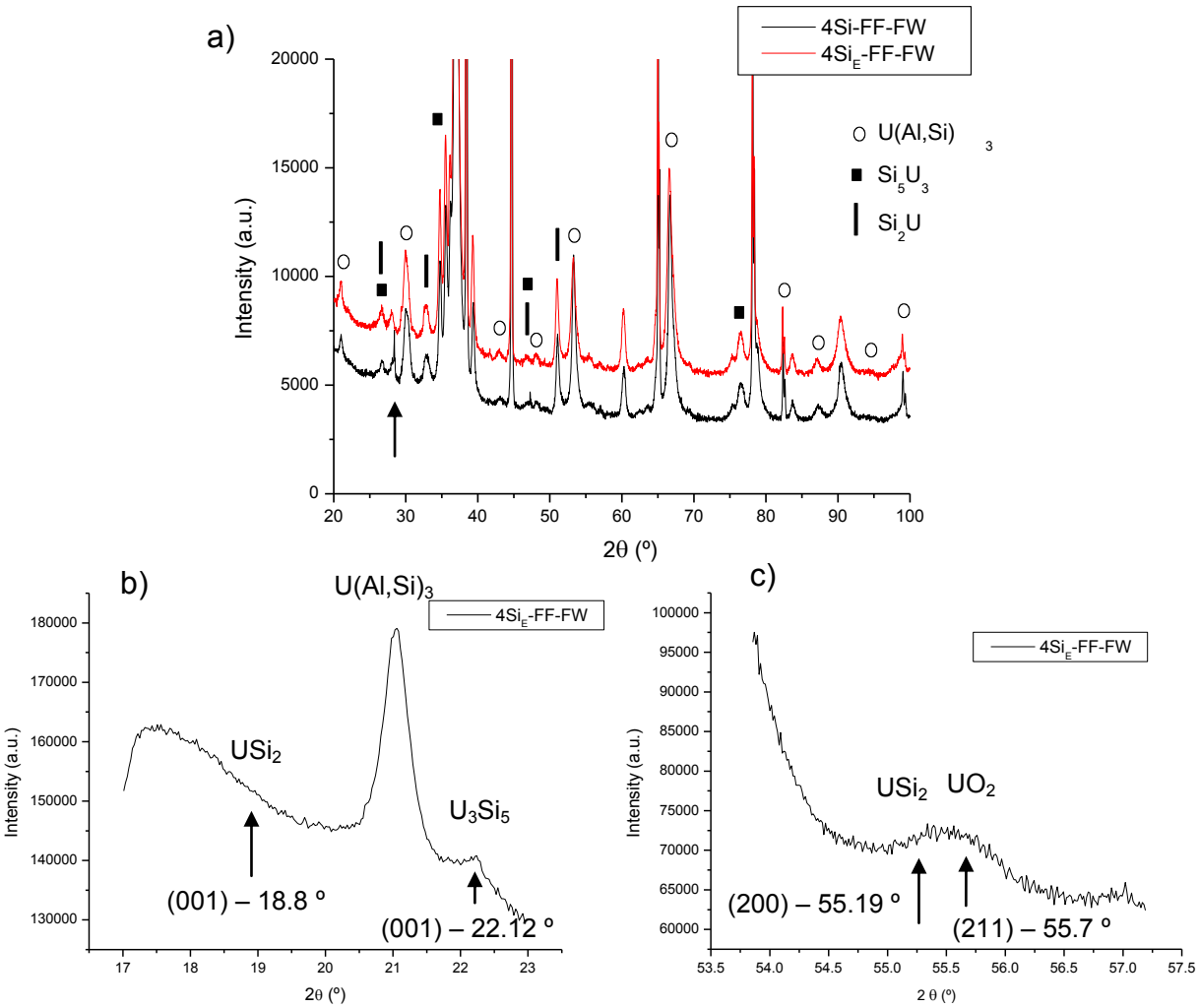


Figure 14. Spectra obtained for miniplates 4Si-FF-FW and $4Si_E$-FF-FW. a) Phases corresponding to IL, b) and c) Identification of U_3Si_5 in the IL - XRD.

From Figures 14 b) and c) it can be concluded that neither (001) nor (200) reflections from USi_2 are evident in these spectra while reflection (001) from U_3Si_5 is observed. According to this we consider that U_3Si_5 is the second Si-rich phase that form IL together with $U(Al,Si)_3$.

4. Conclusions

In this work different miniplates fabricated with U-7Mo atomized particles dispersed in Al-Si matrices were studied. The aim of this work is to obtain during the fabrication process a Si-rich interaction layer that ***completely*** surrounds all U(Mo) particles. Results presented lead to the following conclusions:

After hot rolling process U-7Mo particles developed an oxide layer with different characteristics according particles position in the meat, *peripheral particles* or *inner particles,* in open welded miniplates. The formation of this oxide layer is detrimental to the growth of an interaction layer that completely surrounds all U(Mo) particles. On the other hand neither peripheral nor inner particles developed oxide layer in full welded miniplates during fabrication. In this case the absence of the oxide layer allowed the formation of an interaction layer with the expected characteristics all along the meat.

The addition of 4%Si to Al behaves in an efficient way to ensure Si availability to form interaction layer. Significant differences could not be established between a matrix made by mixing pure Al with pure Si particles and a matrix made by mixing pure Al with eutectic Al(Si) alloy.

Very narrow interaction layer grew by interdiffusion between U(Mo) particles and Al-Si matrices as a consequence of fabrication process surrounding completely almost all U(Mo) particles on full welded miniplates. This interaction layer is mainly formed by $U(Al,Si)_3$ phase with 28 at%Si approximately and U_3Si_5 phase in low amount. The absence of aluminides or Al-Mo-U ternary phases in the interaction layer is promising.

5. Acknowledgement

The authors want to thank the technical staff of Gerencia Materiales-GAEN-CNEA, Departamento ECRI-GCCN-CNEA and Laboratorio de Difracción de Rayos X-Departamento de Física de la Materia Condensada-GAI and ANN-CNEA, for their support.

This work was partially financed by Project PICT-2010-1351, Agencia Nacional de Promoción Cientifica y Tecnológica (Argentina), FONCyT.

References

[1] J.L. Snelgrove, G. L. Hofman, M. K. Meyer, C. L. Trybus, T. C. Wiencek, Nucl. Eng. Design 178 (1997) 119-126.
[2] T.B. Massalski, Binary Alloy Phase Diagrams; second ed., 3, ASM International, 1996, pp. 2682-2683.
[3] M.K. Meyer, G.L. Hofman, S.L. Hayes, C.R. Clark, T.C. Wiencek, J.L. Snelgrove, R.V. Starin, K.H. Kim, J. Nucl. Mat. 304 (2002) 221-236.
[4] G.L. Hofman, Y.S. Kim, M.R. Finlay, J.L. Snelgrove, C. Clark, International meeting on Reduced Enrichment for Research and Test Reactor (RERTR), Chicago, Illinois, USA, 2003.
[5] A. Leenaers, S. Van den Berghe, E. Koonen, C. Jarousse, F. Huet, M. Trotabas, M. Boyard, S. Guillot, L. Sannen, M. Verwerft, J. Nucl. Mater. 335 (2004) 39-47.
[6] S. Van den Berghe, W. Van Renterghem, A. Leenaers, J. Nucl. Mater. 375 (2008) 340-346.
[7] J. Gan, D.D. Keiser Jr, D.M. Wachs, A.B. Robinson, B.D. Miller, T.R. Allen, J. Nucl. Mater. 396 (2010) 234-239.
[8] M. Mirandou, S. Aricó, M. Rosenbusch, M. Ortiz, S. Balart, L. Gribaudo, J. Nucl. Mater. 384 (2009) 268-273.
[9] M.I. Mirandou, S.F. Aricó, S.N. Balart, L.M. Gribaudo, Mater. Charact. 60 (2009) 888-893.
[10] E. Perez, Y. Sohn, D.D. Keiser Jr., Metall. and Mater. Transaction 44 A (2013) 584-595.
[11] X. Iltis, J. Allenou, B. Verhaeghe, H. Palancher, O. Tougait, A. Bonnin, R. Tucoulou, J. Nucl. Mater. 433 (2013) 255-264.

[12] S. Van den Berghe, A. Leenaers, E. Koonen, L. Sannen, Advances in Science and Technology 73 (2010) 78-90.
[13]A. Leenaers, S. Van den Berghe, J. Van Eyken, E. Koonen, F. Charollais, P. Lemione, Y. Calzavara, H. Guyon, C. Jarousse, D. Geslin, D. Wachs, D. Keiser, A. Robinson, G. Hofman, Y.S. Kim, J. Nucl. Mater. 441 (2013) 439-448.
[14] D.D. Keiser Jr, A.B. Robinson, J-F Jue, P. Medvedev, D.M. Wachs, M.R. Finlay, J. Nucl. Mater. 393 (2009) 311-320.
[15] D.D. Keiser Jr, J-F Jue, N.E. Woolstenhulme, E. Ashley, J. Nucl. Mater. 419 (2011) 226-234.
[16] A. Leenears, S. Van den Berghe, C. Datavernier, JNM 440 (2013) 220-228.
[17] S. Van den Berghe, Y. Parthoens, G. Cornelis, A. Leenears, E. Koonen, V. Kuzminov, C. Datavernier, JNM 442 (2013) 60-68.
[18] M. Mirandou, S. Balart, M. Ortiz, M. Granovsky, J. Nucl. Mater. 323 (2003) 29-35.
[19] W. Kraus, G. Nolze, U. Müller, Pulverdiffraktogramme aus Einkristalldaten und Anpassung experimenteller Beugungsaufnahmen, PowderCell 2.3., 2000.
[20] A.E. Dwight, Report Specification Nº ANL –82-14, 1982, 1-39.

NEUTRON IRRADIATION OF U_3Si_5 AND $Al_{43}Mo_4U_6$ COMPOUNDS. FIRST RESULTS.

M. MIRANDOU [(1)*], R. GONZÁLEZ [(1, 2)], S. ARICÓ [(1, 2)] AND A. FORTIS [(1, 2)]

(1) Gerencia Materiales, Gerencia de Área Energía Nuclear.
(2) Instituto de Tecnología "Jorge Sabato", Universidad Nacional de General San Martín.

Comisión Nacional de Energía Atómica (CNEA), Avda. Gral. Paz 1499, B1650KNA, San Martín, Buenos Aires, Argentina.

***corresponding author e-mail**: mirandou@cnea.gov.ar*

ABSTRACT

In the framework of U(Mo) alloys qualification, post- irradiation experiments have shown that the porosity and swelling phenomena observed due to irradiation on dispersed fuel elements are associated to a poor behavior of the interaction layer grown by interdiffusion during fabrication and/or irradiation between U(Mo) particles and the matrix. Fission induced amorphization of some of the phases that form the interaction layer, has been proposed as one explanation to understand the failure.

Out of pile diffusion couples experiments have shown that the phases UAl_3, UAl_4, $Al_{20}Mo_2U$ and $Al_{43}Mo_4U_6$ form the interaction layer when pure Al is used as matrix while $U(Al,Si)_3$, U_3Si_5, USi_2, USi_{2-x}, $Al_{20}Mo_2U$ and $Al_{43}Mo_4U_6$ are identified when Al(Si) is used instead of Al.

The objective of this investigation is to study, independently, the behavior of each phase under neutron irradiation focusing on a possible amorphization.

In this work powders of U_3Si_5 and $Al_{43}Mo_4U_6$ compounds are irradiated in RA1 reactor (Argentina). Samples are analyzed by OM, SEM, EDS, WDS and XRD.

1. Introduction

Reduced Enrichment for Research and Test Reactors (RERTR) non-proliferation program promotes the conversion of research reactors to use low enriched U instead of high enriched U in their cores [1]. In this sense fuel elements should be modified in order to use high density U alloys like U-(7 to 10 wt%)Mo in metastable (bcc) γU phase which have demonstrated a good irradiation behavior [2]. Nevertheless, when dispersion miniplates or full size fuel elements made using pure Al as matrix were tested under irradiation, unacceptable failures appeared that stop final qualification [3, 4]. These failures are associated to the bad behavior under irradiation of the interaction layer (IL) grown by interdiffusion between U(Mo) and the matrix during fabrication and or irradiation. It was proposed that fission induced amorphization affects IL reducing its viscosity and enhancing fission gas mobility inside it [5, 6].

Different laboratories around the world have been working in the characterization of this IL, in pile and out of pile, and in different solution to change its characteristics. From these investigations, the addition of Si to pure Al matrix has arisen as one of the most promising solutions. Concerning the phases that form IL, UAl_3, UAl_4, $Al_{20}Mo_2U$ y $Al_{43}Mo_4U_6$ have been identified when U(Mo)/pure Al is studied meanwhile $U(Al,Si)_3$, U_3Si_5, USi_2, USi_{2-x}, $Al_{20}Mo_2U$ and $Al_{43}Mo_4U_6$ are the ones identified when Al(Si) is used instead of pure Al [7, 8, 9, 10, 11].

The irradiation with 500 keV Kr ions of the phases $U(Al,Si)_3$, UAl_4, $Al_{20}Mo_2U$ and $Al_{43}Mo_4U_6$ [6] showed that among all of them, $Al_{43}Mo_4U_6$ went amorphous at lower dosis (< 1 dpa) and developed big holes at dosis near 100 dpa. This result suggests that this phase could be responsible for the porosity and swelling that provoke the failure under irradiation previously mentioned.

From the statements mentioned above, we consider very important to study, independently, the behavior of each of the phases identified in the ILs under neutron irradiation focusing on a possible amorphization. To start this investigation, U_3Si_5 and $Al_{43}Mo_4U_6$ were selected and powders of these compounds were irradiated in RA1 reactor (Argentina) up to 0.02 dpa. The main reason to select this damage value is to reach a low activation level of the samples in order to decrease the decay times allowing the analysis of the samples in a short time without using hot cells.

In this work details of the melting process, as cast characterization, sample preparation for irradiation and irradiation details are presented for both compounds. Pos-irradiation characterization was performed only for U_3Si_5 sample because $Al_{43}Mo_4U_6$ sample is still too active to be studied. Optical and scanning electron microscopy, energy and wavelength dispersive spectroscopy and x-ray diffraction were used to perform microstructural characterization of the samples.

2. Experimental procedure

Depleted U (0.2 at% ^{235}U – 99.9%), Mo (99.97%), Al (99.99%) and Si (99.95%) were used as starting materials. Three alloys were fabricated by arc melting in a small non-consumable tungsten electrode arc-furnace with a copper crucible under pure argon atmosphere. Each alloy was re-melted five times to promote homogeneity. Only one alloy (50 g) was melted to obtain U_3Si_5 compound using nominal concentration according to its stoichiometry. On the other hand two different alloys (20 g) were necessary to obtain $Al_{43}Mo_4U_6$: the first one using nominal concentration according to its stoichiometry and the other one Mo-enriched following experimental detail in [12]. Information about melted alloys is given in TABLE 1. In some cases thermal treatments were performed in order to optimize relative participation of the compounds of interest in each alloy. To do this, alloys were sealed into quartz tubes under pure Ar atmosphere.

TABLE 1. Summary of relevant alloy fabrication and irradiation data.

Alloy	Nominal composition (at.%)				Expected compound	Irradiation time (h)
	Al	Mo	U	Si		
1	81.15	7.61	11.24	-	$Al_{43}Mo_4U_6$	
2	76.1	13.4	11.3	-	$Al_{43}Mo_4U_6$	728
3			37.5	62.5	U_3Si_5	221

Samples of the three alloys in the as cast condition and after thermal treatments were embedded using conductive polymeric resin and polished up to 1 μm diamond paste to be characterized. Microstructural analysis was performed by optical (OM-Olympus BX60M) and scanning electron microscopy (SEM –Philips SEM 515, and FEI QUANTA 200). Qualitative and quantitative composition determinations were obtained by the use of energy dispersive spectroscopy (EDS-EDAX Phoenix 3.2) and wave length dispersive spectroscopy (WDS – CAMECA SX50) against U, Mo, Al, and Si pure standards respectively. Finally x-ray diffraction was used to identify crystalline structure of the phases (XRD - Philips PW 3710 with *kα* Co radiation and PANalytical-Empyrean with PIXCEL 3d Detector with *kα* Cu radiation). Powders were obtained in an agate mortar and stuck on a special double-sided adhesive tape which has no diffraction peaks in the analyzed angular range. Comparison between theoretical spectrum of

each phase with the experimental spectra was done using POWDERCELL software [13]. A globe box was used for security to obtain and manipulate samples powder.

1g of powder was separated from alloys 2 and 3 to be irradiated in RA1 reactor, thermal flux $7x10^{11}$ n/(cm^3s), up to 0.02 dpa. Irradiation time for each alloy is given in TABLE 1.

Small Al containers were used to introduce powder inside the reactor avoiding dispersion and contamination. After irradiation samples were kept into dry storage till they reach safety doses. Irradiated powders were characterized by OM, SEM and DRX and were prepared in the same way mentioned in the previous paragraph.

3. Results and Discussion

3.1 $Al_{43}Mo_4U_6$ compound: Fabrication process, as cast characterization and irradiation.

As previously mentioned Alloy 1 was melted according to $Al_{43}Mo_4U_6$ stoichiometric concentration. After melting process the alloy was heat treated during 240h at 500ºC.

A multiphase microstructure was observed by optical and scanning electron microscopy for Alloy 1 in the as cast condition (Alloy 1-AC) which, according to crystalline structure identification was formed by UAl_3, UAl_4 and $Al_{20}Mo_2U$ (Figure 1a). In this figure, very low intensity peaks with angular position 2θ = 22º, 31.2º y 38.5º are associated to secondary diffractions of UAl_3 phase for *Kβ Co* radiation. As no any other reflection remained without identification it was concluded that $Al_{43}Mo_4U_6$ compound was not present in the Alloy 1-AC.

After thermal treatment (Alloy 1-TT1) a new crystalline structure identification was performed and no changes were observed concerning identified phases, Figure 1b. Comparing both spectra, some change in the relative intensity of their peaks was evidenced meaning that thermal treatment only modified relative amount of the three phases in the sample.

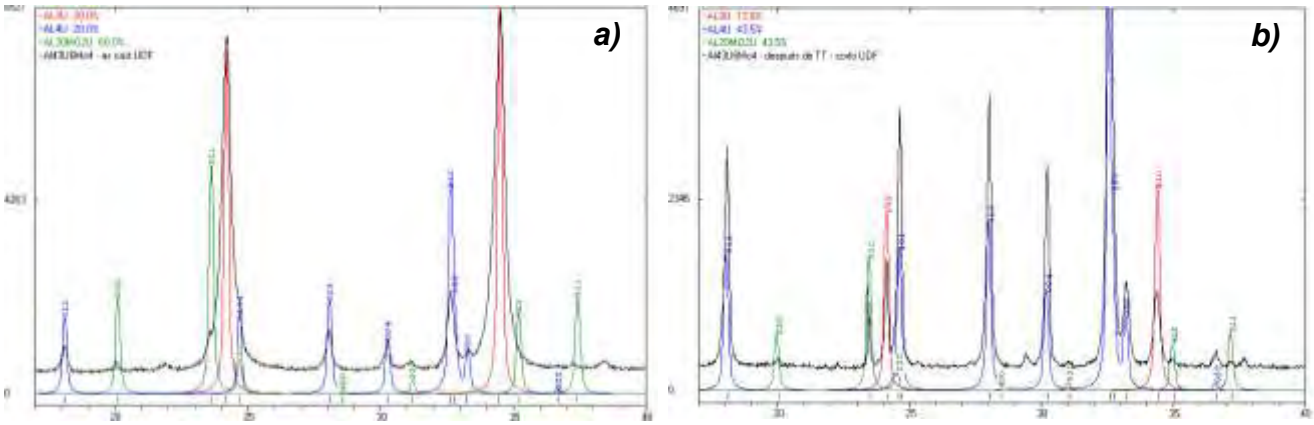


Figure 1. Crystalline structure identification: a) Alloy 1-AC, b) Alloy 1-TT1. XRD

Chemical analysis of Alloy 1-AC revealed that a reduction in Mo concentration was observed after melting process meaning that nominal composition was not stoichiometric as intended, TABLE 2. Neither inhomogeneity in the Alloy 1-AC nor problem during melting process were observed that can easily explain this difference in composition. Further analysis is needed.

Chemical composition of the phases identified by XRD (UAl_3, UAl_4 and $Al_{20}Mo_2U$) and $Al_{43}Mo_4U_6$ together with measured concentration after melting process of Alloy 1-AC were plotted on a Gibbs triangle (in at%) UAl_3 - $MoAl_3$ – Al, Figure 2. As it can be seen in this Figure, measured Alloy 1-AC concentration is located inside a triangle which vertexes are UAl_3, UAl_4 and $Al_{20}Mo_2U$. This means that any thermal treatment performed to this alloy could only change relative amount of these three phases but will probably never promote the formation of the expected compound $Al_{43}Mo_4U_6$.

TABLE 2. Alloy 1-AC concentration before and after melting process.

	Nominal concentration			Measured concentration after melting process		
	Al	***Mo***	***U***	***Al***	***Mo***	***U***
wt%	39.1	13	47.8	41.12	9.54	49.34
at%	81.15	7.61	11.24	83.37	5.5	11.1

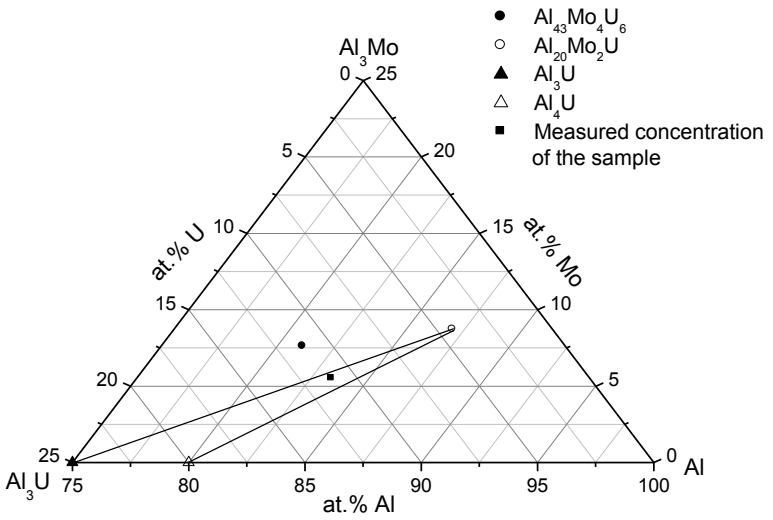


Figure 2. Gibbs triangle showing concentration of phases identified by XRD (UAl_3, UAl_4 and $Al_{20}Mo_2U$), $Al_{43}Mo_4U_6$ and measured concentration of Alloy 1 –AC in at%.

From the results and conclusions presented in previous paragraphs and the experience reported in [12], with a similar problem, a new Alloy (Alloy 2) was melted. According to [12] the starting composition should be chosen enlarged in Mo and reduced in Al respect to the stoichiometric one. Besides, authors propose a thermal treatment of 384 h (2 weeks) at 950 ºC. This thermal treatment was chosen to be performed to Alloy 2 instead of the other one used with Alloy 1.

Figure 3 shows a micrograph of Alloy 2 in the as cast condition (Alloy 2-AC) in which at least three different phases can be observed and were indicated with numbers 1, 2 and 3. Also elements identified in each one are shown. Inside ***zone 1*** Al, Mo and U were identified, inside ***zone 2*** only U and Al are present while ***zone 3*** corresponds to pure Al.

Crystalline structure identification, Figure 4, revealed the presence of $Al_{43}Mo_4U_6$, UAl_3, UAl_4 and Al phases. According to this, ***zone 1*** is formed by $Al_{43}Mo_4U_6$, ***zone 2*** by UAl_3 and/or UAl_4, and ***zone 3*** by pure Al.

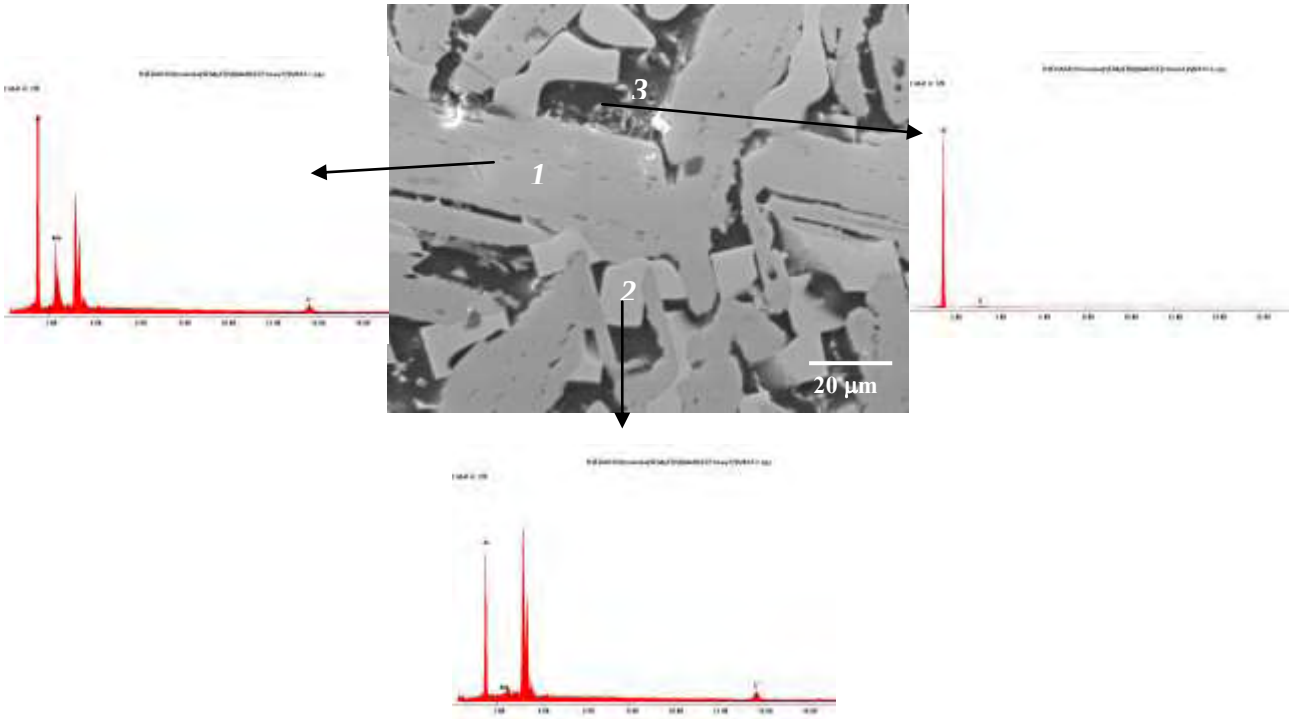


Figure 3. Alloy 2-AC. Three different zones indicated with numbers 1, 2 and 3 together with element identification. SEM and EDS.

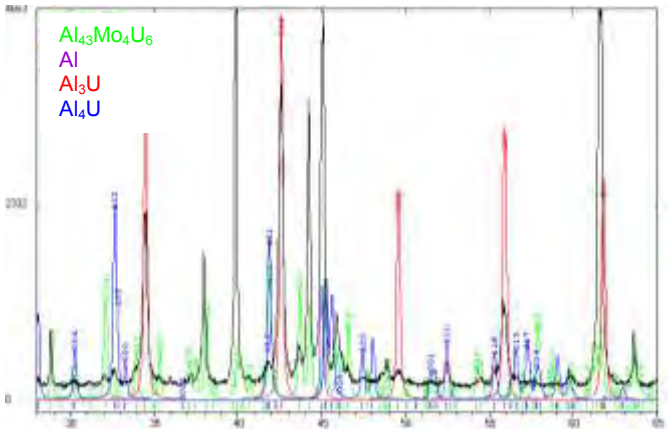


Figure 4. Alloy 2-AC. Crystalline structure identificación. XRD.

Due to the presence of pure Al phase, a thermal treatment of 48h at 580 °C was applied to Alloy 2-AC to promote Al diffusion before subjecting the sample to the final thermal treatment of 384 h at 950 °C. From now on thermal process 48h at 580 °C + 384 h at 950 °C will be called ***TT2***.

After TT2 new crystalline structure identification was performed to Alloy 2-TT2 in which $Al_{43}Mo_4U_6$ and UAl_3 phases were identified being no indications of UAl_4 or pure Al, Figure 5. Besides, point to point concentration measurement, Figure 6, confirm that the compound of interest, $Al_{43}Mo_4U_6$, is present in Alloy 2-TT2.

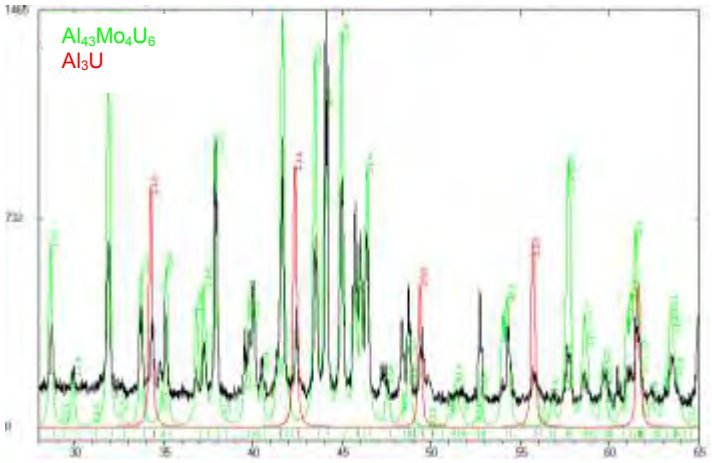


Figure 5. Alloy 2-TT2. Crystalline structure identification. XRD.

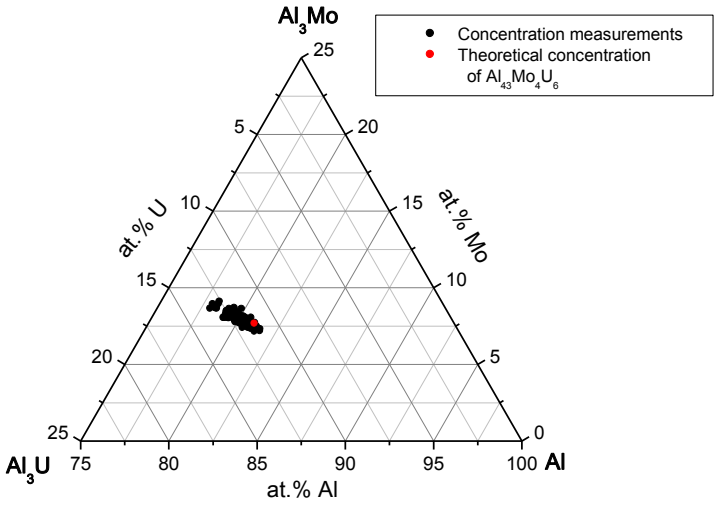


Figure 6. Alloy 2-TT2. Concentration measurements. WDS.

Powder obtained from Alloy 2-TT2 in this condition was used to be irradiated at RA1 reactor during 728 h in order to reach 0.02 dpa. This sample has concluded the irradiation and at the time of this presentation is in dry storage.

3.2. U_3Si_5 compound: Fabrication process, as cast characterization, irradiation and pos-irradiation.

To fabricate Alloy 3, Si and U were melted according U_3Si_5 stoichiometric concentration (see Table 1). A few days after melting sample get into powder without any external action.

SEM observations performed to representative particles of Alloy 3 in the as cast condition (Alloy 3-AC) revealed the presence of, at least, two phases in the sample which are indicated as ***1*** and ***2*** in Figure 7. Clearly seen in the figure, phase indicated as ***2*** is full of cracks which do not progress into phase indicated as ***1***.

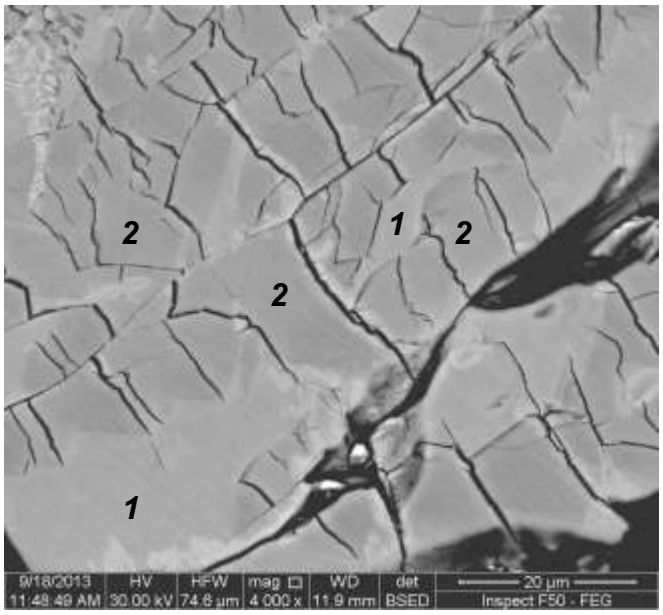


Figure 7. General aspect of representative particles of Alloy 3-AC. SEM

Crystalline structures corresponding to U_3Si_5, USi_{2-x} phases and SiU (in very low amount) together with superficial oxide O_2U were identified by XRD, Figure 8. This information confirms the presence of U_3Si_5 compound in Button 3-AC.

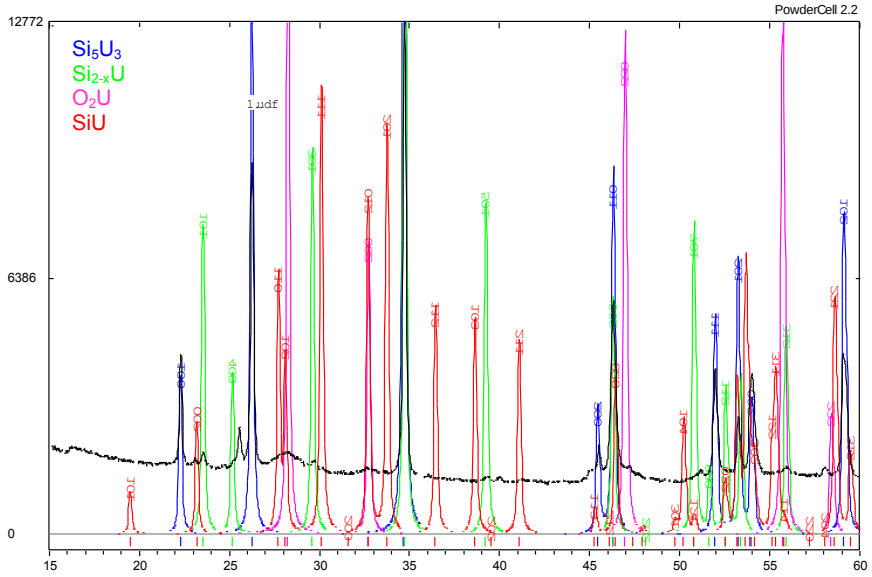


Figure 8. Alloy 3-AC. Crystalline structure identification. XRD.

Powder of Alloy 3-AC was irradiated at RA1 reactor during 221 h in order to reach 0.02 dpa. After irradiation the sample (from now on called Alloy 3-AC-I) spent 270 days in dry storage up to reach safe doses to be manipulated.

New SEM observations and XRD analysis were performed to Alloy 3-AC-I which are showed in Figures 9 and 10. General aspect of particles after irradiation showed the presence of at least two phases. Same crystalline structrues as in Alloy 3-AC were identified for Alloy 3-AC-I being no changes in the background which could be associated to amorphization.

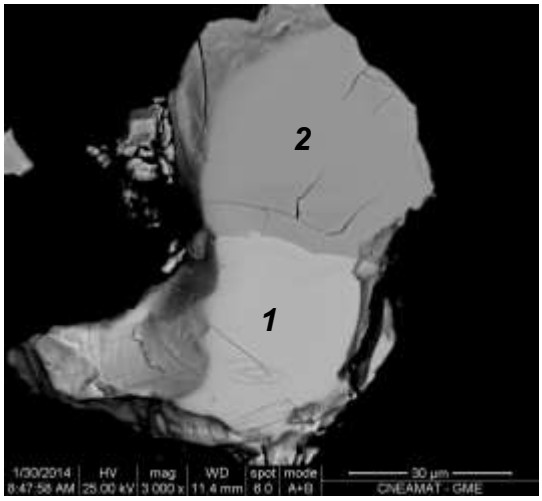


Figure 9. General aspect of representative particles of Alloy 3-AC-I. SEM.

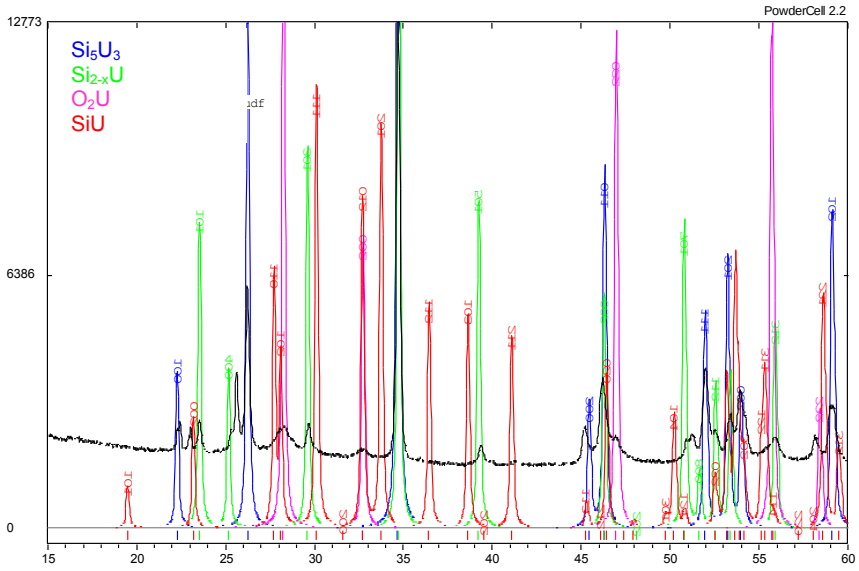


Figure 10. Button 3-AC-I. Crystalline structure identification. XRD

Summarizing information gather from this alloy it can be said that no significative change in morphology and crystalline structure introduced by neutron irradiation could be observed. No evidence of amorphization can be inferred from spectrum in Figure 10.

At this point it is very important to remark that this investigation is in its very beginning and larger irradiations together with higher fluxes (i.e. grater d.p.a.) are mandatory to better characterize compounds behavior under neutron irradiation. However, this investigation was important concerning some details in compounds fabrication process, irradiation devices and irradiated samples handle in relation to characterization equipments.

4. Conclusions

The aim of this work consists in studying, independently, neutron irradiation effects on U_3Si_5 and $Al_{43}Mo_4U_6$ compounds. With this objective, two alloys partially formed by these phases were irradiated at RA1 reactor up to 0.02 dpa. First results of this investigation lead to the following conclusions:

Two different alloys, an stoichiometric one and a non- stoichiometric one, were tested to obtain an alloy mainly formed by $Al4_3U_4Mo_6$ compound. From both of them, the non- stoichiometric one (Al-13.4at%Mo-11.3at.%U) thermally treated at 580ºC-48h + 950ºC-384h allowed achieving the objective. Neutron irradiation effects were not studied yet because sample is still too active to be studied.

Comparing information gather from an alloy partially formed by U_3Si_5 phase before and after irradiation it can be said that significative change either in morphology or in crystalline structure introduced by neutron irradiation could not be observed. No evidence of amorphization can be inferred.

This investigation is in its very beginning and larger irradiations together with higher fluxes are mandatory to better characterize compounds behavior under neutron irradiation. However, this investigation was important concerning some details in compounds fabrication process, irradiation devices and irradiated samples handle in relation to characterization equipments.

5. Acknowledgement

The authors want to thank the technical staff of Gerencia Materiales-GAEN-CNEA, RA1 reactor-GIRCEN-GAEN-CNEA, and Laboratorio de Difracción de Rayos X-Departamento de Física de la Materia Condensada-GAI and ANN-CNEA for their support.

This work was partially financed by Project PICT-2010-1351, Agencia Nacional de Promoción Cientifica y Tecnológica (Argentina), FONCyT.

References

1.- J.L. Snelgrove, G. L. Hofman, M. K. Meyer, C. L. Trybus, T. C. Wiencek, Nucl. Eng. Design 178 (1997) 119-126.
2.- M.K. Meyer, G.L. Hofman, S.L. Hayes, C.R. Clark, T.C. Wiencek, J.L. Snelgrove, R.V. Starin, K.H. Kim, J. Nucl. Mat. 304 (2002) 221-236.
3.- G.L. Hofman, Y.S. Kim, M.R. Finlay, J.L. Snelgrove, C. Clark, International meeting on Reduced Enrichment for Research and Test Reactor (RERTR), Chicago, Illinois, USA, 2003.
4.- A. Leenaers, S. Van den Berghe, E. Koonen, C. Jarousse, F. Huet, M. Trotabas, M. Boyard, S. Guillot, L. Sannen, M. Verwerft, J. Nucl. Mater. 335 (2004) 39-47.
5.- S. Van den Berghe, W. Van Renterghem, A. Leenaers, J. Nucl. Mater. 375 (2008) 340-346.
6.- J. Gan, D.D. Keiser Jr, D.M. Wachs, A.B. Robinson, B.D. Miller, T.R. Allen, J. Nucl. Mater. 396 (2010) 234-239.
7.- M. Mirandou, S. Balart, M. Ortiz, M. Granovsky, J. Nucl. Mater. 323 (2003) 29-35.
8.- M. Mirandou, S. Aricó, M. Rosenbusch, M. Ortiz, S. Balart, L. Gribaudo, J. Nucl. Mater. 384 (2009) 268-273.
9.- M.I. Mirandou, S.F. Aricó, S.N. Balart, L.M. Gribaudo, Mater. Charact. 60 (2009) 888-893.
10.- E. Perez, Y. Sohn, D.D. Keiser Jr., Metall. and Mater. Transaction 44 A (2013) 584-595.
11.- X. Iltis, J. Allenou, B. Verhaeghe, H. Palancher, O. Tougait, A. Bonnin, R. Tucoulou, J. Nucl. Mater. 433 (2013) 255-264.
12. H. Noel, O. Tougait, S. Dubois, Nucl. Mater. 389 (2009) 93-97.
13. Kraus, G. Nolze, U. Müller, Pulverdiffraktogramme aus Einkristalldaten und Anpassung experimenteller Beugungsaufnahmen, PowderCell 2.3., 2000.

INSIGHTS ON THE KINETICS AND MECHANISM BEHAVIORS OF LAYER FORMATION IN UAl_2-Al DIFFUSION COUPLE.

C. MOUSSA, O. TOUGAIT.
[1]*Institut des Sciences Chimiques de Rennes, UMR-CNRS 6226, Université de Rennes 1, Campus de Beaulieu, F-35042 Rennes Cedex - France*

B. STEPNIK
[2]*AREVA-CERCA, 10 Rue Juliette Récamier, 69006 Lyon-France*

ABSTRACT

UAl_x irradiation targets are produced by the thermal reaction between UAl_2 and Al powders. With this respect, the understanding of diffusion mechanism in the UAl_2/Al system is of interest. The present study aims to experimentally evaluate some fundamental features of the growing of the interaction product between UAl_2 and Al by means of diffusion couples experiments. The diffusion couples were prepared using as-cast UAl_2 and pure aluminum in the form of a tri-layer sandwich that was cold worked at 190(10)MPa in a die. The UAl_2-Al interfaces were investigated by SEM-EDS analysis, after heating the couples in a temperature range 575-645℃ for dwell periods up to 70 hours. The growth rate of the interaction layer, that is function of time and temperature, is also influenced by the applied pressure. The major interaction phase, UAl_3, forms in the diffusion zone with planar morphology whereas for longer annealing times and at higher temperatures UAl_4 forms preferentially at the vicinity of both the open pores and cracks of the sample. In terms of mechanism, it can be proposed that the interdiffusion reactions occur in two separate steps (i) formation of UAl_3 from the reaction between UAl_2 and Al, (ii) formation of UAl_4 from the reaction between UAl_3 and Al. The formation of UAl_3 as the first phase was tentatively described according to the normal parabolic behavior of the layer thickening. However, the large dispersion of the data points hindered to evaluate a reliable value of the activation energy.

1. Introduction

Despite the worldwide use of UAl_x dispersion plates as nuclear fuel and irradiation target materials in Research and Test Reactors, the current scientific understanding of diffusion mechanism in the UAl_2/Al system is not clear. To the best of our knowledge, there is no available interdiffusion study between UAl_2 and Al in the open literature. However, the U-Al system has been the subject of numerous studies. From the early work of Storchheim and Zambrow [1], Le Claire and Bear [2], DeLuca and Sumsion [3] and Castleman [4] as main reports, it is believed that the intermetallic layer formation and its growth are mainly controlled by the diffusion of Al and that the major interaction phase is UAl_3. In these studies that will be more precisely described in section 2, it is mentioned that the growth rate of the diffusion zone is function of the temperature, the dwell period and the applied pressure used for the diffusion couple preparation, outlining tricky experimental conditions for such studies.

The study of solid diffusion of Al is considered as a complex system, owing that it depends on various external parameters. Usually two diffusion modes as function of the temperature are discussed (*i*) grain boundary diffusion of Al, more likely below a threshold temperature (*ii*) volume diffusion of Al observed at higher temperature. In the present case, the study is made tangled since UAl_2 is a fragile material, and therefore its micro-hardness

will evolve during the heat-treatment. In addition, the open porosity that forms within the interdiffusion zone constitutes an additional parameter that should be taken into account [5].

The objective of the present study is to experimentally evaluate some fundamental features of the growing of the interaction product between UAl_2 and Al by means of diffusion couple experiments. The morphology and the composition of the interaction phases formed by heat-treatment in the temperature range 550-645°C were mainly characterized by SEM-EDS analysis. The formation of UAl_3 as the first phase allows to evaluate the activation energy by using a parabolic growth law in the temperature range 575-635°C.

2. Relevant results from previous studies on U / Al interdiffusion

The U-Al binary system displays three intermetallic phases, UAl_2 (C15, cF24) with direct solidification from the melt at 1620°C, UAl_3 ($L1_2$, cP4) with peritectic formation from UAl_2 + L at 1350°C and UAl_4 ($D1_b$, oI20) with peritectic formation from UAl_3 + L at 731°C [5].

Storchheim and Zambrow [1] studied the interdiffusion of uranium and aluminium by means of diffusion couples. Two disks one of uranium and one of Al were maintained by applying external pressure of about 152 MPa. The samples were annealed in the temperature range 400-550°C for annealing time of 2 min only. The width of the interaction layer was found to increase with both temperature and applied pressure. The main interaction product was identified as UAl_3. The growth of the diffusion layer was analysed by using a parabolic law in the temperature range 400-550°C, yielding activation energy of 122 $kJ.mol^{-1}$.

Le Claire and Bear [2] prepared diffusion couples with various applied pressures that were heat-treated in the temperature range 480-620°C for annealing time up to 3 hours. They confirm that the main interaction product is UAl_3 and that its thickness increases with the applied pressure. However, UAl_2 and UAl_4 were also observed by X-ray diffraction, with UAl_2 more likely observed in low temperature and high pressure samples whereas UAl_4 was observed in intermediate temperature and low pressure samples. The UAl_3 interdiffusion layer was found to increase parabolically with time at a given temperature, yielding to activation energy of 67 $kJ.mol^{-1}$ for all temperatures and low applied pressure of about 17.2 MPa.

DeLuca and Sumsion [3] by means of diffusion couples, investigate the influence of contaminants such as oxides present on the surfaces of the pieces and the influence of the applied pressure of the U/Al reaction rates. The mutual interdiffusion between Al and U was found with a ratio of 60 to 40 % respectively. UAl_3 was found as the main interaction product, with traces of UAl_2 and UAl_4, that appear above 475°C, whereas, only UAl_2 is observed at low temperature. When UAl_4 is present, it is in the form of powder. The activation energy was found of the order of 77.3 $kJ.mol^{-1}$ in the temperature range 250-550°C.

Castleman [4] performed diffusion couple experiments as the function of the applied pressure in the temperature range 500-600°C and for longer annealing times up to 110h. He confirmed the effect of the pressure on the interdiffusion thickness, and corroborated the assumption of Le Claire and Bear that the pressure effect may shift the equilibrium interface concentrations to enhanced interdiffusion. In all interdiffusion zones, no sign of UAl_4 was found.

3. Experimental Procedures

UAl_2 ingots were melted in an arc-furnace using a non-consumable tungsten electrode and a cooled copper crucible under residual pressure of argon. High purity metals, uranium pieces (99.8 wt.%) and aluminium pieces (99.999 wt.%) were used. The purity of the as-cast ingots was investigated by powder X-ray diffraction revealing a single phase. Disks of UAl_2 were obtained by cutting, to make plate-like samples of approximate 2 x 4 x 4 mm^3 dimensions. The row materials were polished down to 3 µm using diamond paste. Diffusion couples were prepared by embedding an UAl_2 piece between two Al ingots (99.999%), that were cold pressed at 190(10)MPa. The resulting objects were introduced in a clamping

system and maintained at 7N.m during the heat-treatment. These couples were isothermally treated between 550℃ and 6 45℃ for dwell period up to 70 hours under Ar atmosphere.

Each diffusion couple was cut in a perpendicular way to the interface. Two pieces were then mounted in epoxy and polished down to 1 µm for microstructural and elemental analysis using a JEOL 7100F scanning electron microscope equipped with an OXFORD EDS system. Microstructure observations, including thickness measurements and concentration profiles of interaction layers (ILs) in the different diffusion couple specimens, were determined by SEM-EDS.

4. Experimental Results

4.1 Formation of phases and microstructure of the Interaction Layer (IL)

Figure 1 presents the backscattered electron micrographs of some selected diffusion couples UAl_2-Al heat-treated between 550-645℃ for dwell period up to 15h. In agreement with previous study, these experiments show that the kinetic of the interaction layer depends on the temperature of annealing and the dwell period for an initial pressure of 190MPa and a an applied pressure through the clapping system with a tightening torque at 7 N.m.

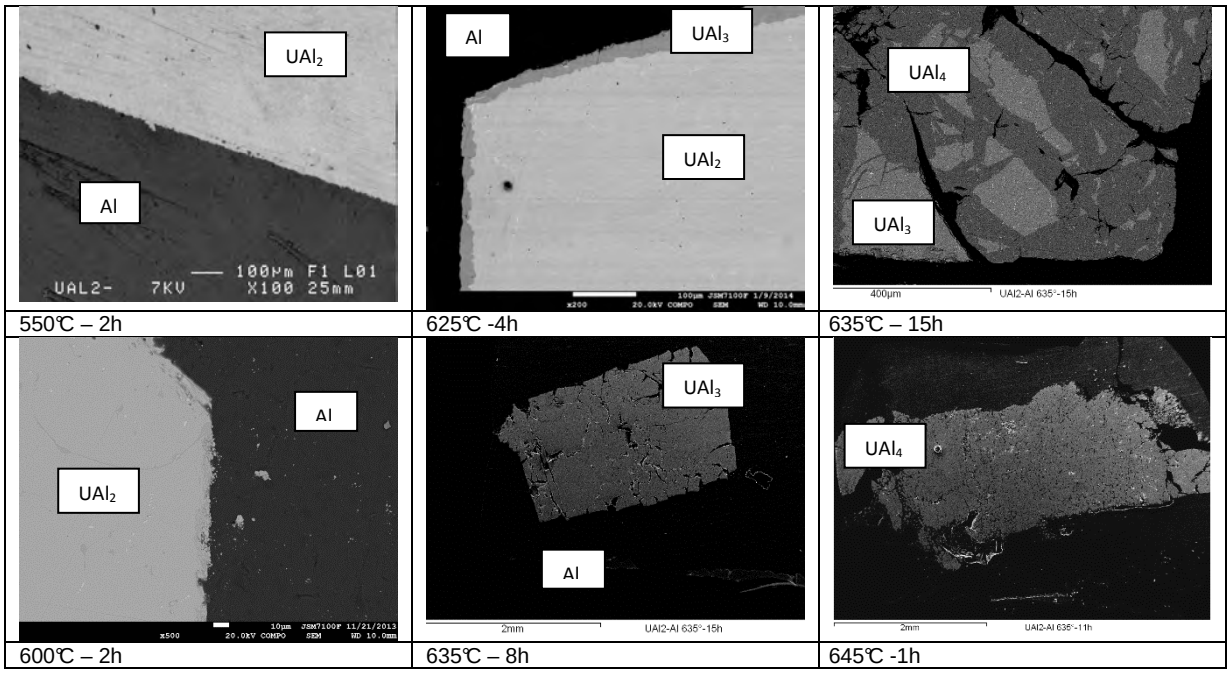


Figure 1. Backscatter electron micrographs of selected UAl_2-Al diffusion couples.

The main features of each of the micrograph depicted on Figure 1 can be summarized for UAl_2-Al diffusion couple experiments, as follows:

- For heat-treatment of 2h at 550℃, there is no sign of any diffusional interaction between UAl_2 and Al, the soldering frontier remains flat and smooth.
- For heat-treatment of 2h at 600℃, there is no obvious growth of a continuous IL, but some motions of matter seems to start at the welding zone where some powdering effects and of some cracks appear. These opening areas seem to act as favourable diffusion paths.
- For heat-treatment of 4h at 625℃ only a continuous IL layer of UAl_3 develops. It has an irregular shape, and their interfaces are nearly parallel to the original interface.
- For heat-treatment of 8h at 635℃, all the UAl_2 phase is consumed and has been transformed to UAl_3 only. The microstructure reveals large pores and cracks, but

the initial shape of the U-based block is kept. The sample contains short, prominent voids that lie in planes perpendicular to the diffusion direction.

- For heat-treatment of 15 h at 635℃, the interact ion product is a mixture of UAl_3 and UAl_4 phases. UAl_4 forms preferentially at the vicinity of the cracks of the sample, but is free of porosity.
- For heat-treatment of 1 h at 645℃, the interacti on product is only formed with UAl_4. The microstructure of the U-based phase shows large open pores and extended cracks. The porosity seems to be uniformly distributed. The initial shape of the UAl_2 block evolves toward powder.

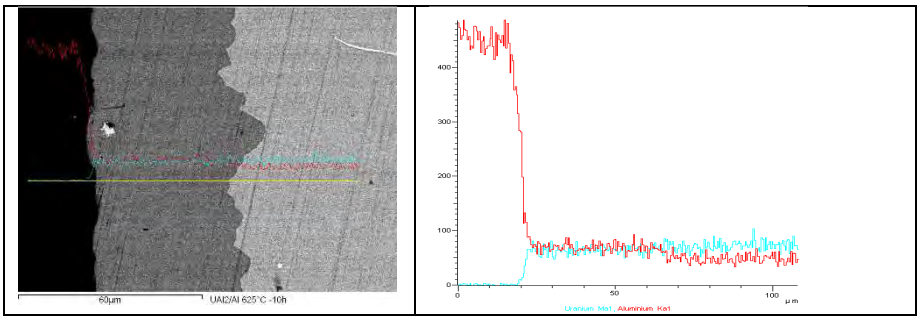
The observations indicate that three domains of temperatures can be defined for these UAl_2-Al diffusion couple experiments carried out for short annealing periods of about few hours. For temperature below 600℃ there was negli gible diffusional interaction. In the temperature range 600-635℃ the main interaction pr oduct is UAl_3 only. This UAl_3 diffusion layer grows with a planar morphology and is free from porosity. For longer dwell periods and for temperatures above 635℃, the richest uranium a luminide phase UAl_4 forms. However, it seems necessary that all the UAl_2 phase has to be transformed into UAl_3 before UAl_4 starts to develop. In terms of mechanism, it can be proposed that the interdiffusion reactions occur in two separated steps (*i*) formation of UAl_3 from the reaction between UAl_2 and Al, (*ii*) formation of UAl_4 from the reaction between UAl_3 and Al.

Regarding the microstructure, the diffusion interaction results in large porosity and formation of cracks, which seems to act as easy diffusion paths for the interdiffusion reactions. The mechanical cohesion of the initial UAl_2 block evolves from a quite homogeneous piece toward a fragile material that tends to decompose into powder when transformed into UAl_4. This is in agreement with the mechanical properties of UAl_4 that is known as a fragile material and with previous obsetrvations [3,6].

4.2 Microstructure of the Interaction Layer at 625°C

The interaction layer of UAl_2-Al diffusion couples was studied at 625℃ for dwel l period up to 46h. Figure 2 gives the backscattered electron micrographs of the intermetallic layer (UAl_3) formed at the interface in the sample annealed at 625℃ for 10h along with the elemental analysis. According to the EDS results, it is found that the composition of the compound layer is UAl_3. The dark, dark gray and gray regions depicted in the micrographs correspond to Al, UAl_3 and UAl_2, respectively. As example of Al concentration profile obtained across the IL, no significant deviation from the stoichiometry except for UAl_3 was observed that is not in agreement with the results of Y. Adda et al., [6] suggesting non-stoichiometric UAl_3 in the interaction layer. The absence of aluminum deficiency at the vicinity of both Al/UAl_3 and UAl_3/UAl_2 interfaces may indicated that the Al may not diffuse at the grain boundaries as it is usually observed for metal-aluminum systems such as Ti-Al or Zr-Al [7, 8].

Considering the shape of the interfaces that is somehow regular at the Al/UAl_3 zone, whereas it is more irregular in the UAl_3/UAl_2 zone, it suggests two different morphologies of grains within the IL. Coarse grains should be expected at the UAl_3/UAl_2 interface whereas fine grains should be expected at the Al/UAl_3 interface. This observation also suggests that some diffusion of UAl_2 has to be considered [8].



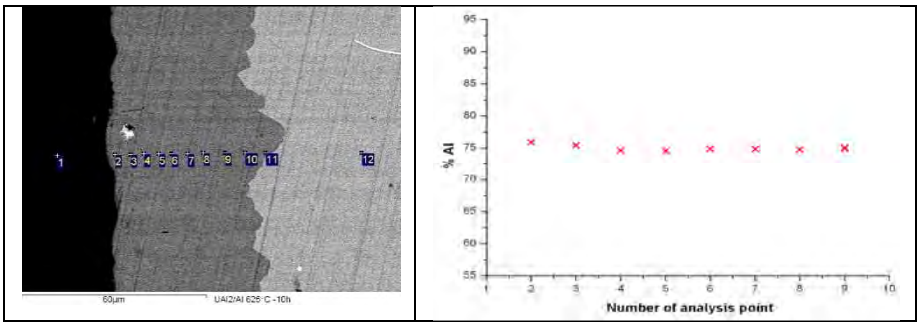


Figure 2. Backscatered electron micrographs of the UAl_2-Al diffusion couple heat-treated at 625℃ for 10h, along with the elemental composition of the interdiffusion zone. a) Continuous analysis points, b) Selected points within the interaction layer

4.3 Growth rate of the UAl_3 interaction product.

A tentative of analysis of the experimental results of the UAl_3 thickness for the UAl_2-Al diffusion couples heat-treated below 635℃ was carr ied out based on the procedure used by Le Claire and Bear [3] for the study of the U-Al diffusion experiments and recently applied by Dickson et al. [9] for the Zr-Al system.

The width of the diffusion zone,*x,* after annealing for time *t* at a fixed pressure and temperature is described according to the simple equation:

$$x = \sqrt{k}.t^{1/n} \qquad (1)$$

Since a diffusion controlled nature of the layer growth is assumed, the IL growth exponent, *n*, is expected to be 2, given the parabolic growth constant *k*.

If diffusion of atoms across the IL is considered to be a temperature activated process, a simple Arrhenius relation should define *k* as function of temperature as follow:

$$k = k_0 . e^{(-\frac{Q}{nRT})} \qquad (2)$$

Where k_o is the temperature-independent constant and Q is the activation energy of UAl_3 thickening.

According to equation (2), the plot of ln *k* (m^2/s) versus reciprocal temperature (K^{-1}), is depicted in figure 3. A large dispersion of data points is observed, which hindered reliable evaluation of the activation energy and pre-exponential factor k_0. The data points should be linear according to the Arrhenius relation.

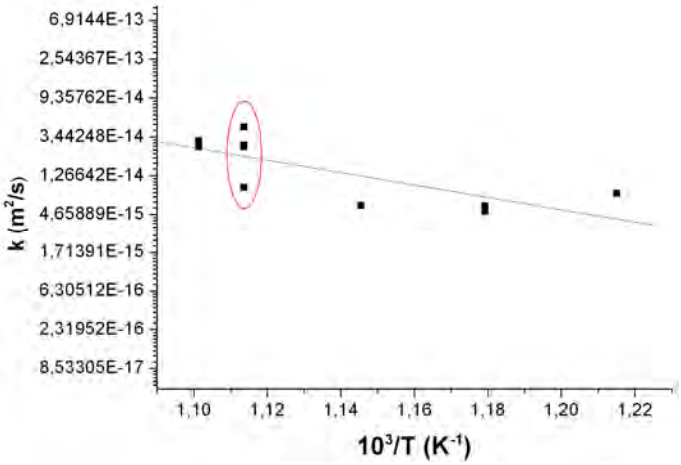


Figure 3: ln *k* versus the reciprocal temperature with linear regression used as guide line for eyes.

5. Conclusion

Since UAl_4 is the thermodynamic stable compound, its formation is expected for the highest temperatures and longest dwell periods. UAl_3 is the kinetic compound and the growth rate of its interaction layer is parabolic with respect to time. The UAl_3 interaction layer grows with a planar morphology and is free from porosity. UAl_3 forms until consuming all the UAl_2 phase. The microstructure of UAl_3 shows the formation of pores and voids that develop in planes perpendicular to the diffusion direction. For longer dwell periods and higher temperatures UAl_4 forms at the vicinity of these voids and cracks that act as favorable zones for the diffusion of Al. When the equilibrium is established between UAl_4 and Al, the interdiffusion material appears fragile and brittle and tends to decompose to powder.

The formation of interaction product involves a series of successive steps, starting from the formation of saturated primary solid solution, nucleation of an intermediate phase and then the growth of the nucleated interaction compound. Since UAl_2 has no homogeneity range, the initial step of the formation of the interaction product starts with the nucleation of UAl_3, which shows no deviation of the stoichiometry (section 4.2).

The temperature dependence of growth of the UAl_3 layer follows an Arrhenius law. The dispersion of data points may be ascribed to experimental conditions which involve the evolution of the pressure during the heat-treatment, (i) the release of the applied pressure of the clamping system with the temperature, (ii) the increase of the internal pressure associated to the formation of UAl_3. The changes of UAl_2 micro hardness with temperature and time should also be considered. The formation of cracks and pores associated to the mechanical properties act as easy diffusion paths for long annealing times.

6. References

[1] S. Storchheim, J.L. Zambrow, Report SEP-102 (1952)

[2] A.D. Le Claire, I.J. Bear, J Nucl. Energy, 2 (1956) 229-242.

[3] L.S. DeLuca, H.T. Sumsion, KAPL -1747, General electric Compagny, New York, 1957

[4] L.S. Castleman, J.Nucl. Mater., 3 (1961) 1-15.

[5] T.B. Massalski, H. Okamoto, P.R. Subramanian, L. Kacprzak (Eds.), BinaryAlloy Phase Diagrams, vols. 1–3, second ed., ASM International, 1990.

[6] Y. Adda, M. Beyeler, A. Kirianenko, B. Pernot, Commissariat à l'Energie Atomique report n°1664, (1961).

[7] A. Laik, K. Bhanumurthy, G.B. Kale, Intermetallics, 12 (2004) 69-74

[8] M. Mirjalili, M. Soltanieh, K. Matsuura, M. Ohno, Intermetallics 32 (2013) 297-302.

[9] J. Dickson, L. Zhou, A Paz y Puente, M. Fu, D.D Keiser Jr, Y.H. Sohn, Intermetallics, 49, (2014) 154-162.

PROGRESS IN DEVELOPMENT OF LARGE, FORMED HIP CANS FOR CLADDING OF U-MO FUEL

K.D. CLARKE, L.A. TUCKER, J.M. CRAPPS, J.E. SCOTT, B. AIKIN, V. VARGAS, M.J. DVORNAK, R.W. HUDSON, D.E. DOMBROWSKI
Materials Science & Technology Division, Los Alamos National Laboratory, PO Box 1663, Los Alamos, NM, 87544 - USA

ABSTRACT

The cladding of LEU U-10Mo fuel foils with 6061 aluminum is being done by solid state bonding in a Hot Isostatic Press (HIP). HIP is performed by encapsulating the fuel assembly in an evacuated stainless steel can. Previous cladding process development efforts have used six-piece, rectangular stainless steel cans, which are welded at the twelve edges of stainless steel sheet. During HIP processing, each weld produces a deviatoric stress distribution, which is less than the full desired bonding pressure. Modeling has shown that a two-piece mild steel formed HIP can produces a more uniform bonding pressure distribution. Experimental demonstration has been done with small, formed mild steel HIP cans and large prototypical size mild steel HIP cans containing U-10Mo fuel foil.

1. Introduction

In support of the United States' nonproliferation and highly enriched uranium (HEU) minimization policies, the U.S. Department of Energy (DOE)/National Nuclear Security Administration's (NNSA) Global Threat Reduction Initiative (GTRI) is actively working to convert civilian research and test reactors from the use of HEU fuel to low enriched uranium (LEU) fuel. GTRI's Reactor Conversion program provides governments and facilities around the world with technical and economic assistance for conversion. If no suitable LEU fuels are available, the program contributes to the development of new LEU fuels. To date, GTRI has converted or verified the shutdown of 87 research reactors worldwide, including 20 domestic facilities. Of the remaining domestic research reactors, five U.S. high performance research reactors (USHPRRs) and one associated critical assembly will require a new high density LEU fuel and fabrication capability, which is currently under development, to convert. Existing qualified fuels do not meet the high fuel density requirements for the operation of these high-performance reactors, which include the Advanced Test Reactor (ATR) at Idaho National Laboratory, the High Flux Isotope Reactor (HFIR) at Oak Ridge National Laboratory, the University of Missouri Research Reactor (MURR), the Massachusetts Institute of Technology Reactor (MITR), and the Department of Commerce's National Bureau of Standards Reactor (NBSR). To maintain performance requirements, the Reactor Conversion program is developing a high-density monolithic plate fuel system, which uses low enriched uranium 10wt% molybdenum (U10Mo) foils clad with aluminum.

The probable processing path for U10Mo alloy monolithic fuel plates for high-powered research and test reactors includes hot isostatic pressing (HIP) to bond the aluminum cladding that encapsulates the fuel foil to the fuel foil and to itself. Initial HIP experiments were performed at Idaho National Laboratory (INL) on approximately ¼ scale "mini" fuel plate samples using a HIP can design intended for these smaller experimental trials [5.1-5.4]. This HIP can design consists of six plates that are assembled and welded to create a box.

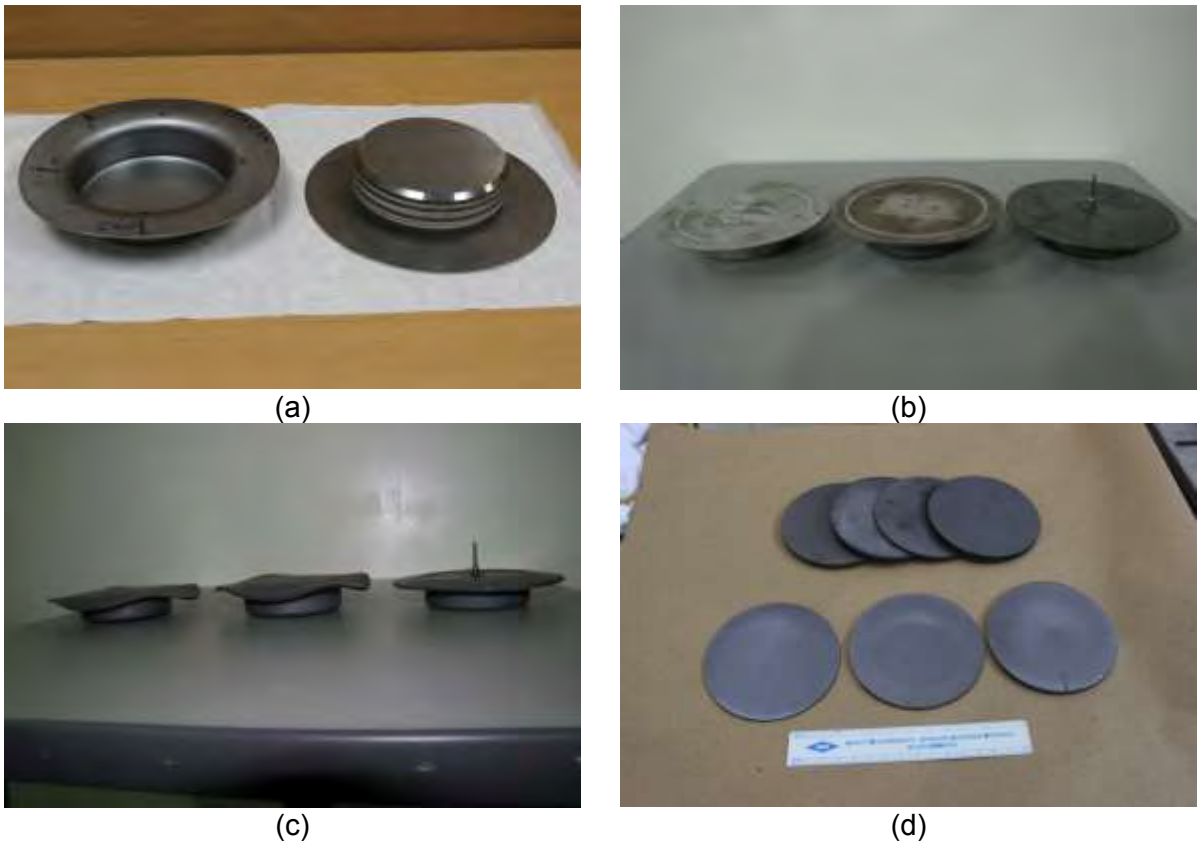
The HIP can is designed to contain a "stackup" of alternating strongbacks (flat steel plates used to separate, transfer uniform stress, and ensure flat fuel plates) and fuel plate layers (including the fuel foil or a surrogate and outer aluminum cladding material). These

experiments showed that, with the addition of a co-rolled zirconium diffusion barrier on the LEU-10Mo alloy fuel foil, the HIP bonding process is a viable method for producing monolithic fuel plates, and HIPed fuel plates have met expectations in irradiation testing. Further experimental trials at Los Alamos National Laboratory (LANL) effectively scaled-up the “mini” can design to produce full-size fuel plates [5.5].

This report summarizes efforts at LANL to produce a HIP can design that is further optimized for higher volume production runs. The production-optimized HIP can design goals were determined by LANL and Babcock & Wilcox (B&W) to include maintaining or improving the quality of the fuel plates produced with the baseline scaled-up mini can design, while minimizing material usage, improving dimensional stability, easing assembly and disassembly, eliminating machining, and significantly reducing welding.

The initial small-scale experiments and modeling have been described in a previous report [5.6] and show that a formed-can approach can achieve the goals described above [5.7-5.9]. Fig 1 shows representative cans from the small-scale trials. The small-scale trials were very successful, produced well-bonded and flat HIPed plates, and showed that the formed-can approach can be used with electron-beam welding or tungsten inert gas (TIG) hand welding (see Fig 1b).

This report summarizes initial efforts to scale-up the formed-can approach to produce fuel plates nominally 63.5 cm (25 inches) long x 12.7 cm (5 inches) wide (hereafter described as “full-scale”). It should be noted that work to develop processing paths to HIP bond the aluminum cladding layer without any HIP can enclosure [5.8] is being performed in parallel to this project, and is described as the “canless” HIP method.



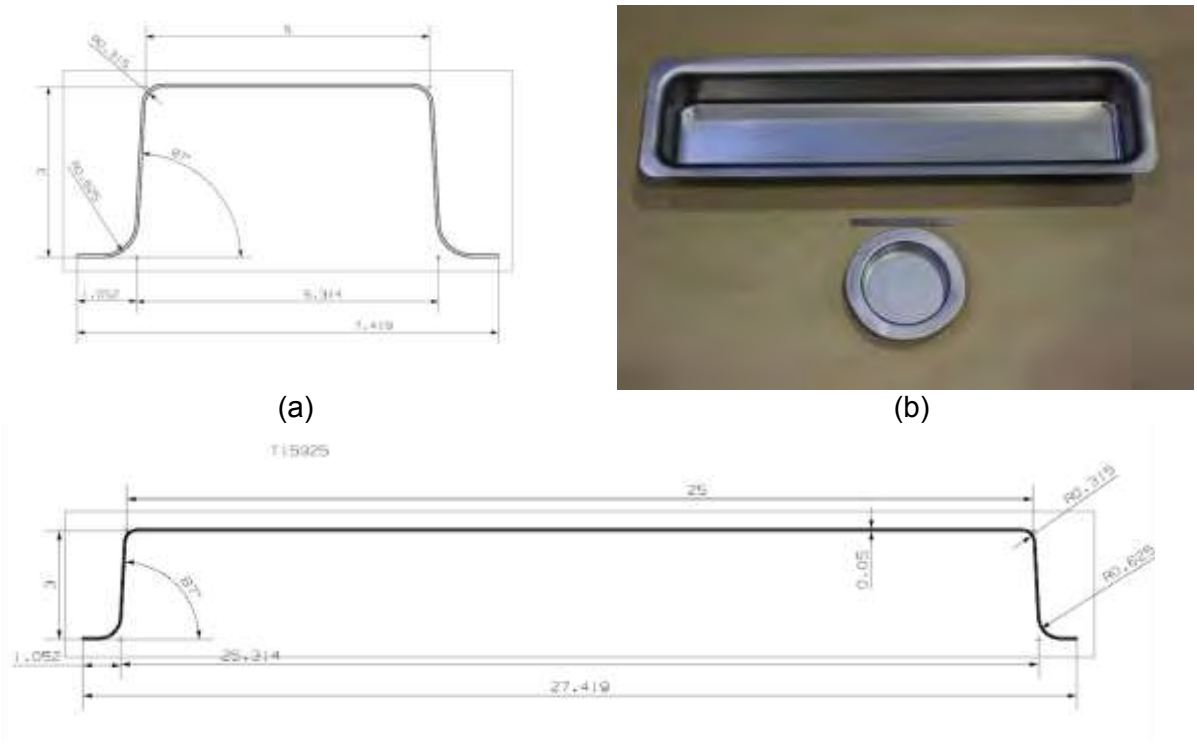
(a) (b) (c) (d)

Fig 1. Representative images of small-scale HIP cans during assembly (a), as welded (b), as-HIPed (c), and three HIPed plates and stacked strongbacks after HIP (d). The inside diameter of the round can is approximately 9 cm (3.5 inches).

2. Results

2.1 Experimental Trials

The first design iteration of the full-scale formed HIP cans have been produced based upon initial small-scale trials [5.6] and finite element analysis results. The dimensions of the formed can and images of the as-formed can are shown in Fig 2.

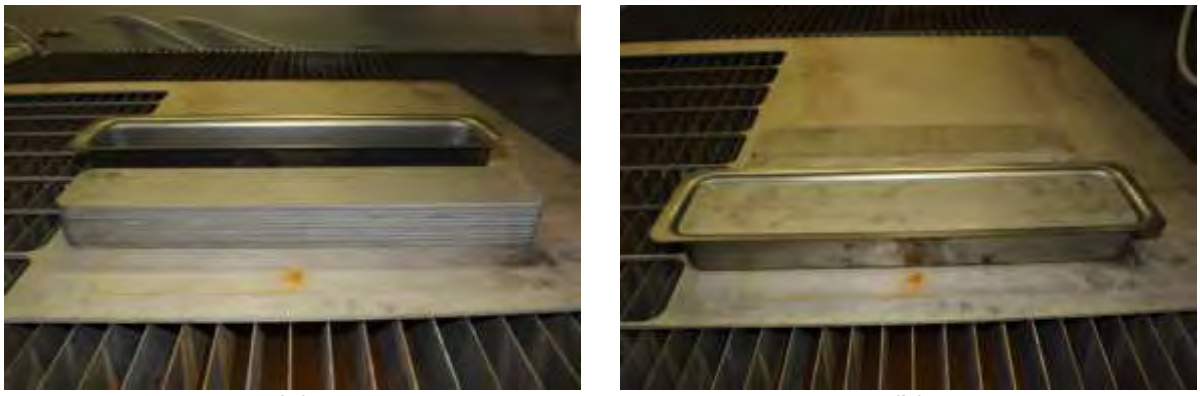


(a) (b)

(c)

Fig 2. Dimensions in inches (a,c) and image (b) of the first iteration of full-scale formed HIP can, compared with a can used for small-scale trials. The material used to form the can is mild steel with a thickness of 1.5 mm. For reference, the length, width, and depth of the can are 63.5, 12.7, and 7.6 cm, respectively.

In addition to the formed cans, the accompanying strongbacks and aluminum plates have been manufactured to produce a stackup to produce a tight fit in the can. Fig 3 shows the stackup of stainless steel plates (strongbacks) and aluminum (cladding) as-machined for the first HIP experiment.



(a) (b)

Fig 3. Machined stackup of 6.35 mm (0.25 inch) thick stainless steel strongbacks and 1 mm (0.037 inch) thick 6061 aluminum plates, both outside (a) and as-assembled (b) in the can.

The HIP processing path to produce an aluminum-clad fuel plate consists of a series of processing steps which were developed using the “mini” HIP cans at INL [5.10, 5.11]. The details of the HIP processing procedures are documented in reference [5.12]. The following basic processing steps have been followed for all HIP can process runs described in this report:

- Prepare stackup materials (steel strongbacks, 6061 Al cladding, U-10Mo fuel foils with Zr co-rolled diffusion barrier or surrogate such as stainless steel or zirconium) and HIP can.
- Ensure correct sizing with dry-run assembly of all components.
- Clean stackup materials and HIP can [5.10, 5.12].
- Assemble stackup materials in HIP can with parting agent (currently MoS_2 aerosol spray).
- Evacuate can and weld lid seams to hermetically seal. This is possible in one step if electron-beam welding within an evacuated chamber is used. GTAW welding requires welding seams, attaching vacuum tube, evacuating HIP can, baking out gasses from HIP can at 350°C, and crimp-welding the vacuum tube. All cans in this report we sealed by electron-beam welding.
- Run HIP cycle at 560°C and 103 MPa (15 ksi) for 90 minutes. Heating and cooling times are approximately 3 hours and 2 hours, respectively, for the LANL HIP equipment. These times are specific to the HIP equipment being used (i.e., larger HIP’s will have slower heating and cooling times).
- Section welds to open can, generally with band saw for formed cans or milling machine for baseline can design.

Three full-scale formed HIP cans have been processed to date, two with only aluminum cladding, and one with one layer including a DU10Mo foil. A representative can during assembly, as-welded, and after HIP processing is shown in Fig 4.

Generally, the formed HIP can performed excellently, showing good deformation over the entire area of the can and resulting in bonded plates that show excellent flatness and consistent thickness over the entire area of the plate. In addition, the can was easy to disassemble, requiring only the removal of the electron-beam welds by band saw to remove the stackup from the can.

For each of the first three cans, however, there have been small breaches in the can at some point during the HIP cycle, as shown in Fig 5. For cans #1 and #2, this occurred on the lid, where the top strongback was smaller in area than the strongback below, which resulted in a tear in the material after it deformed during the HIP cycle. For can #1, this resulted in poor bonding of the aluminum-aluminum plates, but for can #2, the breach likely occurred late enough in the cycle to result in apparently good bonding of the plates.

The stackup was modified for can #3 with a strongback that was slightly larger than the top strongback, to fill the space near the top of the can where the flange radius flares out. This resulted in a small breach underneath the flange on the can itself. Future cans will be processed with strongbacks of equal size to that below it to prevent these breaches.

The current can design includes some characteristics that, based on these initial experiments, may be further optimized. As a result of the trials detailed here, it is likely desirable to (1) reduce the total weight of the can, (2) move from angled walls to vertical walls, and (3) reduce the top and bottom radii in the can. Finite element analyses have been performed to determine the performance of a can with these design changes.

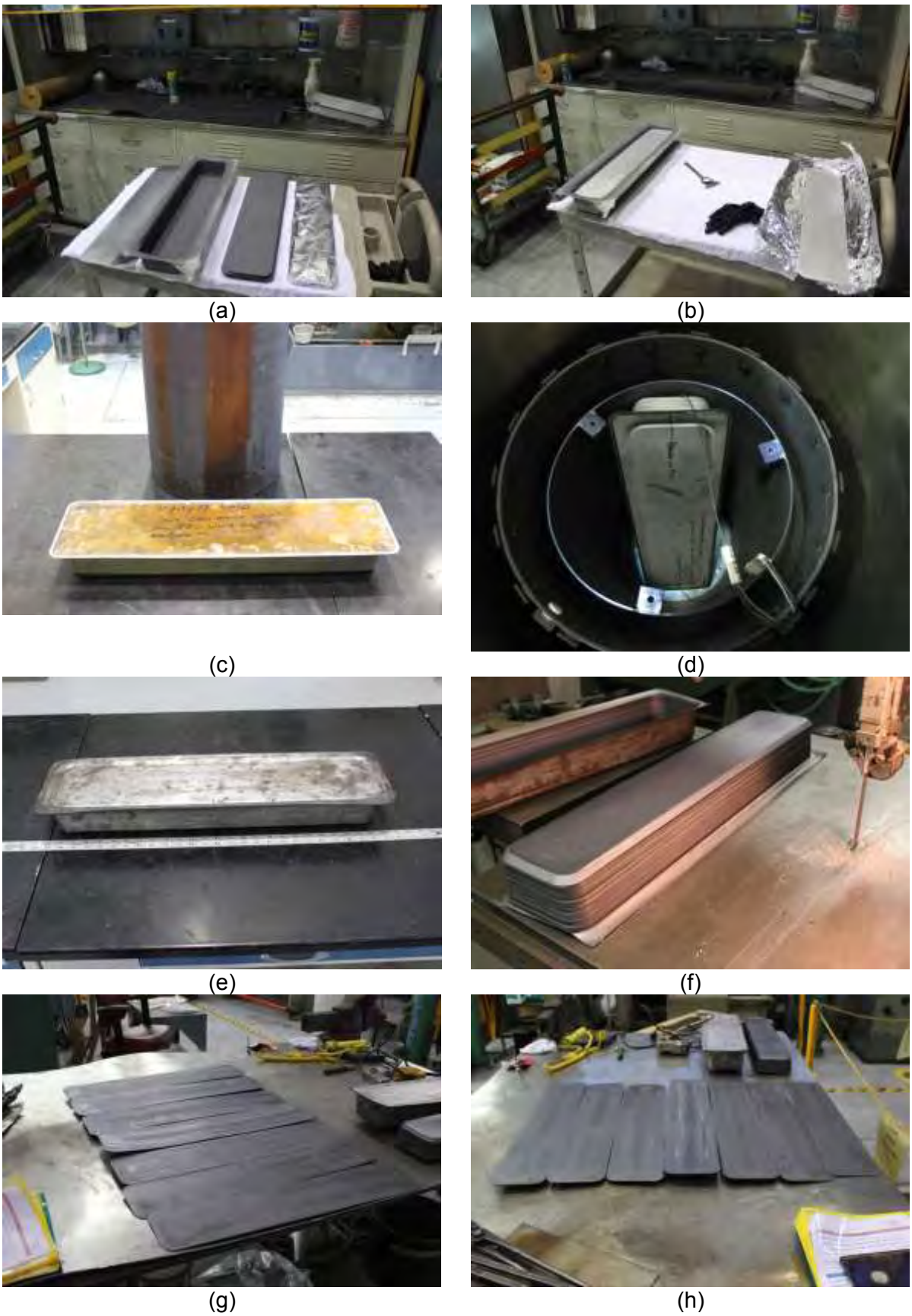
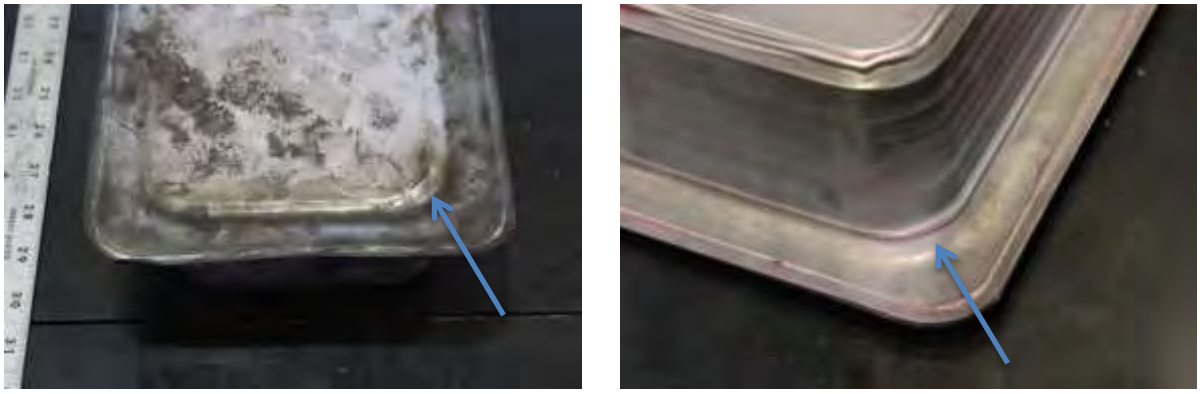


Fig 4. Representative images of the large formed HIP can during assembly (a,b), as-welded (c), in the HIP after the HIP cycle (d), after HIP (e), after opening (f), and the seven as-HIPed plates (g,h).



(a) (b)

Fig 5. Locations of can breaches on cans #1 and #2 (a), and #3 (b)

2.2 Finite Element Modeling

Finite element analyses have been performed on a revised version of the full-scale formed HIP can, and results are shown in Fig. 6. This can design is less deep than the initial design (3.81 cm vs. 7.62 cm), significantly reducing the weight. The walls are vertical, allowing each of the strongbacks and fuel plates in the stackup to be the same size, eliminating the varying size parts required in the can with the angled walls. The vertical walls may make removal of the stackup from the can more difficult, however. Finally, the reduced top and bottom radii of the formed can also eliminate difficulties associated with filling empty areas in the can (near the lid), and reduces the machining required to match the shape of the bottom of the can on the bottom strongback.

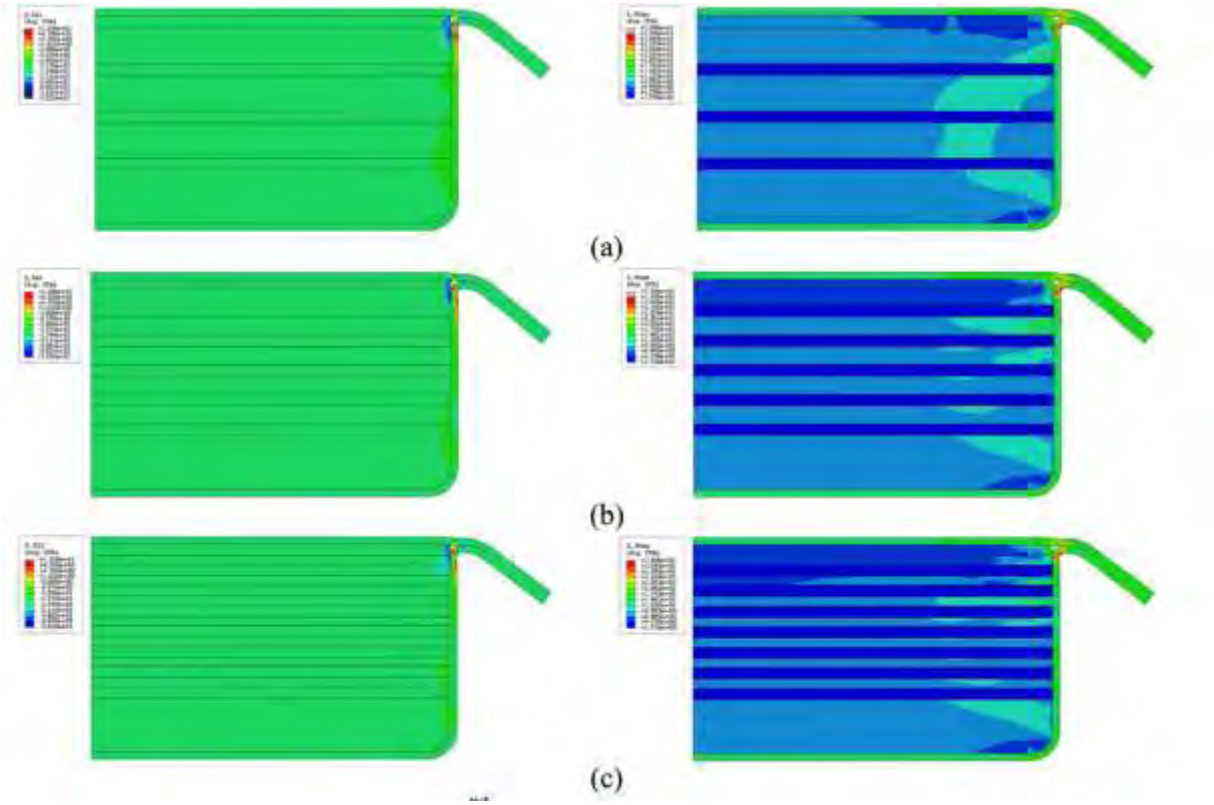


Fig 6. Abaqus finite element analyses of optimized full-scale formed HIP can, showing vertical (S22) stresses in the left image and Von Mises stresses in the right image. Internal stackups including (a) 3, (b) 5, and (c) 7 fuel plates are shown.

Excellent uniform stress distributions are shown, indicating that the optimized can design should perform equivalently to the initial full-scale formed can in producing well-bonded and flat fuel plates that require little further processing. The stackup can also be modified to accommodate seven fuel plates, or more, which reduces the overall number of HIP runs needed to meet production requirements.

3. Summary

The formed HIP can approach offers a viable processing path for producing high-quality HIP-clad fuel plates with reduced time and cost. Stress distributions in all formed can designs have been shown to be uniform, which produces flat plates, minimizing subsequent processing. Further work is required to optimize the can geometry to ensure breaches do not occur during processing and the can is production-ready.

4. Acknowledgements

The authors would like to acknowledge the financial support of the US Department of Energy Global Threat Reduction Initiative Reactor Convert program. Los Alamos National Laboratory, an affirmative action equal opportunity employer, is operated by Los Alamos National Security, LLC, for the National Nuclear Security Administration of the U.S. Department of Energy under contract DE-AC52-06NA25396.

5. References

5.1 D.E. Burkes, D.D. Keiser, D.M. Wachs, J.S. Larson, M.D. Chapple, “Characterization of Monolithic Fuel Foil Properties and Bond Strength”, RRFM 2007, Lyon, France, March 11-15, 2007.

5.2 G.A. Moore, F.J. Rice, N.E. Woolstenhulme, W.D. Swank, D.C. Haggard, J. Jue, B.H. Park, S.E. Steffler, N.P. Hallinan, M.D. Chapple, and D.E. Burkes, “Monolithic Fuel Fabrication Process Development at the Idaho National Laboratory”, RERTR 2008, Washington, D.C., October 5-9, 2008.

5.3 G.A. Moore, F.J. Rice, N.E. Woolstenhulme, J-F. Jue, B.H. Park, S.E. Steffler, N.P. Hallinan, M.D. Chapple, M.C. Marshall, B.I. Mackowiak, C.R. Clark, and B.H. Rabin, “Monolithic Fuel Fabrication Process Development at the Idaho National Laboratory”, RERTR 2009, Beijing, China, November 1-5, 2009.

5.4 J-F. Jue, B.H. Park, C.R. Clark, G.A. Moore, and D.D. Keiser Jr., “Fabrication of Monolithic RERTR Fuels by Hot Isostatic Pressing”, Nuclear Technology, Vol. 172, Nov. 2010, pp. 204-210.

5.5 J. Katz, K. Clarke, B. Mihaila, J. Crapps, B. Aikin, V. Vargas, R. Weinberg, A. Duffield, and D. Dombrowski, “Scale-up of the HIP Bonding Process for Aluminum Clad LEU Reactor Fuel”, RERTR 2011, Santiago, Chile, October 23-27, 2011.

5.6 J. Crapps, K. Clarke, J. Katz, D.J. Alexander, B. Aikin, V.D. Vargas, J.D. Montalvo, D.E. Dombrowski, B. Mihaila, “Development of the hot isostatic press process for monolithic nuclear fuel”, Nuclear Engineering and Design, Vol. 254, January 2013, pp. 43-52.

5.7 K.D. Clarke, J. Crapps, J. Scott, B. Aikin, V. Vargas, M. Dvornak, A. Duffield, R. Weinberg, D. Alexander, J. Montalvo, R. Hudson, B. Mihaila, C. Liu, M. Lovato, D. Dombrowski, “Hot Isostatic Press Can Optimization for Aluminum Cladding of U-10Mo Reactor Fuel Plates: FY12 Final Report and FY 13 Update”, August 2013, Los Alamos National Laboratory LA-UR-13-26706.

5.8 K.D. Clarke, C.E. Cross, R.E. Hackenberg, R.J. McCabe, J.D. Montalvo, M.J. Dvornak, R.L. Edwards, J.M. Crapps, R.R. Trujillo, B. Aikin, V.D. Vargas, K.J. Hollis, T.J. Lienert, B. Mihaila, D.L. Hammon, R.W. Hudson, T.J. Tucker, J.E. Scott, A.N. Duffield, R.Y. Weinberg, and D.E. Dombrowski, “Development of Aluminum-Clad Fuel Plate Processing Through Canned and Canless Hot Isostatic Pressing (HIP), and Studies of Aluminum Cladding Grain Growth during HIP”, RERTR 2012, Warsaw, Poland, October 14-17, 2012.

5.9 N.A. Mara, J. Crapps, T. Wynn, K. Clarke, P. Dickerson, D.E. Dombrowski, B. Mihaila, and A. Antoniu, “Nanomechanical Behavior of U-10Mo/Zr/Al Fuel Assemblies”, RERTR 2011, Santiago, Chile, October 23-27, 2011.

5.10 J-F Jue, B.H. Park, C.R. Clark, G.A. Moore, D.D. Keiser, Jr., “Fabrication of Monolithic RERTR Fuels By Hot Isostatic Pressing”, Nuclear Technology, V. 172, Nov. 2010, pp. 204-210.

5.11 H. Ozaltun, P.G. Medvedev, “Structural Behavior of Monolithic Fuel Plates During Hot Isostatic Pressing and Annealing”, RRFM 2010, Marrackech, Morocco, March 21-25, 2010.

5.12 R.E. Hackenberg, R.J. McCabe, J.D. Montalvo, K.D. Clarke, M.J. Dvornak, R.L. Edwards, J.M. Crapps, R.R. Trujillo, B. Aikin, V.D. Vargas, K.J. Hollis, T.J. Lienert, R.T. Forsyth, and K.L. Harada, “Initial Studies of Process Improvements for Increasing Clad-Clad Interface Grain Growth in Monolithic Fuel Plates”, LANL publication LA-UR-12-25123.

EFFECT OF COLD DEFORMATION AND ANNEALING TEMPERATURE ON U-10Mo FUEL FOIL GEOMETRY

D. J. ALEXANDER, K. D. CLARKE, J. E. SCOTT,
J. D. MONTALVO, D. E. DOMBROWSKI
Materials Science and Technology Division
MST-6 Metallurgy
Los Alamos National Laboratory
P.O. Box 1663, Los Alamos, NM, 87545 – USA

ABSTRACT

LEU U-10Mo fuel fabrication produces a 0.4-mm-thick (0.015 in.) fuel foil by hot deformation and cold deformation. The percentage of cold deformation done has a significant effect on fuel foil residual stress and final fuel foil geometry. This work describes the development of an annealing process to reduce residual stress and improve flat, planar fuel geometry. The results of five different annealing temperatures on the fuel foil geometry are shown for up to five different levels of cold deformation. Microstructural effects at the interface between fuel foil and zirconium diffusion barrier are reviewed.

1. Introduction

In support of the United States' nonproliferation and highly enriched uranium (HEU) minimization policies, the U.S. Department of Energy (DOE)/National Nuclear Security Administration's (NNSA) Global Threat Reduction Initiative (GTRI) is actively working to convert civilian research and test reactors from the use of HEU fuel to low enriched uranium (LEU) fuel. GTRI's Reactor Conversion program provides governments and facilities around the world with technical and economic assistance for conversion. If no suitable LEU fuels are available, the program contributes to the development of new LEU fuels. To date, GTRI has converted or verified the shutdown of 87 research reactors worldwide, including 20 domestic facilities. Of the remaining domestic research reactors, five U.S. high performance research reactors (USHPRRs) and one associated critical assembly will require a new high density LEU fuel and fabrication capability, which is currently under development, to convert. Existing qualified fuels do not meet the high fuel density requirements for the operation of these high-performance reactors, which include the Advanced Test Reactor (ATR) at Idaho National Laboratory, the High Flux Isotope Reactor (HFIR) at Oak Ridge National Laboratory, the University of Missouri Research Reactor (MURR), the Massachusetts Institute of Technology Reactor (MITR), and the Department of Commerce's National Bureau of Standards Reactor (NBSR). To maintain performance requirements, the Reactor Conversion program is developing a high density monolithic plate fuel system which uses low enriched uranium-10wt% molybdenum (U-10Mo) foils clad with aluminum (Al).

The probable method for producing the U-10Mo fuel foils involves casting of the U-10Mo alloy, homogenization, sectioning of the cast ingot into appropriately sized coupons, and machining these coupons to the desired dimensions. After suitable cleaning of all components, the machined coupons are assembled into a steel can, along with thin foils of zirconium (Zr) on each face of the U-10Mo coupon. The assembled can is then welded shut along its edges, to seal the U-10Mo and Zr foils inside, and prevent their exposure to air during the hot rolling, which will roll bond the Zr to the U-10Mo fuel. The role of the Zr is to provide a diffusion barrier between the U-10Mo and an Al cladding layer that will be bonded to the fuel foil at a later stage in the fabrication process. Parting agents are used as necessary to allow the steel can to be removed from the foil after the hot rolling is completed.

After hot rolling, the edges of the steel can are sheared off, and the can is removed from the foil. The foil, now with a Zr layer on each face, is then cold rolled to the final thickness; in this case, the final (total) thickness (Zr + U-10Mo + Zr) is 0.38 mm (0.015 in.).

Although the intent of the hot and cold rolling is to produce flat, smooth foils, this is not always possible, and the foils may be bowed or rippled after rolling, either locally or over the length of the foil. These distortions may affect the final bonding of the Al cladding, which is done by a hot isostatic pressing (HIP) process. Distortions may make it difficult to align the Al cladding with the fuel foil during preparation for the HIP run. The distortion may cause the fuel foil to press against the Al cladding and thus create a thinner area in the cladding layer. Therefore, it would be very helpful if there was a process by which distorted foils could be flattened to remove any distortions.

The present work was carried out to see if a simple annealing treatment could flatten distorted foils. For the same starting conditions (i.e. U-10Mo coupon thickness), 5 levels of cold work, and hence different levels of residual stress, were chosen to span a wide processing range. This in turn required 5 different levels of hot rolling, so that the same final thickness would be reached in all cases. Similarly, 5 different annealing treatments were chosen, again spanning an appropriate processing range of temperatures.

2. Experimental Design and Procedure

Several levels of cold work were chosen, as shown in Table 1. The 4 higher levels of cold work were selected to have strains increasing in equal amounts, with targeted values of true plane strain of 0.4, 0.8, 1.2, and 1.6. A fifth very low level of cold rolling was added, to see if foils could be produced with a minimal level of cold rolling. Five corresponding levels of hot rolling were then calculated, so that the same starting and finishing thicknesses would be maintained for all samples. Five annealing temperatures, from 550 to 750°C, in 50°C increments, were also chosen.

Four casting were produced to supply material for the rolling. The castings were flat plates, nominally 295 mm long by 137 mm tall by 5 mm thick (11.6 by 5.4 by 0.2 in.). The hot top was removed from each plate by electrodischarge machining (EDM), and the plates were then homogenized in vacuum for 4 hours at 1000°C, followed by an oil quench. Each plate was then sectioned by EDM into 6 coupons, nominally 96 mm by 67 mm (3.75 by 2.65 in.). The faces of each coupon were then milled to a final coupon thickness of 3.8 mm (0.150 in.), with approximately equal amounts being removed from both faces; this required multiple passes on each face.

After milling, the coupons were cleaned, and assembled into mild steel cans. A picture frame piece that matched the thickness of the coupon was used to center and align the U-10Mo coupon, and top and bottom plates were 4 mm (0.160 in.) thick. A Zr foil 0.25 mm (0.010 in.) thick was positioned on each face of the U-10Mo coupon. The cleaned and assembled can was clamped to preserve the alignment of the components, transferred to an argon glovebox, and all the edges of the can were welded, to seal the can and prevent exposure of the U and Zr to the atmosphere during hot rolling. The welded can was approximately 135 by 105 by 12.4 mm thick (5.32 by 4.15 by 0.490 in.).

The can was hot rolled after preheating in an air furnace to a temperature of 650°C; the can was reheated after each rolling pass. After the desired final thickness was reached in hot rolling, the can was annealed for 30 minutes at 650°C, and then air cooled. The edges of the can were sheared off, and the foil was removed from the can. The foil was cold rolled to the final thickness of 0.38 mm (0.015 in.)

The cold-rolled foils were trimmed to size, and placed between copper sheets. Vacuum annealing for 1 hour at the chosen temperatures was followed by an oil quench.

% Cold Roll	Final Foil Thick-ness (in.)	Hot-Rolled Foil Thick-ness (in.)	True Strain from Cold Rolling[1]	True Strain (plane strain)[2]		Initial Foil Thick-ness (in.)	Initial Can Thick-ness (in.)	% Hot Roll for Can	Can Thick-ness After HR (in.)	True strain from Hot Rolling[1]	True Strain (plane strain)[2]		Total Strain	Total Plane Strain
5	0.015	0.0158	0.051	0.059		0.170	0.490	90.7	0.0455	2.376	2.745		2.427	2.804
29	0.015	0.021	0.342	0.396		0.170	0.490	87.6	0.0609	2.085	2.408		2.427	2.804
50	0.015	0.030	0.693	0.801		0.170	0.490	82.4	0.0864	1.734	2.003		2.427	2.804
65	0.015	0.043	1.050	1.213		0.170	0.490	74.7	0.1235	1.378	1.592		2.428	2.805
75	0.015	0.060	1.386	1.601		0.170	0.490	64.7	0.1729	1.041	1.203		2.427	2.804

- all rolling is % reduction of thickness
- strains are negative; negative sign omitted for ease of presentation

[1] True strain calculated from thickness change only

[2] True strain calculated assuming plane strain; i.e. no change in foil width during rolling; true plane strain = true strain x 1.155

Table 1. Target rolling reductions and strains for hot and cold rolling

3. Results

The rolling of the cans and foils was readily accomplished. Since the thickness of the U-10Mo foil could not be measured directly during the hot rolling process, the strains could only be estimated based on the can thickness, but the changing can thickness should be a reasonable indicator of the foil strains. After removal of the can, the actual foil thickness was measured, and the actual strain could be determined.

Figure 1 is an example of a typical set of foils, in this case the 12K-641 series. On the left of the image is one piece of the can that was removed after hot rolling. The progressive increase in the hot rolling strain from top to bottom is shown by the increase in length of the can. It is also obvious that hot rolling results in a very rough, pebbly surface for the Du-10Mo foil, which in this case is preserved and shown by the matching inner surface of the can.

On the right side of the figure the corresponding foils are shown after cold rolling. The foils have been trimmed to length, and cut to a final width. The ripples and bows in the different foils can be seen. Also apparent is the dramatic improvement in the surface smoothness of the foils due to the cold rolling.

There are several intriguing aspects of the rolling. Minimal levels of hot rolling are not sufficient to achieve a proper bond between the Zr layer and the Du-10Mo, which is reflected in blisters and other defects on the surface of the finished foils. This can be seen on the top foil, which received only 64% reduction in thickness by hot rolling. At the opposite extreme, very low levels of cold rolling are not sufficient to smooth out the pebbly surface remaining from the hot rolling, so the final surface is rough and uneven. It seems clear that there is some optimal range of hot and cold rolling that is needed to achieve both a satisfactory bond between the Zr and the U-10Mo, and yet still attain a smooth and even cold-rolled finish. The current work shows that the minimum amount of hot rolling is at least 75% reduction in thickness to achieve a satisfactory bond between the Zr and the U-10Mo. At least 25%, and preferably 50% reduction in thickness is needed in cold rolling to achieve a satisfactory surface appearance.

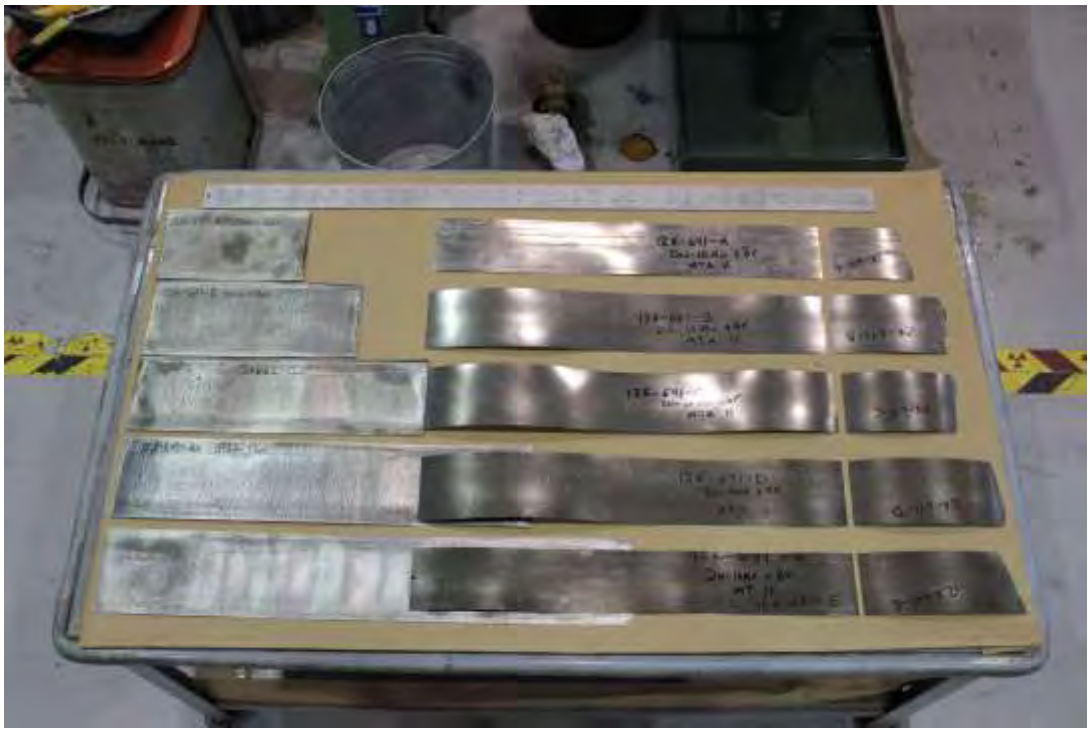


Figure 1. A typical series of 5 foils after cold rolling, and the steel cans from these foils. On the left are the steel cans, and on the right are the trimmed foils after cold rolling.



Figure 2. A series of cold rolled foils prepared for annealing at 650°C. The foils (the same as those shown in Fig. 1) have been placed on a Cu sheet. A similar Cu sheet will be positioned on top of the foils, and weighted. The assembly will be vacuum annealed and oil quenched.

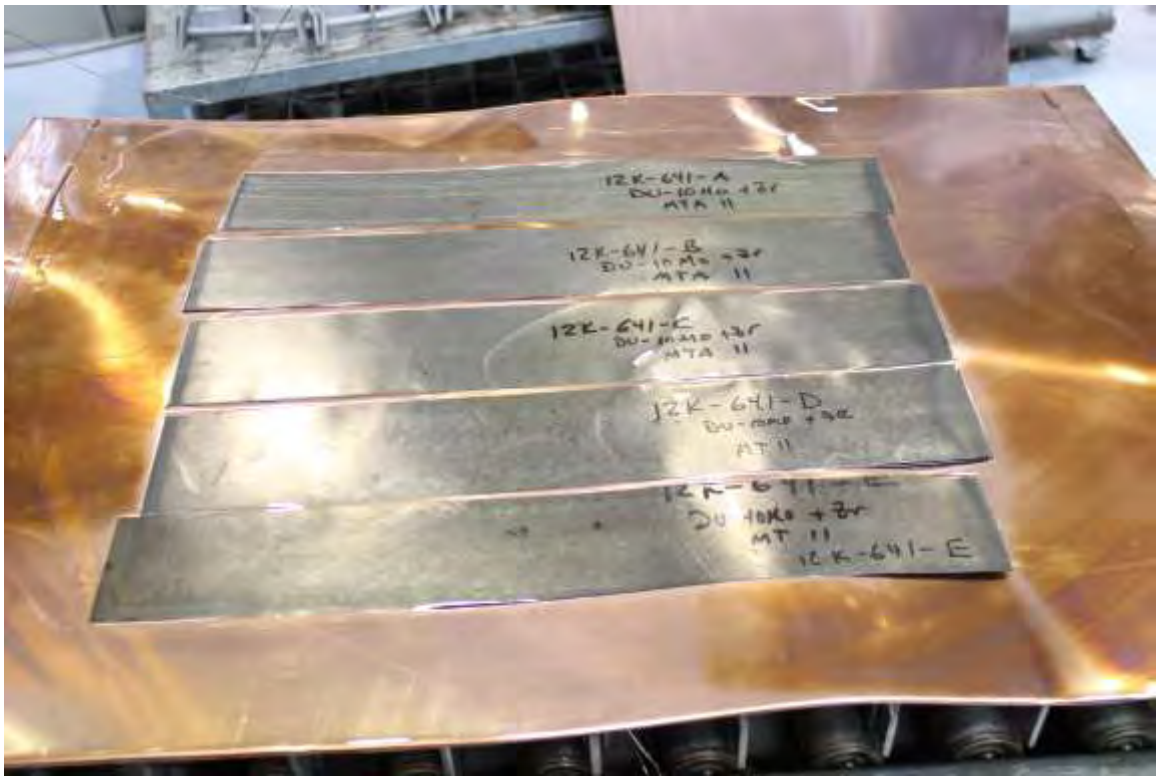


Figure 3. The same foils after vacuum annealing for 1 hour at 650°C, followed by an oil quench. Although the Cu plate has been distorted by the annealing procedure, the individual foils are much flatter and more uniform.

Figure 2 shows the cold rolled foils placed on a copper plate in preparation for annealing. The bows and ripples in typical rolled foils are readily apparent in this view. Another Cu plate, with an additional weight on top, was placed on top of the foils, and the vacuum annealing process was performed. The total mass of the Cu plate and the extra weight was 40 kg (90 lb). Figure 3 shows the same foils after the annealing treatment. The Cu plate has distorted slightly from the annealing process, but the U-10Mo foils are much flatter and smoother that before the anneal. In general, annealing at temperatures of 650°C or higher was able to dramatically improve the flatness of the foils.

The oil quench is needed because of the metastable microstructure in the U-10Mo alloy. The Mo addition stabilizes the gamma phase of the U, but holding the alloy at intermediate temperatures for long times may result in the decomposition of the gamma phase. The oil quench was used rather than a slow cool under vacuum to avoid any possible phase transformations in the gamma phase as the foils slowly cooled to room temperature.

One concern about an annealing process is whether the heat treatment has any effect on the interface between the Zr and the U-10Mo. Sections were taken from the middle of the annealed foils, and mounted and prepared for optical metallography examination. Some typical examples of foils annealed over a range of temperatures are shown in Figure 4. The local variability of the thickness of the Zr diffusion layer is quite noticeable, but the layer is sufficiently thick to serve its intended function. The annealing conditions have resulted in recrystallization of the U-10Mo foil. The interface between the Zr and the U-10Mo does not show any significant growth of any intermetallics that might degrade the strength of this interface, but additional examination at higher magnification than optical metallography permits is needed; i.e. by scanning electron microscopy.

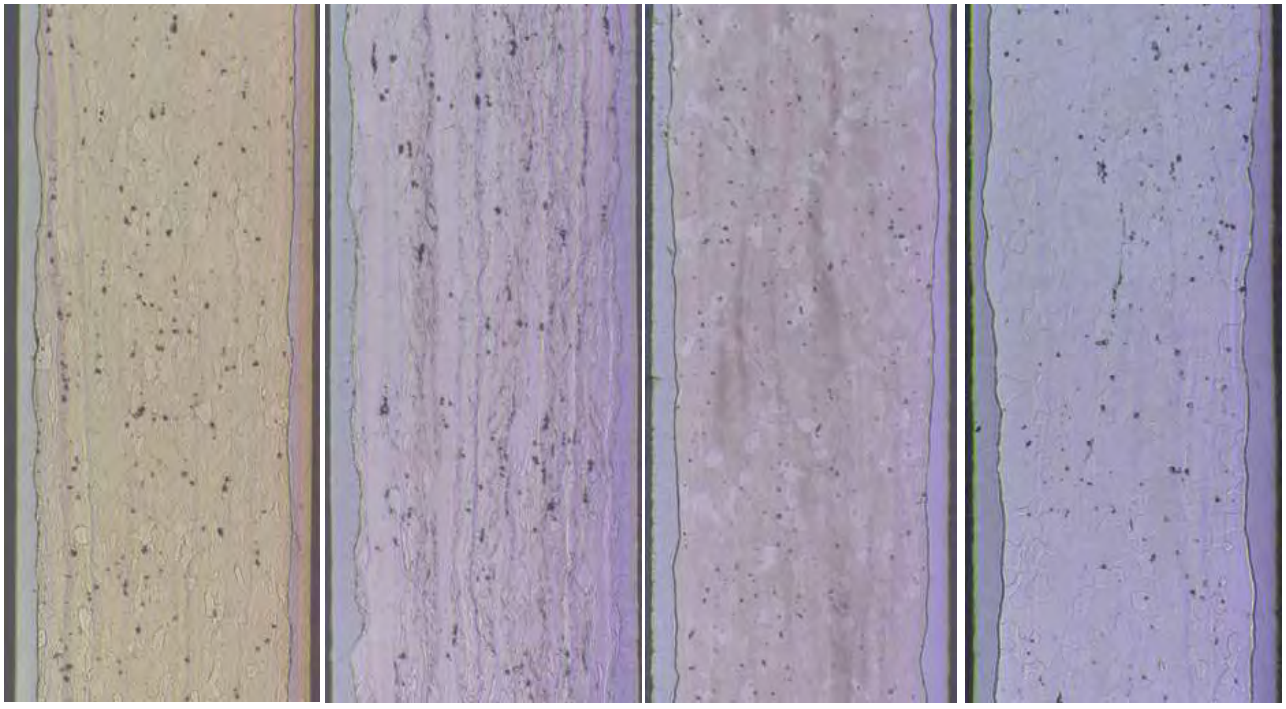


Figure 4. Microstructures of sections through annealed foils; the annealing temperatures are shown for each section. Note the variable thickness of the Zr layer on each edge of each of the foils. Annealing has resulted in recrystallization of the Du-10Mo.

4. Conclusions

1. Hot rolling of the U-10Mo alloy is readily accomplished at 650°C by enclosing the U coupon in a mild steel can, and reheating the can in an air furnace between hot-rolling passes.
2. Hot rolling of cast material results in a rough, pebbled surface on the rolled material.
3. Hot-rolled foils can be cold rolled at room temperature to their desired final thickness.
4. A minimum amount of hot rolling (at least 75% reduction in thickness) is required to achieve a satisfactory bond between the Zr and the U-10Mo material.
5. A minimum amount of cold rolling (25% reduction of thickness, and preferably 50%) is needed to smooth out the rough, irregular surface resulting from hot rolling.
6. Cold rolling may result in ripples and bows in the finished foils.
7. A simple vacuum annealing process in which the foils are placed between Cu plates, with an additional weight on the upper plate (40 kg total mass) can flatten the rippled foils.
8. Annealing temperatures of 650°C or more are effective in flattening the foils.

5. Acknowledgements

The authors would like to acknowledge the financial support of the US Department of Energy Global Threat Reduction Initiative Reactor Convert program. Los Alamos National Laboratory, an affirmative action equal opportunity employer, is operated by Los Alamos National Security, LLC, for the National Nuclear Security Administration of the U.S. Department of Energy under contract DE-AC52-06NA25396. We would like to thank R. M. Aikin, Jr. for the design of the casting mold, J. C. Robison for casting of the U-10Mo plates, T. V. Beard for sectioning the coupons and milling the faces, R. W. Hudson for fabricating the steel cans, R. L. Edwards for cleaning and assembling the steel cans, and A. N. Duffield for assembling and welding the steel cans.

METALLOGRAPHIC STUDY ON ALLOY ZIRCALOY-4 USED IN THE MANUFACTURE OF NUCLEAR USE

ALFREDO G. GONZALEZ [a], CARLOS A. MUÑOZ[a], GUILLERMO J. ARNALDO[b]

[a] *Gerencia Ciclo del Combustible Nuclear, Centro Atómico Constituyentes, Comisión Nacional de Energía Atómica*
b Gerencia de Materiales, Departamento de Caracterización y Fractomecánica, División Metalografía y Ensayos Termomecánicos, Centro Atómico Constituyentes, Comisión Nacional de Energía Atómica, Av. G. Paz 1499 (B1650KNA) San Martín, Buenos Aires, Argentina.

Abstract

In this paper we present the results of the metallographic examination of Zry-4 used in the manufacture of miniplates. The metallographic characterization was performed in order to qualify its microstructures and microhardness. This analysis was carried out for different stages of hot co-rolling, and changes produced in the welding process (method: TIG) to determine if the temperature generated at this stage of manufacture in the miniplate caused changes in the microstructure and microhardness in different areas, from edge to core.

1. INTRODUCTION

Nomenclature

RERTR Reduced Enrichment for Research and Test Reactors

HEU Highly Enriched Uranium

LEU Low Enriched Uranium

GTRI Initiative for Global Threat Reduction

CNEA National Commission of Atomic Energy

RA-3 Argentine Reactor 3

RA-6 Argentine Reactor 6

MTR Material Test Reactor

Zry-4 Zircaloy-4

U-Mo Uranium-Molybdenum

TIG Tungsten Inert Gas

HAZ Heat Affected Zone

RRFM Research Reactor Fuel Management

VHDF Very High Density Fuel

Since 1978 the U.S. has driven the program RERTR, whose goal is the conversion of the core of this type of reactors, which use HEU (90% in the isotope 235U) to LEU (below 20% of 235U).

Since 2003, the RERTR has been strengthened by the GTRI to meet reduced enrichment (HEU to LEU) and to investigate and develop compounds and/or uranium alloys of higher density to meet the decline of the isotope 235U.

CNEA has adhered to both programs timely, carrying out research and development of high-density and low enrichment fuels, in addition in order to enrichment of the reactors RA-3 and RA-6. The former uses uranium oxide as nuclear fuel (U3O8), whereas the latter uses uranium silicide, both LEU.

Since 1998 the CNEA has been conducting research and development of high-density and low-enrichment fuels, to be used in experimental reactors and the type Radioisotope Production MTR. These are studied due to the necessity to reduce the enrichment of uranium compound used as fuel, as 235U isotope below 20%. The compound used in this case is an uranium-molybdenum alloy (U-Mo) [3,4,5,6].

To continue developing this task, the National Commission of Atomic Energy (CNEA – Argentine) generated a special project in 2006, called the "Very High Density Fuels" (Spanish acronym CMAD) [1,2], which is responsible for research and development of these types of nuclear fuels and related tasks. Specifically in the development of these fuels, miniplates are being made, a task prior to the manufacture of fuel plates. The alloy known as Zry-4 is being used as coating material for cover and frame, and in the core the alloy used is uranium-molybdenum (U-Mo).

The alloy Zry-4 is widely known in the nuclear industry because of its low efficiency of neutron capture section and its excellent mechanical properties and corrosion resistance. The miniplate is a set of two covers and one framework of Zry-4 and a U-Mo core, which is welded and then subjected to the process of hot co-rolling. [3,4,5,6].

It is known that the mechanical properties depend strongly on the microstructure of the material and this, in turn, on heat treatments. It was then decided to evaluate the variation of the microstructure and microhardness Zry-4 in the co-rolling steps carried out at T = 650 ° C (the temperature selected for making miniplates), as well as the welding process.

This analysis was made at the different stages of co-rolling, as well as to analyze the changes in the welding process of miniplates (method TIG), in order to determine whether the temperature increase generated at this stage of manufacturing, caused an undesired effect to the core. The above mentioned analysis was carried out in different areas, from the edge of the miniplate to the core.

2. METHODOLOGY

The metallographic study object of this work was carried out following the techniques recommended by the following rules: a) For the preparation of the sample, using the ASTM E-3, b) for the development of the microstructure ASTM E-407, c) and ASTM E-384 for Vickers microhardness testing. For these studies we have used the following technical equipment: Vickers Microhardness Brand Metallographic Microscope Leica and Olympus.

The laminations of strip Zry-4 used for the manufacture of covers and frames, and the miniplate co-lamination were all carried out at 650 ° C.

The strip was laminated from 8mm to 2.4 mm in 10 steps with an average reduction of 11% at each stage. Then it was laminated from 2.4 mm to 1.1 mm in 4 stages with an average reduction of 18% at each stage. The co-lamination of the miniplates was conducted in 15 stages in total with an average reduction of 15%.

Metallographic examination of the strip of Zircaloy 4 and the miniplate was performed through the control of the microstructure and the measurement of microhardness.

3. EXPERIMENTAL RESULTS

3.1. Microstructure analysis strip Zry-4

The microstructure of the strip used to manufacture the frame and the covers was examined.

Figure 1 shows a photograph of samples of 8mm strip before the lamination was carried out



Figure 1. Photographic strip samples of Zry-4 8 mm

A1 is tail rolling (not used). A2 shows the tail away from the lamination, the arrows indicate the direction of the lamination.

Figure 2 shows the grain structure of sample A2, which area is used for the manufacture of covers and frames.



Figure2. Strip microstructure 8 mm

The grains are elongated in the rolling direction.

Figure 3 shows a photograph of the samples of laminated strips from 8 mm to 2.4 mm.

The lamination was carried out in 10 stages with an average reduction of 11% and placed in the oven for 15 minutes each time.

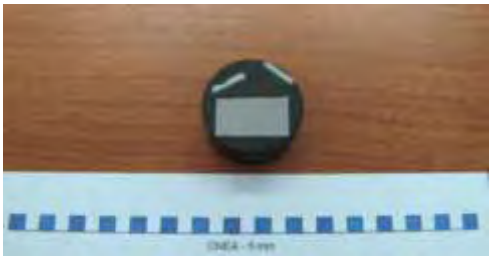


Figure3. Rolled strip up to 2.4 mm

Figure 4 shows a homogeneous structure oriented in the direction of the lamination.



Figure4. Microstructure rolled strip up to 2.4 mm

Figures 5 (a) and (b) show the microstructure of the samples rolled strip of 2.4 mm to 1.1 mm, used in the manufacture of the frame. In this case, lamination was conducted in four stages and placed in the oven for 15 minutes each time.



Figure5. (a) Laminated sample 1.1 mm; (b) Microstructure of rolled strip up to 1.1 mm

As in the previous samples, the grain structure is homogeneous, oriented in the direction of the lamination.

Table 1 shows the microhardness values of each of the three samples.

Table 1. Microhardness of the three samples

STRIP Zry-4	**Microhardness (Hv)**
8,0 mm	258
8,0 mm-2,4 mm	241
2,4 mm - 1,1 mm	225

3.2. Microstructure analysis of miniplate

The microstructure of the Zry-4 miniplate is affected firstly in the welding process by the rise in temperature and the absorption of impurities in the air, and secondly, in the stages of rolling.

Figure 6 shows a photograph of the miniplate uncoated sample on which the effect on the microstructure in the welding process was evaluated.

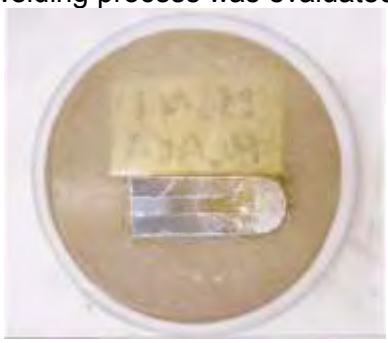


Figure6. Photographic uncoated miniplate sample

Figure 7 shows the external structure of the HAZ called base material. The equiaxial grains are homogeneous, while Figure 8 shows the microstructure of the HAZ, reaching the same 2.5 mm measured from the edge of the miniplate to the center, noting that the structure changes from a material structure phase-based equiaxial α grain acicular to a basket type structure with symmetrical deformations on the edge of the weld. During welding the material is heated to melting temperatures, wherein the base material passes from a granular structure of α-phase to β-phase and then into liquid. Once the material is cooled, the welded zone exhibits an acicular "needle-like" granular structure α grain surrounded with a primary β phase grain boundaries, which is also α widmanstätten structure.

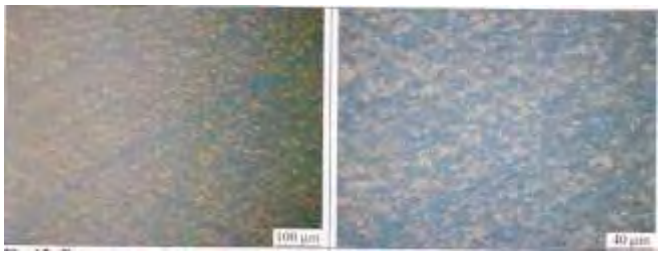


Figure 7 Microstructure of the HAZ



Figure8. Microstructure of the HAZ

3.3. Evaluation of microstructure at the rolling stages

The miniplate was laminated from an initial thickness of 6.5 mm to a final thickness of 1.1 mm. Figure 9 shows the microstructure of the miniplate co-laminated, a thickness of 2.7 mm, which shows a microstructure variation from a base material structure of the α-phase of equiaxial grains, to a HAZ, involving a gradual structural change to the edge laminated miniplate weld with a typical cast structure.

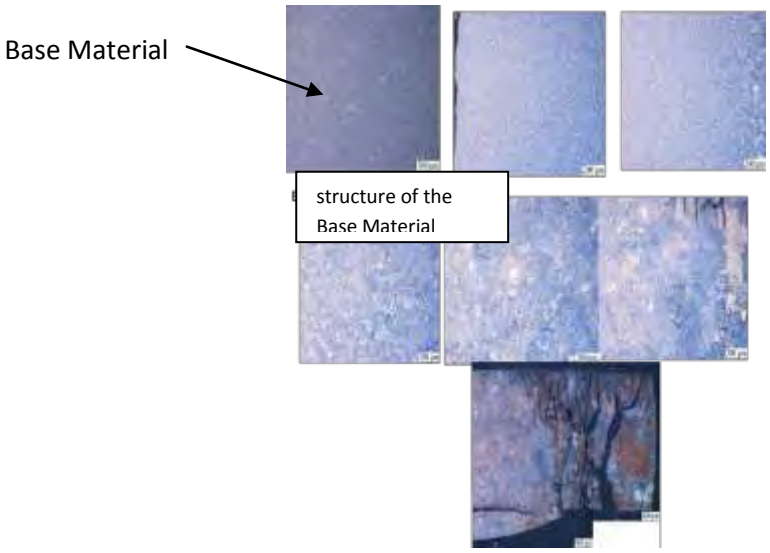


Figure9. Microstructure of rolled to 2.7 mm Miniplate

Figures 10 and 11 show the microstructure of the miniplate rolled from 2.7 mm to 2.4 mm. Like the previous microstructure sample a variation is observed from a base material structure of α-phase of equiaxed grains, to a HAZ gradual structural change, to the edge miniplate weld with a typical laminated structure cast. But the difference with the previous sample is that the cord is cracked at the edges, and more deformed structure is observed in the rolling direction.

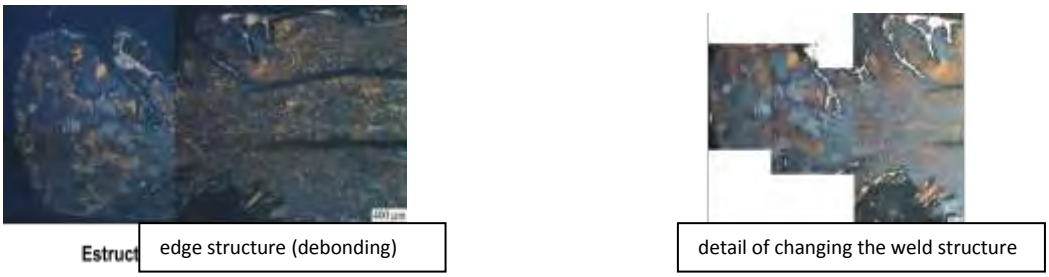


Figure 10 Microstructure of rolled to 2.4 mm miniplate

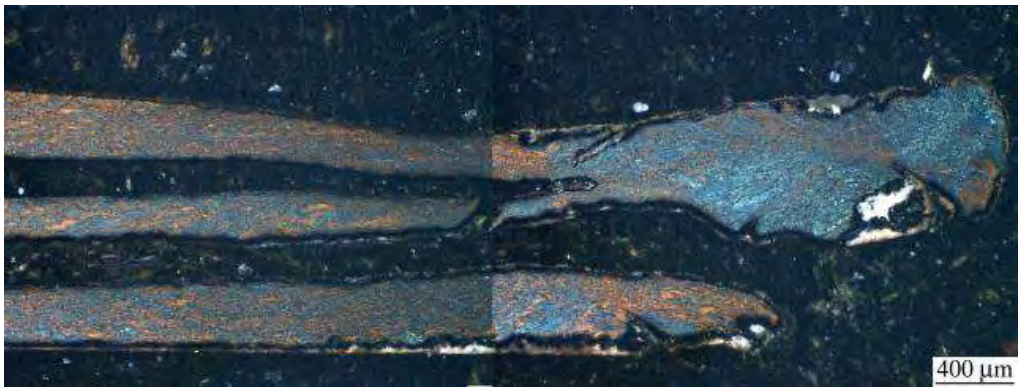


Figure 11. Microstructure of welded edge

In this case the tip shows a brazed miniplate. All the welded area exhibits a very distorted and fissured structure of α-phase grains surrounded by a primary β phase

grain edge, and it seems to have completely lost its acicular grain "needle-like" structure. This is caused by the large deformation suffered by laminating the sample.

3.4 Microhardness evaluation of the lamination steps

Evaluation was performed on the samples microhardness corresponding to different lamination stages. In Figures 11 (a) and (b),12 (a) and (b) , the variation of the microhardness of the miniplate samples is represented: uncoated and 2.7 mm thickness 2.4 mm and 1.1 mm respectively.

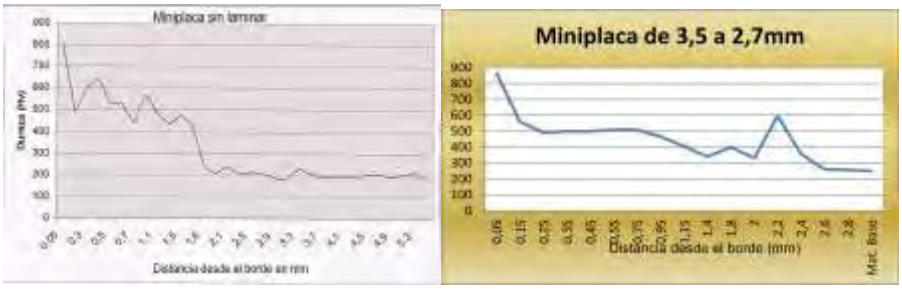


Figure 11. (a) Miniplate microhardness; (b) Microhardness of miniplate

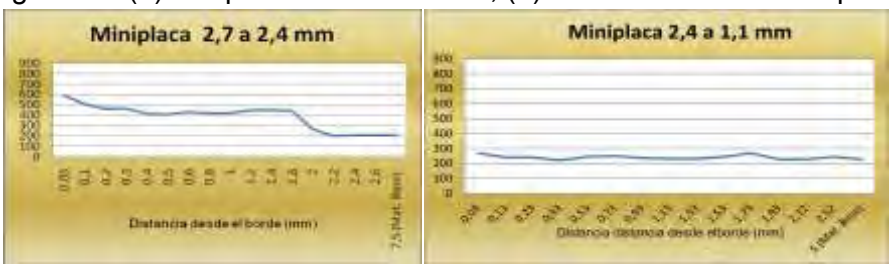


Figure 12 (a) Microhardness; (b) Microhardness miniplate the miniplate

As shown in the graphs, the HAZ has a higher microhardness in the welding process.

Furthermore, as the steps are performed, the microhardness in each sample is homogenized and tends to go down.

4. CONCLUSIONS

Grain size was not significantly different in the lamination stages, both in the starting material (strip of Zry-4) used in the manufacture of covers and frames, and in the samples corresponding to the miniplate because no allotropic change occurred during the temperature transition.

Regarding the samples of the miniplates in the lamination stages, related to the variation of microhardness, there is a greater value in the HAZ, which tends to homogenize it at the end of the lamination as shown in Figure 4.

It is important that the welding process is performed with shielding gas in a controlled atmosphere, as the

Zry-4 and the materials of titanium and niobium are prone to contamination by the components air gases.

It is advisable to weld with heat sink to decrease the effects of the rise temperature produced during this process.

References

[1] López M., Taboada H. Gonzalez A. G.CNEA- “Avances del Proyecto Combustibles de Muy Alta Densidad” in AATN 2010. Buenos Aires, Argentina.

[2] A. G. González, H. Taboada Marisol López, “Progress on Research and Development of VHDF” IFDWG 2009.Beijín, China.

[3] M. López, R. González, A. G. González, H. Taboada “ Advances in the study of high density fuels in CNEA”. RERTR 2009. Beijin, China.www.rertr.anl.gov

[4] Marisol López, Alfredo Gonzalez, Rubén González, , Horacio Taboada.” Monolithic U-Mo based plate development: new findings” RERTR 2010. Lisboa, Portugal. www.rertr.anl.gov

[5] Marisol López, Alfredo Gonzalez, Horacio Taboada. “Summa
ry of temperature influence in the fabrication of monolithic UMo - Zr alloy cladding miniplates” RERTR 2011.Santiago, Chile. www.rertr.anl.gov

[6] Marisol López, Rubén González, Alfredo G. Gonzalez “Improvements done in the development of dispersed and monolithic fuels in CNEA” Research Reactor Fuel Management (RRFM) 2009.Viena, Austria. www.rrfm2009.org

DIGITAL SAFETY AND I&C SYSTEMS AND NEUTRON INSTRUMENTATION SUBSYSTEMS

ING. JIŘÍ MATOUŠEK
I&C, dataPartner s.r.o
Senovážné nám. 241/15, 37001 České Budějovice-Czech Republic

ING. MIROSLAVA KOCHOVÁ
Project management, dataPartner s.r.o
Senovážné nám. 241/15, 37001 České Budějovice-Czech Republic

ABSTRACT

Protection and I&C Systems of research reactors (RR), especially the digital apparatus for neutron flux measuring and evaluation have to be systems with the highest level of safety, reliability and availability, able to manage critical processes.

Many of the currently operated RRs still use analogue I&C and neutron apparatus setup older than 15 years, which leads to possible issues with failing contacts and modules due to their age. Is is also increasingly hard to obtain spare parts. In comparison to power plant reactors, the I&C replacement on RRs is also often limited financially.

DataPartner company deals with development and production of modern modular neutron instrumentation system. The development is based on previous experience in the projects - Neutron instrumentation system of VR-1 reactor at Czech Technical University in Prague and of LR-0 reactor at Nuclear Research Institute in Řež, Czech Republic.

The currently ongoing project, which we are going to present in the poster, is “Protection and Control System Upgrade on LVR-15 10 MW RR” in Řež, Czech Republic. The newest project “TRIGA Mark II 250 kW I&C System Upgrade”, Technical University Vienna, Austria is prepared for implementation in summer 2015.

The neutron instrumentation system allows safety functions for performance power measurement, for power-change measurement and for independent power protection. The neutron flux measurement has modular design and can process signals from various types of fission and ionization chambers (including compensated) in pulse, current or Campbell mode. The neutron instrumentation provides direct outputs to the safety breakers as well as information lines to the control system.

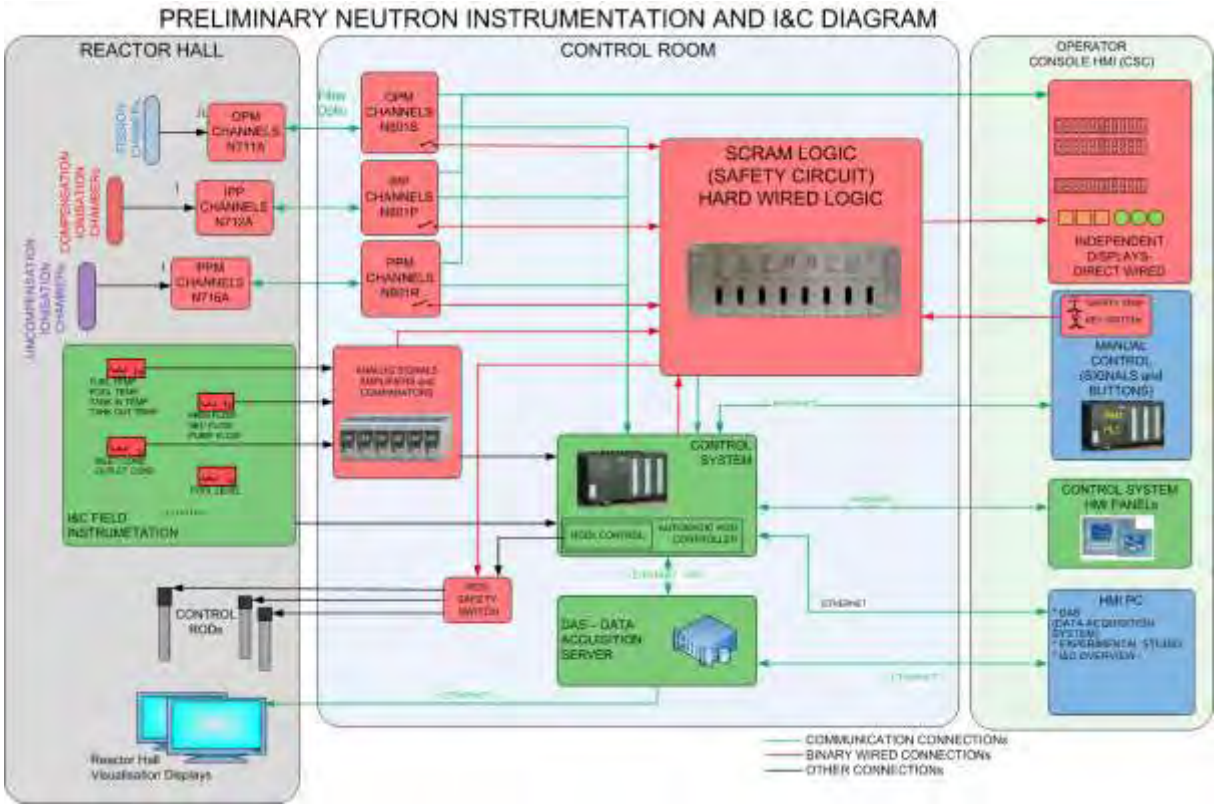
The systems are designed according to IAEA safety standards, guidance and requirements (e.g. No. NS-R-4, NS-G-4.2) to perform safety functions usually classified in A and B categories according to the IEC 61226:2010. As there are very few standards specific for the research reactors, NPP standards (e.g. to IEC 61226, IEC 60880, IEC 61513, IEC IEC 61780) are followed. DataPartner has created methodologies for qualified software and hardware production, reliability calculation and V&V of software and hardware.

The goal of our participation RRFM 2014 is to share our experience of implementing digital safety systems and acquisition of operator requirements for further development and innovations.

1 Neutron Instrumentation - System Design

The new Neutron Instrumentation System (NIS) used in projects mentioned above is usually based on the existing system. The main channels are:

- Wide-range Operational Channels – Operational Power and Period measurements (OPM)
- Wide-range Safety Channels of safety power measurement - Independent Power Protection (IPP)
- Wide-range Pulse Channels - (Pulse Power Measurement - PPM)



Measured signals from the chambers are directly numerically processed to power value and power change rate – period (% per second or period) in Wide-range channels. Power value is converted to common units and can be expressed in % or kW. Actual values are updated every 100 ms and are sent via optical serial line to independent display and via second optical interface to control system. This deterministic time period of data updating assures fast channel failure diagnostics. The time period length is chosen with respect to demands of safety system reaction speed and measured value stability.

The channel disconnects its Safety Relay contacts connected to Scram Logic if measured values breach the preset protection limits or in the case of any internal failure is indicated.

All NI channels consist of the two following modules:

- Primary module for processing neutron chamber signal and converting the analogue signal into digital domain for transmission to the Main Module
- Main Module for comparison of the neutron flux measured values against the safety system setpoints

Technically, these two modules can be located in one metal enclosure (box) or in two separated enclosures depending on interference in given environment.

Channel	**Primary Unit**	**Main Unit**
Wide-range Operational Channel (OPM)	N711A	N801S
Wide-range Safety Channel (IPP)	N712A	N801P
Wide-range Pulse Channel (PPM)	N716A	N801R

NI channels are equipped with test signal generators, which allow auto diagnostics and safety function check (SCRAM signals, neutron chamber voltage measurement, HV power supply voltage measurement) every time before the reactor is started up. The test starts if device switch is turned to ON position or with dedicated buttons on the channel. The channel output safety relays for SCRAM logic are disconnected during entire internal testing.

The safety relay contacts can't close only following the test successful completion. During maintenance and repair of the neutron instrumentation, devices can also be checked using external outputs for each device.

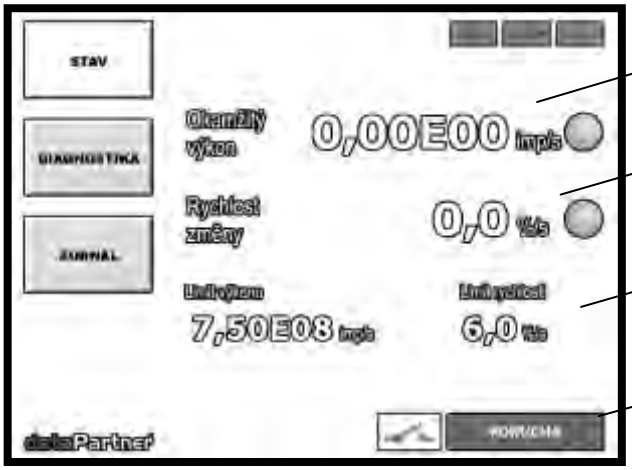
The detector input connections and power supply connections are protected from over-voltage.

If a malfunction in a measurement channel is detected, its SCRAM relay contacts will open to participate in logic to shut the reactor down.

Technical parameters (ranges, inputs from chambers and various outputs) can be adjusted to customer needs, conditions, and requirements.



Figure 1 Installation example - NI RACK for LVR-15



Current power value and alarm icon

Current period value and alarm icon

Current power and period limits

Safety relay state

Figure 2 -Display example

1.1 Proven solution



Figure 3 – LR-0 Installation

Modernization of control equipment of LR-0 reactor (Nuclear Research Institute Řež), training reactor VR-1 Czech Technical University in Prague and the forthcoming Modernization of LVR-15 (Nuclear Research Institute Řež) and TRIGA (technical university in Vienna) are the references. It is therefore standard and already proven solution, customized for special customer requirements.

Implementation of neutron instrumentation equipment includes adaptation to local specifics, such as cabling parameters, noise level, and specific characteristics of the neutron chambers. For example, one adaptation is done by setting of constants, which are hardwired into chamber software and cannot be changed through the user interface. The optimal settings is the part of the delivery and its purpose is to achieve the most appropriate measurement parameters, such as measurement of linearity, static and dynamic response, accuracy, noise immunity, stability, and more.

1.2 Wide-range Operational Channel – (OPM)

1.2.1 Primary unit N711A - Module Description

Module N711A metal enclosure is connected directly to the analog output of neutron ion. chamber.
N711A processes the chamber neutron flux signal by applying the following two technical approaches:

- Counting neutron chamber current pulses per 100 ms at the lowest neutron flux levels
- Measuring power noise of filtered chamber current signal at the higher neutron flux levels

The N711A module simultaneously measures and processes these two signal modes and the resulting outputs are sent in digital form via interface to downstream modules. Actual selection of the representative mode for each neutron flux level is performed by the downstream module in the digital domain.

In case that chamber has on its output symmetrizing transformer, the signal to N711A is routed via desymmetrizing module which consists from transformer enclosed in magnetically shielding case. This module also can make impedance matching. Connection between N711A and desymmetrizing module is made by RG59 cable via UHF connector. The coax cable length must be within 0,5 m. The N711A module also includes adjustable high voltage (HV) power supply for neutron chamber.

EMC rugged metal enclosure (box) provides sufficient mechanical and EMC protection for N711A module. All cables must be routed and terminated to prevent any EMC interference.

Pulse neutron chamber measurement is based on a discriminator with adjustable discriminating level.

Chamber noise power measurement (Campbell) is based on RMS conversion of the input signal with narrowed frequency spectrum. 20 bit analog to digital converter (Sigma-Delta type) is used for conversion of the RMS value to digital format. The signal converter has very high noise immunity with complete noise interference suppression at 50 – 60 Hz levels.

Self-diagnostics and Testing

The following parameters are checked online in each measurement cycle:

1. Neutron chamber internal voltage
2. Neutron chamber supply voltage
3. Discriminating level
4. Programmed memory summary check
5. Parameters for essential CPU configuration registers
6. Execution of all SW steps
7. Data memory using ECC code

Additional tests can be performed (using control commands). However, the following additional tests will void measured data:

1. Connection of pulse generator to the N711A input for verification of the pulse and noise measurement

Communication Interface

N711A module communicates with the downstream system via optical duplex connections using UART interface. Communicated bytes are transmitted via UART with specifically determined structures for upstream/downstream communications. Data packets are validated with 16 bit validation CRC code. The data transmission follows closely reading of new values from A/D converters in period of 100 ms. Validation also includes check of proper logic functions. New controlling data packet is always generated within 10 ms following reception of the results.

Technical Specifications

Operating ambient temperature	-5 to 40 °C
Operating ambient humidity	5 to 90 %
Operating power supply voltage	24 VDC +/- 10%
Current consumption	0,6 A
IAC Channel input resistance	150 Ω
Bandwidth	10kHz to 2,5 MHz
Input Pulse Range	0 to 10^6 imp/s
Input Power Range	10^4 to 10^8 imp/s
Input Current Range	$2x10^{-9}$ to $2x10^{-3}$ A
ADC Power Resolution	20 bit
ADC Current Resolution	20 bit
Discriminator Voltage Resolution	8 bit
Data Clock Period:	100 ms
Communication speed	115 200 bit/s
Adjustable HV Power Supply	0 to 950 V

HV source max current	2 mA
HV setting resolution	12 bits
Testing pulses - amplitude	adjustable 16 bit
Testing pulses - width	selectable in multiplier of two 0,1, 0,2. ... 6,4 µs
Testing pulses - frequency	in decade steps 1, 10, ... 10^6 Hz

1.2.2 Main Unit - N801S

Module N801P receives digital data from upstream module N711A and provides signals for modulation of the reactor power according to active core compensation settings. Processed neutron flux and power change values are compared against setpoints for various reactor alarms and safety trips. The alarm and reactor safety trip setpoints for speed of change are permanently set at certain maximum values. However, these setpoints can be lowered by adjusting coefficient in range of 0-100% from control system.

Module is housed in panel in standard 19“chassis, 4U high. The front part of the module is equipped with various HMI components providing all measured and diagnostic data for N801SP and also upstream module N711A. The module is supplied by two isolated trains of 24 VDC.

N801S front panel includes:

1. LED indicators PWR1, PWR2 for status of two isolated power supplies
2. LED indicator IN-ERR for internal errors of upstream input module
3. LED indicator MY-ERR for internal error of N801P (also flashing during initialization)
4. LED indicator TEST signaling during testing
5. LED indicator for SCH-REL output relay status
6. HEX switches for chamber supply voltage positive adjustments (8 bits)
7. HEX switches for chamber supply voltage negative adjustments (8 bits)
8. Potentiometer for reactor active core compensation adjustment
9. TEST pushbutton
10. INIT pushbutton

Input/Output metal wire cables are connected to the back of N801S with thread lock connectors. Fiber optic cables from N711A are also connected to the back of N801S. The following cables are hooked up to N801S:

1. Fiber-optic cable from upstream module N711A
2. Two 24 VDC power supply cables
3. RS232 cable for communication with control center
4. RS232 cable for communication with two independent displays
5. Output cables for HAV reactor safety system loops

Self-diagnostics and Testing

The following parameters are checked online in each measurement cycle:

1. Internal power supply voltage
2. Programmed memory summary check
3. Parameters for essential CPU configuration registers
4. Execution of all SW steps
5. CPU check by watchdog circuit
6. Data memory using ECC code

Test procedure for upstream module input is initiated by pushing the TEST button. The module N801S disables its outputs to the reactor safety loops including verification that the contacts of output relay are open. Then, the LED indicator TEST is on. List of all performed tests is included in the upstream module N711A documentation.

The TEST LED goes off following the test completion. The flashing LED indicator IN-ERR indicates an error in N711A and it keeps the N801S output to reactor safety loops disabled. Operability can be restored after the error is fixed and the new test is successfully passed. This test is also automatically performed when the N801S module is initialized. After initialization, the N801S signals IN-ERR and disconnects N801S from the reactor safety loop if no data is received within 150 ms. Initialization testing is restored when proper data is received within 30 s and then the IN-ERR signal is disabled. Otherwise, error must be fixed and the test repeated by the TEST button.

If N801S signals MY-ERR (an error in N801S) the N801S input into reactor safety loop is disabled. If the N801S resets itself due to self-diagnostic circuit error, it will signal MY-ERR. The module functions can be restored by pushing the INIT button.

Output Safety Relay SCH-REL functions

SCH-REL contacts are open in case of:

1. N801P initialization
2. N801P testing
3. IN-ERR signals
4. MY-ERR signals
5. Neutron flux is higher than the safety setpoint
6. Reactor power speed change is higher than the safety setpoint
7. Measure value of Neutron flux is lower than the internal safety setpoint (Measurement err)

Otherwise, the relay SCH-REL contacts shall be closed at all times.

Communication Interface

N801S module communicates with the upstream system via optical duplex connections using UART interface. Communicated bytes are transmitted via UART with specifically determined structures for upstream/downstream communications. Data packets are validated with 16 bit validation CRC code. The data transmission upstream follows closely reception of new values.

N801S module communicates via two way RS232 UART interface into the control system. The following parameters are communicated:

Downstream (from N801P to control system)

1. Neutron flux levels [% of nominal reactor power]
2. Speed of change [%/s]
3. Output relay status
4. Cause of output relay trip (module initialization, input error, error of N801S, CPU error, input testing, neutron flux or reactor power speed change value is higher than the safety setpoint)
5. reactor power value is higher than the alarm setpoint
6. reactor power value is higher than the safety trip setpoint
7. N801S module status (initialization, input error, error of N801S, testing, N801S operating)

Upstream (from control system to N801S)

1. Adjustments for coefficient lowering [%]

N801S communicates via one way RS232 UART to two independent displays the following data:

1. Neutron flux level [%]
2. Period [s] = 100 / speed of change [%/s]

Technical Specifications

Operating ambient temperature	-5 to 40 °C
Operating ambient humidity	5 to 90 %
Operating power supply voltage	24 VDC +/- 10%
Current consumption	0,7 A

1.3 Wide-range safety channels (IPP) – Independent Power Protection (IPP)

Inputs for the operational power measurement channels are values from compensation

ionization chambers.

The channels will provide warning and SCRAM signals, which are used by the reactor protection and control logic for generating audiovisual alarms and for initiating fast shutdown.

Manual change of measuring range is not necessary to implement, because the channels are Wide-range. If this function would be required anyway, our device could be modified in such a way.

1.3.1 Primary Unit N712A - Module Description

Module N712A is utilized for direct measurements of neutron current chambers with positive and negative voltage compensation. First, the measured chamber current is processed by the module logarithmic component and then it is converted by A/D converter into digital domain. The converter is Sigma-Delta type with period of 100 ms. The module has very high immunity against interferences at 50 and 60 Hz.

The power supply and chamber signal cables are terminated to terminal blocks on the N712A module. The module is located in the metal enclosure (box) which provides sufficient mechanical and EMC protection.

Self-diagnostics and Testing

The following parameters are checked online in each measurement cycle:

1. Neutron chamber internal voltage
2. Neutron chamber supply voltage
3. Programmed memory summary check
4. Parameters for essential CPU configuration registers
5. Execution of all SW steps
6. Data memory using ECC code

Additional tests can be performed (using control commands). However, the following additional tests will disable measurements from the neutron chamber:

1. Connection of DC current generator to the IDC input in N712A enclosure upstream of N712A module for verification of the measuring and controlling loop functions

Communication Interface

N712A module communicates with the downstream system via optical duplex connections using UART interface. Communicated bytes are transmitted via UART with specifically determined structures for upstream/downstream communications. Data packets are validated with 16 bit validation CRC code. The upstream data transmission follows closely reading of new values from A/D converters in period of 100 ms. Validation also includes check of proper logic functions. New controlling data packet is always generated within 10 ms following reception of the results.

Technical Specifications

Operating ambient temperature	-5 to 40 °C
Operating ambient humidity	5 to 90 %
Operating power supply voltage	24 VDC +/- 10%
Current consumption	0,8 A
Input current range	1^{-10} to 1^{-3} A
ADC current resolution	20 bits
Data Clock Period:	100 ms
Communication speed	115 200 bit/s
HV supply positive	adjustable 10 to 950 V
HV supply negative	adjustable -10 to -950 V
HV adjustment resolution	12 bits
HV supply current	1 mA
Testing current	selectable 10 nA, 1 µA, 100 µA

1.3.2 Primary Unit N801P - Module Description

Module N801P receives digital data from downstream module N712A and provides signals for modulation of the reactor power according to active core compensation settings. Processed neutron flux values are compared against setpoints for various reactor alarms and safety trips. The module evaluates neutron flux minimum limit NMIN.

Module is housed in panel in standard 19“ chassis, 4U high. The front part of the module is equipped with various HMI components providing all measured and diagnostic data for N801P and also upstream module N712A. The module is supplied by two galvanic ally isolated trains of 24 VDC.

N801P front panel includes:

1. LED indicators PWR1, PWR2 for status of two isolated power supplies
2. LED indicator IN-ERR for internal errors of upstream input module
3. LED indicator MY-ERR for internal error of N801P (also flashing during initialization)
4. LED indicator TEST signaling during testing
5. LED indicator for SCH-REL output relay status
6. HEX switches for chamber supply voltage positive adjustments (8 bits)
7. HEX switches for chamber supply voltage negative adjustments (8 bits)
8. Potentiometer for reactor active core compensation adjustment
9. TEST pushbutton
10. INIT pushbutton

Input/Output metal wire cables are connected to the back of N801P with thread lock connectors. Fiber optic cables from N712A are also connected to the back of N801P. The following cables are hooked up to N801P:

1. Fiber-optic cable from upstream module N712A
2. Two 24 VDC power supply cables
3. RS232 cable for communication with control center
4. RS232 cable for communication with two independent displays
5. Output cables for HAV reactor safety system loops
6. Output cables for NMIM

Self-diagnostics and Testing

The following parameters are checked online in each measurement cycle:

1. Internal power supply voltage
2. Programmed memory summary check
3. Parameters for essential CPU configuration registers
4. Execution of all SW steps
5. CPU check by watchdog circuit
6. Data memory using ECC code

Test procedure for upstream module input is initiated by pushing the TEST button. The module N801P disables its outputs to the reactor safety loops including verification that the contacts of output relay are open. Then, the LED indicator TEST is on. List of all performed tests is included in the upstream module N712A documentation.

The TEST LED goes off following the test completion. The flashing LED indicator IN-ERR indicates an error in N712A and it keeps the N801P output to reactor safety loops disabled. Operability can be restored after the error is fixed and the new test is successfully passed. This test is also automatically performed when the N801P module is initialized. After initialization, the N801P signals IN-ERR and disconnects N801P from the reactor safety loop if no data is received within 150 ms. Initialization testing is restored when proper data is received within 30 s and then the IN-ERR signal is disabled. Otherwise, error must be fixed and the test repeated by the TEST button.

If N801P signals MY-ERR (an error in N801P) the N801P input into reactor safety loop is disabled. If the N801P resets itself due to self-diagnostic circuit error, it will signal MY-ERR. The module functions can be restored by pushing the INIT button.

Output Safety Relay SCH-REL functions

SCH-REL contacts are open in case of:

1. N801P initialization
2. N801P testing
3. IN-ERR signals
4. MY-ERR signals
5. Neutron flux is higher than the safety setpoint

Otherwise, the relay SCH-REL contacts shall be closed at all times.

Communication Interface

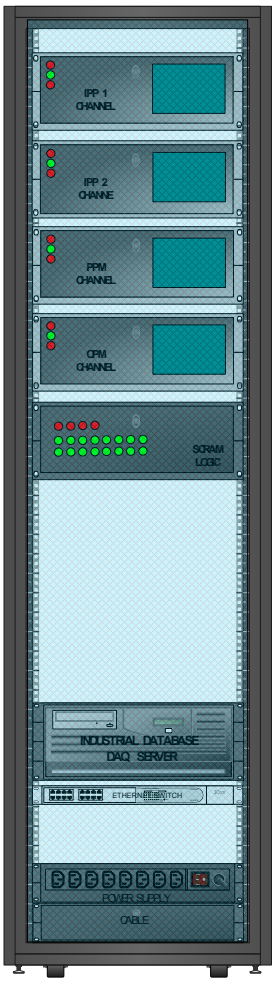
N801P module communicates with the upstream system via optical duplex connections using UART interface. Communicated bytes are transmitted via UART with specifically determined structures for upstream/downstream communications. Data packets are validated with 16 bit validation CRC code. The data transmission follows closely reception of new values.

N801P module communicates via one way RS232 UART interface into the control system. The following parameters are communicated:

1. Neutron flux levels [% of nominal reactor power]
2. Output relay status
3. Cause of output relay trip (module initialization, input error, error of N801P, CPU error, input testing, reactor power value is higher than the safety setpoint)
4. reactor power value is higher than the alarm setpoint
5. reactor power value is higher than the safety trip setpoint
6. N801P module status (initialization, input error, error of N801P, testing, N801P operating)

N801P communicates via one way RS232 UART to two independent displays the following data:

1. Neutron flux level [%]



Technical Specifications

Operating ambient temperature	-5 to 40 °C
Operating ambient humidity	5 to 90 %
Operating power supply voltage	24 VDC +/- 10%
Current consumption	0,7 A

1.4 Wide-range pulse channel – Pulse Power Measurement (PPM)

Design of the project specific N716A and N801R modules is based on N712A and N801P design with small HW differences. However, the SW algorithms and settings will reflect the project specifications, mainly in the following parameters:

- Data time frequency at least 500 µs
- Event Recording (Power Pulse)
- Evaluation of Pulse Power Records (max. Value , Pulse length,)
- Extended Communication Protocol (sending records)
- Different evaluation of safety limits (power integral , max. pulse per hour)

DETERMINATION OF UNCONTROLLED PARAMETERS OF WWR-KN EFAS

YU.S. TCHEREPNIN, S.A. SOKOLOV, S.YU. BULKIN, V.A. LUKICHEV, O.A. KRAVTSOVA, A.I. RADAEV, A.P. DERIKOT

JSC "N.A. Dollezhal research and development institute of rower engineering" (JSC "NIKIET")
Malaya Krasnocelskaya St. 101000 Moscow Russian Federation

1. Introduction

Three experimental fuel assemblies (EFAs) WWR-KN have been irradiated in WWR-K reactor core (Institute of Nuclear Physics, the Republic of Kazakhstan).
The purpose of this fuel assembly irradiation was to test fuel elements (UO2+Al fuel with uranium density (3.0±0.2) g/cm3 and enrichment 19.7 %) up to the average burn-up of 60%. The EFAs were loaded in WWR-K reactor in 07/03/2011 and irradiated under the power up to 6 MW.

2. Object of studies

The objective of neutron and thermo-hydraulic analytical studies is focused on the WWR-K reactor core (WWR-C FAs and three WWR-KN EFAs) at the beginning of the first (see Fig. 1), sixth and ninth test cycles.

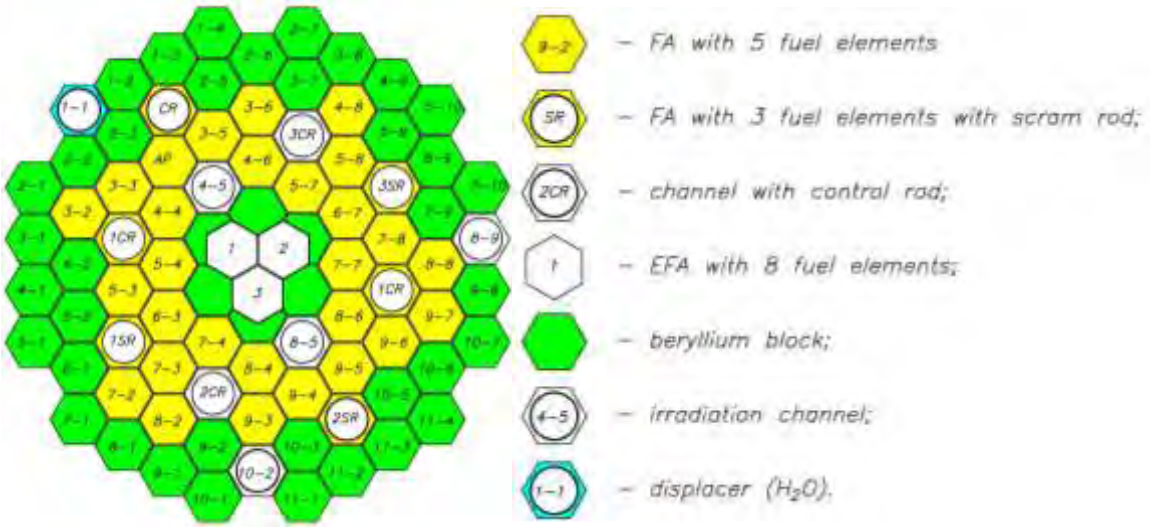


Fig 1 WWR-K core configuration

The aims of this work were the determination of uncontrolled parameters of WWR-KN EFAs on the basis of actual EFA parameters and initial data obtained from the tests.

To prepare compositions of burnet-up FAs with good accuracy, the ^{235}U consumption as a function of burn-up for WWR-C FA and WWR-KN FA was obtained, using MCU-PTR code;

- three WWR-K analytical models were prepared:
  - model 1 – core with heterogeneous description of WWR-C FA and WWR-KN EFA;
  - model 2 – core with heterogeneous description of WWR-KN EFA and homogeneous description of WWR-C FA;
  - model 3 – core with heterogeneous description of WWR-KN EFA and homogeneous description with maximum ^{235}U loading of WWR-C FA.

Neutron calculations was performed using three different models for the beginning of the first, sixth and ninth test cycles. The following data were obtained:

- reactor core neutron parameters with experimentally determined critical position of CPS control rods at minimum controlled reactor power;
- power of WWR-KN EFAs at the beginning of the first, sixth and ninth test cycles with CPS control rods in critical position;
- specific power distribution within the core and 3 EFAs;
- initial data for thermal-hydraulic calculation, including determination of power peaking factor along fuel assemblies and within the core volume; WWR-KN EFA with maximum power rating during the tests with detailed power density distribution output.

3. Main results

Main results of neutron calculation regarding the reactor tests of 3 WWR-KN EFAs at the beginning of the first, sixth and ninth test cycles using different core models are presented in Tab 1.

Parameter	1st cycle			6th cycle		9th cycle	
	Model 1	Model 2	Model 3	Model 1	Model 3	Model 1	Model 3
K_{eff} with CPS control rod in the critical position	0.979	0.987	1.002	0.986	0.994	0.979	1.004
Average ^{235}U burn-up at the BOC, %	22.4			16.8		18.8	
^{235}U max. burn-up in WWR-KN EFA at the BOC, %	0			15.2		25	
Power of 3 WWR-KN EFAs, % reactor power	19.75	19.40	18.60	17.96	17.54	17	15.96
Power peaking factor within the core	2.84			2.41		2.43	

Tab 1: Main results of neutron calculations regarding WWR-KN EFA tests

On the base of results of thermal-hydraulic calculations performed using initial data from neutron calculations (see Tab. 2) and the initial data from the irradiation tests of 3 WWR-KN EFAs, follows parameters were determined:

- experimental hydraulic characteristic of WWR-KN FA and coolant distribution within the gaps between the fuel elements in FAs;
- WWR-KN EFA test parameters at the beginning of the first, sixth and ninth test cycles.

Parameter	1st cycle	6th cycle	9th cycle
Reactor power, MW (based on coolant heating)	5.65	5.66	5.55
Power of 3 EFAs, kW (based on coolant heating)	949	927	786
Power of 3 EFAs, kW (based on neutron calculation)	989	933	825
Maximum power of EFA, kW	333	320	282
Coolant temperature at the core inlet, ^{o}C	32	39	33
Max. cladding temperature, ^{o}C	88	91	79
Max. fuel temperature, ^{o}C	90	93	81
Max. thermal flux, kW/m^2	508	477	423
Thermal flux at the hot point, kW/m^2	374	351	313
Saturation temperature at the hot point, ^{o}C	107.4	107.4	107.4
Surface boiling point, ^{o}C	114.7	114.7	114.2
Margin to surface boiling temperature	1.43	1.39	1.85
EFA thermal reliability coefficient	1	1	1
Safety margin against flow instability	2.1	1.98	2.54

Tab 2: Results of thermo-hydraulic calculations of WWR-KN EFA parameters at the beginning of test cycles

Operation with WWR-KN EFA remains safe in all cycles, i.e. surface boiling at fuel claddings under conditions of 5.55-5.65 MW reactor power, pressure drop in the reactor core of 0.0083-0.009 MPa and coolant temperature at the core inlet of 32-39 ^{o}C is not observed.

The reactor model with the core based on WWR-KN EFAs and WWR-C FA actual parameters was created. This model allows to obtain uncontrolled neutron parameters of EFAs.



European Nuclear Society
Avenue des Arts 56
1000 Brussels, Belgium
Telephone: +32 2 505 30 50 - FAX: +32 2 502 39 02
rrfm2014@euronuclear.org
www.rrfm2014.org